



HAL
open science

Des Galaxies Proches Aux Galaxies Lointaines: Etudes Cinématique et Dynamique

Benoit Epinat

► **To cite this version:**

Benoit Epinat. Des Galaxies Proches Aux Galaxies Lointaines: Etudes Cinématique et Dynamique. Astrophysique [astro-ph]. Université de Provence - Aix-Marseille I, 2008. Français. NNT: . tel-00413769v3

HAL Id: tel-00413769

<https://theses.hal.science/tel-00413769v3>

Submitted on 15 Sep 2009

HAL is a multi-disciplinary open access archive for the deposit and dissemination of scientific research documents, whether they are published or not. The documents may come from teaching and research institutions in France or abroad, or from public or private research centers.

L'archive ouverte pluridisciplinaire **HAL**, est destinée au dépôt et à la diffusion de documents scientifiques de niveau recherche, publiés ou non, émanant des établissements d'enseignement et de recherche français ou étrangers, des laboratoires publics ou privés.

UNIVERSITÉ DE PROVENCE - AIX-MARSEILLE I
ÉCOLE DOCTORALE DE PHYSIQUE ET SCIENCES DE LA MATIÈRE
Laboratoire d'Astrophysique de Marseille

THÈSE DE DOCTORAT

présentée pour obtenir le grade de

Docteur de l'Université de Provence
Spécialité : Astrophysique

par

Benoît EPINAT

DES GALAXIES PROCHES AUX GALAXIES LOINTAINES ÉTUDES CINÉMATIQUE ET DYNAMIQUE

*Soutenue publiquement le jeudi 6 Novembre 2008
Au Laboratoire d'Astrophysique de Marseille
Devant le Jury composé de*

Christian MARINONI _____	Président
Jonathan BLAND-HAWTHORN _____	Rapporteur
Thierry CONTINI _____	Rapporteur
Claudia MENDES DE OLIVEIRA _____	Examinatrice
Éric EMSELLEM _____	Examineur
Matthew LEHNERT _____	Examineur
Philippe AMRAM _____	Directeur
Chantal BALKOWSKI _____	Co-directrice

Remerciements

À mon arrivée au Laboratoire d'Astrophysique de Marseille, au palais Longchamps, j'avais une idée assez vague de ce que serait mon travail. Petit à petit, les briques se sont assemblées pour ébaucher un ouvrage de plus en plus passionnant. Une thèse est un travail solitaire à bien des égards, et pourtant, les participations hétéroclites des uns et des autres ainsi que les échanges sont à la base de tout le travail qui a été effectué. Ce sont en quelques sortes les fondations de l'ouvrage.

Je tiens tout d'abord à remercier Chantal Balkowski qui m'a permis de faire cette thèse en insistant auprès de Philippe Amram pour qu'il propose un sujet. C'est aussi après l'avoir rencontrée à Paris que l'idée de travailler sur les galaxies a germé. Enfin, lors de cette rencontre, j'ai senti le courant passer, ce qui m'a mis en confiance pour arriver au LAM.

J'y ai été chaleureusement accueilli dans l'équipe "Physique des Galaxies" et j'en remercie vivement l'ensemble des membres. Je les remercie également pour toutes les discussions que nous avons eues, tant sur les plans technique avec Jean-Luc, Philippe, Olivier et Jacques que scientifique avec Philippe, Michel, Yvon, Georges, Véronique, Alessandro, Denis et Samuel. C'est cette dualité qui fait l'originalité de cette équipe. L'éloge de l'humour de Michel Marcelin n'étant plus à faire (les remerciements de la thèse de mon propre directeur de thèse montraient déjà la couleur), je veux plutôt le remercier pour sa grande disponibilité, sa pédagogie, ses conseils et la considération qu'il m'a portée.

Je veux aussi remercier les personnes avec lesquelles j'ai partagé mon bureau. Tout d'abord Maxime, stagiaire de Michel, puis Élodie, stagiaire de Philippe avec qui j'ai passé de bons moments. J'ai eu plaisir à m'impliquer dans leurs travaux. Enfin, Henri Plana, "ex" thésard exilé au Brésil qui est venu quelques mois chaque année partager son ancien bureau avec moi et avec qui j'ai eu des discussions très intéressantes et très instructives.

Je remercie Françoise Herniou pour sa relecture finale du manuscrit ainsi que pour d'autres aspects pratiques qui m'ont été utiles tout au long de ma thèse.

À l'aube du vingt-et-unième siècle, l'informatique est un outil indispensable en astronomie, mais lorsqu'on a la poisse et qu'on est novice, comme c'est le cas pour moi, on est alors extrêmement reconnaissant à des personnes telles que Valérie Novak et Jean-Charle Lambert qui s'avèrent être des personnes très compétentes, très patientes, très disponibles et très sympathiques.

L'astronomie est pour moi indissociable de l'observation du ciel. C'est pourquoi les moments forts de ma thèse resteront sans aucun doute les missions d'observation. Débuter ma thèse par une mission à l'observatoire du mont Mégantic au Québec fut une chance d'autant plus grande que j'ai pu assister à une magnifique aurore boréale. Pourtant, ce fut un début un peu difficile puisque je n'avais qu'une vague idée de la physique que j'allais bientôt étudier. De plus, je ne connaissais alors personne. Je tiens donc à remercier Laurent Chemin qui m'a accueilli et m'a à proprement parlé fait débuter ma thèse, m'a présenté l'instrumentation Fabry-Perot, l'acquisition et la réduction des données. Un grand merci aussi à Olivier Daigle qui était avec moi pour la fin de cette mission et qui m'a fait partager ses

programmes de réduction des données. Je remercie également Claude Carignan qui, à cette occasion, m'a accueilli au Laboratoire d'Astronomie Expérimentale de Montréal.

De plus, terminer ma thèse avec deux missions d'observations au WHT (La Palma, Espagne) fut un immense honneur et un réel plaisir. John Beckman est le principal acteur de la réussite de ces missions et je l'en remercie vivement. Je tiens à remercier également toute l'équipe de GH α Fas, et tout particulièrement, Olivier Hernandez et Philippe Balard pour avoir eu la patience de nous apprendre, Marie-Maude et moi-même, à mettre en place l'instrument. Je veux aussi remercier Kambiz, Javier, Sébastien et Marie-Maude pour des parties de ping pong au sommet (de la montagne, bien sûr), pour leur bonne humeur et leur enthousiasme tant pour monter l'instrument que pour faire les observations.

Je remercie toutes les personnes avec lesquelles j'ai eu le plaisir de travailler pendant ma thèse et avec lesquelles, je l'espère, l'aventure continuera.

Je tiens à remercier l'ensemble de mon jury de thèse pour avoir accepté de remplir ce rôle.

Merci en particulier à Claudia Mendes de Oliveira pour m'avoir rassuré lors de ma première prestation orale en anglais à Marseille et pour m'avoir permis de travailler avec son étudiant en thèse, Sergio Torres.

Un grand merci supplémentaire à Thierry Contini pour m'avoir fait participer si naturellement à la collaboration MASSIV lors de ma dernière année de thèse, et pour me permettre de faire mon premier post-doc avec lui à Toulouse. Je tiens d'ailleurs à remercier l'ensemble de la collaboration MASSIV pour la confiance dont chacun des membres m'a gratifié.

Enfin, je ne remercierai probablement jamais assez la personne censée être la moins disponible et qui pourtant a su être là pour moi chaque fois que j'en ai eu besoin (j'ai appris à me jouer de son agenda), je pense bien entendu à mon directeur de thèse, Philippe Amram. Il a été à l'origine de tous mes résultats, de toutes mes collaborations, de mes missions, de mes enseignements, etc., bref, de tout ce qui m'a été profitable et qui a été mentionné dans toutes ces lignes. Il est pour moi bien plus qu'un directeur de thèse. Son sens du partage, son humanité, sa sympathie ont été pour moi un soutien extrêmement appréciable.

Les remerciements non officiels qui suivent me tiennent également à cœur.

Un sujet source de sarcasmes à l'Observatoire de Longchamps, avant qu'on ne déménage au technopôle de Château-Gombert, fut la cantine. Quel casse-tête pour les Universitaires pour pouvoir se restaurer dans une cantine CNRS ! Les étudiants ont subi le même problème. Je remercie donc le président "Momo" d'avoir bien voulu accepter les "squatters" à sa table, ainsi que Christine et Gaby qui étaient aux petits soins avec moi.

Je fais une dédicace toute spéciale (il faut savoir se jouer de sa réputation !) à mes monocycles sans qui ce travail de thèse n'aurait pu aboutir. C'est grâce à eux que je suis venu au laboratoire chaque jour pour avancer mes travaux. D'ailleurs j'avoue qu'ils m'en ont un peu voulu lorsque je leur ai annoncé que je prendrais le métro pour aller sur le site de Château Gombert. Ils ont donc insisté pour m'accompagner dans le métro et me reconduire chez moi de temps à autres.

Merci à l'équipe de monocyclistes de Marseille pour toutes les sorties qui font indéniablement du bien à l'esprit et en particulier à Yvon pour la ballade improvisée à Saint Michel de l'Observatoire (un peu impraticable d'ailleurs) lors de ma mission d'observation de la photométrie des galaxies GHASP.

Je remercie l'ensemble des thésards du LAM, en particulier Benoît pour son aide précieuse lors de la rédaction, ainsi qu'Arthur et Manu pour la détente entre les heures de travail.

Je remercie chaleureusement ma promotion de DEA et Jacqueline pour leur soutien, et plus particulièrement Xavier, Benoît et Marc que j'ai retrouvés avec plaisir lors de multiples conférences.

J'ai également pu compter sur mes amis pendant ces trois années pour passer de bons moments en dehors du labo. Un merci particulier à Guillaume qui m'a soutenu jusqu'au bout en me faisant répéter une ultime fois ma soutenance de thèse le matin même !

Céline, je te remercie pour tout ce que tu as fait pour moi. Ta patience, ton courage, ta relecture de ce manuscrit qui était (du moins à première lecture !) pour toi assez obscur m'ont véritablement aidé à mener ce travail jusqu'au bout.

Je veux finir ces remerciements par ma famille : Maman, Papa, Guillaume, Virginie, Mylaine. Nous avons su nous serrer les coudes, être solidaires et présents les uns pour les autres.

Table des acronymes

ADHOC	Analyse et Dépouillement Homogène des Observations CIGALE
ADHOCw	Analyse et Dépouillement Homogène des Observations CIGALE windows
BHαBar	Big H-Alpha kinematical sample of Barred spiral galaxies
BTFI	Brazilian Tunable Filter Imager
CCD	Charge-Coupled Device
CFHT	Canada-France-Hawaiï Telescope
CIGALE	CInématique des GALaxies
CRAL	Centre de Recherche Astronomique de Lyon
DM	Dark Matter
ELT	Extremely Large Telescope
EAGLE	Elt Ao for GaLaxy Evolution
ESO	European Southern Observatory
FaNTOmM	Fabry-Perot de Nouvelle Technologie pour l'Observatoire du mont Mégantic
FLAMES	Fibre Large Array Multi Element Spectrograph
GÉPI	Galaxies Étoiles Physique et Instrumentation
GHαFaS	Galaxy H-Alpha Fabry-Perot System
GHASP	Gassendi H-Alpha survey of SPirals
GIPSY	Groningen Image Processing SYstem
GIRAFFE	High and Intermediate Resolution Spectrograph
IAC	Instituto de Astrofísica de Canarias
IAG	Instituto de Astronomia, Geofísica e Ciências Atmosféricas
iBTF	imaging Bragg Tunable Filter
ICOS	IC Optical System
IDL	Interactive Data Language
IFTS	Imaging Fourier Transform Spectrometer
IFU	Integral Field Units
IMAGES	Intermediate MAss Galaxy Evolution Sequence
INPE	Instituto Nacional de Pesquisas Espaciais
INT	Isaac Newton Telescope
IPCS	Imaging Photo Counting Systems
LAE	Laboratoire d'Astrophysique Expérimentale
LAM	Laboratoire d'Astrophysique de Marseille
LASER	Light Amplification by the Stimulated Emission of Radiation
LIRG	Luminous Infra-Red Galaxie
LTAO	Laser Tomography Adaptive Optics
MASSIV	Mass ASsembly with SINFONI and VVDS
MMTF	Maryland-Magellan Tunable Filter
MOAO	Multi-Object Adaptive Optics

MOND	MOdified Newtonian Dynamics
NTT	New Technology Telescope
OHP	Observatoire de Haute Provence
ONÉRA	Office National d'Études et de Recherches Aérospatiales
OSIRIS	OH-Suppressing Infra-Red Imaging Spectrograph
PYTHEAS	Prismes, Interféromètres et Trames de lentilles pour l'Holométrie et l'Endoscopie des Astres et des Sources
PSF	Point Spread Function en anglais, Réponse Impulsionnelle en français
SAM	Semi-Analytical method
SESO	Société Européenne de Systèmes Optiques
SINFONI	Spectrograph for INtegral Field Observations in the Near Infrared
SPIE	Society of Photo-Optical Instrumentation Engineers
SOAR	SOuthern Astrophysical Research
TAURUS	Fabry-Perot imaging spectrograph
TTF	Taurus Tunable Filter
USP	Universidade de São Paulo
VLT	Very Large Telescope
VO	Virtual Observatory
VVDS	VIMOS-VLT Deep Survey
WFSpec	Wide Field Spectrograph
WHT	William Herschel Telescope
WMAP	Wilkinson Microwave Anisotropy Probe

Table des matières

Remerciements	i
Table des acronymes	v
Table des matières	vii
Liste des tableaux	xiii
Table des figures	xv
Prélude	1
Introduction	3
1 La spectroscopie à champ intégral avec l'interféromètre de Fabry-Perot	7
1.1 Différentes méthodes pour faire de la spectro-imagerie	7
1.1.1 Spectroscopie, spectrographie ou spectrométrie ?	7
1.1.2 Les systèmes dispersifs	8
1.1.3 Les systèmes interférométriques à balayage	9
1.2 Principes de la spectrométrie avec l'interféromètre de Fabry-Perot	9
1.2.1 Historique de l'interféromètre de Fabry-Perot	9
1.2.2 Relations fondamentales	10
1.2.3 Utilisation classique du Fabry-Perot : pupille ou foyer ?	13
1.2.4 Réalisation d'un sujet de travaux pratiques pour illustrer les possibilités du Fabry-Perot	15
1.2.5 Calibration en longueur d'onde	16
1.2.5.1 La phase parabolique	16
1.2.5.2 Lien entre longueurs d'onde de calibration et d'observation	17
1.2.6 Réflexions parasites	18
1.2.6.1 Méthode pour soustraire les réflexions parasites	19
1.2.7 Quel type de caméra pour des observations Fabry-Perot ?	20

1.3	Développement instrumental pour le 3D-NTT	21
1.3.1	Le 3D-NTT, successeur de CIGALE, GHASP, FaNTOmM et GH α FaS	22
1.3.2	Utilisation des deux Fabry-Perot en cascade	24
1.3.3	Effets de la non-uniformité des surfaces des Fabry-Perot	25
1.3.3.1	Effet de la non-uniformité dans la pupille	25
1.3.3.2	Effet de la non-uniformité au foyer	25
1.3.4	Calibration en longueur d'onde	28
1.4	Étude du concept iBTF et d'une fonction de mérite dans le cadre du projet WFSpec	29
1.4.1	Les concepts de WFSpec	29
1.4.1.1	Concept de champ monolithique : "mono-IFU"	29
1.4.1.2	Concept de champ subdivisé : "multi-IFU"	30
1.4.1.3	Concept de filtre accordable : iBTF	30
1.4.2	Étude comparative d'une fonction de mérite pour les trois concepts	32
1.4.2.1	Détection de galaxies primordiales	32
1.4.2.2	Assemblage de masse dans les galaxies à travers les âges	33
1.4.2.3	Choix du concept de type multi-IFU : EAGLE	34
1.4.3	Quel avenir pour iBTF ?	34
2	GHASP, échantillon cinématique de 203 galaxies locales isolées	37
2.1	Le projet GHASP	37
2.1.1	Définition et objectifs de l'échantillon GHASP	37
2.1.2	Étude du gaz ionisé à partir de la raie H α	40
2.2	Présentation des données scientifiques	42
2.2.1	Des données d'observation aux cartes cinématiques	42
2.2.2	Analyse des cartes de vitesses	43
2.2.3	<u>Article I</u> : GHASP : an H α kinematic survey of spiral and irregular galaxies - VI. New H α data cubes for 108 galaxies	44
2.2.3.1	Introduction	46
2.2.3.2	Observations et réduction des données	47
2.2.3.3	Analyse des données	49
2.2.3.4	Relation de Tully-Fisher	52
2.2.3.5	Résumé et perspectives	54
2.2.3.6	Annexe A : Construction des courbes de rotation	56
2.2.3.7	Annexe B : Notes individuelles sur les galaxies	57
2.2.3.8	Annexe C : Tableaux	69
2.2.3.9	Annexe D : Cartes et diagrammes position-vitesse	76

2.2.3.10	Annexe E : Courbes de rotation	80
2.2.4	<u>Article II</u> : GHASP : An H α kinematic survey of 203 spiral and irregular galaxies - VII. Revisiting the analysis of H α data cubes for 97 galaxies.	81
2.2.4.1	Introduction	82
2.2.4.2	Calibration et profils H α	83
2.2.4.3	Analyse des données	84
2.2.4.4	Relation de Tully-Fisher	85
2.2.4.5	Résumé et conclusions	87
2.2.4.6	Annexe A : Notes individuelles sur les galaxies	88
2.2.4.7	Annexe B : Tableaux	90
2.2.4.8	Annexe C : Profils H α	101
2.2.4.9	Annexe D : Cartes et diagrammes position-vitesse	105
2.2.4.10	Annexe E : Courbes de rotation	106
2.3	Exploitation des données cinématiques	107
2.3.1	Étude de la forme des halos de matière sombre	107
2.3.2	<u>Article III</u> : <i>En préparation</i> - GHASP IX : Kinematical analysis of the whole sample	107
2.3.2.1	Introduction	109
2.3.2.2	Critère d'isolement	110
2.3.2.3	Profils H α intégrés	111
2.3.2.4	Analyse des courbes de rotation	111
2.3.2.5	Signature cinématique des barres	115
2.3.2.6	Dispersion de vitesses du gaz	116
2.3.2.7	Conclusions	116
2.3.2.8	Annexe A : Dispersion de vitesses du disque projetée dans le plan	118
2.3.2.9	Annexe B : Cartes et profils radiaux de dispersion de vitesses	118
3	Cinématique des galaxies à grand décalage spectral	119
3.1	Problématique des galaxies à grand décalage spectral	119
3.1.1	Cosmologie moderne	119
3.1.2	Histoire de l'Univers	120
3.1.3	Galaxies lointaines et spectrographie	121
3.2	Nouvelles observations de galaxies à décalage spectral supérieur à un avec SINFONI	122
3.2.1	Les caractéristiques du spectrographe SINFONI	122
3.2.2	MASSIV : observation de galaxies à grand décalage spectral	123
3.2.3	Observations SINFONI et réduction des données	123
3.2.4	Analyse cinématique des galaxies observées par SINFONI	124

3.2.4.1	Méthode d'analyse	124
3.2.4.2	Commentaires galaxie par galaxie	126
3.3	Observations cinématiques de galaxies à un décalage spectral voisin de 0.6 avec FLAMES/GIRAFFE	129
3.3.1	Les caractéristiques du spectrographe FLAMES/GIRAFFE	129
3.3.2	Étude de la relation de Tully-Fisher avec le programme IMAGES	129
3.4	<u>Article IV</u> : Evidence for strong dynamical evolution in disk galaxies through the last 11 Gyr. <i>GHASP VIII : A local reference sample of rotating disk galaxies for high redshift studies</i>	129
3.4.1	Introduction	132
3.4.2	Des galaxies locales pour simuler des galaxies distantes	133
3.4.3	Échantillon	134
3.4.4	Signatures cinématiques de disques en rotation à grand décalage spectral	140
3.4.5	Ajustement de modèles	141
3.4.6	Analyse	143
3.4.7	Discussion	156
3.4.8	Conclusion	160
3.4.9	Annexe A : Modélisation	163
3.4.10	Annexe B : Tables des paramètres	165
3.4.11	Annexe C : Cartes cinématiques	188
3.4.12	Annexe D : Courbes de rotation	211
	Conclusions et perspectives	223
	Bibliographie du texte en Français	229
	ANNEXES	235
A	Articles et documents concernant l'instrumentation présentée au chapitre 1	237
A.1	<u>Article V</u> : 3D-NTT : a versatile integral field spectro-imager for the NTT	237
A.1.1	Introduction	238
A.1.2	L'instrument	238
A.1.3	Programmes scientifiques	244
A.1.4	Comparaison du 3D-NTT avec d'autres instruments Fabry-Perot	245
A.2	GH α FaS	246
A.2.1	<u>Article VI</u> : GH α FaS : Galaxy H α Fabry-Perot System for the William Herschel Telescope	246
A.2.1.1	Introduction	247

A.2.1.2	Programmes scientifiques	248
A.2.1.3	Un instrument à champ intégral	250
A.2.1.4	Réduction des données	256
A.2.1.5	Conclusions	260
A.2.2	Comment monter GH α FaS ?	263
A.3	<u>Article VII</u> : Wide Field Spectrograph Concepts for the European Extremely Large Telescope	265
A.3.1	Introduction	266
A.3.2	Programmes scientifiques et spécifications	267
A.3.3	Concepts et performances	268
A.3.4	Conclusions	275
B	Aide du programme utilisé pour réduire les données Fabry-Perot présentées au chapitre 2	277
B.1	Le programme principal : computeeverything	277
B.1.1	Description des options de computeeverything	278
B.1.2	Exemple d'utilisation de computeeverything	281
B.2	Quelques autres programmes	283
B.2.1	Addition de cubes de données	283
B.2.1.1	Solution 1 : coaddlambdafiles	283
B.2.1.2	Solution 2 : addcubesastrometry	283
B.2.1.3	Protocole à suivre pour l'addition de cubes	284
B.2.2	Soustraction des reflets parasites : ghost2d et ghost3d	285
B.2.3	Autres routines utiles	286
C	Détermination des vitesses et des dispersions de vitesses (chapitres 2 et 3)	289
C.1	Détermination des paramètres des spectres à raies d'émission	289
C.1.1	La méthode des moments	290
C.1.2	Ajustement d'une gaussienne	291
C.2	Des longueurs d'onde aux vitesses	291
C.2.1	L'effet Doppler-Fizeau	291
C.2.2	Loi de composition des vitesses	292
C.2.2.1	Le décalage spectral est faible	292
C.2.2.2	Le décalage spectral est important	292
C.2.3	Dispersion de vitesses	293

D	Données cinématiques de l'échantillon GHASP décrites au chapitre 2	295
D.1	Cartes cinématiques des galaxies GHASP	296
D.2	Courbes de rotation des galaxies GHASP	347
D.3	Cartes et profils de dispersion de vitesses des galaxies GHASP	359
D.4	Base de données Fabry-Perot	376
E	Étude des modèles de masse (chapitre 2)	377
E.1	<u>Article VIII</u> : GHASP : an H α kinematic survey of spiral and irregular galaxies - V. Dark matter distribution in 36 nearby spiral galaxies	377
E.1.0.1	Introduction	379
E.1.0.2	L'échantillon	380
E.1.0.3	Les données	382
E.1.0.4	Profils de densité et procédure d'ajustement des modèles	384
E.1.0.5	Résultats des modèles	384
E.1.0.6	Discussion	385
E.1.0.7	Résumé et conclusion	388
E.1.0.8	Annexe A : Meilleurs ajustements aux courbes de rotation	389
F	Étude de données à grand décalage spectral (chapitre 3)	399
F.1	<u>Article IX</u> : IMAGES III. The evolution of the near-infrared Tully-Fisher relation over the last 6 Gyr	399
F.1.0.9	Introduction	401
F.1.0.10	Les données	402
F.1.0.11	Méthodologie	403
F.1.0.12	Relation de Tully-Fisher en bande K à $z \sim 0.6$	408
F.1.0.13	Discussion	410
F.1.0.14	Conclusion	412
F.1.0.15	Annexe A : Évolution de la relation de Tully-Fisher en masse stellaire	413

Liste des tableaux

1.1	Comparatif des instruments utilisant un Fabry-Perot en pupille	24
2.1	<u>Article I</u> , Table C1 : Log of the observations.	69
2.2	<u>Article I</u> , Table C2 : Model parameters.	71
2.3	<u>Article I</u> , Table C3 : Galaxy parameters.	73
2.4	<u>Article II</u> , Table B1 : Calibration parameters.	90
2.5	<u>Article II</u> , Table B2 : Model parameters.	93
2.6	<u>Article II</u> , Table B3 : Galaxy parameters.	97
3.1	Paramètres des observations.	123
3.2	Paramètres des modèles cinématiques.	126
3.3	<u>Article IV</u> , Table 1 : Successfulness of the four $z = 1.7$ models to recover $z = 0$ actual parameters.	144
3.4	<u>Article IV</u> , Table 2 : Fits of local and distant Tully-Fisher relation.	155
3.5	<u>Article IV</u> , Table B1 : Galaxy parameters at $z = 0$	166
3.6	<u>Article IV</u> , Table B1 : Exponential disk model on the sample projected at $z = 1.7$	169
3.7	<u>Article IV</u> , Table B1 : Isothermal sphere model on the sample projected at $z = 1.7$	173
3.8	<u>Article IV</u> , Table B1 : “Flat model” on the sample projected at $z = 1.7$	177
3.9	<u>Article IV</u> , Table B1 : Arctangent model on the sample projected at $z = 1.7$	181
3.10	<u>Article IV</u> , Table B1 : Parameters computed without beam smearing correction for the sample projected at $z = 1.7$	185
A.1	<u>Article V</u> , Table 1 : Low resolution mode characteristics.	242
A.2	<u>Article V</u> , Table 2 : High resolution mode characteristics.	243
A.3	<u>Article VI</u> , Table 1 : GH α FaS optical characteristics.	251
A.4	<u>Article VI</u> , Table 2 : GH α FaS optical prescription.	252
A.5	<u>Article VI</u> , Table 3 : GH α FaS Fabry-Perot etalons characteristics at H α	253
A.6	<u>Article VI</u> , Table 4 : Summary of the GH α FaS automated parts.	254
A.7	<u>Article VI</u> , Table 5 : Observed objects with GH α FaS during 6 nights.	260

A.8	<u>Article VII</u> , Table 1 : High level specifications for science case#1 : the Early Universe, the first galaxies and the end of the re-ionization epoch. The objective is to observe statistical samples of $z > 7$ objects, up to redshifts $\sim 10-15$ for a complete census of the formation of the galaxies and of the physical processes that led to the re-ionization of the Universe.	267
A.9	<u>Article VII</u> , Table 2 : High level specifications for science case#2 : the mass assembly of galaxies across cosmic times ($z=[1-5]$). Moderate resolution spectroscopy of homogeneous samples of galaxies for chemical and dynamical analyzes (mapping of absorption and emission line velocities, metallicities, extinction and ionization, etc.) of the galaxies from redshift ~ 1 to 5 for a complete census of baryonic and dark matter assembled and evolved in galaxies.	268
A.10	<u>Article VII</u> , Table 3 : The optical parameters for the monolithic IFU instrument concept.	270
A.11	<u>Article VII</u> , Table 4 : The monolithic wide-field mode concept : expected performance at $2 \mu\text{m}$	271
A.12	<u>Article VII</u> , Table 5 : The optical parameters for the multi-IFU mode instrument concept.	272
A.13	<u>Article VII</u> , Table 6 : The inputs parameters for the Holographic-Tunable Filter concept.	273
E.1	<u>Article VIII</u> , Table 1 : Data used for the analysis of our sample.	381
E.2	<u>Article VIII</u> , Table 2 : Results of the best fits of rotation curves with ISO and NFW models of halo profiles.	383
F.1	<u>Article IX</u> , Table 1 : Principle properties of the sample of 68 galaxies used in this study, ordered by increasing RA (see text).	404
F.2	<u>Article IX</u> , Table 2 : Fits to the local and distant K -band TFRs, using $M_K(AB) = a + b \times \log(V_{flat})$	408
F.3	<u>Article IX</u> , Table A.1 : Fits to the local and distant smTFRs, using $\log(M_{stellar}/M_{\odot}) = a + b \times \log(V_{flat})$	413
F.4	<u>Article IX</u> , Table A.2 : Identified systematic uncertainties that could impact the shift of zero point between the local and the distant smTFRs. Systematic uncertainties on V_{flat} have been converted into $M_{stellar}$ using Eq. (A.1). Negative values tend to reduce the shift of zero point, while positive values have the opposite trend.	414

Table des figures

1.1	Trajet de la lumière à l'intérieur de la cavité Fabry-Perot et construction de l'image à l'infini par l'objectif de la caméra.	11
1.2	Transmission d'un Fabry-Perot théorique (fonction d'Airy), possédant un facteur de réflexion de 0.9 et fonctionnant à l'ordre 798 pour la raie H α (656.3 nm).	12
1.3	Anneaux d'interférences obtenus lors d'une calibration utilisant la raie du Néon à 659.9 nm isolée grâce à un filtre interférentiel à bande étroite. Les différents anneaux correspondent à la même raie observée dans des ordres d'interférences distincts. Les deux images correspondent à deux espacements différents des lames (deux canaux spectraux) : la raie n'est plus transmise à la même position, les longueurs d'onde transmises ont changé avec l'espacement des lames. Le Fabry-Perot utilisé fonctionne à l'ordre 798 pour la raie H α et donc à l'ordre 793 pour cette raie du Néon (équation 1.3).	13
1.4	La fonction d'Airy du Fabry-Perot est modulée par la réponse du filtre interférentiel. Ainsi, seuls les pics de transmission sur la région du spectre à étudier ont une bonne transmission. La raie est échantillonnée en balayant le spectre avec le Fabry-Perot. . .	14
1.5	Effet de l'utilisation d'un Fabry-Perot théorique au foyer du NTT ($F/11$ avec miroir primaire de diamètre 3.58 m et obstruction centrale de 1.16 m), fonctionnant à l'ordre 50 pour la raie H α (656.3 nm) et possédant un facteur de réflexion de 0.73. Trait noir : réponse avec une ouverture nulle. Trait bleu : réponse au foyer Nasmyth du NTT. . . .	14
1.6	La lentille de champ permet de rabattre les rayons afin d'avoir une incidence normale sur le Fabry-Perot, ou sur le filtre interférentiel, placé au plan focal quelle que soit la position dans le champ.	15
1.7	Carte de phase brute (gauche) et variation de la phase brute avec le décalage en pixels par rapport à l'axe optique (droite). La phase est exprimée en canaux spectraux. La courbe en rouge correspond à l'ajustement d'une fonction parabolique repliée.	17
1.8	Carte de phase après déroulement de la phase, dite carte de phase parabolique (gauche) et variation de la phase parabolique avec le décalage en pixels par rapport à l'axe optique (droite). La phase est exprimée en canaux spectraux. La courbe en rouge correspond à l'ajustement d'une fonction parabolique.	18
1.9	Image (champ de UGC 1810) contenant plusieurs réflexions parasites. Les deux réflexions entourées correspondent aux deux types de réflexions corrigeables : focalisée et défocalisée. La réflexion défocalisée est vignettée. Les traits pointillés relient les étoiles et leur réflexion. On observe également sur cette image une réflexion de troisième ordre d'une étoile hors du champ. On remarque sur cet exemple un halo autour des étoiles très brillantes (voir partie 1.2.7).	19

1.10 Schéma de l'ensemble filtre interférentiel, collimateur, Fabry-Perot, objectif, récepteur. Les rayons bleus correspondent à la réflexion générée par la première lame et le filtre interférentiel. Les rayons rouges correspondent à la réflexion générée par la seconde lame et la fenêtre du détecteur.	20
1.11 Effet de la non-uniformité pour un Fabry-Perot théorique en pupille, fonctionnant à l'ordre 798 pour la raie H α (656.3 nm) et possédant un facteur de réflexion de 0.94. Trait noir : réponse sans défaut. Trait bleu : réponse avec les défauts mesurés sur les lames de la SESO.	26
1.12 Interférogramme d'une paire de lames, crédits SESO. L'échelle correspond aux variations d'épaisseur exprimées en nanomètres.	27
1.13 Schéma du foyer du télescope et illustration du positionnement défocalisé de l'interféromètre : $f/D = e/d$	27
1.14 Effet du positionnement du Fabry-Perot à 75 mm du foyer sur l'interférogramme. L'amplitude des défauts d'uniformité des surfaces des lames vus par le montage est atténuée : $min = -3 \text{ nm}$, $max = +2.4 \text{ nm}$	28
1.15 À gauche : Transmission atmosphérique dans l'infrarouge proche (1.4 μm à 2.2 μm). La transmission est supérieure à 0.8 sur des domaines de longueurs d'onde disjoints, couvrant au total moins de 0.5 μm sur les 0.8 μm définissant le domaine spectral des instruments. À droite : Spectre en émission du ciel nocturne dans l'infrarouge proche (1.4 μm à 2.2 μm). Des raies d'émission sont présentes sur tout le spectre.	30
1.16 Vue schématique comparant le fonctionnement des concepts dispersifs "multi-IFU" et "mono-IFU" (en bas) avec le concept à balayage iBTF (en haut). Pour un même temps de pose, tout le spectre est observé avec les systèmes dispersifs sur 30 champs élémentaires (en bas) tandis qu'un seul grand champ est observé en effectuant 30 pas de balayage pour obtenir le tiers utile du spectre (en haut). Au final, le nombre de pixels utilisés est le même : c'est le produit du nombre d'éléments d'échantillonnage spectral par le nombre d'éléments d'échantillonnage spatial.	31
1.17 Facteur de mérite dans le cadre de la détection de galaxies primordiales en fonction de la densité d'objets. La légende est indiquée sur la figure, cependant les courbes correspondant aux cas "mono-IFU" et "multi-IFU" sont confondues. Le facteur de mérite est supérieur pour le concept iBTF car le champ est plus grand et la couverture spectrale est moins importante.	33
1.18 Facteur de mérite dans le cadre de l'assemblage de masse des galaxies en fonction de la densité d'objets. La légende est indiquée sur la figure. À gauche : Pour des densités inférieures à dix galaxies par minute d'arc au carré, le concept "multi-IFU" est largement supérieur aux deux autres concepts. Le facteur de mérite de concept croît très vite tant qu'il y a moins d'objets dans le champ total corrigé par l'optique adaptative que d'IFU. Une fois que chaque IFU observe un objet, la fonction croît comme s'il n'y avait pas d'IFU. Le facteur de mérite du concept "mono-IFU" démarre à un puisqu'on va nécessairement choisir un champ avec au minimum un objet. Celui de l'iBTF démarre plus bas car même si on choisit le champ pour avoir un objet, il est nécessaire de faire 30 expositions pour avoir le spectre complet. À droite : Dès lors que la densité dépasse 80 galaxies par minute d'arc au carré, le concept iBTF devient plus intéressant que le concept "multi-IFU"	34

2.1	Distribution des galaxies GHASP sur la voûte céleste pour des ascensions droites comprises entre 0h et 12h. Les tailles physiques relatives des galaxies (et non les dimensions angulaires) sont respectées. La même échelle est utilisée pour dimensionner les galaxies de la Figure 2.2. Le trait pointillé correspond au plan galactique. On observe une répartition uniforme de galaxies GHASP, hormis dans le plan galactique.	38
2.2	Distribution des galaxies GHASP sur la voûte céleste pour des ascensions droites comprises entre 12h et 24h. Les tailles physiques relatives des galaxies (et non les dimensions angulaires) sont respectées. La même échelle est utilisée pour dimensionner les galaxies de la Figure 2.1. Le trait pointillé correspond au plan galactique. On observe une répartition uniforme de galaxies GHASP, hormis dans le plan galactique.	39
2.3	<u>Article I</u> , Figure 1 : Top panel : distribution of morphological type for almost all of the GHASP sample (201 out of 203 galaxies). Middle panel : distribution of the absolute <i>B</i> -band magnitude for almost all of the GHASP sample (198 out of 203 galaxies). For both the top and middle panels : the blue hash, red hash and residual white represent, respectively, the strongly barred, the moderately barred and the non-barred galaxies. Bottom panel : distribution for almost all of the GHASP sample (198 out of 203 galaxies) in the ‘magnitude-morphological type’ plane distinguishing strongly barred (blue squares), moderately barred (red triangles) and unbarred galaxies (black circles). . . .	48
2.4	<u>Article I</u> , Figure 2 : Dispersion in residual velocity field versus maximum velocity, sorted by Hubble morphological type : black circles $0 \leq t < 2$, red triangles $2 \leq t < 4$, blue squares $4 \leq t < 6$, green rhombuses $6 \leq t < 8$ and pink stars $8 \leq t < 10$. The dashed line represents the linear regression on the data. The points above the dotted line are discussed in Section 3.3. UGC 3334 labelled with an arrow has actually a huge residual velocity dispersion of 54 km s^{-1} (see Table C2).	50
2.5	<u>Article I</u> , Figure 3 : Top panel : kinematical versus morphological (HyperLeda) PAs of the major axis. Galaxies for which no accurate morphological PA has been computed are shown by red open circles ; galaxies having an inclination lower than 25° are displayed by the blue squares ; the other galaxies are represented by black circles. Bottom panel : histogram of the variation between kinematical and morphological PAs. The red hash, blue hash and residual white represent, respectively, the galaxies for which no accurate PA has been measured, for which inclination is lower than 25° and the other galaxies of the sample.	51
2.6	<u>Article I</u> , Figure 4 : Top panel : kinematical versus thick disc morphological inclinations. Middle panel : kinematical versus thin disc morphological inclinations. Top and middle panels : galaxies for which no accurate morphological PA has been computed are shown by red open circles ; galaxies with a difference between the kinematical and morphological PAs larger than 20° are displayed with blue squares ; the other galaxies are represented by black circles. Bottom panel : histogram of the variation between kinematical and morphological inclinations. The red hash, blue hash and residual white represent, respectively, the galaxies for which no accurate PA has been measured, for which the difference between the kinematical and morphological PAs is larger than 20° and the other galaxies of the sample.	52

2.7 Article I, Figure 5 : Tully-Fisher relation for our sample of galaxies. The solid line represents the B magnitude Tully-Fisher relation determined by Tully & Pierce (2000) from nearby galaxies in clusters (Ursa Major, Pisces filament, Coma). Top panel : sorted by inclination – low-inclination galaxies ($i < 25^\circ$) : blue squares ; other galaxies ($i \geq 25^\circ$) : black circles. Middle panel : sorted by V_{max} flags – V_{max} reached : black dots, large size ; V_{max} probably reached : blue squares, medium size ; V_{max} probably not reached : red triangles, small size. Bottom panel : sorted by morphological type – black circles from 0 to 2 ; red triangles from 2 to 4 ; blue squares from 4 to 6 ; green rhombuses from 6 to 8 ; pink stars from 8 to 10 and the dashed line represents the best linear fit to the data. 53

2.8 Article I, Figure D19 : UGC 3740. Top left-hand panel : XDSS blue-band image. Top right-hand panel : $H\alpha$ velocity field. Middle left-hand panel : $H\alpha$ monochromatic image. Middle right-hand panel : $H\alpha$ residual velocity field. The white and black cross is the kinematical centre. The black line is the major-axis, its length represents D_{25} . Bottom panel : position-velocity diagram along the major-axis (full width of 7 pixels), arbitrary flux units. The red line plots the rotation curve computed from the model velocity field along the major-axis (full width of 7 pixel). 76

2.9 Article I, Figure D31 : UGC 4820. Top left-hand panel : XDSS blue-band image. Top right-hand panel : $H\alpha$ velocity field. Middle left-hand panel : $H\alpha$ monochromatic image. Middle right-hand panel : $H\alpha$ residual velocity field. The white and black cross is the kinematical centre. The black line is the major-axis, its length represents D_{25} . Bottom panel : position-velocity diagram along the major-axis (full width of 7 pixels), arbitrary flux units. The red line plots the rotation curve computed from the model velocity field along the major-axis (full width of 7 pixel). 77

2.10 Article I, Figure D45 : UGC 5786. Top left-hand panel : XDSS blue-band image. Top right-hand panel : $H\alpha$ velocity field. Middle left-hand panel : $H\alpha$ monochromatic image. Middle right-hand panel : $H\alpha$ residual velocity field. The white and black cross is the kinematical centre. The black line is the major-axis, its length represents D_{25} . Bottom panel : position-velocity diagram along the major-axis (full width of 7 pixels), arbitrary flux units. The red line plots the rotation curve computed from the model velocity field along the major-axis (full width of 7 pixel). 78

2.11 Article I, Figure D56 : UGC 7154. Top left-hand panel : XDSS blue-band image. Top right-hand panel : $H\alpha$ velocity field. Middle left-hand panel : $H\alpha$ monochromatic image. Middle right-hand panel : $H\alpha$ residual velocity field. The white and black cross is the kinematical centre. The black line is the major-axis, its length represents D_{25} . Bottom panel : position-velocity diagram along the major-axis (full width of 7 pixels), arbitrary flux units. The red line plots the rotation curve computed from the model velocity field along the major-axis (full width of 7 pixel). 79

2.12 Article I, Figure E1 : From the top left-hand panel to the bottom right-hand panel : $H\alpha$ rotation curve of UGC 12893, UGC 89, UGC 94, UGC 1317, UGC 1437 and UGC 1655. 80

2.13 Article II, Figure 1 : $H\alpha$ flux measured by GHASP versus $H\alpha$ flux from James et al. (2004). The dashed line represents the linear regression on the data from which results our calibration. Top panel : calibration for the IPCS 512×512 . Bottom panel : calibration for the IPCS 256×256 83

- 2.14 Article II, Figure 2 : Dispersion in residual velocity field versus maximum velocity, subdivided by Hubble morphological type : black circles $0 \leq t < 2$, red triangles $2 \leq t < 4$, blue squares $4 \leq t < 6$, green rhombuses $6 \leq t < 8$ and pink stars $8 \leq t < 10$. The dashed line represents the linear regression on the data. The points above the dotted line are discussed in Section 3. UGC 3334 labelled with an arrow has actually a huge residual velocity dispersion of 54 km s^{-1} (see Table B2). 84
- 2.15 Article II, Figure 3 : Top panel : kinematical versus morphological (HyperLeda) position angles of the major axis. Galaxies for which no accurate morphological position angle has been computed are shown by red open circles ; galaxies having an inclination lower than 25° are displayed by blue squares ; the other galaxies are represented by black circles. Bottom panel : histogram of the variation between kinematical and morphological position angles. The red hash, blue hash and residual white represent, respectively, the galaxies for which no accurate position angle has been measured, for which inclination is lower than 25° and the other galaxies of the sample. 85
- 2.16 Article II, Figure 4 : Top panel : kinematical versus thick disc morphological inclinations. Middle panel : kinematical versus thin disc morphological inclinations. Top and middle panels : galaxies for which no accurate morphological position angle has been computed are shown by red open circles ; galaxies with a difference between the kinematical and morphological position angles larger than 20° are displayed with blue squares ; the other galaxies are represented by black circles. Bottom panel : histogram of the variation between kinematical and morphological inclinations. The red hash, blue hash and residual white represent, respectively, the galaxies for which no accurate position angle has been measured, for which the difference between the kinematical and morphological position angles is larger than 20° and the other galaxies of the sample. 86
- 2.17 Article II, Figure 5 : Tully-Fisher relation for our sample of galaxies. The solid line represents the B magnitude Tully-Fisher relation determined by Tully & Pierce (2000) from nearby galaxies in clusters (Ursa Major, Pisces filament, Coma). Top panel : subdivided by inclination – low-inclination galaxies ($i < 25^\circ$) : blue squares ; other galaxies ($i \geq 25^\circ$) : black circles. Middle panel : subdivided by V_{max} flags – V_{max} reached : black dots, large size ; V_{max} probably reached : blue squares, medium size ; V_{max} probably not reached : red triangles, small size. Bottom panel : subdivided by morphological type – black circles from 0 to 2 ; red triangles from 2 to 4 ; blue squares from 4 to 6 ; green rhombuses from 6 to 8 ; pink stars from 8 to 10 and the dashed line represents the best linear fit to the data. 86
- 2.18 Article II, Figure C1 : Integrated $H\alpha$ profiles. The profiles have been displayed over three times the spectral range ($\sim 25 \text{ \AA}$, top label or $\sim 1100 \text{ km s}^{-1}$, bottom label). The instrumental intensity in photoelectron per second and per channel is given on the left-hand side Y-axis. The calibrated intensity is displayed on the right-hand side Y-axis. The dashed vertical line indicates the systemic velocity provided by our kinematical models (see Table B2). 101
- 2.19 Article II, Figure D1 : UGC 508. Top left-hand panel : XDSS blue band image. Top right-hand panel : $H\alpha$ velocity field. Middle left-hand panel : $H\alpha$ monochromatic image. Middle right-hand panel : $H\alpha$ residual velocity field. The white and black cross is the kinematical centre. The black line is the major axis, its length represents the D_{25} . Bottom panel : position-velocity diagram along the major axis (full width of 7 pixels), arbitrary flux units. The red line plots the rotation curve computed from the model velocity field along the major axis (full width of 7 pixel). 105

2.20	<u>Article II</u> , Figure E1 : From top left-hand panel to bottom right-hand panel : H α rotation curve of UGC 508, UGC 528, UGC 763, UGC 1117, UGC 1256 and UGC 1736.	106
2.21	<u>Article III</u> , Figure 1 : Histogram of the isolation criterion for 121 out of 203 GHASP galaxies for which the systemic velocity is lower than 800 km s^{-1}	110
2.22	<u>Article III</u> , Figure 2 : Velocity field asymmetry versus rotation curve asymmetry.	111
2.23	<u>Article III</u> , Figure 3 : Asymmetry as a function of (top) magnitude, (middle) morphological type and (bottom) $B - V$ color. Black squares are barred galaxies (B), green triangles are softly barred galaxies (AB) and red stars are unbarred galaxies (A).	112
2.24	<u>Article III</u> , Figure 4 : Comparison of the optical radius and the last radius of the rotation curve with a subdivision by Hubble morphological type : black circles $t \leq 2$, red triangles $2 < t \leq 4$, blue squares $4 < t \leq 6$, green rhombuses $6 < t \leq 8$ and pink stars $t > 8$. Opened symbols are galaxies that are larger than the GHASP field-of-view. The $y = x$ line is plotted as a reference.	112
2.25	<u>Article III</u> , Figure 5 : Tully-Fisher like relation with radius. Only galaxies for which the maximum velocity is reached or probably reached are displayed. Star symbols are used for unbarred, triangles for softly barred and squares for barred galaxies.	112
2.26	<u>Article III</u> , Figure 6 : Inner slope as a function of (top) magnitude, (middle) morphological type, and (bottom) velocity field asymmetry. The left column shows non normalized inner slope whereas the right column shows the inner slope normalized with the maximum velocity and the optical radius. Black open squares are for barred galaxies (B), green triangles are for softly barred galaxies (AB) and red stars are for unbarred galaxies (A).	113
2.27	<u>Article III</u> , Figure 7 : Outer slope as a function of (top) magnitude, (middle) morphological type, and (bottom) velocity field asymmetry. The left column shows non normalized inner slope whereas the right column shows the inner slope normalized with the maximum velocity and the optical radius. Black open squares are for barred galaxies (B), green triangles are for softly barred galaxies (AB) and red stars are for unbarred galaxies (A).	114
2.28	<u>Article III</u> , Figure 8 : Modeled bar galaxy (Hernandez 2005c) with an inclination of 45° . Left : continuum. Right : gas velocity field. The scale is 0.1 kpc per pixel.	115
2.29	<u>Article III</u> , Figure 9 : Bar evolution. Top : position angle of the kinematical minor axis as a function of the position angle of the bar in the plane of the galaxy and bar strength. Bottom : position angle of the kinematical minor axis as a function of the position angle of the bar in the plane of the sky for only 180° . Green dotted line : inclination is 60° . Red dashed line : inclination is 30°	115
2.30	<u>Article III</u> , Figure 10 : From left to right : UGC 5786 monochromatic map, velocity field, velocity dispersion and velocity dispersion modeled from the velocity field and the seeing.	117
3.1	Correspondance entre le décalage spectral et l'âge des galaxies (par rapport à l'époque actuelle)	121
3.2	Vue d'artiste de l'évolution de l'Univers. Crédits : NASA/WMAP science team.	122

3.3 De gauche à droite : image du CFHT en bande I, flux H α , champ de vitesses et carte de dispersion de vitesses. Le flux H α intégré est indiqué sur chaque carte ($10^{-17} \text{ ergs s}^{-1} \text{ cm}^{-1}$). L'échelle est indiquée à gauche et la résolution spatiale (FWHM du seeing plus lissage spatial) est représentée par un cercle sur le champ de vitesses. Le Nord est en haut et l'Est est à gauche. Le centre utilisé pour la cinématique est indiqué par la double croix, et trait indique la position du grand axe du modèle. Les contours de la carte de flux sont superposés sur les cartes cinématiques. Le redshift déduit des données SINFONI est indiqué ainsi que la classification dynamique (RD : disque en rotation, PR : rotation perturbée, MS : système en fusion). 125

3.4 Article IV, Figure 1 : Evolution of the scale with the redshift using the canonical cosmological parameters $H_0 = 71 \text{ km s}^{-1} \text{ Mpc}^{-1}$, $\Omega_m = 0.27$, and $\Omega_\Lambda = 0.73$ 134

3.5 Article IV, Figure 2 : Relative distribution of galaxy properties. Top : optical radius ; Middle : maximum rotation velocity ; Bottom : masses. The black stairs indicates the GHASP local sub-sample, the red hatchings the IMAGES sample and the blue hatchings the SINS sample. In order to show the respective size of the samples (153, 63 and 26 galaxies respectively for GHASP, IMAGES and SINS), arrows and letters with the same colors indicate five galaxies for each sample (G for GHASP, I for IMAGES and S for SINS). 136

3.6 Article IV, Figure 3 : Spatial resolution effects illustrated on eight galaxies illustrating an unambiguous case and the cases described from (i) to (vii) in section 4. The following comments concern each galaxy. Top line : actual high resolution data at $z = 0$. Bottom line : data projected at $z = 1.7$. The spatial scale is labelled in arcsecond on the left side of both lines. From left to right : H α monochromatic maps, velocity fields and velocity dispersion maps. The rainbow scale on the right side of each image represents the flux for the first column and the line-of-sight velocities corrected from instrumental function for the two next columns. The black and white double crosses mark the kinematical center at low redshift, while the black line represents the major axis and ends at the optical radius. More projected galaxies are presented in Appendix C. 138

3.7 Article IV, Figure 4 : Beam smearing effects on a simulation (velocity fields on the top line and velocity dispersion maps on the bottom line) depending on increasing blurring parameter. From left to right, the seeing (represented by a dark disk on the six images) increases from $0.25''$ to $1''$. The pixel size is $0.125''$. The disk scale length is set to 5 kpc (observed at $z = 1.7$), the inclination is 45° and the maximum velocity in the plane of the disk is 200 km.s^{-1} 139

3.8 Article IV, Figure 5 : Example of a rotation curve obtained for a redshifted galaxy. Both rotation curves have been computed from both local and projected UGC 7901 velocity fields presented in Figure 3 : red-open triangles correspond to local full resolution data while black dots come from the data projected at $z = 1.7$ 139

3.9 Article IV, Figure 6 : High resolution rotation curves (black curve) superimposed on velocity fields (color image) of the four models used. From left to right and from top to bottom : exponential disk, isothermal sphere, "flat" and arc-tangent models. The radius (x-axis) is common for the four velocity fields and the four rotation curves. The velocity fields scale is given by the rainbow scale on the right side of the images. The velocity amplitude of the rotation curves is given by the scale on the left side of the y-axis. . . . 142

- 3.10 Article IV, Figure 7 : Kinematical inclination computed at $z = 1.7$ using a “flat model” vs actual kinematical inclination evaluated at $z = 0$. Each circle represents a galaxy. The open ones are galaxies which are stacked to the boundaries allowed for any fit (10 and 80°). The line indicates $y = x$ 144
- 3.11 Article IV, Figure 8 : Difference in the kinematical inclination between actual $z = 0$ galaxies and simulated galaxies $z = 1.7$ using a “flat model” vs the beam smearing parameter B . Each circle represents a galaxy. The open ones are galaxies which are stacked to the boundaries allowed for any fit (10 and 80°). The two dashed lines represent the mean positive and negative errors. 145
- 3.12 Article IV, Figure 9 : Histogram of the difference in kinematical position angles computed at $z = 0$ and at $z = 1.7$ using a “flat model”. 147
- 3.13 Article IV, Figure 10 : Difference in the position angle between actual $z = 0$ galaxies and simulated galaxies $z = 1.7$ using a “flat model” vs the beam smearing parameter B . Each circle represents a galaxy. 147
- 3.14 Article IV, Figure 11 : Mean rotation velocity difference ΔV_c^{mean} between actual $z = 0$ and different $z = 1.7$ rotation curves vs the actual $z = 0$ rotation curve inner slope. Top : ΔV_c^{mean} is the difference between actual $z = 0$ and non-corrected $z = 1.7$ rotation curves. The $z = 1.7$ rotation curves are computed along the major axis of the galaxies. Bottom : ΔV_c^{mean} is the mean difference between actual $z = 0$ and model $z = 1.7$ rotation curves. The $z = 1.7$ rotation curves are computed using a “flat model”. 148
- 3.15 Article IV, Figure 12 : Comparison between the maximum rotation velocities at $z = 0$ (x-axis) and $z = 1.7$ (y-axis). The blue squares (left column) and the black dots (right column) represent respectively the maximum velocities measured along the major axis of the blurred velocity fields and the maximum deduced from the “flat model” fitting. (Top) Velocity fields are truncated at diameters D_{25} (along the major axis). (Bottom) Velocity fields are truncated at diameters $D_{25}/2$ 149
- 3.16 Article IV, Figure 13 : Relative difference between the maximum rotation velocities at $z = 1.7$ and $z = 0$ as a function of the beam smearing parameter B . The symbols are the same than in Figure 12. 150
- 3.17 Article IV, Figure 14 : Example of comparison between high redshift simulated data (left column) and high redshift model mimicking the data (middle column) for the galaxy UGC 7901. A “flat model” has been used here. Top line : velocity field. Bottom line : velocity dispersion map. The difference between the simulated high redshift data (left column) and the model (middle column) is given for both the velocity field and the velocity dispersion map (quadratic difference) on the right column. The velocities are given by the rainbow scales on the right side of the images. 150
- 3.18 Article IV, Figure 15 : Velocity dispersion as a function of projected maximum velocity measured on $z = 0$ velocity fields. Each point represents a galaxy. Blue squares correspond to the seeing-induced central velocity dispersion measured on $z = 1.7$ maps (without applying any corrections). Red-open triangles represent the mean velocity dispersions measured on $z = 0$ galaxies. The black dots correspond to the mean velocity dispersion measured on corrected velocity dispersion maps of $z = 1.7$ galaxies using a “flat model”. The grey dashed and dotted lines respectively indicate the mean velocity dispersion in the IMAGES $z \sim 0.6$ sample and in a sample of forty-two $1 < z < 3$ objects observed with OSIRIS and SINFONI. 151

3.19	<u>Article IV</u> , Figure 16 : Minimum velocity dispersion of $z = 1.7$ galaxies as a function of the mean velocity dispersion at $z = 0$	152
3.20	<u>Article IV</u> , Figure 17 : Ratio between the maximum rotation velocity and the mean velocity dispersion as a function of the maximum rotation velocity. Top. GHASP projected sub-sample. Circles : values uncorrected for the beam smearing. 85% of these circles are within the grey horizontal hatchings zone. Dots : values corrected for the beam smearing using the rotating disk modeling. 85% of these dots are within the purple vertical hatchings zone. The grey and purple hatchings are reported in the Bottom figure for reference. Bottom. Observed high redshift galaxies. Open symbols correspond to observations using AO. Red rhombuses : SINS rotating disks at $z \sim 2$ (Cresci et al. 2009). Orange squares : MASSIV pilot run galaxies at $z \sim 1.5$ (Epinat et al. 2009c). Green triangles : $z \sim 3$ Law et al. (2009) OSIRIS observations. Blue upside down triangles : rotating disks in Wright et al. (2007, 2009) at $z \sim 1.5$ observed with OSIRIS.	153
3.21	<u>Article IV</u> , Figure 18 : Tully-Fisher relation at $z = 0$ – red line – compared with Tully-Fisher relation computed at $z = 1.7$ – black dots and black dashed line –. Open symbols correspond to galaxies that would not be classified as rotating disks at redshift 1.7. The two linear regressions (red line and black dotted line) are computed using only galaxies classified as rotating disks.	156
3.22	<u>Article IV</u> , Figures C : From left to right : XDSS image, $H\alpha$ monochromatic image, velocity field, velocity dispersion map. The white & black crosses mark the kinematical center. The black line is the major axis, its length represents the D_{25} . These maps are not truncated.	189
3.23	<u>Article IV</u> , Figures D : Rotation curves.	211
A.1	<u>Article V</u> , Figure 1 : 3D-NTT optical design (by Immervision, Quebec). The light beam is folded from the Nasmyth focus with 3 mirrors (M1 to M3). Fabry-Perot interferometers can be placed either in the focal plane or in the pupil. A filter wheel contains blocking filters for isolating the interference order of interest.	239
A.2	<u>Article V</u> , Figure 2 : Schematic drawing of the 3D-NTT attached at the Nasmyth derotator of the NTT (violet). The two interferometers are shown as red cylinders (one in the focal plane and one in the pupil plane). Design : F. Rigaud.	239
A.3	<u>Article V</u> , Figure 3 : Photograph of the mechanics of the Tunable Filter of the 3D-NTT. The overall diameter is 30 cm (the useful diameter is 10 cm). The height is 12 cm. The lower right corner insert shows a piezoactuator (not at scale). The three piezoactuators are located at 120° around the central hole. The weight is 16 kg (without glass plates and accessories).	240
A.4	<u>Article V</u> , Figure 4 : Control Interferogram for the worst glass plate of the interferometers of the 3D-NTT. PTV value is 26 nm and rms value is 1.8 nm.	241
A.5	<u>Article V</u> , Figure 5 : Controller board of the interferometer. The "One Euro" coin gives the scale.	241
A.6	<u>Article V</u> , Figure 6 : Quantum efficiency of the $4k \times 4k$ CCD used for the low resolution mode.	242
A.7	<u>Article V</u> , Figure 7 : Quantum efficiency of the L3CCD used for the high resolution mode.	243

- A.8 Article VI, Figure 1 : Two-dimensional optical layout of GH α FaS. The optical design was done in collaboration with Immervision inc. Light beam from telescope comes from the left. The detector (IPCS) can be found at the right-hand side. Different shades of the optical rays represent different positions on the focal plane. See the electronic edition of the PASP for a color version of this figure. 251
- A.9 Article VI, Figure 2 : Spot Diagram of GH α FaS in the detector plane for five different positions of the optical rays at a wavelength of 6560 Å. See the electronic edition of the PASP for a color version of this figure. 251
- A.10 Article VI, Figure 3 : Top view and cut along the optical axis parallel to the optical bread-board at the Nasmyth focus. The optical and mechanical design of GH α FaS has been especially customized for the GHRIL Nasmyth focus of the WHT. The filter wheel can fit four 75-mm filters and, like all the elements of the system, can be controlled remotely via ethernet cables. 253
- A.11 Article VI, Figure 4 : Left : Principle of electron amplification using micro channel plates (MCP) in an image intensifier. Right : Details of high-voltage effect on a micro channel. 254
- A.12 Article VI, Figure 5 : Signal-to-noise ratio comparison : IPCS and CCD at the WHT. The red line shows the S/N for an IPCS, for a 3 hr exposure of 40 cycles with 48 channels, on a 4.2-m telescope with a pixel size of 0.5'' assuming a trough-put of the telescope of 80%. The blue line shows the S/N of a scientific grade CCD with a QE of 90% and a readout noise (σ) of $3e^-$ in the same exposure conditions. The faint detection limit is placed at a S/N of 3. See the electronic edition of the PASP for a color version of this figure. 255
- A.13 Article VI, Figure 6 : Computed nonlinearity of an IPCS detector at different frame rates. See the electronic edition of the PASP for a color version of this figure. 256
- A.14 Article VI, Figure 7 : Examples of derotation. 257
- A.15 Article VI, Figure 8 : Kinematical maps of four objects. Top left : NGC 5427 with NGC 5426. Top right : NGC 4376. Bottom left : NGC 6384. Bottom right : NGC 5954 with NGC 5953. 258
- A.16 Article VI, Figure 9 : H α images of four objects. Top left : NGC 5427 with NGC 5426. Top right : NGC 4376. Bottom left : NGC 6384. Bottom right : NGC 5954 with NGC 5953. 259
- A.17 Article VI, Figure 10 : Left : [N II]658.3 nm image of Planetary Nebula M1-75 with a pixel size of 0.2''. Right : associated expansion velocity field. Range of velocity is from 76 km s⁻¹ to 231 km s⁻¹. 260
- A.18 Article VII, Figure 1 : Monolithic wide-field mode. Left : schematic concept, similar to the MUSE instrument at the VLT. The entrance field of view is split over several modules, each consisting in an image slicer and a spectrograph. Right : 3D view of one of the modules of the instrument. 269
- A.19 Article VII, Figure 2 : The 3D view of all 45 spectrographs constituting the monolithic wide-field mode. 269
- A.20 Article VII, Figure 3 : Multi IFU Mode instrument : (a) the target acquisition system and (b) the 3D view of the 40 channels with the steering mirror, the WFS, and the central telescope focal plane. 271

- A.21 Article VII, Figure 4 : The Holographic-Tunable Filter Instrument. Top : fifty-two spectral bands (blue, green, yellow and red curves) are selected in between the main OH night sky lines (green lines) already lowered by an ad hoc OH-suppression filter. Bottom : imaging Bragg Tunable Filters (i-BTFs) : The light is coming from the right (green arrow) and reaches successively : (1) the tunable filter (2) the 4 scanning i-BTFs (3) the first module containing 16 arms. Each arm contains one i-BTF and one $4k \times 4k$ CCD. The second and third modules are identical to the first one, except that they select the bluer regions of the spectrum. Note : The central beam before the tunable filter contains the whole spectrum. The Airy function is transmitted (Finesse 20), during the scanning process, the whole spectrum is transmitted. Each i-BTF extracts a spectral band on the 0-order beam. 274
- C.1 Exemple d'une raie d'émission (gaussienne) centrée sur la longueur d'onde $\lambda_0 = 6563$ Å, avec une dispersion $\sigma = 0.4$ Å et un continuum de 0.1. Le flux de la raie correspond à l'aire grisée. 290
- D.1 Cartes cinématiques des galaxies GHASP. **En haut à gauche** : Image en bande B (ou R) du XDSS. **En haut à droite** : Champ de vitesse $H\alpha$. **Au milieu à gauche** : Carte monochromatique de flux $H\alpha$. **Au milieu à droite** : Champ de vitesse résiduel lorsqu'il a été possible d'ajuster un modèle de champ de vitesses. La double croix blanche et noire représente le centre cinématique. La ligne noire représente le grand axe et s'arrête au rayon optique ($D_{25}/2$, de Vaucouleurs et al., 1995). **En bas** : Diagramme position-vitesse le long du grand axe (largeur totale de 7 pixels) avec une unité de flux arbitraire. La ligne rouge correspond à la courbe de rotation calculée le long du grand axe du champ de vitesses modèle. 296
- D.2 Courbes de rotation des galaxies GHASP. Les ronds bleus et les croix rouges identifient respectivement le côté qui s'approche et celui qui s'éloigne. La flèche noire indique le rayon optique ($D_{25}/2$, de Vaucouleurs et al., 1995), la flèche grise indique le rayon de transition. 347
- D.3 Dispersion de vitesses des galaxies GHASP. **À gauche** : Carte de dispersion de vitesses. La double croix blanche et noire représente le centre cinématique. La ligne noire représente le grand axe et s'arrête au rayon optique ($D_{25}/2$, de Vaucouleurs et al., 1995). **À droite** : Profil radial de dispersion de vitesses. La flèche noire indique le rayon optique, la flèche grise indique le rayon de transition. 359
- E.1 Article VIII, Figure 1 : Minimum χ^2 obtained with an ISO profile versus an NFW profile. For Figs 1-5 we used three different symbols for the main classes of morphological types of spiral galaxies (early, late and Magellanic). 385
- E.2 Article VIII, Figure 2 : Top panel : Central density (log) of DM versus the core radius (log) of DM for the ISO profile (ISO). Bottom panel : Same for the NFW profile. The solid lines are least-squares fits to our data (excluding the three open squares discussed in Section 6). The dashed line (top panel) is the least-squares fit extracted from fig. 3 of Kormendy & Freeman (2004). The circles surround the points for which ISO is clearly the best model. 386

- E.3 Article VIII, Figure 3 : Top panel : central density (log) of dark halo versus absolute magnitude. Bottom panel : core radius (log) of dark halo versus absolute magnitude. Both are for the ISO models. The solid lines are least-squares fits for our data (excluding the three open squares discussed in Section 6). The dashed lines are the least-squares fits extracted from fig. 3 of Kormendy & Freeman (2004). The circles surround the points for which ISO is clearly the best model. 387
- E.4 Article VIII, Figure 4 : Central surface density (log) of DM (ISO model) as a function of absolute magnitude (given in Table 1, determined from $B_T(0)$ found in the RC3 and our adopted distance). The solid line is a least-squares fit for our data (excluding the three open squares discussed in Section 6). The dashed line is the least-squares fit extracted from fig. 5 of Kormendy & Freeman (2004). The circles surround the points for which ISO is clearly the best model. 387
- E.5 Article VIII, Figure 5 : Core radius (log) of the DM halo (ISO models) as a function of optical disc scalelength (top panel) and $(B - V)$ colour (bottom panel). This last parameter, extracted from the RC3 catalog, could be found for 20 of our galaxies only. The solid lines are least-squares fits obtained with our data (excluding the three open squares discussed in Section 6). The dashed line on the top diagram is the least-squares fit from fig. 1 of Donato et al. (2004). On that diagram we have surrounded HSB, dS and LSB galaxies by circles of growing sizes. 387
- E.6 Article VIII, Figures A : Best-fitting model for the rotation curve with ISO profile (left) and NFW profile (right-hand panel). The dots are for optical velocities, the open circles for HI velocities and the crosses for HI in the central part, not taken into account. The arrow on the X-axis indicates the disc scalelength. 390
- F.1 Article IX, Figure 1 : Illustration of the ΔV_{obs} correction method, for an early-type RC (upper panel, note that $V_{max} > V_{flat}$) and a late-type RC (bottom panel). The blue thick curves represent the input RC of the test, the black curves the best models (see text), and the dash-lines the two alternative RCs with non-optimal r_t . We note that typical r_t values lead to velocity gradients on spatial scales that are much smaller than the typical seeing of ~ 0.8 arcsec. 405
- F.2 Article IX, Figure 2 : Comparison between the ΔV_{model} values obtained in Monte-Carlo simulations of 100 GIRAFFE data-cubes using a 0.8 and 1 arcsec seeing (see text). The black line is a linear fit fixing the intercept to zero. The residual dispersion is ~ 4.3 km s^{-1} 406
- F.3 Article IX, Figure 3 : Examples of kinematical fitting of three $z \sim 0.6$ RD galaxies. From left to right : HST/ACS F775W image with the GIRAFFE IFU superimposed (from Paper I), observed VF (shown with a 5×5 interpolation see Paper I), best modeled VF (shown with a 5×5 interpolation), residual map between the observed and modeled VFs. Relatively large differences are found only close to the minor axis, where departure from pure circular motion is artificially exaggerated by projection effects (see a discussion of this effect in, e.g., Chemin et al. 2006). 407

- F.4 Article IX, Figure 4 : Comparison between the V_{flat} used as inputs to the Monte-Carlo simulations of 100 GIRAFFE data-cubes, with the V_0 values obtained after using the method of correction described in Sect. 3.2. Black dots represent RCs generated using an arctan model (i.e., late-type like RCs), while open circles represent RCs typical of early-type galaxies. Black squares represent simulations where the rotation velocity is not sampled by the IFU (see text). The black line is a linear fit, and the dash lines represent the $1 - \sigma$ residual dispersion $\sim 17 \text{ km s}^{-1}$. Blue stars represent real observations of local galaxies artificially redshifted to $z \sim 0.6$ (see text). 407
- F.5 Article IX, Figure 5 : Correction factors α used to correct ΔV_{obs} for RDs (blue dots ; open blue dots represent the two RD+ galaxies). Small black dots correspond to Monte-Carlo simulations of 100 GIRAFFE data-cubes in the same range of half-light radius, PA, inclination, rotation velocity, and RC gradient (see text). The horizontal dash line represents to the mean correcting factor of 1.25 derived from Monte-Carlo simulations, while the $1 - \sigma$ dispersion around the mean is shown in dash lines. 407
- F.6 Article IX, Figure 6 : Monte-Carlo simulations of the velocity measurement accuracy (see Paper I, for details). The red line shows the corresponding bias (almost zero), while the black dashed lines shows the $1 - \sigma$ error : $\sim 12 \text{ km s}^{-1}$ between $SNR = 3 - 5$, $\sim 5 \text{ km s}^{-1}$ between $SNR = 5 - 10$, and ≤ 2 for $SNR \geq 10$ 408
- F.7 Article IX, Figure 7 : Evolution of the K -band TFR (AB magnitudes). The completeness limit $M_K \sim -20.14$ (corresponding to $M_J = -20.3$, see Sect. 2) is indicated by an horizontal dash line. Blue dots represent RDs (the two RD+ galaxies are represented with open blue dots), green squares PRs, and red triangles CK galaxies. The black line is the local TFR, while the blue dash-line represent a linear fit to the $z \sim 0.6$ TFR (see text). 408
- F.8 Article IX, Figure 8 : K -band TFR derived following the Flores et al. (2006) methodology, for the RD subsample. The black line is the local relation of Verheijen (2001), i.e., the one used as a reference by Flores et al. (2006). Note that K -band magnitudes in the distant sample have been converted into the Vega system using $M_K(Vega) = M_K(AB) - 1.85$. For simplicity, we assume that the K' magnitudes of Verheijen (2001) are roughly equivalent to those derived in the distant sample using the ISAAC Ks filter. The blue line is the SDSS local TFR used as a reference in this study (converted into the Vega system). The blue dash line is a linear fit to the distant RDs, which has a zero point 0.4 mag lower than the local one, fixing the slope to the local value. Open symbols represent galaxies from the new CDFS sample, while full symbols represent galaxies used in Flores et al. (2006). 410
- F.9 Article IX, Figure 9 : Comparison between the rotation velocities V_{F06} obtained using the method of Flores et al. (2006) (i.e., a constant correction factor of 1.2) vs. rotation velocities V_{flat} derived using the new method used in this paper, for the subsample of RDs. V_{F06} underestimates V_{flat} by $\sim 11\%$ on average. Open symbols represent galaxies from the new CDFS sample, while full symbols represent galaxies used in Flores et al. (2006). 411
- F.10 Article IX, Figure A.1 : Evolution of the stellar-mass TFR in the RD subsample (the two RD+ galaxies are represented with open blue dots). The black line is the local smTFR, while the blue dash-line represents a linear fit to the $z \sim 0.6$ smTFR. 413

- F.11 Article IX, Figure A.2 : Histograms of $\log(M_{stellar}/L_K)$ found in the local and distant samples of galaxies using the method of Bell et al. (2003). Both histograms have been re-centered using the median found in the local samples, which allows us to directly infer the evolution of $\log(M_{stellar}/L_K)$ between $z \sim 0.6$ and $z = 0$, i.e., ~ 0.625 dex. Also shown, the evolution of $\log(M_{stellar}/L_K)$ found by Drory et al. (2004) in a sample of intermediate-mass galaxies (black long-dashed line), and Arnouts et al. (2007) in blue star-forming galaxies (blue mixed-line) or independently of the color (black mixed-line). 414

Prélude

La physique, et plus particulièrement l'astronomie, me fait depuis longtemps penser aux poupées gigognes, ces poupées semblables imbriquées les unes dans les autres : une petite poupée dans une poupée un peu plus grande, dans une poupée encore plus grande, etc. En effet, des quarks se regroupent pour former des nucléons qui s'associent entre eux ainsi qu'avec des électrons pour former des atomes. À leur tour, ces atomes s'agglomèrent pour former des molécules. Atomes et molécules forment des structures macroscopiques telles que les objets qui nous entourent ou bien à plus grande échelle les étoiles avec leurs planètes et leurs satellites. Ces systèmes se regroupent pour former des galaxies qui, à leur tour, se regroupent en amas, etc. Cette séquence fait penser à la création de l'Univers, telle qu'on l'imagine au début du vingt-et-unième siècle. En passant d'une échelle à une autre, l'interaction change de nature, de l'interaction forte (nucléaire), à l'interaction faible (gravitation) en passant par l'interaction électromagnétique. Les lois de la physique sont différentes mais ont pourtant des caractéristiques communes.

À l'échelle de temps de l'espèce humaine, la compréhension des mécanismes responsables sur Terre de l'alternance périodique du jour et de la nuit et des saisons, rythmée sur une horloge céleste, a nécessité beaucoup de temps pour émerger et être acceptée. Dès le troisième siècle avant notre ère, Aristarque de Samos avait émis l'hypothèse que les planètes tournent autour du Soleil, sa logique voulant que les plus petits objets tournent autour des plus gros : "Pourquoi faire tourner la torche autour de la mouche ...". Mais il fallut attendre le seizième siècle pour que cette idée soit admise, grâce aux travaux de Copernic qui lui permirent de comprendre que l'alternance entre le jour et la nuit était due à la rotation de la Terre sur elle-même à un rythme régulier et que les saisons résultaient du long trajet de la Terre autour de l'Astre Solaire. Il fallut probablement tant de temps pour en arriver à cette conclusion à cause de la représentation géocentrique de l'Univers défendue par l'Église conjuguée aux difficultés observationnelles. En effet, comme le disait Descartes, "nos sens nous trompent parfois". Ainsi nos sens voient les astres posés sur une sphère céleste à deux dimensions alors qu'ils évoluent en réalité dans un espace à trois dimensions. Kepler interpréta un siècle plus tard le mouvement des planètes autour du Soleil comme étant dû à une force d'intensité décroissante avec le carré de la distance, comme c'est le cas pour l'intensité de la lumière. Galilée, grâce à sa lunette astronomique, apporta de nombreuses preuves observationnelles que la Terre n'est pas le centre du monde, en particulier avec les satellites de Jupiter et les phases de Vénus. Enfin, à la fin du dix-septième siècle, Newton comprit que la force qui fait tourner les astres est due à la masse, et que les lois de gravitation sont universelles, c'est-à-dire qu'elles s'appliquent aussi bien pour expliquer le mouvement des planètes autour du Soleil, que celui de la Lune autour de la Terre ou encore des satellites de Jupiter. Il inventa également le télescope composé de miroirs au lieu de lentilles comme c'est le cas de la lunette. Ces progrès observationnels menèrent, petit à petit, à la découverte en 1924 des galaxies en tant que réels "mondes à part" par Edwin Hubble à partir d'observations au télescope de 2.5 m du mont Wilson.

Des milliards d'étoiles ainsi que de grandes quantités de gaz et de poussières constituent en apparence les galaxies. Chaque galaxie pouvant être considérée comme une entité en soi, il est primordial de comprendre quelle est l'origine de leur cohésion. À l'image des poupées gigognes, on entrevoit

l'analogie avec le système solaire où les planètes sont retenues par l'attraction gravitationnelle due à la masse du Soleil. Les galaxies proches sont le laboratoire idéal de l'astronome pour observer cette cohésion grâce, entre autres, à l'étude de leur cinématique. Les astronomes ne peuvent pas mesurer de vitesses dans les galaxies par l'observation des mouvements apparents, car ils sont trop petits pour être décelés ainsi depuis la Terre à l'échelle de temps d'une vie humaine. Ils mesurent directement la vitesse projetée le long de la ligne de visée en observant la lumière émise par le gaz et par les étoiles. Grâce à l'effet Doppler-Fizeau, le décalage spectral de raies d'absorption des atmosphères stellaires ou bien de raies d'émission du gaz (ou des étoiles) a permis dès les années 1930 de mesurer des vitesses dans des galaxies. De même que pour le système solaire, il est alors nécessaire de représenter les galaxies dans l'espace pour interpréter les vitesses mesurées. La grande résolution spatiale des observations des galaxies les plus proches permet dans certains cas d'affirmer que leur matière est confinée dans un plan. L'interprétation naturelle est alors d'expliquer les mouvements dans ce plan par une rotation due au potentiel gravitationnel de la galaxie. Les premières courbes de rotation de galaxies ont ainsi été mesurées par Burbidge et al. (1960) par spectroscopie à longue fente placée le long du grand axe. Les astronomes s'attendaient alors à observer des courbes de rotation avec une vitesse décroissante à grande échelle étant données la courbe de luminosité exponentielle des galaxies (Kormendy, 1977) et les lois de la gravitation universelle de Newton. Seulement, contre toute attente, les courbes de rotation restent plates à très grande échelle, jusqu'aux derniers points où des vitesses sont mesurables (Bosma, 1978; Rubin et al., 1978). Une explication avancée est que les galaxies possèdent de la matière qu'il est impossible de détecter, la matière sombre ou matière noire (Gunn, 1980) qui représenterait jusqu'à 90% de la masse totale des galaxies. D'autres théories cherchent plutôt à expliquer cette observation par un changement des lois de la physique de Newton. C'est la théorie MOND (Milgrom, 1983).

Aujourd'hui encore, malgré les progrès observationnels, mais peut-être aussi grâce à eux, la cinématique de galaxies proches est source d'interrogations et d'investigations. De plus, avec la possibilité d'observer des galaxies lointaines, se posent de nouvelles questions sur l'évolution de la cinématique des galaxies et sur leur formation. C'est dans ce cadre que cette thèse s'est déroulée, pour apporter une petite pierre à un édifice en construction depuis bien des années...

Introduction

L'étude de données cinématiques de galaxies proches et lointaines est indispensable à la compréhension de la formation, de l'évolution et de la stabilité des galaxies. En effet, la cinématique permet d'estimer la masse dynamique des galaxies, incluant leur matière sombre et leur matière visible. Elle permet également de qualifier le support dynamique et de quantifier le moment angulaire. La comparaison d'échantillons statistiques de galaxies proches et de galaxies lointaines (donc plus jeunes) permet alors de suivre l'évolution dynamique des galaxies à travers les âges. Cependant, la dimension angulaire des galaxies lointaines étant bien inférieure à celle des galaxies proches, il est nécessaire d'utiliser de nouvelles méthodes d'analyse comparative.

L'obtention de données cinématiques a fortement évolué depuis un demi-siècle. Ainsi, l'amélioration des techniques d'observation, plus particulièrement l'essor de l'imagerie électronique et l'augmentation du diamètre des télescopes, a permis le développement de la spectroscopie à champ intégral (appelée aussi spectroscopie 3D). En particulier, l'utilisation de radiotélescopes à synthèse d'ouverture (premières observations par Gottesman et Weliachew, 1975) et l'utilisation d'interféromètres de Fabry-Perot dans le visible (premières observations par Taylor et Atherton, 1980) permettent d'obtenir des cartes de vitesses couvrant l'ensemble du champ des galaxies proches alors que les spectroscopes à longue fente limitent les observations à une unique direction spatiale. La mesure des vitesses projetées en chaque point le long de la ligne de visée dans le disque des galaxies spirales ou lenticulaires permet de calculer la courbe de rotation des galaxies. Cette dernière conduit alors à la détermination de la distribution radiale du potentiel gravitationnel et de la masse galactique lumineuse et sombre. La grande résolution spatiale et spectrale que l'on peut atteindre lors des études cinématiques à champ intégral des galaxies locales permet également de sonder les écarts à la rotation circulaire et d'observer des signatures cinématiques de structures telles que des bras spiraux (Fathi et al., 2008), des barres (Hernandez et al., 2005), des interactions entre galaxies (Amram et al., 2007) ou encore des gauchissements de disques (Christodoulou et al., 1993).

Les premières observations cinématiques de galaxies lointaines (décalage spectral entre 1 et 2) ont été obtenues par spectroscopie à longue fente et datent seulement de 1996 (Vogt et al., 1996). Jusqu'alors, pour des raisons observationnelles, les galaxies lointaines étaient vues comme des sources ponctuelles. En cosmologie, les galaxies étaient alors traditionnellement considérées comme des briques élémentaires traçant les grandes structures. L'étude des propriétés des galaxies permettait ainsi, à partir de grands relevés constitués de dizaines de milliers de galaxies, de contraindre les scénarios de formation de l'Univers par ses propriétés statistiques (Cole et al., 2001; Le Fèvre et al., 2005), sans pour autant avoir à regarder les propriétés dynamiques des galaxies en détail. L'étude cinématique résolue à grand décalage spectral étant devenue possible, elle est désormais utilisée en cosmologie afin d'améliorer la compréhension des mécanismes d'agrégation de la matière et donc de formation des galaxies. Quand la formation d'étoiles fut-elle le plus intense ? Où a-t-elle lieu ? Les populations d'étoiles ont-elles évolué ? Les galaxies se sont-elles formées par accrétion lente de matière ou bien sont-elles le résultat d'interactions et de fusions entre galaxies de faible masse ? Les interactions favorisent-elles la formation d'étoiles ? Comment le support dynamique des galaxies évolue-t-il ?

Ce support est-il ordonné (rotation) ou désordonné (mouvements aléatoires) ? Quelle est la distribution de masse des galaxies ?

Si une galaxie est considérée comme un objet ponctuel, alors sa masse ne peut être déterminée qu'à partir du flux qu'elle émet ou de la largeur des raies de son spectre intégré, c'est-à-dire de la dispersion de vitesses globale qui est une estimation de la vitesse de rotation maximale projetée. Dans le premier cas, c'est la masse stellaire qui est estimée. Le rapport masse-luminosité étant mal contraint, l'incertitude est assez grande. Dans le second cas, il s'agit de la masse dynamique intégrée jusqu'à un rayon donné. Toutefois, l'incertitude reste grande car l'inclinaison est mal contrainte, la distribution de la matière responsable des raies est inconnue et le rayon à l'intérieur duquel est mesurée la masse est mal défini. Les études sur la cinématique résolue à partir de spectrographie à longue fente puis à partir de spectroscopie à champ intégral depuis 2006 seulement (Förster Schreiber et al., 2006; Flores et al., 2006; Law et al., 2007) permettent d'avoir une idée plus précise de la masse dynamique car la vitesse est alors mesurée à un rayon connu et car l'inclinaison et la distribution de matière peuvent être estimées. Ces observations permettent également de contrôler l'accord entre la morphologie et la cinématique et de mesurer des dispersions de vitesses locales et non globales. De plus, si on observe des galaxies en interaction ou en fusion, les observations spectroscopiques à champ intégral permettront dans certains cas de dissocier les composantes et ainsi de donner une estimation non biaisée de la masse. Toutefois, la représentation dans l'espace reste une difficulté majeure pour les galaxies lointaines et ce pour plusieurs raisons : (i) la résolution spatiale reste faible pour ces galaxies malgré l'utilisation de l'optique adaptative ; (ii) le signal provenant de ces galaxies est faible et noyé dans les raies d'émission du ciel nocturne ; (iii) la géométrie de structures jeunes ou en formation peut être bien différente de celle des galaxies locales. Il faudra attendre le développement des ELT (télescopes dont le diamètre sera de l'ordre de quarante mètres) et d'une optique adaptative permettant d'atteindre leur résolution théorique pour obtenir des observations spectroscopiques à champ intégral de galaxies lointaines avec une résolution comparable à celle dont disposent actuellement les observations de galaxies proches. Ces technologies verront le jour dans une dizaine d'années et il est important de préparer ces futures observations dès à présent.

Le travail de cette thèse repose sur l'utilisation de cubes de données cinématiques pour un échantillon de 203 galaxies locales observées dans le cadre du projet GHASP (Gassendi H-Alpha survey of SPirals). Ces cubes de données sont observés autour de la raie H α du gaz d'hydrogène ionisé avec un Fabry-Perot à balayage. L'étude cinématique d'un échantillon de galaxies proches est l'occasion d'affiner les méthodes d'extraction des paramètres cinématiques des disques optiques, de réaliser une étude statistique des propriétés cinématiques des galaxies locales, d'étudier les signatures de mouvements non circulaires, de contraindre la forme des halos de matière noire ainsi que de tester des théories de gravitation modifiée. Par ailleurs, la constitution d'un échantillon de galaxies locales permet de définir des cubes de données cinématiques de référence qui seront utilisés pour étudier la cinématique des galaxies lointaines. Afin de dissocier les biais observationnels des effets d'évolution cinématique, une solution consiste à simuler les galaxies locales telles qu'elles seraient observées si elles étaient aussi éloignées que les galaxies à fort décalage spectral, d'où l'intérêt plus particulier suscité par les données spectroscopiques à champ intégral de galaxies locales.

Dans le premier chapitre, sont exposées les techniques d'observations adaptées à l'étude cinématique des galaxies proches. Leur grande taille angulaire nécessite d'utiliser des techniques permettant d'obtenir un grand champ de vue. L'accent est donc mis sur les techniques d'observations utilisant l'interféromètre de Fabry-Perot et, plus particulièrement, sur ma participation au développement en cours de l'instrument 3D-NTT, développé dans une collaboration entre le LAM (Marseille), le LAE (Montréal) et le GÉPI (Paris) et qui sera sur le ciel fin 2009. Une étude d'un concept d'instrument spectroscopique à grand champ (WFSpec) de première génération pour les ELT est également pré-

sentée. Le deuxième chapitre est consacré au projet GHASP. Ce projet a permis d'obtenir l'échantillon de référence de galaxies locales le plus important observé avec les techniques de Fabry-Perot pour des études cinématiques et dynamiques. Ses objectifs scientifiques y sont présentés et les méthodes de dépouillement et d'analyse des données sont détaillées dans deux articles présentant l'ensemble des données GHASP (Epinat et al., 2008a,b)^{1,2}. Des études cinématiques et dynamiques de cet échantillon local sont également présentées dans ce deuxième chapitre sous forme d'un article en préparation (Epinat et al., 2009b)³. Le troisième chapitre concerne l'étude de données cinématiques de galaxies lointaines obtenues à partir d'instruments à champ intégral. L'analyse cinématique de sept nouvelles galaxies lointaines observées par SINFONI (Epinat et al., 2009c)⁴ y est présentée. Ces données ainsi que d'autres données de la littérature sont alors mises en regard avec l'échantillon de référence GHASP : dans un dernier article (Epinat et al., 2009a)⁵, les galaxies de l'échantillon de référence local sont projetées au décalage spectral des données de la littérature mettant en évidence les biais observationnels ainsi que l'évolution cinématique des galaxies.

L'Annexe A contient des articles dans lesquels je suis impliqué. Ils approfondissent certains points des études instrumentales exposées au chapitre 1 (Marcelin et al., 2008⁶ ; Hernandez et al., 2008b⁷ ; Moretto et al., 2006⁸). L'Annexe B contient l'aide de l'outil de réduction développé pour dépouiller les données GHASP du chapitre 2. L'Annexe C explique comment extraire les données cinématiques à partir d'un spectre. Elle expose les méthodes utilisées pour l'extraction des cartes cinématiques des galaxies locales et lointaines présentées respectivement dans les chapitres 2 et 3. L'Annexe D illustre les données cinématiques (cartes cinématiques, courbes de rotations, profils de dispersion de vitesses et base de données) de l'échantillon GHASP (chapitre 2). L'Annexe E, quant à elle, présente un article auquel j'ai participé (Spano et al., 2008)⁹ concernant la forme des halos de matière sombre des galaxies et qui résulte de l'exploitation des courbes de rotation de l'échantillon GHASP (chapitre 2). Enfin, l'Annexe F expose une étude de la relation de Tully-Fisher à un décalage spectral proche de 0.6 à partir de données GIRAFFE (Puech et al., 2006)¹⁰ pour laquelle j'ai projeté plusieurs galaxies GHASP en utilisant la méthode décrite au chapitre 3 afin de vérifier les biais induits lors de la détermination de la vitesse maximale.

¹Epinat, B., Amram, P., et Marcelin, M. : 2008a, *MNRAS*, **390**, 466

²Epinat, B., Amram, P., Marcelin, M., Balkowski, C., Daigle, O., Hernandez, O., Chemin, L., Carignan, C., Gach, J.-L., et Balard, P. : 2008b, *MNRAS* **388**, 500

³Epinat, B., Amram, P., Marcelin, M., et al. : 2009b, *en préparation*

⁴Epinat, B., Contini, T., Le Fèvre, O., Vergani, D., Garilli, B., Amram, P., Queyrel, J., Tasca, L. et Tresse, L. : 2009c

⁵Epinat, B., Amram, P., Balkowski, C., Marcelin, M. : 2009a

⁶Marcelin, M., Amram, P., Balard, P., Balkowski, C., Boissin, O., Boulesteix, J., Carignan, C., Daigle, O., de Denus-Baillargeon, M.-M., Epinat, B., Gach, J.-L., Hernandez, O., Rigaud, F., et Vallée, P. : 2008, in *Ground-based and Airborne Instrumentation for Astronomy II*, Ian S. McLean ; Mark M. Casali, Editors, 701455, Vol. 7014 of *Presented at the Society of PhotoOptical Instrumentation Engineers (SPIE) Conference*

⁷Hernandez, O., Fathi, K., Carignan, C., Beckman, J., Gach, J.-L., Balard, P., Amram, P., Boulesteix, J., Corradi, R. L. M., de Denus-Baillargeon, M.-M., Epinat, B., Relaño, M., Thibault, S., et Vallée, P. : 2008, *PASP* **120**, 665

⁸Moretto, G., Bacon, R., Cuby, J.-G., Hammer, F., Amram, P., Blais-Ouellette, S., Blanc, P.-E., Devriendt, J., Epinat, B., Fusco, T., Jagourel, P., Hernandez, O., Kneib, J.-P., Montilla, I., Neichel, B., Pécontal, E., Prieto, E., et Puech, M. : 2006, in *Ground-based and Airborne Instrumentation for Astronomy*. Edited by McLean, Ian S. ; Iye, Masanori. *Proceedings of the SPIE, Volume 6269*, pp. 62692G (2006)., Vol. 6269 of *Presented at the Society of Photo-Optical Instrumentation Engineers (SPIE) Conference*

⁹Spano, M., Marcelin, M., Amram, P., Carignan, C., Epinat, B., et Hernandez, O. : 2008, *MNRAS* **383**, 297

¹⁰Puech, M., Flores, H., Hammer, F., Yang, Y., Neichel, B., Lehner t, M., Chemin, L., Nesvadba, N., Epinat, B., Amram, P., Balkowski, C., Cesarsky, C., Dannerbauer, H., di Serego Alighieri, S., Fuentes-Carrera, I., Guiderdoni, B., Kembhavi, A., Liang, Y. C., Östlin, G., Pozzetti, L., Ravikumar, C. D., Rawat, A., Vergani, D., Vernet, J., et Wozniak, H. : 2008, *A&A* **484**, 173

Chapitre 1

La spectroscopie à champ intégral avec l'interféromètre de Fabry-Perot

Résumé

1.1	Différentes méthodes pour faire de la spectro-imagerie	7
1.2	Principes de la spectrométrie avec l'interféromètre de Fabry-Perot	9
1.3	Développement instrumental pour le 3D-NTT	21
1.4	Étude du concept iBTF et d'une fonction de mérite dans le cadre du projet WFSpec	29

Ce chapitre concerne les aspects instrumentaux de cette thèse. La technique de spectroscopie utilisant l'interféromètre de Fabry-Perot est présentée, ainsi que certains aspects de la réduction des données sur lesquels j'ai travaillé. Les études concernant la définition et l'utilisation des Fabry-Perot de l'instrument 3D-NTT auxquelles j'ai participé sont ensuite détaillées. Enfin, dans le cadre de WFSpec, projet de spectrographe à grand champ pour les ELT, je présente une étude que j'ai réalisée sur le facteur de mérite des trois concepts instrumentaux proposés ainsi que ma contribution à l'un de ces concepts, nommé iBTF.

1.1 Différentes méthodes pour faire de la spectro-imagerie

Les études qui sont présentées dans cette thèse concernent principalement des données obtenues avec des instruments utilisant l'interféromètre de Fabry-Perot. Une revue des différents types d'instruments de spectro-imagerie utilisés actuellement est l'occasion de montrer les domaines d'applications des diverses méthodes.

1.1.1 Spectroscopie, spectrographie ou spectrométrie ?

Tout d'abord, commençons par clarifier un peu le vocabulaire de ce que l'on appelle couramment la "spectro". Le préfixe "spectro-" désigne le spectre, soit, en optique, les différentes longueurs d'onde ou bien les fréquences qui composent un faisceau lumineux, en d'autres termes, les couleurs. Le suffixe "-scopie" nous vient du grec et signifie "examiner, observer". La spectroscopie est donc l'examen, l'observation de spectres. Un spectroscope est donc un instrument qui permet d'observer des spectres.

Le suffixe “-graphie” nous vient également du grec et signifie “écrire”. Il fait donc référence à une notion d'enregistrement. La spectrographie désigne donc l'enregistrement des spectres et un spectrographe est un instrument permettant d'enregistrer des spectres. Le suffixe “-métrie” quant à lui, désigne la “mesure”. La spectrométrie consiste donc en la mesure de spectres et un spectromètre est ainsi un instrument permettant la mesure des spectres.

La différence entre chacun de ces termes est subtile. Un spectroscopie doit nous permettre d'observer un spectre à l'oeil, on a donc nécessairement besoin d'un système dispersif, c'est-à-dire qui étale la spectre selon une direction de l'espace, ce qui est le cas d'un prisme ou d'un réseau optique. Pour obtenir un spectrographe, il faut ajouter un système d'acquisition, typiquement une caméra ou une plaque photo. Pour obtenir un spectromètre, il faut une référence, donc un système permettant une calibration en longueur d'onde et/ou en intensité.

La spectroscopie ayant aboutit le siècle dernier à la possibilité de faire de la spectro-imagerie¹, c'est-à-dire obtenir un spectre pour chacun des points d'une image, la terminologie a elle aussi évolué. Ainsi aujourd'hui, un spectrographe désigne un instrument qui permet de faire l'acquisition de spectres sur la surface du récepteur, donc sur une image unique, alors qu'un spectromètre désigne un instrument qui permet la mesure de spectres au cours du temps, en fonction de créneaux de balayage, ce qui nécessite donc plusieurs lectures du récepteur.

1.1.2 Les systèmes dispersifs

Les systèmes dispersifs sont des spectrographes qui utilisent soit des prismes, soit des réseaux, soit les deux. Le phénomène de réfraction permet au prisme de disperser la lumière. C'est la variation de l'indice optique du prisme avec la longueur d'onde qui fait que les différentes composantes du spectre sont réfractées dans des directions différentes. Il y a deux types de réseaux, par réflexion et par transmission, mais dans les deux cas, c'est un phénomène interférométrique dû à sa structure périodique qui en fait un système dispersif. Un autre système optique dispersif peut être créé par l'utilisation d'un réseau accolé sur une face d'un prisme. Ce système s'appelle un Grism² et est utilisé afin de pouvoir utiliser un montage en ligne. En effet, la dispersion du prisme est calculée de manière à compenser la dispersion globale de l'ordre d'interférence utile du réseau. Afin de permettre une mesure avec ces systèmes dispersifs, il est nécessaire de les coupler avec une fente. L'observation ne possède donc qu'une dimension spatiale (le long de la fente) et le spectre est dispersé dans la direction perpendiculaire à la fente.

Cependant, les prismes ne permettent pas d'atteindre des résolutions spectrales très grandes et les réseaux n'ont pas une efficacité optimale car chaque longueur d'onde est dispersée dans plusieurs ordres d'interférence. Par ailleurs, lorsqu'on veut réaliser une cartographie contenant en chaque point une information spectrale, du fait que la dispersion se fait selon une direction spatiale, ces systèmes nécessitent soit plusieurs poses avec déplacement du champ de vue correspondant à la largeur de la fente, soit un couplage avec un système optique comme un découpeur d'image ou des fibres optiques, qui va découper le champ de vue et le réordonner le long d'une fente. Ce type d'instrument 3D est intéressant lorsqu'un grand domaine spectral est nécessaire sur un champ de vue modeste. Néanmoins, cela induit une réduction de données dont la difficulté principale est la reconstruction de l'image. Les systèmes à fibres optiques ont généralement une efficacité faible à cause des pertes dues au couplage avec les fibres. Les observations de galaxies lointaines utilisent ce genre d'instruments car le champ de vue nécessaire est petit.

¹encore appelée spectro 3D ou spectroscopie à champ intégral

²Gr pour *grating* et *ism* pour *prism* (réseau et prisme en anglais)

1.1.3 Les systèmes interférométriques à balayage

Deux types de spectromètres basés sur le phénomène d'interférences optiques permettent naturellement de faire de la spectroscopie à champ intégral. Il s'agit du spectromètre à transformée de Fourier, dit IFTS, et de l'interféromètre de Fabry-Perot. Ces interféromètres ne font que moduler le flux et ne perturbent donc pas le caractère imageur des instruments dans lesquels ils sont placés.

Un spectromètre à transformée de Fourier est un interféromètre de Michelson : ce type d'instrument est composé d'une lame semi-réfléchissante et de deux miroirs, dont un mobile, formant deux voies. La lumière va être décomposée par la lame en deux faisceaux envoyés dans chacune des voies et recomposée après réflexion sur les miroirs, à leur retour sur la lame : les ondes en provenance des deux voies interfèrent. En faisant varier la différence de chemin optique grâce au miroir mobile, il est possible d'enregistrer une série d'interférogrammes. Celle-ci contient la transformée de Fourier du spectre de la lumière en chaque point du champ de vue : pour chaque exposition, l'information enregistrée concerne donc l'ensemble du spectre.

Un spectromètre de Fabry-Perot est un système dynamique composé d'une paire de lames semi-réfléchissantes parallèles. La lumière traversant ce système subit des réflexions multiples entre les lames qui interfèrent à la sortie de l'interféromètre. Pour chaque espacement des lames, seules certaines longueurs d'onde sont transmises par l'interféromètre. Le spectre sur l'ensemble du champ est donc obtenu en faisant varier séquentiellement l'espacement entre les lames. Ce type d'instrumentation est idéal pour étudier la cinématique d'objets étendus (aussi bien les nébuleuses que les galaxies) car le domaine de longueurs d'onde utile peut être ajusté à la dynamique en vitesse de l'objet observé et au bénéfice d'un champ de vue important.

L'IFTS est donc un interféromètre à deux ondes alors que le Fabry-Perot est un interféromètre à ondes multiples. La fonction de transfert dans le cas de l'interféromètre à deux ondes est donc sinusoïdale alors que celle de l'interféromètre à ondes multiples est une fonction d'Airy (voir partie 1.2.2) qui est plus sélective. L'utilisation du Fabry-Perot est une technique éprouvée pour des observations à faible flux du gaz ionisé galactique (Russeau et al., 2005) et extragalactique (Marcelin et al., 1987) alors que l'IFTS est actuellement principalement utilisé pour des applications galactiques stellaires ou planétaires (voir l'article de Maillard, 1996 et les références qui y sont attachées).

Dans la suite, nous nous focalisons sur les instruments utilisant un interféromètre de Fabry-Perot.

1.2 Principes de la spectrométrie avec l'interféromètre de Fabry-Perot

1.2.1 Historique de l'interféromètre de Fabry-Perot

Georgelin et Amram (1995) présentent un historique très détaillé de la découverte du Fabry-Perot et de ses premières applications. Les lignes qui suivent indiquent le contexte scientifique de cette découverte ainsi que les développements et observations astronomiques qui en ont découlé.

Le principe de cet interféromètre repose sur le caractère ondulatoire de la lumière qui fut principalement établi par Thomas Young (1773-1829). Le cadre théorique de l'optique ondulatoire est élaboré un peu plus tard par Augustin Fresnel (1788-1827) et l'expression mathématique de l'interféromètre de Fabry-Perot est déterminée en 1831 par Georges Airy (1801-1892) qui décrit l'addition cohérente de réflexions multiples entre deux surfaces planes (voir partie 1.2.2), grâce à la fonction

éponyme. L'interféromètre de Fabry-Perot a été inventé en 1896 par Charles Fabry (1867-1945) et Alfred Perot (1863-1925) dans le domaine de la métrologie, afin de mesurer très précisément des variations d'épaisseur. Ils pressentent alors déjà la possibilité de placer leur interféromètre au foyer d'un télescope. Les applications de cet interféromètre s'avèrent nombreuses. En 1909, les inventeurs de cet interféromètre l'utilisent dans le but de comparer une lumière monochromatique au mètre étalon, afin d'améliorer la précision des mesures réalisées par Michelson en 1893.

Nous devons les premières utilisations astronomiques de cet interféromètre à Buisson et al. (1914) lorsqu'ils observèrent en 1914 la nébuleuse d'Orion à travers un interféromètre de Fabry-Perot monté sur le télescope de Foucault de 80 cm de l'Observatoire de Marseille. Ces observations leur permirent d'obtenir des informations quant à la cinématique du gaz ionisé de cette nébuleuse. La technique d'observation a été à nouveau utilisée une cinquantaine d'années plus tard par Courtès (1972) afin d'étudier les régions de gaz ionisé (régions HII, voir partie 2.1.2) de notre Galaxie mais également dans d'autres galaxies. Jusqu'alors, ces observations utilisaient un interféromètre de Fabry-Perot dont l'espacement entre les lames est fixe également appelé étalon. Le premier Fabry-Perot à balayage date de 1970 et a été développé à l'Imperial College de Londres, aboutissant quelques années plus tard à un interféromètre contrôlé informatiquement et adapté à l'utilisation au foyer de télescopes (Hicks et al., 1976). Les premières utilisations d'un Fabry-Perot à balayage datent respectivement de 1980, avec le développement de l'instrument TAURUS initialement pour l'INT, et de 1982 avec le développement de l'instrumentation CIGALE par Boulesteix et al. (1984) et ses collaborateurs pour le foyer Cassegrain du télescope de 3.6 m du CFHT. Outre les observations avec étalon par de Vaucouleurs et al. (1974), ces deux instruments conduisirent aux premiers champs de vitesses de galaxies (Taylor et Atherton, 1980; Marcelin et al., 1987), prémices d'une longue pratique d'observations utilisant le Fabry-Perot à balayage au sein de l'équipe Interférométrie du LAM (Boulesteix et al., 1987; Laval et al., 1987; Georgelin et al., 1987; Marcelin et al., 1987; Amram, 1991; Le Coarer et al., 1992; Plana, 1996; Russeil, 1998; Garrido, 2003a). Depuis, de nombreux instruments basés sur l'utilisation de l'interféromètre de Fabry-Perot ont été développés, notamment pour des applications à basse résolution spectrale (Pogge et al., 1995; Bland et Tully, 1989). Dans ce cas, l'interféromètre est nommé filtre accordable. Nous mentionnerons également les TTF et le MMTF qui, avec les instruments de haute résolution spectrale ont inspiré le développement de l'instrument versatile 3D-NNT (voir partie 1.3) par l'équipe Interférométrie du LAM en collaboration avec le GÉPI (observatoire de Paris) et le LAE (Université de Montréal).

Notons également que le principe de l'interféromètre de Fabry-Perot est utilisé pour réaliser les filtres interférentiels très sélectifs (quelques nm) qui sont d'ailleurs utilisés lors des observations astronomiques avec interféromètres de Fabry-Perot (voir Figure 1.4). Le Fabry-Perot est également utilisé pour réaliser des cavités laser. Dans ce cas, les miroirs ne sont plus plans, mais concaves. Enfin le Fabry-Perot est largement utilisé dans le domaine des télécommunications afin de contrôler la longueur d'onde des signaux.

1.2.2 Relations fondamentales

Le Fabry-Perot est composé de deux lames semi-réfléchissantes dont on note les transmissions τ_1 et τ_2 , et les réflectivités ρ_1 et ρ_2 . On note e l'écart entre les lames et n l'indice du matériau entre les lames, qui est de l'air dans nos applications (donc $n = 1$). Considérons un faisceau collimaté d'inclinaison θ par rapport à l'axe optique. En entrée du Fabry-Perot, le champ électrique de l'onde plane est

$$E(\lambda) = U e^{-i\omega t + i\phi_0}$$

où $\omega = 2\pi c/\lambda$ est la fréquence angulaire et ϕ_0 est la phase à l'origine. La différence de chemin optique entre deux réflexions successives de l'onde est (Figure 1.1) :

$$\delta = l_1 - l_2 = 2ne \cos(\theta)$$

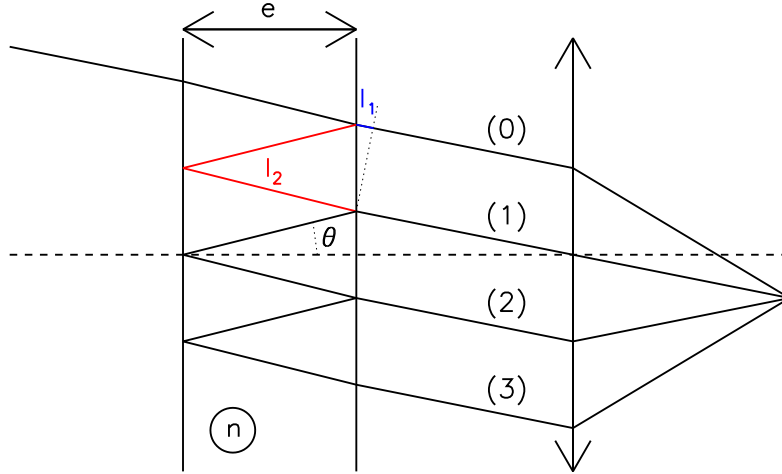


FIG. 1.1: Trajet de la lumière à l'intérieur de la cavité Fabry-Perot et construction de l'image à l'infini par l'objectif de la caméra.

Les ondes qui sortent du Fabry-Perot s'expriment en fonction de k , le nombre d'allers-retours dans la cavité :

$$E_k(\lambda, \theta) = U\tau_1\tau_2(\rho_1\rho_2)^k e^{-i\omega t + i\phi_1 - 2i\pi\frac{k\delta}{\lambda}}$$

Ces ondes vont interférer entre elles à l'infini. L'intensité sortante est donc

$$I(\lambda, \theta) = \left| \sum_{k=0}^{\infty} E_k(\lambda, \theta) \right|^2$$

Posons pour alléger les écritures :

- $\tau = \tau_1\tau_2$
- $\rho = \rho_1\rho_2$
- $I_0 = |U|^2$
- $\phi = 2\pi\frac{2ne \cos(\theta)}{\lambda}$

Nous obtenons

$$I(\lambda, \theta) = I_0\tau^2 \left| \sum_{k=0}^{\infty} (\rho e^{-i\phi})^k \right|^2 = I_0\tau \frac{1}{|1 - \rho e^{-i\phi}|^2}$$

En remarquant que

$$|1 - \rho e^{-i\phi}|^2 = (1 - \rho)^2 \left(1 + \frac{4\rho}{(1 - \rho)^2} \sin^2(\phi/2) \right)$$

et en posant la finesse

$$F = \frac{\pi\sqrt{\rho}}{1 - \rho} \quad (1.1)$$

on obtient l'expression de la fonction d'Airy (Figure 1.2) :

$$I(\lambda, \theta) = I_0 \left(\frac{\tau}{1 - \rho} \right)^2 \frac{1}{1 + \frac{4F^2}{\pi^2} \sin^2(\phi/2)} \quad (1.2)$$

Cette fonction est 2π -périodique en ϕ et maximale pour $\phi = 0 [2\pi]$ soit pour

$$\lambda p = 2ne \cos \theta \quad , \quad \text{avec } p \in \mathbb{N} \quad (1.3)$$

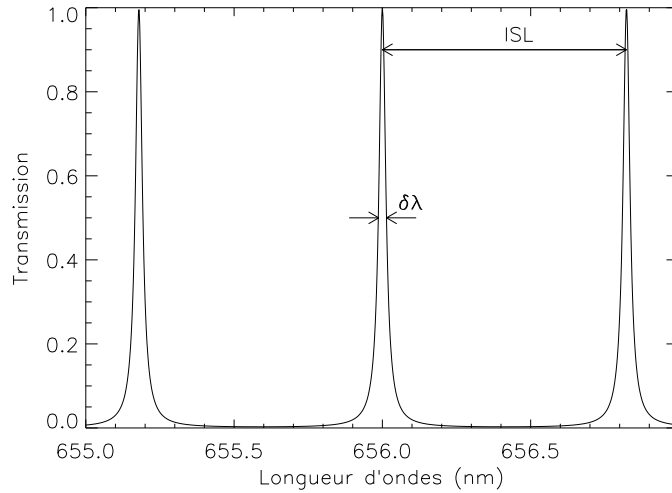


FIG. 1.2: Transmission d'un Fabry-Perot théorique (fonction d'Airy), possédant un facteur de réflexion de 0.9 et fonctionnant à l'ordre 798 pour la raie H α (656.3 nm).

L'équation 1.3 est l'équation fondamentale du Fabry-Perot. À partir de cette équation, on voit clairement que la longueur d'onde va varier dans le champ avec une symétrie circulaire, ce qui explique l'existence d'anneaux d'interférence (correspondant aux divers ordres) dans les interférogrammes lorsqu'on observe une source monochromatique (Figure 1.3). On voit également que, pour une position donnée, plusieurs longueurs d'onde sont transmises. Afin d'éviter la superposition de ces longueurs d'onde, des filtres interférentiels sont généralement utilisés afin de sélectionner l'intervalle spectral contenant la raie d'intérêt (voir Figure 1.4). C'est le cas des instruments Fabry-Perot présentés dans cette thèse.

On appelle intervalle spectral libre (*ISL*) l'intervalle en longueur d'onde séparant deux pics de transmission (voir Figure 1.2) :

$$\lambda_p p = \lambda_{p+1} (p + 1) \quad \text{et} \quad 2 ISL = \lambda_{p-1} - \lambda_{p+1}$$

Donc si l'ordre est grand, on a³ :

$$ISL = \frac{\lambda}{p} \quad (1.4)$$

On peut montrer que la finesse d'un Fabry-Perot est égale à

$$F = \frac{ISL}{\delta\lambda} \quad (1.5)$$

³En toute rigueur on a $ISL = \frac{\lambda_p}{p-1/p}$

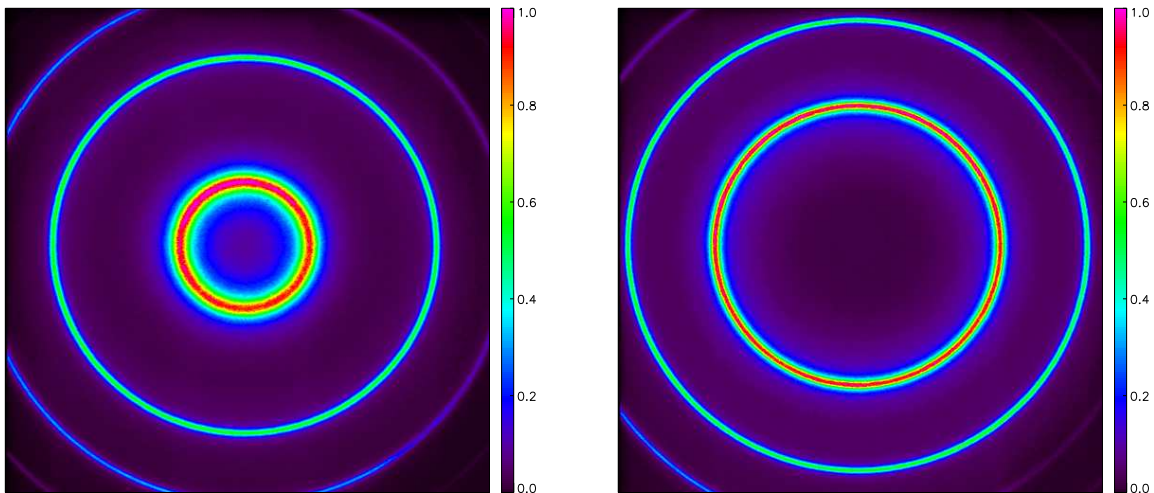


FIG. 1.3: Anneaux d'interférences obtenus lors d'une calibration utilisant la raie du Néon à 659.9 nm isolée grâce à un filtre interférentiel à bande étroite. Les différents anneaux correspondent à la même raie observée dans des ordres d'interférences distincts. Les deux images correspondent à deux espacements différents des lames (deux canaux spectraux) : la raie n'est plus transmise à la même position, les longueurs d'onde transmises ont changé avec l'espacement des lames. Le Fabry-Perot utilisé fonctionne à l'ordre 798 pour la raie $H\alpha$ et donc à l'ordre 793 pour cette raie du Néon (équation 1.3).

où $\delta\lambda$ est l'élément de résolution, typiquement la largeur à mi-hauteur de la PSF (voir Figure 1.2). L'acuité de la fonction d'Airy est donc déterminée par le choix de la réflectivité des lames (équations 1.1 et 1.5).

Par définition, la résolution spectrale d'un instrument est

$$R = \frac{\lambda}{\delta\lambda} \quad (1.6)$$

On en déduit l'expression de la résolution d'un Fabry-Perot à l'aide des équations 1.4 et 1.5 :

$$R = pF \quad (1.7)$$

Les équations 1.3, 1.4, 1.5 et 1.7 sont les relations de base de la spectroscopie Fabry-Perot.

1.2.3 Utilisation classique du Fabry-Perot : pupille ou foyer ?

La relation 1.3 nous montre que les longueurs d'onde transmises par l'interféromètre de Fabry-Perot changent avec l'angle d'incidence du rayon lumineux.

Lorsque le Fabry-Perot est placé dans un faisceau collimaté, chaque angle d'incidence correspond à une position différente sur le champ et la longueur d'onde transmise varie dans le champ. Les défauts de la surface de l'interféromètre interceptée par le faisceau sont moyennés, ce qui provoque généralement un élargissement du pic de transmission, soit une diminution de la finesse, dépendant des défauts moyens. Dans cette configuration, afin de minimiser la surface du Fabry-Perot, ce dernier est généralement placé dans la pupille, d'où le nom d'utilisation en pupille.

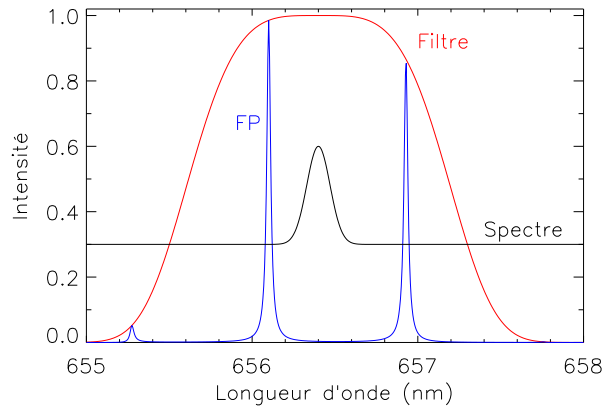


FIG. 1.4: La fonction d'Airy du Fabry-Perot est modulée par la réponse du filtre interférentiel. Ainsi, seuls les pics de transmission sur la région du spectre à étudier ont une bonne transmission. La raie est échantillonnée en balayant le spectre avec le Fabry-Perot.

Lorsque le Fabry-Perot est placé en faisceau convergent, la longueur d'onde transmise pour chacun des rayons composant le faisceau varie selon leur angle d'incidence. Le pic de transmission est alors élargi en chaque point du champ et centré sur une longueur d'onde plus faible qu'à ouverture nulle car l'inclinaison moyenne des rayons est non nulle (Figure 1.5). De plus, la longueur d'onde centrale peut changer selon la position dans le champ. En général, pour que la longueur d'onde ne varie pas, on utilise une lentille de champ afin d'avoir le même angle d'attaque sur le Fabry-Perot en tout point du champ (Figure 1.6). Dans cette configuration, afin de maximiser le champ de vue, le Fabry-Perot est placé dans le plan focal, d'où la dénomination d'utilisation au foyer. Les filtres interférentiels sont habituellement utilisés dans cette configuration.

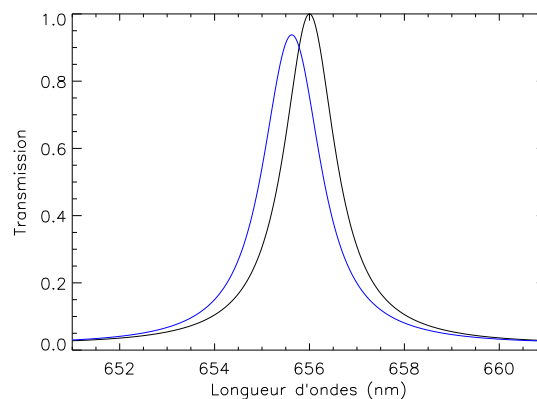


FIG. 1.5: Effet de l'utilisation d'un Fabry-Perot théorique au foyer du NTT ($F/11$ avec miroir primaire de diamètre 3.58 m et obstruction centrale de 1.16 m), fonctionnant à l'ordre 50 pour la raie $H\alpha$ (656.3 nm) et possédant un facteur de réflexion de 0.73 . Trait noir : réponse avec une ouverture nulle. Trait bleu : réponse au foyer Nasmyth du NTT.

Les observations présentées dans cette thèse utilisent l'interféromètre en pupille.

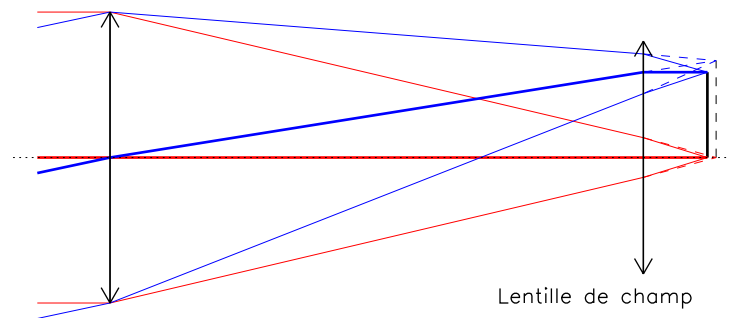


FIG. 1.6: La lentille de champ permet de rabattre les rayons afin d'avoir une incidence normale sur le Fabry-Perot, ou sur le filtre interférentiel, placé au plan focal quelle que soit la position dans le champ.

1.2.4 Réalisation d'un sujet de travaux pratiques pour illustrer les possibilités du Fabry-Perot

Les parties précédentes montrent que l'interféromètre de Fabry-Perot peut être utilisé de plusieurs manières. J'ai repris les concepts des instruments CIGALE et PYHEAS afin de mettre en évidence différentes méthodes permettant de faire de la spectroscopie 3D à partir des propriétés de l'interféromètre de Fabry-Perot dans le cadre des travaux pratiques d'optique des Masters d'Astrophysique et d'Instrumentations Optique et Lasers de l'Université de Provence.

Dans l'instrument CIGALE (ou encore GHASP, FaNTOmM, GH α Fas ou 3D-NTT dont il est question dans la partie 1.3.1), le Fabry-Perot est placé en pupille, entre un collimateur et un objectif de caméra. Ainsi, pour chaque position, plusieurs longueurs d'onde sont transmises. Afin d'éviter la superposition de ces longueurs d'onde, un filtre interférentiel est placé au foyer du collimateur. L'échantillonnage spatial est réalisé par la caméra, et l'échantillonnage spectral est à la fois réalisé par les canaux de balayage du Fabry-Perot et par la caméra puisque la longueur d'onde dépend de la position.

Dans l'instrument PYTHEAS (Le Coarer et al., 1995), la lumière traverse un Fabry-Perot placé dans un faisceau convergent très ouvert avant de former une image sur une trame de micro-lentilles. Cette trame réalise une inversion champ-pupille : l'échantillonnage spatial est réalisé par la trame qui crée des micro-pupilles en sortie. Celles-ci sont imagées sur la caméra par un système afocal constitué d'un collimateur et d'un objectif. Leur lumière est alors dispersée dans le faisceau collimaté par un réseau, ce qui permet de séparer les différents ordres du Fabry-Perot, et ainsi d'utiliser un spectre plus étendu que CIGALE. PYTHEAS est d'une certaine manière l'instrument idéal pour faire de la spectro-imagerie puisqu'il permet de totalement découpler l'information spatiale de l'information spectrale.

Un intérêt pédagogique de PYTHEAS est qu'il emploie plusieurs éléments permettant habituellement de faire de la spectroscopie indépendamment (un Fabry-Perot et un réseau). Par ailleurs, l'utilisation d'une trame de micro-lentilles illustre le fait que l'imagerie et l'échantillonnage spatial ne sont pas forcément réalisés par la caméra. De même l'échantillonnage spectral n'est pas non plus réalisé par la caméra, puisque dans le cas de PYTHEAS, ce sont les différents ordres du Fabry-Perot et ses pas de balayage qui réalisent l'échantillonnage spatial.

La comparaison entre PYTHEAS et CIGALE, quant à elle, permet de mettre en évidence qu'un instrument doit être utilisé et pensé en fonctions des besoins scientifiques :

- CIGALE possède un grand champ de vue pour un intervalle spectral réduit (un seul ordre du Fabry-Perot) et est ainsi adapté à l'étude d'objets très étendus pour lesquels une seule raie est nécessaire, ce qui est le cas de l'étude de la cinématique de galaxies proches.

- PYTHEAS possède un champ de vue réduit mais un intervalle spectral étendu correspondant à quelques centaines d'ordres du Fabry-Perot. Il est ainsi adapté à l'étude d'objets faiblement étendus pour lesquels plusieurs raies sont utiles tels que les noyaux de galaxies ou les amas globulaires.

Cette comparaison permet également de souligner le compromis qui est fait en pratique : il peut être préférable d'utiliser un instrument comme CIGALE permettant d'utiliser pleinement la capacité du récepteur plutôt qu'un instrument idéal comme PYTHEAS qui contiendra moins d'information.

1.2.5 Calibration en longueur d'onde

En utilisation en pupille, nous avons montré que la longueur d'onde varie selon la position sur le champ de vue. Il est donc nécessaire de calibrer les observations en longueur d'onde afin de connaître avec précision la longueur d'onde transmise en chaque position du champ et pour chaque espacement des lames.

En toute rigueur, si on veut une calibration précise, il est nécessaire de calibrer l'instrument à la longueur d'onde d'utilisation car les revêtements de surface des lames du Fabry-Perot peuvent induire un changement de phase à la réflexion dépendant de la longueur d'onde. En d'autre terme, l'épaisseur de la cavité vue par deux ondes planes monochromatiques de longueurs d'onde différentes n'est pas exactement la même. Cela va créer un décalage entre les longueurs d'onde théorique et réellement transmise. Cet effet peut être mesuré et calibré (Garrido et al., 2005). Toutefois, l'effet est généralement suffisamment faible (de l'ordre de quelques pour cent) pour qu'une calibration à une longueur d'onde λ_c voisine de la longueur d'onde de l'objet observé λ soit correcte. De plus, les études cinématiques s'intéressent aux vitesses relatives plutôt qu'aux vitesses absolues.

Pour faire la calibration en longueur d'onde, on utilise une source monochromatique, habituellement une lampe spectrale (au Néon) dont on isole une raie ($\lambda_c = 6592 \text{ \AA}$) en utilisant un filtre interférentiel à bande très étroite ($\sim 1.5 \text{ nm}$) centré sur cette longueur d'onde (Figure 1.4). On réalise l'acquisition d'un cube de calibration en faisant balayer le Fabry-Perot, généralement juste avant et juste après l'observation, pour être dans des conditions de flexion et de température similaires à l'observation. Deux dimensions sont spatiales, la troisième est spectrale. Chaque canal spectral correspond donc à un espacement donné des lames et, spatialement, on observe des anneaux (Figure 1.3).

1.2.5.1 La phase parabolique

Pour un ordre d'interférence donné, la longueur d'onde λ_c d'une source monochromatique est transmise pour des espacements e différents selon la position dans le champ θ (d'après l'équation 1.3). En notant e_θ l'épaisseur pour laquelle λ_c est transmise à l'incidence θ par l'ordre p on obtient

$$e_\theta - e_0 = e_0 \times \left(\frac{1}{\cos \theta} - 1 \right)$$

Le développement limité de cette expression donne

$$e_\theta - e_0 = e_0 \frac{\theta^2}{2}$$

D'où la dénomination de phase parabolique. La carte de phase parabolique est donc une carte où la valeur en chaque point correspond au canal spectral contenant une longueur d'onde de référence. On l'obtient en cherchant pour chaque position spatiale la position de la raie dans la dimension spectrale (Figure 1.7). Il est nécessaire de dérouler la phase pour obtenir la phase parabolique (Figure 1.8).

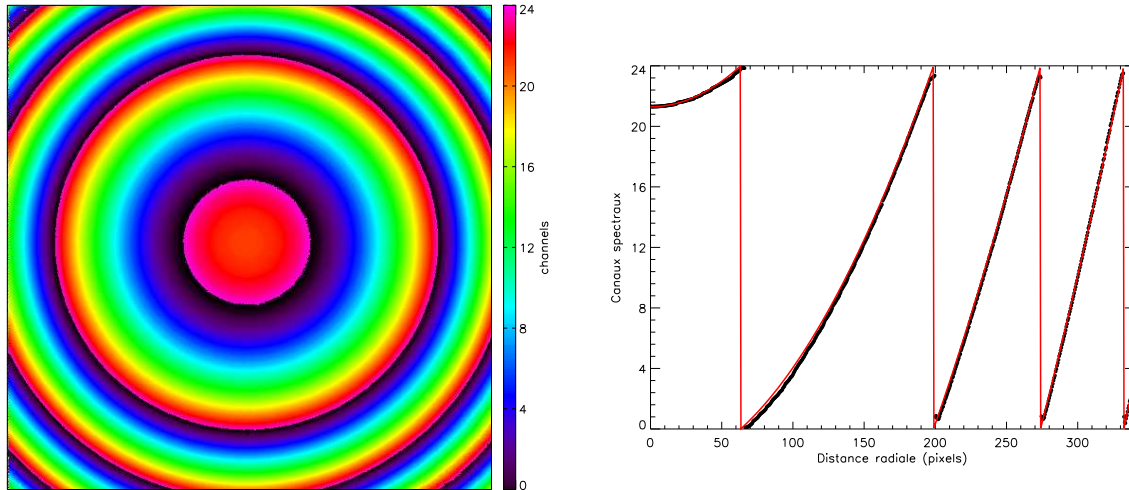


FIG. 1.7: Carte de phase brute (gauche) et variation de la phase brute avec le décalage en pixels par rapport à l'axe optique (droite). La phase est exprimée en canaux spectraux. La courbe en rouge correspond à l'ajustement d'une fonction parabolique repliée.

1.2.5.2 Lien entre longueurs d'onde de calibration et d'observation

Du fait que les longueurs d'onde de calibration λ_c et d'observation λ_s sont différentes, les ordres d'interférences utilisés sont différents pour la calibration (p_c) et l'observation (p_s). Il est donc nécessaire que la calibration soit transposée pour la longueur d'onde d'observation. Le raisonnement présenté dans ce paragraphe est celui que j'ai utilisé afin de programmer la calibration en longueur d'onde du logiciel de réduction de données présenté en Annexe B.

Considérons le canal qui transmet la longueur d'onde de référence λ_r à l'ordre (entier) de référence p_r au centre optique (λ_r et p_r sont fournis par le constructeur du Fabry-Perot, pour une position moyenne des lames). On a alors

$$\lambda_r p_r = \lambda_c (p_c + \varepsilon_c) = \lambda_s (p_s + \varepsilon_s)$$

avec p_c et p_s entiers et $|\varepsilon_c|$ et $|\varepsilon_s|$ inférieurs à 0.5 dans un premier temps (les longueurs d'ondes λ_c et λ_s ne sont pas nécessairement transmises pour ce canal au centre optique). A priori, nous voulons qu'après calibration le canal numéroté $n/2$ (si les canaux sont numérotés de 0 à $n-1$) contienne la longueur d'onde λ_s . La calibration nous permet de savoir pour quel canal ϕ la longueur d'onde λ_c est transmise. Nous pouvons donc déterminer quelle longueur d'onde se trouve au canal ϕ pour l'observation : $\lambda_{s\phi} = \lambda_c p_c / p_s$. On peut alors déterminer le canal ψ où se trouve λ_s :

$$\psi = \phi + n \frac{\lambda_s - \lambda_{s\phi}}{ISL_s}$$

Pour mettre λ_s au canal $n/2$, il faut donc appliquer un décalage Δ en canaux de

$$\Delta = \psi - n/2 = \phi + n \left(\frac{\lambda_s - \lambda_{s\phi}}{ISL_s} - \frac{1}{2} \right)$$

On généralise sur le champ entier en identifiant la phase à ϕ .

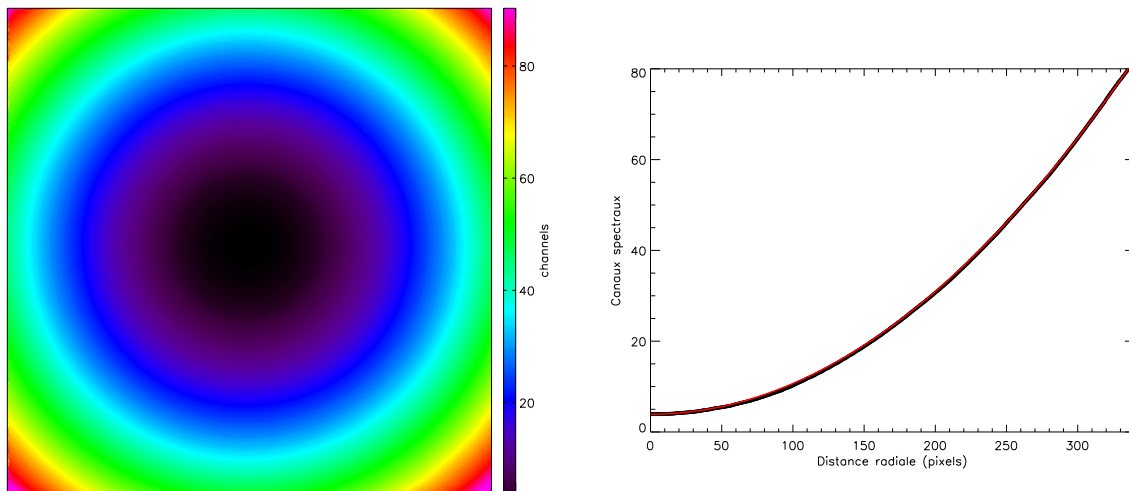


FIG. 1.8: Carte de phase après déroulement de la phase, dite carte de phase parabolique (gauche) et variation de la phase parabolique avec le décalage en pixels par rapport à l'axe optique (droite). La phase est exprimée en canaux spectraux. La courbe en rouge correspond à l'ajustement d'une fonction parabolique.

1.2.6 Réflexions parasites

Du fait de l'utilisation en pupille de l'interféromètre de Fabry-Perot, de nombreuses réflexions sont générées. Certaines d'entre elles peuvent être gênantes. Il est donc nécessaire de comprendre leur origine pour pouvoir corriger numériquement ces réflexions parasites.

Lorsqu'elle entre dans la cavité, la lumière est réfléchi sur les deux interfaces du Fabry-Perot. Pour éviter les reflets, les lames de Fabry-Perot sont trapézoïdales. Ainsi, les faces externes ne peuvent pas induire de réflexion parasite. En revanche, les faces internes ne peuvent pas être inclinées puisque ce sont ces faces qui forment la cavité et vont induire les réflexions parasites, appelées *ghosts* en anglais. Le problème des réflexions parasites dans les étalons de Fabry-Perot a été étudié par Georgelin (1970). En utilisation en pupille, les reflets qui nous gênent principalement sont ceux qui ont lieu sur des surfaces placées dans les plans focaux : les filtres interférentiels ainsi que la fenêtre du détecteur (voir Figure 1.10). Ces deux reflets sont visibles dans nos données et différenciables par le fait que la défocalisation de ces deux reflets n'est pas nécessairement identique (Figure 1.9). En particulier, la position du filtre interférentiel n'a pas besoin d'être strictement au foyer, même si c'est la position qui induit le moins de vignettage, alors que la qualité de l'image nécessite de placer la caméra exactement au foyer. Il faut tout de même noter que si le foyer du collimateur ne coïncide pas exactement avec le foyer du télescope, ce défaut de réglage sera corrigé en ajustant la position de la caméra. Dans ce cas, les deux reflets sont défocalisés, mais en général la défocalisation du reflet ayant lieu sur la caméra est négligeable. Dans les deux cas, le spectre de la réflexion est le même que celui de l'objet réfléchi une fois le cube calibré en longueur d'onde. En effet, dans le cas d'une réflexion sur le filtre interférentiel, le reflet passe à nouveau à travers le Fabry-Perot qui le filtre en longueur d'onde ; dans le cas d'une réflexion sur la fenêtre du détecteur, la longueur d'onde a été filtrée au préalable et la réflexion est exactement symétrique.

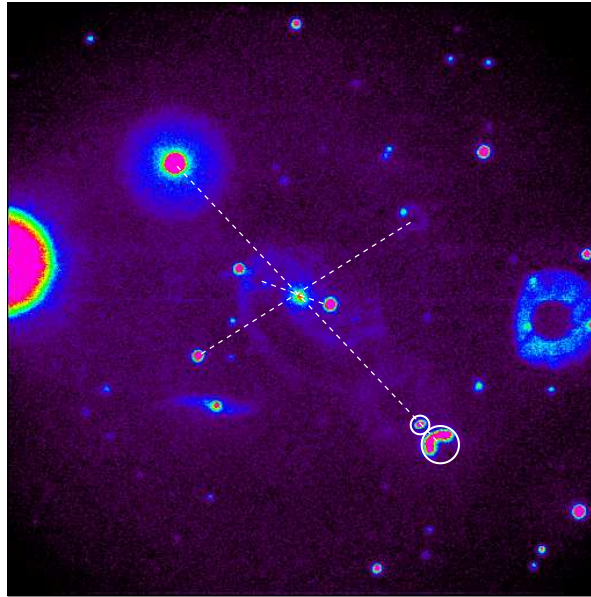


FIG. 1.9: Image (champ de UGC 1810) contenant plusieurs réflexions parasites. Les deux réflexions entourées correspondent aux deux types de réflexions corrigibles : focalisée et défocalisée. La réflexion défocalisée est vignettée. Les traits pointillés relient les étoiles et leur réflexion. On observe également sur cette image une réflexion de troisième ordre d'une étoile hors du champ. On remarque sur cet exemple un halo autour des étoiles très brillantes (voir partie 1.2.7).

1.2.6.1 Méthode pour soustraire les réflexions parasites

J'ai mis au point une méthode afin de soustraire le mieux possible les reflets parasites dans le cube de données (voir l'Annexe B pour l'utilisation pratique de cette méthode). Pour faire ce travail rigoureusement, il faudrait connaître les réglages exacts de l'instrument lors de l'observation tels que la position et l'orientation du filtre interférentiel, de la caméra et du Fabry-Perot. Il faudrait également disposer d'au moins une calibration de ces réflexions parasites afin de connaître les coefficients de réflexion du filtre et de la caméra. Cependant, dans la pratique, aucune calibration autre que celle en longueur d'onde n'est faite. En revanche, dans certaines observations, les étoiles brillantes du champ peuvent servir de référence pour calibrer la soustraction des réflexions parasites. Grâce à la calibration en longueur d'onde, l'axe optique du Fabry-Perot, qui devrait être le centre de réflexion théorique, est déterminé avec précision.

La défocalisation est modélisée par un anneau dont le rayon varie. L'anneau correspond à la pupille du télescope : le miroir primaire et l'obstruction du miroir secondaire (donc le rapport des rayons est connu *a priori*). Le flux réfléchi est réparti sur la surface de l'image de la pupille. On modifie donc les paramètres de réflexion, d'homothétie voire de décalage jusqu'à être satisfait de la correction sur l'étoile de calibration. L'idéal est d'avoir plusieurs étoiles afin d'ajuster au mieux la calibration, car il y a trois paramètres à déterminer pour la réflexion focalisée et quatre pour la réflexion défocalisée :

- le facteur de réflexion,
- l'orientation de la surface réfléchissante par rapport à l'axe optique (deux paramètres),
- la défocalisation de la réflexion défocalisée.

et seulement trois observables :

- le flux réfléchi (réflexion) ;
- la taille de la pupille (défocalisation) ;

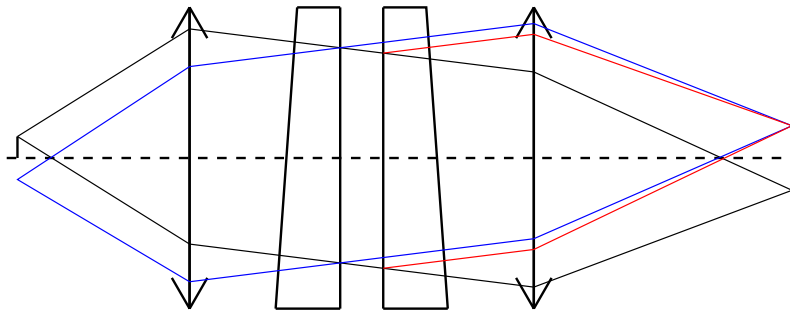


FIG. 1.10: Schéma de l'ensemble filtre interférentiel, collimateur, Fabry-Perot, objectif, récepteur. Les rayons bleus correspondent à la réflexion générée par la première lame et le filtre interférentiel. Les rayons rouges correspondent à la réflexion générée par la seconde lame et la fenêtre du détecteur.

- la position de la réflexion.

La présence de plusieurs objets induisant des réflexions parasites permet de lever la dégénérescence et aussi d'avoir une meilleure précision. Il est toutefois à noter que pour des observations utilisant une caméra à comptage de photons, la réponse n'est pas linéaire à forts flux. Ainsi, une calibration des reflets utilisant des étoiles ou des régions HII trop brillantes peut être biaisée puisque le flux de la réflexion devrait être proportionnel au flux réel de l'objet et non proportionnel au flux mesuré (voir partie 1.2.7).

1.2.7 Quel type de caméra pour des observations Fabry-Perot ?

Les observations Fabry-Perot sont principalement utilisées pour des applications cinématiques sur des objets possédant des raies d'émission (nébuleuses, galaxies, ...). Les temps de pose nécessaires pour obtenir un rapport signal sur bruit suffisant afin de déterminer des cartes de vitesses sont généralement supérieurs à une heure. Selon la position de l'objet sur le ciel ou bien selon qu'on observe en tout début ou en toute fin de nuit, les conditions d'observation peuvent changer durant l'observation : le fond de ciel peut fluctuer, la masse d'air peut évoluer rapidement pour des objets bas sur l'horizon induisant des raies du ciel nocturne d'intensité variable avec le temps. Étant donné que, pour un écartement donné des lames du Fabry-Perot, la longueur d'onde transmise n'est pas partout la même dans le champ et puisqu'il est nécessaire de balayer le spectre (en faisant varier l'espacement des lames) pour obtenir un spectre complet sur tout le champ, les variations des conditions d'observations sont particulièrement gênantes. Afin de moyennner les variations, on procède généralement à l'acquisition de plusieurs spectres complets durant l'observation, en partant du premier canal spectral au dernier puis en repartant du dernier pour aller jusqu'au premier et ainsi de suite.

Les caméras CCD possèdent un bruit de lecture non nul. Une telle séquence d'observation implique donc une perte en terme de rapport signal sur bruit. De plus, le temps de lecture peut durer quelques minutes, ce qui diminue le temps de pose réel sur le ciel. Ces caméras sont tout de même utilisées pour des observations à basse résolution spectrale car le flux reçu est plus important.

Les caméras à comptage de photons (IPCS), en revanche, possèdent un bruit de lecture nul, au détriment d'une efficacité légèrement plus faible (Gach et al., 2002). C'est habituellement ce type de caméra qui est utilisé avec les instruments de type Fabry-Perot, avec l'acquisition d'une trentaine de

cycles courts (environ dix secondes par canal spectral). Ces caméras sont composées d'une photocathode (tube intensificateur) soumise à une très haute tension (supérieure à 1000 V) qui génère 10^6 photo-électrons en moyenne pour un photon incident. Par phosphorescence sur un écran, ces électrons créent un faisceau important de photons. Ces photons sont détectés par un détecteur CCD à lecture rapide (de l'ordre de la dizaine de millisecondes) (voir la Figure 4 de l'article présenté en Annexe A.2.1, notée Figure A.11 dans la table des figures). Ainsi, un photon incident est détecté si le flux généré mesuré est supérieur à un certain seuil, sa position est alors attribuée au barycentre de la tache générée. Cela induit que les rayons cosmiques, habituellement très énergétiques ne sont comptés que comme un unique événement, ce qui rend ce type de caméra insensible au rayonnement cosmique. En revanche, lorsque le flux est important, la réponse devient non linéaire car plusieurs photons peuvent arriver pendant le même pas de lecture, alors qu'un seul photon est compté. Un autre artefact peut survenir lorsque le flux est trop important. Il se forme alors un halo autour de la source (exemple de halo autour d'une étoile visible sur la Figure 1.9). Ce halo peut devenir gênant lorsqu'on utilise un Fabry-Perot à balayage en pupille. Cela est dû au fait que la longueur d'onde transmise change avec le champ et que le spectre du halo n'est pas filtré par le Fabry-Perot. Imaginons qu'une région HII ait un flux induisant un halo, ce halo n'apparaîtra que dans un nombre restreint de canaux spectraux (ceux pour lesquels la transmission du Fabry-Perot sur la région HII correspond à la raie $H\alpha$). Après calibration, ce halo sera donc vu comme une région HII étendue dont le spectre varie avec la position. Il est nécessaire de connaître l'existence de ce phénomène afin d'interpréter correctement le champ de vitesses autour de régions HII de flux très intense. Plus la caméra a une lecture rapide, moins ses artefacts sont importants.

De nouvelles générations de caméras CCD à très faible bruit de lecture et à lecture rapide sont en cours de développement et seront donc utilisables avec des instruments de type Fabry-Perot.

1.3 Développement instrumental pour le 3D-NTT

L'utilisation d'instruments Fabry-Perot sur des télescopes de classe 4 m de diamètre dans des sites dont la qualité du ciel est bonne n'est pas fréquente. Pourtant, ces instruments peuvent permettre de répondre à de nombreuses questions scientifiques. D'un côté, lorsque la résolution spectrale des Fabry-Perot est grande, la cinématique des galaxies proches, des nébuleuses planétaires ainsi que des régions HII de la Galaxie peut être étudiée. D'un autre côté, lorsque la résolution spectrale des Fabry-Perot est faible, l'étude de la physique des régions de formation d'étoiles peut être examinée et il est également envisageable de détecter des galaxies lointaines à fort taux de formation d'étoiles afin d'étudier les phénomènes d'accrétion du gaz et de "feed-back" radiatif.

Afin de permettre de telles études, le projet 3D-NTT (PI : M. Marcelin) a vu le jour, regroupant des scientifiques impliqués dans ces diverses thématiques. Ce projet qui proposait la construction d'un instrument visiteur pour le télescope de l'ESO NTT (La Silla, CHILI) a été accepté. L'instrument 3D-NTT est actuellement en cours de développement et de construction au LAM en collaboration avec le laboratoire du GÉPI (Observatoire de Paris) et le LAE (Université de Montréal) et sera opérationnel au cours du second semestre de l'année 2009. Le 3D-NTT sera installé au foyer Nasmyth ($F/11$) du NTT, télescope de 3.58 m de type Ritchey-Chrétien dont le miroir secondaire qui mesure 0.875 m crée une obstruction de 1.16 m de diamètre. Les caractéristiques générales du 3D-NTT ainsi que ses objectifs scientifiques sont présentés dans l'article de l'Annexe A.1.

1.3.1 Le 3D-NTT, successeur de CIGALE, GHASP, FaNTOmM et GH α FaS

Le projet 3D-NTT est une évolution en termes de technologies utilisées et de méthodes observationnelles qui s'inscrit dans la lignée de CIGALE (PI : J. Boulesteix), GHASP (PI : P. Amram), FaNTOmM (PI : C. Carignan) et GH α FaS (PI : J. Beckman et C. Carignan), précédents instruments développés par le LAM (Observatoire de Marseille) dont les plus récents en collaboration étroite avec le LAE de Montréal. L'IAC a participé à la fabrication de GH α FaS. Comme ses prédécesseurs, le 3D-NTT consiste en un réducteur focal permettant de réduire le nombre d'ouverture du télescope afin d'adapter l'échantillonnage spatial en agrandissant le champ de vue et de diminuer la taille de la pupille pour y placer un Fabry-Perot à balayage. Son dessin optique (Figure 1 de l'article présenté en Annexe A.1, notée Figure A.1 dans la table des figures) a été réalisé par la société Immervision (QUÉBEC). Je ne discute ici que des instruments avec lesquels j'ai eu l'occasion de travailler, CIGALE ayant été utilisé au télescope de 3.6 m de l'ESO (CHILI) de 1990 à 2003.

GHASP est le nom du programme initié en 1998 pour lequel cet instrument a été fabriqué et sur lequel la majeure partie de ma thèse a porté. Cet instrument a été utilisé au foyer Cassegrain du télescope de 1.93 m de diamètre de l'Observatoire de Haute Provence (FRANCE). Deux caméras à comptage de photons ont été utilisées pour GHASP. La première, de 256×256 pixels couvre un champ de vue de $4' \times 4'$ avec un pixel de $0.96''$. Une nouvelle caméra à comptage de photons de 512×512 pixels, avec un pixel de $0.68''$ et un champ couvert de $5.8' \times 5.8'$ est utilisée depuis octobre 2000. Il s'agit d'un tube AsGa (photocathode) qui possède un meilleur rendement quantique que la précédente. Le refroidissement de la caméra est géré par un élément Pelletier dont la température est régulée par un circuit d'eau.

Comme son nom l'indique, FaNTOmM est utilisé au sommet du Mont Mégantic (QUÉBEC), au foyer du télescope de type Ritchey-Chrétien de 1.6 m de diamètre. Il est opérationnel depuis 2002. Il a également déjà été utilisé au CFHT ainsi qu'au foyer du télescope de 3.6 m de l'ESO à La Silla (CHILI). C'est avec cet instrument que j'ai appris à observer et à réduire des données Fabry-Perot, dans le cadre d'un programme d'observations dont l'objectif est de réaliser une mosaïque de la galaxie d'Andromède (M31). La différence principale de cet instrument avec GHASP est le système de refroidissement de la caméra. En effet, cet instrument utilise la cryogénie de Ranque-Hilsh qui consiste à diminuer la température grâce à un système de circulation d'air utilisant de l'air comprimé, un échangeur d'air et un tube de Ranque-Hilsh. La caméra utilisée est une caméra à comptage de photons de 1024×1024 pixels de $0.8''$ sur le ciel, permettant d'obtenir un champ de $19.4' \times 19.4'$.

GH α FaS est utilisé au foyer Nasmyth du WHT (4.2 m de diamètre) à l'observatoire de la Roque de Los Muchachos sur l'île de La Palma (ESPAGNE) depuis l'été 2007 (voir l'article présenté en Annexe A.2.1). Ce foyer se trouve sur l'axe de rotation horizontal de la monture alt-azimutale du télescope, dans une plate-forme qui tourne avec le télescope autour de l'axe de rotation vertical. Afin de ne pas limiter le champ de vue à $2.5' \times 2.5'$, GH α FaS n'utilise pas de dérotateur d'image. Ce type d'observation est rendu possible par l'utilisation d'une caméra à comptage de photons, car le temps d'intégration typique de 10 secondes est suffisamment court pour pouvoir négliger la rotation du champ. Cette caméra possède 1024×1024 pixels couvrant un champ de $3.5' \times 3.5'$ avec un pixel de $0.2''$. Elle utilise le même système de refroidissement que la caméra de GHASP. En revanche, le traitement des données issues de cet instrument doit inclure une routine de dérotation des cubes (Figure 7 de l'article de l'Annexe A.2.1, notée Figure A.14 dans la table des figures). L'avantage du foyer Nasmyth est que l'instrument est fixe sur table optique. Il n'y a donc pas de flexion et il est aisé de modifier des éléments du montage. Suite à mes observations avec cet instrument, j'ai participé à la rédaction d'un manuel expliquant les étapes du montage de l'instrument qui est présenté en Annexe A.2.2. C'est l'utilisation de cet instrument sur table optique qui a motivé le choix d'utiliser un

montage sur marbre plutôt qu'un montage en ligne pour le 3D-NTT afin de faciliter les interventions dans l'instrument, en particulier sur le positionnement des filtres et des Fabry-Perot.

Le 3D-NTT pourra utiliser une caméra CCD de 4096×4096 pixels et une caméra L3CCD de 1600×1600 pixels pouvant fonctionner en mode comptage de photons qui permettront respectivement d'obtenir un champ de vue circulaire de $23'$ et de $12'$ pour un pixel respectif de $0.24''$ et $0.32''$. La quantité d'information sera donc bien supérieure aux précédents instruments.

GHASP, FaNTOmM et GH α FaS utilisent les mêmes Fabry-Perot de grande résolution spectrale fixe mesurant 50 mm de diamètre. Ces Fabry-Perot sont contrôlés par un appareil dénommé CS100 fabriqué par ICOS. Des filtres interférentiels à bande étroite ($\sim 1.5 \text{ nm}$) sont nécessaires afin de sélectionner la raie d'intérêt. L'utilisation de ces filtres constitue une limitation pour couvrir tout le domaine spectral de par leur coût. Le 3D-NTT se démarque par le fait qu'il propose deux modes d'utilisation détaillés dans l'article présenté en Annexe A.1 :

- un mode haute résolution, comme ses prédécesseurs, utilisant la caméra L3CCD en mode comptage de photons, dont l'objectif scientifique principal est l'étude de la cinématique des galaxies proches et des nébuleuses planétaires.
- un mode basse résolution, dit filtre accordable, inspiré des instruments TTF et MMTF, utilisant l'une ou l'autre des caméras et dont les objectifs scientifiques principaux sont l'étude des régions de formation d'étoiles dans les galaxies proches (PI : M. Marcelin) ainsi que la détection de galaxies à fort taux de formation d'étoiles autour de quasars lointains afin d'en étudier les phénomènes d'accrétion de gaz et de "feed-back" radiatif (PI : J. Bland-Hawthorn).

Pour pouvoir répondre à ces objectifs, le 3D-NTT possède deux Fabry-Perot de nouvelle génération. Ces nouveaux Fabry-Perot permettent de couvrir un large domaine spectral (350 nm à 800 nm) grâce à des revêtements de surface optimisés et ont une résolution modulable (100 à 30000 au total pour les deux Fabry-Perot du 3D-NTT) grâce à la grande amplitude de l'espacement entre les lames ($202.5 \mu\text{m}$) permis par des actionneurs piezo-électriques de nouvelle génération. Ces actionneurs sont asservis par un nouveau contrôleur en développement au LAM. Les deux Fabry-Perot possèdent une surface utile de 100 mm . Le premier Fabry-Perot possède une finesse théorique de 50 et un espacement des lames pouvant varier entre $140 \mu\text{m}$ et $340 \mu\text{m}$. Il fournira donc une haute résolution. Le second Fabry-Perot a une finesse théorique de 10 pour un espacement minimum des lames de $2.5 \mu\text{m}$ contraint par l'espacement physique minimum et un espacement maximum de $202.5 \mu\text{m}$ fixé par la course des actionneurs piezo-électriques. Ce Fabry-Perot est également dénommé filtre accordable car il travaille à basse résolution. Le polissage des lames et le dessin de la mécanique des Fabry-Perot ont été réalisés par SESO et les couches minces (revêtements de surface) sont développées et déposées à l'Institut Fresnel.

Les deux Fabry-Perot pourront être utilisés simultanément dans le mode haute résolution : le Fabry-Perot de haute résolution est utilisé en pupille, mais les filtres interférentiels sont alors remplacés par le filtre accordable placé au foyer. Il est tout de même nécessaire d'utiliser des filtres dits de blocage afin de ne sélectionner que l'ordre utile du filtre accordable. Cependant, la largeur des filtres de blocage ($\sim 15 \text{ nm}$) est supérieure d'un ordre de grandeur à celle des filtres interférentiels ($\sim 1.5 \text{ nm}$). Ce dispositif présente l'avantage de permettre l'observation d'objets sur tout le spectre alors que jusqu'à présent, on était limité aux domaines de longueur d'onde pour lesquels on avait des filtres interférentiels. Le champ circulaire dans ce mode est limité à $9'$ de diamètre par la taille physique du Fabry-Perot placé au foyer, ce qui est adapté au champ de la caméra L3CCD.

Le mode basse résolution qui emploie uniquement le filtre accordable et les filtres de blocage possède deux configurations possibles.

- La première est une utilisation classique similaire aux instruments TTF et MMTF, avec le Fabry-Perot placé en pupille. Il est alors nécessaire d'observer plusieurs canaux spectraux et d'ef-

fectuer une correction en longueur d'onde car la longueur d'onde varie avec la position sur le champ.

- La seconde, plus inhabituelle, consiste à utiliser le Fabry-Perot au foyer $F/11$ du NTT. Dans ce cas, le champ est le même que pour le mode haute résolution et la longueur d'onde transmise est la même sur tout le champ sans qu'il ne soit utile d'utiliser de lentille de champ étant donné que le champ de vue est restreint. Ce mode d'observation est rendu possible car l'ouverture est faible au foyer utilisé. En revanche, il est limité à des ordres d'utilisation inférieurs à 80 faute de quoi la transmission diminue de plus de 80% et la résolution est inférieure à la valeur théorique (voir discussion dans la partie 1.2.3).

Toutes ces caractéristiques sont récapitulées dans la Table 1.1. On voit donc que le 3D-NTT présente un très bon compromis entre l'échantillonnage et le champ de vue. Il constitue véritablement un saut technologique par rapport à ses prédécesseurs de par sa résolution modulable et son domaine d'utilisation couvrant tout le visible.

Instrument Caractéristique	GHASP		FaNTOmM	GH α FaS	3D-NTT	
	A	B			HR	BR
Mise en service	1998	2000	2002	2007	2009	2010
Télescope (m)	1.96	1.96	1.6	4.2	3.6	
Nombre d'ouverture	15		8	11	11	
Nombre de pixels	256 ²	512 ²	1024 ²	1024 ²	1600 ²	4096 ²
Taille des pixels (")	0.96	0.68	0.8	0.2	0.32	0.24
Champ circulaire (')	5.6	8.2	27.4	4.9	9 - 12	23
Diamètre FP (mm)	50		50	50	100	100
Finesse des FP	12		12	12	10	50
Domaine de λ (nm)	500 - 750		500 - 750	500 - 750	350 - 800	
Résolution spectrale	~ 10000		~ 10000	~ 10000	30000 - 5000 - 100	

A : Caméra de première génération de GHASP

B : Caméra de seconde génération de GHASP

HR : Mode haute résolution du 3D-NTT

BR : Mode basse résolution du 3D-NTT

TAB. 1.1: Comparatif des instruments utilisant un Fabry-Perot en pupille

Enfin, le logiciel d'acquisition des données ainsi que le logiciel de réduction des données seront basés sur les logiciels utilisés actuellement pour GHASP, FaNTOmM et GH α FaS.

1.3.2 Utilisation des deux Fabry-Perot en cascade

En mode haute résolution, le filtre accordable pourra être utilisé pour sélectionner l'ordre du Fabry-Perot de haut ordre (ou haute résolution spectrale) au lieu d'utiliser une série de filtres interférentiels. Cette utilisation simultanée de deux Fabry-Perot est une des originalités majeures du concept de l'instrument 3D-NTT. Je présente ici une étude que j'ai réalisée montrant les critères qui doivent être respectés afin qu'une telle utilisation soit possible.

En mode haute résolution, on veut couvrir des ordres compris entre 200 et 800, afin d'atteindre des résolutions théoriques entre 10000 et 40000.

Il est alors nécessaire d'ajuster la résolution du Fabry-Perot de bas ordre afin de l'adapter à la dynamique du Fabry-Perot de haut ordre, typiquement son intervalle spectral libre. L'indice 1 réfère au

Fabry-Perot de bas ordre, l'indice 2 à celui de haut ordre, soit celui qui fait le balayage spectral. Le Fabry-Perot de haut ordre va balayer le domaine de longueurs d'onde défini par le pic de transmission du Fabry-Perot de bas ordre. Si on veut une transmission supérieure à 50% sur au moins un intervalle spectral libre du haut ordre, il faut alors satisfaire la relation suivante :

$$\delta\lambda_1 \geq ISL_2$$

Vues les relations 1.4 et 1.6, on peut écrire, après simplifications :

$$R_1 \leq p_2$$

Cette relation doit être vérifiée pour toutes les longueurs d'onde, ainsi que pour tous les ordres p_2 , en particulier pour l'ordre minimum d'utilisation du Fabry-Perot de haut ordre :

$$R_{1min} \leq p_{2min} \quad (1.8)$$

L'ordre minimum du filtre accordable est directement relié à l'espacement minimum que l'on peut atteindre entre les deux lames (de l'ordre de quelques microns). Cet espacement va directement dépendre des revêtements de surface à cause de l'effet de phase qui induit un changement de la cavité vue par l'onde en fonction de la longueur d'onde. Il est à noter que la finesse ne dépend en aucun cas de l'ordre d'utilisation. En revanche, selon les conditions d'utilisation (foyer ou pupille) et selon la qualité de planéité des lames, la finesse expérimentale ne peut qu'être plus faible que la finesse théorique, généralement d'un facteur deux.

Ce sont ces considérations, couplées aux objectifs scientifiques du mode filtre accordable, qui ont permis d'aboutir à la définition d'un Fabry-Perot de bas ordre avec une finesse de 10. Cette finesse assure la possibilité d'atteindre une résolution minimale de 100 sur tout le spectre.

1.3.3 Effets de la non-uniformité des surfaces des Fabry-Perot

La non-uniformité de surface des lames induit des variations d'épaisseur de la cavité Fabry-Perot. Ces variations d'épaisseur induisent donc un décalage de la longueur d'onde transmise selon la position sur la surface du Fabry-Perot. J'ai participé à l'étude de la non-uniformité des surfaces afin de vérifier que les non-uniformités attendues sur les lames ne sont pas critiques pour le projet.

1.3.3.1 Effet de la non-uniformité dans la pupille

La totalité de l'intersection de la pupille et de la surface du Fabry-Perot est éclairée par chaque point du champ, par définition de la pupille. Les défauts de surface vont donc être moyennés et la transmission du Fabry-Perot sera constante sur tout le champ (même profil, même longueur d'onde transmise). L'effet va être uniquement un élargissement du profil théorique, soit une diminution de la finesse, et une diminution de la transmission (Figure 1.11). L'ordre de grandeur de cet effet peut être relié à la valeur des défauts moyens.

1.3.3.2 Effet de la non-uniformité au foyer

Lorsqu'on place le Fabry-Perot au foyer, la largeur du profil ne dépend que de l'ouverture du faisceau (voir partie 1.2.3). J'ai travaillé sur ce point particulier afin de montrer que le filtre accordable

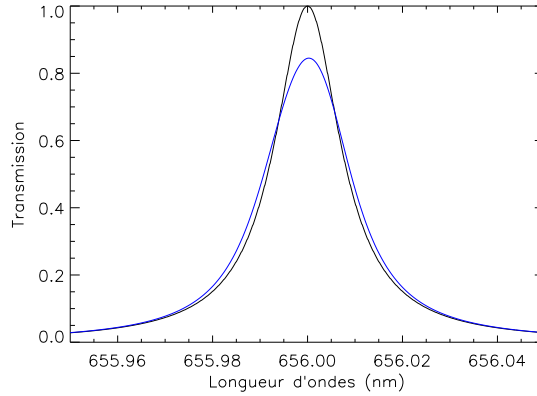


FIG. 1.11: Effet de la non-uniformité pour un Fabry-Perot théorique en pupille, fonctionnant à l'ordre 798 pour la raie H α (656.3 nm) et possédant un facteur de réflexion de 0.94. Trait noir : réponse sans défaut. Trait bleu : réponse avec les défauts mesurés sur les lames de la SESO.

devra être utilisé directement au foyer $F/11$ afin d'éviter la chute de la transmission et l'élargissement du pic. En revanche, la longueur d'onde centrale transmise en chaque point du champ dépend de l'épaisseur locale de la cavité. Le plus grand écart en longueur d'onde transmise dans le champ $d\lambda$ est celui qui va correspondre à la variation maximale d'épaisseur de cavité δe , soit l'erreur de polissage crête à crête :

$$d\lambda = 2\delta e/p$$

On voit donc que l'effet sera d'autant plus important que l'ordre est petit. D'un autre côté, plus l'ordre est faible, plus la largeur théorique du pic de transmission est grande. On veut donc calculer la variation relative de longueur d'onde $d\lambda$ par rapport à la largeur à mi-hauteur du pic de transmission $\delta\lambda$.

D'après les équations 1.4 et 1.5, on déduit que $\delta\lambda = \lambda/(Fp)$. La finesse étant fixe pour un Fabry-Perot donné, $\delta\lambda$ ne dépend que de l'ordre et de la longueur d'onde, on en déduit :

$$d\lambda/\delta\lambda = 2F\delta e/\lambda$$

Cette expression ne dépend plus de l'ordre. Le décalage sera d'autant plus important que l'on travaillera à faibles longueurs d'onde. La finesse théorique du filtre accordable étant de 10 et la variation d'épaisseur de la cavité crête à crête atteignant localement 11 nm selon l'interférogramme fourni par SESO (Figure 1.12) on obtient pour le 3D-NTT :

- à $\lambda = 350$ nm, l'erreur relative est proche de 0.5 ;
- à $\lambda = 656$ nm, l'erreur relative est proche de 0.25.

Si on tient compte de l'ouverture du faisceau ($F/11$), on doit utiliser la finesse réelle à la place de la finesse théorique. Toutefois, on montre que la finesse réelle n'est pas significativement dégradée pour une telle ouverture. Lorsqu'on utilise le filtre accordable comme filtre pour le Fabry-Perot de haut ordre, la largeur à mi-hauteur du filtre accordable est du même ordre de grandeur que l'intervalle spectral libre du Fabry-Perot de haut ordre. La configuration est donc acceptable mais pas optimale dans le bleu.

Étant donné qu'on ne peut pas diminuer la finesse du Fabry-Perot de bas ordre en deçà de 10 (voir partie 1.3.2), une solution pour palier à ce problème est de décaler légèrement le Fabry-Perot du foyer. Ainsi, les défauts de surface de hautes fréquences sont moyennés sur une surface égale à la défocalisation de l'image d'un point situé à l'infini. La taille de la tache en fonction de la défocalisation

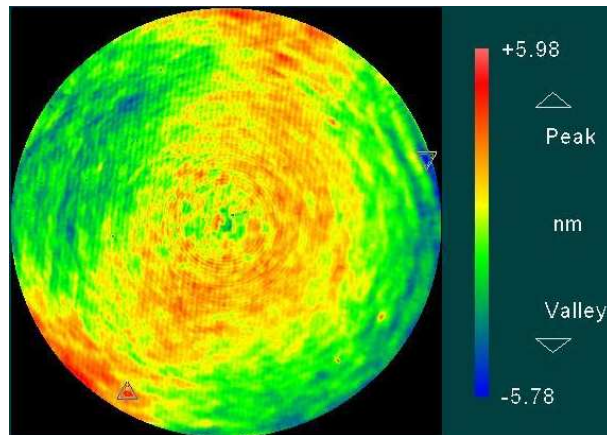


FIG. 1.12: Interférogramme d'une paire de lames, crédits SESO. L'échelle correspond aux variations d'épaisseur exprimées en nanomètres.

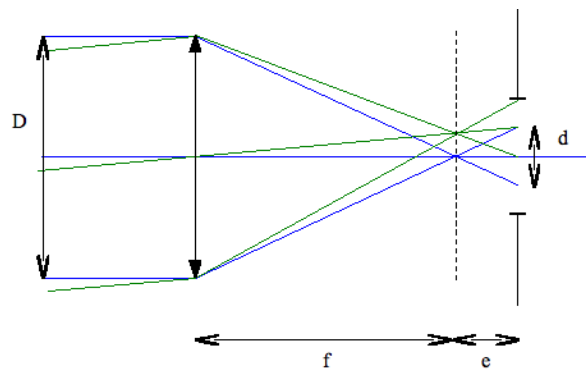


FIG. 1.13: Schéma du foyer du télescope et illustration du positionnement défocalisé de l'interféromètre : $f/D = e/d$.

est aisément calculable à partir des lois de l'optique géométrique (Figure 1.13). Cependant, la taille de la tache doit correspondre à une longueur de cohérence des défauts de surface des lames.

Pour diminuer l'effet par deux, l'interférogramme des lames montre qu'il est nécessaire d'avoir une tache de défocalisation d'au moins 7 mm (Figure 1.14). Cela implique de décaler le Fabry-Perot d'environ 77 mm du plan focal. D'après les plans mécaniques (Figure 2 de l'article de l'Annexe A.1, nommée Figure A.2 dans la table des figures), le Fabry-Perot peut être décalé au maximum de 75 mm du foyer. Cet espacement est suffisant pour réduire l'effet de la non-uniformité des surfaces du Fabry-Perot d'un facteur proche de 2. Cette solution présente l'avantage de libérer le plan focal, permettant par la même occasion d'y placer des masques pour la calibration. De plus, les réflexions parasites éventuelles seront défocalisées et par conséquent moins intenses. D'après le schéma optique, on déduit qu'un tel décalage de 75 mm du foyer va engendrer une perte de champ non vignetté par le Fabry-Perot. Le rayon du champ non vignetté est supérieur à 92.5% du rayon du champ qu'on aurait en plaçant le Fabry-Perot dans le plan focal.

En revanche, cette solution va induire une baisse de la transmission ainsi qu'une faible détérioration de la finesse qui ne devrait pas pénaliser le mode Fabry-Perot de bas ordre en pupille seul. Cette détérioration reste à quantifier.

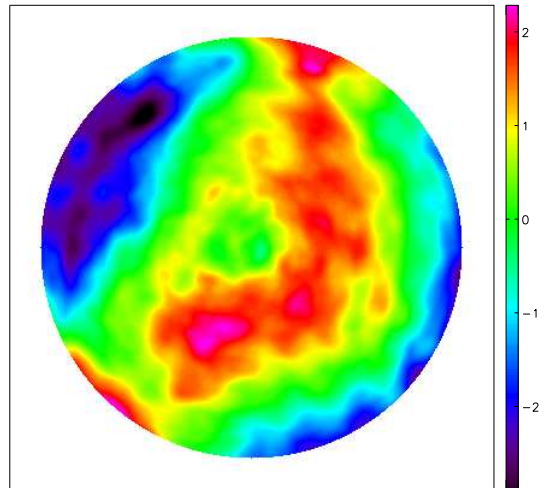


FIG. 1.14: Effet du positionnement du Fabry-Perot à 75 mm du foyer sur l'interférogramme. L'amplitude des défauts d'uniformité des surfaces des lames vus par le montage est atténuée : $\min = -3 \text{ nm}$, $\max = +2.4 \text{ nm}$.

Remarque sur les revêtements de surface : Il est probable que la non-uniformité des revêtements de surface soit plutôt à grande échelle, ce qui peut aggraver le problème présenté dans cette étude.

1.3.4 Calibration en longueur d'onde

Le système de calibration du 3D-NTT utilisera une source accordable (Photon etc) composée d'une lampe super-continuum couplée à une fibre optique afin de réaliser la sélection spectrale. Cette source permettra d'effectuer la calibration à la longueur d'onde d'observation et ainsi d'atténuer les effets de phase. En effet, il n'est pas possible de trouver des raies naturelles dans des sources spectrales à chaque longueur d'onde (environ une par nm). La résolution de cette source sera de 0.1 nm . Cependant, cette résolution sera trop grande pour pouvoir mesurer la réponse impulsionnelle de l'instrument. Il est donc prévu d'introduire dans cette source une lampe spectrale qui pourra être utilisée à la place de la source accordable ou bien en complément de celle-ci. Le système optique adopté pour insérer cette source dans le trajet optique de l'instrument est un écran diffuseur (distribué par Schott). Cet écran sera placé à quelques centimètres du foyer du NTT. La source de calibration doit éclairer un faisceau de fibres optiques multimodes qui permet un éclairage uniforme au niveau de l'écran. Cette solution permet un encombrement minimum. Nous avons testé la faisabilité de cette configuration en laboratoire avec le réducteur focal de l'instrument GHASP, une caméra à comptage de photons, un écran diffuseur de surface quatre fois plus petite que celle de l'écran qui sera utilisé pour le 3D-NTT et avec une source accordable de résolution 0.3 nm . Des anneaux d'interférence ont été obtenus. J'ai vérifié que les flux seraient du même ordre de grandeur avec les composants qui seront utilisés pour le 3D-NTT en tenant compte de la surface de l'écran diffuseur, de l'ouverture de l'instrument, de l'efficacité de la caméra et de la taille du pixel.

Étant donné que l'écran est positionné au foyer du NTT, il sera nécessaire de simuler la pupille du

télescope afin de prendre en compte les effets de déplacement et de déformation du pic de transmission de la réponse instrumentale.

La calibration en longueur d'onde du 3D-NTT en mode haute résolution utilisera la même procédure que celle décrite dans la partie 1.2.5. La calibration en mode basse résolution, quant à elle, est différente car la résolution spectrale ne permet pas de mesurer avec précision des anneaux d'interférence. La méthode sera la même que celle des instruments TTF et MMTF.

1.4 Étude du concept iBTF et d'une fonction de mérite dans le cadre du projet WFSpec

Après les télescopes de classe 10 *m*, la communauté scientifique se tourne vers des projets de télescopes de nouvelle génération de classe 40 *m*. Ces télescopes auront tout particulièrement besoin des dernières technologies d'optique adaptative afin de pouvoir corriger sur un champ de l'ordre de 10' les effets de la turbulence atmosphérique en utilisant plusieurs étoiles lasers (LTAO, MOAO, ...) afin d'atteindre des résolutions spatiales limitées par l'ouverture du télescope (tache d'Airy) dans le but d'observer des objets de petites tailles qui ne peuvent pas être résolus avec les télescopes actuels. Les objectifs principaux de ces télescopes sont donc l'étude de populations stellaires résolues extragalactiques (dans d'autres galaxies que la Voie Lactée), la détection de planètes extra-solaires ainsi que l'étude de l'évolution de l'Univers, en particulier par l'étude à haute résolution de champs profonds.

Dans le cadre de cette dernière thématique, un groupe de travail s'est formé afin de réfléchir à diverses solutions pour réaliser la spectroscopie à champ intégral sur un grand champ pour le futur ELT européen : WFSpec (PI : J.-G. Cuby). J'ai participé à ce groupe de travail pour étudier le concept iBTF, un des trois concepts instrumentaux qui ont émergé du projet et pour lesquels j'ai également défini et étudié la fonction de mérite afin de déterminer le plus performant qui fera l'objet d'une étude plus poussée. Les laboratoires ayant participé à ce projet sont le LAM (Marseille), le CRAL, le GÉPI (Paris) en collaboration avec les entreprises ONÉRA et Photon etc.

1.4.1 Les concepts de WFSpec

Trois études ont été menées sur trois concepts différents avec des spécifications identiques : 48 détecteurs de 4096×4096 pixels, un échantillonnage spatial de 58 mas/pixel adapté à la résolution que l'optique adaptative souhaite atteindre sur ce type de télescopes, une résolution spectrale de 5000 et une couverture spectrale dans l'infrarouge de $1.46 \mu\text{m}$ à $2.21 \mu\text{m}$. Le champ corrigé par l'optique adaptative est supposé atteindre $10' \times 10'$. L'article présentant ces trois concepts est en Annexe A.3. Toutefois, une description sommaire est présentée afin de mettre en évidence les caractéristiques utilisées pour la comparaison de leurs performances.

1.4.1.1 Concept de champ monolithique : "mono-IFU"

Ce concept utilise un champ d'un seul bloc de $0.4' \times 0.4'$ et une couverture spectrale continue. Le champ est découpé en 48 sous-champs par un diviseur de champ ("image splitter"). Chaque sous-champ est découpé et réordonné le long d'une fente virtuelle par un découpeur d'image ("image slicer"). Le spectre de chacune des fentes virtuelles est dispersé par un réseau sur un des 48 récepteurs.

Les Figures 1 et 2 (référencées Figures A.18 et A.19 dans la table des figures) de l'article présenté dans l'Annexe A.3 illustrent ce concept.

1.4.1.2 Concept de champ subdivisé : "multi-IFU"

Ce concept peut utiliser jusqu'à 40 IFU indépendamment positionnés dans le champ corrigé de $10' \times 10'$. Un IFU est composé d'une mosaïque de fibres permettant de couvrir un champ de vue modeste. Les fibres sont réordonnées le long d'une (ou plusieurs) fente et le spectre est dispersé par un réseau. Chaque IFU est imagé sur un (ou plusieurs) des 48 détecteurs, pour un champ total de $0.4' \times 0.4'$. Ce concept est illustré sur la Figure 3 (Figure A.19 dans la table des figures) de l'article présenté dans l'Annexe A.3. Dans la suite nous considérons que cet instrument dispose de 24 IFU.

1.4.1.3 Concept de filtre accordable : iBTF

Au lieu de découper le champ de vue comme dans les concepts précédents, nous avons réfléchi à un concept qui pourrait découper le spectre. En effet, dans le spectre infrarouge, certaines bandes sont très atténuées par l'absorption de l'atmosphère (voir Figure 1.15, gauche). De plus, de nombreuses raies très intenses du ciel nocturne (voir Figure 1.15, droite) font que toute étude spectrale est impossible. En découplant le spectre, les domaines non exploitables vont pouvoir être exclus afin de diminuer le nombre d'éléments spectraux sans perdre d'information utile. Ainsi, tout l'espace détecteur non utilisé par le spectre peut être utilisé pour observer un champ plus grand (voir Figure 1.16). Mon travail sur ce projet a consisté à participer aux réflexions qui ont abouti aux caractéristiques techniques du concept iBTF décrites dans l'article Moretto et al. (2006) (voir l'Annexe A.3) et reprises ci-après. Je me suis plus particulièrement investi dans la définition des domaines spectraux utiles et dans les calculs de temps de pose et de rapports signal sur bruit.

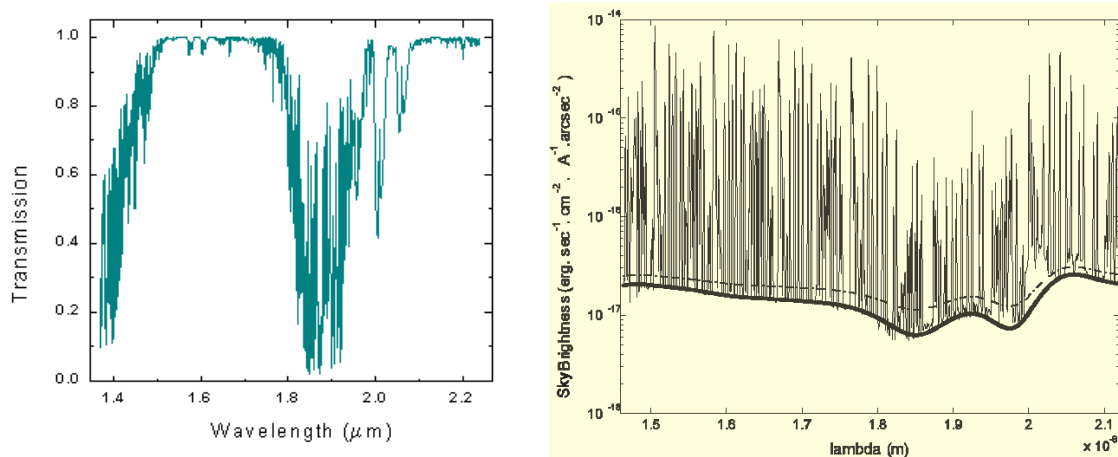


FIG. 1.15: **À gauche** : Transmission atmosphérique dans l'infrarouge proche ($1.4 \mu\text{m}$ à $2.2 \mu\text{m}$). La transmission est supérieure à 0.8 sur des domaines de longueurs d'onde disjointes, couvrant au total moins de $0.5 \mu\text{m}$ sur les $0.8 \mu\text{m}$ définissant le domaine spectral des instruments. **À droite** : Spectre en émission du ciel nocturne dans l'infrarouge proche ($1.4 \mu\text{m}$ à $2.2 \mu\text{m}$). Des raies d'émission sont présentes sur tout le spectre.

Le concept iBTF, comme son nom l'indique, utilise des filtres de Bragg. Ces filtres holographiques permettent d'extraire une composante spectrale d'un faisceau lumineux en la renvoyant dans une di-

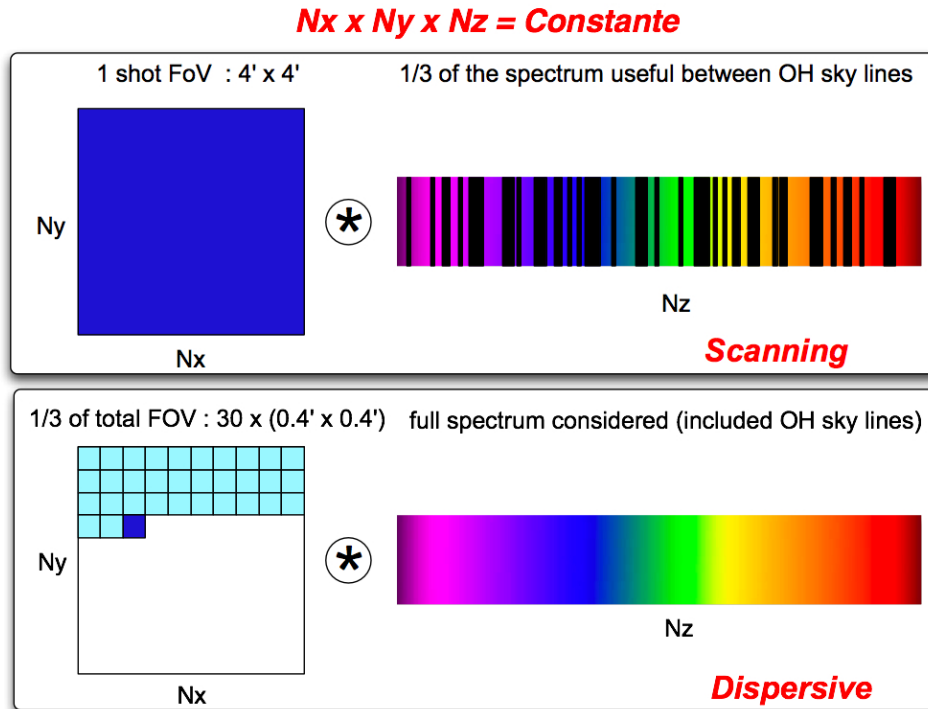


FIG. 1.16: Vue schématique comparant le fonctionnement des concepts dispersifs “multi-IFU” et “mono-IFU” (en bas) avec le concept à balayage iBTF (en haut). Pour un même temps de pose, tout le spectre est observé avec les systèmes dispersifs sur 30 champs élémentaires (en bas) tandis qu’un seul grand champ est observé en effectuant 30 pas de balayage pour obtenir le tiers utile du spectre (en haut). Au final, le nombre de pixels utilisés est le même : c’est le produit du nombre d’éléments d’échantillonnage spectral par le nombre d’éléments d’échantillonnage spatial.

rection différente de celle du faisceau incident, idéalement perpendiculaire. La composante non déviée du faisceau (que l’on appelle l’ordre 0) contient tout le spectre hormis le domaine qui a été extrait. Ainsi en plaçant 48 filtres de Bragg en cascade on va pouvoir extraire 48 bandes spectrales du faisceau principal chacune imagée sur un des 48 récepteurs. La Figure 4 (Figure A.21 dans la table des figures) de l’article présenté dans l’Annexe A.3 illustre ce concept. Cependant, chacune des bandes spectrales extraites de l’ordre 0 ne peut être suffisamment étroite pour atteindre la résolution souhaitée. En utilisant un Fabry-Perot à balayage en amont du faisceau (avant qu’il ne traverse la cascade de filtres de Bragg) et en le faisant balayer, on va ainsi atteindre la résolution souhaitée. En pratique, ce concept ira explorer environ le tiers du domaine spectral total (1400 éléments de résolution sur 4000 au total) en 30 pas de balayage pour obtenir la résolution spectrale de 5000 sur un champ total de $3.8' \times 3.8'$. En revanche, pour obtenir le même rapport signal sur bruit que les autres concepts, le temps de pose doit être 30 fois plus élevé. Cependant, à temps de pose égal, la surface du champ est tout de même trois fois plus grande puisque l’étendue du spectre est réduite d’un facteur trois. Le champ est tellement grand qu’il n’est pas nécessaire de réfléchir à une solution de type “multi-IFU”.

Ce concept purement théorique doit prouver sa faisabilité. En particulier, les premiers filtres de Bragg holographiques seront utilisés dans l’instrument BTFI (PI : C. Mendes de Oliveira) pour le télescope SOAR, un projet mené par l’USP/IAG (São Paulo) en collaboration avec l’INPE (São José dos Campos) et le LAM (Marseille).

1.4.2 Étude comparative d'une fonction de mérite pour les trois concepts

Afin de déterminer le concept le plus performant, j'ai été chargé de réaliser une étude des facteurs de mérite de ces instruments. Traditionnellement, une fonction de mérite doit prendre en compte tous les raffinements, tels que la transmission des optiques, le rendement quantique des détecteurs, le coût de l'instrument, le poids, etc. Pour le projet WFSpec, nous avons élaboré une fonction de mérite simple puisqu'il ne s'agit que de concepts :

$$M = \frac{FOV \times n}{m}$$

FOV est le champ de l'instrument, n est la densité d'objet dans le champ et m est le nombre de poses élémentaires pour obtenir le spectre total. Cette fonction de mérite est simplement le nombre d'objets par exposition élémentaire. Pour le concept iBTF, $m = 30$ car il est nécessaire de faire 30 pas d'échantillonnage spectral alors que pour les autres concepts, $m = 1$ puisqu'une seule exposition permet d'observer l'ensemble du spectre.

Cette étude a nécessité une compréhension précise des spécifications et des contraintes liées aux objectifs scientifiques des instruments. En particulier, WFSpec cherche à répondre à deux objectifs majeurs de l'étude de l'évolution de l'Univers qui sont la détection de galaxies primordiales et l'étude de l'assemblage de masse des galaxies (voir Annexe A.3). L'interprétation de la fonction de mérite diffère selon le cas scientifique étudié.

1.4.2.1 Détection de galaxies primordiales

Ce type d'étude consiste à observer un champ dans une direction de l'espace donnée pendant une longue durée (pouvant aller jusqu'à plusieurs jours) de sorte que des sources faibles émergent du bruit. L'obtention d'un spectre pour chaque élément de résolution spatiale permet d'améliorer la détection des sources par leurs raies d'émission. En effet, si une source possède des raies d'émission, alors le flux est bien plus intense aux longueurs d'onde où sont émises les raies qu'aux autres longueurs d'onde. Le rapport signal sur bruit est donc meilleur à cette longueur d'onde puisque le signal est celui de la raie et le bruit (poissonnien) est la racine carrée de l'ensemble du signal reçu à cette longueur d'onde, soit le signal de la raie ainsi que le flux provenant du fond de ciel et le flux continu de la source. Lorsqu'on utilise une imagerie classique, le flux reste celui de la raie (si on suppose que le continu de la source est faible) alors que le bruit est la racine carrée du flux détecté sur tout le spectre. Outre la détection, un des objectifs est de mesurer le décalage spectral spectroscopique des sources détectées en mesurant la position de plusieurs raies.

Un ELT devrait permettre de détecter des galaxies dont la magnitude en bande AB est inférieure à 28 avec un rapport signal sur bruit de cinq en 15 heures d'observation. À partir de l'extrapolation des observations actuelles ainsi qu'avec les simulations DM et SAM, la densité de galaxies devrait avoisiner les 100 galaxies par minute d'arc au carré pour des décalages spectraux variant de 6 à 15. La fonction de mérite est tracée pour les trois concepts en fonction de la densité de galaxies sur la Figure 1.17.

Le concept le plus performant est iBTF car le champ de vue est plus grand puisqu'on n'observe pas la partie inexploitable du spectre. En revanche, les temps de pose nécessaires sont très longs car on doit balayer le spectre. Étant donné qu'il faudrait typiquement 15 heures par pose élémentaire, cet instrument nécessiterait 450 heures pour observer tout le spectre. Un tel temps de pose, même s'il permet un champ très grand, est assez rédhitoire puisqu'il sera impossible de faire un programme court montrant la faisabilité du projet. Puisque les sources ne sont pas connues *a priori*, le concept

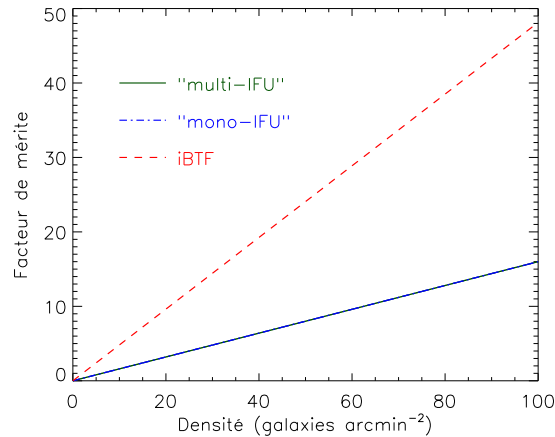


FIG. 1.17: Facteur de mérite dans le cadre de la détection de galaxies primordiales en fonction de la densité d'objets. La légende est indiquée sur la figure, cependant les courbes correspondant aux cas "mono-IFU" et "multi-IFU" sont confondues. Le facteur de mérite est supérieur pour le concept iBTF car le champ est plus grand et la couverture spectrale est moins importante.

"multi-IFU" ne présente aucun avantage en terme de champ de vue comparé au concept "mono-IFU" et leur fonction de mérite est donc identique.

1.4.2.2 Assemblage de masse dans les galaxies à travers les âges

L'objectif est d'étudier en détail la physique de galaxies déjà détectées et dont le décalage spectral spectroscopique est connu. L'étude du spectre (en particulier les raies d'émission) de ces galaxies pour chaque élément de résolution spatiale, va ainsi permettre de cartographier leur taux de formation d'étoiles, leur métallicité mais aussi leur cinématique afin de contraindre les modèles d'évolution des galaxies.

Un ELT devrait permettre de détecter des galaxies dont la magnitude en bande AB est inférieure à 25 avec un rapport signal sur bruit de cinq en huit heures d'observation. À partir d'observations de galaxies à cassure de Lyman⁴ (Steidel et al., 2004; Lehnert et Bremer, 2003), on s'attend, dans cette limite de magnitude, à pouvoir observer environ une dizaine de galaxies par minute d'arc au carré avec un décalage spectral compris entre 1 et 7, et ainsi observer plusieurs galaxies sur un seul champ. La fonction de mérite est tracée pour les trois concepts en fonction de la densité de galaxies sur la Figure 1.18 (gauche).

Contrairement au cas scientifique précédent, le concept "multi-IFU" présente un avantage en terme de champ de vue du fait que les sources sont connues *a priori* : les IFU vont pouvoir être placés n'importe où dans le champ de $10' \times 10'$ corrigé par l'optique adaptative. Le concept "multi-IFU" est donc largement supérieur aux deux autres concepts du fait que le champ total est très large. Le nombre d'IFU a été déterminé pour être adapté aux densités attendues. Notons quand même que plus le décalage spectral est important, plus la densité d'objets devient faible. Cependant, dès lors que la densité est supérieure à 0.2 galaxies par minute d'arc au carré, le concept "multi-IFU" est extrêmement performant puisqu'il y a assez d'objets dans le champ corrigé par l'optique adaptative pour utiliser tous les IFU. Dès lors que tous les IFU sont utilisés, le facteur de mérite croît au même rythme que pour le concept "mono-IFU".

⁴en anglais : Lyman break galaxies

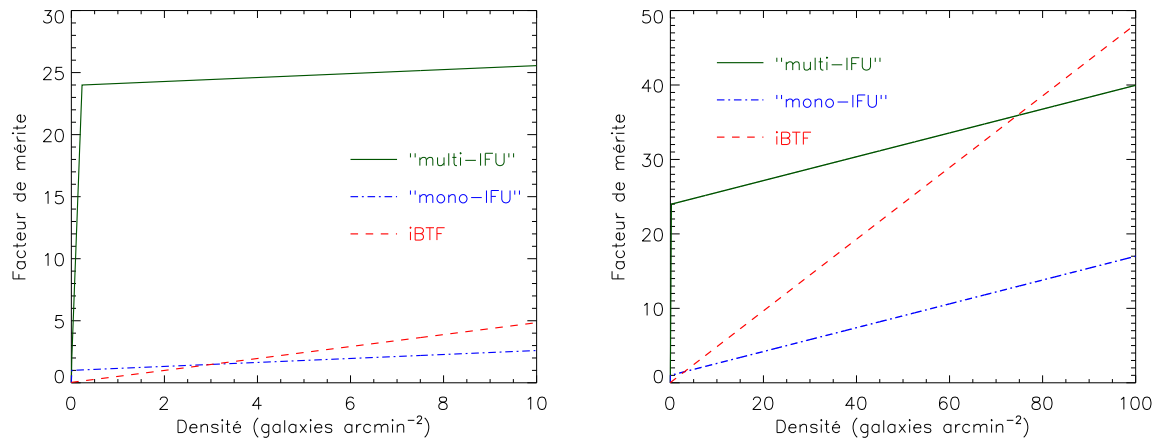


FIG. 1.18: Facteur de mérite dans le cadre de l'assemblage de masse des galaxies en fonction de la densité d'objets. La légende est indiquée sur la figure. **À gauche** : Pour des densités inférieures à dix galaxies par minute d'arc au carré, le concept "multi-IFU" est largement supérieur aux deux autres concepts. Le facteur de mérite de concept croît très vite tant qu'il y a moins d'objets dans le champ total corrigé par l'optique adaptative que d'IUF. Une fois que chaque IFU observe un objet, la fonction croît comme s'il n'y avait pas d'IFU. Le facteur de mérite du concept "mono-IFU" démarre à un puisqu'on va nécessairement choisir un champ avec au minimum un objet. Celui de l'iBTF démarre plus bas car même si on choisit le champ pour avoir un objet, il est nécessaire de faire 30 expositions pour avoir le spectre complet. **À droite** : Dès lors que la densité dépasse 80 galaxies par minute d'arc au carré, le concept iBTF devient plus intéressant que le concept "multi-IFU"

On observe tout de même que le facteur de mérite du concept iBTF croît plus rapidement que pour les deux autres concepts. Pour des densités très élevées, ce concept devient donc plus intéressant que le concept "multi-IFU" (Figure 1.18, droite).

1.4.2.3 Choix du concept de type multi-IFU : EAGLE

La fonction de mérite utilisée permet donc de différencier les différents concepts. En particulier, on voit bien que le projet iBTF constituerait un bon compromis entre les deux thématiques. Cependant, du fait des temps de pose induits par le mode d'observation (balayage du spectre dans le temps) et du fait du faible avancement technologique de ce projet, il n'est pas raisonnable d'envisager l'utilisation de ce concept pour une première génération d'instruments pour les ELT.

Étant donnée l'équivalence en terme de fonction de mérite des deux concepts "mono-IFU" et "multi-IFU" pour la détection de galaxies primordiales et vu l'avantage incomparable que représente la solution "multi-IFU" pour l'étude de l'assemblage de masse dans les galaxies à travers les âges vu la faible densité d'objets attendue, ce concept a été retenu par le groupe de travail WFSpec, même s'il représente une difficulté technologique plus importante que le concept "mono-IFU". Ce projet a été baptisé EAGLE (PI : J.-G. Cuby), acronyme de ELt Ao for GaLaxy Evolution.

1.4.3 Quel avenir pour iBTF ?

Le concept iBTF est un concept innovant tant au point de vue technologique qu'au point de vue observationnel. En effet, il permet de séparer plusieurs composantes spectrales d'une image en une

unique exposition. Le couplage avec un Fabry-Perot permet de doper la résolution spectrale. De plus, l'ordre zéro contenant tous les domaines non extraits peut être imagé. Ainsi, aucune lumière n'est perdue et on peut faire de l'imagerie profonde simultanément à l'acquisition du spectre. Il est dans ce cas intéressant d'utiliser un filtre supprimeur des raies d'émission du ciel nocturne (OH) afin de maximiser le rapport signal sur bruit dans l'ordre zéro (continuum). Par ailleurs, ce concept peut être amélioré en utilisant des filtres de Bragg accordables. Pour le projet WFSpec, la majorité des filtres de Bragg utilisés extraient un domaine spectral fixe. Il est possible de faire varier la bande spectrale moyennant un encombrement plus important afin d'ajouter un système de contrôle. L'accordabilité des filtres de Bragg peut se faire en modifiant leur inclinaison. La difficulté principale vient du fait que pour être capable de faire de l'imagerie avec les filtres de Bragg, il est nécessaire d'en utiliser deux. Le premier sélectionne la bande spectrale mais disperse la lumière comme le ferait un réseau. Le second est utilisé pour compenser cette dispersion. L'accordabilité nécessite de contrôler l'inclinaison des deux filtres simultanément et d'ajuster la position de l'image sur le détecteur. Une autre solution est d'utiliser les propriétés acousto-optiques de cristaux biréfringents : en appliquant une onde ultra sonore au cristal biréfringent (filtre de Bragg) et en faisant varier sa longueur d'onde, la biréfringence du cristal va changer induisant une variation de la bande spectrale.

L'étude de la fonction de mérite a montré que cet instrument est particulièrement adapté pour des thématiques où la densité d'objets est très élevée et pour des objets s'accommodant de temps d'exposition courts ou d'une basse résolution spectrale afin de réduire le nombre de pas de balayage. L'étude de populations stellaires résolues dans les galaxies proches semble donc être la thématique la plus appropriée pour l'utilisation de ce nouveau concept.

Chapitre 2

GHASP, échantillon cinématique de 203 galaxies locales isolées

Résumé

2.1 Le projet GHASP	37
2.2 Présentation des données scientifiques	42
2.3 Exploitation des données cinématiques	107

Ce chapitre présente le projet GHASP et ses objectifs. La production de masse des données cinématiques pour l'échantillon GHASP est décrite dans deux publications. Les nouvelles méthodes utilisées pour obtenir les cartes cinématiques et en extraire les paramètres de projection cinématiques ainsi que les courbes de rotation y sont également détaillées, donnant lieu à une comparaison des paramètres de projection cinématiques et morphologiques et à l'étude de la relation de Tully-Fisher. Ces articles représentent le cœur du travail effectué durant cette thèse. Enfin, une ébauche de l'analyse des propriétés cinématiques de cet échantillon local est présentée sous forme d'un article en préparation.

2.1 Le projet GHASP

2.1.1 Définition et objectifs de l'échantillon GHASP

L'échantillon GHASP est composé de 203 galaxies spirales et irrégulières isolées, observées autour de la raie H α avec l'instrumentation GHASP (partie 1.3.1) entre 1998 et 2004 sur 14 périodes d'observation. C'est l'échantillon contenant le plus grand nombre de galaxies observées avec les techniques de Fabry-Perot à ce jour. Les galaxies sont situées dans l'hémisphère Nord puisqu'elles ont été observées depuis l'Observatoire de Haute Provence dont la latitude est légèrement inférieure à +44° (voir Figures 2.1 et 2.2).

Les détails concernant l'élaboration de l'échantillon sont détaillés dans la thèse d'Olivia Garrido (Garrido, 2003a) qui a effectué une grande partie des observations de ce programme. Les objectifs scientifiques qui ont abouti à la définition de cet échantillon sont multiples :

- Calculer la relation de Tully-Fisher locale ;

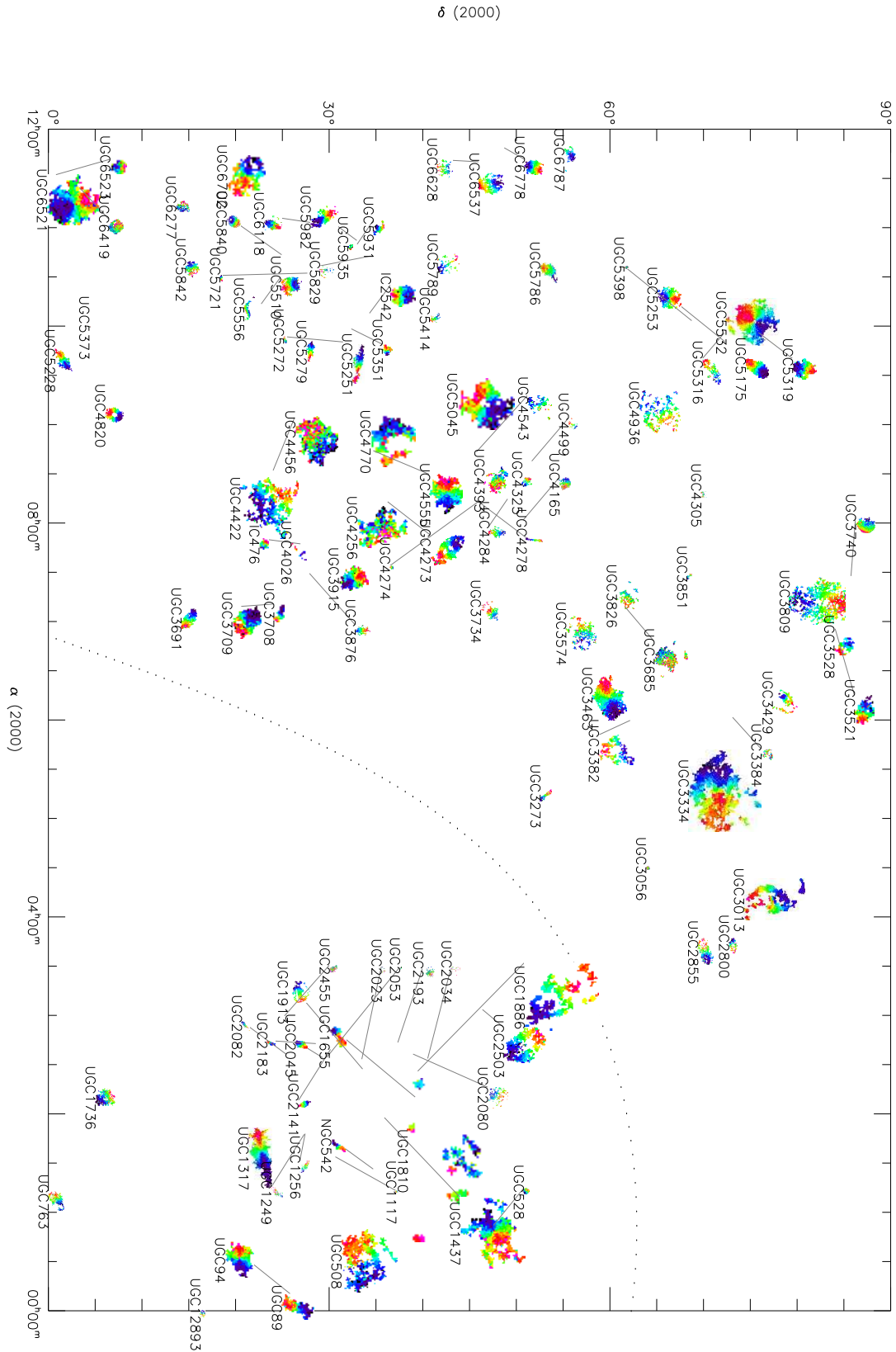


FIG. 2.1: Distribution des galaxies GHASP sur la voûte céleste pour des ascensions droites comprises entre 0h et 12h. Les tailles physiques relatives des galaxies (et non les dimensions angulaires) sont respectées. La même échelle est utilisée pour dimensionner les galaxies de la Figure 2.2. Le trait pointillé correspond au plan galactique. On observe une répartition uniforme de galaxies GHASP, hormis dans le plan galactique.

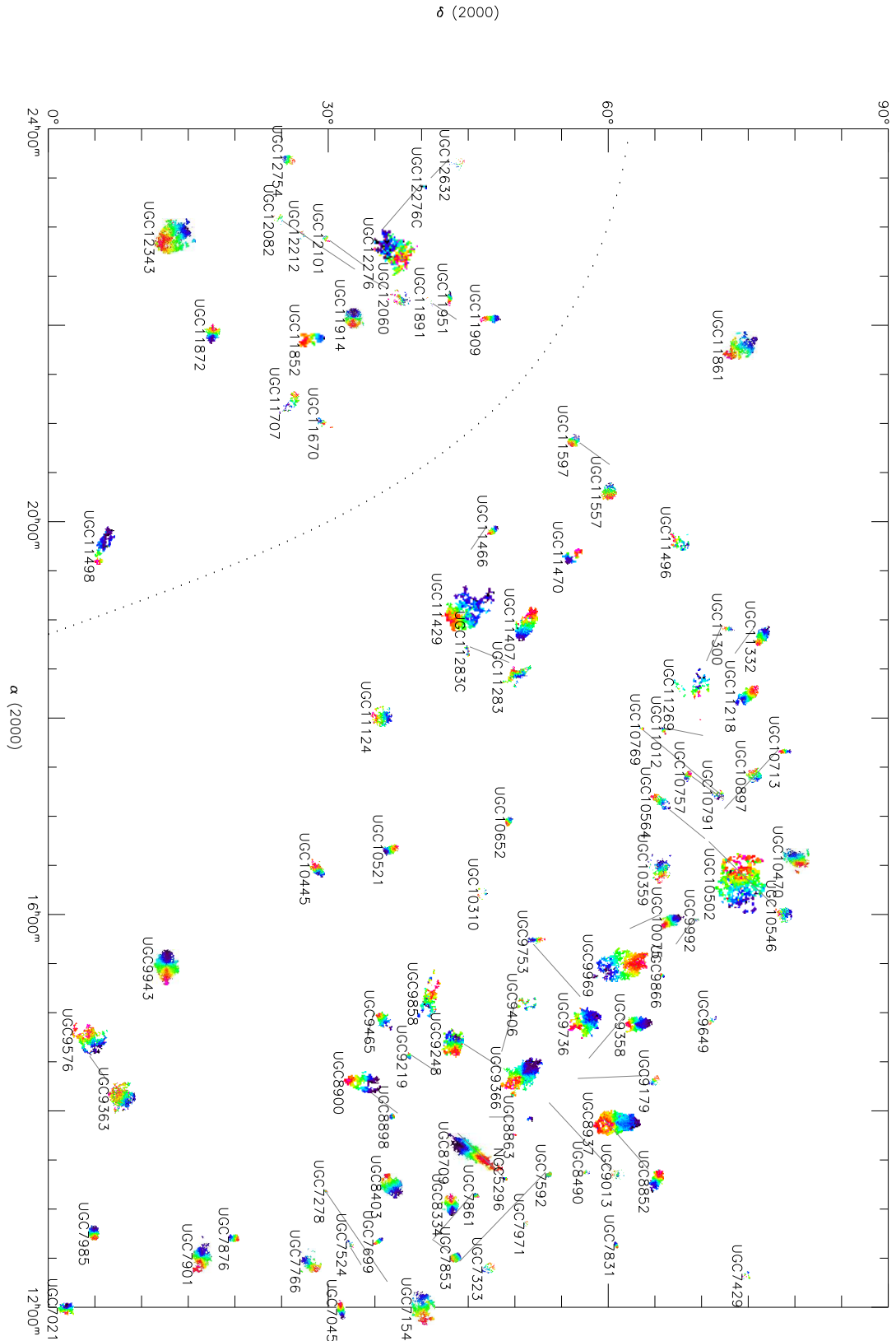


FIG. 2.2: Distribution des galaxies GHASP sur la voûte céleste pour des ascensions droites comprises entre 12h et 24h. Les tailles physiques relatives des galaxies (et non les dimensions angulaires) sont respectées. La même échelle est utilisée pour dimensionner les galaxies de la Figure 2.1. Le trait pointillé correspond au plan galactique. On observe une répartition uniforme de galaxies GHASP, hormis dans le plan galactique.

- Étudier la distribution de matière de la composante lumineuse et du halo de matière sombre, à travers la séquence de Hubble, pour des galaxies à faible et forte brillance de surface et pour un grand intervalle de magnitude. Cette étude se fait habituellement par l'ajustement de modèles de masse sur des courbes de rotation hybrides combinant les données optiques et radio (Barnes et al., 2004; Spano et al., 2008). Une des ambitions de ce programme est de chercher la distribution de masse non plus sur une dimension spatiale (le rayon), mais sur les deux dimensions spatiales en utilisant les champs de vitesses 2D, de l'imagerie à bande large pour déterminer le potentiel 2D des étoiles et des modèles d'évolution spectrophotométrique des étoiles afin de contraindre le rapport masse sur luminosité des galaxies ;
- Comparer la cinématique dans des environnements variés (champ, paires, groupes compacts, galaxies d'amas) afin de dissocier l'évolution propre des galaxies dite séculaire de l'évolution due à une origine extérieure (Garrido et al., 2005) ;
- Produire un échantillon de référence de galaxies locales afin de comparer leur cinématique avec la cinématique de galaxies à grand décalage spectral (Epinat et al., 2007; Puech et al., 2008). Il est primordial de pouvoir dissocier les effets de résolution spatiale et spectrale des effets d'évolution des galaxies ;
- Modéliser les effets de structures non-axisymétriques comme les bras spiraux, les barres, les distorsions ovales en utilisant des simulations numériques N -corps et hydrodynamiques, des études kinémétriques (Krajnović et al., 2006) et la méthode Tremaine-Weinberg pour mesurer les motifs de vitesse des barres, des spirales et des structures internes (Hernandez et al., 2005) ;
- Analyser la dispersion de vitesses du gaz ionisé et chercher des liens avec la dispersion de vitesses des étoiles ;
- Créer des courbes de rotation et des champs de vitesses types (Persic et Salucci, 1991; Persic et al., 1996; Catinella et al., 2006) ;
- Comprendre les liens entre la cinématique (forme de la courbe de rotation, moment angulaire, ...) et les propriétés physiques des galaxies telles que le taux de formation stellaire en comparant, par exemple, à ce qui se passe pour des galaxies à fort taux de formation d'étoiles comme les galaxies bleues compactes.

Certains de ces objectifs ont été abordés pendant la thèse et sont exposés dans les sections 2.3 et 3.4. Ces données servent de point de départ à l'élaboration d'une nouvelle base de données Fabry-Perot présentée en Annexe D.4.

2.1.2 Étude du gaz ionisé à partir de la raie $H\alpha$

La raie $H\alpha$ est le nom que les astronomes utilisent pour faire référence à la raie d'émission produite par les atomes d'hydrogène neutre correspondant à la transition de Balmer α observable dans le rouge (656.3 nm)¹. Elle est générée par la désexcitation des électrons passant du niveau d'énergie $n = 3$ au niveau $n = 2$. Pourtant, la raie $H\alpha$ trace les régions contenant du gaz ionisé. En effet, les régions de gaz ionisé sont des zones de formation stellaire : le rayonnement ultra-violet d'énergie supérieure à 13.6 eV émis par les étoiles jeunes ionise le gaz d'hydrogène neutre à partir duquel elles ont été formées. Dans ce milieu de gaz ionisé (atomes d'hydrogène neutres, protons, électrons, photons ionisants) protons et électrons sont en recombinaison et ionisation permanentes. Lors de la recombinaison d'un électron avec un atome d'hydrogène, la probabilité qu'il utilise la transition de Balmer α pour revenir au repos est environ de 0.5, ce qui explique que le milieu de gaz ionisé émette intensément dans le raie $H\alpha$. Ces régions de gaz ionisé, également appelées régions HII, contiennent également des

¹Historiquement, la série de Balmer a été découverte en premier car c'est la seule à émettre des photons dans le domaine visible.

ions He^+ , O^+ , O^{++} , N^+ , S^+ et S^{++} qui possèdent également des raies d'émission dans le domaine visible. Elles sont principalement situées dans les zones de surdensité de matière que sont les bras spiraux. Cette surdensité comprime le gaz moléculaire provoquant son effondrement et la formation de proto-étoiles. Les étoiles excitatrices étant des étoiles de type OB dont la température effective est comprise entre 25000 et 50000 K , dont la masse est supérieure à $10 M_{\odot}$ et dont la durée de vie est inférieure à 10 millions d'années, les régions HII sont donc de bons traceurs de la formation stellaire récente. Les régions HII observables ont une faible densité électronique (quelques électrons par cm^3), une masse pouvant atteindre $10^4 M_{\odot}$ pour une dimension de l'ordre de la centaine de parsecs et une température électronique de 10000 K . Au delà de la sphère Strömgren à l'intérieur duquel tout le rayonnement ionisant est absorbé, le milieu n'est pas ionisé puisque l'ensemble du rayonnement ionisant a été absorbé en chemin. Ce milieu est donc froid ($\sim 100 K$), ce qui induit l'expansion de ces nébuleuses à une vitesse de l'ordre de la dizaine de km s^{-1} .

Il existe également dans les galaxies des régions de gaz diffus ionisé. Ce gaz diffus a été mis en évidence dès 1971 (Monnet, 1971) dans les régions inter-bras de nombreuses galaxies Sc. Il se présente sous forme de filaments, boucles ou coquilles, notamment au sein du halo et est probablement ionisé par les étoiles du disque. L'émission de ce milieu représente entre 25 et 50% de l'émission $\text{H}\alpha$ totale (Ferguson et al., 1996).

Outre l'information stellaire que les raies d'émission apportent, l'observation de ces raies est particulièrement adaptée à l'étude de la cinématique des galaxies car elles permettent d'obtenir un rapport signal sur bruit bien plus élevé que l'observation de raies d'absorption. Le moment d'ordre 0 de la raie nous donne accès au flux, ce qui est une information quant au taux de formation stellaire et les moments d'ordres supérieurs sont utilisés pour les études cinématiques. L'analyse des moments de raies est détaillée en Annexe C.1.1. La raie $\text{H}\alpha$, qui a une intensité élevée par rapport aux autres raies d'émission du domaine visible, est d'autant plus adaptée aux études cinématiques puisqu'une mesure précise des moments de raies nécessite un rapport signal sur bruit qui augmente avec l'ordre du moment. Toutefois, par rapport aux raies d'absorption stellaires, les raies d'émission présentent l'inconvénient de tracer principalement la cinématique du gaz, donc des structures telles que les spirales, dont les mouvements ne sont pas purement circulaires.

Pendant longtemps, les observations cinématiques ont été réalisées avec des spectrographes à fente placée le long du grand axe déterminé par la morphologie afin d'étudier la raie $\text{H}\alpha$. La plupart des études sur la forme des courbes de rotation ont ainsi utilisé de très grands échantillons observés à partir de spectroscopie à fente (Mathewson et al., 1992; Persic et al., 1996; Catinella et al., 2006). Cependant, depuis une vingtaine d'années, les observations spectroscopiques à champ intégral se multiplient : les techniques de Fabry-Perot permettent d'observer tout le disque optique et les IFU permettent d'observer soit les régions internes de galaxies proches (e.g. Falcón-Barroso et al., 2006), soit les galaxies distante (e.g. Flores et al., 2006; Genzel et al., 2006; Law et al., 2007). L'utilisation d'observations spectroscopiques à champ intégral permet de sonder les mouvements non circulaires dans les galaxies et également de déterminer des courbes de rotation moins biaisées par la présence de structures telles que des bras spiraux ou des barres. Elle permet également d'étudier la cinématique indépendamment de l'étude morphologique. Des cartes cinématiques sont également déduites des observations de la raie HI réalisées avec des radiotélescopes à synthèse d'ouverture. L'avantage des techniques radio est que le gaz neutre peut être détecté sur des échelles supérieures à plusieurs diamètres optiques. La résolution spatiale de ces instruments dépend de la longueur des lignes de base l séparant les diverses antennes (λ/l est la résolution angulaire qui peut être atteinte), de la direction de ces lignes de base et de la latitude de la source. La meilleure résolution pourrait ainsi être atteinte sur Terre en plaçant deux antennes ou plus en des lieux diamétralement opposés de la planète pour avoir les lignes de base les plus longues possibles. Pour des raisons de flux et donc de

durée d'exposition, la résolution spatiale typique en radio est inférieure d'un facteur 10 à celle que le domaine optique atteint usuellement, ce qui fait que les données optiques, en particulier la raie $H\alpha$, sont bien mieux adaptées à l'étude de la courbe de rotation dans les régions internes. Cela est important notamment pour contraindre la forme des halos de matière sombre.

2.2 Présentation des données scientifiques

Les données Fabry-Perot nécessitent une réduction adaptée. Un des premiers logiciels développés pour réduire les données Fabry-Perot est le logiciel CIGALE développé par Jacques Boulesteix au début des années 1980 sur des machines utilisant le système d'exploitation VMS pour réduire les données de l'instrument CIGALE alors installé au CFHT. Par la suite, Jacques Boulesteix développa ADHOC en 1993 puis l'adapta pour Windows (ADHOCw) en 1999. Ce logiciel très éprouvé et très didactique bénéficie de très bons outils de visualisation et de manipulation des données, ainsi que de programmes connexes extrêmement utiles lors des observations. Parallèlement, un autre outil de réduction a été développé sous UNIX en langage C à partir de 1988, puis C++ à partir de 2000 par Étienne Le Coarer pour le dépouillement des données CIGALE observées avec le télescope de 36 cm de la Silla (ESO) correspondant au sondage du plan Galactique et aux nuages de Magellan (Le Coarer et al., 1992). Ce programme dispose d'outils spécifiques pour la visualisation et la décomposition des profils. Il cherche à minimiser l'occupation de l'espace disque par les produits de réduction en utilisant un algorithme de compression et en n'enregistrant que le produit final.

Afin de pouvoir étudier l'échantillon complet de façon homogène, de nouvelles procédures de réduction et d'analyse des données ont été développées (Daigle et al., 2006) sous IDL. Ces nouvelles procédures tendent à être le plus automatisé possible afin de rendre les résultats indépendants de la personne qui analyse les données. J'ai participé activement au développement de certaines routines de ce logiciel de réduction. L'utilisation de l'environnement IDL a été motivé par le fait (i) qu'il fonctionne quel que soit le système d'exploitation utilisé, (ii) qu'IDL possède un environnement de base très riche ainsi que de bibliothèques astronomiques très utiles et (iii) que ce logiciel peut se prêter à modification ou à des ajouts car le code est disponible librement.

2.2.1 Des données d'observation aux cartes cinématiques

La réduction des données a pour objectif de créer un cube de données calibré à partir des interférogrammes d'observation et d'en extraire les cartes cinématiques. Le manuel d'utilisation du programme de réduction présentant les étapes de réduction ainsi que toutes les options de réduction est disponible en Annexe B. Ce manuel d'utilisation a initialement été écrit par Olivier Daigle en français. Je l'ai traduit en anglais et mis à jour avec les modifications que j'ai apportées au programme. Les étapes de réduction appliquées pour réduire l'échantillon GHASP et leurs options sont les suivantes :

- Intégration des données en corrigeant la dérive de suivi du télescope lorsque le champ contient suffisamment d'étoiles. Cette dérive atteint jusqu'à 8 pixels dans certains cas. Les poses élémentaires ayant un flux incompatible avec le flux médian sont supprimées ou remplacées par les poses des cycles d'observation adjacents de manière automatique.
- Création d'un cube calibré en longueur d'onde.
- Soustraction des raies d'émission du ciel nocturne en utilisant un ajustement polynomial d'ordre 2. Dans les quelques cas où la galaxie est trop grande, un spectre médian a été soustrait. Ces raies sont majoritairement produites par les radicaux OH présents dans les couches atmosphériques d'une dizaine de kilomètres d'épaisseur situées à une altitude d'environ 100 km

(Rousselot et al., 2000). Ces radicaux sont créés par la réaction entre l'hydrogène et l'ozone ($H + O_3 \rightarrow OH + O_2$). Le problème principal de ces raies est leur forte et rapide variation spatiale et spectrale.

- Éventuelle suppression des réflexions parasites.
- Éventuelle addition d'observations multiples d'un même objet en utilisant l'astrométrie.
- Lissage spectral de Hanning.
- Lissage spatial adaptatif (inspiré de Cappellari et Copin, 2003) avec un rapport signal sur bruit défini comme étant la racine carrée du flux. L'objectif est d'atteindre un rapport signal sur bruit de 7.
- Calcul de l'astrométrie.
- Correction de l'incertitude sur l'intervalle spectral libre.
- Création des cartes et filtrage.

Un cube de données possède deux dimensions spatiales et une dimension spectrale. Ainsi, un spectre est mesuré pour chaque élément de résolution spatiale (pixel). Pour chaque pixel, on va utiliser le spectre pour mesurer le flux émis par la raie, sa position en longueur d'onde et sa largeur, et ainsi obtenir des cartes pour chacune de ces grandeurs. La méthode utilisée sur l'échantillon GHASP pour extraire ces grandeurs est la méthode des moments : le flux est l'ordre 0 du spectre, la position est l'ordre 1 et la dispersion est l'ordre 2 (voir l'Annexe C.1 pour les détails). On déduit la vitesse et la dispersion de vitesses à partir des mesures en longueur d'onde grâce à l'effet Doppler-Fizeau. L'Annexe C.2 détaille le calcul utilisé pour déterminer la vitesse et la dispersion de vitesses dans le cadre relativiste de l'effet Doppler-Fizeau. La technique de lissage adaptatif est utilisée pour avoir un rapport signal sur bruit correct même dans les régions où le flux est faible, en particulier pour le gaz diffus ionisé qui n'est pas aisé à détecter. Il s'agit d'une accréation de pixels : tant que le rapport signal sur bruit recherché dans le spectre n'est pas atteint, les pixels sont accrétés. Ainsi, le spectre des régions de faible flux n'est pas corrélé avec les régions à fort flux.

2.2.2 Analyse des cartes de vitesses

L'analyse dont il est question ici consiste à extraire les paramètres cinématiques déduits des champs de vitesses et leurs erreurs associées. Ces paramètres sont les paramètres de projection de la galaxie (inclinaison, angle de position du grand axe, vitesse globale de la galaxie dite vitesse systémique) ainsi que la courbe de rotation de la galaxie. Le cœur des méthodes utilisées est décrit dans les articles, je me contente donc ici de mentionner les grandes lignes.

Un modèle de disque fin avec une courbe de rotation paramétrique tirée de Kravtsov et al. (1998) est ajusté aux données par une méthode des moindres carrés afin de déterminer ses paramètres. L'algorithme utilisé est l'algorithme de Levenberg-Marquardt (Vetterling et al., 1989), qui permet d'effectuer l'ajustement de modèles non linéaires aux données. La librairie IDL de Markwardt MPFIT a été utilisée. Cet algorithme utilise les dérivées partielles par rapport aux variables pour converger vers une vallée de moindres carrés. Des cas d'école de champs de vitesses obtenus avec quatre formes de courbes de rotation sont présentés dans la Figure 6 (Figure 3.9 dans la table des figures) de l'article présenté dans la partie 3.4.

Cette méthode a été développée pour deux raisons. Jusqu'à présent, deux méthodes étaient couramment utilisées. La première est une détermination manuelle des paramètres afin de symétriser au mieux la courbe de rotation. Un premier inconvénient de cette méthode est que la détermination des paramètres est dépendante de l'utilisateur, mais le principal problème est que les erreurs ne peuvent pas vraiment être mesurées. Une solution serait la détermination des paramètres indépendamment par plusieurs utilisateurs, ce qui, en pratique, demande beaucoup de temps et de ressources humaines.

La seconde méthode, utilisée par le logiciel GIPSY, est une méthode dite de “tilted ring model”. La galaxie est découpée en anneaux. Pour chaque anneau, un jeu de paramètres est alors ajusté par une méthode de moindres carrés, avec une erreur statistique pour chaque paramètre et pour chaque couronne. Cette méthode est particulièrement adaptée aux données possédant beaucoup de points afin d’avoir une statistique suffisante pour chaque anneau, ce qui est le cas des données H α pour lesquelles un gauchissement des disques est potentiellement observable. De tels gauchissements sont bien plus rares dans le disque optique et donc en H α . La décomposition en anneaux engendre donc une difficulté quant à une définition unique des paramètres de projection pour chaque galaxie. Il était donc nécessaire de faire l’ajustement d’un modèle possédant une seule inclinaison, un seul grand axe, une seule vitesse systémique et un seul et unique centre pour chaque galaxie. Par ailleurs, une détermination robuste et réaliste des erreurs a été mise au point en utilisant la carte des résidus du modèle. Ces méthodes sont décrites en détail dans les articles qui suivent.

Grâce à ces nouvelles méthodes, j’ai pu réduire et analyser l’ensemble de l’échantillon. Deux articles acceptés dans une revue à comité de lecture² ont résulté de ces travaux (Epinat et al., 2008b,a). Ces articles présentent les cartes déduites de la réduction des données ainsi que la comparaison des paramètres de projection déduits de la cinématique et de la morphologie. Une relation de Tully-Fisher est également dérivée à partir de l’échantillon GHASP et des commentaires galaxie par galaxie sont présentés. Ils exposent la description de la cinématique déduite de nos données et la mettent principalement en regard avec les études cinématiques de la littérature.

2.2.3 **Article I : GHASP : an H α kinematic survey of spiral and irregular galaxies - VI. New H α data cubes for 108 galaxies**

Cet article présente les données correspondant aux sept dernières périodes d’observation du programme GHASP. La méthode d’ajustement des modèles y est présentée et chacune des galaxies a été commentée individuellement. Les cartes ainsi que les courbes de rotation sont respectivement présentées en Annexe D.1 et D.2 de la thèse afin de regrouper l’intégralité des images des deux articles.

Nous présentons les observations Fabry-Perot pour un nouvel ensemble de 108 galaxies dans le cadre du programme GHASP. Ce relevé est composé de cubes de données pour 203 galaxies spirales et irrégulières autour de la raie H α afin d’en étudier la cinématique et couvre un grand intervalle de types morphologiques et de magnitudes. Les nouvelles données présentées dans cet article complètent le relevé. L’échantillon GHASP est désormais le plus grand échantillon de données Fabry-Perot jamais publié. L’analyse de l’échantillon complet sera présenté dans de prochains articles. En utilisant les techniques de lissage adaptatif basées sur un maillage de Voronoï, nous avons créé des cubes de données H α à partir desquels les cartes de flux H α , les champs de vitesses ainsi que les champs de vitesses résiduels, les diagrammes position-vitesse, les courbes de rotation et les paramètres cinématiques ont été extraits pour presque toutes les galaxies. La détermination des paramètres cinématiques, des courbes de rotation et des incertitudes associées résulte de nouvelles méthodes implémentées dans la procédure de traitement des données. Cette nouvelle détermination repose sur l’utilisation de la totalité du champ de vitesses 2D et du spectre de puissance du champ de vitesses résiduel alors que les techniques classiques utilisent une décomposition du champ de vitesses en anneaux. Parmi les résultats présentés, nous montrons que les angles de position du grand axe morphologique ont des barres d’erreurs systématiquement plus importantes que pour les déterminations cinématiques, en particulier pour les systèmes faiblement inclinés. Les inclinaisons

²Monthly Notices of the Royal Astronomical Society

morphologiques des galaxies pour lesquelles la détermination de l'angle de position morphologique est très incertaine ne sont pas très fiables. Les galaxies qui ont une forte inclinaison présentent un meilleur accord entre l'inclinaison cinématique et l'inclinaison morphologique calculée en supposant un disque fin. Nous avons utilisé la relation de Tully-Fisher pour vérifier la consistance de nos mesures de vitesses maximales à partir de nos courbes de rotation. Nos données sont en accord avec les précédentes déterminations de la relation de Tully-Fisher provenant de la littérature. Néanmoins, les galaxies de faible inclinaison présentent statistiquement des vitesses supérieures à ce qui est attendu et les galaxies en rotation rapide sont moins lumineuses qu'attendu.

GHASP: an H α kinematic survey of spiral and irregular galaxies – VI. New H α data cubes for 108 galaxies

B. Epinat,^{1*} P. Amram,¹ M. Marcelin,¹ C. Balkowski,² O. Daigle,^{1,3} O. Hernandez,^{1,3}
L. Chemin,² C. Carignan,³ J.-L. Gach¹ and P. Balard¹

¹Laboratoire d'Astrophysique de Marseille, OAMP, Université de Provence & CNRS, 38 rue F. Joliot - Curie, 13388 Marseille, Cedex 13, France

²GEPI, Observatoire de Paris-Meudon, Université Paris VII, 5 Place Jules Janssen, 92195 Meudon, France

³LAE et Observatoire du mont Mégantic, Université de Montréal, C. P. 6128 succ. centre ville, Montréal, Québec, Canada H3C 3J7

Accepted 2008 May 7. Received 2008 May 4; in original form 2008 January 15

ABSTRACT

We present the Fabry–Perot observations obtained for a new set of 108 galaxies in the frame of the Gassendi H α survey of SPirals (GHASP). The GHASP survey consists of 3D H α data cubes for 203 spiral and irregular galaxies, covering a large range in morphological types and absolute magnitudes, for kinematics analysis. The new set of data presented here completes the survey. The GHASP sample is by now the largest sample of Fabry–Perot data ever published. The analysis of the whole GHASP sample will be done in forthcoming papers. Using adaptive binning techniques based on Voronoi tessellations, we have derived H α data cubes from which are computed H α maps, radial velocity fields as well as residual velocity fields, position–velocity diagrams, rotation curves and the kinematical parameters for almost all galaxies. Original improvements in the determination of the kinematical parameters, rotation curves and their uncertainties have been implemented in the reduction procedure. This new method is based on the whole 2D velocity field and on the power spectrum of the residual velocity field rather than the classical method using successive crowns in the velocity field. Among the results, we point out that morphological position angles have systematically higher uncertainties than kinematical ones, especially for galaxies with low inclination. The morphological inclination of galaxies having no robust determination of their morphological position angle cannot be constrained correctly. Galaxies with high inclination show a better agreement between their kinematical inclination and their morphological inclination computed assuming a thin disc. The consistency of the velocity amplitude of our rotation curves has been checked using the Tully–Fisher relationship. Our data are in good agreement with previous determinations found in the literature. Nevertheless, galaxies with low inclination have statistically higher velocities than expected and fast rotators are less luminous than expected.

Key words: galaxies: dwarf – galaxies: irregular – galaxies: kinematics and dynamics – galaxies: spiral.

1 INTRODUCTION

As it is nowadays largely admitted, 2D velocity fields allow the computation of 1D rotation curves in a more robust way than long-slit spectrography. Indeed, first of all, the spatial coverage is larger and moreover, the kinematical parameters are determined a posteriori instead of a priori in long-slit spectrography. In that context, we have undertaken the kinematical 3D Gassendi H α survey of SPirals

(GHASP). The GHASP survey consists of a sample of 203 spiral and irregular galaxies, mostly located in nearby low density environments, observed with a scanning Fabry–Perot for studying their kinematical and dynamical properties through the ionized hydrogen component.

Studying the links between parameters reflecting the dynamical state of a galaxy will help us to have a better understanding of the evolution of galaxies. This sample has been constituted in order:

- (i) to compute the local Tully–Fisher relation;
- (ii) to compare the kinematics of galaxies in different environments (field, pairs, compact groups, galaxies in cluster) for

*E-mail: benoit.epinat@oamp.fr

discriminating secular evolution from an external origin (e.g. Garrido et al. 2005);

(iii) to study the distribution of luminous and dark halo components along the Hubble sequence for high and low surface brightness galaxies, for a wide range of luminosities in combining the optical data with the radio ones (e.g. Barnes, Sellwood & Kosowsky 2004; Spano et al. 2008);

(iv) to model the effect of non-axisymmetric structures like bars, spiral arms, oval distortions, lopsidedness in the mass distribution using both N -body and hydrodynamic numerical simulations (e.g. Hernandez et al., in preparation), kinematic analysis (e.g. Krajnović et al. 2006) and the Tremaine–Weinberg method to measure the bar, spiral and inner structure pattern speeds (Hernandez et al. 2005a);

(v) to analyse the gaseous velocity dispersion and to link it with the stellar one;

(vi) to create template rotation curves (e.g. Persic & Salucci 1991; Persic, Salucci & Stel 1996; Catinella, Giovanelli & Haynes 2006) and template velocity fields;

(vii) to map the 2D mass distribution using 2D velocity field, broad-band imagery and spectrophotometric evolutionary models;

(viii) to search for links between the kinematics (shape of rotation curves, angular momentum, etc.) and the other physical properties of galaxies like star formation rate (e.g. comparison with star-forming galaxies like blue compact galaxies, etc.); and

(ix) to produce a reference sample of nearby galaxies to compare to the kinematics of high-redshift galaxies (Puech et al. 2006; Epinat, Amram & Balkowski 2007). Indeed, it is necessary to disentangle the effects of galaxy evolution from spatial (beam smearing) and spectral resolution effects.

This paper is the sixth of a series called hereafter Paper I–V (Garrido et al. 2002, 2003; Garrido, Marcellin & Amram 2004; Garrido et al. 2005; Spano et al. 2008) presenting the data obtained in the frame of the GHASP survey. The data gathered with the seven first observing runs have been published from Paper I to IV. Dark matter distribution in a subsample of 36 spiral galaxies has been presented in Paper V. This paper presents the last unpublished 101 $H\alpha$ data cubes of the GHASP survey. It includes 108 galaxies (seven data cubes contain two galaxies), providing 106 velocity fields and 93 rotation curves resulting from observational runs eight to fourteen. This represents the largest set of galaxies observed with Fabry–Perot techniques ever published in the same paper (Schommer et al. 1993 sample consists of 75 cluster galaxies in the Southern hemisphere observed with Fabry–Perot techniques and was the largest sample published to date). Including the previous papers (Paper I–IV), the GHASP survey totalizes Fabry–Perot data for 203 galaxies observed from 1998 to 2004. The GHASP sample is by now the largest sample of Fabry–Perot data ever published.

In Section 2, the selection criteria of the GHASP sample, the instrumental set-up of the instrument and the data reduction procedure are described. In Section 3, different momenta of the data cubes are presented as well as the new method to build the rotation curves and to determine the uncertainties. An analysis of the residual velocity fields and of the kinematical parameters is thus given. In Section 4, the Tully–Fisher relation is plotted for the GHASP galaxies presented in this paper. In Section 5, we give the summary and conclusions. In Appendix A, we present some details on the method used to compute the rotation curves. In Appendix B, the comments for each individual galaxy are given. In Appendix C, the different tables are given, while in Appendix D the individual maps and position–velocity diagrams are shown. The rotation

curves are finally displayed in Appendix E, while the numerical tables corresponding to the rotation curves are given in Appendix F.

When the distances of the galaxies are not known, a Hubble constant $H_0 = 75 \text{ km s}^{-1} \text{ Mpc}^{-1}$ is used throughout this paper.

2 OBSERVATIONS AND DATA REDUCTION

2.1 The GHASP sample

The GHASP survey was originally selected to be a subsample complementing the radio survey Westerbork survey of $H\text{I}$ in SPirals galaxies (WHISP) providing $H\text{I}$ distribution and velocity maps for about 400 galaxies (<http://www.astro.rug.nl/whisp>). The first set of GHASP galaxies was selected from the first WHISP website list but some of them have never been observed by WHISP. Thus, only 130 galaxies have finally been observed in both surveys. The comparison between the kinematics of neutral and ionized gas coming from the GHASP and the WHISP data sets is possible for a subsample of 31 dwarf galaxies studied by Swaters et al. (2002) and for another subsample of 19 early-type galaxies analysed by Noordermeer et al. (2005), the remaining part of the WHISP sample being yet unpublished but most of the $H\text{I}$ maps are nevertheless available in the WHISP website.

Most of the GHASP targets were chosen in nearby low-density environments. Nevertheless, some galaxies in pairs or in low density groups have been observed mainly when they were selected by WHISP (see individual comments in Appendix B). Seven galaxies of the GHASP sample are located in nearby clusters (UGC 1437 in the cluster Abell 262, UGC 4422 and 4456 in the Cancer cluster, UGC 6702 in the cluster Abell 1367, UGC 7021, 7901 and 7985 in the Virgo cluster). More Virgo cluster galaxies observed with the same instrument have been published elsewhere (Chemin et al. 2006).

Fig. 1 displays the distribution of the whole GHASP survey in the magnitude–morphological type plane. We have found in the literature measurements for both M_B and Hubble type for 198 galaxies (out of 203 galaxies). Among the sample of 203 galaxies, 83 are strongly barred galaxies (SB or IB) and 53 are moderately barred galaxies (SAB or IAB). The GHASP sample provides a wide coverage in galaxy luminosities ($-16 \leq M_B \leq -22$), thus in galaxy masses from (10^9 to $5 \times 10^{11} M_\odot$) and in morphological types (from Sa to Irregular). The well-known relation for spiral and irregular galaxies between the morphological type and the absolute magnitude is observed through the GHASP sample. Within the dispersion of this relation, the 203 GHASP galaxies are reasonably distributed through the plane down to low-magnitude (≥ -16) and to early-type spirals (≤ 0 , Sa). The whole GHASP data set of galaxies is reasonably representative of the LEDA sample (see Paper IV).

The journal of the observations for the 107 new galaxies is given in Table C1. The 108th galaxy, UGC 11300 has been observed for the third time in order to check the consistency of the new data reduction method (the second observation published in Paper IV was already done in order to compare the new GaAs camera with the ‘S20’ photocathode). Note that the right ascension and the declination given in Table C1 are the coordinates of the kinematical centre (and not the morphological ones given in HyperLeda or in LEDA, except if stated otherwise).

2.2 The instrumental set-up

In order to map the flux distribution and the velocity fields of the sample of galaxies, high spectral resolution 3D data cubes in the $H\alpha$

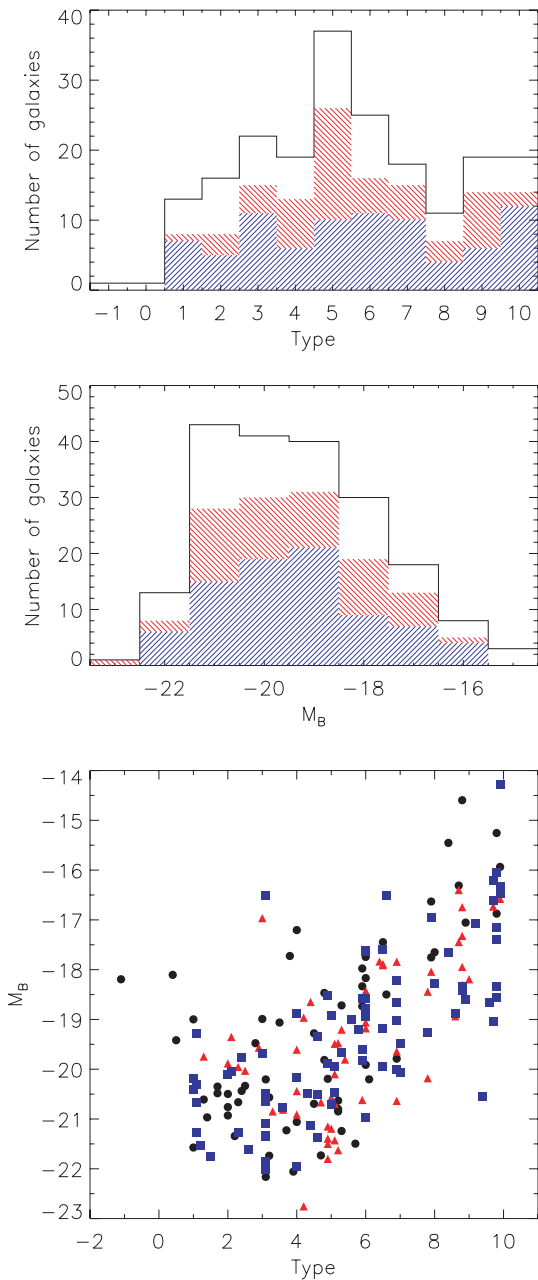


Figure 1. Top panel: distribution of morphological type for almost all of the GHASP sample (201 out of 203 galaxies). Middle panel: distribution of the absolute B -band magnitude for almost all of the GHASP sample (198 out of 203 galaxies). For both the top and middle panels: the blue hash, red hash and residual white represent, respectively, the strongly barred, the moderately barred and the non-barred galaxies. Bottom panel: distribution for almost all of the GHASP sample (198 out of 203 galaxies) in the ‘magnitude–morphological type’ plane distinguishing strongly barred (blue squares), moderately barred (red triangles) and unbarred galaxies (black circles).

line have been obtained. This has been achieved using a focal reducer containing the scanning Fabry–Perot interferometer attached at the Cassegrain focus of the 1.93-m OHP telescope (Observatoire de Haute Provence). The instrument principles and characteristics are the same as for Papers I–V. The detector, a new generation image photon counting system (IPCS), is the same as the one used in Paper IV (with a GaAs photocathode). The pixel size is 0.68 arcsec

(however, the angular resolution of our data is limited by the seeing, about ~ 3 arcsec e.g. Table C1), the field-of-view is 5.8 arcmin^2 and the velocity sampling is $\sim 5 \text{ km s}^{-1}$ (for a resolution of $\sim 10 \text{ km s}^{-1}$).

2.3 The data reduction

The Fabry–Perot technique provides an $H\alpha$ profile inside each pixel, so that a typical velocity field of a GHASP galaxy contains thousands of velocity points. For most of the galaxies observed with GHASP, the velocity field is not limited to the $H \text{ II}$ regions but covers most of the diffuse emission of the disc, as can be seen in the figures. The detection limit of our device is about $10^{-18} \text{ erg cm}^{-2} \text{ s}^{-1} \text{ arcsec}^{-2}$, with a signal-to-noise ratio between 1 and 2 for a typical 2 h exposure time according to fig. 2 of Gach et al. (2002). This insures a good detection of the $H\alpha$ diffuse emission of the disc for most of the galaxies since most of the $H\alpha$ emission found below $1.6 \cdot 10^{-16} \text{ erg cm}^{-2} \text{ s}^{-1} \text{ arcsec}^{-2}$ may be considered as filamentary and/or diffuse according to Ferguson et al. (1996). The way to derive the different moment maps of the 3D data cube ($H\alpha$ line maps and $H\alpha$ velocity fields) are explained in Daigle et al. (2006b) (hereafter D2006). The $H\alpha$ image is a pure monochromatic image of the galaxy (continuum and $[N \text{ II}]$ free).

In a few cases, when the velocity amplitude is comparable or higher than the width of the interference filter, its transmission is not necessarily centred on the systemic velocity and one side of the galaxy may be better transmitted than the other side, leading to an artificial asymmetry in the intensity of the $H\alpha$ emission (see Paper IV for additional explanations as well as in individual comments on each galaxy in Appendix B).

The data processing and the measurements of the kinematical parameters are different from those used in Paper I–V. The data processing used in this paper is basically the same as the one described by D2006. One of the main improvements implemented in this data processing is the use of adaptive spatial binning, based on the 2D Voronoi tessellations method applied to the 3D data cubes, allowing to optimize the spatial resolution to the signal-to-noise ratio. Let us also mention that when enough stars or bright $H \text{ II}$ regions were available in the field-of-view, we corrected the observation from telescope drift (or instrumental flexures) when necessary. Hereafter, we just point out the main difference between the method described in D2006 and the method used in this paper.

The main difference is the criterion used to fix the size of the bins. Indeed, with the spatial adaptive binning technique, a bin is accreting new pixels until it has reached a given criterion given a priori. In D2006, the criterion is the signal-to-noise ratio of the emission line within the bin. For each bin, the noise is determined from the r.m.s. of the continuum (the line free region of the whole spectrum). The signal-to-noise ratio is thus the ratio between the flux in the line and the rms in the continuum. While for the data described in D2006, the number of channels scanned is large enough (36 channels) to determine properly the noise in the continuum, this is not anymore the case here where the number of channels scanned is smaller (24 channels). For the same given spectral resolution (fixed by the interference order and the Finesse of the Fabry–Perot interferometer used), the ratio between the number of channels containing the continuum and the number of channels containing the line is thus larger (by a factor of $3/2$) in D2006 than here. Furthermore, the criterion in D2006 is not relevant anymore for the GHASP data. Instead of the signal-to-noise ratio, the criterion used here is simply the square root of the flux in the line, that is an estimate of the Poisson noise in the line flux.

A second major improvement is the suppression of the ghosts due to reflection at the air–glass interfaces of the interferometer (Georgelin 1970). The reduction routine takes into account the front reflection (between the interference filter and the interferometer) and the back reflection (between the interferometer and the camera detector window). The ghosts are calibrated and then subtracted, thanks to bright stars.

Another major improvement is an automatic cleaning of the velocity fields. The outskirts of a galaxy, where there is no more diffuse H α emission, has to be delimited. Due to residual night sky lines and background emissions (after subtraction), adaptive binning produces large sky bins with a given signal-to-noise ratio or given flux. These bins containing only sky emission are separated from the bins of the galaxy, thanks to a velocity continuity process. The velocity field is divided in several regions where the velocity difference between contiguous bins is lower than a given cut-off value. The regions with too low monochromatic flux and too large bins are erased. The given cut-off fixed a priori is about one-tenth of the total amplitude of the velocity field (let us say 30 km s^{-1} for a velocity field with an overall amplitude of $\sim 300 \text{ km s}^{-1}$).

KARMA (Gooch 1996) and its routine KOORDS have been used to compute the astrometry. XDSS blue-band images or XDSS Red band images when blue image was not available are displayed (see individual captions of Figs D1–D106). Systematic comparison between these broad-band images and the field stars in high-resolution continuum images (with no adaptive binning) were made in order to find the correct World Coordinate System for each image.

3 DATA ANALYSIS

3.1 Different maps from the 3D data cube

For each galaxy, in Appendix D, from Figs D1 to D106, we present up to five frames per figure: the XDSS blue (or red) image (top left-hand panel), the H α velocity field (top right-hand panel), the H α monochromatic image (middle left-hand panel), eventually the H α residual velocity field (middle right-hand panel) and finally the position–velocity diagram along the major-axis (bottom panel) when it can be computed. The white and black cross indicates the centre used for the kinematic analysis (given in Table C1 e.g. Appendix A for determination) while the black line traces the kinematical major-axis deduced from the velocity field analysis (e.g. Section 3.2) or the morphological one (taken from HyperLeda) when no position angle (PA) of the kinematical major-axis could be derived using the kinematic (e.g. Table C2). This line ends at the radius $D_{25}/2$ corresponding to the isophotal level 25 mag arcsec $^{-2}$ in the *B* band (given in Table C3) in order to compare the velocity field extent with the optical disc of the galaxies. Position–velocity diagrams are computed along the axis defined by this black line, using a virtual slit width of seven pixels, and the red line in the position–velocity diagram is the rotation curve deduced from the model velocity field (see the next section) along this virtual slit. When no fit is satisfying (generally because of poor signal-to-noise ratio), we used the real velocity field instead of the model (see individual captions in Figs D1–D106). The rotation curves are found in Appendices E (figures) and F (tables). The colour version of the rotation curves in Appendix E is only available online. Rotation curves are computed and displayed following the method described in Section 3.2. These figures are also available in the website of GHASP: <http://FabryPerot.oamp.fr>.

In order to illustrate the printed version of the paper we have chosen to display the diversity through four galaxies having different morphological types, see Appendices D19 [UGC 3740, SAB(r)c pec], D31 [UGC 4820, S(r)ab], D45 [UGC 5786, SAB(r)b], D56 (UGC 7154, SBcd). Appendix D maps of the other galaxies are only available online.

Only the first page of Appendix F that contains the tables corresponding to the rotation curves of the two first galaxies is displayed in the printed version of the paper, the remaining part of Appendix F being available online.

3.2 Construction of the rotation curves and determination of the uncertainties

A new automatic fitting method has been developed to derive automatically a rotation curve from the 2D velocity field. This method makes the synthesis between (i) the method used in Paper I–IV, (ii) the method based on tilted-ring models found, for instance, in the ROTCUR routine of GIPSY (Begeman 1987) and (iii) the method used by Barnes & Sellwood (2003).

Warps are mainly seen in galactic discs at radii $R > R_{\text{opt}}$. Tilted-ring models have been developed to model the distribution of neutral hydrogen for which warps of the H I disc may be more or less severe. In case of a warp, a monotonic change of the major-axis PA and of the inclination (*i*) is observed.

On the other hand, within the optical disc, the kinematic parameters PA and *i* do not vary significantly and change monotonically with the radius (Paper I–IV and Hernandez et al. 2005b). The variation in PA and *i* with the radius is more likely due to non-circular motions in the plane of the disc (e.g. bars) than to motions out of the plane (like warps) and looks like oscillations around a median value. Thus, we do not allow PA nor *i* to vary with the radius.

Using tilted-ring models, the errors in the parameters are the dispersion of the kinematical parameters over the rings. The method developed here uses the whole residual velocity field to estimate the dispersion induced by non-circular motions and not only the segmented information within each ring as it is the case in tilted-ring models.

Our fitting method is similar to the Barnes & Sellwood (2003) method. Two differences may nevertheless be pointed out. A minor difference is that they use a non-parametric profile, while we fit an analytic function (more details on the building of the rotation curve are given in Appendix A). The major improvement is the computation of the kinematic uncertainties. Indeed, the statistical uncertainty on the fit is unrealistically small (Barnes & Sellwood 2003), because the noise in the data is considered as a blank random noise. That is not the case because the noise in the residual velocity field is mainly due to non-circular motions (bar, oval distortions, spiral arms, local inflows and outflows, etc.) and to the intrinsic turbulence of the gas that have characteristic correlation lengths. In order to take it into account, we compute the errors with the power spectrum of the residual velocity field, applying a Monte Carlo method (see Appendix A).

Rotation curves for the barred galaxies of our sample have been plotted without correction for non-circular motions along the bar.

The rotation curves are sampled with rings. Within the transition radius (defined in Appendix A), the width of the rings is set to match half the seeing. Beyond that radius, each ring contains from 16 to 25 velocity bins.

The curves are plotted with both sides superimposed in the same quadrant, using different symbols for the receding (crosses) and approaching (dots) side (with respect to the centre). The black vertical

arrow in the x -axis represents the radius $D_{25}/2$ while the smaller grey arrow in the x -axis represents the transition radius, always smaller than $D_{25}/2$ by definition.

For galaxies seen almost edge-on (inclination higher than 75°) our model does not describe accurately the rotation of a galaxy since the thickness and the opacity of the disc cannot be neglected anymore. Indeed, on the one hand, it is well known that, due to inner galactic absorption, edge-on galaxies tend to display smoother inner velocity field and rotation curve gradients than galaxies with low or intermediate inclinations and, on the other hand, due to the actual thickness of the disc, motion out of the disc are wrongly interpreted as circular motions in the disc. As a consequence, for most of highly inclined galaxies, the fit converges towards unrealistic low inclination values, leading to modelled velocity fields and rotation curves having too high velocity amplitudes. Thus, for NGC 542, UGC 5279, UGC 5351, UGC 7699, UGC 9219, UGC 10713 and UGC 11332, no rotation curve has been plotted. For them, the position–velocity diagram gives a more suitable information than the rotation curve and allows to follow the peak-to-peak or peak-to-valley velocity distribution along the major-axis.

3.3 Residual velocity fields

As detailed in the previous paragraph and in Appendix A, the main assumption necessary to derive a rotation curve from the observed velocity field is that rotation is dominant and that all non-circular motions are not part of a large-scale pattern. The five kinematical parameters computed from the velocity field to draw the rotation curve are determined from different symmetry properties of the radial velocity field. The influence of small errors in these parameters is to produce patterns with characteristic symmetries in the residual velocity field. This was first illustrated by Warner, Wright & Baldwin (1973) and by van der Kruit & Allen (1978). In their schematic representation of the residual motions in disc galaxies (the modelled velocity field computed from the rotation curve has been subtracted to the observed velocity field), a bad determination of one or several kinematical parameters leads to typical signatures in the residual velocity field (e.g. velocity asymmetry around the major-axis in case of a bad PA determination, etc.). The residual velocity fields plotted for each galaxy in Appendix D clearly show that these typical signatures are not seen, this means that the best determination of the kinematical parameters has been achieved.

The deviation from purely circular velocity can be large. In a forthcoming paper, these residual velocity fields will be analysed in terms of bars and oval distortions, warps, spiral arms (streaming motions), outflows and inflows, etc. (e.g. Fathi et al. 2007).

The mean velocity dispersion on each residual velocity field has been computed for each galaxy and tabulated in Table C2, they range from 4 to 54 km s^{-1} with a mean value around 13 km s^{-1} . Fig. 2 shows that the residual velocity dispersion is correlated with the maximum amplitude of the velocity field (shown by the dashed linear regression), this trend remains if we display the residual velocity dispersion versus the maximum circular velocity (not plotted). Surprisingly, barred galaxies do not have, on average, a higher mean residual velocity dispersion than unbarred galaxies (not plotted). This may be explained by the fact that the number of bins contaminated by the bar is usually rather low with respect to the total bins of the disc. Indeed, this is not the case for discs dominated by a bar. Compared to the general trend, we observe a set of about a dozen of galaxies with a high residual velocity dispersion (points above the dotted line in Fig. 2). These points correspond to galaxies

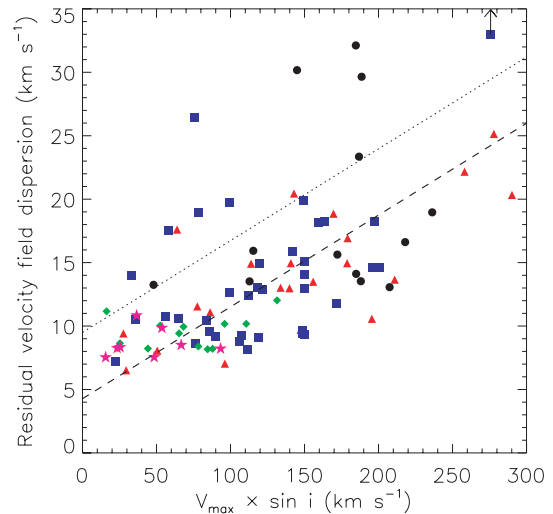


Figure 2. Dispersion in residual velocity field versus maximum velocity, sorted by Hubble morphological type: black circles $0 \leq t < 2$, red triangles $2 \leq t < 4$, blue squares $4 \leq t < 6$, green rhombuses $6 \leq t < 8$ and pink stars $8 \leq t < 10$. The dashed line represents the linear regression in the data. The points above the dotted line are discussed in Section 3.3. UGC 3334 labelled with an arrow has actually a residual velocity dispersion of 54 km s^{-1} (see Table C2).

having strong bar or spiral structure and to data of lower quality: (i) galaxies dominated by strong bars (UGC 89 and UGC 11407), or strong spiral structures (UGC 5786 and UGC 3334) are not correctly described by our model which does not take into account non-axisymmetric motions; (ii) the velocity field of the lower quality data (UGC 1655, UGC 3528, IC 476, UGC 4256, UGC 4456, IC 2542, UGC 6277, UGC 9406 and UGC 11269) presents a mean size of the bins greater than 25 pixels and an integrated total $\text{H}\alpha$ flux lower than 4.5 W m^{-2} (a rough calibration of the total $\text{H}\alpha$ flux of GHASP galaxies using the 26 galaxies we have in common with James et al. 2004 has been made, assuming a spectral ratio of $\text{H}\alpha$ to $[\text{N II}]$ of 3:1). Fig. 2 also shows that, for a given velocity amplitude, this correlation does not clearly depend on the morphological type. We note the well-known fact that late-type galaxies have on average a lower velocity amplitude than early-type ones.

For most of the galaxies seen almost edge-on (i higher than 75°), due to the thickness of the disc, no model has been fitted (see previous subsection) thus no residual velocity fields can be plotted.

3.4 Kinematical parameters

Table C2 gives the input (morphological) parameters of the fits and the results of the fits (output parameters, χ^2 , and parameters of the residual maps). Table C3 gives some fundamental parameters of the galaxies compiled in the literature (morphological and Hubble type, distance, M_B , $D_{25}/2$, axial ratio, H I maps available in the literature), together with maximum velocity parameters computed from the rotation curves (V_{max} , quality flag on V_{max}). The four galaxies larger than our field-of-view are flagged in Table C3. For some galaxies for which the signal-to-noise ratio or the spatial coverage is too low, the fit could not converge correctly and one or two parameters (i and PA) were usually fixed to the morphological values to achieve the fit. These galaxies are flagged with an asterisk (*) in Table C2. When it is the case, parameter determinations are discussed in Appendix B. For some extreme cases, even when i and PA were fixed, the fit does

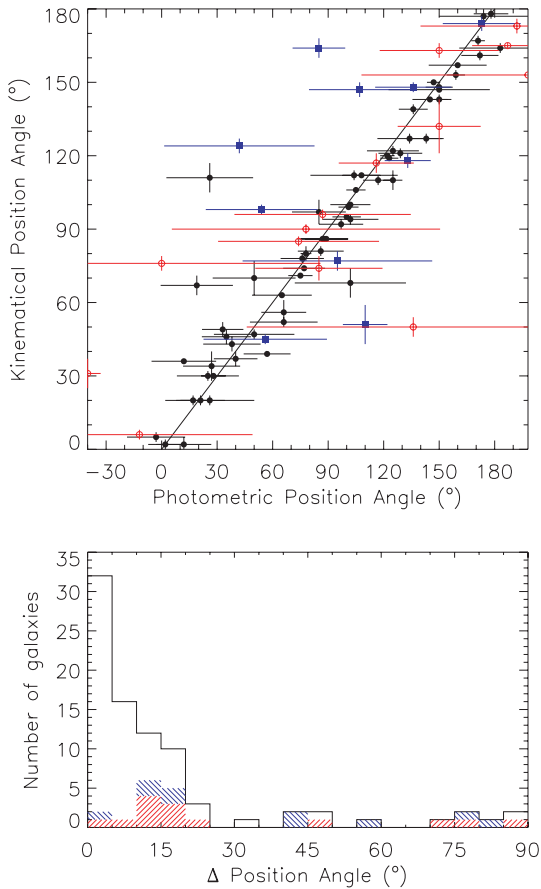


Figure 3. Top panel: kinematical versus morphological (HyperLeda) PAs of the major-axis. Galaxies for which no accurate morphological PA has been computed are shown by the red open circles; galaxies having an inclination lower than 25° are displayed by the blue squares; the other galaxies are represented by the black circles. Bottom panel: histogram of the variation between kinematical and morphological PAs. The red hash, blue hash and residual white represent, respectively, the galaxies for which no accurate PA has been measured, for which inclination is lower than 25° and the other galaxies of the sample.

not converge. In particular for galaxies having high inclinations, then no model was computed (see Section 3.2).

As underlined in Paper I, Garrido (2003) and Paper IV, due to the difference in wavelength between the calibration and the redshifted H α lines, the coating of the Fabry–Perot interferometer induces a small systematic bias (phase shift effect) to the absolute systemic velocities. We tabulate the systemic velocities without correcting them from this phase shift because the dispersion by the phase effect is typically of the same order of magnitude than the dispersion of the systemic velocities found in HyperLeda (Paper IV) and also because the forthcoming analysis and in particular the rotation curves do not depend on this effect.

In Fig. 3, the kinematical PAs obtained by GHASP are compared with the photometric PAs (found in HyperLeda). The error bar on the morphological PA, which is generally not homogeneously given in the literature (or not given at all), has been estimated using the axial ratio and optical radius uncertainties. The galaxy disc in the sky plane is modelled by an ellipse of axial ratio b/a where a is equal to D_{25} . Given the uncertainty on D_{25} , ΔD_{25} , a circle of diameter $D_{25} - \Delta D_{25}/2$ having the same centre as the ellipse is considered. A line passing through the intersection between the ellipse and the

circle and their common centre is thus defined. The angle formed between the major-axis of the ellipse and the previously defined line represents the 1σ uncertainty on the PA.

For all galaxies, HyperLeda references a list of PAs from which they often computed one PA value. HyperLeda does not compute a value when the dispersion or the uncertainty is too large. Indeed, the PA may be quite different from a study to another, depending on (i) the method, (ii) the size of the disc and (iii) the broad-band colours considered by the different authors (non-homogeneity in radius and colour measurements). When no value is computed in HyperLeda, we put the whole list in Table C2. Moreover, to make it readable and to minimize the dispersion on Fig. 3, we only plot the morphological value found closest from the kinematical PA. In Fig. 3, we have distinguished the bulk of galaxies (black circles) for which the agreement is rather good (lower than 20° see Fig. 3, bottom panel) from (i) the galaxies for which no accurate morphological PA has been computed (red open circles) and (ii) the galaxies having an inclination lower than 25° (blue squares). Indeed, some galaxies present a disagreement between kinematical and photometric PAs larger than 20° . Most of these galaxies have (i) a bad morphological determination of the PA or (ii) have kinematical inclinations lower than 25° or (iii) are specific cases (namely UGC 3740, IC 476, UGC 4256, UGC 4422) and are discussed in Appendix B. On the other hand, Fig. 3 shows that morphological PAs have systematically higher uncertainties than kinematical ones; this is specially true for galaxies with low inclination. Quantitatively, for kinematical inclinations greater than 25° , the mean error on morphological PAs is $\sim 3^\circ$, while the mean error on kinematical PAs is $\sim 2^\circ$. For inclinations lower than 25° , the difference in the methods is even larger: the mean error on morphological PAs is $\sim 27^\circ$, while the mean error on kinematical PAs is $\sim 3^\circ$. For comparison, Barnes & Sellwood (2003), using the difference between morphological and kinematical parameters, estimated that non-axisymmetric features introduce inclination and PA uncertainties of 5° on average.

The histogram of the variation between kinematical and morphological PAs given in Fig. 3 (bottom panel) indicates that (i) for more than 60 per cent of these galaxies, the agreement is better than 10° ; (ii) for more than 83 per cent, the agreement is better than 20° ; and (iii) the disagreement is larger than 30° for 15 per cent of these galaxies.

In other words, the position of the slit in long-slit spectroscopy (which is usually based on the major-axis determined from broad-band imagery) with respect to the actual PA may be not negligible, highlighting the strength of the integral field spectroscopy methods to determine the PAs (see also illustrations in Paper IV, Chemin et al. 2006; Daigle et al. 2006a).

In Fig. 4, the inclinations obtained by GHASP are compared with the photometric inclinations. On the top panel, the photometric inclination is the one computed using a correction factor depending on the morphological type (Hubble 1926):

$$\sin^2 i = \frac{1 - 10^{-2 \log r_{25}}}{1 - 10^{-2 \log r_0}}$$

where r_{25} is the apparent flattening, and $\log r_0 = 0.43 + 0.053t$ for the de Vaucouleurs type t ranging from -5 to 7 , and $\log r_0 = 0.38$ for t higher than 7 (Paturel et al. 1997).

In the middle panel, the photometric inclination i is derived from the axial ratio b/a without any correction ($\cos i = b/a$). As for the PAs, the red open circles are the galaxies for which the morphological PA could not be determined accurately. The blue squares are the galaxies for which the difference between morphological and kinematical PAs exceeds 20° .

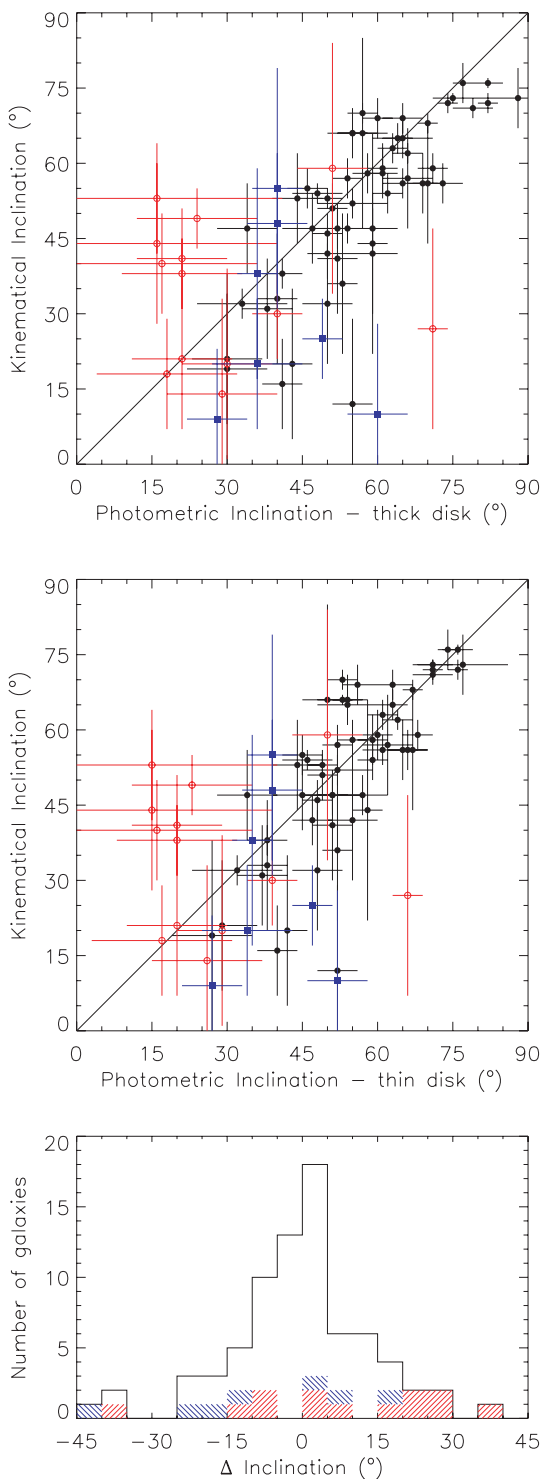


Figure 4. Top panel: kinematical versus thick disc morphological inclinations. Middle panel: kinematical versus thin disc morphological inclinations. Top and middle panels: galaxies for which no accurate morphological PA has been computed are shown by the red open circles; galaxies with a difference between the kinematical and morphological PAs larger than 20° are displayed with the blue squares; the other galaxies are represented by the black circles. Bottom: histogram of the variation between kinematical and morphological inclinations. The red hash, blue hash and residual white represent, respectively, the galaxies for which no accurate PA has been measured, for which the difference between the kinematical and morphological PAs is larger than 20° and the other galaxies of the sample.

The dispersion around the $y = x$ line (equality between the morphological and kinematical inclinations) decreases with the inclination. The main discrepancy is found for low inclinations. The corresponding galaxies are discussed in Appendix B (notes on individual galaxies). On the one hand, the morphological inclination of the galaxies having no robust determination of their morphological PA cannot be constrained correctly. On the other hand, galaxies for which the PA disagreement is relatively high have a high dispersion and their morphological inclination is statistically overestimated.

Excluding these galaxies which have a bad PA estimation, for low inclination systems, kinematical methods may underestimate the inclination or alternatively, morphological estimations may be overestimated. On average, the errors on morphological inclinations ($\sim 6^\circ$) and on kinematical inclinations ($\sim 8^\circ$) are comparable. Whatever be the method used, the determination of the inclination of galaxies having a low inclination remains less accurate than for more inclined galaxies.

The comparison of the two plots in Fig. 4 (top and middle panels) shows that galaxies with high inclination have a better agreement between their kinematical inclination and their morphological inclination computed considering a thin disc. The actual thickness of the disc may not be reproduced by our simple thin disc velocity field modelling. If it is the case, the kinematical inclination may be systematically underestimated. Alternatively, the good agreement between the thin disc morphological inclination and kinematical inclination may mean that the morphological thickness corrections are overestimated.

The histogram of the difference between morphological and kinematical inclinations (Fig. 4, bottom panel) shows that a difference of inclination larger than 10° is found for 40 per cent of the sample.

4 THE TULLY–FISHER RELATION

Among the present sample of 108 galaxies, we have plotted the Tully–Fisher relation (Tully & Fisher 1977, M_B as a function of $\log 2 V_{\max}$) for a subsample of 94 galaxies in Fig. 5. The 14 other galaxies are not considered in the present discussion because (i) for five galaxies the rotation curve does not reach the maximum rotation velocity (UGC 1655, UGC 4393, UGC 6523, UGC 8898 and UGC 9406); (ii) no B magnitude is available for one galaxy (UGC 3685); and (iii) no velocity measurement either on the rotation curve or in the position–velocity diagram is possible for eight other galaxies (see Table C3).

The maximum velocity V_{\max} has been obtained from the fit to the velocity field. The error on V_{\max} is the quadratic combination of the error due to the uncertainty in the inclination (the product $V_{\max} \times \sin i$ is constant) and the median dispersion in the rings of the rotation curve beyond $D_{25}/10$. In the cases where the rotation curve has no point beyond that radius, we replace this term by the intrinsic uncertainty on the velocity determination due to the spectral resolution (8 km s^{-1}). For the highly inclined galaxies for which no correct fit was possible with our method (because it does not take into account the thickness of the disc, see Section 3.2), we computed V_{\max} from the $H\alpha$ position–velocity diagram corrected from the photometric inclination. For them, the error on V_{\max} is simply the intrinsic uncertainty on the velocity determination. For the particular case of UGC 5786, the fit is not good enough to use it to compute V_{\max} because of the long blue northern tail and because of the strong bar. We estimated V_{\max} to 80 km s^{-1} by eye inspection of the rotation curve. These galaxies are flagged in Table C3.

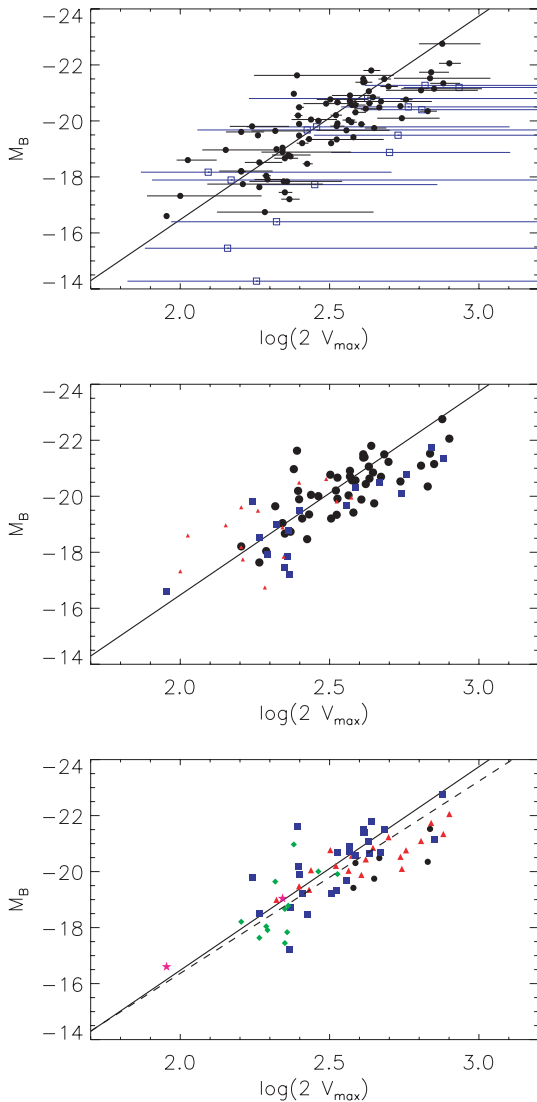


Figure 5. Tully–Fisher relation for our sample of galaxies. The solid line represents the B magnitude Tully–Fisher relation determined by Tully & Pierce (2000) from nearby galaxies in clusters (Ursa Major, Pisces filament, Coma). Top panel: sorted by inclination – low-inclination galaxies ($i < 25^\circ$): blue squares; other galaxies ($i \geq 25^\circ$): black circles. Middle panel: sorted by V_{\max} flags – V_{\max} reached: black dots, large size; V_{\max} probably reached: blue squares, medium size; V_{\max} probably not reached: red triangles, small size. Bottom panel: sorted by morphological type – black circles from 0 to 2; red triangles from 2 to 4; blue squares from 4 to 6; green rhombuses from 6 to 8; pink stars from 8 to 10; the dotted line represents the best linear fit in the data.

The solid line in Fig. 5 is the relation found by Tully & Pierce (2000):

$$M_B = -7.3(\log 2V_{\max} - 2.5) - 20.1.$$

In Fig. 5 (top panel), the error bars on the velocity are displayed and galaxies with inclination lower than 25° are distinguished (blue open squares). We clearly note that these galaxies have statistically higher velocities than expected from the Tully & Pierce (2000) relation. This effect is due to the link between the inclination and velocity determination. Indeed, in the velocity fields, we observe the projected velocity in the line-of-sight: $V_{\text{rot}} \times \sin i$. A given underestimate of the inclination thus leads to a higher overestimate

on maximum velocity for low inclination galaxies than for high inclination galaxies. This also explains the strong trend for low inclination galaxies to exhibit large error bars. Considering this effect, we choose to exclude the 15 galaxies with inclinations lower than 25° from the Tully–Fisher analysis.

Among the 79 remaining galaxies, the maximum velocity V_{\max} is reached for 48 of them (black dots, large size), probably reached for 17 of them (blue squares, medium size) and probably not reached for 14 of them (red triangles, small size). They are distinguished in Fig. 5 (middle panel) and flagged in Table C3. The quality flag on the maximum velocity is deduced (i) from the inspection of the shape of the H α rotation curves and position–velocity diagrams; (ii) from the comparison with H I velocity fields and rotation curves when available (see Table C3); and (iii) from the comparison of the H α velocity fields amplitudes with H I linewidths (see individual comments in Appendix B). It appears from this last point that the H I linewidth at 20 per cent has most often the best agreement with the H α velocity field amplitude (better than the linewidth at 50 per cent). Fig. 5 (middle panel) confirms the two classifications ‘ V_{\max} probably reached’ and ‘ V_{\max} probably not reached’ since for the majority of each class the points are, respectively, in agreement and above the Tully & Pierce (2000) relation. From the two classes ‘ V_{\max} reached’ and ‘ V_{\max} probably reached’, we find the following relation:

$$M_B = (-6.9 \pm 1.6)[\log 2V_{\max} - 2.5] - (19.8 \pm 0.1). \quad (1)$$

This relation is displayed as a dotted line in Fig. 5, in which morphological types are distinguished for the two best classes (black circles from 0 to 2, red triangles from 2 to 4, blue squares from 4 to 6, green rhombuses from 6 to 8 and pink stars from 8 to 10). Coefficients have been computed using the mean of the coefficients obtained (i) using a fit on the absolute magnitudes (as dependent variables) and (ii) using a fit on the velocities (as dependent variables). The difference in the slope determination by these two methods is quite large due to a strong scatter in our data [the error on the parameter in equation (1) is half that difference]. Indeed, usually one uses local calibrators for which distance measurements are accurate (based on Cepheids, red giants branch, members of a same cluster, etc.) leading to a small scatter in the data. From our data, the main difficulty is that the distance determination is mostly based on the systemic velocity corrected from Virgo infall (see Table C3), and that no error bar on the magnitude can be easily estimated. Thus, we have no reason to be more confident on the velocity measurements (mainly affected by inclination determination) than on absolute magnitude measurements. However, despite the dispersion in our data, the resulting parameters using the mean of the two fits are in good agreement with Tully & Pierce (2000), even if our slope is a bit lower. A lower slope had already been observed in H I (Yasuda, Fukugita & Okamura 1997; Federspiel, Tammann & Sandage 1998) and more systematically in optical studies (e.g. Courteau 1997; Rubin, Waterman & Kenney 1999; Márquez et al. 2002; Papers III and IV).

For the Tully–Fisher relation we derived, on the one hand, we observe that fast rotators ($V_{\max} > 300 \text{ km s}^{-1}$; UGC 89, UGC 4422, UGC 4820, UGC 5532, UGC 8900, UGC 8937 and UGC 11470) are less luminous than expected, except maybe for UGC 3334 which is one of the fastest disc rotators (Rubin, Roberts & Ford 1979) (see discussion in Appendix B). This trend can also be observed in several optical studies (Márquez et al. 2002; Papers III and IV). Interestingly, these fast rotators are not observed in H I samples (Tully & Pierce 2000; Federspiel et al. 1998). This may be explained by the shape of the rotation curves of fast rotators: except for UGC 8900,

the rotation curve always reaches the maximum velocity within the first 5 arcsec (i.e. within our seeing). This inner maximum may be missed in H I because of beam smearing, averaging the maximum velocity reached at the centre. Note that the rotation curve of UGC 5532 is clearly decreasing, while the other ones are flat. On the other hand, slow rotators have a small velocity gradient and within the optical regions the maximum could not be reached, whereas H I observations would be able to measure it without any doubt. These two effects could explain the trend observed in optical Tully–Fisher relations.

The result obtained for the Tully–Fisher relation is in agreement with the one obtained with the previous samples (Papers III and IV). The analysis of the whole GHASP sample will be done in a forthcoming paper (Epinat et al., in preparation).

5 SUMMARY AND PERSPECTIVES

The knowledge of the links between the kinematical and dynamical state of galaxies will help us to have a better understanding of the physics and evolution of galaxies. The GHASP sample, which consists of 203 spiral and irregular galaxies covering a wide range of morphological types and absolute magnitudes, has been constituted in order to provide a kinematical reference sample of nearby galaxies. The GHASP galaxies have been observed in the H α line with a scanning Fabry–Perot, providing data cubes.

We present in this paper the last set of 108 galaxies leading to 106 velocity fields and 93 rotation curves. By now, this work consists of the largest sample of galaxies observed with Fabry–Perot techniques ever presented in the same publication. Added to the four previous sets already obtained in the frame of this survey (Paper I–IV), GHASP represents the largest sample of 2D velocity fields of galaxies observed at H α wavelength. For each galaxy, we have presented the H α velocity field, the H α monochromatic image and eventually the H α residual velocity field, the position–velocity diagram along the major-axis and the rotation curve when available.

The following major improvements in the reduction and in the analysis have been developed and implemented.

(i) In order to optimize the spatial resolution for a given signal-to-noise ratio, adaptive binning method, based on the 2D Voronoi tessellations, was used to derive the 3D H α data cubes and to extract from it the line maps and the radial velocity fields.

(ii) The ghosts due to reflections at the air–glass interfaces of the interferometer have been removed in the data cubes.

(iii) The analysis of the faint outskirts or diffuse regions is made automatic.

(iv) The kinematical parameters and their error bars are directly derived from the velocity field.

(v) The uncertainties are estimated from the analysis of the residual velocity field power spectrum.

(vi) The whole 2D velocity field has been used rather than successive crowns in tilted-ring models to compute the rotation curve and the error bars.

The main results of this paper are summarized by the following items.

(i) The absence of typical and well-known bias in the residual velocity fields means that the best determination of the kinematical parameters has been achieved.

(ii) The mean velocity dispersion on each residual velocity field ranges from 6 to 23 km s⁻¹ with a mean value around 13 km s⁻¹ and is strongly correlated with the maximum amplitude of the velocity

field. For a given velocity amplitude, this correlation does not clearly depend on the morphological type. Only strongly barred galaxies have a higher residual velocity dispersion than mild-bared or non-bared galaxies. Peculiar galaxies also show a high residual velocity dispersion.

(iii) The kinematical PAs obtained by GHASP are compared with the photometric PAs. Morphological PAs have systematically higher uncertainties than kinematical ones, this is specially true for galaxies with low inclination. When using long-slit spectroscopy, the PA should be known a priori. This is usually done using morphological determinations based on broad-band imagery. We have shown that in some cases the difference between the PA determined using 2D kinematics and morphologies may be as large as 90° and that in any case the PAs are better determined by 2D kinematics. Thus, large differences between morphological and kinematical PAs may lead us to incorrect rotation curve and maximum velocity determination when using long-slit spectroscopy. This may strongly bias mass distribution models and Tully–Fisher studies, highlighting the strength of integral field spectroscopy with a Fabry–Perot.

(iv) The morphological inclination of the galaxies having no robust determination of their morphological PA cannot be constrained correctly. Galaxies for which the PA disagreement is relatively high have a high dispersion and their morphological inclination is statistically overestimated. Galaxies with high inclination have a better agreement between their kinematical inclination and their morphological inclination computed assuming a thin disc. For galaxies with intermediate disc inclinations (higher than 25° and lower than 75°), to reduce the degrees of freedom in kinematical models, the inclination could be fixed to the morphological value. This is specially true when only low-quality kinematical data are available as it is the case for high-redshift galaxies.

(v) The Tully–Fisher relation found with this new set of data is in good agreement with Tully & Pierce (2000), even if our slope is a bit lower. This trend for a lower slope has already been observed in H I by Yasuda et al. (1997) and Federspiel et al. (1998). Galaxies with inclination lower than 25° have statistically higher velocities than expected from the Tully–Fisher relation derived by Tully & Pierce (2000). Fast rotators ($V_{\max} > 300$ km s⁻¹) are less luminous than expected. This may be explained by the shape of the rotation curves of fast rotators.

ACKNOWLEDGMENTS

The authors warmly thank Dr O. Garrido for leading or participating to most of the observations. They also thank the Programme National Galaxies for supporting the GHASP project in allocating continuously observing time during several years, the Observatoire de Haute-Provence team for its technical assistance during the observations, O. Boissin for his technical help during the observing runs, and J. Boulesteix for permanent support. They thank I. Jégouzo and C. Surace for building the Fabry–Perot Data base. This research has made use of the GOLD Mine Data base and of the NASA/IPAC Extragalactic Data base (NED) which is operated by the Jet Propulsion Laboratory, California Institute of Technology, under contract with the National Aeronautics and Space Administration. The authors have also made an extensive use of the HyperLeda Data base (<http://leda.univ-lyon1.fr>). The Digitized Sky Surveys were produced at the Space Telescope Science Institute under US Government grant NAG W-2166. The images of these surveys are based on photographic data obtained using the Oschin Schmidt Telescope on Palomar Mountain and the UK Schmidt Telescope. The plates

were processed into the present compressed digital form with the permission of these institutions.

REFERENCES

- Amram P., Le Coarer E., Marcelin M., Balkowski C., Sullivan W. T., III, Cayatte V., 1992, *A&AS*, 94, 175
- Amram P., Marcelin M., Balkowski C., Cayatte V., Sullivan W. T., III, Le Coarer E., 1994, *A&AS*, 103, 5
- Arp H., 1966, *Atlas of Peculiar Galaxies*. California Inst. Technology, Pasadena
- Balick B., Heckman T., 1981, *A&A*, 96, 271
- Barnes E. I., Sellwood J. A., 2003, *AJ*, 125, 1164
- Barnes E. I., Sellwood J. A., Kosowsky A., 2004, *AJ*, 128, 2724
- Battaglia G., Fraternali F., Oosterloo T., Sancisi R., 2006, *A&A*, 447, 49
- Begeman K. G., 1987, PhD thesis, Kapteyn Institute
- Bottema R., 1989, *A&A*, 221, 236
- Bottinelli L., Gouguenheim L., Fouque P., Paturel G., 1990, *A&AS*, 82, 391
- Braine J., Combes F., Casoli F., Dupraz C., Gerin M., Klein U., Wielebinski R., Brouillet N., 1993, *A&AS*, 97, 887
- Braun R., Thilker D., Walterbos R. A. M., 2003, *A&A*, 406, 829
- Bravo-Alfaro H., Szomoru A., Cayatte V., Balkowski C., Sancisi R., 1997, *A&AS*, 126, 537
- Broeils A. H., van Woerden H., 1994, *A&AS*, 107, 129
- Carollo C. M., Stiavelli M., Mack J., 1998, *AJ*, 116, 68
- Carozzi N., 1976, *A&A*, 49, 431
- Catinella B., Haynes M. P., Giovanelli R., 2005, *AJ*, 130, 1037
- Catinella B., Giovanelli R., Haynes M. P., 2006, *ApJ*, 640, 751
- Chemin L. et al., 2006, *MNRAS*, 366, 812
- Cote S., Carignan C., Sancisi R., 1991, *AJ*, 102, 904
- Courteau S., 1997, *AJ*, 114, 2402
- Daigle O., Carignan C., Amram P., Hernandez O., Chemin L., Balkowski C., Kennicutt R., 2006a, *MNRAS*, 367, 469
- Daigle O., Carignan C., Hernandez O., Chemin L., Amram P., 2006b, *MNRAS*, 368, 1016 (D2006)
- de Vaucouleurs G., 1979, *ApJ*, 227, 380
- de Vaucouleurs G., Caulet A., 1982, *ApJS*, 49, 515
- Doyle M. T. et al., 2005, *MNRAS*, 361, 34
- Elfhag T., Booth R. S., Hoeglund B., Johansson L. E. B., Sandqvist A., 1996, *A&AS*, 115, 439
- Epinat B., Amram P., Balkowski C., 2007, in Combes F., Palous J., eds, *IAU Symp. Vol. 235, Galaxy Evolution Across the Hubble Time*. Cambridge University Press, Cambridge, p. 401
- Eskridge P. B. et al., 2002, *ApJS*, 143, 73
- Fathi K. et al., 2008, *ApJ*, 645, L17
- Federspiel M., Tammann G. A., Sandage A., 1998, *ApJ*, 495, 115
- Ferguson A. M. N., Wyse R. F. G., Gallagher J. S. III, Hunter D. A., 1996, *AJ*, 111, 2265
- Fridman A. M., Afanasiev V. L., Dodonov S. N., Khoruzhii O. V., Moiseev A. V., Sil'chenko O. K., Zasov A. V., 2005, *A&A*, 430, 67
- Gach, J.-L. et al., 2002, *PASP*, 114, 1043
- García-Barreto J. A., Franco J., Carrillo R., Venegas S., Escalante-Ramírez B., 1996, *Rev. Mex. Astron. Astrofis.*, 32, 89
- Garrido O., 2003, PhD thesis, Université de Provence (France)
- Garrido O., Marcelin M., Amram P., Boulesteix J., 2002, *A&A*, 387, 821
- Garrido O., Marcelin M., Amram P., Boissin O., 2003, *A&A*, 399, 51
- Garrido O., Marcelin M., Amram P., 2004, *MNRAS*, 349, 225
- Garrido O., Marcelin M., Amram P., Balkowski C., Gach J. L., Boulesteix J., 2005, *MNRAS*, 362, 127
- Gavazzi G., Catinella B., Carrasco L., Boselli A., Contursi A., 1998, *AJ*, 115, 1745
- Gavazzi G., Boselli A., Donati A., Franzetti P., Scodreggio M., 2003, *A&A*, 400, 451
- Georgelin Y. P., 1970, *A&A*, 9, 441
- Giovanardi C., Salpeter E. E., 1985, *ApJS*, 58, 623
- Giovanelli R., Haynes M. P., 1993, *AJ*, 105, 1271
- Gooch R., 1996, in Jacoby G. H., Barnes J., eds, *ASP Conf. Ser. Vol. 101, Astronomical Data Analysis Software and Systems V*. Astron. Soc. Pac. San Francisco, p. 80
- Hameed S., Devereux N., 2005, *AJ*, 129, 2597
- Hattori T. et al., 2004, *AJ*, 127, 736
- Haynes M. P., van Zee L., Hogg D. E., Roberts M. S., Maddalena R. J., 1998, *AJ*, 115, 62
- Haynes M. P., Giovanelli R., Salzer J. J., Wegner G., Freudling W., da Costa L. N., Herter T., Vogt N. P., 1999, *AJ*, 117, 1668
- Héraudeau P., Simien F., Maubon G., Prugniel P., 1999, *A&AS*, 136, 509
- Hernandez O., Wozniak H., Carignan C., Amram P., Chemin L., Daigle O., 2005a, *ApJ*, 632, 253
- Hernandez O., Carignan C., Amram P., Chemin L., Daigle O., 2005b, *MNRAS*, 360, 1201
- Hickson P., Kindl E., Auman J. R., 1989, *ApJS*, 70, 687
- Hoffman G. L., Salpeter E. E., Farhat B., Roos T., Williams H., Helou G., 1996, *ApJS*, 105, 269
- Hubble E. P., 1926, *ApJ*, 64, 321
- Huchtmeier W. K., Witzel A., 1979, *A&A*, 74, 138
- Hunter D. A., Elmegreen B. G., 2004, *AJ*, 128, 2170
- Irwin J. A., 1994, *ApJ*, 429, 618
- James P. A. et al., 2004, *A&A*, 414, 23
- Jiménez-Vicente J., Battaner E., 2000, *A&A*, 358, 812
- Kamphuis J. J., Sijbring D., van Albada T. S., 1996, *A&AS*, 116, 15
- Karachentsev I. D., 1972, *Astrofizicheskie Issledovaniia Izvestiya Spetsial'noj Astrofizicheskoy Observatorii*, 7, 3
- Karachentsev I. D., Mineva V. A., 1984a, *Sov. Astron. Lett.*, 10, 105
- Karachentsev I. D., Petit M., 1990, *A&AS*, 86, 1
- Karachentsev I. D., Myneva V. A., 1984b, *Sov. Astron. Lett.*, 10, 235
- Karachentsev I. D., Karachentseva V. E., Huchtmeier W. K., Makarov D. I., 2004, *AJ*, 127, 2031
- Kaufman M., Brinks E., Elmegreen B. G., Elmegreen D. M., Klarić M., Struck C., Thomasson M., Vogel S., 1999, *AJ*, 118, 1577
- Kaufman M., Sheth K., Struck C., Elmegreen B. G., Thomasson M., Elmegreen D. M., Brinks E., 2002, *AJ*, 123, 702
- Knapen J. H., Stedman S., Bramich D. M., Folkes S. L., Bradley T. R., 2004, *A&A*, 426, 1135
- Koopmann R. A., Kenney J. D. P., Young J., 2001, *ApJS*, 135, 125
- Koopmann R. A., Haynes M. P., Catinella B., 2006, *AJ*, 131, 716
- Kornreich D. A., Haynes M. P., Lovelace R. V. E., van Zee L., 2000, *AJ*, 120, 139
- Krajnović D., Cappellari M., de Zeeuw P. T., Copin Y., 2006, *MNRAS*, 366, 787
- Kregel M., van der Kruit P. C., Freeman K. C., 2005, *MNRAS*, 358, 503
- Krumm N., Salpeter E. E., 1979, *AJ*, 84, 1138
- Lang R. H. et al., 2003, *MNRAS*, 342, 738
- Lewis B. M., 1987, *ApJS*, 63, L515
- Márquez I., Moles M., 1996, *A&AS*, 120, 1
- Márquez I., Masegosa J., Moles M., Varela J., Bettoni D., Galletta G., 2002, *A&A*, 393, 389
- Martin C. L., 1998, *ApJ*, 506, 222
- Meyssonnier N., 1984, *A&AS*, 58, 351
- Moustakas J., Kennicutt R. C., Jr, 2006, *ApJS*, 164, 81
- Nilson P., 1973, *Uppsala General Catalogue of Galaxies, Nova Acta Regiae Soc. Sci. Upsaliensis Ser. V*
- Noordermeer E., van der Hulst J. M., Sancisi R., Swaters R. A., van Albada T. S., 2005, *A&A*, 442, 137
- O'Connell R. W., Gallagher J. S., III, Hunter D. A., 1994, *ApJ*, 433, 65
- Paturel G., García A. M., Fouque P., Buta R., 1991, *A&A*, 243, 319
- Paturel G. et al., 1997, *A&AS*, 124, 109
- Paturel G., Fang Y., Petit C., Garnier R., Rousseau J., 2000, *A&AS*, 146, 19
- Persic M., Salucci P., 1991, *ApJ*, 368, 60
- Persic M., Salucci P., Stel F., 1996, *MNRAS*, 281, 27
- Pignatelli E. et al., 2001, *MNRAS*, 323, 188
- Pisano D. J., Wilcots E. M., Liu C. T., 2002, *ApJS*, 142, 161
- Puech M., Hammer F., Flores H., Östlin G., Marquart T., 2006, *A&A*, 455, 119

510 *B. Epinat et al.*

- Rampazzo R., Reduzzi L., Sulentic J. W., Madejsky R., 1995, *A&AS*, 110, 131
- Rasmussen J., Ponman T. J., Mulchaey J. S., 2006, *MNRAS*, 370, 453
- Rhee M.-H., van Albada T. S., 1996, *A&AS*, 115, 407
- Richter O.-G., Huchtmeier W. K., 1991, *A&AS*, 87, 425
- Rossa J., Dettmar R.-J., 2003, *A&A*, 406, 505
- Rownd B. K., Dickey J. M., Helou G., 1994, *AJ*, 108, 1638
- Rubin V. C., Roberts M. S., Ford W. K., Jr, 1979, *ApJ*, 230, 35
- Rubin V. C., Thonnard N., Ford W. K., Jr, 1980, *ApJ*, 238, 471
- Rubin V. C., Thonnard N. T., Ford W. K., Jr, 1982, *AJ*, 87, 477
- Rubin V. C., Waterman A. H., Kenney J. D. P., 1999, *AJ*, 118, 236
- Sandage A., Bedke J., 1994, *The Carnegie Atlas of Galaxies*. Carnegie Institution of Washington with The Flintridge Foundation, Washington, DC
- Sauty S. et al., 2003, *A&A*, 411, 381
- Schneider S. E., Thuan T. X., Magri C., Wadiak J. E., 1990, *ApJS*, 72, 245
- Schommer R. A., Bothun G. D., Williams T. B., Mould J. R., 1993, *AJ*, 105, 97
- Schulman E., Bregman J. N., Brinks E., Roberts M. S., 1996, *AJ*, 112, 960
- Schwartz C. M., Martin C. L., Chandar R., Leitherer C., Heckman T. M., Oey M. S., 2006, *ApJ*, 646, 858
- Sengupta C., Balasubramanyam R., 2006, *MNRAS*, 369, 360
- Shapley A., Fabbiano G., Eskridge P. B., 2001, *ApJS*, 137, 139
- Shostak G. S., van der Kruit P. C., Hummel E., Shaver P. A., van der Hulst J. M., 1982, *A&A*, 115, 293
- Sofue Y., Tomita A., Tutui Y., Honma M., Takeda Y., 1998, *PASJ*, 50, 427
- Spano M., Marcelin M., Amram P., Carignan C., Epinat B., Hernandez O., 2008, *MNRAS*, 383, 297
- Springob C. M., Haynes M. P., Giovanelli R., Kent B. R., 2005, *ApJS*, 160, 149
- Stil J. M., Israel F. P., 2002, *A&A*, 392, 473
- Strickland D. K., Heckman T. M., Colbert E. J. M., Hoopes C. G., Weaver K. A., 2004, *ApJS*, 151, 193
- Swaters R. A., van Albada T. S., van der Hulst J. M., Sancisi R., 2002, *A&A*, 390, 829
- Takase B., Miyauchi-Isobe N., 1991, *Publications of the National Astronomical Observatory of Japan*, 2, 7
- Theureau G., Bottinelli L., Coudreau-Durand N., Gouguenheim L., Hallet N., Loulergue M., Paturel G., Teerikorpi P., 1998, *A&AS*, 130, 333
- Tift W. G., Cocke W. J., 1988, *ApJS*, 67, 1
- Tomita A., Ohta K., Saito M., 1994, *PASJ*, 46, 335
- Tully R. B., Fisher J. R., 1977, *A&A*, 54, 661
- Tully R. B., Pierce M. J., 2000, *ApJ*, 533, 744
- Usui T., Saitō M., Tomita A., 2001, *AJ*, 121, 2483
- van der Hulst J. M., Huchtmeier W. K., 1979, *A&A*, 78, 82
- van der Kruit P. C., Allen R. J., 1978, *ARA&A*, 16, 103
- van Driel W., Marcum P., Gallagher J. S., III, Wilcots E., Guidoux C., Monnier Ragaigine D., 2001, *A&A*, 378, 370
- van Moorsel G. A., 1983, *A&AS*, 54, 19
- van Zee L., 2000, *AJ*, 119, 2757
- Vaughlin I. et al., 1999, *A&AS*, 135, 133
- Vetterling W. T., Flannery B. P., Press W. H., Teukolski S. A., 1989, *Numerical Recipes in FORTRAN - The Art of Scientific Computing*, 2nd edn. Cambridge Univ. Press, Cambridge
- Vogt N. P., Haynes M. P., Herter T., Giovanelli R., 2004, *AJ*, 127, 3273
- Vorontsov-Velyaminov B. A., Krasnogorskaya A. A., 1994, *VizieR Online Data Catalog*, 7062, 0
- Walter F., Weiss A., Martin C., Scoville N., 2002, *AJ*, 123, 225
- Wang Z., Scoville N. Z., Sanders D. B., 1991, *ApJ*, 368, 112
- Warmels R. H., 1988, *A&AS*, 73, 453
- Warner P. J., Wright M. C. H., Baldwin J. E., 1973, *MNRAS*, 163, 163
- Wehner E. H., Gallagher J. S. III, 2005, *ApJ*, 618, L21
- Wilcots E. M., Prescott M. K. M., 2004, *AJ*, 127, 1900
- Wilcots E. M., Turnbull M. C., Brinks E., 2001, *ApJ*, 560, 110
- Yasuda N., Fukugita M., Okamura S., 1997, *ApJS*, 108, 417

APPENDIX A: BUILDING A ROTATION CURVE**A1 The model**

For each of the N independent bins covering the field-of-view of the galaxy, the vector velocity in the frame of the galactic plane is described by the following two components lying in the plane of the galaxy.

- (i) $V_{\text{rot}}(R)$: the rotation velocity; and
- (ii) $V_{\text{exp}}(R)$: the expansion velocity.

There is one component perpendicular to this plane:

- (i) $V_z(R)$: the vertical motion velocity.

The observed radial velocities $V_{\text{obs}}(R)$ is linked to $V_{\text{rot}}(R)$, $V_{\text{exp}}(R)$ and $V_z(R)$ through the following five additional parameters.

- (i) PA: the PA of the major-axis of the galaxy (measured counterclockwise from the north to the direction of the receding side of the galaxy).
- (ii) i : the inclination of the galactic disc with respect to the sky plane.
- (iii) V_{sys} : the systemic velocity of the galaxy.
- (iv) α : the right ascension of the rotation centre.
- (v) δ : the declination of the rotation centre.

through the following equation:

$$V_{\text{obs}} = V_{\text{sys}} + V_{\text{rot}}(R) \cos \theta \sin i + V_{\text{exp}}(R) \sin \theta \sin i + V_z(R) \cos i. \quad (\text{A1})$$

R and θ being the polar coordinates in the plane of the galaxy. The angle in the plane of the galaxy, θ , is linked to the PA, the inclination i , the position x , y and centre x_c , y_c in the sky by the set of equations (A2)–(A7):

$$\cos \theta = R \cos \psi, \quad (\text{A2})$$

$$\sin \theta = R \frac{\sin \psi}{\cos i}, \quad (\text{A3})$$

$$\cos \psi = \frac{(y - y_c) \cos(\text{PA}) - (x - x_c) \sin(\text{PA})}{r}, \quad (\text{A4})$$

$$\sin \psi = -\frac{(x - x_c) \cos(\text{PA}) + (y - y_c) \sin(\text{PA})}{r}, \quad (\text{A5})$$

$$r = \sqrt{(x - x_c)^2 + (y - y_c)^2}, \quad (\text{A6})$$

$$R = r \sqrt{\cos^2 \psi + \frac{\sin^2 \psi}{\cos^2 i}}, \quad (\text{A7})$$

where ψ is the counterclockwise angle in the plane of the sky from the north.

Formally, one has to solve a system of N equations (as many equations as the number N of pixels taken into account) with $8N$ unknowns.

If one makes the assumption that, at the first order, for spiral galaxies, the expansion and vertical motions are negligible with respect to the rotation velocity, equation (A1) becomes

$$V_{\text{obs}}(R) = V_{\text{sys}}(R) + V_{\text{rot}}(R) \cos \theta \sin i.$$

This leads us to solve a system of N equations with $6N$ unknowns.

A usual solution to solve this degenerate system is to fix V_{sys} to a unique value for a given galaxy, and to consider that i , PA, x_c and y_c only depend on the galactic radius (to take warps into account), as it is the case for $V_{\text{rot}}(R)$. The field is decomposed into a certain number of elliptical rings (at given radii, with a given width) for which a set of parameters is computed for the corresponding radii (Begeman 1987). The number of rings being at least one order of magnitude less than N , the system of equations is no more degenerate. The physical width of the rings is typically ranging from 3 to 6 pixels ($\sim 2\text{--}4$ arcsec).

We decided to use a new method. To solve this degenerate system of equations, the number of unknowns is reduced by introducing physical constraints: V_{sys} , i , PA, x_c and y_c are fixed to a unique value for a given galaxy as warps are hardly observed within optical radius.

Moreover, the rotation velocity is approximated by a function with only four parameters:

$$V_{\text{rot}}(R) = V_t \frac{(R/r_t)^g}{1 + (R/r_t)^a}. \quad (\text{A8})$$

A2 Method

The method implemented is a χ^2 -minimization method in the velocity field, using the IDL routine LMFIT. This routine, based on the Levenberg–Marquardt method (as described in section 15.5 of Vetterling et al. 1989), quickly converges towards the best model.

The starting set of parameters is chosen as follows: the rotation centre (x_c , y_c) is supposed to be the nucleus identified in our continuum image (when no nucleus can be seen, either in our images or in other bands, it is chosen as the centre of symmetry of our velocity field), i is derived from the axial ratio found in the literature, the PA is computed from the photometry (or eye-defined by the outer parts of our velocity field when not available), and the systemic velocity is taken from the literature.

In order to have a pretty good estimate of the analytical function parameters (A8), we fit them on this preliminary rotation curve.

We then let free all the parameters. We compute an iterative 3.5σ clipping on the velocity field to reject points that have not been cleaned.

For well-behaved galaxies, the iterative process was quite easy and rapidly converged. However, for some irregular galaxies with asymmetric rotation curves it was hard to converge and we had a strong uncertainty on the kinematical parameters, more especially the inclination which is the less constrained. In some specific cases, marked in Table C2 with an asterisk (*), we then fixed i and/or PA during the fit process.

The rotation curves are computed from the velocity fields, using the previously found projection parameters i , PA, x_c and y_c . A sector of 22.5° in the plane of the galaxy around the minor-axis is excluded, and the points are weighted according to their corresponding $|\cos \theta|$. The rotation curves are sampled with rings.

In the inner parts, the width of the rings is set to match half the seeing, in order to respect Shannon sampling criteria. The transition radius r_t is defined by the first ring that contains more than 25 uncorrelated bins. If r_t is not reached before $D_{25}/10$, r_t is set to $D_{25}/10$. In the outer parts, the rotation curve is computed in successive rings containing the same number of uncorrelated bins, except eventually for the last ring of each side. The number of bins in the rings of the outer parts is set to the number between 16 and 25 that maximizes the number of uncorrelated bins of the last rings of each side. This range (16–25) is found to be the best compromise between the

signal-to-noise ratio and the spatial coverage in each ring. Thus, the width in each ring is variable. The velocity computed for each ring is then always the average of the same number of velocity points.

In the plots of rotation curve, for each individual ring, the vertical error bars are given by the dispersion of the rotation velocities inside the ring, normalized to the number of uncorrelated points inside the ring; the horizontal error bars represent the $\pm 1\sigma$ radius dispersion weighted by $\cos(\theta)$.

A3 Error estimation of the parameters

This method provides a determination of parameters errors, by associating a random noise to the data for which the amplitude can be fixed. However, this error seems unrealistically small. Indeed, the residual velocity field (difference between model and real velocity field) does not appear to be uniformly randomized. It contains the effects of non-axisymmetric motions such as expansion, spiral arms, bars or gas bubble expansion (local expansions), etc., that is to say real physical effects that cannot be described by our simple model. To be more realistic in parameter error determination, we simulate residual velocity fields from the real residual velocity field. We compute its power spectrum and put a random phase. As a result, the new residual field contains the same kind of structure, but placed differently. We then use a Monte Carlo method to estimate the errors: we compute the standard deviation in the parameters found over 250 simulated velocity fields. The advantage of this method is that it is completely automatic, and that it enables to use the whole information to compute global parameters and their errors. We also add 0.5 to the PA uncertainty because of the uncertainty on the astrometry.

The typical accuracy we reach is about 1 arcsec for the position of the rotation centre, $2\text{--}3 \text{ km s}^{-1}$ for the systemic velocity, 2° for the PA of the major-axis, but only $5^\circ\text{--}10^\circ$ for the inclination.

APPENDIX B: NOTES ON INDIVIDUAL GALAXIES

(i) *UGC 12893*. The H α emission is very weak, as confirmed by James et al. (2004) who find a total surface brightness of $0.4 \text{ } 10^{-16} \text{ W m}^{-2}$. The quality of our rotation curve is thus rather poor, anyway a maximum rotation velocity ($\sim 72 \text{ km s}^{-1}$) seems to be reached within the optical limit, adopting the inclination of 19° deduced from our velocity field (HyperLeda gives 30° from the photometry). The width of the H I profile at 20 per cent (75 km s^{-1} from Giovanelli & Haynes 1993 and $\sim 90 \text{ km s}^{-1}$ from Schneider et al. 1990) is in agreement with the amplitude of our H α velocity field and suggests that we actually reach the maximum rotation velocity with our H α rotation curve.

(ii) *UGC 89 (NGC 23)*. Because of the presence of a strong bar in this galaxy, the kinematics method used to determine the inclination is biased. Nevertheless, our kinematical inclination ($33^\circ \pm 13^\circ$) is compatible with the photometric inclination ($40^\circ \pm 4^\circ$) and with the value of 45° from Fridman et al. (2005) (H α Fabry–Perot observations) as well as with the value of 50° from Noordermeer et al. (2005) (H I data from WHISP). Our H α rotation curve reaches a plateau at $\sim 350 \text{ km s}^{-1}$, compatible with its morphological type (SBa) and with the position–velocity diagram from Noordermeer et al. (2005). The steep rise of the H α rotation curve is also in agreement with the H I observation of Noordermeer et al. (2005) and in very good agreement with the H α velocity field

512 *B. Epinat et al.*

of Fridman et al. (2005). Our H α velocity field does not show any obvious evidence for interaction with its companion, UGC 94.

(iii) *UGC 94 (NGC 26)*. The steep rise of the H α rotation curve is in agreement with the H I observation (Noordermeer et al. 2005). The H α rotation curve reaches a plateau at ~ 210 km s $^{-1}$, compatible with its morphological type (Sab). No H α emission can be seen as a counter part of the H I extension to the south-east (Noordermeer et al. 2005). There is no obvious evidence for interaction with its companion, UGC 89, in our H α velocity field.

(iv) *UGC 1013 (NGC 536 and NGC 542)*. An optical rotation curve has been obtained by Vogt et al. (2004) for UGC 1013. Because of bad weather, we could not get a sufficient signal-to-noise ratio when observing that galaxy with GHASP. On the other hand, we have detected, in the same field-of-view, H α emission from its companion NGC 542 (systemic velocity around 4660 km s $^{-1}$ from HyperLeda) with enough signal to get a reliable velocity field.

(v) *UGC 1317 (NGC 697)*. It is the brightest galaxy of the group NGC 677–NGC 697. H I data have been obtained by Giovanardi & Salpeter (1985), by Rhee & van Albada (1996) and by WHISP (website). A good agreement with H I observations within the first 2 arcmin is observed. Outside 2 arcmin, the H I rotation velocities of the receding side increase but we have no H α emission there to check that. There is no obvious evidence for interaction with its companion, NGC 677, in our H α velocity field.

(vi) *UGC 1437 (NGC 753)*. Relatively close to the centre of the A262 cluster, it is not H I deficient, however. It has been already observed in the optical by Rubin, Thonnard & Ford (1980), Amram et al. (1994) (Fabry–Perot data), Courteau (1997) and by Vogt et al. (2004) who found roughly the same kinematical parameters and rotation curves. From their H I rotation curve, Bravo-Alfaro et al. (1997) confirm the flatness of the H α rotation curve even beyond the optical radius ($D_{25}/2$). Although less extended, our H α velocity field is in good agreement with the H I observations by Broeils & van Woerden (1994) and by WHISP (website).

(vii) *UGC 1655 (NGC 828)*. H α emission is detected only in its very centre, so that only the rising part of the H α rotation curve can be plotted. The H α image by Hattori et al. (2004) shows two bright patches on each side of the nucleus. Because of the limited extension of the rotation curve, we could not determine the inclination from the kinematics and adopted the value found in HyperLeda. Anyway, a plateau seems to be reached at ~ 20 arcsec from the centre with a velocity ~ 205 km s $^{-1}$. The rotation curve derived by Márquez et al. (2002) is in agreement with ours and extends a bit further but with a strong dispersion beyond 20 arcsec. Wang, Scoville & Sanders (1991) provide a CO rotation curve limited to a 10 arcsec radius, also in agreement with our H α rotation curve. No H I map is available in the literature but the width of the H I profile at 20 per cent (427 km s $^{-1}$ from Bottinelli et al. 1990; 556 km s $^{-1}$ from Springob et al. 2005) is about twice our H α velocity field amplitude, showing that our H α rotation curve is far from reaching the maximum of the rotation velocity.

(viii) *UGC 1810 and UGC 1813*. Faint H α detection in UGC 1810 despite two hours of integration in good conditions, while a strong H α emitting blob is found in the central region of UGC 1813. Interestingly, two compact H α emitters are detected away from the two galaxies in the eastern and western edges of our field-of-view ($02^{\text{h}}21^{\text{m}}38^{\text{s}}$, $39^{\circ}21'35''$ and $02^{\text{h}}21^{\text{m}}20^{\text{s}}$, $39^{\circ}21'35''$, respectively). These two objects are related with the two galaxies for which we estimate a systemic velocity around 7550 ± 100 km s $^{-1}$, in agreement with WHISP (website), whereas HyperLeda gives a systemic velocity of 7356 km s $^{-1} \pm 57$. They may be intergalactic H II regions. A faint velocity gradient (~ 30 km s $^{-1}$)

is observed in the velocity field of the western object, suggesting that it may be a tidal dwarf galaxy candidate with a systemic velocity around 7680 km s $^{-1}$ (modulo 378 km s $^{-1}$ which is the free spectral range). At the opposite, no velocity gradient is seen in the eastern object having a systemic velocity of 7400 km s $^{-1}$ (modulo 378 km s $^{-1}$).

(ix) *UGC 3056 (NGC 1569, Arp 210)*. Magellanic irregular starburst galaxy (Seyfert I type). We detect a strong H α emission at the centre, causing ghosts in the southern outskirts of the galaxy in our data. This prevented us from computing an accurate velocity field in that region, even though there is some real emission there, as confirmed by the Hunter & Elmegreen (2004) line map. Also, we miss some extended filaments, being too faint or out of our field-of-view. Our H α velocity field is almost uniform and does not show any evidence for rotation. Thus, we could not fit any rotation model to this velocity field and do not show any rotation curve here. However, the velocity field and the position–velocity diagram shows markedly higher velocities at the centre and lower velocities on the north-western side, a feature not clearly seen in previous studies of the ionized gas with long-slit spectroscopy (Tomita, Ohta & Saito 1994; Martin 1998) mostly focused on the filamentary structures. Our position–velocity diagram is compatible with the H I rotation curve of Stil & Israel (2002) that does not show any clearly rising part until 50 arcsec radius.

(x) *UGC 3334 (NGC 1961, Arp 184)*. NGC 1961 is a very bright and massive distorted LINER 2 SAB(rs)b galaxy showing highly irregular outer spiral arms and a pathological disc (Arp 1966). It does not show any nearby companion and no clear double nucleus indicates a merger in progress. Nevertheless, NGC 1961 is the central member of the small group of nine galaxies located in the same velocity interval with a projected separation of 1 Mpc. Two long straight arms tangent to the north-following side of galaxy point towards an extended H I counterpart (Shostak et al. 1982). The amplitude of the WHISP velocity field (website) as well as the width of the H I profile at 20 per cent (~ 700 km s $^{-1}$ from the WHISP website and 690 km s $^{-1}$ from Bottinelli et al. 1990) are fully compatible with the H α velocity field amplitude. The overall resemblance between H α velocity field and H I velocity field is pretty good within the optical disc taking into account the low spatial resolution in the H I data. However, H α kinematics present perturbations all over the disc leading to an asymmetric and wavy rotation curve. The southern spiral arm and the knotty regions in the northern arm present unexpected velocities leading to a model of rotation curve with strong residuals for which it was necessary to constrain the inclination. Our rotation curve is in reasonable agreement with the rotation curve along the major-axis from Rubin et al. (1979) but our rotation curve is almost twice extended on the receding side. Rubin et al. (1979) claimed that NGC 1961, with its total mass greater than $10^{12} M_{\odot}$, was the most massive spiral known. Due to the uncertainties on the inclination and to waves in the rotation curve, the maximum rotation velocity (377 ± 85 km s $^{-1}$) could even be higher. From their optically derived spectra, they concluded to unexplained motions within the system. The H α lines continuously display a double profile (not resolved by Rubin et al. 1979) from the centre to the outermost points of the approaching side (as it can be seen in the H α position–velocity diagram, the most external velocities reach, respectively, ~ 3500 and 3720 km s $^{-1}$). The maximum velocity has been chosen as the mean external velocity. These double profiles in the disc are an additional evidence for the complex history of this galaxy (merging, interaction, stripping) which still needs to be modelled taking into account its disturbed and asymmetric H I distribution and X-ray emission.

(xi) *UGC 3382*. This early-type SBa galaxy presents a lack of H α emission at the centre, we thus miss the inner part of the velocity field within the first 3 kpc. Due to faint H α signal-to-noise ratio in the rest of the disc, our rotation curve is based on a limited number of velocity bins. Despite of this, both sides of the rotation curve agree fairly well. We excluded from the analysis the outermost part of the approaching side because it has no counterpart on the receding side. An inner velocity gradient is well seen in the H I position–velocity diagram (Noordermeer et al. 2005), not in the H α one. Their diagram shows that the rotation curve rises steeply at the centre and suggests that the maximum velocity is rapidly reached, at about 1 arcmin. The amplitude of the H I velocities is in good agreement with that of our H α velocity field, suggesting that we actually reach the maximum rotation velocity within the optical radius, at the end of our H α rotation curve. The morphological and H α kinematical inclinations are the same (21°), while 16° is found from H I data.

(xii) *UGC 3463 (KIG 168)*. Our H α map is in agreement with James et al. (2004) but suffers from bad seeing conditions leading to the confusion of several H II regions. Our rotation curve shows a bump at ~ 10 arcsec likely due to a bar. No H I rotation curve is available. The width of the H I profile at 20 per cent (341 km s^{-1} from Springob et al. 2005 and 334 km s^{-1} from Bottinelli et al. 1990) is in agreement with the amplitude of our H α velocity field, confirming that the maximum velocity is reached before the optical radius $D_{25}/2$.

(xiii) *UGC 3521*. The H α rotation curve is poorly defined at the centre because of the faint H α emission. It rises slowly up to $\sim 165 \text{ km s}^{-1}$ and extends up to about two-third of the optical radius ($D_{25}/2$) without being certain to reach the maximum rotation velocity. No H I rotation curve is available but the width of the H I profile at 20 per cent (381 km s^{-1} from Springob et al. 2005) is higher (by $\sim 50 \text{ km s}^{-1}$) than that of our H α velocity field, suggesting that the plateau is almost reached but not yet.

(xiv) *UGC 3528*. The H α emission is faint. It is sufficient, however, to derive a rotation curve apparently reaching a maximum although it barely reaches half the optical radius. The width of the H I profile at 20 per cent (344 km s^{-1} from Springob et al. 2005) is in good agreement with the amplitude of our H α velocity field, confirming that we do reach the maximum rotation velocity ($D_{25}/2$).

(xv) *UGC 3618 (NGC2308)*. No H α emission is detected thus no image is displayed.

(xvi) *UGC 3685*. Flocculent SBb galaxy whose bar terminates at a well-defined circular ring. The bar is aligned with the kinematic major-axis and there is no clear signature of it in the H α velocity field although a bump can be seen in the H α rotation curve at about 1 kpc. H α emission is mainly seen in a wide ring and in short spiral arms. No H α emission can be seen at the centre except along the bar, in agreement with the James et al. (2004) H α image, but we miss some faint emitting region to the south-east. As seen in the position–velocity diagram, a large velocity dispersion is observed in the nucleus of the galaxy. The photometric inclination is 55° from HyperLeda, 32° from NED and 33° from James et al. (2004). We agree with James et al. (2004) measurement, but we may estimate the uncertainty at $\sim 10^\circ$. Furthermore, if we take into account the very faint outer arms, the disc is rounder. On the other hand, the H I disc, which is about five times more extended than the optical one, is rather circular. It is possible that the inclination should vary with the radius, this should be done on the H I data (not yet published). Moreover, the H α ring is also almost circular. This probably means that the inclination of the galaxy may still be lower. We fit a kinematical inclination of $12^\circ \pm 16^\circ$. Within the error bars, the kinematical

inclination is compatible with the morphological one ($\sim 33^\circ \pm 10^\circ$). The rotation curve rises rapidly within the first 2 kpc as expected for early-type galaxies despite the fact that the bar, aligned with the kinematical major-axis, should lower the inner gradient (Hernandez et al., in preparation). If we exclude this inner structure, the rotation curve seems to grow with a solid body behaviour. The outermost H α regions disconnected from the main body of the disc extend beyond the optical radius $D_{25}/2$. The amplitude of the WHISP velocity field (website) as well as the width of the H I profile at 20 per cent ($\sim 100 \text{ km s}^{-1}$ from the WHISP website, 118 km s^{-1} from Springob et al. 2005 and 103 km s^{-1} from Bottinelli et al. 1990) are almost twice the H α velocity field amplitude. Moreover, regarding the H I velocity gradient, slowly growing up to the H I outskirts, our H α rotation curve probably does not reach the maximum velocity.

(xvii) *UGC 3708 (NGC 2341)*. It forms a pair with UGC 3709. Its H α distribution is asymmetric, brighter on the eastern side. Our H α velocity field suggests an inclination of $44^\circ \pm 16^\circ$, higher than the photometric inclination ($16^\circ \pm 24^\circ$) but compatible with the error bars. No H I velocity field is available. The width of the H I profile at 20 per cent (324 km s^{-1} , Bottinelli et al. 1990) is in agreement with our H α velocity field amplitude, confirming that we reach the maximum rotation velocity.

(xviii) *UGC 3709 (NGC 2342)*. It forms a pair with UGC 3708. The H α rotation curve reaches a plateau with a lower maximum rotation velocity than the one given by Karachentsev & Myneva (1984b), around 250 km s^{-1} instead of 292 km s^{-1} . No H I velocity field is available. The width of the H I profile at 20 per cent (396 km s^{-1} , Bottinelli et al. 1990) is in agreement with our H α velocity field amplitude, confirming that the maximum velocity is reached.

(xix) *UGC 3826 (KIG 188)*. It has a faint H α emission, in agreement with the map presented by James et al. (2004). The rising part of the H α rotation curve is ill-defined, but a plateau seems to be reached within the optical radius. The H I velocity field (WHISP website) shows a velocity amplitude in agreement with our H α velocity field and gives the same overall orientation for the major-axis PA. However, the pattern of the H I isovelocity lines in the central part points at a quite different orientation compared with that suggested by our H α velocity field. The width of the H I profile at 20 per cent given by Springob et al. (2005) (101 km s^{-1}) is significantly larger than the amplitude of our velocity field (almost double) and seems abnormally large when compared with the H I profile obtained by WHISP (website).

(xx) *UGC 3740 (NGC 2276, Arp 25)*. Its spiral pattern is unusual, perhaps because of a tidal encounter with the probable companion NGC 2300 (Karachentsev 1972) or more likely, due to tidal stripping. Indeed, it is a member of a group where stripping has been evidenced (Rasmussen, Ponman & Mulchaey 2006). The western side of our H α image and the velocity field show compression due to stripping by the intragroup medium. Our H α data also reveal low surface brightness filaments extending towards the east, in agreement with James et al. (2004). Our H α rotation curve is very peculiar and asymmetric. A steep velocity rise is observed in the galaxy core. The width of the H I profile at 20 per cent (167 km s^{-1} from Springob et al. 2005) is slightly larger than our H α velocity field amplitude. Nevertheless, the shape of our H α rotation curve suggests that the maximum is reached just after the optical radius ($D_{25}/2$). The CO emission (Elfhag et al. 1996) is distributed in a lopsided fashion, with more emission towards the north-western region.

(xxi) *UGC 3876 (KIG 193)*. Diffuse H α emission can be seen all over the disc, in agreement with James et al. (2004). The H α

514 *B. Epinat et al.*

rotation curve rises slowly beyond the optical radius ($D_{25}/2$) so that we are not sure to reach the maximum rotation velocity. No H I velocity field is available. However, the width of the H I profile at 20 per cent (208 km s^{-1} , Bottinelli et al. 1990) is in good agreement with our H α velocity field amplitude, suggesting that the maximum rotation velocity is effectively reached with our H α rotation curve.

(xxii) *UGC 3915*. Strong H α emission can be seen all over the disc. Our H α rotation curve rises steeply and reaches a plateau around 200 km s^{-1} at about $0.5D_{25}/2$. No strong signature of the bar (aligned with the major-axis) can be seen in our velocity field. A small bump, seen in our rotation curve in the 5 inner arcsec, could be due to the bar. No H I velocity field is available in the literature. The width of the H I profile at 20 per cent (323 km s^{-1} , Bottinelli et al. 1990) is in agreement with our H α velocity field amplitude.

(xxiii) *IC 476*. We detected some H α emission in IC 476, the small companion of UGC 402 (both observed in the same field-of-view). We derive its rotation curve up to about $0.5D_{25}/2$; thus, it is not sure that the maximum rotation velocity is reached. No H I data are available in the literature.

(xxiv) *UGC 4026 (NGC 2449)*. We detected faint H α emission in the low surface brightness galaxy UGC 4026. However, its H α emission is sufficient to derive with confidence a rotation curve up to about $0.5D_{25}/2$. As it seems that we observe the plateau of the rotation curve, the maximum velocity may be reached. A kinematical inclination of $56^\circ \pm 4^\circ$ has been computed, lower than the morphological one of $73^\circ \pm 4^\circ$. The kinematical inclination is very uncertain due to the very low signal-to-noise ratio of our H α data. No H I data are available in the literature.

(xxv) *UGC 4165 (NGC 2500, KIG 224)*. This galaxy belongs to a quartet of galaxies (Sandage & Bedke 1994). Diffuse H α emission is observed in our H α map, in agreement with James et al. (2004). Its short bar is almost aligned with its minor kinematical axis. Within the error bar, a good agreement is observed between the kinematical and morphological inclination. Our H α velocity field is in very good agreement with the WHISP data (website). The width of the H I profile at 20 per cent (101 km s^{-1} from Springob et al. 2005, 114 km s^{-1} from Bottinelli et al. 1990 and 100.9 km s^{-1} from Haynes et al. 1998) is in agreement with our H α velocity field amplitude.

(xxvi) *UGC 4256 (NGC 2532, KIG 232)*. It presents patchy H α emission along its spiral arms. The general pattern of the H α velocity field is in good agreement with the H I velocity field (WHISP website). The PA of the kinematical major-axis of the H α velocity field (116°) is in agreement with the H I one, but is very different from the value given in HyperLeda (26°) and in the RC3 (10°) as already noted by Marquez & Moles (1996). Indeed it is clear that the outermost contours of the galaxy measured from broadband imaging are elongated along the minor kinematical axis. Furthermore, morphological and kinematical inclinations are determined using PAs separated by 90° . Nevertheless, the H I disc is elongated along its kinematical major-axis, leading to an inclination $\sim 30^\circ$. Our H α rotation curve rapidly reaches a plateau climbing up to a maximum velocity $\sim 100 \text{ km s}^{-1}$ around the optical radius ($D_{25}/2$) in agreement with Marquez & Moles (1996) from H α slit spectroscopy.

(xxvii) *UGC 4393 (KIG 250)*. A strong H α emission can be seen along the bar (aligned with the kinematical major-axis) and in the southwestern spiral arm, in agreement with James et al. (2004) H α map. Due to the bar, the H α velocity field is strongly perturbed at the centre. As a consequence, the H α rotation curve is strongly perturbed, with counter-rotation motions at the centre. No H I velocity field is available in the literature. The H I width at 20 per cent (160 km s^{-1} from Springob et al. 2005) is more than

twice our H α velocity field amplitude (70 km s^{-1}). This means that the maximum velocity is not reached in H α . Moreover, due to the presence of the strong bar, the inclination is probably overestimated. Indeed, the external axial ratio of the outermost isophotes leads to an inclination around 35° . However, even with this lower value of inclination, the H I maximum rotation velocity remains slightly lower than expected for such a galaxy, according to the Tully–Fisher relationship.

(xxviii) *UGC 4422 (NGC 2595)*. Located in the Cancer cluster, this barred spiral exhibits a prominent nucleus and distorted outer regions extending up to 70 arcsec ($\sim 18 \text{ kpc}$). H α emission is observed at the centre, in the ring and in the beginning of the bar, in agreement with Gavazzi et al. (1998). Our rotation curve rapidly rises and reaches a plateau at almost 350 km s^{-1} in the innermost 5 arcsec . The shape of the rotation curve is consistent with the Fabry–Perot observations from Amram et al. (1992) and we derive the same set of parameters within the uncertainties. There is a strong discrepancy between the photometric ($49^\circ \pm 4^\circ$) and kinematical inclination ($25^\circ \pm 8^\circ$). No H I velocity map is available. The corrected H I profile width of 321 km s^{-1} from Springob et al. (2005) is in agreement with our H α velocity field amplitude.

(xxix) *UGC 4456 (KIG 260)*. A difference of 82° is observed between the kinematical and morphological major-axis PAs. This difference is due to its low inclination leading to an uncertain morphological determination. Within the error bar, a good agreement is observed between the kinematical and morphological inclinations. No H I velocity map is available. The width of the H I profile at 20 per cent (110 km s^{-1} from Bottinelli et al. 1990 and 105 km s^{-1} from Lewis et al. 1987) is larger than our H α velocity field amplitude although our H α rotation curve rapidly reaches a plateau extending well beyond the optical limit.

(xxx) *UGC 4555 (NGC 2649, KIG 281)*. No H I velocity map is available. The width of the H I profile at 20 per cent (251 km s^{-1} from Bottinelli et al. 1990 and 256 km s^{-1} from Lewis et al. 1987) is in agreement with our H α velocity field amplitude.

(xxxi) *UGC 4770 (NGC 2746)*. In agreement with its morphological type (SBa), it shows a weak and asymmetric H α emission. In particular, no H α is detected within the bar. The H α position–velocity diagram and rotation curve are badly defined due to faint signal-to-noise ratio in the data, especially on the receding side. The maximum velocity $V_{\text{CO}} = 207 \text{ km s}^{-1}$ deduced from the molecular component (Sauty et al. 2003) is in agreement with our H α velocity field amplitude. No H I velocity map is available. The width of the H I profile at 20 per cent (264 km s^{-1} from Bottinelli et al. 1990 and 270 km s^{-1} from Lewis et al. 1987) suggests that H α and the CO rotation curves do not reach the maximum velocity.

(xxxii) *UGC 4820 (NGC 2775, KIG 309)*. H α imaging from Hameed & Devereux (2005) is comparable with our data, showing a flocculent ring of H α emission. Stellar dynamics from Kregel, van der Kruit & Freeman (2005) suggest a maximum velocity of 283 km s^{-1} lower than that suggested by the H α kinematics. No H I velocity map is available in the literature. The width of the H I profile at 20 per cent (435 km s^{-1} from Bottinelli et al. 1990) is in agreement with our H α velocity field amplitude.

(xxxiii) *UGC 5045*. It is a triple-arm barred galaxy that suffers from global distortion and shows ultraviolet (UV) excess (KISO survey, Takase & Miyauchi-Isobe 1991). Its arms are knotty with many H II regions distributed asymmetrically in the disc and no H α emission is detected in the very centre. The rising part of our H α rotation curve is thus missing and the curve looks like a plateau around 400 km s^{-1} , which seems quite high for such an Sc-type

galaxy. Indeed, our H α velocity field suggests a faint inclination (17° only, with an uncertainty of 10°), whereas the photometry suggests $41^\circ \pm 4^\circ$ (HyperLeda). Adopting this last value would lower the plateau of our rotation curve around a more normal value of 200 km s^{-1} , thus casting a doubt on the inclination deduced from our kinematics. No H I velocity map is available but the width of the H I profile at 20 per cent (200 km s^{-1} , Springob et al. 2005) is in agreement with our H α velocity field amplitude. Taking into account the methodology used, and the fact that the velocity field which presents a good signal-to-noise ratio is not strongly disturbed (no bar, symmetric rotation curve), we adopt the kinematic inclination.

(xxxiv) *UGC 5175 (NGC 2977, KIG 363)*. This galaxy shows a strong H α emission. Our H α rotation curve is flat, with a plateau at $\sim 190 \text{ km s}^{-1}$, suggesting a maximum velocity rotation lower than that found by Karachentsev & Mineva (1984a) in the optical. It has been observed in CO by Sauty et al. (2003) who find a linewidth at 50 per cent of 312 km s^{-1} . No H I velocity map is available but the linewidth at 20 per cent of 356 km s^{-1} (Theureau et al. 1998) is comparable with our H α velocity field amplitude.

(xxxv) *UGC 5228*. The H α rotation curve of this strong H α emitter, rises up to a plateau at $\sim 125 \text{ km s}^{-1}$. The H I linewidth of $\sim 270 \text{ km s}^{-1}$ measured by Doyle et al. (2005) is in good agreement with our H α velocity field amplitude.

(xxxvi) *UGC 5251 (NGC 3003)*. As already noted by Rossa & Dettmar (2003), except in the nucleus and in several bright H II regions, the H α emission is rather faint and its distribution asymmetric, like the spiral arms of the galaxy. Such an asymmetry suggests that this galaxy may be disturbed by a dwarf companion. The velocity field is also rather asymmetric. No H I velocity field is available. The width of the H I profile at 20 per cent (305 km s^{-1} from Springob et al. 2005 and 289 km s^{-1} from Bottinelli et al. 1990) is slightly higher (by $\sim 30 \text{ km s}^{-1}$) than the velocity amplitude of our H α velocity field. Thus, the maximum rotation velocity is probably not reached with our H α rotation curve.

(xxxvii) *UGC 5279 (NGC 3026, KIG 377)*. No H I velocity field is available. The width of the H I profile at 20 per cent ($\sim 220 \text{ km s}^{-1}$, Bottinelli et al. 1990) is lower than our H α velocity field amplitude, suggesting that the maximum velocity is reached in our H α position–velocity diagram.

(xxxviii) *UGC 5319 (NGC 3061, KIG 382)*. Its bar, almost aligned with the major-axis, shows no significant signature in our H α velocity field. Our H α rotation curve shows an inclined plateau, continuously rising within the optical limits. The steep rising in the first kpc of the rotation curve for this relatively low mass galaxy may be the signature of a bar. No H I velocity field is available but the width of the H I profile at 20 per cent (233 km s^{-1} from Springob et al. 2005 and 272 km s^{-1} from Lang et al. 2003, HIJASS survey) is significantly higher than the amplitude of our H α velocity field ($\sim 180 \text{ km s}^{-1}$). However, the corrected velocity from Springob et al. (2005) is about 198 km s^{-1} and the width of the H I profile at 50 per cent from Lang et al. (2003) is 189 km s^{-1} which is in better agreement. This disagreement between H I and H α data could indicate that the galaxy is embedded in an H I complex extending much farther out than the optical limit.

(xxxix) *UGC 5351 (NGC 3067)*. This galaxy has been studied in the optical by Rubin, Thonnard & Ford (1982), the PA of the major-axis and the outer velocity gradients agree with both sets of data. Taking into account the difference in distance adopted for that galaxy (28.3 versus 19.3 Mpc), the extensions of the rotation curves agree. The rotation curve in the inner parts from stellar kinematics (Héraudeau et al. 1999) is in very good agreement with the inner part of the H α position–velocity diagram. The full-resolution H I velocity

field (WHISP, Noordermeer et al. 2005) is still too low and does not allow a straightforward comparison with the H α . In particular the bar is not seen in H I, while the signature of the bar is clearly seen in the inner region of the H α velocity field. The H I and H α velocity amplitudes and gas extension are similar but their behaviour along the major-axis seems different. The H α position–velocity diagram suggests that a constant velocity is reached after radius $\sim 5 \text{ arcsec}$, whereas the H I position–velocity diagram does not show such a plateau. The outermost isophotes of the *HST* image (Carollo, Stiavelli & Mack 1998) suggest an almost edge-on galaxy. Due to its high inclination, to avoid contamination due to the thickness of the disc (outer regions along the minor-axis), we have fixed the inclination to 82° from the morphology. The maximum rotation velocity has been computed taking into account this inclination and no rotation curve has been plotted.

(xl) *UGC 5373 (Sextans B, KIG 388)*. This dwarf galaxy is part of the Local Group. Our H α map is in good agreement with the H α maps from Hunter & Elmegreen (2004) and James et al. (2004). The H α velocity field presents a low amplitude velocity gradient ($\sim 30 \text{ km s}^{-1}$) barely visible in the position–velocity diagram. Both major-axis orientation and inclination are difficult to determine; nevertheless, the kinematical major-axis seems to be quite different ($\sim 30^\circ$) from the photometric major-axis probably due to non-circular motions. The H α rotation curve is ill-defined in the central part, with a possible counter-rotation within 15 arcsec from the centre, but rises rapidly beyond 30 arcsec and seems to reach a plateau at about 50 arcsec, in agreement with the H I data from Hoffman et al. (1996) who miss the rising part because of their poor resolution (and possibly lack of H I at the centre). We also agree that this galaxy is almost face-on (from the kinematics we find 10° , with an uncertainty of 18° and (Hoffman et al. 1996) find 18°), whereas the photometry suggests 60° (HyperLeda). However, our very low inclination value may lead us to overestimate the rotation velocities.

(xli) *UGC 5398 (NGC 3077)*. As a member of the M81 group of galaxies it is strongly disrupted by the interaction with M81 and M82. As shown by Walter et al. (2002), its optical image is offset with respect to a prominent H I tidal arm lying at about 4 arcmin east of the galaxy. Our H α map is in good agreement with the one from James et al. (2004). The H α velocity field shows no evidence for rotation, although some velocity gradient can be seen at the edges of the disc, with the lowest velocities observed on the western side (in agreement with Walter et al. 2002 observations, in H I, H α and CO). No H α rotation curve could be derived from our data as one can see it in the velocity field and in the position–velocity diagram.

(xlii) *IC 2542 (KIG 399)*. Kinematic and photometric data lead to a major-axis PA in good agreement but a difference of 20° is observed on the inclination; nevertheless, the difference in the inclination is compatible with the error bars. Our H α rotation curve seems to reach a plateau at almost 300 km s^{-1} within the optical radius ($D_{25}/2$). No H I data are available in the literature.

(xliii) *UGC 5510 (NGC 3162, NGC 3575)*. Our H α rotation curve seems to reach a plateau just before the optical radius ($D_{25}/2$) although the velocities for the receding side are still increasing beyond. No H I velocity field is available. The width of the H I profile at 20 per cent (204 km s^{-1} from van Driel et al. 2001 and 187 km s^{-1} from Bottinelli et al. 1990) is in agreement with our H α velocity field.

(xliv) *UGC 5532 (NGC 3147)*. The H α emission is very weak in the nuclear region and does not allow us to plot the rising part of the H α rotation curve which rapidly reaches (within 1 kpc) a slightly decreasing plateau starting at almost 400 km s^{-1} . No H I

516 *B. Epinat et al.*

velocity map is available. The width of the H I profile at 20 per cent (455 km s^{-1} from Richter & Huchtmeier 1991, and 403 km s^{-1} from Lang et al. 2003) is in agreement with our H α velocity field.

(xlv) *UGC 5556 (NGC 3187, Arp 316, HCG 44D)*. It is a member of the famous compact group HCG 44 (Hickson, Kindl & Auman 1989) strongly interacting with NGC 3190 (Sandage & Bedke 1994). H α emission is only observed along the lenticular central region (the bar) and in the inner arms. The arms are obviously driven by streaming motions due to the interaction with its companion. The PA of the kinematical major-axis of the galaxy is almost perpendicular to the bar. Thus, the velocity field traces the kinematics of the bar and of the streaming motions in the arms but not the kinematics of the disc. Furthermore, we cannot compute a rotation curve. The velocity amplitude perpendicular to the bar across the velocity field is $\sim 150 \text{ km s}^{-1}$, lower than the width of the H I profile at 20 per cent (296 km s^{-1} from van Driel et al. 2001 and 257 km s^{-1} from Bottinelli et al. 1990).

(xlvi) *UGC 5786 (NGC 3310, Arp 217)*. The unusual smooth outer plume on the western side of the galaxy is probably the result of a recent merger (Balick & Heckman 1981). The plume has a smaller radial velocity than the galaxy. Wehner & Gallagher (2005) evidenced a closed loop in the *V* and *R* band that may be tidal debris. Diffuse H α emission, not visible by James et al. (2004), is detected in our H α image all around the galaxy. A large portion of the star formation is located in a central ring surrounding an off-centred nucleus. The central region of the H α velocity field displays an S-shape pattern encircling two velocity peaks leading to two severe bumps in the rotation curve. The bright nucleus exhibits a steep velocity rise. Outside the nuclear region, the velocity decreases and then remains flat along the galaxy major-axis. Despite the evidence for perturbations, the rotation curve is fairly symmetric although showing some oscillations. Outflows are observed in the central region of the galaxy ($\sim 1 \text{ kpc}$) by Schwartz et al. (2006) where we measure large H α linewidths. The width of the H I profile at 20 per cent (330 km s^{-1} from Springob et al. 2005) is significantly larger than the amplitude of our H α velocity field, suggesting that we cannot reach the maximum rotation velocity with our H α data. Indeed, our H α rotation curve clearly reaches a maximum at about 120 km s^{-1} with its central bump at 0.5 kpc but the behaviour of the curve in the outer parts is too chaotic (with a total divergence between receding and approaching side beyond the optical limit) for concluding anything about the true maximum. The kinematical inclination has been determined by excluding the central spiral structure within the first kpc, leading to a rather high inclination of $53^\circ \pm 11^\circ$. This is significantly higher than the morphological inclination of $16^\circ \pm 25^\circ$ (HyperLeda) but the difference remains compatible with the error bars. We finally choose the kinematical inclination.

(xlvii) *UGC 5840 (NGC 3344, KIG 435)*. The H α map is in agreement with Knapen et al. (2004); however, we miss the outermost parts of the galaxy because of our field-of-view (limited to a 4 arcmin diameter in that case because of the use of a 2 inches circular filter). Also, the warp observed in H I (WHISP website) cannot be seen within our field-of-view. Despite the fact that this ringed spiral galaxy is fairly regular, the velocity field is not at all symmetric with respect to the minor-axis. The nuclear region shows a large velocity dispersion, as seen in the position–velocity diagram. The H α rotation curve exhibits a valley where the main spiral structure vanishes in the optical. The width of the H I profile at 20 per cent (166 km s^{-1} from Bottinelli et al. 1990) is in agreement with the amplitude of our H α velocity field. The maximum velocity

found in our H α rotation curve is rather high for such a small galaxy ($D_{25}/2 \sim 6 \text{ kpc}$) of Sbc type.

(xlviii) *UGC 5842 (NGC 3346, KIG 436)*. The H α emission seems relatively poor on the receding side because the interference filter we have used was not perfectly centred on the galaxy. Nevertheless, we were able to derive a quite acceptable rotation curve. The high dispersion of our rotation velocities at the centre is probably due to the bar, then (from 1 to 6 kpc) our rotation curve is slowly rising like a solid body. No H I velocity field is available. The width of the H I profile at 20 per cent (166 km s^{-1} from Bottinelli et al. 1990 and $\sim 180 \text{ km s}^{-1}$ from Tift & Cocke 1988) is in agreement with our H α velocity field suggesting that the maximum rotation velocity is reached. We conclude that a plateau (if any) must begin just beyond the optical radius ($D_{25}/2$) where our H α rotation curve ends after an almost continuously rising tendency.

(xlix) *UGC 6118 (NGC 3504)*. This early-type galaxy presents an almost circular outer ring, and a thin bar (more visible in *JHK* band from NED) embedded in a rather oval structure (axial ratio ~ 0.5). A bulge is visible in the near infrared images. The agreement between our H α map and the one from Hameed & Devereux (2005) is very good. The main bar has a size $\sim 1.2 \text{ arcmin}$. A secondary bar may be suspected in the first $\sim 20 \text{ arcsec}$ around the very bright H α nuclei. An H α spiral structure is observed within the oval structure starting at the end of the inner bar. We find the major kinematical axis to be almost parallel to the bar and the oval structure. Our H α velocity field is almost limited to the central oval structure and the bar, with only a few points in the outer ring. A steep inner rise of the velocities is observed in the galaxy core, otherwise the H α velocities remain roughly constant before 45 arcsec , radius beyond which they begin to increase slightly. This is not observed in the H I position–velocity diagram from WHISP (Noordermeer et al. 2005), and the H I rotation curve slightly increases all along the first arcminute. Their H I velocity field perfectly covers the outer ring and leads to an inclination of 39° . The morphological inclination deduced from the outer ring is $\sim 27^\circ$, while the inclination of the oval structure is $\sim 45^\circ$. The kinematical inclination of 52° deduced from our H α velocity field is consistent with the inclination of the oval distortion. Nevertheless, we computed the rotation curve using the H I inclination because our kinematical inclination mainly relies on velocities measured within the central oval structure. The central region of the velocity field within the bar displays an S-shape pattern encircling two symmetric velocity peaks leading to two strong bumps on the rotation curve (at ~ 0.5 – 1 kpc). Our H α rotation curve is in good agreement with the long-slit observations of Usui, Saitō & Tomita (2001).

(l) *UGC 6277 (NGC 3596, KG 472)*. Except for the first central 15 arcsec , it is a low surface brightness galaxy displaying everywhere weak H α emission. As a result, our H α rotation curve seems to be limited to its rising part. Nevertheless, the velocity amplitude is in agreement with the H I profile of Kornreich et al. (2000), suggesting that our H α rotation curve probably reaches the maximal rotation velocity despite its limited extent (about half the optical radius).

(li) *UGC 6419 (NGC 3664, Arp 05)*. It is one of the prototypical strongly barred magellanic spirals and has a nearby companion, UGC 6418, at 6.2 arcmin . H I Very Large Array (VLA) observations (Wilcots & Prescott 2004) show that the current interactions affect the morphology and the kinematics of the main galaxy. The H I velocity fields of both galaxies are connected, with a large extension ($\sim 10 \text{ arcmin}$) compared with the optical one ($\sim 1 \text{ arcmin}$). The PA of the major-axis of our H α velocity field is almost perpendicular to the H I one. Indeed, the gradient of our H α velocity field is almost

aligned along the bar, which cannot be seen in the H I data due to the low spatial resolution. It is therefore possible that our H α rotation curve does not reflect the rotation of the galaxy but more probably the kinematics of the bar, likely to be affected by non-circular motions. Anyway, the shape of our rotation curve (solid body type) is not surprising for a galaxy of this type, but we find a rather low rotation velocity considering the luminosity of that galaxy. This suggests that the kinematical inclination (66°) as well as the inclination determined from the disc shape when excluding the tidal tail (57°) are too high. Indeed, the axial ratio of the disc including the tidal tail is close to one, suggesting that the galaxy is seen almost face-on. We conclude that the velocities of our H α rotation curve are probably underestimated. Furthermore, the H I velocity field amplitude observed by Wilcots & Prescott (2004) ($\sim 150 \text{ km s}^{-1}$) is about twice ours ($\sim 70 \text{ km s}^{-1}$), suggesting that we do not reach the maximum of the rotation velocity.

(lii) *UGC 6521 (NGC 3719)*. No evidence for interaction with its companion, UGC 6523, can be seen in our H α velocity field which is fairly symmetric. The resulting rotation curve is slightly decreasing beyond 6 kpc. No H I velocity field is available. The width of the H I profile at 20 per cent (397 km s^{-1} , Theureau et al. 1998) is somewhat higher than the amplitude of our H α velocity field but the shape of our rotation curve leaves no doubt that the maximum is effectively reached within the optical limits.

(liii) *UGC 6523 (NGC 3720)*. Nearby companion of UGC 6521. The H α emission is limited to the central regions (about one third the optical radius), thus our H α rotation curve only shows the central rising part of the curve and no clear sign of interaction can be seen. No H I velocity field is available. The width of the H I profile at 20 per cent (393 km s^{-1} from Bottinelli et al. 1990) is much larger (more than three times) than our H α velocity field amplitude, indicating that we are far from reaching the maximum of the rotation velocity.

(liv) *UGC 6787 (NGC 3898)*. Because of the interference filter used for this observation, which was not perfectly centred on the systemic velocity of the galaxy, the H α emission from the eastern side was not transmitted through the filter (a good H α image could be found in Pignatelli et al. 2001). As a consequence, our H α rotation curve is only traced with the approaching side but seems acceptable anyway. It reaches a plateau within the optical radius ($D_{25}/2$) and seems to decrease beyond, in agreement with the H I data from WHISP (Noordermeer et al. 2005). However, the H I data suggest that the rotation curve climbs again beyond 2 arcmin to recover the same velocity level. Also, the steep inner rise of the velocities seen in the H I position–velocity diagram from WHISP is not detected in our H α position–velocity diagram, which is probably due to a too low signal-to-noise ratio of the optical observations. The H α velocities remain constant in the approaching half of the diagram, whereas the H I velocities increase in the same region.

(lv) *UGC 7021 (NGC 4045, NGC 4046)*. The H α emission of this barely barred galaxy is found along the inner ring and at the centre. No diffuse H α is detected otherwise in the disc, which is not surprising for an SAB(r)a galaxy. Our H α map is very similar to the one found in GOLD Mine (Gavazzi et al. 2003). Because H α emission is only detected in the very central area of the optical disc, we use the photometric inclination (56°) rather than the kinematical one (34°). Indeed the kinematical inclination is based only on the inner ring which is supposed to be circular, thus biasing the inclination determination. Our H α rotation curve shows a slowly decreasing plateau starting at $\sim 220 \text{ km s}^{-1}$ and ~ 2 kpc, corresponding to the tip of the bar. The core of the galaxy exhibits two different velocity components, one at $\sim 1920 \text{ km s}^{-1}$ and another one at $\sim 2000 \text{ km s}^{-1}$.

No H I velocity field is available. The width of the H I profile at 20 per cent (337 km s^{-1} , Springob et al. 2005) is in agreement with our H α velocity field amplitude, confirming that we actually reach the maximum of the velocity rotation although our H α rotation curve is far from reaching the optical radius ($D_{25}/2$).

(lvi) *UGC 7045 (NGC 4062)*. This galaxy is a strong H α emitter, as already reported by James et al. (2004). A perfect agreement between photometric and kinematical parameters is observed. Slit spectroscopy observations using H α and [N II] (Sofue et al. 1998) are compatible with ours, showing an H α rotation curve that reaches a slowly rising plateau after about 20 arcsec. The position–velocity diagram derived in H I by Broeils & van Woerden (1994) is affected by beam smearing effects, since the inner part shows a solid body rotation up to almost 1.5 arcmin. At larger radii, however, the optical and radio data are compatible. The velocity dispersion in the central region of our H α rotation curve is rather high, probably due to the bar. The linewidth of the H I profile at 20 per cent (309 km s^{-1} , Springob et al. 2005) is in good agreement with our H α velocity field amplitude.

(lvii) *UGC 7154 (NGC 4145)*. This galaxy, having a bar embedded in a large elliptical bulge, is one of the principal galaxies in the Ursa Major Cluster paired with A1208+40 (Holm 342b) located at 13 arcmin. The H α rotation curve beyond the optical radius ($D_{25}/2$) is mainly traced from emission regions of the spiral arms, leading to large wiggles in the rotation curve. The grand design of the WHISP H I velocity field (website) is compatible with the H α one. The H I maximum rotation velocity of 171 km s^{-1} (Warmels 1988), assuming a 42° inclination, is compatible with our H α value (about 150 km s^{-1} assuming a 65° inclination). Due to beam smearing effects, the inner velocity gradient in H I is nevertheless much lower than in H α and the H I position–velocity diagram suggests a solid body rotation curve up to 2 arcmin from the centre.

(lviii) *UGC 7429 (NGC 4319)*. A very faint H α emission has been detected in two spots for this spiral galaxy, companion of NGC 4291. This detection needs to be confirmed. No H I emission has been detected by Sengupta & Balasubramanyam (2006).

(lix) *UGC 7699*. No H I velocity field is available in the literature. The linewidth of the H I profile at 20 per cent (205 km s^{-1} , Broeils & van Woerden 1994) is in agreement with our H α velocity field amplitude; their position–velocity diagram shows a solid body rotation having the same velocity amplitude as ours but the higher spatial resolution of the H α velocity field enables us to observe deviations from a pure solid body rotation.

(lx) *UGC 7766 (NGC 4559)*. The bar of this galaxy is almost aligned with the major-axis; its signature can be seen on the velocity field as well as on the rotation curve within the first 30 arcsec. Meyssonier (1984) obtained a rotation curve from slit spectroscopy which is in agreement, although it has a much higher dispersion than our H α rotation curve. Our rotation curve is more extended since our velocity field reaches more outer regions although our field-of-view is limited by the size of the interference filter. Krumm & Salpeter (1979) found a flat H I rotation curve from 2 to 7 arcmin. It has been observed more recently by WHISP (website), their position–velocity diagram confirms the flat behaviour of the rotation curve up to 9 arcmin together with the amplitude determined by the previous authors. The width of the H I profile at 20 per cent (254 km s^{-1} , Springob et al. 2005) is in agreement with our H α velocity field amplitude.

(lxi) *UGC 7831 (NGC 4605)*. Diffuse H α emission is observed in the outer disc of this galaxy. Our H α velocity field and rotation curve exhibit a strong asymmetry likely to be explained by the bar. Such an asymmetry is confirmed by the H α + [N II] rotation curve

518 *B. Epinat et al.*

from Rubin et al. (1980) and by Sofue et al. (1998). An *I*-band image (XDSS) clearly provides the morphological centre of the galaxy and leads to the rotation curve presented here. On the other hand, the kinematical centre for this galaxy appears to be shifted by about 10 arcsec eastward from the morphological one but none of them leads to a symmetric inner rotation curve. The receding side of the rotation curve displays a plateau after 40 arcsec, following a solid body shape at the centre, while the approaching side is continuously climbing (note also that the receding side is less luminous than the approaching one). The method described in the paper leads to the rotation curve presented here because it minimizes the dispersion. Nevertheless, this solution is unphysical since it leads to negative rotation velocities for the receding side in the innermost region. To avoid this, the systemic velocity should be somewhat lowered by $\sim 20 \text{ km s}^{-1}$, leading to a worst disagreement between both sides of the rotation curve. Another solution would be to consider another rotation centre but it does not solve the asymmetry problem as explained above. This galaxy has been observed in H I by WHISP (website), their position–velocity diagram is asymmetric, in agreement with our H α position–velocity diagram and rotation curve, and the H I velocity field suggests a warp in the outer parts of the disc.

(Ixii) *UGC 7853 (NGC 4618, Arp 23)*. It forms a physical pair with UGC 7861 (NGC 4625). Assuming a distance for both galaxies of 8.9 Mpc (Moustakas & Kennicutt 2006), their physical separation is only $\sim 22 \text{ kpc}$ (8.5 arcmin). Indeed, these galaxies show obvious signs of interaction (e.g. strong tidal unique tail for both galaxies). Its bar is not centred on the nucleus (Eskridge et al. 2002). Due to the strong southern arm, the morphological centre is offset from the kinematical one. The H α rotation curve displays a solid body shape up to its end ($\sim 150 \text{ arcsec}$) suggesting that the maximum rotation velocity is probably not reached. The H I rotation curve (van Moorsel 1983) decreases beyond 3 arcmin from the centre (note, however, that their beam is larger than 1 arcmin). H I has been also observed by WHISP (website), their position–velocity diagram displays a solid body rotation curve up to $\sim 1.5 \text{ arcmin}$ for the approaching side and a plateau beyond 1 arcmin for the receding side. Their low-resolution velocity field shows a severely warped disc (the PA of the major-axis rotates by 90° between the inner regions and the outermost parts of the H I disc). Taking into account the beam smearing effect, the agreement between the H I and our H α position–velocity diagram and rotation curve is quite acceptable.

(Ixiii) *UGC 7861 (NGC 4625)*. This galaxy is the companion of UGC 7853 (see notes above). Here again the centre of the galaxy is offset from the centre of the velocity field due to the strong southern tidal arm. Our H α rotation curve shows a strong dispersion in the central part (up to 10 arcsec from the centre) then rises slowly as a solid body up to the optical limit (of about 40 arcsec) suggesting that the maximum rotation velocity is probably not reached. Fabry–Perot observations of this galaxy, with the 3.6-m CFHT, have been published by Daigle et al. (2006a), their velocity field and rotation curve are in good agreement with ours. H I has been observed by WHISP (website), their position–velocity diagram suggests a rotation curve with a plateau extending beyond the optical limit, from 1 up to 4 arcmin.

(Ixiv) *UGC 7876 (NGC 4635)*. This isolated galaxy is a member of the Coma1 Cloud (according to GOLD Mine, Gavazzi et al. 2003). The H α rotation curve is asymmetric and the fitting method probably led to an underestimation of the systemic velocity $\sim 10 \text{ km s}^{-1}$. This may be caused by the bar. Its CO emission is very faint (Sauty et al. 2003) and no H I velocity field is available but

the linewidth of the H I profile at 20 per cent (173 km s^{-1} , Springob et al. 2005) is in agreement with our H α velocity field amplitude.

(Ixv) *UGC 7901 (NGC 4651, Arp 189)*. Member of the Virgo cluster, it is a strong H α emitter, particularly in an inner ring from where start the arms. A very good agreement is observed between our H α map and the ones of James et al. (2004), Koopmann, Kenney & Young (2001), and GOLD Mine (Gavazzi et al. 2003). A faint signature of a bar can be seen in the inner regions of our H α velocity field. Our H α rotation curve is in good agreement with that observed by Rubin et al. (1999) from long-slit spectroscopy except that we do not observe the rising trend they observe for the outermost part of the receding side. Such a behaviour seems suspect, all the more since our H α rotation curve is perfectly symmetric and extends farther out, owing to velocities collected far from the major-axis. No H I velocity map is available. The width of the H I profile at 20 per cent (395 km s^{-1} , Springob et al. 2005) is in agreement with our H α velocity field amplitude.

(Ixvi) *UGC 7985 (NGC 4713)*. Member of the Virgo cluster showing a strong H α emission as shown by the same authors as for UGC 7901. The signature of a bar is seen in the inner part of our H α velocity field within a radius of $\sim 30 \text{ arcsec}$. Our H α rotation curve extends farther out than the rotation curve observed by Rubin et al. (1999), beyond the optical radius ($D_{25}/2$). Our rotation curve is fairly symmetric and does not show the strong decrease observed by Rubin et al. (1999) for the receding part around 40 arcsec. No H I velocity map is available but the H I linewidth at 20 per cent (217 km s^{-1} , Springob et al. 2005) is in agreement with our H α velocity field amplitude.

(Ixvii) *UGC 8334 (NGC 5055, M 63)*. M 63 is a very well studied flocculent spiral galaxy. Our observations are fully compatible with the H α Fabry–Perot data observed with the 1.6-m Mont Megantic Telescope (Daigle et al. 2006a). Their rotation curve is more extended, due to a larger field-of-view, but does not reach the optical radius ($\sim 6 \text{ arcmin}$). It possesses a huge H I disc ($\sim 36 \text{ arcmin}$ diameter) strongly warped beyond the optical disc (Battaglia et al. 2006). The agreement between our H α rotation curve and their H I rotation curve is very good but we find a better symmetry for receding and approaching sides from 2 to 10 kpc radius. The position–velocity diagram shows that the velocities steeply rise in the inner 10 arcsec.

(Ixviii) *UGC 8403 (NGC 5112)*. Paired with NGC 5107 at 13.5 arcmin, its H α map shows a very good agreement with that of James et al. (2004). The signature of a weak bar is visible in the inner region of our H α velocity field but it is difficult to see the signature of an interaction with its companion in its velocity field. An attempt of CO detection proved dubious (Braine et al. 1993). It has been observed in H I by Springob et al. (2005), and by WHISP (website). There is a good agreement between the WHISP velocity field and ours and our H α emission is almost as extended as the H I disc. The shape of the H I position–velocity diagram found by WHISP is in very good agreement with our H α position–velocity diagram and rotation curve. Also, the H I linewidth at 20 per cent (226 km s^{-1} , Springob et al. 2005) is in good agreement with our H α velocity field amplitude.

(Ixix) *NGC 5296*. This galaxy has no UGC number. It is the small companion of UGC 8709 (discussed hereafter). Our H α map is deeper than the one by Rossa & Dettmar (2003) but nevertheless does not show any H α emission in the tidal arms seen in their unsharped-mask *R*-band image, the emission being restricted to the central regions ($\sim 1/3 D_{25}/2$). As a consequence, our H α rotation curve only shows the inner rising part. It is difficult to make a direct comparison with the rotation curve obtained by Rampazzo

et al. (1995) because they choose to align their slit in the direction of UGC 8709, which is about 30° different from the true major-axis. However, simulating a slit with their orientation along our H α velocity field shows that our results are consistent. On the WHISP H I velocity field (website), one can hardly distinguish NGC 5296 close to UGC 8709, although it seems to appear as a point source in the average resolution map.

(lxx) *UGC 8709 (NGC 5297)*. It is the large companion of NGC 5296. H α emission is detected in the northern arm but only in the beginning of the southern tidal arm, in agreement with Rossa & Dettmar (2003). The clear signature of a bar can be seen at the centre of the H α velocity field. From the kinematics, we find an inclination ($76^\circ \pm 1^\circ$) slightly smaller than the photometric one ($82^\circ \pm 3^\circ$). It seems that the photometric inclination has been computed from the axial ratio of the disc including the tidal arms. The width of the H I profile at 20 per cent (418 km s^{-1} from van Driel et al. 2001, 413 km s^{-1} from Bottinelli et al. 1990) is in agreement with our H α velocity field amplitude. The H I velocity field has been observed by WHISP (website) and is consistent with ours. The H I position–velocity diagram shows a slightly decreasing plateau beyond 1 arcmin, in agreement with our H α rotation curve. The long-slit rotation curve observed by Rampazzo et al. (1995) also shows a decreasing trend in the outer parts. No CO has been detected in this galaxy (Elfhag et al. 1996).

(lxxi) *UGC 8852 (NGC 5376)*. This galaxy is included in a group together with UGC 8860 (NGC 5379) and UGC 8866 (NGC 5389). Strong H α emission is seen, in particular in a ring located 15 arcsec from the centre. No H I velocity field is available. The width of the H I profile at 20 per cent (402 km s^{-1} , Theureau et al. 1998) is significantly higher than our H α velocity field amplitude ($\sim 320 \text{ km s}^{-1}$). Since our H α rotation curve is still rising in the outer parts, before we reach the optical radius, this suggests that the maximum velocity is not reached.

(lxxii) *UGC 8863 (NGC 5377)*. The detection of H α emission in this early-type SBa galaxy is limited to two faint lobes at about 1 arcmin on each side of the disc. As a consequence our H α rotation curve is reduced to two points (which nevertheless represent 34 independent bins, that is, about a thousand of pixels), one for the receding side and one for the approaching side and we only get a lower limit for the H α maximum rotation velocity of $\sim 190 \text{ km s}^{-1}$. Moreover, even if the signal-to-noise ratio does not allow to compute another velocity bin at the centre of the galaxy, the position–velocity diagram suggests a faint H α emission (yellow spots) allowing us to measure a central gradient of $\sim 40 \text{ km s}^{-1} \text{ arcsec}^{-1}$ (i.e. $\sim 350 \text{ km s}^{-1} \text{ kpc}^{-1}$). Due to beam smearing limitation, this strong gradient cannot be seen in the WHISP position–velocity diagram (Noordermeer et al. 2005). Indeed, the maximum velocity is reached at about 1 arcmin from the centre in H I data leading to a lower velocity gradient of $\sim 3 \text{ km s}^{-1} \text{ arcsec}^{-1}$ (i.e. $\sim 25 \text{ km s}^{-1} \text{ kpc}^{-1}$). Our maximum velocity is probably close to the actual maximum velocity rotation since the width of the H I profile at 20 per cent (391 km s^{-1}) found by Noordermeer et al. (2005) is close to our H α velocity field amplitude.

(lxxiii) *UGC 8898 and UGC 8900 (NGC 5394 and NGC 5395, Arp 84)*. The nuclei of this interacting pair of galaxies are separated by only 1.9 arcmin ($\sim 27 \text{ kpc}$). No H α emission is detected in the tidal arms of UGC 8898, while H α emission is more extended in UGC 8900, in agreement with Kaufman et al. (1999) from Fabry–Perot imaging. The photometric inclination for UGC 8898 is $70^\circ \pm 3^\circ$, quite different from our kinematical inclination ($27^\circ \pm 20^\circ$) which is in fact based on the very central part only (about 15 arcsec diameter). Despite its limited extent, our H α velocity

field of UGC 8898 clearly suggests a PA of the major-axis of 31° , differing by 66° from the one used by Márquez et al. (2002) for long-slit spectroscopy, which they confess is not adequate to elaborate the rotation curve. Indeed, they did not observe any clear rotation within the first 10 arcsec. Our H α rotation curve extends only up to ~ 10 arcsec and we do not reach either a plateau or, probably, the maximum rotation velocity. Because our observations of UGC 8898 have been done through the edge of the transmission function of the interference filter, the spatial coverage of our data is smaller than that of Kaufman et al. (1999). They have also observed UGC 8898 in the CO line (Kaufman et al. 2002) and find a very good agreement between H α and CO data. In agreement with the Fabry–Perot H α velocity field of Kaufman et al. (1999), our H α velocity field of UGC 8900 is not well enough defined to show straightforward evidence for interaction, except that the velocity field is uncompleted and the kinematical major-axis is shifted by 11° from the morphological one, which is a significant difference considering the high inclination of this galaxy. Márquez et al. (2002) have aligned the slit of their spectrograph almost along the morphological major-axis, explaining part of the differences between our rotation curves. Their rotation curve is slightly more extended but much more chaotic and asymmetric, with a markedly smaller velocity amplitude than ours. Both sides of our H α rotation curve are fairly symmetric and show a slowly rising trend (almost solid body like between 20 and 60 arcsec) without ever reaching a plateau. Such a behaviour is unexpected for an Sa-type galaxy and could be due to the interaction with its companion. The kinematical and morphological inclinations of UGC 8900 are compatible within the error bars (they differ by only 9°). H I single dish observations cannot disentangle UGC 8898 from its companion UGC 8900 (van Driel et al. 2001; Theureau et al. 1998). The pair has also been observed in the H I by WHISP (website) and by Kaufman et al. (1999). Taking into account the lower H I spatial resolution, the H I and H α kinematics are compatible, and the H I position–velocity diagram suggests that we actually reach the maximum of the rotation curve at the end of our H α rotation curve.

(lxxiv) *UGC 8937 (NGC 5430)*. Our H α map shows low-emission H α regions that were not detected by García-Barreto et al. (1996). The signature of the strong central bar can be seen in our H α velocity field (S-shape signature). Our rotation curve reaches a plateau within a few arcsec. A strong velocity gradient of $\sim 300 \text{ km s}^{-1}$ is observed between -5 and 5 arcsec, as can be seen in the position–velocity diagram. The H I linewidth at 20 per cent (371 km s^{-1} from Springob et al. 2005, 344 km s^{-1} from Theureau et al. 1998) is slightly smaller than the amplitude of our H α velocity field ($\sim 400 \text{ km s}^{-1}$).

(lxxv) *UGC 9013 (NGC 5474)*. This late-type peculiar dwarf galaxy is the nearest companion of M101 (44 arcmin) and is tidally deformed into a very asymmetric and disturbed object. Our H α velocity field cannot help us finding the rotation centre as it shows a solid body shape. Knapen et al. (2004) show an H α map in good agreement with ours. The H α rotation curve derived from long-slit spectroscopy data by Catinella, Haynes & Giovanelli (2005) cannot be compared directly with ours, because their centre has been chosen to be the ‘pseudo-nucleus’. Several H I studies are available in the literature (Huchtmeier & Witzel 1979; van der Hulst & Huchtmeier 1979; Rownd, Dickey & Helou 1994; Kornreich et al. 2000). Kornreich et al. (2000) and Rownd et al. (1994) used the same data set from the VLA array (35-arcsec beam). The optical part of the galaxy is not affected by the severe warp seen in H I and the solid body rotation seen in H α is compatible with H I data. These authors place the kinematical centre as the symmetry centre of the warp.

520 *B. Epinat et al.*

It is closer to the centre of the outermost optical isophotes than the ‘pseudo-nucleus’. Rownd et al. (1994) assumed an inclination of 21° from a tilted ring model. Their PA of the major-axis at the centre ($\sim 158^\circ$) is in agreement with ours but almost perpendicular to the photometric PA. Due to the presence of the strong tidal arm and the relative low spatial $H\alpha$ coverage, the inclination and centre are in fact difficult to recover. That is why we preferred using the $H\text{I}$ kinematical centre and inclination (21°) consistent with the external axial ratio of the outermost isophotes from the XDSS image. The strange behaviour of the resulting $H\alpha$ rotation curve in the first 40 arcsec could be the signature of strong non-circular motions. We find a maximum velocity rotation $\sim 120 \text{ km s}^{-1}$ at about 70 arcsec, significantly higher than the velocities found by Komreich et al. (2000) even when assuming a very low inclination for the $H\text{I}$ disc. Also the amplitude of our $H\alpha$ velocity field is higher than the $H\text{I}$ velocity field amplitude.

(lxxvi) *UGC 9179 (NGC 5585)*. It is a satellite of M101 (Sandage & Bedke 1994). A good agreement is observed between our $H\alpha$ map and that of James et al. (2004); however, we miss an $H\alpha$ region in the north-east because of our smaller field-of-view. The $H\alpha$ rotation curve is perturbed, due to the presence of the bar and an inner arm-like structure. This galaxy has been observed in $H\text{I}$ by Cote, Carignan & Sancisi (1991) who obtained a velocity field and a rotation curve in agreement with ours although their $H\text{I}$ extent is larger and our $H\alpha$ resolution higher. Our $H\alpha$ rotation velocities are higher because we assume an inclination of 36° (derived from our $H\alpha$ velocity field), whereas the $H\text{I}$ data led to a higher inclination of 51.5° . Both values are nevertheless compatible within the $H\alpha$ error bars. Although the shape of our $H\alpha$ rotation curve suggests that we reach the maximum rotation velocity at the optical limit, the $H\text{I}$ rotation curve from Cote et al. (1991) shows that the true maximum is reached a bit further.

(lxxvii) *UGC 9219 (NGC 5608)*. It has been observed in $H\alpha$ by van Zee (2000) and James et al. (2004), their maps are in agreement with ours. Our $H\alpha$ velocity field amplitude is nevertheless compatible with the $H\text{I}$ linewidth at 20 per cent of 130 km s^{-1} from Bottinelli et al. (1990). No $H\text{I}$ velocity map is available in the literature for this galaxy.

(lxxviii) *UGC 9248 (NGC 5622)*. The $H\alpha$ emission is asymmetric and much brighter on the western side. Nevertheless, the resulting rotation curve is fairly symmetric and reaches a plateau within the optical limit. No $H\text{I}$ velocity map is available in the literature but $H\text{I}$ linewidth measurements at 20 per cent have been done and are compatible with our $H\alpha$ velocity field amplitude although somewhat larger (357 km s^{-1} by Theureau et al. 1998, 349 km s^{-1} by Springob et al. 2005).

(lxxix) *UGC 9358 (NGC 5678)*. Márquez et al. (2002) derived a rotation curve from long-slit spectroscopy which is in good agreement with our $H\alpha$ rotation curve, for both sides. However, since we adopted a slightly lower inclination, our velocities are slightly higher. Their rotation curve is more extended, but the dispersion of their points in the outer parts is quite high, especially on the receding side. Our $H\alpha$ velocity field is perturbed and clearly shows the signature of a bar at the centre (S shape of the isovelocity lines). No $H\text{I}$ velocity map is available in the literature but the width of the $H\text{I}$ profile at 20 per cent (424 km s^{-1} , Springob et al. 2005) is in good agreement with our $H\alpha$ velocity field amplitude.

(lxxx) *UGC 9363 (NGC 5668)*. Our observations are in agreement with previous $H\alpha$ Fabry–Perot observations by Jiménez-Vicente & Battaner (2000). They adopted an inclination of 18° derived by Schulman et al. (1996) from a tilted ring model ap-

plied to VLA $H\text{I}$ data. This inclination is lower than expected from morphology (33°). Our data confirm this tendency, explaining why morphological and kinematical major axes are found to be quite different (40°). Our kinematical estimate of the inclination is close to 0° and leads to unrealistically high rotational velocities. Thus, as Jiménez-Vicente & Battaner (2000), we fixed the inclination to the $H\text{I}$ value of 18° . Schulman et al. (1996) $H\text{I}$ data show a warp starting at 120 arcsec, which is the outermost limit of our $H\alpha$ rotation curve. Indeed, it is possible that the outermost points of our $H\alpha$ rotation curve are affected by this warp, since it shows a clear trend to increase from 80 to 120 arcsec, whereas the $H\text{I}$ observations by Schulman et al. (1996) suggest that the plateau of the curve is already reached at 100 arcsec when correcting for the warp. The width of the $H\text{I}$ profile at 20 per cent (122 km s^{-1} , Springob et al. 2005) is in agreement with our $H\alpha$ velocity field amplitude.

(lxxxii) *UGC 9406 (NGC 5693)*. A short bright bar and an asymmetric disc (with one knotty arm) are observed. This galaxy is paired with UGC 9399 (NGC 5689) at 11.8 arcmin, which may explain the presence of a single arm. Poor $H\alpha$ emission is detected and our $H\alpha$ velocity field shows a strong dispersion, so that it is difficult to draw any reliable rotation curve from our data. The photometric inclination found in the literature varies from 33° (Vorontsov-Velyaminov & Krasnogorskaya 1994) to 51° (HyperLeda). Even when adopting the lowest value of inclination, we find a maximum rotation velocity which remains abnormally low considering the absolute magnitude of this galaxy, suggesting that our $H\alpha$ velocity field is far from reaching the maximum velocity amplitude. Indeed the width of the $H\text{I}$ profile at 20 per cent is 74 km s^{-1} (Bottinelli et al. 1990), whereas our $H\alpha$ velocity field amplitude is smaller than 50 km s^{-1} . No $H\text{I}$ velocity map is available for this galaxy in the literature.

(lxxxiii) *UGC 9465 (NGC 5727)*. A good agreement is observed between our $H\alpha$ map and that of James et al. (2004). No signature of the central bar can be seen in our $H\alpha$ velocity field. It has been observed in $H\text{I}$ by Pisano, Wilcots & Liu (2002) and their velocity field is in good agreement with ours. These authors adopted an inclination of 61° (close to the inclination of 65° we deduced from our $H\alpha$ velocity field) and found a maximum rotation velocity of 93 km s^{-1} in good agreement with our $H\alpha$ value (98 km s^{-1}). The inclination of 90° given in HyperLeda is certainly wrong because this galaxy seems far from being seen edge-on. The inclination deduced from our $H\alpha$ velocity field exactly matches the value suggested by the axial ratio given in NED.

(lxxxiiii) *UGC 9576 (NGC 5774)*. This galaxy is the companion of NGC 5775. There is a good agreement between our $H\alpha$ map and that of James et al. (2004). Márquez et al. (2002) derived a rotation curve from long-slit spectroscopy. However, their slit was 20° away from the true kinematical major-axis, maybe explaining why their rotation curve is more chaotic than ours. Our $H\alpha$ rotation curve is much more symmetric and extends farther out. The width of the $H\text{I}$ profile at 20 per cent (280 km s^{-1}) from Springob et al. (2005) is almost twice our $H\alpha$ velocity field amplitude, which is quite surprising since the shape of our $H\alpha$ rotation curve suggests that we reach the maximum rotation velocity. The value given by Springob et al. (2005) seems nevertheless suspicious as Bottinelli et al. (1990) and Irwin (1994), respectively, found 152 and 179 km s^{-1} (uncorrected for galaxy inclination) for the width of the $H\text{I}$ profile at 20 per cent, which is quite compatible with our $H\alpha$ velocity field amplitude. The detailed $H\text{I}$ velocity field of the pair NGC 5774–NGC 5775 has been observed at the VLA by Irwin (1994). Her velocity field and rotation curve for NGC 5774 are in good agreement with our $H\alpha$ data and have about the same spatial extension. She used the

same method as ours to determine the kinematical parameters and they are in very good agreement with ours.

(lxxxiv) *UGC 9736 (NGC 5874)*. We detect poor and asymmetric H α emission in that galaxy. Our H α rotation curve is nevertheless fairly symmetric and almost reaches the optical limit, with a trend to flatten in its outermost parts. The width of the H I profile at 20 per cent (324 km s^{-1} from Springob et al. 2005, 315 km s^{-1} from Bottinelli et al. 1990) is in agreement with our H α velocity field amplitude and suggests that we actually reach the maximum of the rotation curve. No H I velocity map is available in the literature.

(lxxxv) *UGC 9866 (NGC 5949)*. Comparing our H α map with that of James et al. (2004) shows that our data suffer from bad seeing conditions leading to non-resolved H II regions. However, the H α emission is strong enough so that we have a complete velocity field all over the disc. The H α emission is asymmetric, stronger on the receding side (north-west). Our rotation curve is in very good agreement with the radial velocities measured by Karachentsev & Petit (1990) from slit spectroscopy when correcting for the inclination. Courteau (1997), also from slit spectroscopy, finds a slightly smaller extension for the rotation curve but the velocity width he measures from the flux-weighted rotation profile (213 km s^{-1}) is in agreement with our maximum velocity field amplitude. No H I velocity map is available but the width of the H I profile at 20 per cent (216 km s^{-1} from Springob et al. 2005, 197 km s^{-1} from Bottinelli et al. 1990) is also in good agreement with our H α velocity field amplitude.

(lxxxvi) *UGC 9943 (NGC 5970)*. It forms a pair with IC 1131 at 8 arcmin. H α emission is strong in particular in an inner ring. Our H α rotation curve is in good agreement with the slit spectroscopy one of Márquez et al. (2002). A plateau is clearly reached around 3 kpc. No H I velocity map is available in the literature but the width of the H I profile at 20 per cent (338 km s^{-1} from Springob et al. 2005, 326 km s^{-1} from Bottinelli et al. 1990) is in good agreement with our H α velocity field amplitude.

(lxxxvii) *UGC 10075 (NGC 6015)*. There is a good agreement between our H α map and that of James et al. (2004). We detect, however, some faint emission in an outer spiral arm to the south-east that they do not detect. Our H α rotation curve is in good agreement with the slit spectroscopy observations of Carozzi (1976) when correcting for the different inclinations adopted. However, her detection was not as good, and our rotation curve is almost twice more extended, clearly showing a slowly rising plateau beyond 50 arcsec radius. No H I velocity map is available in the literature but the width of the H I profile at 20 per cent (315 km s^{-1} from Springob et al. 2005, 310 km s^{-1} from Bottinelli et al. 1990) is in good agreement with our H α velocity field amplitude. It has been observed in CO by Braine et al. (1993) who find a strong CO emission at 40 arcsec (2.7 kpc) from the centre.

(lxxxviii) *UGC 10521 (NGC 6207)*. There is a good agreement between our H α map and that of James et al. (2004). Our H α rotation curve is in good agreement with the slit spectroscopy observations by Carozzi (1976) (PA = 15°) and Márquez et al. (2002) (with PA = 22°) when correcting for the different inclinations adopted. No H I velocity map available in the literature but the width of the H I profile at 20 per cent (255 km s^{-1} from Springob et al. 2005, 240 km s^{-1} from Bottinelli et al. 1990) is in good agreement with our H α velocity field amplitude.

(lxxxix) *UGC 10652 (NGC 6283)*. This galaxy is asymmetric, with some bright H α spots and diffuse H α emission all over the disc. An inner H α ring, of some 7 arcsec radius, can be seen at the centre. The morphological inclination of $30^\circ \pm 7^\circ$ is compatible, within the error bars, with the kinematical inclination ($16^\circ \pm 12^\circ$)

deduced from our H α velocity field. The position of the kinematical major-axis differs from the photometric one by 12° . Our H α rotation curve seems to reach a plateau at about 2 kpc (23 arcsec) within the optical limit. No useful H I data are available in the literature for that galaxy.

(xc) *UGC 10713*. We adopted an inclination of 90° for that galaxy, otherwise our method led to a clearly wrong value below 70° , probably because of the odd pattern of our H α velocity field at the centre. It has been observed in H I by WHISP (website) and their velocity field is in agreement with ours, but much more extended. Their H I position–velocity diagram suggests that the rotation curve reaches a plateau at about 1 arcmin radius, just beyond the limits of our H α rotation curve which is limited to the solid body rising part. The H I linewidth at 20 per cent (268 km s^{-1} by Theureau et al. 1998 and 260 km s^{-1} by Springob et al. 2005) is in agreement with our H α velocity field amplitude.

(xci) *UGC 10757*. This galaxy has a velocity of 1168 km s^{-1} . It is located in a triple subgroup with UGC 10762 (NGC 6340) an S0/a galaxy with a peculiar morphology with a series of tightly wound, almost circular, multiple-fragment, relatively thin outer arms surrounding a bulge and a lens at 6.4 arcmin and UGC 10769 which has an Sb pec morphological type located at 6.1 arcmin with a velocity of 1283 km s^{-1} . This system is clearly in interaction as shown by the H I cloud in which the three galaxies are embedded (e.g. WHISP website). This galaxy is asymmetric, with a brighter H α emission at the beginning of the northern spiral arm, also seen in the optical (XDSS) and UV (GALEX) images. The WHISP H I velocity field corresponding to the optical extent of the galaxy (also coinciding with the brightest part of the H I complex) is in agreement with our H α velocity field. However, the pattern of the whole extent of the H I velocity field is quite odd, apparently because of several galaxies interacting there. As a result, the width of the H I profile at 20 per cent found in the literature for that galaxy (283 km s^{-1} from Springob et al. 2005, 276 km s^{-1} from Lang et al. 2003, 222 km s^{-1} from Theureau et al. 1998) is larger than the amplitude of the H α velocity field because a more extended region is embedded in the H I. The shape of the H α rotation curve suggests that we are not far from reaching the maximum rotation velocity within the optical limit.

(xcii) *UGC 10769*. This galaxy has a diffuse disc and no spiral pattern visible. It has a higher velocity than the two other galaxies in the triple system (see UGC 10757 for a detailed discussion). We detect H α emission only in the north-eastern edge of the disc so that no rotation curve can be derived. The secondary peak in the H I distribution corresponds to the same region where the H α is detected.

(xciii) *UGC 10791*. This low surface brightness galaxy has two companions according to the WHISP website. We observe a faint diffuse H α emission throughout the disc insufficient to determine unambiguously its inclination. This galaxy is classified face-on in HyperLeda; nevertheless, it does not look face-on in the XDSS image (see Fig. D93); in addition, the velocity field displays a clear rotation compatible with the H I velocity field (e.g. same PA and velocity amplitude in the central region). Thus, we fixed the inclination to the WHISP value of 34° . The H α distribution extends only until half of the optical radius and thus does not reach the maximum rotation velocity observable in the H I [full width at half-maximum (FWHM): 199 km s^{-1} from Springob et al. 2005, 156 km s^{-1} from Theureau et al. 1998; amplitude of the WHISP velocity field of $\sim 150 \text{ km s}^{-1}$].

(xciv) *UGC 11012 (NGC 6503)*. This galaxy has a strong H α emission all over its disc, with a faint extended feature on the

522 *B. Epinat et al.*

western edge (~ 2 arcmin from the centre). This faint extension cannot be seen in the $H\alpha$ map from Strickland et al. (2004). Our rotation curve clearly reaches a plateau around 80 arcsec, well before the optical limit. Several optical rotation curves are found in the literature but none of them takes this extension into account and their extension is limited to ~ 80 arcsec, whereas ours extends up to 150 arcsec (for the receding side, owing to the mentioned $H\alpha$ extension). Nevertheless, these rotation curves (de Vaucouleurs & Caulet 1982; Karachentsev & Petit 1990) are in very good agreement with our $H\alpha$ rotation curve. $H\beta$ observations made by Bottema (1989) also show a rotation curve in good agreement with ours. The $H\text{I}$ map obtained by Begeman (1987) is more extended than our $H\alpha$ map otherwise both velocity fields are in good agreement, as well as the derived rotation curves. The parameters computed in $H\text{I}$ with a tilted ring model ($PA = -59^\circ.4$, $i = 73^\circ.8$) are in very good agreement with our own parameters.

(xcv) *UGC 11269 (NGC 6667)*. Despite a short exposure time (~ 1 h), our $H\alpha$ observations perfectly match James et al. (2004) $H\alpha$ data who find faint patchy emission. It has been observed in $H\text{I}$ by WHISP (Noordermeer et al. 2005) and their velocity field and rotation curve extend more than four times the optical radius. Our $H\alpha$ position–velocity diagram does not show the steep velocity gradient observed in their $H\text{I}$ position–velocity diagram in the innermost 40 arcsec due to a very noisy and patchy distribution of the ionized gas. The maximum rotation velocity is reached in $H\alpha$, as confirmed by the width of the $H\text{I}$ profile at 20 per cent found by different authors (415 km s^{-1} from Noordermeer et al. 2005, 394 km s^{-1} from Springob et al. 2005, 406 km s^{-1} from Bottinelli et al. 1990). Our $H\alpha$ data suggest that the maximum rotation velocity is reached within the first kpc instead of the first ~ 6 kpc as suggested by the $H\text{I}$ data (Noordermeer et al. 2005).

(xcvi) *UGC 11300 (NGC 6689, NGC 6690)*. This galaxy has been published in Paper IV. See specific comment at the end of this section.

(xcvii) *UGC 11332 (NGC 6654A)*. There is a good agreement between our $H\alpha$ map and that of James et al. (2004). However, our image is affected by very bad seeing conditions (see Table C2) resulting in a diffuse emission around the galaxy that is most probably an artefact. No $H\text{I}$ velocity map is available in the literature. The width of the $H\text{I}$ profile at 20 per cent (331 km s^{-1} from Springob et al. 2005, 315 km s^{-1} from Bottinelli et al. 1990) is significantly larger than our $H\alpha$ velocity field amplitude (about 200 km s^{-1}), suggesting that our $H\alpha$ velocity field does not reach the maximum rotation velocity although it extends up to the optical radius.

(xcviii) *UGC 11407 (NGC 6764)*. The $H\alpha$ emission is conspicuous along the bar and in the arms (particularly the northern arm). Our $H\alpha$ rotation curve has been drawn using the photometric PA of the major-axis and the photometric inclination. It is much chaotic at the centre, up to 20 arcsec (probably because of the strong bar), and then looks on average like that of a solid body rotating disc, although it is markedly asymmetric. The central bar is almost aligned along the photometric major-axis and the $H\text{I}$ velocity field derived from VLA observations (Wilcots, Turnbull & Brinks 2001) leads to the same PA. In the central parts, the isovelocity line patterns show the signature of the strong central bar on both $H\alpha$ and $H\text{I}$ velocity fields. The position–velocity diagram shows a steep velocity rise in the galaxy core. The width of the $H\text{I}$ profile at 20 per cent (291 km s^{-1} from Springob et al. 2005, 293 km s^{-1} from Bottinelli et al. 1990, $\sim 300 \text{ km s}^{-1}$ from Wilcots et al. 2001) is in agreement with our $H\alpha$ velocity field amplitude.

(xcix) *UGC 11466*. We detect a strong $H\alpha$ emission along a bar-like feature. This galaxy has been observed in $H\text{I}$ by WHISP (web-

site) and their high-resolution velocity field is in agreement with our $H\alpha$ velocity field. Their lower resolution maps show a much larger $H\text{I}$ disc but no greater velocity amplitude, suggesting that our $H\alpha$ rotation curve reaches the maximum velocity in the outer parts of the optical disc (also, the WHISP position–velocity diagram is in agreement with our $H\alpha$ position–velocity diagram and rotation curve). This is confirmed by the width of the $H\text{I}$ profile at 20 per cent measured by different authors (247 km s^{-1} from Springob et al. 2005, 239 km s^{-1} from Theureau et al. 1998, 251 km s^{-1} from Kamphuis, Sijbring & van Albada 1996) which is in perfect agreement with our $H\alpha$ velocity field amplitude.

(c) *UGC 11470 (NGC 6824)*. The $H\alpha$ emission is rather faint, and hardly detected on the eastern side of the galaxy because of the interference filter transmission mismatching the systemic velocity. As a result, the rotation curve could be drawn almost only from the approaching side. No $H\text{I}$ velocity map is available in the literature. The width of the $H\text{I}$ profile at 20 per cent (574 km s^{-1} from Springob et al. 2005) is in agreement with the $H\alpha$ velocity amplitude showing that the maximum velocity is reached at a small radius (~ 3 kpc) compared to the optical radius (~ 18 kpc), in agreement with what is expected for such a bright early-type galaxy ($M_B = -21.3$; Sab). There has been no detection of CO in that galaxy by Elfhag et al. (1996).

(ci) *UGC 11496*. The $H\alpha$ emission is very faint in that galaxy, sufficient, however, for drawing a velocity field and deriving an acceptable rotation curve. The $H\text{I}$ velocity field (WHISP website) is in agreement with our $H\alpha$ velocity field but much more extended. The width of the $H\text{I}$ profile at 20 per cent (121 km s^{-1} from Bottinelli et al. 1990) is in agreement with our $H\alpha$ velocity field amplitude and confirms that we reach the maximum rotation velocity as already suggested by the shape of our $H\alpha$ rotation curve, showing a trend to reach a plateau in the outer parts.

(cii) *UGC 11498*. The $H\alpha$ emission is faint and asymmetric in this early-type galaxy (SBb). However, although there is only a few $H\alpha$ emission on the receding side, the shape of our rotation curve suggests that a plateau is reached on both sides. No $H\text{I}$ velocity map is available in the literature. The width of the $H\text{I}$ profile at 20 per cent (509 km s^{-1} from Springob et al. 2005, 500 km s^{-1} from Bottinelli et al. 1990) perfectly matches our $H\alpha$ velocity field amplitude. We find a maximum rotation velocity of 274 km s^{-1} which seems a bit high when taking into account its luminosity.

(ciii) *UGC 11597 (NGC 6946)*. NGC 6946 is a very well studied nearby spiral galaxy. Our $H\alpha$ Fabry–Perot observations are in perfect agreement with the $H\alpha$ Fabry–Perot data recently published by Daigle et al. (2006a) who had a larger field-of-view (we miss the outer parts of the optical disc). We find a kinematical inclination of $40^\circ \pm 10^\circ$ close to their value ($8^\circ.4 \pm 3^\circ$) and compatible with the photometric value ($17^\circ \pm 19^\circ$) within the error bars.

(civ) *UGC 11670 (NGC 7013)*. The $H\alpha$ emission is mainly concentrated in the central part of the disc (with two bright blobs, on each side of the central bulge, along the major-axis) and some emission can be seen on the north-western edge of the optical disc. Our $H\alpha$ rotation curve rapidly reaches a maximum, at about 20 arcsec from the centre (~ 1 kpc), followed by a slight decrease and a plateau. The velocity gradient observed in the inner 20 arcsec of our position–velocity diagram is consistent with that observed in the $H\text{I}$ position–velocity diagram from WHISP (Noordermeer et al. 2005) and their velocity field is in agreement with our $H\alpha$ velocity field but much more extended. The width of the $H\text{I}$ profile at 20 per cent (342 km s^{-1} from Noordermeer et al. 2005, 363 km s^{-1} from Springob et al. 2005, 355 km s^{-1} from Bottinelli et al. 1990) is in good agreement with our $H\alpha$ velocity field amplitude. The

morphological inclination of 90° found in HyperLeda assumes a thick disc. However, assuming a thin disc, the inclination is found to be 68° with a tilted ring fitted to the H I velocity field (Noordermeer et al. 2005) in agreement with the value deduced from our H α velocity field ($65^\circ \pm 2^\circ$) as well as with the inclination deduced from the axial ratio (69°) or other morphological determinations (Vorontsov-Velyaminov & Krasnogorskaya 1994).

(cv) *UGC 11872 (NGC 7177)*. Our H α map has a mottled appearance, in agreement with that of James et al. (2004); however, our observations suffer from bad seeing conditions. Our H α rotation curve rapidly reaches a well-defined and symmetric plateau, extending up to the optical radius. The rotation curve obtained by Márquez et al. (2002) reaches the plateau more rapidly (10 arcsec instead of 20 arcsec) but they find it at a lower value since they assume a surprisingly high inclination (79° , while we find 47° from our H α velocity field, which is closer to the morphological value of 54°). Furthermore, slit spectroscopy of the inner part of the galaxy by Héraudeau et al. (1999) confirms that the maximum velocity is not reached before 20 arcsec. No H I velocity map is available in the literature; however, H I linewidths have been measured (314 km s^{-1} from Springob et al. 2005, 317 km s^{-1} from Bottinelli et al. 1990) and are in agreement with our H α velocity field amplitude. Moreover, a radio synthesis observation has been done (Rhee & van Albada 1996) to derive a position–velocity diagram. It shows a solid body rotation as far out as 1 arcmin which is likely to be explained by beam smearing effects.

(cvi) *UGC 12082*. The H α emission in this low-luminosity nearby galaxy is rather patchy. Our H α map is in agreement with that of James et al. (2004). The H I velocity field (WHISP website) confirms our PA determination for the major-axis in the central part. It is, however, much more extended than the H α one and shows a

strong warp of the H I disc. The WHISP position–velocity diagram suggests that we do not reach the maximum velocity within the optical radius although the shape of our H α rotation curve shows a trend to reach a plateau in the outer parts. The H I linewidth at 20 per cent confirms that point, since all the values found in the literature (95 km s^{-1} from Braun, Thilker & Walterbos 2003, 103 km s^{-1} from Springob et al. 2005, 79 km s^{-1} from Bottinelli et al. 1990) are markedly larger than the amplitude of our H α velocity field.

NB. The following targets, already published in the previous GHASP papers, have been observed again in different conditions (filters, seeing, transparency, exposure time, etc.) in order to check if the quality of the data may be improved: UGC 2023, UGC 2034, UGC 3734, UGC 11300 and UGC 12060. The results are fully consistent with the previous set of observations without any significant improvement so that we do not present the new data in this paper, except for UGC 11300.

We present the new observation for UGC 11300 mainly to compare the new method of reduction presented in this paper with the previous GHASP papers. We observe a general good agreement in velocities as well as in radial extension. The adaptive spatial binning enables us now: (1) to plot velocity measurement in the outskirts of the approaching side; (2) to increase the spatial resolution within the inner 30 arcsec ($\sim 1 \text{ kpc}$); and (3) to underline that the error bars are correlated with the spatial resolution and the quality of the data (the error bars are generally smaller and a wide range of amplitudes are observed).

APPENDIX C: TABLES

Table C1. Log of the observations.

N° UGC (1)	N° NGC (2)	α (2000) (3)	δ (2000) (4)	λ_c (\AA) (5)	FWHM (\AA) (6)	Date (7)	Exposure time (s) (8)	Seeing (arcsec) (9)
12893		00 ^h 00 ^m 28 ^s .0	17°13′ 09″	6582.8	10.6	2003 October 25	8640	2.6
89	23	00 ^h 09 ^m 53 ^s .4	25°55′ 24″	6660.3	20.0	2002 September 5	720	2.6
				6660.3	20.0	2002 September 6	1920	4.3
				6660.2	20.0	2002 September 7	6000	2.6
94	26	00 ^h 10 ^m 25 ^s .9	25°49′ 54″	6660.3	20.0	2002 September 3	6240	2.9
1013	536	01 ^h 26 ^m 21 ^s .8 ^s	34°42′ 11″	6675.0	20.0	2002 September 10	1920	4.8
				6675.2	20.0	2002 September 8	1920	2.4
NGC 542	542	01 ^h 26 ^m 21 ^s .8 ^s	34°42′ 11″	6675.0	20.0	2002 September 10	1920	4.8
				6675.2	20.0	2002 September 8	1920	2.4
1317	697	01 ^h 51 ^m 17 ^s .6	22°21′ 28″	6628.4	20.0	2002 September 10	4800	3.4
1437	753	01 ^h 57 ^m 42 ^s .2	35°54′ 58″	6660.2	20.0	2002 September 3	6720	3.8
1655	828	02 ^h 10 ^m 09 ^s .7	39°11′ 25″	6693.1	22.6	2000 October 24	12 720	3.9
1810		02 ^h 21 ^m 28 ^s .7 ^s	39°22′ 32″	6735.0	20.0	2002 September 7	7200	3.6
3056	1569	04 ^h 30 ^m 49 ^s .2 ^s	64°50′ 53″	6560.3	12.0	2001 November 21	6000	2.7
3334	1961	05 ^h 42 ^m 04 ^s .6	69°22′ 43″	6654.9	20.6	2001 November 20	5040	3.1
3382		05 ^h 59 ^m 47 ^s .7	62°09′ 28″	6658.0	20.0	2003 October 25	4080	3.6
				6658.0	20.0	2003 October 30	7920	4.6
3463		06 ^h 26 ^m 55 ^s .8	59°04′ 47″	6627.6	20.0	2003 March 6	6960	7.2
3521		06 ^h 55 ^m 00 ^s .1	84°02′ 30″	6659.3	20.0	2003 March 8	8400	3.4
3528		06 ^h 56 ^m 10 ^s .6	84°04′ 44″	6659.3	20.0	2003 March 8	8400	3.4
3618	2308	06 ^h 58 ^m 37 ^s .6 ^s	45°12′ 38″	6689.5	20.0	2003 March 4	6000	2.4
3685		07 ^h 09 ^m 05 ^s .9	61°35′ 44″	6603.2	12.0	2002 March 17	5520	3.0
3708	2341	07 ^h 09 ^m 12 ^s .0	20°36′ 11″	6674.2	20.0	2003 March 2	6480	3.3
3709	2342	07 ^h 09 ^m 18 ^s .1	20°38′ 10″	6674.2	20.0	2003 March 2	6480	3.3
3826		07 ^h 24 ^m 28 ^s .0	61°41′ 38″	6601.6	12.0	2002 March 20	4560	3.2
3740	2276	07 ^h 27 ^m 13 ^s .1	85°45′ 16″	6613.7	11.1	2002 March 15	4800	3.4

524 *B. Epinat et al.*Table C1 – *continued*

N° UGC (1)	N° NGC (2)	α (2000) (3)	δ (2000) (4)	λ_c (Å) (5)	FWHM (Å) (6)	Date (7)	Exposure time (s) (8)	Seeing (arcsec) (9)
3876		07 ^h 29 ^m 17 ^s .5	27°54'00''	6581.7	10.6	2004 March 18	6000	3.4
				6581.7	10.6	2004 March 19	9600	3.4
3915		07 ^h 34 ^m 55 ^s .8	31°16'34''	6659.2	20.0	2003 March 3	6000	3.4
IC 476		07 ^h 47 ^m 16 ^s .5	26°57'03''	6659.2	20.0	2003 March 7	6240	3.0
4026	2449	07 ^h 47 ^m 20 ^s .4	26°55'48''	6659.2	20.0	2003 March 7	6240	3.0
4165	2500	08 ^h 01 ^m 53 ^s .2	50°44'15''	6573.7	11.4	2002 March 16	4800	3.0
				6573.6	11.4	2002 March 17	4800	2.5
4256	2532	08 ^h 10 ^m 15 ^s .2	33°57'24''	6674.3	20.0	2004 March 17	6960	2.4
4393		08 ^h 26 ^m 04 ^s .4	45°58'02''	6611.1	11.1	2004 March 20	6960	3.5
4422	2595	08 ^h 27 ^m 42 ^s .0	21°28'45''	6658.4	20.0	2003 March 9	7200	2.7
4456		08 ^h 32 ^m 03 ^s .5	24°00'39''	6688.7	20.0	2004 March 22	6720	4.8
4555	2649	08 ^h 44 ^m 08 ^s .4	34°43'02''	6658.7	20.0	2004 March 23	6960	5.9
4770	2746	09 ^h 05 ^m 59 ^s .4	35°22'38''	6718.7	20.0	2004 March 24	7920	4.3
4820	2775	09 ^h 10 ^m 20 ^s .1	07°02'17''	6593.0	10.1	2003 March 6	8400	6.3
5045		09 ^h 28 ^m 10 ^s .2	44°39'52''	6734.3	20.0	2003 March 9	6960	2.5
5175	2977	09 ^h 43 ^m 46 ^s .8	74°51'35''	6628.5	20.0	2004 March 23	5520	6.9
5228		09 ^h 46 ^m 03 ^s .8	01°40'06''	6602.9	12.0	2003 March 4	9120	2.8
5251	3003	09 ^h 48 ^m 36 ^s .4	33°25'17''	6593.9	10.1	2002 March 15	1680	3.1
5279	3026	09 ^h 50 ^m 55 ^s .1	28°33'05''	6594.2	10.1	2004 March 16	6000	2.7
5319	3061	09 ^h 56 ^m 12 ^s .0	75°51'59''	6613.9	11.1	2004 March 17	7200	2.4
5351	3067	09 ^h 58 ^m 21 ^s .3	32°22'12''	6593.7	10.1	2003 March 7	7200	4.1
5373		10 ^h 00 ^m 00 ^s .5	05°19'58''	6571.0	11.4	2004 March 22	7680	4.6
5398	3077	10 ^h 03 ^m 20 ^s .0	68°44'01''	6563.7	12.0	2003 March 8	7920	3.2
IC 2542		10 ^h 07 ^m 50 ^s .5	34°18'55''	6689.7	20.0	2004 March 21	7440	4.1
5510	3162	10 ^h 13 ^m 31 ^s .7	22°44'14''	6592.3	10.1	2003 March 2	6240	3.5
5532	3147	10 ^h 16 ^m 53 ^s .5	73°24'03''	6630.3	9.6	2002 March 19	4560	3.3
				6623.1	8.6	2002 March 20	1920	3.3
5556	3187	10 ^h 17 ^m 47 ^s .9	21°52'24''	6593.9	10.1	2002 March 17	5760	3.1
5786	3310	10 ^h 38 ^m 45 ^s .9	53°30'12''	6584.2	10.6	2002 March 20	4080	4.1
5840	3344	10 ^h 43 ^m 31 ^s .1	24°55'21''	6573.7	11.4	2002 March 20	5760	3.3
5842	3346	10 ^h 43 ^m 39 ^s .0	14°52'18''	6584.2	10.6	2004 March 20	6000	3.5
6118	3504	11 ^h 03 ^m 11 ^s .3	27°58'20''	6593.9	10.1	2002 March 18	5760	2.4
6277	3596	11 ^h 15 ^m 06 ^s .2	14°47'12''	6580.8	10.6	2004 March 19	10 320	2.9
6419	3664	11 ^h 24 ^m 24 ^s .6	03°19'36''	6593.9	10.1	2003 April 27	6960	3.5
6521	3719	11 ^h 32 ^m 13 ^s .4	00°49'09''	6689.2	20.0	2003 March 5	6960	3.7
6523	3720	11 ^h 32 ^m 21 ^s .6	00°48'14''	6689.2	20.0	2003 March 5	6960	3.7
6787	3898	11 ^h 49 ^m 15 ^s .6	56°05'04''	6584.3	10.6	2002 March 19	3600	2.9
				6584.2	10.6	2002 March 20	5760	3.3
7021	4045	12 ^h 02 ^m 42 ^s .3	01°58'36''	6602.6	12.0	2003 March 4	7200	4.3
7045	4062	12 ^h 04 ^m 03 ^s .8	31°53'42''	6581.1	10.6	2004 March 18	6000	2.1
7154	4145	12 ^h 10 ^m 01 ^s .4	39°53'02''	6584.2	10.6	2002 March 21	5520	4.2
7429	4319	12 ^h 21 ^m 43 ^s .1	75°19'22''	6592.1	10.1	2003 March 3	6960	4.3
7699		12 ^h 32 ^m 48 ^s .0	37°37'18''	6573.9	14.0	2004 March 22	6720	4.6
7766	4559	12 ^h 35 ^m 57 ^s .3	27°57'38''	6583.3	10.6	2002 June 17	2400	1.9
7831	4605	12 ^h 39 ^m 59 ^s .7	61°36'29''	6565.7	12.0	2002 June 15	3840	2.2
7853	4618	12 ^h 41 ^m 33 ^s .1	41°09'05''	6573.6	11.4	2002 March 18	5040	2.6
7861	4625	12 ^h 41 ^m 52 ^s .9	41°16'25''	6575.7	11.4	2002 June 16	3840	3.3
7876	4635	12 ^h 42 ^m 39 ^s .3	19°56'44''	6584.3	10.6	2004 March 17	6720	3.0
7901	4651	12 ^h 43 ^m 42 ^s .7	16°23'35''	6581.7	10.6	2004 March 19	8160	3.8
7985	4713	12 ^h 49 ^m 57 ^s .9	05°18'42''	6574.1	11.4	2003 April 26	6240	5.4
8334	5055	13 ^h 15 ^m 49 ^s .4	42°01'46''	6572.9	13.7	2002 June 14	4320	2.3
8403	5112	13 ^h 21 ^m 56 ^s .6	38°44'05''	6584.2	10.6	2002 March 21	4080	4.4
NGC 5296	5296	13 ^h 46 ^m 18 ^s .7	43°51'04''	6615.4	11.1	2002 June 13	6000	3.2
8709	5297	13 ^h 46 ^m 23 ^s .7	43°52'20''	6615.4	11.1	2002 June 13	6000	3.2
8852	5376	13 ^h 55 ^m 16 ^s .1	59°30'25''	6610.2	11.1	2003 March 5	2880	2.8
				6609.9	11.1	2003 March 7	4800	3.7
8863	5377	13 ^h 56 ^m 16 ^s .7	47°14'08''	6601.1	12.0	2004 March 26	5040	3.3
8898	5394	13 ^h 58 ^m 33 ^s .7	37°27'12''	6651.1	20.6	2002 March 18	4320	2.7
8900	5395	13 ^h 58 ^m 38 ^s .0	37°25'28''	6651.1	20.6	2002 March 18	4320	2.7
8937	5430	14 ^h 00 ^m 45 ^s .8	59°19'43''	6628.2	20.0	2003 March 3	8880	4.4
9013	5474	14 ^h 05 ^m 02 ^s .0	53°39'08''	6565.2	12.0	2002 June 14	5040	2.3

Table C1 – continued

N° UGC (1)	N° NGC (2)	α (2000) (3)	δ (2000) (4)	λ_c (Å) (5)	FWHM (Å) (6)	Date (7)	Exposure time (s) (8)	Seeing (arcsec) (9)
9179	5585	14 ^h 19 ^m 48 ^s .1	56°43'45''	6570.7	11.4	2004 March 20	8160	3.1
9219	5608	<i>14^h23^m17.5^s</i>	<i>41°46'34''</i>	6573.7	11.4	2004 March 22	6480	4.7
9248	5622	14 ^h 26 ^m 12 ^s .2	48°33'51''	6655.2	20.6	2004 March 21	10 800	4.8
9358	5678	14 ^h 32 ^m 05 ^s .6	57°55'16''	6603.0	12.0	2004 March 19	7680	4.3
9363	5668	14 ^h 33 ^m 24 ^s .4	04°27'02''	6594.1	10.1	2003 April 26	8160	2.8
9406	5693	14 ^h 36 ^m 11 ^s .1	48°35'06''	6612.6	11.1	2003 April 28	6000	3.3
9465	5727	14 ^h 40 ^m 26 ^s .1	33°59'23''	6594.1	10.1	2004 March 17	6480	3.4
9576	5774	14 ^h 53 ^m 42 ^s .5	03°34'57''	6594.2	10.1	2003 April 27	6840	4.1
9736	5874	15 ^h 07 ^m 51 ^s .9	54°45'08''	6629.1	20.0	2003 March 2	3840	4.8
9866	5949	15 ^h 28 ^m 00 ^s .6	64°45'46''	6572.2	11.4	2004 March 24	5280	6.9
9943	5970	15 ^h 38 ^m 30 ^s .0	12°11'11''	6602.5	12.0	2003 March 4	8400	4.3
10075	6015	15 ^h 51 ^m 25 ^s .3	62°18'36''	6580.9	10.6	2004 March 18	5760	3.2
10521	6207	16 ^h 43 ^m 03 ^s .7	36°49'55''	6582.1	10.6	2003 April 28	2400	3.0
				6582.1	10.6	2003 April 29	5280	3.9
10652	6283	16 ^h 59 ^m 26 ^s .5	49°55'20''	6584.2	10.6	2003 April 26	2880	3.2
				6584.2	10.6	2003 April 27	3120	4.1
10713		<i>17^h04^m33.7^s</i>	<i>72°26'45''</i>	6585.5	10.6	2002 September 4	5040	2.4
10757		17 ^h 10 ^m 13 ^s .4	72°24'38''	6586.0	10.6	2002 June 17	5280	2.4
10769		<i>17^h11^m33.5^s</i>	<i>72°24'07''</i>	6592.9	10.1	2002 June 17	5280	2.1
10791		17 ^h 14 ^m 38 ^s .5	72°23'56''	6593.1	10.1	2002 June 15	6000	2.6
11012	6503	17 ^h 49 ^m 26 ^s .3	70°08'40''	6562.2	8.8	2002 September 6	5040	2.6
11269	6667	18 ^h 30 ^m 39 ^s .7	67°59'14''	6615.5	11.1	2002 June 17	3840	2.3
11300	6689	18 ^h 34 ^m 49 ^s .9	70°31'28''	6584.4	10.6	2002 September 5	5040	3.7
11332	6654A	<i>18^h39^m25.2^s</i>	<i>73°34'48''</i>	6594.7	10.1	2002 September 10	7200	5.5
11407	6764	19 ^h 08 ^m 16 ^s .4	50°55'59''	6615.0	11.1	2002 September 11	6480	2.6
11466		19 ^h 42 ^m 59 ^s .1	45°17'58''	6583.0	10.6	2002 June 16	5040	2.3
11470	6824	19 ^h 43 ^m 40 ^s .8	56°06'34''	6628.6	20.0	2002 September 6	3600	2.2
11496		19 ^h 53 ^m 01 ^s .8	67°39'54''	6611.3	11.1	2002 June 18	5520	1.9
11498		19 ^h 57 ^m 15 ^s .1	05°53'24''	6628.0	20.0	2003 October 25	8400	4.3
11597	6946	20 ^h 34 ^m 52 ^s .5	60°09'12''	6562.3	8.8	2002 June 14	5280	2.4
11670	7013	21 ^h 03 ^m 33 ^s .7	29°53'50''	6581.9	10.6	2002 September 11	7440	2.7
11872	7177	22 ^h 00 ^m 41 ^s .2	17°44'18''	6584.8	10.6	2002 September 10	7200	4.7
12082		22 ^h 34 ^m 11 ^s .3	32°51'42''	6582.1	10.6	2002 September 2	7440	2.8

Column (1): name of the galaxy in the UGC catalogue except for NGC 542, IC 476, IC 2542 and NGC 5296 that do not have UGC name. Column (2): name in the NGC catalogue when available. Columns (3) and (4): coordinates (in J2000) of the centre of the galaxy used for the kinematic study except for those in italic (taken from HyperLeda). Column (5): central wavelength of the interference filter used. Column (6): FWHM of the interference filter. Column (7): date of the observations. Column (8): total exposure time in second. Column (9): seeing in arcsec.

Table C2. Model parameters.

N° UGC (1)	$V_{\text{sys_Leda}}$ (km s ⁻¹) (2)	$V_{\text{sys_FP}}$ (km s ⁻¹) (3)	i_{Morph} (°) (4)	i_{Kin} (°) (5)	PA_{Morph} (°) (6)	PA_{Kin} (°) (7)	\overline{Res} (10 ⁻³ km s ⁻¹) (8)	σ_{res} (km s ⁻¹) (9)	χ_{red}^2 (10)
12893	1102 ± 7	1097 ± 2	30 ± 8	19 ± 19	95 ± 51	77 [#] ± 5	-28.1	8	1.2
89	4564 ± 3	4510 ± 5	40 ± 4	33 ± 13	174 ± 24	177 ± 4	42.5	23	8.6
94	4592 ± 4	4548 ± 2	50 ± 4	42 ± 5	102 ± 15	94 ± 2	-3.9	13	2.7
1013	5190 ± 4		80 ± 3		68 ± 5				
NGC 542	4660 ± 8		90		143 ± 6				
1317	3111 ± 5	3090 ± 2	75 ± 4	73 ± 1	105 ± 5	106 ± 1	-1.3	15	3.3
1437	4893 ± 4	4858 ± 2	52 ± 3	47 ± 4	134 ± 17	127 [#] ± 2	-0.8	18	5.2
1655	5340 ± 16	5427 ± 7	45 ± 9	45 ± 18*		138 [#] ± 6	-2744.9	30	15.4
1810	7556 ± 21		75 ± 3		42 ± 6				
3056	-100 ± 7		65 ± 7		120 ± 12				
3334	3934 ± 4	3952 ± 13	47 ± 7	47 ± 14*	85 ± 15	97 [#] ± 6	9.9	54	46.0
3382	4497 ± 6	4489 ± 2	21 ± 10	21 ± 14	30 ^{2M} /168 ^{Pa} ± 61	6 [#] ± 2	-11.5	16	4.1
3463	2692 ± 4	2679 ± 3	63 ± 3	63 ± 3	117 ± 8	110 ± 2	-0.1	15	3.6
3521	4426 ± 7	4415 ± 2	61 ± 3	58 ± 5	76 ± 12	78 [#] ± 3	3.2	16	4.1
3528	4421 ± 18	4340 ± 5	59 ± 5	42 ± 12	38 ± 16	43 [#] ± 4	-17.8	32	17.6
3618	5851 ± 6		49 ± 5		171 ± 16				
3685	1796 ± 4	1795 ± 1	55 ± 4	12 ± 17	133 ± 12	118 [#] ± 4	-1.3	9	1.4
3708	5201 ± 26	5161 ± 4	16 ± 24	44 ± 16	136 ^{Ni} ± 90	50 [#] ± 4	-11.6	18	5.4

Table C2 – continued

N° UGC (1)	$V_{\text{sys,Leda}}$ (km s^{-1}) (2)	$V_{\text{sys,FP}}$ (km s^{-1}) (3)	i_{Morph} ($^\circ$) (4)	i_{Kin} ($^\circ$) (5)	PA_{Morph} ($^\circ$) (6)	PA_{Kin} ($^\circ$) (7)	\overline{Res} ($10^{-3} \text{ km s}^{-1}$) (8)	σ_{res} (km s^{-1}) (9)	χ^2_{red} (10)
3709	5223 ± 50	5292 ± 4	46 ± 4	55 ± 4	66 ± 18	52 [#] ± 2	-4.7	18	5.3
3826	1733 ± 3	1724 ± 2	30 ± 9	20 ± 19	160 ^{2M} /85 ^{Ni} ± 34	74 [#] ± 5	135.4	9	1.2
3740	2417 ± 6	2416 ± 2	40 ± 6	48 ± 14	19 ± 20	67 [#] ± 4	<0.1	11	1.7
3876	860 ± 7	854 ± 2	61 ± 3	59 ± 5	178 ± 9	178 [#] ± 3	-0.2	10	1.6
3915	4679 ± 7	4659 ± 3	59 ± 5	47 ± 4	25 ± 17	30 ± 2	6.8	13	2.7
IC 476	4734 ± 32	4767 ± 3	40 ± 5	55 ± 24	102 ± 30	68 ± 6	-5.9	18	5.5
4026	4782 ± 11	4892 ± 3	73 ± 4	56 ± 4	136 ± 8	139 ± 2	4.0	19	5.7
4165	515 ± 4	504 ± 1	21 ± 9	41 ± 10	74 ^{Pa} ± 43	85 [#] ± 2	-0.4	10	1.6
4256	5252 ± 5	5252 ± 3	36 ± 4	38 ± 21	26 ± 23	111 [#] ± 6	15.9	26	11.1
4393	2126 ± 5	2119 ± 4	50 ± 5	50 ± 9*	50 ± 22	70 [#] ± 7	0.6	11	1.7
4422	4333 ± 4	4321 ± 2	49 ± 4	25 ± 8	12 ± 17	36 ± 2	-18.3	20	6.2
4456	5497 ± 23	5470 ± 1	28 ± 6	9 ± 14	42 ± 41	124 ± 3	7.3	14	3.1
4555	4235 ± 6	4235 ± 2	21 ± 12	38 ± 7	140 ^{2M} /78 ^{SDSS} ± 72	90 ± 2	0.5	15	3.5
4770	7063 ± 9	7026 ± 3	36 ± 9	20 ± 13	54 ± 30	98 [#] ± 3	-36.8	14	3.0
4820	1355 ± 4	1350 ± 2	41 ± 4	38 ± 3	160 ± 16	157 ± 2	<0.1	13	2.7
5045	7716 ± 23	7667 ± 2	41 ± 4	16 ± 9	136 ± 21	148 ± 2	-2.8	13	2.7
5175	3052 ± 11	3049 ± 2	65 ± 4	56 ± 3	145 ± 9	143 ± 2	-2.3	13	2.9
5228	1873 ± 7	1869 ± 2	82 ± 2	72 ± 2	122 ± 4	120 ± 2	-0.7	9	1.3
5251	1481 ± 3	1465 ± 3	88 ± 9	73 ± 6	78 ± 3	80 [#] ± 3	<0.1	15	3.5
5279	1488 ± 4		90		83 ± 4				
5319	2448 ± 9	2439 ± 1	40 ± 5	30 ± 9	125 ^{2M} /7 ^{Pa} ± 19	165 [#] ± 2	-21.0	9	1.3
5351	1473 ± 4		82 ± 6		105 ± 4				
5373	302 ± 3	291 ± 2	60 ± 6	10 ± 18	110 ± 12	51 ± 8	-0.5	8	0.9
5398	14 ± 5		40 ± 10		45 ± 23				
IC 2542	6113 ± 20	6111 ± 2	43 ± 4	20 ± 15	173 ± 21	174 ± 3	-0.9	20	6.3
5510	1301 ± 3	1298 ± 2	38 ± 5	31 ± 10	26 ± 24	20 [#] ± 3	-0.3	10	1.4
5532	2812 ± 8	2802 ± 1	33 ± 9	32 ± 3	150 ± 27	147 ± 1	<0.1	14	2.9
5556	1581 ± 3		75 ± 2		105 ± 5				
5786	990 ± 3	992 ± 4	16 ± 25	53 ± 11	18 ^{SDSS} ± 90	153 ± 5	-574.4	18	4.9
5840	582 ± 4	580 ± 1	18 ± 14	18 ± 11		153 [#] ± 3	<0.1	12	2.1
5842	1261 ± 10	1245 ± 1	34 ± 6	47 ± 9	104 ± 24	112 [#] ± 2	-1.5	10	1.7
6118	1539 ± 5	1525 ± 2	27 ± 7	39 ± 8*	150 ^{2M} /57 ^{Pa} ± 32	163 [#] ± 3	16.3	11	1.9
6277	1192 ± 3	1191 ± 3	17 ± 16	17 ± 17*	0 ^{2M} ± 86	76 ± 3	-5.1	19	5.7
6419	1365 ± 24	1381 ± 2	57 ± 5	66 ± 19	27 ± 15	34 ± 7	-1.8	8	0.9
6521	5879 ± 5	5842 ± 2	50 ± 3	46 ± 4	21 ± 13	20 ± 2	-0.9	17	4.5
6523	5913 ± 13	5947 ± 2	24 ± 7	24 ± 14*	36 ^{Va} /12 ^{Pa} /1 ^{Pa} ± 52	173 [#] ± 3	-6.4	13	2.8
6787	1173 ± 3	1157 ± 3	57 ± 3	70 ± 2	108 ± 10	112 ± 2	-0.7	17	4.4
7021	1979 ± 8	1976 ± 3	56 ± 4	56 ± 7*	89 ± 11	86 [#] ± 2	-0.6	14	3.1
7045	770 ± 6	758 ± 1	70 ± 2	68 ± 2	101 ± 5	99 ± 2	0.2	10	1.5
7154	1011 ± 28	1009 ± 1	64 ± 3	65 ± 3	100 ± 8	95 [#] ± 2	<0.1	12	2.3
7429	1476 ± 24		73 ± 3		162 ± 7				
7699	496 ± 1		78 ± 2		32 ± 4				
7766	814 ± 3	807 ± 1	65 ± 4	69 ± 3	150 ± 7	143 [#] ± 2	<0.1	12	2.4
7831	147 ± 4	136 ± 3	70 ± 3	56 ± 12	125 ± 5	110 [#] ± 5	<0.1	9	1.2
7853	537 ± 4	530 ± 2	58 ± 5	58 ± 28*	40 ± 12	37 [#] ± 4	12.8	8	1.1
7861	611 ± 4	598 ± 1	47 ± 6	47 ± 24*	116 ^{Pa} /30 ^{SDSS} ± 20	117 [#] ± 4	<0.1	11	1.9
7876	955 ± 8	944 ± 1	44 ± 5	53 ± 9	3 ± 22	164 [#] ± 3	0.3	8	1.1
7901	799 ± 2	788 ± 2	50 ± 3	53 ± 2	77 ± 11	74 [#] ± 2	<0.1	12	2.2
7985	653 ± 3	642 ± 2	24 ± 12	49 ± 6	110 ^{2M} /87 ^{Ha} /153 ^{Pa} /100 ^{Ni} /88 ^{SDSS} ± 48	96 [#] ± 3	-0.1	8	1.0
8334	508 ± 3	484 ± 1	55 ± 5	66 ± 1	102 ± 11	100 ± 1	-0.1	11	1.7
8403	969 ± 4	975 ± 2	54 ± 3	57 ± 4	129 ± 12	121 ± 2	-0.1	9	1.3
NGC 5296	2243 ± 3	2254 ± 2	65 ± 6	65 ± 4	12 ± 15	2 ± 3	-6.2	4	0.3
8709	2407 ± 13	2405 ± 3	82 ± 3	76 ± 1	147 ± 4	150 [#] ± 2	0.1	15	3.3
8852	2023 ± 17	2075 ± 1	55 ± 7	52 ± 3	65 ± 16	63 ± 2	0.9	10	1.5
8863	1796 ± 7	1789 ± 4	77 ± 4	77 ± 13*	38 ± 5	38 [#] ± 7*	-41.4	14	3.3
8898	3464 ± 10	3448 ± 2	71 ± 3	27 ± 20	30 ^{2M} /140 ^{Pa} /117 ^{SDSS} ± 7	31 ± 6	41.5	7	0.7
8900	3466 ± 11	3511 ± 3	66 ± 5	57 ± 10	172 ± 10	161 ± 2	5.8	20	6.6
8937	2968 ± 9	2961 ± 5	50 ± 5	32 ± 12	177 ± 16	5 [#] ± 3	2361.4	19	5.7
9013	255 ± 23	262 ± 1	50 ± 4	21 ± 16*	85 ± 14	164 ± 4	1.8	7	0.8
9179	302 ± 2	293 ± 2	53 ± 3	36 ± 14	33 ± 11	49 ± 4	<0.1	9	1.4
9219	666 ± 11		81 ± 6		99 ± 9				
9248	3867 ± 6	3865 ± 2	58 ± 3	58 ± 4	86 ± 12	81 [#] ± 2	3.5	15	3.6

Table C2 – continued

N° UGC (1)	$V_{\text{sys_Leda}}$ (km s $^{-1}$) (2)	$V_{\text{sys_FP}}$ (km s $^{-1}$) (3)	i_{Morph} ($^\circ$) (4)	i_{Kin} ($^\circ$) (5)	PA_{Morph} ($^\circ$) (6)	PA_{Kin} ($^\circ$) (7)	\overline{Res} (10^{-3} km s $^{-1}$) (8)	σ_{res} (km s $^{-1}$) (9)	χ^2_{red} (10)
9358	1907 \pm 4	1912 \pm 3	62 \pm 3	54 \pm 4	2 \pm 9	2 [#] \pm 2	2.3	15	3.5
9363	1584 \pm 3	1577 \pm 1	33 \pm 6	18 \pm 14*	107 \pm 27	147 \pm 3	3.2	8	1.1
9406	2279 \pm 2	2281 \pm 2	51 \pm 7	59 \pm 25	60 ^{2M} /150 ^{SDSS} \pm 22	132 \pm 12	78.0	11	2.0
9465	1495 \pm 3	1485 \pm 2	90	65 \pm 4	143 \pm 9	127 \pm 3	0.3	8	1.1
9576	1565 \pm 5	1555 \pm 2	52 \pm 4	41 \pm 11	125 \pm 14	122 \pm 3	-0.4	10	1.6
9736	3128 \pm 4	3135 \pm 2	51 \pm 3	51 \pm 5	57 \pm 13	39 [#] \pm 2	2.9	14	3.2
9866	427 \pm 4	430 \pm 1	69 \pm 3	56 \pm 6	150 \pm 7	148 \pm 2	-5.1	7	0.8
9943	1958 \pm 4	1946 \pm 1	48 \pm 5	54 \pm 2	87 \pm 14	86 [#] \pm 2	-0.1	9	1.4
10075	831 \pm 3	827 \pm 1	66 \pm 3	62 \pm 2	28 \pm 7	30 [#] \pm 1	<0.1	9	1.4
10521	852 \pm 2	832 \pm 2	71 \pm 3	59 \pm 3	17 \pm 7	20 \pm 2	0.7	9	1.2
10652	1092 \pm 26	1089 \pm 1	30 \pm 7	21 \pm 13	56 \pm 33	45 [#] \pm 3	0.6	8	1.0
10713	1073 \pm 4		90		8 \pm 4				
10757	1168 \pm 8	1210 \pm 2	59 \pm 3	44 \pm 22	66 \pm 12	56 \pm 6	0.7	11	1.8
10769	1230 \pm 13		57 \pm 4		41 \pm 16				
10791	1328 \pm 6	1318 \pm 3	0	34 \pm 20*		92 \pm 4	726.5	10	1.7
11012	36 \pm 12	25 \pm 1	74 \pm 2	72 \pm 2	123 \pm 5	119 [#] \pm 2	0.4	8	1.0
11269	2590 \pm 6	2563 \pm 6	60 \pm 3	69 \pm 4	97 \pm 12	92 [#] \pm 3	3.8	30	14.4
11300	488 \pm 3	480 \pm 2	77 \pm 2	76 \pm 4	171 \pm 4	167 \pm 3	<0.1	10	1.6
11332	1569 \pm 25		82 \pm 2		65 \pm 3				
11407	2412 \pm 4	2402 \pm 8	64 \pm 3	64 \pm 22*	65 \pm 9	65 \pm 10*	1.0	20	6.6
11466	820 \pm 9	826 \pm 3	55 \pm 3	66 \pm 5	35 \pm 13	46 [#] \pm 3	-0.3	13	2.6
11470	3530 \pm 40	3546 \pm 5	47 \pm 6	47 \pm 7	50 \pm 22	47 \pm 3	258.0	25	10.7
11496	2105 \pm 6	2115 \pm 2	0	44 \pm 16		167 \pm 4	135.8	9	1.2
11498	3266 \pm 8	3284 \pm 4	79 \pm 4	71 \pm 2	75 \pm 7	71 [#] \pm 2	-23.4	22	7.9
11597	46 \pm 3	40 \pm 2	17 \pm 19	40 \pm 10		61 [#] \pm 3	0.4	13	2.5
11670	778 \pm 3	776 \pm 3	90	65 \pm 2	159 \pm 5	153 [#] \pm 2	0.8	16	3.9
11872	1147 \pm 5	1140 \pm 1	54 \pm 6	47 \pm 3	88 \pm 13	86 \pm 2	-0.1	13	2.7
12082	803 \pm 2	792 \pm 2	29 \pm 11	14 \pm 19		143 \pm 5	0.6	8	1.1

Column (1): name in the UGC catalogue (see Table C1). Column (2): systemic velocity found in the HyperLeda data base. Column (3): systemic velocity deduced from our velocity field analysis. Column (4): morphological inclination from HyperLeda (Paturel et al. 1997). Column (5): inclination deduced from the analysis of our velocity field; those marked with an asterisk (*) have been fixed equal to morphological value, except for UGC 6118, UGC 9013, UGC 9363 and UGC 10791 for which we used inclinations determined from H1 data (see Table C3). Column (6): morphological PA from HyperLeda, except for those marked (*Ha*: Haynes et al. 1999; *Ni*: Nilson 1973; *PA*: Paturel et al. 2000; *SDSS*: 2006 Sloan Digital Sky Survey, DR5; *2M*: Two-Micron All-Sky Survey team 2003, 2MASS extended objects; *Va*: Vauglin et al. 1999). Column (7): PA deduced from our velocity field; those marked with an asterisk (*) have been fixed equal to morphological value. The symbol[#] indicates that the PA refers to the approaching side. Column (8): mean residual velocity in the whole velocity field. Column (9): residual velocity dispersion in the whole velocity field. Column (10): reduced χ^2 of the model.

Table C3. Galaxy parameters.

N° UGC (1)	t (2)	Type (3)	D Mpc (4)	M_B (mag) (5)	b/a (6)	$i_{b/a}$ ($^\circ$) (7)	$D_{25}/2$ (arcsec kpc $^{-1}$) (8)	V_{max} flag (km s $^{-1}$) (9)	V_{max} (10)	H1 data (11)
12893	8.4 \pm 0.8	Sd	12.5 ^{la}	-15.5	0.89 \pm 0.06	27 \pm 7	34 \pm 5/2.1 \pm 0.3	72 \pm 67	2	
89	1.2 \pm 0.6	SBa	64.2 ^{Mo}	-21.5	0.79 \pm 0.04	38 \pm 3	46 \pm 4/14.5 \pm 1.4	343 \pm 117	1	W ^{N05}
94	2.4 \pm 0.6	S(r)ab	64.2 ^{Mo}	-20.4	0.68 \pm 0.04	47 \pm 3	34 \pm 3/10.5 \pm 0.8	209 \pm 21	1	W ^{N05}
1013	3.1 \pm 0.2	SB(r)b pec	70.8	-22.0	0.31 \pm 0.03	72 \pm 2	88 \pm 6/30.1 \pm 2.0			W ^{Web}
NGC 542	2.8 \pm 3.9	Sb pec	63.7	-19.5	0.22 \pm 0.03	77 \pm 2	34 \pm 6/10.4 \pm 1.7	125 \pm 8 ^{PV}	2	
1317	4.9 \pm 0.7	SAB(r)c	42.2	-21.5	0.33 \pm 0.04	71 \pm 2	114 \pm 7/23.4 \pm 1.5	205 \pm 9	1	W ^{Web}
1437	4.9 \pm 1.0	SABc	66.8	-21.8	0.63 \pm 0.03	51 \pm 2	43 \pm 5/13.8 \pm 1.7	218 \pm 15	1	W ^{Web}
1655	1.0 \pm 0.5	Sa	73.0	-21.6	0.75 \pm 0.09	42 \pm 8	86 \pm 10/30.3 \pm 3.5	205 \pm 64	4	
1810	3.1 \pm 0.6	Sb pec	102.4	-22.2	0.36 \pm 0.02	69 \pm 1	52 \pm 4/26.0 \pm 2.0			W ^{Web}
3056	9.6 \pm 1.2	IB	2.5 ^{Oc}	-18.7	0.57 \pm 0.06	55 \pm 4	119 \pm 9/1.4 \pm 0.1			
3334	4.2 \pm 1.0	SABb	55.6	-22.8	0.70 \pm 0.07	45 \pm 6	132 \pm 8/35.7 \pm 2.2	377 \pm 85	1	W ^{Web}
3382	1.0 \pm 0.4	SB(r)a	62.8	-20.4	0.94 \pm 0.05	20 \pm 9	38 \pm 4/11.5 \pm 1.1	322 \pm 207	2	W ^{N05}
3463	4.7 \pm 0.9	SABc	38.6	-20.7	0.49 \pm 0.03	61 \pm 2	66 \pm 4/12.4 \pm 0.8	168 \pm 9	1	
3521	4.8 \pm 1.8	Sc	62.6	-19.8	0.52 \pm 0.03	59 \pm 2	35 \pm 4/10.7 \pm 1.1	167 \pm 12	3	
3528	2.0 \pm 0.3	SBab	61.8	-20.1	0.58 \pm 0.06	55 \pm 4	41 \pm 5/12.2 \pm 1.6	276 \pm 66	2	
3618	2.0 \pm 0.3	Sab	80.0	-20.9	0.70 \pm 0.05	46 \pm 4	44 \pm 4/16.9 \pm 1.4			
3685	3.0 \pm 0.4	SB(r)b	26.3 ^{la}	-19.7	0.61 \pm 0.04	52 \pm 3	57 \pm 4/7.3 \pm 0.5	133 \pm 177	3	W ^{Web}
3708	4.5 \pm 1.7	Sbc pec	70.0	-20.7	0.96 \pm 0.11	15 \pm 23	25 \pm 6/8.3 \pm 2.0	235 \pm 69	1	

Table C3 – *continued*

N° UGC (1)	t (2)	Type (3)	D (Mpc) (4)	M_B (mag) (5)	b/a (6)	$i_{b/a}$ ($^\circ$) (7)	$D_{25}/2$ (arcsec kpc $^{-1}$) (8)	V_{\max} flag (km s $^{-1}$) (9)	V_{\max} (10)	H I data (11)
3709	5.7 ± 1.6	Sc	70.7	-21.5	0.71 ± 0.05	45 ± 4	35 ± 3/12.1 ± 1.1	241 ± 14	1	
3826	6.5 ± 0.8	SABc	25.7 ^{Ja}	-17.9	0.87 ± 0.07	29 ± 8	98 ± 9/12.2 ± 1.2	74 ± 66	1	W ^{Web}
3740	5.4 ± 0.6	SAB(r)c pec	17.1 ^{Sh}	-19.8	0.78 ± 0.06	39 ± 5	67 ± 5/5.5 ± 0.4	87 ± 20	2	W ^{Web}
3876	6.5 ± 0.8	Scd	14.5 ^{Ja}	-17.4	0.50 ± 0.03	60 ± 2	57 ± 4/4.0 ± 0.3	112 ± 10	2	
3915	4.6 ± 1.6	SBc	63.6	-21.4	0.55 ± 0.06	57 ± 4	34 ± 6/10.3 ± 1.7	205 ± 16	1	
IC 476	4.2 ± 2.6	SABb	63.9	-19.0	0.78 ± 0.05	39 ± 5	18 ± 3/5.7 ± 0.8	71 ± 22	3	
4026	2.0 ± 0.4	Sab	64.7	-20.8	0.41 ± 0.03	66 ± 2	43 ± 4/13.5 ± 1.2	285 ± 14	2	
4165	6.9 ± 0.4	SBcd	11.0 ^{Mo}	-18.2	0.94 ± 0.05	20 ± 8	74 ± 5/3.9 ± 0.2	80 ± 18	1	W ^{Web}
4256	5.2 ± 0.6	SABc	71.7	-21.6	0.82 ± 0.04	35 ± 4	50 ± 4/17.3 ± 1.3	123 ± 59	1	W ^{Web}
4393	4.6 ± 1.3	SBc	31.5 ^{Ja}	-19.3	0.66 ± 0.05	49 ± 4	44 ± 7/6.7 ± 1.1	47 ± 10	4	
4422	4.9 ± 0.6	SAB(r)c	58.1	-21.1	0.68 ± 0.04	47 ± 3	51 ± 5/14.4 ± 1.4	354 ± 95	1	
4456	5.2 ± 0.6	S(r)c	74.0	-20.8	0.89 ± 0.04	27 ± 5	31 ± 3/11.0 ± 1.1	212 ± 321	1	
4555	4.0 ± 0.6	SABb	58.0	-20.9	0.94 ± 0.07	20 ± 11	45 ± 5/12.7 ± 1.4	185 ± 30	1	
4770	1.1 ± 0.6	SBa	95.9	-21.3	0.83 ± 0.07	34 ± 8	48 ± 5/22.3 ± 2.3	330 ± 195	3	
4820	1.7 ± 0.8	S(r)ab	17.1 ^{Sh}	-20.3	0.79 ± 0.04	38 ± 4	127 ± 6/10.6 ± 0.5	337 ± 20	1	
5045	5.0 ± 0.5	SAB(r)c	105.1	-21.2	0.76 ± 0.04	40 ± 4	35 ± 3/18.0 ± 1.5	429 ± 228	1	
5175	3.2 ± 0.7	Sb	44.1	-20.6	0.48 ± 0.05	61 ± 3	62 ± 5/13.2 ± 1.1	188 ± 10	1	
5228	4.9 ± 0.5	SBc	24.7	-19.9	0.25 ± 0.02	76 ± 1	68 ± 5/8.2 ± 0.6	125 ± 9	1	
5251	4.3 ± 0.8	SBbc pec	21.5	-20.5	0.22 ± 0.01	77 ± 1	142 ± 7/14.8 ± 0.7	125 ± 9	3	W ^{Web}
5279	9.7 ± 1.1	IB	21.3	-19.0	0.27 ± 0.02	74 ± 1	67 ± 5/6.9 ± 0.5	110 ± 8 ^{PV}	1	
5319	5.3 ± 0.6	SB(r)c	35.8	-19.7	0.77 ± 0.05	39 ± 4	47 ± 3/8.2 ± 0.6	180 ± 47	2	
5351	2.1 ± 0.6	SABa	19.3 ^{Sh}	-19.4	0.32 ± 0.04	71 ± 2	62 ± 3/5.8 ± 0.3	135 ± 8 ^{PV}	1	W ^{N05}
5373	9.9 ± 0.3	IB	1.4 ^{Ka}	-14.3	0.62 ± 0.05	52 ± 4	148 ± 10/1.0 ± 0.1	90 ± 162	2	
5398	7.9 ± 3.8	Sd	3.8 ^{Ka}	-17.8	0.81 ± 0.08	36 ± 8	162 ± 13/3.0 ± 0.2			
IC 2542	4.6 ± 1.3	SBc	83.4	-20.5	0.75 ± 0.04	42 ± 4	31 ± 3/12.4 ± 1.2	290 ± 192	2	
5510	4.6 ± 1.0	SAB(r)c	18.6	-19.3	0.80 ± 0.05	37 ± 5	64 ± 6/5.8 ± 0.5	167 ± 44	1	
5532	3.9 ± 0.6	Sbc	41.1	-22.1	0.85 ± 0.08	32 ± 8	122 ± 10/24.2 ± 1.9	398 ± 24	1	W ^{Web}
5556	5.0 ± 0.8	SBc pec	22.2	-18.9	0.32 ± 0.02	71 ± 1	67 ± 4/7.2 ± 0.4			W ^{Web}
5786	4.0 ± 0.1	SAB(r)b	14.2 ^{Sh}	-19.6	0.96 ± 0.11	15 ± 23	54 ± 6/3.7 ± 0.4	80 ± 15	3	W ^{Web}
5840	4.0 ± 0.3	SB(r)bc	6.9 ^{Ka}	-18.9	0.95 ± 0.07	17 ± 13	200 ± 10/6.7 ± 0.3*	251 ± 138	1	W ^{Web}
5842	6.0 ± 0.4	SBc	15.2 ^{Sh}	-18.8	0.83 ± 0.05	34 ± 5	79 ± 5/5.8 ± 0.4	115 ± 18	2	
6118	2.1 ± 0.6	SB(r)ab	19.8 ^{Sh}	-20.0	0.90 ± 0.05	26 ± 7	74 ± 5/7.1 ± 0.4	137 ± 24	1	W ^{N05}
6277	5.1 ± 0.5	SABc	16.9	-19.5	0.96 ± 0.07	17 ± 15	106 ± 9/8.7 ± 0.7	268 ± 257	2	V ^{K00}
6419	8.9 ± 0.9	SBm	18.8	-18.6	0.65 ± 0.04	50 ± 3	44 ± 4/4.0 ± 0.4	53 ± 11	3	V ^{W04}
6521	3.7 ± 0.9	S(r)bc	78.6	-21.2	0.67 ± 0.03	48 ± 2	50 ± 3/19.1 ± 1.2	249 ± 18	1	
6523	1.4 ± 1.1	Sa	80.0	-21.0	0.92 ± 0.04	23 ± 7	32 ± 3/12.5 ± 1.3	118 ± 63	4	
6787	1.7 ± 0.8	Sab	18.9	-20.5	0.60 ± 0.03	53 ± 2	104 ± 6/9.5 ± 0.5	232 ± 11	2	W ^{N05}
7021	1.3 ± 0.8	SAB(r)a	26.8	-19.7	0.62 ± 0.04	52 ± 3	77 ± 5/10.0 ± 0.6	223 ± 18	1	
7045	5.3 ± 0.6	SABc	11.4 ^{Mo}	-19.2	0.39 ± 0.03	67 ± 2	124 ± 6/6.9 ± 0.3	160 ± 9	1	
7154	6.9 ± 0.4	SBcd	16.2	-20.0	0.46 ± 0.03	63 ± 2	139 ± 9/10.9 ± 0.7	145 ± 9	1	W ^{Web}
7429	2.4 ± 0.7	SB(r)ab	23.7	-19.8	0.40 ± 0.03	67 ± 2	73 ± 5/8.4 ± 0.6			
7699	6.0 ± 0.6	SBc	9.3	-17.6	0.28 ± 0.01	74 ± 1	108 ± 6/4.9 ± 0.3	92 ± 8 ^{PV}	1	
7766	6.0 ± 0.4	SBc	13.0	-21.0	0.46 ± 0.05	63 ± 3	317 ± 15/20.0 ± 1.0*	120 ± 9	1	W ^{Web}
7831	4.9 ± 0.4	SBc	5.2 ^{Ka}	-18.5	0.39 ± 0.03	67 ± 2	177 ± 8/4.5 ± 0.2	92 ± 15	2	W ^{Web}
7853	8.6 ± 1.1	SBm	8.9 ^{Mo}	-18.9	0.64 ± 0.05	50 ± 3	106 ± 6/4.6 ± 0.3	110 ± 35	3	W ^{Web}
7861	8.8 ± 0.7	SAB(r)m pec	10.2 ^{Mo}	-17.3	0.75 ± 0.05	41 ± 4	41 ± 4/2.0 ± 0.2	50 ± 21	3	W ^{Web}
7876	6.5 ± 0.9	SABc	14.5	-17.9	0.72 ± 0.05	44 ± 4	58 ± 7/4.1 ± 0.5	98 ± 14	2	
7901	5.2 ± 0.6	Sc pec	20.7 ^{Sh}	-20.6	0.66 ± 0.03	49 ± 3	115 ± 6/11.6 ± 0.6	215 ± 10	1	
7985	6.9 ± 0.5	SBcd	13.7 ^{Mo}	-18.7	0.92 ± 0.08	23 ± 11	51 ± 5/3.4 ± 0.3	112 ± 13	1	
8334	4.0 ± 0.2	Sbc	9.8	-21.1	0.61 ± 0.06	53 ± 4	356 ± 20/16.9 ± 1.0	214 ± 9	1	
8403	5.8 ± 0.6	SBc	19.1 ^{Ja}	-19.2	0.61 ± 0.04	52 ± 3	90 ± 6/8.3 ± 0.6	128 ± 10	1	W ^{Web}
NGC 5296	-1.1 ± 0.8	S0-a	32.8	-18.2	0.58 ± 0.04	54 ± 3	28 ± 3/4.5 ± 0.5	80 ± 9	3	W ^{Web}
8709	4.9 ± 0.8	SABc pec	35.0	-21.4	0.24 ± 0.02	76 ± 1	112 ± 7/19.0 ± 1.1	207 ± 9	1	W ^{Web}
8852	2.3 ± 0.6	SAB(r)a	30.6	-20.0	0.62 ± 0.08	52 ± 6	77 ± 9/11.4 ± 1.3	187 ± 10	3	
8863	1.1 ± 0.4	SBa	25.5 ^{Ko}	-20.3	0.39 ± 0.03	67 ± 2	108 ± 5/13.4 ± 0.6	193 ± 13	2	W ^{N05}
8898	3.1 ± 0.6	SBb pec	49.0	-20.5	0.41 ± 0.03	66 ± 2	79 ± 6/18.7 ± 1.3	65 ± 45	4	W ^{Web}
8900	3.2 ± 0.6	Sb pec	49.2	-21.7	0.47 ± 0.06	62 ± 4	75 ± 8/17.8 ± 1.8	346 ± 37	2	W ^{Web}
8937	3.1 ± 0.4	SBb	49.0 ^{Mo}	-21.1	0.67 ± 0.06	48 ± 4	69 ± 6/16.4 ± 1.4	320 ± 105	1	
9013	6.0 ± 0.3	Sc pec	7.2 ^{Ka}	-18.2	0.66 ± 0.04	49 ± 3	72 ± 5/2.5 ± 0.2	62 ± 45	2	V ^{R94}
9179	6.9 ± 0.4	SABc	5.7 ^{Ka}	-17.8	0.61 ± 0.03	52 ± 2	128 ± 8/3.5 ± 0.2	111 ± 36	3	
9219	9.7 ± 1.4	IB	10.2 ^{Ja}	-16.6	0.44 ± 0.03	64 ± 2	49 ± 4/2.4 ± 0.2	45 ± 8 ^{PV}	2	
9248	3.1 ± 0.5	Sb	54.9	-20.2	0.57 ± 0.03	55 ± 2	40 ± 4/10.6 ± 1.0	166 ± 11	1	

Table C3 – continued

N° UGC	t	Type	D (Mpc)	M_B (mag)	b/a	$i_{b/a}$ ($^\circ$)	$D_{25}/2$ (arcsec kpc $^{-1}$)	V_{\max} flag (km s $^{-1}$)	V_{\max}	H I data
(1)	(2)	(3)	(4)	(5)	(6)	(7)	(8)	(9)	(10)	(11)
9358	3.3 \pm 0.8	SABb	29.1	-20.8	0.52 \pm 0.03	59 \pm 2	94 \pm 6/13.3 \pm 0.9	221 \pm 14	1	
9363	6.9 \pm 0.4	S(r)cd	22.3	-19.8	0.84 \pm 0.05	33 \pm 6	57 \pm 5/6.2 \pm 0.5	143 \pm 105	1	V ^{S96}
9406	6.9 \pm 0.4	SB(r)cd	33.8	-19.0	0.64 \pm 0.08	50 \pm 6	44 \pm 8/7.3 \pm 1.3	19 \pm 10	4	
9465	7.9 \pm 0.9	SABd	26.4 ^{Ja}	-18.0	0.40 \pm 0.03	67 \pm 2	23 \pm 3/3.0 \pm 0.4	97 \pm 9	1	
9576	6.9 \pm 0.4	SABc pec	27.4 ^{Ja}	-19.6	0.63 \pm 0.05	51 \pm 4	51 \pm 4/6.8 \pm 0.6	104 \pm 25	1	V ^{I94}
9736	5.0 \pm 0.7	SABc	45.4	-20.6	0.65 \pm 0.03	49 \pm 2	71 \pm 4/15.7 \pm 1.0	193 \pm 16	1	
9866	4.0 \pm 0.3	S(r)bc	7.4 ^{Ja}	-17.2	0.41 \pm 0.03	65 \pm 2	55 \pm 4/2.0 \pm 0.1	116 \pm 11	2	
9943	5.0 \pm 0.6	SB(r)c	28.0	-20.7	0.69 \pm 0.05	46 \pm 4	82 \pm 5/11.1 \pm 0.7	185 \pm 10	1	
10075	6.0 \pm 0.4	Sc	14.7 ^{Ja}	-19.9	0.44 \pm 0.04	64 \pm 3	174 \pm 9/12.4 \pm 0.7	168 \pm 9	1	
10521	4.9 \pm 0.7	Sc	18.0 ^{Mo}	-20.2	0.38 \pm 0.03	68 \pm 2	106 \pm 9/9.3 \pm 0.7	124 \pm 9	1	
10652	3.8 \pm 2.6	S(r)bc	18.2	-17.7	0.87 \pm 0.05	29 \pm 6	33 \pm 3/2.9 \pm 0.3	141 \pm 82	2	
10713	3.0 \pm 0.4	Sb	18.3	-19.0	0.19 \pm 0.02	79 \pm 1	54 \pm 7/4.8 \pm 0.7	105 \pm 8 ^{PV}	2	W ^{Web}
10757	6.0 \pm 0.4	Sc	19.5	-17.7	0.53 \pm 0.04	58 \pm 2	36 \pm 4/3.4 \pm 0.4	81 \pm 33	3	W ^{Web}
10769	3.0 \pm 0.5	SABb	20.0	-17.0	0.59 \pm 0.04	54 \pm 3	28 \pm 3/2.7 \pm 0.3			W ^{Web}
10791	8.8 \pm 0.5	SABm	21.7	-16.7	1.00 \pm 0.13	0 \pm 0	56 \pm 9/5.9 \pm 0.9	96 \pm 49	3	W ^{Web}
11012	5.9 \pm 0.7	Sc	5.3 ^{Ka}	-18.7	0.33 \pm 0.03	71 \pm 2	185 \pm 11/4.7 \pm 0.3	117 \pm 9	1	
11269	2.0 \pm 0.5	SABa	35.0 ^{Ja}	-19.9	0.56 \pm 0.04	56 \pm 3	56 \pm 5/9.5 \pm 0.8	202 \pm 13	1	W ^{N05}
11300	6.4 \pm 0.9	SABc	8.4 ^{Ja}	-17.8	0.28 \pm 0.01	74 \pm 1	99 \pm 5/4.0 \pm 0.2	114 \pm 9	2	W ^{Web}
11332	7.0 \pm 0.5	SBcd	23.0 ^{Ja}	-19.5	0.21 \pm 0.01	78 \pm 1	63 \pm 5/7.1 \pm 0.5	91 \pm 8 ^{PV}	3	
11407	3.6 \pm 0.6	SBbc	35.8	-20.8	0.49 \pm 0.03	61 \pm 2	75 \pm 6/13.0 \pm 1.0	159 \pm 31	1	V ^{W01}
11466	4.8 \pm 1.9	Sc	14.2	-18.5	0.59 \pm 0.03	54 \pm 2	45 \pm 4/3.1 \pm 0.3	133 \pm 10	1	W ^{Web}
11470	2.2 \pm 0.6	Sab	50.8	-21.3	0.71 \pm 0.07	45 \pm 5	72 \pm 9/17.8 \pm 2.2	380 \pm 40	2	
11496	8.8 \pm 0.5	Sm	31.9		1.00 \pm 0.13	0 \pm 0	57 \pm 9/8.9 \pm 1.3	96 \pm 29	2	W ^{Web}
11498	3.1 \pm 0.7	SBb	44.9	-20.5	0.32 \pm 0.04	71 \pm 2	84 \pm 9/18.2 \pm 1.9	273 \pm 9	1	
11597	5.9 \pm 0.3	SABc	5.9 ^{Ka}	-20.6	0.96 \pm 0.09	16 \pm 18	342 \pm 14/9.8 \pm 0.4*	154 \pm 32	3	
11670	0.5 \pm 1.0	S(r)a	12.8	-19.4	0.33 \pm 0.03	71 \pm 2	125 \pm 7/7.7 \pm 0.4	190 \pm 9	1	W ^{N05}
11872	2.5 \pm 0.5	SAB(r)b	18.1 ^{Ko}	-20.0	0.63 \pm 0.07	51 \pm 5	85 \pm 6/7.4 \pm 0.5	183 \pm 12	1	
12082	8.7 \pm 0.8	SABm	10.1 ^{Ja}	-16.4	0.90 \pm 0.07	26 \pm 10	81 \pm 9/3.9 \pm 0.4	105 \pm 137	3	W ^{Web}

Column (1): name of the galaxy in the UGC catalogue (see Table C1). Column (2): morphological type from the de Vaucouleurs classification (de Vaucouleurs 1979) in the HyperLeda data base. Column (3): morphological type from the HyperLeda data base. Column (4): distance D , deduced from the systemic velocity taken in NED corrected from Virgo infall, assuming $H_0 = 75 \text{ km s}^{-1} \text{ Mpc}^{-1}$, except for those marked (*Ja*: James et al. 2004; *Ka*: Karachentsev et al. 2004; *Ko*: Koopmann, Haynes & Catinella 2006; *Mo*: Moustakas & Kennicutt 2006; *Oc*: O’Connell, Gallagher & Hunter 1994; *Sh*: Shapley, Fabbiano & Eskridge 2001). Column (5): absolute B magnitude from D and apparent corrected B magnitude (HyperLeda). Column (6): axial ratio from HyperLeda. Column (7): inclination derived from the axial ratio ($\arccos b/a$). Column (8): isophotal radius at the limiting surface brightness of 25 B mag arcsec $^{-2}$, from HyperLeda (Paturel et al. 1991) in arcsecond and kpc adopting the distance given in column (4); an asterisk (*) indicates that the galaxy is larger than GHASP field-of-view. Column (9): maximum velocity, V_{\max} , derived from the fit of the velocity field discussed in Section 3.2, or from the position–velocity diagram (marked with^{PV}). Column (10): quality flag on V_{\max} (1: reached; 2: probably reached; 3 probably not reached; 4: not reached). Column (11): aperture synthesis H I data references: W for WHISP data (*S02*: Swaters et al. 2002; *N05*: Noordermeer et al. 2005; *web*: <http://www.astro.rug.nl/whisp/>); V for VLA data (*I94*: Irwin 1994; *R94*: Rownd et al. 1994; *S96*: Schulman et al. 1996; *K00*: Kornreich et al. 2000; *W01*: Wilcots et al. 2001; *W04*: Wilcots & Prescott 2004).

APPENDIX D: INDIVIDUAL MAPS AND POSITION-VELOCITY DIAGRAMS

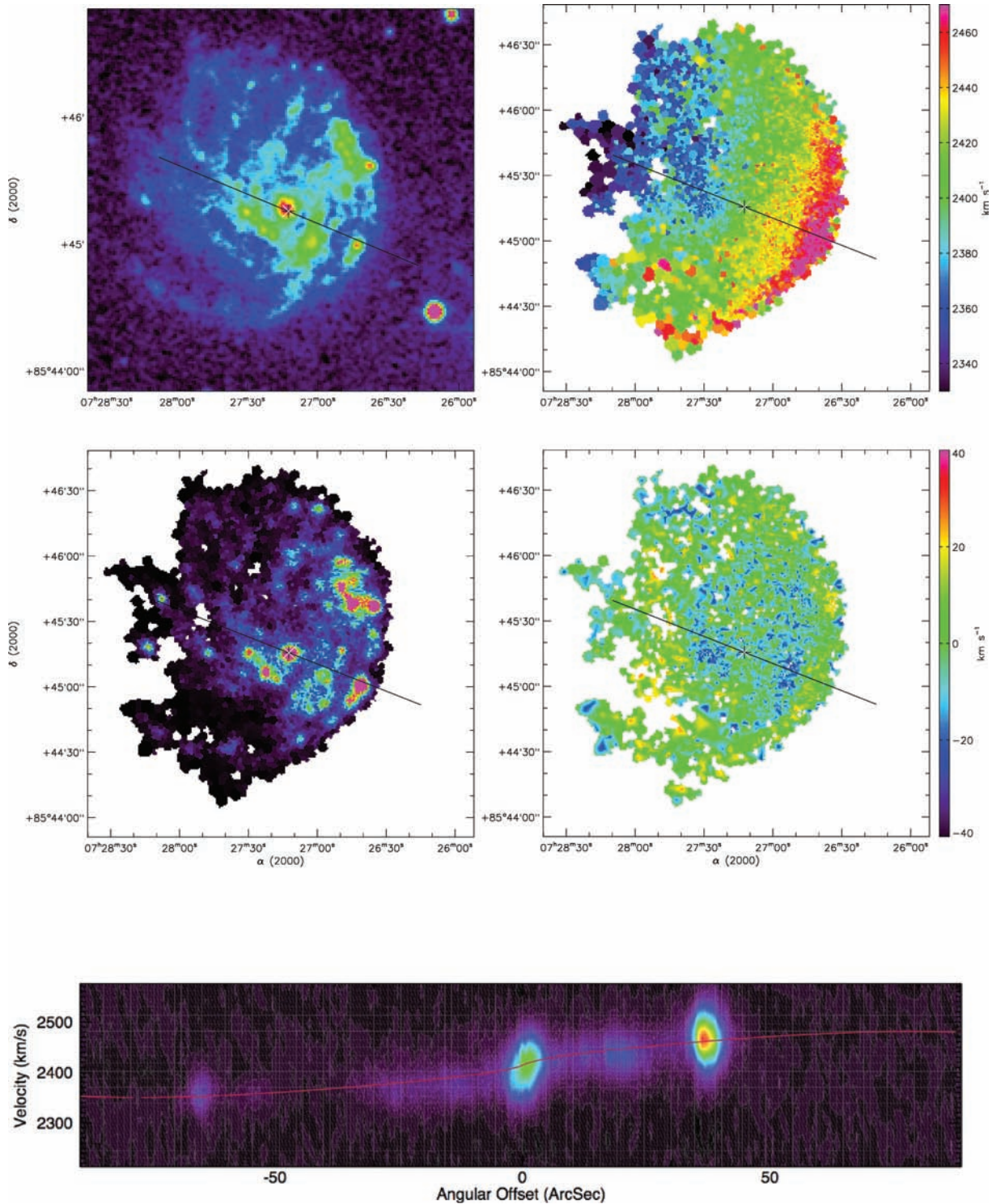


Figure D19. UGC 3740. Top left-hand panel: X-ray image. Top right-hand panel: $H\alpha$ velocity field. Middle left-hand panel: $H\alpha$ monochromatic image. Middle right-hand panel: $H\alpha$ residual velocity field. The white and black cross is the kinematical centre. The black line is the major-axis, its length represents D_{25} . Bottom panel: position-velocity diagram along the major-axis (full width of 7 pixels), arbitrary flux units. The red line plots the rotation curve computed from the model velocity field along the major-axis (full width of 7 pixels).

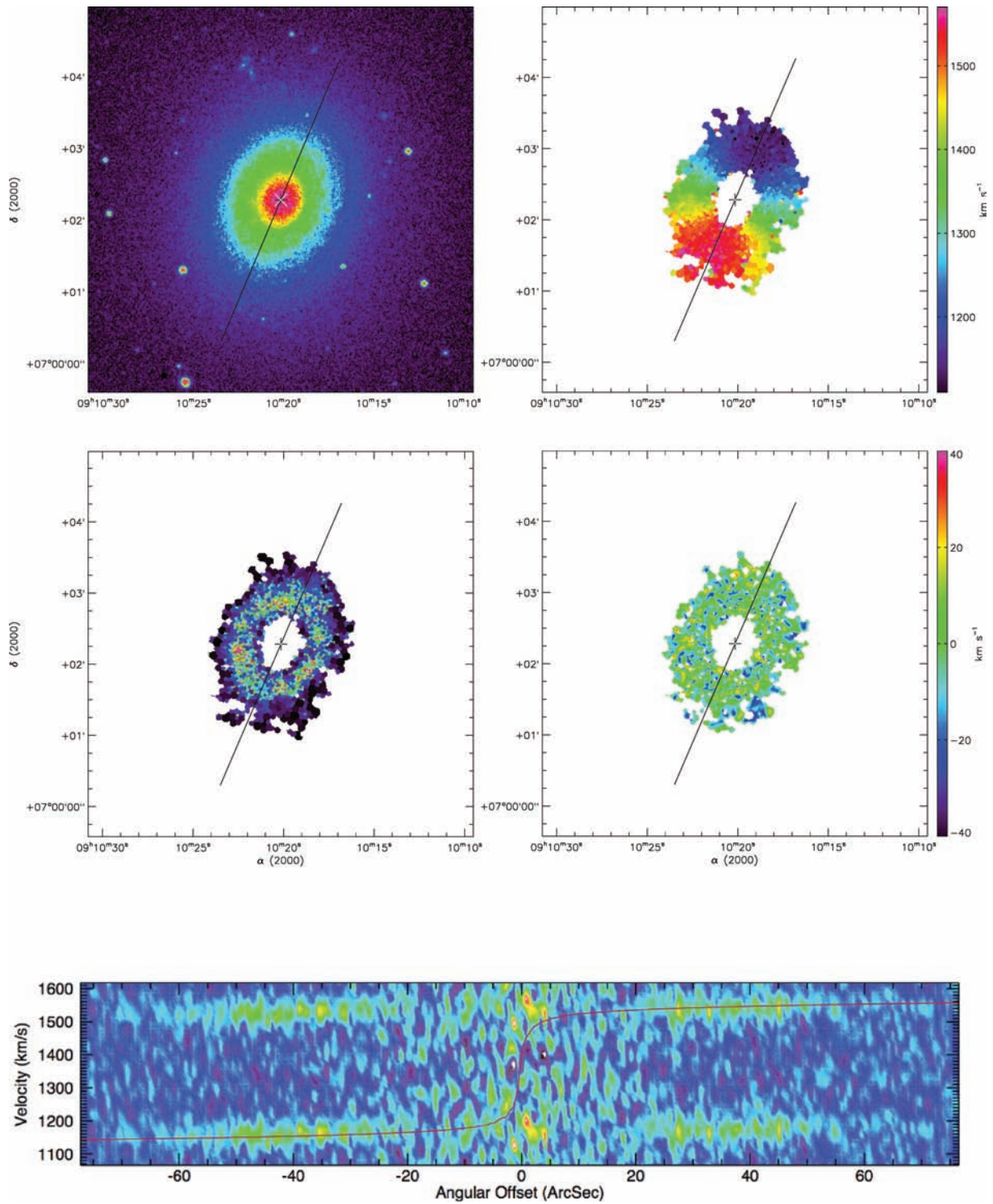


Figure D31. UGC 4820. Top left-hand panel: XDSS blue-band image. Top right-hand panel: $H\alpha$ velocity field. Middle left-hand panel: $H\alpha$ monochromatic image. Middle right-hand panel: $H\alpha$ residual velocity field. The white and black cross is the kinematical centre. The black line is the major-axis, its length represents D_{25} . Bottom panel: position-velocity diagram along the major-axis (full width of 7 pixels), arbitrary flux units. The red line plots the rotation curve computed from the model velocity field along the major-axis (full width of 7 pixel).

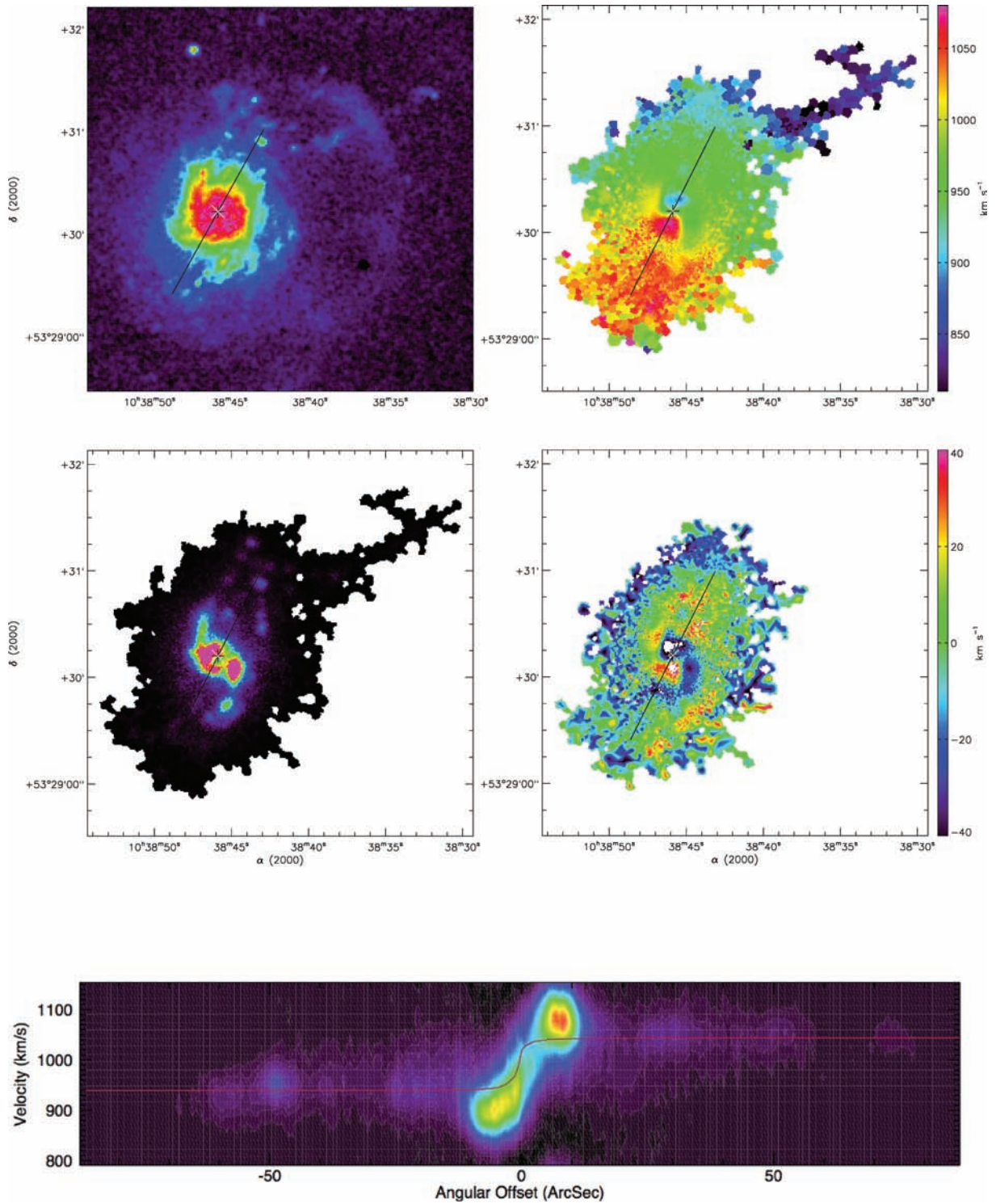


Figure D45. UGC 5786. Top left-hand panel: X-ray image. Top right-hand panel: H α velocity field. Middle left-hand panel: H α monochromatic image. Middle right-hand panel: H α residual velocity field. The white and black cross is the kinematical centre. The black line is the major-axis, its length represents D_{25} . Bottom panel: position–velocity diagram along the major-axis (full width of 7 pixels), arbitrary flux units. The red line plots the rotation curve computed from the model velocity field along the major-axis (full width of 7 pixel).

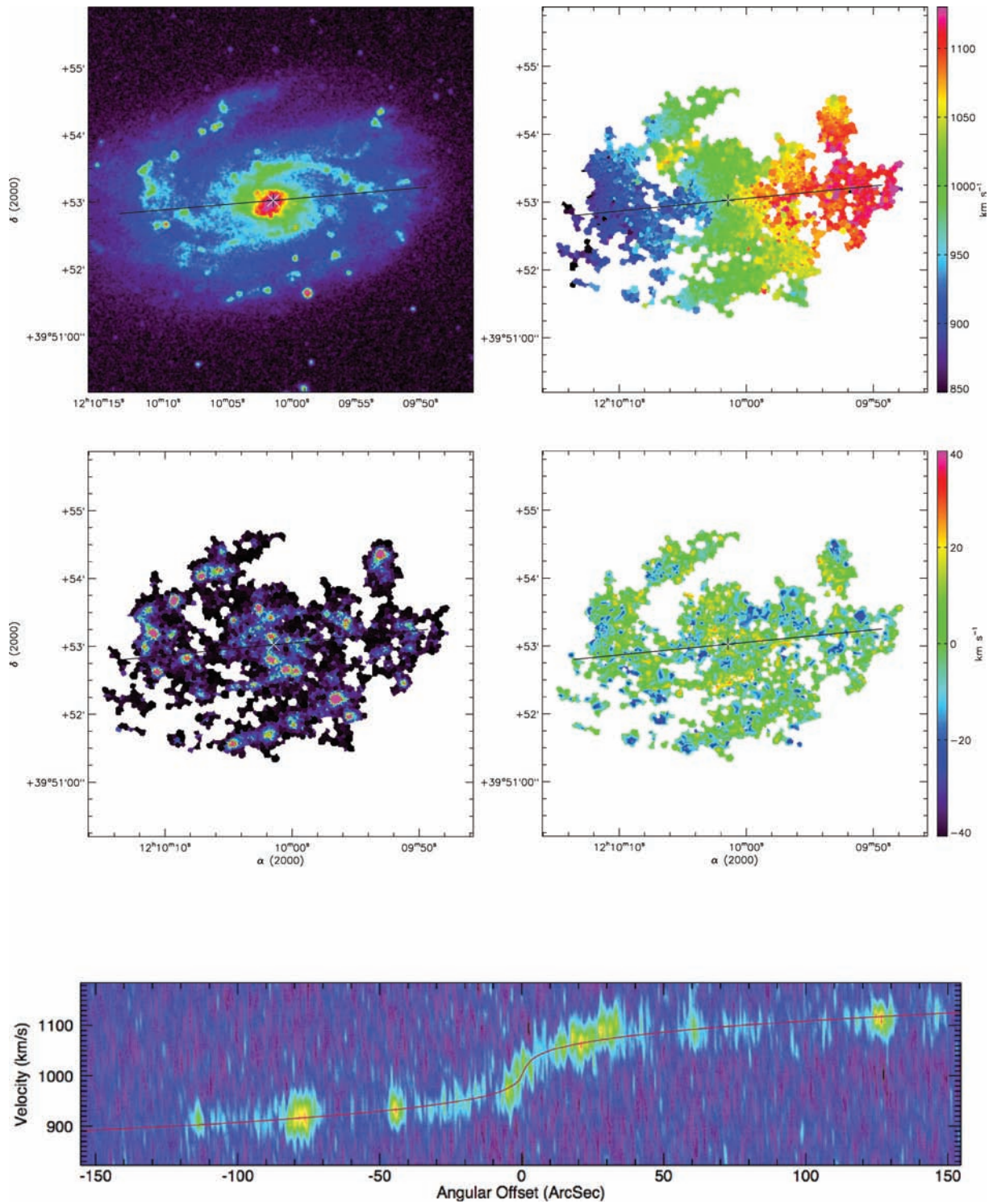


Figure D56. UGC 7154. Top left-hand panel: XDSS blue-band image. Top right-hand panel: $H\alpha$ velocity field. Middle left-hand panel: $H\alpha$ monochromatic image. Middle right-hand panel: $H\alpha$ residual velocity field. The white and black cross is the kinematical centre. The black line is the major-axis, its length represents D_{25} . Bottom panel: position–velocity diagram along the major-axis (full width of 7 pixels), arbitrary flux units. The red line plots the rotation curve computed from the model velocity field along the major-axis (full width of 7 pixel).

APPENDIX E: ROTATION CURVES

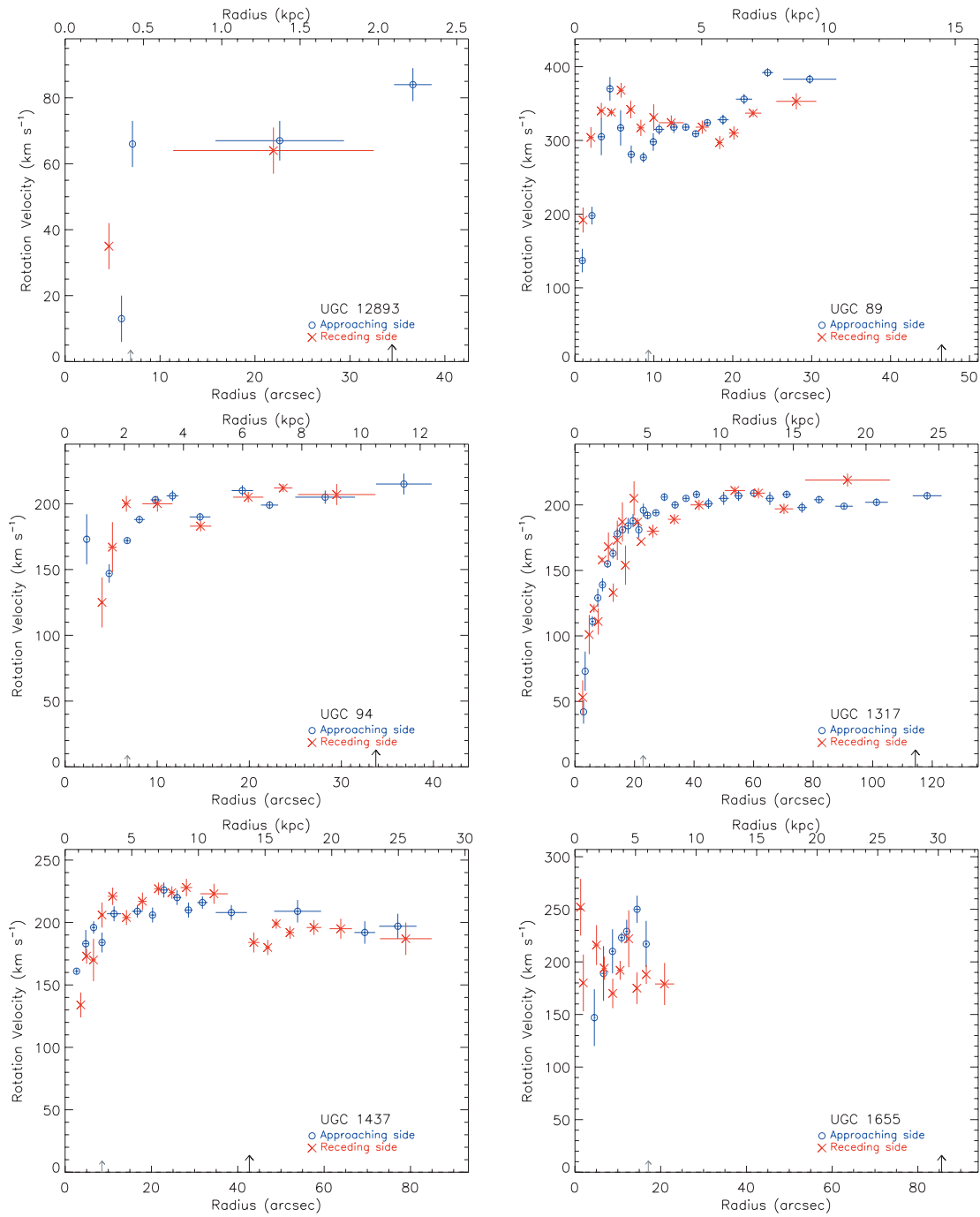


Figure E1. From the top left-hand panel to the bottom right-hand panel: H α rotation curve of UGC 12893, UGC 89, UGC 94, UGC 1317, UGC 1437 and UGC 1655.

2.2.4 Article II : GHASP : An H α kinematic survey of 203 spiral and irregular galaxies - VII. Revisiting the analysis of H α data cubes for 97 galaxies.

De même que pour l'article précédent, les cartes ainsi que les courbes de rotation sont respectivement présentées en Annexe D.1 et D.2 de la thèse.

Afin de disposer d'un échantillon homogène, réduit et analysé en utilisant les mêmes procédures, nous présentons dans cet article une nouvelle réduction et une nouvelle analyse pour un ensemble de 97 galaxies déjà publiées dans des articles antérieurs (Garrido et al., 2002, 2003b, 2004, 2005), mais en utilisant désormais les nouvelles procédures adoptées pour l'ensemble de l'échantillon (voir partie 2.2.3). Le programme d'observations GHASP est à présent terminé. Cet article présente les paramètres cinématiques pour l'ensemble de l'échantillon. Pour la première fois, les profils intégrés de la raie H α ont été calculés et sont présentés pour tout l'échantillon. Le flux H α total déduit de ces profils a été utilisé afin de déterminer une calibration en flux pour les 203 galaxies de GHASP. Cet article confirme les conclusions déjà suggérées par l'étude de la moitié de l'échantillon concernant (i) la précision de mesure des angles de position du grand axe qui est accrue en utilisant des données cinématiques, (ii) la difficulté d'obtenir des estimations robustes des inclinaisons morphologiques et cinématiques, en particulier pour les galaxies de faible inclinaison et (iii) l'accord excellent entre la relation de Tully-Fisher déterminée à partir de notre échantillon et ces précédentes déterminations provenant de la littérature.

GHASP: an H α kinematic survey of 203 spiral and irregular galaxies – VII. Revisiting the analysis of H α data cubes for 97 galaxies

B. Epinat,^{*} P. Amram and M. Marcelin

Laboratoire d'Astrophysique de Marseille, OAMP, Université Aix-Marseille and CNRS, 38 rue Frédéric Joliot-Curie, 13388 Marseille Cedex 13, France

Accepted 2008 July 31. Received 2008 July 31; in original form 2008 July 18

ABSTRACT

The Gassendi H α survey of SPirals survey (GHASP) consists of 3D H α data cubes for 203 spiral and irregular galaxies, covering a large range in morphological types and absolute magnitudes, for kinematics analysis. It is the largest sample of Fabry–Perot data published up to now. In order to provide an homogenous sample, reduced and analysed using the same procedure, we present in this paper the new reduction and analysis for a set of 97 galaxies already published in previous papers but now using the new data reduction procedure adopted for the whole sample. The GHASP survey is now achieved and the whole sample is reduced using the adaptive binning techniques based on Voronoi tessellations. We have derived H α data cubes from which are computed H α maps, radial velocity fields as well as residual velocity fields, position–velocity diagrams, rotation curves and kinematical parameters for almost all galaxies. The rotation curves, the kinematical parameters and their uncertainties are computed homogeneously using the new method based on the power spectrum of the residual velocity field. This paper provides the kinematical parameters for the whole sample. For the first time, the integrated H α profiles have been computed and are presented for the whole sample. The total H α fluxes deduced from these profiles have been used in order to provide a flux calibration for the 203 GHASP galaxies. This paper confirms the conclusions already drawn from half the sample concerning (i) the increased accuracy of position angles measurements using kinematical data, (ii) the difficulty to have robust determinations of both morphological and kinematical inclinations in particular for low-inclination galaxies and (iii) the very good agreement between the Tully–Fisher relationship derived from our data and previous determinations found in the literature.

Key words: galaxies: dwarf – galaxies: irregular – galaxies: kinematics and dynamics – galaxies: spiral.

1 INTRODUCTION

The Gassendi H α survey of SPirals (GHASP) survey consists of a large sample of spiral and irregular galaxies observed with a scanning Fabry–Perot for studying their kinematical and dynamical properties through the ionized hydrogen component. The goals of this study have been described in Epinat et al. (2008). The GHASP sample is by now the largest homogenous sample of Fabry–Perot data ever published, comprising 3D data for 203 galaxies. This paper is the seventh of a series called hereafter Paper I to VI (Garrido et al. 2002, 2003; Garrido, Marcelin & Amram 2004; Garrido et al. 2005; Spano et al. 2007; Epinat et al. 2008) presenting the data obtained in the frame of the GHASP survey. The observations were lead during 14 observing runs at the ‘Observatoire de Haute Provence (OHP)’, France, from 1998 to 2004. The survey is now achieved.

The observing runs number 8 to 14 have been presented in Paper VI, which relies on a set of 108 galaxies, providing 106 velocity fields and 93 rotation curves. Those data have been reduced with the new data reduction procedure (see Paper VI, and references therein). The data presented in this paper are those of the seven first observing runs (already presented in Papers I to IV) that have been re-reduced using the same method as in Paper VI. It also contains data for UGC 3382 and UGC 11300 that have been improved by adding new data (runs 3, 5 and 6) to the ones already published in Paper VI (runs 10 and 13). Thus, the data presented here consist of a set of 97 galaxies, providing 96 velocity fields and 82 rotation curves.

To be clear on the goals and limits of this work, we summarize hereafter what we present and what we do not in this paper. We present

(i) the new individual maps and position–velocity diagrams in Appendix D (on line data only);

^{*}E-mail: benoit.epinat@oamp.fr

(ii) the new rotation curves, in Appendix E and the new corresponding tables in Appendix F.

In this paper, we lead the same kind of analysis as the one presented in Paper VI concerning:

- (i) the study of the parameters of the kinematical models;
- (ii) the study of the residual velocity fields;
- (iii) the Tully–Fisher relation.

Because it is useful to display and analyse all the data together, we put here in the same tables (in Appendix B) the new parameters and results already published in Paper VI so that the reader does not have to compile tables coming from different publications. With respect to Papers I to IV, some distances and absolute magnitudes have been recomputed (using better estimations). For the whole GHASP sample, we make a new analysis on an absolute flux calibration made using the data calibrated by James et al. (2004) and the integrated $H\alpha$ profiles deduced from our data cubes.

Because this has been discussed in previous papers, we do not present any more:

- (i) the morphological types and luminosity distributions of the whole GHASP sample (see Paper VI);
- (ii) the data reduction procedure used here, including the computation of the rotation curves, the determination of the kinematical parameters and the determination of the uncertainties (see Paper VI);
- (iii) the instrumental set-up of the instrument for the data reduced in this paper (see Papers I to IV);
- (iv) the individual comments for each galaxy (see Papers I to IV), except when the new reduction procedure leads to new comments or to conclusions notably different from the previous ones (see Appendix A).

In Section 2, we make an indirect flux calibration of the $H\alpha$ profiles. In Section 3, we present the data and in Section 4 we compute the Tully–Fisher relation. In Section 5, we give the summary and conclusions. When the distances of the galaxies are not known, a Hubble constant $H_0 = 75 \text{ km s}^{-1} \text{ Mpc}^{-1}$ is used throughout this paper.

2 CALIBRATION AND $H\alpha$ PROFILES

Even if direct flux calibration is always possible using well calibrated and extended $H\alpha$ emitters like planetary nebulae (Dopita & Hua 1997), during the observations, we decided not to calibrate our data, thus saving observing time. Indeed, our major scientific goal was not to use the Fabry–Perot technique to make photometric studies but kinematic ones. We estimated that $H\alpha$ flux calibrations require additional observing times ranging from 25 to 33 per cent. Nevertheless, an indirect calibration of the total $H\alpha$ flux of the 201/203 galaxies from the GHASP sample has been made using 69 of the 71 galaxies we have in common with James et al. (2004). From their study using narrow-band filters including $H\alpha$ and $[\text{N II}]$, James et al. (2004) provided calibrated fluxes for their sample of 334 galaxies. Our spectral resolution allows us to resolve the $H\alpha$ line, moreover the full width half maximum (FWHM) of the narrow-band filters is narrow enough to reject $[\text{N II}]$. This is not the case for James et al. (2004) who do not separate $H\alpha$ from $[\text{N II}]$ lines. We have corrected this effect assuming a mean and constant spectral ratio $H\alpha/[\text{N II}]=3$. The distinct calibrations have been made depending on the observing set up. Indeed, the GHASP sample has been obtained using a 256×256 Imaging Photon Counting System (IPCS) until 2000 March (runs number 1 to 4) and with

a new 512×512 IPCS since 2000 October (runs number 5 to 14), with respective pixel scales of 0.96 and 0.68 arcsec (given in Table B1). We reject from the calibration the galaxies for which we have added data observed with both detectors. Their flux was computed a posteriori by taking into account the response of each detector and the corresponding exposure time. To compute the total $H\alpha$ flux for each galaxy, we compute the $H\alpha$ profile by summing the flux in the spectrum of each spatial element (see Appendix C). To minimize the foreground sky contamination, only the spatial elements used to compute the different moments (monochromatic images, velocity fields, ...) have been added. We use the velocity field in order to disentangle free spectral range overlaps. We correct the fluxes from the interference filter response, taking into account the aperture of the instrument, the inclination of the filter and its temperature during the observations. We subtract the continuum taking into account the periodicity of the Fabry–Perot transmission (difference between the free spectral range of the interferometer and the FWHM of the interference filter). The systemic velocity computed from the kinematical model (vertical dashed line in Fig. C1) is globally well centred on the integrated $H\alpha$ profile. Fig. 1 shows the comparison between James et al. (2004) fluxes and our estimated

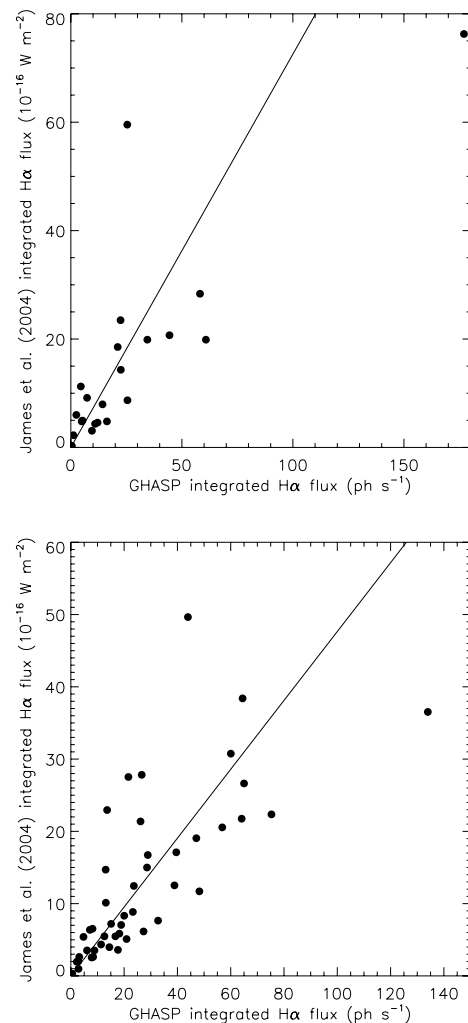


Figure 1. $H\alpha$ flux measured by GHASP versus $H\alpha$ flux from James et al. (2004). The dashed line represents the linear regression on the data from which results our calibration. Top panel: calibration for the IPCS 512×512 . Bottom panel: calibration for the IPCS 256×256 .

468 *B. Epinat, P. Amram and M. Marcelin*

fluxes for the old IPCS (top panel) and the new IPCS (bottom panel). The linear regressions are plotted with the dashed lines and their coefficients are, respectively, $0.73 \pm 0.13 \times 10^{-16}$ and $0.48 \pm 0.06 \times 10^{-16} \text{ W m}^{-2} \text{ ph}^{-1} \text{ s}$. The fluxes estimated from this calibration are presented in Table B1.

3 DATA ANALYSIS

As detailed in Paper VI, the same procedure (adaptive binning, sky subtraction, ghost removals, ...) has been used to compute the data cubes and the maps deduced from these cubes. For each galaxy, in Appendix D (available online only), from Fig. D1 to D96, when possible, we present five frames per figure: the second generation Sky Survey XDSS blue (or red) image (top left-hand panel), the $H\alpha$ velocity field (top right-hand panel), the $H\alpha$ monochromatic image (middle left-hand panel) and, when a model fits the velocity field, the $H\alpha$ residual velocity field (middle right-hand panel) and finally, the position–velocity diagram along the major axis (bottom panel). The white and black double crosses indicate the centres used for the kinematical analysis (given in Table B1, see Paper VI for details) while the black line traces the kinematical major axis deduced from the velocity field analysis (see Paper VI) or the morphological one (taken from HyperLeda) when no position angle of the kinematical major axis could be derived using the kinematics (e.g. Table B2). This line ends at the radius $D_{25}/2$ corresponding to the isophotal level 25 mag arcsec⁻² in the *B* band (given in Table B3) in order to compare the velocity field extent with the optical disc of the galaxies. Position–velocity diagrams are computed along the axis defined by this black line, using a virtual slit width of seven pixels. The red line superimposed on the position–velocity diagram is the rotation curve deduced from the model velocity field along this virtual slit (see Paper VI). When no fit is satisfactory (generally because of poor signal-to-noise ratio), we used the real velocity field instead of the model (see individual captions in Figures D1 to D96). The rotation curves are given in Appendix E (figures) and F (tables). They are computed and displayed following the method described in Paper VI. These figures are also available on the Fabry–Perot data base: <http://FabryPerot.oamp.fr/>. Appendix F (that contains the tables corresponding to the rotation curves) is available online only. The curves are plotted with both sides superimposed in the same quadrant, using different symbols for the receding (crosses) and approaching (dots) side (with respect to the centre). The black vertical arrow on the *X*-axis represents the radius $D_{25}/2$ while the smaller grey arrow on the *X*-axis represents the transition radius (defined in Paper VI), always smaller than $D_{25}/2$ by definition.

For galaxies seen almost edge-on (inclination higher than 75°), our model does not describe accurately the rotation of a galaxy (see Paper VI). Furthermore, for UGC 1249, UGC 2082, UGC 3851, UGC 4278, UGC 5272, UGC 5935 and UGC 11909, neither rotation curve nor residual velocity fields have been plotted. For them, the position–velocity diagram gives more suitable information than the rotation curve and allows the peak-to-peak or peak-to-valley velocity distribution along the major axis to be followed.

The rotation curves recomputed in this paper may be different from the ones published in Papers I to V since: (i) the adaptive binning gives different weights to low signal-to-noise ratio regions in the velocity field from which is computed the rotation curve; (ii) the exclusion sector around the minor axis is always set at 22.5° (in the galaxy plane) contrarily to what had been done in previous papers where the exclusion sector varied from one galaxy to the other; (iii) the inclination and major axis position angle may be different and (iv) the centre may have changed. Indeed, as has been

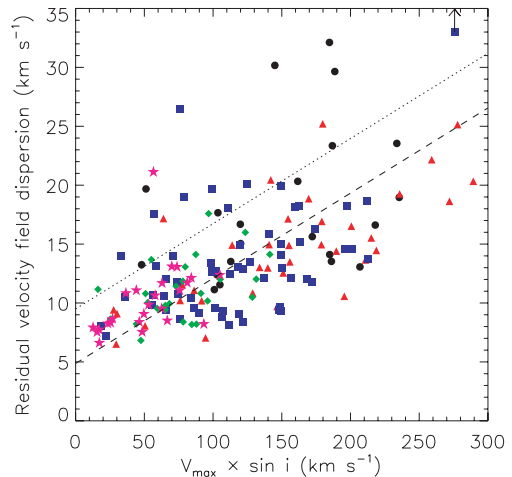


Figure 2. Dispersion in residual velocity field versus maximum velocity, subdivided by Hubble morphological type: black circles $0 \leq t < 2$, red triangles $2 \leq t < 4$, blue squares $4 \leq t < 6$, green rhombuses $6 \leq t < 8$ and pink stars $8 \leq t < 10$. The dashed line represents the linear regression on the data. The points above the dotted line are discussed in Section 3. UGC 3334 labelled with an arrow has actually a huge residual velocity dispersion of 54 km s^{-1} (see Table B2).

done in Paper VI, the velocity field centre chosen to compute the rotation curve matches the morphological centre (nucleus) when it is unambiguously defined from the morphology. No comment is given in Appendix A unless the differences between the previous and the new velocity fields and rotation curves lead to inconsistent results.

The mean velocity dispersion on each residual velocity field has been computed for each galaxy and tabulated in Table B2. The details on the computation and the analysis of residual velocity fields are given in Paper VI. Taking into account the whole sample, the plot presented in Paper VI has been updated in Fig. 2. It still shows that the residual velocity dispersion is correlated with the maximum amplitude of the velocity field (shown by the dashed linear regression). We observe a set of galaxies with a high residual velocity dispersion (points above the dotted line in Fig. 2). These points correspond to galaxies: (i) dominated by strong bars (UGC 89, UGC 3013, UGC 11283 and UGC 11407), or strong spiral structures (UGC 5786 and UGC 3334) and not correctly described by our model which does not take into account non-axisymmetric motions; (ii) having velocity fields of lower quality (UGC 1655, UGC 1736, UGC 3382, UGC 3528, IC 476, UGC 4256, UGC 4456, UGC 4543, IC 2542, UGC 6277, UGC 6523, UGC 9406, UGC 10502, UGC 11269, UGC 11891 and UGC 12276), all these galaxies present a mean size of the bins greater than 25 pixels and an integrated total $H\alpha$ flux on average lower than $2.7 \pm 2.6 \times 10^{-16} \text{ W m}^{-2}$. We also confirm that there is no evidence for correlations between the residual velocity dispersion and the morphological type or the presence of a bar (when it is not dominating the potential of the galaxy).

The morphological parameters (input parameters of the fits) and the results of the fits (kinematical parameters, χ^2 , and parameters of the residual maps) are given in Table B2. Morphological types, distances, absolute magnitudes M_B , optical radii $D_{25}/2$, axis ratios and references for $H\alpha$ velocity fields compiled from the literature are given in Table B3, together with maximum velocity parameters computed from the rotation curves (V_{max} and quality flag on V_{max}). The 25 galaxies larger than the field of view of the instrument are flagged in column 8 of Table B3. The galaxies for which it was

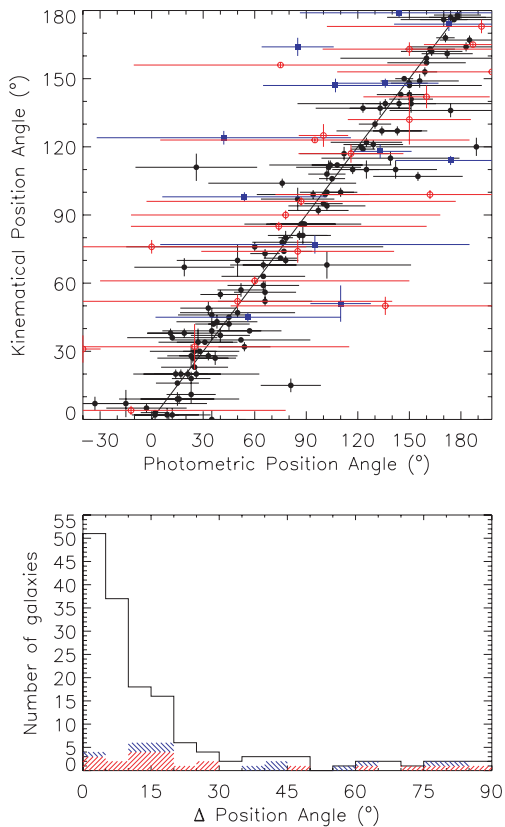


Figure 3. Top panel: kinematical versus morphological (HyperLeda) position angles of the major axis. Galaxies for which no accurate morphological position angle has been computed are shown by red open circles; galaxies having an inclination lower than 25° are displayed by blue squares; the other galaxies are represented by black circles. Bottom panel: histogram of the variation between kinematical and morphological position angles. The red hash, blue hash and residual white represent, respectively, the galaxies for which no accurate position angle has been measured, for which inclination is lower than 25° and the other galaxies of the sample.

necessary to decrease the degrees of freedom of the model have their fixed parameters flagged with an asterisk (*) in Table B2 (see Paper VI for more details).

The kinematical position angles obtained by GHASP are compared with the photometric position angles (found in HyperLeda) and plotted in Fig. 3. The error bar on the morphological position angle has been estimated using the axis ratio and optical radius uncertainties; for clarity, only one morphological position angle is plotted (see Paper VI). In Fig. 3, we have used special symbols for galaxies with no accurate morphological position angle (red open circles) and with an inclination lower than 25° (blue squares). Most of the galaxies showing a disagreement in position angles larger than 20° present: (i) a bad morphological determination of the position angle; or (ii) a kinematical inclination lower than 25° ; or (iii) are specific cases discussed in Appendix A or Appendix B of Paper VI (namely these galaxies are: UGC 3013, UGC 3740, IC 476, UGC 4256, UGC 4273, UGC 4422, UGC 4543, UGC 5931, UGC 10310, UGC 10359, UGC 10470, UGC 10445, UGC 10897, UGC 11283, UGC 11861 and UGC 12060). Morphological position angles of low-inclination galaxies have systematically higher uncertainties than kinematical ones (see Fig. 3). For kinematical inclinations greater than 25° , the mean error on morphological position angles is $\sim 20^\circ$ and the mean error on kinematical position

angles is $\sim 2^\circ$. For inclinations lower than 25° , the difference is larger: the mean error on morphological position angles is $\sim 40^\circ$ while the mean error on kinematical position angles is $\sim 3^\circ$. For the whole sample, the histogram of the variation between kinematical and morphological position angles given in Fig. 3 (bottom panel) indicates that (i) for 57 per cent of the galaxies, the agreement is better than 10° ; (ii) for 79 per cent, the agreement is better than 20° and (iii) the disagreement is larger than 30° for 15 per cent of the galaxies. The conclusion addressed in Paper VI remains valid, i.e. integral field spectroscopy constitutes the best technique to determine position angles and as a consequence, rotation curves.

The kinematical and morphological inclinations are compared in Fig. 4. On the top panel, the photometric inclination is computed using a correction factor depending on the morphological type (see Paper VI). On the middle panel, the photometric inclination is derived from the axis ratio. Galaxies for which the morphological position angle could not be determined accurately are represented by red open circles while galaxies with a difference between morphological and kinematical position angles larger than 20° are displayed with blue squares. The conclusions given in Paper VI are still valid: (i) the agreement between photometric and kinematical inclinations is better for high-inclination galaxies; (ii) morphological inclination determination is unreliable if the measure of the position angle is not reliable; (iii) the errors on morphological and kinematical inclinations are comparable; (iv) kinematical methods may underestimate (or morphological method overestimate) the inclination and (v) the kinematical inclinations are closer to the morphological inclinations when the latter are computed without any correction for the morphological type (see Fig. 4 top and middle panels). The histogram of the difference between morphological and kinematical inclinations (Fig. 4, bottom panel) shows that a difference of inclination larger than 10° is found for less than 40 per cent of the sample. Taking into account the whole GHASP sample, the number of galaxies by bin is higher and the histogram is more symmetrical with respect to that computed in Paper VI.

4 THE TULLY–FISHER RELATION

Among the whole sample of 203 galaxies, we have plotted the Tully–Fisher relation (Tully & Fisher 1977, M_B as a function of $\log 2 V_{\max}$) for a subsample of 177 galaxies in Fig. 5. The 26 other galaxies are not considered in the present discussion because (i) for seven galaxies the rotation curve does not reach the maximum rotation velocity (UGC 1117, UGC 1655, UGC 2455, UGC 4393, UGC 6523, UGC 8898 and UGC 9406); (ii) no B magnitude is available for three galaxies (UGC 2800, UGC 11496 and UGC 12212) and (iii) no velocity measurement, either on the rotation curve or position–velocity diagram is possible for 16 other galaxies (see Table B3). The maximum velocity V_{\max} and its error have been obtained from the fit to the velocity field and the solid line in Fig. 5 is the relation found by Tully & Pierce (2000) (see Paper VI).

In Fig. 5 (top panel), the error bars on the velocity are displayed and galaxies with inclination lower than 25° are distinguished (blue open squares). As already noted in Paper VI, these galaxies have statistically higher velocities than expected from the Tully & Pierce (2000) relation and have large error bars. Considering this effect, we choose to exclude the 22 galaxies with inclinations lower than 25° from the Tully–Fisher analysis (see Paper VI). Among the 155 remaining galaxies, the maximum velocity V_{\max} is reached for 76 of them (black dots, large size), probably reached for 44 of them (blue squares, medium size) and probably not reached for 35 of them (red triangles, small size). They are distinguished in Fig. 5 (middle

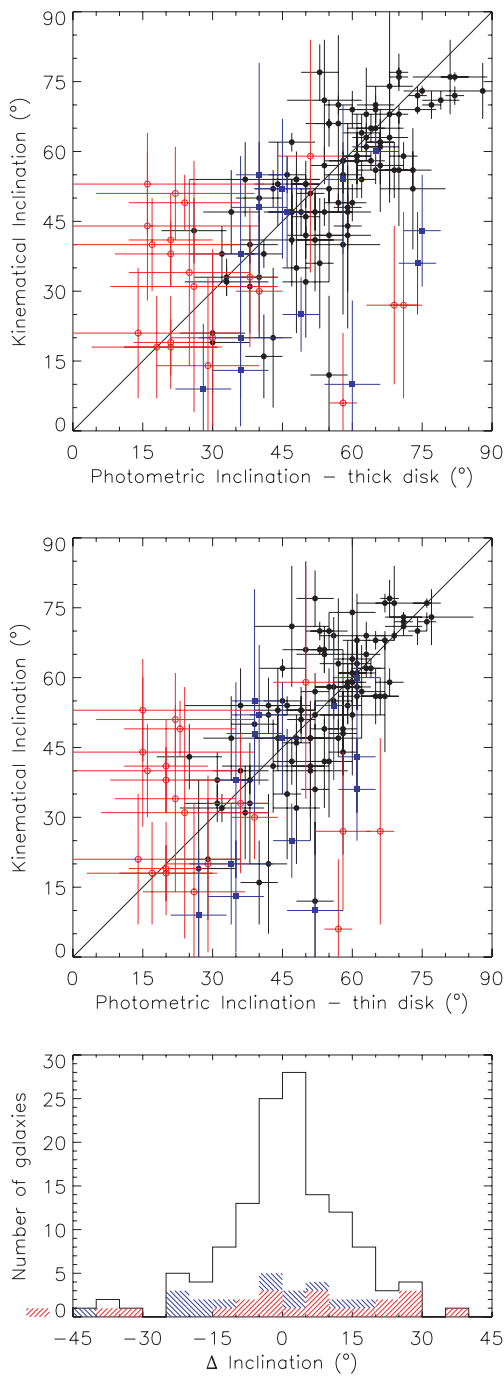
470 *B. Epinat, P. Amram and M. Marcelin*

Figure 4. Top panel: kinematical versus thick disc morphological inclinations. Middle panel: kinematical versus thin disc morphological inclinations. Top and middle panels: galaxies for which no accurate morphological position angle has been computed are shown by red open circles; galaxies with a difference between the kinematical and morphological position angles larger than 20° are displayed with blue squares; the other galaxies are represented by black circles. Bottom panel: histogram of the variation between kinematical and morphological inclinations. The red hash, blue hash and residual white represent, respectively, the galaxies for which no accurate position angle has been measured, for which the difference between the kinematical and morphological position angles is larger than 20° and the other galaxies of the sample.

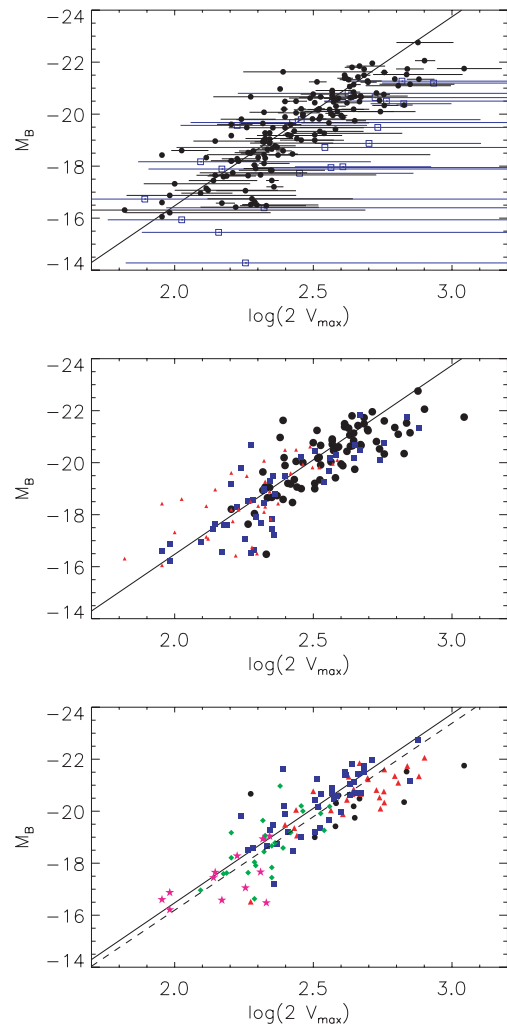


Figure 5. Tully–Fisher relation for our sample of galaxies. The solid line represents the B magnitude Tully–Fisher relation determined by Tully & Pierce (2000) from nearby galaxies in clusters (Ursa Major, Pisces filament, Coma). Top panel: subdivided by inclination – low-inclination galaxies ($i < 25^\circ$): blue squares; other galaxies ($i \geq 25^\circ$): black circles. Middle panel: subdivided by V_{\max} flags – V_{\max} reached: black dots, large size; V_{\max} probably reached: blue squares, medium size; V_{\max} probably not reached: red triangles, small size. Bottom panel: subdivided by morphological type – black circles from 0 to 2; red triangles from 2 to 4; blue squares from 4 to 6; green rhombuses from 6 to 8; pink stars from 8 to 10 and the dashed line represents the best linear fit to the data.

panel) and flagged in Table B3. The quality flag on the maximum velocity is given in Table B3 (see Paper VI).

Fig. 5 (middle panel) confirms the two classifications ‘ V_{\max} probably reached’ and ‘ V_{\max} probably not reached’ since for the majority of each class the points are respectively in agreement and above the Tully & Pierce (2000) relation. From the two classes ‘ V_{\max} reached’ and ‘ V_{\max} probably reached’, we find the following relation (see Paper VI for additional details):

$$M_B = (-7.2 \pm 1.2)(\log 2V_{\max} - 2.5) - (19.8 \pm 0.1). \quad (1)$$

This relation is displayed as a dashed line in Fig. 5, in which morphological types are distinguished for the two best classes (black circles from 0 to 2, red triangles from 2 to 4, blue squares from 4 to 6, green rhombuses from 6 to 8 and pink stars from 8 to 10). The slope of the linear regression computed here from the whole

GHASP sample is now exactly the same as the one computed by Tully & Pierce (2000) (this slope was found to be somewhat lower in Paper VI), and its uncertainty has been reduced by a factor of 0.75. For the Tully–Fisher relation, we note that fast rotators ($V_{\max} > 300 \text{ km s}^{-1}$: UGC 89, UGC 508, UGC 3429, UGC 4422, UGC 4820, UGC 5532, UGC 8900, UGC 8937, UGC 9969 and UGC 11470) are less luminous than expected. This trend has already been noted and discussed in Paper VI.

5 SUMMARY AND CONCLUSIONS

The knowledge of the links between the kinematical and dynamical state of galaxies helps us to increase our understanding of the physics and evolution of galaxies. The GHASP sample, which consists of 203 spiral and irregular galaxies, covering a wide range of morphological types and absolute magnitudes, has been constituted in order to provide a kinematical reference sample of nearby galaxies. The galaxies have been observed in the $H\alpha$ line using Fabry–Perot techniques, leading to the construction of data cubes. This sample is by now the largest set of galaxies ever homogeneously observed with Fabry–Perot techniques. Major improvements in the reduction (adaptive binning techniques, ghost suppression, treatment of faint outskirts regions, etc.) and the analysis (determination of the rotation curve and kinematical parameters and their uncertainties, etc.) have been developed and implemented in the data reduction procedure and homogeneously applied to the whole GHASP sample (see Paper VI for additional details).

In this paper, 97 galaxies have been re-reduced using adaptive binning techniques in order to provide homogeneous data for the whole sample. For each galaxy, we have presented the $H\alpha$ velocity field, the $H\alpha$ monochromatic image and eventually the $H\alpha$ residual velocity field, the position–velocity diagram along the major axis and the rotation curve, when available, leading for the whole sample to 200 velocity fields and 177 rotation curves.

From the data cubes, integrated $H\alpha$ profiles have also been produced. A post calibration has allowed to compute indirect absolute $H\alpha$ flux for all the galaxies belonging to the GHASP sample. This post calibration has been done using fluxes for 69 galaxies found in the literature (James et al. 2004).

We confirm and strengthen most of the results already obtained from half the sample as following.

(i) A high-quality model has been achieved to represent the axisymmetric rotational component of the galaxies since no typical signatures for biases are observed in the residual velocity fields. This means that the residuals observed in the residual velocity field are due to actual non-circular motions and not to an incorrect determination of the kinematical parameters (position of the centre, position angle, inclination and rotation velocity). In addition, the position–velocity diagrams confirm the validity of the rotation curves.

(ii) The mean residual velocity dispersion is strongly correlated with the maximum amplitude of the velocity field. For a given velocity range, this correlation does not clearly depend on the morphological type. However, strongly barred galaxies have a higher residual velocity dispersion than mild-barred or unbarred galaxies. Peculiar galaxies also show a high residual velocity dispersion.

(iii) The determinations of kinematical position angles are robust whatever the inclination of the galaxy whereas morphological position angles are poorly determined for low-inclination systems. Moreover, morphological position angles have systematically higher uncertainties than kinematical ones. This is a major argument for deriving rotation curves from integral field spectroscopy rather than long slit spectroscopy instruments that could lead to incorrect

positioning of the slit (a difference between the morphological and kinematical position angles larger than 30° is found for ~ 15 per cent of the GHASP sample). This may strongly bias mass distribution models and Tully–Fisher studies. In order to build a mass model, the stellar mass distribution derived from the surface brightness profile is combined with the rotation curve deduced from the velocity field. The position angles of the major axis deduced from the surface brightness image and from the velocity field should be identical. The important inconsistencies may appear if these position angles are misaligned.

(iv) Galaxies with poor determination of their morphological position angles have usually unreliable and overestimated morphological inclinations. The agreement between kinematical and morphological inclinations is better when assuming a thin disc, in particular, for high-inclination galaxies. For galaxies with intermediate disc inclinations (higher than 25° and lower than 75°), to improve the quality of the rotation curve, it is possible to reduce the degrees of freedom in kinematical models by fixing the inclination to the morphological value. This is specially true when only low-quality kinematical data are available as it is the case for high-redshift galaxies.

(v) The use of the whole GHASP sample leads to a Tully–Fisher relationship in perfect agreement with Tully & Pierce (2000), despite important differences in the selection of both samples. With respect to the result presented in Paper VI, the use of the whole sample increases the agreement with Tully & Pierce (2000). Three comments should be underlined: (i) galaxies with inclination lower than 25° are inappropriate for Tully–Fisher relation determination since their estimated velocities are easily overestimated; (ii) fast rotators ($V_{\max} > 300 \text{ km s}^{-1}$) are maybe less luminous (than expected from the Tully–Fisher relation) and (iii) for fast rotators and high-luminosity galaxies, the agreement with the Tully–Fisher relation is better when the morphological inclination of the galaxy is computed without taking into account the increasing thickness of the disc when the morphological type of the galaxies moves from early to late types.

From these data and analysis, it is now possible to address the scientific drivers on the whole GHASP sample in forthcoming papers.

ACKNOWLEDGMENTS

The authors warmly thank their collaborators: Philippe Balard, Chantal Balkowski, Jacques Boulesteix, Olivier Boissin, Claude Carignan, Laurent Chemin, Olivier Daigle, Jean-Luc Gach, Olivia Garrido and Olivier Hernandez for having participated to the previous works making possible the new analyse of the observations. They thank Isabelle Jégouzo and Christian Surace for building the Fabry–Perot data base. The authors wish to thank the referee Dr P. James who helped improving the manuscript. They also thank the Programme National Galaxies for supporting the GHASP project in allocating continuously observing time during several years, the Observatoire de Haute-Provence team for its technical assistance during the observations. This research has made use of the NASA/IPAC Extragalactic Data base (NED) which is operated by the Jet Propulsion Laboratory, California Institute of Technology, under contract with the National Aeronautics and Space Administration. The authors have also made an extensive use of the HyperLeda data base (<http://leda.univ-lyon1.fr>). The Digitized Sky Surveys were produced at the Space Telescope Science Institute under US Government grant NAG W-2166. The images of these surveys are based on photographic data obtained using the Oschin Schmidt

472 *B. Epinat, P. Amram and M. Marcelin*

Telescope on Palomar Mountain and the UK Schmidt Telescope. The plates were processed into the present compressed digital form with the permission of these institutions.

REFERENCES

- de Vaucouleurs G., 1979, *ApJ*, 227, 380
 Dopita M. A., Hua C. T., 1997, *ApJS*, 108, 515
 Epinat B., Amram C., Balkowski C., Daigle O., Hernandez L., Chemin L., Carignan C., Gash J.-L., Balard P., 2008, 388, 500
 Garrido O., Marcelin M., Amram P., Boulesteix J., 2002, *A&A*, 387, 821
 Garrido O., Marcelin M., Amram P., Boissin O., 2003, *A&A*, 399, 51
 Garrido O., Marcelin M., Amram P., 2004, *MNRAS*, 349, 225
 Garrido O., Marcelin M., Amram P., Balkowski C., Gach J. L., Boulesteix J., 2005, *MNRAS*, 362, 127
 Haynes M. P., Giovanelli R., Salzer J. J., Wegner G., Freudling W., da Costa L. N., Herter T., Vogt N. P., 1999, *AJ*, 117, 1668
 Irwin J. A., 1994, *ApJ*, 429, 618
 James P. A. et al., 2004, *A&A*, 414, 23
 Karachentsev I. D., Karachentseva V. E., Huchtmeier W. K., Makarov D. I., 2004, *AJ*, 127, 2031
 Koopmann R. A., Haynes M. P., Catinella B., 2006, *AJ*, 131, 716
 Kornreich D. A., Haynes M. P., Lovelace R. V. E., van Zee L., 2000, *AJ*, 120, 139
 Laine S., Gottesman S. T., 1998, *MNRAS*, 297, 1041
 Marcum P. M. et al., 2001, *ApJS*, 132, 129
 Moustakas J., Kennicutt R. C., Jr, 2006, *ApJS*, 164, 81
 Nilson P., 1973, *Uppsala General Catalog of Galaxies*, *Nova Acta Regiae Soc. Sci. Upsaliensis Ser. V*
 Noordermeer E., van der Hulst J. M., Sancisi R., Swaters R. A., van Albada T. S., 2005, *A&A*, 442, 137
 O’Connell R. W., Gallagher J. S., III, Hunter D. A., 1994, *ApJ*, 433, 65
 Paturel G., Garcia A. M., Fouque P., Buta R., 1991, *A&A*, 243, 319
 Paturel G. et al., 1997, *A&AS*, 124, 109
 Paturel G., Fang Y., Petit C., Garnier R., Rousseau J., 2000, *A&AS*, 146, 19
 Rownd B. K., Dickey J. M., Helou G., 1994, *AJ*, 108, 1638
 Saha A., Thim F., Tammann G. A., Reindl B., Sandage A., 2006, *ApJS*, 165, 108
 Schulman E., Bregman J. N., Brinks E., Roberts M. S., 1996, *AJ*, 112, 960
 Shapley A., Fabbiano G., Eskridge P. B., 2001, *ApJS*, 137, 139
 Spano M., Marcelin M., Amram P., Carignan C., Epinat B., Hernandez O., 2007, *MNRAS*, 1084
 Springob C. M., Masters K. L., Haynes M. P., Giovanelli R., Marinoni C., 2007, *ApJS*, 172, 599
 Swaters R. A., 1999, PhD thesis, Rijksuniversiteit Groningen
 Swaters R. A., van Albada T. S., van der Hulst J. M., Sancisi R., 2002, *A&A*, 390, 829
 Swaters R. A., Madore B. F., van den Bosch F. C., Balcells M., 2003, *ApJ*, 583, 732
 Tully R. B., Fisher J. R., 1977, *A&A*, 54, 661
 Tully R. B., Pierce M. J., 2000, *ApJ*, 533, 744
 Tully R. B., Verheijen M. A. W., Pierce M. J., Huang J.-S., Wainscoat R. J., 1996, *AJ*, 112, 2471
 van der Kruit P. C., Allen R. J., 1978, *ARA&A*, 16, 103
 Vauglin I. et al., 1999, *A&AS*, 135, 133
 Wilcots E. M., Prescott M. K. M., 2004, *AJ*, 127, 1900
 Wilcots E. M., Turnbull M. C., Brinks E., 2001, *ApJ*, 560, 110
 Williams B. A., Yun M. S., Verdes-Montenegro L., 2002, *AJ*, 123, 2417

APPENDIX A: NOTES ON INDIVIDUAL GALAXIES

UGC 508. H_I inclination (25°, Noordermeer et al. 2005) as well as photometric inclination (14°, from an axis ratio of 0.97) lead to a very high maximum rotation velocity (~550 km s⁻¹). From Tully–Fisher relationship, its absolute magnitude M_B suggests a maximum

velocity around 270 km s⁻¹, leading to an axis ratio of 0.5 (hence an inclination of 60°). This strongly barred galaxy shows moreover clear evidence for interaction, resulting in a perturbed morphology and velocity field. This biases the determination of the inclination by morphological as well as kinematical methods, leading to an unrealistically high-maximum rotation velocity.

UGC 1117. This galaxy is the famous M33. Because of the limited field of view of GHASP, we only observed the solid body central part of the rotation curve. The external round shape structures in the different images are due to edge-effects of the interference filter vignetting the field of view.

UGC 1249. No rotation curve has been computed because of its high inclination (90°).

UGC 1256. Within ~25 arcsec (~1 kpc), the rotation curve shows negative rotation velocity. This is due to the fact that the bar is almost parallel to the major axis.

UGC 1736. The kinematical centre chosen in Paper IV is different from the morphological centre chosen here, leading to a different rotation curve.

UGC 1913. Same comment as for UGC 1736.

UGC 2023. Despite the fact that this galaxy has been observed again (2 h exposure time on 2002 September 11) and that these data have been compared and added to the data presented in Paper II, the signal-to-noise ratio remains very weak. From the *R*-band image observed by James et al. (2004), it is now possible to accurately determine the centre of that very low surface brightness object. The major axis position angle and the inclination have been set to the values determined from H_I data Swaters (1999). The kinematical centre chosen in Paper II is quite different from the one used here (13 arcsec westward now, which is 0.5 kpc), leading to a very different shape for the rotation curve. Despite the fact that the systemic velocities are almost the same, in Paper II the rotation curve reaches a plateau at ~20 arcsec whereas, with the new rotation centre, the rotation curve now shows a solid body shape up to 60 arcsec.

UGC 2034. Despite the fact that this galaxy has been observed again for 1.5 h (on 2002 September 12) and that these data have been compared and added to the data presented in Paper II, the signal-to-noise ratio remains very weak. Due to the lack of rotation and spatial coverage, our model does not converge. Thus, the parameters have been set to H_I values from Swaters (1999).

UGC 2045. A difference of 6° is computed between the major axis position angle given in this paper and in Paper IV. This is due to the warp which biases the automatic determination of the major axis position angle with respect to the morphological one. It leads to a little change, however, in the rotation curve. The maximum rotation velocity is thus directly taken from the position–velocity diagram plot.

UGC 2053. The signal-to-noise ratio and the total H α flux of this galaxy are very low. The new maps are not much different from the ones published in Paper II, so that they are not presented here.

UGC 2080. The determination of the inclination of this almost face-on galaxy leads to lower value when using the kinematics than when using the morphology. A too low inclination leads to a maximum rotation velocity too high with respect to its magnitude and optical radius. The distance of this nearby galaxy is not accurately determined, but even if the distance is underestimated by a factor of 2, the kinematical inclination is still too low. Thus, the inclination has been set to the morphological value.

UGC 2082. Using the rule defined in Paper VI, we have not plotted the rotation curve of this edge-on galaxy. The maximum rotation velocity may be not reached.

UGC 2141. The signature of a strong bar is clearly visible in the velocity field. It is almost aligned with the major axis and may explain the difference between the value of major axis position angle found in this study and that published in Paper IV (7°). The major axis position angle probably changes with radius within the optical limits for this galaxy. Because of the resulting uncertainty on the major axis position angle, the maximum rotation velocity of that galaxy has been determined directly from its velocity field.

UGC 2183. The inclination computed here ($41 \pm 10^\circ$) is similar to the morphological one (47°) but quite different from that found in H I by Swaters (1999) and adopted in Paper IV (62°). The value 90° suggested by Noordermeer et al. (2005) from optical measurements does not seem realistic.

UGC 2455. The velocity field of this faint low surface brightness galaxy shows a small amplitude making difficult the determination of the rotation curve which is, moreover, affected by a strong bar.

UGC 3013. The determination of the morphological position angle is biased by a strong bar and spiral arms.

UGC 3382. This galaxy has been published in Paper VI from data coming only from run 13. Nevertheless, this galaxy was already observed in run 5 but never published because the signal-to-noise ratio was too low. In this paper, the data from both runs have been added, leading to higher signal-to-noise ratio data and smaller bins allowing a refinement in the kinematical parameters.

UGC 3429. The nucleus of the galaxy is probably hidden behind a dust lane, so that its true position is hard to find on the continuum images because of strong absorption. Thus, we use the centre making the central part of the rotation curve most symmetric. This leads to a satisfactory position for the rotation centre on the continuum image when assuming that the dust lane is symmetrical with respect to the major axis. Beyond 65 arcsec, the rotation curve is unsure, due to obvious strong non-circular motions in the velocity field of this post-merger candidate (Marcum et al. 2001).

UGC 3574. With respect to Paper I, the inclination has been reduced from 30 to $19 \pm 10^\circ$, this new value is more compatible with the morphological one (21°) but leads to a very high maximum rotation velocity with respect to its faint absolute magnitude ($M_B = -18.0$, James et al. 2004). For this nearby object ($V_{\text{sys}} = 1433 \text{ km s}^{-1}$), the distance determined using the Hubble relationship (corrected from Virgo infall) is nevertheless unsure, as can also be suspected from its maximal H α extension reaching ~ 2.5 its optical radius.

UGC 3851. The ghost on the data (located on the northern side of the image) has been removed. No rotation curve has been computed because of its high inclination and to the fact that the velocity field corresponding to the very bright region south of the galaxy may be an artefact due to the detector.

UGC 4273. The determination of the morphological position angle is biased by the bar and spiral arms.

UGC 4278. No rotation curve has been computed because of its high inclination (90°).

UGC 4284. The rotation curve is more symmetrical using a kinematical centre 5 arcsec south from the morphological centre. However, to have a consistent analysis with the rest of the sample, we decided to keep the morphological centre.

UGC 4305. The centre has been changed from Paper III, and is now more to the East. It has been determined from a Two-Micron All-Sky Survey (2MASS) image in the infrared. This centre still gives a fairly symmetric rotation curve. It coincides approximately with the H I kinematical centre but absolutely not with the optical centre of isophotes. The counter rotation seen in the rotation curve of Paper III is not seen anymore in the new rotation curve due to the new centre. However, peculiar motions are still seen in the

velocity field near the optical centre of isophotes. Depending on the centre chosen for kinematical analysis, they can be interpreted as the non-regular motions or as a counter rotation.

UGC 4499. The inclination has been set to the value computed by Swaters et al. (2003).

UGC 4543. The morphological position angle of this galaxy is difficult to estimate due to its ‘Magellanic’ structure.

UGC 4936. The inclination found now is 17° lower than the one published in Paper III. This value is more compatible with the absolute magnitude of the galaxy as well as its optical radius.

UGC 5272. The position–velocity diagram displays a solid body structure characteristic of a bar like structure or an edge-on galaxy. The optical and H α images both look like a bar rather than a disc galaxy, suggesting a morphological inclination close to 90° . Thus, no rotation curve has been plotted. The H I inclination is 59° , computed from a different major axis position angle (20°), this is an additional argument in favour of the bar like structure seen in the H α image.

UGC 5721. The uncommon rotation curve results from the very irregular velocity field perturbed by a strong bar.

UGC 5931. The morphological position angle of this galaxy is difficult to estimate due to the interaction with its close companion UGC 5935.

UGC 5935. No rotation curve has been computed because of its high inclination, close to 90° .

UGC 6537. The rotation centre has been assumed to be the strong nucleus, leading to an asymmetric rotation curve in the outer regions, compatible with the asymmetric velocity field. In Paper III, in order to get a symmetric rotation curve, the rotation centre had been shifted by 7 arcsec (~ 0.5 kpc) with respect to the nucleus, and the major axis position angle rotated by 6° .

UGC 7278. This galaxy does not show any evidence for rotation. However, a velocity amplitude of about 10 km s^{-1} is observed on its velocity field.

UGC 7524. The velocity field only covers the bar of the galaxy which is almost aligned with the H I major axis position angle, thus no rotation curve has been plotted. Furthermore, only the central part of this galaxy is seen in our field of view.

UGC 7592. This galaxy does not show any evidence for rotation. However, a velocity amplitude of about 25 km s^{-1} is observed on its velocity field.

UGC 10310. The morphological position angle is difficult to estimate due to the nature of this barred Magellanic galaxy.

UGC 10359. The determination of the morphological position angle is biased by a strong bar and spiral arms.

UGC 10445. The presence of a bar and spiral arms makes both morphological and kinematical position angles determinations difficult.

UGC 10470. A strong bar in this galaxy biases the determination of the major axis position angle and the inclination. For the latter, we adopted the value suggested by the morphological axis ratio (34° from the NED).

UGC 10502. The kinematical inclination is much higher than the morphological one (24° from the axis ratio). Since this galaxy is interacting, its morphological inclination may be underestimated because of its open spiral arms distorted by streaming motions. The average morphological inclination given in Hyperleđa is instead 40° , still lower than the kinematical one.

UGC 10897. The morphological position angle is poorly determined for this low-inclination galaxy.

UGC 11124. The inclination is difficult to determine because of a strong bar in this interacting galaxy. The kinematical inclination

474 *B. Epinat, P. Amram and M. Marcelin*

(51°) is higher than the morphological one determined from the axis ratio (22°). Despite the fact that the external isocontours seem almost round, the luminosity of this galaxy is nevertheless more consistent with a high inclination than with a lower one with respect to its rotation velocity.

UGC 11283. The presence of a strong bar and spiral arms makes both morphological and kinematical position angle determinations difficult.

UGC 11429. The very peculiar velocity field of this galaxy, which is in pair, displays a concave curvature towards the South on both sides of the galaxy. Thus, the residual velocity field shows a very high dispersion and a signature typical of a rotation curve having a rotation centre abnormally displaced towards the South on the major axis (van der Kruit & Allen 1978). This is obviously not the case from the morphology.

UGC 11861. The morphological position angle of this galaxy is difficult to estimate due to its ‘Magellanic’ structure.

UGC 11909. No rotation curve has been computed because of its high inclination (90°).

UGC 11951. The rotation curve published in Paper II is incorrect due to a typo in the value of the position angle of the major axis.

UGC 12060. This galaxy is irregular, barred and has a low surface brightness. These features make the morphological position angle determination difficult.

UGC 12276. The previous data reduction (Paper IV) missed a large part of the velocity field.

UGC 12276c. The total H α diameter of the galaxy (~ 8 arcsec) is not much larger than the seeing spot of the observations (~ 5 arcsec). Thus, no rotation curve has been computed.

UGC 12632. The very high velocity bump on the blue side of the H α rotation curve is also visible in the H I data (Swaters 1999).

APPENDIX B: TABLES

Table B1. Calibration parameters.

N° UGC (1)	N° NGC (2)	α (2000) (3)	δ (2000) (4)	Exposure time (s) (5)	Scale (arcsec) (6)	Flux ($10^{-16} \text{ W m}^{-2}$) (7)	Paper (8)
12893		00 ^h 00 ^m 28 ^s .0	17°13′ 09″	8640	0.68	0.3 ± 0.1	VI
89	0023	00 ^h 09 ^m 53 ^s .4	25°55′ 24″	8640	0.68	3.3 ± 0.4	VI
94	0026	00 ^h 10 ^m 25 ^s .9	25°49′ 54″	6240	0.68	2.2 ± 0.3	VI
508	0266	00 ^h 49 ^m 47 ^s .8	32°16′ 40″	9720	0.68	4.8 ± 0.6	IV
528	0278	00 ^h 52 ^m 04 ^s .6	47°33′ 01″	3600	0.96	75.4 ± 13.1	II
763	0428	01 ^h 12 ^m 55 ^s .7	00°58′ 53″	4680	0.68	27.8 ± 3.3	IV
1013	0536	01 ^h 26 ^m 21 ^s .9	34°42′ 11″	3840	0.68		VI
	0542	01 ^h 26 ^m 30 ^s .9	34°40′ 31″	3840	0.68	0.5 ± 0.1	VI
1117	0598	01 ^h 33 ^m 51 ^s .0	30°39′ 35″	5760	0.68	$\geq 97.6 \pm 11.6$	IV
1249		01 ^h 47 ^m 29 ^s .9	27°19′ 60″	6000	0.96	$\geq 17.8 \pm 3.1$	II
1256	0672	01 ^h 47 ^m 54 ^s .7	27°25′ 57″	11040	0.96	$\geq 25.9 \pm 4.5$	II
1317	0697	01 ^h 51 ^m 17 ^s .6	22°21′ 28″	4800	0.68	8.3 ± 1.0	VI
1437	0753	01 ^h 57 ^m 42 ^s .2	35°54′ 58″	6720	0.68	7.9 ± 0.9	VI
1655	0828	02 ^h 10 ^m 09 ^s .7	39°11′ 25″	12720	0.68	0.3 ± 0.1	VI
1736	0864	02 ^h 15 ^m 27 ^s .7	06°00′ 08″	7560	0.68	6.2 ± 0.7	IV
1810		02 ^h 21 ^m 28 ^s .7	39°22′ 32″	7200	0.68	2.1 ± 0.2	VI
1886		02 ^h 26 ^m 00 ^s .6	39°28′ 15″	6120	0.68	3.2 ± 0.4	IV
1913	0925	02 ^h 27 ^m 17 ^s .3	33°34′ 44″	3960	0.68	$\geq 44.9 \pm 5.3$	IV
2023		02 ^h 33 ^m 18 ^s .5	33°29′ 30″	14160	0.96	3.9 ± 0.7	II
2034		02 ^h 33 ^m 42 ^s .9	40°31′ 41″	15840	0.96	1.5 ± 0.3	I
2045	0972	02 ^h 34 ^m 13 ^s .4	29°18′ 40″	6120	0.68	22.4 ± 2.7	IV
2053		02 ^h 34 ^m 29 ^s .3	29°44′ 60″	9120	0.96	0.3 ± 0.1	II
2082		02 ^h 36 ^m 16 ^s .2	25°25′ 25″	7200	0.96	4.0 ± 0.7	II
2080		02 ^h 36 ^m 27 ^s .9	38°58′ 09″	21840	0.96	12.9 ± 2.2	I
2141	1012	02 ^h 39 ^m 14 ^s .9	30°09′ 04″	5040	0.68	23.0 ± 2.7	IV
2183	1056	02 ^h 42 ^m 48 ^s .3	28°34′ 27″	5760	0.68	3.4 ± 0.4	IV
2193	1058	02 ^h 43 ^m 30 ^s .1	37°20′ 28″	7920	0.68	6.5 ± 0.8	IV
2455	1156	02 ^h 59 ^m 42 ^s .3	25°14′ 13″	3840	0.96	32.2 ± 5.6	I
2503	1169	03 ^h 03 ^m 34 ^s .8	46°23′ 10″	7200	0.68	4.5 ± 0.5	IV
2800		03 ^h 40 ^m 03 ^s .6	71°24′ 19″	8880	0.96	2.0 ± 0.4	I
2855		03 ^h 48 ^m 20 ^s .7	70°07′ 57″	7200	0.96	25.0 ± 4.3	II
3013	1530	04 ^h 23 ^m 26 ^s .7	75°17′ 44″	3360	0.68	4.8 ± 0.6	IV
3056	1569	04 ^h 30 ^m 49 ^s .2	64°50′ 52″	6000	0.68	270.5 ± 32.0	VI
3273		05 ^h 17 ^m 45 ^s .1	53°33′ 01″	4800	0.68	3.6 ± 0.4	IV
3334	1961	05 ^h 42 ^m 04 ^s .6	69°22′ 43″	5040	0.68	20.2 ± 2.4	VI
3382		05 ^h 59 ^m 47 ^s .7	62°09′ 28″	19200	0.68	0.4 ± 0.1	VI
3384		06 ^h 01 ^m 37 ^s .2	73°07′ 01″	4320	0.68	1.4 ± 0.2	IV
3429	2146	06 ^h 18 ^m 38 ^s .4	78°21′ 26″	6480	0.68	30.7 ± 3.6	IV
3463		06 ^h 26 ^m 55 ^s .8	59°04′ 47″	6960	0.68	11.1 ± 1.3	VI

Table B1 – continued

N° UGC (1)	N° NGC (2)	α (2000) (3)	δ (2000) (4)	Exposure time (s) (5)	Scale (arcsec) (6)	Flux (10^{-16} W m $^{-2}$) (7)	Paper (8)
3574		06 ^h 53 ^m 10 ^s .4	57°10'40''	10080	0.96	$\geq 8.7 \pm 1.5$	I
3521		06 ^h 55 ^m 00 ^s .1	84°02'30''	8400	0.68	0.7 ± 0.1	VI
3528		06 ^h 56 ^m 10 ^s .6	84°04'44''	8400	0.68	0.3 ± 0.1	VI
3618	2308	06 ^h 58 ^m 37 ^s .6	45°12'38''	6000	0.68		VI
3691		07 ^h 08 ^m 01 ^s .4	15°10'39''	3960	0.68	12.2 ± 1.4	IV
3685		07 ^h 09 ^m 05 ^s .9	61°35'44''	5520	0.68	8.0 ± 0.9	VI
3708	2341	07 ^h 09 ^m 12 ^s .0	20°36'11''	6480	0.68	1.2 ± 0.1	VI
3709	2342	07 ^h 09 ^m 18 ^s .1	20°38'10''	6480	0.68	4.2 ± 0.5	VI
3734	2344	07 ^h 12 ^m 28 ^s .7	47°10'00''	11040	0.68	$\geq 3.7 \pm 0.4$	IV
3826		07 ^h 24 ^m 28 ^s .0	61°41'38''	4560	0.68	4.0 ± 0.5	VI
3809	2336	07 ^h 27 ^m 03 ^s .9	80°10'42''	9120	0.96	$\geq 25.4 \pm 4.4$	III
3740	2276	07 ^h 27 ^m 13 ^s .1	85°45'16''	4800	0.68	63.8 ± 7.6	VI
3851	2366	07 ^h 28 ^m 51 ^s .9	69°12'31''	7200	0.96	$\geq 128.5 \pm 22.3$	III
3876		07 ^h 29 ^m 17 ^s .5	27°54'00''	15600	0.68	1.5 ± 0.2	VI
3915		07 ^h 34 ^m 55 ^s .8	31°16'34''	6000	0.68	9.3 ± 1.1	VI
IC476		07 ^h 47 ^m 16 ^s .5	26°57'03''	6240	0.68	0.2 ± 0.1	VI
4026	2449	07 ^h 47 ^m 20 ^s .4	26°55'48''	6240	0.68	0.5 ± 0.1	VI
4165	2500	08 ^h 01 ^m 53 ^s .2	50°44'15''	9600	0.68	13.6 ± 1.6	VI
4256	2532	08 ^h 10 ^m 15 ^s .2	33°57'24''	6960	0.68	2.9 ± 0.3	VI
4273	2543	08 ^h 12 ^m 57 ^s .9	36°15'16''	6240	0.68	9.0 ± 1.1	IV
4274	2537	08 ^h 13 ^m 14 ^s .9	45°59'31''	2640	0.96	15.3 ± 2.7	III
4278		08 ^h 13 ^m 58 ^s .9	45°44'37''	7200	0.96	$\geq 14.9 \pm 2.6$	III
4284	2541	08 ^h 14 ^m 40 ^s .2	49°03'42''	7440	0.96	$\geq 34.0 \pm 5.9$	III
4305		08 ^h 19 ^m 18 ^s .4	70°43'03''	6240	0.96	$\geq 94.2 \pm 16.4$	III
4325	2552	08 ^h 19 ^m 20 ^s .0	50°00'31''	6240	0.96	3.8 ± 0.7	I
4393		08 ^h 26 ^m 04 ^s .4	45°58'02''	6960	0.68	5.4 ± 0.6	VI
4422	2595	08 ^h 27 ^m 42 ^s .0	21°28'45''	7200	0.68	3.2 ± 0.4	VI
4456		08 ^h 32 ^m 03 ^s .5	24°00'39''	6720	0.68	2.0 ± 0.2	VI
4499		08 ^h 37 ^m 41 ^s .5	51°39'10''	10560	0.96	3.5 ± 0.6	I
4543		08 ^h 43 ^m 21 ^s .4	45°44'10''	13680	0.96	2.8 ± 0.5	III
4555	2649	08 ^h 44 ^m 08 ^s .4	34°43'02''	6960	0.68	1.5 ± 0.2	VI
4770	2746	09 ^h 05 ^m 59 ^s .4	35°22'38''	7920	0.68	0.6 ± 0.1	VI
4820	2775	09 ^h 10 ^m 20 ^s .1	07°02'17''	8400	0.68	9.5 ± 1.1	VI
4936	2805	09 ^h 20 ^m 20 ^s .4	64°06'10''	6960	0.96	16.6 ± 2.9	III
5045		09 ^h 28 ^m 10 ^s .2	44°39'52''	6960	0.68	3.5 ± 0.4	VI
5175	2977	09 ^h 43 ^m 46 ^s .8	74°51'35''	5520	0.68	5.2 ± 0.6	VI
5228		09 ^h 46 ^m 03 ^s .8	01°40'06''	9120	0.68	7.3 ± 0.9	VI
5251	3003	09 ^h 48 ^m 36 ^s .4	33°25'17''	1680	0.68	23.1 ± 2.7	VI
5253	2985	09 ^h 50 ^m 21 ^s .9	72°16'47''	6960	0.96	9.5 ± 1.7	I
5272		09 ^h 50 ^m 22 ^s .4	31°29'16''	8160	0.96	6.9 ± 1.2	III
5279	3026	09 ^h 50 ^m 55 ^s .3	28°33'04''	6000	0.68	5.0 ± 0.6	VI
5316	3027	09 ^h 55 ^m 40 ^s .4	72°12'13''	6240	0.96	8.7 ± 1.5	I
5319	3061	09 ^h 56 ^m 12 ^s .0	75°51'59''	7200	0.68	3.2 ± 0.4	VI
5351	3067	09 ^h 58 ^m 21 ^s .2	32°22'12''	7200	0.68	8.2 ± 1.0	VI
5373		10 ^h 00 ^m 00 ^s .5	05°19'58''	7680	0.68	6.0 ± 0.7	VI
5398	3077	10 ^h 03 ^m 20 ^s .0	68°44'01''	7920	0.68	20.9 ± 2.5	VI
5414	3104	10 ^h 03 ^m 57 ^s .1	40°45'21''	7200	0.96	11.8 ± 2.1	III
IC2542		10 ^h 07 ^m 50 ^s .5	34°18'55''	7440	0.68	1.6 ± 0.2	VI
5510	3162	10 ^h 13 ^m 31 ^s .7	22°44'14''	6240	0.68	18.9 ± 2.2	VI
5532	3147	10 ^h 16 ^m 53 ^s .5	73°24'03''	6480	0.68	27.8 ± 3.3	VI
5556	3187	10 ^h 17 ^m 47 ^s .9	21°52'24''	5760	0.68	3.2 ± 0.4	VI
5721	3274	10 ^h 32 ^m 16 ^s .9	27°40'08''	8160	0.96	5.3 ± 0.9	I
5786	3310	10 ^h 38 ^m 45 ^s .9	53°30'12''	4080	0.68	183.5 ± 21.7	VI
5789	3319	10 ^h 39 ^m 09 ^s .4	41°41'11''	6300	0.96	$\geq 16.0 \pm 2.8$	I
5829		10 ^h 42 ^m 43 ^s .7	34°26'54''	11760	0.96	$\geq 3.3 \pm 0.6$	I
5840	3344	10 ^h 43 ^m 31 ^s .1	24°55'21''	5760	0.68	$\geq 60.4 \pm 7.2$	VI
5842	3346	10 ^h 43 ^m 39 ^s .0	14°52'18''	6000	0.68	9.9 ± 1.2	VI
5931	3395	10 ^h 49 ^m 50 ^s .2	32°58'59''	10320	0.96	10.5 ± 1.8	I
5935	3396	10 ^h 49 ^m 55 ^s .2	32°59'27''	10320	0.96	10.2 ± 1.8	I
5982	3430	10 ^h 52 ^m 11 ^s .5	32°56'59''	10080	0.96	8.3 ± 1.4	I
6118	3504	11 ^h 03 ^m 11 ^s .3	27°58'20''	5760	0.68	27.4 ± 3.2	VI
6277	3596	11 ^h 15 ^m 06 ^s .2	14°47'12''	10320	0.68	9.4 ± 1.1	VI

476 *B. Epinat, P. Amram and M. Marcelin*

Table B1 – continued

N° UGC (1)	N° NGC (2)	α (2000) (3)	δ (2000) (4)	Exposure time (s) (5)	Scale (arcsec) (6)	Flux ($10^{-16} \text{ W m}^{-2}$) (7)	Paper (8)
6419	3664	11 ^h 24 ^m 24 ^s .6	03°19'36"	6960	0.68	12.2 ± 1.4	VI
6521	3719	11 ^h 32 ^m 13 ^s .4	00°49'09"	6960	0.68	3.6 ± 0.4	VI
6523	3720	11 ^h 32 ^m 21 ^s .6	00°48'14"	6960	0.68	1.4 ± 0.2	VI
6537	3726	11 ^h 33 ^m 21 ^s .2	47°01'45"	6240	0.96	≥73.8 ± 12.8	III
6628		11 ^h 40 ^m 05 ^s .7	45°56'33"	5760	0.96	7.9 ± 1.4	III
6702	3840	11 ^h 43 ^m 59 ^s .0	20°04'37"	5280	0.68	2.9 ± 0.3	IV
6778	3893	11 ^h 48 ^m 38 ^s .4	48°42'38"	10080	0.96	18.4 ± 3.2	I
6787	3898	11 ^h 49 ^m 15 ^s .6	56°05'04"	9360	0.68	2.0 ± 0.2	VI
7021	4045	12 ^h 02 ^m 42 ^s .3	01°58'36"	7200	0.68	4.6 ± 0.5	VI
7045	4062	12 ^h 04 ^m 03 ^s .8	31°53'42"	6000	0.68	13.8 ± 1.6	VI
7154	4145	12 ^h 10 ^m 01 ^s .4	39°53'02"	5520	0.68	30.3 ± 3.6	VI
7278	4214	12 ^h 15 ^m 39 ^s .1	36°19'41"	5040	0.96	142.4 ± 24.8	III
7323	4242	12 ^h 17 ^m 30 ^s .2	45°37'12"	7200	0.96	18.5 ± 3.2	III
7429	4319	12 ^h 21 ^m 43 ^s .1	75°19'22"	6960	0.68	0.1 ± 0.1	VI
7524	4395	12 ^h 25 ^m 48 ^s .9	33°32'48"	8400	0.96	≥17.7 ± 3.1	I
7592	4449	12 ^h 28 ^m 10 ^s .9	44°05'33"	2880	0.96	429.6 ± 74.7	III
7699		12 ^h 32 ^m 48 ^s .1	37°37'20"	6720	0.68	8.3 ± 1.0	VI
7766	4559	12 ^h 35 ^m 57 ^s .3	27°57'38"	2400	0.68	≥50.4 ± 6.0	VI
7831	4605	12 ^h 39 ^m 59 ^s .7	61°36'29"	3840	0.68	62.1 ± 7.4	VI
7853	4618	12 ^h 41 ^m 33 ^s .1	41°09'05"	5040	0.68	49.8 ± 5.9	VI
7861	4625	12 ^h 41 ^m 52 ^s .9	41°16'25"	3840	0.68	6.3 ± 0.7	VI
7876	4635	12 ^h 42 ^m 39 ^s .3	19°56'44"	6720	0.68	4.1 ± 0.5	VI
7901	4651	12 ^h 43 ^m 42 ^s .7	16°23'35"	8160	0.68	12.7 ± 1.5	VI
7971	4707	12 ^h 48 ^m 22 ^s .9	51°09'57"	13200	0.96	0.8 ± 0.1	I
7985	4713	12 ^h 49 ^m 57 ^s .9	05°18'42"	6240	0.68	28.6 ± 3.4	VI
8334	5055	13 ^h 15 ^m 49 ^s .4	42°01'46"	4320	0.68	≥88.2 ± 10.4	VI
8403	5112	13 ^h 21 ^m 56 ^s .6	38°44'05"	4080	0.68	30.5 ± 3.6	VI
8490	5204	13 ^h 29 ^m 36 ^s .5	58°25'09"	13920	0.96	≥16.2 ± 2.8	I
	5296	13 ^h 46 ^m 18 ^s .7	43°51'04"	6000	0.68	0.8 ± 0.1	VI
8709	5297	13 ^h 46 ^m 23 ^s .7	43°52'20"	6000	0.68	15.2 ± 1.8	VI
8852	5376	13 ^h 55 ^m 16 ^s .1	59°30'25"	7680	0.68	4.4 ± 0.5	VI
8863	5377	13 ^h 56 ^m 16 ^s .7	47°14'08"	5040	0.68	0.4 ± 0.1	VI
8898	5394	13 ^h 58 ^m 33 ^s .7	37°27'12"	4320	0.68	1.0 ± 0.1	VI
8900	5395	13 ^h 58 ^m 38 ^s .0	37°25'28"	4320	0.68	5.6 ± 0.7	VI
8937	5430	14 ^h 00 ^m 45 ^s .8	59°19'43"	8880	0.68	10.7 ± 1.3	VI
9013	5474	14 ^h 05 ^m 02 ^s .0	53°39'08"	5040	0.68	≥18.8 ± 2.2	VI
9179	5585	14 ^h 19 ^m 48 ^s .1	56°43'45"	8160	0.68	12.5 ± 1.5	VI
9219	5608	14 ^h 23 ^m 17 ^s .5	41°46'34"	6480	0.68	2.9 ± 0.3	VI
9248	5622	14 ^h 26 ^m 12 ^s .2	48°33'51"	10800	0.68	1.8 ± 0.2	VI
9358	5678	14 ^h 32 ^m 05 ^s .6	57°55'16"	7680	0.68	8.8 ± 1.0	VI
9366	5676	14 ^h 32 ^m 46 ^s .8	49°27'29"	5040	0.68	34.7 ± 4.1	IV
9363	5668	14 ^h 33 ^m 24 ^s .4	04°27'02"	8160	0.68	≥21.5 ± 2.5	VI
9406	5693	14 ^h 36 ^m 11 ^s .1	48°35'06"	6000	0.68	0.9 ± 0.1	VI
9465	5727	14 ^h 40 ^m 26 ^s .1	33°59'23"	6480	0.68	4.2 ± 0.5	VI
9576	5774	14 ^h 53 ^m 42 ^s .5	03°34'57"	6840	0.68	11.3 ± 1.3	VI
9649	5832	14 ^h 57 ^m 46 ^s .2	71°40'53"	5520	0.68	3.9 ± 0.5	IV
9736	5874	15 ^h 07 ^m 51 ^s .9	54°45'08"	3840	0.68	2.8 ± 0.3	VI
9753	5879	15 ^h 09 ^m 46 ^s .8	57°00'01"	5040	0.68	18.7 ± 2.2	IV
9858		15 ^h 26 ^m 41 ^s .6	40°33'53"	5280	0.68	6.9 ± 0.8	IV
9866	5949	15 ^h 28 ^m 00 ^s .6	64°45'46"	5280	0.68	7.2 ± 0.9	VI
9943	5970	15 ^h 38 ^m 30 ^s .0	12°11'11"	8400	0.68	16.0 ± 1.9	VI
9969	5985	15 ^h 39 ^m 37 ^s .2	59°19'54"	18840	0.96	12.3 ± 2.1	I
9992		15 ^h 41 ^m 47 ^s .9	67°15'14"	5760	0.68	0.5 ± 0.1	IV
10075	6015	15 ^h 51 ^m 25 ^s .3	62°18'36"	5760	0.68	27.1 ± 3.2	VI
10310		16 ^h 16 ^m 18 ^s .5	47°02'45"	12340	0.96	1.8 ± 0.3	I
10359	6140	16 ^h 20 ^m 56 ^s .9	65°23'23"	4560	0.68	≥17.9 ± 2.1	IV
10470	6217	16 ^h 32 ^m 39 ^s .1	78°11'53"	7920	0.68	35.9 ± 4.2	IV
10445		16 ^h 33 ^m 47 ^s .7	28°59'05"	4320	0.68	8.7 ± 1.0	IV
10502		16 ^h 37 ^m 37 ^s .8	72°22'26"	3120	0.68	6.9 ± 0.8	IV
10521	6207	16 ^h 43 ^m 03 ^s .7	36°49'55"	7680	0.68	10.3 ± 1.2	VI
10546	6236	16 ^h 44 ^m 34 ^s .4	70°46'47"	5280	0.68	13.0 ± 1.5	IV
10564	6237	16 ^h 46 ^m 22 ^s .5	70°21'20"	4560	0.68	6.9 ± 0.8	IV

Table B1 – continued

N° UGC (1)	N° NGC (2)	α (2000) (3)	δ (2000) (4)	Exposure time (s) (5)	Scale (arcsec) (6)	Flux (10^{-16} W m $^{-2}$) (7)	Paper (8)
10652	6283	16 ^h 59 ^m 26 ^s .5	49°55'20"	6000	0.68	6.4 ± 0.8	VI
10713		17 ^h 04 ^m 33 ^s .7	72°26'44"	5040	0.68	1.9 ± 0.2	VI
10757		17 ^h 10 ^m 13 ^s .4	72°24'38"	5280	0.68	2.8 ± 0.3	VI
10769		17 ^h 11 ^m 33 ^s .5	72°24'07"	5280	0.68	0.1 ± 0.1	VI
10791		17 ^h 14 ^m 38 ^s .5	72°23'56"	6000	0.68	0.0 ± 0.1	VI
10897	6412	17 ^h 29 ^m 37 ^s .5	75°42'16"	6960	0.96	16.3 ± 2.8	II
11012	6503	17 ^h 49 ^m 26 ^s .3	70°08'40"	5040	0.68	25.3 ± 3.0	VI
11124		18 ^h 07 ^m 27 ^s .6	35°33'51"	3600	0.68	8.4 ± 1.0	IV
11218	6643	18 ^h 19 ^m 46 ^s .7	74°34'06"	7200	0.96	42.2 ± 7.3	II
11269	6667	18 ^h 30 ^m 39 ^s .7	67°59'14"	3840	0.68	1.1 ± 0.1	VI
11283		18 ^h 33 ^m 52 ^s .4	49°16'41"	8640	0.96	10.4 ± 1.8	II
11283c		18 ^h 34 ^m 00 ^s .7	49°22'21"	7200	0.96	0.6 ± 0.1	II
11300	6689	18 ^h 34 ^m 49 ^s .9	70°31'27"	17520	0.96	≥9.3 ± 1.6	II IV VI
11332	6654A	18 ^h 39 ^m 25 ^s .2	73°34'48"	7200	0.68	15.6 ± 1.8	VI
11407	6764	19 ^h 08 ^m 16 ^s .4	50°55'59"	6480	0.68	6.6 ± 0.8	VI
11429	6792	19 ^h 20 ^m 57 ^s .4	43°07'57"	6000	0.68	4.4 ± 0.5	IV
11466		19 ^h 42 ^m 59 ^s .1	45°17'58"	5040	0.68	14.2 ± 1.7	VI
11470	6824	19 ^h 43 ^m 40 ^s .8	56°06'34"	3600	0.68	2.9 ± 0.3	VI
11496		19 ^h 53 ^m 01 ^s .8	67°39'54"	5520	0.68	0.9 ± 0.1	VI
11498		19 ^h 57 ^m 15 ^s .1	05°53'24"	8400	0.68	1.9 ± 0.2	VI
11557		20 ^h 24 ^m 00 ^s .7	60°11'41"	4320	0.68	10.0 ± 1.2	IV
11597	6946	20 ^h 34 ^m 52 ^s .5	60°09'12"	5280	0.68	≥103.2 ± 12.2	VI
11670	7013	21 ^h 03 ^m 33 ^s .7	29°53'50"	7440	0.68	2.9 ± 0.3	VI
11707		21 ^h 14 ^m 31 ^s .8	26°44'05"	4320	0.68	6.9 ± 0.8	IV
11852		21 ^h 55 ^m 59 ^s .4	27°53'53"	6480	0.68	0.6 ± 0.1	IV
11861		21 ^h 56 ^m 24 ^s .2	73°15'39"	4800	0.68	9.5 ± 1.1	IV
11872	7177	22 ^h 00 ^m 41 ^s .2	17°44'18"	7200	0.68	6.3 ± 0.7	VI
11891		22 ^h 03 ^m 33 ^s .8	43°44'57"	10560	0.96	0.6 ± 0.1	II
11909		22 ^h 06 ^m 16 ^s .4	47°15'10"	4320	0.68	13.8 ± 1.6	IV
11914	7217	22 ^h 07 ^m 52 ^s .5	31°21'32"	6120	0.68	20.2 ± 2.4	IV
11951	7231	22 ^h 12 ^m 30 ^s .2	45°19'42"	7200	0.96	14.7 ± 2.6	II
12060		22 ^h 30 ^m 34 ^s .0	33°49'09"	18000	0.96	4.1 ± 0.7	I
12082		22 ^h 34 ^m 11 ^s .3	32°51'42"	7440	0.68	1.3 ± 0.2	VI
12101	7320	22 ^h 36 ^m 03 ^s .5	33°56'52"	4680	0.68	2.3 ± 0.3	IV
12212		22 ^h 50 ^m 30 ^s .6	29°08'20"	9360	0.96	1.0 ± 0.2	II
12276	7440	22 ^h 58 ^m 32 ^s .6	35°48'08"	4680	0.68	3.1 ± 0.4	IV
12276c		22 ^h 58 ^m 41 ^s .4	35°48'33"	4680	0.68	0.2 ± 0.1	IV
12343	7479	23 ^h 04 ^m 56 ^s .7	12°19'21"	5520	0.68	31.0 ± 3.7	IV
12632		23 ^h 29 ^m 58 ^s .7	40°59'25"	5760	0.68	3.4 ± 0.4	IV
12754	7741	23 ^h 43 ^m 54 ^s .4	26°04'31"	10800	0.96	≥44.1 ± 7.7	I

(1) Name of the galaxy in the UGC catalogue except for NGC 542, IC 476, IC 2542 and NGC 5296 that do not have UGC name. (2) Name in the NGC catalogue when available. (3) and (4) Coordinates (in 2000) of the centre of the galaxy used for the kinematic study except those in *italic* (taken from HyperLeda). (5) Total exposure time in second. (6) Pixel scale in arcsec. (7) Flux deduced from the comparison with James et al. (2004) data. When the galaxy is larger than the field of view (see Table B3), we only have a lower limit on the integrated H α flux. (8) Publication papers.

Table B2. Model parameters.

N° UGC (1)	$V_{\text{sys_Leda}}$ (km s $^{-1}$) (2)	$V_{\text{sys_FP}}$ (km s $^{-1}$) (3)	i_{Morph} ($^\circ$) (4)	i_{Kin} ($^\circ$) (5)	PA_{Morph} ($^\circ$) (6)	PA_{Kin} ($^\circ$) (7)	$\overline{\text{Res}}$ (10^{-3} km s $^{-1}$) (8)	σ_{res} (km s $^{-1}$) (9)	χ_{red}^2 (10)
12893	1102 ± 7	1097 ± 2	30 ± 8	19 ± 19	95 ± 90	77 [#] ± 5	−28.1	8	1.2
89	4564 ± 3	4510 ± 5	40 ± 4	33 ± 13	174 ± 37	177 ± 4	42.5	23	8.6
94	4592 ± 4	4548 ± 2	50 ± 4	42 ± 5	102 ± 22	94 ± 2	−3.9	13	2.7
508	4665 ± 4	4641 ± 2	15 ± 27	25 ± 7*	95 ^{2M} ± 90	123 ± 2	−0.2	24	8.7
528	639 ± 7	628 ± 1	14 ± 22	21 ± 14	50 ^{2M} /30 ^{Hα} ± 90	52 ± 3	0.6	9	1.3
763	1156 ± 4	1148 ± 2	48 ± 5	54 ± 6	112 ± 26	117 ± 3	−0.4	12	2.3
1013	5190 ± 4		80 ± 3		68 ± 7				
NGC 542	4660 ± 8		90 ± 0		143 ± 8				
1117	−182 ± 3	−191 ± 1	56 ± 5	56 ± 16*	23 ± 11	18 [#] ± 3	2.1	9	1.4

478 *B. Epinat, P. Amram and M. Marcelin*

Table B2 – continued

N° UGC (1)	$V_{\text{sys_Leda}}$ (km s $^{-1}$) (2)	$V_{\text{sys_FP}}$ (km s $^{-1}$) (3)	i_{Morph} ($^\circ$) (4)	i_{Kin} ($^\circ$) (5)	PA_{Morph} ($^\circ$) (6)	PA_{Kin} ($^\circ$) (7)	$\overline{\text{Res}}$ (10^{-3} km s $^{-1}$) (8)	σ_{res} (km s $^{-1}$) (9)	χ^2_{red} (10)
1249	340 ± 14		90 ± 0		150 ± 8				
1256	424 ± 6	428 ± 1	70 ± 2	76 ± 2	66 ± 9	73 ± 2	1.0	13	2.5
1317	3111 ± 5	3090 ± 2	75 ± 4	73 ± 1	105 ± 8	106 ± 1	-1.3	15	3.3
1437	4893 ± 4	4858 ± 2	52 ± 3	47 ± 4	134 ± 26	127 [#] ± 2	-0.8	18	5.2
1655	5340 ± 16	5427 ± 7	45 ± 9	45 ± 18*		138 [#] ± 6	-2744.9	30	15.4
1736	1561 ± 2	1522 ± 2	48 ± 3	35 ± 14	24 ± 21	27 ± 3	-6.5	18	5.1
1810	7556 ± 21		75 ± 3		42 ± 9				
1886	4859 ± 23	4836 ± 3	47 ± 5	62 ± 2	52 ± 40	35 ± 2	0.8	19	5.9
1913	554 ± 4	536 ± 2	59 ± 3	48 ± 9	102 ± 11	108 [#] ± 3	-12.7	12	2.2
2023	604 ± 6	593 ± 2	15 ± 30	19 ± 18*		135 [#] ± 9*	<0.1	7	0.7
2034	579 ± 6	567 ± 2	37 ± 12	19 ± 23*	170 ± 57	162 [#] ± 17*	-0.3	8	1.0
2045	1546 ± 3	1525 ± 3	66 ± 4	61 ± 8	151 ± 14	139 [#] ± 4	-3.7	17	4.4
2053	1026 ± 5		66 ± 9		43 ± 23				
2082	707 ± 3		87 ± 4		133 ± 3				
2080	903 ± 5	893 ± 1	25 ± 12	25 ± 9*	75 ^{2M} ± 85	156 [#] ± 2	-0.1	10	1.5
2141	985 ± 4	965 ± 3	68 ± 5	74 ± 23	23 ± 14	11 [#] ± 5	-11.6	11	1.9
2183	1546 ± 7	1475 ± 4	47 ± 11	41 ± 10	160 ± 50	159 ± 3	-2.0	12	2.1
2193	517 ± 6	519 ± 1	58 ± 3	6 ± 15	100 ± 14	125 [#] ± 6	<0.1	8	1.0
2455	374 ± 2	367 ± 2	43 ± 7	51 ± 30*	25 ± 28	83 [#] ± 21*			
2503	2387 ± 4	2377 ± 2	57 ± 3	49 ± 2	31 ± 16	34 ± 1	-8.4	16	3.8
2800	1174 ± 5	1174 ± 2	73 ± 7	52 ± 13	103 ± 19	111 [#] ± 4	0.9	12	2.2
2855	1202 ± 4	1188 ± 2	68 ± 2	68 ± 2	110 ± 10	100 ± 2	-0.6	19	5.4
3013	2468 ± 14	2453 ± 6	58 ± 3	58 ± 8*	81 ± 18	15 [#] ± 4	-3.5	25	10.0
3056	-100 ± 7		65 ± 7		120 ± 17				
3273	616 ± 7	615 ± 2	90 ± 0	82 ± 7	45 ± 12	42 ± 4	4.0	12	2.4
3334	3934 ± 4	3952 ± 13	47 ± 7	47 ± 14*	85 ± 21	97 [#] ± 6	9.9	54	46.0
3382	4497 ± 6	4490 ± 2	21 ± 10	18 ± 6	30 ^{2M} /168 ^{Pa} ± 90	4 [#] ± 2	-2.2	18	5.0
3384	1088 ± 3		45 ± 7		62 ± 59				
3429	898 ± 6	868 ± 4	37 ± 12	54 ± 8	123 ± 28	137 [#] ± 3	-7.6	17	4.3
3463	2692 ± 4	2679 ± 3	63 ± 3	63 ± 3	117 ± 12	110 ± 2	-0.1	15	3.6
3574	1441 ± 3	1433 ± 1	21 ± 8	19 ± 10	10 ^{2M} /121 ^{Ha} /162 ^{Pa} ± 90	99 ± 3	<0.1	12	2.3
3521	4426 ± 7	4415 ± 2	61 ± 3	58 ± 5	76 ± 17	78 [#] ± 3	3.2	16	4.1
3528	4421 ± 18	4340 ± 5	59 ± 5	42 ± 12	38 ± 24	43 [#] ± 4	-17.8	32	17.6
3618	5851 ± 6		49 ± 5		171 ± 24				
3691	2202 ± 4	2203 ± 2	62 ± 4	64 ± 4	65 ± 19	68 [#] ± 3	<0.1	10	1.7
3685	1796 ± 4	1795 ± 1	55 ± 4	12 ± 17	133 ± 18	118 [#] ± 4	-1.3	9	1.4
3708	5201 ± 26	5161 ± 4	16 ± 24	44 ± 16	136 ^{Ni} ± 90	50 [#] ± 4	-11.6	18	5.4
3709	5223 ± 50	5292 ± 4	46 ± 4	55 ± 4	66 ± 27	52 [#] ± 2	-4.7	18	5.3
3734	969 ± 5	966 ± 1	26 ± 7	43 ± 7	144 ± 59	139 ± 2	7.7	12	2.2
3826	1733 ± 3	1724 ± 2	30 ± 9	20 ± 19	160 ^{2M} /85 ^{Ni} ± 56	74 [#] ± 5	135.4	9	1.2
3809	2202 ± 4	2200 ± 1	58 ± 4	58 ± 2	178 ± 17	177 [#] ± 1	<0.1	14	3.3
3740	2417 ± 6	2416 ± 2	40 ± 6	48 ± 14	19 ± 29	67 [#] ± 4	<0.1	11	1.7
3851	99 ± 2		90 ± 0		30 ± 7				
3876	860 ± 7	854 ± 2	61 ± 3	59 ± 5	178 ± 14	178 [#] ± 3	-0.2	10	1.6
3915	4679 ± 7	4659 ± 3	59 ± 5	47 ± 4	25 ± 26	30 ± 2	6.8	13	2.7
IC 476	4734 ± 32	4767 ± 3	40 ± 5	55 ± 24	102 ± 49	68 ± 6	-5.9	18	5.5
4026	4782 ± 11	4892 ± 3	73 ± 4	56 ± 4	136 ± 12	139 ± 2	4.0	19	5.7
4165	515 ± 4	504 ± 1	21 ± 9	41 ± 10	74 ^{Pa} ± 86	85 [#] ± 2	-0.4	10	1.6
4256	5252 ± 5	5252 ± 3	36 ± 4	38 ± 21	26 ± 35	111 [#] ± 6	15.9	26	11.1
4273	2458 ± 18	2398 ± 2	65 ± 5	60 ± 4	54 ± 15	32 [#] ± 2	-2.3	14	3.3
4274	445 ± 3	430 ± 1	69 ± 6	27 ± 17		175 ± 3	<0.1	8	1.1
4278	558 ± 4		90 ± 0		172 ± 3				
4284	559 ± 3	536 ± 2	61 ± 3	59 ± 9	170 ± 14	176 ± 3	0.5	10	1.4
4305	158 ± 2	139 ± 1	51 ± 6	40 ± 27*	15 ± 21	9 [#] ± 4			
4325	518 ± 4	508 ± 2	68 ± 4	63 ± 14	52 ± 14	57 ± 3	-0.4	11	2.0
4393	2126 ± 5	2119 ± 4	50 ± 5	50 ± 9*	50 ± 35	70 [#] ± 7	0.6	11	1.7
4422	4333 ± 4	4321 ± 2	49 ± 4	25 ± 8	12 ± 26	36 ± 2	-18.3	20	6.2
4456	5497 ± 23	5470 ± 1	28 ± 6	9 ± 14	42 ± 74	124 ± 3	7.3	14	3.1
4499	692 ± 4	682 ± 1	80 ± 6	50 ± 14*	151 ± 13	141 ± 4	0.5	7	0.7
4543	1960 ± 4	1948 ± 2	45 ± 6	52 ± 15	174 ± 36	136 [#] ± 4	0.7	14	3.0
4555	4235 ± 6	4235 ± 2	21 ± 12	38 ± 7	140 ^{2M} /78 ^{SDSS} ± 90	90 ± 2	0.5	15	3.5
4770	7063 ± 9	7026 ± 3	36 ± 9	20 ± 13	54 ± 48	98 [#] ± 3	-36.8	14	3.0

Table B2 – continued

N° UGC (1)	$V_{\text{sys_Leda}}$ (km s $^{-1}$) (2)	$V_{\text{sys_FP}}$ (km s $^{-1}$) (3)	i_{Morph} ($^\circ$) (4)	i_{Kin} ($^\circ$) (5)	PA_{Morph} ($^\circ$) (6)	PA_{Kin} ($^\circ$) (7)	$\overline{\text{Res}}$ (10 $^{-3}$ km s $^{-1}$) (8)	σ_{res} (km s $^{-1}$) (9)	χ_{red}^2 (10)
4820	1355 \pm 4	1350 \pm 2	41 \pm 4	38 \pm 3	160 \pm 23	157 \pm 2	<0.1	13	2.7
4936	1733 \pm 5	1728 \pm 1	36 \pm 6	13 \pm 12	174 \pm 32	114 [#] \pm 2	0.2	10	1.4
5045	7716 \pm 23	7667 \pm 2	41 \pm 4	16 \pm 9	136 \pm 31	148 \pm 2	−2.8	13	2.7
5175	3052 \pm 11	3049 \pm 2	65 \pm 4	56 \pm 3	145 \pm 14	143 \pm 2	−2.3	13	2.9
5228	1873 \pm 7	1869 \pm 2	82 \pm 2	72 \pm 2	122 \pm 6	120 \pm 2	−0.7	9	1.3
5251	1481 \pm 3	1465 \pm 3	88 \pm 9	73 \pm 6	78 \pm 4	80 [#] \pm 3	<0.1	15	3.5
5253	1322 \pm 7	1322 \pm 2	38 \pm 6	40 \pm 4	176 \pm 31	176 [#] \pm 2	−0.7	13	2.5
5272	520 \pm 3		90 \pm 0		118 \pm 6				
5279	1488 \pm 4		90 \pm 0		83 \pm 6				
5316	1059 \pm 3	1031 \pm 2	70 \pm 2	77 \pm 4	130 \pm 9	130 \pm 3	−5.4	14	3.2
5319	2448 \pm 9	2439 \pm 1	40 \pm 5	30 \pm 9	125 ^{2M} /7 ^{Pa} \pm 29	165 [#] \pm 2	−21.0	9	1.3
5351	1473 \pm 4		82 \pm 6		105 \pm 6				
5373	302 \pm 3	291 \pm 2	60 \pm 6	10 \pm 18	110 \pm 18	51 \pm 8	−0.5	8	0.9
5398	14 \pm 5		40 \pm 10		45 \pm 35				
5414	603 \pm 3	592 \pm 2	54 \pm 8	71 \pm 13	35 \pm 29	39 [#] \pm 4	−0.4	13	2.7
IC 2542	6113 \pm 20	6111 \pm 2	43 \pm 4	20 \pm 15	173 \pm 32	174 \pm 3	−0.9	20	6.3
5510	1301 \pm 3	1298 \pm 2	38 \pm 5	31 \pm 10	26 \pm 37	20 [#] \pm 3	−0.3	10	1.4
5532	2812 \pm 8	2802 \pm 1	33 \pm 9	32 \pm 3	150 \pm 42	147 \pm 1	<0.1	14	2.9
5556	1581 \pm 3		75 \pm 2		105 \pm 7				
5721	537 \pm 4	527 \pm 6	62 \pm 3	62 \pm 30*	95 \pm 14	95 [#] \pm 21*	0.2	14	3.1
5786	990 \pm 3	992 \pm 4	16 \pm 25	53 \pm 11	18 ^{SDSS} \pm 90	153 \pm 5	0.5	17	4.6
5789	742 \pm 2	730 \pm 2	63 \pm 3	68 \pm 10	37 \pm 12	27 \pm 3	4.0	8	1.1
5829	630 \pm 3	626 \pm 2	25 \pm 13	34 \pm 20		18 [#] \pm 6	−0.5	9	1.2
5840	582 \pm 4	580 \pm 1	18 \pm 14	18 \pm 11		153 [#] \pm 3	<0.1	12	2.1
5842	1261 \pm 10	1245 \pm 1	34 \pm 6	47 \pm 9	104 \pm 36	112 [#] \pm 2	−1.5	10	1.7
5931	1621 \pm 3	1604 \pm 3	58 \pm 4	54 \pm 16	35 \pm 20	180 [#] \pm 5	10.2	13	2.9
5935	1656 \pm 7		90 \pm 0		99 \pm 14				
5982	1583 \pm 6	1573 \pm 2	58 \pm 4	55 \pm 4	33 \pm 17	28 \pm 2	−1.5	15	3.6
6118	1539 \pm 5	1525 \pm 2	27 \pm 7	39 \pm 8*	150 ^{2M} /57 ^{Pa} \pm 50	163 [#] \pm 3	16.3	11	1.9
6277	1192 \pm 3	1191 \pm 3	17 \pm 16	17 \pm 17*	0 ^{2M} \pm 90	76 \pm 3	−5.1	19	5.7
6419	1365 \pm 24	1381 \pm 2	57 \pm 5	66 \pm 19	27 \pm 23	34 \pm 7	−1.8	8	0.9
6521	5879 \pm 5	5842 \pm 2	50 \pm 3	46 \pm 4	21 \pm 19	20 \pm 2	−0.9	17	4.5
6523	5913 \pm 13	5947 \pm 2	24 \pm 7	24 \pm 14*	36 ^{Va} /12 ^{Pa} /51 ^{Pa} \pm 90	173 [#] \pm 3	−6.4	13	2.8
6537	862 \pm 5	856 \pm 2	49 \pm 5	47 \pm 5	14 \pm 19	20 [#] \pm 2	−0.2	12	2.3
6628	850 \pm 5	863 \pm 1	33 \pm 10	20 \pm 20*	144 \pm 58	179 \pm 2	1.4	10	1.4
6702	7372 \pm 10	7332 \pm 2	32 \pm 7	38 \pm 6	60 \pm 75	76 [#] \pm 2	8.4	15	3.6
6778	969 \pm 4	951 \pm 1	60 \pm 3	49 \pm 4	162 \pm 15	163 [#] \pm 2	2.7	12	2.3
6787	1173 \pm 3	1157 \pm 3	57 \pm 3	70 \pm 2	108 \pm 15	112 \pm 2	−0.7	17	4.4
7021	1979 \pm 8	1976 \pm 3	56 \pm 4	56 \pm 7*	89 \pm 17	86 [#] \pm 2	−0.6	14	3.1
7045	770 \pm 6	758 \pm 1	70 \pm 2	68 \pm 2	101 \pm 8	99 \pm 2	0.2	10	1.5
7154	1011 \pm 28	1009 \pm 1	64 \pm 3	65 \pm 3	100 \pm 11	95 [#] \pm 2	<0.1	12	2.3
7278	291 \pm 2		44 \pm 9						
7323	517 \pm 4	505 \pm 1	51 \pm 4	51 \pm 11*	19 \pm 21	38 \pm 3	<0.1	10	1.5
7429	1476 \pm 24		73 \pm 3		162 \pm 10				
7524	317 \pm 3		90 \pm 0		127 \pm 7				
7592	204 \pm 3		63 \pm 5		47 \pm 16				
7699	496 \pm 1		78 \pm 2		32 \pm 6				
7766	814 \pm 3	807 \pm 1	65 \pm 4	69 \pm 3	150 \pm 10	143 [#] \pm 2	<0.1	12	2.4
7831	147 \pm 4	136 \pm 3	70 \pm 3	56 \pm 12	125 \pm 7	110 [#] \pm 5	<0.1	9	1.2
7853	537 \pm 4	530 \pm 2	58 \pm 5	58 \pm 28*	40 \pm 17	37 [#] \pm 4	12.8	8	1.1
7861	611 \pm 4	598 \pm 1	47 \pm 6	47 \pm 24*	116 ^{Pa} /30 ^{SDSS} \pm 31	117 [#] \pm 4	<0.1	11	1.9
7876	955 \pm 8	944 \pm 1	44 \pm 5	53 \pm 9	3 \pm 34	164 [#] \pm 3	0.3	8	1.1
7901	799 \pm 2	788 \pm 2	50 \pm 3	53 \pm 2	77 \pm 16	74 [#] \pm 2	<0.1	12	2.2
7971	467 \pm 6	457 \pm 2	26 \pm 18	31 \pm 27	25 ^{Ni} \pm 90	32 \pm 11	0.3	8	1.0
7985	653 \pm 3	642 \pm 2	24 \pm 12	49 \pm 6	110 ^{2M} /87 ^{Ha} /153 ^{Pa} /100 ^{Ni} /88 ^{SDSS} \pm 90	96 [#] \pm 3	−0.1	8	1.0
8334	508 \pm 3	484 \pm 1	55 \pm 5	66 \pm 1	102 \pm 16	100 \pm 1	−0.1	11	1.7
8403	969 \pm 4	975 \pm 2	54 \pm 3	57 \pm 4	129 \pm 17	121 \pm 2	−0.1	9	1.3
8490	202 \pm 2	190 \pm 1	58 \pm 8	40 \pm 15	5 \pm 17	167 \pm 3	−0.2	11	1.8
NGC 5296	2243 \pm 3	2254 \pm 2	65 \pm 6	65 \pm 4	12 \pm 22	2 \pm 3	−6.2	4	0.3
8709	2407 \pm 13	2405 \pm 3	82 \pm 3	76 \pm 1	147 \pm 5	150 [#] \pm 2	0.1	15	3.3
8852	2023 \pm 17	2075 \pm 1	55 \pm 7	52 \pm 3	65 \pm 24	63 \pm 2	0.9	10	1.5
8863	1796 \pm 7	1789 \pm 4	77 \pm 4	77 \pm 13*	38 \pm 8	38 [#] \pm 7*	−41.4	14	3.3

480 *B. Epinat, P. Amram and M. Marcelin*

Table B2 – continued

N° UGC (1)	$V_{\text{sys_Leda}}$ (km s^{-1}) (2)	$V_{\text{sys_FP}}$ (km s^{-1}) (3)	i_{Morph} ($^\circ$) (4)	i_{Kin} ($^\circ$) (5)	PA_{Morph} ($^\circ$) (6)	PA_{Kin} ($^\circ$) (7)	$\overline{\text{Res}}$ ($10^{-3} \text{ km s}^{-1}$) (8)	σ_{res} (km s^{-1}) (9)	χ^2_{red} (10)
8898	3464 ± 10	3448 ± 2	71 ± 3	27 ± 20	30 ^{2M} /140 ^{Pa} /117 ^{SDSS} ± 10	31 ± 6	41.5	7	0.7
8900	3466 ± 11	3511 ± 3	66 ± 5	57 ± 10	172 ± 15	161 ± 2	5.8	20	6.6
8937	2968 ± 9	2961 ± 5	50 ± 5	32 ± 12	177 ± 23	5 [#] ± 3	2361.4	19	5.7
9013	255 ± 23	262 ± 1	50 ± 4	21 ± 16*	85 ± 21	164 ± 4	1.8	7	0.8
9179	302 ± 2	293 ± 2	53 ± 3	36 ± 14	33 ± 16	49 ± 4	<0.1	9	1.4
9219	666 ± 11		81 ± 6		99 ± 13				
9248	3867 ± 6	3865 ± 2	58 ± 3	58 ± 4	86 ± 18	81 [#] ± 2	3.5	15	3.6
9358	1907 ± 4	1912 ± 3	62 ± 3	54 ± 4	2 ± 14	2 [#] ± 2	2.3	15	3.5
9366	2102 ± 3	2109 ± 2	66 ± 3	62 ± 2	45 ± 10	45 [#] ± 2	-0.6	14	2.9
9363	1584 ± 3	1577 ± 1	33 ± 6	18 ± 14*	107 ± 42	147 ± 3	3.2	8	1.1
9406	2279 ± 2	2281 ± 2	51 ± 7	59 ± 25	60 ^{2M} /150 ^{SDSS} ± 36	132 ± 12	78.0	11	2.0
9465	1495 ± 3	1485 ± 2	90 ± 0	65 ± 4	143 ± 14	127 ± 3	0.3	8	1.1
9576	1565 ± 5	1555 ± 2	52 ± 4	41 ± 11	125 ± 21	122 ± 3	-0.4	10	1.6
9649	447 ± 4	440 ± 1	70 ± 3	54 ± 6*	40 ± 12	55 [#] ± 3	<0.1	10	1.6
9736	3128 ± 4	3135 ± 2	51 ± 3	51 ± 5	57 ± 19	39 [#] ± 2	2.9	14	3.2
9753	771 ± 3	764 ± 2	74 ± 4	69 ± 1	2 ± 8	3 ± 2	0.5	11	1.8
9858	2621 ± 3	2638 ± 3	90 ± 0	75 ± 2	78 ± 6	70 ± 2	0.6	17	4.6
9866	427 ± 4	430 ± 1	69 ± 3	56 ± 6	150 ± 11	148 ± 2	-5.1	7	0.8
9943	1958 ± 4	1946 ± 1	48 ± 5	54 ± 2	87 ± 20	86 [#] ± 2	-0.1	9	1.4
9969	2519 ± 3	2516 ± 2	63 ± 3	61 ± 1	15 ± 12	16 ± 1	7.4	19	5.4
9992	426 ± 4		60 ± 5						
10075	831 ± 3	827 ± 1	66 ± 3	62 ± 2	28 ± 10	30 [#] ± 1	<0.1	9	1.4
10310	716 ± 3	702 ± 2	42 ± 11	42 ± 20*	165 ± 47	7 [#] ± 7	<0.1	11	2.0
10359	907 ± 4	911 ± 2	32 ± 8	44 ± 12*	76 ± 43	104 [#] ± 3	<0.1	13	2.5
10470	1368 ± 3	1354 ± 2	45 ± 5	34 ± 9*	155 ± 26	107 [#] ± 2	-0.6	10	1.6
10445	962 ± 3	961 ± 2	46 ± 4	47 ± 12	142 ± 24	110 ± 4	-0.4	11	1.8
10502	4297 ± 5	4291 ± 2	40 ± 5	50 ± 5	94 ± 33	99 ± 2	-0.2	20	6.4
10521	852 ± 2	832 ± 2	71 ± 3	59 ± 3	17 ± 10	20 ± 2	0.7	9	1.2
10546	1280 ± 4	1268 ± 2	55 ± 3	42 ± 10	9 ± 19	2 [#] ± 3	-2.9	14	3.1
10564	1132 ± 4	1120 ± 2	53 ± 4	77 ± 6	156 ± 23	149 ± 3	0.9	11	2.1
10652	1092 ± 26	1089 ± 1	30 ± 7	21 ± 13	56 ± 54	45 [#] ± 3	0.6	8	1.0
10713	1073 ± 4		90 ± 0		8 ± 7				
10757	1168 ± 8	1210 ± 2	59 ± 3	44 ± 22	66 ± 18	56 ± 6	0.7	11	1.8
10769	1230 ± 13		57 ± 4		41 ± 24				
10791	1328 ± 6	1318 ± 3	0 ± 0	34 ± 20*		92 ± 4	726.5	10	1.7
10897	1334 ± 3	1313 ± 1	31 ± 6	31 ± 17*	139 ± 40	115 ± 3	0.3	13	2.7
11012	36 ± 12	25 ± 1	74 ± 2	72 ± 2	123 ± 7	119 [#] ± 2	0.4	8	1.0
11124	1608 ± 4	1606 ± 2	22 ± 17	51 ± 10		2 [#] ± 3	-0.4	11	1.8
11218	1483 ± 2	1477 ± 2	64 ± 3	58 ± 2	36 ± 11	42 ± 2	-0.5	12	2.3
11269	2590 ± 6	2563 ± 6	60 ± 3	69 ± 4	97 ± 18	92 [#] ± 3	3.8	30	14.4
11283	1963 ± 5	1944 ± 4	34 ± 7	34 ± 17*	9 ± 58	120 ± 5	-3.7	18	4.9
11283c	1963 ± 5		68 ± 3		82 ± 14				
11300	488 ± 3	482 ± 1	77 ± 2	70 ± 3	171 ± 5	168 ± 2	-1.6	12	2.3
11332	1569 ± 25		82 ± 2		65 ± 5				
11407	2412 ± 4	2402 ± 8	64 ± 3	64 ± 22*	65 ± 13	65 ± 10*	1.0	20	6.6
11429	4642 ± 4	4679 ± 7	61 ± 3	61 ± 16*	23 ± 14	28 [#] ± 6			
11466	820 ± 9	826 ± 3	55 ± 3	66 ± 5	35 ± 20	46 [#] ± 3	-0.3	13	2.6
11470	3530 ± 40	3546 ± 5	47 ± 6	47 ± 7	50 ± 33	47 ± 3	258.0	25	10.7
11496	2105 ± 6	2115 ± 2	0 ± 0	44 ± 16		167 ± 4	135.8	9	1.2
11498	3266 ± 8	3284 ± 4	79 ± 4	71 ± 2	75 ± 10	71 [#] ± 2	-23.4	22	7.9
11557	1388 ± 4	1392 ± 1	29 ± 16	29 ± 22*		96 [#] ± 3	0.1	11	1.8
11597	46 ± 3	40 ± 2	17 ± 19	40 ± 10	60 ^{Sp} ± 90	61 [#] ± 3	0.4	13	2.5
11670	778 ± 3	776 ± 3	90 ± 0	65 ± 2	159 ± 7	153 [#] ± 2	0.8	16	3.9
11707	906 ± 4	897 ± 2	65 ± 4	70 ± 4	65 ± 21	59 ± 3	0.3	11	1.8
11852	5850 ± 8	5821 ± 3	47 ± 5	47 ± 7	16 ± 35	9 [#] ± 3	4.1	20	6.8
11861	1477 ± 4	1476 ± 2	75 ± 4	43 ± 12	11 ± 14	38 [#] ± 3	<0.1	16	4.0
11872	1147 ± 5	1140 ± 1	54 ± 6	47 ± 3	88 ± 19	86 ± 2	-0.1	13	2.7
11891	461 ± 4	466 ± 6	43 ± 10	43 ± 23*		119 ± 10	11.1	21	7.4
11909	1106 ± 5		90 ± 0		1 ± 6				
11914	951 ± 2	945 ± 1	33 ± 7	33 ± 4	88 ± 34	86 [#] ± 2	0.2	15	3.5
11951	1085 ± 10	1085 ± 2	81 ± 8	76 ± 8	88 ± 14	81 [#] ± 4	0.2	12	2.4
12060	884 ± 5	879 ± 2	74 ± 4	36 ± 11	147 ± 18	7 [#] ± 3	-0.4	12	2.2

Table B2 – continued

N° UGC (1)	$V_{\text{sys_Leda}}$ (km s $^{-1}$) (2)	$V_{\text{sys_FP}}$ (km s $^{-1}$) (3)	i_{Morph} ($^\circ$) (4)	i_{Kin} ($^\circ$) (5)	PA_{Morph} ($^\circ$) (6)	PA_{Kin} ($^\circ$) (7)	$\overline{\text{Res}}$ (10^{-3} km s $^{-1}$) (8)	σ_{res} (km s $^{-1}$) (9)	χ^2_{red} (10)
12082	803 \pm 2	792 \pm 2	29 \pm 11	14 \pm 19		143 \pm 5	0.6	8	1.1
12101	777 \pm 3	770 \pm 2	58 \pm 5	58 \pm 9*	133 \pm 18	137# \pm 4	0.5	13	2.8
12212	892 \pm 4	899 \pm 2	71 \pm 9	71 \pm 27*		82 \pm 7	0.9	13	2.8
12276	5664 \pm 4	5642 \pm 2	38 \pm 6	33 \pm 15	160 ^{Pa} /55 ^{2M} \pm 37	142# \pm 5	9.2	20	6.2
12276c	5664 \pm 4		24 \pm 10		41 ^{Pa} \pm 90				
12343	2381 \pm 3	2371 \pm 2	43 \pm 4	52 \pm 4	25 \pm 19	23# \pm 2	−0.3	16	4.2
12632	422 \pm 5	415 \pm 2	37 \pm 13	46 \pm 16*		47 \pm 4	−0.4	9	1.3
12754	753 \pm 9	742 \pm 2	50 \pm 3	53 \pm 5	163 \pm 18	162# \pm 2	0.2	13	2.8

(1) Name in the UGC catalogue (see Table B1). (2) Systemic velocity found in HyperLeda data base. (3) Systemic velocity deduced from our velocity field analysis. (4) Morphological inclination from HyperLeda (Paturel et al. 1997). (5) Inclination deduced from the analysis of our velocity field; those marked with an asterisk (*) have been fixed equal to morphological value from HyperLeda, except UGC 9649, UGC 10359, UGC 10470 for which we used morphological inclinations from NED, and UGC 508, UGC 2023, UGC 2034, UGC 2455, UGC 4499, UGC 6118, UGC 6628, UGC 9013, UGC 9363, UGC 10791 and UGC 12632 for which we used inclinations determined from H I data (see Table B3). (6) Morphological position angle from HyperLeda, except for those marked (Ha: Haynes et al. 1999; Ni: Nilson 1973; Pa: Paturel et al. 2000; SDSS: 2006 Sloan Digital Sky Survey, DR5; Sp: Springob et al. 2007; 2M: Two-Micron All-Sky Survey team 2003, 2MASS extended objects; Va: Vauglin et al. 1999). (7) Position angle deduced from our velocity field; those marked with an asterisk (*) have been fixed equal to morphological value. The symbol# indicates that the position angle refers to the approaching side. (8) Mean residual velocity on the whole velocity field. (9) Residual velocity dispersion on the whole velocity field. (10) Reduced χ^2 of the model.

Table B3. Galaxy parameters.

N° UGC (1)	t (2)	Type (3)	D (Mpc) (4)	M_b (mag) (5)	b/a (6)	$i_{b/a}$ ($^\circ$) (7)	$D_{25/2}$ (arcsec kpc $^{-1}$) (8)	V_{max} (km s $^{-1}$) (9)	V_{max} flag (10)	H I data (11)
12893	8.4 \pm 0.8	Sd	12.5 ^{Ja}	−15.5	0.89 \pm 0.06	27 \pm 7	34 \pm 5/2.1 \pm 0.3	72 \pm 67	2	
89	1.2 \pm 0.6	SBa	64.2 ^{Mo}	−21.5	0.79 \pm 0.04	38 \pm 3	46 \pm 4/14.5 \pm 1.4	343 \pm 117	1	W ^{N05}
94	2.4 \pm 0.6	S(r)ab	64.2 ^{Mo}	−20.4	0.68 \pm 0.04	47 \pm 3	34 \pm 3/10.5 \pm 0.8	209 \pm 21	1	W ^{N05}
508	1.5 \pm 0.9	SBab	63.8	−21.8	0.97 \pm 0.11	14 \pm 25	85 \pm 7/26.3 \pm 2.2	553 \pm 127	1	W ^{N05}
528	2.9 \pm 1.1	SABb	12.1	−19.6	0.97 \pm 0.09	14 \pm 21	72 \pm 5/4.2 \pm 0.3	84 \pm 52	1	W ^{Web}
763	8.6 \pm 1.0	SABm	12.7 ^{Ja}	−18.9	0.74 \pm 0.04	42 \pm 3	85 \pm 6/5.2 \pm 0.4	104 \pm 11	1	
1013	3.1 \pm 0.2	SB(r)b pec	70.8	−22.0	0.31 \pm 0.03	72 \pm 2	88 \pm 6/30.1 \pm 2.0			W ^{Web}
NGC 542	2.8 \pm 3.9	Sb pec	63.7	−19.5	0.22 \pm 0.03	77 \pm 2	34 \pm 6/10.4 \pm 1.7	125 \pm 8 ^{PV}	2	
1117	6.0 \pm 0.4	Sc	0.9 ^{Sa}	−18.9	0.58 \pm 0.06	54 \pm 4	1863 \pm 64/8.1 \pm 0.3*	79 \pm 17	4	
1249	8.8 \pm 0.6	SBm pec	7.2 ^{Ka}	−18.3	0.38 \pm 0.05	68 \pm 3	193 \pm 11/6.7 \pm 0.4*	65 \pm 8 ^{PV}	3	W ^{S02}
1256	6.0 \pm 0.3	SBc pec	7.2 ^{Ka}	−18.9	0.39 \pm 0.02	67 \pm 1	210 \pm 12/7.3 \pm 0.4*	105 \pm 9	2	W ^{Web}
1317	4.9 \pm 0.7	SAB(r)c	42.2	−21.5	0.33 \pm 0.04	71 \pm 2	114 \pm 7/23.4 \pm 1.5	205 \pm 9	1	W ^{Web}
1437	4.9 \pm 1.0	SABc	66.8	−21.8	0.63 \pm 0.03	51 \pm 2	43 \pm 5/13.8 \pm 1.7	218 \pm 15	1	W ^{Web}
1655	1.0 \pm 0.5	Sa	73.0	−21.6	0.75 \pm 0.09	42 \pm 8	86 \pm 10/30.3 \pm 3.5	205 \pm 64	4	
1736	5.1 \pm 0.6	SABc	17.6 ^{Ja}	−20.1	0.69 \pm 0.03	46 \pm 3	112 \pm 7/9.5 \pm 0.6	193 \pm 68	3	
1810	3.1 \pm 0.6	Sb pec	102.4	−22.2	0.36 \pm 0.02	69 \pm 1	52 \pm 4/26.0 \pm 2.0			W ^{Web}
1886	3.6 \pm 0.6	SABb	66.5	−20.8	0.70 \pm 0.06	45 \pm 5	16 \pm 3/5.1 \pm 0.8	267 \pm 8	1	W ^{Web}
1913	7.0 \pm 0.4	SBcd	9.3 ^{Ka}	−20.1	0.53 \pm 0.04	58 \pm 3	319 \pm 13/14.4 \pm 0.6*	105 \pm 16	3	W ^{Web}
2023	9.9 \pm 0.6	I	7.8 ^{Ja}	−15.9	0.97 \pm 0.11	13 \pm 27	77 \pm 10/2.9 \pm 0.4	53 \pm 49	3	W ^{S02}
2034	9.7 \pm 1.1	IAB	10.1	−16.7	0.84 \pm 0.10	33 \pm 10	90 \pm 11/4.4 \pm 0.5	39 \pm 46	2	W ^{S02}
2045	2.0 \pm 0.4	Sab	22.7 ^{Mo}	−20.5	0.48 \pm 0.05	61 \pm 3	112 \pm 10/12.4 \pm 1.1	185 \pm 16 ^{PV}	3	W ^{N05}
2053	9.9 \pm 0.4	IB	12.7	−16.3	0.55 \pm 0.08	56 \pm 6	56 \pm 8/3.4 \pm 0.5			W ^{S02}
2082	5.9 \pm 0.5	Sc	10.2	−18.3	0.19 \pm 0.01	79 \pm 1	156 \pm 7/7.7 \pm 0.4	100 \pm 8 ^{PV}	3	W ^{Web}
2080	6.0 \pm 0.3	SABc	13.7	−19.2	0.91 \pm 0.08	24 \pm 11	127 \pm 11/8.5 \pm 0.7	131 \pm 42	1	W ^{Web}
2141	0.4 \pm 1.5	S0-a	12.2 ^{Ja}	−18.1	0.50 \pm 0.03	60 \pm 2	63 \pm 5/3.7 \pm 0.3	157 \pm 20 ^{PV}	3	W ^{N05}
2183	1.0 \pm 0.4	Sa	18.6 ^{Ja}	−19.0	0.73 \pm 0.11	43 \pm 9	56 \pm 11/5.1 \pm 1.0	160 \pm 32	1	W ^{N05}
2193	5.3 \pm 0.6	Sc	9.8 ^{Mo}	−18.7	0.55 \pm 0.04	57 \pm 2	74 \pm 5/3.5 \pm 0.2	174 \pm 423	2	W ^{Web}
2455	9.8 \pm 0.6	IB	7.8 ^{Ka}	−18.6	0.78 \pm 0.06	38 \pm 5	86 \pm 6/3.3 \pm 0.2	21 \pm 12	4	W ^{S02}
2503	2.6 \pm 1.0	SB(r)b	34.4 ^{Ko}	−21.6	0.59 \pm 0.03	54 \pm 2	97 \pm 6/16.2 \pm 1.1	285 \pm 12	1	W ^{Web}
2800	9.9 \pm 0.7	I	20.6 ^{Sw}		0.50 \pm 0.06	60 \pm 4	70 \pm 9/7.0 \pm 0.9	103 \pm 20	2	W ^{Web}
2855	5.1 \pm 0.6	SABc	17.5 ^{Ja}	−21.4	0.41 \pm 0.03	65 \pm 2	106 \pm 7/9.0 \pm 0.6	229 \pm 9	1	W ^{Web}
3013	3.1 \pm 0.5	SB(r)b	36.3	−21.3	0.57 \pm 0.03	55 \pm 2	55 \pm 5/9.6 \pm 0.8	212 \pm 21	1	W ^{Web}
3056	9.6 \pm 1.2	IB	2.5 ^{Oc}	−18.7	0.57 \pm 0.06	55 \pm 4	119 \pm 9/1.4 \pm 0.1			
3273	8.8 \pm 1.2	SAB(r)m	12.2 ^{Sw}	−18.3	0.33 \pm 0.04	71 \pm 3	77 \pm 11/4.6 \pm 0.7	106 \pm 7	3	W ^{Web}
3334	4.2 \pm 1.0	SABb	55.6	−22.8	0.70 \pm 0.07	45 \pm 6	132 \pm 8/35.7 \pm 2.2	377 \pm 85	1	W ^{Web}
3382	1.0 \pm 0.4	SB(r)a	62.8	−20.4	0.94 \pm 0.05	20 \pm 9	38 \pm 4/11.5 \pm 1.1	335 \pm 111	2	W ^{N05}

482 *B. Epinat, P. Amram and M. Marcelin*

Table B3 – continued

N° UGC	t	Type	D (Mpc)	M_b (mag)	b/a	$i_{b/a}$ ($^\circ$)	$D_{25}/2$ (arcsec kpc $^{-1}$)	V_{\max} (km s $^{-1}$)	V_{\max} flag	H I data
(1)	(2)	(3)	(4)	(5)	(6)	(7)	(8)	(9)	(10)	(11)
3384	8.8 ± 0.5	Sm	17.0	-14.6	0.77 ± 0.06	40 ± 5	13 ± 2/1.0 ± 0.2			W ^{Web}
3429	2.3 ± 0.7	SBab pec	17.9 ^{Mo}	-21.3	0.81 ± 0.11	36 ± 11	159 ± 8/13.8 ± 0.7	322 ± 30	1	
3463	4.7 ± 0.9	SABc	38.6	-20.7	0.49 ± 0.03	61 ± 2	66 ± 4/12.4 ± 0.8	168 ± 9	1	
3574	5.9 ± 0.5	Sc	21.8 ^{Ja}	-18.0	0.94 ± 0.05	20 ± 8	44 ± 4/4.7 ± 0.4*	202 ± 96	1	W ^{Web}
3521	4.8 ± 1.8	Sc	62.6	-19.8	0.52 ± 0.03	59 ± 2	35 ± 4/10.7 ± 1.1	166 ± 12	3	
3528	2.0 ± 0.3	SBab	61.8	-20.1	0.58 ± 0.06	55 ± 4	41 ± 5/12.2 ± 1.6	276 ± 66	2	
3618	2.0 ± 0.3	Sab	80.0	-20.9	0.70 ± 0.05	46 ± 4	44 ± 4/16.9 ± 1.4			
3691	6.1 ± 1.0	S(r)c	28.9 ^{Sh}	-20.2	0.50 ± 0.06	60 ± 4	61 ± 8/8.5 ± 1.1	143 ± 10	2	
3685	3.0 ± 0.4	SB(r)b	26.3 ^{Ja}	-19.7	0.61 ± 0.04	52 ± 3	57 ± 4/7.3 ± 0.5	133 ± 177	3	W ^{Web}
3708	4.5 ± 1.7	Sbc pec	70.0	-20.7	0.96 ± 0.11	15 ± 23	25 ± 6/8.3 ± 2.0	234 ± 69	1	
3709	5.7 ± 1.6	Sc	70.7	-21.5	0.71 ± 0.05	45 ± 4	35 ± 3/12.1 ± 1.1	241 ± 14	1	
3734	4.4 ± 0.9	SABb	15.9 ^{Ja}	-18.6	0.90 ± 0.04	25 ± 6	62 ± 5/4.7 ± 0.3*	108 ± 16	1	W ^{Web}
3826	6.5 ± 0.8	SABc	25.7 ^{Ja}	-17.9	0.87 ± 0.07	29 ± 8	98 ± 9/12.2 ± 1.2	74 ± 66	1	W ^{Web}
3809	4.0 ± 0.3	SB(r)bc	32.9	-22.0	0.56 ± 0.05	56 ± 3	150 ± 12/24.0 ± 1.9*	258 ± 9	1	
3740	5.4 ± 0.6	SAB(r)c pec	17.1 ^{Sh}	-19.8	0.78 ± 0.06	39 ± 5	67 ± 5/5.5 ± 0.4	87 ± 20	2	W ^{Web}
3851	9.8 ± 0.6	IB	3.4 ^{Sh}	-17.1	0.33 ± 0.02	71 ± 1	132 ± 8/2.2 ± 0.1*	65 ± 8 ^{PV}	3	W ^{S02}
3876	6.5 ± 0.8	Scd	14.5 ^{Ja}	-17.4	0.50 ± 0.03	60 ± 2	57 ± 4/4.0 ± 0.3	112 ± 10	2	
3915	4.6 ± 1.6	SBc	63.6	-21.4	0.55 ± 0.06	57 ± 4	34 ± 6/10.3 ± 1.7	205 ± 16	1	
IC 476	4.2 ± 2.6	SABb	63.9	-19.0	0.78 ± 0.05	39 ± 5	18 ± 3/5.7 ± 0.8	70 ± 22	3	
4026	2.0 ± 0.4	Sab	64.7	-20.8	0.41 ± 0.03	66 ± 2	43 ± 4/13.5 ± 1.2	284 ± 14	2	
4165	6.9 ± 0.4	SBcd	11.0 ^{Mo}	-18.2	0.94 ± 0.05	20 ± 8	74 ± 5/3.9 ± 0.2	80 ± 18	1	W ^{Web}
4256	5.2 ± 0.6	SABc	71.7	-21.6	0.82 ± 0.04	35 ± 4	50 ± 4/17.3 ± 1.3	123 ± 59	1	W ^{Web}
4273	3.1 ± 0.4	SBb pec	35.4 ^{Ja}	-20.7	0.48 ± 0.05	61 ± 3	65 ± 6/11.2 ± 1.1	219 ± 11	1	W ^{Web}
4274	8.4 ± 1.6	SBd	6.9 ^{Ka}	-17.7	0.53 ± 0.05	58 ± 4	62 ± 8/2.1 ± 0.3	102 ± 57	2	W ^{S02}
4278	6.5 ± 0.8	SBc	9.6	-19.2	0.14 ± 0.01	82 ± 1	87 ± 6/4.0 ± 0.3*	80 ± 8 ^{PV}	2	W ^{S02}
4284	6.0 ± 0.4	SABc	9.8	-18.4	0.52 ± 0.03	59 ± 2	91 ± 6/4.3 ± 0.3*	118 ± 14	3	W ^{Web}
4305	9.8 ± 0.8	I	3.4 ^{Sw}	-16.9	0.70 ± 0.05	45 ± 4	200 ± 12/3.3 ± 0.2*	48 ± 28	2	W ^{S02}
4325	9.0 ± 0.5	SABm	10.9 ^{Mo}	-18.2	0.54 ± 0.03	57 ± 2	89 ± 6/4.7 ± 0.3	85 ± 13	3	W ^{S02}
4393	4.6 ± 1.3	SBc	31.5 ^{Ja}	-19.3	0.66 ± 0.05	49 ± 4	44 ± 7/6.7 ± 1.1	47 ± 10	4	
4422	4.9 ± 0.6	SAB(r)c	58.1	-21.1	0.68 ± 0.04	47 ± 3	51 ± 5/14.4 ± 1.4	353 ± 94	1	
4456	5.2 ± 0.6	S(r)c	74.0	-20.8	0.89 ± 0.04	27 ± 5	31 ± 3/11.0 ± 1.1	211 ± 321	1	
4499	7.9 ± 0.8	SBd	12.2 ^{Ja}	-17.0	0.45 ± 0.03	63 ± 2	57 ± 5/3.4 ± 0.3	62 ± 13	2	W ^{S02}
4543	8.0 ± 0.5	Sd	30.3 ^{Sw}	-17.6	0.77 ± 0.05	40 ± 5	37 ± 4/5.4 ± 0.5	70 ± 15	2	W ^{S02}
4555	4.0 ± 0.6	SABb	58.0	-20.9	0.94 ± 0.07	20 ± 11	45 ± 5/12.7 ± 1.4	185 ± 30	1	
4770	1.1 ± 0.6	SBa	95.9	-21.3	0.83 ± 0.07	34 ± 8	48 ± 5/22.3 ± 2.3	330 ± 194	3	
4820	1.7 ± 0.8	S(r)ab	17.1 ^{Sh}	-20.3	0.79 ± 0.04	38 ± 4	127 ± 6/10.6 ± 0.5	336 ± 20	1	
4936	6.9 ± 0.3	SAB(r)c	25.6 ^{Ko}	-20.6	0.81 ± 0.06	35 ± 6	102 ± 7/12.6 ± 0.8	264 ± 227	2	
5045	5.0 ± 0.5	SAB(r)c	105.1	-21.2	0.76 ± 0.04	40 ± 4	35 ± 3/18.0 ± 1.5	429 ± 228	1	
5175	3.2 ± 0.7	Sb	44.1	-20.6	0.48 ± 0.05	61 ± 3	62 ± 5/13.2 ± 1.1	188 ± 10	1	
5228	4.9 ± 0.5	SBc	24.7	-19.9	0.25 ± 0.02	76 ± 1	68 ± 5/8.2 ± 0.6	125 ± 9	1	
5251	4.3 ± 0.8	SBbc pec	21.5	-20.5	0.22 ± 0.01	77 ± 1	142 ± 7/14.8 ± 0.7	125 ± 9	3	W ^{Web}
5253	2.3 ± 0.9	Sab	21.1	-20.7	0.81 ± 0.05	36 ± 5	108 ± 7/11.1 ± 0.7	235 ± 17	1	W ^{N05}
5272	9.8 ± 0.6	IB	7.1 ^{Ka}	-16.1	0.23 ± 0.02	76 ± 1	48 ± 4/1.7 ± 0.2	45 ± 8 ^{PV}	3	W ^{S02}
5279	9.7 ± 1.1	IB	21.3	-19.0	0.27 ± 0.02	74 ± 1	67 ± 5/6.9 ± 0.5	110 ± 8 ^{PV}	1	
5316	6.5 ± 0.8	SBc	17.6	-19.9	0.38 ± 0.03	68 ± 2	100 ± 7/8.6 ± 0.6	145 ± 9	3	W ^{Web}
5319	5.3 ± 0.6	SB(r)c	35.8	-19.7	0.77 ± 0.05	39 ± 4	47 ± 3/8.2 ± 0.6	180 ± 47	2	
5351	2.1 ± 0.6	SABa	19.3 ^{Sh}	-19.4	0.32 ± 0.04	71 ± 2	62 ± 3/5.8 ± 0.3	135 ± 8 ^{PV}	1	W ^{N05}
5373	9.9 ± 0.3	IB	1.4 ^{Ka}	-14.3	0.62 ± 0.05	52 ± 4	148 ± 10/1.0 ± 0.1	90 ± 162	2	
5398	7.9 ± 3.8	Sd	3.8 ^{Ka}	-17.8	0.81 ± 0.08	36 ± 8	162 ± 13/3.0 ± 0.2			
5414	9.9 ± 0.2	IAB(r)	10.0 ^{Sw}	-16.6	0.68 ± 0.08	47 ± 6	90 ± 10/4.3 ± 0.5	74 ± 10	2	W ^{S02}
IC 2542	4.6 ± 1.3	SBc	83.4	-20.5	0.75 ± 0.04	42 ± 4	31 ± 3/12.4 ± 1.2	290 ± 192	2	
5510	4.6 ± 1.0	SAB(r)c	18.6	-19.3	0.80 ± 0.05	37 ± 5	64 ± 6/5.8 ± 0.5	167 ± 44	1	
5532	3.9 ± 0.6	Sbc	41.1	-22.1	0.85 ± 0.08	32 ± 8	122 ± 10/24.2 ± 1.9	398 ± 24	1	W ^{Web}
5556	5.0 ± 0.8	SBc pec	22.2	-18.9	0.32 ± 0.02	71 ± 1	67 ± 4/7.2 ± 0.4			W ^{Web}
5721	6.6 ± 0.8	SBcd	6.5 ^{Ka}	-16.5	0.50 ± 0.03	60 ± 2	49 ± 4/1.5 ± 0.1	99 ± 29	3	W ^{S02}
5786	4.0 ± 0.1	SAB(r)b	14.2 ^{Sh}	-19.6	0.96 ± 0.11	15 ± 23	54 ± 6/3.7 ± 0.4	80 ± 15	3	W ^{Web}
5789	5.9 ± 0.4	SBc	14.1 ^{Sa}	-19.6	0.49 ± 0.04	61 ± 2	109 ± 7/7.4 ± 0.5*	131 ± 10	3	W ^{Web}
5829	9.7 ± 0.9	IB	9.0 ^{Sw}	-16.2	0.92 ± 0.07	22 ± 11	135 ± 9/5.9 ± 0.4*	48 ± 26	2	W ^{S02}
5840	4.0 ± 0.3	SB(r)bc	6.9 ^{Ka}	-18.9	0.95 ± 0.07	17 ± 13	200 ± 10/6.7 ± 0.3*	251 ± 138	1	W ^{Web}
5842	6.0 ± 0.4	SBc	15.2 ^{Sh}	-18.8	0.83 ± 0.05	34 ± 5	79 ± 5/5.8 ± 0.4	115 ± 18	2	
5931	5.9 ± 0.5	SBc pec	21.2 ^{Sh}	-19.8	0.55 ± 0.05	56 ± 4	52 ± 6/5.3 ± 0.6	157 ± 32	3	

Table B3 – continued

N° UGC (1)	t (2)	Type (3)	D (Mpc) (4)	M_b (mag) (5)	b/a (6)	$i_{b/a}$ ($^\circ$) (7)	$D_{25/2}$ (arcsec kpc $^{-1}$) (8)	V_{\max} (km s $^{-1}$) (9)	V_{\max} flag (10)	H I data (11)
5935	9.4 \pm 1.5	SBm pec	26.4 ^{Sw}	-20.5	0.41 \pm 0.04	66 \pm 2	93 \pm 11/11.9 \pm 1.4		4	W ^{S02}
5982	5.1 \pm 0.7	SBc	20.8 ^{Sh}	-20.0	0.56 \pm 0.05	56 \pm 4	120 \pm 10/12.1 \pm 1.0	199 \pm 13	1	W ^{Web}
6118	2.1 \pm 0.6	SB(r)ab	19.8 ^{Sh}	-20.0	0.90 \pm 0.05	26 \pm 7	74 \pm 5/7.1 \pm 0.4	137 \pm 24	1	W ^{N05}
6277	5.1 \pm 0.5	SABc	16.9	-19.5	0.96 \pm 0.07	17 \pm 15	106 \pm 9/8.7 \pm 0.7	270 \pm 258	2	V ^{K00}
6419	8.9 \pm 0.9	SBm	18.8	-18.6	0.65 \pm 0.04	50 \pm 3	44 \pm 4/4.0 \pm 0.4	53 \pm 11	3	V ^{W04}
6521	3.7 \pm 0.9	S(r)bc	78.6	-21.2	0.67 \pm 0.03	48 \pm 2	50 \pm 3/19.1 \pm 1.2	249 \pm 18	1	
6523	1.4 \pm 1.1	Sa	80.0	-21.0	0.92 \pm 0.04	23 \pm 7	32 \pm 3/12.5 \pm 1.3	118 \pm 63	4	
6537	5.1 \pm 0.5	SB(r)c	14.3 ^{Tu}	-20.5	0.67 \pm 0.05	48 \pm 4	158 \pm 9/11.0 \pm 0.6*	187 \pm 17	1	W ^{Web}
6628	8.8 \pm 1.0	SAB(r)m	15.3 ^{Sw}	-17.9	0.87 \pm 0.07	30 \pm 8	65 \pm 6/4.8 \pm 0.5	183 \pm 168	3	W ^{S02}
6702	1.3 \pm 1.0	Sa	99.8	-20.6	0.86 \pm 0.05	31 \pm 6	24 \pm 3/11.5 \pm 1.5	195 \pm 23	1	
6778	5.1 \pm 0.8	SABc pec	15.5 ^{Sh}	-20.7	0.53 \pm 0.03	58 \pm 2	81 \pm 6/6.1 \pm 0.4	223 \pm 14	2	W ^{Web}
6787	1.7 \pm 0.8	Sab	18.9	-20.5	0.60 \pm 0.03	53 \pm 2	104 \pm 6/9.5 \pm 0.5	232 \pm 10	2	W ^{N05}
7021	1.3 \pm 0.8	SAB(r)a	26.8	-19.7	0.62 \pm 0.04	52 \pm 3	77 \pm 5/10.0 \pm 0.6	223 \pm 18	1	
7045	5.3 \pm 0.6	SABc	11.4 ^{Mo}	-19.2	0.39 \pm 0.03	67 \pm 2	124 \pm 6/6.9 \pm 0.3	160 \pm 9	1	
7154	6.9 \pm 0.4	SBcd	16.2	-20.0	0.46 \pm 0.03	63 \pm 2	139 \pm 9/10.9 \pm 0.7	145 \pm 9	1	W ^{Web}
7278	9.8 \pm 0.5	IB	2.9 ^{Sh}	-17.4	0.78 \pm 0.08	39 \pm 8	204 \pm 12/2.9 \pm 0.2			W ^{S02}
7323	8.0 \pm 0.4	SBd	8.1 ^{Sw}	-18.3	0.70 \pm 0.04	45 \pm 3	114 \pm 7/4.5 \pm 0.3	84 \pm 15	2	W ^{S02}
7429	2.4 \pm 0.7	SB(r)ab	23.7	-19.8	0.40 \pm 0.03	67 \pm 2	73 \pm 5/8.4 \pm 0.6			
7524	8.8 \pm 0.7	SB(r)m	4.6 ^{Ko}	-18.4	0.33 \pm 0.02	71 \pm 1	125 \pm 8/2.8 \pm 0.2*	45 \pm 8 ^{PV}	3	W ^{S02}
7592	9.8 \pm 0.5	IB	2.9 ^{Sh}	-18.3	0.58 \pm 0.04	54 \pm 3	140 \pm 9/2.0 \pm 0.1			W ^{S02}
7699	6.0 \pm 0.6	SBc	9.3	-17.6	0.28 \pm 0.01	74 \pm 1	108 \pm 6/4.9 \pm 0.3	92 \pm 8 ^{PV}	1	
7766	6.0 \pm 0.4	SBc	13.0	-21.0	0.46 \pm 0.05	63 \pm 3	317 \pm 15/20.0 \pm 1.0*	120 \pm 9	1	W ^{Web}
7831	4.9 \pm 0.4	SBc	5.2 ^{Ka}	-18.5	0.39 \pm 0.03	67 \pm 2	177 \pm 8/4.5 \pm 0.2	92 \pm 15	2	W ^{Web}
7853	8.6 \pm 1.1	SBm	8.9 ^{Mo}	-18.9	0.64 \pm 0.05	50 \pm 3	106 \pm 6/4.6 \pm 0.3	110 \pm 35	3	W ^{Web}
7861	8.8 \pm 0.7	SAB(r)m pec	10.2 ^{Mo}	-17.3	0.75 \pm 0.05	41 \pm 4	41 \pm 4/2.0 \pm 0.2	50 \pm 21	3	W ^{Web}
7876	6.5 \pm 0.9	SABc	14.5	-17.9	0.72 \pm 0.05	44 \pm 4	58 \pm 7/4.1 \pm 0.5	98 \pm 14	2	
7901	5.2 \pm 0.6	Sc pec	20.7 ^{Sh}	-20.6	0.66 \pm 0.03	49 \pm 3	115 \pm 6/11.6 \pm 0.6	215 \pm 10	1	
7971	8.7 \pm 0.5	Sm	8.4 ^{Sw}	-16.3	0.92 \pm 0.11	24 \pm 15	66 \pm 8/2.7 \pm 0.3	33 \pm 27	3	W ^{S02}
7985	6.9 \pm 0.5	SBcd	13.7 ^{Mo}	-18.7	0.92 \pm 0.08	23 \pm 11	51 \pm 5/3.4 \pm 0.3	112 \pm 13	1	
8334	4.0 \pm 0.2	Sbc	9.8	-21.1	0.61 \pm 0.06	53 \pm 4	356 \pm 20/16.9 \pm 1.0*	214 \pm 9	1	
8403	5.8 \pm 0.6	SBc	19.1 ^{Ja}	-19.2	0.61 \pm 0.04	52 \pm 3	90 \pm 6/8.3 \pm 0.6	128 \pm 10	1	W ^{Web}
8490	8.9 \pm 0.4	Sm	4.7 ^{Sh}	-17.1	0.64 \pm 0.07	51 \pm 5	135 \pm 8/3.1 \pm 0.2*	90 \pm 29	2	W ^{S02}
NGC 5296	-1.1 \pm 0.8	S0-a	32.8	-18.2	0.58 \pm 0.04	54 \pm 3	28 \pm 3/4.5 \pm 0.5	80 \pm 9	3	W ^{Web}
8709	4.9 \pm 0.8	SABc pec	35.0	-21.4	0.24 \pm 0.02	76 \pm 1	112 \pm 7/19.0 \pm 1.1	207 \pm 9	1	W ^{Web}
8852	2.3 \pm 0.6	SAB(r)a	30.6	-20.0	0.62 \pm 0.08	52 \pm 6	77 \pm 9/11.4 \pm 1.3	186 \pm 10	3	
8863	1.1 \pm 0.4	SBa	25.5 ^{Ko}	-20.3	0.39 \pm 0.03	67 \pm 2	108 \pm 5/13.4 \pm 0.6	191 \pm 13	2	W ^{N05}
8898	3.1 \pm 0.6	SBb pec	49.0	-20.5	0.41 \pm 0.03	66 \pm 2	79 \pm 6/18.7 \pm 1.3	65 \pm 45	4	W ^{Web}
8900	3.2 \pm 0.6	Sb pec	49.2	-21.7	0.47 \pm 0.06	62 \pm 4	75 \pm 8/17.8 \pm 1.8	345 \pm 37	2	W ^{Web}
8937	3.1 \pm 0.4	SBb	49.0 ^{Mo}	-21.1	0.67 \pm 0.06	48 \pm 4	69 \pm 6/16.4 \pm 1.4	320 \pm 105	1	
9013	6.0 \pm 0.3	Sc pec	7.2 ^{Ka}	-18.2	0.66 \pm 0.04	49 \pm 3	72 \pm 5/2.5 \pm 0.2*	62 \pm 45	2	V ^{R94}
9179	6.9 \pm 0.4	SABc	5.7 ^{Ka}	-17.8	0.61 \pm 0.03	52 \pm 2	128 \pm 8/3.5 \pm 0.2	111 \pm 36	3	
9219	9.7 \pm 1.4	IB	10.2 ^{Ja}	-16.6	0.44 \pm 0.03	64 \pm 2	49 \pm 4/2.4 \pm 0.2	45 \pm 8 ^{PV}	2	
9248	3.1 \pm 0.5	Sb	54.9	-20.2	0.57 \pm 0.03	55 \pm 2	40 \pm 4/10.6 \pm 1.0	166 \pm 11	1	
9358	3.3 \pm 0.8	SABb	29.1	-20.8	0.52 \pm 0.03	59 \pm 2	94 \pm 6/13.3 \pm 0.9	221 \pm 14	1	
9366	4.7 \pm 0.9	Sc	37.7 ^{Mo}	-21.7	0.45 \pm 0.03	63 \pm 2	107 \pm 6/19.6 \pm 1.2	241 \pm 9	1	W ^{Web}
9363	6.9 \pm 0.4	S(r)cd	22.3	-19.8	0.84 \pm 0.05	33 \pm 6	57 \pm 5/6.2 \pm 0.5*	143 \pm 105	1	V ^{S96}
9406	6.9 \pm 0.4	SB(r)cd	33.8	-19.0	0.64 \pm 0.08	50 \pm 6	44 \pm 8/7.3 \pm 1.3	19 \pm 10	4	
9465	7.9 \pm 0.9	SABd	26.4 ^{Ja}	-18.0	0.40 \pm 0.03	67 \pm 2	23 \pm 3/3.0 \pm 0.4	97 \pm 9	1	
9576	6.9 \pm 0.4	SABc pec	27.4 ^{Ja}	-19.6	0.63 \pm 0.05	51 \pm 4	51 \pm 4/6.8 \pm 0.6	104 \pm 25	1	V ^{I94}
9649	3.1 \pm 0.7	SBb	7.7 ^{Ja}	-16.5	0.42 \pm 0.03	65 \pm 2	56 \pm 5/2.1 \pm 0.2	94 \pm 11	2	W ^{Web}
9736	5.0 \pm 0.7	SABc	45.4	-20.6	0.65 \pm 0.03	49 \pm 2	71 \pm 4/15.7 \pm 1.0	192 \pm 16	1	
9753	3.5 \pm 0.7	Sbc	12.4 ^{Sh}	-19.1	0.36 \pm 0.04	69 \pm 2	114 \pm 7/6.8 \pm 1.0	138 \pm 9	1	W ^{Web}
9858	4.0 \pm 0.5	SABb	38.2	-20.4	0.20 \pm 0.02	79 \pm 1	118 \pm 12/21.8 \pm 2.3	160 \pm 9	2	W ^{Web}
9866	4.0 \pm 0.3	S(r)bc	7.4 ^{Ja}	-17.2	0.41 \pm 0.03	65 \pm 2	55 \pm 4/2.0 \pm 0.1	114 \pm 11	2	
9943	5.0 \pm 0.6	SB(r)c	28.0	-20.7	0.69 \pm 0.05	46 \pm 4	82 \pm 5/11.1 \pm 0.7	185 \pm 10	1	
9969	3.1 \pm 0.3	SB(r)b	36.0 ^{Sh}	-21.4	0.50 \pm 0.03	60 \pm 2	119 \pm 7/20.8 \pm 1.3	311 \pm 9	1	W ^{Web}
9992	9.8 \pm 0.6	I	10.4	-15.3	0.61 \pm 0.05	52 \pm 4	44 \pm 6/2.2 \pm 0.3			W ^{S02}
10075	6.0 \pm 0.4	Sc	14.7 ^{Ja}	-19.9	0.44 \pm 0.04	64 \pm 3	174 \pm 9/12.4 \pm 0.7	168 \pm 9	1	
10310	9.2 \pm 0.6	SBm	12.7 ^{Sw}	-17.1	0.80 \pm 0.09	37 \pm 9	77 \pm 10/4.7 \pm 0.6	66 \pm 27	3	W ^{S02}
10359	5.6 \pm 0.6	SBc pec	16.0	-19.0	0.85 \pm 0.07	32 \pm 8	63 \pm 5/4.9 \pm 0.4*	143 \pm 30	1	W ^{Web}
10470	4.0 \pm 0.2	SB(r)bc	21.2 ^{Ja}	-20.2	0.73 \pm 0.05	43 \pm 4	67 \pm 5/6.9 \pm 0.5	164 \pm 39	1	W ^{Web}
10445	6.0 \pm 0.9	SB(r)c pec	16.9 ^{Ja}	-17.6	0.71 \pm 0.04	45 \pm 3	57 \pm 4/4.7 \pm 0.3	77 \pm 17	2	W ^{Web}

Table B3 – continued

N° UGC	t	Type	D (Mpc)	M_b (mag)	b/a	$i_{b/a}$ ($^\circ$)	$D_{25/2}$ (arcsec kpc $^{-1}$)	V_{\max} (km s $^{-1}$)	V_{\max} flag	H I data
(1)	(2)	(3)	(4)	(5)	(6)	(7)	(8)	(9)	(10)	(11)
10502	5.3 ± 0.6	Sc	61.2	−21.2	0.78 ± 0.05	39 ± 4	60 ± 5/17.9 ± 1.5	163 ± 14	1	W ^{Web}
10521	4.9 ± 0.7	Sc	18.0 ^{Mo}	−20.2	0.38 ± 0.03	68 ± 2	106 ± 9/9.3 ± 0.7	124 ± 9	1	
10546	6.0 ± 0.5	SABc	20.4 ^{Ja}	−19.1	0.59 ± 0.04	54 ± 3	55 ± 5/5.4 ± 0.4	106 ± 22	1	W ^{Web}
10564	6.5 ± 0.8	SBC	18.4 ^{Ja}	−17.6	0.62 ± 0.05	52 ± 3	37 ± 4/3.3 ± 0.3	75 ± 8	2	W ^{Web}
10652	3.8 ± 2.6	S(r)bc	18.2	−17.7	0.87 ± 0.05	29 ± 6	33 ± 3/2.9 ± 0.3	141 ± 82	2	
10713	3.0 ± 0.4	Sb	18.3	−19.0	0.19 ± 0.02	79 ± 1	54 ± 7/4.8 ± 0.7	105 ± 8 ^{PV}	2	W ^{Web}
10757	6.0 ± 0.4	Sc	19.5	−17.7	0.53 ± 0.04	58 ± 2	36 ± 4/3.4 ± 0.4	81 ± 33	3	W ^{Web}
10769	3.0 ± 0.5	SABb	20.0	−17.0	0.59 ± 0.04	54 ± 3	28 ± 3/2.7 ± 0.3			W ^{Web}
10791	8.8 ± 0.5	SABm	21.7	−16.7	1.00 ± 0.13	0 ± 0	56 ± 9/5.9 ± 0.9	95 ± 48	3	W ^{Web}
10897	5.2 ± 0.5	SABc	20.5 ^{Ja}	−19.5	0.86 ± 0.05	30 ± 6	64 ± 4/6.3 ± 0.4	113 ± 56	2	W ^{Web}
11012	5.9 ± 0.7	Sc	5.3 ^{Ka}	−18.7	0.33 ± 0.03	71 ± 2	185 ± 11/4.7 ± 0.3	117 ± 9	1	
11124	5.9 ± 0.5	SBC	23.7 ^{Ja}	−18.6	0.93 ± 0.10	22 ± 16	67 ± 10/7.7 ± 1.1	96 ± 15	2	W ^{Web}
11218	5.2 ± 0.6	Sc	22.8 ^{Ko}	−20.8	0.48 ± 0.03	61 ± 2	100 ± 5/11.0 ± 0.6	185 ± 9	1	W ^{Web}
11269	2.0 ± 0.5	SABa	35.0 ^{Ja}	−19.9	0.56 ± 0.04	56 ± 3	56 ± 5/9.5 ± 0.8	202 ± 13	1	W ^{N05}
11283	7.8 ± 0.9	SBd	31.3 ^{Sw}	−19.3	0.86 ± 0.05	31 ± 6	40 ± 4/6.1 ± 0.7	173 ± 73	2	W ^{Web}
11283c	5.4 ± 2.2	Sc	31.3 ^{Sw}	−16.5	0.41 ± 0.03	66 ± 2	28 ± 3/4.2 ± 0.5			W ^{Web}
11300	6.4 ± 0.9	SABc	8.4 ^{Ja}	−17.8	0.28 ± 0.01	74 ± 1	99 ± 5/4.0 ± 0.2*	112 ± 9	2	W ^{Web}
11332	7.0 ± 0.5	SBcd	23.0 ^{Ja}	−19.5	0.21 ± 0.01	78 ± 1	63 ± 5/7.1 ± 0.5	91 ± 8 ^{PV}	3	
11407	3.6 ± 0.6	SBbc	35.8	−20.8	0.49 ± 0.03	61 ± 2	75 ± 6/13.0 ± 1.0	158 ± 30	1	V ^{W01}
11429	3.1 ± 0.5	SBb	65.2	−21.8	0.53 ± 0.03	58 ± 2	63 ± 4/19.8 ± 1.3	232 ± 35	2	W ^{Web}
11466	4.8 ± 1.9	Sc	14.2	−18.5	0.59 ± 0.03	54 ± 2	45 ± 4/3.1 ± 0.3	133 ± 10	1	W ^{Web}
11470	2.2 ± 0.6	Sab	50.8	−21.3	0.71 ± 0.07	45 ± 5	72 ± 9/17.8 ± 2.2	380 ± 40	2	
11496	8.8 ± 0.5	Sm	31.9		1.00 ± 0.13	0 ± 0	57 ± 9/8.9 ± 1.3	96 ± 29	2	W ^{Web}
11498	3.1 ± 0.7	SBb	44.9	−20.5	0.32 ± 0.04	71 ± 2	84 ± 9/18.2 ± 1.9	274 ± 9	1	
11557	7.8 ± 0.9	SABd	19.7 ^{Sw}	−18.4	0.90 ± 0.11	26 ± 14	59 ± 8/5.7 ± 0.8	105 ± 72	2	W ^{S02}
11597	5.9 ± 0.3	SABc	5.9 ^{Ka}	−20.6	0.96 ± 0.09	16 ± 18	342 ± 14/9.8 ± 0.4*	154 ± 32	3	
11670	0.5 ± 1.0	S(r)a	12.8	−19.4	0.33 ± 0.03	71 ± 2	125 ± 7/7.7 ± 0.4	190 ± 9	1	W ^{N05}
11707	7.9 ± 1.0	Sd	15.9 ^{Sw}	−16.6	0.57 ± 0.03	55 ± 2	31 ± 3/2.4 ± 0.3	97 ± 5	2	W ^{S02}
11852	1.0 ± 0.5	SBA	80.1	−20.2	0.72 ± 0.05	44 ± 4	28 ± 3/10.8 ± 1.3	221 ± 27	2	W ^{N05}
11861	7.8 ± 0.9	SABd	25.1 ^{Sw}	−20.2	0.48 ± 0.03	61 ± 2	54 ± 4/6.5 ± 0.5	181 ± 39	2	W ^{S02}
11872	2.5 ± 0.5	SAB(r)b	18.1 ^{Ko}	−20.0	0.63 ± 0.07	51 ± 5	85 ± 6/7.4 ± 0.5	183 ± 12	1	
11891	9.9 ± 0.5	I	9.0	−16.4	0.78 ± 0.08	39 ± 8	100 ± 15/4.3 ± 0.6	83 ± 35	3	W ^{Web}
11909	4.5 ± 1.6	Sbc	17.7	−19.3	0.20 ± 0.01	78 ± 1	61 ± 6/5.2 ± 0.5	110 ± 8 ^{PV}	2	W ^{Web}
11914	2.5 ± 0.7	S(r)ab	15.0 ^{Ko}	−20.3	0.86 ± 0.06	31 ± 6	135 ± 7/9.8 ± 0.5	285 ± 26	1	W ^{N05}
11951	1.1 ± 0.8	SBA	17.4	−19.3	0.36 ± 0.04	69 ± 3	51 ± 8/4.3 ± 0.7	106 ± 7	3	W ^{N05}
12060	9.9 ± 0.5	IB	15.7 ^{Sw}	−16.5	0.49 ± 0.03	61 ± 2	33 ± 4/2.5 ± 0.3	107 ± 27	1	W ^{S02}
12082	8.7 ± 0.8	SABm	10.1 ^{Ja}	−16.4	0.90 ± 0.07	26 ± 10	81 ± 9/3.9 ± 0.4	105 ± 137	3	W ^{Web}
12101	6.6 ± 0.9	Scd	15.1 ^{Sh}	−18.5	0.55 ± 0.06	57 ± 4	77 ± 7/5.6 ± 0.5	94 ± 12	3	V ^{W02}
12212	8.7 ± 0.5	Sm	15.5 ^{Sw}		0.51 ± 0.07	59 ± 5	59 ± 10/4.4 ± 0.7	78 ± 15	4	W ^{Web}
12276	1.1 ± 0.5	SB(r)a	77.8	−20.7	0.81 ± 0.06	36 ± 5	34 ± 3/12.8 ± 1.1	94 ± 37	2	W ^{N05}
12276c	5.1 ± 5.0	S?	77.8	−17.4	0.92 ± 0.06	23 ± 9	9 ± 2/3.3 ± 0.7			W ^{N05}
12343	4.4 ± 0.9	SBbc	26.9 ^{Ja}	−21.1	0.75 ± 0.03	42 ± 3	109 ± 5/14.2 ± 0.6	221 ± 14	1	V ^{L98}
12632	8.7 ± 0.5	SABm	8.0	−17.4	0.83 ± 0.11	34 ± 11	127 ± 14/4.9 ± 0.6	69 ± 19	2	W ^{S02}
12754	6.0 ± 0.4	SBC	8.9 ^{Sw}	−18.6	0.65 ± 0.03	49 ± 2	109 ± 6/4.7 ± 0.3*	123 ± 11	1	W ^{Web}

(1) Name of the galaxy in the UGC catalogue (see Table B1). (2) Morphological type from the de Vaucouleurs classification (de Vaucouleurs 1979) in HyperLeda data base. (3) Morphological type from HyperLeda data base. (4) Distance D , deduced from the systemic velocity taken in NED corrected from Virgo infall, assuming $H_0 = 75 \text{ km s}^{-1} \text{ Mpc}^{-1}$, except for those marked (*Ja*: James et al. 2004; *Ka*: Karachentsev et al. 2004; *Ko*: Koopmann, Haynes & Catinella 2006; *Mo*: Moustakas & Kennicutt 2006; *Oc*: O’Connell, Gallagher & Hunter 1994; *Sa*: Saha et al. 2006; *Sh*: Shapley, Fabbiano & Eskridge 2001; *Tu*: Tully et al. 1996). (5) Absolute B magnitude from D and apparent corrected B magnitude (HyperLeda). (6) Axis ratio from HyperLeda. (7) Inclination derived from the axis ratio ($\arccos b/a$). (8) Isophotal radius at the limiting surface brightness of 25 B mag arcsec $^{-2}$, from HyperLeda (Paturel et al. 1991) in arcsec and kpc adopting the distance given in column 4; an asterisk (*) indicates that the galaxy is larger than GHASP field of view. (9) Maximum velocity, V_{\max} , derived from the fit of the velocity field or from the position–velocity diagram (marked with ^{PV}). (10) Quality flag on V_{\max} (1: reached; 2: probably reached; 3 probably not reached; 4: not reached). (11) Aperture synthesis H I data references: W for WHISP data (S02: Swaters et al. 2002; N05: Noordermeer et al. 2005; web: <http://www.astro.rug.nl/whisp/>); V for VLA data (I94: Irwin 1994; R94: Rownd, Dickey & Helou 1994; S96: Schulman et al. 1996; L98: Laine & Gottesman 1998; K00: Komreich et al. 2000; W01: Wilcots, Turnbull & Brinks 2001; W02: Williams, Yun & Verdes-Montenegro 2002; W04: Wilcots & Prescott 2004).

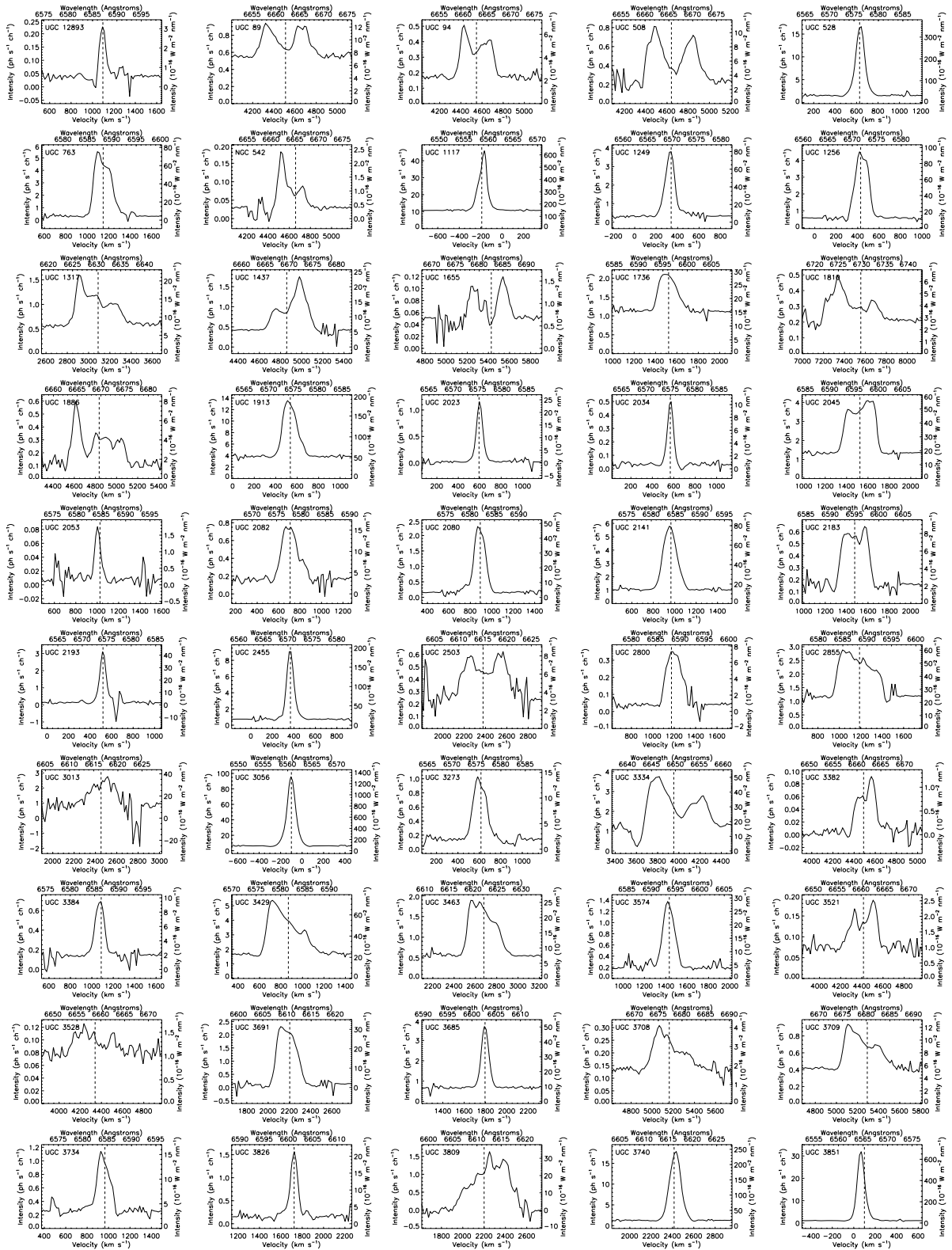
APPENDIX C: H α PROFILES

Figure C1. Integrated H α profiles. The profiles have been displayed over three times the spectral range ($\sim 25 \text{ \AA}$, top label or $\sim 1100 \text{ km s}^{-1}$, bottom label). The instrumental intensity in photoelectron per second and per channel is given on the left-hand side Y-axis. The calibrated intensity is displayed on the right-hand side Y-axis. The dashed vertical line indicates the systemic velocity provided by our kinematical models (see Table B2).

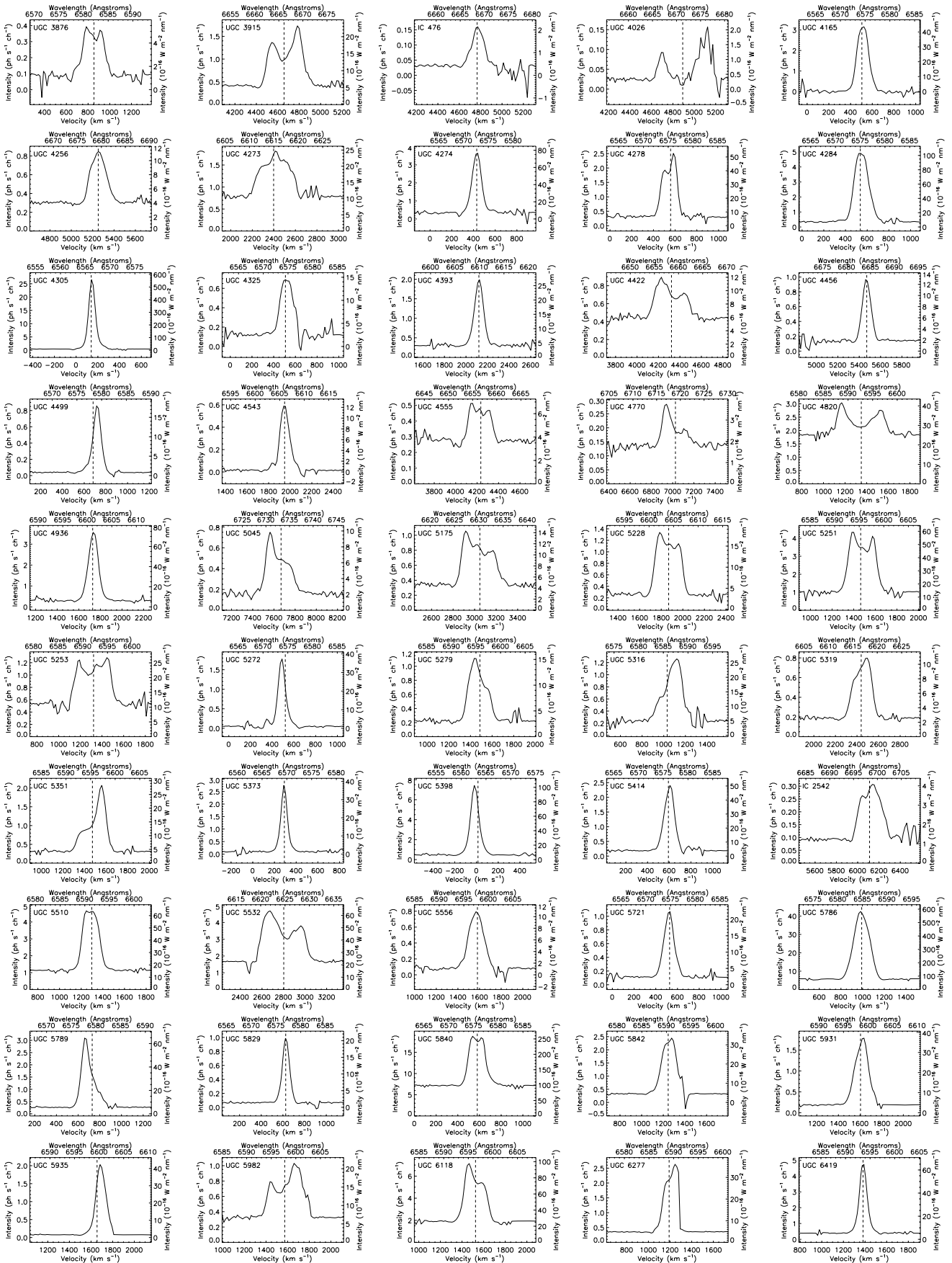
486 *B. Epinat, P. Amram and M. Marcelin*

Figure C1 – continued

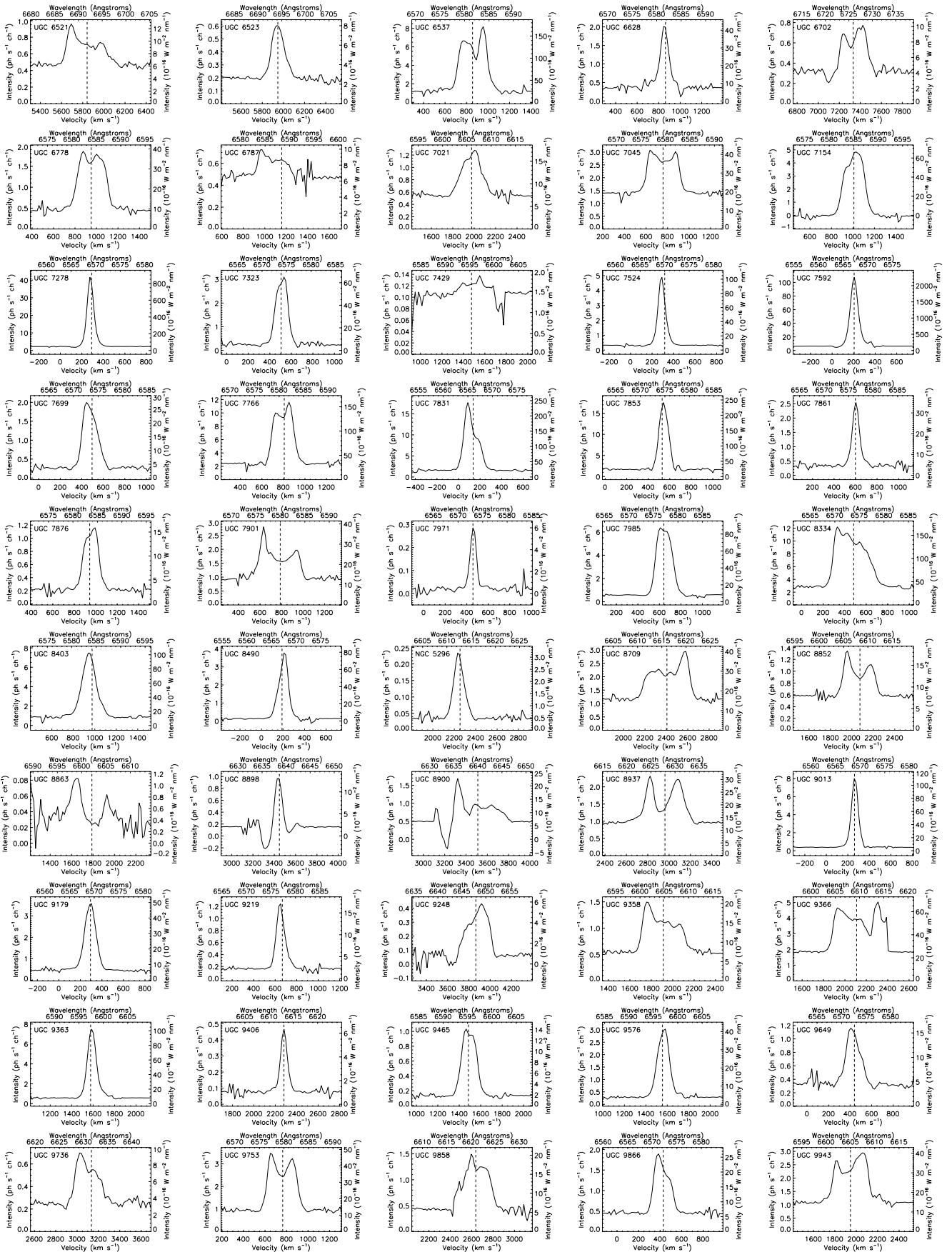


Figure C1 – continued

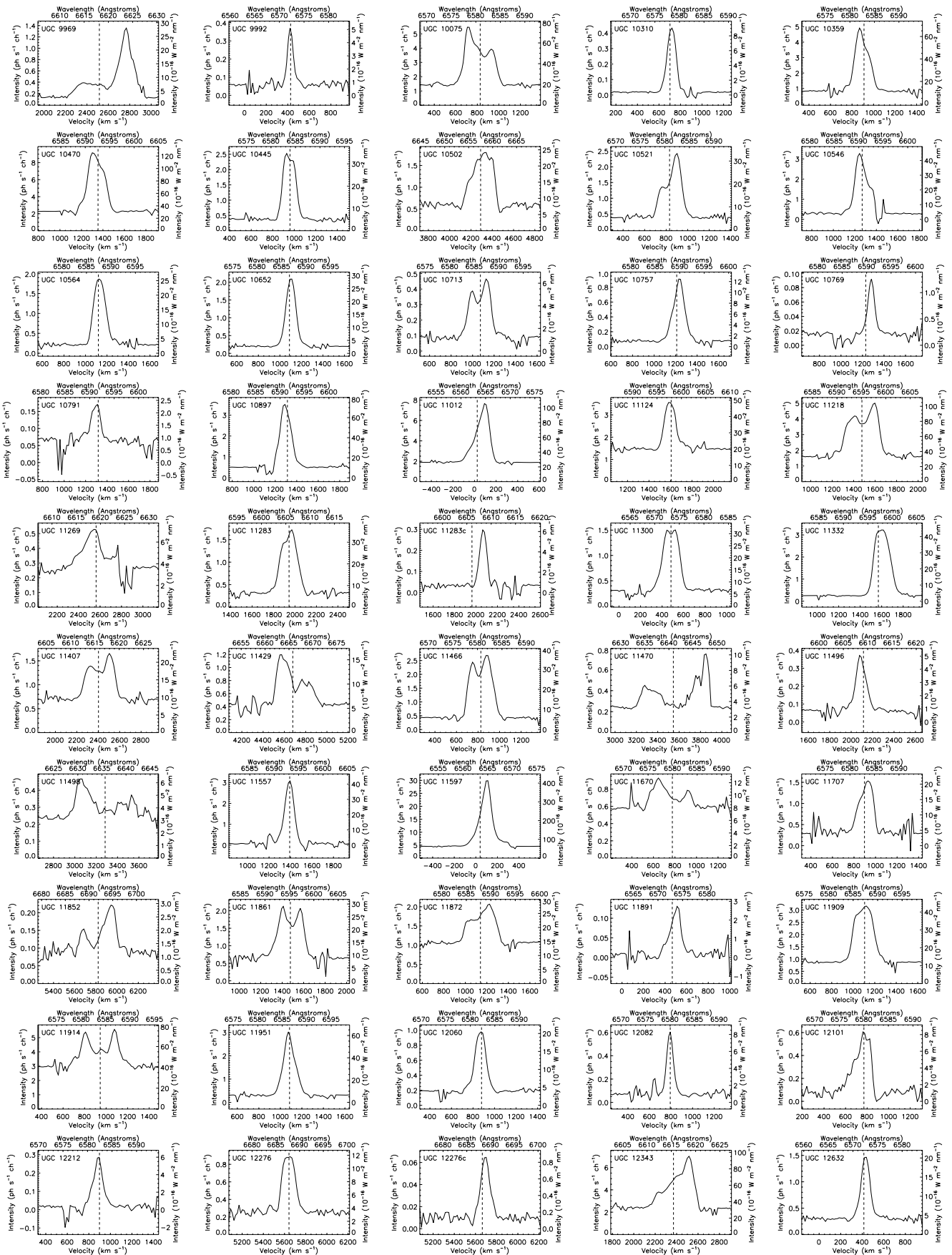
488 *B. Epinat, P. Amram and M. Marcelin*

Figure C1 – continued

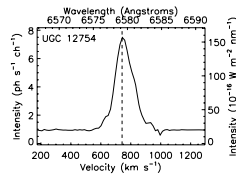


Figure C1 – continued

APPENDIX D: INDIVIDUAL MAPS AND POSITION-VELOCITY DIAGRAMS

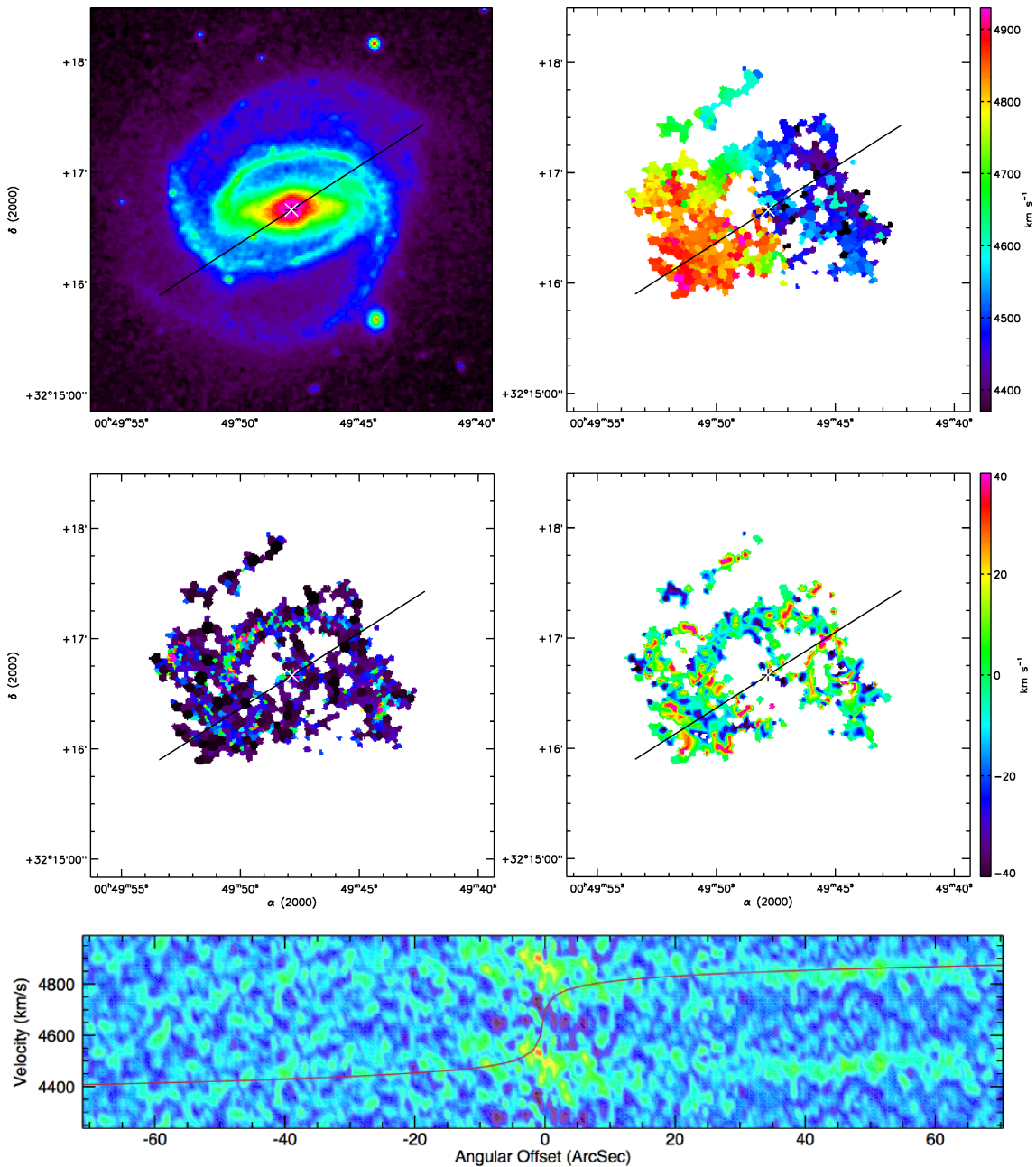


Figure D1. UGC 508. Top left-hand panel: XDSB blue band image. Top right-hand panel: $H\alpha$ velocity field. Middle left-hand panel: $H\alpha$ monochromatic image. Middle right-hand panel: $H\alpha$ residual velocity field. The white and black cross is the kinematical centre. The black line is the major axis, its length represents the D_{25} . Bottom panel: position–velocity diagram along the major axis (full width of 7 pixels), arbitrary flux units. The red line plots the rotation curve computed from the model velocity field along the major axis (full width of 7 pixel).

490 *B. Epinat, P. Amram and M. Marcelin*

APPENDIX E: ROTATION CURVES

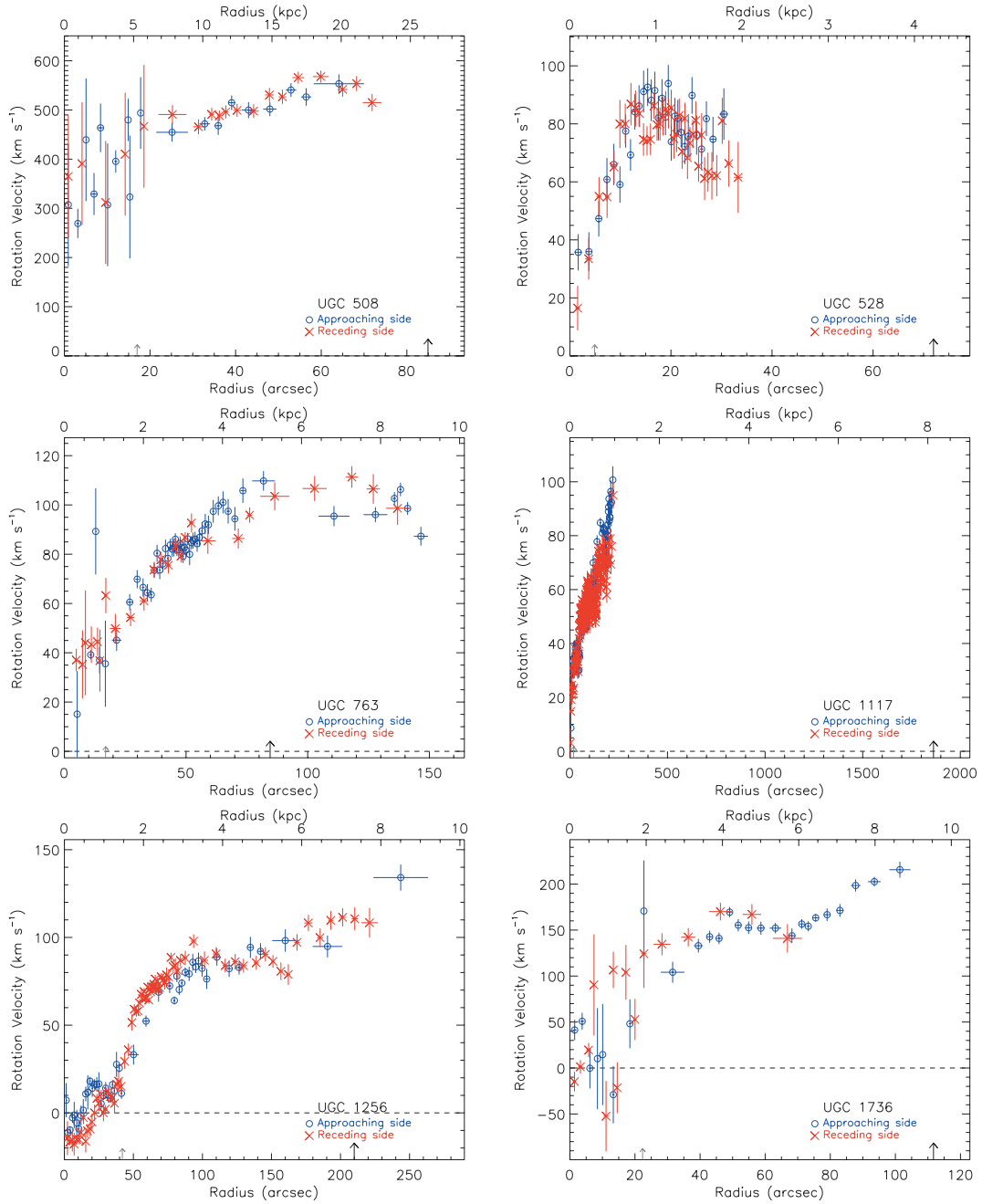


Figure E1. From top left-hand panel to bottom right-hand panel: H α rotation curve of UGC 508, UGC 528, UGC 763, UGC 1117, UGC 1256 and UGC 1736.

2.3 Exploitation des données cinématiques

Les données de l'échantillon GHASP sont désormais réduites de manière homogène et les paramètres de projection cinématiques sont déterminés pour l'ensemble de l'échantillon. L'étude cinématique et dynamique de l'échantillon complet peut désormais être effectuée. Des études ont déjà été réalisées par Garrido et al. (2005); Spano et al. (2008) sur des parties de l'échantillon. Des études similaires en cours sur l'ensemble de l'échantillon sont présentées dans cette partie.

2.3.1 Étude de la forme des halos de matière sombre

J'ai participé à une étude présentée dans l'Annexe E sur les modèles de masse de 36 galaxies de l'échantillon (Spano et al., 2008). Les courbes de rotation des galaxies GHASP sont combinées à des données radio lorsque celles-ci existent dans la littérature. Cela permet d'accroître l'extension des courbes afin de mieux contraindre les modèles. Ces modèles décomposent les courbes de rotation en une composante lumineuse déduite d'observations photométriques, une composante gazeuse déduite des observation du gaz HI et d'un halo de matière sombre. Les données photométriques sont elles-mêmes décomposées en un disque confiné dans un plan et en un bulbe sphérique. Deux types de halos de matière sombre ont été utilisés : un modèle de sphère isotherme et un modèle de Navarro-Frenk-White suggéré par les simulations cosmologiques. Les observations photométriques des galaxies GHASP auxquelles j'ai participé sont actuellement en cours à l'Observatoire de Haute Provence. Les données photométriques ne sont donc pas disponibles pour tout l'échantillon GHASP. C'est pourquoi cette étude a été restreinte à 36 galaxies. Les principaux résultats sur ce sous-échantillon sont (i) que le modèle isotherme ajuste mieux les données que le modèle Navaro-Frenk-White et (ii) que quel que soit le modèle, le rayon de cœur des halos est corrélé à leur densité centrale : les galaxies de faible luminosité ont un petit rayon de cœur et une grande densité centrale alors que les halos de galaxies plus lumineuses ont un rayon de cœur plus grand et une densité centrale plus faible. Il en résulte que la densité de surface des halos est à peu près constante quel que soit le modèle et quelle que soit la magnitude absolue, et donc le type de la galaxie.

Suite à cette étude, j'ai travaillé sur de nouveaux programmes permettant d'ajuster d'autres types de halos de matière sombre. En particulier, j'ai co-encadré deux stages de Master première année (Élodie Giovannoli, Loïc Guennou) afin de tester respectivement un modèle de type Einasto (Merritt et al., 2006) et un modèle avec un potentiel de Yukawa (Piazza et Marinoni, 2003). Ces deux modèles possèdent des paramètres libres additionnels par rapport aux modèles utilisés par Spano et al. (2008) et sont donc moins contraints. Une investigation plus poussée de ces modèles est encore nécessaire.

Des routines permettant l'ajustement d'un modèle de disque exponentiel afin de palier au manque de données photométriques ont été écrites dans le but de réaliser une étude préliminaire des modèles de masse de l'ensemble de l'échantillon GHASP.

2.3.2 Article III : *En préparation* - GHASP IX : Kinematical analysis of the whole sample

J'ai initié des études cinématiques à partir de l'échantillon GHASP complet durant ma thèse. Je présente ces études sous forme d'article en préparation (Epinat et al., 2009b) dont la forme finale sera probablement très différente de la forme actuelle puisque chaque domaine d'investigation sera développé pour donner éventuellement lieu, au final, à plusieurs articles disjoints.

Ce travail est en cours. L'échantillon GHASP complet compte 203 galaxies spirales et irrégulières principalement dans des environnements peu denses et est désormais réduit de manière homogène. L'analyse cinématique de l'ensemble de l'échantillon GHASP est présentée. Nous confirmons les résultats obtenus par Garrido et al. (2005) à partir de la moitié de l'échantillon : (i) le gaz ionisé est présent sur l'ensemble du disque optique ; (ii) l'asymétrie cinématique croît pour les galaxies plus bleues, plus faiblement lumineuses et de type plus tardif ce qui met en évidence que les galaxies en rotation lente ne sont pas capable d'homogénéiser leur distribution de masses ; (iii) en moyenne, la pente interne des courbes de rotation décroît lorsque la luminosité diminue, lorsque le type morphologique devient tardif ou lorsque l'asymétrie cinématique croît ; (iv) la pente externe des courbes de rotation tend à croître lorsque l'on considère des galaxies plus faiblement lumineuses, de type plus tardif ou présentant une plus forte asymétrie cinématique. Ces résultats sont préliminaires en vue d'étudier la possibilité d'ajuster un Courbe de Rotation Universelle (Persic et al., 1996; Catinella et al., 2006; Noordermeer et al., 2007). En plus de ces analyses déjà ébauchées par le passé, une comparaison des profils $H\alpha$ et HI intégrés est menée : l'accord est correct pour plus de 75% de l'échantillon. Par ailleurs, les signatures de barres sur les champs de vitesses sont étudiées à partir de simulations numériques (Hernandez, 2005a) en vue de futures études sur les échantillons GHASP et $BH\alpha$ Bar (échantillon de galaxies barrées). Nous montrons que la présence d'une barre devrait être détectable à partir du champ de vitesses $H\alpha$. Les cartes de dispersion de vitesses sont également présentées ainsi que les profils de dispersion de vitesses qui en ont été déduits (voir l'Annexe D.3 de la thèse). À partir de ces données, nous montrons que la dispersion de vitesses du gaz est assez homogène pour l'échantillon local GHASP et qu'elle est plus faible que la dispersion de vitesses stellaire. Seule une minorité des galaxies présente un pic de dispersion central ou bien d'autres caractéristique marquées. L'effet du seeing ("beam smearing effect") sur les cartes de dispersion de vitesses est également présenté.

In preparation - GHASP IX: Kinematical analysis of the whole sample

Epinat B.¹, Amram, P.¹, Marcelin, M.¹, Balkowski, C.² et al.

¹Laboratoire d'Astrophysique de Marseille, OAMP, Université de Provence & CNRS, 38 rue Frédéric Joliot-Curie, 13388 Marseille Cedex 13 France

²Galaxies Etoiles Physique et Instrumentation, Observatoire de Paris-Meudon, Université Paris VII, 5 Place Jules Janssen, 92195 Meudon, France.

Accepted. Received; in original form

ABSTRACT

This is an ongoing work. The whole GHASP sample contains 203 spiral and irregular galaxies in low density environments and is now reduced using the same methods. The kinematical analysis of the whole GHASP sample is presented. We confirm the results obtained from half the sample (Garrido et al. 2005): (i) the ionized gas is present all over the optical disks; (ii) the kinematical asymmetry increases for bluer, fainter, later-type galaxies showing that slow rotators are not able to homogenize the distribution of mass; (iii) the inner slope of the rotation curves decreases, in average, with decreasing brightness, increasing morphological type or increasing asymmetry and (iv) the outer slope of the rotation curves tends to increase when considering fainter, later-type or asymmetric galaxies. These results are preliminary for studying the possibility to fit an Universal Rotation Curve. Additionally to this previous analysis, we make a comparison of $H\alpha$ and HI integrated profiles: the agreement is rather good for more than 75% of the sample. Moreover, we study bar signatures on $H\alpha$ velocity fields from numerical simulations for further investigations on both GHASP and BH α Bar (barred galaxies sample) samples. We show that the presence of a bar should be detected in $H\alpha$ velocity fields. GHASP velocity dispersion maps are also presented and velocity dispersion profiles have been derived. We show from these data that the gaseous velocity dispersion is homogeneous for the local GHASP sample and lower than stellar velocity dispersion. We show that very few galaxies present a central peak in their velocity dispersion maps or other strong features. The effect of the seeing (beam smearing effect) on the velocity dispersion is also presented.

1 INTRODUCTION

This paper is the ninth of a series presenting and analyzing the observational data obtained in the frame of the GHASP survey (acronym for Gassendi $H\alpha$ survey of SPIrals). This survey consists in mapping the distribution of the ionized hydrogen of field galaxies using a scanning Fabry-Perot interferometer at the 1.93 m telescope of the Observatoire de Haute-Provence. High resolution 2D velocity fields (with a sampling about 5 km s^{-1} in velocity and $3''$ in spatial resolution) in the $H\alpha$ line of hydrogen are derived. The GHASP survey is now achieved and consists of 3D $H\alpha$ data cubes for 203 spiral and irregular galaxies, covering a large range in morphological types and absolute magnitudes, for kinematics analysis. The GHASP sample is by now the largest sample of Fabry-Perot data ever published. In order to provide homogenous data reduction procedure on the whole sample, we have reanalyzed the data using adaptive binning techniques based on Voronoi tessellations (Epinat et al. 2008a, paper VII of the GHASP series). We have derived $H\alpha$ data cubes from which are computed $H\alpha$ maps, radial velocity

fields as well as residual velocity fields, position-velocity diagrams, rotation curves and the kinematical parameters for almost all of the observed galaxies.

Velocity fields enable to deduce rotation curves in a more robust way than slit spectra (which most often assume that both kinematical and photometric axis are confused). GHASP galaxies were first chosen to cover the plane “galaxy mass - galaxy morphological type” for a large range of luminosity ($-15 \leq M_b \leq -22$) and morphological types (from Sa to irregular). Furthermore, they were chosen in low-density environment, excluding cluster, group or pair galaxies.

The search for links between the shape of rotation curves (RCs after) and physical properties of galaxies has been the subject of many studies: Tully & Fisher (1977) have shown that both luminosity and maximal velocity are tightly linked. Rubin et al. (1985) then showed that in fact the maximal rotational velocity is linked both with the luminosity and the morphological type. Persic & Salucci (1991) noted that both the shape of the RCs and luminosity are linked and derived an universal rotation curve (1996) which mainly depends on the luminosity. However, Verheijen (1997) and

2 *B. Epinat et al.*

Sofue et al. (1999) showed that the URC is not able to reproduce systematically the inner and outer parts of their RCs.

The goal of this paper is, first of all, to check if the main kinematical properties based on the study of half the GHASP sample (Garrido et al. 2005, paper IV of the GHASP series) are confirmed for the whole sample. Studying all the links between parameters reflecting the dynamical state of a galaxy will help us to have a better understanding of the evolution of galaxies. More precisely, the first approach is based on the study of the variation of the $H\alpha$ extension over optical radius ratio and the study of the shape of the RCs (in terms of inner, outer slopes and degree of asymmetry of the RCs). However, in that paper we do not differentiate isolated galaxies from softly interacting galaxies as was done in paper IV.

From the whole GHASP sample other topics can be studied. Barred galaxies velocity fields are mainly studied using harmonic decompositions (Krajnović et al. 2006; Fathi et al. 2007) and the Tremaine-Weinberg method (Hernandez et al. 2005c) in order to derive bars pattern speed. Harmonic decompositions are suited for high resolution velocity fields, however, they do not allow to disentangle between bars or arms. Moreover, this method does not seem to be adapted for bar detection at high redshift studies since its use on high- z simulations of SINGS galaxies (Shapiro et al. 2008) is only able to roughly disentangle major mergers from rotating disks. Bar signatures on velocity fields need to be searched in order to permit their detection in high redshift galaxies for which no broad band high resolution imagery is available. The GHASP and BH α Bar (Hernandez et al. 2005b) samples combined together provide enough barred galaxies in order to make a detailed study.

The gaseous velocity dispersion has never been studied in detail in local field galaxies. However, it is actually used in high redshift studies as an indicator of the gravitational support and as an estimator of dynamical mass (Förster Schreiber et al. 2006). Comparisons between gaseous and stellar velocity dispersion are mandatory to understand the links between both components. The velocity dispersion maps derived for the whole GHASP sample are an unique occasion for studying gaseous velocity dispersion properties.

In section 2 we compute the isolation criterion for the GHASP sample. In section 3 we make a comparison between the integrated $H\alpha$ profiles and the HI ones. In section 4, the rotation curve shape is studied. In section 5, we investigate the signature of bars in $H\alpha$ velocity fields. In section 6 the gaseous velocity dispersion is analyzed. In section 7 we give the conclusions.

2 ISOLATION CRITERION

The isolation criterion has been estimated for GHASP galaxies. It is defined from numerical simulations (Athanasoula 1984) as the logarithmic ratio between external and internal forces:

$$f' = \log \frac{F_{\text{external}}}{F_{\text{internal}}} = 3 \log \frac{R}{b} + \log \frac{M_C}{M_G} \quad (1)$$

Where R is the radius of the galaxy, b is the impact parameter (the closest approach pericenter distance between the galaxy and the companion), M_C and M_G are respectively

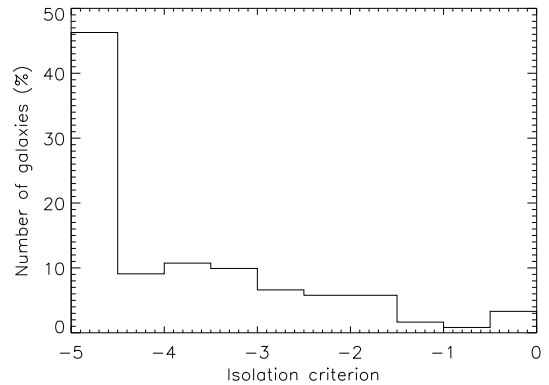


Figure 1. Histogram of the isolation criterion for 121 out of 203 GHASP galaxies for which the systemic velocity is lower than 800 km s^{-1} .

the mass of the companion and of the galaxy. Since masses are not direct estimates and because the physical separation between two objects depends on the accuracy of the distance measurements as well as on the projection effects, in practice, it is estimated according Varela et al. (2004) via equation 2:

$$f = 3 \log \frac{D_{25}/2}{D_p} + 0.4(m_G - m_C) \quad (2)$$

In this equation, $D_{25}/2$ is the angular optical radius, D_p is the projected angular separation, m_C and m_G are the respective apparent magnitudes of the companion and of the galaxy, that gives an idea about the stellar masses of the galaxies.

However, evaluating this criterion is still a tricky task for local galaxies due to the major problem of evaluating their distance. Indeed, it is usual to define the distance from the Hubble law. However, the accuracy of this law is poor since relative motions between close galaxies can be as large as 1000 km s^{-1} that is equivalent in term of distances to more than 13 kpc (considering a Hubble constant of $H_0 = 75 \text{ km s}^{-1} \text{ Mpc}^{-1}$). Since a velocity range of $\pm 700 \text{ km s}^{-1}$ is necessary in order not to miss close neighbors, we decided to exclude galaxies with velocities lower than 800 km s^{-1} that could be interacting with galaxies with negative systemic velocities or even with the Milky Way. An angular radius of 5° around each galaxy has been chosen to search for neighbors using the SIMBAD data base. It corresponds at least to a physical separation of 1 Mpc . Thus it has been possible to estimate the isolation criterion for only 121 galaxies of GHASP sample. Refinements should be developed in order to compute the criterion for the closest galaxies, by using more accurate distance estimates. A full 3D galaxy distribution should be used. Nevertheless, we can probe the isolation criterion for more than half the sample. The histogram is presented in Figure 1. Galaxies with isolation criterion lower than -5 are represented in the first histogram bin.

Galaxies with isolation criterion greater than -2 are the small companions in pair galaxies, the principal galaxy being less affected by the gravitational potential of the companion.

3 INTEGRATED H α PROFILES

An eye inspection has been done in order to compare HI WHISP profiles and our H α profiles. This concerns 120 out of the 201 GHASP galaxies for which an integrated H α spectrum has been computed. A general good agreement is observed. In particular, it has been underlined in the previous papers that the velocity amplitude of the integrated HI profiles is in good agreement with the H α velocity amplitude. This is thus recovered in the H α profiles. Measurements and quantitative comparison will be done. The shape as also been compared and we found that:

- the agreement is very good for 59 galaxies (half the sub sample);
- the agreement is satisfying for 29 galaxies;
- 30 galaxies present a disagreement, mostly because a single profile is observed in H α whereas a double horn profile is observed in HI;
- 2 galaxies have a very low signal to noise ratio.

These comparison show the ability of H α observations to map the velocity fields, and to reach the maximum velocity.

4 ROTATION CURVE ANALYSIS

4.1 Kinematical asymmetries

The asymmetry is mainly computed for morphology studies (Conselice et al. 2000). The morphological asymmetry parameter is computed from 2D images and is defined as:

$$A_{abs} = \frac{\sum |I_0 - I_{180}|}{2 \sum |I_0|} \quad (3)$$

They find a strong correlation of the asymmetry with the morphological types as well as with the color. Garrido et al. (2005) computed the rotation curve asymmetry for half the GHASP sample using the formula defined by Dale & Uson (2003):

$$A_{rc} = \left[\sum \frac{\|V(R) - V(-R)\|}{\sqrt{\sigma^2(R) + \sigma^2(-R)}} \right] / \left[\frac{1}{2} \sum \frac{\|V(R) + V(-R)\|}{\sqrt{\sigma^2(R) + \sigma^2(-R)}} \right] \quad (4)$$

where $\sigma(R)$ is the uncertainty in the data at radial position R . This definition presents the advantage that it takes into account the velocity dispersion (or the uncertainty) of each velocity measurement. With the new method used (Epinat et al. 2008b), the rotation curve is computed independently for each side. In order to have velocity measurements at the same radius, the rotation curve is split within a regular radius grid, and for each radius, a velocity is computed for each side taking into account the measurements of the rotation curves within the ring. The number of bins is taken into account to weight the measurements but also to compute the global uncertainty. However, since the rotation curve averages the variations in the velocity field due to non circular motion but also to an eventual non symmetric potential, we defined a new asymmetry parameter computed from the 2D velocity field. The definition we propose is similar to the morphological asymmetry definition given in equation 3:

$$A_{vf} = \frac{\sum w|V_0 + V_{180}|}{\sum w(|V_0| + |V_{180}|)} \quad (5)$$

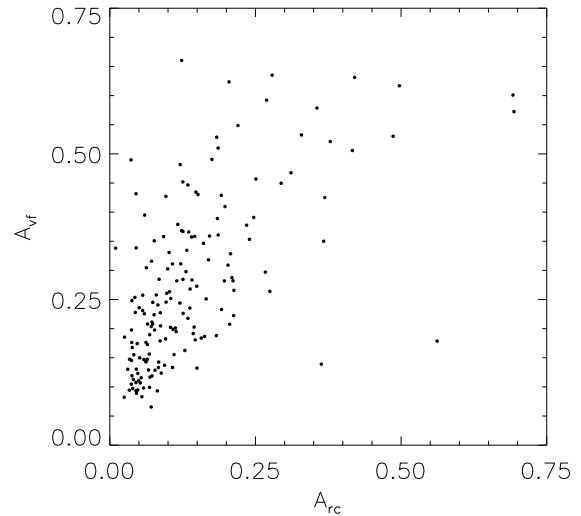


Figure 2. Velocity field asymmetry versus rotation curve asymmetry.

There are two main differences with the morphological definition: (i) a weight is introduced in order to take into account the size of the bins created by adaptive binning techniques, and (ii) the subtraction in equation 3 becomes an addition since the velocity is an odd moment (cosine azimuthal dependency).

This method presents the advantage that it takes into account the whole 2D information. Indeed, some fluctuations may happen along the minor axis as well as along the major axis that is mainly used to compute the rotation curve. It also enables to compute an asymmetry parameter for non rotating objects for which it was not possible to derive a rotation curve. The asymmetry parameters defined according to equation 5 needs some work before it can be computed. First of all, it is necessary to know the kinematical centre. Secondly, the systemic velocity has to be subtracted with accuracy in order to consider only the galaxy motions. When no model fits the data (Epinat et al. 2008b), the kinematical centre is chosen as the morphological centre, and the central velocity is considered to be the systemic velocity found from the literature (cf. Epinat et al. 2008a). Such a definition leads to a maximum asymmetry of one, the minimum asymmetry being zero. In contrast with the morphological method, it is not possible to measure velocities at each position. Thus, only positions for which both sides have measurements are taken into account. For each position, the weight w is inversely proportional to the sum of the bin sizes of each side. The very centre has been excluded since a small misplacement of the center generates artificial asymmetries. The asymmetry is computed until the optical radius.

Velocity field asymmetries and rotation curve asymmetries are compared for the whole GHASP sample in figure 2.

A good correlation exists between these two parameters, strengthening the choice of this new definition for the kinematical asymmetry, compared with that used by Garrido et al. 2005. We may notice however that this parameter should not be used as a bar signature since bars have symmetric

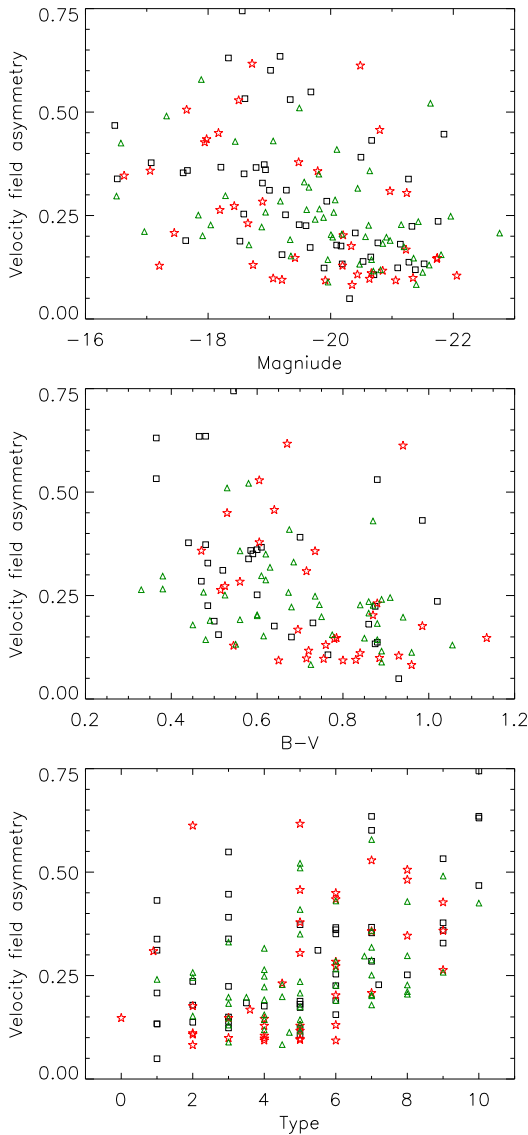
4 *B. Epinat et al.*

Figure 3. Asymmetry as a function of (top) magnitude, (middle) morphological type and (bottom) $B - V$ color. Black squares are barred galaxies (B), green triangles are softly barred galaxies (AB) and red stars are unbarred galaxies (A).

potentials. An axial symmetry should then be computed instead of a central symmetry.

Our asymmetry parameter has been plotted as a function of magnitude, color and morphological type in Figure 3. Correlations are observed, confirming the trends already observed by Garrido et al. 2005: the velocity field asymmetry tends to decrease with increasing brightness, increasing morphological type and decreasing $B - V$.

Kinematical asymmetry parameter will be studied with the radius.

4.2 Rotation curves shape

Figure 4 presents the comparison between the optical radius (defined from RC3 catalog as $D_{25}/2$, de Vaucouleurs et al. 1995) confirms for the whole sample the result previously found by Garrido et al. (2005): our rotation curves/velocity

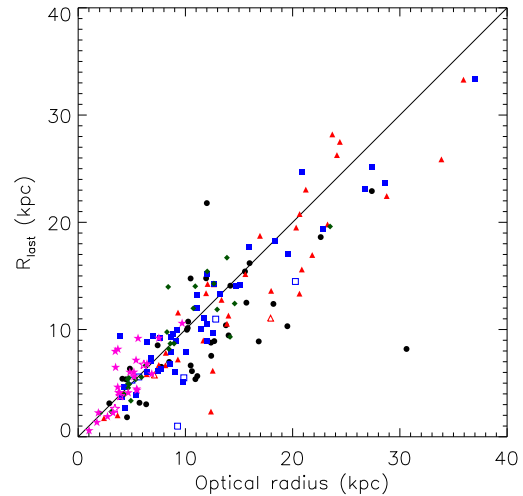


Figure 4. Comparison of the optical radius and the last radius of the rotation curve with a subdivision by Hubble morphological type: black circles $t \leq 2$, red triangles $2 < t \leq 4$, blue squares $4 < t \leq 6$, green rhombuses $6 < t \leq 8$ and pink stars $t > 8$. Open symbols are galaxies that are larger than the GHASP field-of-view. The $y = x$ line is plotted as a reference.

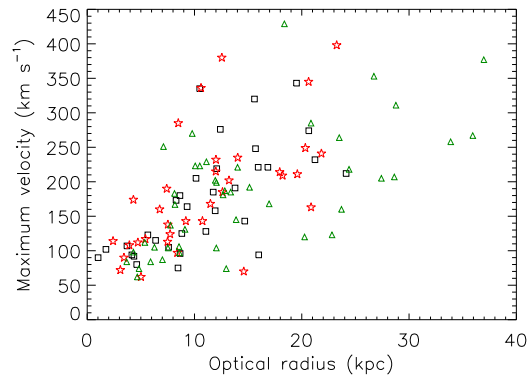


Figure 5. Tully-Fisher like relation with radius. Only galaxies for which the maximum velocity is reached or probably reached are displayed. Star symbols are used for unbarred, triangles for softly barred and squares for barred galaxies.

fields statistically reach the optical radius. This means that ionized gas is present all over the optical disks. Early type galaxies ($t \leq 4$) are those for which, statistically, the $H\alpha$ extent is lower compared to the optical radius.

Figure 5 shows an expected correlation between the maximum velocity and the optical radius. The galaxies for which we are not sure to reach the maximum velocity are not plotted. No clear influence of the presence of a bar can be seen on the observed correlation.

Several approaches can be used in order to study the rotation curves shape. The first approach presented here is a slope approach. Rotation curves are fitted with a five parameters Zhao function (Kravtsov et al. 1998):

$$V(R) = V_t \frac{(R/R_t)^g}{[1 + (R/R_t)^a]^{(g+b)/a}} \quad (6)$$

The advantage of this function is that it can reproduce

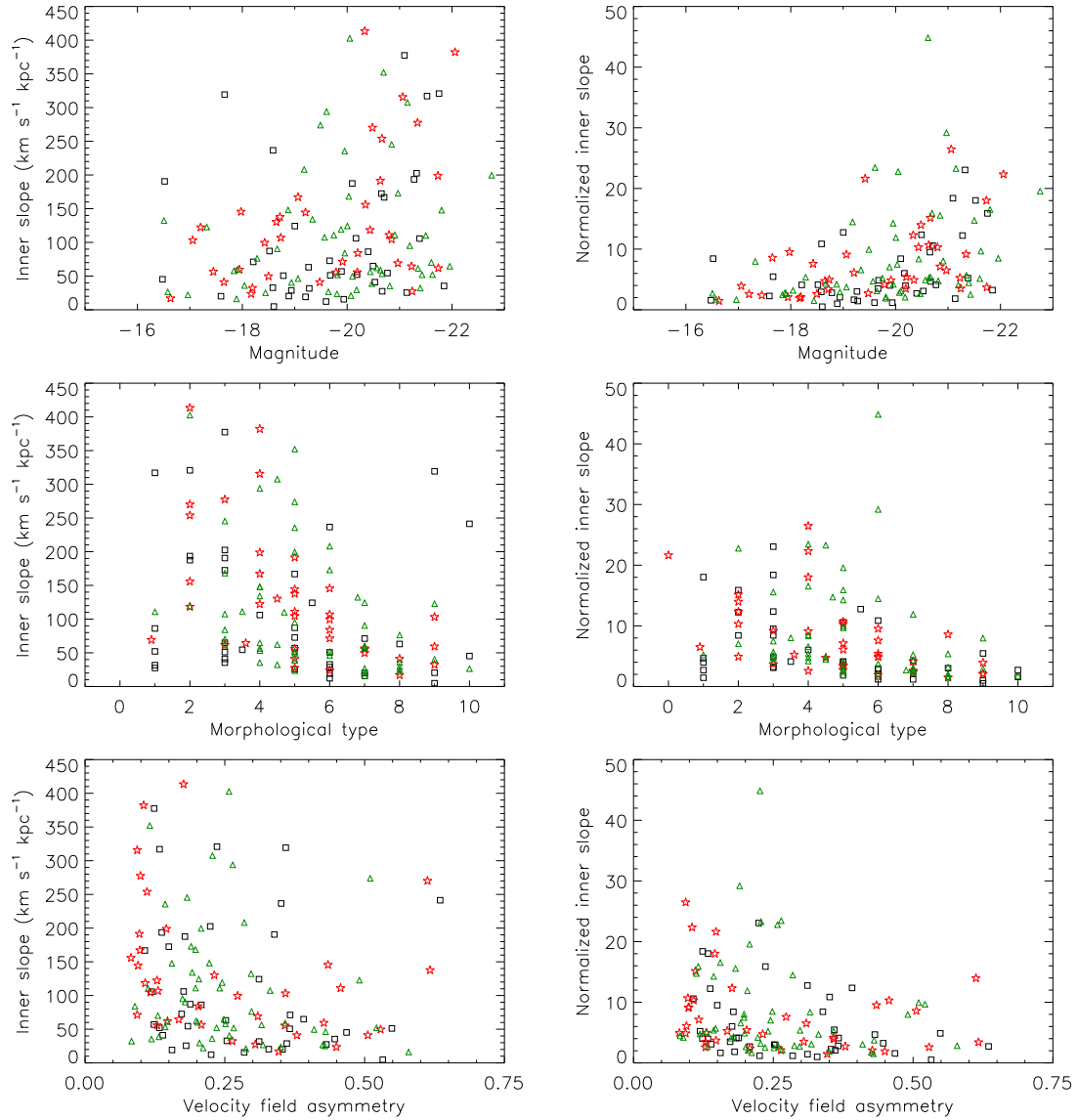


Figure 6. Inner slope as a function of (top) magnitude, (middle) morphological type, and (bottom) velocity field asymmetry. The left column shows non normalized inner slope whereas the right column shows the inner slope normalized with the maximum velocity and the optical radius. Black open squares are for barred galaxies (B), green triangles are for softly barred galaxies (AB) and red stars are for unbarred galaxies (A).

any type of rotation curve. However, since it contains a large number of free parameters, several set of parameters can lead to almost the same rotation curve and it can describe low confidence level rotation curves. We observed that the set of free parameters can be reduced to four by setting $g = 1$. This only imposes the inner shape of the rotation curve ($V \sim V_t \times R/R_t$) to be linear. However, the inner slope is not defined as the ratio V_t/R_t since it happens that the transition radius R_t is small compared to the first points of the rotation curves. Instead, an inner radius R_{in} is defined as the radius of the first rotation curve point when it is larger than both $0.7R_t$ and $3''$. Otherwise, it is equal to the maximum of those two last values. In practice, it is usual that R_t is of the order of the optical radius. To avoid determining an inner slope at such a radius, R_{in} is at most $0.5D_{25}/2$. Thus, the inner

slope is equal to

$$S_{in} = V(R_{in})/R_{in}$$

The error on S_{in} is the difference between the inner slope and the slope for a radius equal to $1.1R_{in}$.

At large radii, equation 6 is equivalent to $V \sim V_t \times (R/R_t)^{-b}$. However, at large radii, the model is not constrained correctly. We thus prefer to define an outer radius R_{out} equal to the last radius of the rotation curve lower than the optical radius. The outer slope S_{out} is then the derivative function at R_{out} :

$$S_{out} = \frac{V_t}{R_t} \frac{1 - b(R_{out}/R_t)^a}{[1 + (R_{out}/R_t)^a]^{1+(1+b)/a}}$$

The error on the outer slope is defined as the difference between the outer slope and the slope of the function at a radius equal to $0.9R_{out}$.

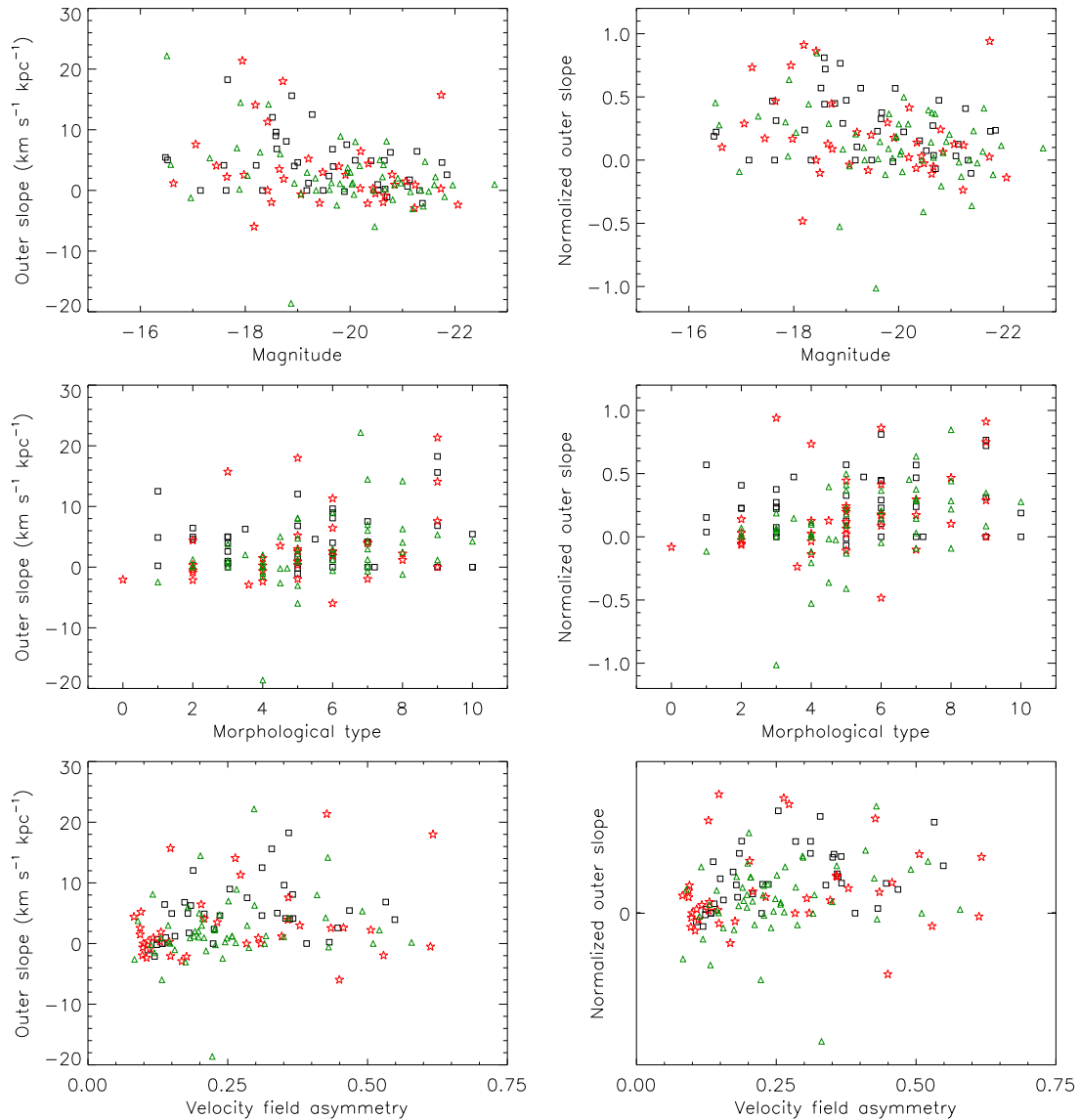
6 *B. Epinat et al.*

Figure 7. Outer slope as a function of (top) magnitude, (middle) morphological type, and (bottom) velocity field asymmetry. The left column shows non normalized inner slope whereas the right column shows the inner slope normalized with the maximum velocity and the optical radius. Black open squares are for barred galaxies (B), green triangles are for softly barred galaxies (AB) and red stars are for unbarred galaxies (A).

In Figure 6, the inner slope is displayed as a function of the B-band magnitude, the morphological numerical type and the asymmetry parameter of the velocity field. Since inclination i uncertainty leads to an uncertain scale factor of the rotation curve (the product $\sin i \times V_{max}$ is constant), the inner slope has been normalized by both the maximum velocity and the optical radius.

A correlation is found between the inner slope and the magnitude. More precisely, one can see that the inner slope varies on a wide range for bright galaxies whereas it exhibits only small values for less luminous galaxies. Since the morphological type is correlated with the magnitude and with the velocity field asymmetry (see Fig. 3 for this last one), it is not surprising that a correlation is also observed between the inner slope and the morphological type as well as between the inner slope and the velocity field asymmetry. All of these

correlations are somewhat better (less dispersed) when considering the normalized inner slope (right plots on Figure 4) but not that different. In any case we confirm the results found from half the sample by Garrido et al. (2005) when plotting the inner slope as a function of the morphological type or as a function of the rotation curve asymmetry: the inner slope of the RCs decreases, in average, for later types as well as for increasing asymmetry.

We find that the inner slope is larger for unbarred galaxies than for barred galaxies. Such a result had been found already by Garrido et al. (2005) from half the GHASP sample. For the whole sample we now find a median inner slope of $65 \text{ km s}^{-1} \text{kpc}^{-1}$ for barred galaxies, $76 \text{ km s}^{-1} \text{kpc}^{-1}$ for softly barred ones and $107 \text{ km s}^{-1} \text{kpc}^{-1}$ for unbarred ones. However, since barred and unbarred galaxies have not exactly the same distribution within morphological types

(in average GHASP barred galaxies are less massive than GHASP unbarred galaxies), this result needs to be confirmed. Furthermore, such a result can be biased by non circular motions due to the bar itself.

As well as for the inner slope, the dependency of the outer slope with magnitude, morphological type and asymmetry has been probed in Figure 7. The correlations are not as tight as with the inner slope. However, one can see that the brightest galaxies statistically exhibit the lowest outer slopes (same thing for earliest types and smallest asymmetric velocity fields).

Here again we confirm the results found from half the sample by Garrido et al. (2005) when plotting the outer slope as a function of the morphological type or as a function of the rotation curve asymmetry: the outer slope tends to increase when considering later-type (hence fainter) or asymmetric isolated galaxies.

The second approach aims at deriving an universal rotation curve depending on the magnitude of the galaxy as suggested by Persic et al. (1996); Catinella et al. (2006); Noordermeer et al. (2007). It is suggested that halo density is directly correlated with galaxy luminosity. This can also be inferred from mass models. The previous approach already gives the trend of the templates to search.

5 VELOCITY FIELD BAR SIGNATURES

Most of spiral galaxies contains central bars. Gas streaming appears in the bar inducing non circular motions around the centre. Specific Fabry-Perot observations have been done in order to study bar kinematics (BH α Bar sample containing 21 barred and softly barred galaxies). In particular, the Tremaine-Weinberg method enabled to compute the pattern speed of bars (Hernandez et al. 2005b). Moreover, a third of the GHASP sample contains barred galaxies (B) and another third contains softly barred galaxies (AB).

In the frame of these samples a study has been initiated in order to search for bar signatures in velocity fields. Such signatures may be detectable on high redshift galaxies for which the bar is not visible in broad band imaging with poor spatial resolution. A method has been developed on N-body+SPH simulations developed by Hernandez (2005a). Continuum images and gas velocity fields are computed with a given inclination from the simulation at given stages of the evolution of the simulation (Figure 8). During its evolution, the bar position changes within the galaxy plane and the strength of the bar increases (Figure 9). Thus, these simulations enable to study the effects of bar strength and position with respect to the major axis on the velocity field.

Bar position and strength is computed on the continuum image from a two dimensions gaussian fit of the bar. The strength of a bar is estimated by:

$$s = 1 - w/l$$

where w/l is the ratio of the width and the length of the bar estimated by the gaussian.

Due to the bar potential, the velocity field is distorted in the inner region as can be observed in Figure 8. In particular, the iso-velocity zero (called kinematical minor axis hereafter) is not perpendicular anymore with respect to the

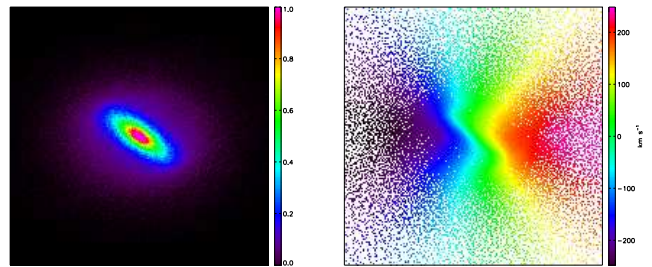


Figure 8. Modeled bar galaxy (Hernandez 2005a) with an inclination of 45° . Left: continuum. Right: gas velocity field. The scale is 0.1 kpc per pixel.

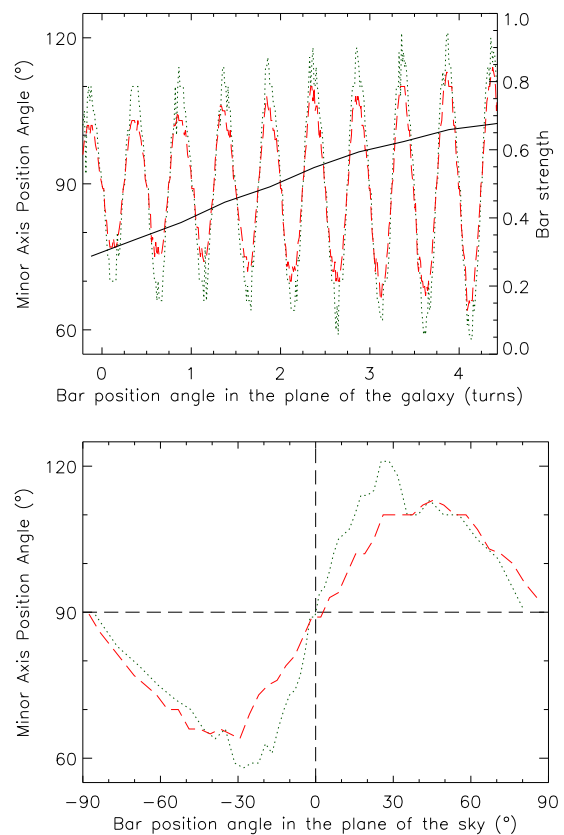


Figure 9. Bar evolution. Top: position angle of the kinematical minor axis as a function of the position angle of the bar in the plane of the galaxy and bar strength. Bottom: position angle of the kinematical minor axis as a function of the position angle of the bar in the plane of the sky for only 180° . Green dotted line: inclination is 60° . Red dashed line: inclination is 30° .

major axis aligned with the X-axis. We suggest that the position angle of the minor axis with respect to the major axis can be used as a bar signature. Using the bar length and width, we create a rectangular mask over which the velocity dispersion of the velocity field is computed. This dispersion is computed for each angle of the mask with a step of one degree. The position angle of the mask for which the dispersion is minimum defines the position angle of kinematical minor axis.

8 *B. Epinat et al.*

In Figure 9, the position angle of the kinematical minor axis is plotted versus bar position with respect to the major axis for the same galaxy projected on the sky using two inclinations of 30° and 60° . The strength of the bar is overplotted. We observe that the kinematical minor axis is perpendicular to the major axis when the bar is parallel or perpendicular to the major axis. The deviation of the minor axis is found to be maximum when the bar is 45° from the major axis in the plane of the disk. Moreover, this deviation increases with the inclination as well as with the strength of the bar. If we consider the position angle of the bar in the plane of the sky, the behavior is less regular in particular for high inclinations. Due to inclination effects, when the bar has a strength lower than 0.3, it is possible that the position angle of the bar is misidentified on the continuum image since it looks round and it is very faint. In such case, the use of the velocity field can help in disentangling the real bar position.

This method will be applied on GHASP and BH α Bar local samples in order to check that the method correctly describes observed galaxies and is not strongly biased by spiral arms, or rings. This method will be generalized to the same samples but projected at high redshift (as presented in Epinat et al. 2009) to test the ability of detecting bars from the kinematics.

6 GASEOUS VELOCITY DISPERSION

Only velocity fields and flux maps of GHASP galaxies have been published in previous papers (Epinat et al. 2008b,a) since the velocity dispersion maps were not used to recover the projection parameters. However, these dispersion maps have been computed during the reduction procedure using the barycenter method. The velocity dispersions have been corrected from instrumental point spread function (PSF) using the relation:

$$\sigma = \sigma_{obs}^2 - \sigma_{PSF}^2$$

The PSF is estimated from the wavelength calibration cube.

The velocity dispersion profiles have been derived from the velocity dispersion maps using a similar method as for the rotation curves in Epinat et al. (2008b): the velocity dispersion map containing one unique point per bin is decomposed into rings using the same projection parameters (inclination and position angle) and the same transition radius as for the rotation curves. The transition radius defines an inner and an outer regions. In the inner regions, the ring width is half the seeing whereas in the outer region, the number of bins per ring is 50. This number of bin has been chosen larger than for rotation curves since the velocity dispersion is more sensitive to the signal to noise ratio (second order moment) than the velocity (first order moment). No exclusion sector is defined and no distinction is made between receding and approaching sides since the velocity dispersion is an odd moment (Begeman 1987; Krajnović et al. 2006). The velocity dispersion maps and profiles are displayed in Appendix B. Identical velocity dispersion maps cuts have been chosen for the whole sample (from 0 to 60 km s^{-1}) in order to facilitate the comparison.

We observe that gas velocity dispersion is usually low ($24 \pm 5 \text{ km s}^{-1}$) compared to stellar velocity dispersions

($> 50 \text{ km s}^{-1}$ Shapiro et al. 2003). Moreover the profiles are rather flat. However in $\sim 15\%$ galaxies, we observe that velocity dispersion is peaked in the centre. In several case, the central peak can be partly explained by beam smearing effects. UGC 5786 is the galaxy that presents the strongest central feature in its velocity dispersion maps. It displays an “S” shape. For this galaxy, the velocity shear component of the velocity map has been estimated from the velocity field, the flux map and from the seeing (Figure 10). The central “S” shape is recovered satisfactorily using the methods exposed in Epinat et al. (2009). The velocity shear using this method is underestimated since we do not know the actual velocity field nor the flux distribution map without the effect of the seeing. Thus to compute such a dispersion map we assumed the observed velocity field and monochromatic map as being the high resolution ones. However, the overall velocity dispersion decrease cannot be explained by beam smearing effects. This method should be used to disentangle seeing effects from actual velocity dispersion features on the GHASP sample. However, when no dispersion feature is observed, this should mean that the spatial resolution is good enough to trace the velocity gradient.

In several cases of galaxies showing no rotation, but large star formation (UGC 3056, UGC 5398, UGC 7278) a central peak is observed and thus cannot be explained by beam smearing effects.

Interestingly, some galaxies present a pattern in the velocity dispersion maps. For instance, UGC 7985 clearly exhibits a feature along the minor axis that could be explained by projection effects and non isotropic velocity dispersions. Using a decomposition as in Shapiro et al. (2003) could give an idea of the physical processes. In particular that would mean that the radial velocity dispersion is larger than the rotational velocity dispersion. Appendix A gives the details on the assumptions for such a decomposition. In some other cases (e.g. UGC 7853), the velocity dispersion is larger on one side. This suggests that the gas is warmer on one side or that gas accretion is occurring on that side. In UGC 10470, the velocity dispersion is larger in the spiral arms.

7 CONCLUSIONS

Most of the preliminary results found by Garrido et al. (2005) when analyzing half of the GHASP sample of galaxies are confirmed in this study based on the whole sample of 203 galaxies.

About the extension of the RCs, we find that our H α rotation curves/velocity fields statistically reach the optical radius. This means that ionized gas is present all over the optical disks.

About the shape of the RCs, we find that the asymmetry of the velocity fields increases when we consider bluer, fainter, later-type galaxies showing that slow rotators are not able to homogenize the distribution of mass. The inner slope of the RCs decreases, in average, with decreasing brightness, increasing morphological type or increasing asymmetry. We find that the inner slope is larger (almost double) for unbarred galaxies than for barred galaxies. This result must be taken with care however, since the barred galaxies are not uniformly distributed among the different morphological types of our sample and, furthermore, the in-

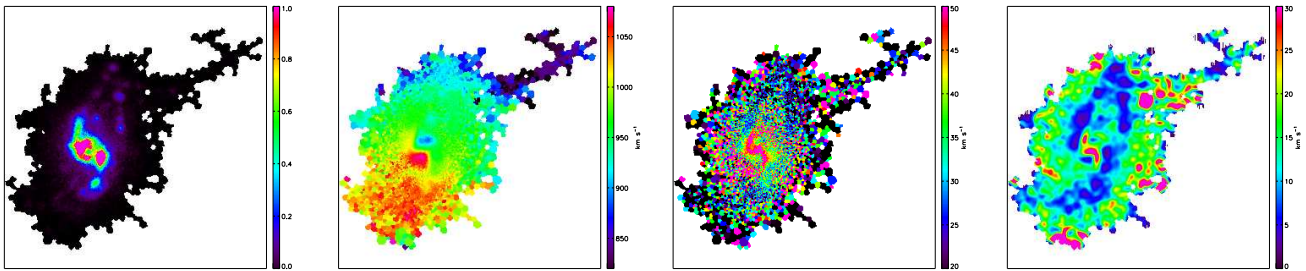
In preparation - *GHASP IX: Kinematical analysis of the whole sample* 9

Figure 10. From left to right: UGC 5786 monochromatic map, velocity field, velocity dispersion and velocity dispersion modeled from the velocity field and the seeing.

ner slope is likely to be biased by non circular motions due to the bar itself. The outer slope of the RCs tends to increase when considering fainter, later-type or asymmetric galaxies. No significant difference can be seen between the outer slope of barred and unbarred galaxies. More generally, the presence of a bar does not seem to affect the outer velocity slope, neither the degree of asymmetry of the distribution of matter, nor the maximal velocity determination. The only difference we find is that barred galaxies seem to exhibit a smaller range of variation of the inner slope of the RCs.

H α integrated profiles are compared to HI ones. They show a rather good agreement that confirms the ability of H α data to derive the maximum rotation velocity.

The influence of bars on the gas kinematics has been studied from numerical models. These models suggest that a signature should be detected on H α velocity fields. It depends on the inclination of the disk and on the orientation of the bar with respect to the major axis. This signature consists in a rotation of the kinematical minor axis and is more likely observed for inclined disks when the bar is neither aligned nor perpendicular to the major axis.

Gaseous velocity dispersion maps are also presented and velocity dispersion profiles have been derived. They show that local galaxies gaseous velocity dispersion is homogeneous for the GHASP sample and lower ($\sim 25 \text{ km s}^{-1}$) than the stellar one. Moreover the dispersion maps are mostly featureless. However, it has been shown that the dispersion maps are sensitive to the spatial resolution.

This work is on going, and the studies presented in this paper will be more deeply investigated.

REFERENCES

- Athanassoula E., 1984, *Phys. Rep.*, 114, 319
- Begeman K. G., 1987, PhD thesis, Kapteyn Institute, (1987)
- Catinella B., Giovanelli R., Haynes M. P., 2006, *ApJ*, 640, 751
- Conselice C. J., Bershady M. A., Jangren A., 2000, *ApJ*, 529, 886
- Dale D. A., Uson J. M., 2003, *AJ*, 126, 675
- de Vaucouleurs G., de Vaucouleurs A., Corwin H. G., Buta R. J., Paturel G., Fouque P., 1995, *VizieR Online Data Catalog*, 7155, 0
- Epinat B., Amram P., Balkowski C., Marcelin M., 2009, in preparation
- Epinat B., Amram P., Marcelin M., 2008a, *MNRAS*, 390, 466
- Epinat B., Amram P., Marcelin M., Balkowski C., Daigle O., Hernandez O., Chemin L., Carignan C., Gach J.-L., Balard P., 2008b, *MNRAS*, 388, 500
- Fathi K., Ven G. V. D., Peletier R., Emsellem E., Falcón-Barroso J., Cappellari M., Zeeuw T. D., 2007, *Two-Dimensional Kinematics of a Bar and Central Disk in NGC5448. Island Universes - Structure and Evolution of Disk Galaxies*, p. 125
- Förster Schreiber et al. N. M., 2006, *ApJ*, 645, 1062
- Garrido O., Marcelin M., Amram P., Balkowski C., Gach J. L., Boulesteix J., 2005, *MNRAS*, 362, 127
- Hernandez O., 2005a, PhD thesis, Université de Montréal (Canada)
- Hernandez O., Carignan C., Amram P., Chemin L., Daigle O., 2005b, *MNRAS*, 360, 1201
- Hernandez O., Wozniak H., Carignan C., Amram P., Chemin L., Daigle O., 2005c, *ApJ*, 632, 253
- Krajnović D., Cappellari M., de Zeeuw P. T., Copin Y., 2006, *MNRAS*, 366, 787
- Kravtsov A. V., Klypin A. A., Bullock J. S., Primack J. R., 1998, *ApJ*, 502, 48
- Noordermeer E., van der Hulst J. M., Sancisi R., Swaters R. S., van Albada T. S., 2007, *MNRAS*, 376, 1513
- Persic M., Salucci P., 1991, *ApJ*, 368, 60
- Persic M., Salucci P., Stel F., 1996, *MNRAS*, 281, 27
- Rubin V. C., Burstein D., Ford Jr. W. K., Thonnard N., 1985, *ApJ*, 289, 81
- Shapiro K. L., Gerssen J., van der Marel R. P., 2003, *AJ*, 126, 2707
- Shapiro et al. K. L., 2008, *ApJ*, 682, 231
- Sofue Y., Tutui Y., Honma M., Tomita A., Takamiya T., Koda J., Takeda Y., 1999, *ApJ*, 523, 136
- Tully R. B., Fisher J. R., 1977, *A&A*, 54, 661
- Varela J., Moles M., Márquez I., Galletta G., Masegosa J., Bettoni D., 2004, *A&A*, 420, 873
- Verheijen M. A. W., 1997, PhD thesis, PhD thesis, Univ. Groningen, The Netherlands, (1997)

10 *B. Epinat et al.*

APPENDIX A: VELOCITY DISPERSION PROJECTION

We can generally defined the velocity dispersion by the relation:

$$\sigma_{ab}^2 = \overline{V_a V_b} - \overline{V_a} \overline{V_b} \quad (\text{A1})$$

We make the hypothesis that the ionized gas emission happens in the galactic plane. Thus we express the line of sight velocity (Epinat et al. 2008b) of a single particle:

$$V_{los} = V_{sys} + V_\theta \cos \theta \sin i + V_r \sin \theta \sin i + V_z \cos i \quad (\text{A2})$$

where θ is the azimuthal angle in the galactic plane.

Thus, we wish at expressing $\overline{V_{los}^2}$ and $\overline{V_{los}}^2$ to compute σ_{los}^2 .

As V_{sys} is constant, we deduce that:

$$\begin{aligned} \sigma_{los}^2 &= (\sigma_\theta^2 \cos^2 \theta + \sigma_r^2 \sin^2 \theta) \sin^2 i + \sigma_z^2 \cos^2 i \\ &+ 2(\sigma_{r\theta}^2 \cos \theta \sin \theta \sin^2 i + \sigma_{\theta z}^2 \sin \theta \cos i \sin i + \sigma_{rz}^2 \sin \theta \cos i \sin i) \end{aligned} \quad (\text{A3})$$

These expressions are only valid for motions observed in the galactic plane. They are not valid anymore for bulges (in particular if we observe the stellar component).

There are a lot of parameters. We need to make hypothesis in order to simplify this expression. By assuming a disk transparent and a symmetry with respect to the galactic plan, we can approximate that $\overline{V_z} = 0$. The assumption that rotation motions are preponderant used to compute rotation curves implies $\overline{V_r} = 0$.

However, the problem is more difficult for the velocity dispersion. When the stellar population is distributed symmetrically, $\sigma_{r\theta}$ and σ_{rz} are equal to zero (Shapiro et al. 2003). Thus it remains only three parameters that can vary with the radius. The epicycle approximation enables to link two of them:

$$\frac{\sigma_\theta^2}{\sigma_r^2} = \frac{1}{2} \left(1 + \frac{\partial \ln V_\theta}{\partial \ln R} \right) \quad (\text{A4})$$

R being the radius in the pane of the galaxy.

$$\sigma_{los}^2 = (\sigma_\theta^2 \cos^2 \theta + \sigma_r^2 \sin^2 \theta) \sin^2 i + \sigma_z^2 \cos^2 i \quad (\text{A5})$$

The vertical velocity dispersion does not depend on the azimuthal angle. For a flat rotation curve, according to equation A4, $\sigma_r^2 = 2\sigma_\theta^2$. For a solid body rotation curve $\sigma_r^2 = \sigma_\theta^2$

APPENDIX B: VELOCITY DISPERSION MAPS AND RADIAL PROFILES OF GHASP GALAXIES

Chapitre 3

Cinématique des galaxies à grand décalage spectral

Résumé

3.1	Problématique des galaxies à grand décalage spectral	119
3.2	Nouvelles observations de galaxies à décalage spectral supérieur à un avec SINFONI	122
3.3	Observations cinématiques de galaxies à un décalage spectral voisin de 0.6 avec FLAMES/GIRAFFE	129
3.4	Article IV : Evidence for strong dynamical evolution in disk galaxies through the last 11 Gyr. GHASP VIII : A local reference sample of rotating disk galaxies for high redshift studies	129

Ce chapitre expose les objectifs de l'étude de la cinématique résolue des galaxies à grand décalage spectral. De nouvelles données cinématiques obtenues par SINFONI sur le VLT sont présentées et interprétées. Enfin, un article présente l'utilisation de l'échantillon cinématique de galaxies proches GHASP afin de simuler des galaxies observées à grand décalage spectral. Les biais d'observations sont ainsi mis en évidence et la comparaison des propriétés dynamiques des galaxies locales et des galaxies à grand décalage spectral est faite en s'appuyant sur les observations de galaxies à grand décalage spectral de la littérature. Cet article est un des points clés de cette thèse.

3.1 Problématique des galaxies à grand décalage spectral

3.1.1 Cosmologie moderne

Le développement de la cosmologie moderne a été rendu possible grâce à des avancées théoriques, avec le développement de la théorie de la relativité générale par Einstein en 1915, et observationnelles, lorsque Edwin Hubble mit fin en 1924 au débat quant à la nature extragalactique des nébuleuses spirales grâce à l'observation d'étoiles variables dans la galaxie NGC 6822.

À partir des équations de la relativité générale, le cadre théorique prend forme. Le principe cosmologique énoncé par Einstein repose sur le principe Copernicien (l'homme n'a pas une position privilégiée et l'Univers doit donc être partout le même) et stipule que l'Univers est uniforme et isotrope

et que le temps est universel. Cela permet de définir des métriques et ainsi, à partir des équations d'Einstein, d'établir des relations théoriques entre la courbure de l'Univers et son contenu en matière-énergie. La seule métrique générale à respecter le principe cosmologique est la métrique dite de Friedmann-Robertson-Walker :

$$ds^2 = c^2 dt^2 - R(t)^2 \left[\frac{dr^2}{1 - kr^2} + r^2(d\theta^2 + \sin^2\theta d\phi^2) \right]$$

Les distances sont décomposées en un produit entre un facteur d'échelle $R(t)$ dépendant du temps et une coordonnée comobile indépendante du temps. La géométrie de l'Univers dépend de la valeur du paramètre k .

La découverte de Hubble, quant à elle, est la première d'une série de découvertes observationnelles. Elle permet à Hubble de montrer que l'Univers est en expansion et d'estimer celle-ci par la constante de Hubble, alors estimée à $H_0 = 540 \text{ km s}^{-1} \text{ Mpc}^{-1}$. Cette découverte est explicable dans le cadre de la cosmologie, le paramètre de Hubble est alors égal à :

$$H(t) \equiv \frac{\dot{R}(t)}{R(t)}$$

La constante de Hubble est la valeur actuelle de la vitesse d'expansion de l'Univers (à $t = 0$). Dès lors les observations de galaxies distantes se sont multipliées afin de déterminer les paramètres cosmologiques avec la précision la meilleure possible. Ces paramètres cosmologiques ont été introduits par les divers modèles d'Univers. Ils consistent en :

- le facteur de décélération $q_0 = -\frac{\ddot{R}}{\dot{R}^2}(t = 0) = -\frac{\dot{R}(t=0)}{H_0^2}$
- le paramètre de densité Ω_m , défini comme le rapport de la densité de matière-énergie actuelle de l'Univers ρ_0 sur la densité critique $\rho_c = 3H_0^2/8\pi G$, G étant la constante universelle de gravitation
- la constante cosmologique Λ qui intervient dans le calcul du paramètre de densité du vide $\Omega_\Lambda = \Lambda/3H_0^2$.

Pour un Univers plat, on a $\Omega_m + \Omega_\Lambda = 1$. Actuellement, la détermination des paramètres cosmologiques à partir des observations de WMAP donne $H_0 = 72 \pm 5 \text{ km s}^{-1} \text{ Mpc}^{-1}$ et $\Omega_m = 0.27 \pm 0.04$. De plus, les modèles privilégiés actuellement sont des modèles d'Univers plat. Ces valeurs ont été utilisées pour les études présentées dans cette thèse. Elles permettent de dater les galaxies observées à un certain décalage spectral en calculant le temps de parcours des photons dans le modèle cosmologique adopté. La Figure 3.1 présente la relation entre le décalage spectral et l'âge des galaxies pour trois cosmologies différentes. On parle de grand décalage spectral à partir de 1 et de décalage spectral intermédiaire entre 0.1 et 1.

3.1.2 Histoire de l'Univers

D'après ces modèles cosmologiques d'évolution de l'Univers, celui-ci est né il y a 13.7 ± 0.13 milliards d'années à partir d'une singularité lors du Big Bang. Après le Big Bang, l'Univers s'est refroidi et neutrons et protons se sont combinés pour former de l'hydrogène neutre. Plus tard, les premières étoiles se sont formées par effondrement des nuages d'hydrogène. Le flux ultraviolet alors émis par ces étoiles ionisa à nouveau l'Univers le rendant ainsi transparent. La datation exacte de la ré-ionisation de l'Univers est encore très incertaine ($6 < z < 14$), c'est pourquoi les preuves observationnelles de cette ré-ionisation sont aujourd'hui recherchées (3.2).

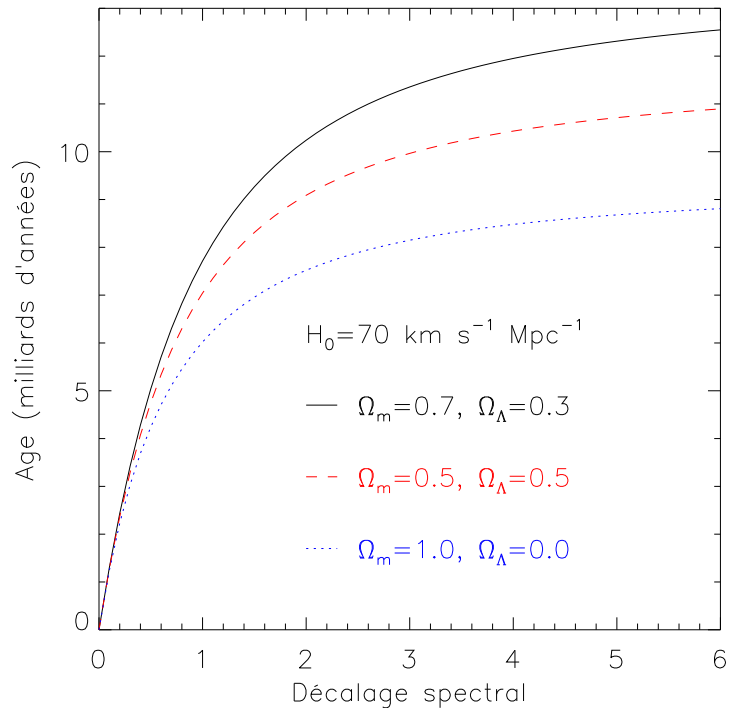


FIG. 3.1: Correspondance entre le décalage spectral et l'âge des galaxies (par rapport à l'époque actuelle)

3.1.3 Galaxies lointaines et spectrographie

Jusqu'à présent, les observations de galaxies à moyen et grand décalage spectral utilisaient des spectrographes à longue fente. Ces observations ont permis d'obtenir des échantillons de galaxies conséquents (Erb et al., 2003, 2004; Weiner et al., 2006). Cependant, la largeur de la fente est bien souvent trop importante pour pouvoir réaliser un échantillonnage spatial fin : les points hors de l'axe de la fente contribuent fortement au spectre mesuré et la courbe de rotation obtenue est biaisée (Weiner et al., 2006). De plus, les erreurs d'alignement de la fente avec le grand axe cinématique sont fréquentes puisqu'il n'est pas aisé de mesurer ce paramètre à partir d'observations photométriques peu résolues.

L'utilisation de spectrographes à champ intégral tels que SINFONI ou FLAMES/GIRAFFE sur le VLT et OSIRIS sur un des télescopes de 10 m de l'observatoire du Keck a été une avancée significative puisqu'elle a permis l'observation résolue de la cinématique de galaxies jusqu'à un décalage spectral de 3 (Förster Schreiber et al., 2006; Genzel et al., 2006; Law et al., 2007; Yang et al., 2008). Grâce à ces observations, l'information cinématique est disponible sur l'ensemble du champ. Il devient donc envisageable d'utiliser des méthodes sophistiquées afin de corriger la courbe de rotation de ces galaxies de la contribution des points hors du grand axe. Cependant, étant donné que la taille des dégradations dues à la turbulence atmosphérique est du même ordre de grandeur que les galaxies observées, ces corrections doivent être validées et les biais estimés.

Un des objectifs de ces observations est de pouvoir détecter des proto-galaxies dont les caractéristiques seraient bien différentes des galaxies connues à ce jour. L'utilisation combinée d'imagerie à haute résolution (observation à partir de l'espace ou bien utilisant l'optique adaptative) avec des observations cinématiques est actuellement le meilleur moyen pour répondre à cet objectif. Cependant,

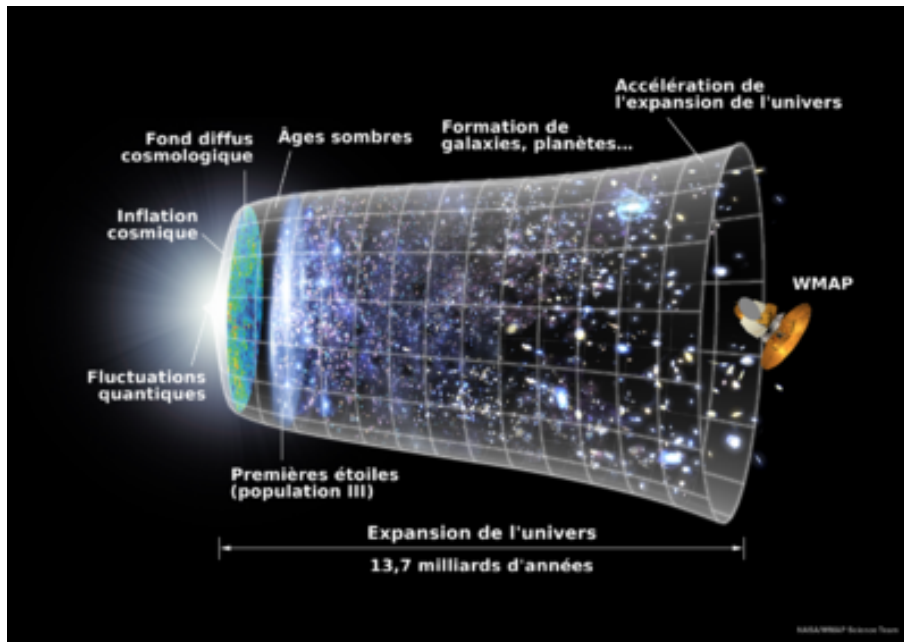


FIG. 3.2: Vue d'artiste de l'évolution de l'Univers. Crédits : NASA/WMAP science team.

le faible signal en provenance des objets les plus lointains constitue la principale limitation. Toutefois, on peut d'ores et déjà sonder l'évolution des structures à travers les âges et, en particulier, essayer de comprendre si les galaxies actuelles se sont formées par accrétion lente de matière, par fusion de galaxies plus petites ou par d'autres phénomènes. L'évolution du support gravitationnel des structures peut également être étudiée afin de déterminer l'époque à laquelle ce support est devenu organisé.

3.2 Nouvelles observations de galaxies à décalage spectral supérieur à un avec SINFONI

3.2.1 Les caractéristiques du spectrographe SINFONI

SINFONI est un spectrographe à champ intégral fonctionnant dans le proche infrarouge ($1.1 - 2.45 \mu\text{m}$) installé au foyer Cassegrain du VLT UT4 (8 m , au CHILI) qui peut utiliser un module d'optique adaptative. Cet instrument utilise un découpeur d'image ("image slicer") afin de placer tout le champ le long d'une fente virtuelle et de disperser la lumière avec un réseau. Quatre réseaux sont employés afin de couvrir quatre bandes spectrales (J, H, K, H+K) avec quatre résolutions spectrales différentes (respectivement 2000, 3000, 4000 et 1500). Selon le mode d'utilisation de l'instrument plusieurs tailles de pixels peuvent être utilisées. Généralement, lors d'observations sans optique adaptative, un pixel de $0.25''$ pour un champ de $8'' \times 8''$ est utilisé alors que les observations avec optique adaptative utilisent un pixel de $0.1''$ pour un champ de $3'' \times 3''$. Étant donné que la fente doit être échantillonnée sur au moins deux pixels afin de respecter le critère de Shannon pour l'échantillonnage spectral, l'échantillonnage spatial dans la direction de largeur de la fente est deux fois plus fin. Ainsi généralement les données sont interpolées suivant l'autre direction (la longueur) pour fournir un échantillonnage spatial de $0.125''$ ou de $0.05''$ selon le mode d'observation.

Étant donnée l'amplitude spectrale, il est fréquent que plusieurs raies d'émission soient présentes.

En particulier, lorsque la raie H α est étudiée, les doublets d'azote [NII] (6548 et 6584 Å) et du soufre [SII] (6716 et 6731 Å) sont également observés dans le domaine spectral.

3.2.2 MASSIV : observation de galaxies à grand décalage spectral

Durant ma thèse, j'ai pris part à la collaboration internationale MASSIV (PI : T. Contini). Comme son nom l'indique, le programme MASSIV a pour objectif l'étude de l'assemblage de masse des galaxies en utilisant des données spectroscopiques obtenues avec SINFONI sur le VLT. Pour cela, environ 140 galaxies sont choisies parmi les galaxies du catalogue VVDS pour des décalages spectraux compris entre 1 et 1.8. L'échantillon de base du VVDS présente l'avantage d'être complet et représentatif des populations de galaxies lointaines. C'est le sondage spectroscopique le plus profond et couvrant le plus grand champ. Ainsi, pour chaque galaxie, un décalage spectral spectroscopique est déterminé avec précision (Le Fèvre et al., 2005). Cela permet de sélectionner des galaxies dont les raies d'émission sont intercalées entre les plus fortes raies du ciel nocturne dans le proche infrarouge, ce qui est impossible à réaliser lorsqu'on ne dispose que du décalage spectral photométrique à cause de son incertitude. À partir des observations du programme MASSIV, il sera possible de réaliser une description détaillée de la proportion des différents types dynamiques (disques en rotation, sphéroïdes, galaxies en fusion, ...) dans cette gamme de décalage spectral, et de suivre l'évolution des lois d'échelle comme la relation Masse-Métallicité et la relation de Tully-Fisher afin de contraindre les scénarios d'évolution des galaxies.

3.2.3 Observations SINFONI et réduction des données

Les données SINFONI présentées ici sont des données préliminaires au programme MASSIV. De même que pour le programme MASSIV, ces sept galaxies ont été choisies dans l'échantillon VVDS. Elles ont été observées en bande H durant des périodes d'observations de quatre nuits, du 5 au 8 septembre 2005 et du 12 au 15 novembre 2006 sans optique adaptative avec un pixel de $0.250'' \times 0.125''$ et un champ carré de $8''$ de côté (voir Table 3.1).

VVDS ID	α (J2000)	δ (J2000)	z_{VVDS}	Exposition (hours)	Seeing ($''$)
020182331	02 : 26 : 44.260	-04 : 35 : 51.89	1.2286	3	0.93
020261328	02 : 27 : 11.049	-04 : 25 : 31.60	1.5291	1	0.61
220596913	22 : 14 : 29.184	+00 : 22 : 18.89	1.2667	1.75	0.47
220584167	22 : 15 : 23.038	+00 : 18 : 47.01	1.4637	1.75	0.77
220544103	22 : 15 : 25.708	+00 : 06 : 39.53	1.3970	1	0.69
220015726	22 : 15 : 42.455	+00 : 29 : 03.59	1.3091	2	0.55
220014252	22 : 17 : 45.690	+00 : 28 : 39.47	1.3097	2	0.61

TAB. 3.1: Paramètres des observations.

La réduction des données SINFONI a pour but de créer un cube de données calibré en longueur d'onde, corrigé du flat instrumental et du biais de la caméra, et pour lequel les raies d'émission du ciel nocturne ont été soustraites. La réjection des rayons cosmiques doit également être effectuée puisque ces données sont obtenues par une caméra CCD. La réduction doit également permettre de combiner les différentes observations nécessaires pour pouvoir éviter d'avoir un nombre trop important de rayons cosmiques. L'ESO met à la disposition des utilisateurs de SINFONI les logiciels

de réduction ESOREX et GASGANO qui utilisent tous deux les mêmes procédures de réduction des données. ESOREX utilise la ligne de commande alors que GASGANO utilise une interface graphique. Les étapes les plus importantes de la réduction des données SINFONI sont la soustraction des raies du ciel nocturne et la combinaison des différentes expositions en un cube final. La soustraction du ciel est effectuée en utilisant les expositions adjacentes. Toutefois, d'autres méthodes sont possibles, comme la soustraction d'un spectre médian. La recombinaison des cubes est faite en utilisant les décalages relatifs des pointés du télescope par rapport à une étoile brillante de référence. Par ailleurs, pour chaque observation de galaxies, une étoile standard tellurique est observée afin de permettre la calibration en flux. Pour l'étude cinématique qui est présentée ici, cette calibration en flux n'est pas primordiale. En revanche, les étoiles de référence sont utiles pour mesurer le seeing des observations afin de l'inclure dans les modèles.

Les cartes cinématiques présentées en Figure 3.3 ont été obtenues en utilisant un programme que j'ai développé sous IDL à partir des routines utilisées par le programme de réduction des données Fabry-Perot. Ce programme détermine les paramètres de la raie en utilisant un ajustement gaussien (voir Annexe C) et détermine également des cartes d'erreurs. Il permet également l'ajustement simultané de plusieurs raies. Un lissage spatial gaussien (largeur à mi-hauteur de 2 pixels) a été effectué sur le cube avant le calcul des cartes cinématiques. Les cartes de dispersion de vitesses ont été corrigées de la résolution spectrale de SINFONI déterminée à partir du spectre de raies du ciel nocturne. Ce programme sera utilisé pour le programme MASSIV conjointement à GIPSY. Les images de gauche ont été obtenues en bande I au CFHT. Ce sont les images avec le meilleur seeing ($< 0.65''$) du "CFHT legacy survey" pour les galaxies du champs à deux heures et celle du "CFH12K/CFHT" (McCracken et al., 2003) pour les galaxies du champ à 22 heures.

3.2.4 Analyse cinématique des galaxies observées par SINFONI

3.2.4.1 Méthode d'analyse

J'ai contribué de manière significative à l'analyse cinématique de ces galaxies. Pour chaque galaxie, l'inclinaison et l'angle de position du grand axe morphologique ont été estimés à partir des images en bande I avec le logiciel GALFIT (Peng et al., 2002). Ce programme prend en compte la valeur du seeing afin d'ajuster un modèle. Les inclinaisons ont également été mesurées à partir de la mesure des rapports d'axe en utilisant la méthode décrite dans la section 3.4.6 de l'article de la partie 3.4 et présentent un très bon accord avec les valeurs estimées par GALFIT. Pour les VVDS020261328 et VVDS220015726 pour lesquelles GALFIT détermine un inclinaison nulle, les inclinaisons déterminées à partir du rapport d'axe ont été utilisées.

Ces paramètres morphologiques ont servi de paramètres de départ à l'ajustement d'un modèle cinématique sur les champs de vitesses 2D. Ce modèle consiste en un disque fin en rotation dont la courbe de rotation est croissante dans les parties internes et plate à grand rayon. Il est similaire à celui utilisé par Wright et al. (2007) :

$$V(r) = V_t \frac{r}{r_t}$$

lorsque $r < r_t$ et pour $r \geq r_t$:

$$V(r) = V_t$$

La méthode utilisée pour prendre en compte le seeing de l'observation est décrite dans l'article présenté dans la partie 3.4. Les paramètres du modèle sont l'inclinaison, l'angle de position du grand axe, la vitesse d'éloignement global de la galaxie (convertie en terme de redshift dans la Table 3.2), le centre cinématique, V_t et r_t . Étant donné le faible nombre de pixels, l'inclinaison est difficilement

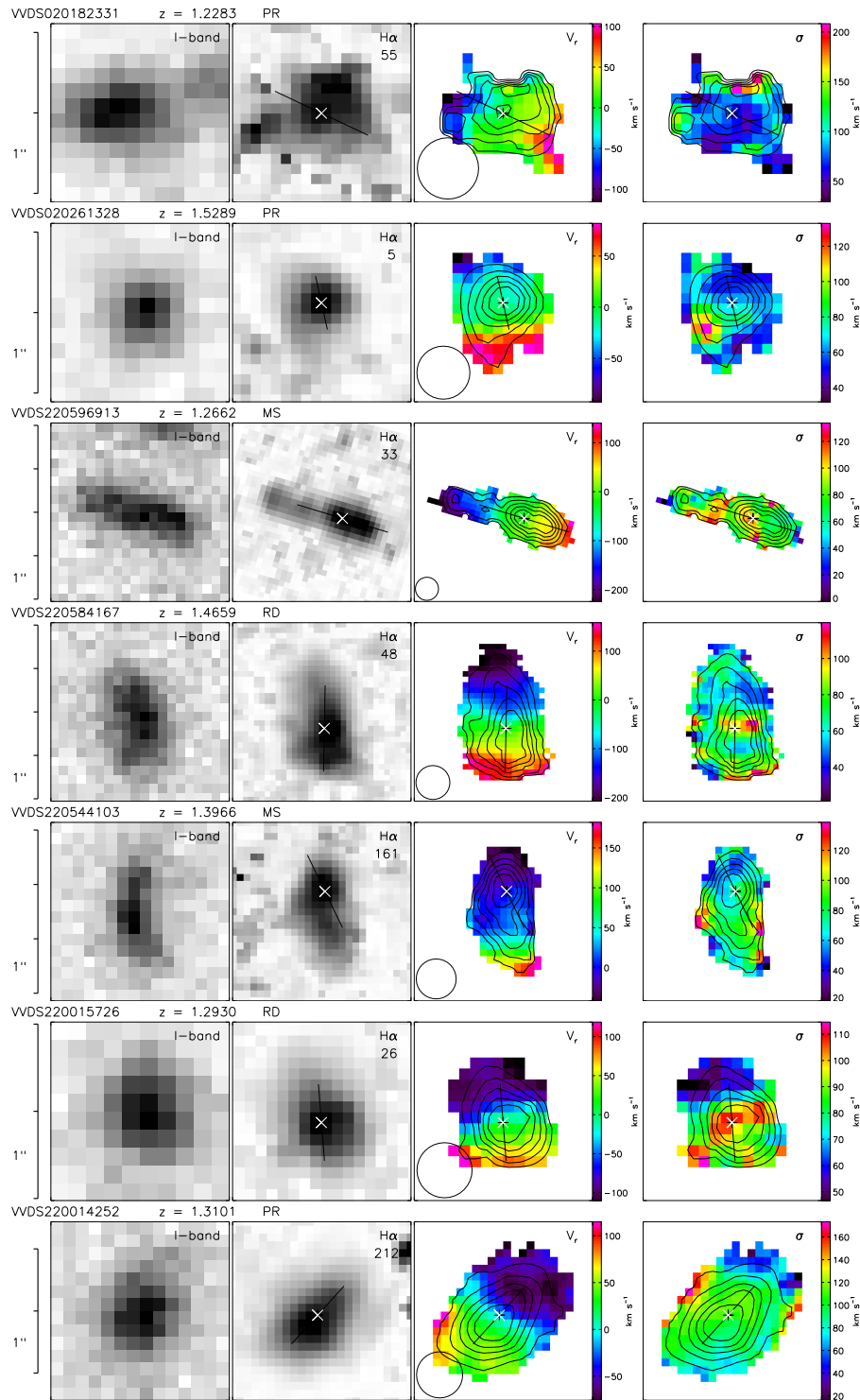


FIG. 3.3: De gauche à droite : image du CFHT en bande I, flux $H\alpha$, champ de vitesses et carte de dispersion de vitesses. Le flux $H\alpha$ intégré est indiqué sur chaque carte ($10^{-17} \text{ ergs s}^{-1} \text{ cm}^{-1}$). L'échelle est indiquée à gauche et la résolution spatiale (FWHM du seeing plus lissage spatial) est représentée par un cercle sur le champ de vitesses. Le Nord est en haut et l'Est est à gauche. Le centre utilisé pour la cinématique est indiqué par la double croix, et trait indique la position du grand axe du modèle. Les contours de la carte de flux sont superposés sur les cartes cinématiques. Le redshift déduit des données SINFONI est indiqué ainsi que la classification dynamique (RD : disque en rotation, PR : rotation perturbée, MS : système en fusion).

VVDS ID	$z_{H\alpha}$	Inclination ($^{\circ}$)	Position Angle ($^{\circ}$)	r_t ($''$)	V_t ($km\ s^{-1}$)	σ_0 ($km\ s^{-1}$)	V_{max} ($km\ s^{-1}$)
020182331	1.22832	52	244	0.55	134	71	134
020261328	1.52891	47	192	0.77	195	55	194
220596913	1.26619	66	253	2.80	325	76	177
220584167	1.46588	49	178	1.24	280	47	280
220544103	1.39659	61	205	6.73	762	70	146
220015726	1.29300	25	184	0.12	323	38	323
220014252	1.31014	48	137	0.12	103	92	103

TAB. 3.2: Paramètres des modèles cinématiques.

contrainte. Elle a donc été fixée à la valeur déterminée par la morphologie. Cependant, lorsque cette inclinaison est nulle, une inclinaison de 10° a été utilisée. De plus, le centre a également été contraint à être situé au centre de l'émission $H\alpha$ (soit le pic, soit le centre des isophotes externes, voir Figure 3.3). À partir des meilleurs ajustements, une carte de dispersion de vitesses modèle a été calculée. Celle-ci ne contient que les effets liés au gradient de vitesse non résolu dû au manque de résolution spatiale (voir l'Annexe 3.4.9 de l'article présenté dans la partie 3.4). Cette carte de dispersion est soustraite quadratiquement aux cartes de dispersion de vitesses observées afin d'examiner la dispersion de vitesses intrinsèque de la galaxies. La dispersion moyenne (pondérée par l'inverse de la carte d'erreur associée) σ_0 mesurée sur les cartes ainsi corrigées est présentée dans la Table 3.2 avec les autres paramètres du modèle. La vitesse maximale est déterminée comme étant la vitesse atteinte par le modèle au point le plus éloigné du centre. Cette modélisation a pour but d'aider dans l'interprétation cinématique des galaxies, afin de voir si leur cinématique peut être expliquée par un disque en rotation.

3.2.4.2 Commentaires galaxie par galaxie

Une interprétation de la cinématique individuelle de chaque galaxie à laquelle j'ai contribué est présentée.

VVDS020182331

Le flux $H\alpha$ de cette galaxie est principalement émis au centre. Le champ de vitesses de cette galaxie est perturbé. Les résidus important d'une raie du ciel (14605\AA) perturbent la mesure des paramètres des raies et sont à l'origine de la forte dispersion de vitesses ainsi que du maximum local du flux, tous deux au Nord. L'incertitude sur la mesure des vitesses n'est inférieure à $20\text{ km}\cdot\text{s}^{-1}$ que sur un diamètre d'une seconde d'arc au centre. Sur cette région, un modèle de disque en rotation est acceptable. La dispersion de vitesses corrigée est élevée ($71\text{ km}\cdot\text{s}^{-1}$) et le support dynamique de cet objet n'est pas clairement dominé par la rotation ($V_{max}/\sigma_0 = 1.9$). L'objet proche, visible sur l'image en bande I, n'est pas détecté en $H\alpha$, ce qui indique que cet objet est soit une source d'avant ou d'arrière plan, soit un compagnon qui forme peu ou pas d'étoiles et avec lequel VVDS020182331 pourrait interagir. Cette dernière hypothèse pourrait expliquer que VVDS020182331 ait une rotation perturbée.

VVDS020261328

La carte de flux est piquée au centre et présente une extension faiblement lumineuse au Sud. La carte de dispersion de vitesses présente un pic à $\sim 120\text{ km}\cdot\text{s}^{-1}$ au Sud-Est. Le champ de vitesses

montre clairement un gradient de vitesses d'environ 100 km.s^{-1} sur un rayon de $0.8''$ qui est toutefois irrégulier. L'ajustement d'un modèle de disque en rotation suggère que seul le centre de la galaxie est détecté puisque le plateau n'est pas atteint. Il montre également que le pic de dispersion de vitesses ne peut pas être attribué aux effets du seeing. Cette galaxie est considérée comme un disque avec une rotation perturbée et dont le support dynamique est principalement dû à la rotation ($V_{max}/\sigma_0 = 3.5$).

VVDS220596913

La carte de flux $H\alpha$ présente deux composantes principales séparées de 12.5 kpc ($1.5''$) qu'on ne distingue pas sur l'image en bande I. La composante la plus lumineuse est située du côté Ouest et est elle-même constituée de deux pics d'intensité égale. L'autre composante située à l'Est est bien moins lumineuse. Elle présente un faible gradient de vitesses et deux pics de dispersion de vitesses ($\sim 100 \text{ km.s}^{-1}$). L'un correspond à la région la plus intense, l'autre est plus diffus et est situé sur la zone de transition entre les deux composantes principales où l'émission est la plus diffuse (rapport signal sur bruit d'environ quatre). Cette forte dispersion de vitesses pourrait être une signature de fusion comme c'est le cas pour le groupe compact de Hickson H31 (Amram et al., 2007). Le gradient de vitesses de la composante faiblement lumineuse fait un angle de 20° avec celui de la composante la plus brillante, ce qui suggère, de même que la distribution de flux irrégulière, que ce système est composé d'au moins deux galaxies en cours de fusion. Bien qu'un unique disque en rotation composé de grands blocs (comme observés par Bournaud et al., 2008) ne puisse être exclus (induisant $V_{max}/\sigma_0 = 2.3$), l'ajustement de la composante la plus brillante seule donne de meilleurs résultats. Cela suggère que cette composante est en rotation avec une vitesse de rotation maximale de $\sim 200 \text{ km.s}^{-1}$. Le centre a été fixé entre les deux pics de flux de la composante brillante et l'inclinaison a été estimée à 55° . Cet objet est donc classé comme étant un système en cours de fusion.

VVDS220584167

VVDS220584167 est l'objet qui possède l'émission $H\alpha$ la plus étendue de l'échantillon. Il présente un pic de dispersion de vitesses proche du centre allongé. L'observation est affectée par de forts résidus dus à une raie du ciel (16195\AA) qui induisent de fortes incertitudes sur la mesure des paramètres des raies, plus particulièrement au Sud. Le champ de vitesses est asymétrique et la galaxie possède une morphologie irrégulière en bande I, ce qui suggère l'existence d'une forte barre. De plus, le décalage observé entre les morphologies en bande I et $H\alpha$ suggère qu'un violent épisode de formation stellaire est en cours. Le champ de vitesses est ajusté raisonnablement par un modèle de disque en rotation et le pic de dispersion de vitesses n'est pas expliqué par ce modèle puisque ce dernier ne simule pas l'effet de la barre sur le champ de vitesses. Le support dynamique de cet objet est dominé par la rotation ($V_{max}/\sigma_0 = 5.6$). Cette galaxie est donc classée comme étant un disque en rotation possédant une barre.

VVDS220544103

La carte de flux $H\alpha$ montre deux pics séparés d'environ 6 kpc ($0.75''$). Cette galaxie possède une morphologie irrégulière aussi bien en $H\alpha$ qu'en bande I. La variation de vitesse le long de la composante principale (Nord) est faible ($\sim 30 \text{ km.s}^{-1}$) alors que celle de la composante la plus faible (Sud) est élevée ($\sim 120 \text{ km.s}^{-1}$). Les deux gradients ont globalement la même direction (la vitesse augmente du Nord au Sud). Les lignes d'isovitesse sont perpendiculaires à la morphologie tordue et allongée de l'objet. Les pics les plus intenses de dispersion de vitesses sont situés sur les bords où le rapport signal sur bruit est le plus faible. Hormis ces pics, la carte de dispersion de vitesses présente un pic allongé proche du pic de flux $H\alpha$. L'ajustement d'un modèle de disque en rotation au système

entier induit $V_{max}/\sigma_0 = 2.1$, mais ne semble cependant pas optimum et l'hypothèse d'un objet constitué de deux galaxies (ou plus) en cours de fusion semble plus appropriée. C'est objet est donc classé comme un système en fusion.

VVDS220015726

Les régions centrales ont un signal important alors que les régions avec un faible signal sont affectées par des résidus dus à la proximité de la raie H α avec deux raies de ciel très intenses (15053Å et 15056Å). La carte de flux est piquée au centre, au même endroit où la dispersion de vitesses est maximale ($\sim 100 \text{ km.s}^{-1}$). Les cartes cinématiques de cette galaxie sont bien reproduites par un modèle de disque en rotation. En particulier, la dispersion de vitesses centrale est très bien expliquée par la faible résolution spatiale. VVDS220015726 est clairement dominée par la rotation ($V_{max}/\sigma_0 = 8.5$) puisque c'est le disque en rotation le plus rapide de l'échantillon ($V_{max} = 323 \text{ km.s}^{-1}$) mais aussi l'objet avec la plus faible dispersion de vitesses ($\sigma_0 = 38 \text{ km.s}^{-1}$). Cette galaxie est classée comme étant un disque en rotation.

VVDS220014252

La carte de flux H α présente un pic allongé ainsi qu'une émission diffuse dans les régions externes. Le pic ne correspond pas exactement au centre des isophotes externes. La carte de flux suggère également un bras à l'Ouest. Le champ de vitesses ressemble à celui d'un disque en rotation sauf à l'extrême Ouest, où les vitesses sont plus grandes qu'attendues. Un modèle de disque en rotation s'ajuste toutefois bien au champ de vitesses, en particulier lorsque le centre cinématique est fixé au centre des isophotes externes. La vitesse de rotation maximale est relativement basse (103 km.s^{-1}) mais le modèle montre qu'elle est atteinte proche du centre. Le côté Nord-Ouest du champ de vitesses présente un maximum local suivi d'une faible chute de vitesses. Autours de ce maximum, les profils sont larges et asymétriques. Des profils larges (plus de 150 km.s^{-1}) sont également observés au Nord-Est avec un rapport signal sur bruit plus grand que cinq. La dispersion de vitesses n'est pas piquée au centre et est élevée partout. De plus, la dispersion de vitesses moyenne de cette galaxie est la plus grande de tout l'échantillon (92 km.s^{-1}). Le modèle montre clairement que la dispersion de vitesses n'est pas due à la résolution. Les profils larges et asymétriques observés laissent supposer qu'ils sont en fait des profils doubles non résolus, ce qui pourrait être une signature d'interactions (Amram et al., 2007). De plus, le support dynamique n'est pas dominé par la rotation puisque $V_{max}/\sigma_0 = 1.1$. Cette galaxie est donc classée comme ayant une rotation perturbée, et connaissant potentiellement un épisode de fusions mineures.

Finalement, sur l'ensemble de ces observations, seule une minorité est bien reproduite par un modèle de disque en rotation. En effet, des écarts au modèle et des pics de dispersion de vitesses sont observés pour presque toutes les galaxies présentées, sans qu'il soit pour autant possible de les attribuer au gradient de vitesse non résolu. Par ailleurs, la dispersion de vitesses est de l'ordre de 80 km s^{-1} , ce qui n'est pas habituel dans l'Univers local. Cela suggère que les disques sont de nature différente. L'interprétation de ces observations pourrait être améliorée en utilisant des images observées à partir de l'espace ou avec optique adaptative.

3.3 Observations cinématiques de galaxies à un décalage spectral voisin de 0.6 avec FLAMES/GIRAFFE

3.3.1 Les caractéristiques du spectrographe FLAMES/GIRAFFE

FLAMES/GIRAFFE (PI : F. Hammer) est un spectrographe à champ intégral fonctionnant dans le visible (370 – 900 nm) installé au foyer Nasmyth du VLT UT2 (8 m, au CHILI). FLAMES est le nom du système permettant de positionner les fibres dans un champ de vue de 25 minutes d'arc de diamètre. GIRAFFE est le nom du spectrographe qui permet d'obtenir des résolutions spectrales allant de 7500 à 30000 grâce à deux réseaux. Trois modes d'utilisation sont possibles. Le premier permet de positionner 132 fibres indépendantes dans le champ de vue (MEDUSA) afin d'observer des objets ponctuels. Le second consiste en un unique champ rectangulaire de 22×14 micro-lentilles (ARGUS). Enfin, le dernier mode (IFU) possède 15 sous-champs de 20 micro-lentilles qui peuvent être placés simultanément mais indépendamment dans le champ de vue de FLAMES. Pour ce dernier mode, l'échantillonnage spatial est de $0.52''$ par micro-lentille, ce qui induit un champ de $\sim 3.12'' \times 2.08''$. C'est le mode utilisé pour observer la cinématique de galaxies lointaines, grâce au doublet [OII] (3727 et 3728.5 \AA).

3.3.2 Étude de la relation de Tully-Fisher avec le programme IMAGES

L'objectif du programme IMAGES (PI : F. Hammer) est d'étudier l'assemblage de masses des galaxies depuis $z = 1$. Pour cela, un échantillon de galaxies avec un décalage spectral $0.4 < z < 0.75$ est en cours d'observation par l'instrument FLAMES/GIRAFFE. Cet échantillon compte actuellement 68 galaxies (Flores et al., 2006; Puech et al., 2006; Yang et al., 2008; Neichel et al., 2008; Puech et al., 2008).

À partir de ces observations, l'évolution de relation de Tully-Fisher a été étudiée par (Puech et al., 2008). J'ai contribué à cette étude en utilisant une partie réduite de l'échantillon GHASP afin d'évaluer la qualité de la détermination des vitesses de rotation de l'échantillon IMAGES. Pour cela, j'ai projeté les galaxies GHASP (la méthode est décrite dans la partie 3.4) à un décalage spectral de 0.6 dans les conditions d'observation de l'échantillon IMAGES : un pixel de $0.52''$ et un seeing de $0.8''$. L'utilisation des données GHASP a permis de vérifier sur des données réelles les barres d'erreurs estimées à partir de simulations numériques. Le résultat principal de cette étude présentée en Annexe F est que, d'après la comparaison entre la relation de Tully-Fisher locale et celle obtenue à partir de l'échantillon IMAGES, les galaxies auraient doublé leur masse stellaire entre $z \sim 0.6$ et $z \sim 0$.

3.4 Article IV : Evidence for strong dynamical evolution in disk galaxies through the last 11 Gyr. *GHASP VIII : A local reference sample of rotating disk galaxies for high redshift studies*

Un des objectifs de l'échantillon GHASP annoncés dans le chapitre 2 est la création d'un échantillon de référence afin de mieux comprendre l'étude des galaxies à grand décalage spectral et de les comparer aux galaxies locales. L'échantillon GHASP étant désormais complet, j'ai utilisé l'ensemble

des données de l'échantillon afin de simuler un échantillon de référence de 153 galaxies locales observées dans les mêmes conditions de résolution spatiale que les galaxies dont le décalage spectral est $z \sim 1.7$. Ce travail est présenté sous forme d'un article¹ (Epinat et al., 2009a).

Les galaxies à grand décalage spectral sont observées avec une faible résolution spatiale à cause de leur éloignement. Nous avons utilisé les cubes de données H α observés avec un Fabry-Perot de 153 galaxies proches isolées sélectionnées dans le programme GHASP (Gassendi H α survey of SPirals) afin de dissocier les effets de résolution spatiale de l'évolution cinématique des galaxies. Nous avons simulé des cubes de données de galaxies à un décalage spectral $z = 1.7$ en utilisant un pixel de $0.125''$ et un seeing de $0.5''$ à partir desquels ont été déterminées des cartes de flux H α , de vitesses et de dispersion de vitesses. Nous avons montré que le gradient interne est affaibli et qu'il est responsable d'un pic de dispersion de vitesses. Des modèles simples de disques en rotation ont été ajustés à ces données possédant une faible résolution spatiale afin de déterminer les paramètres cinématiques des galaxies et leur courbe de rotation. La détermination de l'inclinaison n'est pas fiable et la position du centre est délicate. L'angle de position du grand axe est retrouvé avec une précision meilleure que 5° pour 70% de l'échantillon. Ces modèles permettent également de retrouver statistiquement la vitesse de rotation maximale ainsi de la dispersion de vitesses intrinsèque. Ceci valide l'utilisation de la relation de Tully-Fisher pour les galaxies à grand décalage spectral. Nous avons cependant noté que le manque de résolution induit une pente plus faible à grand décalage spectral. Nous avons également conclu que les principaux paramètres cinématiques sont mieux contraints pour les galaxies dont le rayon est supérieur à trois fois la largeur à mi-hauteur du seeing. Les données simulées ont été comparées aux données de galaxies observées avec VLT/SINFONI, Keck/OSIRIS et VLT/GIRAFFE dans la gamme de décalage spectral $3 > z > 0.4$ permettant de suivre l'évolution de onze à quatre Gyr. Nous avons montré que, pour les galaxies dominées par la rotation, la classification basée sur l'utilisation du pic de dispersion de vitesses comme signature de disques en rotation peut s'avérer erronée pour les rotateurs lents ou présentant une courbe de rotation en corps solide. C'est le cas pour $\sim 30\%$ de notre échantillon. Nous avons mis en évidence que la grande dispersion de vitesses observée dans les galaxies à grand décalage spectral n'est pas reproduite avec l'échantillon local projeté, à moins d'utiliser la dispersion de vitesses non corrigée des effets de résolution. Cela signifie sans ambiguïté que, contrairement aux galaxies locales évoluées, il existe à grand décalage spectral au moins une famille de galaxies pour laquelle une fraction significative du support dynamique est due à des mouvements aléatoires. Il faudra néanmoins s'assurer que ces propriétés ne sont pas dues à d'importants biais de sélection avant de pouvoir conclure que la formation d'un disque gazeux instable et transitoire est un processus commun dans la formation des galaxies.

¹Monthly Notices of the Royal Astronomical Society

Mon. Not. R. Astron. Soc. 000, 000–000 (2009)

Evidence for strong dynamical evolution in disk galaxies through the last 11 Gyr. *GHASP VIII: A local reference sample of rotating disk galaxies for high redshift studies*

Epinat B.^{1,2}, Amram P.¹, Balkowski C.³, Marcelin M.¹

¹Laboratoire d'Astrophysique de Marseille, Université de Provence, CNRS, 38 rue Frédéric Joliot-Curie, F-13388 Marseille Cedex 13, France

²Laboratoire d'Astrophysique de Toulouse-Tarbes, Université de Toulouse, CNRS, 14 Avenue Édouard Belin, F-31400 Toulouse, France

³Galaxies Etoiles Physique et Instrumentation, Observatoire de Paris-Meudon, Université Paris VII, 5 Place Jules Janssen, F-92195 Meudon, France.

Accepted. Received; in original form

ABSTRACT

Due to their large distances, high redshift galaxies are observed at a very low spatial resolution. In order to disentangle the evolution of galaxy kinematics from low resolution effects, we have used Fabry-Perot 3D H α data-cubes of 153 nearby isolated galaxies selected from the Gassendi H α survey of SPirals (GHASP) to simulate data-cubes of galaxies at redshift $z = 1.7$ using a pixel size of 0.125'' and a 0.5'' seeing. We have derived H α flux, velocity and velocity dispersion maps. From these data, we show that the inner velocity gradient is lowered and is responsible for a peak in the velocity dispersion map. This signature in the velocity dispersion map can be used to make a kinematical classification, but misses 30% of the regular rotating disks in our sample. Toy-models of rotating disks have been built to recover the kinematical parameters and the rotation curves from low resolution data. The poor resolution makes the kinematical inclination uncertain and the position of galaxy center difficult to recover. The position angle of the major axis is retrieved with an accuracy higher than 5° for 70% of the sample. Toy-models also enable to retrieve statistically the maximum velocity and the mean velocity dispersion of galaxies with a satisfying accuracy. This validates the use of the Tully-Fisher relation for high redshift galaxies but the loss of resolution induces a lower slope of the relation despite the beam smearing corrections. We conclude that the main kinematic parameters are better constrained for galaxies with an optical radius at least as large as three times the seeing. The simulated data have been compared to actual high redshift galaxies data observed with VLT/SINFONI, Keck/OSIRIS and VLT/GIRAFFE in the redshift range $3 > z > 0.4$, allowing to follow galaxy evolution from eleven to four Gyr. For rotation-dominated galaxies, we find that the use of the velocity dispersion central peak as a signature of rotating disks may misclassify slow and solid body rotators. This is the case for $\sim 30\%$ of our sample. We show that the projected local data cannot reproduce the high velocity dispersion observed in high redshift galaxies except when no beam smearing correction is applied. This unambiguously means that, unlike local evolved galaxies, there exists at high redshift at least a population of disk galaxies for which a large fraction of the dynamical support is due to random motions. We should nevertheless insure that these features are not due to important selection biases before concluding that the formation of an unstable and transient gaseous disk is a general galaxy formation process.

Key words: galaxies: spiral; galaxies: irregular; galaxies: kinematics and dynamics; galaxies: high-redshift; galaxies: evolution; galaxies: formation.

2 *B. Epinat et al.*

1 INTRODUCTION

Formation and evolution of galactic disks is one of the most important unsolved questions of extragalactic astronomy and is probably a key clue to merge cosmological models and galaxy building-up mechanisms. The understanding of the rate and the processes followed by galaxies of different masses to assemble, the relative importance of mergers versus continuous gas accretion infall onto the disk, the connection between bulge and disk formation and more widely the dynamical evolution, the rate of metal enrichment, the evolution of ratio between the baryonic and dark matter masses and mass distribution, the angular momentum transfers during these processes are among some of the fundamental and open questions.

Since the mid 1990s, large ground-based telescopes combined with space observatory multiwavelength observations allow to tackle observationally the question of galaxy formation. The challenges for the future are also to extend the study of galaxy formation to the earliest phases, at $z > 6$, and to chart the progress of galaxy formation in detail down to lower redshifts. Morphological and photometric studies point out that high redshift galaxies do not show well-defined shapes and their colors indicate a rapid star formation. Galaxies undergo strong evolution from irregular clumps of star formation into the Hubble sequence valid in the local universe (Papovich et al. 2005). Global properties such as stellar mass, population age, star formation rate, large-scale gaseous outflows, active galactic nucleus fraction have been extensively studied by numerous authors (Dickinson et al. 2003; Steidel et al. 2004; Reddy et al. 2006). The epoch of galaxy formation may span over a broad period probably over 5 Gyrs. At redshifts $z \sim 2$, galaxies are thought to be accumulating the majority of their stellar mass and a wide variety of evolutionary states from young and active star-forming to massive and passively evolving galaxies are observed. At redshifts $z \sim 1$, the pattern of spiral and elliptical galaxies observed in the nearby universe has settled into place even if the fraction of peculiar galaxies is higher (Glazebrook et al. 1995; Abraham et al. 1996; Lotz et al. 2008). However, it is still unknown whether the majority of star formation occurs in flattened disk-like or alternatively in non-equilibrium systems. More widely, it is clear that we do not yet understand the dynamical state of galaxies during this period in which they are forming the bulk of their stars (Law et al. 2007).

More than one thousand high redshift galaxies (mainly Lyman-break galaxies up to $z \sim 3$) have a spectroscopic redshift (e.g. Steidel et al. 2003). Samples of galaxies have been observed with long slit spectrographs to study their kinematics and dynamics. Pioneer observations of $z \sim 1$ disk galaxies have been obtained by Vogt et al. (1996, 1997). Observations of galaxies at higher redshift were more recently obtained (Erb et al. 2003, 2004, 2006; Weiner et al. 2006; Kassin et al. 2007). Studies using NIR slit or integral field unit (IFU) spectroscopy of H α emission under seeing limited conditions have suggested that at least a subset of high redshift galaxies have a disk-like morphology and show large organized rotation, which may indicate the formation of an early galactic disk (Erb et al. 2003). Kassin et al. (2007) showed from long slit spectroscopy kinematical data and HST restframe B-band morphology that a correla-

tion between peculiar kinematics and peculiar or merger-like morphology exists at $z \sim 1$.

However, at high redshift, the small angular size of the galaxies ($\sim 0.5 - 1.5''$), comparable to the size of the seeing halo which imposes to set-up a large width for the slit, is a serious observational difficulty. The difficulty is even enhanced by the fact that irregular galaxy morphology may induce possible strong misalignment of the slit with respect to the kinematic major axis. Moreover, with slit spectroscopy, it is not possible to study internal kinematics features like spiral arms or bars. For these reasons, the use of integral field spectroscopy has been overcome using seeing-limited and adaptive optics (AO) assisted integral field unit spectroscopy to obtain two-dimensional maps of these galaxies. Due to obvious observational difficulties, the advent of large telescopes and specialized focal instrumentations were necessary to map in 3D some of these galaxies. Nowadays, kinematics and dynamics of intermediate to high redshift ($0.4 < z < 3$) galaxies are being increasingly studied with integral field instruments on 8/10-meters class telescopes. IMAGES survey (Flores et al. 2006; Puech et al. 2006; Yang et al. 2008; Neichel et al. 2008; Puech et al. 2008; Rodrigues et al. 2008) contains 63 velocity fields and velocity dispersion maps of intermediate galaxies ($0.4 < z < 0.75$) observed with the integral-field spectrograph FLAMES/GIRAFFE at the VLT in the optical, in order to probe the dynamical evolution, in particular in the Tully-Fisher relation. The SINS survey has been carried out with the integral-field spectrograph SINFONI at the VLT (Förster Schreiber et al. 2009 and references therein). They have analyzed the 2D H α kinematics for 63 high redshift galaxies ($1.3 < z < 2.6$) in the near infra-red (among 80 galaxies observed). They realized sub-kpc resolution AO assisted observations using SINFONI for eight galaxies plus four $z \sim 3$ Lyman Break Galaxies. Similar programs are under progress also using SINFONI at redshift ~ 1.5 (Epinat et al. 2009b, Queyrel et al. 2009, Contini et al. in preparation) and using OSIRIS at Keck Observatory at redshift ~ 1.5 (Wright et al. 2007, 2009) and $z \sim 3$ (Law et al. 2007, 2009).

The question of the assembly of galaxies via major dissipative mergers or internal secular processes has been recently intensely debated in the literature. Based on the analysis of H α velocity fields, velocity dispersion maps and flux distributions, all the different teams advocated that disk candidates are distinguishable from merger candidates. Förster Schreiber et al. (2009) classified the whole SINS sample and concluded that a third of galaxies has rotation-dominated kinematics, another third is composed of interacting or merging systems and the last third has dispersion-dominated kinematics. Epinat et al. (2009b) reached the same conclusions from the MASSIV pilot run. Wright et al. (2009) and Law et al. (2009) gave conclusions compatible with this classification. However, the large picture that emerges in terms of galaxy formation is still a bit confused. Genzel et al. (2008, 2006) and Förster Schreiber et al. (2006) claimed that a secular process of assembly forms bulges and disks in massive galaxies at $z \sim 2$. Robertson & Bullock (2008) nevertheless suggested that the observation of high redshift disk galaxies like the one presented in Genzel et al. (2006) is consistent with the hypothesis that gas-rich mergers play an important role in disk formation at high redshift. Law et al. (2007, 2009) and Nesvadba et al. (2008) argued

that galaxies display irregular kinematics more related to merging or gas cooling systems than rotating disks and concluded that the high velocity dispersions observed in most of the galaxies at $z \sim 2$ may be due neither to a ‘merger’ nor to a ‘disk’, but to the result of instabilities related to cold gas accretion becoming dynamically dominant. Epinat et al. (2009b) advocated that several processes are acting at these epochs. Among them, merging seems to play a key role. Close pairs of galaxies expected to merge in less than 1 Gyr, indicate that the hierarchical build up of galaxies at the peak of star formation is fully in progress. The dominant ‘perturbed rotators’ may include a significant fraction of galaxies with minor mergers in progress or cold gas accretion along streams of the cosmic web, producing a high velocity dispersion.

The unusual kinematics, the high gas fraction and star formation rates in high redshift galaxies have been observed quite recently and attempts to explain them have been done. One explanation is that these young galaxies may have experienced gas-rich major or minor mergers (e.g. Semelin & Combes 2002; Robertson & Bullock 2008). An alternative or complementary scenario may be that early-stage galactic disks accrete large amounts of low angular momentum gas from the cosmic web and thus contain huge quantities of cold gas which fragments and collapses to form violent starbursts (e.g. Immeli et al. 2004b; Bournaud et al. 2007; Elmegreen et al. 2007).

In that last scenario, large star formation may have happened in dispersion-dominated transitory disks rather than in rotationally supported gaseous disks as predicted in current galaxy formation theories. Through secular evolution processes, these unstable disks may lead to the formation of the nowadays bulges and thick disks. Filamentary gas accretion mechanisms should be no more observable nowadays since large amounts of low angular momentum cold gas do not exist anymore. As a consequence, merging is the only mechanism able to fuel galaxies with large amounts of fresh gas in the local universe while at higher redshifts alternative mechanisms may have been in strong concurrence.

Selection effects in the different observations are induced by the relatively low number of galaxies studied and cosmic variance effects. For obvious observational reasons, preferentially extended and bright emission lines galaxies were selected. The prevalence of large velocity shears (large galaxies) or large velocity dispersions (mergers, etc.) in these sources may thus be a product of the selection criteria.

At high redshift, the best seeing-limited observations cover ~ 5 kpc and provide only 2 or 3 spatial resolution elements across the major axis of a typical galaxy. Seeing limited studies may miss velocity structures on spatial scales smaller than that of the seeing halo, thus these kinematical measurements are insufficient to claim rotation without using a model to deconvolve the beam smearing effect. The use of IFU instead of long slit spectrograph minimizes the problem but does not solve it completely. Current integral field surveys at redshift $z > 0.5$ lack of a reference that would be affected by the same observation and methodological biases. This is for instance necessary to probe a possible evolution in the Tully-Fisher relation or to probe a possible evolution in the dynamical support (rotation or dispersion). A solution is the use of N-body/hydrodynamical simulations of galaxies projected at high redshift as done by Kronberger et al.

(2007). A complementary approach, tackled in this work, is to use real data and project them at high redshift, with the same observing conditions as the real high redshift observations.

In section 2 we describe previous simulations of high redshift data from nearby kinematical data. In section 3, we describe the GHASP subsample selection and the simulation of redshifted galaxies. We test the validity of a galaxy classification based on the kinematical maps in section 4. We present the velocity maps analysis method in section 5, we comment the results in section 6, then discuss them in section 7. A conclusion is provided in section 8. The model used to recover the high resolution velocity fields and rotation curves from the projected local data set of galaxies is more widely detailed in Appendix A. The fit parameters and the beam smearing parameter for each galaxy are given in Appendix B. The maps of local sample projected at high redshift are displayed in Appendix C and the rotation curves corresponding to actual data and different models are given in Appendix D. Appendixes B, C and D are provided online only.

Throughout this paper we use a standard cosmology with $H_0 = 71 \text{ km s}^{-1} \text{ Mpc}^{-1}$, $\Omega_m = 0.27$, and $\Omega_\Lambda = 0.73$. We have chosen to project our sample at the critical cosmological scale of redshift 1.7 which is in addition representative of the scale of galaxies from four to eleven Gyr ($0.4 < z < 3$). In such a cosmology, at redshift $z = 1.7$, $1''$ corresponds to 8.56 kpc.

2 LOCAL GALAXIES TO SIMULATE DISTANT GALAXIES

To learn about galaxy evolution, a method is to compare primordial galaxies to nowadays ones. Because of their large distances, high redshift galaxies are obviously not observable with the same spatial sampling as low redshift galaxies. To compare nearby and distant galaxies, it is thus necessary to disentangle distance effects from evolution ones.

Due to the lost of spatial resolution, (i) it is difficult to disentangle rotators from mergers; (ii) the determination of the kinematical parameters (position angle of the major axis, center, inclination, systemic velocities) is more difficult; (iii) the structures within the galaxies (bars, rings, spiral arms, bubbles, etc.) as well as the disk/bulbe/halo mass distributions in the inner regions are smoothed when not erased.

The comparison between nearby galaxies projected at high redshift and observed distant galaxies can help identifying signatures of mergers, kinematical parameters and internal galaxy features and shapes.

Even at low redshift, while the spatial resolution is high enough to allow detailed analysis, controversy may exist on the nature and on the history of peculiar galaxies such as interacting, mergers or starforming galaxies. This is the case for instance for the nearby gas rich Hickson compact group HCG 31 which displays a low velocity dispersion ($\sim 60 \text{ km s}^{-1}$) and an intense star formation rate. Three scenarios have been put forward to explain the nature of this object: (i) these are two systems that are in a pre-merger phase (Amram et al. 2004; Verdes-Montenegro et al. 2005; Amram et al. 2007), (ii) the system is a late-stage

4 *B. Epinat et al.*

merger (Williams et al. 1991) or (iii) it is a single interacting galaxy (Richer et al. 2003). At $z = 0.013$, the actual redshift of the group, high spatial and spectral Fabry-Perot observations allow to observe that the broader $H\alpha$ profiles (larger than 30 km s^{-1}) are located in the overlapping regions between the two main galaxies (HCG 31 A and C). This clearly maps the shock between the two galaxies and the subsequent starburst regions (Amram et al. 2004, 2007). What would tell us the observations of a compact group like HCG 31 ($z = 0.013$) when observed at higher redshift? To illustrate the answer to this question for this specific compact group, beam smearing effects have been tested by Amram et al. (2008). At $z = 0.15$, it becomes already difficult to count how many galaxies are involved in the system and the broadening of the $H\alpha$ profiles would be interpreted as an indicator of rotating disk. This system could thus be catalogued as a rotator instead of a merger (Flores et al. 2006). At $z = 0.60$, disentangling the system is a real challenge. This illustrates the difficulty to retrieve the true nature and the history of high redshift galaxies from observations affected by a too small spatial resolution.

As illustrated by the previous example, spatial resampling of nearby galaxies has already been used to simulate distant galaxies in order to interpret integral field data as well as long slit observations (Rix et al. 1997; Weiner et al. 2006; Flores et al. 2006; Puech et al. 2008; Shapiro et al. 2008; Amram et al. 2008), but a systematic comparison has never been done for a large local reference sample.

The systematics induced by the beam smearing effects have been studied in Amram et al. (2008) who have projected the data cube of the galaxies used to study the local Tully-Fisher (TF) relation for CGs (Mendes de Oliveira et al. 2003) at different redshifts. They pointed out several features: (i) high redshift galaxies have smoother rotation curves than local galaxies, a “solid-bodyfication” of the rotation curve is observed; (ii) nothing indicates that the maximum velocity of the rotation curve is reached, leading to uncertainties in the Tully-Fisher relation determination.

In order to analyze the kinematics of high redshift galaxies, control samples of nearby galaxies, with well studied kinematics, are necessary. Compact groups are probably extreme cases difficult to describe even if they have probably been more frequent in the past than nowadays. Close-by interacting galaxies may also lead to inextricable confusion if the separation between the galaxies is not large enough to disentangle the individual galaxies. Star forming galaxies dominated by bright HII regions producing strong winds may also lead to misinterpretation when the spatial resolution is not high enough to access the main mass component. Before studying these difficult kinds of galaxies which will be considered in further works, in the present paper we have considered more quiescent galaxies. We study the smoothing of these signatures by using the GHASP sample in order to simulate high redshift galaxies. The aim of this work is to know whether atmospheric seeing may mask more complex structures than simple flattened disk-like configuration and to test different models enabling to recover the structures and the kinematic parameters.

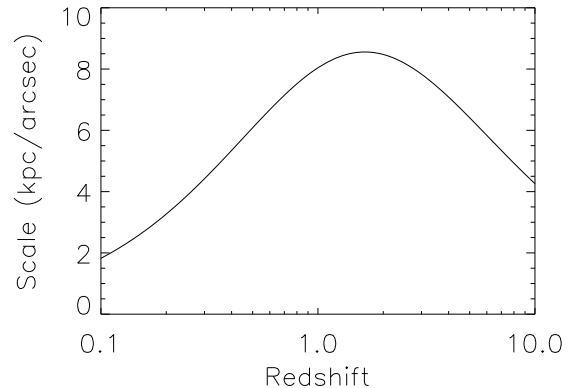


Figure 1. Evolution of the physical length scale with the redshift using the canonical cosmological parameters $H_0 = 71 \text{ km s}^{-1} \text{ Mpc}^{-1}$, $\Omega_m = 0.27$, and $\Omega_\Lambda = 0.73$.

3 THE SAMPLE

3.1 GHASP: the local dataset

Fabry-Perot observations from the GHASP survey (Epinat et al. 2008b,c) have been used for this work. The GHASP sample contains 203 local galaxies, mainly isolated spirals and irregulars, observed through their $H\alpha$ line. These data consist of high spectral resolution ($\sim 5 - 10 \text{ km s}^{-1}$) and seeing-limited data cubes. Nearby galaxies present a broad range of luminosities/masses and morphological types and provide a wide range of kinematical signatures (shape of the velocity fields and of the rotation curves as well as presence of non circular structures like bars, spiral arms, etc.). This sample is thus particularly well adapted to be compared with what is thought to be the ancestors of the actual rotating disks.

We have corrected some local distances computed from the Hubble law using the systemic velocities, since the Hubble constant in the GHASP paper ($H_0 = 75 \text{ km s}^{-1} \text{ Mpc}^{-1}$) differs from the one used in the present paper ($H_0 = 71 \text{ km s}^{-1} \text{ Mpc}^{-1}$).

3.2 The redshifted dataset

153 galaxies belonging to the GHASP sample have been projected to redshift $z = 1.7$ and constitute the so-called “redshifted dataset”. We describe in this section the selection criteria and the techniques applied to project the data cubes taking into account several constraints (distance, foreground contaminations, seeing, resampling, etc.) and to compute the moment maps.

3.2.1 Physical length scale

Considering the standard cosmology chosen in this paper and ignoring evolutionary effects, the angular size of galaxies decreases with the distance from redshifts $z \sim 0$ to $z \sim 1.7$ and thus increases for redshifts $z > 1.7$ (see Figure 1). We have chosen to set the galaxies at their lower angular size, i.e. at the redshift $z = 1.7$ leading to a physical

scale of 8.56 kpc/arcsec . This physical scale is representative of high redshift galaxies for which 3D observations are available today. Indeed, the physical scale of 8.56 kpc/arcsec computed at $z = 1.7$ decreases only by 20% in the range of redshifts $z \sim 0.63 - 4.34$. Thus, this physical scale correctly matches actual observations of high redshift galaxies done with integral field spectroscopy instruments such as SINFONI (Förster Schreiber et al. 2009), OSIRIS (Law et al. 2009; Wright et al. 2007, 2009) and FLAMES/GIRAFFE (Flores et al. 2006; Yang et al. 2008).

3.2.2 Flux re-scaling

Direct comparison between low and high redshift galaxy fluxes is not straightforward since high redshift galaxies do have higher star formation rates and higher luminosities than at low redshift. Nevertheless, instead of giving arbitrary units for $\text{H}\alpha$ fluxes, we have computed the expected flux F_i at redshift $z = 1.7$ for each galaxy, using the flux F_0 computed from the calibration in Epinat et al. (2008b), the distance d of the galaxy and the luminous distance at redshift 1.7 ($d_l = 12.865 \text{ Gpc}$) using equation 1:

$$F_i = F_0 \times \frac{d^2}{d_l^2} \quad (1)$$

$\text{H}\alpha$ monochromatic maps presented in Appendix C have been calibrated using equation 1.

3.2.3 Cleaning from background contaminations

In order to exclude most of the foreground stars from the Milky Way as well as to reduce residual night sky lines contribution, regions where no ionized gas was detected in the local data cubes have been masked on each channel. Indeed, sky contribution is large since it is integrated over a large angular size (around $10'$ square).

3.2.4 Blurring, resampling and noise addition

The wavelength range of the data cube has been extended from 24 to 72 channels in order to remove interfringe effects due to the spectrum periodicity of Fabry-Perot interferometers (Epinat 2008a). Each channel of the cube has been blurred by a two dimensional gaussian simulating the seeing. The width of this gaussian has been computed taking into account the seeing measured on the $z = 0$ data so that the seeing halo for redshifted galaxies is simulated by a two dimensional gaussian function of $0.5''$ FWHM. This halo of $0.5''$ matches the best average spatial resolution that can be reached without AO. This operation is computed in the Fourier space.

The spatial sampling has been set to $0.125''$, to mimic the SINFONI pixel size. To avoid any interpolation, the binning is the merging of an integer number of real pixels that corresponds to the closest simulated size obtained for a redshift $z = 1.7$. The ratio seeing/pixel size has been set to be identical for each galaxy. Thus the mean scale for our sample is 8.5 kpc/arcsec with a standard deviation of 0.3 kpc/arcsec .

In the present study, no spectral binning or smoothing

has been applied in order to dissociate these two resolution effects on 3D data (this test will be done in a forthcoming work).

No noise has been added in the datacubes. Our goal is to study the beam smearing effects in the data to test the ability to recover the kinematical parameters. Indeed, if noise is added on the spectra simultaneously to blurring, it will not be straightforward to unambiguously disentangle the lack of spatial resolution from the low signal-to-noise ratio. Adding noise reduces the detectability at low intensity levels, does not strongly bias velocity distribution but affects velocity dispersion measurements. The signal-to-noise ratio of the simulated data (ranging from ~ 3 to ~ 50) is higher than real high redshift observations (ranging from ~ 2 to ~ 10 , e.g. Epinat et al. 2009b). The signal-to-noise ratio slightly varies from one galaxy to the other since the binning is not the same.

3.2.5 Cleaning procedures on redshifted data

A cleaning procedure has been applied on redshifted data to remove spurious measurements outside of the galaxies. We used the following criteria that ensure to avoid discontinuities on the edges of the velocity fields: the velocity dispersion must be larger than 5 km s^{-1} , which is lower than the spectral resolution of our data, and the signal-to-noise ratio (defined as the ratio of the $\text{H}\alpha$ monochromatic flux over the RMS among spectral elements in the continuum at that pixel times the full width of the line) must be larger than 2.7. This cleaning corresponds to the maps presented in Appendix C.

3.2.6 Computing the moment maps for redshifted data

The different maps have been computed using the barycenter method described in Daigle et al. (2006) and already used to compute the local maps in Epinat et al. (2008b,c). Velocity dispersion maps have been corrected from the spectral PSF considered to be described by a gaussian function using the following classical relation:

$$\sigma_{corr}^2 = \sigma_{obs}^2 - \sigma_{PSF}^2 \quad (2)$$

3.2.7 Selection of a sub-sample

To avoid artifacts and to produce a realistic sample, only a sub-sample of GHASP galaxies has been used to simulate galaxies at high redshift. Some galaxies coming from the GHASP sample have been rejected. The selection criteria are described hereafter.

I. Actual observations of high redshift galaxies are limited in flux and in size. We have discarded too small and too faint galaxies and “uncomplete” observations:

(i) galaxies with an optical radius smaller than 3.2 kpc ($3/4$ of the seeing at $z = 1.7$);

(ii) galaxies having less than 20 pixels after cleaning;

(iii) galaxies with an integrated $\text{H}\alpha$ emission fainter than $10^{-22} \text{ W m}^{-2}$;

(iv) “uncomplete” observations, i.e. galaxies larger than the field-of-view (see Epinat et al. 2008b) (for which $\text{H}\alpha$ emission is missed, the comparison has been made with $\text{H}\alpha$

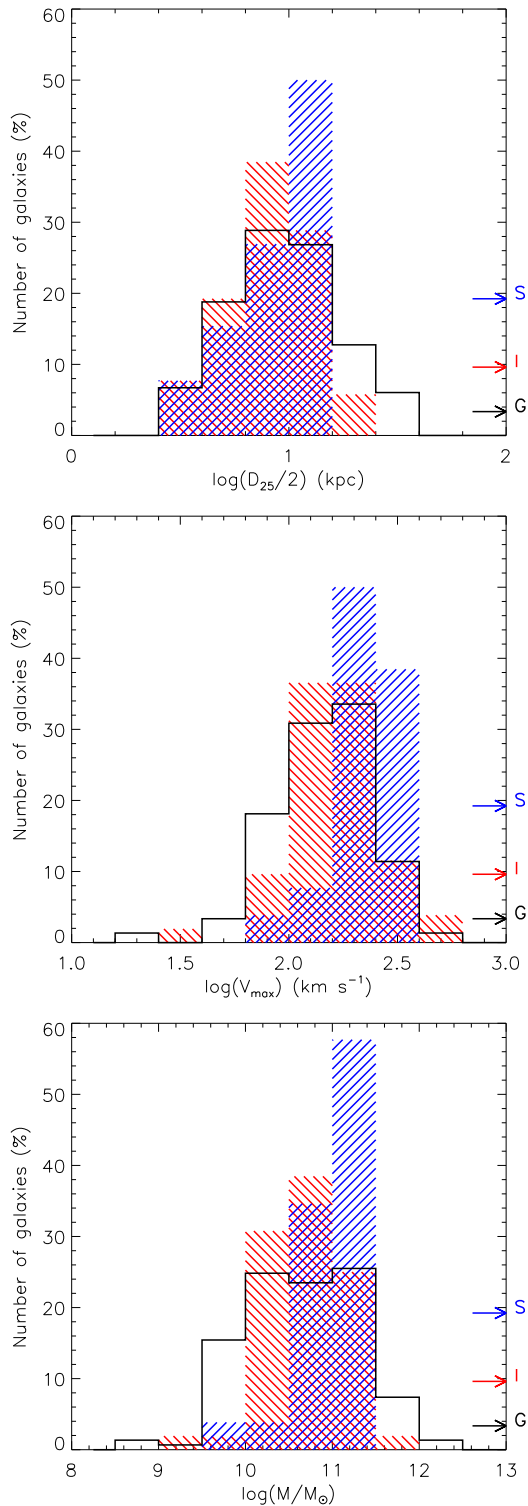
6 *B. Epinat et al.*

Figure 2. Relative distribution of galaxy properties. Top: optical radius; Middle: maximum rotation velocity; Bottom: masses. The black stairs indicates the GHASP local sub-sample, the red hatching the IMAGES sample and the blue hatching the SINS sample. In order to show the respective size of the samples (153, 63 and 26 galaxies respectively for GHASP, IMAGES and SINS), arrows and letters with the same colors indicate five galaxies for each sample (G for GHASP, I for IMAGES and S for SINS).

images when available from NED database) as well as galaxies showing a non uniform H α emission due to filter transmission problems.

II. Pair galaxies are analyzed separately when their angular separation at high redshift is large enough (typically 0.5'') to clearly disentangle them. Only the two pairs UGC 5931/5935 and UGC 8709/NGC 5296 are presented on the same maps in Appendix C. Only UGC 8709 is analyzed since it is clear on projected maps that NGC 5296 is only a small satellite. The pair UGC 5931/5935 is the only one that could be interpreted as a single galaxy at redshift $z \sim 1.7$ thus the couple is analyzed as a single galaxy, UGC 5931.

In summary, the sub-sample resulting from these criteria contains 153 galaxies (or close pair galaxies) among the 203 GHASP galaxies. Thus, our sample contains 153 simulated high signal-to-noise ratio, high spectral resolution ($\sim 10 \text{ km s}^{-1}$), sky subtracted data cubes of galaxies observed at a redshift $z \sim 1.7$ under good seeing conditions (0.5'' seeing) with a 0.125'' spatial sampling.

Some examples of the original and blurred maps are given in Figure 3: for each galaxy, the top line presents the actual maps already presented in Epinat et al. (2008b,c) whereas the bottom one corresponds to the blurred maps for the same galaxy projected at redshift 1.7. The whole set is presented in Appendix C: the original XDSS image, as well as the blurred H α flux, velocity field and the velocity dispersion maps are given for each galaxy of the sub-sample. On each map of Figure 3 and Appendix C, the white and black double crosses mark the center used for the analysis while the black line represents the major axis used or derived from the analysis. This line ends at the optical radius taken from the RC3 catalog (see Table B1).

In Appendix D, we present the rotation curves of redshifted galaxies. The black dots correspond to the rotation curve along the major axis (determined from high resolution data, see Table B1). The velocities are measured on the velocity field for the pixels intercepted by the major axis and are deprojected from inclination. The colored lines are the high resolution rotation curves obtained from the models fit on the velocity fields (see section 5). The red-open triangles correspond to the high resolution rotation curves from Epinat et al. (2008b,c). These authors have computed the rotation curves from H α data cubes obtained from adaptive binning techniques based on Voronoi tessellations. Original improvements, based on the whole 2D velocity field and on the power spectrum of the residual velocity field rather than the classical method using fit in annuli or tilted ring model has been used to compute the rotation curves. The kinematical parameters (inclination, position angle, systemic velocity and center) were not allowed to vary with the radius.

3.2.8 Distribution of the sub-sample

Figure 2 presents the relative distribution for the three following galaxy parameters: optical radius ($D_{25}/2$), maximum rotation velocity (V_{max}) and total mass (M) computed within the optical radius for three different samples.

$$M = \frac{V_{max}^2 \times D_{25}/2}{G} \quad (3)$$

These samples are: (i) the GHASP sub-sample previously defined (black stairs); (ii) the IMAGES sample (red

hatchings) observed with FLAMES/GIRAFFE (Flores et al. 2006; Puech et al. 2006; Yang et al. 2008; Neichel et al. 2008; Puech et al. 2008) and (iii) the 26 galaxies from SINS sample (blue hatchings) for which these measurements are available so far, and that are mainly classified as rotating disks (Förster Schreiber et al. 2009; Cresci et al. 2009). For comparison, the total amount of galaxies of each sample being different (153 for GHASP, 63 for IMAGES and 26 for SINS), we have marked on the histograms of Figure 2 a reference level of five galaxies for each sample with arrows of the same color as the histograms (G for GHASP, I for IMAGES and S for SINS). The GHASP local sample contains galaxies over a broader mass range resulting from larger galaxies and slowest rotators than the two other samples. The lack of very large galaxies at high redshift can be explained by both evolution effect and observational biases due to a poorer signal-to-noise ratio, inducing underestimated radii. We may also notice that GHASP barred galaxies are on average smaller than unbarred galaxies. This biases the comparison that can be done between barred and unbarred galaxies since we expect the parameters determination accuracy to be correlated with the size of redshifted galaxies. The bias induced between barred and unbarred GHASP galaxies does not affect the global comparison with high redshift galaxies. Moreover, even if high redshift and local distributions are different, the simulated maps are suited for studying biases in the kinematical parameters determination since the GHASP sub-sample covers the whole mass, extent and velocity ranges observed at high redshift. It is however interesting to notice that almost no high redshift galaxies from both IMAGES and SINS samples are slow rotators even if they are on average smaller objects. This is probably due to magnitude selection effects and could indicate that no $H\alpha$ is detected in the outer regions (nevertheless, Cresci et al. 2009 found a good agreement between the radii measured in K -band and in $H\alpha$). Moreover, high redshift samples are not selected in a statistically complete way since they aim at observing galaxies with resolved kinematics.

3.2.9 Velocity field extent

As already underlined in paragraph 3.2.4, our redshifted sample benefits from a high signal-to-noise ratio, thus, our velocity fields are probably more extended than what observation facilities would enable for real high redshift observations. The extent of local velocity fields is close to the optical radius value as underlined by Garrido et al. (2005). The mean value of optical radius for our GHASP sub-sample is 11 kpc (median value is 9 kpc), with a dispersion of 7 kpc . The lowest value is 3 kpc and the highest value is 35 kpc . For comparison, we have converted half light radii ($r_{1/2}$) taken from the literature for high redshift objects into optical radii (r_{opt}) assuming an exponential distribution of light: $r_{opt} = 1.9r_{1/2}$.

IMAGES galaxies observed with FLAMES/GIRAFFE in the redshift range $0.4 < z < 0.75$ by Neichel et al. (2008) have a mean optical radius of 9 kpc with a scatter of ± 4 kpc , which is comparable to our sample. Their smallest galaxy is 2.9 kpc and the largest is 19.5 kpc . On average, the 16 galaxies observed with OSIRIS by Law et al. (2009) with redshifts from 2 to 3 extend up to 1.1 ± 0.3 kpc . These values are very low. This could be partially attributed to the different

estimators. Indeed, the disk dimensions are deduced from the ionized gas flux map, which is not completely suitable for comparison. The four $z \sim 1.5$ redshift galaxies observed by Wright et al. (2007) with OSIRIS using AO extend up to 4.9 ± 1.1 kpc in optical radius. Förster Schreiber et al. (2006, 2009) and Cresci et al. (2009) have provided half light radius measurements for 26 galaxies (mainly for rotating disks) out of the 63 SINS galaxies. The mean optical radius is 9.1 ± 3.3 kpc , the smallest galaxy radius is 3.2 kpc and the largest one is 14.5 kpc , which is still slightly smaller than for the GHASP sample. The nine galaxies with redshift ranging between 1 and 1.5 presented by Epinat et al. (2009b) have optical radii of 10.3 ± 4.1 kpc . The sizes are ranging from 5.3 kpc to 17.3 kpc . Except for high redshift galaxies observed with the OSIRIS instrument that uses AO facility (Law et al. 2009; Wright et al. 2007, 2009), the extent of high redshift galaxy velocity fields is rather similar to the ones of our sub-sample. However, there is no case for galaxies larger than 20 kpc as already noticed from the histogram in Figure 2. The smaller extent of observations with AO facility could be explained by the use of a very small pixel scale (50 mas for both OSIRIS and SINFONI in AO mode) that induces a loss in flux detection. Indeed, for constant surface brightness objects, it is necessary to use longer exposures when using a smaller pixel scale to reach a given signal-to-noise ratio, even with a negligible read-out noise.

On the other hand, due to selection criteria effects on high redshift sample, we would expect to observe large galaxies but evolution processes have the opposite effect. In conclusion, since local data have a better signal-to-noise ratio and on average a larger spatial extent, in section 6, we have truncated the images of all the galaxies at the optical radius to mimic high redshift galaxies. However, the maps presented in Appendix C are not truncated.

3.3 Biases induced by spatial resolution effects

At redshift $z = 0$, the use of optical spectroscopy is the best way to probe the inner shape of rotation curves since the inner regions are usually not well resolved with HI radio observation (for GHASP data already observed in HI in the WHISP survey by Noordermeer et al. 2005, the typical resolution is ~ 5 kpc). Optical rotation curves are not always extended enough to determinate reliable maximum velocities (Garrido et al. 2005). Complementarily, HI data are used to trace the outer regions of rotation curves since HI generally extends further away. At high redshift, the situation regarding the spatial resolution in optical or in infrared becomes comparable to HI at local redshift, but still with a smaller extent. Thus, the biases due to spatial resolution effects for our sample are somewhat similar to HI beam smearing effects for local galaxies (see section 6.1 for a discussion on the beam smearing parameter). Our projected sample gives a good opportunity to revisit these biases, and to point out specific biases in the optical or in the infrared since we exactly know how the high resolution kinematical maps look like.

From the comparison between the original and redshifted maps given in Figure 3 in the case of UGC 07901 (top-left), we note that:

(i) The apparent size of the galaxy seems to be enlarged while in fact, flux limits reduce it. Indeed, the emitting re-

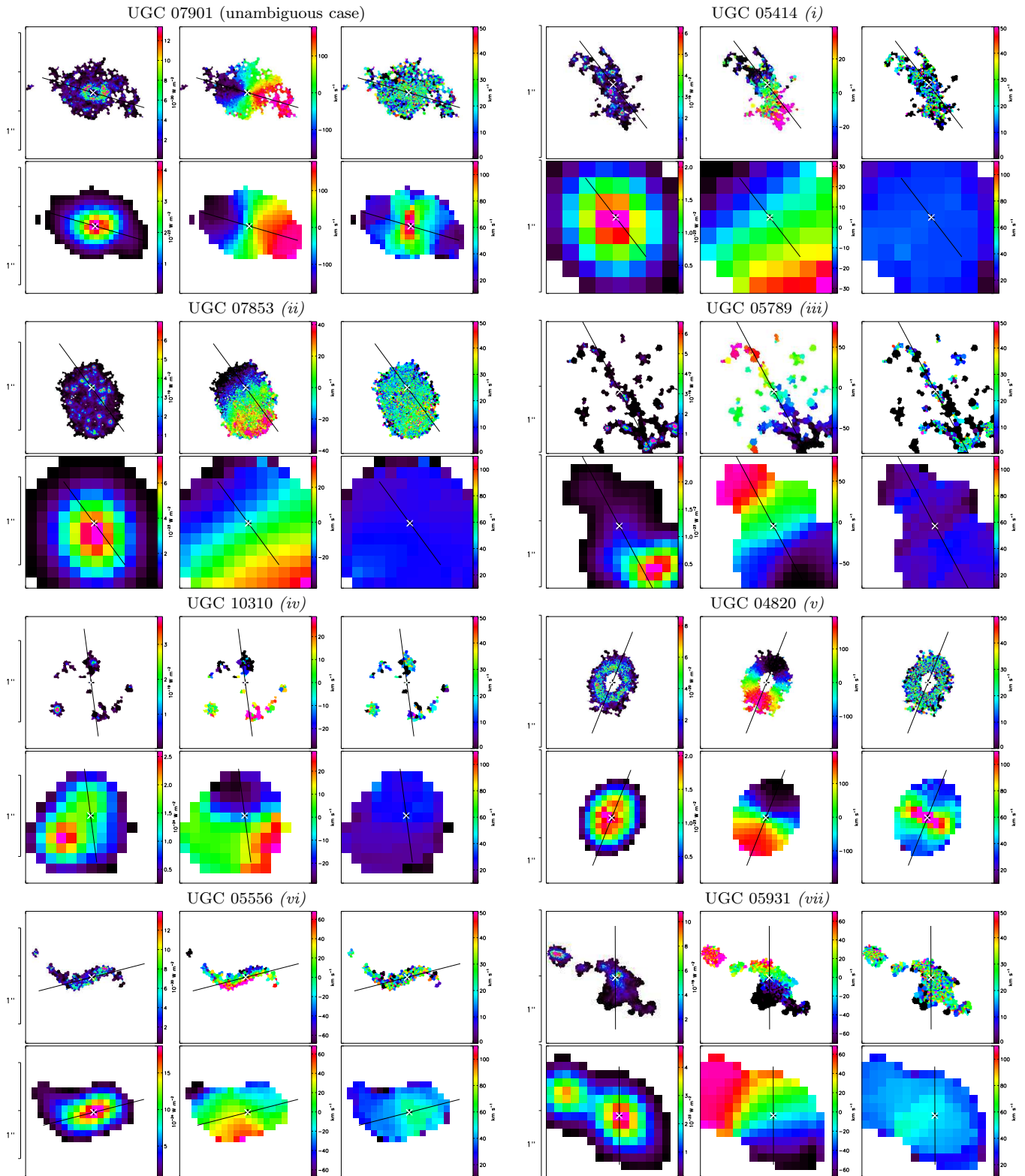
8 *B. Epinat et al.*

Figure 3. Spatial resolution effects illustrated on eight galaxies illustrating an unambiguous case and the cases described from (i) to (vii) in section 4. The following comments concern each galaxy. Top line: actual high resolution data at $z = 0$. Bottom line: data projected at $z = 1.7$. The spatial scale is labelled in arcsecond on the left side of both lines. From left to right: $H\alpha$ monochromatic maps, velocity fields and velocity dispersion maps. The rainbow scale on the right side of each image represents the flux for the first column and the line-of-sight velocities corrected from instrumental function for the two next columns. The black and white double crosses mark the kinematical center at low redshift, while the black line represents the major axis and ends at the optical radius. More projected galaxies are presented in Appendix C.

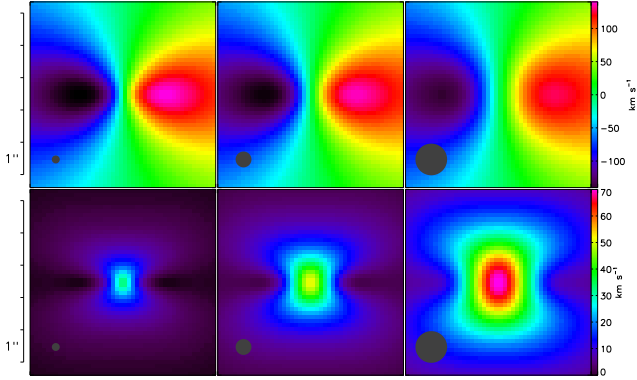


Figure 4. Beam smearing effects on a simulation (velocity fields on the top line and velocity dispersion maps on the bottom line) depending on increasing blurring parameter. From left to right, the seeing (represented by a dark disk on the six images) increases from $0.25''$ to $1''$. The pixel size is $0.125''$. The disk scale length is set to 5 kpc (observed at $z = 1.7$), the inclination is 45° and the maximum velocity in the plane of the disk is 200 km s^{-1} .

gions in the blurred images are artificially extended toward outer regions of the galaxy where there is in fact no emission. This is due to beam smearing that spreads out the flux over the PSF. In actual observations, depending on the signal-to-noise ratio, these faint outer regions should not exist.

(ii) Concerning the $\text{H}\alpha$ monochromatic map, we totally lose the details of the inner ring distribution and the emission is only present in the central peak of the blurred images.

(iii) The velocity gradient is lowered along the major axis while the velocity gradient is increased across the minor axis. Indeed, both velocity fields nevertheless present the usual “spider” shape. However, the isovelocity lines are more open for the high redshift galaxy than for the $z = 0$ galaxy. If one does not take into account the beam smearing, this could be interpreted as a lower inclination for the redshifted galaxy (the same conclusion would be reached by looking at the morphology due to the fact that the relative enlargement is higher for the minor axis than for the major axis).

(iv) The velocity dispersion maps are quite different. The bottom-right map shows the velocity dispersion affected by beam smearing, the top-right map displays the velocity dispersion for each point of the galaxy, referred hereafter as the local velocity dispersion and noted σ . We aim to measure this quantity in order to estimate the pressure support for both nearby and distant galaxies. The local velocity dispersion does not display any strong feature whereas the velocity dispersion map at high redshift clearly shows a central peak elongated along the minor axis. As already discussed by other authors (e.g. Weiner et al. 2006; Flores et al. 2006), this peak is only due to beam smearing effects: for each pixel, the resulting line is the combination of lines at various wavelengths (velocities) weighted by the real flux and is thus enlarged. The enlargement is maximum where the projected velocity gradient is the highest (see Appendix A for details).

Both redshifted velocity field and velocity dispersion map contain information on the true velocity field itself. In Figure 4, in order to illustrate this effect that is responsible for both points (iii) and (iv), an exponential disk model has been drawn in order to compute velocity fields and velocity

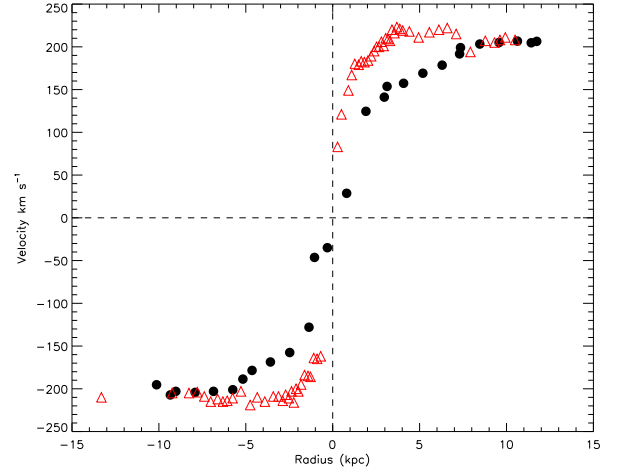


Figure 5. Example of a rotation curve obtained for a redshifted galaxy. Both rotation curves have been computed from both local and projected UGC 7901 velocity fields presented in Figure 3: red-open triangles correspond to local full resolution data while black dots come from the data projected at $z = 1.7$.

dispersion maps with increasing seeing ranging from $0.25''$ to $1''$. The disk scale length has been set to 5 kpc and the maximum velocity of the rotation curve to 200 km s^{-1} . The inclination has been fixed to 45° . The flux contribution follows an exponential disk, and the local velocity dispersion σ is null everywhere. We observe that the velocity shear vanishes whereas the velocity dispersion peak increases. The behavior would be the same with an increasing pixel size or with a decreasing disk scale length. If the local velocity dispersion has a constant value σ in the field, the resulting velocity dispersion map is the quadratic sum of σ with the previously computed blurred velocity dispersion map. It results that the peak is more attenuated for galaxies with a high local velocity dispersion.

In addition to these effects on the maps, the beam smearing will modify the shape of the rotation curve, which will eventually look like a solid body rotation curve. This is illustrated in Figure 5 where the rotation curve at low redshift (red-open triangles) is over-plotted on the rotation curve derived from the major axis of the redshifted velocity field (black dots). At high redshift, the inner velocity gradient is lowered whereas the outer gradient becomes higher. It can be noticed that the maximum velocity seems to be reached at larger radii (around 8 kpc instead of 3 kpc) on both the velocity field and the rotation curve of the projected galaxy. This is due to the fact that, for this specific ring galaxy, the blurred $\text{H}\alpha$ distribution is dominated by the contribution of the ring. Since it is close to the center, the velocity of the ring has a strong weight and is reached rapidly. At larger radii, the contribution of the $\text{H}\alpha$ ring remains important and tends to lower the plateau. For most of the nearby galaxies observed at high spatial resolution with a flatter $\text{H}\alpha$ distribution, the inner slope is also shallower (see Appendix D, e.g. UGC 11872). For galaxies with a lower extent, the maximum velocity is not reached on the rotation curve (see Appendix D, e.g. UGC 528). With HI data at low redshift, this would not be true since, the ex-

tent being larger, the external plateau could be reached. However, mostly for massive spiral galaxies, we see that the maximum velocity is reached close to the center in $H\alpha$, the rotation curve may even be decreasing afterward. Epinat et al. (2008c) suggested that this could be a possible explanation for the difference observed in Tully-Fisher relations obtained from $H\alpha$ and HI data for the most massive galaxies.

4 KINEMATICAL SIGNATURES OF HIGH REDSHIFT ROTATING DISKS

4.1 Kinematical classification

The velocity dispersion map feature discussed in the previous section is typical of a rotating disk with a rather uniform flux distribution and with a projected velocity gradient larger than 100 km s^{-1} , due to the strong inner velocity gradient. Flores et al. (2006) use this signature to provide a dynamical classification for high redshift galaxies (for $z \sim 0.6$): “rotating disks” present a central velocity dispersion peak, “perturbed rotators” show a peak (slightly) offset from the center and objects having “complex kinematics” (e.g. mergers) display featureless velocity dispersion maps. The GHASP sample contains mainly rotating disks, thus we can use it to probe this classification. We find that around 70% of the sample would be correctly classified (i.e. entering in the category “rotating disks”). Nevertheless, the remaining fraction of the sample would be misclassified for the following reasons (see Figure 3 for illustrations of each case):

(i) disks in rotation with a low velocity gradient (face-on, low mass galaxies, high velocity dispersion in the velocity field with respect to the rotation velocity amplitude) show a very faint or no central velocity dispersion peak (see Appendix C, e.g. UGC 3685, UGC 3851, UGC 5414 -Fig. 3-, UGC 6628, UGC 11557);

(ii) disks showing a solid body rotation curve have the same velocity gradient everywhere in the field and thus no peak of velocity shear can be observed in the velocity dispersion map (see Appendix C, e.g. UGC 6419, UGC 7853 -Fig. 3-);

(iii) asymmetries in the $H\alpha$ distribution can induce an offset velocity dispersion peak (hence misclassified as “perturbed rotators”) since the resulting velocity dispersion map is the combination of velocity field shears weighted by the $H\alpha$ monochromatic flux (see Appendix A and Appendix C, e.g. UGC 4393, UGC 5316, UGC 5789 -Fig. 3-);

(iv) galaxies with a patchy $H\alpha$ emission seem to have a continuous emission once projected at high redshift from which can result peculiar velocity fields and velocity dispersion maps (see Appendix C, e.g. UGC 10310 in Fig. 3);

(v) a central hole (or ring) in the flux distribution can be completely blurred depending on the actual size of the galaxies (see Appendix C, e.g. UGC 3382, UGC 4820 -Fig. 3-, UGC 5045);

(vi) the presence of a strong bar can induce very peculiar velocity fields with an apparent position angle of the major axis completely biased (see Appendix C, UGC 5556 being the most impressive case -Fig. 3-);

(vii) using only broad band images, very close pairs (see Appendix C, e.g. UGC 5931 & UGC 5935 in Fig. 3) can appear as a single galaxy with two main clumps. Kinematical

data are helpful to distinguish single galaxies from systems composed by two or more galaxies. A paired galaxies system or even a compact group of galaxies may look like a single perturbed galaxy when they are in fact composed of distinct galaxies in interaction or just seen close in projection on the sky plane. Reciprocally, chaotic single galaxies composed by bright clumps may look like multiple systems. In a given field-of-view, multiple galaxies can be identified using the discontinuities in the velocity gradients, the variation of the major axis position angle and the possible multiple components along the line-of-sight in the line profiles (e.g. Amram et al. 2007). Velocity discontinuities are obvious when the different galaxies are rotating in apparent opposite directions but are also visible when the galaxies are rotating with the same apparent spin. Within a given pixel, multiple components in the line profiles can be identified by the relative difference in velocities and often also by difference in flux ratio. In the case of UGC 5931/35 the velocity field looks disturbed even though the actual velocity field is more regular, the position angle of the major axis is biased and the velocity dispersion signature of a rotating disk is partly lost.

In addition to these effects, this classification cannot be used for galaxies with a high local velocity dispersion since the peak in the velocity dispersion map is smoothed.

4.2 IMAGES classification

GIRAFFE observations, in the frame of the IMAGES program (Yang et al. 2008; Neichel et al. 2008; Puech et al. 2008; Rodrigues et al. 2008), provided a sample of 63 galaxies (including those of Flores et al. 2006 and Puech et al. 2006) ranging from $z = 0.4$ to $z = 0.75$ representative of the population of emission line galaxies more massive than $1.5 \times 10^{10} M_{\odot}$ (see Figure 6 in Yang et al. 2008). In this sample, Yang et al. (2008) found 32% of regular “rotating disks”. A lower limit of the number of “anomalous kinematics (perturbed and complex)” galaxies can be given considering that absorption line galaxies are not perturbed. Yang et al. (2008) estimated that absorption line galaxies represent 40% of the total population of galaxies at $z \sim 0.6$. Thus, taking into account all the galaxies (emission and absorption line galaxies) in that redshift range, these authors found that at least $41 \pm 7\%$ of them have anomalous kinematics (not relaxed), including $26 \pm 7\%$ with complex dynamics (not simply pressure or rotationally supported). The merger hypothesis is favored by these authors to explain this complex dynamics. Even if the condition of projection of the local GHASP sample of galaxies presented in this paper is built to match the SINFONI observations rather the GIRAFFE ones, a comparison between local galaxies and galaxies at intermediate redshift (IMAGES/GIRAFFE) may also be done. Indeed, the seeing conditions (without AO) are statistically the same, the sizes of the galaxies do not dramatically differ between redshift $z = 1.7$ and $z = 0.6$ (at $z = 1.7$, $1'' \sim 8.6 \text{ kpc}$ and at $z = 0.6$, $1'' \sim 6.7 \text{ kpc}$, see Figure 1), the main difference is the sampling of the seeing on the CCD, the one of SINFONI ($0.125''$) being approximately four times higher than that of GIRAFFE ($0.52''$). Nevertheless, the spectral sampling is higher in GIRAFFE ($22 - 30 \text{ km s}^{-1}$) than in SINFONI ($67 - 160 \text{ km s}^{-1}$) but lower than in GHASP ($\sim 17 \text{ km s}^{-1}$). On the one hand, from the comparison be-

tween IMAGES and GHASP, it can be concluded that actual disks in rotation with emission lines at intermediate redshift look like local disks in rotation projected at high redshift but the absence of perturbed disks in the local sample does not allow to conclude if perturbed disks at intermediate redshift look like perturbed local galaxies. On the other hand, due to the items developed in section 4.1 (ordered from the most to the least relevant), we have shown that 30% of the rotating disks may be misclassified using the classification given by Flores et al. (2006). At high redshift, this is particularly critical for galaxies where noise in the outer parts of the velocity field causes off-center dispersion peak. The “corrected” number of rotating disks in IMAGES sample of 63 galaxies may be underestimated by a factor 1.4. In other words, the fraction of rotating disks found in IMAGES may pass from 32% (see above) to 44%. Reciprocally, the fraction of galaxies with anomalous kinematics for the total population, including absorption and emission line galaxies, may thus be lowered from 41% (see above) to 33%. This gives a lower limit to the fraction of galaxies having anomalous kinematics. Indeed, it is likely that a fraction of absorption line galaxies are perturbed and also have anomalous kinematics. In addition, based on the observed dynamics in the IMAGES survey and the possible misclassification due to the faint spatial sampling (no AO and large pixel scale) combined to the small spatial coverage (due to the small sizes of the galaxies) and the low SNR in some cases, the anomalous kinematics and even the complex dynamics for several galaxies could be due to unrelaxed gas disk without involving, in all the cases, a merger. Indeed, Liang et al. (2006) estimated that the gas content in intermediate galaxies at $z \sim 0.6$ was twice larger than in galaxies at the current epoch and that one cannot exclude transient episodes of intense gas accretion making the disk unstable during a relatively short period.

To conclude, the kinematical classification made by Flores et al. (2006) is relevant for a reasonable fraction of rotating disks, assuming that the local velocity dispersion is lower than the rotation velocity. However, low velocity gradient in the velocity field, solid body shape for the rotation curve, flux asymmetries in the H α distribution and other asymmetries like strong bars could cause the IMAGES sample to look more perturbed than it actually is.

5 FITTING METHOD

5.1 General model

To recover the actual kinematic parameters (those from high resolution data) through the degenerate blurred data cube, it is absolutely necessary to model the blurred data. Models consisting in a thin planar disk have been used to retrieve (i) the projection parameters (inclination i with respect to the line of sight, position angle of the major axis PA and systemic velocity V_{sys}) and (ii) the kinematical parameters (center of rotation, rotation velocity and local velocity dispersion σ both as a function of the radius). No hypothesis is done on the nature of the gravitational support (rotation or pressure). The only assumption we do is that the gaseous disk is infinitely thin without any supposition on the amplitude of the velocity dispersion. To constrain the kinematical parameters, this general model allows the use of the blurred

velocity fields alone, the blurred velocity dispersion maps alone or the combination of both.

5.2 Method used

In the following, we have only used the blurred velocity fields. A discussion on this choice is provided in section 5.4. The velocity field is supposed to be axisymmetric and the rotation curve is described by two parameters: the maximum velocity of the model V_t and a transition radius r_t . To avoid any *a priori* shape for the rotation curve describing the redshifted data, we have tested four different models of rotation curve in order to evaluate which ones describe at best the data. These four models all have two free parameters (r_t and V_t). We have chosen rotation curves that have been used for such studies in the literature and which may have rising, flat or decreasing shape: (1) an exponential disk as used for the SINS sample (Cresci et al. 2009); (2) an isothermal sphere as used in mass models (Spano et al. 2008); (3) a model described by an inner linear slope to reach V_t and a plateau after r_t (referred hereafter as “flat model”) as used for OSIRIS data (Wright et al. 2007, 2009); and finally (4) a model described by an arctangent function as used for the IMAGES sample (Puech et al. 2008). The two first models may have a physical meaning, the two last are well known to fit rotation curves of local galaxies. Except for the arctangent model, the maximum velocity of the model V_t is reached at the transition radius r_t . Ideally, to increase the flexibility of the fit, it should be useful to use a rotation curve described by three parameters, but the addition of one more parameter makes the fit difficult to converge since the number of free parameters is already of the same order than the number of data measurements. These models are described in Appendix A (section A5) and illustrated in Figure 6 (using $r_t = 11$ kpc, $V_t = 190$ km s $^{-1}$ and $i = 45^\circ$). In Appendix D, we have over-plotted the four models to the rotation curves (exponential disk in red, isothermal sphere in green, “flat model” in black, and arctangent function in blue). Thus, the global model contains seven parameters (i , PA , V_{sys} , V_t , r_t and the center coordinates). They are determined from a Levenberg-Marquardt nonlinear least-squares χ^2 minimization (Press et al. 1992) and the statistical errors of the fits have been used (see Tables B2 to B5). Since a simple thin rotating disk model is not suited for the description of highly inclined disks, we set an upper limit of 80° to the inclination. Moreover, due to the degeneracy between the velocity and the inclination, we set a minimum inclination of 10° to avoid unrealistically high rotation velocities. It results that 16 galaxies have been excluded from the fitting and thus only 137 out of the 153 galaxies of our sub-sample have been used for the studies presented hereafter.

5.3 Computing method and limitations

From the model parameters previously defined, a high resolution velocity field model is created. Then, the seeing has to be taken into account. In order to do that, ideally, one should know the high resolution line flux map and create a high resolution data cube. Indeed, the line flux weights the contribution of each high resolution spatial element. From observations, it is not yet possible to know the high reso-

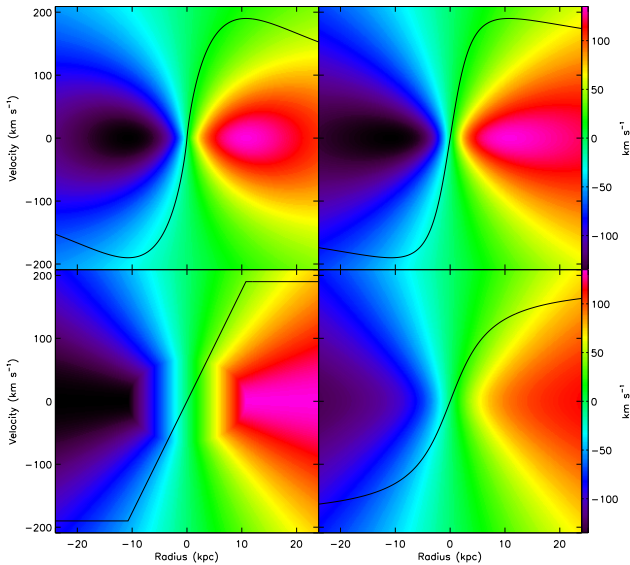


Figure 6. High resolution rotation curves (black curve) superimposed on velocity fields (color image) of the four models used. From left to right and from top to bottom: exponential disk, isothermal sphere, “flat” and arctangent models. The radius (x-axis) is common for the four velocity fields and the four rotation curves. The velocity fields scale is given by the rainbow scale on the right side of the images. The velocity amplitude of the rotation curves is given by the scale on the left side of the y-axis.

lution line flux map. One solution is to use flux distribution models. However, the GHASP local dataset shows that such assumption is abusive since some galaxies display rings, asymmetry or holes. An other solution would be to perform deconvolution from the observed maps. In this study, we simply use the low resolution line map that we interpolate. The method we adopted is more robust than deconvolution technics, but will not recover holes, rings, asymmetries, etc. However, the seeing blur will decrease their effect. Creating a model data cube is a time consuming task. It is possible to avoid the creation of high resolution data cubes by assuming that the H α line is locally well described by a gaussian. This formalism enables to compute directly the blurred velocity field and velocity dispersion map from the seven parameters of the model and is equivalent to generate high resolution data cubes that also need the same assumption. Analytical details are presented in Appendix A. In equation A23, giving the expression of the blurred velocity dispersion, the first term represents the local velocity dispersion contribution whereas the second term corresponds to a velocity shear feature induced by beam smearing effects.

5.4 Local velocity dispersion maps

To constrain the kinematical parameters, the generic model presented in section 5.1 allows the use of the blurred velocity fields alone, the blurred velocity dispersion maps alone or the combination of both. In the forthcoming analysis, the kinematical model has been constrained using the blurred velocity fields only. Indeed, the blurred velocity dispersion maps do not add any constraining power, thus, adding a

dispersion parameter to the model is not necessary to fit the data. In a second step, the model has been used to correct the beam smearing effects in the velocity dispersion map (see Appendix A).

To demonstrate that the use of the velocity dispersion map is not necessary to constrain the kinematical parameters, we have attempted to combine it to the velocity field in order to retrieve the parameters of the model. In order to model the expected local velocity dispersion map an additional hypothesis concerning the physical nature of the velocity dispersion is needed. We may choose the local velocity dispersion to be constant (i.e. the same value everywhere in the plane of the galaxy). This hypothesis, being a possibility since it is mainly what is observed in the GHASP sample (Epinat 2008a, Epinat et al., in preparation), leads to a satisfying agreement with the parameters of the local sample. However, if this method works for the GHASP sample, this is mainly due to the fact that, for nearby galaxies, the velocity shear is high with respect to the local velocity dispersion and the signal-to-noise ratio is high. This might not be the case for distant galaxies for which the signal-to-noise ratio is lower and for which the physical nature of the velocity dispersion is unknown. In addition, even if the method using a unique and constant velocity dispersion works, it not necessary since (i) this parametrical approach needs the introduction of one or more parameters to describe the local velocity dispersion map (radial and azimuthal dependencies, etc.); (ii) the projection parameters and the velocity gradient can be recovered using the velocity field alone; (iii) the constant velocity dispersion could also be retrieved from the velocity field only (see equation A23); (iv) the velocity shear cannot be constrained efficiently when lower than the local velocity dispersion and (v) from a technical point of view, the low signal-to-noise ratio affects more strongly the velocity dispersion (second order momentum) than the velocity (first order momentum) and this would lead to larger uncertainties, in particular for the velocity determination.

To summarize, we favor the method using the velocity field alone since it allows to avoid any *a priori* hypothesis on the local velocity dispersion. The velocity dispersions are corrected from beam smearing effect using the parameters of the model.

5.5 Residual maps of nearby and high redshift galaxies

Velocity fields and rotation curves of low redshift galaxies exhibit a large range of shapes and despite a large number of attempts, no “universal” rotation curve is adequate to describe the large variety and complexity of velocity gradients of rotationally supported galaxies. In nearby spirals observed at high spatial and spectral resolutions, typical deviations of $\sim 10 - 20 \text{ km s}^{-1}$ caused by non circular motion (spiral arms, bar, etc.) are locally observed (Sofue & Rubin 2001; Epinat et al. 2008b,c). Subtracting model describing galaxies dominated by circular motions from the GHASP data thus lead to mean residuals equal to zero and r.m.s. lower than 20 km s^{-1} (Epinat et al. 2008b,c). The velocities observed in the residual velocity fields of both nearby and projected samples have typically the same amplitude. This indicates that the method does not create artefacts.

6 ANALYSIS

6.1 Beam smearing parameter

Since Burbidge & Burbidge (1975), it is known that the turnover radius of a rotation curve for a given galaxy differs if determined from optical line or from HI 21 cm line studies. This is due to the large beams generally used in 21 cm line observations. This artifact may induce spurious effects, for instance, in the determination of the luminous and dark matter distributions and on the internal shape and properties of dark haloes (e.g. Blais-Ouellette et al. 1999). A suitable parameter to characterize the effect of the beam on radio HI data is the ratio R/b , i.e. the ratio between the (Holmberg) radius R of a galaxy and the half-power beamwidth b . Mimicking this definition given by Bosma (1978) suitable for HI data, we define hereafter the so-called “beam smearing parameter” B , ratio between the optical radius of a given galaxy and the seeing FWHM s during its observation (see Table B6 in Appendix B for B values):

$$B = \frac{D_{25}/2}{s} \quad (4)$$

Following Bosma (1978), a “believable” rotation curve in the HI may be obtained from a 2D velocity field when B is greater or equal to seven. This criterion quantifies the spatial sampling needed to model the rotation of a galaxy. Thus, it may be exported to any sampling problem, independently on the nature of the probed component (neutral or ionized gas). In others words, the rotation curve must contain at least seven independent measurements on both sides of the galaxy.

Thanks to the advent of AO, leading to a resolution of typically $0.1''$, we will find $B \gtrsim 10$, for a galaxy with a size $\geq 2''$. Thus, the determination of the kinematical parameters of the galaxy such as the dynamical center, its inclination, position angle and its maximum rotational velocity (V_c^{max}) becomes reliable. When B is large enough, V_c^{max} may be computed from the rotation curve rather than from the width of the central velocity dispersion, in the center of the galaxy.

Yang et al. (2008) estimated that galaxies extending over less than six spatial pixels may lead to a less robust kinematical classification than for more extended galaxies. This is the case for compact galaxies having their half light radius (~ 1 kpc) within one GIRAFFE pixel ($0.52''$). The same authors estimated that with a median spatial coverage of nine pixels at signal-to-noise ratio > 4 the classification is robust and unambiguous.

The beam smearing parameter B in the projected sample ranges from 0.8 to 8.4 (see Table B6), but half of them has $B < 2.4$. In the next sections we will show that an acceptable agreement between high and low resolution rotation curves is only given for $B > 6 - 7$. Nevertheless, $B \geq 2 - 3$ allows the determination of the position angle of the major axis and of the maximum rotation velocity.

6.2 Galaxy projection parameters determination

In this paragraph, the four models described in section 5 have been tested to recover the different kinematical parameters at high redshift discussed hereafter (Tables B2 to

B5). The quality of the models at $z = 1.7$ is tested by their ability to retrieve the parameters at $z = 0$ (given in Table B1). Table 1 presents the percentage of galaxies which are better described by these different models. It shows that the “flat model” is the one that statistically has the best recovery of almost all the parameters. Since the difference with the other models is small in terms of the RMS, it could be that the “flat model” recovers the parameters best because it somehow yields more robust fit. However, this may also reflect the flat general trend of nearby galaxy rotation curves outside the inner solid body part. Indeed, the exponential disk and isothermal sphere rotation curve models are decreasing beyond r_t while the arctangent is rising. From the nowadays observed rotation curves of high redshift galaxies, there is no evidence for decreasing or rising rotation curves. A fraction of the rotation curves are still rising at the last observed point but this is probably because the maximum rotation velocity is not reached. This effect is even worse due to beam smearing effects and moreover to the fact that high redshift galaxies are probably smaller. In the following sections, the plots only show the results obtained using this model.

6.2.1 The center

In nearby galaxies for which high resolution data are available, the determination of the center is very sensitive to the method used to find it. The center may be fixed by the morphology, i.e. the position of the galaxy nucleus seen on high resolution broad-band images in the near infrared or even in the optical. Alternatively it can be computed using the kinematics and becomes very sensitive to asymmetries in the rotation curve, especially in its solid body domain. In this case, it is computed by making the central regions of the rotation curve as symmetric as possible. In best fit model techniques based on least square computations (e.g. ROTCUR in GIPSY package, Begeman 1987) the position of the center may strongly depend on the value of the other kinematical parameters as well as on asymmetries in moment maps ($m = 1$ effects like lopsidedness). The kinematical center may thus be offset by ~ 1 kpc with respect to the morphological center (Hernandez et al. 2005; Chemin et al. 2006). For nearby galaxies, the offset may be much larger than the seeing (up to $60''$), and thus may not be explained by spatial resolution effects. The shift between the center position of the galaxy determined from the photometry and from the kinematics is clearly a function of the morphological type of the galaxy. The strongest discrepancies occur for later type spirals for which the morphological center is not always easy to identify (Hernandez et al. 2005).

In addition to the previous spurious effects, in high redshift data, the determination of the center is strongly affected by the low spatial resolution, the size of the seeing disk being equal to several kpc. Indeed, due to the small number of independent velocity measurements in the velocity field compared to the large number of free kinematical parameters, whatever the model used is, best fit models cannot converge to fix the center. Due both to the low spatial resolution and to the apparent small size of the disk due to flux detection limitation (or intrinsic small size since, in the cold dark matter scenario, the first objects originated from gravitational collapse of the initial fluctuations are smaller),

Table 1. Successfulness of the four $z = 1.7$ models to recover $z = 0$ actual parameters.

Model	Successfulness ⁽¹⁾					RMS ⁽²⁾			
	i ^(a) %	PA ^(b) %	V_c^{max} ^(c) %	σ ^(d) %	RC ^(e) %	i ^(a) °	PA ^(b) °	V_c^{max} ^(c) $km\ s^{-1}$	σ ^(d) $km\ s^{-1}$
Exponential disk	27	29	26	15	37	15	5.8	24.9	8.8
Isothermal sphere	10	8	15	10	12	15	5.8	22.7	8.5
“Flat model”	51	39	41	51	29	14	5.7	22.9	8.0
Arctangent	12	24	18	24	22	16	5.8	21.9	7.9

(1): Percentage of galaxies better described by each model.

(2): RMS between true and fitted parameters for each model.

(a): Kinematical inclination.

(b): Kinematical position angle of the major axis.

(c): Maximum velocity. The RMS is computed from the relative difference between the maximum velocities at $z = 1.7$ and $z \sim 0$ ($\Delta V_c^{max}/V_c^{max}$).

(d): Local velocity dispersion.

(e): Rotation curve shape agreement quantified by the residuals ΔV_c^{mean} between the actual rotation curve at $z = 0$ and the model rotation curve at $z = 1.7$ (cf. section 6.3).

rotation curves for high redshift galaxies tend to show solid body shapes and thus do not display a clear turnover, even if we observe a plateau at high spatial resolution. This effect makes almost impossible the determination of the position of the center using either the method of symmetrization of rotation curves or best fit models.

To determine the position of the center, the central peak induced by the inner velocity gradient observed in the velocity dispersion maps is not more helpful than the $H\alpha$ intensity maps at the same spatial resolution. For galaxies with $B_{\lambda} > 3$ for which the rotation curve shows a slope break, the center may be found from the velocity fields. Moreover, actual high redshift galaxies seem to show large local velocity dispersions (see paragraph 6.5), which makes even more difficult to distinguish the velocity dispersion peak.

In this work, as it has been done for instance in Epinat et al. (2008b), the center of the velocity fields chosen to compute the rotation curves has been fixed *a priori* to match the morphological centers (nuclei) from high resolution images. This method could easily be applied to real high redshift data using for instance HST imagery.

In conclusion, due to the lack of spatial resolution, photometric centers from high resolution broad-band images should be used because kinematical ones are not reliable.

6.2.2 The inclination

The determination of the inclination of a galaxy disk with respect to the plane of the sky is a key parameter since it fixes the amplitude of the maximum rotation parameter V_c^{max} . It is a critical kinematical parameter to determine for high redshift galaxies. For instance, a disk rotating at $V_c^{max} = 200\ km\ s^{-1}$ inclined by 35° with respect to the plane of the sky, might be confused with a disk rotating at $V_c^{max} = 160$ or $270\ km\ s^{-1}$ if the inclination is respectively overestimated by 10° (25°) or underestimated by 10° (45°). Thus, wrong determinations of the inclination increase the dispersion of V_c^{max} hence, for instance, the scatter in the Tully-Fisher relation.

Kinematical inclination

Due to the degeneracy between the inclination and the

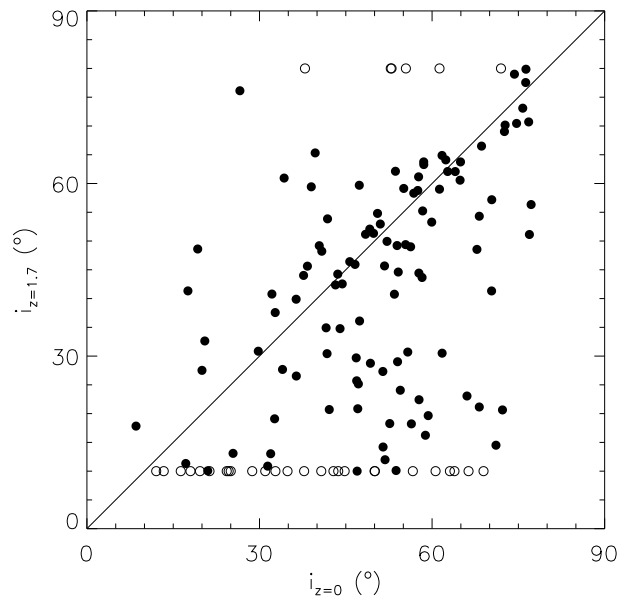


Figure 7. Kinematical inclination computed at $z = 1.7$ using a “flat model” vs actual kinematical inclination evaluated at $z = 0$. Each circle represents a galaxy. The open ones are galaxies which are stacked to the boundaries allowed for any fit (10 and 80°). The line indicates $y = x$.

maximum rotation velocity in kinematical projection models, the inclination is probably the most difficult parameter to recover, even for high resolution kinematical data of local galaxies (Palunas & Williams 2000; Epinat et al. 2008b). Morphological inclination measured on high spatial resolution images is in global agreement with the kinematical inclination but with a rather large scatter. Figure 7 presents the comparison between the kinematical inclinations derived from high resolution velocity fields on the local data in Epinat et al. (2008b) and those obtained from the fit to the redshifted dataset derived using the “flat model”. A high scatter is observed. The four models lead to the same uncertainties in the determination of the inclination but the “flat model” enables to determine an

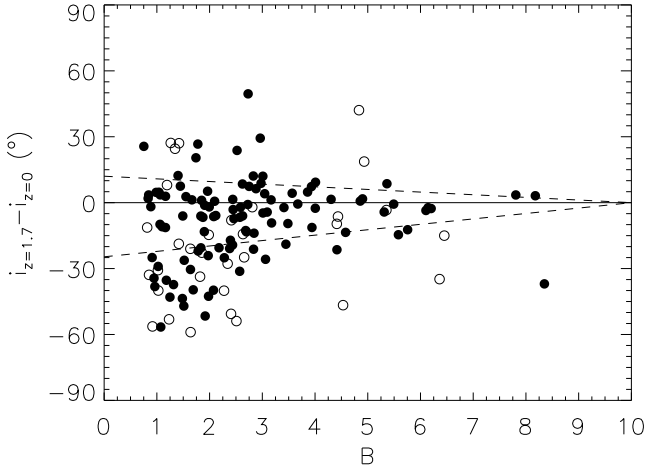


Figure 8. Difference in the kinematical inclination between actual $z = 0$ galaxies and simulated galaxies at $z = 1.7$ using a “flat model” vs the beam smearing parameter B . Each circle represents a galaxy. The open ones are galaxies which are stacked to the boundaries allowed for any fit (10 and 80°). The two dashed lines represent the mean positive and negative errors.

inclination for 77% of the sample while the three other models recover an inclination only for $58 \pm 2\%$ of the sample (“flat model” provides less galaxies with inclination set to the extreme values 10° and 80° compared to the other models). It is also the one which statistically provides the best estimate of the inclination (see Table 1). The four models lead to a RMS between true and fitted inclinations equal to $15 \pm 1^\circ$ and a median equal to $8 \pm 1^\circ$, which means that the inclination can only be recovered with an error lower than $\sim 8^\circ$ in 50% of cases. The standard deviation and the median are also smaller for the “flat model” than for the other models, when considering only the 70 galaxies for which the four models recover an inclination.

Figure 8 shows that, for high redshift galaxies, the scatter in the determination of the kinematical inclination decreases when the beam smearing parameter B increases. It seems that two regimes are observed depending on B below or above 3. The scatter around $i_{z=1.7} - i_{z=0} = 0$ is very large for $B \lesssim 3$ and clearly smaller when $B \gtrsim 3$. Moreover, for $B \gtrsim 3$, we clearly observe that the blurring of the data induces underestimated inclinations in average. This may be explained by the fact that the isovelocity lines are more “open” for low values of B (see discussion in section 3.3). Making the assumption that (i) the discontinuity observed between two regimes is mainly due to numerical instabilities (as suggested by the statistical error bars, not plotted for clarity), (ii) the actual inclination may be recovered for $B \gtrsim 10$ and (iii) the accuracy in the determination of the inclination could reasonably be well quantified by a linear function of B . Two linear fits (represented by the two dashed lines on Figure 8) have been made to model the mean error on the underestimate and on the overestimate of the inclination respectively. The fits avoid the galaxies for which the inclination has been stacked to its lower of higher boundary (open symbols). The equations are:

If $0 < B < 10$,

$$i_{z=1.7} - i_{z=0} = -1.2 \times B + 12 \quad \text{for } i_{z=1.7} - i_{z=0} > 0$$

$$i_{z=1.7} - i_{z=0} = +2.5 \times B - 25 \quad \text{for } i_{z=1.7} - i_{z=0} < 0 \quad (5)$$

While if $B \geq 10$,

$$i_{z=1.7} - i_{z=0} = 0 \quad (6)$$

These formulae are helpful in the case the inclination is determined from the kinematics because they provide the error bars as a function of the beam smearing parameter B .

Morphological inclination

Due to the small angular size of high redshift galaxies, the determination of morphological inclination needs to take into account the seeing. Programs widely used like SEXTRACTOR (Bertin & Arnouts 1996), or like any two-dimensional Gaussian fit, provide axis length measurements that need to be corrected for beam smearing in order to compute the inclination. Models taking into account seeing effects, such as GIM2D (Simard et al. 2002) or GALFIT (Peng et al. 2002) have been developed to compute morphological parameters. In order to model the effect of the seeing, we have created two sets of high resolution models of thin inclined galactic disks using an exponential disk surface brightness radial profile with a disk scale length R_d and a flat luminosity function truncated at $R_{opt} = 3.2R_d$. The disk scale length R_d has been set to various physical lengths (2, 3, 4, 5 and 6 kpc) to see the evolution when the beam smearing parameter $B = R_{opt}/s$ varies and the disks have been inclined from 10° to 80° with a step of 10° .

We have projected these models at redshift $z = 1.7$ using a seeing of $0.5''$ and a pixel size of $0.125''$, as we did with our kinematical data. The axis lengths were determined on both projected and high resolution images using Gauss2dfit IDL routine as the FWHMs of the 2D gaussian function. This fitting procedure gives very accurate results on high resolution images whatever the luminosity profile is, but the lengths are not identical. The effect of the seeing is very well reproduced, for all inclinations, disk scale lengths and luminosity profiles by assuming that the measured major and minor axis a_m and b_m are quadratically overestimated by a fraction C of the seeing FWHM s :

$$\cos i = \frac{b}{a} = \sqrt{\frac{b_m^2 - C^2 \times s^2}{a_m^2 - C^2 \times s^2}} \quad (7)$$

where a , b and i are respectively the actual major axis, small axis and disk inclination. The fraction C almost does not depend on the luminosity profile. Thus for an exponential luminosity profile, $C = 1.014 \pm 0.002$, and for a flat profile, $C = 1.015 \pm 0.010$, which is in both cases very close to 1. The better accuracy obtained for the exponential distribution reflects the fact that an exponential distribution is better described by a gaussian distribution than the flat distribution. Since (i) the high resolution image can be well reproduced by a 2D gaussian function and (ii) blurring the image with the seeing consists in convolving the high resolution image with a 2D gaussian function, it is reasonable that the blurred image is well reproduced by a 2D gaussian function whose measured axis are the quadratic combinations of the true lengths with the seeing.

16 *B. Epinat et al.*

In addition to beam smearing effects, the presence of large clumps may bias the morphological inclination determination. Indeed, numerical simulations as well as observations show that no more than 5-10 large clumps are seen in a disk of a high redshift galaxy. In the case where the inclination is measured using the H α image, even if these large clumps are randomly distributed through the disk, they will visually induce an overestimation of the actual disk inclination. One may preferentially use high resolution broad-band imaging tracing the bulk of stars rather than bright stars located in those clumps.

In conclusion, the inclination should be derived from broad-band images, with high resolution if possible, in order to better constrain the model and to relax from one unity the number of free parameters. Ideally, to avoid contamination due to clumps of star formation in the determination of the inclination, the inclination of the old stellar disk should be measured in the near-infrared rest-frame of the galaxy. We have given a simple correction of beam smearing effects to determine the inclination from axis ratio. When no high resolution imagery is available, we have provided a model to estimate the uncertainties on kinematical inclination. In the following sections, we have fixed the inclination to the kinematical inclination derived at redshift zero.

6.2.3 The position angle of the major axis

Similarly to a bad determination of the inclination, a wrong determination of the position angle of the major axis will lower the maximum rotation velocity V_c^{max} . The use of integral field spectroscopy enables to compute reliable kinematical position angles of the major axis.

For nearby galaxies

The kinematical and photometric position angles have been compared for the whole GHASP sample (Epinat et al. 2008b). The histogram of the variation between kinematical and morphological position angles indicates that for 57% of the galaxies, the agreement is better than 10°; for 79%, the agreement is better than 20° and the disagreement is larger than 30° for 15% of the galaxies. Most of the galaxies showing a disagreement in position angles larger than 20° present a bad morphological determination of the position angle, a kinematical inclination lower than 25° or are specific cases due essentially to the presence of bar and spirals arms. In conclusion, the agreement between morphological and kinematical position angles is satisfactory for rotating disks but not very good for low inclination systems ($i \leq 25^\circ$) and strongly barred galaxies. In any case, integral field spectroscopy constitutes the best technique to determine position angles and as a consequence, rotation curves.

Comparison with projected galaxies

We have compared the kinematical position angles derived from high resolution velocity fields (Epinat et al. 2008b), with those computed from the redshifted data as illustrated on Figure 9 on which the “flat model”, that gives the best estimate for more galaxies than the other models (see Table 1), has been used. Whatever the model used, for more than 70% of the data set, the agreement is better than 5°. Less than 8% have a disagreement larger than 10°. When the

inclination is a free parameter, the estimate of position angles remains as accurate. This is to be pointed out since a good position angle estimate is mandatory to recover the true rotation curve. The accuracy is even better for large galaxies as seen in Figure 10: the agreement is better than 5° for more than 78% of the galaxies with a beam smearing parameter greater than 3. Bars also induce the strongest disagreements, as well as a low H α extent (e.g. UGC1655).

Signature of non-circular motions

The comparison between morphological and kinematical position angles at high redshift should be used to assess the presence of strong bars as well as other non rotation motions. To be able to do that, accurate measurements of morphological position angles are necessary and one should preferentially use high resolution imaging. Indeed, high redshift galaxies are less regular and have peculiar and more disturbed velocity fields than nearby galaxies like the ones studied in the GHASP sample. Thus, the signature of these peculiarities should be quantified through the comparison between morphological and kinematical position angles.

Low inclination high redshift galaxies

The projected GHASP sample may be used to test the biases introduced by long slit observations. One may underline the well known effect that measured rotation velocity declines as misalignment increases. As already mentioned by Weiner et al. (2006) who used a simulated high redshift galaxy from $z = 0$ Fabry-Perot observation, there is a lack of galaxies with high rotation for misaligned slits. Clearly, measuring rotation velocity from a misaligned slit is subject to large errors for galaxies with low inclination. Thus nearly round shaped galaxies (ellipticity $e < 0.25$) should absolutely be avoided for long slit spectrography.

In conclusion, due to their small angular size and beam smearing effects, high redshift galaxies are poorly sampled and appear rounder than they really are. From any type of galaxies and any inclination, the GHASP sample allows us to conclude that the kinematical position angle of 2D projected velocity fields are recovered with an accuracy better than 5° in more than 70% of the cases, giving a higher limit taking into account that high redshift galaxies are intrinsically more disturbed than nearby galaxies. We have stressed that the position angle of the major axis of low ellipticity high redshift disks, are better determined *a posteriori* from 2D velocity fields than *a priori* from imagery, as it is done for long slit observations and finally that the difference between the morphological and the kinematical position angles gives a signature of non axi-symmetric motions.

6.2.4 Systemic velocity

The determination of the systemic velocities is not fundamental but it allows to test again the validity of the models. The systemic velocities are reasonably well recovered from all the models: the systemic velocity can be recovered within $6 \pm 1 \text{ km s}^{-1}$ for half the sample (depending on the model used). This value is probably an upper limit but we have to keep in mind that this value remains rather low because the position of the center has been fixed.

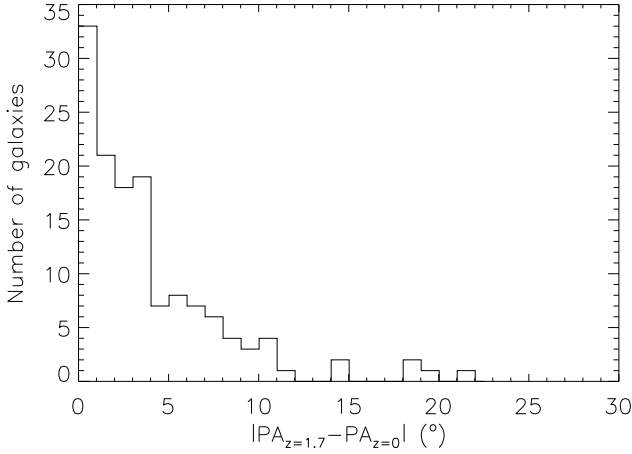


Figure 9. Histogram of the difference in kinematical position angles computed at $z = 0$ and at $z = 1.7$ using a “flat model”.

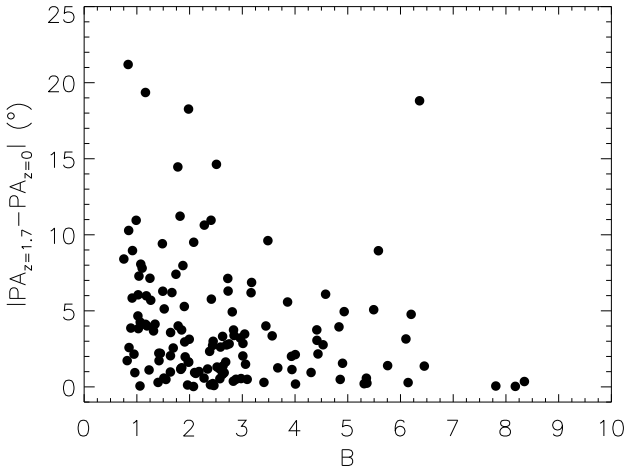


Figure 10. Difference in the position angle between actual $z = 0$ galaxies and simulated galaxies $z = 1.7$ using a “flat model” vs the beam smearing parameter B . Each circle represents a galaxy.

6.3 Shapes of the rotation curves

In cases where $B \gtrsim 10$, it may become possible to address the problem of the shape of the inner density profile in spirals (CORE vs CUSPY controversy) for high redshift galaxies. This problem remains one of the five main further challenges to Λ CDM theory (Primack 2007). With the help of AO, for the largest and brightest galaxies, it will be possible to model the mass distribution in high redshift galaxies in separating luminous from dark halo contribution. It is not possible to separate them using the best data observed without AO (i.e with $B < 3$), e.g. for galaxy Q2343-BX610 located at $z \sim 2.2$ (Förster Schreiber et al. 2006). The question is nevertheless addressable on high quality data obtained with AO, e.g. for galaxy BzK-15504 (Genzel et al. 2006) for which $B \sim 6$. Indeed, in our projected sample for which the beam smearing parameter B ranges from 0.8 to 8.4, an acceptable agreement between high and low resolution rotation curves is only given for the three galaxies with $B > 7$ (cf. rotation curves of UGC 01886, UGC 03334 and UGC 03809 in Appendix D). Five

other galaxies having $6 < B < 7$ already show noticeable differences in the inner parts of their rotation curve.

In order to quantify the ability to recover the shape of the rotation curves for high redshift galaxies, we computed the difference between redshifted rotation curves and original rotation curves at $z = 0$. To avoid biases due to the rotation curve sampling we recomputed velocities with a radial step of 0.5 kpc . On local rotation curves, this is achieved by computing the mean value within radial ranges of 0.5 kpc weighted by the number of bins used to compute the high resolution rotation curves presented in Epinat et al. (2008b,c). On the rotation curves computed along the major axis of the redshifted velocity field, we interpolate the rotation curve within the required radii. For the models, velocities can be computed at any radius.

The difference between the rotation curves is quantified using the parameter ΔV_c^{mean} measuring the mean rotation velocity difference along the whole rotation curves:

$$\Delta V_c^{mean} = \frac{\sum_{i=1}^{n_1} [V_0(r_i) - V_z(r_i)] + \sum_{j=1}^{n_2} [V_z(r_j) - V_0(r_j)]}{n_1 + n_2} \quad (8)$$

where r_i and r_j are respectively the radii for receding and approaching sides, V_0 is the high resolution rotation curve and V_z is the rotation curve of the redshifted data (it can either be the one from the major axis or from the models). The ΔV_c^{mean} parameter enables to distinguish an overestimate from an underestimate of the rotation curves. Figure 11 (top) shows that ΔV_c^{mean} between $z = 0$ actual rotation curves and $z = 1.7$ non-corrected rotation curves is strongly correlated with the inner slope of $z = 0$ galaxies. The inner slope has been computed from a fit to the high resolution rotation curve (cf. Epinat 2008a). $\Delta V_c^{mean} > 0$ indicates that the $z = 0$ rotation curves always display higher mean rotation velocity than the projected $z = 1.7$ rotation curves. Indeed, galaxies with large inner slopes are more affected by the beam smearing. Figure 11 (bottom) displays that ΔV_c^{mean} between $z = 0$ actual rotation curves and $z = 1.7$ “flat model” rotation curves is on average equal to zero and not correlated with the inner slope of $z = 0$ galaxies. ΔV_c^{mean} is positive as much as negative, meaning that the model respectively overestimates and underestimates the mean rotation curves. The scatter around the axis $\Delta V_c^{mean} = 0$ is nevertheless large (mean errors can be as large as $\pm 50 \text{ km s}^{-1}$), pointing out the difficulty to retrieve the actual shape of the rotation curves even if the general trend is recovered. These comments remain valid for the three other rotation curve models. The rotation curve shape can thus hardly be used for mass modeling. Using this parameter to quantify the ability to recover the actual shape of rotation curves, we find that the exponential disk model statistically gives a better description followed by the “flat model” (see Table 1).

We also compared the inner slopes measured from $z = 0$ rotation curves and from the model rotation curves. The scatter around $y = x$ line is very large, indicating that the use of such models to constrain mass modeling is not sufficient. AO observations are thus mandatory for mass modeling.

We find that galaxies with a beam smearing parameter $B \gtrsim 3$ tend to present larger ΔV_c^{mean} , but this trend is not very significant. This is due to the fact that large galaxies are

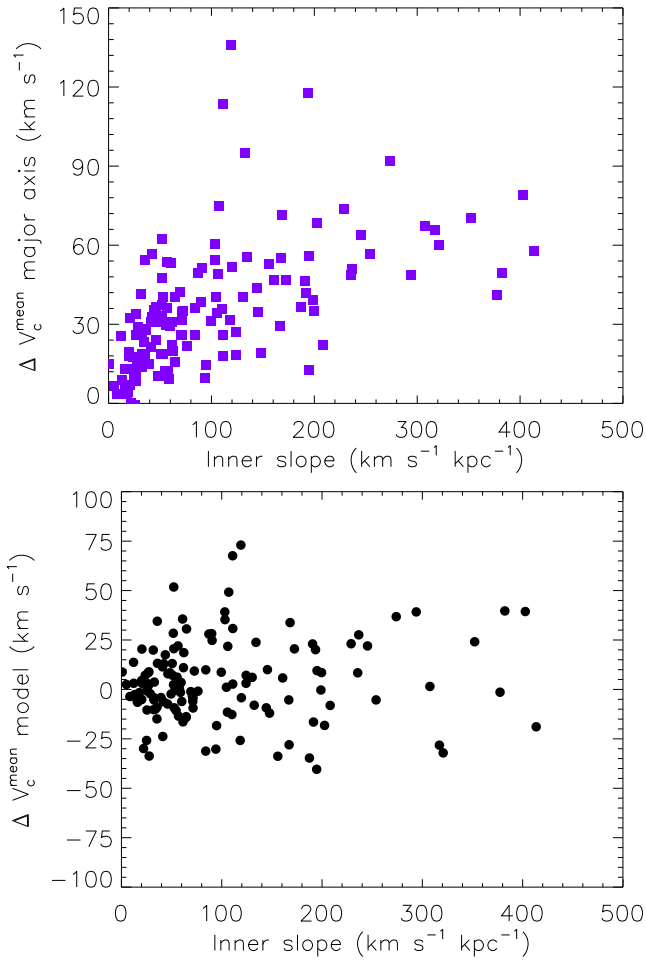
18 *B. Epinat et al.*

Figure 11. Mean rotation velocity difference ΔV_c^{mean} between actual $z = 0$ and different $z = 1.7$ rotation curves vs the actual $z = 0$ rotation curve inner slope. Top: ΔV_c^{mean} is the mean difference between actual $z = 0$ and non-corrected $z = 1.7$ rotation curves. The $z = 1.7$ rotation curves are computed along the major axis of the galaxies. Bottom: ΔV_c^{mean} is the mean difference between actual $z = 0$ and model $z = 1.7$ rotation curves. The $z = 1.7$ rotation curves are computed using a “flat model”.

also the fastest rotators and thus have larger inner slopes of the rotation curve. These large slopes are often explained by the presence of bulges and are well known in massive local galaxies dominated in their central region by the luminous matter distribution. However, without any high resolution broad band images, it is difficult to assess the presence of such bulges in high redshift galaxies. Furthermore, the rotation curve shape for high redshift galaxies is unknown and the presence of a bulge is not mandatory to observe a large inner velocity gradient.

On the other hand, rotation curves based on large clumps velocity measurements tend to underestimate the tangential velocity of the disk. These clumps have a radial velocity component which has to be taken into account (Bournaud, private communication). Thus, AO observations are needed to observe disk regions uncontaminated by the blurring of large clumps.

We conclude that the distance effect is too important

to recover a reliable rotation curve shape, in particular in the inner regions, whatever the beam smearing is up to at least 6 (for larger values, our statistics are very poor), due to the sharper rotation curve shapes of large and massive galaxies. On the other hand, the unknown shape of high redshift rotation curves makes this comparison very approximate since if the slope is lower, the rotation curve shape should be better recovered.

6.4 Maximum rotation velocity analysis

Even without having a complete knowledge of the shape of a rotation curve, the first order analysis of kinematical data may allow a determination of the maximum rotation velocity of the rotation curve V_c^{max} . The latter is an important parameter to recover since it constrains the total amount of dynamical mass of the galaxies and is used for the analysis of the Tully-Fisher relation.

Two methods have been tested to retrieve this parameter. The first one consists in using the rotation curve computed along the major axis, which is equivalent to simulate a long slit aligned with the major axis, without taking beam smearing into account. With long slit spectroscopy, it is however possible to use models that take into account the seeing as done, e.g., by Weiner et al. (2006), but it is not straightforward to evaluate the contribution due to regions outside the slit. The second one consists in using the rotation curve models that account for the beam smearing. For both, V_c^{max} is estimated from the maximum amplitude of the rotation curve within the extent of the velocity field along the major axis. In Figure 12, we compare the maximum rotation velocity determined by Epinat et al. (2008b) with those determined from these two methods. The model presented in this Figure is the “flat model”.

6.4.1 Major axis rotation curve

The maximum rotation velocity V_{rc}^{max} directly determined from the rotation curve along the major axis without accounting for beam smearing is systematically underestimated for galaxies with rotation velocities lower than $\sim 150 \text{ km s}^{-1}$. The effect is even worse when we only consider the rotation curve limited to half the optical radius as it is shown on the Figure 12 (bottom). The maximum rotation velocity derived from rotation curve along the major axis (i.e. equivalent to rotation curves obtained using long slit spectroscopy instruments considering a good alignment with the actual position angle) is reliable for galaxies with an optical radius larger than three times the seeing ($B > 3$), as seen in Figure 13 on which the relative difference between the maximum rotation velocities at $z = 1.7$ and $z = 0$ is plotted as a function of the beam smearing parameter B . The maximum rotation velocities determined from the rotation curve along the major axis are systematically underestimated by more than 25% for galaxies with B lower than 2.5. A correction to recover the actual maximum rotation velocity V_c^{max} depending on the beam smearing parameter B can be applied for smaller galaxies by making the assumption that the rotation curve shape is rather similar for high

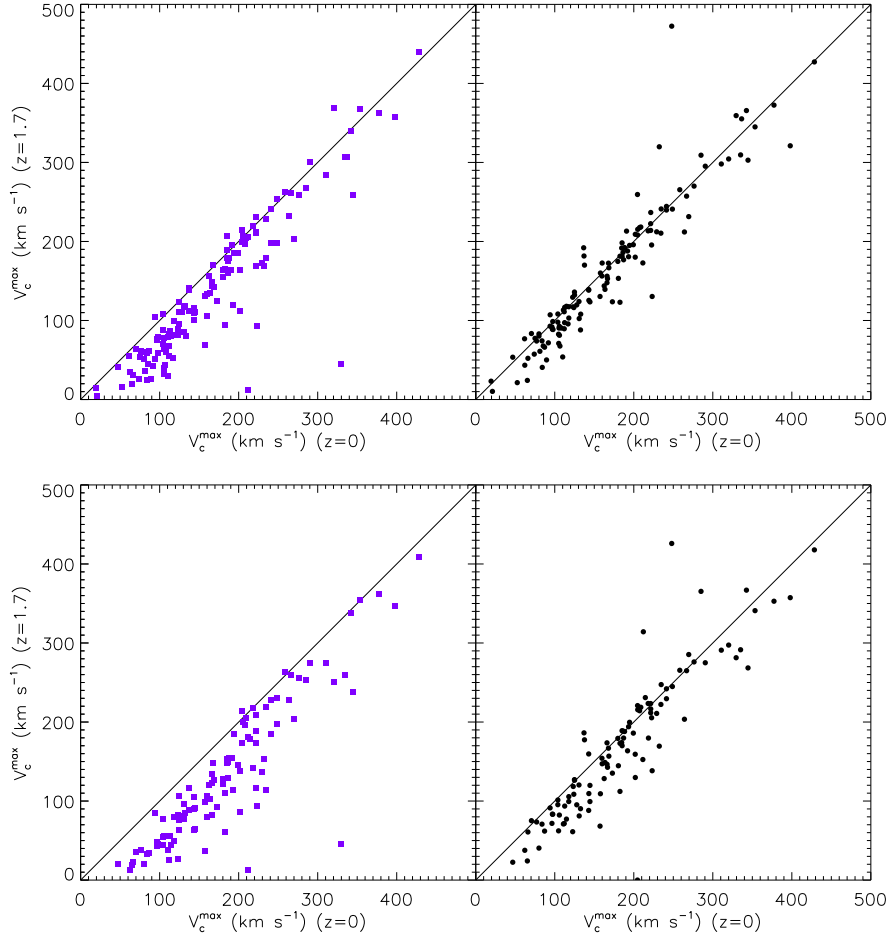


Figure 12. Comparison between the maximum rotation velocities at $z = 0$ (x-axis) and $z = 1.7$ (y-axis). The blue squares (left column) and the black dots (right column) represent respectively the maximum velocities measured along the major axis of the blurred velocity fields and the maximum deduced from the “flat model” fitting. (Top) Velocity fields are truncated at diameters D_{25} (along the major axis). (Bottom) Velocity fields are truncated at diameters $D_{25}/2$.

redshift and local galaxies:

$$V_c^{max} = \frac{V_{rc}^{max}}{0.1(\pm 0.2) + 0.36 B} \quad (9)$$

The uncertainty given in parenthesis provides a range of corrections: the lower limit for the correction is given for $0.1 + 0.2$ and the upper limit for $0.1 - 0.2$.

This method may be improved in taking into account the beam smearing affecting the data along the major axis. Nevertheless, high redshift galaxies are strongly affected by the slit effect since they are poorly sampled due to their small angular size. Indeed, their angular size measured along the minor axis is comparable to the width of the long slit. In addition, the width of the long slit is usually larger than the seeing. Thus, without additional assumption on the spatial or spectral distribution, a confusion between the velocity and the position remains (slit effect). Moreover, flux distribution outside the slit is not constrained in long slit observations. Thus, assumptions on flux distribution are needed to take into account the contribution of external points to the velocity measurements.

6.4.2 Velocity field model

The model fitting enables to recover more reliable maximum rotation velocities even for slow rotators (Figure 12). The four rotation curve models have been compared. We find that the “flat model” statistically recovers better values than the other models (see Table 1). In particular, the three other models give very large maximum rotation velocities in a few case. In the case of exponential disk and isothermal halo models, this is due to the shape of these models that contains a central “bump”. In the case of the arctangent function, this is due to the fact that no plateau is reached unless the transition radius is very small (e.g. Appendix D). Due to the beam smearing, the models are mostly constrained by the inner regions that are more luminous. Indeed, one can observe the rather good agreement of the inner slope of the four models for all the rotation curves presented in Appendix D. The difficulty to recover the maximum rotation velocity for slow rotators is due to the fact that these galaxies are in addition intrinsically smaller, typically of the order of the beam size. The maximum rotation velocities derived from model fitting are statistically in good agreement with the actual

20 *B. Epinat et al.*

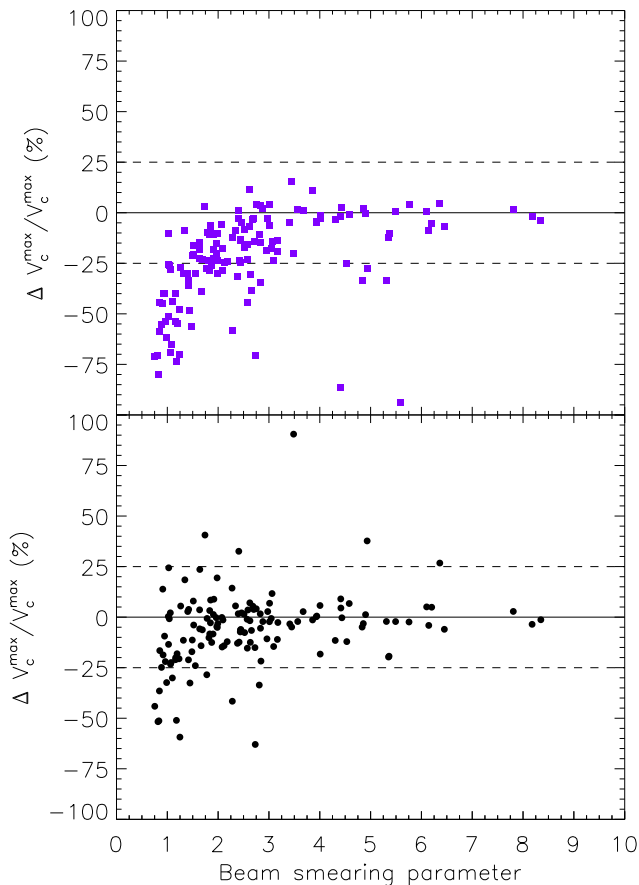


Figure 13. Relative difference between the maximum rotation velocities at $z = 1.7$ and $z = 0$ as a function of the beam smearing parameter B . The symbols are the same as in Figure 12.

maximum rotation velocities. This is especially convincing for the “flat model” (used in Figure 13) for which the determination is better than 25% even for galaxies with B as low as 1. The three other models may overestimate the maximum rotation velocities for some galaxies with B smaller than 2.

In conclusion, we have stressed that the use of integral field instruments sampling the seeing, enables a more robust modeling since off-axis points can be taken into account with less confusion than long slit spectrographs because they have an additional spatial dimension and allow to avoid slit effects. Moreover, we have shown that, using a simple flat rotation curve to model the disk, the maximum velocity can be recovered with an accuracy better than 25%, even for galaxies with a beam smearing parameter as low as 1.

6.5 Velocity dispersion analysis

6.5.1 Mean velocity dispersion and velocity shear

The local velocity dispersion σ is a non trivial physical parameter to recover. Indeed, as explained in Appendix A, for each pixel, the measured velocity dispersion σ_1 is the

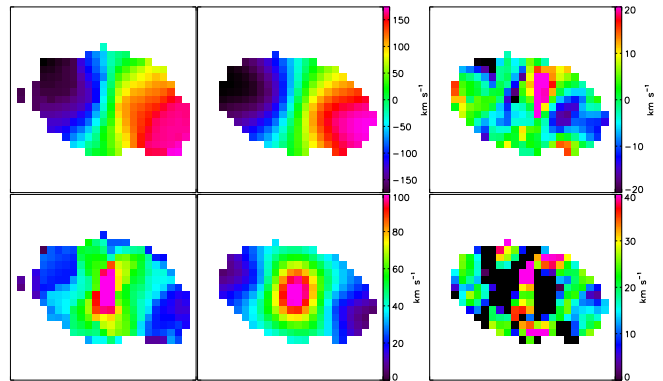


Figure 14. Example of comparison between high redshift simulated data (left column) and high redshift model mimicking the data (middle column) for the galaxy UGC 7901. A “flat model” has been used here. Top line: velocity field. Bottom line: velocity dispersion map. The difference between the simulated high redshift data (left column) and the model (middle column) is given for both the velocity field and the velocity dispersion map (quadratic difference) on the right column. The velocities are given by the rainbow scales on the right side of the images.

quadratic combination of the local velocity dispersion plus a velocity shear feature induced by beam smearing effects. The velocity shear feature can however be extracted from the high resolution modeled velocity field if it correctly describes the observed velocity field. This requires a good estimate of the spatial PSF. Theoretically, as it is the case for the velocity field modeling, the velocity shear feature of the velocity dispersion map also needs the knowledge of a high spatial resolution line emission map.

The local velocity dispersion component is also affected by the low spatial resolution. Thus if we consider that the local velocity dispersion of the gas depends on the gravitational potential, we have to correct the velocity dispersion component from this effect. It is thus necessary to use a velocity dispersion model. In the present study, we avoid this by assuming that the local gas velocity dispersion is almost constant as observed in local galaxies (Epinat et al., in preparation). Thus, we measure the local velocity dispersion as the mean value of the velocity dispersion map quadratically corrected from the velocity shear term derived from the velocity field modeling (illustrated in Figure 14). Weiner et al. (2006) used both velocity and velocity dispersion to constrain their model, using a constant velocity dispersion model. This is an alternative approach from the method used in this paper. This has been discussed in section 5.

The velocity dispersion estimate also depends on the spectral resolution of the data. Our data that have a very high spectral resolution better than 10000 are probably not affected by spectral resolution effects. Spectral resolution effects will be studied in a forthcoming paper since we aim at probing spatial resolution effects only in the present study. Another difficulty with this parameter is its sensitivity to the signal-to-noise ratio that is usually low for high redshift observations. We do not consider this effect here since our data are not affected by a low signal-to-noise ratio. Moreover, if a constant local velocity dispersion model is assumed, all the points of the map should have the same velocity dispersion. There should be at least several points in the map with

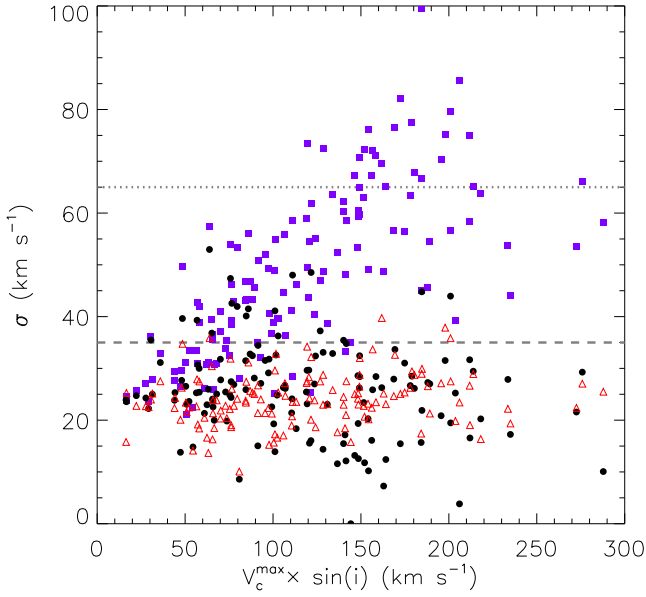


Figure 15. Velocity dispersion as a function of projected maximum velocity measured on $z = 0$ velocity fields. Each point represents a galaxy. Blue squares correspond to the seeing-induced central velocity dispersion measured on $z = 1.7$ maps (without applying any corrections). Red-open triangles represent the mean velocity dispersions measured on $z = 0$ galaxies. The black dots correspond to the mean velocity dispersion measured on corrected velocity dispersion maps of $z = 1.7$ galaxies using a “flat model”. The grey dashed and dotted lines respectively indicate the mean velocity dispersion in the IMAGES $z \sim 0.6$ sample and in a sample of forty-two $1 < z < 3$ objects observed with OSIRIS and SINFONI.

a sufficient signal-to-noise ratio in order to do an accurate measurement.

We conclude that a model is helpful to disentangle the velocity shear present in the velocity dispersion map from the local velocity dispersion. This is dramatically true for galaxies with a small beam smearing parameter.

6.5.2 Velocity dispersions vs rotation velocities

In Figure 15, the velocity dispersion is plotted as a function of the projected maximum velocity (observed at $z = 0$) corrected for the inclination. Red-open triangles represent the velocity dispersion measurements for the local data. No dependency is observed with the projected maximum velocity. The local velocity dispersion does not depend either on the total radial velocity amplitude of the galaxy, suggesting that it does not depend on the galaxy mass. Blue squares represent seeing-induced velocity dispersions measured at the center of $z = 1.7$ velocity dispersion maps and show a clear correlation with the projected maximum velocity. However, a large scatter is observed. This may be explained by the dependency of rotation curve shape with the true maximum velocity (Rubin et al. 1985; Persic et al. 1996; Catinella et al. 2006), in particular, the inner gradient is larger for fast rotators. These fast rotators observed with a low inclination should thus present a higher central velocity dispersion peak than slower rotators observed with a high inclination. This

trend shows that the central velocity dispersion gives an indication about the shape of the inner rotation curve as well as the maximum velocity. The black dots represent the mean velocity dispersion measured on corrected velocity dispersion maps using a “flat model” being the one that statistically allows the best recovery of the local velocity dispersion (see Table 1). By comparing the error on the corrected velocity dispersion and the beam smearing parameter B (not plotted), we note that the correction is statistically underestimated for galaxies with $B < 2$, and often overestimated for other galaxies, probably due to both an insufficient resolution for the line flux maps and the rotation curve shape that rises rapidly for faster rotators. However, the correction is satisfactory since no strong correlation is seen anymore with the projected maximum velocity. Moreover, due to its low local velocity dispersion, the GHASP sample provides a strong constrain on the method. Indeed, the velocity shear contribution to the blurred velocity dispersion maps may be negligible for dispersion-dominated galaxies.

In conclusion, we have noticed that the mean gaseous local velocity dispersion does not depend on the mass for nearby galaxies contrarily to the projected sample. We have shown that the model we used for the projected galaxies is suitable to model high redshift kinematics. Indeed, it allows to remove the unresolved velocity shear contribution due to beam smearing and thus to recover the uniform velocity dispersion observed in nearby galaxies.

6.5.3 Velocity dispersion estimation used for the IMAGES sample

Flores et al. (2006) used the minimum observed value in the velocity dispersion maps in order to have an estimate of the local velocity dispersion. Indeed, it is necessary to discard from this measurement all the pixels affected by the velocity shear.

To test this method with our reference sample, the minimum velocity dispersion of the uncorrected and uncut velocity dispersion map has been compared to the mean velocity dispersion at $z = 0$. We find that using such an estimate, the velocity dispersion is underestimated by a mean factor around 2. We obtained a good agreement by estimating the velocity dispersion as the mean of the points with the 20% lowest velocity dispersion values on the redshifted velocity dispersion map, not limited to the optical radius. The comparison between this estimate and the mean velocity dispersion at $z = 0$ is presented in Figure 16. Such an estimate has been motivated by the fact that $z = 0$ velocity dispersion fluctuates from one region to another one. Moreover, the velocity dispersion is often slightly lower in the outer parts of galaxies (Epinat et al. in preparation), thus, the mean velocity dispersion at $z = 0$ should be larger than the outer velocity dispersion. Such velocity dispersion measurements depend on the map extent, and thus on the signal-to-noise ratio of high redshift observations. This makes the estimator sensitive to this parameter in particular for rotation-dominated galaxies. Indeed, for dispersion-dominated galaxies, the local velocity dispersion may be easier to recover as the velocity shear is relatively less important. Note that this comparison with FLAMES/GIRAFFE data only indicates a trend since the sampling used in the present paper does not match the sampling of IMAGES dataset.

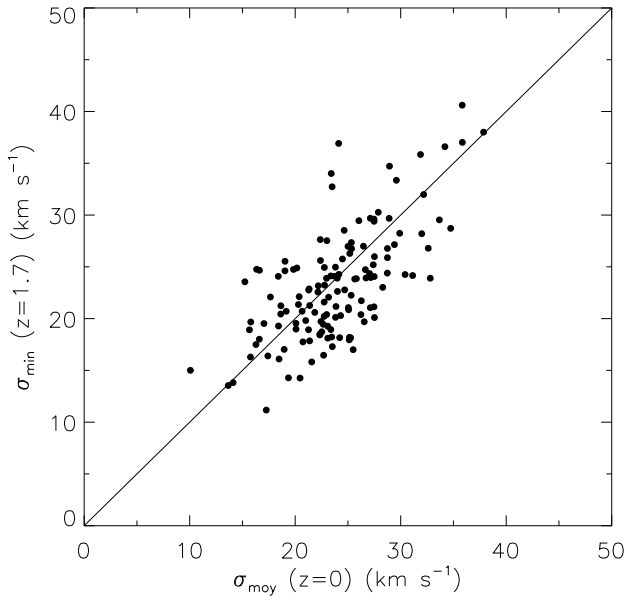


Figure 16. Minimum velocity dispersion of $z = 1.7$ galaxies as a function of the mean velocity dispersion at $z = 0$.

The conclusion is that this method allows to estimate the local velocity dispersion without the help of any model. However, it is very sensitive to both the signal-to-noise ratio and to the radial extent of the galaxy.

6.5.4 Unresolved beam and line-of-sight effects

The GHASP sample of local galaxies allows to test if high local velocity dispersions observed at high redshift may be the result of the integration, within a seeing disk, along the line-of-sight of individual HII regions.

From an observational point of view, in GHASP disks, the very central regions being excluded, the typical size of a bin for which the $H\alpha$ emission has a signal-to-noise ratio ~ 7 ranges from less than 0.1 kpc (one pixel) for the intense $H\alpha$ knots to $\sim 0.5 \text{ kpc}$ for the most diffuse regions (Epinat et al. 2008b,c).

The local velocity dispersion within those bins (signal-to-noise ratio ~ 7) ranges from 10 to 30 km s^{-1} . When these local galaxies are projected at high redshift, a seeing disk ($\sim 0.5''$) may thus contain more than 100 bins, mixing along the line-of-sight the velocity components of several tens to several hundreds of individual regions. Taking into account the local velocity dispersion at $z = 0$ and the number of regions integrated within a seeing disk at high redshift, even with the high spectral resolution of GHASP (which is not reached by far by any IFU spectrographs on 8-10 meter-class telescopes), the different components are undiscernible in the spectrum along the line-of-sight.

In conclusion, one has no way to know if the large local velocity dispersions seen in high redshift galaxies are due to very large, extended and massive clumps or, at the opposite, to the addition and the superposition along the line-of-sight within a seeing disk of a large amount of individual smaller clumps. This should be addressed using high resolution obser-

vations of the luminosity distribution (HST, AO or future JWST imaging).

6.5.5 Velocity dispersion evolution with the redshift

In order to study the evolution of the velocity dispersion with the redshift, we have compared the GHASP local sample with IMAGES sample (at $z \sim 0.6$) and with $z > 1$ samples observed with SINFONI and OSIRIS. We have estimated the minimum value of the velocity dispersion map for each of the 63 galaxies of the IMAGES sample following Flores et al. (2006) and we have used the velocity dispersion values given by the authors for 42 $1 < z < 3$ galaxies observed with SINFONI (SINS and MASSIV pilot run) and OSIRIS.

At $z = 0$, the GHASP sample used in this paper provides a mean local velocity dispersion of $24 \pm 5 \text{ km s}^{-1}$. The mean local velocity dispersion for the whole IMAGES sample is $35 \pm 18 \text{ km s}^{-1}$ while it reaches $\sim 65 \pm 25 \text{ km s}^{-1}$ for $1 < z < 3$ galaxies (as illustrated by the dashed and dotted lines in Figure 15).

Moreover, it is interesting to notice that the mean local velocity dispersion in the IMAGES sample does not significantly differ for “rotating disk” ($37 \pm 10 \text{ km s}^{-1}$), “perturbed rotation” ($34 \pm 24 \text{ km s}^{-1}$) and “complex kinematics” ($35 \pm 17 \text{ km s}^{-1}$). Using an alternative approach to compute the local velocity dispersion (excluding the central hot region and weighting by the signal-to-noise ratio after a 1-sigma bootstrapping), Puech et al. (2007) estimated slightly higher values ($\sim 45 \text{ km s}^{-1}$), but the previous conclusion does not change. This may indicate that different physical mechanisms (cosmological gas accretion, galaxy accretions, turbulence generated by self-gravity and/or star formation, etc.) may occur for galaxies having different histories and however lead to velocity dispersions having typically the same value. Alternatively, considering that a fraction of IMAGES “perturbed rotators” may be classified as “rotating disks” (see section 4), this could explain why no clear difference in the velocity dispersion is observed between both categories.

Contrarily to what is observed for nearby galaxies (see Figure 15), as already noticed in Epinat et al. (2009b), for $z > 1$ galaxies, the maximum rotation velocities decreases when the local velocity dispersion increases (if we exclude the values from Law et al. 2009, since the latter are limited to the very inner part of the galaxies). Indeed, for the local GHASP sample, when no correction for beam smearing is applied, the velocity dispersion increases with the maximum rotation velocity. When the correction is applied, the velocity dispersion of these galaxies is not correlated to the maximum rotation velocity.

In conclusion, we note a clear and continuous increase of the local velocity dispersion with the redshift. This indicates an evolution of the galactic dynamics through the ages, from eleven Gyr ($z \sim 2.5$) to six Gyr ($z \sim 0.6$) up to now ($z \sim 0$). This might be due to the evolution of the dynamical support (dispersion towards rotation via e.g. violent relaxation processes) and/or to the evolution of non-circular motions (instabilities due to the presence of bars, etc.) and/or chaotic motions (turbulence, energy injection due to high star formation rates and/or AGNs).

6.6 Gravitational support

The ratio of the maximum circular rotation velocity V_c^{max} and the local velocity dispersion σ measures the nature of the gravitational support of a system in equilibrium. A high circular velocity compared to velocity dispersion ($V_c^{max}/\sigma > 1$) is the signature of a rotation-dominated gravitational support, whereas a lower ratio ($V_c^{max}/\sigma < 1$) is the signature of a dispersion-dominated system, as it is the case for elliptical galaxies. For nearby spirals, characteristic values for the local gaseous velocity dispersion σ range from 10 to 40 $km s^{-1}$ (see Figure 15).

An interesting possible probe of the state of dynamical galaxy evolution is given by the behavior of this ratio V_c^{max}/σ with the redshift. To test the beam smearing effects on the measure of the ratio V_c^{max}/σ , we have computed it for the projected GHASP sub-sample and compared it to actual distant galaxies. The ratio V_c^{max}/σ as a function of V_c^{max} has been plotted in Figure 17 for both local (top) and high redshift observed galaxies (bottom).

We have plotted GHASP local galaxies projected at $z = 1.7$ using dots. These points have been computed using the maximum velocity V_c^{max} derived from kinematics modeling and the velocity dispersion σ corrected for beam smearing effects as explained in section 6.5. Since the GHASP sample is mainly composed of rotation-dominated galaxies, our sub-sample shows values of the ratio V_c^{max}/σ lower than 2 only for very slow rotators ($V_c^{max} < 100 km s^{-1}$) and values ranging from 5 to 20 for rotators ranging from 100 to 400 $km s^{-1}$. This ratio is strongly correlated with V_c^{max} for local galaxies (slope 0.048 $km^{-1} s$), but with a large scatter. The correlation is expected since the velocity dispersion of the gas is rather constant with the maximum velocity for local galaxies, and the large scatter is due to the difficulty to recover both V_c^{max} and σ for the projected galaxies because of beam smearing effects. We have also plotted with circles the values without any correction for the beam smearing: the maximum velocity being computed from the rotation curve along the major axis and the velocity dispersion being estimated as the mean of the uncorrected velocity dispersion maps. The corresponding regions in which 85% of the points are lying have been reported on both plots of Figure 17 using vertical purple and grey horizontal hatchings. They respectively refer to beam smearing corrected and uncorrected points (see sections 6.4 and 6.5). Since the uncorrected maximum velocity and velocity dispersion are respectively underestimated and overestimated, grey and purple areas show only a small overlap. This grey area represents the “worst” estimation for the redshifted dataset.

From long slit spectrography, line-of-sight kinematic line widths (σ) of several hundreds good-quality measurements galaxies at $z \sim 1$, Weiner et al. (2006) roughly divided their sample into rotation ($V_c^{max}/\sigma > 1$) and dispersion-dominated galaxies ($V_c^{max}/\sigma < 1$). Dispersion-dominated galaxies are blue, mostly irregular and are not elliptical galaxies. These authors conclude that these galaxies probably have a disordered kinematics that is integrated over by the seeing.

Förster Schreiber et al. (2006) found that their three best rotators candidates at $z \sim 2$ show $V_c^{max}/\sigma \sim 2 - 4$, they concluded that these very gas rich disks are dynamically hot, geometrically thick and unstable to global star for-

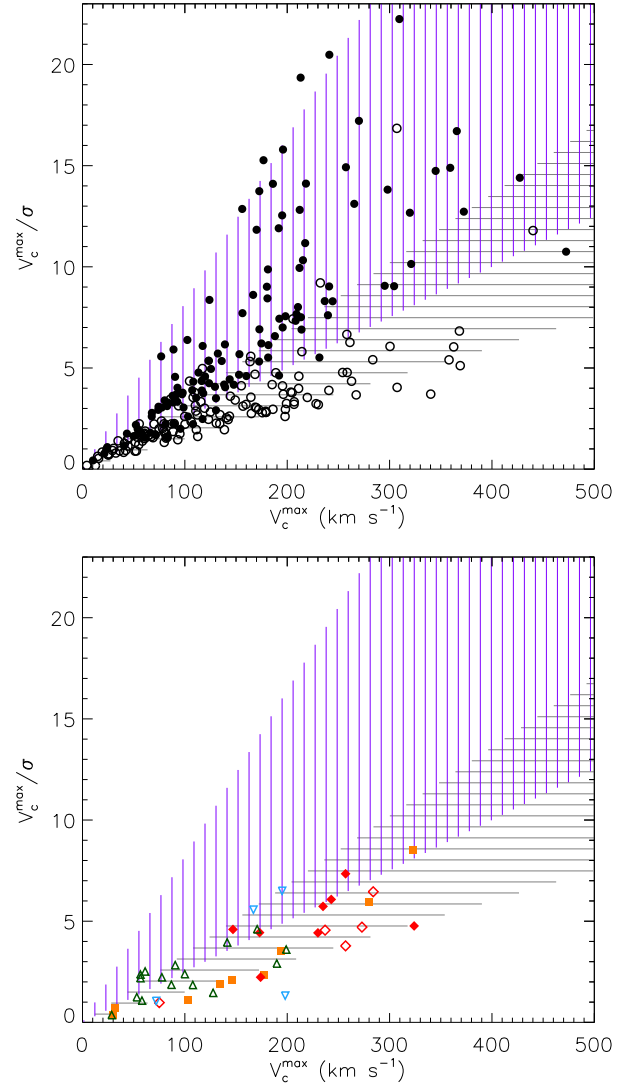


Figure 17. Ratio between the maximum rotation velocity and the mean velocity dispersion as a function of the maximum rotation velocity. **Top.** GHASP projected sub-sample. Circles: values uncorrected for the beam smearing. 85% of these circles are within the grey horizontal hatchings zone. Dots: values corrected for the beam smearing using the rotating disk modeling. 85% of these dots are within the purple vertical hatchings zone. The grey and purple hatchings are reported in the Bottom figure for reference. **Bottom.** Observed high redshift galaxies. Open symbols correspond to observations using AO. Red rhombuses: SINS rotating disks at $z \sim 2$ (Cresci et al. 2009). Orange squares: MASSIV pilot run galaxies at $z \sim 1.5$ (Epinat et al. 2009b). Green triangles: $z \sim 3$ Law et al. (2009) OSIRIS observations. Blue upside down triangles: rotating disks in Wright et al. (2007, 2009) at $z \sim 1.5$ observed with OSIRIS.

mation and fragmentation. These authors argue that these observations may be described by simulations (Immeli et al. 2004a) of gas-rich disks in which clumpy fragmentation disks are unstable and star forming clumps evolve by fuelling the galaxy center by dynamical friction and finally form a central bulge on ~ 1 Gyr time scale. Genzel et al. (2008) and Cresci et al. (2009) extended the SINS sample first described by Förster Schreiber et al. (2006) to 13 rotating disks candi-

dates for which local velocity dispersion has been measured. They found $V_c^{max}/\sigma \sim 1 - 6$ with a mean value of 4.6.

Using 16 galaxies in the same range of redshift ($z \sim 2$), Law et al. (2009) found $V_c^{max}/\sigma \sim 0.1 - 1$ with a mean value of 0.5. These values are notably different from the SINS sample. As mentioned in section 3.2.9, the mean radius of the galaxies observed by Law et al. (2009) is eight times lower than for SINS galaxies. Moreover, their parameters (maximum velocity and velocity dispersion) are not corrected for the beam smearing and for inclination. Indeed, their maximum rotation velocity is the half of the whole shear whereas the velocity dispersion is flux-weighted, i.e. dominated by the inner regions. Similarly to Genzel et al. (2008), Law et al. (2009) concluded that the high velocity dispersion they observe may be neither a merger nor a disk, but rather the result of instabilities related to cold gas accretion.

In the redshift range of $1.2 < z < 1.7$, a compilation of 13 galaxies classified as rotators extracted from Wright et al. (2007), Wright et al. (2009) and Epinat et al. (2009b) provides $V_c^{max}/\sigma \sim 0.4 - 8.5$ with a mean value of 3.1. These values are comparable to the ones found at higher redshifts. Epinat et al. (2009b) argued that, considering the samples presently available, several processes may drive galaxy evolution. For instance, for their perturbed rotators, it is not straightforward to disentangle whether the high velocity dispersion is the result of gas accretion or gas rich minor mergers.

Bournaud et al. (2008) found $V_c^{max}/\sigma \sim 1 - 2$ (not corrected for inclination) for a clumpy galaxy at $z = 1.6$ and proposed an internal fragmentation formation scenario of a gas-rich primordial disk becoming unstable. In comparing their SINFONI observations to numerical models, Bournaud et al. (2007) concluded that (i) complex morphology can result from the internal evolution of an unstable gas-rich disk galaxy and (ii) irregularities in the velocity field (\sim several tens of $km\ s^{-1}$) can be explained by clump-clump interactions that cause the individual velocity of each clump to differ significantly from the initial rotation velocity.

In Figure 17 (bottom), we have over-plotted the points corresponding to real high redshift galaxies. The values of these points have been corrected for beam smearing. Green triangles correspond to the galaxies observed by Law et al. (2007, 2009) at $z \sim 3$ with OSIRIS. These authors did not provide the inclination of the disks, thus we have used a mean statistic inclination of 45° to compute the maximum rotation velocity in the galaxy plane. Moreover, we have corrected these velocities for beam smearing effect using the lower limit given in equation 9. This correction only provides lower values for V_c^{max} since, due to the very small extent of these objects, the plateaus may not be reached. The local velocity dispersion has also been estimated from the velocity dispersion maps using the estimation given in section 6.5.3 instead of the flux-weighted velocity dispersion provided in Law et al. (2009) uncorrected for beam smearing effects. Blue upside down triangles are the rotating disks also observed with OSIRIS by Wright et al. (2007, 2009) at $z \sim 1.5$. Orange squares are galaxies part of MASSIV pilot run (Epinat et al. 2009b) and red rhombuses correspond to SINS rotating disks Cresci et al. (2009), both observed with SINFONI. Open symbols correspond to AO corrected observations. SINFONI setup in natural seeing observation has a pixel size of $0.125''$ and a seeing around $0.5''$. Observations

using AO use a pixel size of $0.05''$ with a seeing up to $0.2''$. SINFONI spectral resolution is 4500 ($70\ km\ s^{-1}$) in K band, 3000 ($100\ km\ s^{-1}$) in H band and 1900 ($160\ km\ s^{-1}$) in J band. OSIRIS observations are using AO devices in order to have a seeing up to $0.1''$ and use a pixel size of $0.05''$ with a spectral resolution of 3600 ($85\ km\ s^{-1}$).

All these authors observed that, for a given circular velocity, V_c^{max}/σ is lower for high redshift galaxies than for local galaxies. Several of them corrected for beam smearing but others did not. Since beam smearing artificially causes lower values of V_c^{max}/σ , the values for the projected sample obtained without correcting for the beam smearing effects provide a lower limit for nearby disks. Figure 17 shows that V_c^{max}/σ values for high redshift galaxies, derived taking into account the seeing, are below this lower limit. This is thus a strong evidence for dynamical evolution between $z > 1.5$ and $z \sim 0$.

We observe that the correlation for high redshift galaxies has a lower slope ($0.014\ km^{-1}\ s$) than for local galaxies, showing that high redshift galaxies are more dispersion-dominated. Ideally, to probe the gravitational potential, dispersion measurements should be done on the non collisional stellar component rather than on the collisional gas component. However, stellar kinematics are unreachable at high redshift with the current instrumentation. We could also notice that it is possible that the extent of high redshift galaxies may be lower than for low redshift galaxies and thus the maximum velocity may be missed. Another care is that it is probable that high redshift surveys have selection biases. Moreover, all these high redshift observations have a much lower spectral resolution than the local sample. We expect from this low spectral resolution that velocity dispersion correction is less accurate and thus that velocity dispersion measurements have much larger uncertainties.

6.7 Tully-Fisher relation

The Tully-Fisher relation is a way to constrain galaxy formation models as well as to probe the dynamical stability of galaxies.

We computed the B-band Tully-Fisher relation for both local and redshifted GHASP sub-sample. As it has been done in Epinat et al. (2008b,c), the Tully-Fisher relation has been computed as the mean relation from the one obtained using a fit on absolute magnitudes as dependent variable and the one obtained using a fit on velocities as dependent variable. The errors are estimated as the difference between those two fits.

The GHASP sample is limited to rotating disks. It does not contain strongly interacting galaxies nor galaxies supported by random pressure. Nevertheless, as discussed in section 4, once projected and following the classification done by Flores et al. (2006), the kinematics of some galaxies may resemble to perturbed rotators. We first did not exclude any galaxy since we want to compare the scatter using the same projection parameters for both. Moreover, at high redshift, all the galaxies could be interpreted as rotating disks since they all present a velocity gradient at high redshift. Epinat et al. (2008b) found a slope of -7.2 ± 1.2 from the whole GHASP sample but excluding several galaxies because of their low inclinations (that induce strong uncertainties), or because their maximum velocity is proba-

Table 2. Fits of local and distant Tully-Fisher relation.

Sample	Band	Slope a ^(a)	Zero point b ^(a)	Comment
GHASP local whole sample	B	-7.2 ± 1.2	-3.97 ^(d)	Free slope, from Epinat et al. (2008b)
GHASP local sub-sample, RD ^(b) + PR ^(c)	B	-6.2 ± 2.2	-6.23 ^(d)	Free slope
GHASP projected sub-sample, RD + PR	B	-5.2 ± 1.9	-8.68 ^(d)	Free slope
GHASP local sub-sample, RD	B	-7.4 ± 1.7	-3.50 ^(d)	Free slope
GHASP projected sub-sample, RD	B	-6.6 ± 1.4	-5.38 ^(d)	Free slope
GHASP projected sub-sample, RD	B	-7.4	-3.67 ± 0.10	Fixed slope
SDSS local subsample	K	-6.88 ± 0.57	-6.54 ± 1.33	Free slope, from Puech et al. (2008)
IMAGES $z \sim 0.6$, RD	K	-7.24 ± 1.04	-5.07 ± 2.37	Free slope, from Puech et al. (2008)
IMAGES $z \sim 0.6$, RD	K	-6.88	-5.88 ± 0.09	Fixed slope, from Puech et al. (2008)

(a): Tully-Fisher relation: $M = a \times \log V_c^{max} + b$. (b): RD refers to rotating disks. (c): PR to perturbed rotators. (d): Error bar on the zero point is not provided for the GHASP sample when the slope is free since it is very sensitive to changes in the slope. Keeping the slope fixed would lead to errors around 0.1.

bly not reached. From the local sub-sample defined in the present paper, the slope is estimated to -6.2 ± 2.2 . This lower slope (although within the errors) can be explained by selection biases (see section 3.2.7): we only excluded the smallest galaxies, but not those that do not reach their maximum velocity or those with an inclination lower than 25° . In particular, low mass galaxies hardly reach their maximum velocity within the optical radius, and Epinat et al. (2008b) have shown that the fastest rotators present a lower slope since they are less luminous than expected from local Tully-Fisher relation. The Tully-Fisher relation derived from the redshifted dataset is still lower (-5.2 ± 1.9) but compatible with the one derived from the local sub-sample within the error bars (see Table 2). This lower slope can be explained by beam smearing effects. Indeed, as shown in section 6.4, the maximum velocity is more difficult to recover for slow rotators than for fast rotators for which the model is better constrained. The scatter for those two slopes are rather similar and larger than the one derived by Epinat et al. (2008b), due to selection effects, in particular, the inclination inducing the strong scatter.

Absolute K-band magnitudes have been obtained for the IMAGES sample (Flores et al. 2006). Unfortunately, K-band photometry for the GHASP sample is not available, thus, we compare the B-band Tully-Fisher relation for the GHASP sample to the K-band Tully-Fisher relation for the IMAGES sample (Puech et al. 2008). This induces color-luminosity biases (e.g. Sakai et al. 2000; Verheijen 2001). This data obtained with FLAMES/GIRAFFE instrument have a spectral resolution very similar to that of the GHASP redshifted data. Let’s notice however that GIRAFFE has a lower spatial resolution ($0.8''$ seeing and $0.52''/\text{pixel}$) than our simulations and a small spatial extent (6 by 4 spaxels).

Since a simple magnitude correction consists in adding a given value, the slopes should be comparable. Our slope is found to be lower than theirs (see Table 2). Their magnitude range however is tighter than ours as shown in Figure 2 and our sample thus contains lower luminosity systems for which the maximum velocity has not been derived with confidence. The slope determination is also highly dependent on the fitting method used. Surprisingly, assuming no evolution effects, we would have expected from IMAGES data a Tully-Fisher relation with a lower slope due to the instrumental spatial resolution differences between both samples. Indeed, the slope of the Tully-Fisher relation obtained from the pro-

jected GHASP sample is lower than the one obtained from high spatial resolution rotation curves (see Table 2). In addition, we have checked that this effect remains true whatever the magnitude range, in particular when the faintest galaxies are excluded.

In order to derive the Tully-Fisher relation in the same conditions as Puech et al. (2008), we also computed a Tully-Fisher relation using only galaxies that would be classified as “rotating disks”. Indeed, we noticed on the Tully-Fisher relation plots that some of the galaxies that Puech et al. (2008) classified as “complex kinematics” and “perturbed rotators” have their counterparts in our sub-sample, corresponding to galaxies that would be misclassified. By using “perturbed rotators” and “rotating disks” to derive their slope, they would probably have found a lower slope. Indeed, this is the trend that we observe when we use the whole GHASP sub-sample (see Table 2). In Figure 18 GHASP galaxies classified as “rotating disks” correspond to full points, and galaxies misclassified are displayed as open circles. The red continuous and black dashed lines correspond to the Tully-Fisher relation computed when using only galaxies that would be classified as “rotating disks” respectively for local and redshifted samples. These determinations are consistent with local determination: from the non redshifted sample we find a slope of -7.4 ± 1.7 and for the redshifted sample we find a slope of -6.6 ± 1.4 that is in agreement with the one derived at redshift $z \sim 0.6$ by (Puech et al. 2008). However, the trend is still to find a lower slope for the redshifted sample, although the difference is lower than the statistical error bars. The scatter also then becomes lower. Indeed, using only galaxies that would be classified as rotating disks imply that most of the low inclination systems are excluded as well as those with a solid body rotation curve for which the maximum is not determined with confidence. The use of the GHASP sample may indicate that the differentiation between “rotating disks” and “perturbed rotators” could be incorrect since GHASP galaxies misclassified as “perturbed rotators” are actually “rotating disks” and have the same behavior in our Tully-Fisher relation that in $z \sim 0.6$ relation. However, this classification enables in fact to exclude galaxies for which the lack of spatial resolution induces biases in the parameters determination.

Since Puech et al. (2008) used K-band magnitudes, we cannot compare directly the Tully-Fisher zero point. However, the comparison between local and high redshift zero

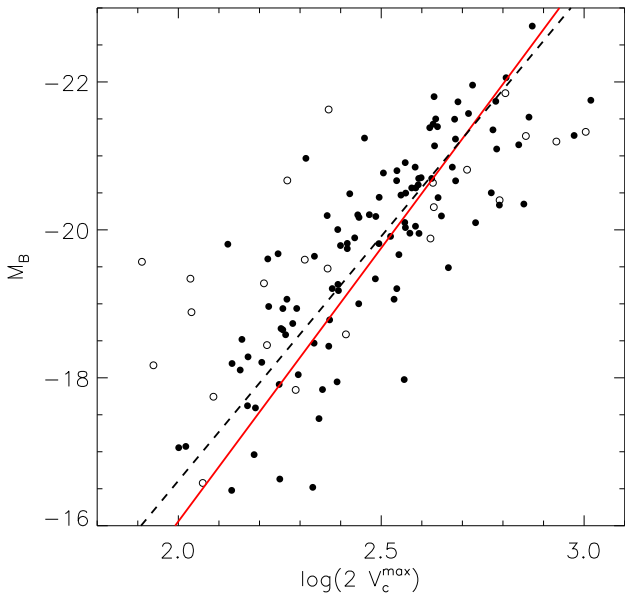


Figure 18. Tully-Fisher relation at $z = 0$ – red line – compared with Tully-Fisher relation computed at $z = 1.7$ – black dots and black dashed line –. Open symbols correspond to galaxies that would not be classified as rotating disks at redshift 1.7. The two linear regressions (red line and black dotted line) are computed using only galaxies classified as rotating disks.

point can be probed. The Tully-Fisher zero point b is defined by Puech et al. (2008) as

$$M = a \times \log V_c^{\max} + b \quad (10)$$

In order to compare the zero point of their $z \sim 0.6$ sample and local value (from a SDSS sub-sample), they fixed the slope of the high redshift Tully-Fisher to the local slope. Thus, they found a galaxy brightening of 0.66 ± 0.14 magnitude from $z \sim 0.6$ to $z = 0$ that would indicate that galaxies double their stellar mass between these two epochs. They conclude that rotating disks observed at $z \sim 0.6$ should be rapidly transforming their gas into stars. We did the same comparison on our local and redshifted galaxies by fixing the slope to -7.4 found from the local galaxies classified as “rotating disks”. We found that beam smearing effects cannot account for the brightening suggested by Puech et al. (2008) since it leads to a difference of the zero point in Tully-Fisher relation equivalent to a loss of brightness of 0.17 ± 0.10 magnitude. Considering that the uncertainty is of the same order of magnitude than the difference of zero point, we conclude that both local and redshifted zero points are compatible. This result would indicate that the significant evolution of the Tully-Fisher zero point with respect to the error bars observed by Puech et al. (2008) is not accounted for by beam smearing effects.

In this section, we have discussed:

- The comparison between the local Tully-Fisher relation for the GHASP sample with the Tully-Fisher relation for the GHASP sample projected at high redshift. The conclusions are that the slope of the Tully-Fisher relation is lowered by beam smearing effects within the error bars

and that the zero point of this relation is not significantly modified. This supports that the evolution of the zero point in the Tully-Fisher relation, observed by Puech et al. (2008), cannot be explained by beam smearing effects.

- The comparison between the slope of the Tully-Fisher relation for the GHASP sample projected at high redshift with the slope of the Tully-Fisher relation for the IMAGES sample. The conclusion is that the slopes of the Tully-Fisher relations derived from the GHASP sample projected at high redshift and from the IMAGES sample are compatible within the errors. Nevertheless, the latter comparison is limited (i) by the distributions in mass or in velocity of both samples that do not match, (ii) by the fact that the magnitude in the GHASP sample is computed in the B-band whereas it is computed in the K-band for the IMAGES sample and (iii) by the fitting methods used to compute the Tully-Fisher relation coefficients that are not exactly the same.

7 DISCUSSION

A common explanation for massive galaxies having irregular kinematics and high nuclear gas fraction is that they may have undergone major mergers of gas-rich galaxies. On the other hand, models linking cosmological simulations to galaxy evolution (e.g. Ocvirk et al. 2008; Dekel et al. 2009) proposed a scenario where galaxies at $z \sim 2$ accrete significant amounts of cold gas which form unstable gaseous disks. Immeli et al. (2004a), followed by other authors, relaunched an old debate in suggesting that, in early-stage galactic disks, efficient gas cooling could have led to high cold gas fractions, which then fragmented due to self-gravity and collapsed to form a nuclear starburst. The kinematics of the brightest nebular emitting regions may be relatively featureless and may dominate the entire line emitting regions through the galaxy up to observable radii. The absence of shear may be a transient effect vanishing to further lower surface brightness ionized gas at later evolutionary stage.

7.1 Formation and evolution of high redshift gaseous disk

For rotating disks, at a resolution of a few kiloparsecs, it is challenging to know whether the large velocity dispersion observed in high redshift galaxies is due to (i) cold gas accretion, (ii) gas rich minor merger accretion events (e.g. Semelin & Combes 2002) or (iii) wet major mergers. The three scenarios may fuel the disk in fresh gas. Scenario (i) might have two origins, internal or external to the galaxy. Indeed, huge reservoirs of gas, gravitationally bound to the galaxy (Pfenniger & Combes 1994), may fuel the galaxies in cold gas as well as cold gas accretion flowing from the intergalactic medium. Both accretion mechanisms may lead to gas instabilities, cloud fragmentation and collapse, thus finally to strong starburst activity (Immeli et al. 2004b; Bournaud et al. 2008). The existence of a disk in rotation does not prove that it has been formed by continuous gas accretion. Indeed, if the initial spins of the progenitors are not too different, old wet major merger events may produce a rotating

disk after a timescale > 0.5 Gyr (shorter than the nowadays timescale) indistinguishable from a disk formed by the two other mechanisms. Alternatively, the presence of large reservoirs of gas around disk galaxies (Daddi et al. 2008) indicates that large amounts of gas are available to fuel the star formation. If minor mergers (10:1 to 50:1) occur with a high frequency, relaxation processes eject the pre-existing stars from the disk to the spheroid or to the thick disk. From an observational point of view, these stars are undistinguishable from the ones belonging to the thin disk. The formation of a spheroid or a thick disk will not perturb significantly the disk kinematics and its signature would be difficult to detect directly. Nevertheless, the stabilization of the disk due to these structures should be indirectly observable: they will diminish the star formation inducing less sub-structures as $H\alpha$ and UV clumps. A gaseous or stellar disk stable to all axisymmetric perturbations requires the Toomre's parameters $Q > 1$ (Safronov 1960; Toomre 1964). Giant star-forming clumps observed in high redshift galaxies, in which the star formation is as high as $100 - 1000 M_{\odot} \text{ yr}^{-1}$, require high turbulent speeds and a dense disk with few stars in a spheroid (Bournaud & Elmegreen 2009). The formation of these clumps requires that most of the stars and the gas lie in a rotating disk during the clump formation, otherwise $Q > 1$, the disk is stable and massive clumps do not form. Indeed, halo as well as stellar spheroid stabilize the disk and make the disk too stable to allow giant clumps to develop. The distribution, size and mass of these clumps may be considered as indirect indicators of the disk formation history. At the opposite, smooth diffuse gas accretion is not supposed to be efficient to form a stellar spheroid and instabilities dominate the disks and are observable through deep imaging addressing the formation of clumps. For very minor mergers (e.g. mass ratio $> 100:1$), the dwarf galaxies are dislocated by the tidal field once they experience the gravitational field of the main galaxy. Torn by tidal field, this kind of accretion resembles very much to diffuse gas accretion. For a baryonic mass galaxy of $10^{10} M_{\odot}$, these satellites have masses lower than $10^8 M_{\odot}$. If these galaxies exist, they are not detectable in observations or in numerical simulations, due to the lack of spatial resolution.

Large turbulence in the neutral gas disk could be provided by energy dissipation due to rapid external gas accretion (cosmological filaments, outer disk gas reservoirs). The huge sizes, masses and velocity dispersions of star-forming clumps still need to be understood. Taniguchi & Shioya (2001) favored a multiple merger origin similar to what is observed in several local compact groups. Noguchi (1999), Immeli et al. (2004a,b), Bournaud et al. (2007, 2008) proposed that, resulting from Jeans instabilities, primordial gaseous disk could fragment into several dense clumps. If the gas accretion is large and fast enough, the disk may become unstable leading to clumps formation with Jeans length-scale of $1 - 2$ kpc and Jeans mass-scale of $\sim 10^{8-9} M_{\odot}$. Unfortunately, the kpc-scale turbulence in the neutral atomic gas component (or the molecular gas via its CO content) has never been observed at high redshift. The presence of large clumps indicates nevertheless that it should be higher than in the local universe.

Disks observed at high redshift may be short-lived and not the precursors of today disk galaxies. Indeed, new pictures emerge in the literature in which young thick disks

form by cold flows (Dekel et al. 2009; Kereš et al. 2009) and other types of diffuse gas accretion (Semelin & Combes 2005), bulges form by internal and clump-driven evolution (Elmegreen et al. 2008; Genzel et al. 2008), and the thin disk forms later by further smooth accretion (e.g., Bournaud & Combes 2002). Models discussed in Bournaud et al. (2007, 2008) predict that velocity shear tracing the initial gas rotation should be observed but with high velocity dispersion as shown by the observations of high redshift galaxies. In simulations including external gas accretion (Bournaud et al. 2008), the relatively thin initial disk (700 pc) becomes thicker ($\sim 1 - 2$ kpc). This is due to gravitational heating processes linked to clump formation processes. Stars formed in clumps constitute the thick disk or merge in the central bulge. The gas which has not been transformed in stars during the clump phase cools down and falls down in the pre-existing thin stellar disk.

The standard model indicates that massive galaxies formed earlier, thus having accreted their mass earlier and having been unstable at higher redshifts. As a consequence, their clumps should have been dispersed in the bulge or in the thick disk at earlier epochs than for less massive galaxies. Indeed, a bulge component seems to be already present in the most massive galaxies in the SINS sample.

7.2 What do observations of high redshift galaxies show?

7.2.1 Seeing-limited observations

Observations with a seeing disk of ~ 4 kpc ($\sim 0.5''$) do not allow to sample the internal substructures of high redshift galaxies. Nevertheless, they are easier to obtain than AO ones. On the one hand, they do not require natural or laser guide star and, on the other hand, the larger pixel scale allow to observe the disk outskirts which have a lower surface brightness.

The bulk of SINS galaxies have been observed without AO (51 out of 63 galaxies) with a seeing disk of $\sim 0.6''$. Many SINS galaxies are bright and large, they have been selected from previous long slit observations (Erb et al. 2003, 2006) on the basis of consequent velocity shear and/or velocity dispersion. Among the 51 galaxies, 14 of them are classified as rotating disks (Cresci et al. 2009). These authors did not point out specific conclusions linked to the absence of AO and invoke the need for gas accretion to form disk as suggested by the predictions of the latest N-body/hydrodynamical simulations of disk formation and evolution (e.g. Dekel et al. 2009).

In the frame of the MASSIV program, nine galaxies have been observed with a mean seeing of $0.65''$ in the redshift range $1.2 < z < 1.6$ during a pilot run. Epinat et al. (2009b) found that six of them are compatible with rotators. They distinguished two rotating disks and four perturbed rotators showing a high velocity dispersion. For the MASSIV program, a special care is given in the selection of the targets. No definitive conclusion can yet be drawn. In particular for their perturbed rotators, they concluded that the high velocity dispersion may be the signature of gas accretion as well as gas rich minor mergers.

In conclusion, the SINS survey and the MASSIV pilot run reach roughly the same conclusion that almost a third of

28 *B. Epinat et al.*

high redshift galaxies has rotation-dominated disks, another third has dispersion-dominated disks while the last third is composed of merging galaxy candidates. This is consistent with previous results obtained with long slit spectroscopy data by Weiner et al. (2006) and Kassin et al. (2007) who found one third of dispersion-dominated disks from more statistically complete samples. Forthcoming integral field spectroscopy data, like the MASSIV sample, will help in distinguishing between the various processes of galaxy formation acting at these redshifts. Indeed, the MASSIV sample has been selected from the VIMOS-VLT Deep Survey (Le Fèvre et al. 2005), which is both statistically representative of the overall population and volume complete, based on the measured masses and on-going star formation rate (Contini et al. et al., in preparation).

7.2.2 Adaptive optics observations

Adaptive optics observations allow to reach the kpc-scale which is a large improvement to analyze the internal kinematics of high redshift galaxies.

In the frame of the SINS program, twelve galaxies have been observed with SINFONI assisted by AO (Förster Schreiber et al. 2009). Only five of them, classified as rotating disks, have been published up to now (Genzel et al. 2008). The first observation by Genzel et al. (2006) of a high redshift galaxy (BzK 15504 at $z = 2.38$) with an angular resolution of 150 mas (~ 1 kpc) exhibits a resolved velocity shear which is nevertheless not well fitted by a simple disk model. With AO, the line-of-sight velocity dispersion remains high at high radii ($\sigma \sim 60 - 100$ km s⁻¹) and the residual velocity map between the observed velocity field and the model (best-fitting exponential disk) shows deviations larger than 100 km s⁻¹. Genzel et al. (2006) argued that it may be explained by radial gas inflows fuelling the central AGN.

The galaxy 1E0657-56 at $z = 3.2$ being strongly lensed, SINFONI observations without AO of this object lead to a spatial resolution of ~ 200 pc in the source plane, even better than AO resolution for non lensed galaxies. The position-velocity diagram within the central kpc of this galaxy looks like a rotating L_{*} nearby spiral galaxy (Nesvadba et al. 2006) suggesting that, in some cases at least, a significant amount of mass could be already in place on small physical scale at $z \geq 3$.

OSIRIS instrument also assisted by AO has been used by Law et al. (2007, 2009) and Wright et al. (2007, 2009) for observing a total of 25 high redshift galaxies. Law et al. (2009) provide 16 galaxies at $z \sim 2 - 3$, including at most five rotating disks, resolved with a PSF $\sim 110 - 150$ mas. These authors concluded that, even for galaxies showing clear velocity gradients, rotation may not be the dominant mechanism of physical support. They refuted a simple bimodal disk/merger classification scheme but underlined the dynamical importance of cold gas accretion. At lower redshifts (~ 1.5), Wright et al. (2007, 2009) have observed nine galaxies, four of them have been classified as rotating disks. Among these four cases, two look like local disks while due to their high velocity dispersion, the two other ones look more like unstable disks.

7.2.3 High velocity dispersion in high redshift galaxies: comparison with local galaxies

We have shown in this work that, although the seeing-limited observations of intermediate and high redshift galaxies (from $z \sim 0.4$ to $z \sim 3$) suffer from significant beam smearing effects, it is not sufficient to explain the increase of velocity dispersion with the redshift. Moreover, AO observations of high redshift galaxies reaching the lower limit of the kpc-scale also display a high velocity dispersion. This unambiguously indicates a clear and continuous dynamical evolution in disk galaxies through the last eleven Gyr. Three mechanisms act simultaneously and are responsible for gaseous velocity dispersion: turbulence due to local gravity, feedback linked to star formation processes and infall in the potential well of the galaxy. It is a challenging question to quantify the contribution of each processes.

Galaxies at earlier stages of evolution are observed to be very different from nowadays galaxies. Their high star formation rate of $\sim 10^{2-3} M_{\odot}$ per year has no equivalent in the local universe. This high star formation rate could be fuelled by large amounts of neutral and molecular gas. Theoretical calculations as well as observational evidence show that molecular cloud-cloud collision account for a substantial fraction of the star formation in the Galaxy (e.g. Tan 2000, Sato et al. 2000 and references therein). In high redshift galaxies, high velocity dispersions up to 100 km s⁻¹ are observed in the warm phase of the gas on several kpc-scale, the velocity dispersion of the cold phase of the gas and of the stellar component being not observable. Very extended (as large as ~ 1 kpc) and massive star forming clumps ($\sim 10^{8-9} M_{\odot}$) are observed at redshift ≥ 1 , (e.g. Elmegreen et al. 2007 and references therein). Corresponding high-mass clumps do not exist in local galaxies, even in high star forming objects, where their masses do not exceed $\sim 10^6 M_{\odot}$. On deca/hecto pc-scale, the typical velocity dispersion of the cold gas phase in the interstellar medium of local galaxies is of the order of 5 km s⁻¹: even in massive molecular clouds observed in local HII regions (e.g. $\sim 2.10^5 M_{\odot}$ in NGC 7538, Minn & Greenberg 1975), the internal velocity dispersion does not exceed ~ 5 km s⁻¹. The formation of OB-stars associations leads to the ionization of smaller clumps, the so-called HII regions. Local gaseous velocity dispersion in nearby galaxies within HII regions spans only between 10 and 30 km s⁻¹ (see section 6.5 and Weiner et al. 2006). During the strongest phase of star formation, mainly due to supernova activity, the ionized gas component is more turbulent and its velocity dispersion higher although not as high as observed in high redshift galaxies.

The mean rotation velocity of the ionized gas component may be similar to the unobserved neutral gas component (atomic or molecular). The spatial distribution of the ionized gas is more clumpy and its velocity dispersion higher than the neutral gas. It follows the distribution and dynamics of young stars and the stellar winds induced by them. Strong supernovae winds, large bubbles in expansion increase the velocity dispersion of the ionized gas and participate to the turbulent motions linked to star formation processes. However, turbulent motions observed through the ionized gas component, on kpc-scale structures, probably cannot be explained by star formation processes only. External mechanisms, like cosmological gas accretion, combined

to local self-gravity are needed to provide additional energy to sustain the high velocity dispersions (Lehnert et al. 2009) and thus, should be present also in the neutral gas component. In nearby galaxies, a fraction of the local velocity dispersion observed in the gas is due to turbulence linked to mass density contrasts generated for instance by $m = 2$ perturbations (spiral arms). At higher redshift, since gas density is higher, this turbulence linked to local gravity may increase and it will not indicate that the disk is unstable.

7.2.4 Large clumps observed in high redshift galaxies: huge HII regions or conglomerate of small clumps?

Galaxies are increasingly clumpy with redshift (Conselice et al. 2005). A large fraction of their luminous mass (up to 30%) and optical light (up to 50%) is confined to a few kpc-size clumps (Elmegreen & Elmegreen 2005). These clumps are probably formed inside the galactic disk rather than entered from outside in a merger (Bournaud & Elmegreen 2009). They are specific to high redshift galaxies that do not have spirals, nor bulges or exponential profiles. These clumps tell us about galaxy evolution and could be progenitors of modern spiral disks.

If these gaseous clumps are gravitationally bound and dynamically relaxed, they may trace the gravitational potential as it should be shown by the hidden stellar velocity dispersion. If one considers that the clumps observed at high redshift proceed from molecular clouds gravitationally bound as massive as $\sim 10^9 M_\odot$, extrapolation of the scaling relation of Larson (1981) leads to internal velocity dispersion not higher than $\sim 25 \text{ km s}^{-1}$. To reach internal velocity dispersions $\sim 100 \text{ km s}^{-1}$, like those observed in clumps at high redshift, clump progenitors should have the mass of a massive galaxy ($\sim 10^{12} M_\odot$). These huge clumps may not be gravitationally linked systems or may be bound but not in equilibrium. The scaling relations of Larson (1981) are not valid to describe the physics of these clumps.

Many numerical works have been concerned with collision between so-called high-mass clouds which nevertheless do not exceed $\sim 10^3 M_\odot$ (e.g. Chapman et al. 1992). These clouds are obviously much less massive than the large clumps observed at high redshift. Nevertheless, one might expect a collision between two high-mass clouds to consist of many smaller-scale collisions between the clouds of lower mass of which the clumps are composed maybe down to $\sim 10 M_\odot$ (e.g. Kitsionas et al. 2008). These clumps may be the result of a high star-formation occurring at this stage but most massive clumps predicted in models simulating disk instability have a velocity dispersion $\sim 20 - 30 \text{ km s}^{-1}$ (Immeli et al. 2004a) or $40 - 50 \text{ km s}^{-1}$ (Bournaud et al. 2008). In other words, the mean local velocity scatter around circular motions (i.e. the dispersion in the rest frame of a disk in circular motion) expected from simulations ranges from 20 to 50 km s^{-1} . The circular rotation of the clumps is given by the mean potential well of the galaxy (disk+dark halo) but clump-clump (2-body gravitational) interaction induces their velocity dispersion with an amplitude lower than 50 km s^{-1} . The high velocity dispersion observed on 2D velocity dispersion maps may be due to integration through the line-of-sight within the size of the unresolved observed beam. Very strong winds due to supernova activity may also

increase the local velocity dispersion in the ionized gas component.

7.2.5 Large clumps at kpc-scale resolution

In this paper, we do not focus on merging systems but only on rotators for which three mechanisms of formation are possible: major mergers, minor mergers and gas accretion.

The assembly of galaxies at redshifts $z \sim 1 - 2$ which have clumps embedded in what appears to be a disk is unlikely to be mostly driven by hierarchical merging of smaller galaxies. Indeed, the formation of giant clumps (with the masses, sizes and elongations typically observed) in massive and highly turbulent disks, requires that the dominant process of mass assembly be some smooth accretion of cold and diffuse gas (Bournaud & Elmegreen 2009). This is consistent with the picture in which young thick disks form by cold flows (Dekel et al. 2009; Kereš et al. 2009). However, the actual physical nature and the characterization of these clumps request further attention before disentangling different mechanisms occurring at different epoch of galaxy assembly.

The nature of the massive clumps observed in high redshift galaxies is well established from imaging (Conselice et al. 2005; Elmegreen & Elmegreen 2005). Nevertheless, the lack of spatial resolution does not allow to fully characterize them. Indeed, large clumps with large velocity dispersions might be composed of several unresolved smaller clumps. Even if it is well established that the sizes, the luminosities, the velocity dispersion and thus the masses of these clumps are large with respect to the clumps observed in lower redshift galaxies, it may not be excluded that their ‘oversized’ geometric and kinematics properties is due to the lack of resolution and to the fact that they are not resolved. In any cases, their physics is poorly understood and need higher spatial resolution to be modeled through numerical simulations. The high velocity dispersion in high redshift galaxies may be due to the blended kinematics of neighboring, self-gravitating clouds. The low spatial resolution (limited by the seeing) combined with the low spectral resolution make difficult the deconvolution by both spatial and spectral instrumental PSF. Thus these large star forming clumps observed at high redshift maybe consist of the conglomerate of unresolved smaller scales clumps. In that case, the large velocity dispersion observed on kpc-scale in high redshift galaxies may thus be the result of the velocity dispersion of the different small clouds composing the unresolved clumps, rather than a local velocity dispersion within a large individual star-forming clump. Sub-kpc data are needed to observe sub-clumps in order to know if they are gravitationally bound or just spatial resolution effects.

Only high resolution observations may enable to compute velocity fields and rotation curves uncontaminated by the blurring of the data (see section 6.3). IFU AO observations provide in one shot a kpc-scale sampling both on the morphology and on the kinematics. These data are needed to sample the velocity field, rotation curve and velocity dispersion map, as discussed in section 6, and to recognize the disk formation mechanisms printed in the morphology and the kinematics.

8 CONCLUSION

Due to the lack of spatial resolution, consequence of their large distance, observations of galaxies at high redshift are affected by beam smearing effects. The different moment maps (intensity maps, velocity fields, velocity dispersion maps, etc.) as well as the one dimensional plots (line profiles, rotation curves, etc.) are severally blurred on kpc-scale. For instance, beam smearing effects completely modify the shape of the rotation curves in inducing artificially a solid body shape trend (i.e. a lower inner slope and a higher outer slope than real).

In this work, in order to study the biases induced by beam smearing effects existing in observation of high redshift galaxies and to provide new tools and recipes to analyse high redshift galaxies, we have used 3D data cubes for a large sample of local galaxies. This sample of nearby galaxies consists of 153 objects observed with Fabry-Perot technics belonging to the GHASP sample. We have simulated observations of this sample at redshift 1.7 and have attempted to recover hidden information from the blurred velocity fields and velocity dispersion maps using simple kinematical models. The conclusions can be summarized through the different items as follows:

(I) The analysis led in this work enables us to test the validity of high redshift dynamical classification made by Flores et al. (2006); Yang et al. (2008) to distinguish rotating disks from mergers. We have shown that, using this classification, most of the rotating disks are correctly classified but we have also pointed out that around 30% of disk galaxies would be misclassified as perturbed rotators, or even complex kinematics. This may lower the fraction of galaxies with anomalous or perturbed kinematics in the IMAGES sample from 41% to 33%. This work will be further completed in projecting at high redshift a local sample of galaxies showing complex kinematics (mergers, close binaries, compact groups, blue compact galaxies) in order to evaluate the fraction of these systems which would be misclassified as rotating disks.

(II) This sample was used to test the relevance of recovering the actual dynamical parameters of high redshift galaxies (inclination, position angle of the major axis, center, maximum rotation velocity, etc.) taking into account the lack of spatial resolution quantified by a “beam smearing parameter” B , ratio between the optical galactic radius ($D_{25}/2$) and the seeing FWHM. Actual observations generally lead to a B parameter lower or equal to 2-3 without AO (e.g. Förster Schreiber et al. 2006) or even $B \gtrsim 6$ when using AO (e.g. Genzel et al. 2008). The “recipes” to recover the dynamical parameters are the following:

- the position of the kinematical center is poorly constrained by the kinematics and should be fixed using high resolution broad-band images. When no clear center can be deduced from sub-kpc images of high redshift galaxies, as it is often the case, the position of the center is strongly affected by beam smearing effects. The determination of the center estimated by the symmetrization of the rotation curves is not reliable for galaxies showing a solid body shape at all radii, which is likely the case for galaxies with $B \lesssim 3$;
- the inclination needs to be constrained by high reso-

lution morphologies since the agreement is better between high resolution morphological inclinations and high resolution kinematical inclinations than between high redshift and low redshift kinematical inclinations. The beam smearing however needs to be taken into account. In addition to the possible corrections already discussed in the literature (e.g. Simard et al. 2002; Peng et al. 2002), a simple way to do it consists in correcting half light radius major and minor axis by subtracting quadratically the seeing. The uncertainties in the determination of the kinematical inclination can be quantified by a linear function of the beam smearing parameter B ;

- the position angle of the major axis is recovered with an accuracy better than 5° for 70% of the sample using a 2D velocity field using simple rotating disk models, even with a rather low spatial resolution ($B \sim 2$);
- the observed velocity dispersion of the gas is strongly correlated with the velocity shear of the galaxy, especially in the inner regions. The local velocity dispersion σ can be statistically recovered (i) by subtracting quadratically the velocity dispersion map model deduced from the velocity field modeling although with a large scatter or (ii) by considering regions with the lowest values that are the less affected by beam smearing. The larger the local velocity dispersion is, the weaker the above correlation is;
- the maximum velocity is statistically fairly well recovered for galaxies larger than three times the seeing in radius (i.e. with $B > 3$), even if this limit probably depends on the unknown high redshift shape of the rotation curves. For galaxies with $B < 3$, we provide a correction of the maximum velocity as a function of B . The use of a simple velocity field modeling enables to recover statistically the maximum velocity with an error lower than 25% in almost any case. We have also shown that a simple model of rotation curve consisting of a solid body part and a flat plateau statistically gives better estimates of the maximum velocity compared to exponential disk, isothermal sphere or arctangent rotation curve models;
- the local GHASP sub-sample of galaxies was also used to test different rotation curve models to recover the actual rotation curves, i.e. unaffected by beam smearing effects. A direct comparison between actual high resolution data ($z = 0$) and various models was done in this purpose. In average, the various models are able to recover the general trend of the actual $z = 0$ rotation curves but the scatter around the mean difference in the rotation curves (ΔV_c^{mean}) is large, pointing out the difficulty to retrieve the actual shapes. Moreover, observations having a value of $B \lesssim 3$ do not allow suitable beam smearing corrections to recover the rough shape of the rotation curve whatever the model used. In order to be able to address problematics linked to the shape of the rotation curve (e.g. CORE vs CUSPY controversy about the inner density profile in spirals) for high redshift galaxies, $B \gtrsim 10$ are necessary.

(III) Finally, this sample of local and evolved galaxies projected at high redshift has been compared to samples of actual high redshift galaxies observed using integral field capabilities (SINFONI, OSIRIS, GIRAFFE) to disentangle evolution effects from distance effects. By applying the same methods of analysis on both projected and observed samples, a relative comparison can be done to probe the kine-

mational evolution of galaxies, since the same observational biases exist in both samples. Our results suggest (i) that the trend in the evolution of the Tully-Fisher relation observed by Puech et al. (2008) is not due to beam smearing effects and (ii) that, except if no beam smearing correction is done on actual high redshift data, the high local velocity dispersion observed in high redshift galaxies cannot be reproduced in the local projected sample. This unambiguously means that, at the opposite of local evolved galaxies, it exists from redshifts $z \sim 3$ to $z \sim 1$ at least a population of disk galaxies for which a large fraction of the dynamical support is not only due to rotation but also to velocity dispersion. At $z \sim 0.6$, galaxies show intermediate velocity dispersions between local and higher redshift galaxies. This demonstrates a strong and continuous dynamical evolution in disk galaxies through the last eleven Gyr ($z \sim 2.5$). This conclusion is relevant at least for some galaxies among the relatively small sample of high redshift galaxies observed using IFU to date. Indeed, one cannot exclude important observation biases in the selection of the targets which was dictated by the feasibility of the observations rather than by strong considerations on the representativity of a given epoch by a set of galaxies correctly selected using for instance luminosity or mass functions. For a given observing time, multi-slit spectroscopy enables to observe larger samples than IFU techniques. However, due to the low spatial coverage per galaxy, long slit data does not allow a complete kinematical analysis.

The low numerical value for $(V_c^{max}/\sigma \sim 1 - 2)$ is a convincing evidence for the existence of a population of thick and transient turbulent gas disks in high redshift galaxies. However, the large turbulence is a consequence of the large amount of gas which induces feedback, local gravitational disturbances and infall processes. It does not prove that the disk is formed by continuous gas accretion rather than by frequent wet minor mergers or old wet major mergers (Robertson & Bullock 2008). If these thick disks are still seen later, they may be transformed into bulges and central galactic black hole. On the other hands, it has to be surveyed if the high redshift galaxies observed to date are representative of their epoch of formation or, alternatively, if the sample is biased by selection effects. These open questions justify the MASSIV on-going program (Contini et al. in preparation, Epinat et al. 2009b, Queyrel et al. 2009) dealing with galaxies ranging from $z \sim 1.0$ to $z \sim 1.8$ and selecting the targets using criteria making them representative of given epochs.

The spatial resolution reached by AO observations enables to reduce significantly the beam smearing effects. In this paper, the limits of the determination of kinematical parameters for high redshift galaxies observed under seeing limited conditions have been discussed: morphological and kinematical AO observations in the redshift range $0.5 < z < 3$ are essential to discuss the different scenarios of mass assembly and galaxy evolution.

In forthcoming works, the effects of spectral resolution and of the noise will be studied using the GHASP sample and local disturbed disk galaxies as compact groups galaxies (Torres et al. in preparation), blue compact star forming galaxies, strongly barred galaxies, mergers, close binaries will be compared to high redshift galaxies using the same methods presented in this paper.

The data used for this work will be available in a database under construction containing Fabry-Perot data <http://fabryperot.oamp.fr/>, enabling to retrieve directly from the database redshifted datacubes with a given seeing, pixel size and spectral resolution. This database will also contain data from several other Fabry-Perot surveys (barred galaxies; galaxies in clusters, in compact groups; blue compact galaxies, etc.).

ACKNOWLEDGEMENTS

We thank David R. Law for kindly providing us before publication their velocity and velocity dispersion maps (Law et al. 2009). We thank Frédéric Bournaud for discussion. We also thank the referee, Benjamin Weiner, for careful reading of the manuscript and useful comments that helped to improve the paper.

REFERENCES

- Abraham R. G., van den Bergh S., Glazebrook K., Ellis R. S., Santiago B. X., Surma P., Griffiths R. E., 1996, *ApJS*, 107, 1
- Amram P., Balkowski C., de Oliveira C. M., Plana H., Epinat B., 2008, in Wada K., Combes F., eds, Mapping the Galaxy and Nearby Galaxies From Nearby to High Redshift Compact Group of Galaxies. p. 261
- Amram P., Mendes de Oliveira C., Plana H., Balkowski C., Hernandez O., 2007, *A&A*, 471, 753
- Amram P., Mendes de Oliveira C., Plana H., Balkowski C., Hernandez O., Carignan C., Cypriano E. S., Sodré Jr. L., Gach J. L., Boulesteix J., 2004, *ApJ*, 612, L5
- Begeman K. G., 1987, PhD thesis, Kapteyn Institute, (1987)
- Bertin E., Arnouts S., 1996, *A&AS*, 117, 393
- Blais-Ouellette S., Carignan C., Amram P., Côté S., 1999, *AJ*, 118, 2123
- Bosma A., 1978, PhD thesis, Groningen Universiteit
- Bournaud F., Combes F., 2002, *A&A*, 392, 83
- Bournaud F., Daddi E., Elmegreen B. G., Elmegreen D. M., Nesvadba N., Vanzella E., di Matteo P., Le Tiran L., Lehnert M., Elbaz D., 2008, *A&A*, 486, 741
- Bournaud F., Elmegreen B. G., 2009, *ApJ*, 694, L158
- Bournaud F., Elmegreen B. G., Elmegreen D. M., 2007, *ApJ*, 670, 237
- Burbidge E. M., Burbidge G. R., 1975, The Masses of Galaxies. Galaxies and the Universe, p. 81
- Catinella B., Giovanelli R., Haynes M. P., 2006, *ApJ*, 640, 751
- Chapman S., Pongracic H., Disney M., Nelson A., Turner J., Whitworth A., 1992, *Nature*, 359, 207
- Chemin L., Balkowski C., Cayatte V., Carignan C., Amram P., Garrido O., Hernandez O., Marcelin M., Adami C., Boselli A., Boulesteix J., 2006, *MNRAS*, 366, 812
- Conselice C. J., Blackburne J. A., Papovich C., 2005, *ApJ*, 620, 564
- Contini T. et al., 2009, in preparation
- Cresci G., Hicks E. K. S., Genzel R. et al., 2009, *ApJ*, 697, 115

- Daddi E., Dannerbauer H., Elbaz D., Dickinson M., Morrison G., Stern D., Ravindranath S., 2008, *ApJ*, 673, L21
- Daigle O., Carignan C., Hernandez O., Chemin L., Amram P., 2006, *MNRAS*, 368, 1016
- de Vaucouleurs G., de Vaucouleurs A., Corwin Jr. H. G., Buta R. J., Paturel G., Fouque P., 1992, *VizieR Online Data Catalog*, 7137, 0
- Dekel A., Birnboim Y., Engel G., Freundlich J., Goerdt T., Mumcuoglu M., Neistein E., Pichon C., Teyssier R., Zinger E., 2009, *Nature*, 457, 451
- Dickinson M., Papovich C., Ferguson H. C., Budavári T., 2003, *ApJ*, 587, 25
- Elmegreen B. G., Bournaud F., Elmegreen D. M., 2008, *ApJ*, 688, 67
- Elmegreen B. G., Elmegreen D. M., 2005, *ApJ*, 627, 632
- Elmegreen D. M., Elmegreen B. G., Ravindranath S., Coe D. A., 2007, *ApJ*, 658, 763
- Epinat B., 2008a, PhD thesis, Université de Provence (France)
- Epinat B., Amram P., Marcelin M., 2008b, *MNRAS*, 390, 466
- Epinat B., Amram P., Marcelin M., Balkowski C., Daigle O., Hernandez O., Chemin L., Carignan C., Gach J.-L., Balard P., 2008c, *MNRAS*, 388, 500
- Epinat B., Amram P., Marcelin M. et al., 2009a, in preparation
- Epinat B., Contini T., Le Fevre O., Vergani D., Amram P., Garilli B., Queyrel J., Tasca L., Tresse L., 2009b, accepted for publication in *A&A*, ArXiv e-prints 0903.1216
- Erb D. K., Shapley A. E., Steidel C. C., Pettini M., Adelberger K. L., Hunt M. P., Moorwood A. F. M., Cuby J.-G., 2003, *ApJ*, 591, 101
- Erb D. K., Steidel C. C., Shapley A. E., Pettini M., Adelberger K. L., 2004, *ApJ*, 612, 122
- Erb D. K., Steidel C. C., Shapley A. E., Pettini M., Reddy N. A., Adelberger K. L., 2006, *ApJ*, 647, 128
- Flores H., Hammer F., Puech M., Amram P., Balkowski C., 2006, *A&A*, 455, 107
- Förster Schreiber N. M., Genzel R., Bouche N. et al., 2009, submitted to *ApJ*, ArXiv e-prints 0903.1872
- Förster Schreiber N. M., Genzel R., Lehnert M. D. et al., 2006, *ApJ*, 645, 1062
- Garrido O., Marcelin M., Amram P., Balkowski C., Gach J. L., Boulesteix J., 2005, *MNRAS*, 362, 127
- Genzel R., Burkert A., Bouché N. et al., 2008, *ApJ*, 687, 59
- Genzel R., Tacconi L. J., Eisenhauer F. et al., 2006, *Nature*, 442, 786
- Glazebrook K., Ellis R., Santiago B., Griffiths R., 1995, *MNRAS*, 275, L19
- Hernandez O., Carignan C., Amram P., Chemin L., Daigle O., 2005, *MNRAS*, 360, 1201
- Immeli A., Samland M., Gerhard O., Westera P., 2004a, *A&A*, 413, 547
- Immeli A., Samland M., Westera P., Gerhard O., 2004b, *ApJ*, 611, 20
- Kassin S. A., Weiner B. J., Faber S. M., Koo D. C., Lotz J. M., Diemand J., Harker J. J., Bundy K., Metevier A. J., Phillips A. C., Cooper M. C., Croton D. J., Konidaris N., Noeske K. G., Willmer C. N. A., 2007, *ApJ*, 660, L35
- Kereš D., Katz N., Fardal M., Davé R., Weinberg D. H., 2009, *MNRAS*, 395, 160
- Kitsionas S., Whitworth A. P., Klessen R. S., 2008, in IAU Symposium Vol. 249 of IAU Symposium, SPH simulations of star/planet formation triggered by cloud-cloud collisions. pp 271–278
- Kronberger T., Kapferer W., Schindler S., Ziegler B. L., 2007, *A&A*, 473, 761
- Larson R. B., 1981, *MNRAS*, 194, 809
- Law D. R., Steidel C. C., Erb D. K., Larkin J. E., Pettini M., Shapley A. E., Wright S. A., 2007, *ApJ*, 669, 929
- Law D. R., Steidel C. C., Erb D. K., Larkin J. E., Pettini M., Shapley A. E., Wright S. A., 2009, *ApJ*, 697, 2057
- Le Fevre O., Vettolani G., Garilli et al., 2005, *A&A*, 439, 845
- Lehnert M. D., Nesvadba N. P. H., Tiran L. L., Matteo P. D., van Driel W., Douglas L. S., Chemin L., Bournaud F., 2009, *ApJ*, 699, 1660
- Liang Y. C., Hammer F., Flores H., 2006, *A&A*, 447, 113
- Lotz J. M., Davis M., Faber et al., 2008, *ApJ*, 672, 177
- Mendes de Oliveira C., Amram P., Plana H., Balkowski C., 2003, *AJ*, 126, 2635
- Minn Y. K., Greenberg J. M., 1975, *ApJ*, 196, 161
- Neichel B., Hammer F., Puech M. et al., 2008, *A&A*, 484, 159
- Nesvadba N. P. H., Lehnert M. D., Davies R. I., Verma A., Eisenhauer F., 2008, *A&A*, 479, 67
- Nesvadba N. P. H., Lehnert M. D., Eisenhauer F., Genzel R., Seitz S., Davies R. I., Saglia R. P., Lutz D., Tacconi L., Bender R., Abuter R., 2006, *ApJ*, 650, 661
- Noguchi M., 1999, *ApJ*, 514, 77
- Noordermeer E., van der Hulst J. M., Sancisi R., Swaters R. A., van Albada T. S., 2005, *A&A*, 442, 137
- Ocvirk P., Pichon C., Teyssier R., 2008, *MNRAS*, 390, 1326
- Palunas P., Williams T. B., 2000, *AJ*, 120, 2884
- Papovich C., Dickinson M., Giavalisco M., Conselice C. J., Ferguson H. C., 2005, *ApJ*, 631, 101
- Paturel G., Petit C., Prugniel P., Theureau G., Rousseau J., Brouty M., Dubois P., Cambrésy L., 2003, *A&A*, 412, 45
- Peng C. Y., Ho L. C., Impey C. D., Rix H.-W., 2002, *AJ*, 124, 266
- Persic M., Salucci P., Stel F., 1996, *MNRAS*, 281, 27
- Pfenniger D., Combes F., 1994, *A&A*, 285, 94
- Press W. H., Teukolsky S. A., Vetterling W. T., Flannery B. P., 1992, *Numerical recipes in FORTRAN. The art of scientific computing*
- Primack J. R., 2007, *Nuclear Physics B Proceedings Supplements*, 173, 1
- Puech M., Flores H., Hammer F. et al., 2008, *A&A*, 484, 173
- Puech M., Hammer F., Flores H., Östlin G., Marquart T., 2006, *A&A*, 455, 119
- Puech M., Hammer F., Lehnert M. D., Flores H., 2007, *A&A*, 466, 83
- Queyrel J., Contini T., Perez-Montero E., Garilli B., Le Fevre O., Kissler-Patig M., Epinat B., Vergani D., Tresse L., Amram P., Lemoine-Busserolle M., 2009, submitted to *A&A*, ArXiv e-prints 0903.1211
- Reddy N. A., Steidel C. C., Fadda D., Yan L., Pettini M., Shapley A. E., Erb D. K., Adelberger K. L., 2006, *ApJ*, 644, 792
- Richer M. G., Georgiev L., Rosado M., Bullesos A., Valdez-Gutiérrez M., Dultzin-Hacyan D., 2003, *A&A*, 397, 99

- Rix H.-W., Guhathakurta P., Colless M., Ing K., 1997, *MNRAS*, 285, 779
- Robertson B. E., Bullock J. S., 2008, *ApJ*, 685, L27
- Rodrigues M., Flores H., Hammer F., Liang Y. C., 2008, in Knapen J. H., Mahoney T. J., Vazdekis A., eds, *Pathways Through an Eclectic Universe Vol. 390 of Astronomical Society of the Pacific Conference Series, Evolution of the Mass-Metallicity Relation from IMAGES*. p. 318
- Rubin V. C., Burstein D., Ford Jr. W. K., Thonnard N., 1985, *ApJ*, 289, 81
- Safronov V. S., 1960, *Annales d'Astrophysique*, 23, 979
- Sakai S., Mould J. R., Hughes S. M. G., Huchra J. P., Macri L. M., Kennicutt Jr. R. C., Gibson B. K., Ferrarese L., Freedman W. L., Han M., Ford H. C., Graham J. A., Illingworth G. D., Kelson D. D., Madore B. F., Sebo K., Silbermann N. A., Stetson P. B., 2000, *ApJ*, 529, 698
- Sato F., Hasegawa T., Whiteoak J. B., Miyawaki R., 2000, *ApJ*, 535, 857
- Semelin B., Combes F., 2002, *A&A*, 388, 826
- Semelin B., Combes F., 2005, *A&A*, 441, 55
- Shapiro K. L., Genzel R., Förster Schreiber N. M. et al., 2008, *ApJ*, 682, 231
- Simard L., Willmer C. N. A., Vogt N. P., Sarajedini V. L., Phillips A. C., Weiner B. J., Koo D. C., Im M., Illingworth G. D., Faber S. M., 2002, *ApJS*, 142, 1
- Sofue Y., Rubin V., 2001, *ARA&A*, 39, 137
- Spano M., Marcellin M., Amram P., Carignan C., Epinat B., Hernandez O., 2008, *MNRAS*, 383, 297
- Steidel C. C., Adelberger K. L., Shapley A. E., Pettini M., Dickinson M., Giavalisco M., 2003, *ApJ*, 592, 728
- Steidel C. C., Shapley A. E., Pettini M., Adelberger K. L., Erb D. K., Reddy N. A., Hunt M. P., 2004, *ApJ*, 604, 534
- Tan J. C., 2000, *ApJ*, 536, 173
- Taniguchi Y., Shioya Y., 2001, *ApJ*, 547, 146
- Toomre A., 1964, *ApJ*, 139, 1217
- Torres S. et al., 2009, in preparation
- Verdes-Montenegro L., Del Olmo A., Yun M. S., Perea J., 2005, *A&A*, 430, 443
- Verheijen M. A. W., 2001, *ApJ*, 563, 694
- Vogt N. P., Forbes D. A., Phillips A. C., Gronwall C., Faber S. M., Illingworth G. D., Koo D. C., 1996, *ApJ*, 465, L15
- Vogt N. P., Phillips A. C., Faber S. M., Gallego J., Gronwall C., Guzman R., Illingworth G. D., Koo D. C., Lowenthal J. D., 1997, *ApJ*, 479, 121
- Weiner B. J., Willmer C. N. A., Faber S. M., Melbourne J., Kassin S. A., Phillips A. C., Harker J., Metevier A. J., Vogt N. P., Koo D. C., 2006, *ApJ*, 653, 1027
- Williams B. A., McMahon P. M., van Gorkom J. H., 1991, *AJ*, 101, 1957
- Wright S. A., Larkin J. E., Barczys M., Erb D. K., Iserlohe C., Krabbe A., Law D. R., McElwain M. W., Quirrenbach A., Steidel C. C., Weiss J., 2007, *ApJ*, 658, 78
- Wright S. A., Larkin J. E., Law D. R., Steidel C. C., Shapley A. E., Erb D. K., 2009, *ApJ*, 699, 421
- Yang Y., Flores H., Hammer F. et al., 2008, *A&A*, 477, 789

APPENDIX A: THE MODEL

A1 Real light distribution

We note $S(x, y, \lambda)$ the spectral distribution of light at position (x, y) at wavelength λ . This spectral distribution contains continuum (C) and line emission (L):

$$S(x, y, \lambda) = L(x, y, \lambda) + C(x, y) \quad (\text{A1})$$

The line flux or monochromatic flux is defined by equation A2:

$$M(x, y) = \int_{\lambda} L(x, y, \lambda) d\lambda \quad (\text{A2})$$

The velocity (first moment of the line) is defined by equation A3:

$$V(x, y) \equiv \overline{V(x, y)} = \frac{\int_{\lambda} L(x, y, \lambda) v(\lambda) d\lambda}{M(x, y)} \quad (\text{A3})$$

And finally, the local velocity dispersion (second moment of the line) is defined by equation A4:

$$\sigma(x, y)^2 \equiv \overline{V(x, y)^2} - \overline{V(x, y)}^2 \quad (\text{A4})$$

where

$$\overline{V(x, y)^2} = \frac{\int_{\lambda} L(x, y, \lambda) v(\lambda)^2 d\lambda}{M(x, y)} \quad (\text{A5})$$

These are ideally the quantities that one wants to estimate. However this is not obvious as spectral PSF and spatial PSF are not Dirac distributions, and because instruments sample the light distributions through pixels and spectral channels.

A2 Spectral PSF and sampling effects

The effect of the spectral PSF is a convolution with the spectrum:

$$S_1(x, y, \lambda) = L \otimes_{\lambda} PSF_{\lambda} + C \quad (\text{A6})$$

PSF_{λ} being the spectral PSF. The spectral PSF can be considered constant within the wavelength range. Since the continuum does not vary with wavelength (by definition) it can be considered as null.

Spectral sampling is equivalent to convolving the spectrum with a “door” function:

$$S_2(x, y, \Lambda_i) = \int_{\Lambda_i - \Delta\lambda/2}^{\Lambda_i + \Delta\lambda/2} S_1(x, y, \lambda) d\lambda \quad (\text{A7})$$

As spectral channels are contiguous, and because the spectral PSF does not introduce any loss in flux, the monochromatic flux can be expressed as:

$$M(x, y) = \sum_i S_2(x, y, \Lambda_i) \quad (\text{A8})$$

By assuming that the rectangle method is giving a good estimate of integrals, that is true only when the spectral resolution (PSF and sampling) enables to oversample the line, the following equations can then be written:

$$\sum_i S_2(x, y, \Lambda_i) v(\Lambda_i) \approx \int_{\lambda} S(x, y, \lambda) v(\lambda) d\lambda \quad (\text{A9})$$

$$\sum_i S_2(x, y, \Lambda_i) v(\Lambda_i)^2 \approx \int_{\lambda} S(x, y, \lambda) v(\lambda)^2 d\lambda \quad (\text{A10})$$

34 *B. Epinat et al.*

This is the first approximation. It enables to deduce:

$$V(x, y) \equiv \overline{V(x, y)} = \frac{\sum_i S_2(x, y, \Lambda_i) v(\Lambda_i)}{M(x, y)} \quad (\text{A11})$$

$$\overline{V(x, y)^2} = \frac{\sum_i S_2(x, y, \Lambda_i) v(\Lambda_i)^2}{M(x, y)} \quad (\text{A12})$$

and then to express the velocity dispersion as in equation A4.

A3 Spatial PSF and sampling effects

The spatial PSF, noted PSF_{xy} is due to diffraction limit (Airy disk) as well as to seeing conditions. However, the induced defaults have to be compared with velocity variations.

A3.1 Spatial PSF effects

The effect of the spatial PSF is a 2D convolution with the images:

$$S_3(x, y, \Lambda) = S_2(x, y, \Lambda) \otimes_{xy} PSF_{xy} \quad (\text{A13})$$

One can measure

$$M_0(x, y) = \sum_i S_3(x, y, \Lambda_i) \quad (\text{A14})$$

And deduce from analytical computing that

$$M_0 = M \otimes_{xy} PSF_{xy} \quad (\text{A15})$$

The measurement of the moments is also biased by this convolution :

$$\overline{V_0^\alpha} = \frac{[\overline{V^\alpha} M] \otimes_{xy} PSF_{xy}}{M_0} \quad (\text{A16})$$

By combining equation A4 and A16 we deduce the square of the blurred velocity dispersion before sampling:

$$\sigma_0^2 = \frac{[\sigma^2 M] \otimes_{xy} PSF_{xy}}{M_0} + \frac{[\overline{V^2} M] \otimes_{xy} PSF_{xy}}{M_0} - \left(\frac{[\overline{V} M] \otimes_{xy} PSF_{xy}}{M_0} \right)^2 \quad (\text{A17})$$

A3.2 Sampling effects

Spatial sampling is equivalent to convolve each frame with a 2D “door” function. Thus the measured spectrum is:

$$S_4(X, Y, \Lambda) = \int_{X-\Delta x/2}^{X+\Delta x/2} \int_{Y-\Delta y/2}^{Y+\Delta y/2} S_3(x, y, \Lambda) dx dy \quad (\text{A18})$$

To have lighter notations, the notation $\int_{pix} dx dy$ is used instead of $\int_{X-\Delta x/2}^{X+\Delta x/2} \int_{Y-\Delta y/2}^{Y+\Delta y/2} dx dy$. The measured quantities are noted with the index 1 ($M_1, V_1, \overline{V_1^\alpha}, \sigma_1$).

The observed flux is:

$$M_1(X, Y) = \sum_i S_4(X, Y, \Lambda_i) \quad (\text{A19})$$

from which is deduced the link with the real monochromatic flux, by assuming that the spatial PSF does not depend neither on the wavelength nor on the position:

$$M_1(X, Y) = \int_{pix} M \otimes_{xy} PSF_{xy} dx dy \quad (\text{A20})$$

In other words, the measured flux is the sum of the PSF convolved flux in one pixel. Within the same hypothesis, we deduce the observed momenta:

$$\overline{V_1^\alpha}(X, Y) = \frac{\int_{pix} [M \overline{V^\alpha}] \otimes_{xy} PSF_{xy} dx dy}{M_1} \quad (\text{A21})$$

and thus, the expression of the observed velocity:

$$V_1(X, Y) \equiv \overline{V_1^1}(X, Y) = \frac{\int_{pix} [M \overline{V}] \otimes_{xy} PSF_{xy} dx dy}{M_1} \quad (\text{A22})$$

and the square of the observed velocity dispersion:

$$\sigma_1^2(X, Y) \equiv \overline{V_1(X, Y)^2} - \overline{V_1(X, Y)}^2 = \frac{\int_{pix} [\sigma^2 M] \otimes_{xy} PSF_{xy} dx dy}{M_1} + \frac{\int_{pix} [\overline{V^2} M] \otimes_{xy} PSF_{xy} dx dy}{M_1} - \left(\frac{\int_{pix} [\overline{V} M] \otimes_{xy} PSF_{xy} dx dy}{M_1} \right)^2 \quad (\text{A23})$$

A4 Comments

The previous set of equations is obtained with a very few hypothesis. It enables to understand why low resolution makes kinematical studies critical, in particular at high redshift. Moreover, it can be used as the basis to write kinematical models: it is possible to avoid the modeling of a data cube in order to gain computing time and resources. Modeling a velocity field is sufficient providing that we make some hypothesis on the flux distribution. Indeed, even if the flux distribution is known at the observing resolution, in the previous set of equations, we see the need for high resolution flux map. Ideally, high resolution narrow band observations should be provided to improve the modeling (using Tunable Filters for instance on space telescopes). HST data could also be used but making the approximation that the maps are tracing the gas distribution.

These equations also enable to disentangle resolution effects from real dispersion features in the velocity dispersion maps. Indeed, equation A23 presents a natural decomposition in two terms: a local velocity dispersion one and a velocity shear one due to the beam smearing. By using a satisfying velocity field model, unresolved velocity gradient can be subtracted quadratically from the velocity dispersion map. The remaining term is thus the local dispersion convolved with the spatial PSF. This term contains the signature of the spectral PSF. In particular, by making the hypothesis that the local velocity dispersion σ is constant, what seems to be the case for the gaseous component for local galaxies, then the expression is simplified:

$$\sigma_1^2 = \sigma^2 + \frac{\int_{pix} [\overline{V^2} M] \otimes_{xy} PSF_{xy} dx dy}{M_1} - \left(\frac{\int_{pix} [\overline{V} M] \otimes_{xy} PSF_{xy} dx dy}{M_1} \right)^2 \quad (\text{A24})$$

In the case one wants to constrain models with the velocity dispersion map, a velocity dispersion model has to be built.

A5 Rotation curve models

Four models are used in this paper. These four models are only described with two parameters having the same physical signification: the maximum velocity V_t of the function,

and the radius at which it is reached r_t (hereafter called transition radius) except for the arctangent model since the maximum velocity is reached at infinity. The transition radius is constrained to measure at least one pixel.

A5.1 First model: exponential disk

This model describes a galaxy whose luminosity profile is fit with an exponential law, and for which the gravitation potential is uniquely due to the stars (no dark matter halo). It is a Freeman disk.

$$V(r) = \frac{r}{r_0} \sqrt{\pi G \Sigma_0 r_0 (I_0 K_0 - I_1 K_1)} \quad (\text{A25})$$

Where r_0 is the exponential radius, Σ_0 is the central disk surface density, I_i and K_i are the i -order modified Bessel function evaluated at $0.5r/r_0$. The maximum velocity $V_t \sim 0.88\sqrt{\pi G \Sigma_0 r_0}$ is reached at $r_t \sim 2.15r_0$. This model is the one used in Förster Schreiber et al. (2006).

A5.2 Second model: isothermal sphere

This model describes the rotation curve due to an isothermal sphere dark matter halo. Spano et al. (2008) have shown that this model is the best fit model for local galaxies.

$$V(r) = \sqrt{4\pi G \rho_0 r_c^2 \left[\frac{r_c}{r} \ln \left(\frac{r}{r_c} + \sqrt{1 + \frac{r^2}{r_c^2}} \right) - \frac{1}{\sqrt{1 + \frac{r^2}{r_c^2}}} \right]} \quad (\text{A26})$$

Where r_c is the core radius and ρ_0 is the central halo density. The maximum velocity $V_t \sim 0.54\sqrt{4\pi G \rho_0 r_c^2}$ is reached at $r_t \sim 2.92r_c$. This model should be used when the contribution of the stars to the gravitation potential is negligible (i.e. for LSB galaxies).

A5.3 Third model: “flat model”

This model does not describe any classical mass distribution. However, it can describe correctly lots of observed rotation curves of local galaxies, in particular those reaching a plateau.

$$V(r) = V_t \frac{r}{r_t}, \text{ for } r < r_t, \quad (\text{A27})$$

$$V(r) = V_t, \text{ for } r \geq r_t. \quad (\text{A28})$$

This model is that used in Wright et al. (2007).

A5.4 Fourth model: arctangent

This model is used by Puech et al. (2008). The rotation curve is described by an arctangent function. Since the maximum velocity is reached asymptotically for an infinite radius, the transition radius r_t is defined as the radius for which the velocity reaches 70% of the asymptotic velocity V_t :

$$V(r) = V_t \frac{2}{\pi} \arctan \frac{2r}{r_t} \quad (\text{A29})$$

This function is rather similar to the “flat model” but is smoother. Moreover, the plateau is not clearly reached, thus it is more likely a rotation curve with an increasing plateau.

APPENDIX B: TABLES

Table B1: Galaxy parameters at $z = 0$

Galaxy	$i_{z=0}^{(a)}$ °	$PA_{z=0}^{(b)}$ °	$D_{25}/2^{(c)}$ kpc	$M_B^{(d)}$ mag	$V_c^{max (e)}$ $km s^{-1}$	$\sigma^{(f)}$ $km s^{-1}$	V_c^{max}/σ	$S_{in}^{(g)}$ $km s^{-1} kpc^{-1}$
UGC 89	33 ± 13	177 ± 4	18.5	-21.5	343 ± 117	30 ± 17	11.4 ± 7.6	317 ± 26
UGC 94	42 ± 5	94 ± 2	17.2	-20.4	209 ± 21	23 ± 15	9.1 ± 6.0	118 ± 7
UGC 508	25 ± 7	123 ± 1	25.9	-21.8	553 ± 127	22 ± 16	25.1 ± 19.2	321 ± 24
UGC 528	21 ± 14	52 ± 3	3.5	-19.6	84 ± 52	24 ± 11	3.5 ± 2.7	103 ± 8
UGC 763	54 ± 6	117 ± 3	7.1	-18.9	104 ± 11	23 ± 13	4.5 ± 2.6	34 ± 2
NGC 542	90 ± 1	143 ± 9	9.9*	-19.5	125 ± 8	28 ± 16	4.5 ± 2.6	—
UGC 1249	90 ± 1	150 ± 9	6.9	-18.3	65 ± 8	15 ± 15	4.3 ± 4.4	—
UGC 1256	76 ± 2	73 ± 2	7.2	-18.9	105 ± 9	17 ± 13	6.2 ± 4.8	29 ± 1
UGC 1317	73 ± 1	106 ± 1	26.0	-21.5	205 ± 9	27 ± 15	7.6 ± 4.2	110 ± 5
UGC 1437	47 ± 4	-53 ± 2	23.1	-21.8	218 ± 15	23 ± 18	9.5 ± 7.4	148 ± 10
UGC 1655	45 ± 18	-42 ± 6	29.0	-21.6	205 ± 64	16 ± 20	12.8 ± 16.5	195 ± 18
UGC 1736	35 ± 14	27 ± 2	11.3	-20.1	193 ± 68	19 ± 17	10.2 ± 9.8	50 ± 1
UGC 1886	62 ± 2	35 ± 1	34.0	-20.8	267 ± 8	19 ± 14	14.1 ± 10.4	27 ± 3
UGC 2045	61 ± 8	-41 ± 4	10.3	-20.5	137 ± 8	34 ± 11	4.0 ± 1.3	229 ± 15
UGC 2082	87 ± 4	133 ± 4	7.5	-18.3	100 ± 8	13 ± 14	7.7 ± 8.3	—
UGC 2080	25 ± 9	-24 ± 1	8.6	-19.2	131 ± 42	14 ± 13	9.4 ± 9.2	208 ± 16
UGC 2141	74 ± 23	-169 ± 4	4.2	-18.1	105 ± 8	30 ± 10	3.5 ± 1.2	36 ± 1
UGC 2455	51 ± 30	-97 ± 21	3.6	-18.6	21 ± 12	16 ± 14	1.3 ± 1.4	48 ± 4
UGC 2800	52 ± 13	-69 ± 3	6.5	—	103 ± 20	10 ± 13	10.3 ± 13.5	32 ± 1
UGC 2855	68 ± 2	100 ± 2	10.5	-21.4	229 ± 9	19 ± 15	12.1 ± 9.5	52 ± 1
UGC 3013	58 ± 8	-165 ± 3	22.8	-21.3	212 ± 21	29 ± 15	7.3 ± 3.8	203 ± 12
UGC 3334	47 ± 14	-83 ± 5	35.0	-22.8	377 ± 85	27 ± 16	14.0 ± 8.9	200 ± 7
UGC 3382	18 ± 6	-176 ± 2	9.9	-20.4	335 ± 111	17 ± 15	19.7 ± 18.6	58 ± 4
UGC 3384	45 ± 7	62 ± 59	4.1	-14.6	335 ± 111	21 ± 16	—	—
UGC 3429	54 ± 8	-43 ± 2	14.9	-21.3	248 ± 8	36 ± 14	6.9 ± 2.7	194 ± 6
UGC 3463	63 ± 3	110 ± 2	16.1	-20.7	168 ± 9	29 ± 14	5.8 ± 2.8	53 ± 3
UGC 3574	19 ± 10	99 ± 2	12.5	-18.0	202 ± 96	18 ± 14	11.2 ± 10.2	146 ± 7
UGC 3521	58 ± 5	-102 ± 2	9.7	-19.8	166 ± 12	21 ± 14	7.9 ± 5.3	46 ± 3
UGC 3528	42 ± 12	-137 ± 3	11.7	-20.1	276 ± 66	17 ± 14	16.2 ± 13.9	187 ± 11
UGC 3691	64 ± 4	-112 ± 2	8.7	-20.2	143 ± 10	29 ± 12	4.9 ± 2.1	84 ± 5
UGC 3685	12 ± 17	-62 ± 3	12.0	-19.7	133 ± 177	23 ± 13	5.8 ± 8.4	51 ± 1
UGC 3708	44 ± 16	-130 ± 4	8.0	-20.7	234 ± 69	40 ± 15	5.8 ± 2.8	132 ± 7
UGC 3709	55 ± 4	-128 ± 2	13.4	-21.5	241 ± 14	38 ± 16	6.3 ± 2.7	94 ± 6
UGC 3734	43 ± 7	139 ± 2	3.7	-18.6	108 ± 16	20 ± 14	5.4 ± 3.9	130 ± 3
UGC 3809	58 ± 2	-3 ± 1	32.1	-22.0	258 ± 9	16 ± 15	16.1 ± 15.1	65 ± 1
UGC 3740	48 ± 14	-113 ± 4	6.6	-19.8	87 ± 20	30 ± 10	2.9 ± 1.2	12 ± 2
UGC 3851	90 ± 1	30 ± 8	3.8	-17.1	65 ± 8	18 ± 12	3.6 ± 2.4	—
UGC 3876	59 ± 5	-2 ± 2	4.5	-17.4	112 ± 10	21 ± 15	5.3 ± 3.8	42 ± 3
UGC 3915	47 ± 4	30 ± 2	9.6	-21.4	205 ± 16	32 ± 14	6.4 ± 2.8	106 ± 6
IC 476	55 ± 24	68 ± 6	5.4*	-19.0	70 ± 22	27 ± 14	2.6 ± 1.6	52 ± 4
UGC 4165	41 ± 10	-95 ± 2	4.4	-18.2	80 ± 18	22 ± 13	3.6 ± 2.3	71 ± 1
UGC 4256	38 ± 21	-69 ± 6	21.6	-21.6	123 ± 59	32 ± 18	3.8 ± 2.8	52 ± 4
UGC 4273	60 ± 4	-148 ± 2	11.4	-20.7	219 ± 11	21 ± 16	10.4 ± 8.0	172 ± 12
UGC 4278	90 ± 1	172 ± 4	6.2	-19.2	80 ± 8	20 ± 12	4.0 ± 2.4	—
UGC 4284	59 ± 9	176 ± 3	8.5	-18.4	118 ± 14	16 ± 12	7.4 ± 5.6	100 ± 4
UGC 4325	63 ± 14	57 ± 3	5.2	-18.2	85 ± 13	19 ± 13	4.5 ± 3.1	32 ± 1
UGC 4393	50 ± 9	-110 ± 7	9.7	-19.3	47 ± 10	28 ± 11	1.7 ± 0.7	8 ± 1
UGC 4422	25 ± 8	36 ± 1	25.3	-21.1	353 ± 94	23 ± 17	15.3 ± 12.1	308 ± 12
UGC 4456	9 ± 14	124 ± 3	18.5	-20.8	211 ± 321	25 ± 15	8.4 ± 13.8	111 ± 9
UGC 4499	50 ± 14	141 ± 3	4.4	-17.0	62 ± 13	20 ± 13	3.1 ± 2.1	22 ± 1
UGC 4555	38 ± 7	90 ± 2	12.7	-20.9	185 ± 30	24 ± 15	7.7 ± 5.0	111 ± 6
UGC 4770	20 ± 13	-82 ± 2	21.4	-21.3	330 ± 194	21 ± 17	15.7 ± 15.7	28 ± 3
UGC 4820	38 ± 3	157 ± 1	10.0	-20.3	336 ± 20	23 ± 14	14.6 ± 8.9	156 ± 13
UGC 4936	13 ± 12	-66 ± 2	22.2	-20.6	264 ± 227	20 ± 13	13.2 ± 14.2	59 ± 1
UGC 5045	16 ± 9	148 ± 2	17.4	-21.2	429 ± 228	28 ± 14	15.3 ± 11.2	95 ± 5
UGC 5175	56 ± 3	143 ± 1	11.0	-20.6	188 ± 10	34 ± 13	5.5 ± 2.1	71 ± 4
UGC 5228	72 ± 2	120 ± 1	8.3	-19.9	125 ± 9	27 ± 10	4.6 ± 1.7	57 ± 2

Table B1: *continued*

Galaxy	$i_{z=0}$ ^(a) °	$PA_{z=0}$ ^(b) °	$D_{25}/2$ ^(c) kpc	M_B ^(d) mag	V_c^{max} ^(e) km s ⁻¹	σ ^(f) km s ⁻¹	V_c^{max}/σ	S_{in} ^(g) km s ⁻¹ kpc ⁻¹
UGC 5251	73 ± 6	-100 ± 3	17.0	-20.5	125 ± 9	27 ± 11	4.6 ± 1.9	39 ± 1
UGC 5253	40 ± 4	-4 ± 1	13.3	-20.7	235 ± 17	21 ± 15	11.2 ± 8.0	254 ± 19
UGC 5279	90 ± 1	83 ± 7	7.9	-19.0	110 ± 8	26 ± 11	4.2 ± 1.8	-
UGC 5316	77 ± 4	130 ± 2	10.3	-19.9	145 ± 9	18 ± 15	8.1 ± 6.7	16 ± 1
UGC 5319	30 ± 9	-15 ± 1	8.2	-19.7	180 ± 47	25 ± 12	7.2 ± 3.9	73 ± 1
UGC 5351	82 ± 6	105 ± 7	6.5	-19.4	135 ± 8	32 ± 11	4.2 ± 1.5	-
UGC 5414	71 ± 13	-141 ± 4	4.6	-16.6	74 ± 10	20 ± 14	3.7 ± 2.6	26 ± 1
IC 2542	20 ± 15	174 ± 3	11.7*	-20.5	290 ± 192	33 ± 15	8.8 ± 7.1	71 ± 1
UGC 5510	31 ± 10	-160 ± 2	7.7	-19.3	167 ± 44	26 ± 11	6.4 ± 3.2	134 ± 7
UGC 5532	32 ± 3	147 ± 1	22.0	-22.1	398 ± 24	27 ± 14	14.7 ± 7.7	382 ± 30
UGC 5556	75 ± 2	105 ± 8	9.0	-18.9	398 ± 24	27 ± 14	-	-
UGC 5786	53 ± 11	153 ± 5	6.0	-19.6	80 ± 15	36 ± 11	2.2 ± 0.8	294 ± 27
UGC 5789	68 ± 10	27 ± 3	12.0	-19.6	131 ± 10	20 ± 11	6.6 ± 3.6	12 ± 1
UGC 5842	47 ± 9	-68 ± 2	6.0	-18.8	115 ± 18	24 ± 15	4.8 ± 3.1	51 ± 1
UGC 5931	54 ± 16	0 ± 4	6.1	-19.8	157 ± 32	27 ± 13	5.8 ± 3.0	52 ± 3
UGC 5982	55 ± 4	28 ± 2	11.4	-20.0	199 ± 13	23 ± 14	8.7 ± 5.3	236 ± 19
UGC 6118	39 ± 8	-17 ± 3	7.3	-20.0	137 ± 24	31 ± 13	4.4 ± 2.0	403 ± 35
UGC 6277	17 ± 17	76 ± 3	9.3	-19.5	270 ± 258	24 ± 17	11.2 ± 13.4	274 ± 14
UGC 6419	66 ± 19	34 ± 6	5.3	-18.6	53 ± 11	26 ± 10	2.0 ± 0.9	5 ± 1
UGC 6521	46 ± 4	20 ± 2	19.2	-21.2	249 ± 18	26 ± 15	9.6 ± 5.6	64 ± 4
UGC 6523	24 ± 14	-7 ± 3	10.5	-21.0	118 ± 63	35 ± 13	3.4 ± 2.2	69 ± 5
UGC 6537	47 ± 5	-160 ± 2	12.1	-20.5	187 ± 17	18 ± 12	10.4 ± 7.0	25 ± 3
UGC 6628	20 ± 20	179 ± 2	6.1	-17.9	183 ± 168	17 ± 14	10.8 ± 13.3	60 ± 2
UGC 6702	38 ± 6	-104 ± 2	14.7	-20.6	195 ± 23	24 ± 15	8.1 ± 5.2	120 ± 11
UGC 6778	49 ± 4	-17 ± 1	9.5	-20.7	223 ± 14	25 ± 11	8.9 ± 4.0	352 ± 23
UGC 7021	56 ± 7	-94 ± 1	9.9	-19.7	223 ± 18	29 ± 14	7.7 ± 3.8	111 ± 6
UGC 7045	68 ± 2	99 ± 1	6.4	-19.2	160 ± 9	23 ± 11	7.0 ± 3.3	144 ± 4
UGC 7154	65 ± 3	-85 ± 1	13.1	-20.0	145 ± 9	23 ± 12	6.3 ± 3.3	124 ± 7
UGC 7278	44 ± 9	-20 ± 27	3.4	-17.4	145 ± 9	19 ± 11	-	-
UGC 7323	51 ± 11	38 ± 2	5.6	-18.3	84 ± 15	16 ± 13	5.2 ± 4.4	76 ± 4
UGC 7699	78 ± 2	32 ± 6	4.9	-17.6	92 ± 8	24 ± 11	3.8 ± 1.8	-
UGC 7831	56 ± 12	-70 ± 4	4.1	-18.5	92 ± 15	26 ± 9	3.5 ± 1.4	87 ± 2
UGC 7853	58 ± 28	-143 ± 3	5.1	-18.9	110 ± 35	24 ± 9	4.6 ± 2.3	20 ± 1
UGC 7876	53 ± 9	-16 ± 2	4.1	-17.9	98 ± 14	23 ± 11	4.3 ± 2.1	60 ± 1
UGC 7901	53 ± 2	-106 ± 1	11.3	-20.6	215 ± 10	25 ± 13	8.6 ± 4.5	191 ± 10
UGC 7985	49 ± 6	-84 ± 2	5.1	-18.7	112 ± 13	27 ± 10	4.1 ± 1.6	90 ± 1
UGC 8403	57 ± 4	121 ± 2	10.5	-19.2	128 ± 10	25 ± 10	5.1 ± 2.1	13 ± 1
UGC 8490	40 ± 15	167 ± 2	3.2	-17.1	90 ± 29	19 ± 13	4.7 ± 3.6	103 ± 4
UGC 8709	76 ± 1	-30 ± 1	27.1	-21.4	207 ± 9	27 ± 11	7.7 ± 3.1	32 ± 2
UGC 8852	52 ± 3	63 ± 1	8.8	-20.0	186 ± 10	25 ± 11	7.4 ± 3.3	84 ± 2
UGC 8863	77 ± 13	-142 ± 6	13.0	-20.3	191 ± 13	26 ± 13	7.3 ± 3.7	-
UGC 8898	27 ± 20	31 ± 6	11.7	-20.5	65 ± 45	23 ± 8	2.8 ± 2.2	65 ± 5
UGC 8900	57 ± 10	161 ± 2	19.5	-21.7	345 ± 37	25 ± 13	13.8 ± 7.3	62 ± 3
UGC 8937	32 ± 12	-175 ± 2	14.8	-21.1	320 ± 105	33 ± 15	9.7 ± 5.4	377 ± 34
UGC 9013	21 ± 16	164 ± 4	4.7	-18.2	62 ± 45	23 ± 10	2.7 ± 2.3	24 ± 1
UGC 9179	36 ± 14	49 ± 3	4.5	-17.8	111 ± 36	21 ± 11	5.3 ± 3.3	46 ± 3
UGC 9219	81 ± 6	99 ± 13	3.7	-16.6	45 ± 8	26 ± 13	1.7 ± 0.9	-
UGC 9248	58 ± 4	-99 ± 2	13.1	-20.2	166 ± 11	24 ± 15	6.9 ± 4.3	61 ± 1
UGC 9358	54 ± 4	-178 ± 2	13.3	-20.8	221 ± 14	29 ± 11	7.6 ± 2.9	245 ± 22
UGC 9366	62 ± 2	-135 ± 1	20.7	-21.7	241 ± 9	29 ± 14	8.3 ± 4.0	199 ± 13
UGC 9363	18 ± 14	147 ± 3	10.2	-19.8	143 ± 105	24 ± 11	6.0 ± 5.2	55 ± 2
UGC 9406	59 ± 25	132 ± 11	8.5	-19.0	19 ± 10	25 ± 12	0.8 ± 0.5	1 ± 1
UGC 9465	65 ± 4	127 ± 2	8.1	-18.0	97 ± 9	25 ± 10	3.9 ± 1.6	36 ± 1
UGC 9576	41 ± 11	122 ± 2	11.4	-19.6	104 ± 25	24 ± 11	4.3 ± 2.2	27 ± 2
UGC 9649	54 ± 6	-125 ± 2	3.9	-16.5	94 ± 11	19 ± 12	4.9 ± 3.2	191 ± 11
UGC 9736	51 ± 5	-141 ± 1	14.3	-20.6	192 ± 16	24 ± 14	8.0 ± 4.7	62 ± 4
UGC 9753	69 ± 1	3 ± 1	7.1	-19.1	138 ± 9	23 ± 13	6.0 ± 3.4	167 ± 4
UGC 9858	75 ± 2	70 ± 2	22.4	-20.4	160 ± 9	23 ± 15	7.0 ± 4.6	56 ± 1

Table B1: *continued*

Galaxy	$i_{z=0}^{(a)}$ °	$PA_{z=0}^{(b)}$ °	$D_{25}/2^{(c)}$ kpc	$M_B^{(d)}$ mag	$V_c^{max (e)}$ km s ⁻¹	$\sigma^{(f)}$ km s ⁻¹	V_c^{max}/σ	$S_{in}^{(g)}$ km s ⁻¹ kpc ⁻¹
UGC 9943	54 ± 2	-94 ± 1	11.1	-20.7	185 ± 10	26 ± 12	7.1 ± 3.3	167 ± 9
UGC 9969	61 ± 1	16 ± 1	27.2	-21.4	311 ± 9	22 ± 16	14.1 ± 10.3	61 ± 2
UGC 10075	62 ± 2	-150 ± 1	10.9	-19.9	168 ± 9	25 ± 10	6.7 ± 2.7	71 ± 2
UGC 10310	42 ± 20	-173 ± 6	4.9	-17.1	66 ± 27	22 ± 12	3.0 ± 2.0	20 ± 1
UGC 10359	44 ± 12	-76 ± 2	13.9	-19.0	143 ± 30	21 ± 14	6.8 ± 4.8	124 ± 7
UGC 10470	34 ± 9	-73 ± 2	8.8	-20.2	164 ± 39	27 ± 13	6.1 ± 3.3	106 ± 5
UGC 10445	47 ± 12	110 ± 4	6.4	-17.6	77 ± 17	23 ± 12	3.3 ± 1.9	36 ± 1
UGC 10502	50 ± 5	99 ± 2	19.8	-21.2	163 ± 14	19 ± 16	8.6 ± 7.3	27 ± 1
UGC 10521	59 ± 3	20 ± 2	7.3	-20.2	124 ± 9	27 ± 10	4.6 ± 1.7	53 ± 3
UGC 10546	42 ± 10	-178 ± 3	8.1	-19.1	106 ± 22	22 ± 14	4.8 ± 3.2	44 ± 3
UGC 10564	77 ± 6	149 ± 3	8.0	-17.6	75 ± 8	23 ± 12	3.3 ± 1.7	20 ± 1
UGC 10713	90 ± 1	8 ± 7	4.6	-19.0	105 ± 8	26 ± 11	4.0 ± 1.7	–
UGC 10757	44 ± 22	56 ± 5	3.9	-17.7	81 ± 33	28 ± 13	2.9 ± 1.8	90 ± 5
UGC 10897	31 ± 17	115 ± 3	7.1	-19.5	113 ± 56	18 ± 15	6.3 ± 6.1	41 ± 1
UGC 11012	72 ± 2	-61 ± 1	5.1	-18.7	117 ± 9	24 ± 10	4.9 ± 2.1	107 ± 3
UGC 11124	51 ± 10	-178 ± 3	8.2	-18.6	96 ± 15	22 ± 13	4.4 ± 2.7	33 ± 1
UGC 11218	58 ± 2	42 ± 1	11.9	-20.8	185 ± 9	22 ± 13	8.4 ± 5.0	105 ± 6
UGC 11269	69 ± 4	-88 ± 2	11.3	-19.9	202 ± 13	27 ± 14	7.5 ± 3.9	119 ± 11
UGC 11283	34 ± 17	120 ± 4	7.8	-19.3	173 ± 73	22 ± 14	7.9 ± 6.0	42 ± 4
UGC 11283C	68 ± 3	300 ± 15	4.0*	-16.5	173 ± 73	17 ± 15	–	–
UGC 11300	70 ± 3	168 ± 2	4.4	-17.8	112 ± 9	17 ± 14	6.6 ± 5.5	161 ± 7
UGC 11332	82 ± 2	65 ± 5	8.3	-19.5	91 ± 8	29 ± 10	3.1 ± 1.1	–
UGC 11407	64 ± 22	65 ± 9	11.3	-20.8	158 ± 30	28 ± 12	5.6 ± 2.6	55 ± 3
UGC 11429	61 ± 16	-152 ± 5	20.1	-21.8	232 ± 35	20 ± 16	11.6 ± 9.4	35 ± 1
UGC 11466	66 ± 5	-134 ± 3	3.9	-18.5	133 ± 10	32 ± 12	4.2 ± 1.6	195 ± 6
UGC 11496	44 ± 16	167 ± 3	9.2	–	96 ± 29	24 ± 13	4.0 ± 2.5	18 ± 1
UGC 11557	29 ± 22	-84 ± 3	5.9	-18.4	105 ± 72	23 ± 13	4.6 ± 4.1	25 ± 1
UGC 11707	70 ± 4	59 ± 2	7.9	-16.6	97 ± 5	21 ± 13	4.6 ± 2.9	16 ± 1
UGC 11852	47 ± 7	-171 ± 2	15.9	-20.2	221 ± 27	25 ± 18	8.8 ± 6.5	41 ± 4
UGC 11861	43 ± 12	-142 ± 2	12.0	-20.2	181 ± 39	24 ± 15	7.5 ± 5.0	21 ± 1
UGC 11872	47 ± 3	86 ± 1	7.7	-20.0	183 ± 12	26 ± 14	7.0 ± 3.8	168 ± 9
UGC 11909	90 ± 1	1 ± 6	7.2	-19.3	110 ± 8	27 ± 12	4.1 ± 1.8	–
UGC 11914	33 ± 4	-94 ± 1	8.0	-20.3	285 ± 26	20 ± 15	14.2 ± 10.8	413 ± 31
UGC 11951	76 ± 8	-99 ± 4	4.6	-19.3	106 ± 7	25 ± 13	4.2 ± 2.2	32 ± 1
UGC 12060	36 ± 11	-173 ± 3	3.5	-16.5	107 ± 27	14 ± 15	7.6 ± 8.4	27 ± 2
UGC 12276	33 ± 15	-38 ± 5	15.1	-20.7	94 ± 37	22 ± 16	4.3 ± 3.5	19 ± 2
UGC 12343	52 ± 4	-157 ± 1	15.1	-21.1	221 ± 14	25 ± 14	8.8 ± 5.0	25 ± 1
UGC 12754	53 ± 5	-18 ± 2	5.3	-18.6	123 ± 11	15 ± 15	8.2 ± 8.2	237 ± 13

(a): Inclination from Epinat et al. (2008b).

(b): Position angle of the major axis from Epinat et al. (2008b).

(c): Optical radius from the RC3 catalog (de Vaucouleurs et al. 1992) or from the HyperLeda database (refereed by an asterisk *, Paturel et al. 2003).

(d): B-band magnitude from the HyperLeda database (Paturel et al. 2003).

(e): Maximum velocity from Epinat et al. (2008b).

(f): Mean local velocity dispersion.

(g): Inner slope of the rotation curve. No value is provided when no high resolution rotation curve is computed (edge on galaxies, Epinat et al. 2008b,c).

Table B2: Exponential disk model on the sample projected at $z = 1.7$

Galaxy ^(a)	$i_{z=1.7}$ ^(b)	$PA_{z=1.7}$ ^(c)	r_t ^(d) kpc	V_t ^(e) $km\ s^{-1}$	V_c^{max} ^(f) $km\ s^{-1}$	σ ^(g) $km\ s^{-1}$	V_c^{max}/σ	ΔV_c^{mean} ^(h) $km\ s^{-1}$	S_{in} ⁽ⁱ⁾ $km\ s^{-1}\ kpc^{-1}$
UGC 89	10*	169 ± 1	4.3 ± 0.1	401 ± 1	401	21 ± 20	19.4	-22	492
UGC 94	22 ± 1	91 ± 1	4.9 ± 0.1	232 ± 1	232	16 ± 15	14.5	-10	250
UGC 508	10*	121 ± 1	10.2 ± 0.1	549 ± 1	549	27 ± 16	20.2	19	308
UGC 528	10*	54 ± 3	∞	∞	44	35 ± 2	1.3	33	127*
UGC 763	18 ± 9	119 ± 1	4.4 ± 0.1	103 ± 1	103	27 ± 5	3.8	-5	122
NGC 542	-	-	-	-	-	-	-	-	-
UGC 1249	-	-	-	-	-	-	-	-	-
UGC 1256	10*	67 ± 1	7.3 ± 0.7	96 ± 2	96	25 ± 5	3.8	-4	73
UGC 1317	70 ± 1	103 ± 1	11.5 ± 0.1	229 ± 1	229	23 ± 15	9.8	1	115
UGC 1437	46 ± 1	-60 ± 1	8.7 ± 0.1	234 ± 1	234	29 ± 15	8.2	8	152
UGC 1655	10*	-61 ± 1	1.1 ± 0.1	420 ± 1	420	0 ± 0	> 100	-81	1628
UGC 1736	11 ± 10	28 ± 1	11.2 ± 0.2	194 ± 2	189	22 ± 13	8.6	-7	100
UGC 1886	63 ± 1	34 ± 1	13.1 ± 0.1	272 ± 1	272	16 ± 11	17.3	10	122
UGC 2045	10*	-30 ± 1	12.5 ± 0.5	234 ± 5	167	31 ± 22	5.3	25	108
UGC 2082	-	-	-	-	-	-	-	-	-
UGC 2080	10*	-23 ± 1	5.9 ± 0.1	130 ± 1	130	16 ± 6	8.3	-3	119
UGC 2141	80*	-158 ± 3	∞	∞	71	41 ± 2	1.7	34	20*
UGC 2455	10*	-76 ± 8	∞	∞	10	24 ± 1	0.4	8	3*
UGC 2800	43 ± 4	-75 ± 1	5.6 ± 0.3	94 ± 1	94	9 ± 9	10.6	-7	90
UGC 2855	37 ± 3	97 ± 1	11.3 ± 0.1	225 ± 1	225	19 ± 12	12.1	-5	115
UGC 3013	61 ± 35	-156 ± 1	∞	∞	502	26 ± 19	19.2	-19	24*
UGC 3334	10*	-83 ± 1	16.7 ± 0.1	400 ± 1	400	32 ± 19	12.7	19	143
UGC 3382	43 ± 1	-174 ± 1	10.5 ± 0.1	327 ± 2	327	14 ± 11	22.9	-4	179
UGC 3384	-	-	-	-	-	-	-	-	-
UGC 3429	10*	-34 ± 1	12.7 ± 0.8	319 ± 11	301	44 ± 30	6.8	31	146
UGC 3463	62 ± 1	108 ± 1	10.3 ± 0.1	176 ± 1	176	32 ± 9	5.5	-3	98
UGC 3574	48 ± 1	102 ± 1	10.3 ± 0.2	192 ± 1	192	20 ± 6	9.5	5	107
UGC 3521	53 ± 1	-105 ± 1	6.7 ± 0.1	162 ± 1	162	13 ± 13	12.5	-7	133
UGC 3528	51 ± 1	-134 ± 1	2.7 ± 0.1	302 ± 1	302	13 ± 18	22.7	-36	558
UGC 3691	68 ± 2	-114 ± 1	46.5 ± 4.4	283 ± 19	147	34 ± 9	4.4	9	39
UGC 3685	10*	-67 ± 1	5.5 ± 0.2	92 ± 1	92	24 ± 4	3.8	8	90
UGC 3708	10*	-119 ± 1	1.1 ± 0.1	291 ± 1	291	15 ± 22	19.8	-80	1161
UGC 3709	55 ± 1	-132 ± 1	9.2 ± 0.1	257 ± 1	257	36 ± 19	7.1	-11	157
UGC 3734	10*	136 ± 1	1.1 ± 0.1	124 ± 1	124	6 ± 7	19.3	3	498
UGC 3809	60 ± 1	-3 ± 1	11.9 ± 0.1	271 ± 1	271	20 ± 15	13.2	-10	132
UGC 3740	54 ± 3	-113 ± 1	9.3 ± 0.9	75 ± 3	72	37 ± 2	2.0	11	46
UGC 3851	-	-	-	-	-	-	-	-	-
UGC 3876	61 ± 6	5 ± 1	4.5 ± 0.5	115 ± 2	115	32 ± 8	3.6	-9	135
UGC 3915	39 ± 1	30 ± 1	4.1 ± 0.1	225 ± 1	225	28 ± 16	8.2	-7	288
IC 476	80*	64 ± 1	∞	∞	84	25 ± 12	3.3	20	29*
UGC 4165	10*	-99 ± 1	2.1 ± 0.3	88 ± 3	88	22 ± 7	4.0	-9	202

Table B2: *continued*

Galaxy ^(a)	$i_{z=1.7}$ ^(b) °	$PA_{z=1.7}$ ^(c) °	r_t ^(d) kpc	V_t ^(e) $km\ s^{-1}$	V_c^{max} ^(f) $km\ s^{-1}$	σ ^(g) $km\ s^{-1}$	V_c^{max}/σ	ΔV_c^{mean} ^(h) $km\ s^{-1}$	S_{in} ⁽ⁱ⁾ $km\ s^{-1}\ kpc^{-1}$
UGC 4256	70 ± 1	-65 ± 1	21.1 ± 0.4	124 ± 2	123	47 ± 8	2.6	44	36
UGC 4273	53 ± 1	-149 ± 1	10.2 ± 0.1	190 ± 1	190	27 ± 10	6.9	18	106
UGC 4278	—	—	—	—	—	—	—	—	—
UGC 4284	67 ± 1	176 ± 1	18.8 ± 1.0	158 ± 5	110	20 ± 10	5.5	7	51
UGC 4325	11 ± 35	57 ± 1	1.1 ± 0.1	104 ± 1	104	14 ± 10	7.3	-24	428
UGC 4393	10*	-110 ± 1	∞	∞	58	31 ± 5	1.9	-4	6*
UGC 4422	20 ± 1	35 ± 1	9.8 ± 0.1	364 ± 1	364	25 ± 15	14.4	44	211
UGC 4456	14 ± 4	124 ± 1	14.9 ± 0.2	184 ± 1	184	25 ± 5	7.3	32	73
UGC 4499	10*	145 ± 1	1.1 ± 0.1	110 ± 1	110	4 ± 7	26.2	-56	448
UGC 4555	44 ± 1	91 ± 1	8.6 ± 0.1	187 ± 1	187	19 ± 11	9.7	5	122
UGC 4770	10*	-79 ± 1	26.5 ± 0.3	397 ± 2	378	25 ± 13	15.2	-29	93
UGC 4820	10*	156 ± 1	1.9 ± 0.1	458 ± 2	458	1 ± 3	> 100	-71	1123
UGC 4936	18 ± 2	-66 ± 1	11.1 ± 0.1	226 ± 1	226	22 ± 6	10.5	-4	117
UGC 5045	10*	146 ± 1	10.1 ± 0.1	447 ± 1	447	30 ± 9	14.8	-8	252
UGC 5175	48 ± 1	143 ± 1	6.3 ± 0.1	199 ± 1	199	26 ± 9	7.5	-11	173
UGC 5228	10*	119 ± 1	5.1 ± 0.1	143 ± 1	143	24 ± 14	6.0	-15	150
UGC 5251	63 ± 2	-102 ± 1	11.9 ± 0.1	136 ± 1	136	24 ± 11	5.7	-9	66
UGC 5253	45 ± 1	-5 ± 1	3.6 ± 0.1	266 ± 1	266	10 ± 13	27.1	-5	382
UGC 5279	—	—	—	—	—	—	—	—	—
UGC 5316	10*	127 ± 1	26.7 ± 1.3	167 ± 5	131	20 ± 7	6.5	-9	39
UGC 5319	31 ± 2	-11 ± 1	7.7 ± 0.2	181 ± 1	181	28 ± 7	6.4	4	131
UGC 5351	—	—	—	—	—	—	—	—	—
UGC 5414	10*	-151 ± 3	∞	∞	56	32 ± 2	1.8	10	24*
IC 2542	34 ± 1	174 ± 1	7.1 ± 0.1	304 ± 1	304	33 ± 12	9.3	-17	236
UGC 5510	10*	-161 ± 1	9.2 ± 0.3	166 ± 2	164	33 ± 5	5.0	20	103
UGC 5532	30 ± 1	147 ± 1	6.5 ± 0.1	381 ± 1	381	29 ± 13	13.2	29	319
UGC 5556	—	—	—	—	—	—	—	—	—
UGC 5786	80*	154 ± 1	∞	∞	83	53 ± 4	1.6	39	16*
UGC 5789	59 ± 2	31 ± 1	20.0 ± 0.6	123 ± 2	114	17 ± 9	6.8	-2	37
UGC 5842	70 ± 3	-68 ± 1	52.3 ± 17.0	330 ± 82	118	32 ± 7	3.7	13	41
UGC 5931	10*	9 ± 1	∞	∞	128	37 ± 6	3.4	28	27*
UGC 5982	49 ± 1	31 ± 1	6.6 ± 0.1	202 ± 1	202	12 ± 13	16.4	4	168
UGC 6118	80*	-25 ± 1	∞	∞	191	42 ± 20	4.6	39	33*
UGC 6277	10*	76 ± 1	6.6 ± 0.4	243 ± 5	236	42 ± 8	5.6	26	202
UGC 6419	10*	40 ± 3	1.4 ± 0.7	30 ± 7	30	27 ± 1	1.1	2	94
UGC 6521	47 ± 1	20 ± 1	8.6 ± 0.1	256 ± 1	256	27 ± 14	9.4	6	167
UGC 6523	10*	-6 ± 1	2.4 ± 0.1	115 ± 1	115	39 ± 8	2.9	-8	235
UGC 6537	27 ± 1	-164 ± 1	4.6 ± 0.1	188 ± 1	188	10 ± 10	18.3	-18	217
UGC 6628	42 ± 7	-179 ± 1	8.4 ± 1.1	142 ± 8	138	23 ± 7	6.0	0	95
UGC 6702	45 ± 1	-107 ± 1	5.5 ± 0.1	215 ± 1	215	16 ± 14	13.5	20	210
UGC 6778	28 ± 2	-18 ± 1	7.9 ± 0.1	204 ± 1	204	29 ± 12	7.0	19	145
UGC 7021	27 ± 3	-105 ± 1	6.1 ± 0.2	140 ± 1	140	45 ± 12	3.1	69	124

Table B2: *continued*

Galaxy ^(a)	$i_{z=1.7}$ ^(b) °	$PA_{z=1.7}$ ^(c) °	r_t ^(d) kpc	V_t ^(e) $km\ s^{-1}$	V_c^{max} ^(f) $km\ s^{-1}$	σ ^(g) $km\ s^{-1}$	V_c^{max}/σ	ΔV_c^{mean} ^(h) $km\ s^{-1}$	S_{in} ⁽ⁱ⁾ $km\ s^{-1}\ kpc^{-1}$
UGC 7045	34 ± 12	100 ± 1	4.9 ± 0.1	178 ± 1	178	11 ± 12	16.1	-15	191
UGC 7154	62 ± 1	-84 ± 1	15.7 ± 0.2	135 ± 1	133	24 ± 7	5.6	2	51
UGC 7278	-	-	-	-	-	-	-	-	-
UGC 7323	10*	35 ± 1	5.0 ± 0.5	77 ± 2	77	24 ± 5	3.2	-3	82
UGC 7699	-	-	-	-	-	-	-	-	-
UGC 7831	10*	-69 ± 1	8.1 ± 3.9	94 ± 21	65	43 ± 6	1.5	25	64
UGC 7853	10*	-149 ± 2	∞	∞	53	27 ± 2	1.9	20	14*
UGC 7876	10*	-18 ± 1	3.9 ± 0.8	93 ± 3	93	27 ± 3	3.4	-7	122
UGC 7901	45 ± 1	-107 ± 1	5.1 ± 0.1	243 ± 1	243	15 ± 16	16.3	-7	253
UGC 7985	55 ± 6	-88 ± 1	7.5 ± 1.3	98 ± 7	93	40 ± 4	2.3	23	72
UGC 8403	61 ± 1	120 ± 1	18.9 ± 0.4	146 ± 2	132	26 ± 6	5.0	-6	47
UGC 8490	33 ± 35	176 ± 2	3.4 ± 3.3	52 ± 8	50	31 ± 4	1.6	34	78
UGC 8709	74 ± 1	-26 ± 1	13.0 ± 0.1	222 ± 1	222	18 ± 15	12.5	-15	100
UGC 8852	10*	63 ± 1	4.0 ± 0.1	198 ± 1	198	14 ± 14	14.1	-26	256
UGC 8863	46 ± 19	-143 ± 1	35.9 ± 2.5	327 ± 14	214	19 ± 13	11.5	-18	58
UGC 8898	73 ± 6	38 ± 2	1.1 ± 0.1	33 ± 1	33	22 ± 3	1.5	21	133
UGC 8900	10*	163 ± 1	21.8 ± 0.1	357 ± 1	327	11 ± 15	29.0	0	100
UGC 8937	10*	-179 ± 1	10.3 ± 0.1	322 ± 1	322	37 ± 21	8.7	28	179
UGC 9013	10*	156 ± 2	6.1 ± 3.4	46 ± 9	45	25 ± 1	1.8	5	41
UGC 9179	10*	49 ± 1	12.6 ± 3.7	155 ± 27	118	24 ± 3	4.9	7	72
UGC 9219	-	-	-	-	-	-	-	-	-
UGC 9248	60 ± 1	-92 ± 1	10.4 ± 0.1	155 ± 1	154	36 ± 14	4.3	29	85
UGC 9358	48 ± 1	-175 ± 1	8.6 ± 0.1	243 ± 1	243	29 ± 17	8.4	16	158
UGC 9366	63 ± 1	-136 ± 1	9.2 ± 0.1	254 ± 1	254	30 ± 16	8.4	0	157
UGC 9363	10*	153 ± 1	7.5 ± 0.1	128 ± 1	128	25 ± 3	5.1	3	95
UGC 9406	10*	151 ± 2	50.3 ± 34.4	55 ± 28	26	24 ± 4	1.1	8	7
UGC 9465	60 ± 4	130 ± 1	25.3 ± 2.4	151 ± 9	108	33 ± 5	3.3	11	37
UGC 9576	50 ± 1	119 ± 1	15.9 ± 0.3	119 ± 1	115	25 ± 4	4.6	-3	44
UGC 9649	10*	-131 ± 1	∞	∞	101	27 ± 8	3.7	25	34*
UGC 9736	54 ± 1	-145 ± 1	15.0 ± 0.1	201 ± 1	200	29 ± 12	6.9	9	79
UGC 9753	10*	0 ± 1	1.9 ± 0.1	216 ± 3	216	1 ± 4	> 100	-48	551
UGC 9858	70 ± 1	70 ± 1	14.0 ± 0.2	167 ± 1	167	22 ± 16	7.6	14	70
UGC 9943	60 ± 1	-95 ± 1	8.0 ± 0.1	207 ± 1	207	29 ± 13	7.1	0	145
UGC 9969	59 ± 1	16 ± 1	12.9 ± 0.1	312 ± 1	312	22 ± 17	14.1	3	141
UGC 10075	16 ± 4	-149 ± 1	7.3 ± 0.1	173 ± 1	173	21 ± 11	8.0	-7	131
UGC 10310	31 ± 10	-154 ± 1	1.1 ± 0.1	78 ± 1	78	21 ± 5	3.7	-16	320
UGC 10359	37 ± 3	-83 ± 1	22.7 ± 0.8	196 ± 5	181	23 ± 9	7.9	-2	53
UGC 10470	28 ± 2	-64 ± 1	6.8 ± 0.1	143 ± 1	143	34 ± 7	4.1	18	115
UGC 10445	25 ± 6	105 ± 1	3.6 ± 0.2	78 ± 1	78	26 ± 4	3.0	-7	111
UGC 10502	52 ± 1	101 ± 1	15.2 ± 0.1	149 ± 1	149	33 ± 10	4.6	6	58
UGC 10521	10*	18 ± 1	3.4 ± 0.1	124 ± 1	124	26 ± 10	4.8	-10	186
UGC 10546	35 ± 3	174 ± 1	6.5 ± 0.2	95 ± 1	95	28 ± 8	3.4	14	80

Table B2: *continued*

Galaxy ^(a)	$i_{z=1.7}$ ^(b) °	$PA_{z=1.7}$ ^(c) °	r_t ^(d) kpc	V_t ^(e) $km\ s^{-1}$	V_c^{max} ^(f) $km\ s^{-1}$	σ ^(g) $km\ s^{-1}$	V_c^{max}/σ	ΔV_c^{mean} ^(h) $km\ s^{-1}$	S_{in} ⁽ⁱ⁾ $km\ s^{-1}\ kpc^{-1}$
UGC 10564	77 ± 5	148 ± 1	20.5 ± 3.3	100 ± 9	78	26 ± 5	3.0	2	30
UGC 10713	—	—	—	—	—	—	—	—	—
UGC 10757	55 ± 20	52 ± 2	4.8 ± 3.4	53 ± 10	52	39 ± 2	1.3	22	59
UGC 10897	10*	114 ± 1	21.7 ± 3.3	183 ± 18	118	30 ± 6	3.9	10	51
UGC 11012	80*	−65 ± 2	12.7 ± 5.6	122 ± 28	83	48 ± 7	1.7	46	56
UGC 11124	10*	−180 ± 1	30.2 ± 2.9	156 ± 10	102	25 ± 4	4.1	2	32
UGC 11218	41 ± 1	39 ± 1	7.4 ± 0.1	198 ± 1	198	17 ± 14	11.5	−2	148
UGC 11269	73 ± 1	−84 ± 1	45.1 ± 1.6	360 ± 9	224	28 ± 19	8.0	68	51
UGC 11283	56 ± 1	135 ± 1	3.5 ± 0.1	131 ± 1	131	29 ± 11	4.5	16	193
UGC 11283C	—	—	—	—	—	—	—	—	—
UGC 11300	10*	162 ± 2	8.3 ± 4.2	118 ± 24	105	28 ± 10	3.7	10	80
UGC 11332	—	—	—	—	—	—	—	—	—
UGC 11407	24 ± 5	82 ± 1	45.6 ± 1.5	285 ± 7	176	36 ± 10	4.9	−14	40
UGC 11429	80*	−157 ± 1	∞	∞	356	25 ± 14	14.1	−18	19*
UGC 11466	10*	−143 ± 2	4.0 ± 1.5	113 ± 6	113	49 ± 8	2.3	8	146
UGC 11496	44 ± 2	167 ± 1	18.8 ± 0.9	118 ± 3	102	23 ± 7	4.5	−6	38
UGC 11557	10*	−86 ± 1	12.4 ± 1.8	104 ± 8	89	27 ± 6	3.3	−3	49
UGC 11707	53 ± 5	54 ± 1	7.7 ± 0.3	93 ± 1	93	15 ± 10	6.0	−7	67
UGC 11852	13 ± 3	−171 ± 1	5.5 ± 0.1	230 ± 1	230	7 ± 10	33.5	−21	223
UGC 11861	41 ± 1	−150 ± 1	17.3 ± 0.2	174 ± 1	167	27 ± 9	6.1	0	60
UGC 11872	10*	82 ± 1	8.0 ± 0.1	193 ± 2	190	34 ± 14	5.6	29	135
UGC 11909	—	—	—	—	—	—	—	—	—
UGC 11914	19 ± 1	−93 ± 1	1.8 ± 0.1	426 ± 3	426	2 ± 6	> 100	−62	1130
UGC 11951	79 ± 35	−100 ± 5	∞	∞	69	37 ± 4	1.9	26	17*
UGC 12060	80*	177 ± 1	∞	∞	68	26 ± 5	2.6	3	20*
UGC 12276	39 ± 1	−44 ± 1	6.9 ± 0.1	97 ± 1	97	23 ± 8	4.2	0	78
UGC 12343	51 ± 1	−157 ± 1	15.1 ± 0.1	222 ± 1	222	31 ± 10	7.2	−19	87
UGC 12754	80*	−24 ± 1	∞	∞	128	32 ± 8	4.0	28	25*

(a): Galaxies for which no parameter is provided are those for which the fit was not possible.

(b): Inclination deduced from the fit. The error is a statistical error and thus gives a lower limit. The asterisk * indicates that the inclination was stacked to one boundary.

(c): Position angle of the major axis deduced from the fit with the inclination fixed to the value in Table B1. The error is a statistical error and thus gives a lower limit.

(d): Scale length radius of the model (defined in Appendix A) deduced from the fit with the inclination fixed to the value in Table B1. The error is a statistical error and thus gives a lower limit.

(e): Velocity of the model (defined in Appendix A) deduced from the fit with the inclination fixed to the value in Table B1. The error is a statistical error and thus gives a lower limit.

(f): Maximum velocity of the model within R_{last} (see Table B6). The error is the same as in column (e) and thus not take into account the uncertainty on the inclination.

(g): Local velocity dispersion (beam smearing corrected).

(h): Mean difference of the model rotation curve with the actual rotation curve at $z = 0$.

(i): Inner slope of the rotation curve from the model. The asterisk * indicates that only the slope is constrained by the model.

Table B3: Isothermal sphere model on the sample projected at $z = 1.7$

Galaxy ^(a)	$i_{z=1.7}$ ^(b) °	$PA_{z=1.7}$ ^(c) °	r_t ^(d) kpc	V_t ^(e) $km\ s^{-1}$	V_c^{max} ^(f) $km\ s^{-1}$	σ ^(g) $km\ s^{-1}$	V_c^{max}/σ	ΔV_c^{mean} ^(h) $km\ s^{-1}$	S_{in} ⁽ⁱ⁾ $km\ s^{-1}\ kpc^{-1}$
UGC 89	10*	170 ± 1	2.7 ± 0.1	406 ± 1	406	20 ± 17	20.8	-43	478
UGC 94	22 ± 1	91 ± 1	3.6 ± 0.1	231 ± 1	231	15 ± 13	15.2	-21	201
UGC 508	10*	121 ± 1	7.0 ± 0.1	552 ± 1	552	27 ± 16	20.2	-3	246
UGC 528	10*	54 ± 3	1.1 ± 0.1	44 ± 2	44	35 ± 2	1.3	30	130
UGC 763	18 ± 8	119 ± 1	4.2 ± 0.2	101 ± 1	101	27 ± 5	3.7	-7	76
NGC 542	-	-	-	-	-	-	-	-	-
UGC 1249	-	-	-	-	-	-	-	-	-
UGC 1256	10*	67 ± 1	7.4 ± 0.7	94 ± 2	94	25 ± 5	3.7	-3	40
UGC 1317	70 ± 1	103 ± 1	9.3 ± 0.1	225 ± 1	225	22 ± 13	10.4	-7	75
UGC 1437	45 ± 1	-59 ± 1	5.7 ± 0.1	234 ± 1	234	28 ± 15	8.5	-5	128
UGC 1655	10*	-61 ± 1	1.1 ± 0.1	319 ± 1	319	0 ± 0	> 100	-63	875
UGC 1736	10*	28 ± 1	11.9 ± 0.2	193 ± 2	188	22 ± 13	8.6	-4	51
UGC 1886	64 ± 1	34 ± 1	10.7 ± 0.1	268 ± 1	268	16 ± 11	16.9	7	79
UGC 2045	10*	-30 ± 1	10.4 ± 0.3	208 ± 3	171	31 ± 22	5.5	24	62
UGC 2082	-	-	-	-	-	-	-	-	-
UGC 2080	10*	-23 ± 1	5.7 ± 0.2	128 ± 1	128	16 ± 6	8.2	-4	71
UGC 2141	80*	-158 ± 3	∞	∞	71	41 ± 2	1.7	34	19*
UGC 2455	13 ± 35	-76 ± 11	∞	∞	10	24 ± 1	0.4	8	3*
UGC 2800	43 ± 4	-75 ± 1	5.9 ± 0.3	93 ± 1	93	9 ± 9	10.5	-6	49
UGC 2855	35 ± 3	97 ± 1	12.0 ± 0.1	223 ± 1	222	19 ± 12	11.9	-2	58
UGC 3013	40 ± 35	-156 ± 1	∞	∞	503	26 ± 19	19.2	-18	22*
UGC 3334	10*	-83 ± 1	14.4 ± 0.1	387 ± 1	387	31 ± 20	12.6	18	84
UGC 3382	43 ± 1	-174 ± 1	11.3 ± 0.1	325 ± 2	324	14 ± 11	22.7	-4	90
UGC 3384	-	-	-	-	-	-	-	-	-
UGC 3429	10*	-34 ± 1	9.8 ± 0.3	270 ± 5	269	44 ± 30	6.1	36	86
UGC 3463	62 ± 1	108 ± 1	10.7 ± 0.1	174 ± 1	174	32 ± 8	5.4	-3	51
UGC 3574	48 ± 1	102 ± 1	10.6 ± 0.2	189 ± 1	189	20 ± 6	9.3	7	56
UGC 3521	54 ± 1	-105 ± 1	6.7 ± 0.1	160 ± 1	160	13 ± 12	12.4	-8	75
UGC 3528	53 ± 1	-134 ± 1	1.5 ± 0.1	313 ± 3	313	14 ± 18	22.4	-64	649
UGC 3691	65 ± 2	-114 ± 1	25.3 ± 0.9	187 ± 5	145	34 ± 9	4.3	10	23
UGC 3685	10*	-67 ± 1	4.8 ± 0.3	91 ± 1	91	24 ± 4	3.7	7	59
UGC 3708	10*	-119 ± 1	1.1 ± 0.1	240 ± 1	240	22 ± 27	11.2	-52	681
UGC 3709	56 ± 1	-132 ± 1	9.1 ± 0.1	253 ± 1	253	36 ± 19	7.1	-11	87
UGC 3734	10*	136 ± 1	1.1 ± 0.1	103 ± 1	103	15 ± 7	7.0	3	294
UGC 3809	61 ± 1	-3 ± 1	12.6 ± 0.1	269 ± 1	269	21 ± 15	13.1	-14	67
UGC 3740	54 ± 3	-113 ± 1	9.3 ± 0.7	72 ± 3	71	37 ± 2	1.9	12	24
UGC 3851	-	-	-	-	-	-	-	-	-
UGC 3876	63 ± 6	5 ± 1	4.7 ± 0.6	114 ± 2	114	32 ± 8	3.6	-8	77
UGC 3915	38 ± 1	30 ± 1	2.6 ± 0.1	228 ± 1	228	25 ± 17	9.0	-17	273
IC 476	80*	64 ± 1	∞	∞	83	25 ± 12	3.3	21	28*
UGC 4165	10*	-99 ± 1	1.3 ± 0.6	89 ± 7	89	21 ± 8	4.2	-13	217

Table B3: *continued*

Galaxy ^(a)	$i_{z=1.7}$ ^(b)	$PA_{z=1.7}$ ^(c)	r_t ^(d)	V_t ^(e)	V_c^{max} ^(f)	σ ^(g)	V_c^{max}/σ	ΔV_c^{mean} ^(h)	S_{in} ⁽ⁱ⁾
	$^\circ$	$^\circ$	kpc	$km\ s^{-1}$	$km\ s^{-1}$	$km\ s^{-1}$		$km\ s^{-1}$	$km\ s^{-1}\ kpc^{-1}$
UGC 4256	80*	-65 ± 1	21.9 ± 0.3	122 ± 1	121	47 ± 8	2.6	47	17
UGC 4273	53 ± 1	-149 ± 1	11.3 ± 0.1	190 ± 1	190	28 ± 10	6.9	20	53
UGC 4278	—	—	—	—	—	—	—	—	—
UGC 4284	66 ± 1	176 ± 1	15.9 ± 0.4	140 ± 2	111	20 ± 10	5.5	8	28
UGC 4325	10*	56 ± 1	1.1 ± 0.1	81 ± 1	81	20 ± 10	4.1	-16	240
UGC 4393	10*	-110 ± 1	∞	∞	58	31 ± 5	1.9	-4	6*
UGC 4422	19 ± 1	35 ± 1	7.6 ± 0.1	360 ± 1	360	24 ± 14	14.7	34	148
UGC 4456	16 ± 3	124 ± 1	15.0 ± 0.2	181 ± 1	181	25 ± 5	7.2	33	38
UGC 4499	10*	145 ± 1	1.1 ± 0.1	89 ± 1	89	9 ± 9	9.4	-47	259
UGC 4555	44 ± 1	91 ± 1	8.5 ± 0.1	185 ± 1	185	19 ± 11	9.7	5	68
UGC 4770	10*	-79 ± 1	28.8 ± 0.2	394 ± 2	376	25 ± 13	15.2	-30	43
UGC 4820	10*	156 ± 1	1.1 ± 0.1	451 ± 1	451	3 ± 7	> 100	-56	1315
UGC 4936	14 ± 2	-66 ± 1	10.9 ± 0.1	222 ± 1	222	22 ± 6	10.3	-3	64
UGC 5045	10*	146 ± 1	9.4 ± 0.1	439 ± 1	439	30 ± 9	14.6	-12	146
UGC 5175	48 ± 1	143 ± 1	6.2 ± 0.1	196 ± 1	196	26 ± 8	7.4	-11	99
UGC 5228	10*	118 ± 1	4.8 ± 0.1	139 ± 1	139	25 ± 12	5.6	-15	90
UGC 5251	62 ± 2	-102 ± 1	12.6 ± 0.1	135 ± 1	135	24 ± 11	5.7	-7	34
UGC 5253	47 ± 1	-5 ± 1	2.2 ± 0.1	269 ± 1	269	9 ± 12	31.5	-17	383
UGC 5279	—	—	—	—	—	—	—	—	—
UGC 5316	10*	127 ± 1	22.3 ± 0.6	148 ± 2	131	20 ± 7	6.6	-8	21
UGC 5319	31 ± 2	-11 ± 1	8.3 ± 0.2	180 ± 1	180	28 ± 7	6.4	6	68
UGC 5351	—	—	—	—	—	—	—	—	—
UGC 5414	10*	-151 ± 3	21.5 ± 16.8	101 ± 59	58	32 ± 2	1.8	10	15
IC 2542	34 ± 1	174 ± 1	7.6 ± 0.1	302 ± 1	302	33 ± 12	9.2	-14	125
UGC 5510	10*	-161 ± 1	9.5 ± 0.2	164 ± 2	162	33 ± 5	4.9	21	54
UGC 5532	33 ± 1	147 ± 1	3.6 ± 0.1	395 ± 1	395	28 ± 12	14.1	7	346
UGC 5556	—	—	—	—	—	—	—	—	—
UGC 5786	80*	154 ± 1	∞	∞	83	53 ± 4	1.6	39	15*
UGC 5789	57 ± 2	31 ± 1	19.4 ± 0.4	117 ± 1	112	17 ± 9	6.7	0	19
UGC 5842	66 ± 3	-68 ± 1	20.6 ± 1.9	171 ± 12	118	32 ± 7	3.7	14	26
UGC 5931	10*	9 ± 1	∞	∞	130	37 ± 6	3.5	28	21*
UGC 5982	49 ± 1	31 ± 1	6.6 ± 0.1	199 ± 1	199	12 ± 13	16.0	3	95
UGC 6118	80*	-25 ± 1	∞	∞	192	42 ± 20	4.6	39	31*
UGC 6277	10*	76 ± 1	7.3 ± 0.4	244 ± 5	236	42 ± 8	5.6	30	105
UGC 6419	10*	41 ± 3	1.1 ± 0.1	26 ± 1	26	27 ± 1	1.0	1	77
UGC 6521	47 ± 1	20 ± 1	6.8 ± 0.1	252 ± 1	252	27 ± 15	9.5	-3	117
UGC 6523	10*	-6 ± 1	1.5 ± 0.1	115 ± 2	115	39 ± 8	2.9	-11	238
UGC 6537	27 ± 1	-164 ± 1	3.6 ± 0.1	186 ± 1	186	11 ± 10	17.3	-23	162
UGC 6628	39 ± 6	-179 ± 1	8.2 ± 0.8	137 ± 6	134	23 ± 7	5.8	2	52
UGC 6702	44 ± 1	-107 ± 1	3.5 ± 0.1	214 ± 1	214	15 ± 13	14.3	3	192
UGC 6778	28 ± 2	-18 ± 1	8.3 ± 0.1	203 ± 1	202	29 ± 12	7.0	21	76
UGC 7021	28 ± 3	-105 ± 1	5.9 ± 0.2	136 ± 1	136	45 ± 12	3.0	69	72

Table B3: *continued*

Galaxy ^(a)	$i_{z=1.7}$ ^(b) °	$PA_{z=1.7}$ ^(c) °	r_t ^(d) kpc	V_t ^(e) $km\ s^{-1}$	V_c^{max} ^(f) $km\ s^{-1}$	σ ^(g) $km\ s^{-1}$	V_c^{max}/σ	ΔV_c^{mean} ^(h) $km\ s^{-1}$	S_{in} ⁽ⁱ⁾ $km\ s^{-1}\ kpc^{-1}$
UGC 7045	12 ± 35	100 ± 1	5.2 ± 0.2	175 ± 1	175	12 ± 12	14.9	-14	106
UGC 7154	62 ± 1	-84 ± 1	16.5 ± 0.2	133 ± 1	131	24 ± 7	5.5	4	25
UGC 7278	-	-	-	-	-	-	-	-	-
UGC 7323	10*	35 ± 1	5.2 ± 0.6	76 ± 2	76	24 ± 5	3.2	-2	46
UGC 7699	-	-	-	-	-	-	-	-	-
UGC 7831	10*	-69 ± 1	7.7 ± 2.5	88 ± 13	67	43 ± 6	1.6	26	36
UGC 7853	10*	-149 ± 2	∞	∞	54	27 ± 2	2.0	20	11*
UGC 7876	10*	-18 ± 1	3.9 ± 1.0	91 ± 3	91	27 ± 3	3.3	-7	73
UGC 7901	44 ± 1	-107 ± 1	3.9 ± 0.1	240 ± 1	240	14 ± 14	17.0	-13	193
UGC 7985	55 ± 6	-88 ± 1	7.8 ± 1.0	96 ± 5	93	40 ± 4	2.3	23	39
UGC 8403	60 ± 1	120 ± 1	17.9 ± 0.3	137 ± 1	130	26 ± 5	4.9	-5	24
UGC 8490	35 ± 35	176 ± 2	∞	∞	50	30 ± 4	1.6	31	63*
UGC 8709	74 ± 1	-26 ± 1	13.9 ± 0.1	220 ± 1	220	19 ± 15	11.8	-15	50
UGC 8852	10*	63 ± 1	3.1 ± 0.1	195 ± 1	195	12 ± 14	15.6	-32	196
UGC 8863	42 ± 17	-142 ± 1	27.8 ± 1.0	273 ± 6	215	18 ± 12	12.1	-20	31
UGC 8898	75 ± 6	38 ± 2	1.1 ± 0.1	27 ± 1	27	22 ± 3	1.2	24	79
UGC 8900	10*	163 ± 1	20.9 ± 0.1	338 ± 1	322	11 ± 14	28.8	4	51
UGC 8937	15 ± 1	-179 ± 1	8.7 ± 0.1	315 ± 1	315	36 ± 21	8.8	23	114
UGC 9013	10*	156 ± 2	6.4 ± 3.1	46 ± 8	45	25 ± 1	1.8	6	22
UGC 9179	10*	49 ± 1	10.3 ± 1.6	135 ± 12	117	24 ± 3	4.9	8	41
UGC 9219	-	-	-	-	-	-	-	-	-
UGC 9248	60 ± 1	-92 ± 1	11.2 ± 0.1	154 ± 1	153	36 ± 14	4.3	31	43
UGC 9358	48 ± 1	-175 ± 1	9.1 ± 0.1	241 ± 1	241	29 ± 17	8.3	17	83
UGC 9366	64 ± 1	-136 ± 1	8.8 ± 0.1	249 ± 1	249	30 ± 16	8.3	-1	89
UGC 9363	10*	153 ± 1	8.0 ± 0.2	128 ± 1	128	25 ± 3	5.0	4	50
UGC 9406	10*	151 ± 2	24.7 ± 5.7	34 ± 6	26	24 ± 4	1.1	9	4
UGC 9465	62 ± 3	130 ± 1	18.4 ± 0.8	122 ± 4	106	33 ± 5	3.2	12	21
UGC 9576	50 ± 1	119 ± 1	16.7 ± 0.2	117 ± 1	114	25 ± 4	4.5	-1	22
UGC 9649	10*	-131 ± 1	∞	∞	102	27 ± 8	3.7	25	27*
UGC 9736	54 ± 1	-145 ± 1	16.0 ± 0.1	199 ± 1	198	29 ± 12	6.8	12	39
UGC 9753	10*	0 ± 1	1.1 ± 0.1	210 ± 1	210	2 ± 7	93.3	-50	605
UGC 9858	70 ± 1	70 ± 1	14.3 ± 0.2	164 ± 1	164	22 ± 16	7.5	16	36
UGC 9943	60 ± 1	-95 ± 1	7.7 ± 0.1	204 ± 1	204	28 ± 13	7.2	-1	83
UGC 9969	59 ± 1	16 ± 1	11.5 ± 0.1	307 ± 1	307	22 ± 17	14.1	-1	83
UGC 10075	21 ± 3	-149 ± 1	7.3 ± 0.1	170 ± 1	170	21 ± 11	8.1	-6	73
UGC 10310	33 ± 10	-154 ± 1	1.1 ± 0.1	62 ± 1	62	23 ± 5	2.7	-12	182
UGC 10359	36 ± 3	-83 ± 1	18.3 ± 0.4	169 ± 2	166	23 ± 9	7.2	0	29
UGC 10470	28 ± 2	-64 ± 1	7.5 ± 0.1	142 ± 1	142	35 ± 7	4.1	19	60
UGC 10445	23 ± 7	105 ± 1	3.2 ± 0.2	76 ± 1	76	25 ± 4	3.0	-8	74
UGC 10502	52 ± 1	101 ± 1	15.7 ± 0.1	147 ± 1	147	33 ± 10	4.5	7	29
UGC 10521	10*	18 ± 1	2.8 ± 0.1	122 ± 1	122	26 ± 10	4.7	-12	137
UGC 10546	36 ± 3	174 ± 1	7.1 ± 0.2	95 ± 1	95	28 ± 8	3.4	15	42

Table B3: *continued*

Galaxy ^(a)	$i_{z=1.7}$ ^(b) °	$PA_{z=1.7}$ ^(c) °	r_t ^(d) kpc	V_t ^(e) $km\ s^{-1}$	V_c^{max} ^(f) $km\ s^{-1}$	σ ^(g) $km\ s^{-1}$	V_c^{max}/σ	ΔV_c^{mean} ^(h) $km\ s^{-1}$	S_{in} ⁽ⁱ⁾ $km\ s^{-1}\ kpc^{-1}$
UGC 10564	74 ± 6	148 ± 1	17.5 ± 1.5	90 ± 4	78	26 ± 5	3.0	3	16
UGC 10713	—	—	—	—	—	—	—	—	—
UGC 10757	56 ± 20	52 ± 2	4.9 ± 3.5	53 ± 10	51	39 ± 2	1.3	23	33
UGC 10897	10*	114 ± 1	15.4 ± 1.0	145 ± 6	118	30 ± 6	3.9	11	29
UGC 11012	80*	−65 ± 2	11.3 ± 2.9	112 ± 15	85	48 ± 7	1.8	48	31
UGC 11124	10*	−180 ± 1	19.9 ± 0.8	118 ± 3	100	25 ± 4	4.0	3	19
UGC 11218	42 ± 1	39 ± 1	7.6 ± 0.1	195 ± 1	195	17 ± 13	11.5	−1	81
UGC 11269	70 ± 1	−84 ± 1	29.3 ± 0.4	270 ± 3	222	28 ± 19	7.9	71	29
UGC 11283	58 ± 1	135 ± 1	2.8 ± 0.1	129 ± 1	129	29 ± 11	4.4	13	143
UGC 11283C	—	—	—	—	—	—	—	—	—
UGC 11300	10*	162 ± 2	7.2 ± 2.5	109 ± 13	104	28 ± 10	3.7	9	48
UGC 11332	—	—	—	—	—	—	—	—	—
UGC 11407	10*	82 ± 1	30.7 ± 0.5	218 ± 3	175	35 ± 11	4.9	−13	22
UGC 11429	80*	−157 ± 1	∞	∞	357	25 ± 14	14.2	−18	18*
UGC 11466	10*	−143 ± 2	4.2 ± 1.8	112 ± 7	111	49 ± 8	2.3	9	84
UGC 11496	44 ± 2	167 ± 1	17.0 ± 0.5	109 ± 2	101	23 ± 7	4.4	−4	20
UGC 11557	10*	−86 ± 1	11.0 ± 1.0	95 ± 4	88	27 ± 6	3.3	−2	27
UGC 11707	54 ± 5	54 ± 1	8.1 ± 0.4	92 ± 1	92	15 ± 10	5.9	−7	35
UGC 11852	10*	−172 ± 1	5.4 ± 0.1	226 ± 1	226	7 ± 10	31.2	−23	131
UGC 11861	42 ± 1	−150 ± 1	17.5 ± 0.1	169 ± 1	164	27 ± 9	6.0	1	30
UGC 11872	10*	82 ± 1	8.4 ± 0.1	191 ± 1	188	34 ± 14	5.6	31	71
UGC 11909	—	—	—	—	—	—	—	—	—
UGC 11914	10 ± 2	−93 ± 1	1.1 ± 0.1	397 ± 1	397	5 ± 8	87.9	−57	1144
UGC 11951	80*	−100 ± 5	∞	∞	72	37 ± 4	1.9	25	16*
UGC 12060	23 ± 35	177 ± 1	∞	∞	68	26 ± 5	2.6	3	19*
UGC 12276	39 ± 1	−44 ± 1	5.7 ± 0.1	96 ± 1	96	23 ± 9	4.2	−1	53
UGC 12343	51 ± 1	−157 ± 1	17.1 ± 0.1	224 ± 1	223	31 ± 9	7.2	−17	41
UGC 12754	80*	−24 ± 1	∞	∞	128	32 ± 8	4.0	28	24*

(a): Galaxies for which no parameter is provided are those for which the fit was not possible.

(b): Inclination deduced from the fit. The error is a statistical error and thus gives a lower limit. The asterisk * indicates that the inclination was stacked to one boundary.

(c): Position angle of the major axis deduced from the fit with the inclination fixed to the value in Table B1. The error is a statistical error and thus gives a lower limit.

(d): Scale length radius of the model (defined in Appendix A) deduced from the fit with the inclination fixed to the value in Table B1. The error is a statistical error and thus gives a lower limit.

(e): Velocity of the model (defined in Appendix A) deduced from the fit with the inclination fixed to the value in Table B1. The error is a statistical error and thus gives a lower limit.

(f): Maximum velocity of the model within R_{last} (see Table B6). The error is the same as in column (e) and thus not take into account the uncertainty on the inclination.

(g): Local velocity dispersion (beam smearing corrected).

(h): Mean difference of the model rotation curve with the actual rotation curve at $z = 0$.

(i): Inner slope of the rotation curve from the model. The asterisk * indicates that only the slope is constrained by the model.

Table B4: “Flat model” on the sample projected at $z = 1.7$

Galaxy ^(a)	$i_{z=1.7}$ ^(b) °	$PA_{z=1.7}$ ^(c) °	r_t ^(d) kpc	V_t ^(e) km s ⁻¹	V_c^{max} ^(f) km s ⁻¹	σ ^(g) km s ⁻¹	V_c^{max}/σ	ΔV_c^{mean} ^(h) km s ⁻¹	S_{in} ⁽ⁱ⁾ km s ⁻¹ kpc ⁻¹
UGC 89	19 ± 1	171 ± 1	1.0 ± 0.1	366 ± 1	366	22 ± 18	16.7	-28	363
UGC 94	21 ± 1	91 ± 1	1.0 ± 0.1	218 ± 1	218	15 ± 13	14.1	-26	224
UGC 508	10*	122 ± 1	1.0 ± 0.1	519 ± 1	519	28 ± 16	18.6	-32	517
UGC 528	10*	54 ± 3	1.1 ± 0.1	41 ± 2	41	35 ± 2	1.1	39	38
UGC 763	24 ± 6	119 ± 1	1.2 ± 0.3	98 ± 1	98	26 ± 5	3.8	-10	83
NGC 542	-	-	-	-	-	-	-	-	-
UGC 1249	-	-	-	-	-	-	-	-	-
UGC 1256	78 ± 6	67 ± 1	3.0 ± 0.2	90 ± 2	90	25 ± 5	3.6	-2	30
UGC 1317	69 ± 1	103 ± 1	3.0 ± 0.1	215 ± 1	215	21 ± 12	10.3	-13	72
UGC 1437	46 ± 1	-58 ± 1	1.1 ± 0.1	213 ± 1	213	28 ± 15	7.5	-12	203
UGC 1655	10*	-61 ± 1	1.1 ± 0.1	259 ± 1	259	0 ± 0	> 100	-40	228
UGC 1736	10*	28 ± 1	4.7 ± 0.1	181 ± 1	181	21 ± 14	8.4	-2	38
UGC 1886	65 ± 1	35 ± 1	6.3 ± 0.1	257 ± 1	257	17 ± 11	14.9	2	41
UGC 2045	10*	-30 ± 1	3.5 ± 0.1	182 ± 1	182	30 ± 22	6.1	23	52
UGC 2082	-	-	-	-	-	-	-	-	-
UGC 2080	10*	-23 ± 1	1.6 ± 0.2	124 ± 1	124	15 ± 7	8.4	-8	80
UGC 2141	79 ± 35	-158 ± 4	∞	∞	71	41 ± 2	1.7	35	19*
UGC 2455	53 ± 35	-76 ± 9	∞	∞	10	24 ± 1	0.4	8	3*
UGC 2800	46 ± 3	-75 ± 1	2.8 ± 0.1	91 ± 1	91	9 ± 9	10.6	-4	33
UGC 2855	49 ± 1	98 ± 1	5.0 ± 0.1	212 ± 1	212	17 ± 12	12.8	2	42
UGC 3013	44 ± 35	-156 ± 1	∞	∞	505	26 ± 19	19.3	-18	22*
UGC 3334	10 ± 1	-84 ± 1	4.4 ± 0.1	373 ± 1	373	29 ± 20	12.7	9	84
UGC 3382	41 ± 1	-174 ± 1	5.0 ± 0.1	310 ± 1	310	14 ± 11	22.2	0	62
UGC 3384	-	-	-	-	-	-	-	-	-
UGC 3429	45 ± 35	-33 ± 1	10.5 ± 4.2	600 ± 238	472	44 ± 34	10.7	20	57
UGC 3463	62 ± 1	108 ± 1	5.3 ± 0.1	173 ± 1	173	32 ± 9	5.3	0	33
UGC 3574	49 ± 1	102 ± 1	4.3 ± 0.1	180 ± 1	180	20 ± 6	9.0	10	42
UGC 3521	55 ± 1	-105 ± 1	2.7 ± 0.1	156 ± 1	156	12 ± 12	12.9	-7	58
UGC 3528	54 ± 1	-135 ± 1	1.0 ± 0.1	270 ± 1	270	16 ± 20	17.2	-35	277
UGC 3691	62 ± 2	-115 ± 1	6.8 ± 0.1	138 ± 2	138	33 ± 10	4.2	10	20
UGC 3685	10*	-67 ± 1	1.7 ± 0.5	88 ± 1	88	24 ± 4	3.6	7	51
UGC 3708	10*	-118 ± 1	1.1 ± 0.1	211 ± 1	211	26 ± 30	8.0	-8	191
UGC 3709	59 ± 1	-131 ± 1	1.4 ± 0.1	240 ± 1	240	32 ± 20	7.6	-30	167
UGC 3734	10*	136 ± 1	1.1 ± 0.1	90 ± 1	90	20 ± 6	4.6	6	83
UGC 3809	61 ± 1	-3 ± 1	6.0 ± 0.1	265 ± 1	265	20 ± 15	13.1	-14	44
UGC 3740	51 ± 3	-113 ± 1	3.5 ± 0.1	66 ± 1	66	37 ± 2	1.8	14	19
UGC 3851	-	-	-	-	-	-	-	-	-
UGC 3876	63 ± 6	5 ± 1	2.0 ± 0.2	111 ± 2	111	32 ± 8	3.5	-6	55
UGC 3915	30 ± 1	30 ± 1	1.0 ± 0.1	208 ± 1	208	28 ± 16	7.3	-12	208
IC 476	80*	64 ± 1	∞	∞	83	25 ± 12	3.3	21	28*
UGC 4165	10*	-99 ± 1	1.1 ± 0.1	80 ± 1	80	24 ± 7	3.4	-6	75

Table B4: *continued*

Galaxy ^(a)	$i_{z=1.7}$ ^(b) °	$PA_{z=1.7}$ ^(c) °	r_t ^(d) kpc	V_t ^(e) $km\ s^{-1}$	V_c^{max} ^(f) $km\ s^{-1}$	σ ^(g) $km\ s^{-1}$	V_c^{max}/σ	ΔV_c^{mean} ^(h) $km\ s^{-1}$	S_{in} ⁽ⁱ⁾ $km\ s^{-1}\ kpc^{-1}$
UGC 4256	80*	-65 ± 1	9.3 ± 0.1	117 ± 1	117	47 ± 8	2.5	52	13
UGC 4273	53 ± 1	-148 ± 1	5.2 ± 0.1	185 ± 1	185	27 ± 11	6.8	21	36
UGC 4278	—	—	—	—	—	—	—	—	—
UGC 4284	64 ± 1	176 ± 1	5.2 ± 0.1	117 ± 1	117	19 ± 10	6.1	9	23
UGC 4325	10*	56 ± 1	1.1 ± 0.1	68 ± 1	68	24 ± 8	2.8	-5	64
UGC 4393	10*	-111 ± 1	8.8 ± 0.3	54 ± 2	54	31 ± 5	1.7	-4	6
UGC 4422	13 ± 1	35 ± 1	1.4 ± 0.1	345 ± 1	345	23 ± 13	14.7	2	250
UGC 4456	18 ± 3	124 ± 1	5.0 ± 0.1	173 ± 1	173	25 ± 5	6.9	31	35
UGC 4499	10*	145 ± 1	1.1 ± 0.1	77 ± 1	77	14 ± 10	5.6	-30	71
UGC 4555	44 ± 1	91 ± 1	3.2 ± 0.1	181 ± 1	181	18 ± 11	9.9	3	56
UGC 4770	10*	-79 ± 1	11.8 ± 0.1	359 ± 1	359	24 ± 13	14.9	-34	31
UGC 4820	10*	156 ± 1	1.1 ± 0.1	355 ± 1	355	4 ± 9	92.6	-34	331
UGC 4936	10*	-66 ± 1	3.9 ± 0.1	212 ± 1	212	21 ± 7	9.9	-2	54
UGC 5045	10*	146 ± 1	1.0 ± 0.1	427 ± 1	427	30 ± 10	14.4	-18	436
UGC 5175	49 ± 1	143 ± 1	2.8 ± 0.1	192 ± 1	192	26 ± 9	7.4	-9	68
UGC 5228	21 ± 18	118 ± 1	2.1 ± 0.1	136 ± 1	136	25 ± 11	5.3	-14	65
UGC 5251	70 ± 1	-102 ± 1	5.4 ± 0.1	132 ± 1	132	23 ± 12	5.7	-4	24
UGC 5253	49 ± 1	-5 ± 1	1.1 ± 0.1	241 ± 1	241	12 ± 13	20.5	-5	216
UGC 5279	—	—	—	—	—	—	—	—	—
UGC 5316	56 ± 5	128 ± 1	7.2 ± 0.1	126 ± 1	126	17 ± 9	7.3	-6	17
UGC 5319	31 ± 2	-11 ± 1	3.7 ± 0.1	175 ± 1	175	28 ± 7	6.2	9	47
UGC 5351	—	—	—	—	—	—	—	—	—
UGC 5414	15 ± 35	-149 ± 3	3.6 ± 0.9	57 ± 6	57	32 ± 2	1.8	8	16
IC 2542	33 ± 1	174 ± 1	3.5 ± 0.1	295 ± 1	295	33 ± 12	9.1	-3	85
UGC 5510	11 ± 6	-161 ± 1	3.8 ± 0.1	153 ± 1	153	33 ± 5	4.7	24	40
UGC 5532	41 ± 1	146 ± 1	1.0 ± 0.2	321 ± 1	321	32 ± 12	10.1	40	313
UGC 5556	—	—	—	—	—	—	—	—	—
UGC 5786	80*	154 ± 1	∞	∞	83	53 ± 4	1.6	39	15*
UGC 5789	54 ± 2	31 ± 1	6.8 ± 0.1	102 ± 1	102	16 ± 8	6.4	3	15
UGC 5842	60 ± 2	-68 ± 1	5.0 ± 0.2	118 ± 3	118	31 ± 7	3.7	13	23
UGC 5931	10 ± 35	9 ± 1	∞	∞	130	37 ± 6	3.5	28	21*
UGC 5982	49 ± 1	31 ± 1	3.1 ± 0.1	196 ± 1	196	12 ± 13	15.8	8	64
UGC 6118	59 ± 4	-25 ± 1	∞	∞	192	42 ± 20	4.6	39	31*
UGC 6277	11 ± 12	76 ± 1	3.0 ± 0.1	231 ± 3	231	42 ± 8	5.5	37	76
UGC 6419	23 ± 35	41 ± 3	1.1 ± 0.1	21 ± 1	21	28 ± 1	0.8	3	20
UGC 6521	46 ± 1	20 ± 1	1.0 ± 0.1	241 ± 1	241	27 ± 15	9.0	-14	243
UGC 6523	10*	-6 ± 1	1.0 ± 0.1	103 ± 1	103	40 ± 8	2.6	-1	103
UGC 6537	26 ± 1	-164 ± 1	1.1 ± 0.1	177 ± 1	177	12 ± 10	15.3	-26	165
UGC 6628	28 ± 8	-179 ± 1	3.0 ± 0.2	123 ± 3	123	23 ± 7	5.4	4	41
UGC 6702	46 ± 1	-106 ± 1	0.9 ± 0.1	195 ± 1	195	16 ± 13	12.5	-4	208
UGC 6778	29 ± 1	-18 ± 1	3.6 ± 0.1	196 ± 1	196	28 ± 14	7.0	24	54
UGC 7021	31 ± 3	-105 ± 1	2.3 ± 0.1	130 ± 1	130	45 ± 12	2.9	68	57

Table B4: *continued*

Galaxy ^(a)	$i_{z=1.7}$ ^(b) °	$PA_{z=1.7}$ ^(c) °	r_t ^(d) kpc	V_t ^(e) km s ⁻¹	V_c^{max} ^(f) km s ⁻¹	σ ^(g) km s ⁻¹	V_c^{max}/σ	ΔV_c^{mean} ^(h) km s ⁻¹	S_{in} ⁽ⁱ⁾ km s ⁻¹ kpc ⁻¹
UGC 7045	21 ± 20	100 ± 1	2.5 ± 0.1	173 ± 1	173	13 ± 13	13.7	-9	68
UGC 7154	61 ± 1	-85 ± 1	6.6 ± 0.1	124 ± 1	124	23 ± 8	5.4	7	19
UGC 7278	-	-	-	-	-	-	-	-	-
UGC 7323	14 ± 28	35 ± 1	2.3 ± 0.2	74 ± 1	74	24 ± 5	3.1	-1	32
UGC 7699	-	-	-	-	-	-	-	-	-
UGC 7831	18 ± 35	-69 ± 1	2.8 ± 0.5	80 ± 5	72	43 ± 6	1.7	28	29
UGC 7853	22 ± 35	-149 ± 2	∞	∞	54	27 ± 2	2.0	20	11*
UGC 7876	18 ± 35	-18 ± 1	1.7 ± 0.5	89 ± 3	89	27 ± 3	3.3	-6	54
UGC 7901	41 ± 1	-107 ± 1	1.1 ± 0.1	226 ± 1	226	15 ± 13	14.6	-17	214
UGC 7985	52 ± 6	-88 ± 1	3.1 ± 0.2	90 ± 3	90	40 ± 4	2.2	25	29
UGC 8403	58 ± 1	120 ± 1	6.3 ± 0.1	120 ± 1	120	26 ± 5	4.6	-3	19
UGC 8490	65 ± 35	176 ± 2	∞	∞	50	31 ± 4	1.6	35	32*
UGC 8709	73 ± 1	-25 ± 1	6.9 ± 0.1	218 ± 1	218	19 ± 14	11.2	-10	31
UGC 8852	12 ± 3	63 ± 1	1.1 ± 0.1	186 ± 1	186	13 ± 14	14.1	-31	175
UGC 8863	51 ± 5	-141 ± 1	8.2 ± 0.1	213 ± 1	213	11 ± 11	19.4	-31	26
UGC 8898	76 ± 6	37 ± 2	1.1 ± 0.1	24 ± 1	24	22 ± 3	1.1	31	23
UGC 8900	10*	164 ± 1	7.7 ± 0.1	303 ± 1	303	10 ± 13	30.1	11	39
UGC 8937	13 ± 1	-179 ± 1	1.1 ± 0.1	304 ± 1	304	34 ± 19	9.0	-1	284
UGC 9013	10 ± 35	156 ± 2	2.7 ± 0.7	43 ± 4	43	25 ± 1	1.8	7	16
UGC 9179	27 ± 20	49 ± 1	3.3 ± 0.2	113 ± 4	113	24 ± 3	4.8	8	34
UGC 9219	-	-	-	-	-	-	-	-	-
UGC 9248	59 ± 1	-92 ± 1	4.8 ± 0.1	148 ± 1	148	35 ± 14	4.2	36	31
UGC 9358	49 ± 1	-175 ± 1	4.2 ± 0.1	237 ± 1	237	29 ± 18	8.3	22	56
UGC 9366	64 ± 1	-136 ± 1	3.7 ± 0.1	244 ± 1	244	29 ± 16	8.3	0	66
UGC 9363	10*	153 ± 1	3.7 ± 0.1	125 ± 1	125	25 ± 3	5.0	6	34
UGC 9406	16 ± 35	151 ± 2	6.0 ± 0.4	23 ± 1	23	24 ± 4	1.0	9	4
UGC 9465	64 ± 2	130 ± 1	5.6 ± 0.1	99 ± 1	99	32 ± 6	3.0	13	18
UGC 9576	48 ± 1	119 ± 1	6.7 ± 0.1	108 ± 1	108	25 ± 4	4.3	2	16
UGC 9649	29 ± 35	-131 ± 1	4.3 ± 0.9	122 ± 18	107	27 ± 8	3.9	23	28
UGC 9736	55 ± 1	-145 ± 1	6.6 ± 0.1	188 ± 1	188	29 ± 12	6.6	19	28
UGC 9753	10*	-1 ± 1	1.1 ± 0.1	170 ± 1	170	14 ± 19	11.8	-28	157
UGC 9858	70 ± 1	70 ± 1	5.7 ± 0.1	156 ± 1	156	20 ± 17	7.7	22	27
UGC 9943	62 ± 1	-94 ± 1	2.6 ± 0.1	198 ± 1	198	26 ± 13	7.6	-5	77
UGC 9969	59 ± 1	16 ± 1	1.1 ± 0.1	298 ± 1	298	22 ± 17	13.8	-16	269
UGC 10075	31 ± 2	-149 ± 1	3.2 ± 0.1	167 ± 1	167	19 ± 12	8.6	-4	52
UGC 10310	30 ± 13	-153 ± 1	1.1 ± 0.1	52 ± 1	52	24 ± 4	2.2	-5	49
UGC 10359	35 ± 2	-83 ± 1	5.7 ± 0.1	139 ± 1	139	23 ± 9	6.2	3	24
UGC 10470	28 ± 2	-64 ± 1	3.5 ± 0.1	139 ± 1	139	34 ± 7	4.0	22	40
UGC 10445	21 ± 8	105 ± 1	1.1 ± 0.1	74 ± 1	74	25 ± 4	2.9	-9	70
UGC 10502	51 ± 1	100 ± 1	6.6 ± 0.1	144 ± 1	144	32 ± 10	4.4	9	22
UGC 10521	20 ± 7	18 ± 1	1.2 ± 0.2	116 ± 1	116	27 ± 9	4.4	-9	99
UGC 10546	35 ± 3	174 ± 1	3.2 ± 0.1	93 ± 1	93	28 ± 8	3.3	18	29

Table B4: *continued*

Galaxy ^(a)	$i_{z=1.7}$ ^(b) °	$PA_{z=1.7}$ ^(c) °	r_t ^(d) kpc	V_t ^(e) km s ⁻¹	V_c^{max} ^(f) km s ⁻¹	σ ^(g) km s ⁻¹	V_c^{max}/σ	ΔV_c^{mean} ^(h) km s ⁻¹	S_{in} ⁽ⁱ⁾ km s ⁻¹ kpc ⁻¹
UGC 10564	71 ± 7	148 ± 1	5.7 ± 0.2	77 ± 2	77	25 ± 5	3.0	5	14
UGC 10713	—	—	—	—	—	—	—	—	—
UGC 10757	43 ± 35	52 ± 2	3.5 ± 1.2	61 ± 12	61	39 ± 2	1.6	28	18
UGC 10897	10*	114 ± 1	4.7 ± 0.1	117 ± 2	117	30 ± 6	3.9	11	25
UGC 11012	80*	-65 ± 2	3.8 ± 0.5	98 ± 7	96	48 ± 7	2.0	49	26
UGC 11124	27 ± 6	180 ± 1	5.8 ± 0.1	92 ± 1	92	25 ± 4	3.7	4	16
UGC 11218	44 ± 1	39 ± 1	3.3 ± 0.1	192 ± 1	192	16 ± 14	11.9	1	57
UGC 11269	67 ± 1	-86 ± 1	8.3 ± 0.1	209 ± 1	209	27 ± 19	7.7	73	25
UGC 11283	61 ± 1	135 ± 1	1.1 ± 0.1	124 ± 1	124	29 ± 11	4.2	13	112
UGC 11283C	—	—	—	—	—	—	—	—	—
UGC 11300	41 ± 35	162 ± 2	2.2 ± 0.5	97 ± 5	97	26 ± 10	3.7	6	43
UGC 11332	—	—	—	—	—	—	—	—	—
UGC 11407	10*	79 ± 1	8.3 ± 0.1	160 ± 1	160	35 ± 11	4.6	-11	19
UGC 11429	80*	-157 ± 1	17.9 ± 0.2	320 ± 4	320	25 ± 14	12.7	-15	18
UGC 11466	10*	-143 ± 2	1.7 ± 0.7	108 ± 5	108	49 ± 8	2.2	10	63
UGC 11496	44 ± 2	168 ± 1	5.8 ± 0.1	94 ± 1	94	23 ± 7	4.2	-2	16
UGC 11557	10*	-86 ± 1	3.9 ± 0.2	83 ± 2	83	27 ± 6	3.1	-1	21
UGC 11707	57 ± 4	54 ± 1	3.6 ± 0.1	89 ± 1	89	15 ± 10	5.9	-7	25
UGC 11852	36 ± 1	-172 ± 1	2.3 ± 0.1	223 ± 1	223	7 ± 10	30.6	-24	97
UGC 11861	42 ± 1	-150 ± 1	6.6 ± 0.1	153 ± 1	153	27 ± 9	5.7	3	23
UGC 11872	25 ± 3	82 ± 1	3.5 ± 0.1	181 ± 1	181	33 ± 15	5.5	34	52
UGC 11909	—	—	—	—	—	—	—	—	—
UGC 11914	10*	-93 ± 1	1.1 ± 0.1	309 ± 1	309	10 ± 14	30.3	-19	285
UGC 11951	80 ± 35	-103 ± 5	5.3 ± 2.0	95 ± 22	81	36 ± 4	2.2	20	18
UGC 12060	40 ± 35	177 ± 1	∞	∞	68	26 ± 5	2.6	3	19*
UGC 12276	38 ± 1	-43 ± 1	1.0 ± 0.1	93 ± 1	93	23 ± 9	4.0	-5	95
UGC 12343	50 ± 1	-157 ± 1	7.5 ± 0.1	214 ± 1	214	31 ± 9	6.9	-10	29
UGC 12754	80*	-24 ± 1	6.1 ± 0.8	149 ± 19	129	32 ± 8	4.1	28	25

(a): Galaxies for which no parameter is provided are those for which the fit was not possible.

(b): Inclination deduced from the fit. The error is a statistical error and thus gives a lower limit. The asterisk * indicates that the inclination was stacked to one boundary.

(c): Position angle of the major axis deduced from the fit with the inclination fixed to the value in Table B1. The error is a statistical error and thus gives a lower limit.

(d): Scale length radius of the model (defined in Appendix A) deduced from the fit with the inclination fixed to the value in Table B1. The error is a statistical error and thus gives a lower limit.

(e): Velocity of the model (defined in Appendix A) deduced from the fit with the inclination fixed to the value in Table B1. The error is a statistical error and thus gives a lower limit.

(f): Maximum velocity of the model within R_{last} (see Table B6). The error is the same as in column (e) and thus not take into account the uncertainty on the inclination.

(g): Local velocity dispersion (beam smearing corrected).

(h): Mean difference of the model rotation curve with the actual rotation curve at $z = 0$.

(i): Inner slope of the rotation curve from the model. The asterisk * indicates that only the slope is constrained by the model.

Table B5: Arctangent model on the sample projected at $z = 1.7$

Galaxy ^(a)	$i_{z=1.7}$ ^(b) °	$PA_{z=1.7}$ ^(c) °	r_t ^(d) kpc	V_t ^(e) km s ⁻¹	V_c^{max} ^(f) km s ⁻¹	σ ^(g) km s ⁻¹	V_c^{max}/σ	ΔV_c^{mean} ^(h) km s ⁻¹	S_{in} ⁽ⁱ⁾ km s ⁻¹ kpc ⁻¹
UGC 89	10*	172 ± 1	1.0 ± 0.1	389 ± 1	274	24 ± 20	11.6	-15	490
UGC 94	21 ± 1	91 ± 1	1.0 ± 0.1	232 ± 1	163	17 ± 14	9.4	-17	302
UGC 508	10*	122 ± 1	1.0 ± 0.1	536 ± 1	378	28 ± 16	13.5	-22	679
UGC 528	10*	54 ± 3	1.1 ± 0.1	48 ± 2	33	36 ± 2	0.9	40	57
UGC 763	14 ± 11	119 ± 1	1.1 ± 0.1	107 ± 1	76	27 ± 5	2.8	-10	126
NGC 542	-	-	-	-	-	-	-	-	-
UGC 1249	-	-	-	-	-	-	-	-	-
UGC 1256	10*	67 ± 1	2.7 ± 0.5	107 ± 4	75	26 ± 4	2.9	-4	51
UGC 1317	69 ± 1	103 ± 1	1.1 ± 0.1	221 ± 1	156	21 ± 12	7.3	-21	265
UGC 1437	46 ± 1	-58 ± 1	1.1 ± 0.1	221 ± 1	155	29 ± 15	5.3	-5	267
UGC 1655	10*	-60 ± 1	1.1 ± 0.1	285 ± 1	201	0 ± 0	> 100	-37	318
UGC 1736	10*	28 ± 1	5.7 ± 0.1	241 ± 3	170	22 ± 13	7.7	-5	54
UGC 1886	65 ± 1	35 ± 1	1.0 ± 0.1	262 ± 1	184	17 ± 11	11.0	3	320
UGC 2045	10*	-30 ± 1	4.7 ± 0.2	253 ± 4	169	31 ± 21	5.4	23	69
UGC 2082	-	-	-	-	-	-	-	-	-
UGC 2080	10*	-23 ± 1	1.2 ± 0.1	135 ± 2	95	15 ± 6	6.2	-7	148
UGC 2141	80*	-158 ± 4	∞	∞	71	41 ± 2	1.7	35	19*
UGC 2455	27 ± 35	-76 ± 9	∞	∞	10	24 ± 1	0.4	8	3*
UGC 2800	43 ± 4	-75 ± 1	1.9 ± 0.2	104 ± 3	73	9 ± 9	8.3	-8	69
UGC 2855	35 ± 3	97 ± 1	5.2 ± 0.1	268 ± 2	189	19 ± 12	10.0	-4	66
UGC 3013	52 ± 35	-156 ± 1	∞	∞	505	26 ± 19	19.3	-18	22*
UGC 3334	10*	-83 ± 1	3.6 ± 0.1	415 ± 1	293	30 ± 20	9.7	3	147
UGC 3382	43 ± 1	-174 ± 1	4.2 ± 0.1	379 ± 3	267	14 ± 11	18.6	-7	114
UGC 3384	-	-	-	-	-	-	-	-	-
UGC 3429	10*	-34 ± 1	4.7 ± 0.2	341 ± 8	240	44 ± 30	5.4	34	92
UGC 3463	62 ± 1	108 ± 1	2.9 ± 0.1	188 ± 1	133	32 ± 8	4.1	-6	83
UGC 3574	48 ± 1	102 ± 1	4.0 ± 0.1	218 ± 2	154	20 ± 6	7.6	4	70
UGC 3521	54 ± 1	-105 ± 1	1.7 ± 0.1	173 ± 1	122	13 ± 12	9.7	-15	126
UGC 3528	55 ± 1	-135 ± 1	1.0 ± 0.1	293 ± 1	206	16 ± 20	12.7	-25	381
UGC 3691	66 ± 2	-114 ± 1	13.9 ± 0.5	255 ± 7	146	34 ± 9	4.3	10	23
UGC 3685	10*	-67 ± 1	1.1 ± 0.1	94 ± 1	66	24 ± 4	2.7	6	112
UGC 3708	63 ± 2	-118 ± 1	1.1 ± 0.1	240 ± 1	169	27 ± 31	6.2	-2	277
UGC 3709	56 ± 1	-132 ± 1	2.0 ± 0.1	267 ± 1	188	35 ± 19	5.4	-21	168
UGC 3734	10*	136 ± 1	1.1 ± 0.1	103 ± 1	73	21 ± 5	3.4	5	120
UGC 3809	62 ± 1	-3 ± 1	3.9 ± 0.1	299 ± 1	211	20 ± 15	10.4	-20	97
UGC 3740	54 ± 3	-113 ± 1	4.2 ± 0.4	89 ± 4	63	37 ± 2	1.7	12	27
UGC 3851	-	-	-	-	-	-	-	-	-
UGC 3876	62 ± 7	5 ± 1	1.4 ± 0.4	126 ± 6	89	32 ± 8	2.8	-10	112
UGC 3915	25 ± 1	30 ± 1	1.0 ± 0.1	222 ± 1	156	31 ± 16	5.1	-5	282
IC 476	80*	64 ± 1	∞	∞	83	25 ± 12	3.3	21	28*
UGC 4165	10*	-99 ± 1	1.1 ± 0.1	91 ± 1	64	25 ± 6	2.6	-5	108

Table B5: *continued*

Galaxy ^(a)	$i_{z=1.7}$ ^(b) °	$PA_{z=1.7}$ ^(c) °	r_t ^(d) kpc	V_t ^(e) km s ⁻¹	V_c^{max} ^(f) km s ⁻¹	σ ^(g) km s ⁻¹	V_c^{max}/σ	ΔV_c^{mean} ^(h) km s ⁻¹	S_{in} ⁽ⁱ⁾ km s ⁻¹ kpc ⁻¹
UGC 4256	80*	-65 ± 1	10.4 ± 0.2	152 ± 2	107	47 ± 8	2.3	46	19
UGC 4273	53 ± 1	-149 ± 1	4.6 ± 0.1	225 ± 1	158	28 ± 10	5.7	19	62
UGC 4278	—	—	—	—	—	—	—	—	—
UGC 4284	66 ± 1	176 ± 1	8.2 ± 0.3	183 ± 4	110	20 ± 10	5.5	8	28
UGC 4325	10*	56 ± 1	1.1 ± 0.1	76 ± 1	53	26 ± 7	2.1	-3	91
UGC 4393	10*	-110 ± 1	∞	∞	58	31 ± 5	1.9	-4	6*
UGC 4422	10*	35 ± 1	1.1 ± 0.1	359 ± 1	253	24 ± 13	10.5	10	415
UGC 4456	18 ± 3	124 ± 1	4.8 ± 0.1	203 ± 2	143	25 ± 5	5.7	28	54
UGC 4499	10*	145 ± 1	1.1 ± 0.1	87 ± 1	61	15 ± 11	4.1	-29	103
UGC 4555	45 ± 1	91 ± 1	2.1 ± 0.1	198 ± 1	140	19 ± 11	7.5	-3	123
UGC 4770	10*	-79 ± 1	13.5 ± 0.2	494 ± 3	348	25 ± 13	14.0	-29	47
UGC 4820	10*	156 ± 1	1.1 ± 0.1	386 ± 1	272	5 ± 10	49.9	-25	458
UGC 4936	10*	-66 ± 1	3.3 ± 0.1	244 ± 2	172	21 ± 7	8.0	-10	94
UGC 5045	10*	146 ± 1	1.4 ± 0.1	453 ± 1	319	30 ± 9	10.6	-15	398
UGC 5175	48 ± 1	143 ± 1	1.2 ± 0.1	204 ± 1	144	24 ± 10	5.9	-17	209
UGC 5228	10*	118 ± 1	1.1 ± 0.1	145 ± 1	102	26 ± 11	3.9	-18	170
UGC 5251	63 ± 2	-102 ± 1	4.8 ± 0.1	156 ± 1	110	24 ± 11	4.6	-9	41
UGC 5253	50 ± 1	-5 ± 1	1.1 ± 0.1	260 ± 1	183	14 ± 16	13.4	3	297
UGC 5279	—	—	—	—	—	—	—	—	—
UGC 5316	10*	127 ± 1	11.3 ± 0.4	191 ± 4	130	20 ± 7	6.5	-8	22
UGC 5319	31 ± 2	-11 ± 1	3.3 ± 0.1	212 ± 2	149	28 ± 7	5.3	4	82
UGC 5351	—	—	—	—	—	—	—	—	—
UGC 5414	10*	-150 ± 3	8.7 ± 6.3	111 ± 53	57	32 ± 2	1.8	10	16
IC 2542	34 ± 1	174 ± 1	2.5 ± 0.1	339 ± 2	239	33 ± 12	7.3	-22	172
UGC 5510	10*	-161 ± 1	4.3 ± 0.1	201 ± 3	142	33 ± 5	4.3	20	59
UGC 5532	43 ± 1	146 ± 1	1.0 ± 0.1	354 ± 1	249	31 ± 12	8.1	31	439
UGC 5556	—	—	—	—	—	—	—	—	—
UGC 5786	80*	154 ± 1	∞	∞	83	53 ± 4	1.6	39	15*
UGC 5789	56 ± 2	31 ± 1	9.9 ± 0.2	152 ± 2	107	17 ± 9	6.4	-1	20
UGC 5842	67 ± 3	-68 ± 1	11.5 ± 1.2	236 ± 19	118	32 ± 7	3.7	14	26
UGC 5931	10*	9 ± 1	∞	∞	130	37 ± 6	3.5	28	21*
UGC 5982	48 ± 1	31 ± 1	1.4 ± 0.1	209 ± 1	147	11 ± 12	13.0	-6	187
UGC 6118	80*	-25 ± 1	∞	∞	192	42 ± 20	4.6	39	31*
UGC 6277	10*	76 ± 1	3.2 ± 0.2	296 ± 8	208	42 ± 8	5.0	28	118
UGC 6419	10*	42 ± 3	1.1 ± 0.1	24 ± 1	17	28 ± 1	0.6	3	28
UGC 6521	46 ± 1	20 ± 1	1.0 ± 0.1	250 ± 1	176	27 ± 14	6.5	-7	321
UGC 6523	10*	-5 ± 1	1.0 ± 0.1	114 ± 1	80	40 ± 8	2.0	2	145
UGC 6537	23 ± 1	-164 ± 1	1.1 ± 0.1	189 ± 1	133	12 ± 10	11.0	-23	224
UGC 6628	40 ± 6	-179 ± 1	3.8 ± 0.5	169 ± 9	119	23 ± 7	5.2	1	57
UGC 6702	47 ± 1	-105 ± 1	0.9 ± 0.1	205 ± 1	145	17 ± 14	8.8	7	279
UGC 6778	26 ± 2	-18 ± 1	3.3 ± 0.1	238 ± 2	168	29 ± 12	5.8	19	92
UGC 7021	32 ± 3	-105 ± 1	1.7 ± 0.1	148 ± 3	104	45 ± 12	2.3	63	113

Table B5: *continued*

Galaxy ^(a)	$i_{z=1.7}$ ^(b) °	$PA_{z=1.7}$ ^(c) °	r_t ^(d) kpc	V_t ^(e) km s ⁻¹	V_c^{max} ^(f) km s ⁻¹	σ ^(g) km s ⁻¹	V_c^{max}/σ	ΔV_c^{mean} ^(h) km s ⁻¹	S_{in} ⁽ⁱ⁾ km s ⁻¹ kpc ⁻¹
UGC 7045	10*	100 ± 1	1.5 ± 0.1	190 ± 3	134	12 ± 10	11.2	-17	164
UGC 7154	62 ± 1	-84 ± 1	7.7 ± 0.1	165 ± 1	116	24 ± 7	4.9	3	27
UGC 7278	-	-	-	-	-	-	-	-	-
UGC 7323	10*	35 ± 1	1.8 ± 0.4	87 ± 4	61	24 ± 5	2.5	-3	61
UGC 7699	-	-	-	-	-	-	-	-	-
UGC 7831	10*	-69 ± 1	3.6 ± 1.6	110 ± 21	66	43 ± 6	1.6	26	39
UGC 7853	10*	-149 ± 2	∞	∞	54	27 ± 2	2.0	20	11*
UGC 7876	10*	-18 ± 1	1.1 ± 0.1	99 ± 1	69	27 ± 3	2.6	-9	116
UGC 7901	36 ± 1	-107 ± 1	1.1 ± 0.1	240 ± 1	169	19 ± 16	9.1	-10	289
UGC 7985	56 ± 6	-88 ± 1	3.6 ± 0.7	118 ± 9	83	40 ± 4	2.1	23	42
UGC 8403	60 ± 1	120 ± 1	9.2 ± 0.2	178 ± 2	126	26 ± 5	4.8	-5	25
UGC 8490	28 ± 35	176 ± 2	1.1 ± 0.1	57 ± 2	40	31 ± 4	1.3	33	67
UGC 8709	75 ± 1	-25 ± 1	4.5 ± 0.1	245 ± 1	173	19 ± 15	8.9	-19	69
UGC 8852	10*	63 ± 1	1.1 ± 0.1	201 ± 1	142	17 ± 15	8.5	-23	241
UGC 8863	41 ± 19	-142 ± 1	14.4 ± 0.6	358 ± 9	214	18 ± 12	11.8	-19	32
UGC 8898	79 ± 5	37 ± 2	1.1 ± 0.1	28 ± 1	20	22 ± 3	0.9	31	33
UGC 8900	10*	163 ± 1	9.7 ± 0.1	420 ± 1	296	11 ± 14	26.9	2	55
UGC 8937	10*	-179 ± 1	1.1 ± 0.1	320 ± 1	225	35 ± 20	6.5	5	380
UGC 9013	10*	156 ± 2	2.7 ± 2.0	55 ± 14	39	25 ± 1	1.6	5	26
UGC 9179	10*	49 ± 1	5.2 ± 1.0	175 ± 19	117	24 ± 3	4.9	8	43
UGC 9219	-	-	-	-	-	-	-	-	-
UGC 9248	62 ± 1	-92 ± 1	4.6 ± 0.1	182 ± 1	129	36 ± 14	3.6	30	50
UGC 9358	47 ± 1	-175 ± 1	2.9 ± 0.1	269 ± 1	189	29 ± 17	6.5	13	117
UGC 9366	64 ± 1	-136 ± 1	1.5 ± 0.1	257 ± 1	181	30 ± 16	6.0	-11	218
UGC 9363	10*	153 ± 1	2.7 ± 0.1	143 ± 2	101	25 ± 3	4.0	2	68
UGC 9406	10*	151 ± 2	13.2 ± 3.3	45 ± 8	26	24 ± 4	1.1	9	4
UGC 9465	62 ± 3	130 ± 1	9.5 ± 0.5	160 ± 5	106	33 ± 5	3.2	11	21
UGC 9576	50 ± 1	119 ± 1	8.0 ± 0.1	147 ± 1	104	25 ± 4	4.1	-2	23
UGC 9649	10*	-131 ± 1	∞	∞	102	27 ± 8	3.7	25	28*
UGC 9736	54 ± 1	-145 ± 1	6.9 ± 0.1	240 ± 1	169	29 ± 12	5.8	10	44
UGC 9753	63 ± 4	-1 ± 1	1.1 ± 0.1	188 ± 1	132	17 ± 23	7.6	-24	220
UGC 9858	71 ± 1	70 ± 1	6.1 ± 0.1	196 ± 2	138	22 ± 15	6.2	13	41
UGC 9943	61 ± 1	-95 ± 1	1.7 ± 0.1	216 ± 1	153	28 ± 12	5.5	-8	158
UGC 9969	59 ± 1	16 ± 1	1.3 ± 0.1	310 ± 1	218	22 ± 17	9.8	-11	309
UGC 10075	19 ± 3	-149 ± 1	2.1 ± 0.1	186 ± 1	131	20 ± 11	6.5	-10	113
UGC 10310	41 ± 9	-153 ± 1	1.1 ± 0.1	58 ± 1	41	24 ± 5	1.7	-4	70
UGC 10359	36 ± 3	-83 ± 1	9.6 ± 0.2	223 ± 3	157	23 ± 9	6.8	-1	30
UGC 10470	28 ± 2	-64 ± 1	2.9 ± 0.1	166 ± 2	117	34 ± 7	3.4	16	73
UGC 10445	12 ± 14	105 ± 1	1.1 ± 0.1	82 ± 1	58	26 ± 4	2.2	-7	99
UGC 10502	52 ± 1	101 ± 1	5.1 ± 0.1	165 ± 1	116	33 ± 9	3.6	3	41
UGC 10521	64 ± 2	17 ± 1	1.1 ± 0.1	128 ± 1	90	29 ± 9	3.1	-7	150
UGC 10546	36 ± 3	174 ± 1	2.6 ± 0.2	109 ± 2	77	28 ± 8	2.8	14	53

Table B5: *continued*

Galaxy ^(a)	$i_{z=1.7}$ ^(b) °	$PA_{z=1.7}$ ^(c) °	r_t ^(d) kpc	V_t ^(e) km s ⁻¹	V_c^{max} ^(f) km s ⁻¹	σ ^(g) km s ⁻¹	V_c^{max}/σ	ΔV_c^{mean} ^(h) km s ⁻¹	S_{in} ⁽ⁱ⁾ km s ⁻¹ kpc ⁻¹
UGC 10564	74 ± 7	148 ± 1	9.0 ± 1.0	117 ± 7	78	26 ± 5	3.0	3	17
UGC 10713	—	—	—	—	—	—	—	—	—
UGC 10757	57 ± 21	52 ± 2	∞	∞	43	39 ± 2	1.1	21	42*
UGC 10897	10*	114 ± 1	8.0 ± 0.6	190 ± 10	117	30 ± 6	3.9	11	30
UGC 11012	80*	-65 ± 2	5.9 ± 1.9	147 ± 25	84	48 ± 7	1.7	48	32
UGC 11124	10*	-180 ± 1	10.4 ± 0.5	156 ± 5	100	25 ± 4	4.0	3	19
UGC 11218	40 ± 1	39 ± 1	2.1 ± 0.1	212 ± 1	150	17 ± 12	9.0	-6	129
UGC 11269	71 ± 1	-84 ± 1	16.0 ± 0.3	366 ± 4	222	28 ± 19	7.9	71	29
UGC 11283	62 ± 1	134 ± 1	1.1 ± 0.1	137 ± 1	97	30 ± 11	3.2	15	158
UGC 11283C	—	—	—	—	—	—	—	—	—
UGC 11300	10*	162 ± 2	3.1 ± 1.6	130 ± 23	92	28 ± 10	3.3	8	54
UGC 11332	—	—	—	—	—	—	—	—	—
UGC 11407	10*	82 ± 1	16.4 ± 0.3	291 ± 4	175	36 ± 11	4.9	-13	23
UGC 11429	80*	-157 ± 1	∞	∞	357	25 ± 14	14.2	-18	18*
UGC 11466	10*	-143 ± 2	1.5 ± 1.3	125 ± 21	88	49 ± 8	1.8	8	110
UGC 11496	44 ± 2	167 ± 1	8.7 ± 0.3	141 ± 3	100	23 ± 7	4.4	-5	21
UGC 11557	10*	-86 ± 1	5.3 ± 0.6	120 ± 7	84	27 ± 6	3.2	-2	29
UGC 11707	54 ± 5	53 ± 1	3.0 ± 0.2	105 ± 2	74	15 ± 10	4.8	-7	45
UGC 11852	10*	-172 ± 1	1.1 ± 0.1	236 ± 1	167	8 ± 10	22.0	-34	285
UGC 11861	41 ± 1	-150 ± 1	8.3 ± 0.1	211 ± 1	149	27 ± 9	5.5	0	33
UGC 11872	10*	82 ± 1	3.4 ± 0.1	225 ± 2	159	34 ± 14	4.7	29	85
UGC 11909	—	—	—	—	—	—	—	—	—
UGC 11914	10*	-93 ± 1	1.1 ± 0.1	335 ± 1	236	12 ± 17	20.4	-9	393
UGC 11951	80*	-100 ± 5	∞	∞	71	37 ± 4	1.9	25	16*
UGC 12060	44 ± 35	177 ± 2	∞	∞	68	26 ± 5	2.6	3	19*
UGC 12276	37 ± 1	-43 ± 1	1.0 ± 0.1	97 ± 1	69	23 ± 8	3.0	-4	126
UGC 12343	51 ± 1	-157 ± 1	7.8 ± 0.1	275 ± 1	194	31 ± 10	6.2	-18	45
UGC 12754	80*	-24 ± 1	∞	∞	128	32 ± 8	4.0	28	24*

(a): Galaxies for which no parameter is provided are those for which the fit was not possible.

(b): Inclination deduced from the fit. The error is a statistical error and thus gives a lower limit. The asterisk * indicates that the inclination was stacked to one boundary.

(c): Position angle of the major axis deduced from the fit with the inclination fixed to the value in Table B1. The error is a statistical error and thus gives a lower limit.

(d): Scale length radius of the model (defined in Appendix A) deduced from the fit with the inclination fixed to the value in Table B1. The error is a statistical error and thus gives a lower limit.

(e): Velocity of the model (defined in Appendix A) deduced from the fit with the inclination fixed to the value in Table B1. The error is a statistical error and thus gives a lower limit.

(f): Maximum velocity of the model within R_{last} (see Table B6). The error is the same as in column (e) and thus not take into account the uncertainty on the inclination.

(g): Local velocity dispersion (beam smearing corrected).

(h): Mean difference of the model rotation curve with the actual rotation curve at $z = 0$.

(i): Inner slope of the rotation curve from the model. The asterisk * indicates that only the slope is constrained by the model.

Table B6: Parameters computed without beam smearing correction for the sample projected at $z = 1.7$.

Galaxy	B ^(a)	V_{rc}^{max} ^(b) $km\ s^{-1}$	σ_{cen} ^(c) $km\ s^{-1}$	σ_{min} ^(d) $km\ s^{-1}$	$V_{rc}^{max}/\sigma_{cen}$	ΔV_c^{mean} ^(e) $km\ s^{-1}$	R_{last} ^(f) kpc
UGC 89	4.6	340	100	28	3.4	66	9.8
UGC 94	4.4	205	62	20	3.3	32	11.7
UGC 508	6.5	514	54	23	9.6	60	21.7
UGC 528	0.8	25	36	24	0.7	60	1.9
UGC 763	1.6	89	47	24	1.9	23	7.1
NGC 542	2.5	—	43	23	—	—	6.6
UGC 1249	1.6	—	31	21	—	—	4.7
UGC 1256	1.7	64	40	25	1.6	29	7.2
UGC 1317	6.1	207	70	21	2.9	36	23.8
UGC 1437	5.5	220	71	18	3.1	19	23.1
UGC 1655	6.4	214	35	16	6.1	13	7.8
UGC 1736	2.7	119	41	17	2.9	11	8.5
UGC 1886	8.2	261	44	14	5.9	10	31.5
UGC 2045	2.4	139	73	37	1.9	74	4.0
UGC 2082	1.7	—	35	25	—	—	3.0
UGC 2080	2.0	117	22	14	5.2	22	8.5
UGC 2141	1.0	40	49	33	0.8	54	3.8
UGC 2455	0.8	4	24	20	0.2	11	3.6
UGC 2800	1.5	81	28	15	2.9	19	5.6
UGC 2855	2.4	172	58	26	2.9	37	10.5
UGC 3013	5.6	13	68	24	0.2	68	22.8
UGC 3334	8.4	363	66	24	5.5	35	31.6
UGC 3382	2.5	307	25	11	12.2	12	9.9
UGC 3384	1.0	—	30	25	—	—	0.0
UGC 3429	3.5	198	80	41	2.5	118	8.2
UGC 3463	3.7	170	60	27	2.8	19	16.1
UGC 3574	3.0	164	31	16	5.3	35	12.5
UGC 3521	2.4	144	48	20	3.0	24	9.6
UGC 3528	3.0	258	45	16	5.7	37	7.1
UGC 3691	2.0	100	49	26	2.1	26	8.7
UGC 3685	2.8	119	27	16	4.4	19	12.0
UGC 3708	1.8	179	70	54	2.6	95	4.2
UGC 3709	3.0	198	75	38	2.6	10	13.3
UGC 3734	0.9	60	35	22	1.7	40	3.7
UGC 3809	7.8	263	64	25	4.1	−4	24.5
UGC 3740	1.6	61	39	24	1.5	26	6.6
UGC 3851	0.9	—	29	23	—	—	1.8
UGC 3876	1.0	83	52	21	1.6	33	4.5
UGC 3915	2.4	199	71	28	2.8	34	9.4
IC 476	1.3	64	42	30	1.5	33	3.0
UGC 4165	1.0	60	34	20	1.8	26	4.4
UGC 4256	4.8	82	54	36	1.5	63	18.3
UGC 4273	2.6	168	54	23	3.1	47	11.4
UGC 4278	1.4	—	28	9	—	—	5.7
UGC 4284	2.0	100	39	19	2.6	31	5.7
UGC 4325	1.2	44	38	21	1.2	26	4.1
UGC 4393	2.3	41	33	20	1.2	4	9.7
UGC 4422	5.8	368	63	22	5.8	67	21.9
UGC 4456	4.0	206	28	18	7.4	18	16.2
UGC 4499	1.0	55	27	20	2.1	0	4.3
UGC 4555	2.9	189	46	17	4.1	26	12.1
UGC 4770	4.4	45	28	18	1.6	−15	17.6
UGC 4820	2.3	307	86	34	3.6	53	5.8
UGC 4936	5.4	232	26	14	8.9	9	18.6
UGC 5045	4.4	440	44	23	10.1	14	17.2
UGC 5175	2.5	179	72	30	2.5	35	8.5

56 *B. Epinat et al.*Table B6: *continued*

Galaxy	$B^{(a)}$	$V_{rc}^{max (b)}$ $km s^{-1}$	$\sigma_{cen}^{(c)}$ $km s^{-1}$	$\sigma_{min}^{(d)}$ $km s^{-1}$	$V_{rc}^{max}/\sigma_{cen}$	$\Delta V_c^{mean (e)}$ $km s^{-1}$	$R_{last}^{(f)}$ kpc
UGC 5228	1.9	111	59	24	1.9	36	8.3
UGC 5251	4.0	123	50	21	2.5	15	12.9
UGC 5253	3.0	228	72	21	3.2	57	9.0
UGC 5279	1.9	—	47	27	—	—	7.8
UGC 5316	2.4	99	33	19	3.0	7	10.3
UGC 5319	1.8	165	46	21	3.6	35	7.5
UGC 5351	1.5	—	65	31	—	—	4.5
UGC 5414	1.1	26	37	21	0.7	26	4.6
IC 2542	2.8	300	55	24	5.5	26	8.3
UGC 5510	1.8	149	47	24	3.2	56	7.4
UGC 5532	5.4	358	75	25	4.8	50	18.7
UGC 5556	2.2	—	47	27	—	—	0.0
UGC 5786	1.4	51	57	37	0.9	49	5.5
UGC 5789	2.8	86	25	19	3.4	3	12.0
UGC 5842	1.4	80	43	24	1.9	31	5.7
UGC 5931	1.5	69	47	29	1.5	47	6.1
UGC 5982	2.6	186	65	18	2.9	49	9.9
UGC 6118	1.7	141	56	24	2.5	79	6.2
UGC 6277	2.1	203	53	37	3.8	92	4.8
UGC 6419	1.2	16	30	22	0.5	7	5.3
UGC 6521	4.9	254	63	20	4.0	16	18.5
UGC 6523	2.6	82	50	29	1.7	42	5.4
UGC 6537	2.8	160	52	22	3.0	13	10.4
UGC 6628	1.4	94	31	18	3.1	29	6.1
UGC 6702	3.9	185	55	18	3.4	52	14.6
UGC 6778	2.2	169	57	29	3.0	71	7.4
UGC 7021	2.3	93	67	35	1.4	114	6.3
UGC 7045	1.5	134	60	28	2.2	44	6.4
UGC 7154	3.1	111	39	19	2.9	18	13.1
UGC 7278	0.8	—	24	15	—	—	0.0
UGC 7323	1.3	59	37	17	1.6	22	5.3
UGC 7699	1.1	—	46	25	—	—	3.9
UGC 7831	1.0	42	46	29	0.9	49	2.5
UGC 7853	1.2	29	32	23	0.9	33	5.1
UGC 7876	0.9	59	43	25	1.4	29	3.8
UGC 7901	2.7	207	82	21	2.5	42	11.3
UGC 7985	1.2	67	43	25	1.6	51	5.1
UGC 8403	2.4	110	36	23	3.0	9	10.5
UGC 8490	0.8	26	31	21	0.8	54	2.5
UGC 8709	6.2	196	57	24	3.5	28	22.4
UGC 8852	2.1	176	67	27	2.6	36	6.8
UGC 8863	3.1	164	21	15	8.0	5	9.8
UGC 8898	2.7	19	24	19	0.8	40	2.2
UGC 8900	4.5	259	58	17	4.4	31	12.6
UGC 8937	3.4	369	76	27	4.8	41	14.4
UGC 9013	1.1	35	26	20	1.4	18	4.7
UGC 9179	1.1	80	35	23	2.2	37	4.5
UGC 9219	0.9	—	32	23	—	—	2.6
UGC 9248	3.2	144	60	26	2.4	53	10.0
UGC 9358	3.0	230	77	27	3.0	64	10.7
UGC 9366	4.9	241	65	30	3.7	39	16.0
UGC 9363	2.4	109	28	20	4.0	30	10.2
UGC 9406	2.0	15	25	18	0.6	15	8.2
UGC 9465	1.9	80	43	22	1.8	28	8.1
UGC 9576	2.8	108	31	20	3.5	9	11.4
UGC 9649	0.9	52	39	25	1.3	46	3.8
UGC 9736	3.6	195	53	24	3.7	20	13.4
UGC 9753	1.6	113	72	24	1.6	55	6.3

Table B6: *continued*

Galaxy	B ^(a)	V_{rc}^{max} ^(b) $km\ s^{-1}$	σ_{cen} ^(c) $km\ s^{-1}$	σ_{min} ^(d) $km\ s^{-1}$	$V_{rc}^{max}/\sigma_{cen}$	ΔV_c^{mean} ^(e) $km\ s^{-1}$	R_{last} ^(f) kpc
UGC 9858	5.3	106	49	22	2.2	54	22.4
UGC 9943	2.6	207	65	27	3.2	29	10.5
UGC 9969	6.1	284	54	28	5.3	22	21.3
UGC 10075	2.6	142	59	26	2.4	32	9.5
UGC 10310	1.2	30	29	18	1.0	18	4.9
UGC 10359	3.2	116	37	19	3.2	27	13.3
UGC 10470	2.1	134	51	24	2.6	49	8.8
UGC 10445	1.5	61	34	19	1.8	18	6.4
UGC 10502	4.3	157	55	20	2.8	17	19.8
UGC 10521	1.7	95	56	30	1.7	40	6.0
UGC 10546	1.9	78	41	21	1.9	36	6.4
UGC 10564	1.8	54	34	23	1.6	19	7.7
UGC 10713	1.0	–	51	31	–	–	4.0
UGC 10757	0.9	36	43	30	0.9	38	3.5
UGC 10897	1.6	87	39	24	2.2	31	5.8
UGC 11012	1.2	53	59	33	0.9	75	3.7
UGC 11124	2.0	77	32	23	2.4	14	8.2
UGC 11218	2.7	179	67	26	2.7	41	9.2
UGC 11269	2.6	112	46	20	2.5	136	11.3
UGC 11283	1.8	125	49	19	2.5	57	7.8
UGC 11283C	0.9	–	21	19	–	–	0.0
UGC 11300	1.0	55	45	20	1.2	47	4.4
UGC 11332	1.9	–	42	26	–	–	7.7
UGC 11407	2.5	131	59	26	2.2	12	11.3
UGC 11429	4.9	169	39	25	4.3	–7	20.1
UGC 11466	0.9	80	62	32	1.3	56	3.9
UGC 11496	2.1	68	26	21	2.6	4	9.2
UGC 11557	1.4	70	31	19	2.2	10	5.9
UGC 11707	1.9	75	35	18	2.1	13	7.9
UGC 11852	3.9	211	49	18	4.3	22	8.4
UGC 11861	2.7	155	40	25	3.8	7	12.0
UGC 11872	1.8	165	64	24	2.6	71	6.3
UGC 11909	1.7	–	43	25	–	–	7.2
UGC 11914	1.9	267	76	25	3.5	58	6.6
UGC 11951	1.1	33	40	27	0.8	42	4.6
UGC 12060	0.8	44	31	14	1.4	34	3.5
UGC 12276	3.9	105	21	16	5.0	5	15.1
UGC 12343	3.4	211	56	27	3.7	0	15.1
UGC 12754	1.3	90	41	24	2.2	51	5.3

(a): Beam smearing parameter: $B = \frac{D_{25}/2}{s}$, s being the seeing.

(b): Maximum velocity measured on the rotation curve along the major axis at $z = 1.7$.

(c): Central velocity dispersion from the uncorrected velocity dispersion map.

(d): Mean velocity dispersion from the 20% smallest values.

(e): Mean difference of the rotation curve measured along the major axis at $z = 1.7$ with the actual rotation curve at $z = 0$.

(f): Radius of the last point (maps were cut at $D_{25}/2$).

58 *B. Epinat et al.*

APPENDIX C: MAPS

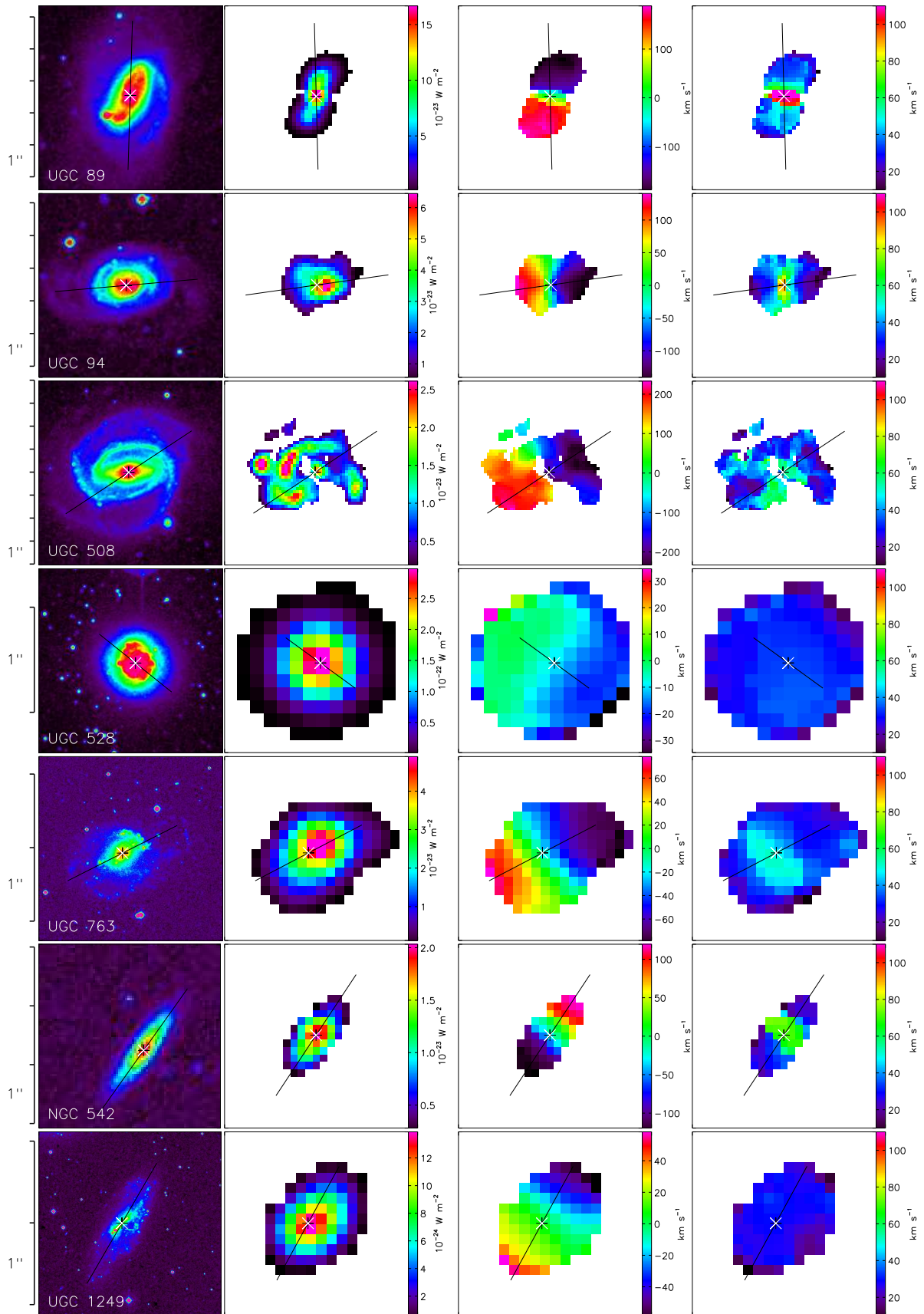


Figure C1. From left to right: XDSS image, $H\alpha$ monochromatic image, velocity field, velocity dispersion map. The white & black crosses mark the kinematical center. The black line is the major axis, its length represents the D_{25} . These maps are not truncated.

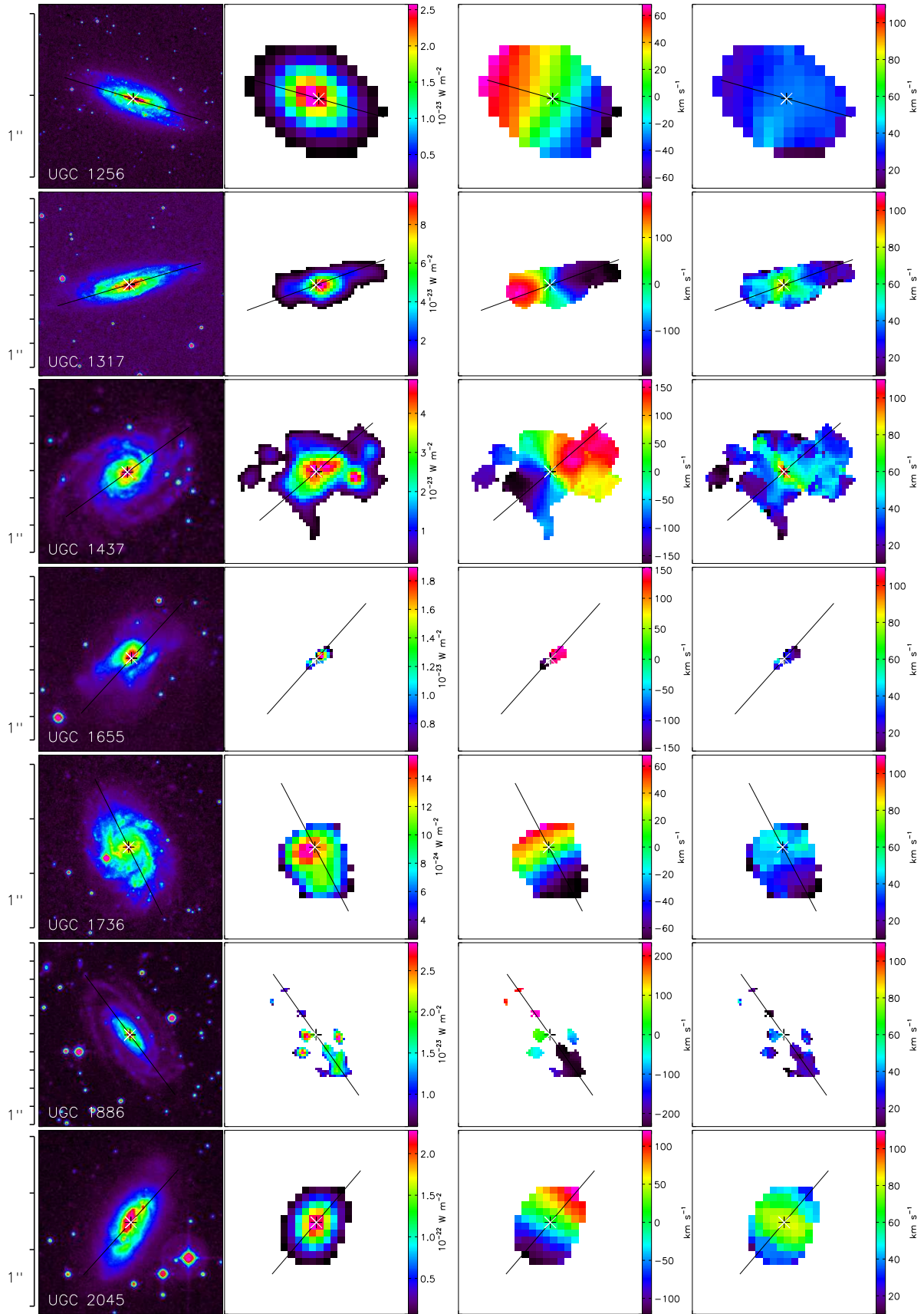
60 *B. Epinat et al.*

Figure C2. From left to right: XDFSS image, $H\alpha$ monochromatic image, velocity field, velocity dispersion map. The white & black crosses mark the kinematic center. The black line is the major axis, its length represents the D_{25} . These maps are not truncated.

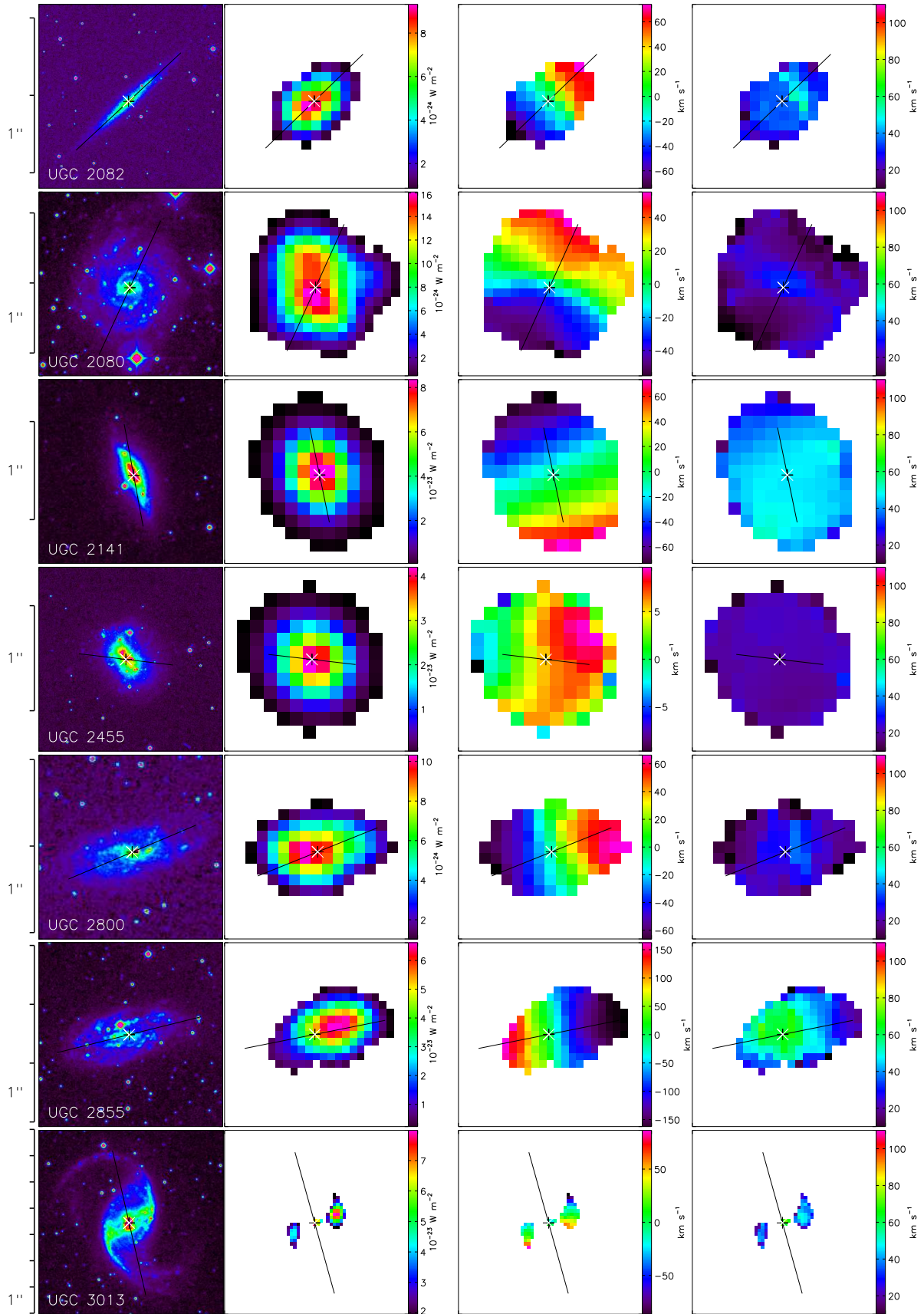


Figure C3. From left to right: XDS image, H α monochromatic image, velocity field, velocity dispersion map. The white & black crosses mark the kinematical center. The black line is the major axis, its length represents the D_{25} . These maps are not truncated.

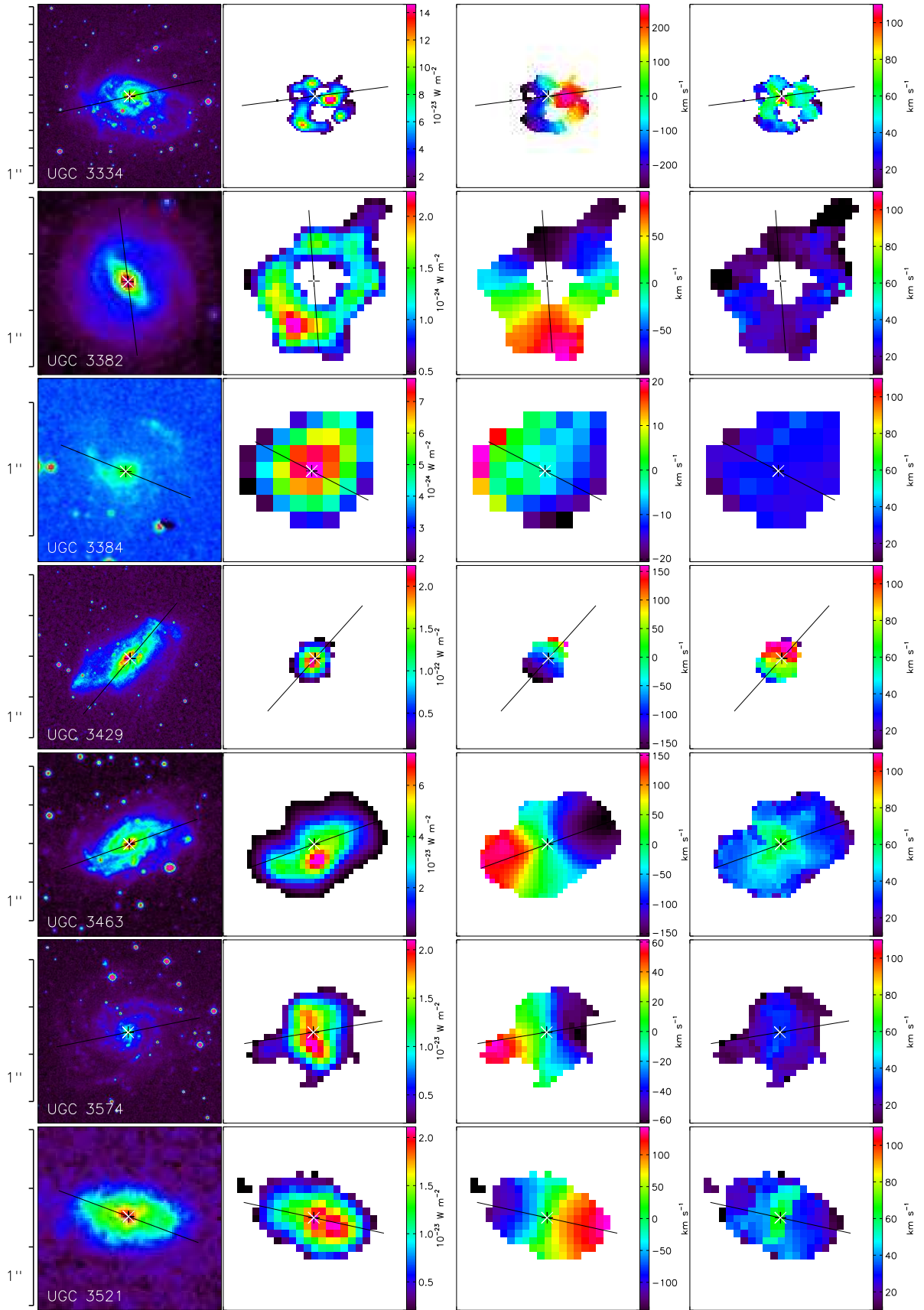
62 *B. Epinat et al.*

Figure C4. From left to right: X-ray image, $H\alpha$ monochromatic image, velocity field, velocity dispersion map. The white & black crosses mark the kinematic center. The black line is the major axis, its length represents the D_{25} . These maps are not truncated.

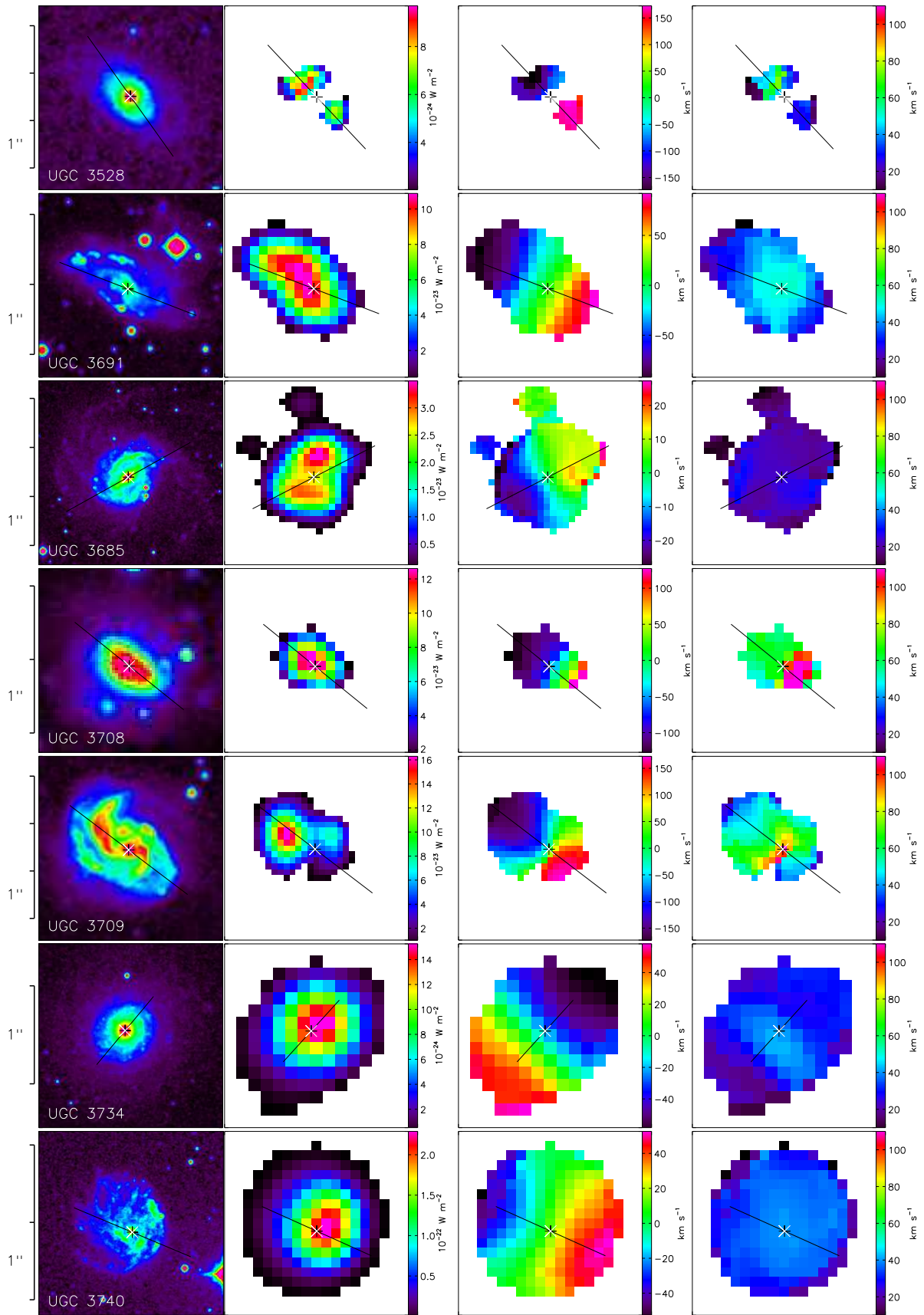


Figure C5. From left to right: XDS image, $H\alpha$ monochromatic image, velocity field, velocity dispersion map. The white & black crosses mark the kinematical center. The black line is the major axis, its length represents the D_{25} . These maps are not truncated.

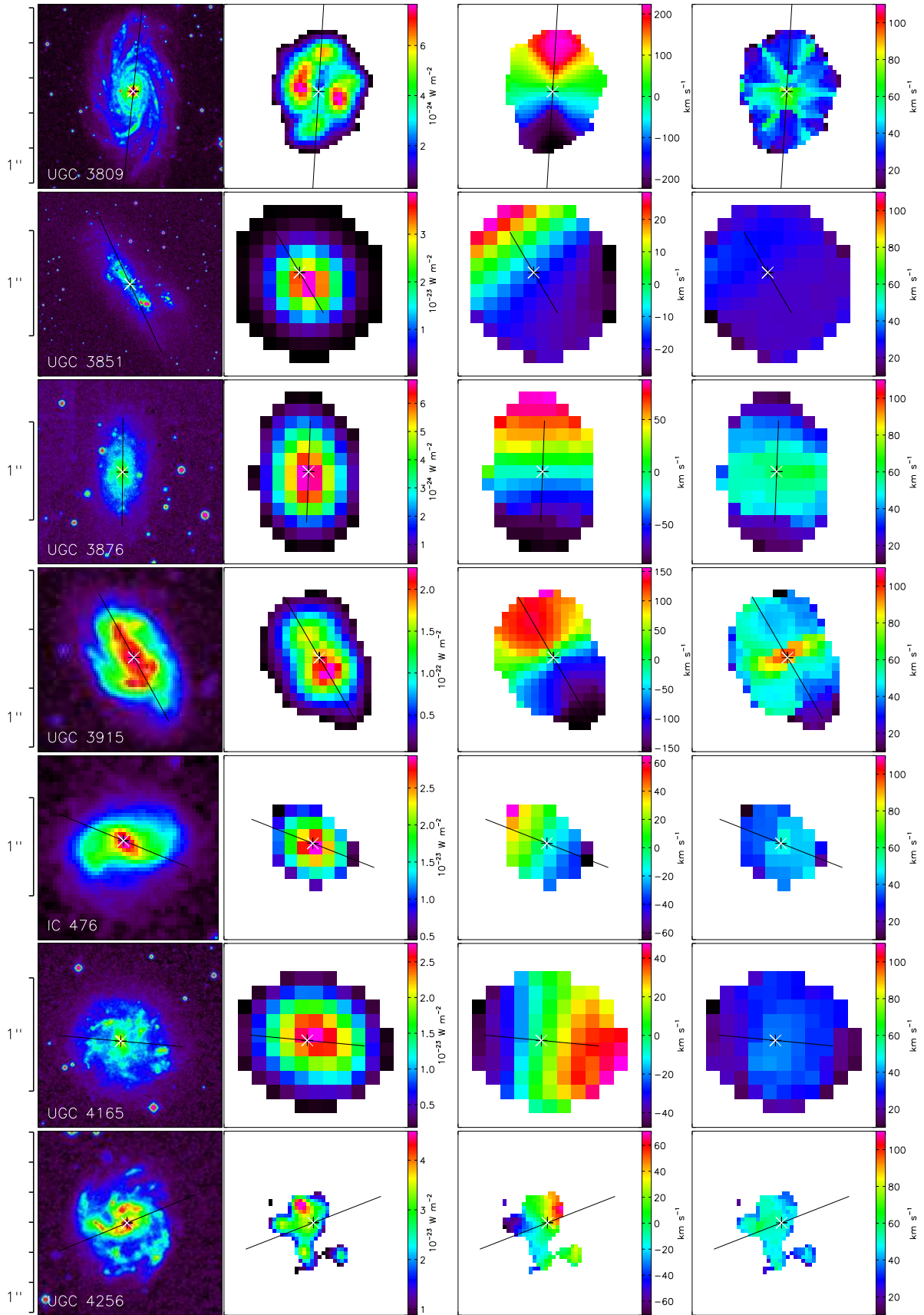
64 *B. Epinat et al.*

Figure C6. From left to right: XDSS image, $H\alpha$ monochromatic image, velocity field, velocity dispersion map. The white & black crosses mark the kinematic center. The black line is the major axis, its length represents the D_{25} . These maps are not truncated.

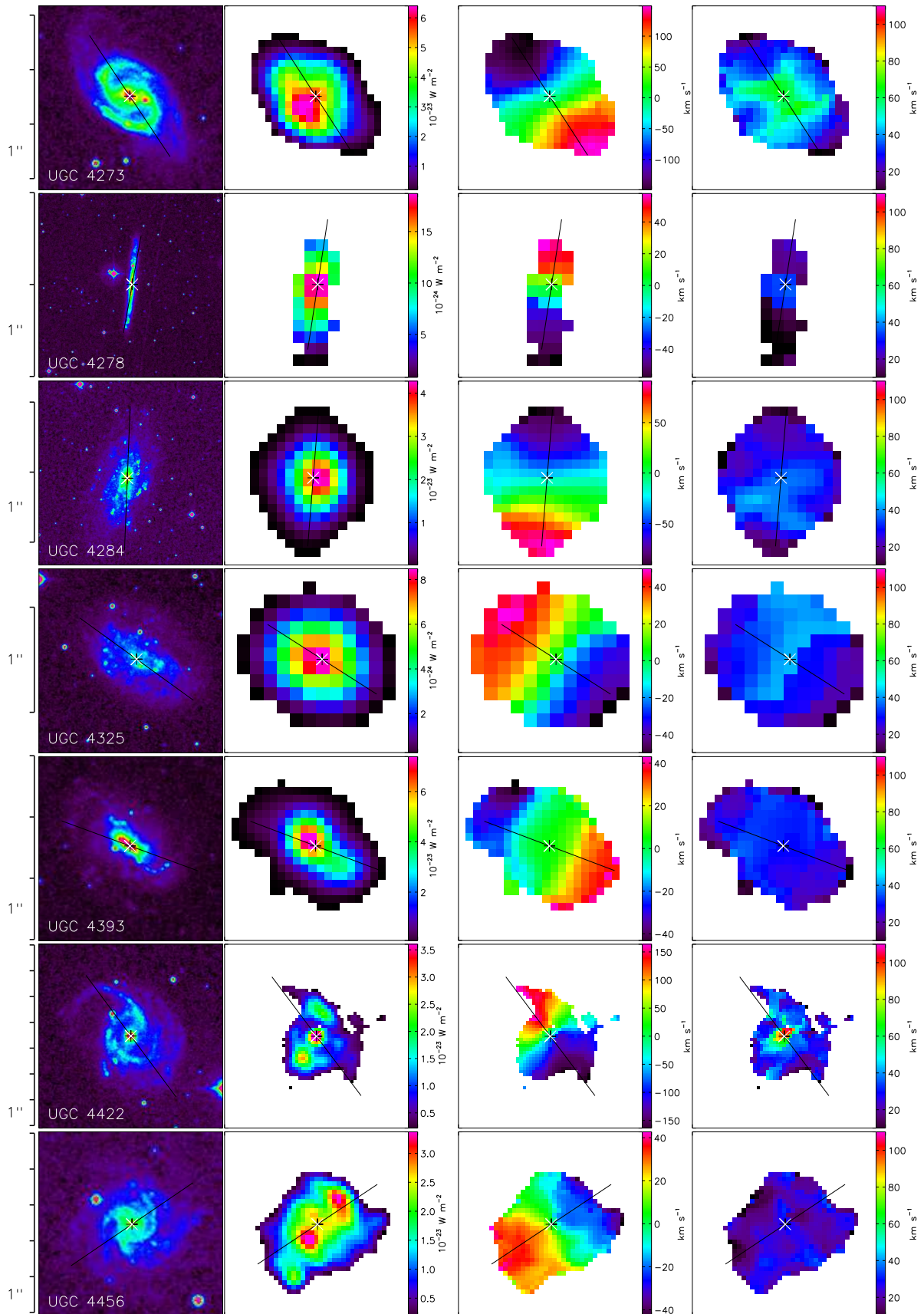


Figure C7. From left to right: XDSS image, H α monochromatic image, velocity field, velocity dispersion map. The white & black crosses mark the kinematical center. The black line is the major axis, its length represents the D_{25} . These maps are not truncated.

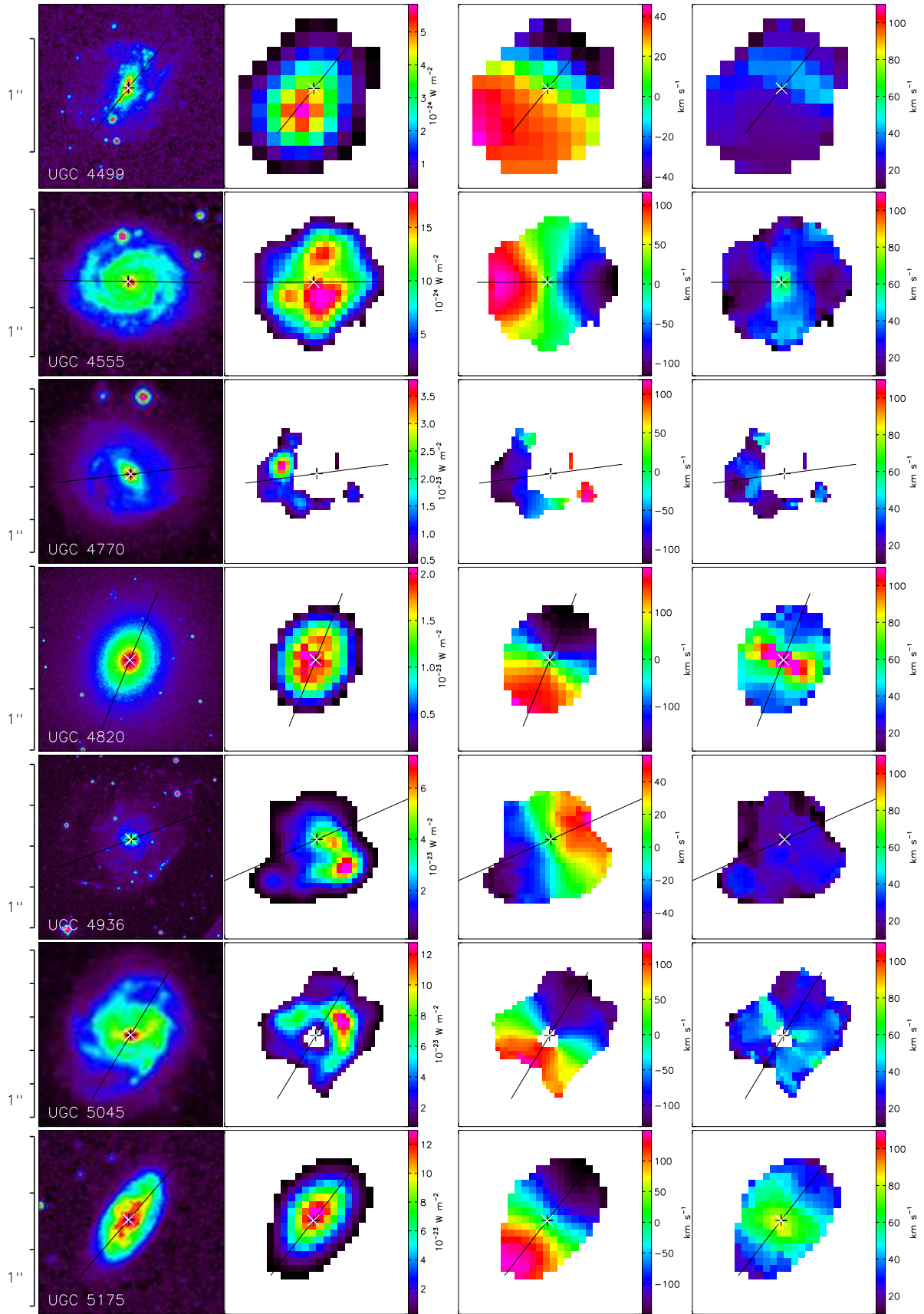
66 *B. Epinat et al.*

Figure C8. From left to right: X-ray image, $H\alpha$ monochromatic image, velocity field, velocity dispersion map. The white & black crosses mark the kinematic center. The black line is the major axis, its length represents the D_{25} . These maps are not truncated.

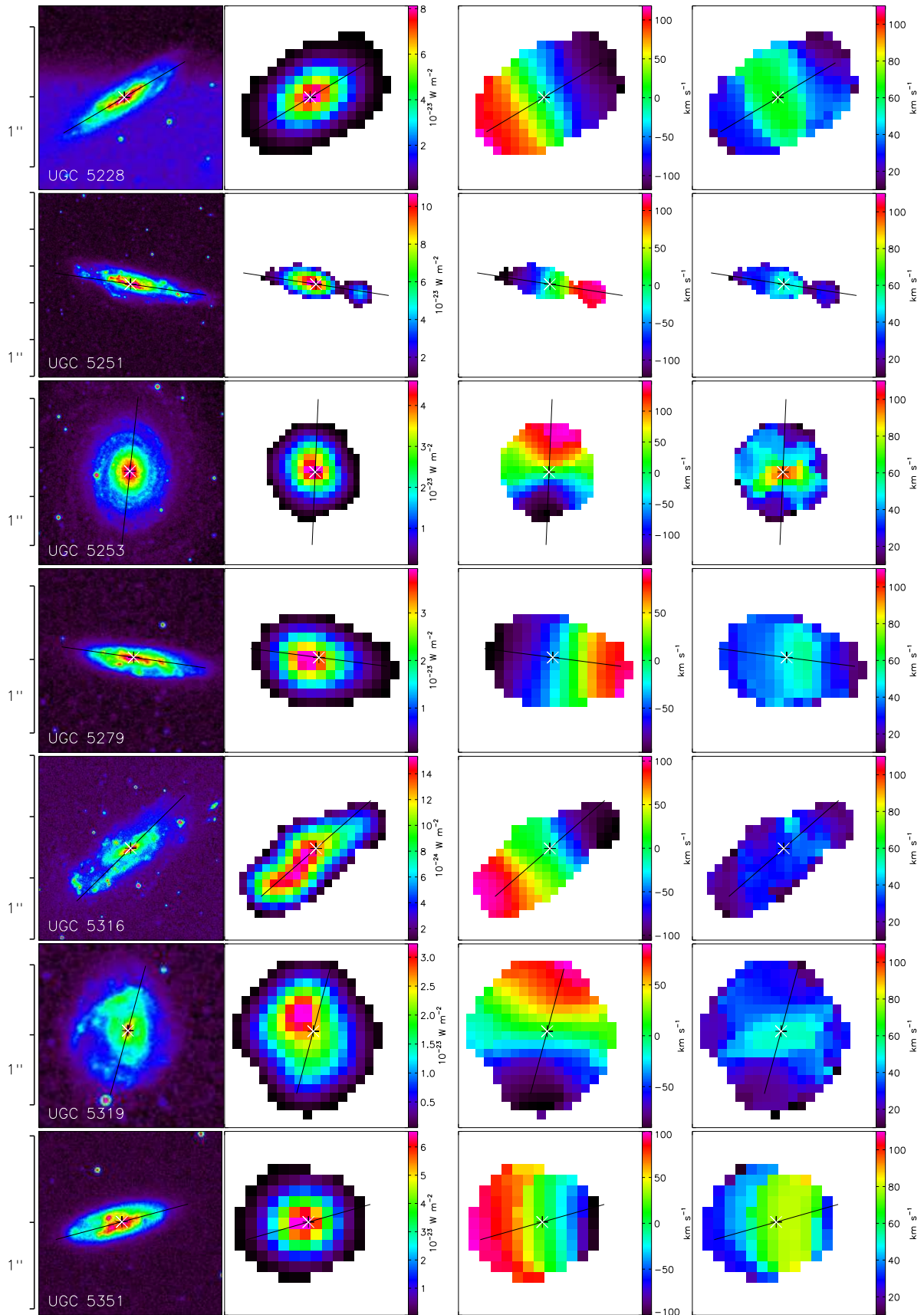


Figure C9. From left to right: XDSS image, H α monochromatic image, velocity field, velocity dispersion map. The white & black crosses mark the kinematical center. The black line is the major axis, its length represents the D_{25} . These maps are not truncated.

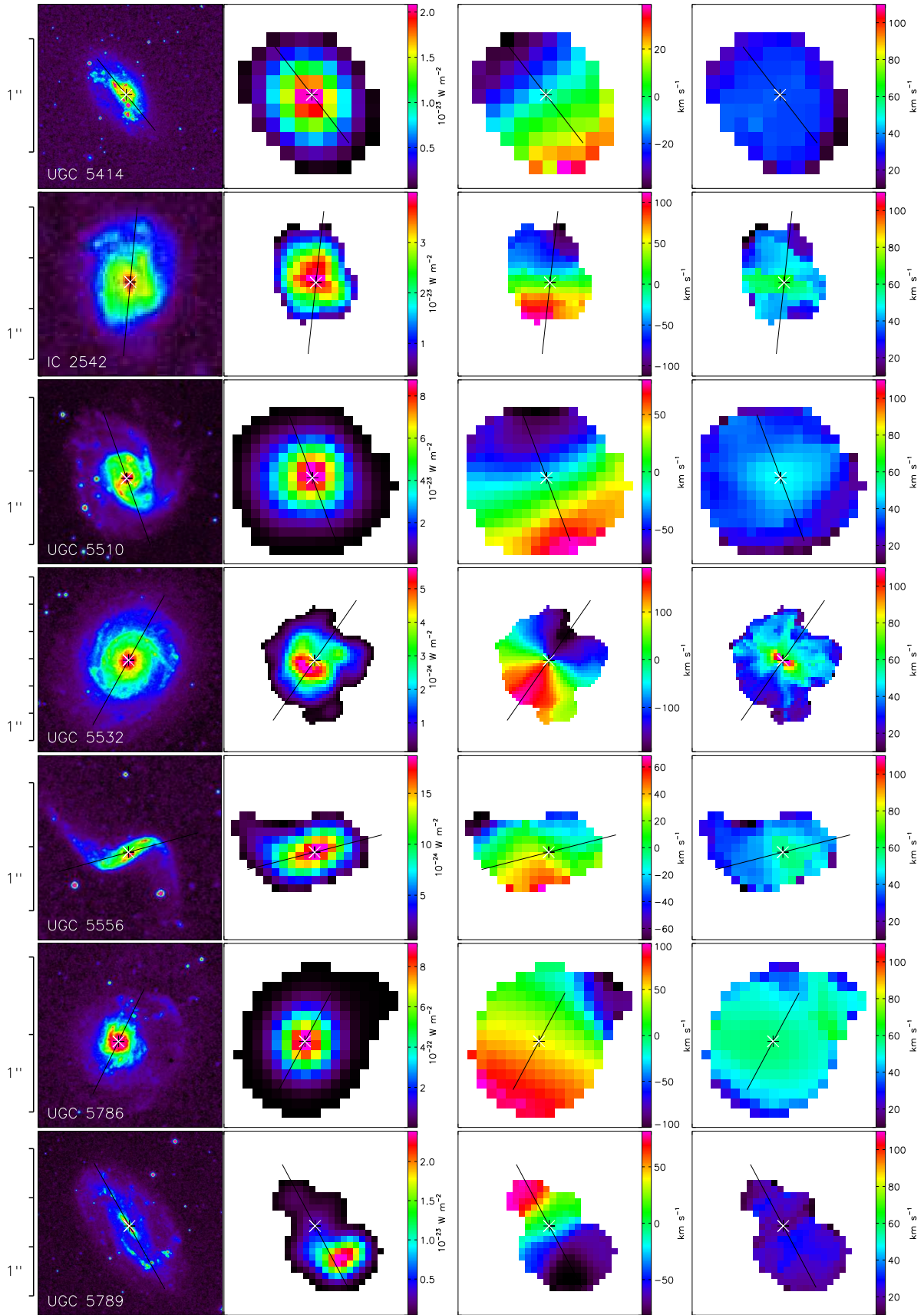
68 *B. Epinat et al.*

Figure C10. From left to right: XDRS image, $H\alpha$ monochromatic image, velocity field, velocity dispersion map. The white & black crosses mark the kinematic center. The black line is the major axis, its length represents the D_{25} . These maps are not truncated.

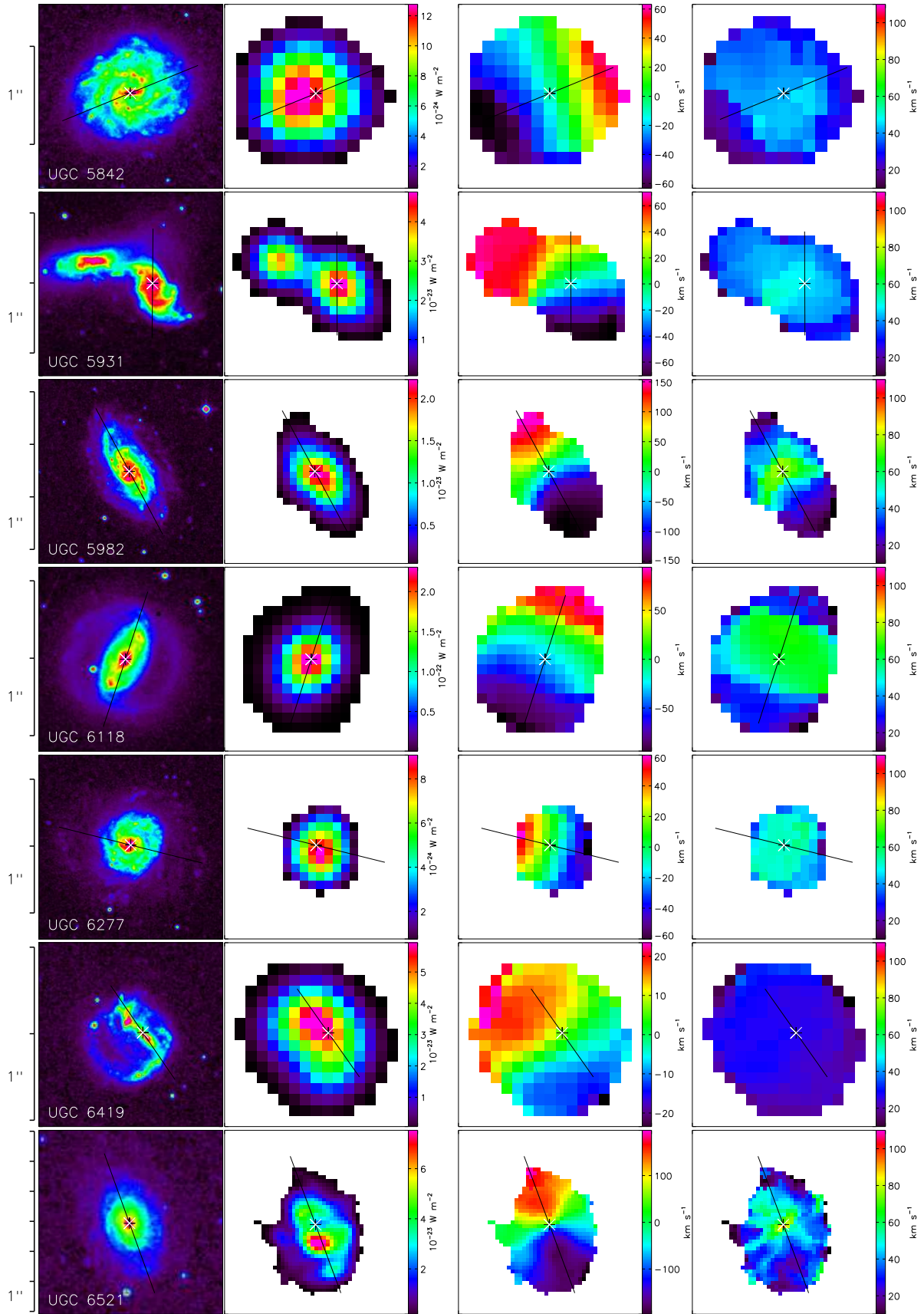


Figure C11. From left to right: XDRS image, $H\alpha$ monochromatic image, velocity field, velocity dispersion map. The white & black crosses mark the kinematical center. The black line is the major axis, its length represents the D_{25} . These maps are not truncated.

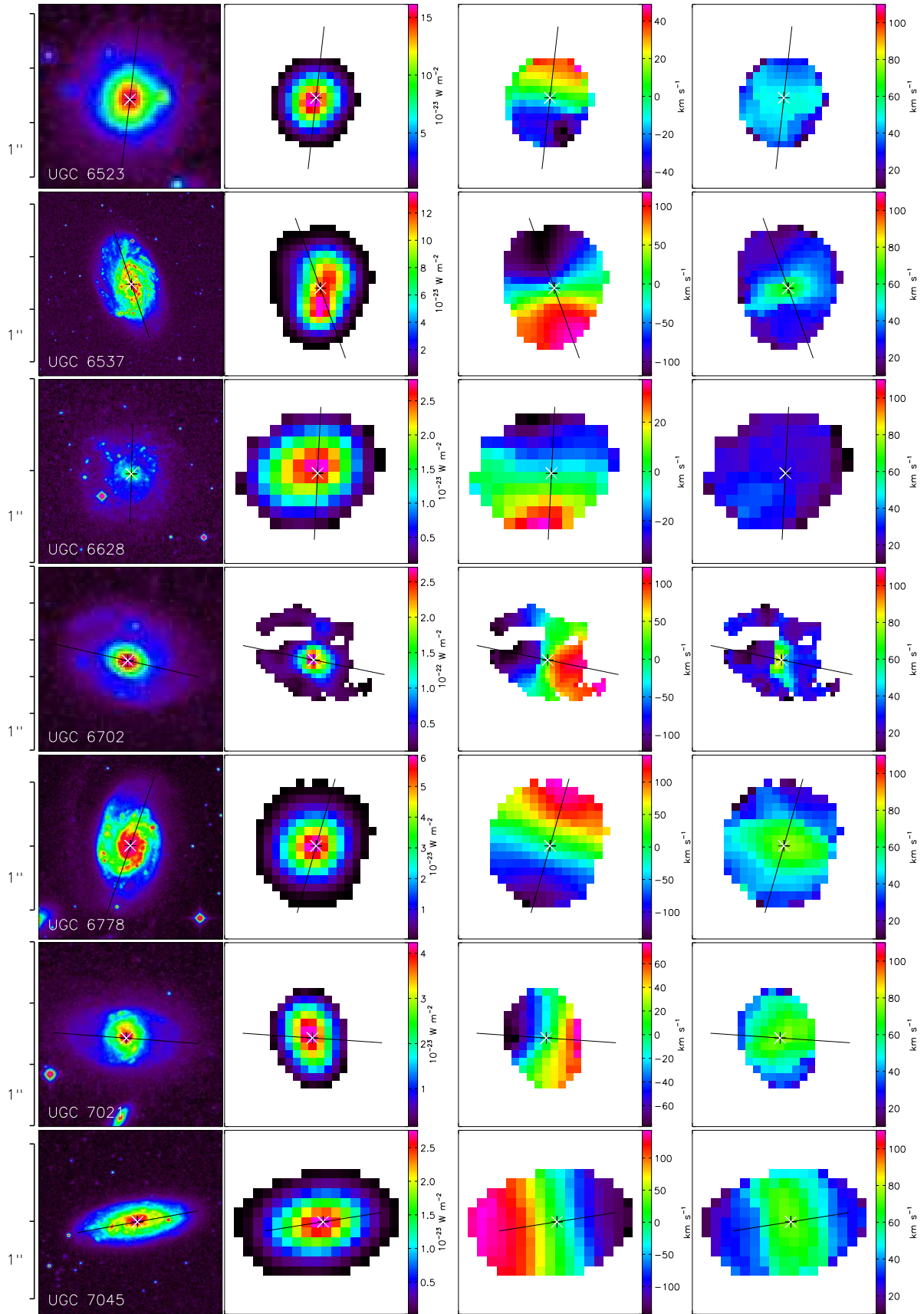
70 *B. Epinat et al.*

Figure C12. From left to right: X-DSS image, $H\alpha$ monochromatic image, velocity field, velocity dispersion map. The white & black crosses mark the kinematic center. The black line is the major axis, its length represents the D_{25} . These maps are not truncated.

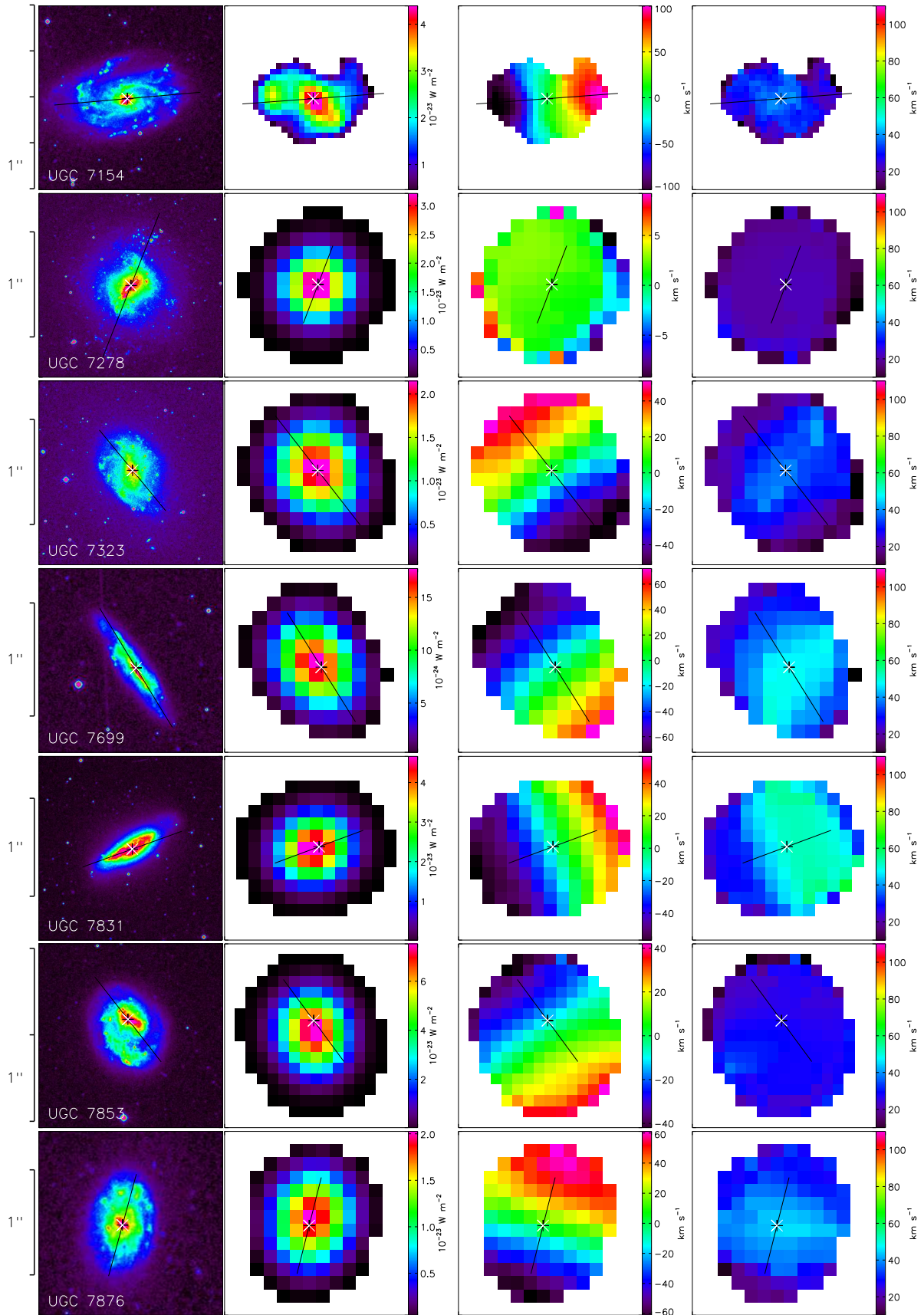


Figure C13. From left to right: X-DSS image, $H\alpha$ monochromatic image, velocity field, velocity dispersion map. The white & black crosses mark the kinematical center. The black line is the major axis, its length represents the D_{25} . These maps are not truncated.

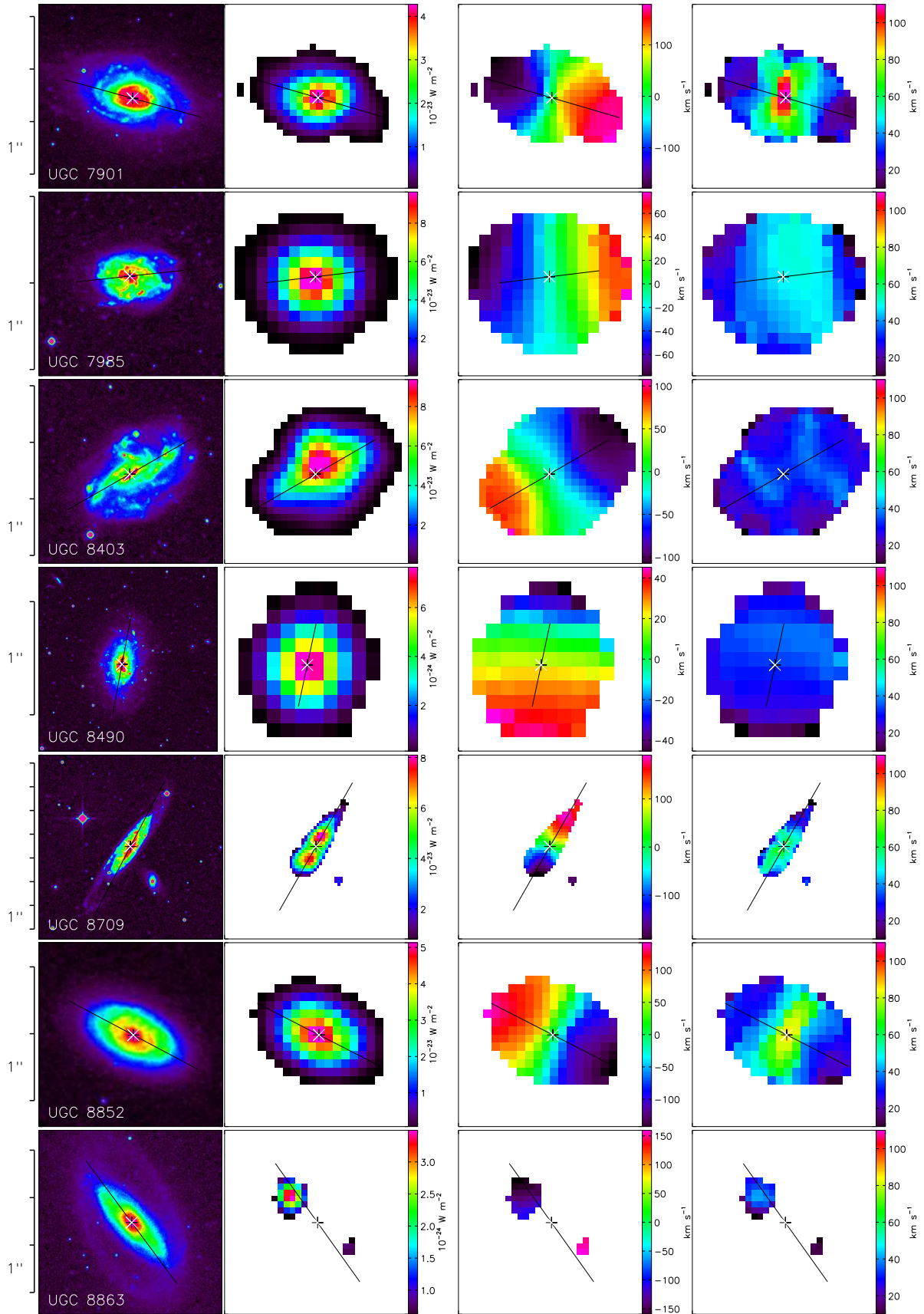
72 *B. Epinat et al.*

Figure C14. From left to right: X-DSS image, $H\alpha$ monochromatic image, velocity field, velocity dispersion map. The white & black crosses mark the kinematic center. The black line is the major axis, its length represents the D_{25} . These maps are not truncated.

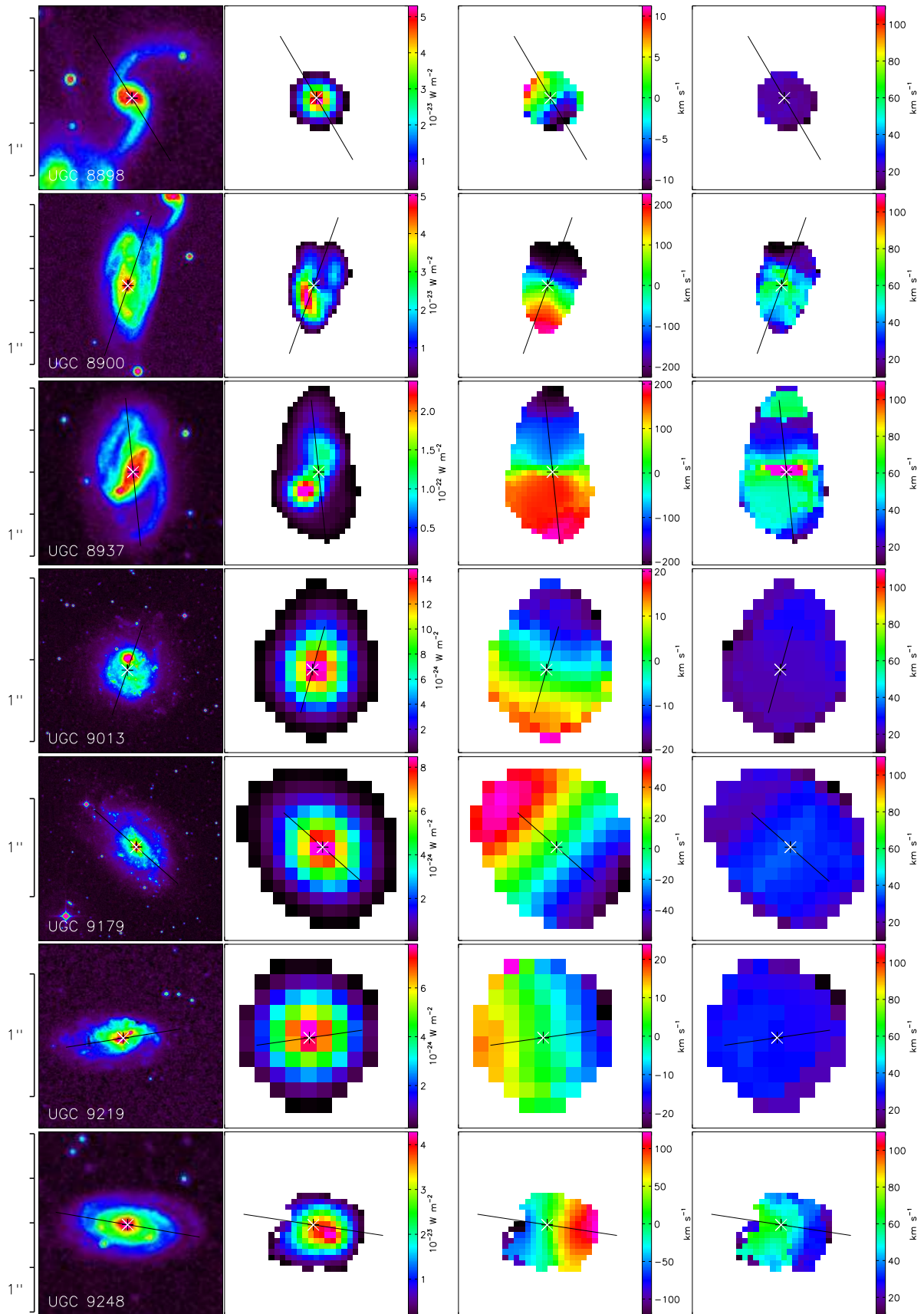


Figure C15. From left to right: XDRS image, $H\alpha$ monochromatic image, velocity field, velocity dispersion map. The white & black crosses mark the kinematical center. The black line is the major axis, its length represents the D_{25} . These maps are not truncated.

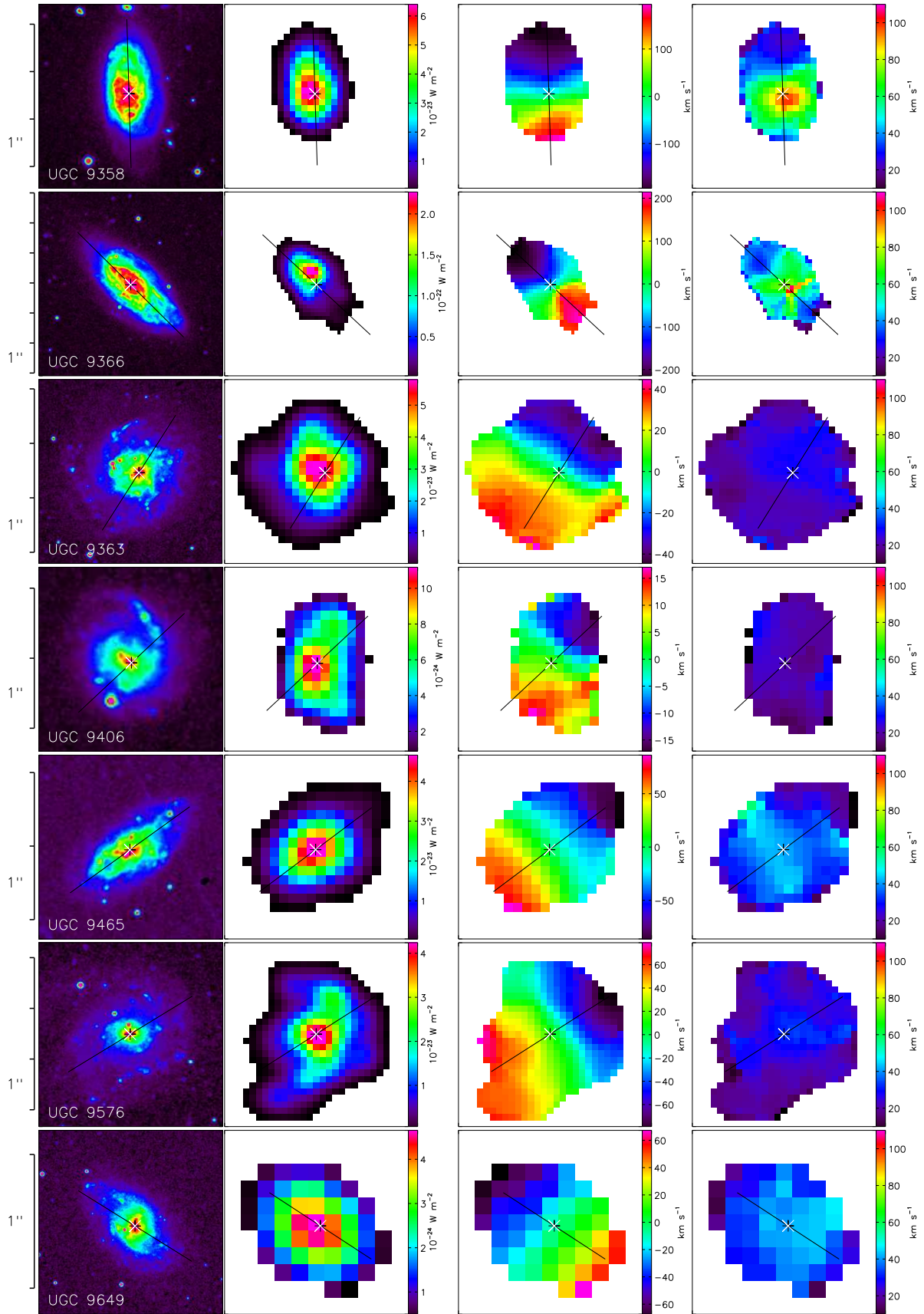
74 *B. Epinat et al.*

Figure C16. From left to right: X-DSS image, H α monochromatic image, velocity field, velocity dispersion map. The white & black crosses mark the kinematic center. The black line is the major axis, its length represents the D_{25} . These maps are not truncated.

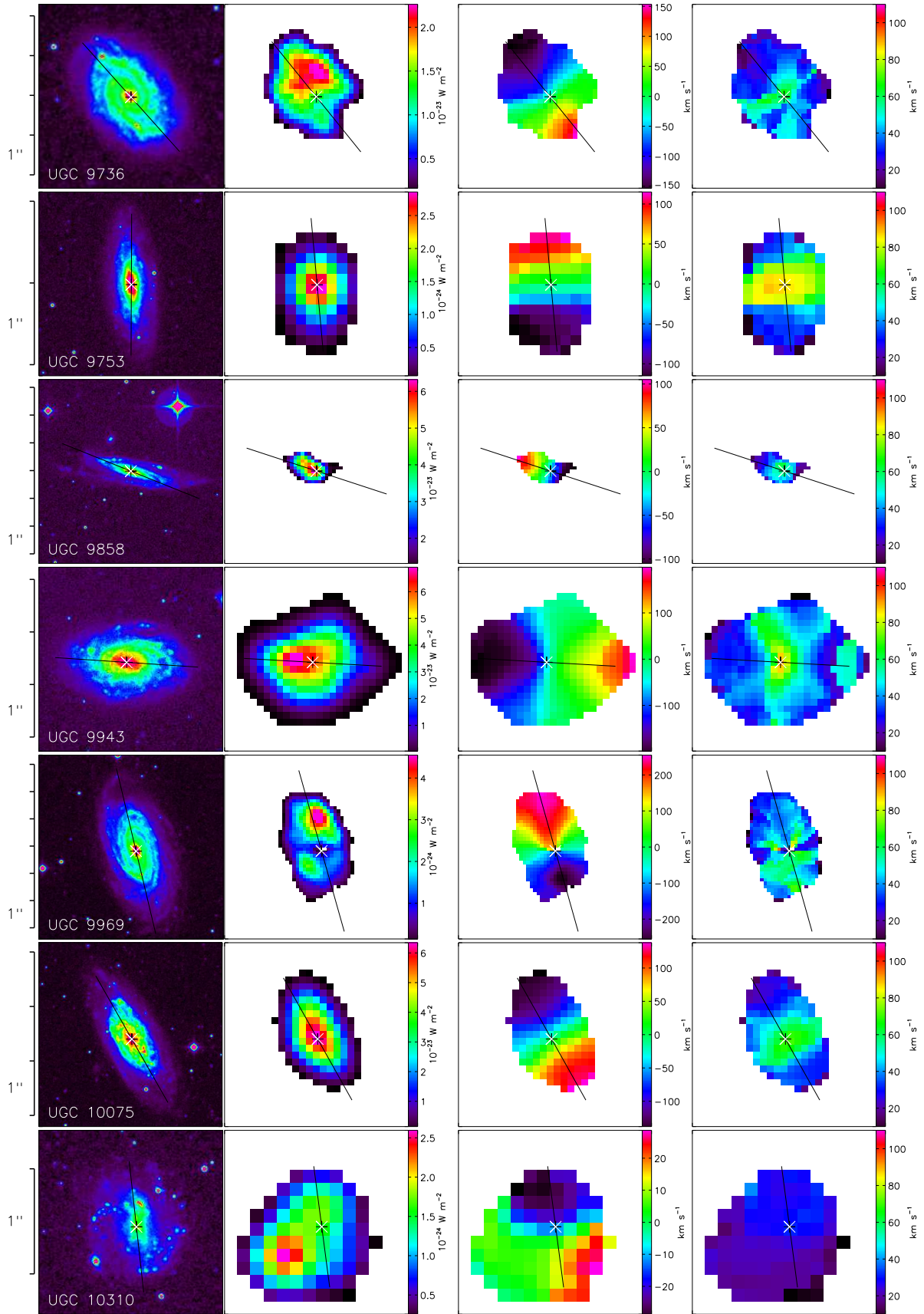


Figure C17. From left to right: X-ray image, $H\alpha$ monochromatic image, velocity field, velocity dispersion map. The white & black crosses mark the kinematical center. The black line is the major axis, its length represents the D_{25} . These maps are not truncated.

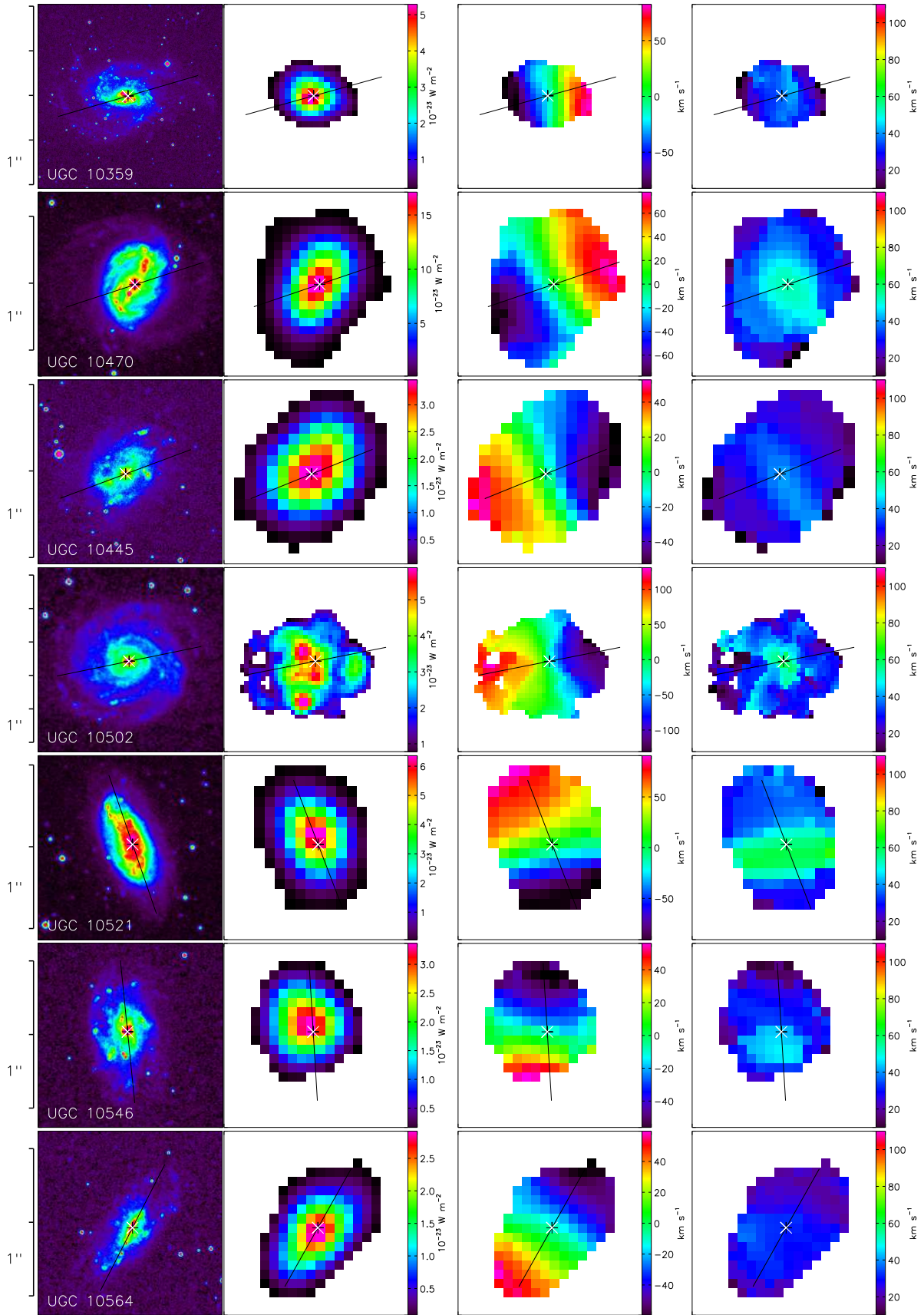
76 *B. Epinat et al.*

Figure C18. From left to right: XDRS image, $H\alpha$ monochromatic image, velocity field, velocity dispersion map. The white & black crosses mark the kinematic center. The black line is the major axis, its length represents the D_{25} . These maps are not truncated.

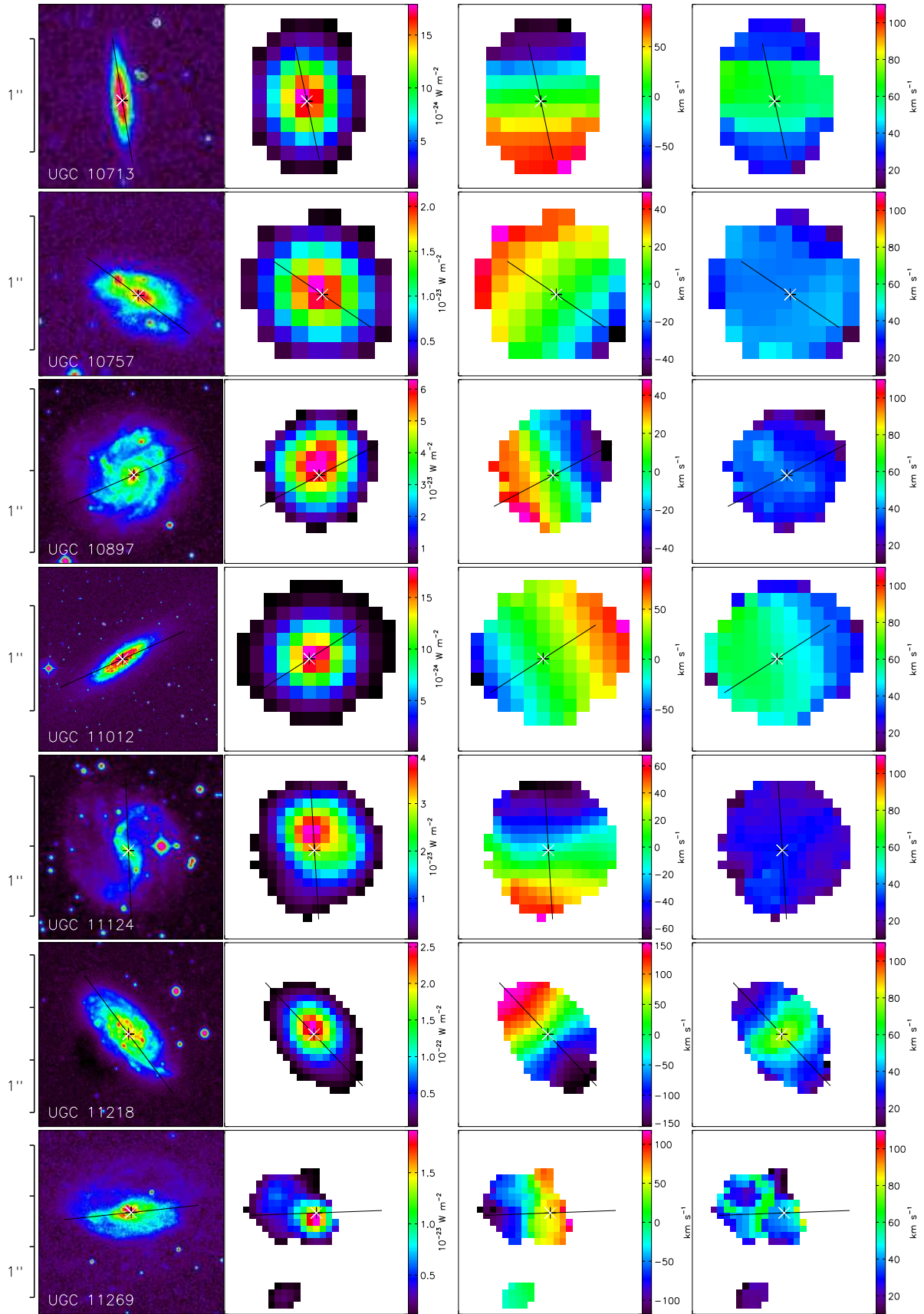


Figure C19. From left to right: X-DSS image, $H\alpha$ monochromatic image, velocity field, velocity dispersion map. The white & black crosses mark the kinematical center. The black line is the major axis, its length represents the D_{25} . These maps are not truncated.

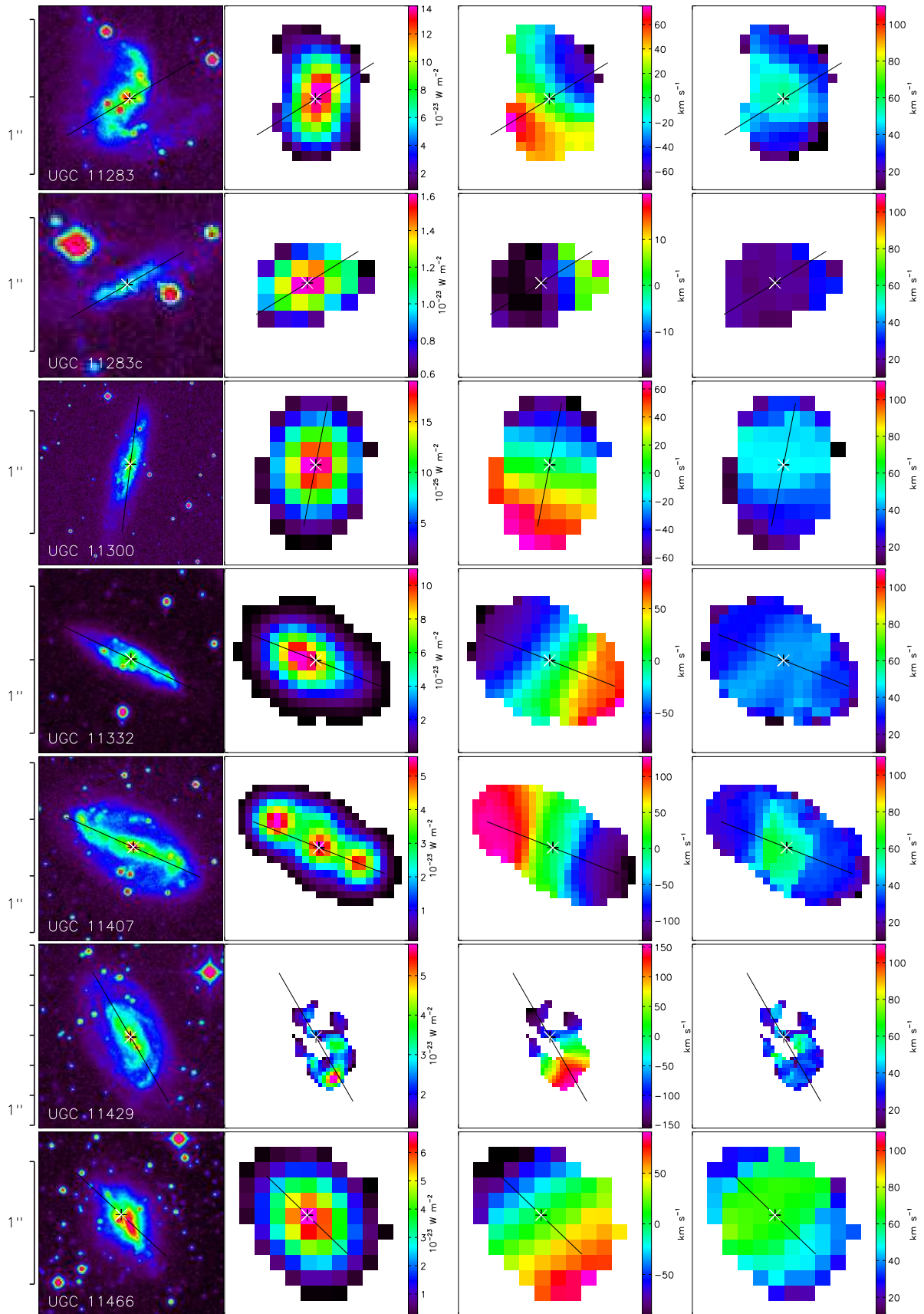
78 *B. Epinat et al.*

Figure C20. From left to right: XDRS image, H α monochromatic image, velocity field, velocity dispersion map. The white & black crosses mark the kinematic center. The black line is the major axis, its length represents the D_{25} . These maps are not truncated.

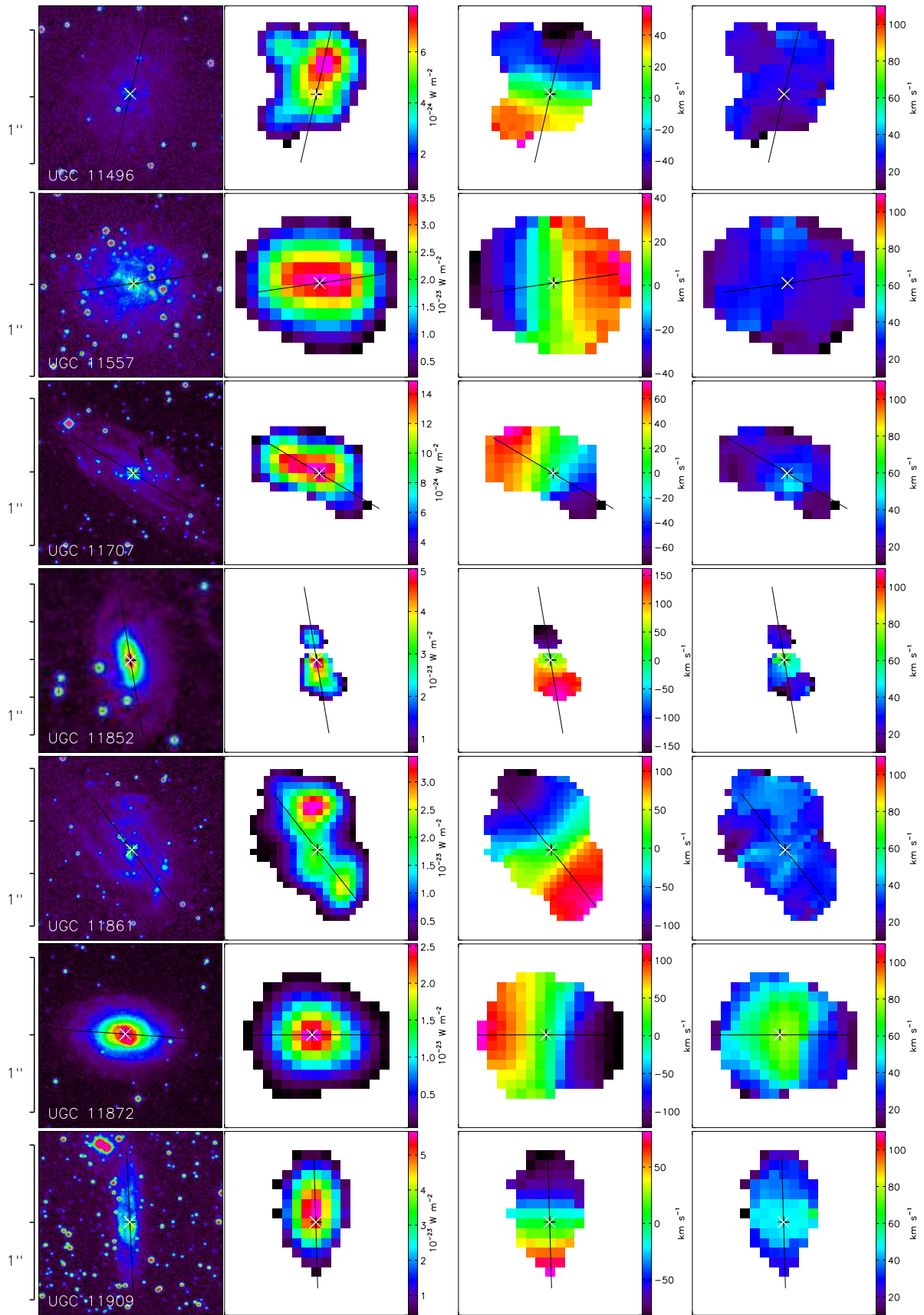


Figure C21. From left to right: X-DSS image, $H\alpha$ monochromatic image, velocity field, velocity dispersion map. The white & black crosses mark the kinematical center. The black line is the major axis, its length represents the D_{25} . These maps are not truncated.

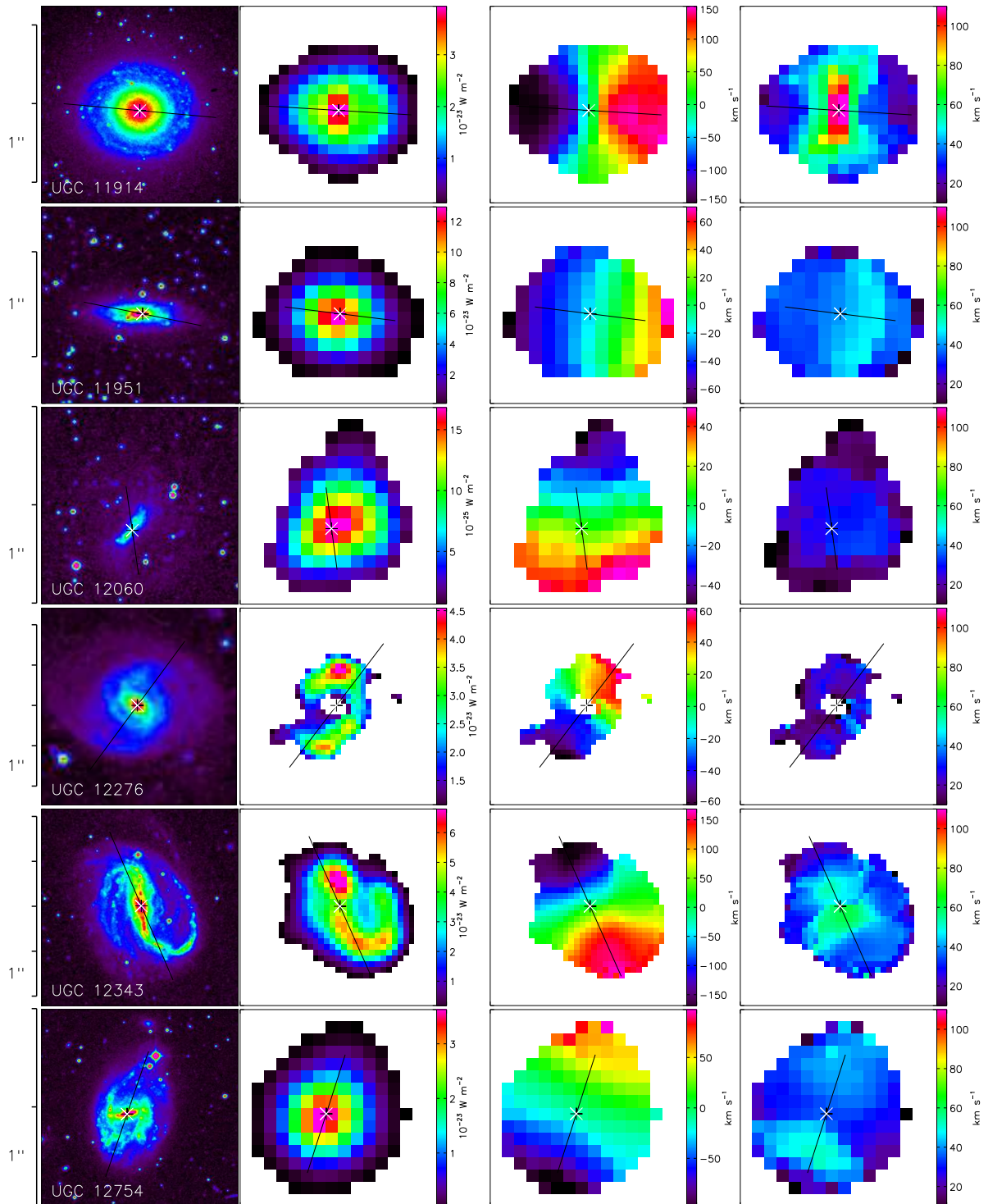
80 *B. Epinat et al.*

Figure C22. From left to right: X-ray image, $H\alpha$ monochromatic image, velocity field, velocity dispersion map. The white & black crosses mark the kinematic center. The black line is the major axis, its length represents the D_{25} . These maps are not truncated.

APPENDIX D: ROTATION CURVES

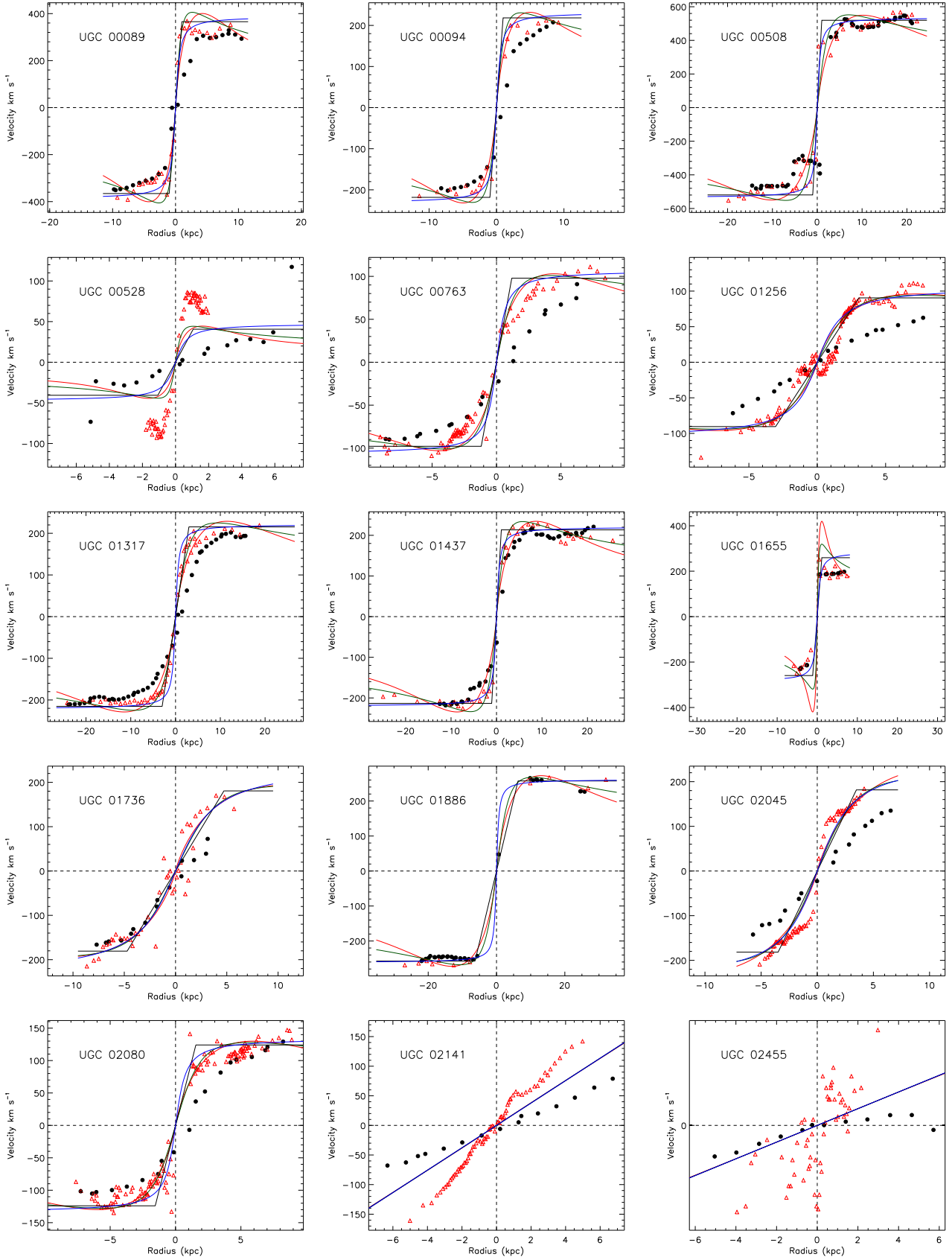
82 *B. Epinat et al.*

Figure D1. High redshift rotation curves along the major axis (black dots), actual rotation curves at redshift zero (red-open triangles) and high resolution rotation curve models (red line: exponential disk; green line: isothermal sphere; black line: “flat model”; blue line: arc-tangent function).

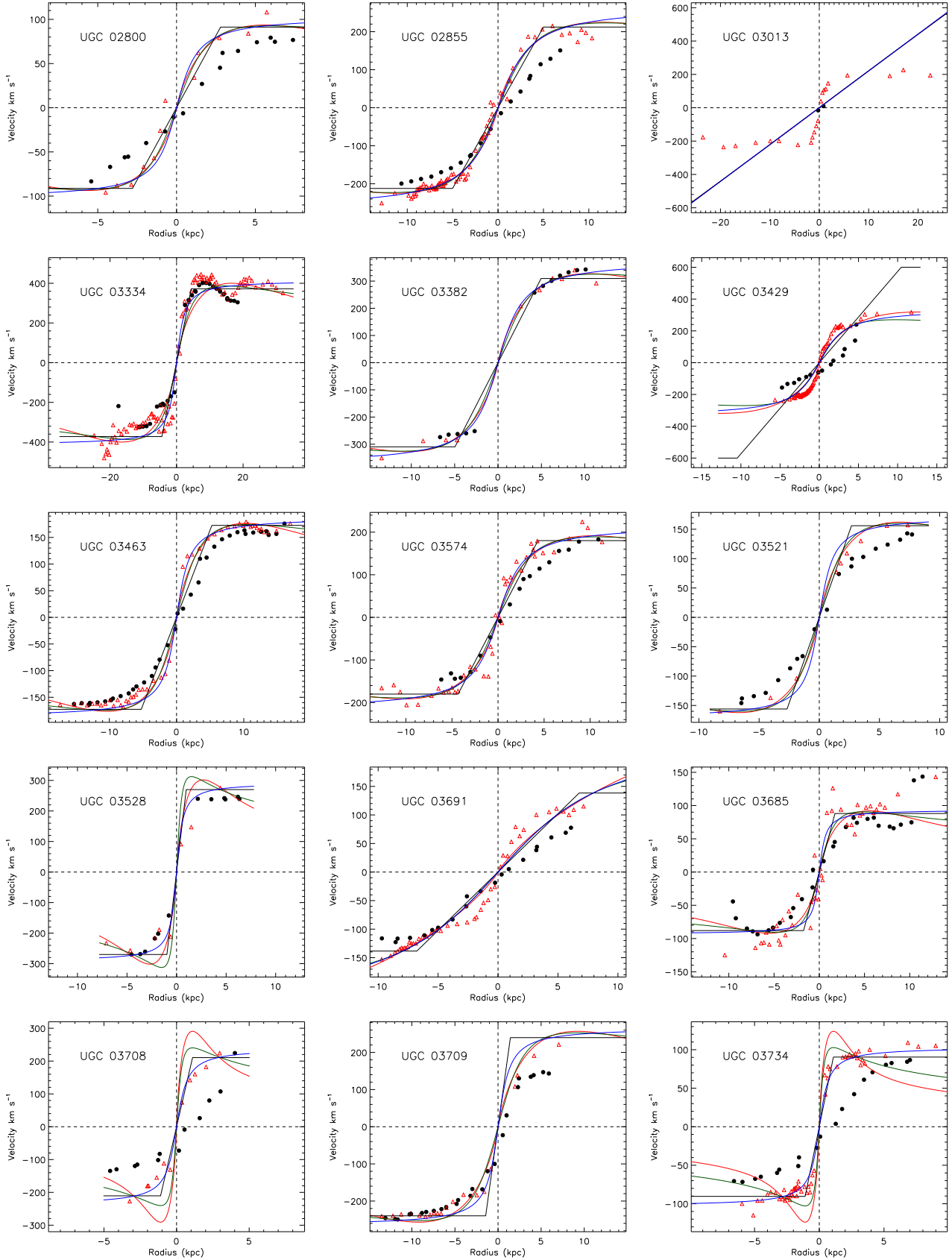


Figure D2. High redshift rotation curves along the major axis (black dots), actual rotation curves at redshift zero (red-open triangles) and high resolution rotation curve models (red line: exponential disk; green line: isothermal sphere; black line: “flat model”; blue line: arc-tangent function).

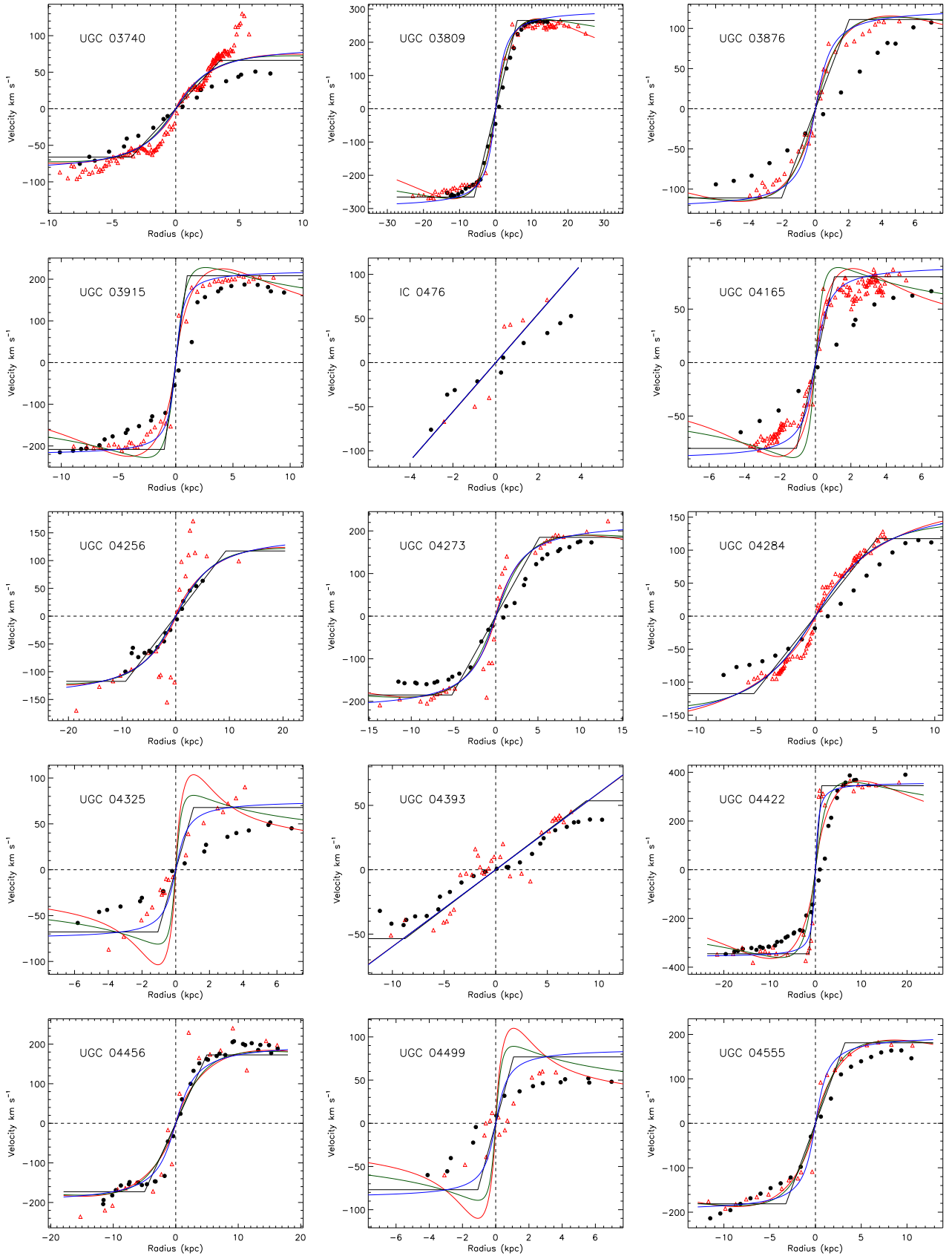


Figure D3. High redshift rotation curves along the major axis (black dots), actual rotation curves at redshift zero (red-open triangles) and high resolution rotation curve models (red line: exponential disk; green line: isothermal sphere; black line: “flat model”; blue line: arc-tangent function).

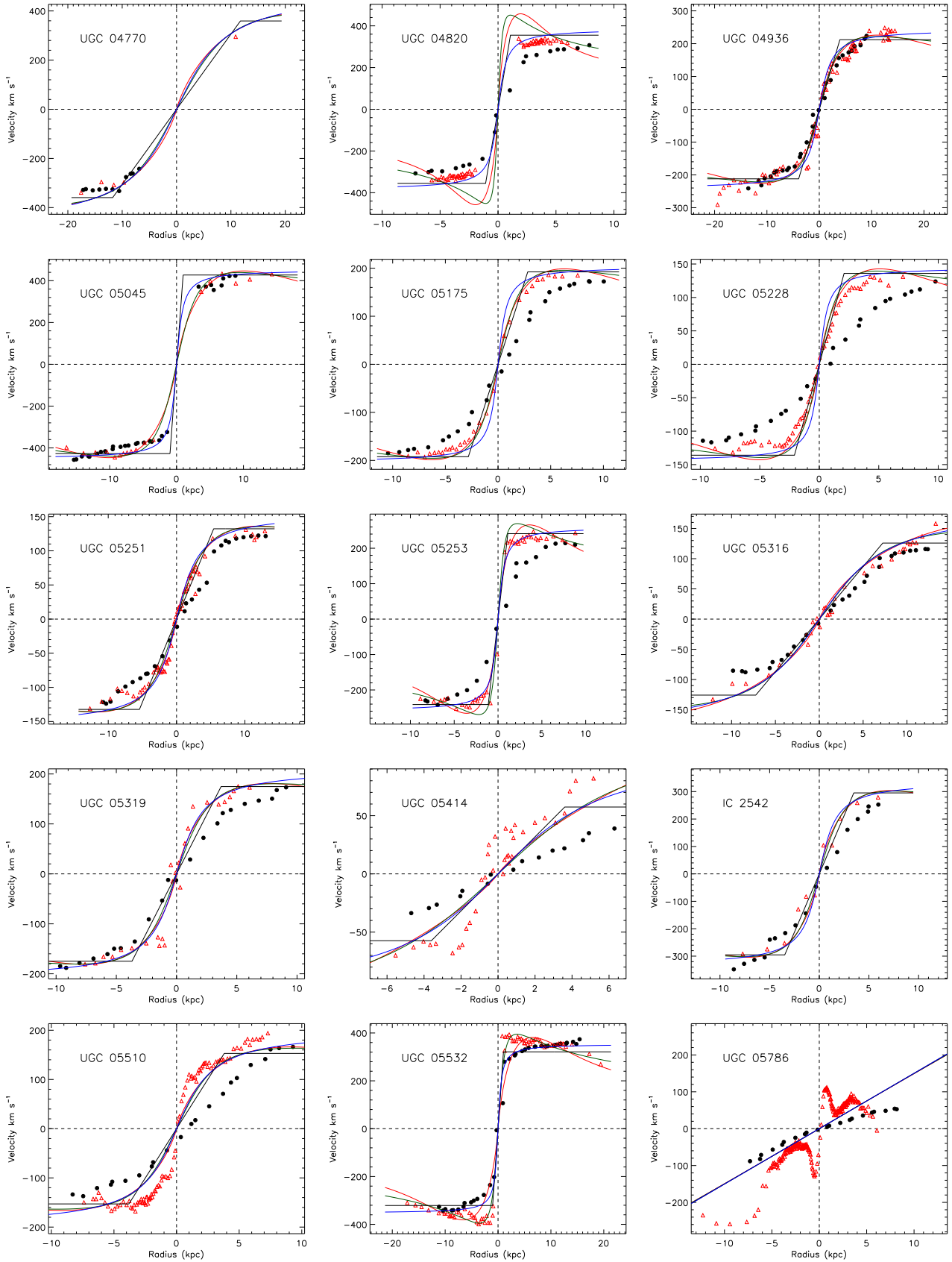


Figure D4. High redshift rotation curves along the major axis (black dots), actual rotation curves at redshift zero (red-open triangles) and high resolution rotation curve models (red line: exponential disk; green line: isothermal sphere; black line: “flat model”; blue line: arc-tangent function).

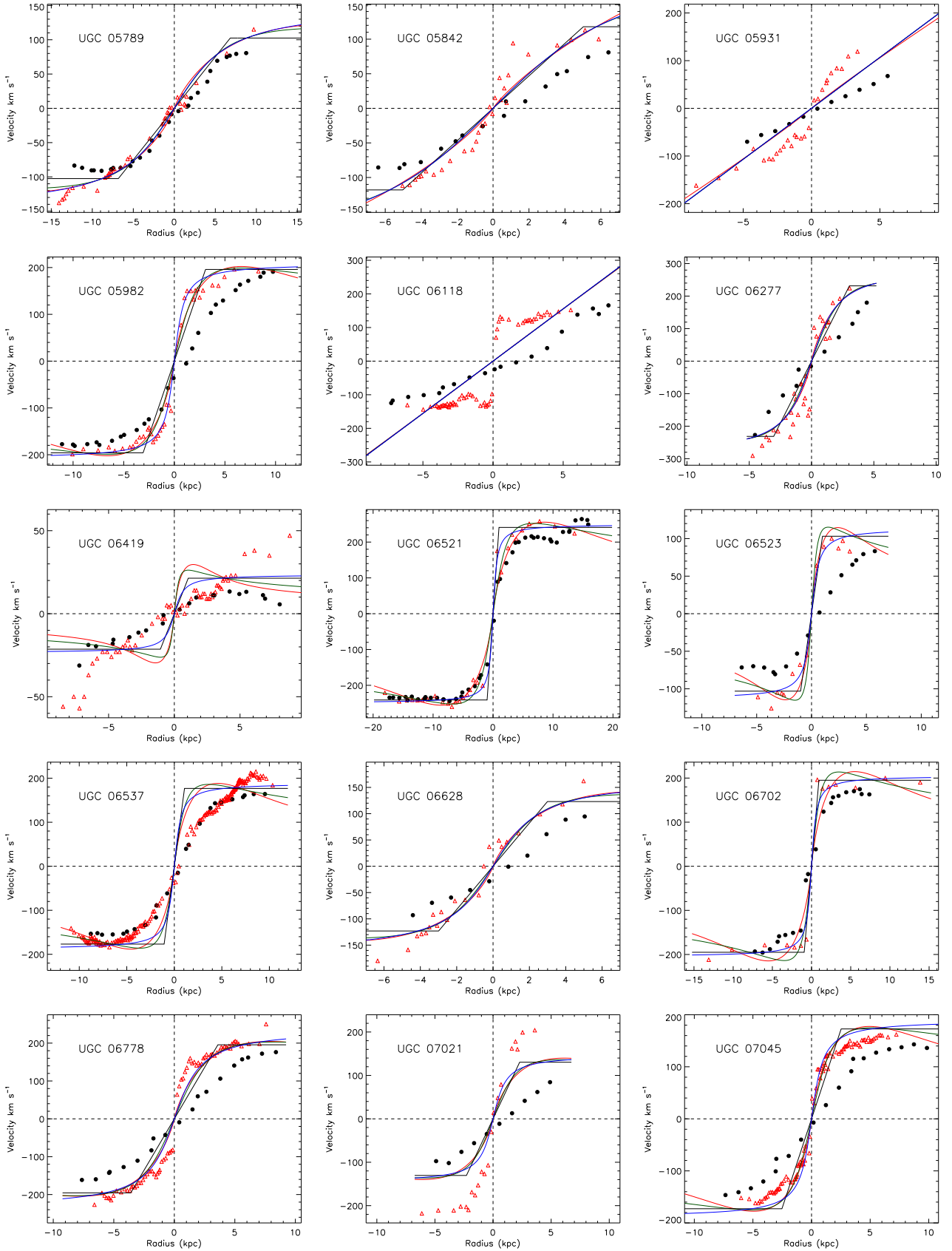
86 *B. Epinat et al.*

Figure D5. High redshift rotation curves along the major axis (black dots), actual rotation curves at redshift zero (red-open triangles) and high resolution rotation curve models (red line: exponential disk; green line: isothermal sphere; black line: “flat model”; blue line: arc-tangent function).

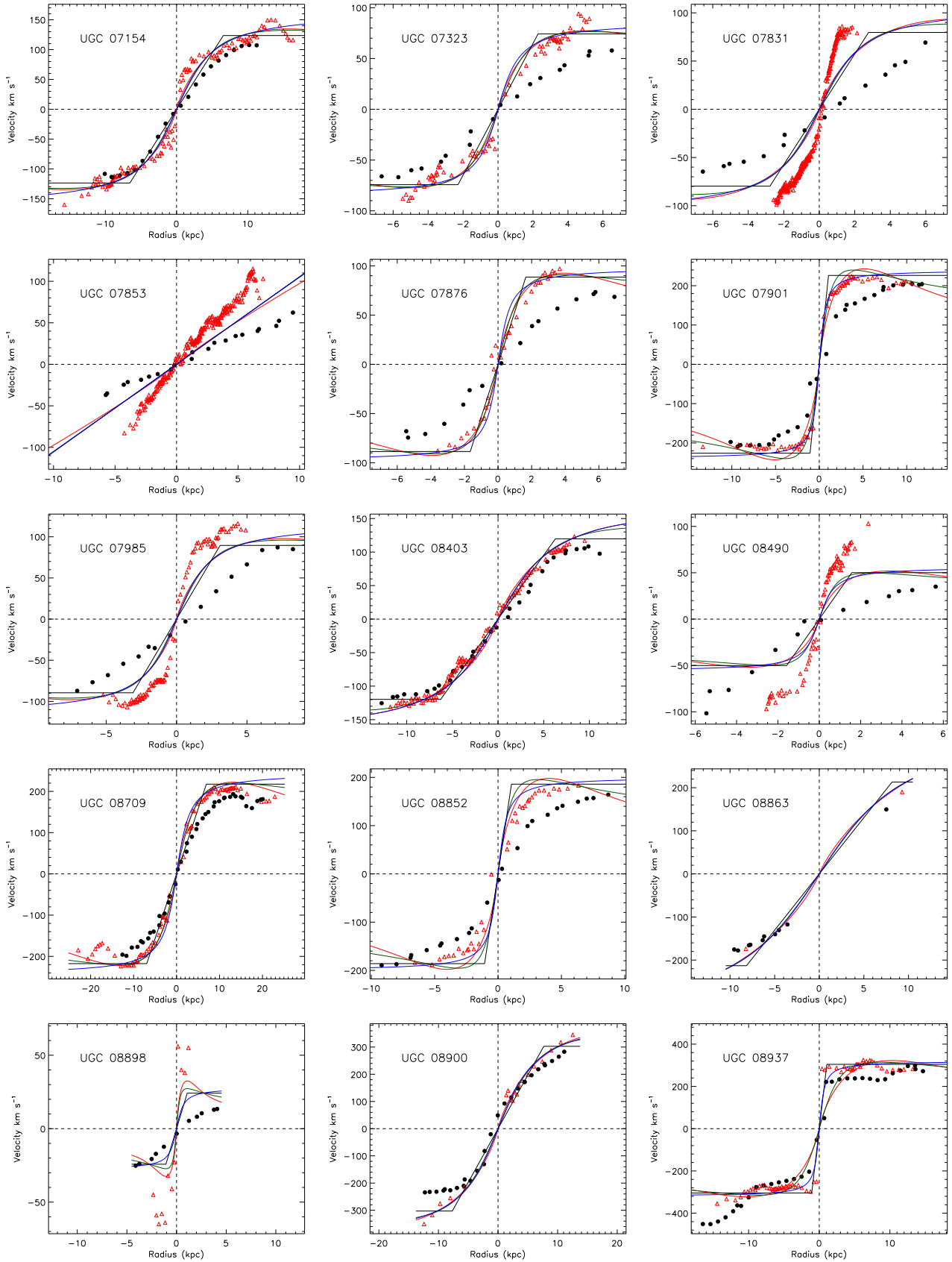


Figure D6. High redshift rotation curves along the major axis (black dots), actual rotation curves at redshift zero (red-open triangles) and high resolution rotation curve models (red line: exponential disk; green line: isothermal sphere; black line: “flat model”; blue line: arc-tangent function).

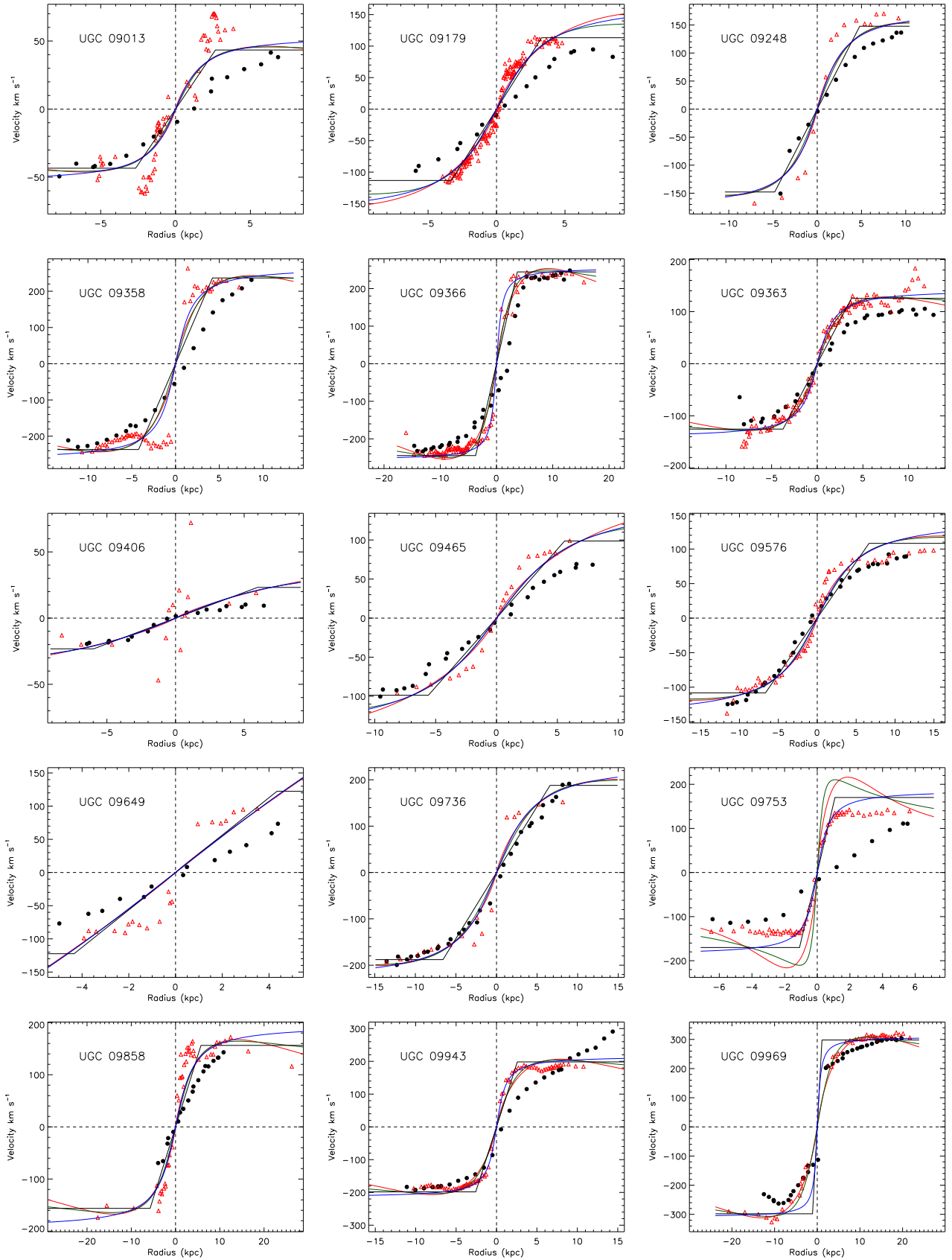


Figure D7. High redshift rotation curves along the major axis (black dots), actual rotation curves at redshift zero (red-open triangles) and high resolution rotation curve models (red line: exponential disk; green line: isothermal sphere; black line: “flat model”; blue line: arc-tangent function).

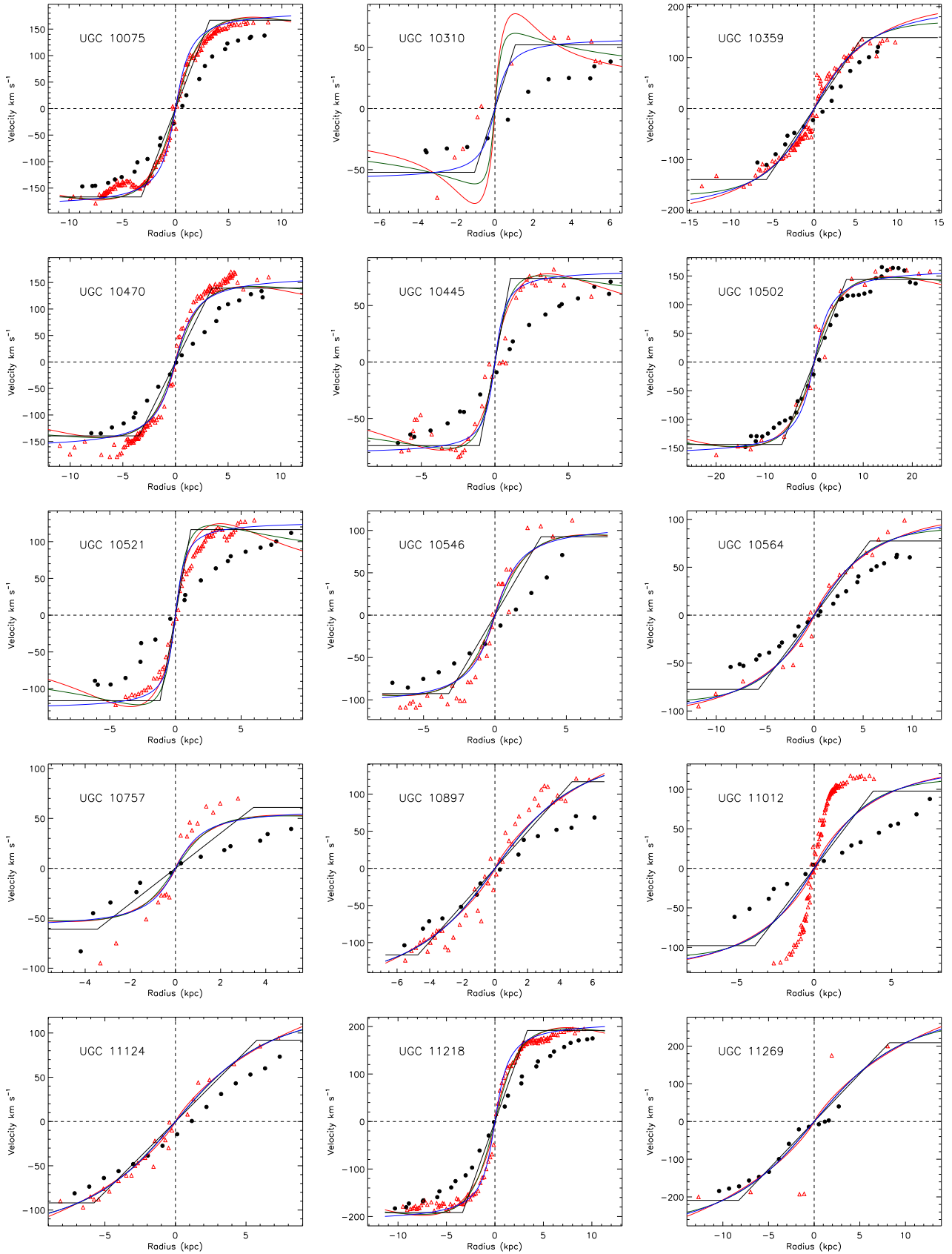


Figure D8. High redshift rotation curves along the major axis (black dots), actual rotation curves at redshift zero (red-open triangles) and high resolution rotation curve models (red line: exponential disk; green line: isothermal sphere; black line: “flat model”; blue line: arc-tangent function).

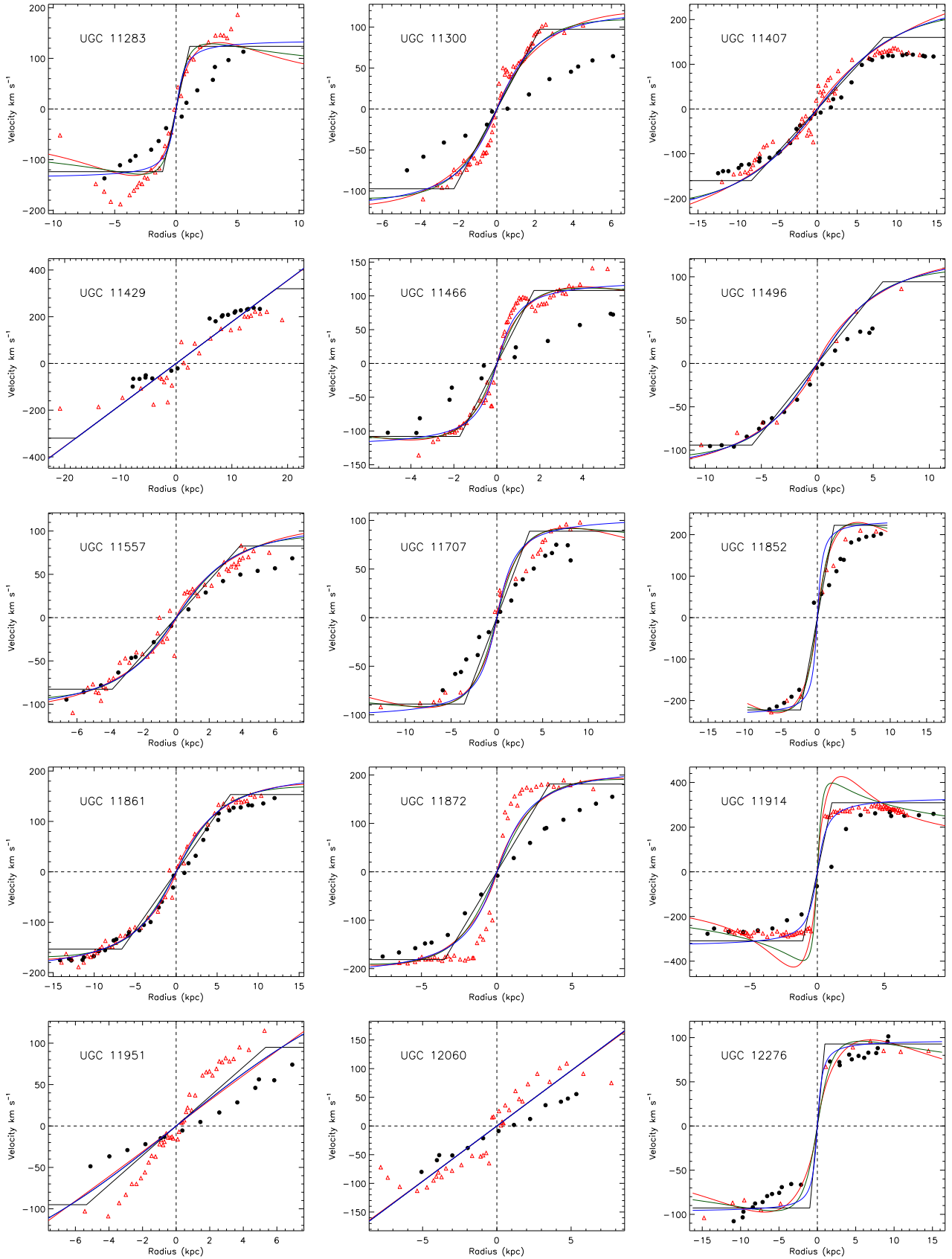
90 *B. Epinat et al.*

Figure D9. High redshift rotation curves along the major axis (black dots), actual rotation curves at redshift zero (red-open triangles) and high resolution rotation curve models (red line: exponential disk; green line: isothermal sphere; black line: “flat model”; blue line: arc-tangent function).

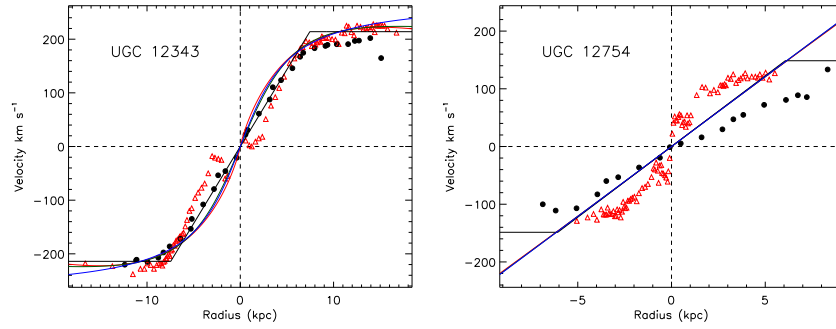


Figure D10. High redshift rotation curves along the major axis (black dots), actual rotation curves at redshift zero (red-open triangles) and high resolution rotation curve models (red line: exponential disk; green line: isothermal sphere; black line: “flat model”; blue line: arc-tangent function).

Conclusions et perspectives

L'étude de la cinématique et de la dynamique des galaxies proches et lointaines permet de contraindre les mécanismes physiques à l'origine de la formation des galaxies, de leur évolution et de leur stabilité actuelle. Grâce à l'utilisation des données spectroscopiques à champ intégral obtenues par interférométrie Fabry-Perot sur l'échantillon de galaxies proches GHASP, j'ai pu, au cours de cette thèse, initier l'étude cinématique de ces galaxies et sonder les effets liés à la faible résolution spatiale des données cinématiques actuelles des galaxies lointaines afin de dissocier les effets de distance des effets d'évolution.

Instrumentation

L'importance d'utiliser une instrumentation adaptée aux besoins spécifiques de mon travail de thèse m'a amené à m'impliquer dès le début de ma thèse dans le projet 3D-NTT, instrument qui sera sur le ciel fin 2009. J'ai ainsi participé à la définition des spécifications des deux Fabry-Perot contenus dans cet instrument et de leurs modes d'utilisation respectifs. Un de ces Fabry-Perot possédera une faible résolution spectrale et pourra être utilisé en pupille ou au foyer du télescope. Dans ce dernier cas, il pourra être utilisé conjointement au second Fabry-Perot de grande résolution afin de sélectionner la bande passante utile. Le choix des résolutions de chacun des deux Fabry-Perot est le résultat de cette utilisation combinée ainsi que des besoins scientifiques des différents modes d'observation du 3D-NTT : le mode basse résolution permettra principalement d'étudier les caractéristiques du milieu interstellaire dans les galaxies proches grâce à des cartes d'extinction et d'abondances, ainsi que de détecter des galaxies lointaines grâce à leurs raies d'émission et d'étudier les phénomènes d'accrétion de gaz et de "feed-back" radiatif ; le mode haute résolution sera destiné à l'étude de la cinématique d'objets à raies d'émission tels que des nébuleuses planétaires, des régions HII Galactiques et des galaxies locales. Je me suis également investi dans la calibration en longueur d'onde de cet instrument et, étant donnée l'expérience que j'ai acquise pour la réduction de données Fabry-Perot durant cette thèse, je prendrai activement part à la mise en place du logiciel de réduction des données issues du 3D-NTT. Par ailleurs, le VLT étant une réplique du NTT à plus grande échelle, le 3D-NTT a été conçu pour pouvoir devenir un 3D-VLT moyennant un nombre de modifications minimales. Je pourrais participer à une telle mise à niveau de l'instrument.

Par ailleurs, en vue des futures observations des galaxies lointaines et dans le cadre du développement de l'ELT européen, j'ai pris part à un projet concernant un spectrographe à grand champ dédié à l'étude de la formation des galaxies primordiales : WFSpec. Cela a été pour moi l'occasion de travailler sur un concept innovant, l'iBTF. Ce concept propose d'utiliser des filtres de Bragg afin de sélectionner plusieurs bandes spectrales tout en préservant l'imagerie, et un Fabry-Perot afin de doper la résolution spectrale. Dans le cadre de ce projet je me suis également penché sur les deux autres concepts proposés afin d'en étudier le facteur de mérite. Cette étude a permis de déterminer qu'un concept "multi-IFU", rebaptisé EAGLE, est le plus adapté à l'étude des galaxies primordiales. Il

en résulte aussi que le concept iBTF est adapté à des thématiques scientifiques possédant une très forte densité d'objets dans le champ, comme par exemple l'étude de populations stellaires résolues dans les galaxies proches. Je compte prolonger mon investissement dans les projets d'instruments spectroscopiques pour les ELT que sont l'iBTF et EAGLE. Par ailleurs, les ELT observeront principalement dans l'infrarouge car cette bande spectrale permet d'effectuer une correction plus fine des effets de la turbulence atmosphérique. Il est donc primordial de réfléchir à des solutions permettant de réduire la contribution des nombreuses raies du ciel dans ce domaine de longueurs d'onde pour faire de l'imagerie en bande large. Dans cette perspective, j'envisage de m'impliquer dans le développement de filtres supprimeurs des raies du ciel nocturne.

Enfin, la réduction et l'utilisation de données Fabry-Perot nécessitant une bonne compréhension de cet interféromètre, je me suis penché durant ma thèse sur diverses solutions de spectroscopie Fabry-Perot. Je les ai reprises pour élaborer un sujet de travaux pratiques pour des étudiants de Master afin de les initier à la spectroscopie Fabry-Perot.

Galaxies de l'Univers local : GHASP

Le projet GHASP a pour objectif principal de constituer un échantillon de référence de galaxies spirales et irrégulières locales situées dans des environnements peu denses pour des études cinématiques et dynamiques et notamment pour la comparaison avec les galaxies distantes. Cet échantillon est composé de 203 galaxies pour lesquelles des cubes de données ont été obtenus autour de la raie H α avec un instrument utilisant un interféromètre de Fabry-Perot au télescope de 1.93 m de l'OHP.

Durant ma thèse, afin de disposer de données réduites de manière homogène pour effectuer l'analyse cinématique, j'ai, dans un premier temps, réalisé la réduction de l'ensemble des données cinématiques de l'échantillon GHASP en utilisant de nouvelles procédures de réduction. Ces procédures ont permis d'obtenir des cartes cinématiques de meilleure qualité notamment grâce à la correction des erreurs de guidage du télescope, à l'exclusion des poses élémentaires présentant des anomalies de flux, à la soustraction éventuelle de reflets parasites et surtout grâce à l'emploi d'un maillage adaptatif pour assurer un rapport signal sur bruit correct tout en préservant l'indépendance de l'information entre mailles adjacentes. À partir des cartes cinématiques ainsi déduites, les paramètres de projection cinématiques et les courbes de rotation ont été déterminés en vue de leur exploitation scientifique. Une extraction robuste des paramètres de projection cinématiques et des courbes de rotation mettant à profit l'intégralité de l'information à deux dimensions du champ de vitesses en lui ajustant un modèle de disque fin en rotation a été mise en place parallèlement à une détermination réaliste des erreurs associées utilisant le spectre de puissance du champ de vitesses résiduel. Les principaux résultats de l'analyse cinématique de l'échantillon GHASP, initiée durant cette thèse, sont énumérés ci-après.

1. La relation de Tully-Fisher obtenue à partir de l'échantillon GHASP est en très bon accord avec les déterminations précédentes de la littérature. Cependant, l'échantillon GHASP suggère l'existence d'une famille de galaxies en rotation rapide pour lesquelles la luminosité est plus faible qu'attendue d'après la relation de Tully-Fisher. Par ailleurs, nous avons montré que les galaxies de faible inclinaison doivent être exclues de l'étude de cette relation car l'incertitude sur leur vitesse de rotation déprojetée est grande et cette vitesse est de ce fait souvent surestimée.
2. L'angle de position du grand axe est déterminé de manière plus précise à partir des données cinématiques, en particulier pour les galaxies de faible inclinaison. Pour les galaxies fortement barrées, la détermination de l'angle de position cinématique peut être biaisée et dépend de l'orientation de la barre.

3. Les inclinaisons cinématiques et morphologiques sont déterminées avec une précision équivalente ($\sim 7 \pm 1^\circ$).
4. À partir des courbes de rotation de 36 galaxies GHASP, il a été montré qu'un profil de sphère isotherme décrit mieux la densité des halos de matière sombre qu'un profil de Navarro-Frenk-White. De plus, les halos de matière sombre possèdent une densité de surface constante, indépendante du type morphologique ou de la magnitude. Les observations photométriques des galaxies GHASP sont en cours afin de pouvoir utiliser l'échantillon complet. Toutefois, des études préliminaires sur tout l'échantillon peuvent d'ores et déjà être menées en utilisant un modèle de disque exponentiel pour décrire le disque stellaire. L'ajustement de modèles de masses sur l'ensemble des galaxies de l'échantillon permettra de mieux contraindre les caractéristiques des halos de matière sombre. Des modèles plus sophistiqués seront aussi utilisés. De plus, le développement de méthodes d'ajustement à partir d'imagerie et de champs de vitesses à deux dimensions, au lieu de profils de luminosité et de courbes de rotation à une dimension, devrait permettre de mieux contraindre la forme des halos de matière sombre.
5. L'utilisation de l'échantillon complet permet de confirmer que la pente interne des courbes de rotation des galaxies croît avec leur masse. Une légère corrélation entre la pente externe et la magnitude a également pu être mise en évidence. Ces indices suggèrent qu'une description de la courbe de rotation à partir d'un nombre réduit de paramètres doit être possible "en moyenne". Les propriétés et la validité d'une courbe de rotation universelle seront donc étudiées en détail. Des courbes de rotation et des champs de vitesses typiques ("templates") seront également déduits à partir des données GHASP.
6. L'étude préliminaire des cartes et des profils de dispersion des vitesses du gaz dans les galaxies GHASP montre que la dispersion de vitesses du gaz varie assez faiblement avec la position. De même la valeur moyenne de la dispersion de vitesses varie très peu d'une galaxie à l'autre et est proche de 20 km s^{-1} . Nous avons également montré que la dispersion de vitesses centrale augmente lorsque la résolution spatiale est trop faible par rapport au gradient de vitesses central, ce qui n'est généralement pas le cas pour les galaxies proches étant donnée la grande résolution spatiale des observations. Une étude plus poussée de la dispersion de vitesses du gaz ionisé sera menée, afin (i) de chercher des corrélations avec les paramètres physiques des galaxies comme le type morphologique ou la magnitude, (ii) de la comparer à la dispersion de vitesses des étoiles et (iii) de déterminer les liens qui existent entre les dispersions azimutale, radiale et perpendiculaire au plan du disque, en utilisant des modèles de déprojection des cartes de dispersion de vitesses.

En plus des travaux présentés précédemment initiés à partir de l'échantillon GHASP, d'autres points clés seront étudiés. En particulier, l'effet des potentiels barrés sur les champs de vitesses sera approfondi. Une étude des effets de la barre sur la cinématique des galaxies à partir de simulations numériques de galaxies barrées a mis en évidence une corrélation entre l'angle de la barre et la position du petit axe cinématique. La recherche de cette corrélation dans l'échantillon de galaxies barrées BH α Bar et dans l'échantillon GHASP fait partie des perspectives de cette thèse. De plus, les résultats pourront être confrontés à l'étude kinématique de ces échantillons qui devrait permettre de mettre en évidence des potentiels non axi-symétriques. Enfin, l'influence du milieu dans lequel évoluent les galaxies sur leur cinématique sera étudiée. Pour cela, il sera nécessaire de confronter l'échantillon GHASP à des échantillons de galaxies dans des environnements différents (amas, groupes, groupes compacts, binaires, etc.). L'objectif de la base de données Fabry-Perot, projet auquel j'ai participé, est justement de mettre à la disposition de la communauté scientifique les observations de galaxies de ces divers échantillons déjà observés et à venir. En particulier, le 3D-NTT permettra d'observer de nouveaux échantillons.

Galaxies de l'Univers lointain

La compréhension des mécanismes de formation des galaxies et leur évolution à travers les âges est un des défis de ce début de siècle. Quand et comment la matière s'est-elle condensée pour former les structures observées dans l'Univers proche ? D'où leur stabilité résulte-t-elle ? Quand les galaxies ont-elles formé leurs étoiles ? Quand les disques stellaires se sont-ils formés ? L'étude de la cinématique des galaxies permet de donner des indices pour répondre à ces questions. Cependant, l'observation des galaxies lointaines est fortement handicapée par la faible résolution spatiale due à leur faible dimension angulaire.

Afin d'aider à l'interprétation des données cinématiques de ces galaxies lointaines, l'échantillon GHASP a été projeté à grand décalage spectral (~ 1.7), dans les conditions d'observation obtenues sans optique adaptative. Les biais observationnels dus au manque de résolution spatiale ont ainsi pu être étudiés.

1. Le manque de résolution spatiale induit une diminution du gradient de vitesse, cependant, celui-ci se retrouve en partie dans les cartes de dispersion de vitesses sous forme d'un pic central.
2. La courbe de rotation mesurée le long du grand axe des galaxies lointaines présente une forme typique de rotation en corps solide, en particulier car la pente interne est fortement diminuée par les effets de résolution. De plus, la vitesse maximale déterminée à partir de cette courbe de rotation est fortement sous-estimée pour les galaxies dont la dimension est inférieure à trois fois la tache du seeing.
3. L'ajustement de modèles cinématiques aux champs de vitesses prenant en compte la faible résolution spatiale permet statistiquement de retrouver la vitesse maximale avec une précision meilleure que 25% et l'angle de position du grand axe cinématique avec une précision meilleure que 5° pour des galaxies aussi petites que la tache du seeing. Cependant, le centre et l'inclinaison sont bien plus délicats à déterminer, ce qui démontre l'intérêt d'utiliser des images du continuum en bande large obtenues par optique adaptative ou à partir de l'espace. En particulier, la valeur de l'inclinaison fixe l'amplitude de la courbe de rotation déprojetée.
4. La dispersion de vitesses intrinsèque peut être retrouvée à partir des modèles car ils permettent de soustraire la contribution due au gradient de vitesse.
5. Les courbes de rotation des modèles sont plus fidèles aux courbes de rotation réelles que les courbes de rotation mesurées le long du grand axe. Cependant, la forme de la courbe des modèles est simpliste puisque ces modèles ne possèdent que deux paramètres.

L'utilisation conjointe des données GHASP projetées et des données cinématiques à champ intégral de galaxies à grand décalage spectral de la littérature a permis de mettre en évidence des effets d'évolution.

1. Le résultat majeur est que la dispersion de vitesses des galaxies possédant un décalage spectral $z > 1$ est plus grande que pour les galaxies locales, impliquant que les disques observés à grand décalage spectral sont de nature différente. Il pourrait s'agir de disques épais créés par accrétion de nuages de gaz possédant une forte formation stellaire dont le support dynamique serait moins organisé que localement. Par contre, la dispersion de vitesses des galaxies possédant un décalage spectral $z \sim 0.6$ est assez similaire à celle des galaxies locales, ce qui implique que les disques actuels étaient déjà formés il y a six milliards d'années.
2. Le programme IMAGES, pour lequel 68 galaxies ont actuellement été observées à un décalage spectral $z \sim 0.6$ par FLAMES/GIRAFFE dans le visible, a été mis en place afin d'étudier l'assemblage de masses des galaxies depuis $z = 1$. En particulier, l'évolution de la relation de Tully-Fisher a été étudiée. L'étude comparative de cette relation à partir de l'échantillon IMAGES

et à partir de l'échantillon GHASP (projeté et local) semble confirmer la conclusion avancée par Puech et al. (2008) selon laquelle les galaxies auraient doublé leur masse stellaire depuis six milliards d'années. Par ailleurs, une étude est actuellement en cours avec l'utilisation conjointe des échantillons GHASP et IMAGES afin de sonder l'évolution du moment cinétique des galaxies. Un sous-échantillon de GHASP représentatif de l'échantillon IMAGES sera extrait et projeté dans les mêmes conditions d'observation.

3. Le projet MASSIV a pour objectif d'observer un échantillon de plus de cent galaxies avec un décalage spectral $1 < z < 1.8$ dans un large intervalle de masses stellaires en vue d'étudier l'assemblage de masses dans ce domaine de décalage spectral. Ces observations sont obtenues par SINFONI, avec optique adaptative pour certaines d'entre elles. Les données SINFONI préliminaires à ce programme présentées dans cette thèse montrent que la cinématique des galaxies avec un décalage spectral $z > 1$ est comparable à la cinématique de disques en rotation mais avec une forte dispersion de vitesses ($\sim 100 \text{ km s}^{-1}$), souvent piquée à diverses positions et corrélée au flux de la raie observée. Ces observations sont en accord avec les autres observations de la littérature et avec les conclusions avancées au point 1. Dans le cadre du projet MASSIV, je mettrai à profit l'expérience acquise durant cette thèse afin de prendre part au dépouillement des données et à leur analyse. La constitution d'un échantillon complet et représentatif et sa comparaison avec des échantillons locaux et des simulations numériques permettra d'aboutir à des conclusions solides quant à la formation et l'évolution des structures.

Afin de réaliser la comparaison des galaxies lointaines et locales, il est nécessaire de disposer d'échantillons de référence locaux de galaxies dans divers environnements. Les méthodes de projection et d'analyse appliquées à l'échantillon GHASP seront employées afin de projeter des galaxies binaires, des galaxies d'amas, des galaxies bleues compactes et des groupes compacts. L'utilisation du 3D-NTT pour observer de tels échantillons de galaxies sera déterminante. Par ailleurs, la signature cinématique des barres mise en évidence sur les simulations numériques sera recherchée sur les échantillons GHASP et BH α Bar projetés afin de déterminer quelle résolution est nécessaire pour mettre en évidence des structures barrées à grand décalage spectral sur les données cinématiques. Enfin, de la même manière que les effets de la résolution spectrale ont été étudiés à partir de l'échantillon GHASP, j'utiliserai cet échantillon afin de déterminer si la relativement faible résolution spectrale des données SINFONI ($\sim 80 \text{ km s}^{-1}$ contre $\sim 20 \text{ km s}^{-1}$ pour GHASP) a une incidence majeure sur leur analyse cinématique.

L'arrivée future des ELT permettra d'observer les galaxies lointaines avec une résolution spatiale comparable à celle qui est aujourd'hui obtenue sur les galaxies proches. Cela ouvrira la voie à des études cinématiques poussées incluant l'évolution de la distribution de matière dans les galaxies, et de la forme des halos de matière sombre à travers les âges...

Bibliographie du texte en Français

- Amram, P. : 1991, *Ph.D. thesis*, Université de Provence (France)
- Amram, P., Mendes de Oliveira, C., Plana, H., Balkowski, C., et Hernandez, O. : 2007, *A&A* **471**, 753
- Barnes, E. I., Sellwood, J. A., et Kosowsky, A. : 2004, *AJ* **128**, 2724
- Bland, J. et Tully, R. B. : 1989, *AJ* **98**, 723
- Bosma, A. : 1978, *Ph.D. thesis*, Groningen Universiteit
- Boulesteix, J., Georgelin, Y., Marcelin, M., et Monnet, G. : 1984, in A. Boksenberg et D. L. Crawford (eds.), *Society of Photo-Optical Instrumentation Engineers (SPIE) Conference Series*, Vol. 445 of *Society of Photo-Optical Instrumentation Engineers (SPIE) Conference Series*, pp 37–41
- Boulesteix, J., Georgelin, Y. P., Le Coarer, E., Marcelin, M., et Monnet, G. : 1987, *A&A* **178**, 91
- Bournaud, F., Daddi, E., Elmegreen, B. G., Elmegreen, D. M., Nesvadba, N., Vanzella, E., di Matteo, P., Le Tiran, L., Lehnert, M., et Elbaz, D. : 2008, *A&A* **486**, 741
- Buisson, H., Fabry, C., et Bourget, H. : 1914, *ApJ* **40**, 241
- Burbidge, E. M., Burbidge, G. R., et Prendergast, K. H. : 1960, *ApJ* **131**, 282
- Cappellari, M. et Copin, Y. : 2003, *MNRAS* **342**, 345
- Catinella, B., Giovanelli, R., et Haynes, M. P. : 2006, *ApJ* **640**, 751
- Christodoulou, D. M., Tohline, J. E., et Steiman-Cameron, T. Y. : 1993, *ApJ* **416**, 74
- Cole, S., Norberg, P., Baugh, C. M., Frenk, C. S., Bland-Hawthorn, J., Bridges, T., Cannon, R., Colless, M., Collins, C., Couch, W., Cross, N., Dalton, G., De Propris, R., Driver, S. P., Efstathiou, G., Ellis, R. S., Glazebrook, K., Jackson, C., Lahav, O., Lewis, I., Lumsden, S., Maddox, S., Madgwick, D., Peacock, J. A., Peterson, B. A., Sutherland, W., et Taylor, K. : 2001, *MNRAS* **326**, 255
- Courtès, G. : 1972, *Vistas in Astronomy* **14**, 81
- Daigle, O., Carignan, C., Hernandez, O., Chemin, L., et Amram, P. : 2006, *MNRAS* **368**, 1016
- de Vaucouleurs, G., de Vaucouleurs, A., Corwin, H. G., Buta, R. J., Paturel, G., et Fouque, P. : 1995, *VizieR Online Data Catalog* **7155**, 0
- de Vaucouleurs, G., de Vaucouleurs, A., et Pence, W. : 1974, *ApJ* **194**, L119
- Epinat, B., Amram, P., et Balkowski, C. : 2007, in F. Combes et J. Palous (eds.), *IAU Symposium*, Vol. 235 of *IAU Symposium*, pp 401–401

- Epinat, B., Amram, P., Balkowski, C., et Marcelin, M. : 2009a
- Epinat, B., Amram, P., et Marcelin, M. : 2008a, *MNRAS* **390**, 466
- Epinat, B., Amram, P., Marcelin, M., et al. : 2009b, *en préparation*
- Epinat, B., Amram, P., Marcelin, M., Balkowski, C., Daigle, O., Hernandez, O., Chemin, L., Carignan, C., Gach, J.-L., et Balard, P. : 2008b, *MNRAS* **388**, 500
- Epinat, B., Contini, T., Le Fevre, O., Vergani, D., Garilli, B., Amram, P., Queyrel, J., Tasca, L., et Tresse, L. : 2009c
- Erb, D. K., Shapley, A. E., Steidel, C. C., Pettini, M., Adelberger, K. L., Hunt, M. P., Moorwood, A. F. M., et Cuby, J.-G. : 2003, *ApJ* **591**, 101
- Erb, D. K., Steidel, C. C., Shapley, A. E., Pettini, M., et Adelberger, K. L. : 2004, *ApJ* **612**, 122
- Falcón-Barroso, J., Bacon, R., Bureau, M., Cappellari, M., Davies, R. L., de Zeeuw, P. T., Emsellem, E., Fathi, K., Krajnović, D., Kuntschner, H., McDermid, R. M., Peletier, R. F., et Sarzi, M. : 2006, *MNRAS* **369**, 529
- Fathi, K., Beckman, J. E., Lundgren, A. A., Carignan, C., Hernandez, O., Amram, P., Balard, P., Boulesteix, J., Gach, J.-L., Knapen, J. H., et Relaño, M. : 2008, *ApJ* **675**, L17
- Ferguson, A. M. N., Wyse, R. F. G., Gallagher, III, J. S., et Hunter, D. A. : 1996, *AJ* **111**, 2265
- Flores, H., Hammer, F., Puech, M., Amram, P., et Balkowski, C. : 2006, *A&A* **455**, 107
- Förster Schreiber, N. M., Genzel, R., Lehnert, M. D., Bouché, N., Verma, A., Erb, D. K., Shapley, A. E., Steidel, C. C., Davies, R., Lutz, D., Nesvadba, N., Tacconi, L. J., Eisenhauer, F., Abuter, R., Gilbert, A., Gillessen, S., et Sternberg, A. : 2006, *ApJ* **645**, 1062
- Gach, J.-L., Hernandez, O., Boulesteix, J., Amram, P., Boissin, O., Carignan, C., Garrido, O., Marcelin, M., Östlin, G., Plana, H., et Rampazzo, R. : 2002, *PASP* **114**, 1043
- Garrido, O. : 2003a, *Ph.D. thesis*, Université de Provence (France)
- Garrido, O., Marcelin, M., et Amram, P. : 2004, *MNRAS* **349**, 225
- Garrido, O., Marcelin, M., Amram, P., Balkowski, C., Gach, J. L., et Boulesteix, J. : 2005, *MNRAS* **362**, 127
- Garrido, O., Marcelin, M., Amram, P., et Boissin, O. : 2003b, *A&A* **399**, 51
- Garrido, O., Marcelin, M., Amram, P., et Boulesteix, J. : 2002, *A&A* **387**, 821
- Genzel, R., Tacconi, L. J., Eisenhauer, F., Förster Schreiber, N. M., Cimatti, A., Daddi, E., Bouché, N., Davies, R., Lehnert, M. D., Lutz, D., Nesvadba, N., Verma, A., Abuter, R., Shapiro, K., Sternberg, A., Renzini, A., Kong, X., Arimoto, N., et Mignoli, M. : 2006, *Nature* **442**, 786
- Georgelin, Y. M., Boulesteix, J., Georgelin, Y. P., Laval, A., et Marcelin, M. : 1987, *A&A* **174**, 257
- Georgelin, Y. P. : 1970, *A&A* **9**, 441

- Georgelin, Y. P. et Amram, P. : 1995, in G. Comte et M. Marcelin (eds.), *IAU Colloq. 149 : Tridimensional Optical Spectroscopic Methods in Astrophysics*, Vol. 71 of *Astronomical Society of the Pacific Conference Series*, p. 382
- Gottesman, S. T. et Weliachew, L. : 1975, *ApJ* **195**, 23
- Gunn, J. E. : 1980, *Royal Society of London Philosophical Transactions Series A* **296**, 313
- Hernandez, O. : 2005a, *Ph.D. thesis*, Université de Montréal (Canada)
- Hernandez, O., Fathi, K., Carignan, C., Beckman, J., Gach, J.-L., Balard, P., Amram, P., Boulesteix, J., Corradi, R. L. M., de Denus-Baillargeon, M.-M., Epinat, B., Relaño, M., Thibault, S., et Vallée, P. : 2008b, *PASP* **120**, 665
- Hernandez, O., Wozniak, H., Carignan, C., Amram, P., Chemin, L., et Daigle, O. : 2005, *ApJ* **632**, 253
- Hicks, T. R., Reay, N. K., et Stephens, C. L. : 1976, *A&A* **51**, 367
- Kormendy, J. : 1977, *ApJ* **217**, 406
- Krajnović, D., Cappellari, M., de Zeeuw, P. T., et Copin, Y. : 2006, *MNRAS* **366**, 787
- Kravtsov, A. V., Klypin, A. A., Bullock, J. S., et Primack, J. R. : 1998, *ApJ* **502**, 48
- Laval, A., Boulesteix, J., Georgelin, Y. P., Georgelin, Y. M., et Marcelin, M. : 1987, *A&A* **175**, 199
- Law, D. R., Steidel, C. C., Erb, D. K., Larkin, J. E., Pettini, M., Shapley, A. E., et Wright, S. A. : 2007, *ApJ* **669**, 929
- Le Coarer, E., Amram, P., Boulesteix, J., Georgelin, Y. M., Georgelin, Y. P., Marcelin, M., Joulie, P., et Urios, J. : 1992, *A&A* **257**, 389
- Le Coarer, E., Bensammar, S., Comte, G., Gach, J. L., et Georgelin, Y. : 1995, *A&AS* **111**, 359
- Le Fèvre, O., Vettolani, G., Garilli, B., Tresse, L., Bottini, D., Le Brun, V., Maccagni, D., Picat, J. P., Scaramella, R., Scodreggio, M., Zanichelli, A., Adami, C., Arnaboldi, M., Arnouts, S., Bardelli, S., Bolzonella, M., Cappi, A., Charlot, S., Ciliegi, P., Contini, T., Foucaud, S., Franzetti, P., Gavignaud, I., Guzzo, L., Ilbert, O., Iovino, A., McCracken, H. J., Marano, B., Marinoni, C., Mathez, G., Mazure, A., Meneux, B., Merighi, R., Paltani, S., Pellò, R., Pollo, A., Pozzetti, L., Radovich, M., Zamorani, G., Zucca, E., Bondi, M., Bongiorno, A., Busarello, G., Lamareille, F., Mellier, Y., Merluzzi, P., Ripepi, V., et Rizzo, D. : 2005, *A&A* **439**, 845
- Lehnert, M. D. et Bremer, M. : 2003, *ApJ* **593**, 630
- Maillard, J. P. : 1996, *Appl. Opt.* **35**, 2734
- Marcelin, M., Amram, P., Balard, P., Balkowski, C., Boissin, O., Boulesteix, J., Carignan, C., Daigle, O., de Denus-Baillargeon, M.-M., Epinat, B., Gach, J.-L., Hernandez, O., Rigaud, F., et Vallée, P. : 2008, in *Ground-based and Airborne Instrumentation for Astronomy II*, Ian S. McLean ; Mark M. Casali, Editors, 701455, Vol. 7014 of *Presented at the Society of Photo-Optical Instrumentation Engineers (SPIE) Conference*
- Marcelin, M., Le Coarer, E., Boulesteix, J., Georgelin, Y., et Monnet, G. : 1987, *A&A* **179**, 101
- Mathewson, D. S., Ford, V. L., et Buchhorn, M. : 1992, *ApJS* **81**, 413

- McCracken, H. J., Radovich, M., Bertin, E., Mellier, Y., Dantel-Fort, M., Le Fèvre, O., Cuillandre, J. C., Gwyn, S., Foucaud, S., et Zamorani, G. : 2003, *A&A* **410**, 17
- Merritt, D., Graham, A. W., Moore, B., Diemand, J., et Terzić, B. : 2006, *AJ* **132**, 2685
- Milgrom, M. : 1983, *ApJ* **270**, 371
- Monnet, G. : 1971, *A&A* **12**, 379
- Moretto, G., Bacon, R., Cuby, J.-G., Hammer, F., Amram, P., Blais-Ouellette, S., Blanc, P.-E., Devriendt, J., Epinat, B., Fusco, T., Jagourel, P., Hernandez, O., Kneib, J.-P., Montilla, I., Neichel, B., Pécontal, E., Prieto, E., et Puech, M. : 2006, in *Ground-based and Airborne Instrumentation for Astronomy. Edited by McLean, Ian S.; Iye, Masanori. Proceedings of the SPIE, Volume 6269, pp. 62692G (2006).*, Vol. 6269 of *Presented at the Society of Photo-Optical Instrumentation Engineers (SPIE) Conference*
- Neichel, B., Hammer, F., Puech, M., Flores, H., Lehnert, M., Rawat, A., Yang, Y., Delgado, R., Amram, P., Balkowski, C., Cesarsky, C., Dannerbauer, H., Fuentes-Carrera, I., Guiderdoni, B., Kembhavi, A., Liang, Y. C., Nesvadba, N., Östlin, G., Pozzetti, L., Ravikumar, C. D., di Serego Alighieri, S., Vergani, D., Vernet, J., et Wozniak, H. : 2008, *A&A* **484**, 159
- Noordermeer, E., van der Hulst, J. M., Sancisi, R., Swaters, R. S., et van Albada, T. S. : 2007, *MNRAS* **376**, 1513
- Peng, C. Y., Ho, L. C., Impey, C. D., et Rix, H.-W. : 2002, *AJ* **124**, 266
- Persic, M. et Salucci, P. : 1991, *ApJ* **368**, 60
- Persic, M., Salucci, P., et Stel, F. : 1996, *MNRAS* **281**, 27
- Piazza, F. et Marinoni, C. : 2003, *Physical Review Letters* **91(14)**, 141301
- Plana, H. : 1996, *Ph.D. thesis*, Université de Provence (France)
- Pogge, R. W., Atwood, B., Byard, P. L., O'Brien, T. P., Peterson, B. M., Lame, N. J., et Baldwin, J. A. : 1995, *PASP* **107**, 1226
- Puech, M., Flores, H., Hammer, F., Yang, Y., Neichel, B., Lehnert, M., Chemin, L., Nesvadba, N., Epinat, B., Amram, P., Balkowski, C., Cesarsky, C., Dannerbauer, H., di Serego Alighieri, S., Fuentes-Carrera, I., Guiderdoni, B., Kembhavi, A., Liang, Y. C., Östlin, G., Pozzetti, L., Ravikumar, C. D., Rawat, A., Vergani, D., Vernet, J., et Wozniak, H. : 2008, *A&A* **484**, 173
- Puech, M., Hammer, F., Flores, H., Östlin, G., et Marquart, T. : 2006, *A&A* **455**, 119
- Rousselot, P., Lidman, C., Cuby, J.-G., Moreels, G., et Monnet, G. : 2000, *A&A* **354**, 1134
- Rubin, V. C., Thonnard, N., et Ford, Jr., W. K. : 1978, *ApJ* **225**, L107
- Russeil, D. : 1998, *Ph.D. thesis*, Université de Provence (France)
- Russeil, D., Adami, C., Amram, P., Le Coarer, E., Georgelin, Y. M., Marcelin, M., et Parker, Q. : 2005, *A&A* **429**, 497
- Spano, M., Marcelin, M., Amram, P., Carignan, C., Epinat, B., et Hernandez, O. : 2008, *MNRAS* **383**, 297

- Steidel, C. C., Shapley, A. E., Pettini, M., Adelberger, K. L., Erb, D. K., Reddy, N. A., et Hunt, M. P. : 2004, *ApJ* **604**, 534
- Taylor, K. et Atherton, P. D. : 1980, *MNRAS* **191**, 675
- Vetterling, W. T., Flannery, B. P., Press, W. H., et Teukolski, S. A. : 1989, *Numerical Recipes in FORTRAN - The Art of Scientific Computing - Second Edition*, University Press, Cambridge
- Vogt, N. P., Forbes, D. A., Phillips, A. C., Gronwall, C., Faber, S. M., Illingworth, G. D., et Koo, D. C. : 1996, *ApJ* **465**, L15
- Weiner, B. J., Willmer, C. N. A., Faber, S. M., Melbourne, J., Kassin, S. A., Phillips, A. C., Harker, J., Metevier, A. J., Vogt, N. P., et Koo, D. C. : 2006, *ApJ* **653**, 1027
- Wright, S. A., Larkin, J. E., Barczys, M., Erb, D. K., Iserlohe, C., Krabbe, A., Law, D. R., McElwain, M. W., Quirrenbach, A., Steidel, C. C., et Weiss, J. : 2007, *ApJ* **658**, 78
- Yang, Y., Flores, H., Hammer, F., Neichel, B., Puech, M., Nesvadba, N., Rawat, A., Cesarsky, C., Lehnert, M., Pozzetti, L., Fuentes-Carrera, I., Amram, P., Balkowski, C., Dannerbauer, H., di Serego Alighieri, S., Guiderdoni, B., Kembhavi, A., Liang, Y. C., Östlin, G., Ravikumar, C. D., Vergani, D., Vernet, J., et Wozniak, H. : 2008, *A&A* **477**, 789

UNIVERSITÉ DE PROVENCE - AIX-MARSEILLE I
ÉCOLE DOCTORALE DE PHYSIQUE ET SCIENCES DE LA MATIÈRE
Laboratoire d'Astrophysique de Marseille

THÈSE DE DOCTORAT

présentée pour obtenir le grade de

Docteur de l'Université de Provence
Spécialité : Astrophysique

par

Benoît EPINAT

DES GALAXIES PROCHES AUX GALAXIES LOINTAINES ÉTUDES CINÉMATIQUE ET DYNAMIQUE

ANNEXES

Annexe A

Articles et documents concernant l'instrumentation présentée au chapitre 1

Résumé

A.1 Article V : 3D-NTT : a versatile integral field spectro-imager for the NTT	237
A.2 GHαFaS	246
A.3 Article VII : Wide Field Spectrograph Concepts for the European Extremely Large Telescope	265

Cette annexe contient des documents concernant les instruments présentés dans le chapitre 1. En particulier, les plans, les schémas ainsi que les principaux objectifs scientifiques des instruments sont présentés dans des publications.

A.1 **Article V : 3D-NTT : a versatile integral field spectro-imager for the NTT**

Un premier article concernant le projet 3D-NTT (PI : M. Marcelin) (partie 1.3) a été publié dans les comptes-rendus de la conférence SPIE qui s'est tenue à Marseille en juin 2008 (Marcelin et al., 2008) suite à la présentation d'un poster.

Le 3D-NTT est un spectro-imageur à champ intégral pour le visible permettant deux modes d'observation : un mode basse résolution avec un filtre accordable ($R \sim 300$ à 6000) possédant un grand champ de vue ($17' \times 17'$) et un mode haute résolution ($R \sim 10000$ à 40000) avec un Fabry-Perot à balayage ($7' \times 7'$). Il sera utilisé comme instrument visiteur sur le NTT à partir de 2009. Deux grands programmes seront menés : "Caractérisation du milieu interstellaire de galaxies proches grâce à des cartes 2D d'extinction et d'abondances" (PI : M. Marcelin) et "Accrétion de gaz et feed-back radiatif dans les premiers âges de l'Univers" (PI : J. Bland Hawthorn). Ils utiliseront tous deux principalement le mode filtre accordable. Cet instrument est en cours de construction au sein d'une collaboration entre le LAM (Marseille), le GÉPI (Paris) et le LAE (Montréal). L'adresse du site internet de cet instrument est <http://www.astro.umontreal.ca/3DNTT>.

3D-NTT: a versatile integral field spectro-imager for the NTT

M. MARCELIN ^(a), P. AMRAM ^(a), P. BALARD ^(a), C. BALKOWSKI ^(b), O. BOISSIN ^(a), J. BOULESTEIX ^(a), C. CARIGNAN ^(c), O. DAIGLE ^(c), M-M. de DENUS BAILLARGEON ^(c), B. EPINAT ^(a), J-L. GACH ^(a), O. HERNANDEZ ^(c), F. RIGAUD ^(b), P. VALLÉE ^(c).

^(a) LAM, CNRS UMR6111 et Université de Provence, 38 rue Frédéric Joliot-Curie, 13013 Marseille FRANCE

^(b) GEPI, Observatoire de Paris, CNRS UMR 8111 et Université Paris 7, 5 Place Janssen 92195 Meudon Cedex FRANCE

^(c) LAE, Université de Montréal, C. P. 6128 succ. centre ville, Montréal, Québec, H3C 3J7 CANADA

ABSTRACT

The 3D-NTT is a visible integral field spectro-imager offering two modes. A low resolution mode ($R \sim 300$ to $6\,000$) with a large field of view Tunable Filter ($17' \times 17'$) and a high resolution mode ($R \sim 10\,000$ to $40\,000$) with a scanning Fabry-Perot ($7' \times 7'$). It will be operated as a visitor instrument on the NTT from 2009. Two large programmes will be led: "Characterizing the interstellar medium of nearby galaxies with 2D maps of extinction and abundances" (PI M. Marcelin) and "Gas accretion and radiative feedback in the early universe" (PI J. Bland Hawthorn). Both will be mainly based on the Tunable Filter mode. This instrument is being built as a collaborative effort between LAM (Marseille), GEPI (Paris) and LAE (Montréal). The website adress of the instrument is : <http://www.astro.umontreal.ca/3DNNT>

Keywords : Fabry-Perot, Integral field spectro-imager, Tunable Filter.

1 INTRODUCTION

Now that large telescopes, 8m to 10m diameter, are producing a wide quantity of data, their interpretation necessitates complementary informations that can be more easily obtained with smaller telescopes, 4m class for instance. Indeed, owing to their greater availability, these instruments are better adapted to key programmes of survey type, allowing statistical studies necessary for preparing observations on larger size telescopes. For instance, the detailed study of a large number of nearby galaxies with a 4m class telescope will help defining the typical objects that will serve as a reference for distant galaxies to be observed with 8-10m class telescopes.

2 THE INSTRUMENT

The 3D-NTT is a visible integral field spectro-imager that will be attached at the Nasmyth focus of the NTT. Basically it is a focal reducer inside which Fabry-Perot interferometers of low or high interference order can be placed separately or simultaneously, offering different observing modes. There are two main modes, a low resolution mode (detailed in section 2.3) and a high resolution mode (detailed in section 2.4). This instrument is being built as a collaborative effort between LAM (Marseille), GEPI (Paris) and LAE (Montréal). Details on the instrument and management of the project can be found on the website of the instrument: <http://www.astro.umontreal.ca/3DNNT>

2.1 The focal reducer

Basically, the 3D-NTT is a focal reducer bringing the original f:11 focal ratio of the NTT to f:2.9. A collimator provides a parallel beam, with a 70mm pupil diameter. Fabry-Perot interferometers can be placed either in the pupil or in the focal plane (or both simultaneously) depending on the observing mode. Figure 1 shows the optical design, with the location of the main planes where the interferometers can be placed (focal plane and pupil plane). Figure 2 shows a 3D schematic view of the instrument when attached at the Nasmyth focus of the NTT.

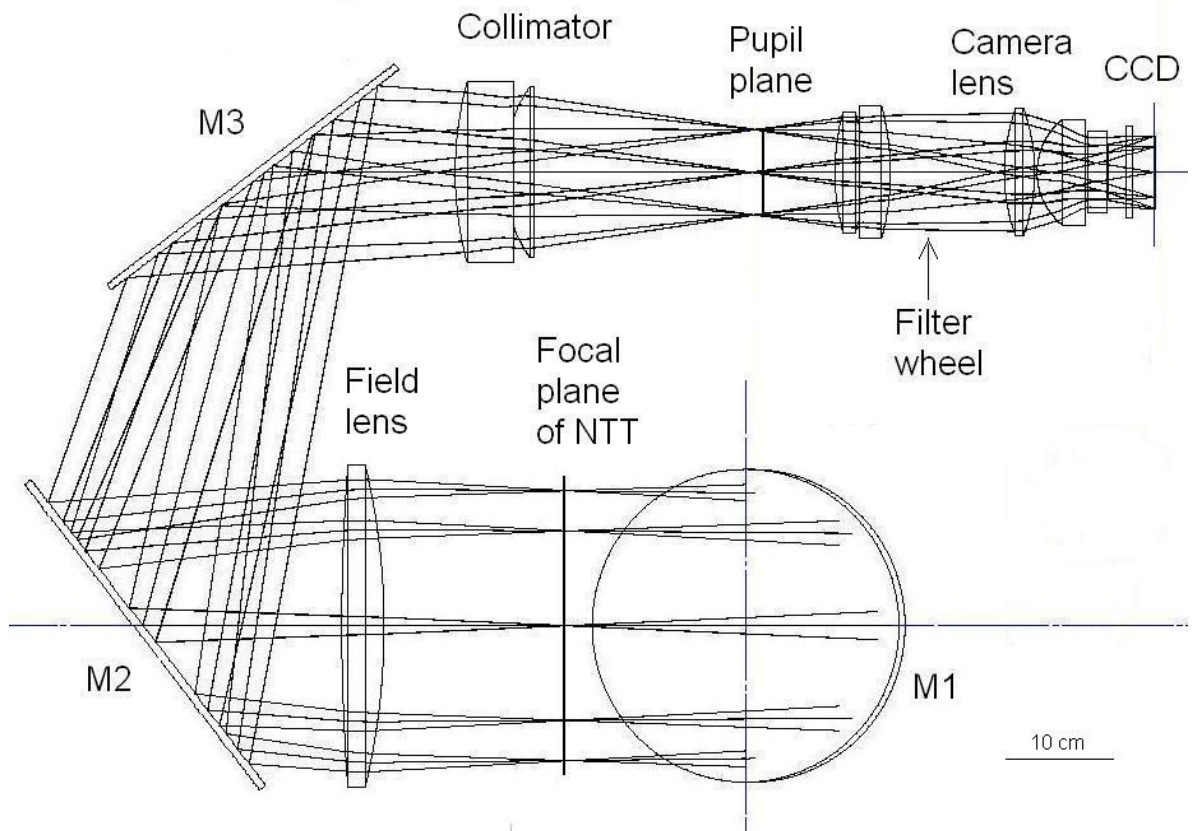


Fig. 1. 3D-NTT optical design (by Immervision, Québec). The light beam is folded from the Nasmyth focus with 3 mirrors (M1 to M3). Fabry-Perot interferometers can be placed either in the focal plane or in the pupil. A filter wheel contains blocking filters for isolating the interference order of interest.

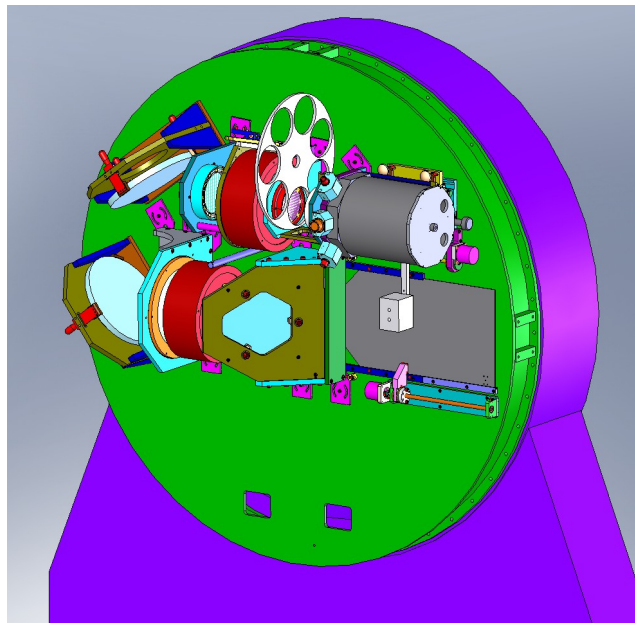


Fig. 2. Schematic drawing of the 3D-NTT attached at the Nasmyth derotator of the NTT (violet). The two interferometers are shown as red cylinders (one in the focal plane and one in the pupil plane). Design : F. Rigaud.

2.2 The Tunable Filter

The masterpiece of the 3D-NTT is a new technology Fabry-Perot with long range piezoelectric actuators (from a few microns to 200 microns) manufactured by CEDRAT (Fig.3). With such a tunable spacing between its two glass plates, the interferometer can be used either as a Tunable Filter when the spacing is small, typically a few microns (the FWHM of the filter can be tuned from ~ 0.2 to 6 nm and its central wavelength can be selected all over the visible spectrum, from 350 to 850 nm) or as a standard scanning Fabry-Perot for larger spacings, then allowing to scan a selected spectral line.

Two such devices can be placed inside the 3D-NTT, allowing two main operating modes with low or high resolution. Both are identical, only the coatings of the glass plates are different.

For the low resolution mode, the Tunable Filter is used alone. It can be placed either in the pupil (then offering a wide field of view, $17^\circ \times 17^\circ$) or in the focal plane. The field of view is then smaller (9° circular) but there is no phase shift effect and the transmitted wavelength is then the same all over the field. See details about the low resolution mode in section 2.3.

For the high resolution mode, the Tunable Filter is placed in the focal plane where it is used for selecting the line of interest that we want to scan with the second interferometer, at high resolution order, placed in the pupil. The Tunable Filter is then used as a classical interference filter, with the advantage that its wavelength (and FWHM) can be tuned at the desired values for the scientific purpose aimed at, whereas series of filters often have mismatches or even gaps at many interesting wavelengths. See details about the high resolution mode in section 2.4.



Fig. 3. Photograph of the mechanics of the Tunable Filter of the 3D-NTT. The overall diameter is 30 cm (the useful diameter is 10 cm). The height is 12 cm. The lower right corner insert shows a piezoactuator (not at scale). The three piezoactuators are located at 120° around the central hole. The weight is 16kg (without glass plates and accessories).

The glass plates of the two interferometers have been polished by SESO (Société Européenne de Systèmes Optiques) who also designed the mechanics of the interferometer. The plates are paired with different diameters (13 and 16 cm \varnothing) but the useful diameter is 10 cm. For the four plates, the polishing quality is high, with an rms value ranging from 1.2 to 1.8 nm and a PTV value ranging from 8 nm to 26 nm. Indeed the high PTV values are due to very local defects and remain within the goal specifications. As an example, Figure 4 shows the control interferogram for the worst plate.

The piezoactuators are monitored by a controller that enables to keep the plates parallel (owing to capacitive sensors manufactured by FOGALE Nanotech) and to scan the spacing between the plates. As can be seen on Figure 5, showing a photograph of the controller board, the gain in size is evident when compared with commercially available devices (such as the well known CS100 from Queensgate/ICOS). The accuracy of the positioning of the plates offered by our controller is 10nm over a 200 μ m range [1].

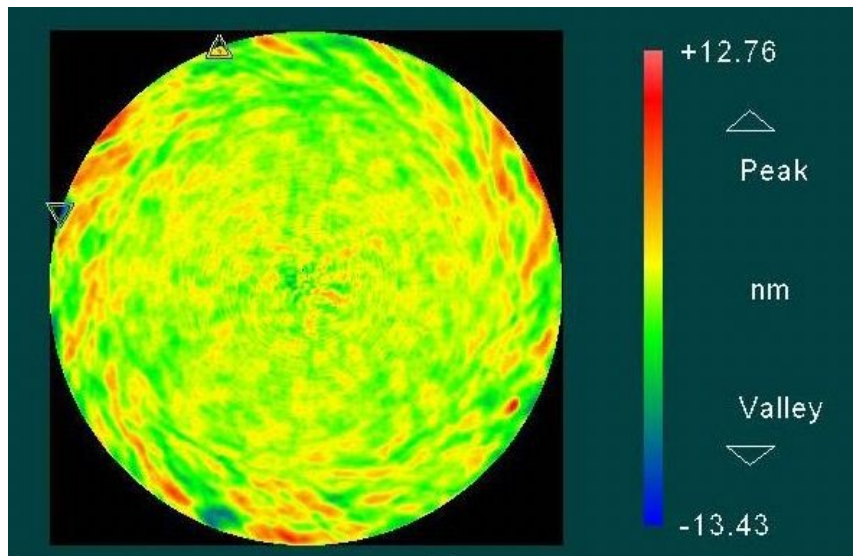


Fig. 4. Control Interferogram for the worst glass plate of the interferometers of the 3D-NTT. PTV value is 26 nm and rms value is 1.8 nm.

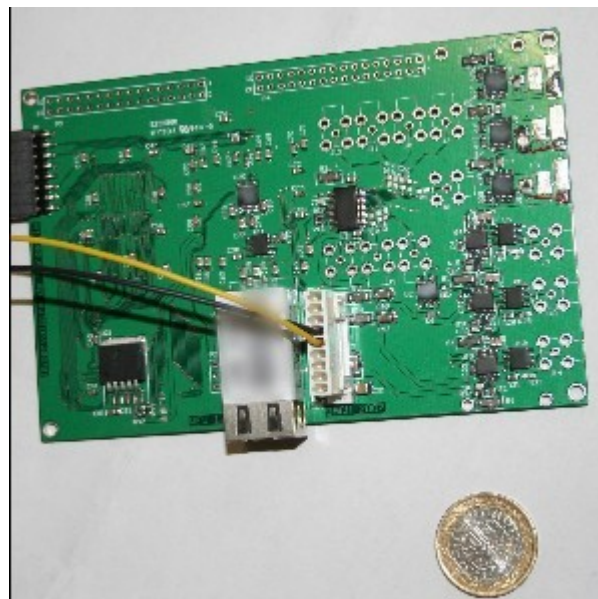


Fig. 5. Controller board of the interferometer. The "One Euro" coin gives the scale.

2.3 Low resolution mode

This mode will be mainly used to produce monochromatic images at selected wavelengths all over the visible range, with typical bandwidths of 0.5 to 5 nm.

For the low resolution mode the Tunable Filter is used alone and can be placed either in the focal plane or in the pupil plane. When placed in the focal plane, the field of view is circular (9 arcmin diameter) and uses but a small part of the detector surface, however it is interesting because the transmitted wavelength is the same across the whole field of view. When placed in the pupil plane, the field of view is much larger (17 arcmin x 17 arcmin) and covers the whole surface of the 4k x 4k detector. However, the transmitted wavelength is slightly shifting from center to edge (it is the so called "phase shift effect") with a typical value of 2 nm from center to edge. This effect, although it can be taken into account

when observing (since the wavelength shift can be perfectly known) raises constraints on the scientific programmes that can be led with this configuration. So, even if the price to pay is a reduction in terms of field of view, it can be better to observe with the Tunable Filter in the focal plane for some programmes.

The interference order p will range from 30 to 600 (at H alpha wavelength). Because the coating of the Tunable Filter will offer an almost constant Finesse around 10 [2], the resolution R will range from 300 to 6 000 since $R = p F$.

The wavelength range covered will be 350-850 nm, mainly limited by the detector quantum efficiency (see Figure 6). The detector used for the low resolution mode is a 4k x 4k CCD from EEV (with 12µm pixels). The high sensitivity in the blue will allow to reach the [OII] line at 372.7 nm which is of peculiar interest for metallicity measurements.

The main characteristics for the low resolution mode are summarized in Table 1.

Table 1. Low resolution mode characteristics

LOW RESOLUTION MODE	
Field of view	17' x 17' when TF in pupil or 9' Ø when TF in focal plane
Wavelength range	350 to 850 nm
Spectral Resolution	300 to 6 000 (at H alpha)
<u>CCD</u>	
EEV 4096 x 4096 with 12 µm pixels	
Scale	0.25"/pixel

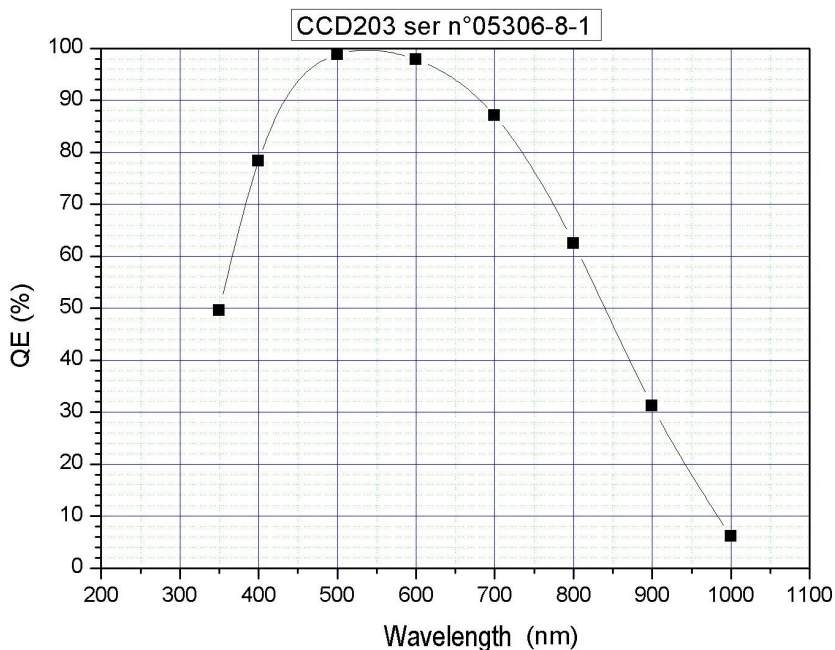


Fig. 6. Quantum efficiency of the 4kx4k CCD used for the low resolution mode.

2.4 High resolution mode

This mode will be mainly used for obtaining velocity fields of emission line objects. The selected line will be scanned by a high order Fabry-Perot interferometer placed in the pupil plane of the instrument. The interference order p of the interferometer will range from 200 to 800 (at H alpha wavelength). Because the coating of the Tunable Filter will offer an almost constant Finesse around 50 [2], the resolution R will range from 10 000 to 40 000 since $R = p F$.

When operating in the high resolution mode, two interferometers are placed inside the 3D-NTT, as shown in Figure 2. The line to be scanned is selected by the Tunable Filter placed in the focal plane and used, in that case, as a classical interference filter. The advantage is that the central wavelength can be accurately tuned at the required wavelength, which is barely the case when using series of filters. For instance, when scanning the H alpha line of a galaxy in order to get its velocity field, one often has difficulties to find a filter matching at best the redshifted line. A Tunable Filter allows to be always perfectly centered on the observed line. Another advantage is that there is no aging problem, whereas classical interference filters have their transmitted wavelength shifting toward the blue with time.

The wavelength range covered will be 400-850 nm, mainly limited by the detector quantum efficiency (see Figure 7). The detector used for the high resolution mode is a 1600 x 1600 L3CCD from EEV (with 16 μ m pixels). The interest of such a device is that it can operate in photon counting mode because it has very low spurious charges generation rate and sub-electron (< 0.1 electron) effective readout noise [3]. This enables to scan rapidly the interferometer (typically 5 to 10s exposure time for a given spacing of the plates) and to average out the changes in transparency due to weather conditions or airmass variations along the exposure.

The main characteristics for the high resolution mode are summarized in Table 2.

Table 2. High resolution mode characteristics

HIGH RESOLUTION MODE	
Field of view	8.5' x 8.5'
Wavelength range	400 to 850 nm
Spectral Resolution	10 000 to 40 000 (at H alpha)
<u>CCD</u>	
	EEV L3CCD 1600 x 1600 with 16 μ m pixels
Scale	0.33"/pixel

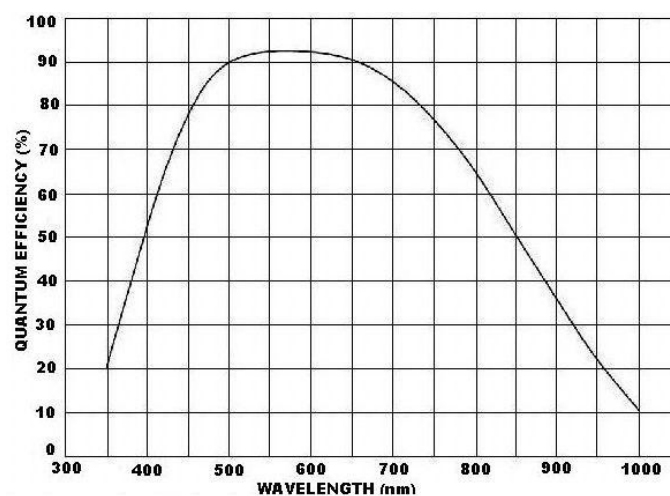


Fig. 7. Quantum efficiency of the L3CCD used for the high resolution mode.

3 THE SCIENTIFIC DRIVERS

Because of its ability to work at low or high resolution, the 3D-NTT can be used for a large variety of scientific programmes. However, it will focus on Large Programmes, two of them having already been approved by the Observing Programme Committee of ESO.

3.1 The Large Programmes

The two Large Programmes approved by ESO's OPC are : "*Characterizing the interstellar medium of nearby galaxies with 2D maps of extinction and abundances*" (PI M. Marcelin) covering 51 nights (over 2 periods) and "*Gas accretion and radiative feedback in the early universe*" (PI J. Bland Hawthorn) covering 20 nights (over 2 periods).

The first Large Programme aims at observing the ionized gas in SINGS galaxies (43 out of 75 can be observed from La Silla) with Tunable Filter in order to map the stellar formation as well as the dust extinction and metal abundance (from line ratios maps). The observed lines will be:

[OII] 372.7 nm, H beta 486.1 nm, [OIII] 495.9 - 500.7 nm, [NII] 654.8 - 658.4 nm, H alpha 656.3 nm

The aim is to better understand the nature, origin and evolution of these galaxies, comparing the 3D-NTT maps with maps obtained in FIR (MIPS/Spitzer) and UV (Galax) for a detailed analysis of extinction and its relation with other physical quantities such as metal abundance.

The data obtained for nearby galaxies will have a high resolution (both spatial and spectral) and will serve as a reference sample for studies at larger redshift led with larger telescopes (later with ELT).

The second Large Programme aims at observing some 30 quasars at $z \sim 2$ in the Lyman alpha line (redshifted at 380 to 400 nm for $z \sim 2.2$ to 2.3) with the Tunable Filter, with 5 deep images for each target (one at the quasar redshift, two blueshifted and two redshifted).

The aim is to detect galaxies with a high stellar formation rate around these quasars, in order to check if quasars with a high UV luminosity suppress the stellar formation around them as suggested by recent observations with the TTF on the AAT (Barr et al. 2004 and Francis & Bland-Hawthorn 2005).

If such an observation is confirmed, it will put strong constraints on the cosmological models.

3.2 Other programmes

A lot of programmes can be led with the 3D-NTT. Its low resolution mode alone already offers many possibilities as has been demonstrated by the TTF on the AAO [4].

Among the many possible programmes that could be led with such an instrument, one can mention the following ones (ordered from nearby to more distant objects):

The Galaxy, with both low and high resolution mode:

Physics of Planetary nebulae and HII regions (velocity fields, extinction, density and temperature maps)

Nearby galaxies, with low resolution mode:

Low- z super-wind galaxies and shocked gas

Search for warm ionized gas around nearby radio galaxies

Identification and mapping of star forming galaxies

Nearby galaxies, with high resolution mode:

A Search for Planetary Nebulae around nearby elliptical galaxies (tracing the large scale velocity field of galaxies)

The origin and fate of faint ionized gas in the halos of irregular dwarf galaxies

On the lifetime of grand design spiral patterns

Detailed kinematic study of interacting galaxy pairs

Tracing the eventful life of galaxies in low density environments

Nearby galaxies, with both low and high resolution mode:

Ionized Gas in Star-forming and luminous infrared galaxies

The origin of asymmetries in isolated galaxies

Compact groups of galaxies with both low and high resolution mode:

Kinematics of the member galaxies and diffuse ionized intragroup gas

Mergers kinematics

Gaseous outflows from member galaxies and intra-group medium enrichment

AGN, with low resolution mode:

Ionization Cones: Probing the Accretion Mode of Obscured Active Galactic Nuclei

Seyfert 2 and LINERS as well as filamentary ionized structures in clusters

Clusters with low resolution mode:

Ionized gas in intracluster medium

Distant galaxies with low resolution mode:

Search for high-redshift gravitationally lensed galaxies.

4 COMPARISON OF 3D-NTT WITH OTHER TF DEVICES

The other Tunable Filters operating by now on telescopes are MMTF on Magellan and OSIRIS on Grantecan. There is also a project, named BTFI, on SOAR.

Compared with these instruments, the main advantages of the 3D-NTT are:

- Large Field of View 17'x17' (much better than BTFI, 3' and OSIRIS 6.7' but smaller than MMTF 27') and a FOV 10' Ø without "phase-shift" effect.
- Blue sensitivity (MMTF only operates above 500nm)
- Possibility of high resolution mode (also possible on BTFI but not possible on MMTF nor OSIRIS)

The main disadvantage of the 3D-NTT is that it will operate without Adaptive Optics. However, this is not a big trouble since the 3D-NTT will operate with a large field of view and the NTT itself provides very good seeing conditions, often around 0.5 arcsec.

ACKNOWLEDGEMENTS

The authors wish to thank the Région PACA (Provence Alpes Côte d'Azur) the PNG (Programme National Galaxies) and the CSAA from INSU (Commission Spécialisée Astronomie Astrophysique de l'Institut des Sciences de l'Univers) for their financial support. They thank the Pôle Instrumental du GEPI (laboratoire Galaxies & Etoiles, Physique et Instrumentation) from Observatoire de Paris for its precious help in the making of the 3D-NTT as well as the Conseil Scientifique de l'Observatoire de Paris. They also acknowledge support from the Natural Sciences and Engineering Research Council of Canada and the Fonds Québécois de la recherche sur la nature et les technologies. They are indebted to Emanuela Pompei and Gerardo Ihle (ESO) for their advices concerning the adaptation of the instrument to the NTT. They thank Joss Bland-Hawthorn for his wise help, based on the experience of the TTF on the AAT, both from a technical and scientific point of view. They also thank all the collaborators involved in the meetings devoted to the science to be led with the 3D-NTT who helped defining the main characteristics of the instrument.

REFERENCES

- [1] L.E.M. Cavalcanti, J-L Gach, P. Balard, C. Mendes de Oliveira, K. Taylor, P. Amram, S. Blais-Ouellette, C. Carignan, O. Daigle, M. Marcelin, "Etalon controller for the BTFI & 3D-NTT" Optical Complex Systems Conference OCS 2008. Cannes, 17-19 march 2008. (2008)
- [2] M-M. De Denus Baillargeon, L. Abel Tiberini, M. Lequime, P. Amram, C. Carignan, B. Epinat, J-L. Gach, O. Hernandez, M. Marcelin, "Developing high-performance reflective coatings for the tunable filter and the high-order interferometer of the 3D-NTT", SPIE Conference Astronomical Telescopes and Instrumentation. Marseille, 23-28 June 2008. (2008)
- [3] O. Daigle, J-L Gach, C. Guillaume, C. Carignan, S. Blais-Ouellette, "CCCP: a new CCD controller for counting photons" SPIE Conference Astronomical Telescopes and Instrumentation. Marseille, 23-28 June 2008. (2008)
- [4] J. Bland-Hawthorn and L. Kedziora-Chudczer, "Taurus Tunable Filter - Seven Years of Observing" Publications of the Astronomical Society of Australia, 20, 242-251 (2003)

A.2 GH α FaS

A.2.1 Article VI : GH α FaS : Galaxy H α Fabry-Perot System for the William Herschel Telescope

Un article sur la première lumière de l'instrument GH α FaS (présenté dans la partie 1.3.1) a été publié par Hernandez et al. (2008b) dans une revue à comité de lecture¹.

GH α FaS, un nouvel instrument à Fabry-Perot, est désormais opérationnel au William Herschel Telescope (WHT). Il a été monté pour la première fois au foyer Nasmyth du WHT (4.2 m) à La Palma en juillet 2007. Utilisant une technologie moderne, avec une résolution spectrale de l'ordre de $R \sim 15000$, une résolution spatiale limitée par la turbulence atmosphérique et un champ de vue circulaire de $4.8'$, GH α FaS apportera un nouveau regard sur le gaz ionisé émettant dans la raie H α dans l'univers proche. Beaucoup de programmes scientifiques peuvent être étudiés avec un Fabry-Perot à balayage sur un télescope de 4.2 m couplé à des conditions atmosphériques de qualité. Les galaxies, mais aussi les régions HII, les nébuleuses planétaires, les restes de supernova et le milieu interstellaire diffus sont autant de sujets pour lesquels des données uniques peuvent être obtenues rapidement. Des astronomes du Laboratoire d'Astrophysique Expérimentale (LAE) de Montréal, du Laboratoire d'Astrophysique de Marseille (LAM-OAMP) et de l'Instituto de Astrofísica de Canarias (IAC) ont inauguré GH α FaS en étudiant en détail la dynamique de plusieurs galaxies spirales proches. Un ensemble d'outils robustes de réduction et d'analyse des cubes de données obtenus par GH α FaS a également été développé.

¹Publications of the Astronomical Society of the Pacific

GH α FaS: Galaxy H α Fabry-Perot System for the William Herschel Telescope

O. HERNANDEZ,¹ K. FATHI,^{2,6} C. CARIGNAN,¹ J. BECKMAN,^{2,7} J.-L. GACH,³ P. BALARD,³ P. AMRAM,³ J. BOULESTEIX,³
 R. L. M. CORRADI,⁸ M.-M. DE DENUS-BAILLARGEON,^{1,9} B. EPINAT,³ M. RELAÑO,⁵ S. THIBAUT,⁴ AND P. VALLÉE¹

Received 2007 November 22; accepted 2008 April 29; published 2008 June 4

ABSTRACT. GH α FaS, a new Fabry-Perot system, is now available at the William Herschel Telescope (WHT). It was mounted, for the first time, at the Nasmyth focus of the 4.2-m WHT on La Palma in 2007 July. Using modern technology, with a spectral resolution of the order $R \sim 15,000$, and with a seeing-limited spatial resolution, GH α -FAS will provide a new look at the H α -emitting gas over a 4.8' circular field in the nearby universe. Many science programs can be done on a 4.2-m class telescope in world-class seeing conditions with a scanning Fabry-Perot. Not only galaxies but H II regions, planetary nebulae, supernova remnants, and the diffuse interstellar medium are subjects for which unique data can be acquired rapidly. Astronomers from the Laboratoire d'Astrophysique Expérimentale (LAE) in Montréal, the Laboratoire d'Astrophysique de Marseille (LAM-OAMP), and the Instituto de Astrofísica de Canarias (IAC), have inaugurated GH α FaS by studying in detail the dynamics of some nearby spiral galaxies. A robust set of state-of-the-art tools for reducing and analyzing the data cubes obtained with GH α FaS has also been developed.

Online material: color figures

1. INTRODUCTION

From 2007 July 2 to July 8, the new private instrument GH α -FAS¹⁰ was commissioned on the William Herschel Telescope (WHT). The acronym GH α FaS stands for Galaxy H α Fabry-Perot (FP) System, and gives an idea of the nature and the prime use of the instrument. It is a new generation FP interferometer, whose chief and powerful advantage is its high-sensitivity photon-counting detector coupled to a large field of view. GH α -FAS (which sounds like the Spanish word “gafas,” for a pair of glasses) is used on the Ground-based High Resolution

Imaging Laboratory (GHRIL) platform of the Nasmyth focus of the WHT.

GH α FaS is an improved version of the scanning Fabry-Perot system FaNTOMM (Hernandez et al. 2003), which is a resident instrument at the Observatoire du mont Mégantic (OmM) 1.6-m telescope and which has also been used as a visitor instrument on the Canada-France-Hawaii (CFH) and ESO La Silla 3.6-m telescopes. The complete system is composed of a focal reducer, a calibration unit, a filter wheel for the order sorter filters, an FP etalon and an image photon-counting system (IPCS) camera. The IPCS is composed of an Hamamatsu intensifier multichannel plates (MCP) tube that intensifies every generated electron coming from the photocathode by a factor of 10^7 . Each photon event, recorded on a DALSA CCD, is then analyzed by a centering algorithm. With this amplification, the camera has essentially no readout noise. Because of this, a zero-noise IPCS is to be preferred to CCDs at very low flux level (Gach et al. 2002), even if the GaAs IPCS has only a detector quantum efficiency (DQE) of $\sim 26\%$. Moreover, because of the fast scanning capability, it can average out the variation of atmospheric transmission, which is not possible with the long integration times needed per channel for the CCDs in order to beat the readout noise.

In the last three years, around 150 galaxies were observed with the FaNTOMM system on the OMM, CFH, and ESO La Silla telescopes in the context of three large surveys: the SINGS samples (Daigle et al. 2006b & Dicaire et al. 2008), a survey of barred galaxies, the *BH α BAR* sample (Hernandez et al. 2005), and a sample of Virgo spirals (Chemin et al. 2006). While the first scientific justification was to derive high-spatial-resolution optical-rotation curves for mass-modeling purposes, the data were

¹Laboratoire d'Astrophysique Expérimentale, Observatoire du mont Mégantic & Département de physique, Université de Montréal, C.P. 6128 succ. centre ville, Montréal, PQ, Canada H3C 3J7; :olivier@astro.umontreal.ca.

²Instituto de Astrofísica de Canarias, C/ Vía Láctea s/n, 38200 La Laguna, Tenerife, Spain.

⁶Stockholm Observatory, AlbaNova University Center, 106 91 Stockholm, Sweden.

⁷Consejo Superior de Investigaciones Científicas, Spain.

³Laboratoire d'Astrophysique de Marseille, Observatoire Astronomique Marseille-Provence, Université de Provence & CNRS, 2 place Le Verrier, 13248 Marseille Cedex 4, France.

⁸Isaac Newton Group, Apartado de Correos 321, 38700 Santa Cruz de la Palma, Spain.

⁹Institut Fresnel, CNRS & Universités Aix Marseille, 13397 Marseille Cedex 20, France.

⁵Dpto. Física Teórica y del Cosmos, Universidad de Granada, Avda. Fuente Nueva s/n, 18071 Granada, Spain.

⁴IMMERVISION, 2020 University, suite 2420, Montréal, PQ, Canada H3A 2A5.

¹⁰More information can be found at <http://www.iac.es/proyecto/ghafas/>.

666 HERNANDEZ ET AL.

also used by IAC astronomers to constrain the role of gravitational perturbations as well as feedback from individual H II regions on the evolution of structures in galaxies (Fathi et al. 2007) and by a Berkeley-Munich group, the GÉPI group at Observatoire de Paris and Laboratoire d'Astrophysique de Marseille (LAM), to compare those local samples to high- z galaxies.

GH α FAS comes with its own custom-designed focal reducer developed to be optically and mechanically compatible with the Nasmyth focus of the WHT. The system has its own control and data acquisition system. It has a 4' circular field with a 0.4'' pixel and a minimum of $\sim 5 \text{ km s}^{-1}$ velocity resolution. Full acquisition and reduction software (mainly based on IDL routines) is provided by the Montréal and IAC groups. The project will be done in three phases. For Phase I (2007 July), the optical system (focal reducer, filter wheel, and calibration unit) has been delivered to the WHT and used with the Marseilles IPCS camera for this first run. For Phase II (beginning of 2008), an improved GaAs IPCS will be added to the system. Phase III (mid-2008) will provide an FP controller to replace the old CS100 technology (provided by IC Optical, formerly Queen's Gate) and possibly a Tunable Source to calibrate the data at the observing wavelength.

GH α FAS is presented in this paper. Section 2 describes the science cases for the GH α FAS instrument, while § 3 discusses the technical details of the instrument. In § 4, the data preparation and reduction procedures are presented while a sample of the first results is shown. The conclusions are given in § 5.

2. GH α FAS SCIENCE DRIVERS

Several instruments exist that provide two-dimensional maps for kinematical and population analysis of galaxies or other astronomical objects. Those observations are mainly based on two different techniques of wavelength separation: dispersive or scanning. The former uses fibers (*Virus*: Hill et al. 2006; *Argus*: Kaufer et al. 2003; *Integral*: Arribas et al. 1998), micro-lenses (first concept done by Courtes 1982; *Tiger*: Bacon et al. 1995; *Sauron*: Bacon et al. 2001), or image slicers (*SINFONI*: Eisenhauer et al. 2003; *MUSE*: Henault et al. 2004; *WIFES*: Dopita et al. 2007; *SWIFT*: Thatte et al. 2006; *FRIDA*: López et al. 2006, and references therein) and the latter, Fabry-Perot etalons in a pupil (*FANTOMM*: Hernandez et al. 2003; *Cigale*: Boulesteix et al. 1984; *HIFI*: Bland et al. 1990; *Taurus*: Atherton et al. 1982). GH α FAS is a scanning instrument with the largest field of view (FOV) with such a spatial resolution (0.4'' pixel $^{-1}$ in low mode and 0.2'' pixel $^{-1}$ in high-spatial-resolution mode) on a 4-m class telescope.

Two-dimensional kinematics is a very powerful technique for studying the structure and evolution of extended sources. Galaxy dynamics, the distribution of dark matter, the dynamical and physical state of star-forming regions, circum nuclear starburst and fueling of active galactic nuclei, detection of kinematically decoupled components, dynamics and physical state of planetary nebulae, and supernova-driven winds and feedback

mechanisms are just a few phenomena which can be studied with this technique.

Large spectral-range spectrographs are commonly used to analyze the stellar population and stellar and gaseous kinematics of relatively small (1 kpc) regions of nearby galaxies or entire galaxies at high redshifts (e.g., de Zeeuw et al. 2002; Genzel et al. 2006; Peletier et al. 2007; Emsellem et al. 2007; Marquart et al. 2007). The low-redshift studies have shown that morphological methods are not a sufficient tool for galaxy classification and supplementary kinematical and population data are necessary for understanding galaxy evolution. High-redshift, two-dimensional kinematical studies have shown that galaxy disks are more disturbed at $z \sim 1$ than locally.

Large spatial-coverage instruments have been successful at studying the state and dynamics of galaxies and of the interstellar medium (e.g., Zurita et al. 2004; Hernandez et al. 2005a; Chemin et al. 2006; Sluis & Williams 2006; Daigle et al. 2006b; Fathi et al. 2007a; Relaño et al. 2005, 2007; Rosado et al. 2007; Amram et al. 2007). These studies have observationally confirmed the important role of gravitational perturbations on the evolution of galaxies, which are now accepted to be the main drivers for morphological transformations.

2.1. H II Region Studies and Interaction of Stellar Winds with the ISM

The internal kinematics of H II regions are of interest because of the light shed on the evolutionary properties of the massive stars that ionize them and on their interaction with the surrounding ISM. A key issue here is that the velocity dispersion measured in H α of the majority of H II regions observed in external galaxies, which are necessarily selected as the most luminous regions, is found to be supersonic. A basic question is what is the source of input energy to maintain these line widths, and the linked possibility that the line widths could be used as a luminosity index and, hence, as a distance-measuring standard candle. A long-term debate was opened by Terlevich & Melnick (1981), who suggested that the line widths vary as the fourth power of the luminosity and that this reflects virial equilibrium within the regions. This was addressed in some detail by Chu & Kennicutt (1994a) in a study of 30 Doradus, and by Chu & Kennicutt (1994b), who found, for a large sample of bright H II regions, that their line profiles are broadened by turbulence as well as wind-induced line splittings; i.e., that, in general, virialization cannot be assumed. These studies are merely pointers to the wealth of physical inference that will be available using GH α FAS to investigate how metals are distributed around galaxies by the outflows from H II regions and by similar flows around galactic centres, and how the ionization structure of H II regions relates to their kinematic structure.

2.2. Planetary Nebulae and Ionized Stellar Outflows

In the last two decades, the extraordinary variety of morphologies of planetary nebulae (PNe) has been widely recognized

(e.g., Balick & Frank 2002). Their study is crucial in order to fully understand mass loss, the physical process that governs the latest evolution of low mass stars and plays a basic role in the chemical enrichment of galaxies. A precise determination of the 6D geometry and kinematics of PNe requires 2D spectroscopy, at a resolution $R \geq 30,000$ for “normal” PNe (and lower for the highly collimated, high-velocity components) and in the brightest nebular emission lines ([O III], [H α], and [N II]). GH α FAS can provide an efficient and accurate way to observe all the different macro and microstructures present in the nebulae, which include—often in the same object—multiple spherical shells, bipolar or multipolar lobes, point-symmetrical features, symmetric knots, filaments, and jets. Comparison of the images and radial velocity fields with sophisticated radiative-hydrodynamical simulations (e.g., García-Segura et al. 1999) can then reveal the physical processes at work in shaping PNe. By obtaining fully monochromatic images of the nebulae in different emission lines, we can determine the density, temperature, and ionization degree, throughout the objects. This is also essential for a proper 3D modeling of the nebulae and a correct determination of their physico-chemical properties (cf. Gonçalves et al. 2006). Ultimately, the most important questions to be answered are the following ones: Why do stars lose their spherical symmetry at the tip of the asymptotic giant branch or immediately after? Can single stars do it, or is the majority of the observed PNe the result of binary evolution (e.g., Moe & de Marco 2006)?

2.3. Structure and Evolution of Nearby Spiral Galaxies

The evolution of structures in galaxies is given by the interactions with neighboring galaxies, gravitational perturbations, and/or winds from star-forming regions. The IAC, LAE, and LAM groups have developed a set of robust data analysis tools that were used successfully on previous Fabry-Perot observations covering out to 12 kpc in the nearby grand-design Sc spiral galaxy, M 74. These tools are optimized to investigate the large-scale dynamics as well as feedback from individual H II regions into their surrounding interstellar medium in order to study the evolution of structures in galaxies using two-dimensional kinematical observations (Zurita et al. 2001; Hernandez et al. 2005a, 2005b; Fathi et al. 2005, 2007a, 2007b). After the careful examination of the resonance structures by measuring the pattern speeds of the bars in M 100 (Hernandez et al. 2005b), NGC 1068 (Emsellem et al. 2006), and NGC 6946 (Fathi et al. 2007b), there is now a solid framework for kinematically studying the resonant interaction in disks of galaxies. The combination of these studies with the emerging theoretical foundation (Maciejewski 2006; Maciejewski & Athanassoula 2007; Athanassoula 2005) has opened the possibility of adding the global kinematical information to the local effects at or near the Lindblad and ultraharmonic resonance radii, and compare the strength and degree of symmetry of the density waves. Such quantification is important to study to what degree bars infer dynamical mixing of the gas and stars in their parent disks.

2.4. Fueling of Active Galactic Nuclei

Due to the mass concentration toward the center of the gravitational potential in galaxies, their nuclear region are suitable environments for the formation of supermassive black holes (SMBHs), which can become active by infall of interstellar gas. Recent works (Tremaine et al. 2002 and references therein) show, in addition, that the mass of the SMBH is proportional to that of the bulge of its host galaxy. This relation suggests a connection between the large-scale properties of galaxies and the nuclear properties (Haehnelt & Kauffmann 2000). The process responsible for such a relation has to transfer matter and angular momentum within galaxies. Pioneer works have proposed that bars can trigger the mass flows to help grow and feed SMBHs in galaxies (e.g., Shlosman et al. 1989), but observations have not confirmed this. Thus, measuring the velocity at which gas is falling from the outer parts of a galaxy toward the center is imperative for constraining the links between large-scale properties and activity in the nucleus of galaxies. The dynamical analysis methods developed in Fathi et al. (2005, 2006) have shown to be useful for quantifying the kinematical effects of gravitational perturbations due to bars and spiral arms. Applying these methods to high-spatial-resolution data for a large number of objects, delivered by GH α FAS, will provide necessary details required for linking the kiloparsec-scale kinematics with the parsec-scale processes.

2.5. Dynamical Masses of the Galaxies in the Virgo Cluster

The large size and homogeneity of surveys of local galaxies (SDSS, 2dF, 2MASS) have yielded extraordinary advances in our understanding of galaxy structure and evolution. One of the most important realizations of galaxy formation studies is the recent detection from SDSS and 2dF of a robust bimodality in the distribution of galaxy properties, with a characteristic transition scale at stellar mass $\sim 3 \times 10^{10} M_{\odot}$, corresponding to a halo (virial) circular velocity $V \sim 120 \text{ km s}^{-1}$ (Kauffmann et al. 2003; Dekel & Birnboim 2006). However, large surveys like the SDSS lack measurements of the *dynamical mass*, because it must include coverage to luminosities below the fundamental galaxy transition scale at $V \sim 120 \text{ km s}^{-1}$. Central to such a study, the number of galaxies per unit volume as a function of halo circular velocity—the circular velocity function, $N(V)$ —is a robust prediction of cosmological models that has never been *directly* tested (Klypin et al. 1999; Newman & Davis 2002). The Virgo cluster is an ideal laboratory for analyzing, in depth, these processes using GH α FAS observations.

2.6. Kinematics of High-Redshift Galaxies

In studying high-redshift galaxies, it is necessary to disentangle distance effects from evolution ones (e.g., Förster Schreiber et al. 2006). Even at low redshifts, controversy may exist on the nature and on the history of merging, interacting (including

668 HERNANDEZ ET AL.

compact groups [CGs] of galaxies) or even blue compact galaxies that are suspected of constituting a large fraction of the primordial building blocks leading to the present-day galaxies (e.g., Kunth & Östlin 2000; Amram et al. 2004, 2007). In compact groups, high spatial and spectral resolution data from GH α FAS allow observation that the broader H α profiles are located in the overlapping regions between the galaxies within a group. At higher redshift such a broadening would be interpreted as an indicator of rotating disk, and this system could have been catalogued like a rotator instead of a merger (Flores et al. 2006). On the other hand, in cases when the spatial resolution increases, it becomes possible to address the problem of the shape of the inner density profile in spirals (CORE vs CUSP controversy), which remains one of the five main further challenges to the Λ CDM theory proposed by Singh (2006).

The lack of resolution induce series of biases: (i) the size of the galaxy is artificially enlarged but, in the same time, the size of the galaxy is diminished due to flux limitations; (ii) the inclination is lowered when the spatial resolution decreases; (iii) the velocity gradient is lowered along the major axis while, in the same time, the velocity gradient is enlarged toward the minor axis. The consequence is that there is often no indication that the maximum velocity of the rotation curve is reached, leading to uncertainties in the TF relation determination. In addition, the (fine) structures within the galaxies (bars, rings, spiral arms, bubbles, etc.) are attenuated or erased and the determination of the other kinematical parameters (position angle, center, inclination) becomes highly uncertain.

3. THE REAL INTEGRAL FIELD UNIT

GH α FAS is a real integral field unit (IFU): for each pixel of the IPCS, one spectrum is available. Integral field units make use of lenslet arrays, fiber bundles, or slitlets to scan the two-dimensional area of interest for observations. GH α FAS omits the intermediate constructions, and delivers one unique spectrum for each IPCS spectrum. There is no cross talk between the GH α -FAS spectra, and each pixel corresponds to one spectrum, as opposed to each lenslet or fiber, which in reality cover more than one pixel on the CCD. In this sense, GH α FAS is the real IFU. This kind of instrument is called “ecological” where no information mixing is possible between spatial and spectral information.

GH α FAS is composed of a focal reducer, a filter wheel, a Fabry-Perot etalon, an IPCS as the detector, and a calibration arm (neon source). Data acquisition and instrument controls are done with a PC via ethernet. Table 1 presents optical characteristics of GH α FAS.

3.1. Optical and Mechanical Design

The Nasmyth foci of the WHT offer two optical modes: one with an optical derotator (in the UV/optical) provides a FOV of $2.5' \times 2.5'$ with a throughput of 75%, while the other, without derotator, gives access to a FOV of $5' \times 5'$ with no optical

throughput degradation. In the design of the optical system, two cases—one with derotator and one without—were studied. Taking into account the numerous scientific cases exposed above, we opted to keep the FOV ($5' \times 5'$) as large a possible and decided not to use the optical derotator, which implied that a post observation alignment of the data had to be developed (see § 4.1).

Optical calculations and optimization were done using ZEMAX. Table 2 presents the detailed optical prescription. The optical prescription for GH α FAS is beginning at surface numbered 9. Before the ninth surface, the prescription is the one the WHT for the nasmyth focus. The focal reducer stands on the optical table of the GHRIL platform at the second Nasmyth focus of the WHT. It has a total length of 770 mm (distance from the field lens to the detector plane). The length between the focal plane and the field lens is 50 mm and between the field lens and the collimator lens 345 mm. The total free space of the collimated beam between the collimator lens and the first meniscus of the objective is 200 mm. In the collimated beam the pupil has a diameter of 40 mm (angles are less than 5° on the pupil) in order to use etalon with an aperture diameter greater than 45 mm and avoid any vignetting (see Fig. 1).

Globally, as GH α FAS is scanning small wavelength ranges (typically the FWHM of a filter is 15 Å), it should be considered as an achromatic system. The optical calculations, design, and manufacturing were relatively simple. This configuration allowed us to use 3 commercial lenses while two custom lenses had to be fabricated by BMV Optical Technologies¹¹. The optical performances are shown in Table 1 and the spot diagram is given in Figure 2.

From left to right, the optical beam will meet (a) the focal plane, where a mask has been put to avoid any diffuse light, (b) the field lens (surface 10 in the optical prescription in Table 2), (c) the collimator lens (surface 12), (d) a filter in the filter wheel, (e) the Fabry-Perot etalon in the pupil, (f) the first objective lens (surface 20), (g) the second objective lens (surface 23), (h) the last objective lens (surface 25), to be, finally, focused on the detector. Perpendicular to the optical axis, in the plane of the optical table, between the field lens and the collimator, the calibration unit (replication of the focal plane of the telescope) is founded. The calibration unit is in place when the calibration mirror is in the optical axis.

Finally, Table 3 presents the available Fabry-Perot etalons showing the ability of GH α FAS to reach high resolution by simply changing the etalon, an operation that can be done in less than 2 minutes.

The spot diagram (Fig. 2) shows the optical performances of the instrument. It clearly stresses the size of the optical spot on the detector in various positions (conjugated of various positions on the sky). It is given for only a wavelength (6560 Å) as observations are typically done in H α mode. The spot size is sampled by 1 pixel in the center and in almost the detector, whereas 2 pixel are

¹¹ BMV Optical Technologies 26 Concourse Gate, Ottawa, Ontario, Canada K2E 7T7.

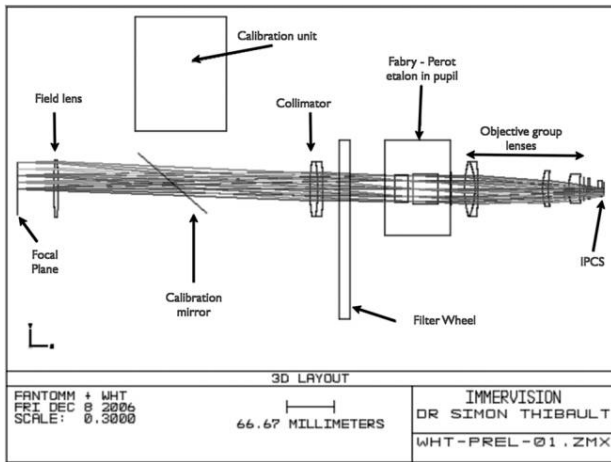


FIG. 1.—Two-dimensional optical layout of GH α FaS. The optical design was done in collaboration with Immersion inc. Light beam from telescope comes from the left. The detector (IPCS) can be found at the right-hand side. Different shades of the optical rays represent different positions on the focal plane. See the electronic edition of the PASP for a color version of this figure.

needed to have 50% of the encircled energy on the edges of the detector. The instrument is able to well sample the seeing (typically 0.6'' pixel⁻¹ to 0.8'' pixel⁻¹) with 2 pixels.

The mechanical design was performed at the Université de Montréal. All parts are made of aluminum. The lens' cylinders were painted inside to avoid any parasite reflection and included different masks. Lenses have been tested with a Zygo interferometer to check their quality. The optical and mechanical integration were done at Montreal, whereas the IPCS–Focal reducer integration was done at Marseille. Figure 3 presents a top view and a cut along the optical axis parallel to the optical breadboard of the instrument on the optical table of the GHRIL.

Finally, the calibration arm, with its mirror-controlled arm, has a neon lamp for calibration purpose. The Ne [6598] emis-

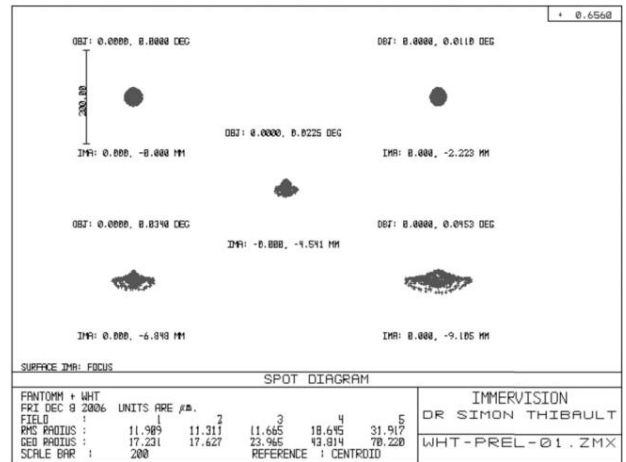


FIG. 2.—Spot Diagram of GH α FaS in the detector plane for five different positions of the optical rays at a wavelength of 6560 Å. See the electronic edition of the PASP for a color version of this figure.

sion is used to calibrate the phase shifts of the Fabry-Perot etalon. This lamp will be replaced, at a later stage, by a Photon etc Tunable Source (see <http://www.photonetc.com>), which is able to provide any calibration wavelength.

GH α FaS is fully automated and controlled via ethernet modules. Table 4 presents a summary of all automated items in their operation modes. The filter wheel, the shutter, and the calibration arms have their own ethernet modules designed by J-L. Gach and P. Ballard from LAM. The IPCS has its own dedicated link and network to avoid a mixing of the information between ethernet modules and data. The etalon is controlled via a RS-232 link with its CS100 controller.

3.2. Detector: State of the Art IPCS

3.2.1. IPCS

The IPCS is composed of a photocathode placed in front of a commercial CCD, which amplifies the photons (from a factor 10⁵ to 10⁷; see Gach et al. 2002; Hernandez et al. 2003 and references therein for a complete description and history of such devices). It provides a system where the detection of a photon is around 10⁶ times above the readout noise of the commercial CCD. Therefore, the IPCS has essentially no readout noise.

The photocathode in the WHT camera is a GaAs type HAMAMATSU V7090-61¹² with a quantum efficiency of $\lesssim 26\%$ (this value includes the loss due to the MCP stack). The spectral range is from 400 to 850 nm and is very flat over these wavelengths. It uses two microchannel plates to provide an electron amplification (after the photoelectric effect that converts photons to electrons) of 10⁷ (see Fig. 4). Each channel is 6 μm wide.

¹²Useful documentation can be found directly on this Web site: <http://www.astro.umontreal.ca/fantommm/Description/v7090u.pdf>.

Detector (low spatial resolution mode)	CCD, 512 × 512 pixels @ 25 μm
Detector (high spatial resolution mode)	CCD, 1k × 1k pixels @ 12.5 μm
Physical FOV	12.8 × 12.8 mm
FOV (HR & LR modes)	202'' × 202''
FOV (HR & LR modes on diag.)	285''
Focal scale (LR mode)	0.394'' pixels ⁻¹
Focal scale (HR mode)	0.197'' pixels ⁻¹
Pupil diameter	40 mm
Image Quality	50% EE ³ in 0.4'' from 0 to 0.7 FOV 50% EE < 1 everywhere else
Spectral range	450 to 850 nm
Geometric distortion	< 0.7%
F/number in	10.94
F/number out	2.75

670 HERNANDEZ ET AL.

TABLE 2
 GH α FAS OPTICAL PRESCRIPTION

Surf	Type	Comment	Radius	Thickness	Glass	Diameter	Conic
OBJ	STD ^a		Infinity	Infinity	...	0	0
1	STD		Infinity	400	...	4193.45	0
2	STD		Infinity	0	...	4192.817	0
3	STD		Infinity	7994.4	...	4192.817	0
4	STD		Infinity	105.9	...	4180.168	0
5 -STO	STD	primary mirror	-20879	-8034.961	mirror	4180.001	-1
6	STD	secondary mirror	-6231.38	9969.75	mirror	971.8717	-2.53287
7	STD		Infinity	84	...	0	0
8	STD		Infinity	481	...	113.7209	0
9	STD		Infinity	50.39427	...	72.51192	0
10	STD	011-4780	259.5	7.9	BK7	77.6889	0
11	STD		Infinity	350	...	77.49541	0
12	STD	PAC096	258.954	11	BK7	56.79739	0
13	STD		-256.371	6.5	SF5	55.89834	0
14	STD		-1092.828	100	...	55.25999	0
15	STD	top plate	Infinity	19.05	F _{silica}	37.92693	0
16	STD		Infinity	7	...	35.88337	0
17	STD	bottom plate	Infinity	35	F _{silica}	36.86071	0
18	STD		Infinity	18	...	41.64935	0
19	STD	Distance (fix)	Infinity	18.54656	...	45.24545	0
20	STD	PAC095	140.89	14.5	BK7	49.38644	0
21	STD		-101.72	4	F4	49.47157	0
22	STD		-465.06	90	...	49.71964	0
23	STD	Custom 1	87.01528	10	SF6	49.44784	0
24	STD		182.7571	30.15954	...	47.36752	0
25	STD	Custom 2	57.38259	10	SF11	38.995	0
26	STD		115.5478	6	...	35.35846	0
27	STD		Infinity	6.35	...	32.6863	0
28	STD		Infinity	2	Sapphire	29.02896	0
29	STD		Infinity	11.85	...	28.39365	0
30	STD		Infinity	5.5	1.47	21.56853	0
31	STD		Infinity	0	...	19.45602	0
32	STD		Infinity	2	...	19.45602	0
33	TS ^b	Detector	-	0	...	18.3041	-
34- IMA	STD	Focus	Infinity	18.3041	0

NOTE.—^a Standard.
^b Standard.

Finally, the electrons are projected onto a P-43 phosphor screen via a bundle of optical fibers and then is imaged on the focal plane of a DALSA fast readout commercial CCD (Panthera 1M60) using two objectives (from LINOS technology). Data are then transferred to an acquisition computer using the “camera link” cable via an optical hub and to a dedicated ethernet link at 1 Gbits s⁻¹ (Balard et al. 2006).

3.2.2. Cooling System: The PELTIER Effect Simplified

A simple commercial PELTIER effect system is used to cool down the photocathode to its optimal temperature, which is -30°C. This PELTIER effect system is also coupled with a liquid cooling system to evacuate heat from the IPCS. The Dalsa

CCDs do not need to be cooled as photons (electrons) are amplified and well above the readout noise. The mean thermal noise of the cathode is 5 events per frame at -10°C, which is equivalent to 0.7 photon hour⁻¹ pixel⁻¹ and drops to 3 events per frame at -30°C. This dark current should drop to 0.4 events per frame if it were due only to the thermal emissivity of the photocathode. This background noise, which shows no dependence on temperature, can be explained by K⁴⁰ beta disintegration, which is present in the MCP glass (Siegmond et al., 1988). Recent investigations carried out in collaboration with Biospace lab company¹³ showed that using intensifier input windows free

¹³ More information can be found at <http://www.biospace.fr/>.

TABLE 3
GH α FAS FABRY-PEROT ETALONS CHARACTERISTICS AT HA

Etalon name	p ^a	FSR ^b km s ⁻¹	\mathcal{F} ^c	\mathcal{F}_e ^d	R ^e
Mégantic 1	765	391.9	22	17	16065
OM2	798	375.7	25	12	19950
OM3	2604	115.1	15	9	39060
OM4	609	492.3	30	24	18270
OM5	1938	154.7	56	32	108528
CFHT	1162	258.0	17	12	19754

NOTE.—^a interference order.
^b Free spectral range.
^c Finesse for a pupil point.
^d Effective finesse.
^e Spectral resolution.

of potassium decreases the minimal background noise achievable by a factor of 10.

3.3. IPCS Advantages

The readout noise affects CCDs at low light levels when very faint flux objects are observed. Classical CCDs reach nowadays high quantum efficiency (up to 95%), and very low readout noise (down to 2–3 electrons and may be 1 in a near future, Gach et al. 2003). With the IPCS, observations of faint flux objects are split into several short ones (in particular, this method also helps reduce pollution by cosmic rays). Thus, the maximal signal-to-noise ratio (S/N) per pixel achievable by an “ideal” CCD is described by

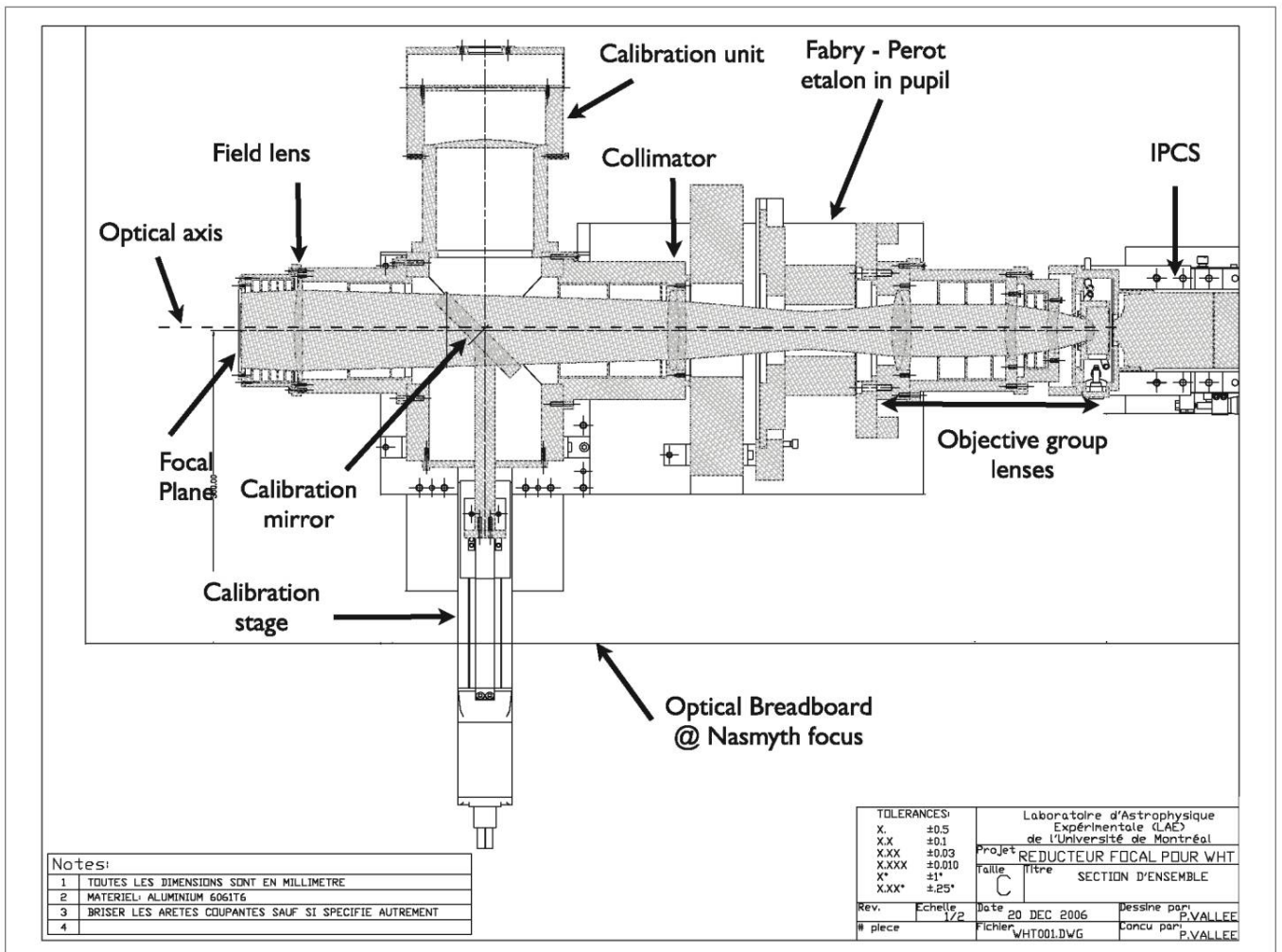


Fig. 3.—Top view and cut along the optical axis parallel to the optical breadboard at the Nasmyth focus. The optical and mechanical design of GH α FAS has been especially customized for the GHRIL Nasmyth focus of the WHT. The filter wheel can fit four 75-mm filters and, like all the elements of the system, can be controlled remotely via ethernet cables.

672 HERNANDEZ ET AL.

TABLE 4
 SUMMARY OF THE GH α FAS AUTOMATED PARTS

Part name	Controlled by	Operation
Calibration arm	ethernet module	calibration
Calibration lamp	ethernet module	calibration
Calibration mirror	ethernet module	calibration
Calibration stage	ethernet module	calibration
Fabry-Perot etalon	CS 100 via RS 232	observation & calibration
Filter wheel	ethernet module	observation & calibration

$$S/N = \frac{N}{\sqrt{N + n\sigma^2 + T}}, \quad (1)$$

where N is the number of photons collected per pixel during the exposure time, σ the readout noise of the CCD in electrons, and T the thermal noise in electrons per pixel. Although the T term is close to zero in more recent CCD or IPCS devices and can be neglected, additional limitations constrain the usage of CCDs. n is the number of exposures. The S/N decreases dramatically when N is small and n is large. This is the case in multiplex instruments (scanning instruments). For an IPCS, the S/N is described by the following formula:

$$S/N = \frac{N}{\sqrt{N + T}} \approx \sqrt{N}. \quad (2)$$

As IPCS, in fact, do not have readout noise, they are also less affected by cosmic rays because one event is seen as one photon only—a decisive advantage with respect to CCDs, where long exposures are required in the case of faint objects. Although the first generation of IPCS had a poorer quantum efficiency with respect to CCDs and were affected by image distortion, they were still competitive in multiplex instruments or in speckle interferometry because of the absence of readout noise.

Multiplex instruments collect a large number of images. For example, the scanning Fabry-Perot FANTOMM uses up to 64

channels to reconstruct the interferometric map of an object emission line, in order to determine its velocity field, monochromatic image, and velocity dispersion maps (see Hernandez et al., 2003). The global S/N of a multiplex observation (S/N_m) is the quadratic sum of the S/N s of each channel, since there is no noise correlation between channels. Neglecting thermal noise, the S/N_m is given by

$$S/N_m = \sqrt{n \left(\frac{N/n}{\sqrt{N/n + \sigma^2}} \right)^2} = \frac{N}{\sqrt{N + n\sigma^2}}, \quad (3)$$

where N is the number of photons expected during the whole exposure, n the number of channels, and σ the readout noise of the CCD.

During multiplex observations, the emission usually appears only in a few channels, which could be different for each pixel according to the Doppler shift. Experience with CIGALE and FANTOMM showed that, emission lines appear most of the time in only 25% of the channels. This lowers the above “ideal” S/N_m . The “worst” case is when the line is detected only in 2 channels. This does not affect the comparison between CCD and IPCS usage, but gives a more precise idea of the kind of objects that could be observed with such instruments. In this “worst” case the S/N_m is given by

$$S/N_m = \sqrt{2 \left(\frac{N/n}{\sqrt{N/n + \sigma^2}} \right)^2} = \frac{2N/n}{\sqrt{2N/n + 2\sigma^2}}. \quad (4)$$

Because of the very small readout time (10 ms with the WHT camera and 25 ms with the FANTOMM one), in the case of an IPCS, it is possible to observe each channel several times during the observation and then average the sky variations (because the first and last images may not be comparable in terms of seeing and transparency when observing with a ground-based tele-

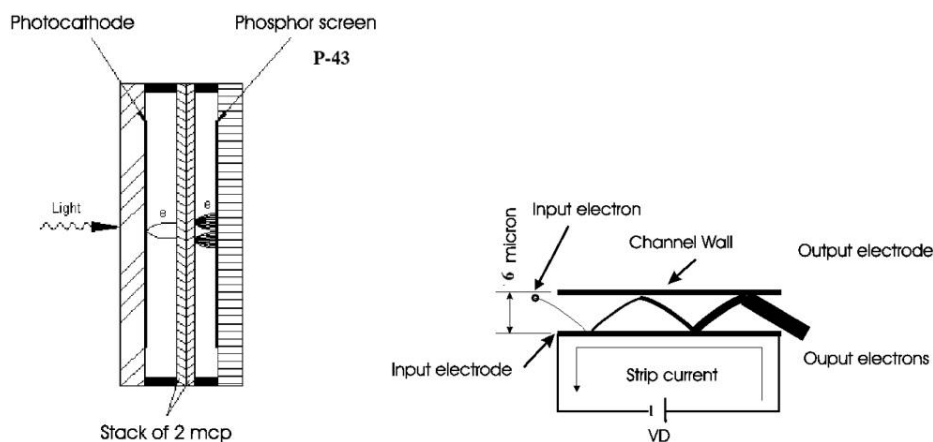


Fig. 4.—Left: Principle of electron amplification using micro channel plates (MCP) in an image intensifier. Right: Details of high-voltage effect on a micro channel.

scope). Typically, each channel is observed 5 to 15 s, and when the last channel has been integrated, the first is observed again. Each set of n channels is called a cycle, the duration of which is typically 5 to 15 minutes (depending on the exposure time per channel and the number of channels). The cycle exposure time must be under the OH timescale variations (typically 15 minutes; see Ramsay et al. 1992). Individual cycles are then summed to obtain the S/N required without any loss of events. Many short cycles are then preferred to a single cycle with sky variation. The overlay time of the data acquisition system is under 10 ms, so an exposure time of, at least, 1 s per channel, e.g. 48 s per cycle, is the shortest optimal exposure time. The experience of the LAE and LAM teams lead channel exposure time to 5 s, so a cycle time of around 5 minutes. The total observation consists of several cycles. S/N_m can be rewritten as:

$$S/N_m = \frac{\frac{2N}{n}}{\sqrt{\frac{2N}{n} + 2m\sigma^2}}, \quad (5)$$

where N is the number of photons expected during the whole exposure, n the number of channels, m the number of cycles, and σ the readout noise of the CCD. Meanwhile, the IPCS S/N_m obtained is independent of the number of cycles and the atmosphere-free S/N is

$$S/N_m = \sqrt{\frac{2N}{n}}. \quad (6)$$

These two equations are used to generate Figure 5. The faint detection limit is for a S/N of 3. It can be seen on this figure that an IPCS can reach higher S/N than a classical CCD for very faint fluxes.

The measured QE of the whole system (including MCP losses) was measured to be 26% at H α . The overall system presents the same characteristics as the IPCS of FANTOMM (Gach et al. 2002; Hernandez et al. 2003). The system is limited by the process itself. The Dalsa camera can be read with two speeds depending on the binning mode (1024×1024 pixels or 512×512 pixels) chosen. When two events occur within the same frame (16.6 ms or 10 ms) at the same location, only one event is counted instead of two. The mean number M of missed photons can be evaluated assuming a Poissonian process for the photon emission by the following equation:

$$M = N \times \left(1 - \frac{1 - e^{-\lambda}}{\lambda}\right), \quad (7)$$

where $\lambda = N/\text{frame per second}$ is the mean number of photons expected during the resolved period of the detector and N the total number of photons.

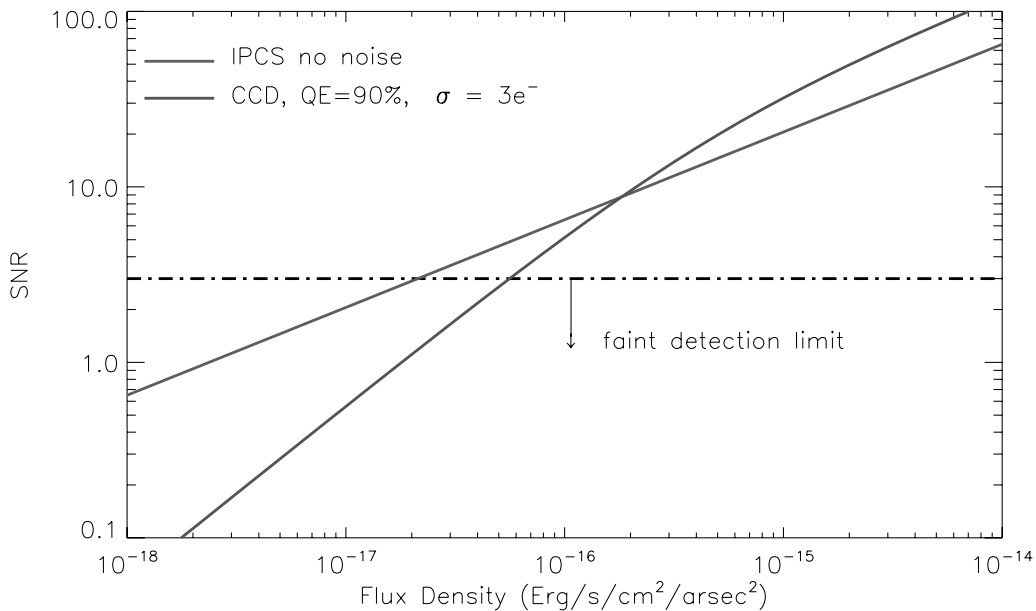


FIG. 5.—Signal-to-noise ratio comparison: IPCS and CCD at the WHT. The red line shows the S/N for an IPCS, for a 3 hr exposure of 40 cycles with 48 channels, on a 4.2-m telescope with a pixel size of 0.5" assuming a trough-put of the telescope of 80%. The blue line shows the S/N of a scientific grade CCD with a QE of 90% and a readout noise (σ) of $3e^-$ in the same exposure conditions. The faint detection limit is placed at a S/N of 3. See the electronic edition of the PASP for a color version of this figure.

674 HERNANDEZ ET AL.

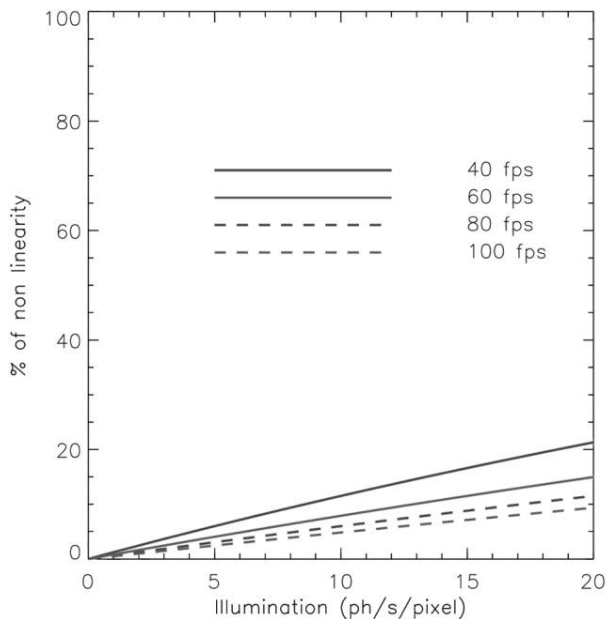


FIG. 6.—Computed nonlinearity of an IPCS detector at different frame rates. See the electronic edition of the PASP for a color version of this figure.

Figure 6 shows the percentage of nonlinearity of an IPCS detector at different possible frame rates. This shows that the system loses its linearity when the flux increases. Therefore this detector is used exclusively for faint fluxes. Figure 6 shows also that this effect is less important for higher frame rates. The blue lines (dot or continuous) represent the FANTOMM GaAs system, and the red one is the improved GH α FAS camera.

4. DATA REDUCTION

4.1. Data Preparation

As GH α FAS is mounted on the optical table of the Nasmyth focus, our observations are affected by the field rotation. The optical derotator provided by the Isaac Newton Group (ING) of Telescopes has the disadvantage of covering a field of only $2.5' \times 2.5'$, which is too small for the scientific programs envisaged for GH α FAS. Our observation strategy allows us to store the image of the individual channel separately, which is ideal for derotating the observed cube a posteriori (for examples of derotation, see Figure 7). Following the information provided on the ING web pages, the field rotation is $\approx 0.29''$, i.e., negligible, during the exposure of each individual cycle (~ 4 minutes).

Most of the data reduction steps are carried out using an IDL-based data reduction package developed by Daigle et al. (2006b). However, because we do not use the optical derotator, the data are affected by the rotation. In order to correct for this effect, we combine Daigle's reduction package with a number of

available packages, KARMA¹⁴, SWARP¹⁵ and IMWCS¹⁶. The complete steps of the GH α FAS data reduction are

1. We create an initial and rough estimate of the data quality by reducing the observed data cube. This step allows also a good phase calibration, which we use to reduce the individual cycles.
2. We reduce each individual observed cycle.
3. We create a cube image for each reduced cycle. Investigating each of these images, we have found that for almost all the observed galaxies, the effect of the sky rotation is marginal within the 4 minutes exposure to scan one cycle. This is also confirmed by the ING Web pages.
4. The collapsed cube image of each individual cycle is then used to find the three brightest point sources. The IMWCS and KARMA tools are then used to include the appropriate keywords in the header of each image.
5. We found that a simple rotational transformation does not provide the adequate accuracy, hence we use the SWARP package to match all cycles regardless of the complexity of the transformation required.
6. We apply the same transformation to each individual channel within each cycle, and rebuild a corrected version of the data cube.
7. Finally, we reduce the corrected data cube following all the standard reduction procedures presented in Daigle et al. (2006b).

Note that this process is made possible only because our detector has a high time resolution and has no readout noise. This reduction process does not add any excess noise to the observational data and keeps the very high overall sensitivity of the instrument.

4.2. Data Reduction and Derivation of the H α Kinematics

GH α FAS data reduction involves the standard Fabry-Perot data reduction steps: cube construction, phase calibration, sky subtraction, and kinematics derivation, which is done using the software package of Daigle et al. (2006b) and the GIPSY package (Vogelaar & Terlouw 2001).

By construction, GH α FAS covers a reasonably large field in order to observe nearby extended objects and provide simultaneous sky coverage to allow for reliable sky subtraction. However, some galaxies extend beyond the full GH α FAS field. In order to sample the sky variations properly during the long observation of the object, the telescope is pointed to a blank field away from the galaxy once every three cycles. The sky cubes are thereafter treated in the same way as the galaxy cube. The re-

¹⁴More information is available at the Karma homepage, <http://www.atnf.csiro.au/computing/software/karma>.

¹⁵More information can be found at the Terapix Web site, <http://terapix.iap.fr>.

¹⁶See the Image World Coordinate Setting Program Web site, <http://tdc-www.harvard.edu/software/wcstools/imwcs>, for more information.

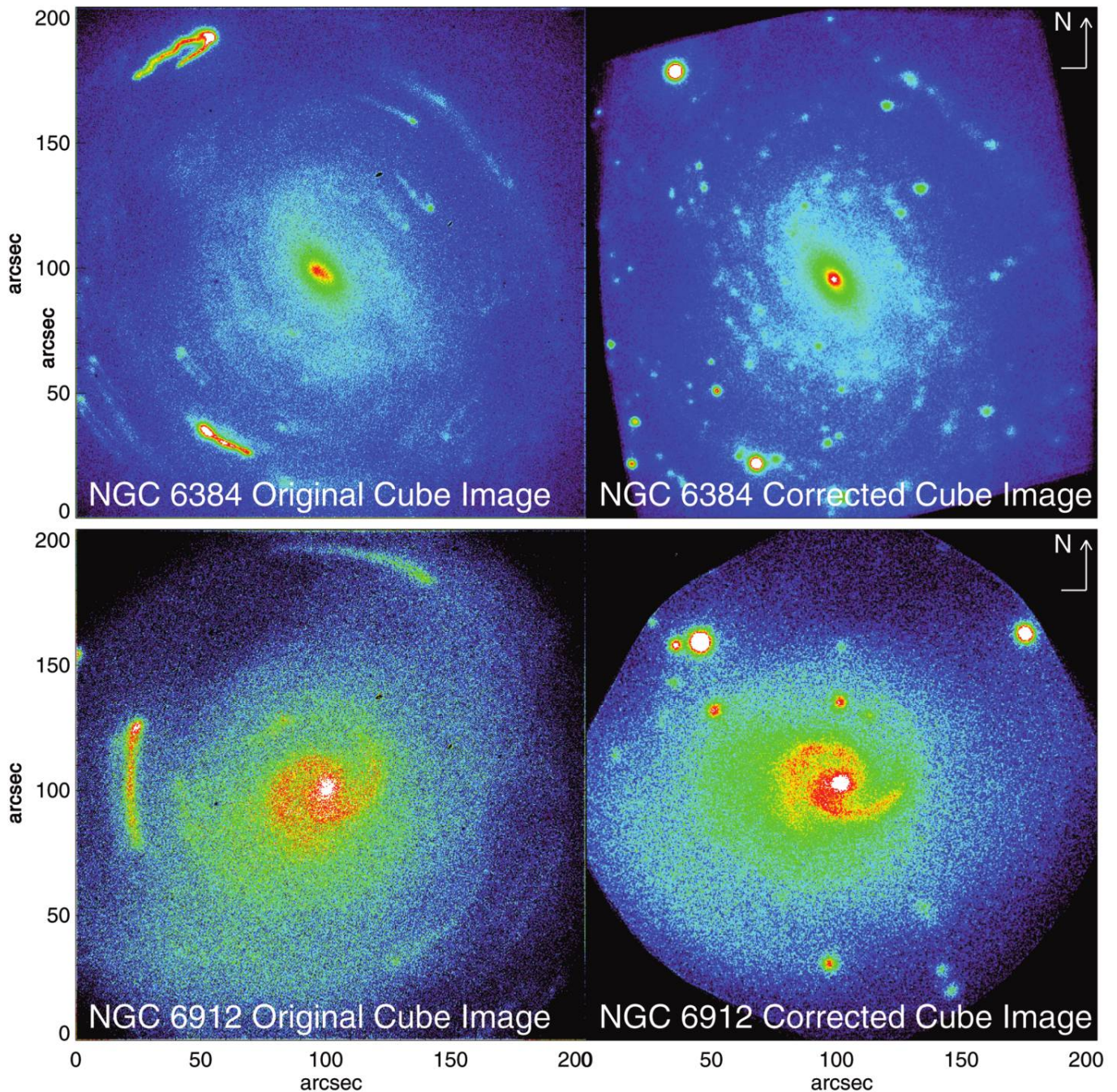


FIG. 7.—Examples of derotation.

duced sky cube is then rescaled to the galaxy count level and subtracted from the galaxy cube. In order to examine the accuracy of the sky subtraction procedure, the sky cube is used in four different ways before subtraction from the galaxy. All the sky spectra are then rearranged to build one spectrum representative of the entire sky cube, but also fitted with first, third, and fourth order polynomials to each channel image of the sky cube.

Subtracting each sky representation separately, we end up with four different reduced galaxy cubes.

The free spectra range (FSR) determines the depth of the data cube and is a function of the observed wavelength (λ) and the interference order (p) at this wavelength: $\text{FSR} = \lambda/p$. The number of channels is linked to the finesse of the Airy function of the etalon (in fact, the number of channel respects the Nyquist cri-

676 HERNANDEZ ET AL.

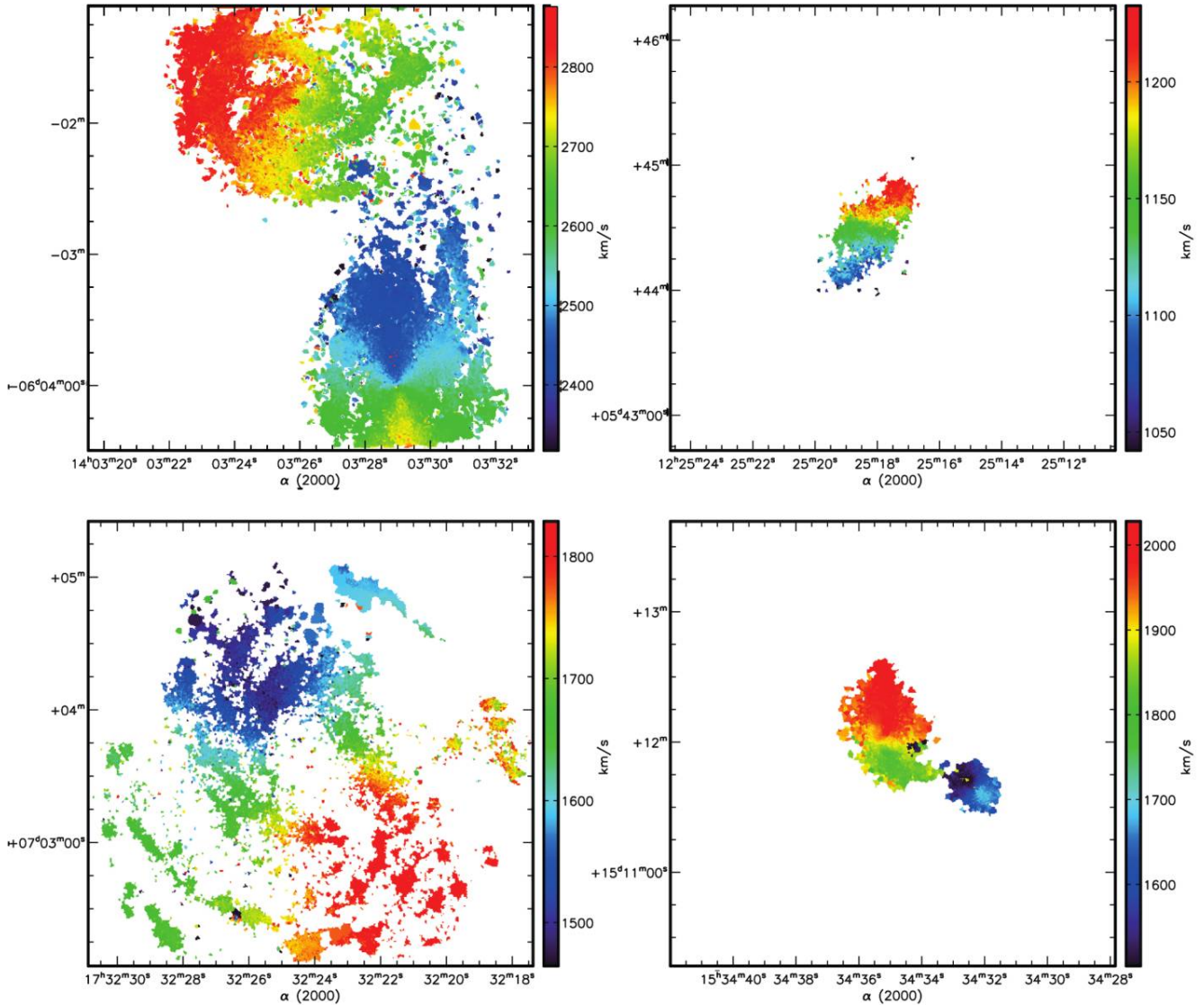


FIG. 8.—Kinematical maps of four objects. *Top left:* NGC 5427 with NGC 5426. *Top right:* NGC 4376. *Bottom Left:* NGC 6384. *Bottom right:* NGC 5954 with NGC 5953

teria: $n = 2.2 \times$ the effective Finesse) and has no relation to the FSR. To study normal galaxies, a FSR of 0.8 nm (360 kms at $H\alpha$) is used. If the velocity range of a galaxy (with its inclination factor) is larger than the FSR (which is not frequent), one will find in order -1 or $+1$ the rest of the velocity field (filters, used in front of the etalon, typically block all etalon order except $p + 1, p, p - 1$). So a jump in the velocity field is generally found and easily corrected. This could happen with active galactic nuclei of galaxy. In that particular case, another etalon is used to increase the FSR. Table 2 presents the FSR for different etalons.

Each reduced galaxy cube is treated independently to derive the $H\alpha$ kinematics by means of deriving the moment maps with consistency checks by applying single Gaussian profiles to the

spectra (e.g., Fathi et al. 2007a). Analyzing the kinematical maps, it was found that the sky subtraction does not significantly change the derived kinematics. In order to gain more field coverage, a two-dimensional Voronoi tessellation method (Cappellari & Copin 2003; Daigle et al 2006b) was applied on the faint regions of the observed field. Finally, the maps were cleaned by removing all values that are derived from spectra with amplitude-over-noise (A/N) less than 10 (the noise being the standard deviation of the parts of the spectra outside the $H\alpha$ emission line). Although this seems a strict criterion, it was chosen to continue the analysis of the velocity field based on spectra that are reliable not only for deriving reliable velocities, but also velocity dispersion. $\text{GH}\alpha\text{FAS}$ instrumental dispersion has been measured using the neon lamp and was found

to be $\sigma_{\text{inst}} = \text{FWHM}/2.35 = 2.5 \text{ km s}^{-1}$. It was then subtracted quadratically from the H α velocity dispersion, and the derived velocities were corrected for the Heliocentric velocity drift.

To give an idea of the efficiency of the pipeline reduction, two panels of results are given, representing the scientific drivers of the instrument. The final kinematical maps are presented in Figure 8 for four objects while H α monochromatic images are

represented in Figure 9. Finally, monochromatic image in the [N II] line and the first order of the PNe M1-75 is presented in Figure 10. It is not the goal of this paper to comment, analyze, or derive kinematical parameters. The final, complete, and detailed data reduction and analysis will be available in forthcoming papers.

Finally, the status of the data reduction of the first run (17 objects) over 6 nights is presented in Table 5.

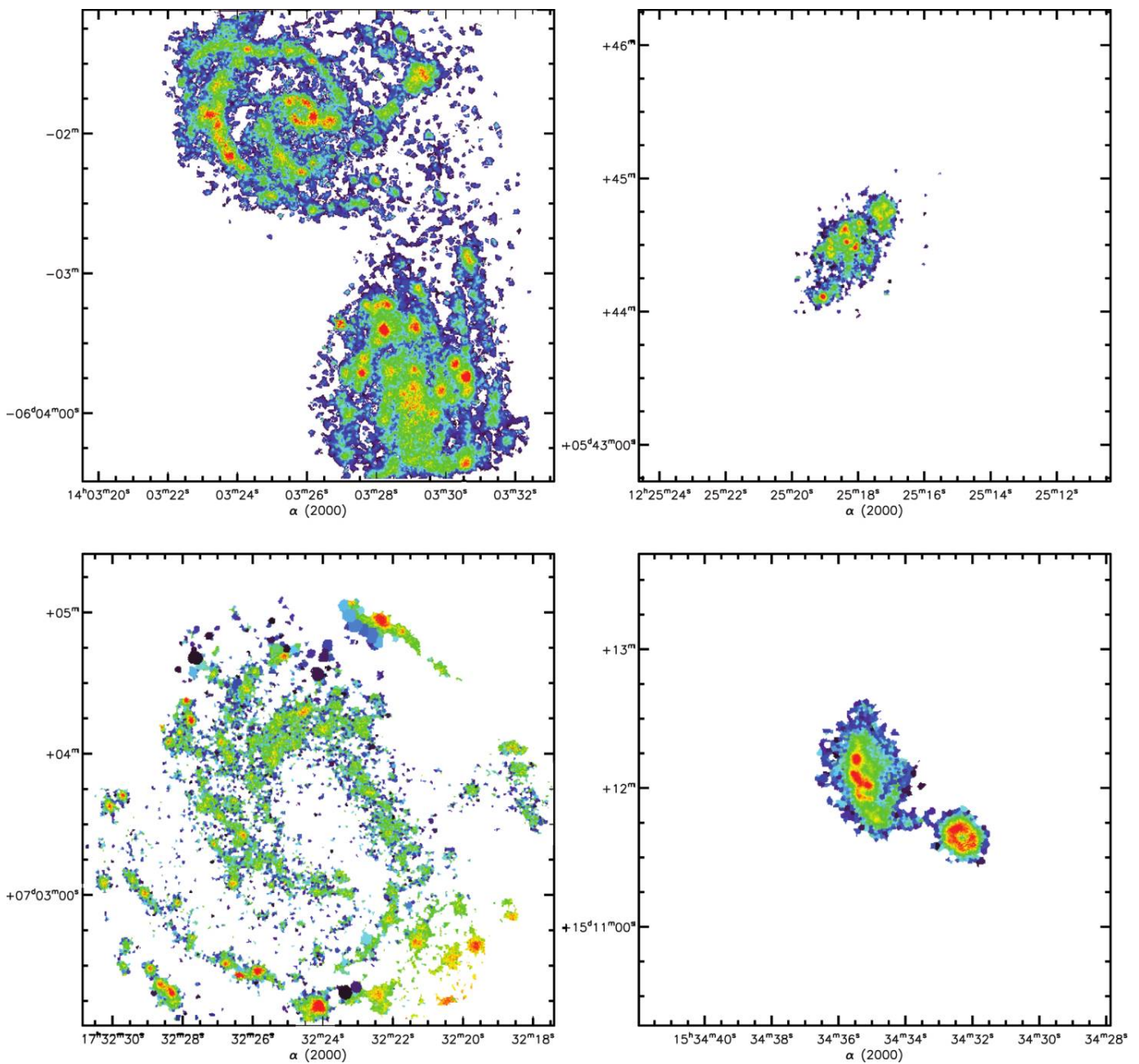


Fig. 9.—H α images of four objects. *Top left*: NGC 5427 with NGC 5426. *Top right*: NGC 4376. *Bottom Left*: NGC 6384. *Bottom right*: NGC 5954 with NGC 5953

678 HERNANDEZ ET AL.

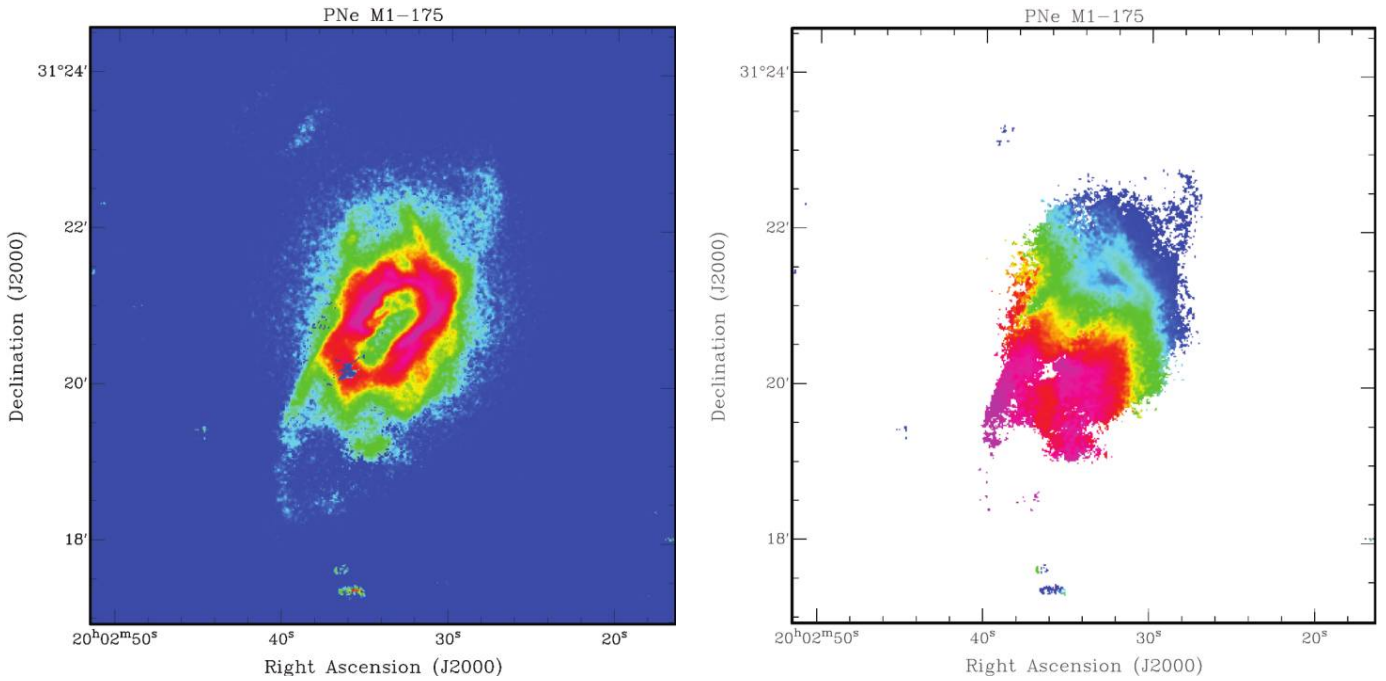


FIG. 10.—*Left*: [N II]658.3 nm image of Planetary Nebula M1-75 with a pixel size of $0.2''$. *Right*: associated expansion velocity field. Range of velocity is from 76 km s^{-1} to 231 km s^{-1}

5. CONCLUSIONS

GH α FAS, a new Fabry-Perot system with high spatial and spectral resolution has been presented. GH α FAS offers the largest FOV of such instrument on a 4-m class telescope. It is also

the most versatile instrument capable of studying ISM to high-redshift galaxies.

GH α FAS provides a FOV of $202'' \times 202''$ with two spatial resolutions: $0.4'' \text{ pixels}^{-1}$ or $0.2'' \text{ pixels}^{-1}$ (hard-binned mode). Different spectral resolutions can be achieved simply by chan-

TABLE 5
 OBSERVED OBJECTS WITH GH α FAS DURING 6 NIGHTS

Name	R.A.	decl.	V_{sys}	Night	(Seeing)	Status
NGC 4376	12 25 18.0	+05 44 28	1136	6	0.7	Reduced
NGC 4594	12 39 59.4	-11 37 23	1024	4	2.0	Reduced Dicaire et al 2008
NGC 5236	13 37 00.9	-29 51 57	513	5	0.7	Reduced Fathi et al 2008
NGC 5427	14 03 26.0	-06 01 51	2618	2	1.5	Reduced
NGC 5850	15 07 07.7	+01 32 39	2556	3	2.0	Reduced
NGC 5954	15 34 35.1	+15 11 54	1959	2	1.5	Reduced
NGC 6118	16 21 48.6	-02 17 00	1573	6	0.6	Reduced
NGC 6384	17 32 24.3	+07 03 37	1665	1	1.8	Reduced
NGC 6643	18 19 46.4	+74 34 06	1484	2	1.5	In progress
NGC 6643	18 19 46.4	+74 34 06	1484	2	Imaging	In progress
NGC 6912	20 26 52.1	-18 37 02	6968	3	2.5	Reduced
NGC 6912	20 26 52.1	-18 37 02	6968	6	0.8	Reduced
NGC 6962	20 47 19.1	+00 19 15	4211	4	1.8	Reduced
KPG 552	21 07 44.0	+03 52 30	7767	5	0.6	Reduced
KPG 591	23 47 01.6	+29 28 17	4845	4	1.5	Reduced
PN M1-75	20 04 44.1	+31 27 24	3890 ^a	5	0.8	Reduced
Arp 278	22 19 28.6	+29 23 32	4718	6	0.8	Reduced

NOTE.—All objects that were successfully observed during the commissioning run of six nights.^aDistance measured in parsecs. Note that NGC 6912 was observed twice in order to achieve improved spatial resolution, and the planetary nebula, PN M1-75, was observed in high-resolution mode with $0.2'' \text{ pixel}^{-1}$.

ging etalon in the pupil space. With the actual bank of etalon available, spectral resolution varies from 8000 to 110,000. The use of tunable filters (in development both at LAE and LAM) would also improve the versatility of this instrument. The high-performance no readout-noise detector, in the GH α FAS version, remains the best detector to be used with faint flux science cases. It allows, at the same time, real-time data acquisition (the astronomical object is seen live during observation), on-sky reduction, and real-time OH sky line removing. Finally, a robust reduction pipeline, for complete data reduction, is available and can be obtained at <http://www.astro.umontreal.ca/fantommm/reduction>.

Development of GH α FAS was formulated in the summer of 2006 by the IAC, and conception, design, and realization began in the beginning of 2006 December at LAE. The first lights were obtained only 6 months later in the summer of 2007. This fast schedule was possible because of the expertise developed at LAM, Observatoire de Marseille, and LAE at University of Montreal, through the building of FANTOMM and CIGALE. While GH α FAS was constructed as a private instrument, it is expected to become a visitor instrument at WHT in less than two years.

GH α FAS should be considered as a high-performance instrument but also as a lab test of much more complicated instruments such as the 3D-NTT (<http://www.astro.umontreal.ca/>

3dntt), the Brazilian Tunable Filter : BTFi (<http://www.astro.iag.usp.br/~btfi>) and the SMART tunable Filter for the E-ELT (Moretto et al. 2006). Those instruments will use GH α FAS technology but with many improved features, such as EMCCD (Daigle et al. 2006a), customs large tunable filters, and a new tunable filter made with Volume Phase gratings (Blais-Ouellette et al. 2006).

We would like to thank the staff of the WHT, where the data were obtained, for their continuing support. Special thanks also to Olivier Boissin for his help before and during the commissioning of the instrument. We also acknowledge support from the Natural Sciences and Engineering Research Council of Canada and the Fonds Québécois de la recherche sur la nature et les technologies. This research has benefitted from support by the following projects: AYA2004-28251-CO2-01 and AYA2007-67625-CO2-01 of the Spanish Ministry of Education and Science, and P3/86 of the Instituto de Astrofísica de Canarias. K. F. acknowledges support from the Wenner-Gren foundations, the Royal Swedish Academy of Sciences' Hierta-Retzius foundation, and the IAC project P3/86. Monica Relaño acknowledges support from the Juan de la Cierva Fellowship Program and the project AYA2004-08251-CO2-00. We are grateful to Daniel Fabricant, associate editor of PASP, for helpful comments.

REFERENCES

- Amram, P., Mendes de Oliveira, C., Plana, H., Balkowski, C., & Hernandez, O. 2007, *A&A*, 471, 753
- Amram, P. et al. 2004, *ApJ*, 612, L5
- Arribas, S. et al. 1998, in *ASP Conf. Ser. 152, Fiber Optics in Astronomy III*, ed. S. Arribas, E. Mediavilla, & F. Watson (San Francisco: ASP), 149
- Athanassoula, E. 2005, *Celest. Mech. Dyn. Astron.*, 91, 9
- Atherton, P. D., Taylor, K., Pike, C. D., Harmer, C. F. W., Parker, N. M., & Hook, R. N. 1982, *MNRAS*, 201, 661
- Bacon, R. et al. 1995, *A&AS*, 113, 347
- . 2001, *MNRAS*, 326, 23
- Balard, P. et al. 2006, *Scientific Detectors for Astronomy 2005, Astrophysics and Space Science Library*, Vol. 336, ed. J. E. Beletic, J. W. Beletic, & P. Amico (New York: Springer), 117
- Balick, B., & Frank, A. 2002, *ARA&A*, 40, 439
- Blais-Ouellette, S., Daigle, O., & Taylor, K. 2006, *Proc. SPIE*, 6269, 62695H
- Bland, J., Tully, R. B., & Cecil, G. N. 1990, *Proc. SPIE*, 1235, 590
- Boulesteix, J., Georgelin, Y., Marcelin, M., & Monnet, G. 1984, *Proc. SPIE*, 445, 37
- Cappellari, M., & Copin, Y. 2003, *MNRAS*, 342, 345
- Chemin, L., Balkowski, C., Cayatte, V., Carignan, C., Amram, P., Garrido, O., Hernandez, O., Marcelin, M., Adami, C., Boselli, A., & Boulesteix, J. 2006, *MNRAS*, 366, 812
- Chu, Y.-H., & Kennicutt, R. C. Jr. 1994a, *ApJ*, 425, 720
- . 1994b, *Ap&SS*, 216, 253
- Courtes, G. 1982, in *IAU Colloq. 67, Instrumentation for Astronomy with Large Optical Telescopes*, ed. C. Humphries (New York: Springer), 123
- Daigle, O., Carignan, C., Blais-Ouellette, & S. 2006a, *Proc. SPIE*, 6276, 62761F
- Daigle, O., Carignan, C., Amram, P., Hernandez, O., Chemin, L., Balkowski, C., & Kennicutt, R. 2006b, *MNRAS*, 367, 469
- Dekel, A., & Birnboim, Y. 2006, *MNRAS*, 368, 2
- de Zeeuw, P. T. et al. 2002, *MNRAS*, 329, 513
- Dicaire, I., et al. 2008, *MNRAS*, 385, 553
- Dopita, M., Hart, J., McGregor, P., Oates, P., Bloxham, G., & Jones, D. 2007, *Ap&SS*, 310, 255
- Eisenhauer, F. et al. 2003, *Proc. SPIE*, 4841, 1548
- Emsellem, E., Fathi, K., Wozniak, H., Ferruit, P., Mundell, C. G., & Schinnerer, E. 2006, *MNRAS*, 365, 367
- Emsellem, E., et al. 2007, *MNRAS*, 379, 401
- Fathi, K., Beckman, J. E., Zurita, A., Relaño, M., Knapen, J. H., Daigle, O., Hernandez, O., & Carignan, C. 2007, *A&A*, 466, 905
- Fathi, K., Toonen, S., Falcón-Barroso, J., Beckman, J. E., Hernandez, O., Daigle, O., Carignan, C., & de Zeeuw, T. 2007, *ApJ*, 667, L137
- Fathi, K., van de Ven, G., Peletier, R. F., Emsellem, E., Falcón-Barroso, J., Cappellari, M., & de Zeeuw, T. 2005, *MNRAS*, 364, 773
- Fathi, K. et al. 2008, *ApJL*, 675, L17
- Flores, H., Hammer, F., Puech, M., Amram, P., & Balkowski, C. 2006, *A&A*, 455, 107
- Förster Schreiber, N. M. et al. 2006, *ApJ*, 645, 1062
- Gach, J.-L., Darson, D., Guillaume, C., Goillandeau, M., Cavadore, C., Balard, P., Boissin, O., & Boulesteix, J. 2003, *PASP*, 115, 1068
- Gach, J.-L., Hernandez, O., Boulesteix, J., Amram, P., Boissin, O., Carignan, C., Garrido, O., Marcelin, M., Östlin, G., Plana, H., & Rampazzo, R. 2002, *PASP*, 114, 1043

680 HERNANDEZ ET AL.

- García-Segura, G., Langer, N., Różyczka, M., & Franco, J. 1999, *ApJ*, 517, 767
- Genzel, R. et al. 2006, *Nature*, 442, 786
- Gonçalves, D. R., Ercolano, B., Carnero, A., Mampaso, A., & Corradi, M. R. L. 2006, *MNRAS*, 365, 1039
- Haehnelt, M. G., & Kauffmann, G. 2000, *MNRAS*, 318, L35
- Henault, F. et al. 2004, *Proc. SPIE*, 5492, 909
- Hernandez, O., Carignan, C., Amram, P., Chemin, L., & Daigle, O. 2005, *MNRAS*, 360, 1201
- Hernandez, O., Gach, J.-L., Carignan, C., & Boulesteix, J. 2003, *Proc. SPIE*, 4841, 1472
- Hernandez, O., Wozniak, H., Carignan, C., Amram, P., Chemin, L., & Daigle, O. 2005, *ApJ*, 632, 253
- Hill, G. J. et al. 2006, *Proc. SPIE*, 6269, 62692J
- Kauffmann et al. 2003, *MNRAS*, 341, 54
- Klypin et al. 1999, *ApJ*, 522, 82
- Kunth, D., & Östlin, G. 2000, *AAPR*, 10, 1
- Maciejewski, W. 2006, *MNRAS*, 371, 451
- Maciejewski, W., & Athanassoula, E. 2007, *MNRAS*, 380, 999
- Marquart, T., Fathi, K., Östlin, G., Bergvall, N., Cumming, R. J., & Amram, P. 2007, *A&A*, 474, L9
- Moe, M., & De Marco, O. 2006, *ApJ*, 650, 916
- Moretto, G. et al. 2006, *Proc. SPIE*, 6269, 62692G
- Newman, & Davis 2002, *ApJ*, 564, 567
- Peletier, R. F. et al. 2007, *MNRAS*, 379, 445
- Relaño, M., & Beckman, J. E. 2005, *A&A*, 430, 911
- Relaño, M., Beckman, J. E., Daigle, O., & Carignan, C. 2007, *A&A*, 467, 1117
- Rosado, M., Arias, L., & Ambrocio-Cruz, P. 2007, *AJ*, 133, 89
- Shlosman, I., Frank, J., & Begelman, M. C. 1989, *Nature*, 338, 45
- Siegmund, O. H. W. 1988, *Proc. SPIE*, 982, 108
- Singh, S. 2006, *Nature*, 440, 1114
- Sluis, A. P. N., & Williams, T. B. 2006, *AJ*, 131, 2089
- Terlevich, R., & Melnick, J. 1981, *MNRAS*, 195, 839
- Thatte, N., Tecza, M., Clarke, F., Goodsall, T., Lynn, J., Freeman, D., & Davies, R. L. 2006, *Proc. SPIE*, 6269, 62693L
- Tremaine, S. et al. 2002, *ApJ*, 574, 740
- Vogelaar, M. G. R., & Terlouw, J. P. 2001, *ASPC*, 238, 358
- Zurita, A., Relaño, M., Beckman, J. E., & Knapen, J. H. 2004, *A&A*, 413, 73
- Zurita, A., Rozas, M., & Beckman, J. E. 2001, *Ap&SS*, 276, 491

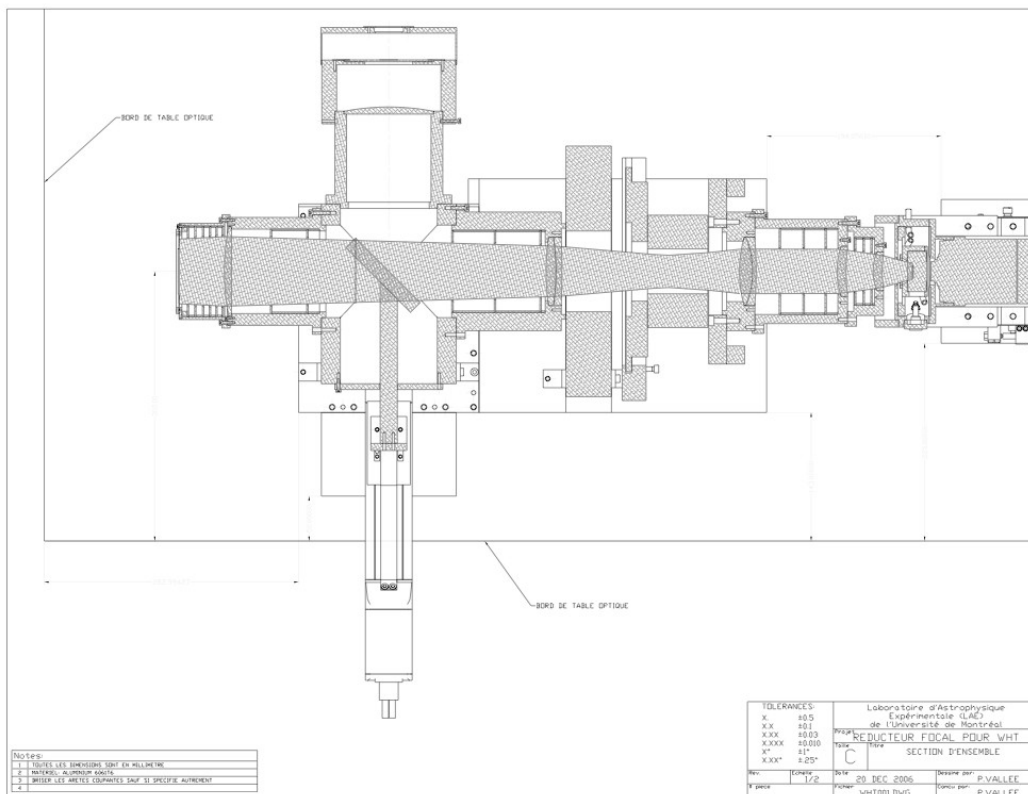
A.2.2 Comment monter GH α FaS ?

Durant les deux périodes d'observation de l'année 2008 qui ont suivi les premières observations de juillet 2007, un manuel pour le montage de l'instrument a été rédigé par Marie-Maude de Denus Baillargeon et moi-même. Il décrit toutes les opérations à réaliser (assemblage des éléments optiques, câblage des éléments, réglages optiques, configuration réseau), étape par étape, images à l'appui afin que l'utilisateur de l'instrument ait tous les éléments pour que la mission d'observation soit un succès. Je ne présente ici que la première page de ce manuel.

GH α FAS INSTRUMENT SETUP

1. Mechanical assembly

For the mechanical assembly, each part is identified with a number. The numerical number is important, start with GFS0001, then mount on it GFS0002 and so on. A lot of screws are situated under the assemblies. See the InstructionsAssemblage.txt file for more details. (Note : the filter wheel shall not be installed between the focal reducer and the FP etalon, as shown on the schematics below, but in front of the focal reducer). Clean the optics before assembling all the parts.



The light diffuser (depolished glass) has to be fixed between the calibration mirror and the calibration lamp (to the aluminum structure with shim stops).

The table has been marked with a felt-pen to indicate the appropriate position for the assembly (i.e. roughly on the optical axis and at focus position).

The camera can be mounted on its holder but must not be put in place before having completed the alignment procedure (see section 3). The FP etalon, the motorized calibration mirror and the filter wheel should also be put in place only once the alignment with the laser is finished, but they all can be mounted on their holders.

A.3 Article VII : Wide Field Spectrograph Concepts for the European Extremely Large Telescope

Cet article a été publié dans les comptes-rendus de la conférence SPIE qui a eu lieu à Orlando en juin 2006 par Moretto et al. (2006). Il discute des objectifs scientifiques du projet WFSpec et présente les trois concepts présentés dans la section 1.4.

Les spécifications de haut niveau liées aux programmes scientifiques pour un spectrographe à grand champ sur un Extremely Large Telescope (ELT) ainsi que les divers concepts envisagés sont présentés. Les dessins préliminaires correspondant aux différents concepts instrumentaux sont exposés : un champ intégral monolithique (IFU), un champ intégral subdivisé (multi-IFU) et un nouveau type de filtre accordable. Ce travail s'intègre dans les activités effectuées dans le cadre du groupe de travail "Instrumentation" du "ELT Design Study", un programme subventionné par la Communauté Européenne, Framework Programme 6.

Wide Field Spectrograph Concepts for the European Extremely Large Telescope

G. Moretto^a, R. Bacon^b, J.-G. Cuby^a, F. Hammer^c,
P. Amram^a, S. Blais-Ouellette^d, P.-E. Blanc^a, J. Devriendt^b, B. Epinat^a, T. Fusco^c, P. Jagourel^b,
O. Hernandez^a, J.-P. Kneib^a, I. Montilla^b, B. Neichel^{c,e}, E. Pécontal^b, E. Prieto^a, M. Puech^c

^aLaboratoire d'Astrophysique de Marseille (LAM), Marseille 13376, France

^bCentre de Recherche Astronomique de Lyon (CRAL), Saint Genis Laval 69561, France

^cObservatoire de Paris (GEPI), Meudon 92195, France

^dPhoton etc, 5155 Decelles Avenue, Montréal, Québec, H3T 2B1, Canada

^eONERA, BP72 - 29 avenue de la Division Leclerc, 92322 Chatillon, France

ABSTRACT

We report on the science case high level specifications for a wide field spectrograph instrument for an Extremely Large Telescope (ELT) and present possible concepts. Preliminary designs are presented which resort to different instrument concepts: monolithic integral field (IFU), multi-IFU, and a smart tunable filter. This work is part of the activities performed in the work package 'Instrumentation' of the 'ELT Design Study', a programme supported by the European Community, Framework Programme 6.

Keywords: Extremely Large Telescope, Instrumentation.

1. INTRODUCTION

A technology development program towards a European Extremely Large Telescope (ELT) has been launched by the European Commission through the Framework Program 6 (FP6): the ELT Design Study. One work package in this study deals with instrument studies¹. In a first phase, several 'small studies' will be performed, eventually followed by point design studies for a few of the instruments initially considered. As part of this exercise, several French laboratories joined to perform one of the 'small studies' for a wide field spectrograph, dubbed WFSPEC. WFSPEC is aimed at observing the high redshift Universe and investigate the mass assembly of galaxies across cosmic times.

The objectives of the study are to establish, from the science case, the high level specifications for the instrument; perform conceptual design(s); evaluate performance; evaluate development risks and mitigations and finally compare the various solutions. We present preliminary designs based on three different concepts: monolithic IFU, multi-IFU, and a smart tunable filter. Work is in progress and the final evaluation of the various technical solutions is beyond the scope of this paper which only deals with the high level specifications derived from the science case and with the presentation of the 3 instrument concepts.

2. SCIENCE CASE AND HIGH LEVEL SPECIFICATIONS

Two highlight ELT science cases are the observation of the first objects in the Universe for understanding how the galaxies formed and how the Universe was re-ionized, and the physical study of the mass assembly of galaxies across cosmic times for understanding how dark and baryonic matter assembled in galaxies from the first cosmological seeds. The high level specifications for both science cases are indicated table 1 and 2. Both specification sets are to a large extent similar, allowing to consider both science cases at once for the same instrument. WFSPEC is in essence a wide field near IR spectroscopic facility with high multiplex capabilities.

Table 1. High level specifications for science case#1: the Early Universe, the first galaxies and the end of the re-ionization epoch². The objective is to observe statistical samples of $z > 7$ objects, up to redshifts $\sim 10-15$ for a complete census of the formation of the galaxies and of the physical processes that led to the re-ionization of the Universe

Specification	Minimum	Goal	Note
FOV (diameter)	5 arcmin	10 arcmin	<ul style="list-style-type: none"> Target density if of the order of a few, possibly a few tens, per square arcminutes at $z \sim 6-7$, decreasing sharply with redshift
Spectral Resolution	5000	8000	<ul style="list-style-type: none"> Digital OH suppression requires spectral resolution higher than 3000. Resolving ISM lines $\sim 10-20$ km/s, typical of the galaxy masses of distant objects.
Wavelength Range	0.9-1.8 μm	0.8-2.5 μm	<ul style="list-style-type: none"> The gain of the K-band is marginal : there will be typically only a few objects per field accessible at $z > 15$ ($\text{Ly}\alpha$) or even at $z > 10$ (HeII)
Multiplex	20	> 100	<ul style="list-style-type: none"> Number of objects in homogeneous samples to be observed at once for statistical studies
Individual Object field of view	0.5" x 0.5"	1" x 1"	<ul style="list-style-type: none"> The typical size of high-z objects is of the order of 200-400 mas, half-light diameter
Spatial Sampling	60 mas	30 mas	<ul style="list-style-type: none"> To sample the galaxy sizes with $\sim 10 \times 10$ pixels This requires Adaptive Optics correction either full field or locally where the targets are
Closest distance between objects	Few arcsec	Few arcsec	<ul style="list-style-type: none"> To investigate high amplification regions in cluster gravitational lenses.
Observing Time	> 10 hrs per setting	10 hrs per setting	<ul style="list-style-type: none"> Critically depends on the AO performance

Table 2. High level specifications for science case#2: the mass assembly of galaxies across cosmic times ($z=[1-5]$). Moderate resolution spectroscopy of homogeneous samples of galaxies for chemical and dynamical analyzes (mapping of absorption and emission line velocities, metallicities, extinction and ionization, etc.) of the galaxies from redshift ~ 1 to 5 for a complete census of baryonic and dark matter assembled and evolved in galaxies

Specification	Minimum	Goal	Note
FOV (diameter)	5 arcmin	10 arcmin	<ul style="list-style-type: none"> For homogeneous samples of galaxies for statistical studies
Spatial Resolution	100 mas	50 mas	<ul style="list-style-type: none"> Size of HII regions $\sim 0.1-0.2$ kpc.
Spectral Resolution	5000	10000	<ul style="list-style-type: none"> Digital OH suppression requires spectral resolution higher than 3000. Resolving ISM lines $\sim 10-20$ km/s. Similar requirement for resolving satellite motions
Wavelength Range	1.2-2.2 μm	0.8-2.5 μm	<ul style="list-style-type: none"> The I band is marginally important for this science case: above $z = 1.4$ the OII 3727 line is already above 0.9 μm
Number of objects	20	> 100	<ul style="list-style-type: none"> Up to a few tens of galaxies at once at $z \sim [1-2]$ with typical sizes $2'' \times 2''$, and, in addition, satellite galaxies (up to 10 per galaxy, faint and small) to probe matter distribution in galaxy halos
Size of objects	$2'' \times 2''$		
Spatial Sampling	50 mas	20 mas	
Closest distance between objects	Few arcsec	Few arcsec	<ul style="list-style-type: none"> Mergers and massive companions.
Observing Time			<ul style="list-style-type: none"> About 1 to 10 nights per field. Deeper exposures have to be considered, e.g. to detect lines from faint satellites. For example, at $z=3$, the typical flux of the halo galaxies is about 10^{-19} to 10^{-20} ergs s⁻¹ cm⁻², down to $m_{AB}=27-28$.

3. CONCEPTUAL DESIGNS AND PERFORMANCE

Three different conceptual designs have been investigated for WFSPEC: a multi-integral field mode (multi-IFU), a monolithic integral field mode (mono-IFU) and a holographic-tunable filter mode (smart tunable filter). We present below the main characteristics for each of those three concepts. The purpose of analyzing several concepts was to avoid a priori biases for any particular concept, with the final goal of evaluating all concepts against the science cases and allowing a quantitative estimate of the factors of merit for each solution.

3.1 Monolithic Integral Field (IFU) Concept

The monolithic concept provides a continuous field-of-view (FOV) of 24×24 arcsec² sampled at 56 mas. As shown in Figure 1, a field splitter separates the FOV in 5×9 sub-fields, each of them feeding a module featuring an image slicer, a collimator and a spectrograph with a $4k \times 4k$ IR detector, dispersing the $[1.46-2.21]$ μm range at a spectral resolution of 5000. 3D spectroscopy of the full field of view allows *blind detection* of emission-line high-redshift objects which may have continuum emission that is too faint to be detected in broad-band imaging.

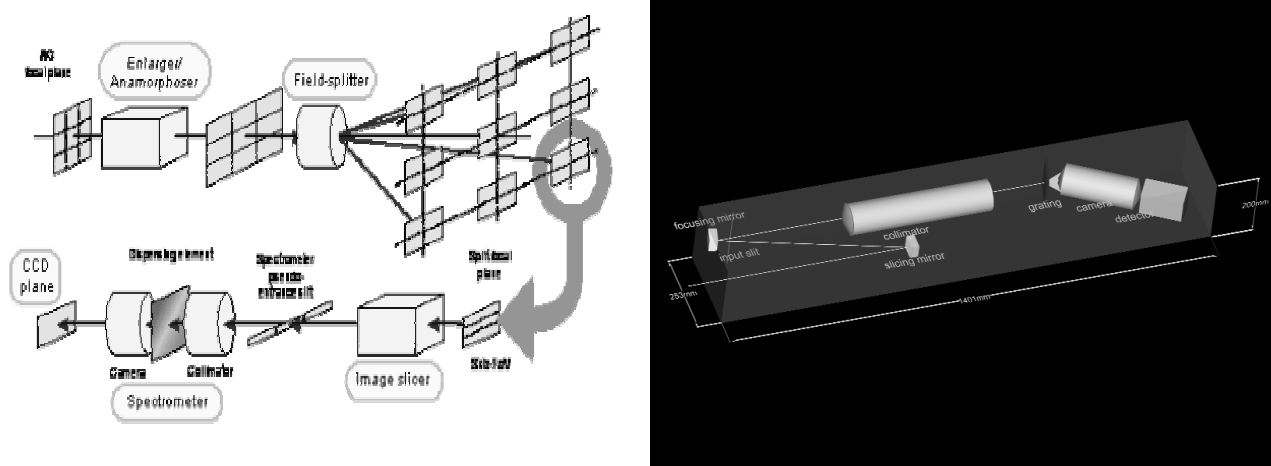


Fig. 1. Monolithic wide-field mode. Left: schematic concept, similar to the MUSE³ instrument at the VLT. The entrance field of view is split over several modules, each consisting in an image slicer and a spectrograph. Right: 3D view of one of the modules of the instrument.

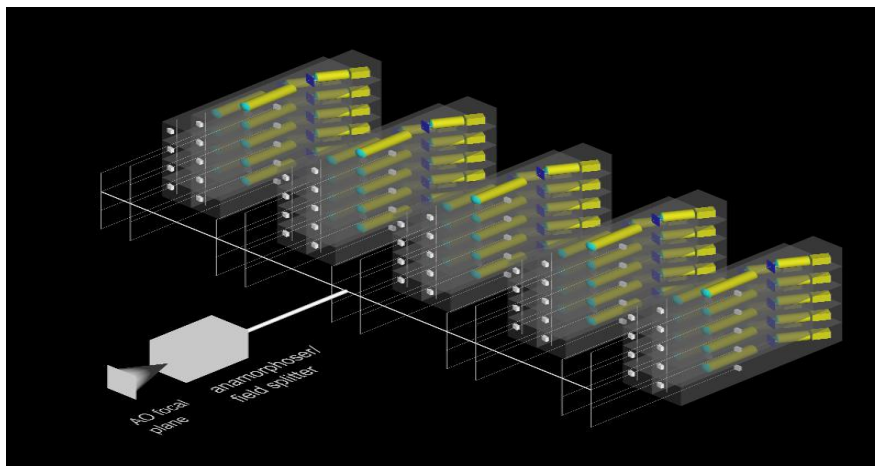


Fig. 2. The 3D view of all 45 spectrographs constituting the monolithic wide-field mode

This instrument concept is ideally suited to crowded fields of view with high target density and / or for extremely faint emitting line objects that are not detected in broad band imaging. Simulations of high redshift Ly α emitters show that the density of objects could be as high as 70 objects/arcmin² down to line fluxes of $\sim 5 \times 10^{-20}$ erg.s⁻¹.cm⁻² in the redshift range [7-15]. The instrument could therefore observe ~ 10 of these objects without any a priori knowledge of their position.

Table 3 summarizes the inputs parameters considering a future ELT (42m) and IR detectors of 4096x4096 pixels. The number of modules and the number of pixels in the cross-dispersion direction are a trade-off between the field-of-view and the spatial resolution. For the given 5000 spectral resolution a configuration of 45 modules is needed as presented in Figure 2. Such concept can work initially in GLAO assisted mode and later (initially if available) with Laser Tomography Adaptive

Optics (LTAO) for full performance⁴. Bearing in mind a cryogenic instrument a compact and packed configuration was chosen.

Table. 3. The optical parameters for the monolithic IFU instrument concept.

Spectral Resolution	5000	Total Pixels	755×10^6
Spectral Range (μm)	1.46-2.21	Pixel/Module	17×10^6
Throughput	0.25	Number of Exposures	80
Telescope Diameter (m)	42	Exposure Time (hours)	1
Telescope Focal Ratio	15	Medium Seeing (arcsec)	0.8
Pixel Size (μm)	20	GLAO Correction (arcsec)	0.3
Read-Out-Noise (e^-)	10	LTAO Correction (arcsec)	0.065
Dark current (e^-/s)	0.07	FOV (arcsec^2)	24×24
SNR	5	Spatial Sampling (arcsec)	0.056
Pixels in Dispersion Direction	4096	Samples	429
Pixel in Cross-Dispersion Direction	4096	F# camera	1.8/3.6
Dispersion/Pixel (\AA)	1.83	Modules	45

The performance of the system has been calculated considering that the system operates with ground layer AO (GLAO) correction. The expected performance of GLAO is to concentrate 40% of the energy in a circle of radius 200 mas in a 0.5 arcmin field of view in the K-band². The expected performance at $2 \mu\text{m}$ is presented in Table 4. The limiting line flux is calculated for an unresolved emission line. The number of pixels used for source extraction is optimized in order to obtain the best result. In the case of medium seeing, by integrating 20 pixels we recover 74% of the flux, in the GLAO-corrected case integrating over 4 pixels allows to recover 45% of the flux, in the LTAO-corrected case integrating over 2 pixels allows to recover 87% of the flux. The point spread function (PSF) used to calculate these values is a Gaussian function. In the LTAO case 85% of the energy is in a Gaussian function of FWHM 64 mas and 15% of the energy is in a halo of FWHM 80 mas. In the GLAO case 80% of the energy is in a Gaussian of FWHM 300 mas and the remaining 20% is in a halo of FWHM 100 mas.

Table 4. The monolithic wide-field mode concept: expected performance at 2 μm.

seeing	Medium Uncorrected	GLAO-Corrected	LTAO-Corrected	Diffraction-Limit	Resolved Source
limiting flux ($10^{-20} \text{erg s}^{-1} \text{cm}^{-2} \text{A}^{-1}$)	1.4	0.45	0.12	0.05	16
limiting AB magnitude	25.9	27.5	29.0	30	23.7
limiting line flux ($10^{-20} \text{erg s}^{-1} \text{cm}^{-2}$)	7	2.4	0.6	0.3	80

3.2 Multi-Integral Field Concept

The multi-IFU concept⁵ features 30 to 40 independent channels distributed over the 5 to 10 arcminutes unvignetted field of view of the telescope. Target selection - Figure 3(a) - relies on pick-off and beam steering mirrors which direct the light from any position in the focal plane to fixed instrument channels which individually consist in an adaptive optics dedicated deformable mirror, an image slicer system and a spectrograph as presented in Figure 3(b). The individual size of the Integral Field Units is of the order of $1 \times 1 \text{arcsec}^2$ with spatial sampling of the order of $30 \pm 10 \text{milliarcsec}$.

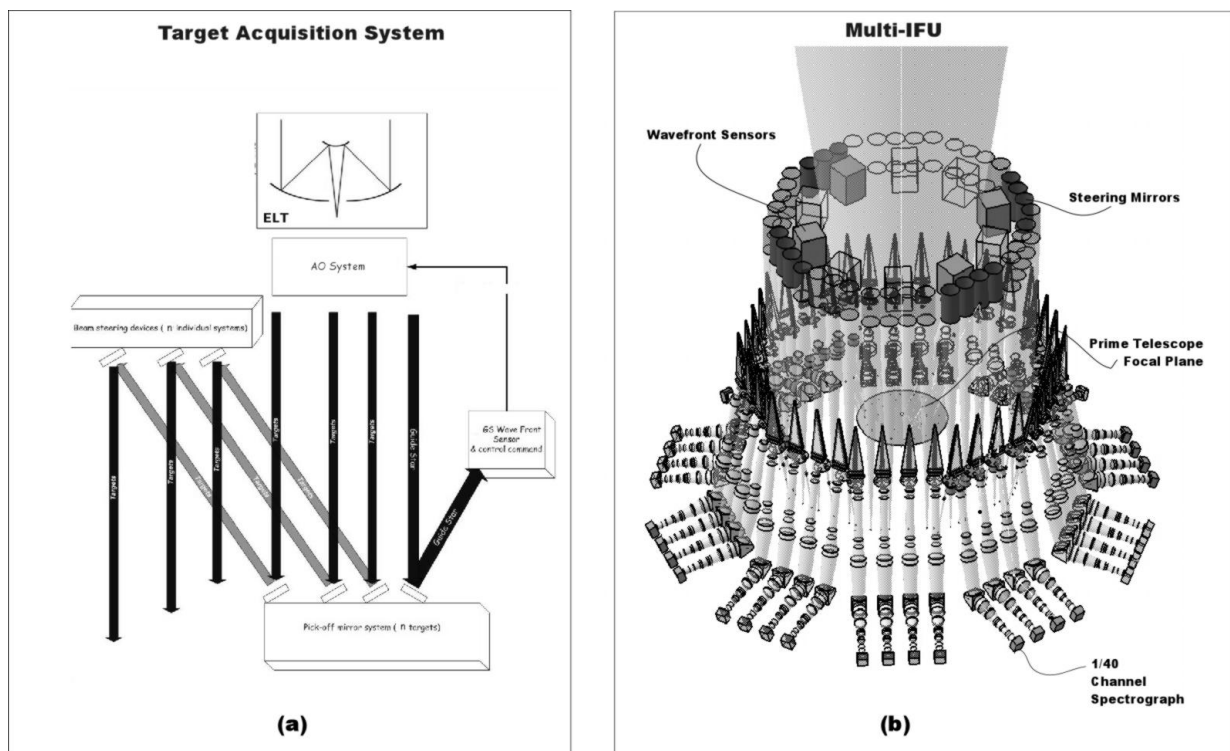


Fig. 3. Multi IFU Mode instrument: (a) the target acquisition system and (b) the 3D view of the 40 channels with the steering mirror, the WFS, and the central telescope focal plane.

This instrument concept relies on the so-called Multi-Object Adaptive Optics (MOAO) which locally corrects the distortions introduced by the atmospheric turbulence on each target. Several WFS (wavefront sensors) located in the telescope focal plane are fed by the same pick-off mirrors in the telescope focal plane to measure the turbulent wavefront over the field of view and correct it locally in open loop. The spectral resolution is ~ 5000 for OH avoidance and detailed physical studies. Higher spectral resolutions can be accommodated on some or all channels. Image quality of the order of 0.1 to 0.2 arcsec (resp. 0.05 to 0.07) can be achieved using Natural Guide Stars (NGS) (resp. Laser Guide Stars - LGS) in MOAO mode. Initial performance with Ground Layer Adaptive Optics (GLAO) correction if MOAO cannot be deployed at telescope first light will allow 0.3-0.4 arcsec image quality to be achieved.

Table 5 summarizes the input parameters assuming an ELT diameter of 42m. The concept of pick/off steering mirrors requires a large back focal distance at telescope focus of up to 2 meters. The instrument occupies a large volume of $\sim 40 \text{ m}^3$ and would need good access for integration and maintenance. The total volume of the continuous-IFU instrument, including the access space for maintenance, is 17 m^3 . A gravity stable platform is desirable in both cases.

Table. 5. The optical parameters for the multi-IFU mode instrument concept.

FOV (arcsec ²)	5'x5'
Individual FOV	1.5''x1.5''
Number of IFU	Up to 40
Number of pixel per IFU	60 x 60
Spatial sampling (arcsec)	0.025
Spectral coverage	(I,Z),J,H,K
Pixel size	18 μm
Detector format	4096x4096
F# camera	3.53 x 7.06
Pixel in cross dispersion direction	4096

3.3 Holographic-Tunable Filter Concept

The concept presented in this section is a third one based on tunable filters (Fabry-Perot) and imaging Bragg tunable filters (i-BTFs, based on Volume Phase Holographic grating systems⁶). It uses two dispersive systems: several volume phase holographic gratings for the low resolution dispersion ($R=250$) and one tunable filter ($R=5000$) for the high resolution dispersion. As presented in Figure 4-top, fifty-two spectral bands (blue, green, yellow and red curves*) are selected in between the main OH night sky lines (green lines) already lowered by an *ad hoc* filter. The principle of operation is to use a tunable filter generating a Dirac comb function (in wavelength) and to image the field of view in as many wavelengths of this comb as possible (in practice 52 images in the 52 spectral bands defined by the 52 imaging Bragg tunable filters). Scanning 20 times the tunable filter allows a full coverage of each spectral band. In total 20 times 52 narrow band images provide complete imaging of the field of view at a spectral resolution of ~ 5000 over about a 1/3 of the spectral range from 0.8 to 2.5 μm (note that another $\sim 1/3$ of the spectral range is in practice useless because of poor atmospheric transmission and / or too strong and crowded OH emission).

The system consists of:

1. A tunable filter allowing to reach the high resolution during the scanning process, where 20 scans in each large band is necessary to reach $R=5000$. The thin red vertical lines (Figure 4-top) represent the Airy function of the tunable filter (the *Finesse* is given by the ratio between the distance of two adjacent red line and the width of a

* Please send us an e-mail (wfspec@clio.univ-lyon1.fr) for a color version of the figure

- red line), which allows the scanning of the whole spectrum (0.8 to 2.5 microns) simultaneously through 20 steps.
2. A succession of 52 imaging Bragg tunable filters (i-BTFs), each of them with a spectral resolution $R=250$ selecting a wavelength band between the strongest night sky lines. These 52 i-BTFs consist in:
 - a. Three arms of 16 i-BTFs each, hold fixed in order to select and isolate regions with high atmospheric transmission and low or moderate OH emission. The three arms are basically identical, selecting the spectral bands from blue to red.
 - b. Four tunable i-BTFs which selects 4 tunable spectral ranges in regions not covered by the fixed i-BTFs. This adds flexibility to the final spectral coverage covered by the instrument, depending on the science case. These 4 tunable i-BTFs are in practice located in front of the 3 arms of 16 i-BTFs.

As presented in Figure 4-bottom each VPH has one 4kx4k CCD associated to it. The central input light beam before the tunable filter contains the whole spectrum. The Airy function (or Dirac comb) is transmitted (Finesse 20) during the scanning process and the whole spectrum is transmitted. Each i-BTF extracts a spectral band on the 0-order beam. Table 6 summarizes the inputs parameters considering a 42 m ELT.

Table. 6. The inputs parameters for the Holographic-Tunable Filter concept.

FOV (arcsec ²)	4'x4' AO Corrected
Telescope Diameter	42m
Spectral Resolution	5000
Spectral coverage	0.8 - 2.46μm (I,J,H,K)
Pixel size	52mas
Detector format	4096x4096
Number of Detectors	52
Number of Scanning i-BTFs	4
Number of Static i-BTFs	48
Number of Tunable Filter	1

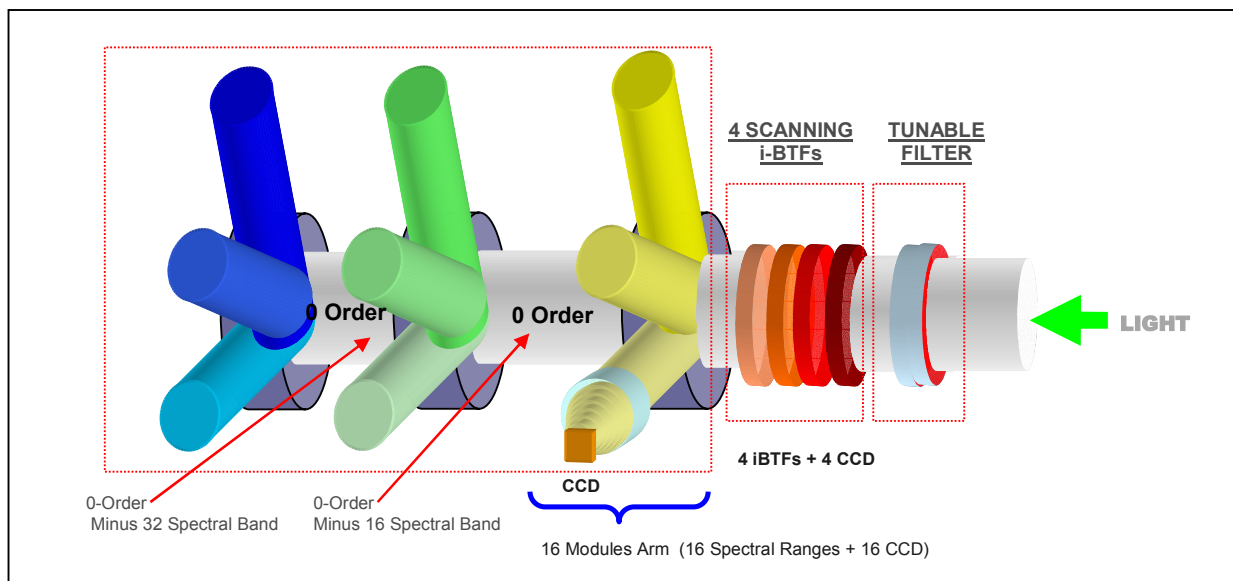
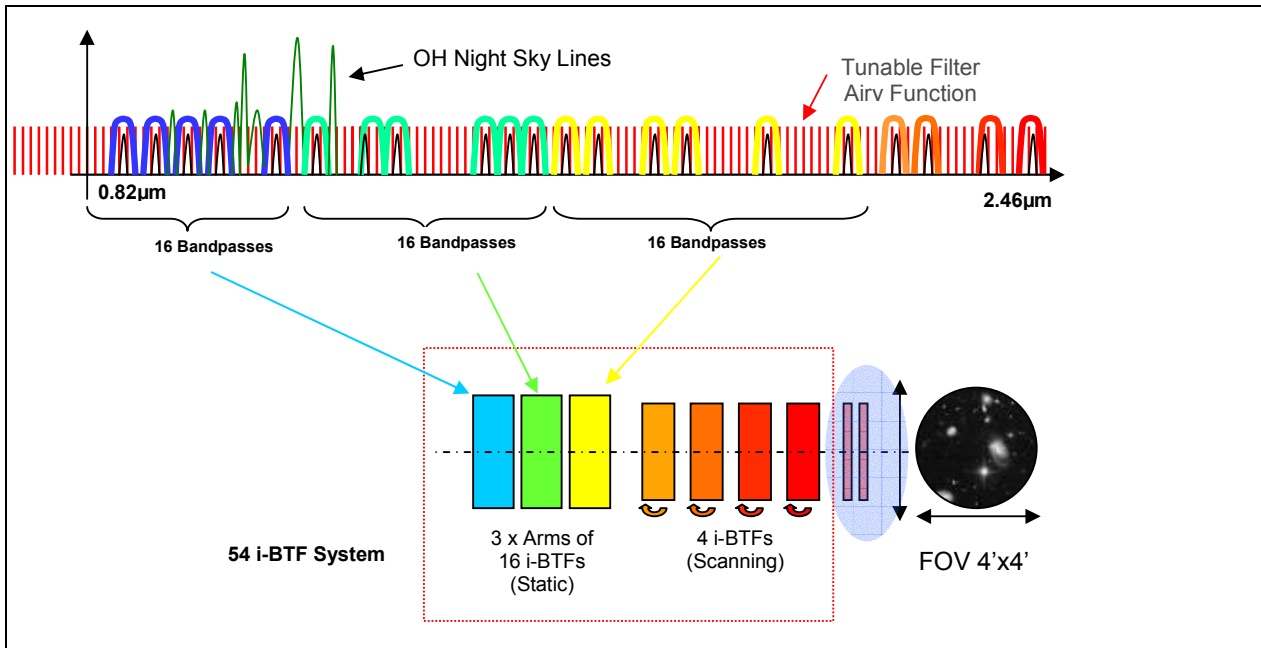


Fig. 4. The Holographic-Tunable Filter Instrument. Top: fifty-two spectral bands (blue, green, yellow and red curves) are selected in between the main OH night sky lines (green lines) already lowered by an *ad hoc* OH-suppression filter⁷. Bottom: imaging Bragg Tunable Filters (i-BTFs): The light is coming from the right (green arrow) and reaches successively: (1) the tunable filter (2) the 4 scanning i-BTFs (3) the first module containing 16 arms. Each arm contains one i-BTF and one 4kx4k CCD. The second and third modules are identical to the first one, except that they select the bluer regions of the spectrum. Note: The central beam before the tunable filter contains the whole spectrum. The Airy function is transmitted (Finesse 20), during the scanning process, the whole spectrum is transmitted. Each i-BTF extracts a spectral band on the 0-order beam.

4. CONCLUSIONS

We have presented 3 different conceptual designs for a wide field ELT spectrograph dedicated to the study of the high z Universe and of the mass assembly of galaxies across cosmic times. The concepts are: monolithic IFU, multi-IFU, and a holographic-tunable filter. Work is still in progress to evaluate each solution in terms of risks and mitigations and provide a factor of merit for the various science cases. After this is done, further work will continue for a detailed study of one concept, possibly two if the concepts allow to cover other science cases.

ACKNOWLEDGEMENTS

This work was supported by CNRS/INSU and by the European Community (Framework Programme 6, ELT Design Study, contract No 011863).

REFERENCES

1. C R Cunningham, E. Atad-Ettdgui, R. Bacon, B. Brandl, J-G Cuby, G. Dalton, W. Dent, S. D'Odorico, I. Egan, C. Evans^a, F. Hammer, N. Hubin, P. Jagourel, F. Kerber, R. Lenzen, I. Montilla, G. Moretto, S. Morris, E. Prieto, A. Quirrenbach, M. Redfern, O. Ryan, M. Strachan and C. Verinaud, "*ELT Instrument Concepts: Impact on Telescope and Adaptive Optics Design*", In this conference SPIE 6269-65, Orlando, USA, 2006.
2. Cuby J.-G., Kneib J.-P., Hammer F., Prieto E., Marteaud M., Vola P., Jagourel P., Blanc P.-E., Fusco T., The First Galaxies: Instrument requirements and concept study for OWL, 2005, Proc. IAUS 232
3. Bacon et al., Probing unexplored territories with MUSE, a second generation instrument for the VLT. These proceedings, 6269-19
4. Le Louarn, M., "*Preliminary AO simulations for a 30-60 m ELT*". Internal Note, 2006
5. Cuby J.-G., Kneib J.-P., Prieto E., Blanc P.-E., Marteaud M., Vola P., Jagourel P., Hammer F., Fusco T., MOMFIS, the Multi-Object IR Spectrograph for OWL, 2005, Proceedings of the Ringberg workshop on Instrumentation for Extremely Large Telescopes, <http://www.mpia-hd.mpg.de/ELT/Manuscripts/Cuby.pdf>
6. Blais-Ouellette et al., The imaging Bragg Tunable Filter, 2006, these proceedings, 6269-200
7. Blais-Ouellette et al., Atmospheric lines suppressing filters: toward a mature technology, 2006, these proceedings, 6269-63

Annexe B

Aide du programme utilisé pour réduire les données Fabry-Perot présentées au chapitre 2

Résumé

B.1 Le programme principal : <code>computeeverything</code>	277
B.2 Quelques autres programmes	283

Au cours de cette thèse, le programme de réduction écrit en langage IDL a été amélioré et utilisé pour la réduction des données GHASP présentées dans le chapitre 2. J'ai donc mis le manuel d'utilisation à jour dans une version traduite en anglais présentée dans cette annexe. Actuellement, ce programme de réduction ne gère que les données acquises par les caméras à comptage de photons. Pour les données obtenues avec une caméra CCD, il est donc nécessaire de créer préalablement un cube de données en utilisant par exemple le logiciel "ADHOCw".

B.1 Le programme principal : `computeeverything`

The main procedure is called **`computeeverything`**. By launching this procedure, all the steps of the reduction will be managed :

- Integration of observation files (.ada) ;
- Creation of a wavelength calibration phase map from calibration observations ;
- Wavelength calibration of the cube ;
- Spectral smoothing of the cube ;
- Spectral correction of the cube using night sky spectrum from the cube itself ;
- Night sky spectrum subtraction ;
- Adaptive binning and/or spatial smoothing of the data cube ;
- Construction of kinematical maps (continuum, line flux, radial velocity, velocity dispersion) ;
- Computation of the astrometry for all the products using "Karma/Koords" software (semi-automatic) ;
- Correction of the free spectral range uncertainty ;
- Cleaning of the maps ;
- Automatic adjustment of a data cube from a user modified velocity field.

B.1.1 Description des options de computeeverything

The syntax to call the procedure is :

pro computeeverything, dir, cieldir, calibdir, adadir, conffile = conffile, name = name, astron = astron, plot = plot, fits = fits, correctguiding = correctguiding, guidingnobreak = guidingnobreak, ignorecycle = ignorecycle, spectral_smooth = spectral_smooth, snr = snr, targetsn = targetsn, fwhm = fwhm, remove_sky = remove_sky, ohmap_remove_sky = ohmap_remove_sky, ohmap_degree = ohmap_degree, maps = maps, clean = clean, manual_clean = manual_clean, fsr=fsr, align = align, thresholdalign = thresholdalign, maxalign = maxalign, passalign = passalign, coadd = coadd, continuumflat = continuumflat, noflat = noflat, autorvmonolevel = autorvmonolevel, expand = expand, adjustrv_nosmooth = adjustrv_nosmooth, tryhard_voro = tryhard_voro, calibadhoc = calibadhoc, startfromneb = startfromneb, adacielfdir = adacielfdir, scalefactorciel = scalefactorciel, exit_at_end = exit_at_end

The most important options of this procedure can be summarized in a configuration file (fits header format) produced by the user friendly Qt based program **reducWizard** available at <http://www.astro.umontreal.ca/~odaigle/reduction>. This program uses information given by the user and can also use information stored in observation files (.adt and .adp files). Thus the syntax become lighter :

pro computeeverything, conffile = conffile, align = align, thresholdalign = thresholdalign, maxalign = maxalign, passalign = passalign, coadd = coadd, continuumflat = continuumflat, noflat = noflat, autorvmonolevel = autorvmonolevel, expand = expand, adjustrv_nosmooth = adjustrv_nosmooth, tryhard_voro = tryhard_voro, calibadhoc = calibadhoc, startfromneb = startfromneb, adacielfdir = adacielfdir, scalefactorciel = scalefactorciel, exit_at_end = exit_at_end

For clarity, are first presented options that can be set using **reducWizard** facility. The location for setting the parameters is given in italic between brackets :

- **conffile** : String variable containing the name of the configuration file created by **reducWizard**.
- **name** : String variable containing the name of the object (*Params / Object name*). Note that it will be used for astrometry purpose only.
- **dir** : String variable containing the directory name in which the products of the data reduction are stored (*Data / Output directory*). This directory should contain an .adp file with the information about the observation when no configuration file created by **reducWizard** is not used.
- **calibdir** : String vector variable containing the directory names where are stored the raw calibration files (*Data / Calibration directory, directories separated by a coma*).
- **adadir** : String variable containing the directory name in which the raw data is stored (*Data / Observation directory*).
- **cielfdir** : String variable containing the directory name in which are located subdirectories with the calibration and the observation. This keyword is used for convenience, in order to avoid to have to specify the whole path twice for the two keywords **calibdir** and **adadir**. When using **reducWizard**, the whole path is automatically given in **adadir** and **calibdir**.
- **astrom** : Binary value specifying that astrometry during the reduction is desired (*Data / Misc / Semi-automatic astrometry (through koords)*). The astrometry is performed using the software “Koords” from “Karma” package. The user will have to interact manually with “Koords”. However, reference XDSS data is automatically downloaded from DSS server. Be sure to have an internet connexion and to have provided a correct name for your object or to download reference images by yourself previously. Default is 0 : no astrometry.

- **plot** : Binary value indicating that maps and graphics have to be displayed (1) or not (0) during the reduction (*Data / Misc / Plot while working*). Note that setting this option to 0 is problematic with options requiring user to interact. Default is 0.
- **fits** : Binary value indicating that files must be save in fits format (1) or in “ADHOCw” format (0) (*Data / Misc / Output to fits files (instead of AD ? files)*). Default is 0, i.e. “ADHOCw” format.
- **correctguiding** : Binary value setting the telescope guiding error correction option (*Data / Integration / Guiding correction*). Set to one if guiding correction is required during integration of observation files (.ada). In that case, user is asked to choose at least three reference stars on the first cycle, the instructions are written in IDL terminal. If not enough stars are present, the guiding correction can be aborted by middle clicking and the configuration file (if used) will be updated accordingly. The position of the reference stars are stored in stars.ad1 file. The file format is : line 0 : x first star position, line 1 : y first star position, line 2 : x second star position, etc. Default is 0 : no guiding correction.
- **guidingnobreak** : Binary value specifying if a step of the guiding system has happened during the observation (*also Data / Integration / Guiding correction*). This was frequently at Mont Megantic Observatory, Canada, during observations of SINGS sample. Set to 0 if a step happened. Default is 1 : no step.
- **ignorecycle** : Vector of integers indicating the cycles to ignore during the integration process of raw data (*Data / Integration / Cycles to ignore separated by a coma*).
- **spectral_smooth** : Spectral smoothing options (2-elements vector). A post wavelength calibration spectral smoothing can be done (first element) (*Data / Spectral / Neb spectral smoothing*). Spectral smoothing is usually done after the wavelength calibration (second element) (*Data / Spectral / Lambda spectral smoothing*). Set to 0 for no spectral smoothing, to 1 for a hanning spectral smoothing, to 2 for a three channels gaussian smoothing. Default is [0,1] : hanning spectral smoothing after the calibration.
- **spatial_smooth** : Spatial smoothing options (2-elements vector). A post wavelength calibration spatial smoothing can be done (first element) (*Data / Spatial / Neb spatial smoothing*). However spatial smoothing is usually done after the wavelength calibration (second element) (*Data / Spatial / Lambda spatial smoothing*). Set to 0 if no spatial smoothing, to 1 if the voronoi adaptive binning technique have to be used (not available before wavelength calibration), to 2 for a 3×3 pixels binning or to 4 for a two dimension gaussian smoothing. Default is [0,0] : no spatial smoothing.
- **snr** : Signal to noise ratio definition for voronoi adaptive binning (*Data / Spatial / SN method*). Five definitions are available :
 - (1) $\frac{line_flux}{\sqrt{line_flux+line_width_continuum^2}}$, (2) $\frac{line_flux}{line_width_continuum}$, (3) $\frac{barycenter_heigth}{\sigma_continuum}$,
 - (4) $\frac{line_flux}{\sqrt{pixel_flux}}$: the pixel flux is the sum of all the channels of the original data cube (without any correction), (5) $\sqrt{line_flux}$: it is a poissonnian like signal to noise ratio definition. Default is 1.
- **targetsn** : Target signal to noise ratio for voronoi adaptive binning (*Data / Spatial / SN*). Default is 5.
- **fwhm** : Full width at half maximum in pixels of the two dimension gaussian smoothing (*Data / Spatial / FWHM*). This is a 2-elements vector, the first element used for the post wavelength calibration smoothing, and the second for the last smoothing. Default is [2,3].
- **remove_sky** : Binary value specifying if sky spectrum has to be removed from the data cube (*Data / Sky / Sky subtraction*). 0 : no. 1 : yes. Default is 1.
- **ohmap_remove_sky** : Method specifying the method that has to be used to subtract the sky (*also Data / Sky / Sky subtraction*). Four methods are possibles. (1) Median spectrum ; (2) Sky cube polynomial fitting ; (3) Sky from the interferograms (non wavelength calibrated data cube),

usual method for Tunable Filter data. Better if no smoothing before the wavelength calibration is done ; (4) Sky cube interpolation. For photon counting camera data, (2) usually gives the best results. Default is 1.

- **ohmap_degree** : Degree of the polynomial sky cube fitting (*Data / Sky / Polynomial degree*). Default is 4.
- **maps** : 3-elements binary vector. First element : Total line width map (*Data / Maps / Total width*). Second elements : Dispersion in the continuum map (*Data / Maps / Continuum sigma*). Third element : Barycenter height (*Data / Maps / Barycenter height*). Set to 1 for desired maps. Default is [0,0,0] (none of these maps).
- **clean** : Binary value indicating if cleaning is desired (*Data / Maps / Clean maps*). Set to 1 to try cleaning. Default is 0.
- **manual_clean** : Binary value indicating whether regions for cleaning are given by the user (1) or are computed automatically (0) (*Data / Maps / Manually choose regions*). Default is 0.
- **fsr** : Binary value indicating whether free spectral range jumps may be corrected (1) or not (0) (*Data / Maps / Correct FSR jumps*). In the case the correction is requested, user is prompted to define a polygonal region by clicking on the map. When the region is selected, the user may indicate if the free spectral range has to be added (+) or subtracted (-). The map is then updated and the user can choose another region if necessary by answering the prompt. Default is 1.

The other options are only available using command line or using the option available in *Data / Misc / Use modified launch command* with **reducWizard**. They are presented hereafter :

- **align** : Binary value that specifies that a spectral correction using sky spectrum has to be done. 0 : no. 1 : yes. Default is 0.
- **thresholdalign** : Cross correlation factor value beyond which a spectrum is considered to be dominated by sky spectrum. Cross correlation is done with respect to the data cube median spectrum. The value must range from 0 to 1. Default is 0.9.
- **maxalign** : Maximum spectral correction in channel that can be done by the spectral correction routine. Value must range from 2 and the number of spectral channels of the data cube. Default is the number of spectral channels.
- **passalign** : Maximum number of iterations for spectral correction using sky cube. The value must be greater than 0. Usually, the algorithm should converge in two or three iterations. Default is 20.
- **coadd** : Binary value that specifies if the directory dir contains a data cube that have been coadded (using the routine `coadd_lambda_files`). 0 : no. 1 : yes. When this option is set, only cube whose name contains the string `-coadd` are used. Default is 0.
- **continumflat** : During spectral correction using sky cube, this option tells the routine that the *flat* must be computed using the continuum level of each sky pixel (1) or that it must be computed using the data cube itself where it is not dominated by the object (0). Default is 0.
- **noflat** : This option tells that no flat has to be applied on the data cube (1) during the spectral correction using sky cube. Otherwise, the cube is corrected (0). Default is 1.
- **autorvmonolevel** : Monochromatic flux beyond which an automatic search of emission lines correlated with the brightest neighbor lines has to be done.
- **expand** : By default, the adaptive binning routine using only regions where calibration is considered as valid in order to eliminate vignetted areas. However, when using coadded cubes, this masking is no more valid. If the program `coaddlambdafiles` has been used with the option `expand = 1`, this keyword has to be set to 1.
- **tryhard_voro** : Adaptive binning algorithm accretes spectra in order to reach the requested signal to noise. However, it happens that the signal to noise diminishes when adding a new spectrum. This event makes the bin aborted and all the pixels of this bin are excluded for further

bin accretion. Setting this parameter to 1 makes the previous pixels still usable (but not the one that made the signal to noise ratio diminish in order to avoid an infinite loop on its spectrum) but increases the computing time. Default and recommended is 1.

- **calib_adhoc** : If one wants to use a calibration computed using “ADHOCw”, this parameter must be set to one, and the file Phas_prb.AD2 must be present in the object directory. Otherwise, the calibration is computed by the data reduction software (0). Default is 0.
- **startfromneb** : This option is particularly important since it enables to avoid the integration steps and to start from a non wavelength calibrated cube (has to be used for CCD observations instead of photon counting cameras). The cube must be called neb.ad3, be present in the object directory and the parameter must be set to one. Default is 0.
- **adaciendir** : Specifies the directory in which are located observation files of the sky (when a sky has been observed, for instance because the object covers the whole field of view). By default, the sky is computed from the object cube.
- **scalefactorciel** : This option must be used when the previous option is used. It tells the program how to compensate the integration time between object and sky observations. For instance, if the object has been observed twice the time for the sky, this parameter has to be set to 2.
- **exit_at_end** : This option make the program quit IDL at the end of execution. Default is 0. When the reduction is launch from **reducWizard**, this keyword is set to 1.

B.1.2 Exemple d'utilisation de computeeverything

computeeverything, 'ngc5713', '/home/user/observations/ciel', ['M282', 'M284'], 'M283', targetsn = 7, spatial_smooth = [0,1], align = 1, plot = 1, correctguiding = 1, spatial_smooth = [0,0], ignorecycle = [5, 6, 8].

This calling sequence of **computeeverything** proceeds to the data reduction of observations located in **/home/user/observations/ciel/M283** directory, using calibrations placed in **/home/user/observations/ciel/M282** and **/home/user/observations/ciel/M284**. Cycles 5, 6 and 8 are discarded. A guiding correction will be done (**correctguiding = 1**) during the integration of observation data without searching for a guiding break (since **guidingnobreak** is set to 1 by default). The integrated data cube is then calibrated in wavelength before a hanning spectral smoothing is applied on the data (by default **spectral_smooth** is set to [0,1]). The data cube wavelength calibration is calibrated by using sky lines (**align = 1**). The next step is the subtraction of a sky cube computed from a 4 degrees polynomial fit (default is **remove_sky = 1**, **ohmap_remove_sky = 1** and **ohmap_degree = 4**). Then an adaptive spatial binning with a target signal to noise ratio of 7 is done (**spatial_smooth = [0,1]** and **targetsn = 5**), and the maps are created. The following files are created :

- **calibration.ad3** : Calibration cube resulting from the addition of the two calibrations located in **M282** and **M284**.
- **cal_prb.ad2, cal_bru.ad2, cal_sum.ad2, cal_rv.ad2, cal_cen.ad1, cal_finesse.ad1, cal_valid.fits** : Files extracted from the calibration cube. **cal_prb.ad2** : parabolic phase file used to convert an interferogram cube into a wavelength ordered cube. **cal_bru.ad2** : raw phase file that contains the position in channel of the calibration line barycenter. **cal_sum.ad2** : File containing the sum of the spectrum for each pixel of the calibration cube. **cal_rv.ad2** : Position of the calibration line barycenter after applying the calibration to the calibration cube itself in order to check the validity of the parabolic phase. **cal_cen.ad2** : Position (x,y) of the center of the calibration rings. **cal_finesse.ad2** : Finesse computed in the whole calibration cube. **cal_valid.fits** : Mask indicating where the calibration is valid in order to eliminated vignettted areas.

- **neb.ad3** : Interferogram data cube obtained from the integration of the observation data located in **M283**.
- **adasort.txt** : File containing the rejected channels and cycles during integration.
- **valid_reg.fits** : Mask indicating where the observation is valid in order to eliminate vignettted areas due to filters.
- **stars.ad1** : File storing the position of stars used for guiding correction.
- **lambda.ad3** : Wavelength calibrated cube after applying the parabolic phase correction to **neb.ad3**.
- **lambda-SZ1.ad3** : Data cube after hanning spectral smoothing.
- **lambda-SZ1-aligned.ad3** : Data cube after alinement using sky lines.
- **lambda-SZ1-aligned-OHmap.ad3** : Sky subtracted data cube.
- **iciel.ad3** : Sky cube.
- **ohmap-SZ1.ad2** : Mask indicating the regions from which the sky cube as been computed.
- **lambda-SZ1-aligned-OHmap-sn07-binned.ad3** : Cube on which have been applied the adaptive binning with a signal to noise ratio of 7. This cube contains the raw result of bin accretion.
- **lambda-SZ1-aligned-OHmap-sn07.ad3** : Cube lambda-SZ1-aligned-OHmap-sn07-binned.ad3 on which a Delaunay triangulation has been applied in order to smooth bin edges.
- **lambda-SZ1-aligned-OHmap-sn07-binned-adjusted.ad3** : Cube lambda-SZ1-aligned-OHmap-sn07-binned.ad3 on which an automatic search of emission lines in low line flux regions has been done using correlation with neighbor strong emission lines.
- **lambda-SZ1-aligned-OHmap-sn07-adjusted.ad3** : Cube lambda-SZ1-aligned-OHmap-sn07-binned-adjusted.ad3 on which a Delaunay triangulation has been applied in order to smooth bin edges.
- **rv-SZ1-aligned-OHmap.ad2, mono-SZ1-aligned-OHmap.ad2, cont-SZ1-aligned-OHmap.ad2, disp-SZ1-aligned-OHmap.ad2** : Radial velocity (**rv**), line monochromatic flux (**mono**), continuum (**cont**) et velocity dispersion (**disp**) maps extracted from the cube lambda-SZ1-aligned-OHmap.ad3.
- **rv-SZ1-aligned-OHmap-sn07-binned.ad2, mono-SZ1-aligned-OHmap-sn07-binned.ad2, cont-SZ1-aligned-OHmap-sn07-binned.ad2, disp-SZ1-aligned-OHmap-sn07-binned.ad2** : Radial velocity (**rv**), line monochromatic flux (**mono**), continuum (**cont**) et velocity dispersion (**disp**) maps extracted from the cube lambda-SZ1-aligned-OHmap-sn07-binned.ad3.
- **rv-SZ1-aligned-OHmap-sn07.ad2, mono-SZ1-aligned-OHmap-sn07.ad2, cont-SZ1-aligned-OHmap-sn07.ad2, disp-SZ1-aligned-OHmap-sn07.ad2** : Radial velocity (**rv**), line monochromatic flux (**mono**), continuum (**cont**) et velocity dispersion (**disp**) maps extracted from the cube lambda-SZ1-aligned-OHmap-sn07.ad3.
- **rv-SZ1-aligned-OHmap-sn07-binned-adjusted.ad2, mono-SZ1-aligned-OHmap-sn07-binned-adjusted.ad2, cont-SZ1-aligned-OHmap-sn07-binned-adjusted.ad2, disp-SZ1-aligned-OHmap-sn07-binned-adjusted.ad2** : Radial velocity (**rv**), line monochromatic flux (**mono**), continuum (**cont**) et velocity dispersion (**disp**) maps extracted from the cube lambda-SZ1-aligned-OHmap-sn07-binned-adjusted.ad3.
- **rv-SZ1-aligned-OHmap-sn07-adjusted.ad2, mono-SZ1-aligned-OHmap-sn07-adjusted.ad2, cont-SZ1-aligned-OHmap-sn07-adjusted.ad2, disp-SZ1-aligned-OHmap-sn07-adjusted.ad2** : Radial velocity (**rv**), line monochromatic flux (**mono**), continuum (**cont**) et velocity dispersion (**disp**) maps extracted from the cube lambda-SZ1-aligned-OHmap-sn07-adjusted.ad3.
- **binSize-SZ1-aligned-OHmap-sn07.ad2** : Map indicating for each pixel the size of the bin to which it belongs for an adaptive binning with a target signal to noise of 7.
- **binnum-SZ1-aligned-OHmap-sn07.ad2** : Map indicating for each pixel the index of the bin to which it belongs for an adaptive binning with a target signal to noise of 7.
- **binCentroid-SZ1-aligned-OHmap-sn07.ad2** : Mask indicating the centroids of the bins for an

adaptive binning with a target signal to noise of 7. There is one point per bin.

- **signal-SZ1-aligned-OHmap-sn07.ad2** : Signal map for an adaptive binning with a target signal to noise of 7.
- **noise-SZ1-aligned-OHmap-sn07.ad2** : Noise map for an adaptive binning with a target signal to noise of 7.
- **sn-SZ1-aligned-OHmap-sn07.ad2** : Signal to noise ratio map for an adaptive binning with a target signal to noise of 7.
- **skyflat.ad2** : Amplitude correction applied on the cube when alining with sky lines (for creating lambda-SZ1-aligned.ad3).
- **offset.ad2** : Spectral correction (expressed in spectral channels) applied on the cube when alining with sky lines (for creating lambda-SZ1-aligned.ad3).

B.2 Quelques autres programmes

B.2.1 Addition de cubes de données

Two routines are available to perform this job.

B.2.1.1 Solution 1 : **coaddlambdfiles**

This procedure can be used in order to add two data cubes. Cubes must be observed with the same interferometer since no spectral adjustment is done (only a translation). The procedure can find the spatial and spectral translations to perform in order to add two cubes by itself. When the cubes have only few common information, a file called **alignzone.adz** can be created in the directories of both cubes to add. The zone defined in each files should correspond approximately to the same zone on the galaxy. The translation is then computed from this zone.

The calling sequence of the procedure is

coaddlambdfiles, *dirs*, *align = align*, *remove_sky = remove_sky*, *spectral_smooth = spectral_smooth*, *ohmap_remove_sky = ohmap_remove_sky*, *expand = expand*.

The options are the following :

- **dirs** : Directories in which is stored the data. At least two directories have to be specified. The result is created in the first directory.
- **align**, **remove_sky**, **ohmap_remove_sky**, **spectral_smooth**, : These option must be identical to the one used to create the cube by **computeeverything**. They are used by **coaddlambdfiles** in order to find which cube to add.
- **expand** : By default, **coaddlambdfiles** creates files with the same size as the file of the first directory. When addition is done in order to enlarge the field of view, this option must be set to one.

B.2.1.2 Solution 2 : **addcubesastrometry**

This procedure has been developed since the astrometry has been integrated to the reduction pipeline. It uses this information in order to recover the translations needed to add the cubes. It also

uses information stored in cubes header in order to compute the translation needed in the spectral direction.

The calling sequence of the procedure is

addcubesastrometry, *dir1*, *dir2*, *diradd*, *filename*.

The options are the following :

- **dir1** : Directories in which is stored the first cube.
- **dir2** : Directories in which is stored the second cube.
- **diradd** : Directories in which is computed the added cube.
- **filename** : Name of the files to be added that have to be the same for both cubes. It is also the name of the added cube but with the string **-coadd** before the extension.

B.2.1.3 Protocole à suivre pour l'addition de cubes

Before adding cubes, it is necessary to create them in an identical way. Here is an example for the reduction of galaxy NGC 5033. Since it has been observed using two different interference filters, the cubes have to be added before applying the last steps of reduction (adaptive binning, maps extraction, ...).

computeeverything, 'ngc5033-1', '/home/user/observations/ciel', ['W021', 'W024'], 'W022', *spectral_smooth* = [0,1], *align* = 1, *plot* = 1, *correctguiding* = 1, *spatial_smooth* = [0,0].

computeeverything, 'ngc5033-2', '/home/user/observations/ciel', ['W021', 'W024'], 'W023', *spectral_smooth* = [0,1], *align* = 1, *plot* = 1, *correctguiding* = 1, *spatial_smooth* = [0,0].

coaddlambdafiles, ['ngc5033-1', 'ngc5033-2'], *align* = 1, *spectral_smooth* = 1

or

addcubeastrometry, 'ngc5033-1', 'ngc5033-2', 'ngc5033-1', 'lambda-SZ1-aligned-OHmap.ad3'

computeeverything, 'ngc5033-1', '/home/user/observations/ciel', ['W021', 'W024'], 'W022', *spectral_smooth* = [0,1], *align* = 1, *plot* = 1, *correctguiding* = 1, *spatial_smooth* = [0,1], *tryhard_voro* = 1, *targets_n* = 7, *coadd* = 1

The two first calls to ***computeeverything*** make the basic data reduction for the two observations : integration with guiding correction, hanning spectral smoothing, sky line alignment, sky subtraction. Note that spatial adaptive binning is not done at this stage. The results are respectively stored in **ngc5033-1** and **ngc5033-2** directories.

The call of the two adding functions makes the same job. It uses files **lambda-SZ1-aligned-OHmap.ad3** previously created in directories **ngc5033-1** and **ngc5033-2** and make the addition in directory **ngc5033-1** with the name **lambda-SZ1-aligned-OHmap-coadd.ad3**.

Last call to ***computeeverything*** takes this cube and does the last reduction steps. All the created files will contain the substring **-coadd** in their names.

B.2.2 Soustraction des reflets parasites : **ghost2d** et **ghost3d**

It can happen that observations are affected by ghosts. A ghost subtraction routine is available in order to subtract two kinds of ghosts that are usually present on the data : a focused one and a defocused one. In order to do a clean ghost subtraction, a set of parameters needs to be adjusted by the user. First of all, a full reduction has to be done in order to determine the calibration center (center of the reflections) but also to check the existence of such ghosts. Usually, they are present because of bright line emitting regions. In such a case, the ghost is visible on the velocity field as a symmetrical region with the same velocity. The use of adaptive binning makes the detection of ghost easier. In order to do an accurate subtraction, it is better if the observation contains several bright stars that cause several ghosts.

The procedure is the following in order to adjust the parameters : One must use the routine **ghost2d**. The calling sequence is :

```
result = ghost2d(image = image, center = center, refl1 = refl1, refl2 = refl2, rin = rin, rout = rout,
homot = homot, ex1 = ex1, ey1 = ey1, ex2 = ex2, ey2 = ey2)
```

Here are some explanations about the inputs :

- **image** : This image should be the sum over spectral dimension of the cube **neb.ad3** or **lambda.ad3**. The ghost subtraction will be calibrated using this image.
- **center** : This is the center of reflection. If one is working in the reduction directory, by default the programs search for the center specified in **cal_cen.ad1**, which should be the center for ghosts.
- **refl1** : This is the reflection factor of the focused ghost. By default this parameters is set to 0.01.
- **refl2** : This is the reflection factor of the defocused ghost. By default this parameters is set to 0.1.
- **rin** : The defocused ghost is simply modeled as the pupil of the instrument, that is usually a circular mirror (primary) with a circular obstruction (secondary mirror). This parameter is the radius in pixel of the inner obstruction as observed on the ghost. Default is 10 pixels
- **rout** : This is the radius in pixel of the primary mirror. Default is 38 pixels.
- **homot** : Due to defocus, this reflection is usually not exactly symmetrical to the object. An homothetic factor is then needed to recover correctly the ghost position. Default is 1 (no homothetic).
- **ex1** : It is possible that the center needs to be adjusted for the focused reflection. This is the shift in pixel in x direction.
- **ey1** : This is the shift in pixel in y direction.
- **ex2** : It is possible that the center needs to be adjusted for the defocused reflection. This is the shift in pixel in x direction.
- **ey2** : This is the shift in pixel in y direction.

The function returns the corrected image. The user has to display it in order to check if the subtraction has been done correctly. Ghost parameters have to be adjusted separately for both reflections, by setting the reflection factor of the other reflection to 0. For the focused reflection, one should start to adjust the center (using parameters **ex1** and **ey1**) and then the reflection factor. For the defocused reflection, one should start to adjust the center (using parameters **ex2** and **ey2**) and the homothetic factor. Once it is done, the pupil shape should be adjusted (parameters **rin** and **rout**). Then the reflection factor can be adjusted. Once these adjustments are done, a complete ghost subtraction has to be done, and eventually further adjustments can be made.

The ghost subtraction now needs to be performed on the data cube calibrated in wavelength or not by using the routine **ghost3d**. The calling sequence is :

$result = \mathbf{ghost3d}(cube = cube, center = center, refl1 = refl1, refl2 = refl2, rin = rin, rout = rout, homot = homot, ex1 = ex1, ey1 = ey1, ex2 = ex2, ey2 = ey2)$

The parameters must be set to the values previously determined. The function returns the ghost subtracted data cube that the user has to write using **writefits** or **writead3** functions (depending on the format chosen for reduction). It is better if the header/trailer of the non ghost subtracted cube is attached to the corrected cube. One can now restart data reduction by renaming the corrected cube as the non corrected one. A copy of the non corrected cube should be done for backup in case the subtraction is still not accurate enough. All the products of the reduction after cube creation have to be deleted in order that the reduction starts from the corrected cube.

B.2.3 Autres routines utiles

In this section, the most useful routines for manipulating data are described. All the routines used for data reduction are available on the website <http://www.astro.umontreal.ca/fantommm/reduction>.

- **readad3(file_name, trailer, xyz = re)**. This function returns the cube read from the ad3 file file_name. The cube trailer is put in the variable *trailer* if specified. The trailer has the format of the structure `ad3_trailer`, defined in the file `ad3_trailer__define.pro`. This routine can read gzipped files `.ad3.gz`. The cube is oriented as $[x,y,z]$ when the variable `xyz = 1`. By default, the cube is oriented as $[z,x,y]$ (z is the spectral dimension).
- **writead3(file_name, cube, trailer, data_xyz = dx, write_xyz = dw)**. This function writes the cube `cube` in the `.ad3` file `ad3`, with its trailer if specified in variable `trailer`. If no trailer is specified, a generic trailer is attached to the cube. The keyword `data_xyz` specifies the orientation of the input cube : `data_xyz = 0` means that the orientation is $[z,x,y]$ (default) whereas `data_xyz = 1` means that the orientation is $[x,y,z]$. The keyword `write_xyz` tells how to write the file. When `write_xyz = 0`, the cube is written as $[z,x,y]$ (default). When `write_xyz = 1`, the cube is written as $[x,y,z]$. The file is gzipped when the field `was_compressed` of the `ad3_trailer` structure is set to 1 or if the file name contains the extension `.gz`.
- **readad2(file_name, trailer)** : This function returns the image read from the ad2 file file_name. The image trailer is put in the variable *trailer* if specified. The trailer has the format of the structure `ad2_trailer`, defined in the file `ad2_trailer__define.pro`
- **writead2(file_name, image, trailer)** : This function writes the image `image` in the `.ad2` file `ad2`, with its trailer if specified in variable `trailer`. If no trailer is specified, a generic trailer is attached to the image.
- **readad1(file_name)** : This function reads a `.ad1` file and returns its contents.
- **writead1(file_name, data)** : This function creates a `.ad1` file and writes the contents of the variable `data`.
- **ad3ToFits(ad3, fits, fits_xyz = fx)** : This function converts the `.ad3` file `ad3` into the `.fits` file `fits`. The fits header will be created from the ad3 trailer. The option `fits_xyz` tells how to write the file : `fits_xyz = 0` writes the dimensions as $[z,x,y]$ and `fits_xyz = 1` writes the dimension as $[x,y,z]$. Default is `fits_xyz = 1`.
- **ad2ToFits(ad2, fits)** : This function converts the `.ad2` file `ad2` into the `.fits` file `fits`. The fits header will be created from the ad2 trailer.
- **fitsToAd3(fits, ad3, trailer, ad3_xyz = ax)** : This function converts the `.fits` file `fits` into the `.ad3` file `ad3`. The variable `trailer` contains the trailer that will be happened to the file. The ad3 trailer will be completed with the fits header information. The option `ad3_xyz` tells how to write the file :

ad3_xyz = 0 writes the dimensions as [z,x,y] and ad3_xyz = 1 writes the dimension as [x,y,z]. Default is ad3_xyz = 0.

- **fitsToAd2(fits, ad2, trailer)** : This function converts the .fits file fits into the .ad2 file ad2. The variable trailer contains the trailer that will be happened to the file. The ad2 trailer will be completed with the fits header information.

Annexe C

Détermination des vitesses et des dispersions de vitesses (chapitres 2 et 3)

Résumé

C.1 Détermination des paramètres des spectres à raies d'émission	289
C.2 Des longueurs d'onde aux vitesses	291

Cette annexe explique comment déterminer la vitesse et la dispersion de vitesses à partir d'un spectre d'une raie d'émission : les paramètres de la raie (flux, position, largeur) peuvent être déterminés par la méthode des moments (utilisée pour les données GHASP présentées au chapitre 2 et dans la partie 3.4) ainsi que par la méthode de l'ajustement d'une gaussienne à la raie d'émission (utilisée pour les données SINFONI présentées dans la partie 3.2) ; enfin l'effet Doppler-Fizeau dans le cadre relativiste est utilisé pour convertir les longueurs d'onde en vitesses.

C.1 Détermination des paramètres des spectres à raies d'émission

Les paramètres d'intérêt des spectres à raies d'émission sont le niveau de continuum du spectre, le flux de la raie, sa position et sa largeur qui est généralement définie soit comme sa largeur à mi-hauteur, soit comme sa dispersion (voir Figure C.1). Il existe plusieurs méthodes pour déterminer ces paramètres. Certaines méthodes peuvent prendre en compte les effets d'asymétrie des raies dus à des phénomènes d'absorption liés à l'inclinaison des galaxies, à l'existence de profils doubles ou encore à des profils bruités. Cependant, les méthodes utilisées au cours de cette thèse n'ont pas pris en compte ces effets. En particulier, lorsque l'inclinaison des galaxies était supérieure à 75° , plutôt que d'utiliser la courbe de rotation, nous avons préféré utiliser le diagramme position-vitesse à partir duquel il est possible de mesurer les vitesses en utilisant l'enveloppe externe des profils. Cette partie expose deux méthodes classiques : la méthode des moments, utilisée pour déterminer les cartes cinématiques des données GHASP (parties 2.1 et 3.4), et la méthode d'ajustement d'une gaussienne, utilisée pour les données SINFONI (partie 3.2).

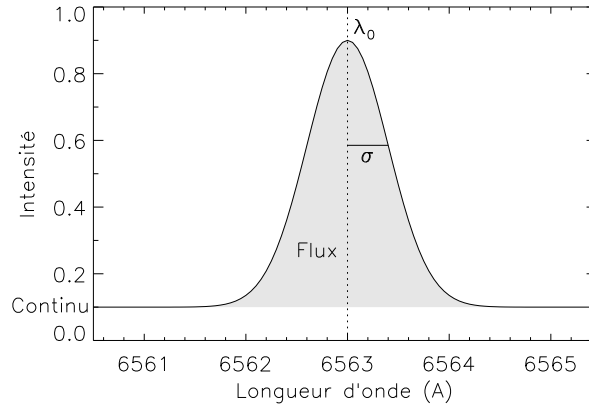


FIG. C.1: Exemple d'une raie d'émission (gaussienne) centrée sur la longueur d'onde $\lambda_0 = 6563 \text{ \AA}$, avec une dispersion $\sigma = 0.4 \text{ \AA}$ et un continuum de 0.1. Le flux de la raie correspond à l'aire grisée.

C.1.1 La méthode des moments

Le spectre S mesuré est discrétisé par l'échantillonnage en longueur d'onde. On peut le décomposer en une raie $R(\lambda_i)$ et un continuum C :

$$S(\lambda_i) = R(\lambda_i) + C$$

Le continuum est généralement estimé à partir des éléments du spectre qui sont hors de la raie : la méthode calcule la moyenne des éléments du spectre dont le flux est inférieur à un seuil. Celui-ci est déterminé à partir du profil : le maximum du profil est mesuré et le seuil correspond à la valeur du flux du premier élément autour de la raie pour lequel le flux remonte.

Une fois le continuum déterminé, on peut calculer les moments de la raie d'émission. Le flux F est alors défini comme étant la somme du flux pour chaque longueur d'onde élémentaire :

$$F = \sum_i R(\lambda_i) = \sum_i \lambda_i^0 R(\lambda_i)$$

Cela correspond à la définition du moment d'ordre zéro de la raie. La longueur d'onde Λ de la raie va être définie comme étant son barycentre, soit sa longueur d'onde moyenne :

$$\Lambda = \frac{\sum_i \lambda_i^1 R(\lambda_i)}{F}$$

Ceci correspond au moment d'ordre un de la raie. La dispersion σ de la raie est l'écart moyen entre chaque longueur d'onde élémentaire du spectre de la raie et le barycentre Λ précédemment défini :

$$\sigma = \sqrt{\frac{\sum_i (\lambda_i - \Lambda)^2 R(\lambda_i)}{F}}$$

La dispersion est ainsi déterminée à partir du moment centré d'ordre deux de la raie. En pratique, pour écourter le temps de calcul, l'algorithme utilisé emploie la relation suivante :

$$\sigma = \sqrt{\frac{\sum_i \lambda_i^2 R(\lambda_i)}{F} - \Lambda^2}$$

On pourrait également calculer les ordres successifs afin de déterminer des paramètres d'asymétrie de la raie. Cependant, plus l'ordre est élevé, plus il est nécessaire d'avoir un spectre de bonne qualité. Cette méthode possède l'avantage de ne rien présupposer sur le spectre, en particulier sur sa symétrie.

C.1.2 Ajustement d'une gaussienne

Généralement, le spectre de raies d'émission est relativement bien décrit par une fonction gaussienne. Ainsi, on ajuste le spectre par une fonction gaussienne superposée à un continuum C :

$$S(\lambda) = I_0 \exp - \frac{(\lambda - \Lambda)^2}{2\sigma^2} + C$$

où I_0 est le maximum de la raie, Λ est la position de la raie et σ est la dispersion en longueur d'onde de la raie. Ce sont les paramètres libres à ajuster par la méthode des moindres carrés. Le flux F est égal à l'intégrale de la fonction gaussienne :

$$F = I_0 \sigma \sqrt{2\pi}$$

On relie également la largeur à mi-hauteur $FWHM$ à la dispersion de vitesses :

$$FWHM = 2 \sqrt{2 \ln 2} \sigma$$

Cette méthode possède l'avantage d'être moins sensible au rapport signal sur bruit. Par contre, cette méthode suppose que la raie est symétrique, ce qui n'est pas forcément le cas. Cependant, cette méthode a été principalement utilisée pour des données SINFONI (section 3.2) dont la faible résolution spectrale induit une symétrisation des profils. De plus, il est plus aisé d'effectuer les corrections de la réponse instrumentale pour déterminer la dispersion de la raie. En effet, si on considère que la réponse instrumentale ainsi que le profil réel sont gaussiens, alors le profil observé est la convolution de deux gaussiennes. On montre alors que ce profil est également gaussien et que sa largeur est la somme quadratique des largeurs respectives de ces gaussiennes. Cette correction quadratique est largement utilisée, même lorsque la dispersion de vitesses n'est pas déterminée à partir de cette méthode.

Un autre avantage de cette méthode est que le bruit du spectre peut être pris en compte pour l'ajustement. Il est également possible d'ajuster simultanément plusieurs raies d'émission en supposant que ces raies ont toutes les mêmes caractéristiques, ce qui peut accroître la précision de l'estimation.

C.2 Des longueurs d'onde aux vitesses

Le passage des longueurs d'onde aux vitesses est possible grâce l'effet Doppler-Fizeau. Étant donné que l'un des objets de cette thèse est l'étude de galaxies lointaines, les effets relativistes doivent être pris en compte pour déterminer les vitesses. L'effet Doppler-Fizeau doit alors être déterminé à partir des lois de la relativité restreinte.

C.2.1 L'effet Doppler-Fizeau

L'effet Doppler est un phénomène généré par le déplacement de la source d'une onde par rapport à un observateur. Il est dû à la vitesse de propagation finie de l'onde et est nommé effet Doppler-Fizeau dans le cas d'ondes lumineuses. L'effet Doppler-Fizeau relie la fréquence émise par la source

v_0 et la fréquence mesurée par le récepteur v_m selon l'expression générale :

$$v_0 = v_m \frac{\sqrt{1 - \beta^2}}{1 + \beta \cos \theta} \quad (\text{C.1})$$

$\beta = V/c$ où V est la vitesse relative de la source par rapport au récepteur, c est la célérité de la lumière et θ est l'angle formé entre la ligne de visée et la direction propre du mouvement.

Habituellement, les mouvements relativistes sont dus à l'expansion de l'Univers et se font principalement le long de la visée. On utilise donc la formule de l'effet Doppler-Fizeau longitudinal ($\theta = 0$) :

$$v_0 = v_m \sqrt{\frac{1 - \beta}{1 + \beta}} \quad (\text{C.2})$$

Pour nos applications, il est nécessaire d'exprimer la vitesse V en fonction de la longueur d'onde mesurée $\lambda_m = c/v_m$ et de la longueur d'onde au repos $\lambda_0 = c/v_0$. On obtient à partir de l'équation C.2 :

$$V = c \frac{(z + 1)^2 - 1}{(z + 1)^2 + 1} \quad (\text{C.3})$$

où z est le décalage spectral : $z = \frac{\lambda_m - \lambda_0}{\lambda_0}$.

C.2.2 Loi de composition des vitesses

Lorsqu'on observe la cinématique des galaxies, les vitesses mesurées correspondent à la composition d'un mouvement d'éloignement global de la galaxie et de mouvements internes à la galaxie. Il est nécessaire de prendre en compte le changement de référentiel afin d'avoir une détermination correcte des vitesses.

C.2.2.1 Le décalage spectral est faible

Lorsque le décalage spectral est faible ($z \ll 1$), l'équation C.3 se simplifie :

$$V = c \times z \quad (\text{C.4})$$

Cela correspond donc au cas où la vitesse est faible. Dans ce cas, la composition des vitesses peut se faire dans l'approximation Newtonienne et la vitesse observée est simplement la somme de la vitesse d'entraînement et de la vitesse dans le référentiel de la galaxie.

C.2.2.2 Le décalage spectral est important

Des galaxies dont le décalage spectral est supérieur à 1 sont présentées dans la partie 3.2. Pour ces galaxies, il est nécessaire de faire la composition des vitesses en utilisant les lois de la relativité restreinte. Notons λ_0 la longueur d'onde au repos de la raie observée. Notons V les vitesses, λ les longueurs d'onde et $z = \frac{\lambda - \lambda_0}{\lambda_0}$ les décalages spectraux. L'indice e indique qu'il s'agit de valeurs correspondant à l'entraînement et l'indice m est réservé aux valeurs mesurées. Enfin, notons V_r la vitesse dans le référentiel de la galaxie observée (r pour relative). Toutes les vitesses sont des vitesses le long de la ligne de visée.

Les lois de composition des vitesses de la relativité restreinte donnent :

$$V_r = \frac{V_m - V_e}{1 - \frac{V_m V_e}{c^2}} \quad (\text{C.5})$$

On peut écrire l'équation C.3 pour V_e et V_m et ainsi obtenir en utilisant l'équation C.5 après simplification :

$$V_r = c \frac{(z_m + z_e + 2)(z_m - z_e)}{(z_m + 1)^2 + (z_e + 1)^2} \sim c \frac{z_m - z_e}{1 + z_e} \quad (\text{C.6})$$

Ce qui donne en termes de longueurs d'onde :

$$V_r \sim c \frac{\lambda_m - \lambda_e}{\lambda_e} \quad (\text{C.7})$$

L'équivalence finale provient du fait que les mouvements dans la galaxies sont d'amplitude négligeable par rapport à la vitesse d'éloignement.

Finalement, tout se passe comme si la longueur d'onde au repos était λ_e au lieu de λ_0 . Il n'y a qu'une dilatation du spectre.

C.2.3 Dispersion de vitesses

Étant donné que la largeur de raie naturelle est négligeable par rapport à la réponse impulsionnelle spectrale des spectrographes utilisés et que cette même réponse impulsionnelle est inférieure à la largeur de raie observée, cette dernière s'explique par une dispersion de vitesses le long de la ligne de visée. La dispersion de vitesses est donc directement liée à la dispersion de la raie en longueur d'onde. Il est alors légitime d'exprimer la dispersion de la raie en unité de vitesses. En différenciant l'équation C.7 par rapport à la variable λ_m on obtient :

$$dV_r \sim c \frac{d\lambda_m}{\lambda_e} \quad (\text{C.8})$$

Dans certains cas, plusieurs raies sont observées. Elles peuvent alors être utilisées simultanément pour obtenir la vitesse et la dispersion des vitesses. Il est donc utile d'exprimer la dispersion de vitesses en fonction du décalage spectral puisqu'il est le même quelle que soit la raie :

$$dV_r \sim c \frac{dz_m}{1 + z_e} \quad (\text{C.9})$$

Ces équations ne sont rigoureusement valables que lorsque la dispersion de vitesse est négligeable par rapport à la célérité de la lumière car on a supposé que la vitesse varie linéairement avec la longueur d'onde (ou le décalage spectral) en utilisant la différenciation. Cette hypothèse est vérifiée en pratique.

Annexe D

Données cinématiques de l'échantillon GHASP décrites au chapitre 2

Résumé

D.1 Cartes cinématiques des galaxies GHASP	296
D.2 Courbes de rotation des galaxies GHASP	347
D.3 Cartes et profils de dispersion de vitesses des galaxies GHASP	359
D.4 Base de données Fabry-Perot	376

Les deux articles présentés dans le chapitre 2 présentent les données GHASP. Les cartes cinématiques constituent deux annexes à chacun de ces articles qui sont uniquement disponibles en ligne. Les courbes de rotation sont incluses dans des annexes qui font partie du corps principal de l'article. Cependant, plutôt que de montrer les cartes et les courbes de rotation des deux sous-échantillons de manière disjointe, j'ai rassemblé dans cette annexe l'ensemble des cartes cinématiques et des courbes de rotation des articles pour toutes les galaxies en les ordonnant par ascension droite croissante. De plus, les cartes de dispersion de vitesses et les profils de dispersion de vitesses qui en sont déduits sont également présentés dans cette annexe. Une présentation succincte de la base de données Fabry-Perot est faite.

D.1 Cartes cinématiques des galaxies GHASP

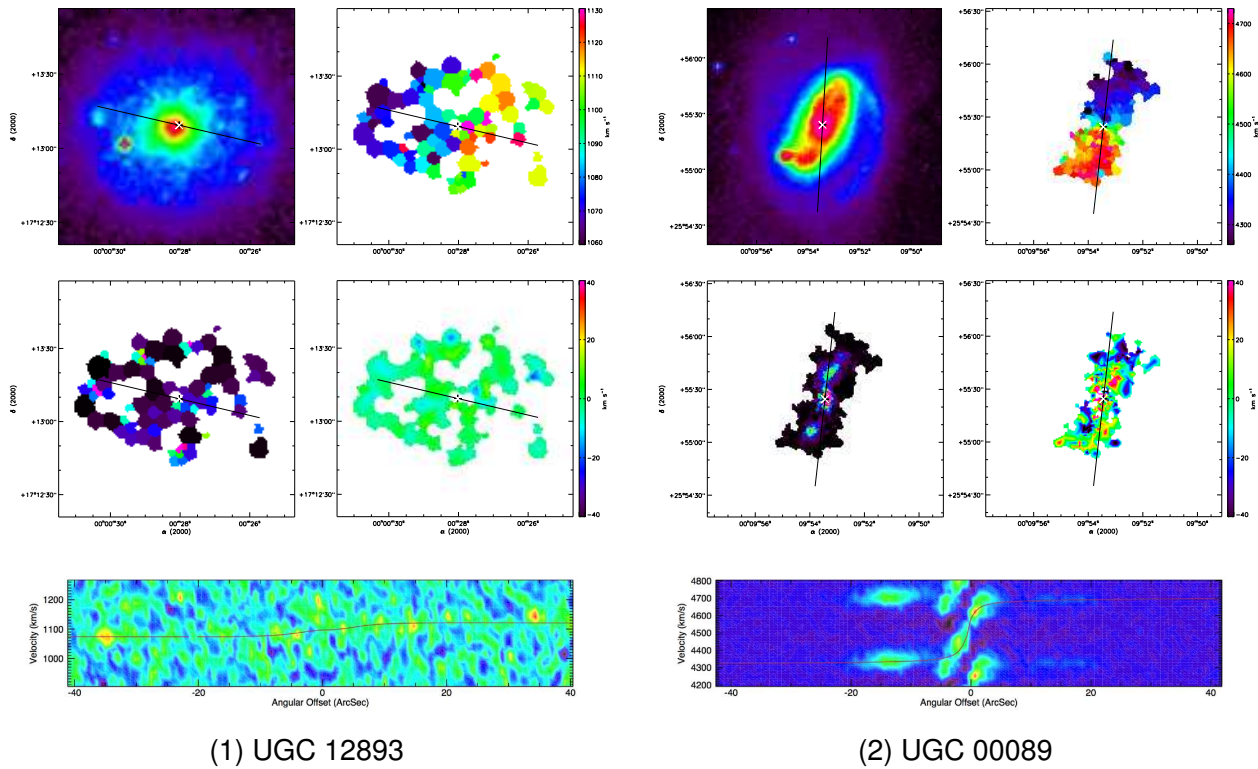
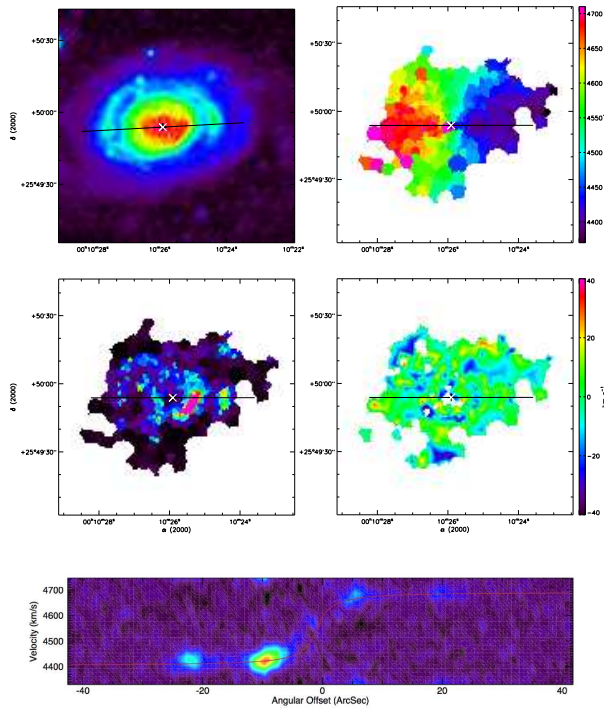
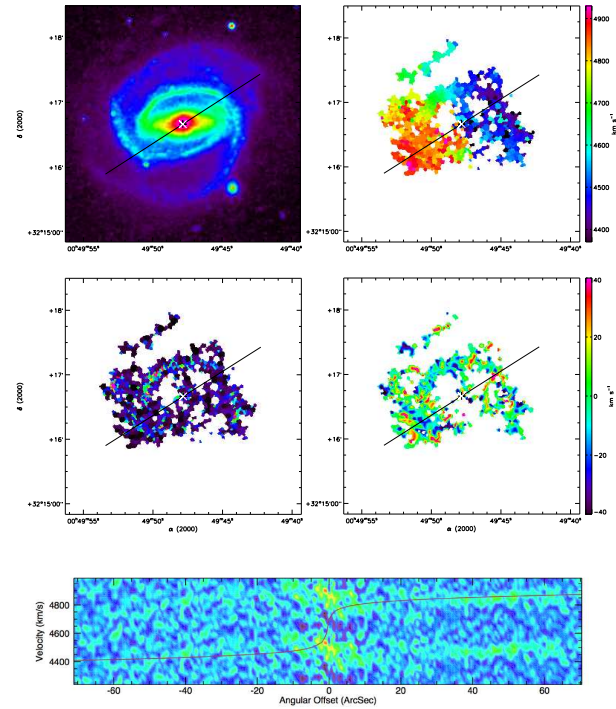


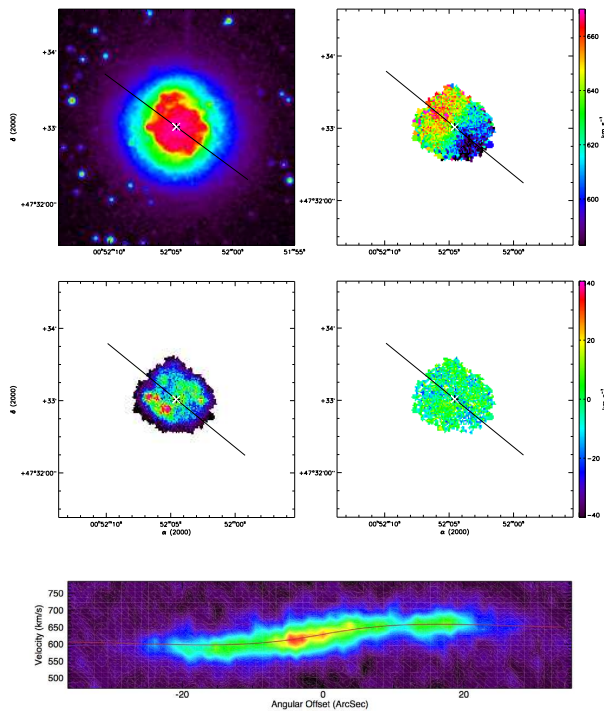
FIG. D.1: Cartes cinématiques des galaxies GHASP. **En haut à gauche** : Image en bande B (ou R) du XDSS. **En haut à droite** : Champ de vitesse $H\alpha$. **Au milieu à gauche** : Carte monochromatique de flux $H\alpha$. **Au milieu à droite** : Champ de vitesse résiduel lorsqu'il a été possible d'ajuster un modèle de champ de vitesses. La double croix blanche et noire représente le centre cinématique. La ligne noire représente le grand axe et s'arrête au rayon optique ($D_{25}/2$, de Vaucouleurs et al., 1995). **En bas** : Diagramme position-vitesse le long du grand axe (largeur totale de 7 pixels) avec une unité de flux arbitraire. La ligne rouge correspond à la courbe de rotation calculée le long du grand axe du champ de vitesses modèle.



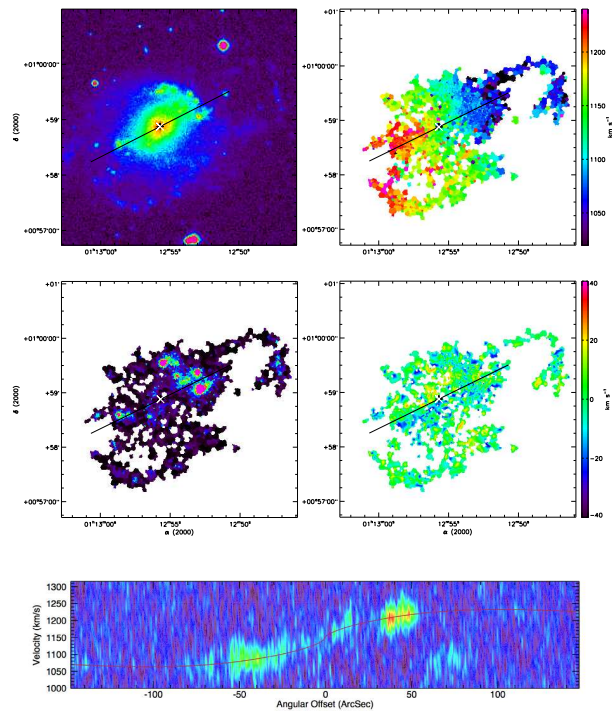
(3) UGC 00094



(4) UGC 00508

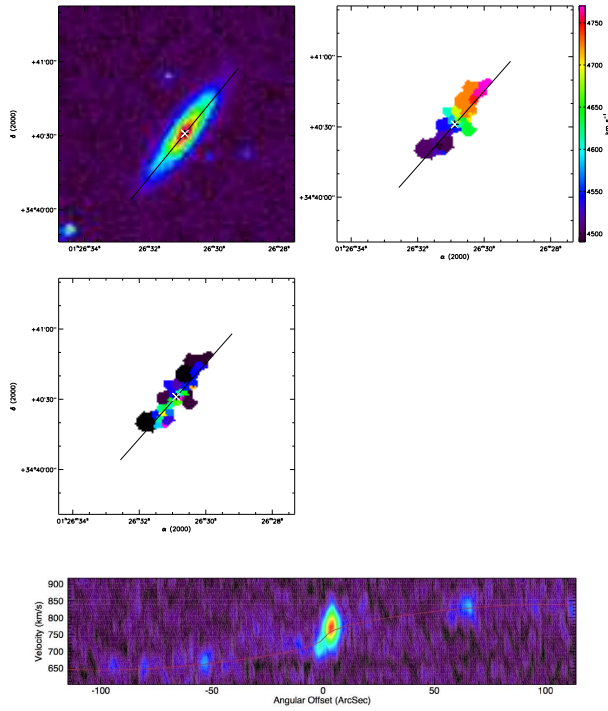


(5) UGC 00528

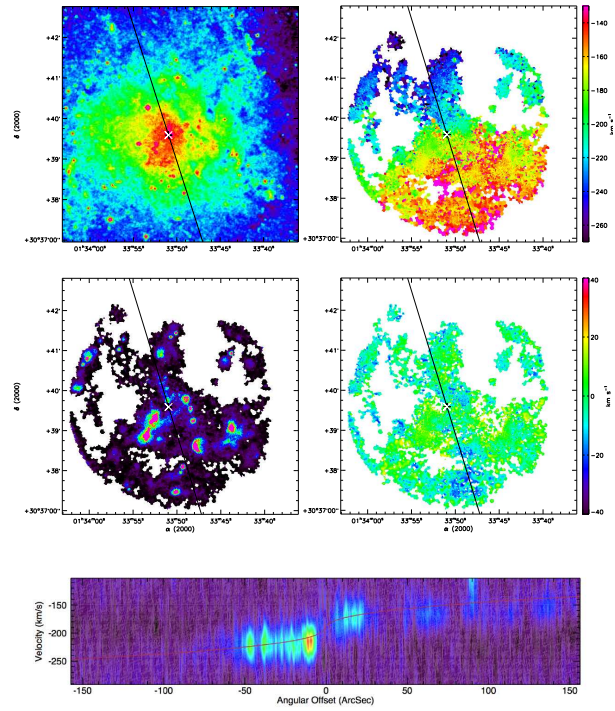


(6) UGC 00763 (XDSS en bande R)

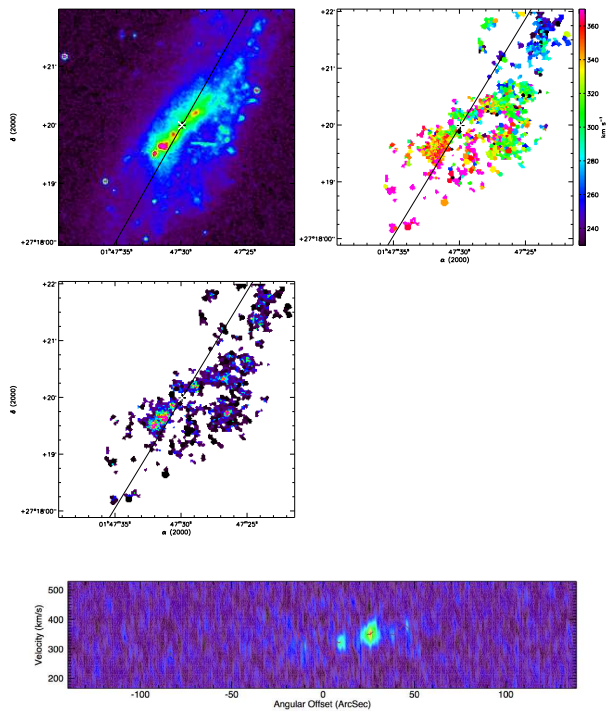
FIG. D.1 : suite



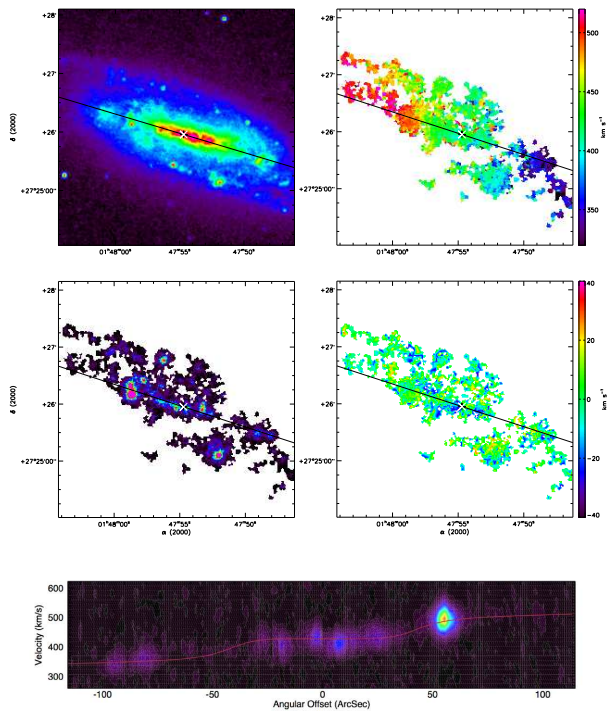
(7) NGC 0542



(8) UGC 01117 (XDSS en bande R)

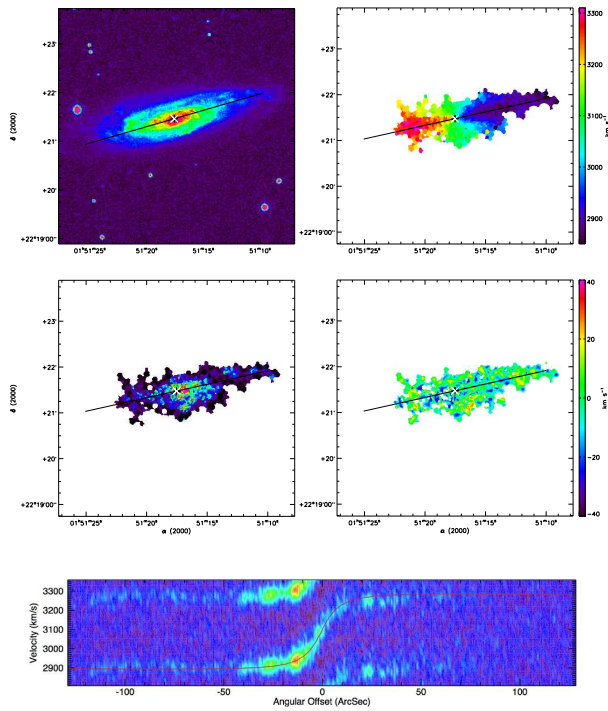


(9) UGC 01249

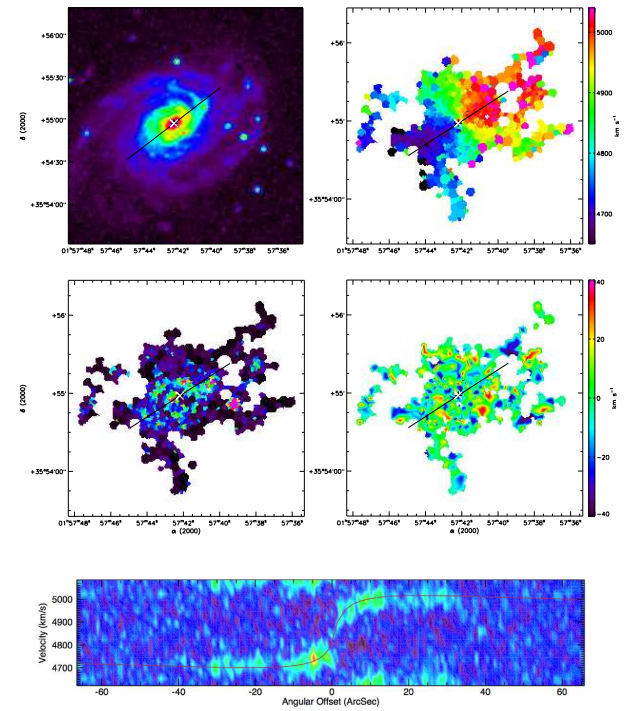


(10) UGC 01256

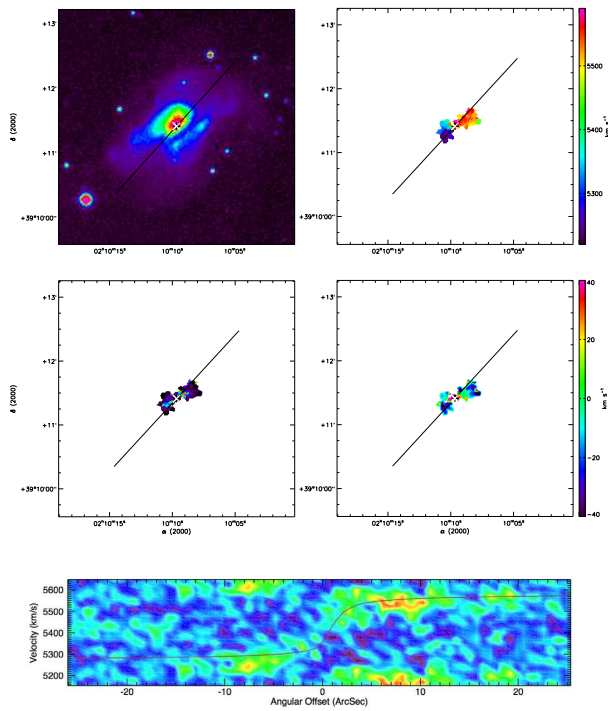
FIG. D.1 : suite



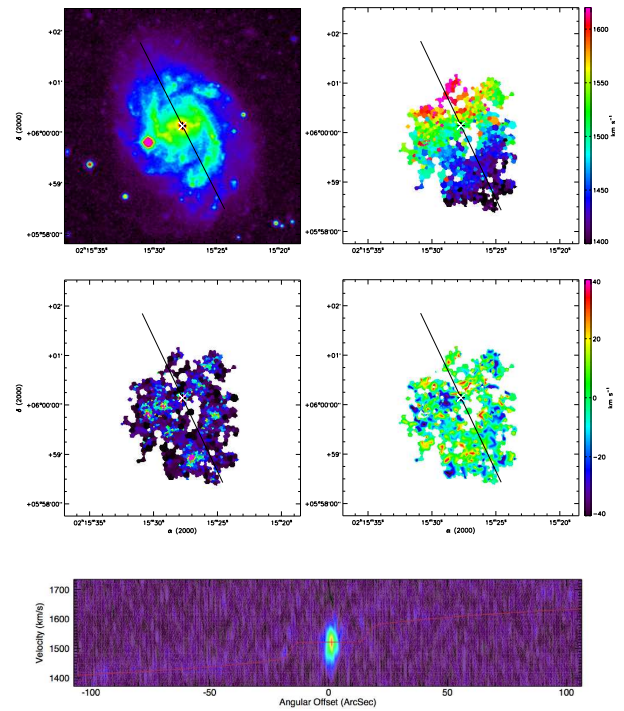
(11) UGC 01317



(12) UGC 01437

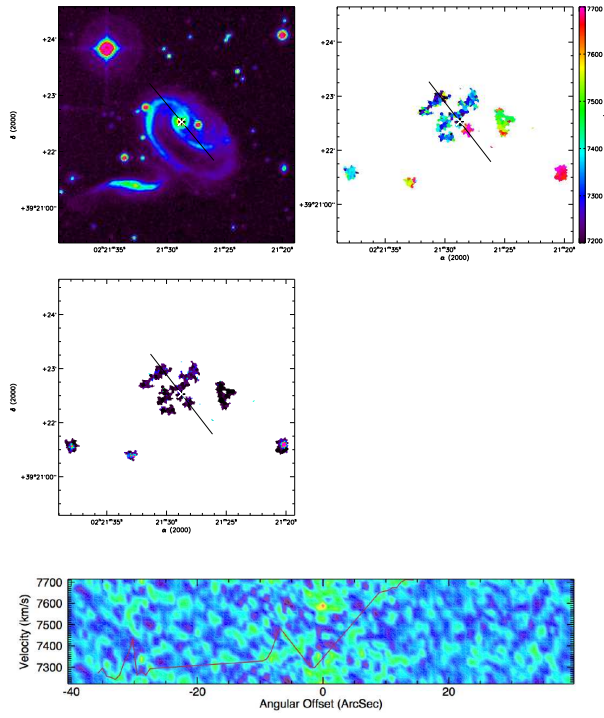


(13) UGC 01655

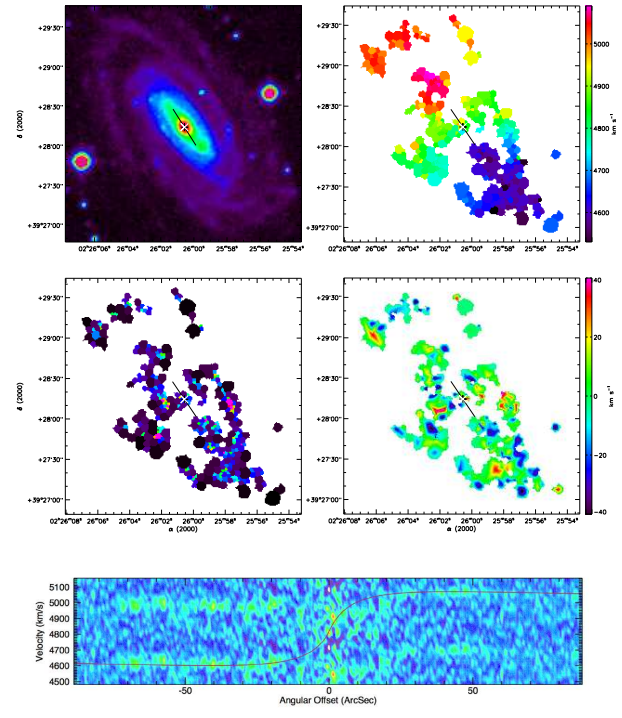


(14) UGC 01736

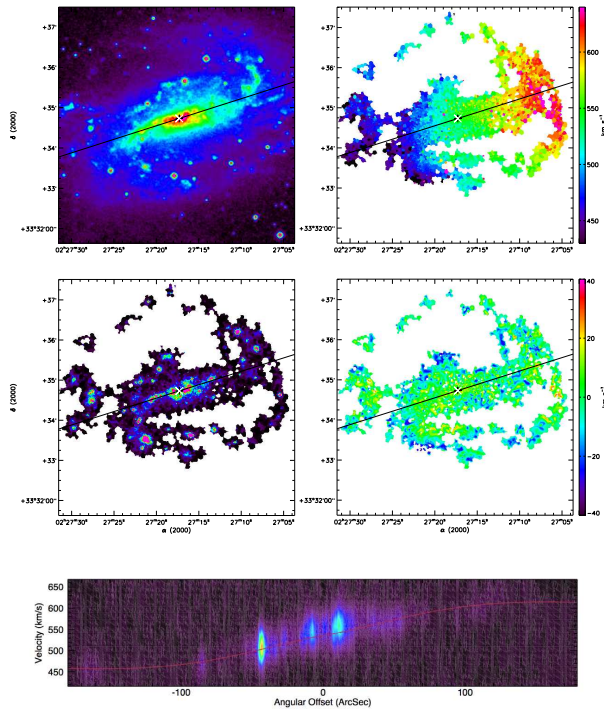
FIG. D.1 : suite



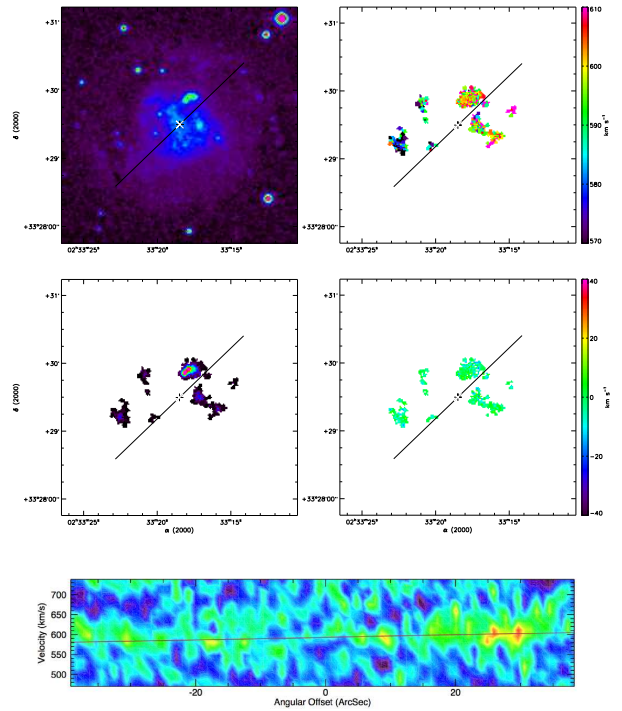
(15) UGC 01810



(16) UGC 01886

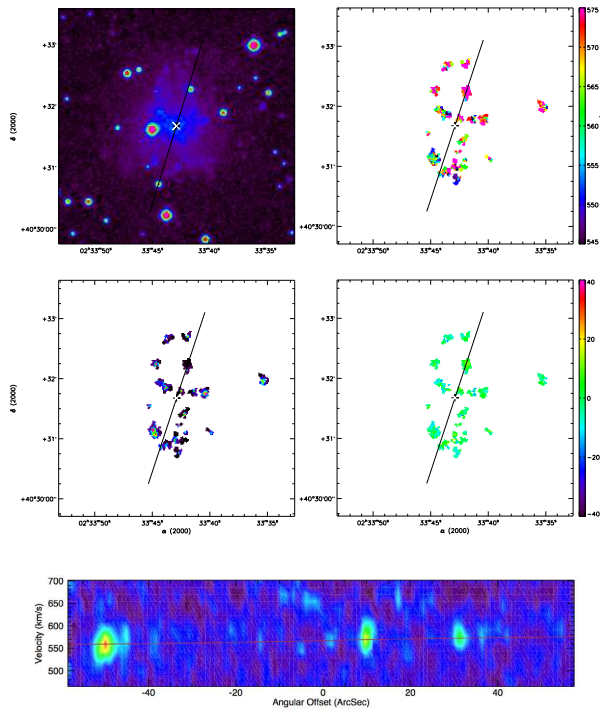


(17) UGC 01913

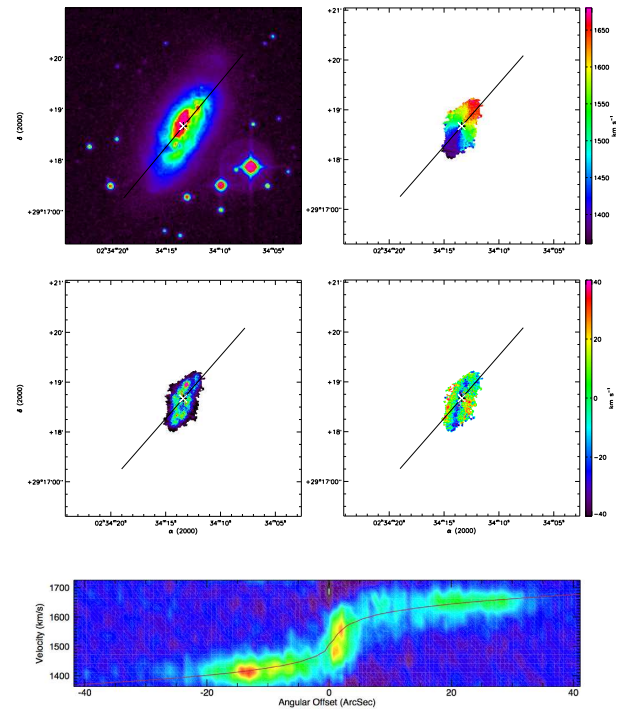


(18) UGC 02023

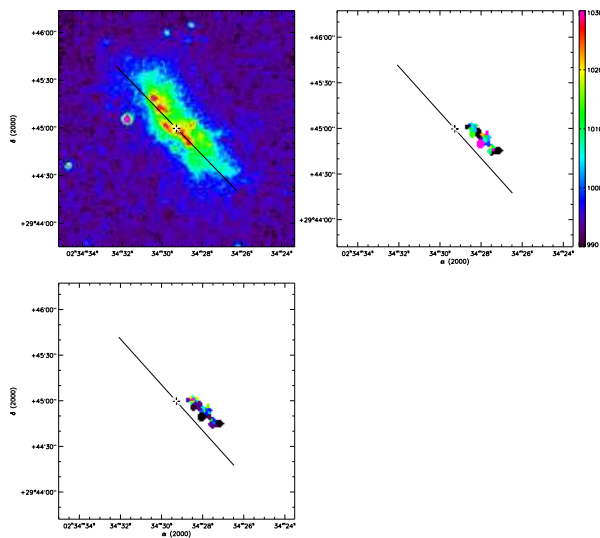
FIG. D.1 : suite



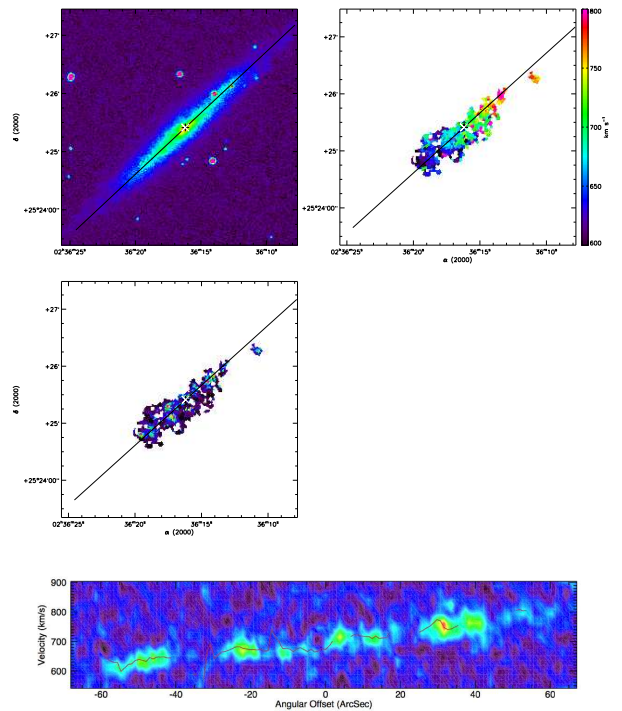
(19) UGC 02034



(20) UGC 02045

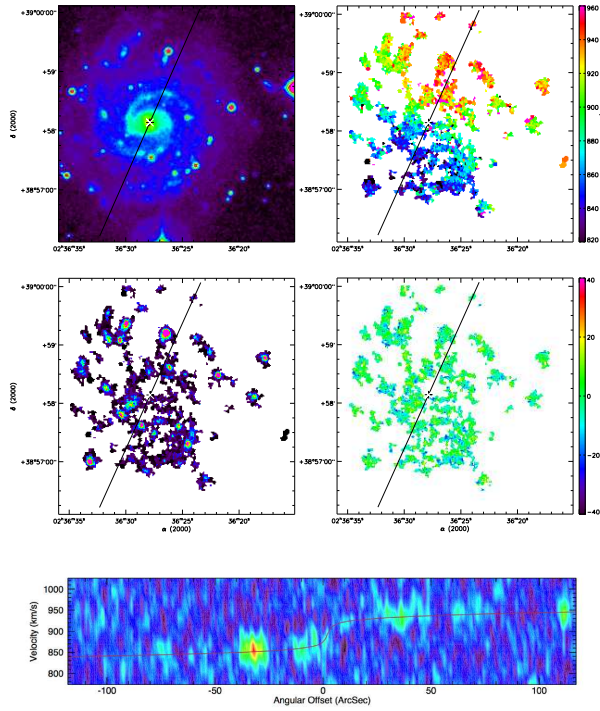


(21) UGC 02053

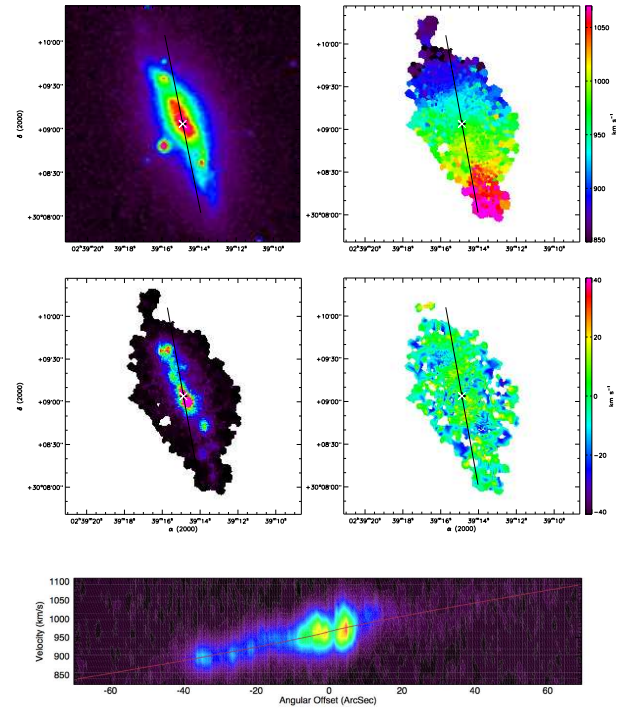


(22) UGC 02082

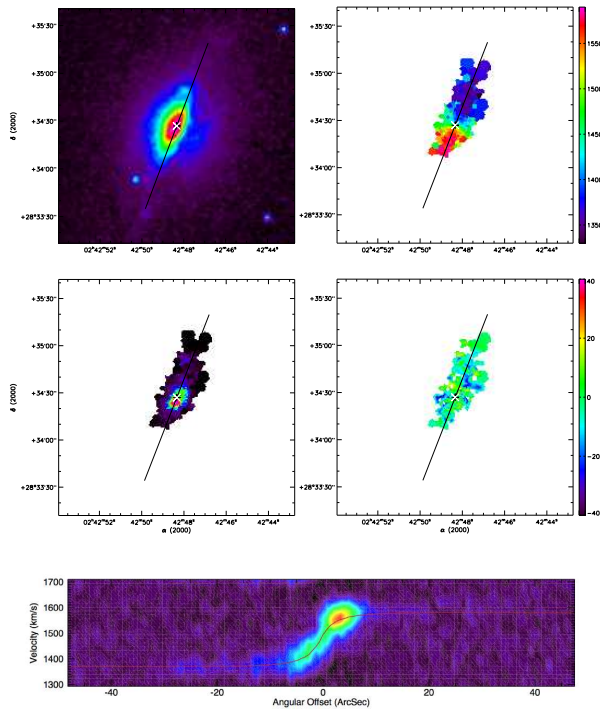
FIG. D.1 : suite



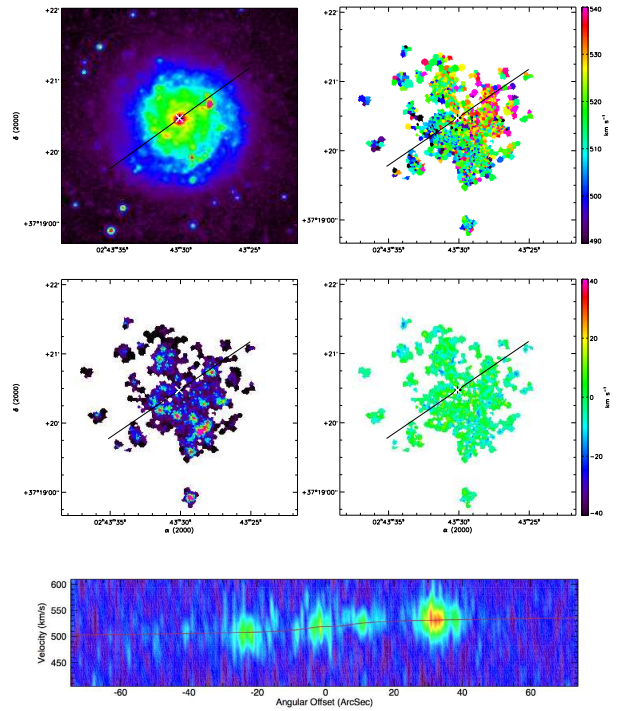
(23) UGC 02080



(24) UGC 02141

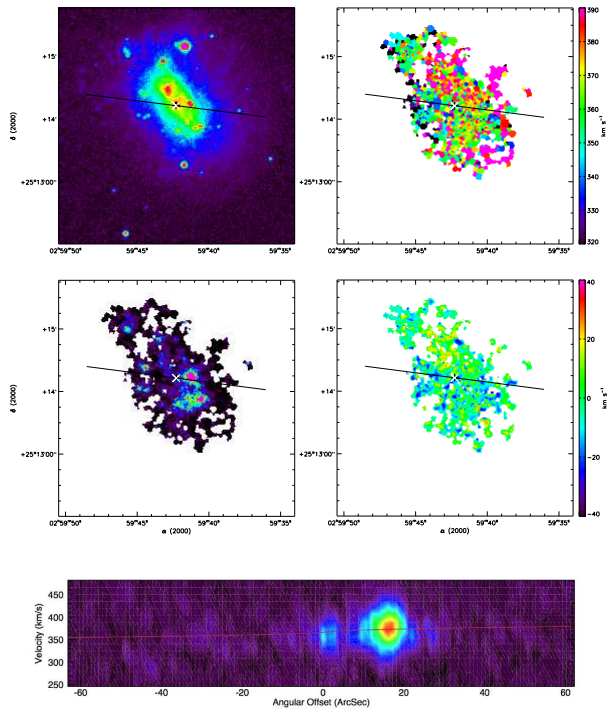


(25) UGC 02183

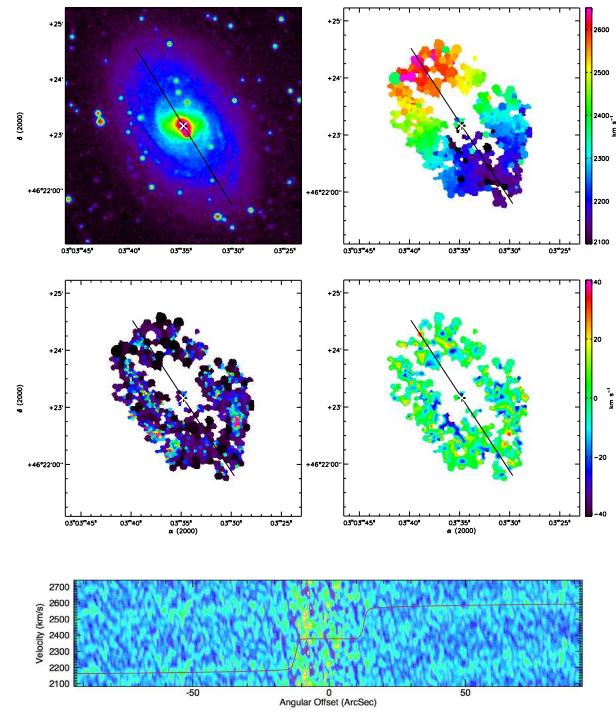


(26) UGC 02193

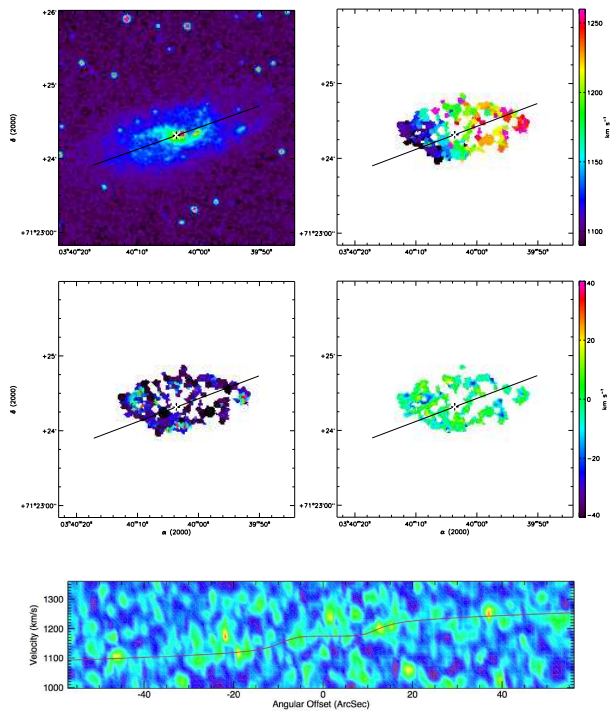
FIG. D.1 : suite



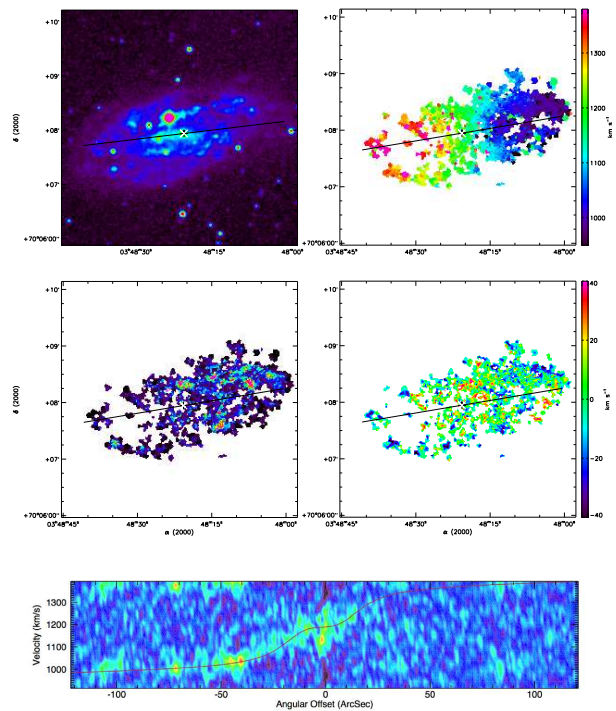
(27) UGC 02455



(28) UGC 02503

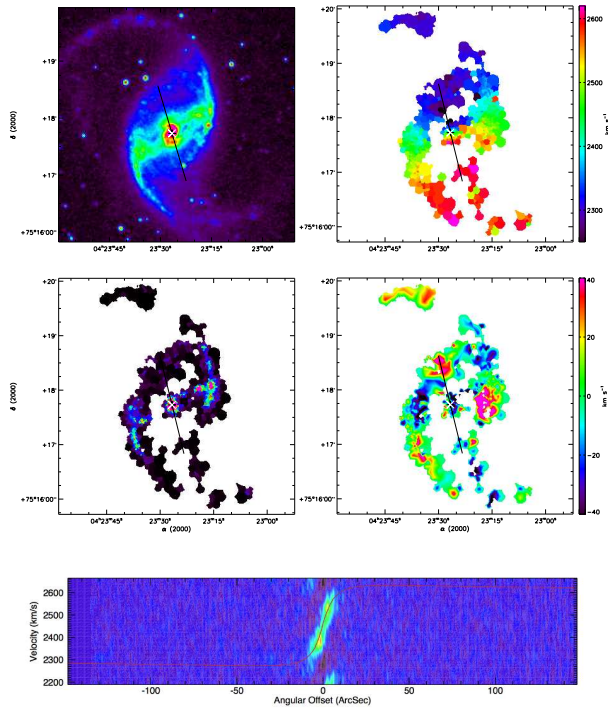


(29) UGC 02800

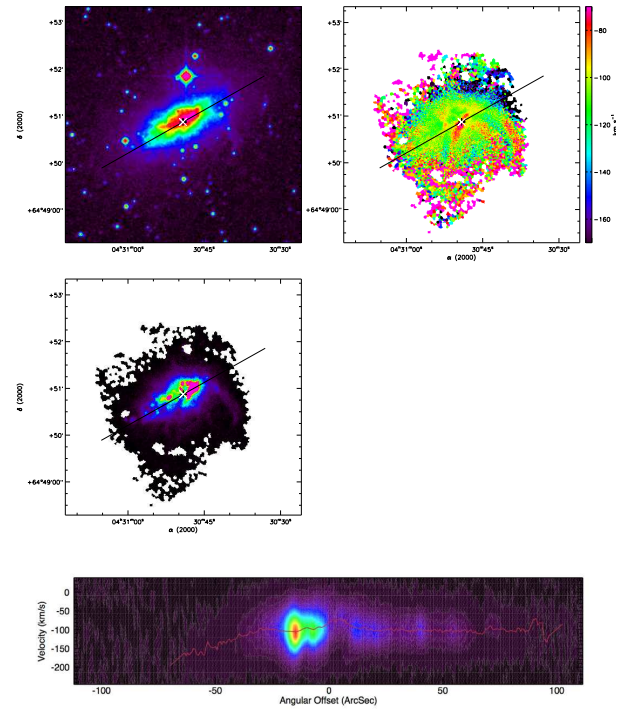


(30) UGC 02855

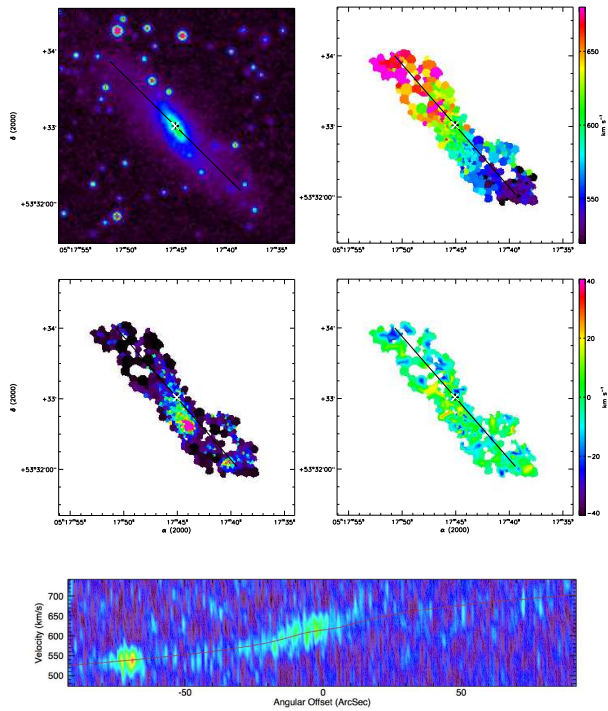
FIG. D.1 : suite



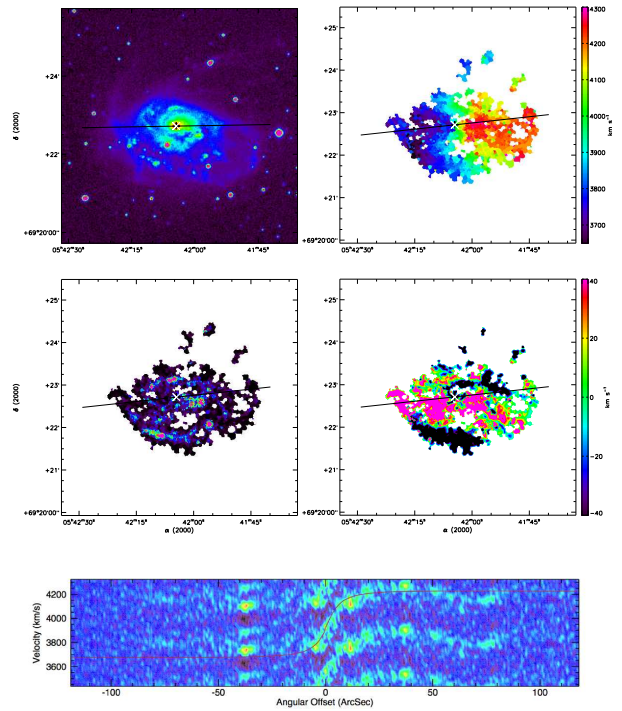
(31) UGC 03013



(32) UGC 03056 (XDSS en bande R)

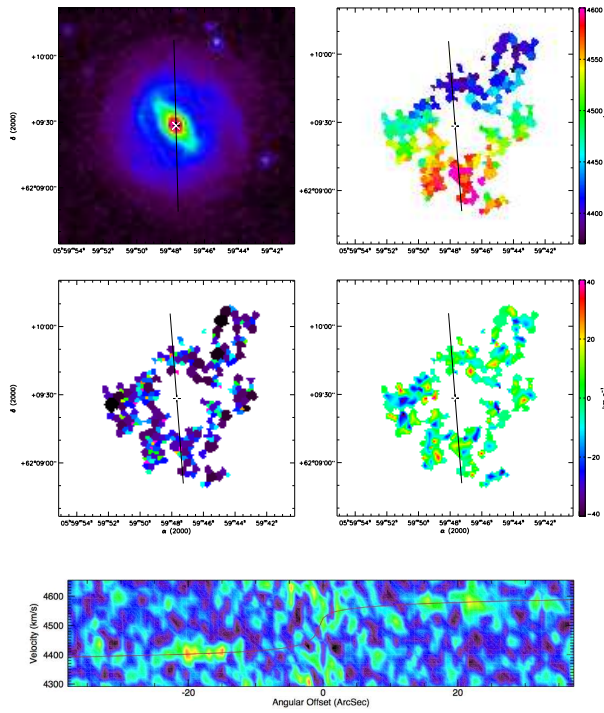


(33) UGC 03273

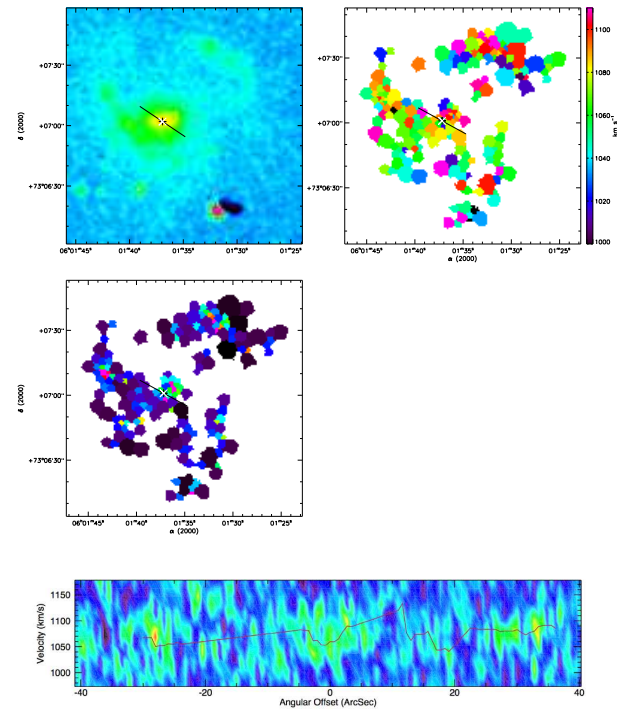


(34) UGC 03334

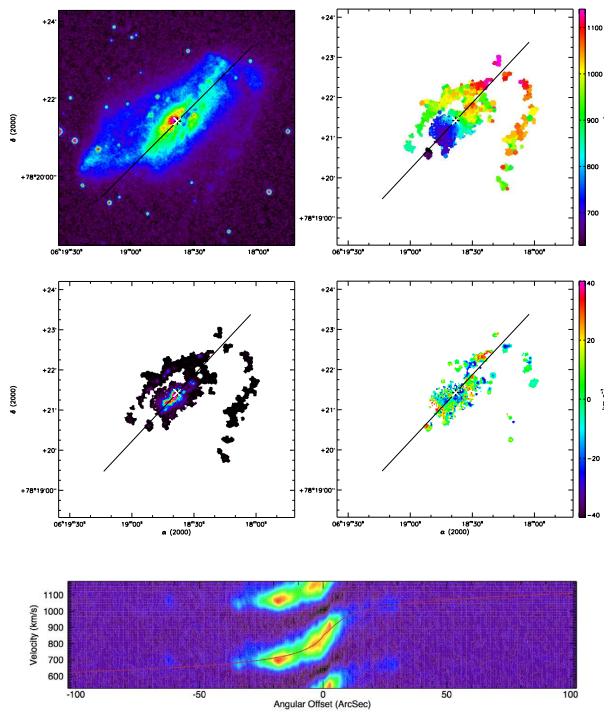
FIG. D.1 : suite



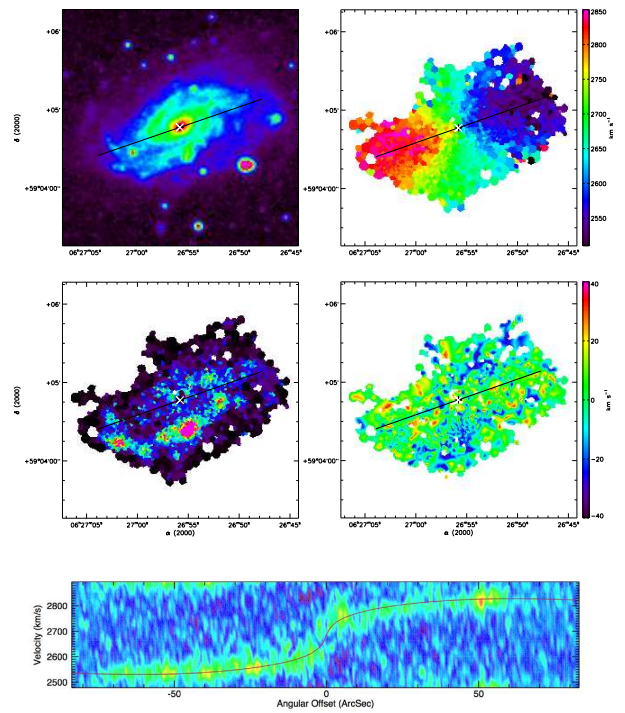
(35) UGC 03382



(36) UGC 03384

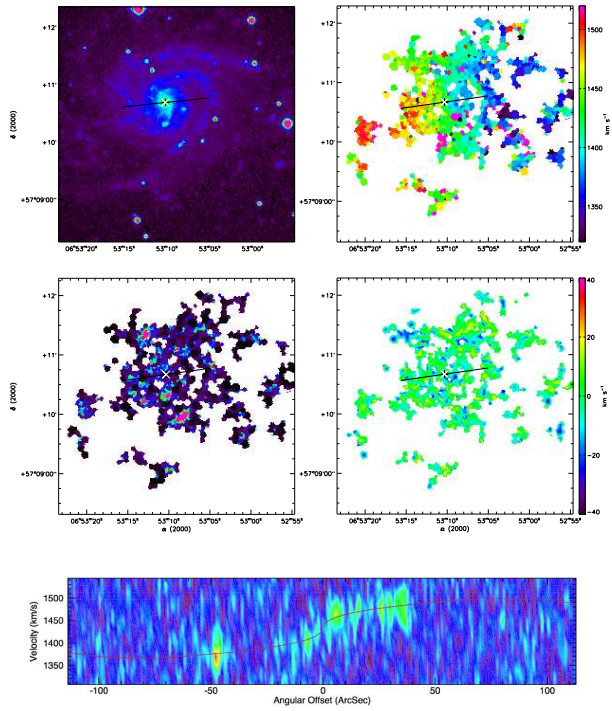


(37) UGC 03429

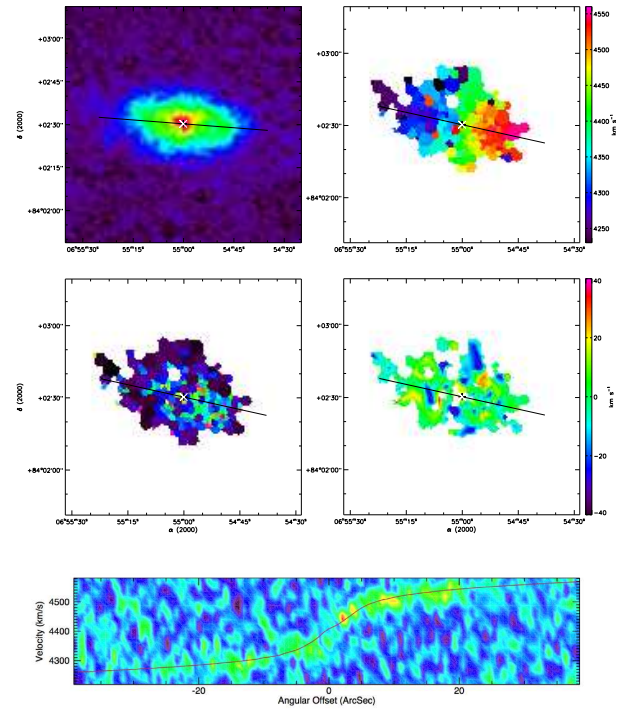


(38) UGC 03463

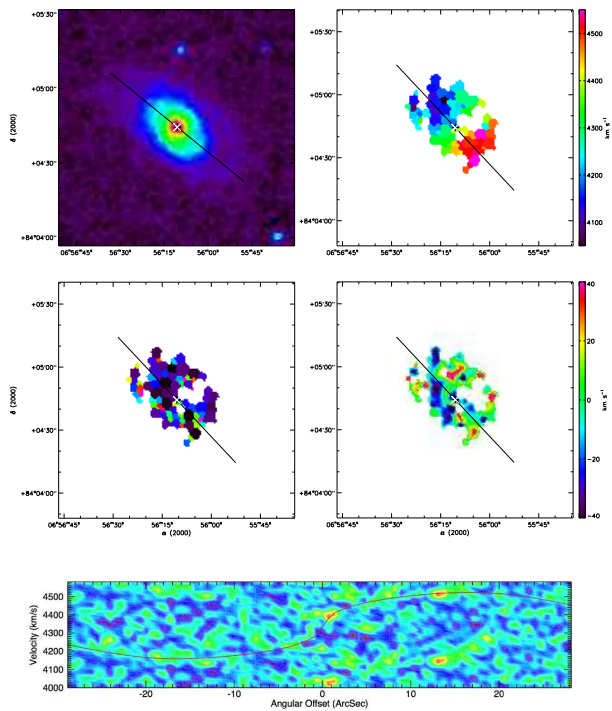
FIG. D.1 : suite



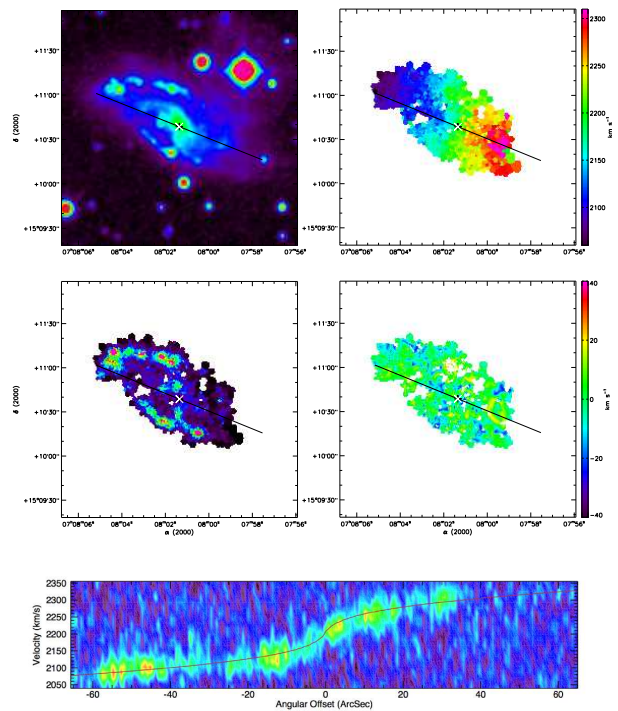
(39) UGC 03574



(40) UGC 03521

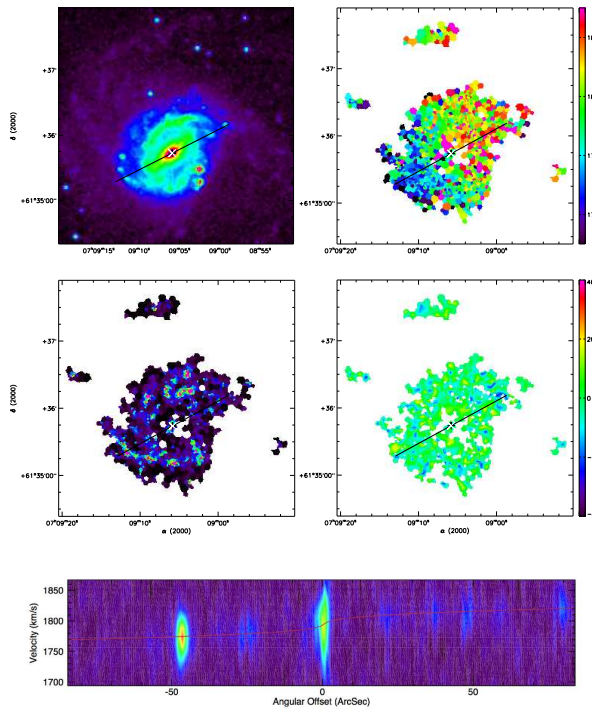


(41) UGC 03528

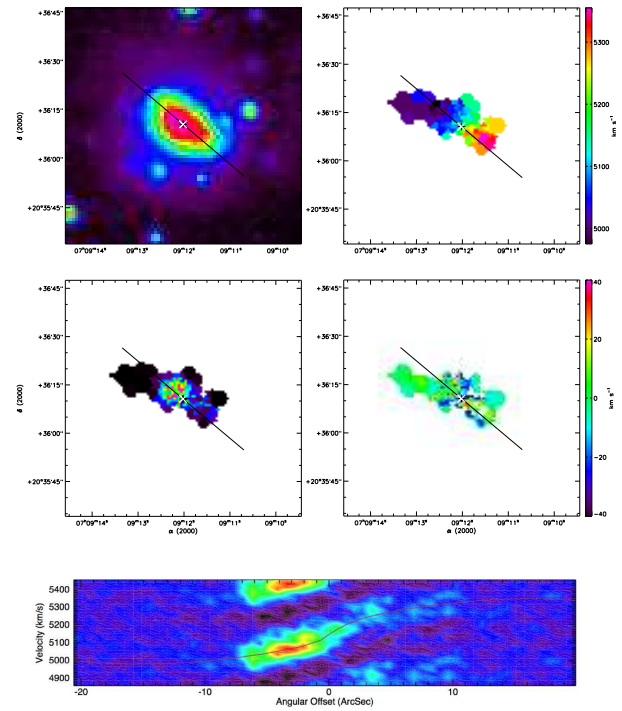


(42) UGC 03691

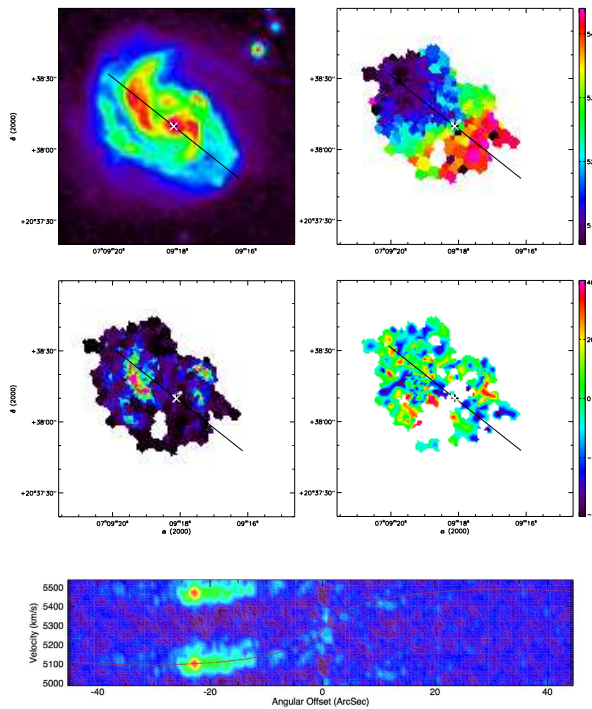
FIG. D.1 : suite



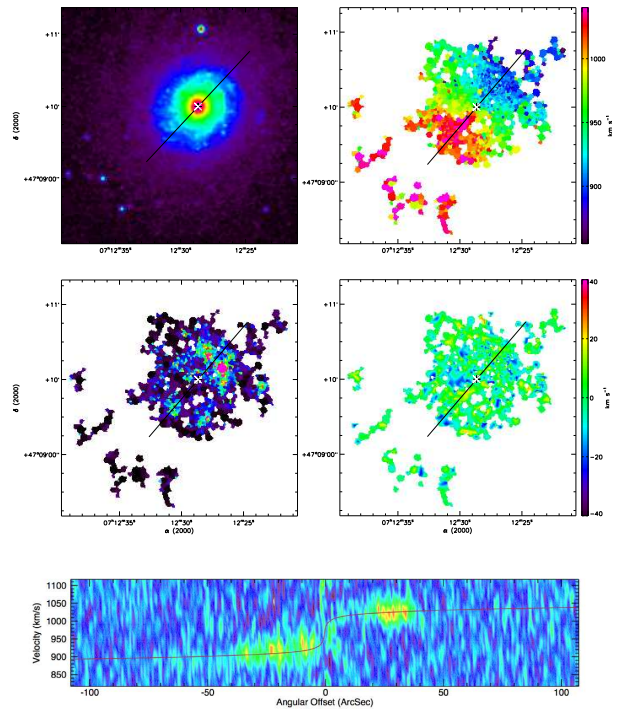
(43) UGC 03685



(44) UGC 03708

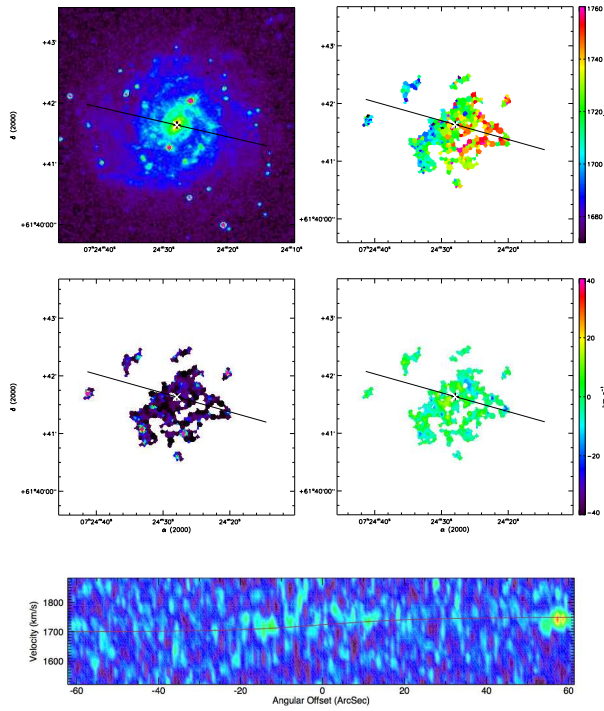


(45) UGC 03709

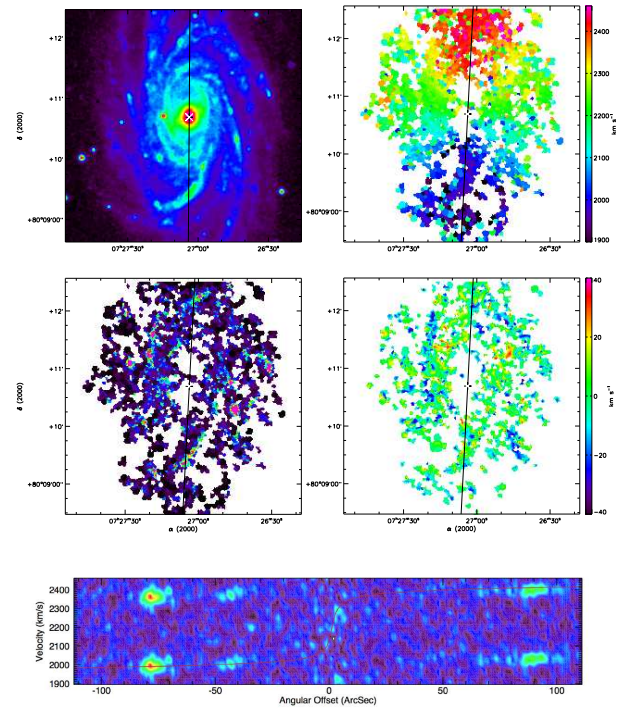


(46) UGC 03734

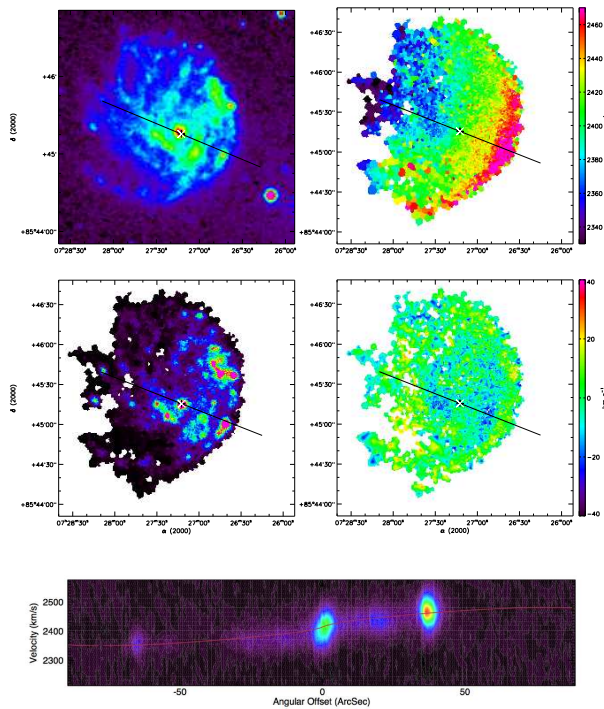
FIG. D.1 : suite



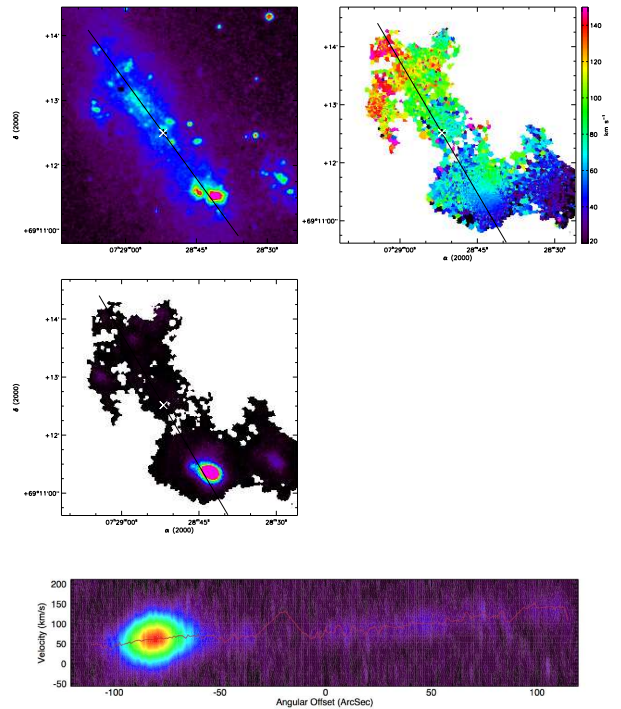
(47) UGC 03826



(48) UGC 03809

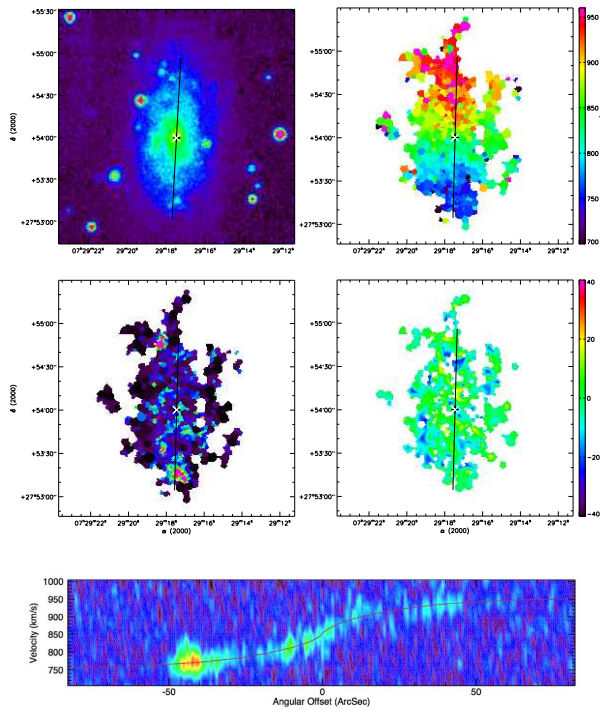


(49) UGC 03740

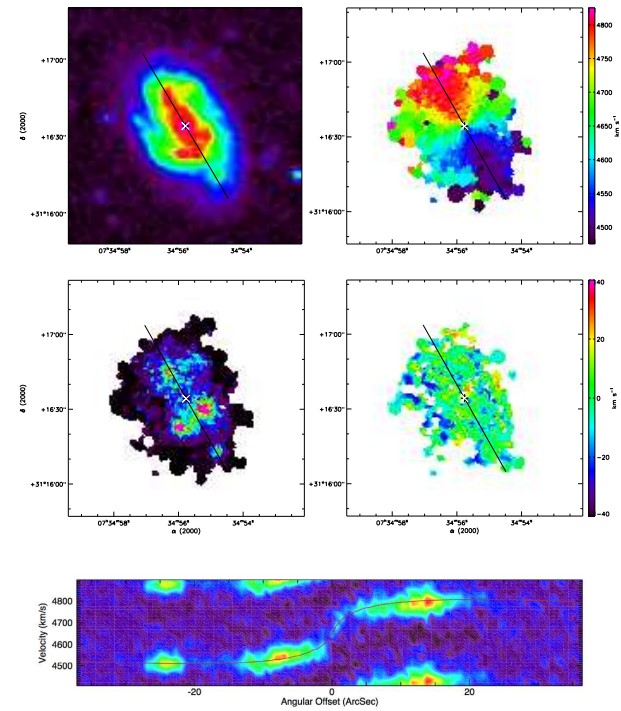


(50) UGC 03851

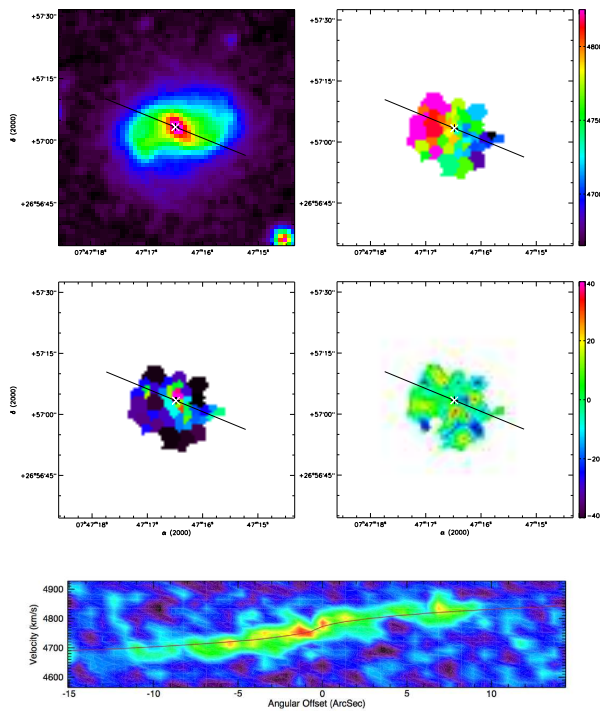
FIG. D.1 : suite



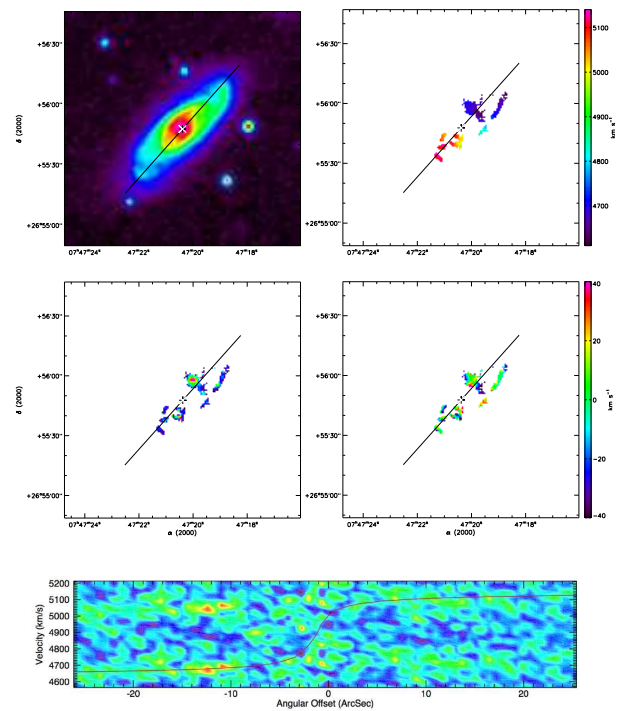
(51) UGC 03876



(52) UGC 03915

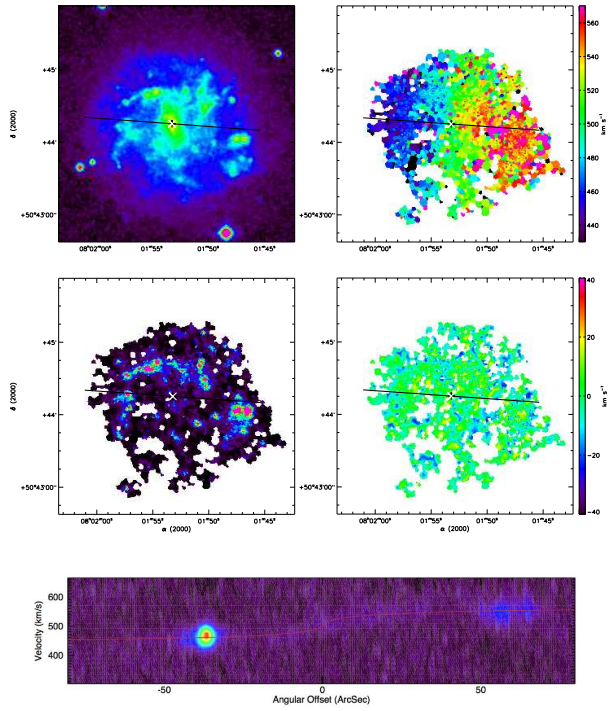


(53) IC 0476

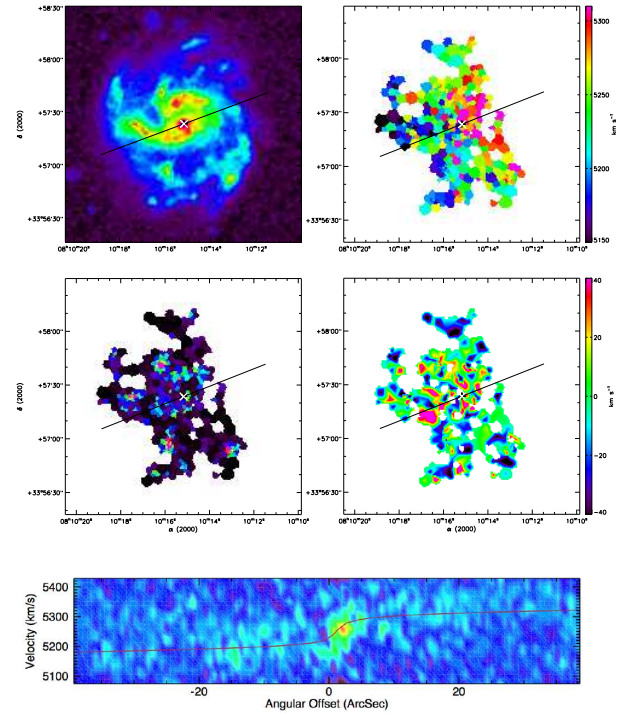


(54) UGC 04026

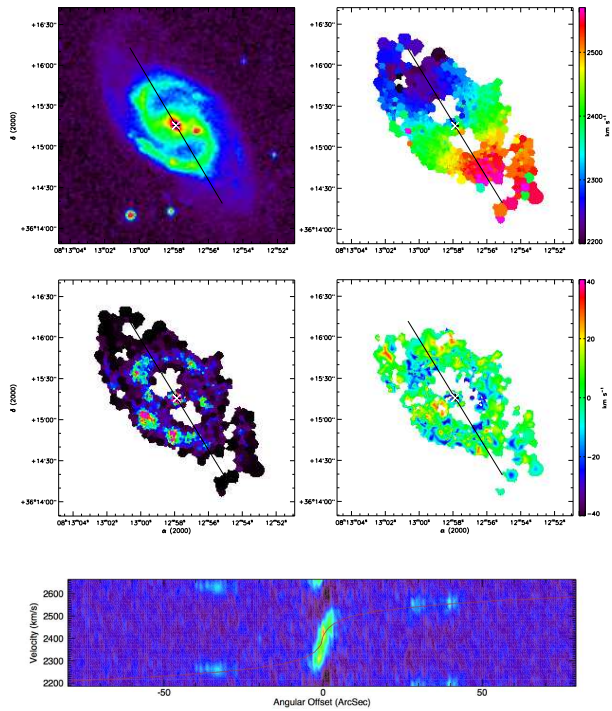
FIG. D.1 : suite



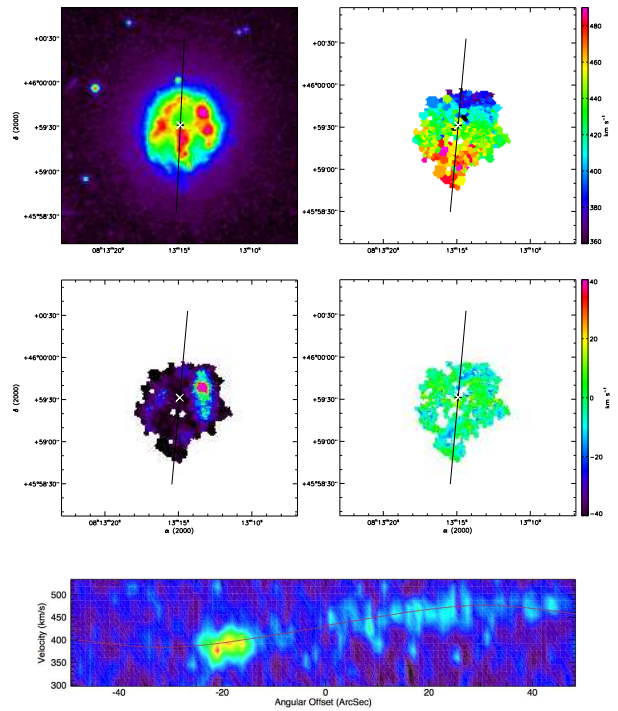
(55) UGC 04165



(56) UGC 04256

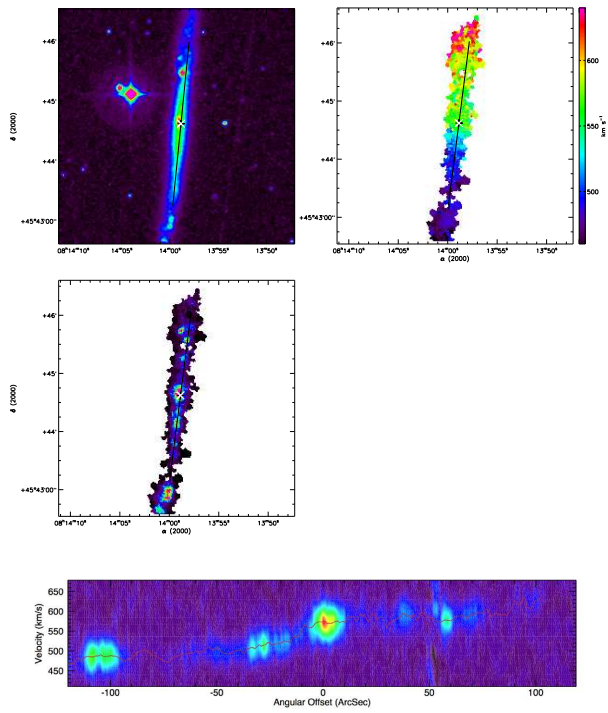


(57) UGC 04273

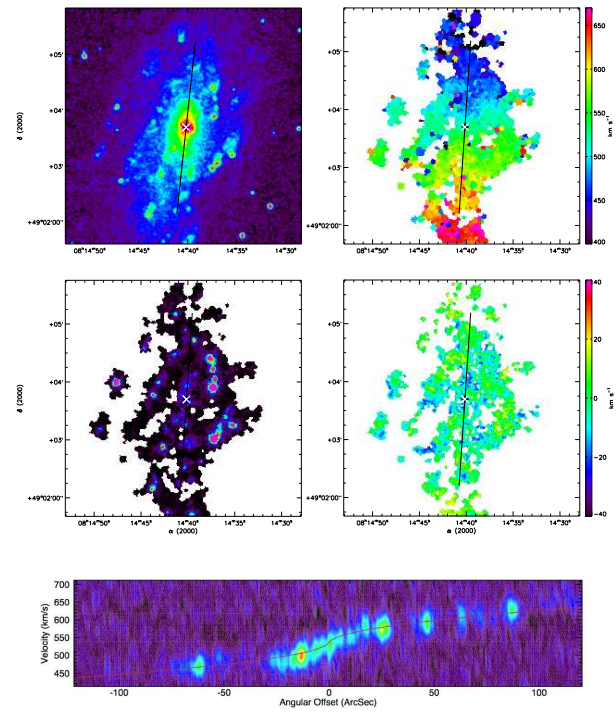


(58) UGC 04274

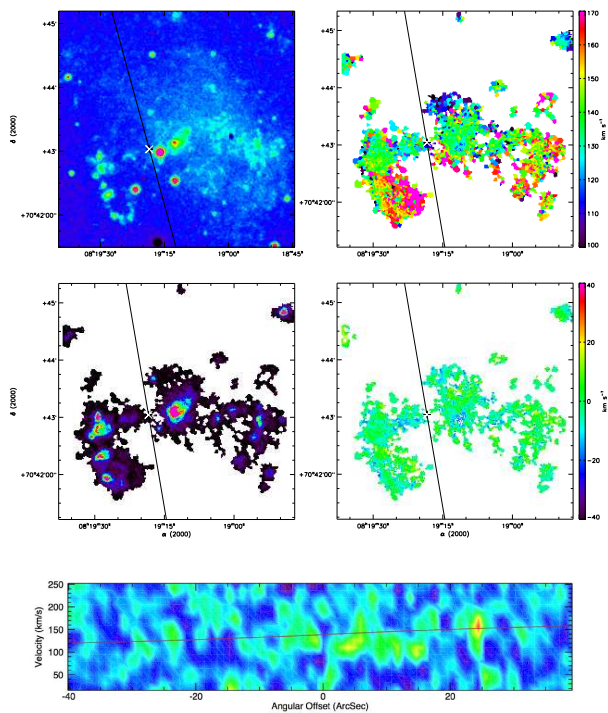
FIG. D.1 : suite



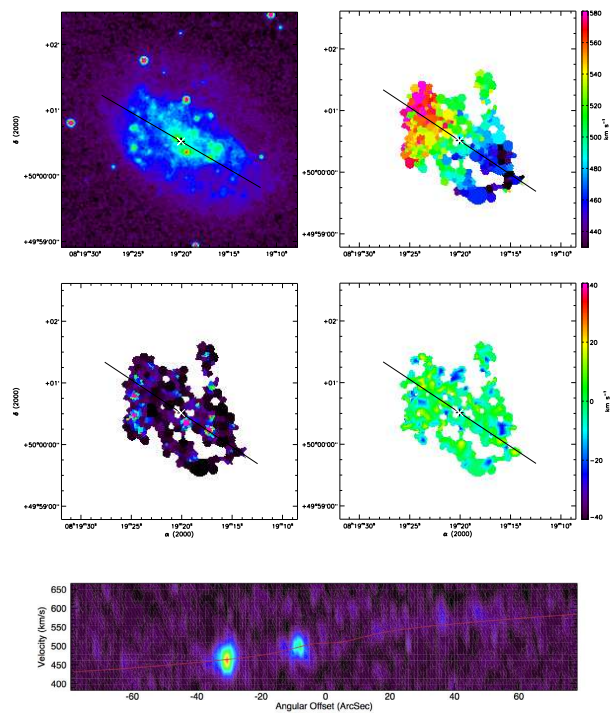
(59) UGC 04278



(60) UGC 04284

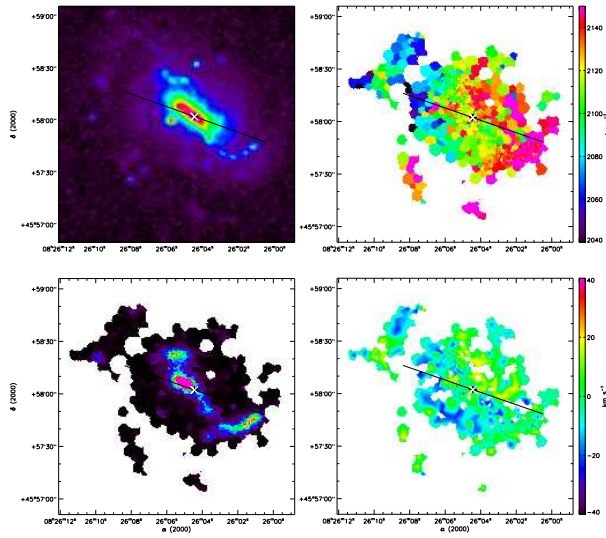


(61) UGC 04305

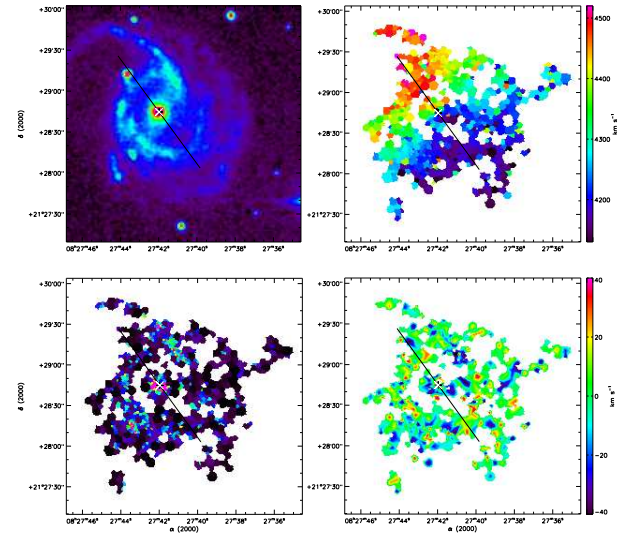


(62) UGC 04325

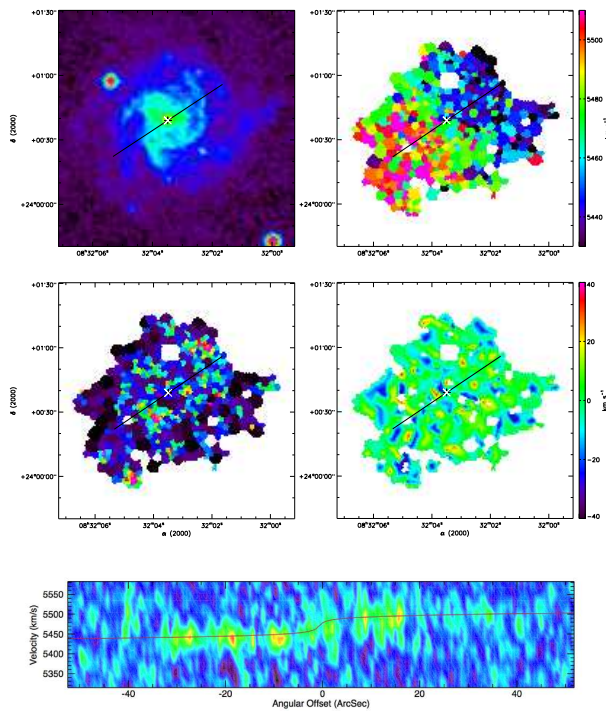
FIG. D.1 : suite



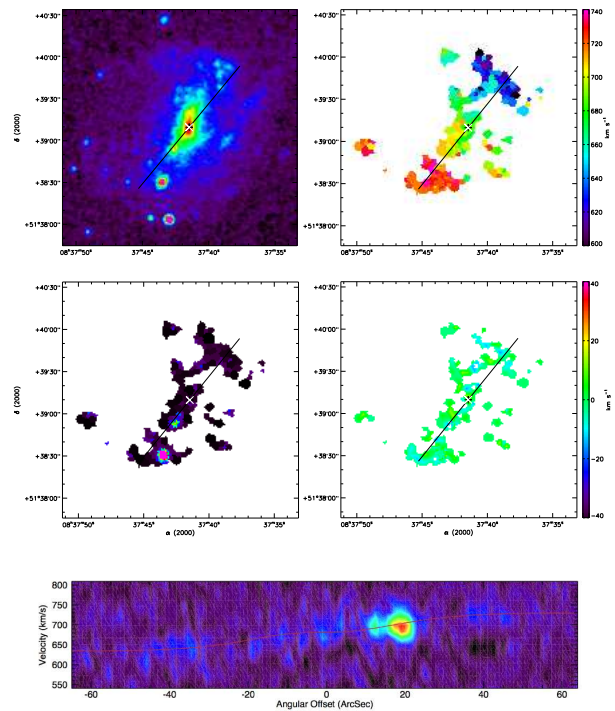
(63) UGC 04393



(64) UGC 04422

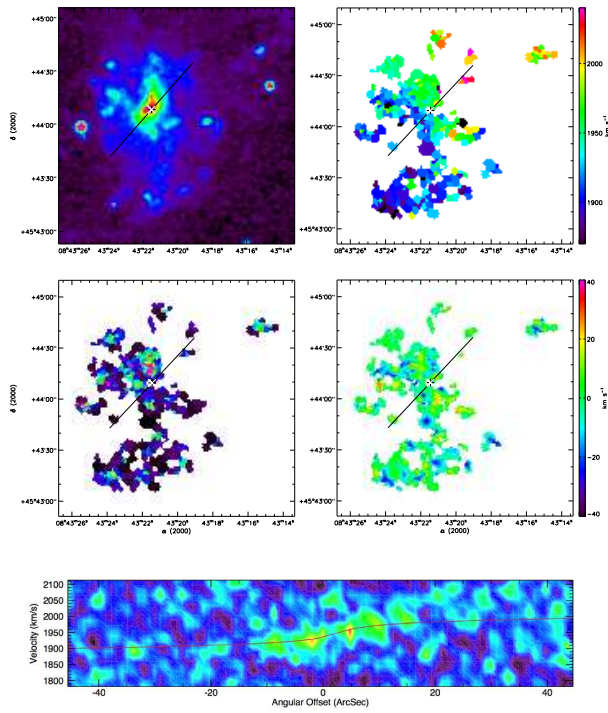


(65) UGC 04456

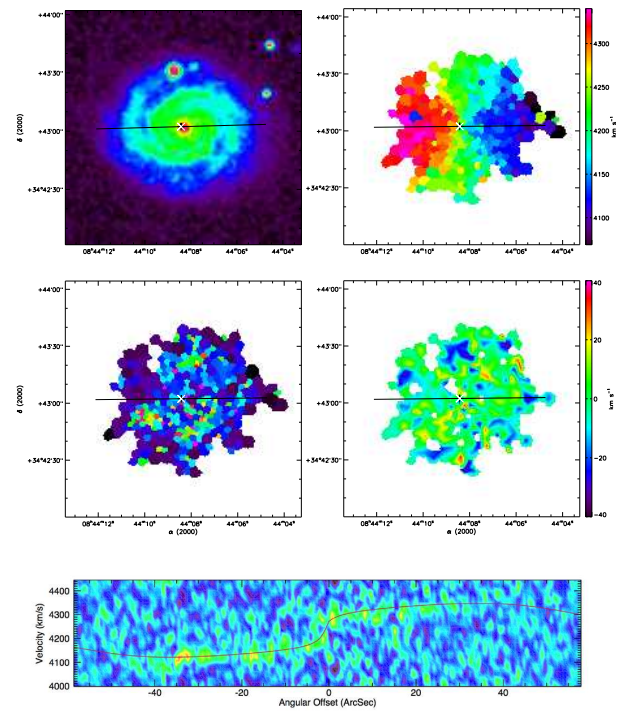


(66) UGC 04499

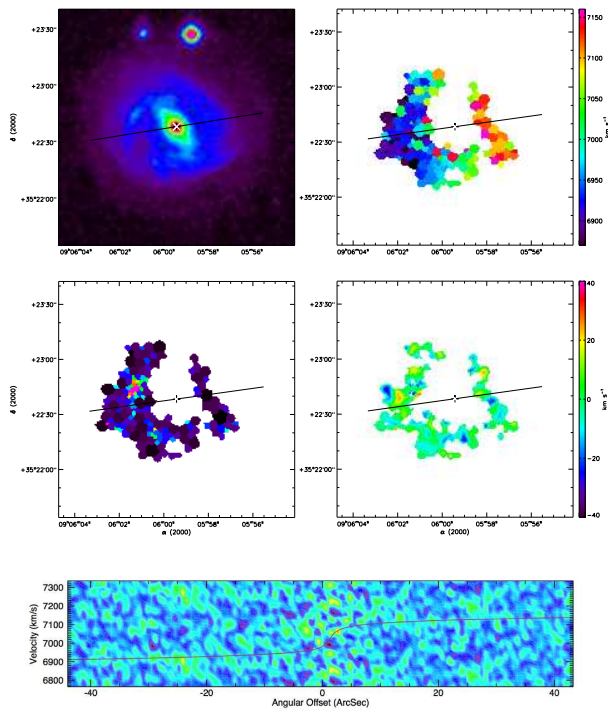
FIG. D.1 : suite



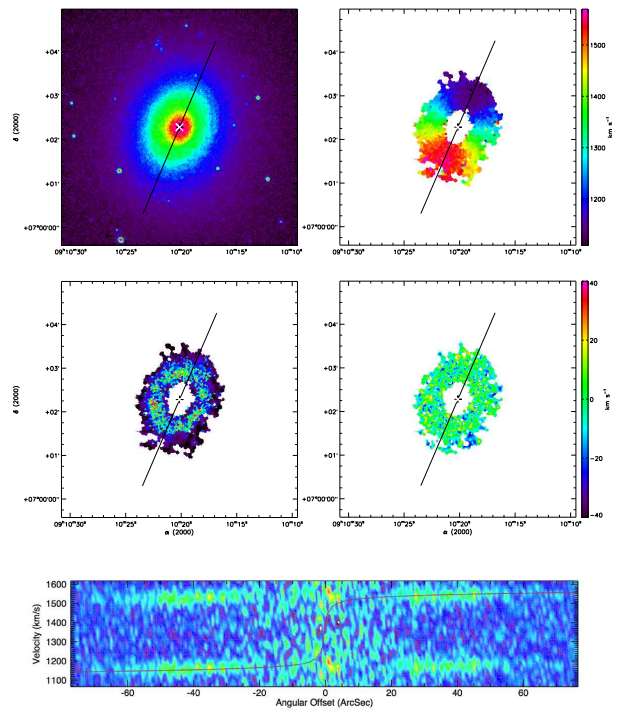
(67) UGC 04543



(68) UGC 04555

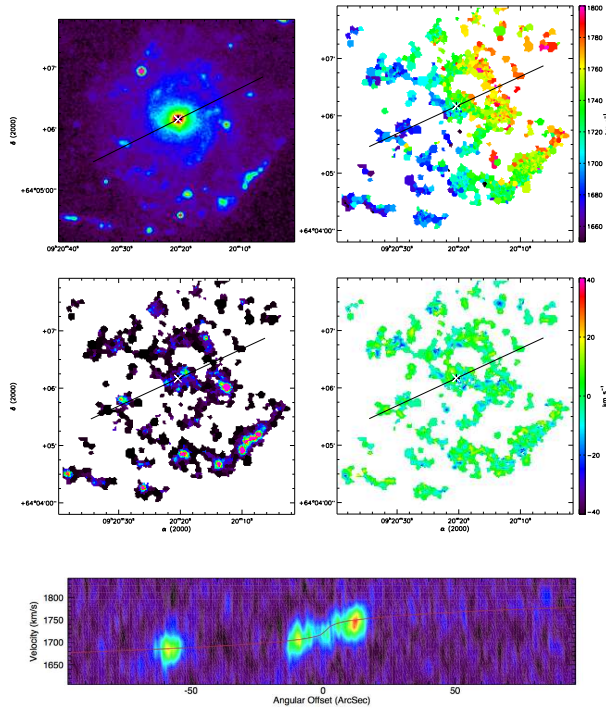


(69) UGC 04770

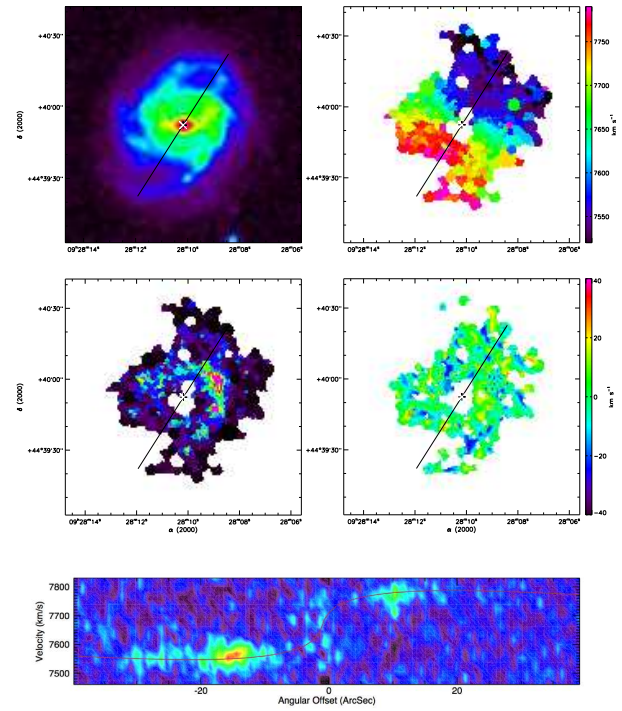


(70) UGC 04820

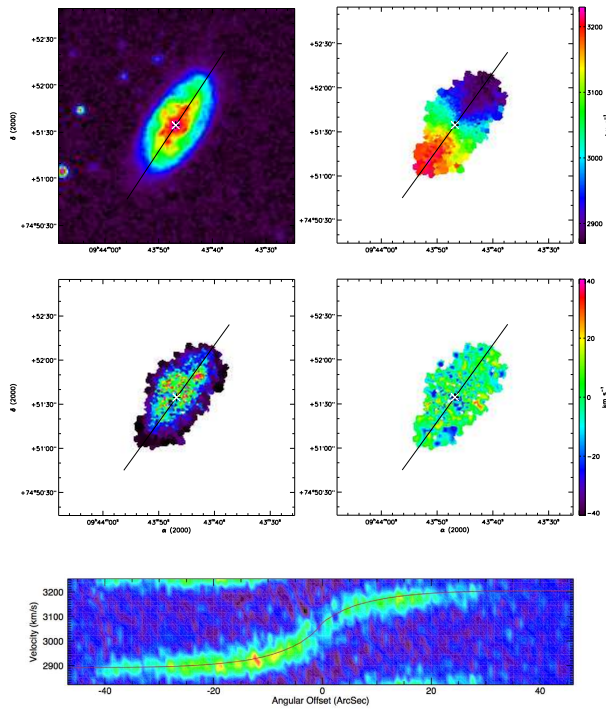
FIG. D.1 : suite



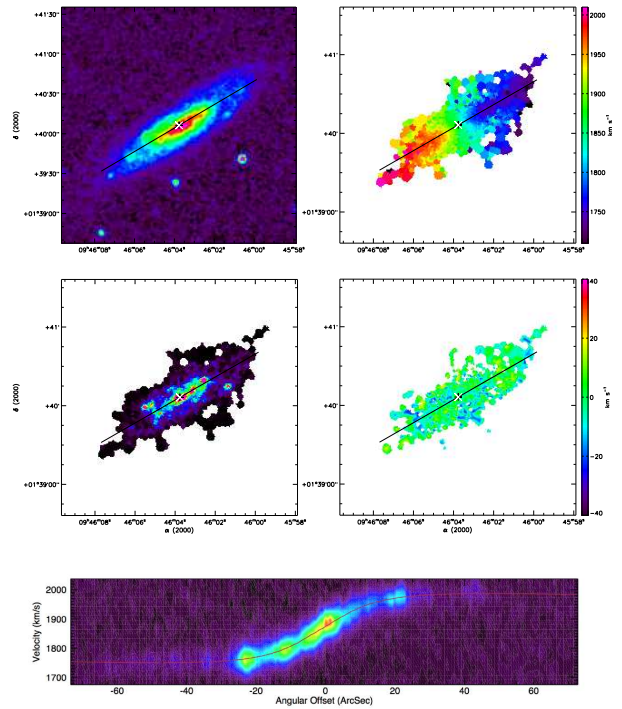
(71) UGC 04936 (XDSS en bande R)



(72) UGC 05045

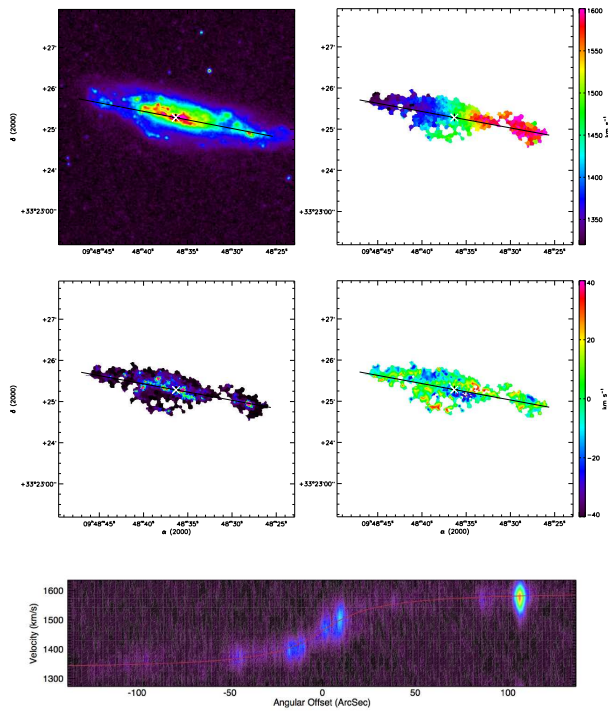


(73) UGC 05175

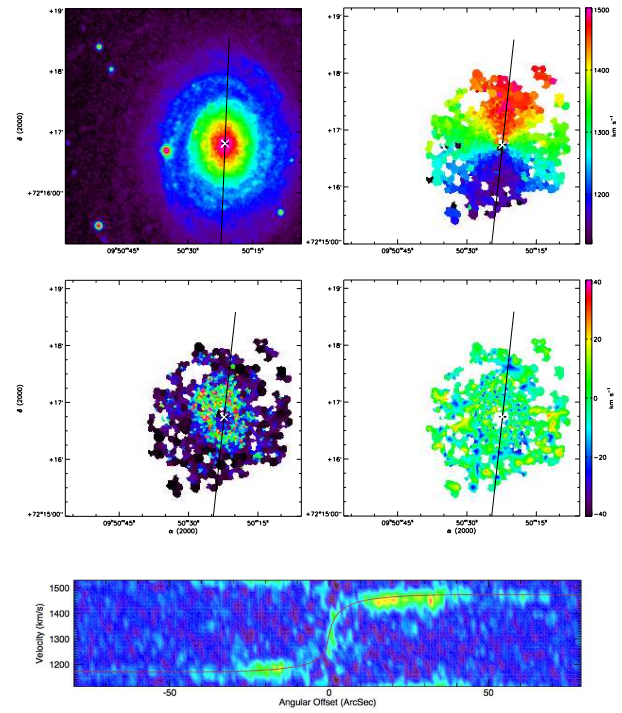


(74) UGC 05228 (XDSS en bande R)

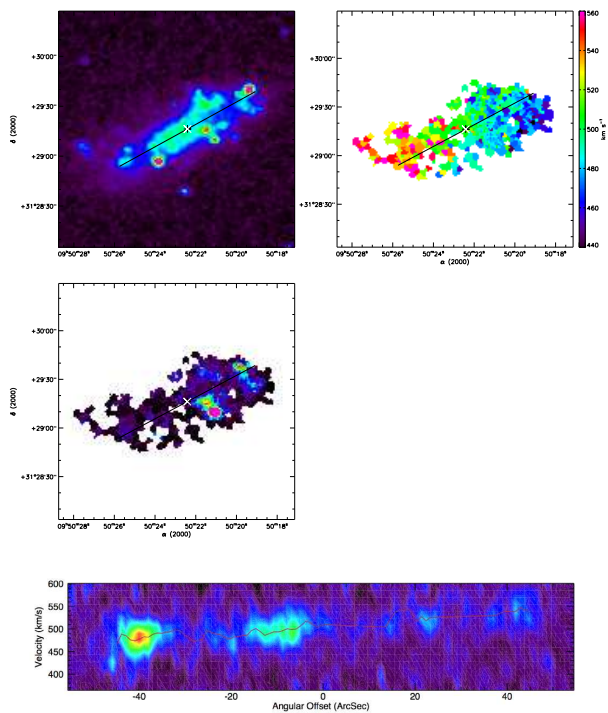
FIG. D.1 : suite



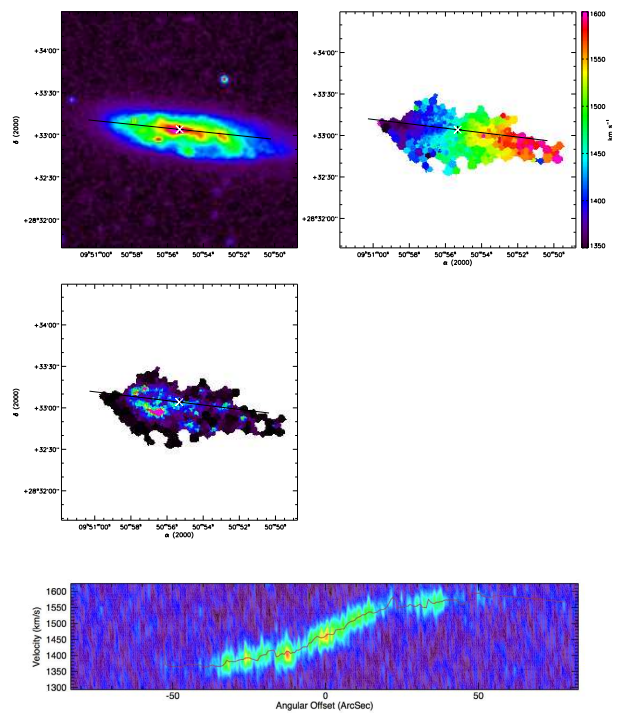
(75) UGC 05251



(76) UGC 05253

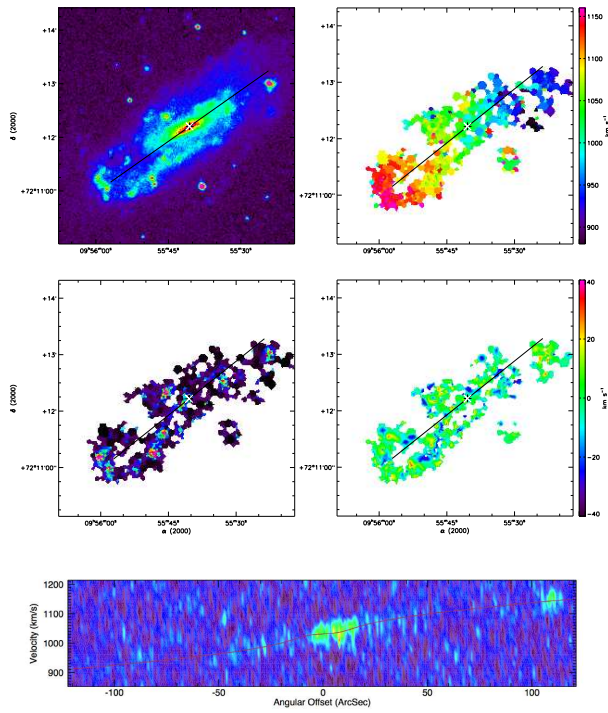


(77) UGC 05272

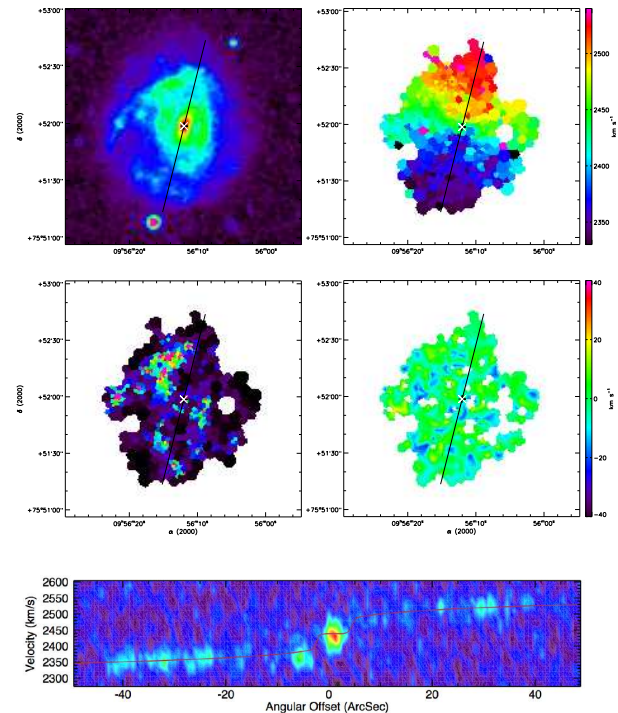


(78) UGC 05279

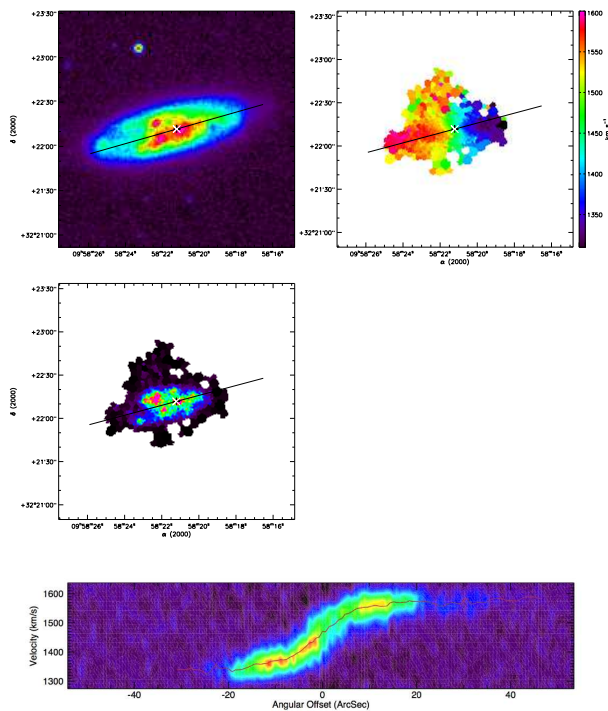
FIG. D.1 : suite



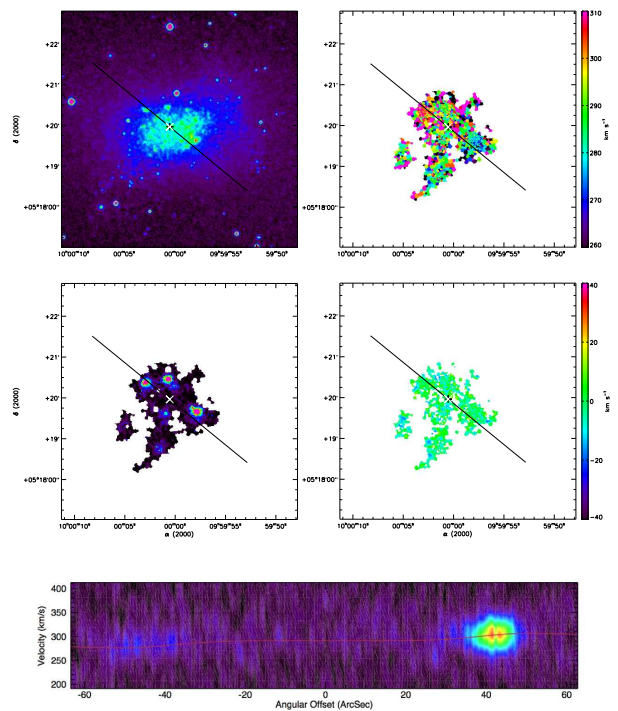
(79) UGC 05316



(80) UGC 05319

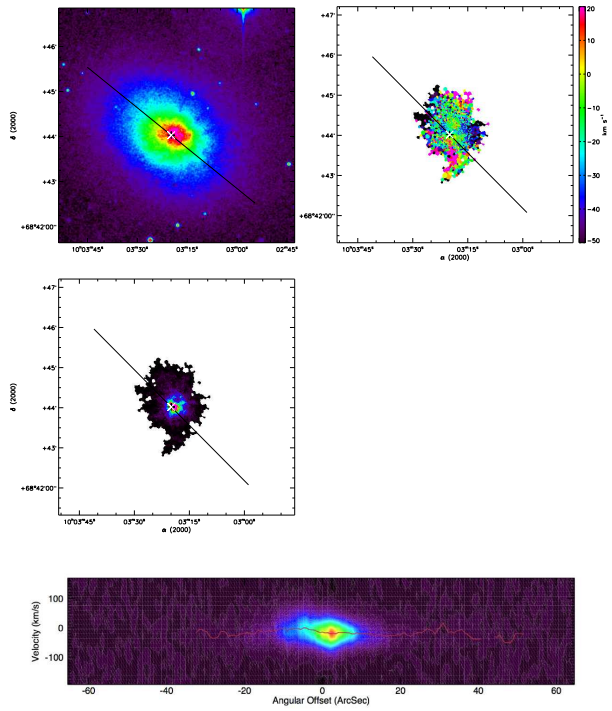


(81) UGC 05351

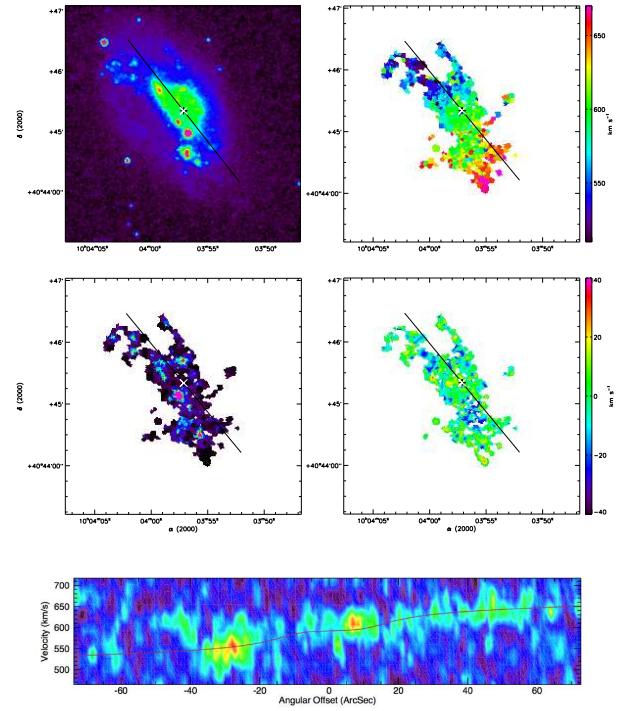


(82) UGC 05373

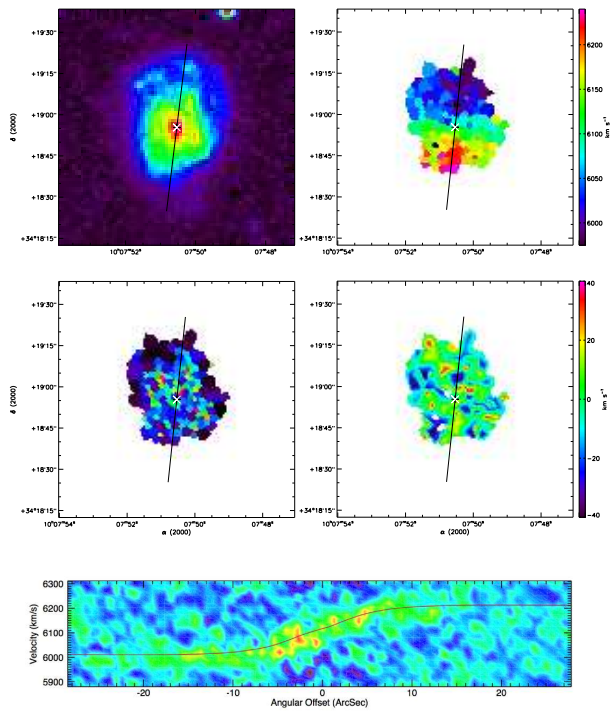
FIG. D.1 : suite



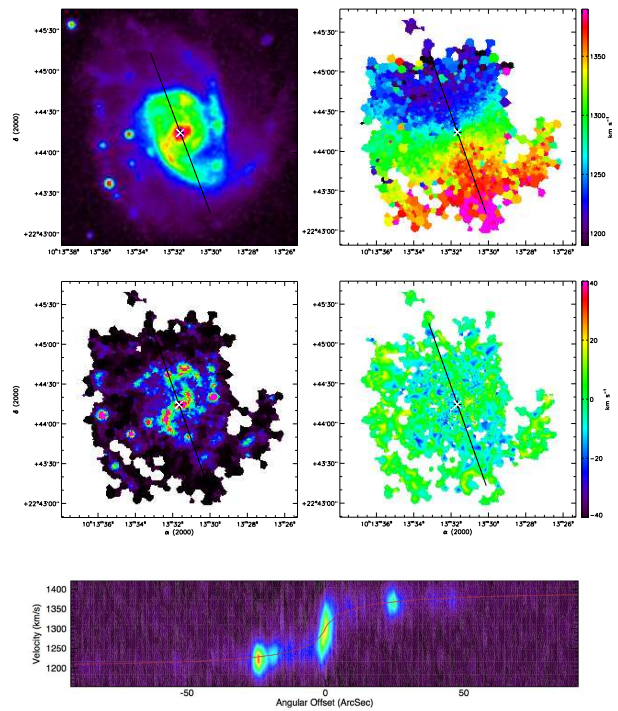
(83) UGC 05398



(84) UGC 05414

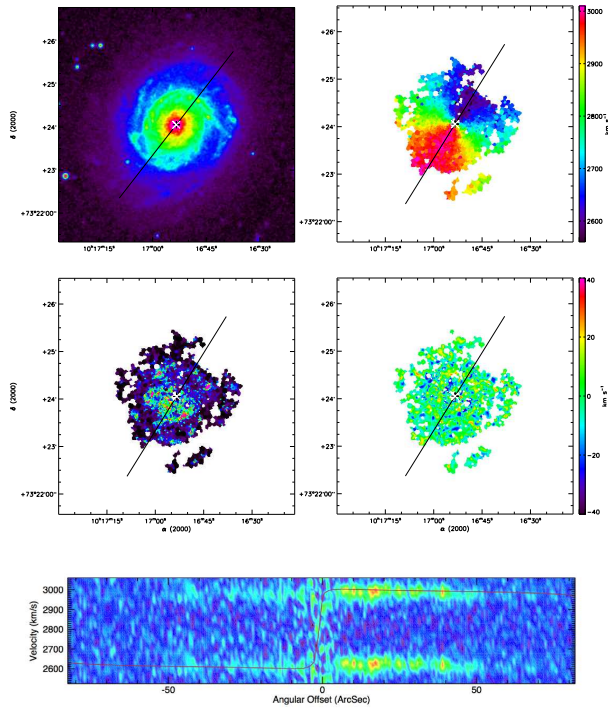


(85) IC 2542

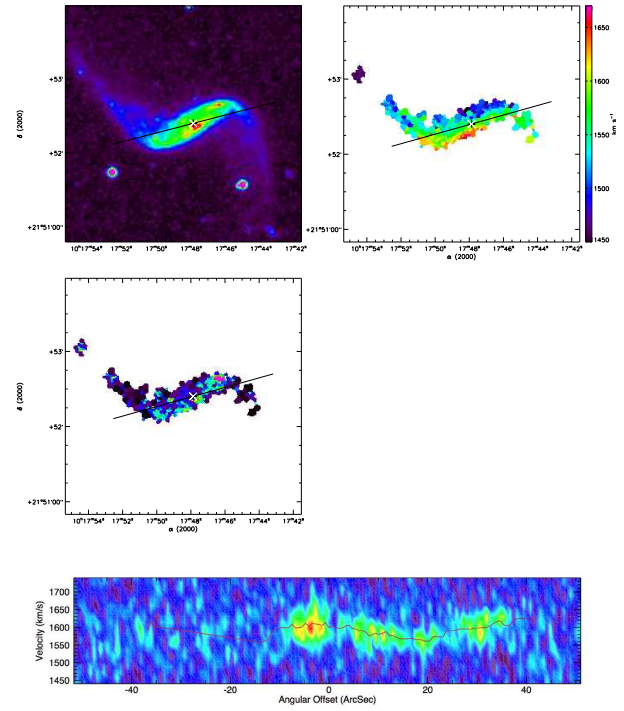


(86) UGC 05510

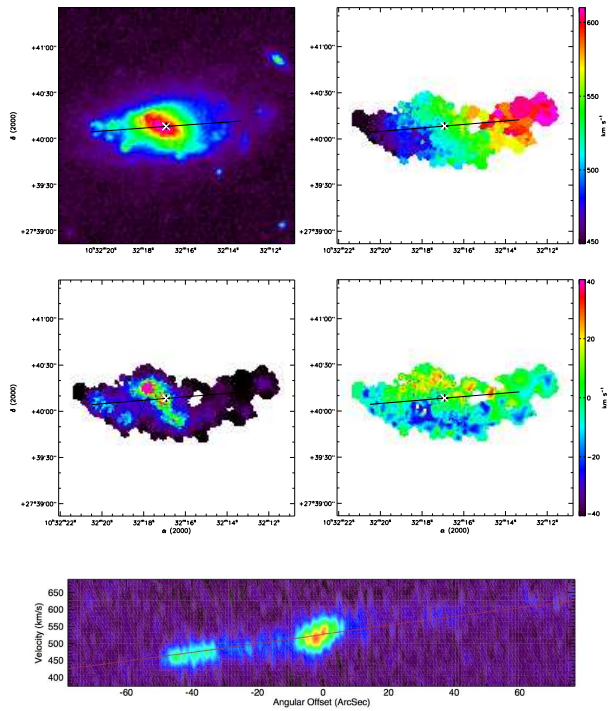
FIG. D.1 : suite



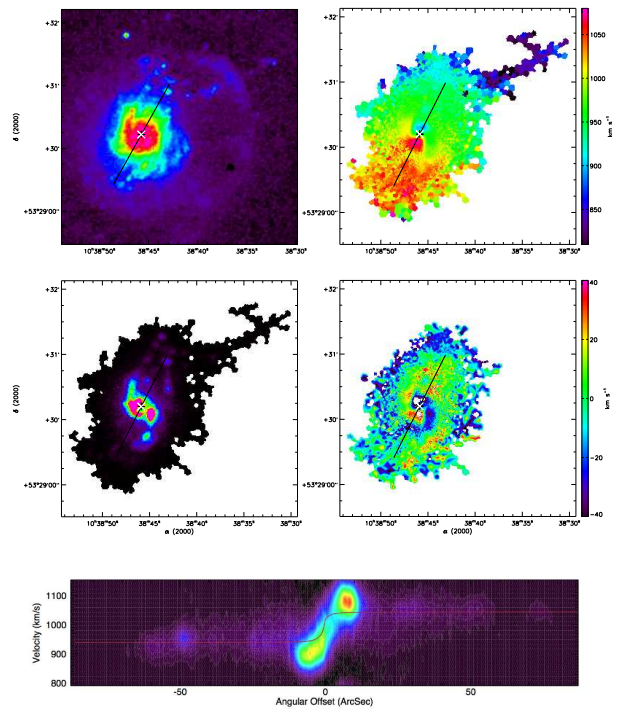
(87) UGC 05532



(88) UGC 05556

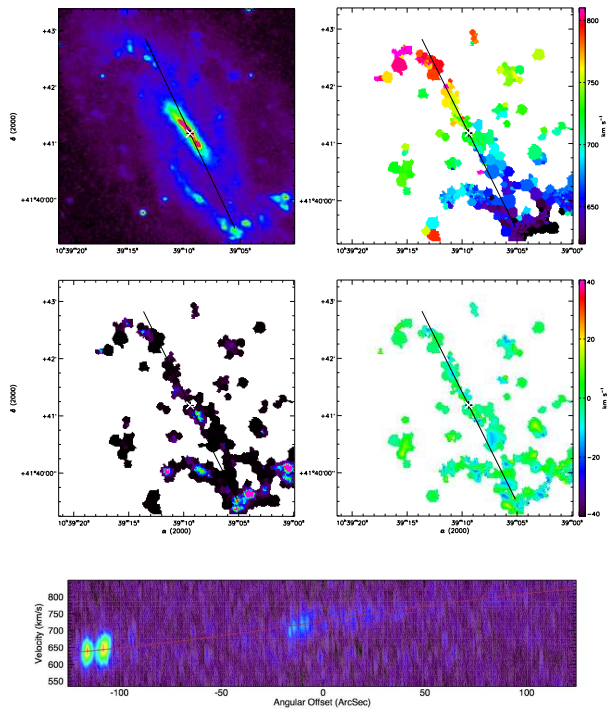


(89) UGC 05721

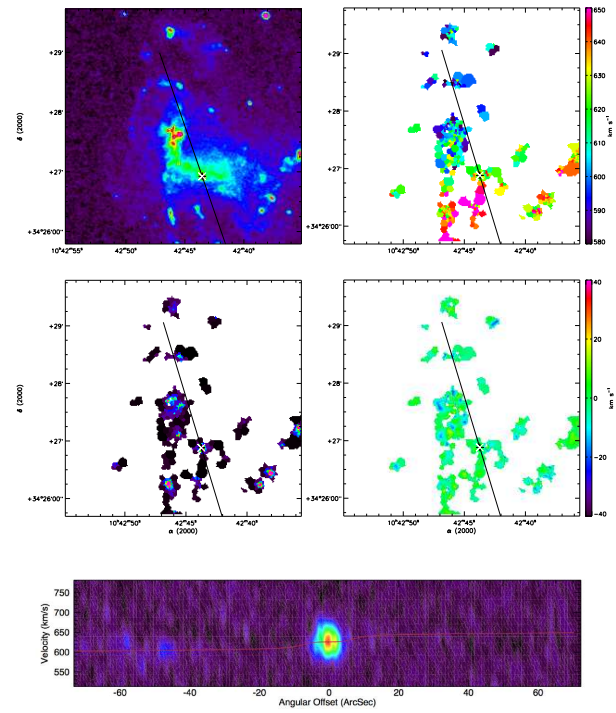


(90) UGC 05786

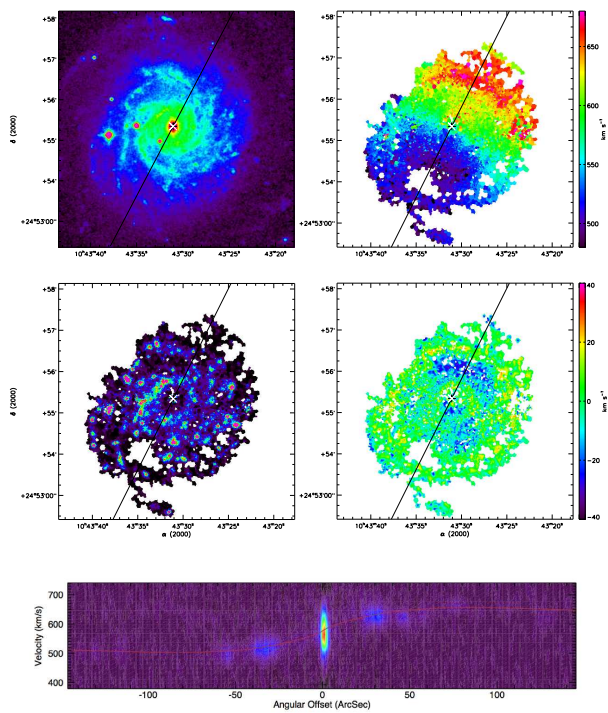
FIG. D.1 : suite



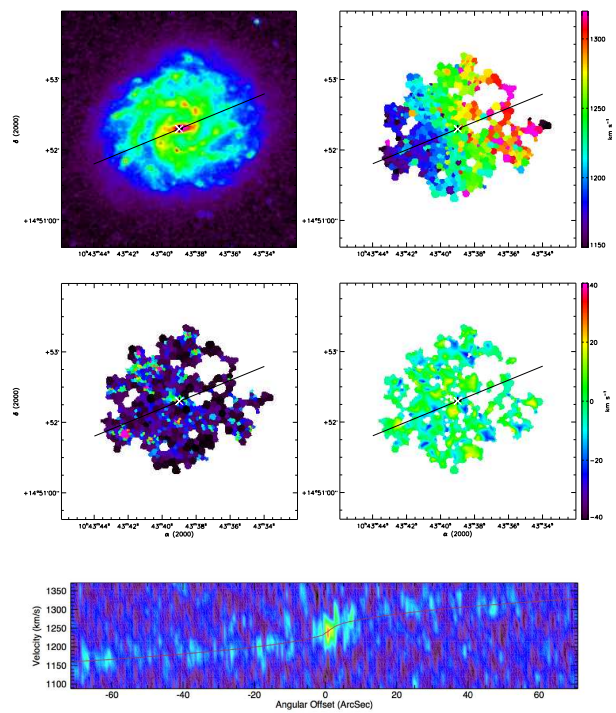
(91) UGC 05789



(92) UGC 05829

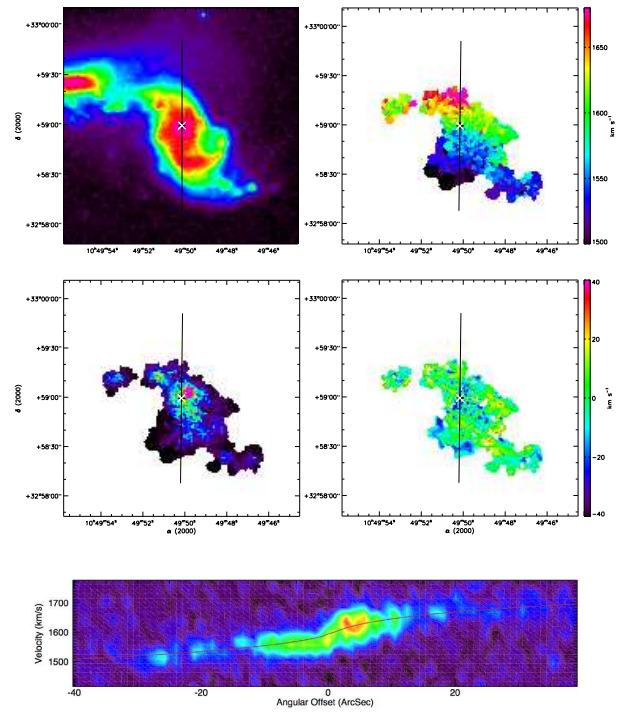


(93) UGC 05840

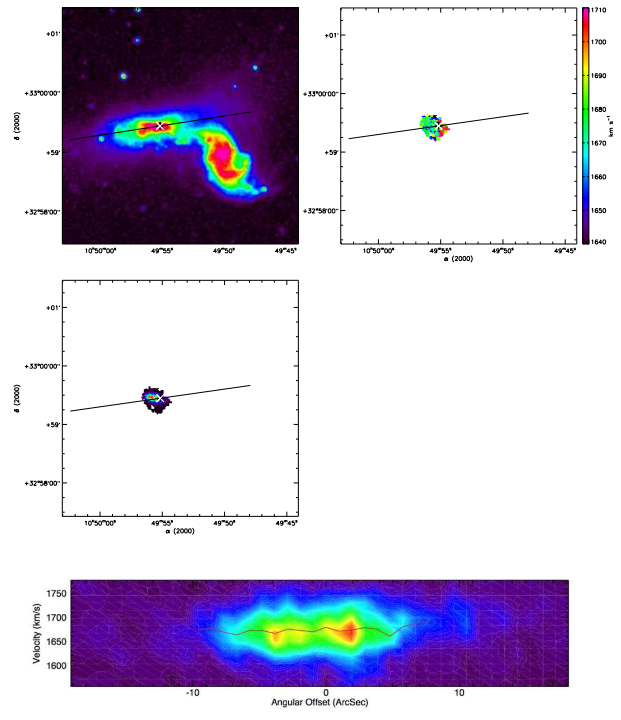


(94) UGC 05842

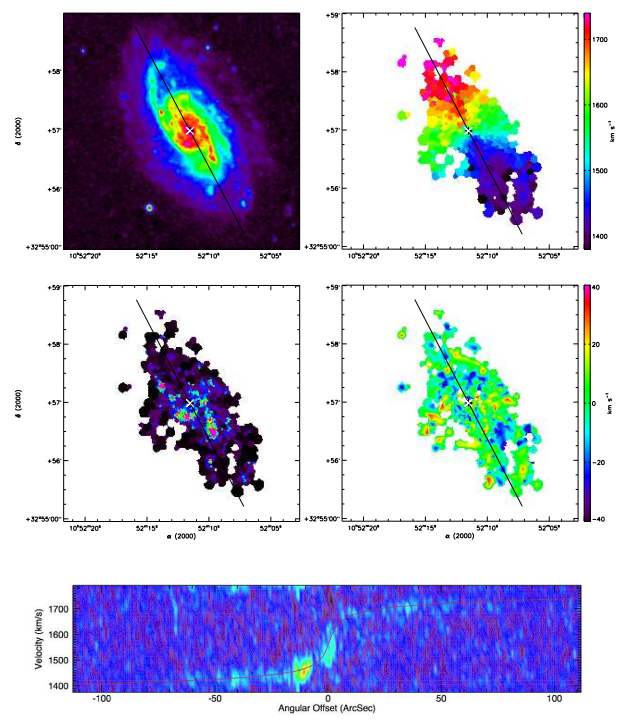
FIG. D.1 : suite



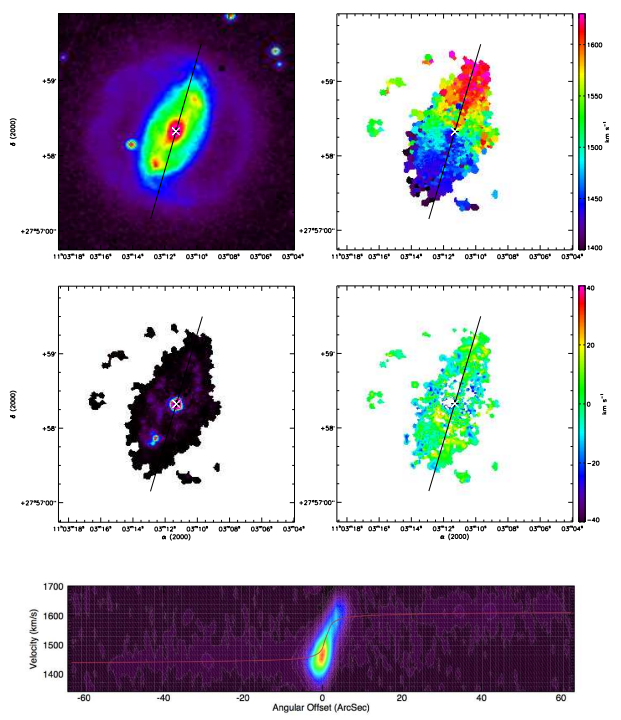
(95) UGC 05931



(96) UGC 05935

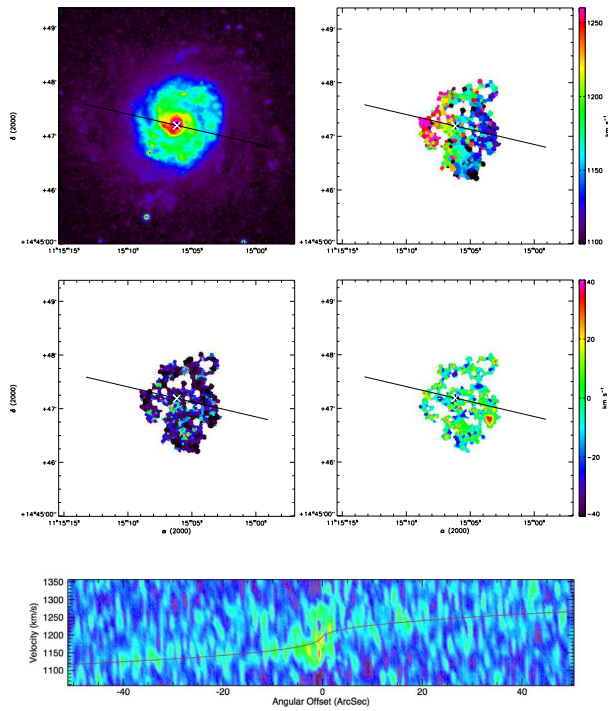


(97) UGC 05982

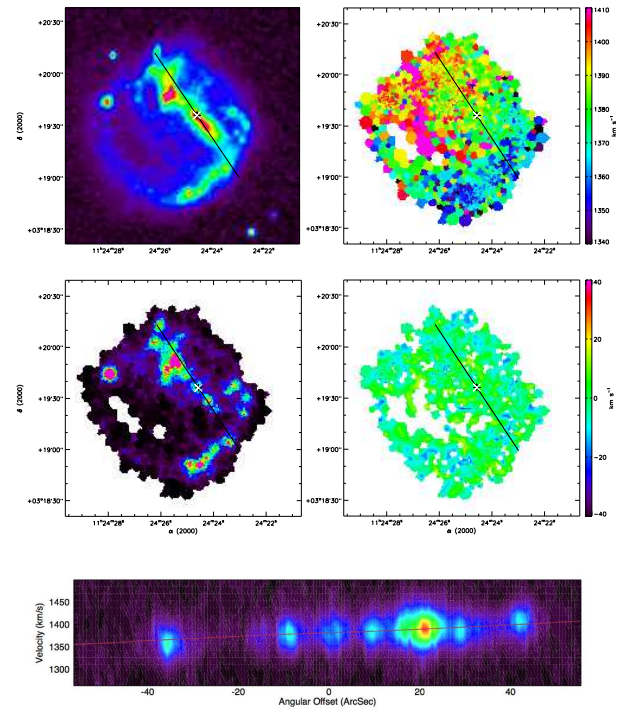


(98) UGC 06118

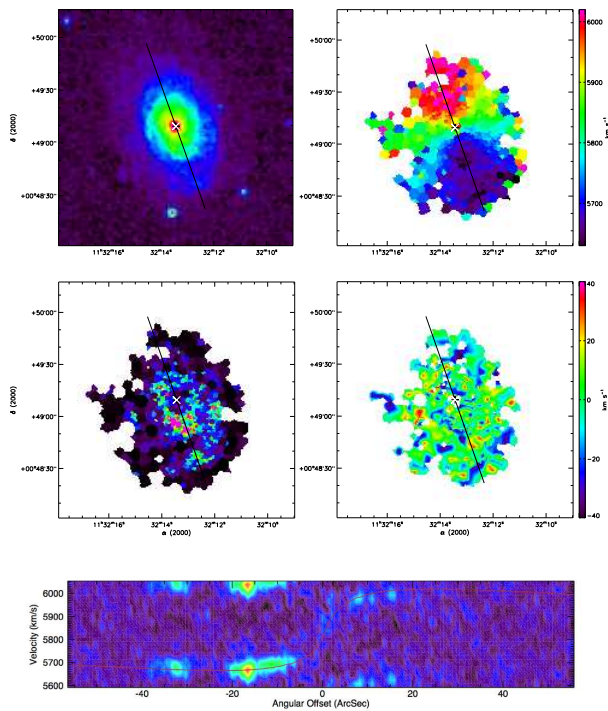
FIG. D.1 : suite



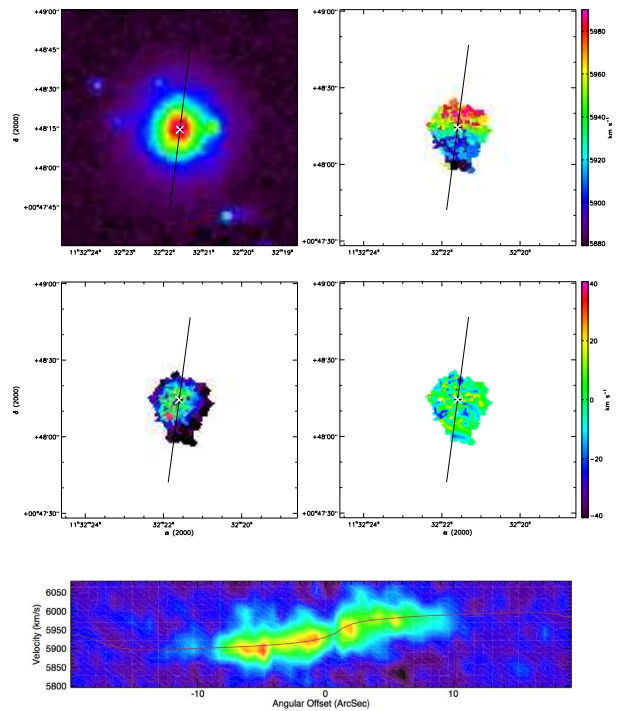
(99) UGC 06277



(100) UGC 06419



(101) UGC 06521 (XDSS en bande R)



(102) UGC 06523 (XDSS en bande R)

FIG. D.1 : suite

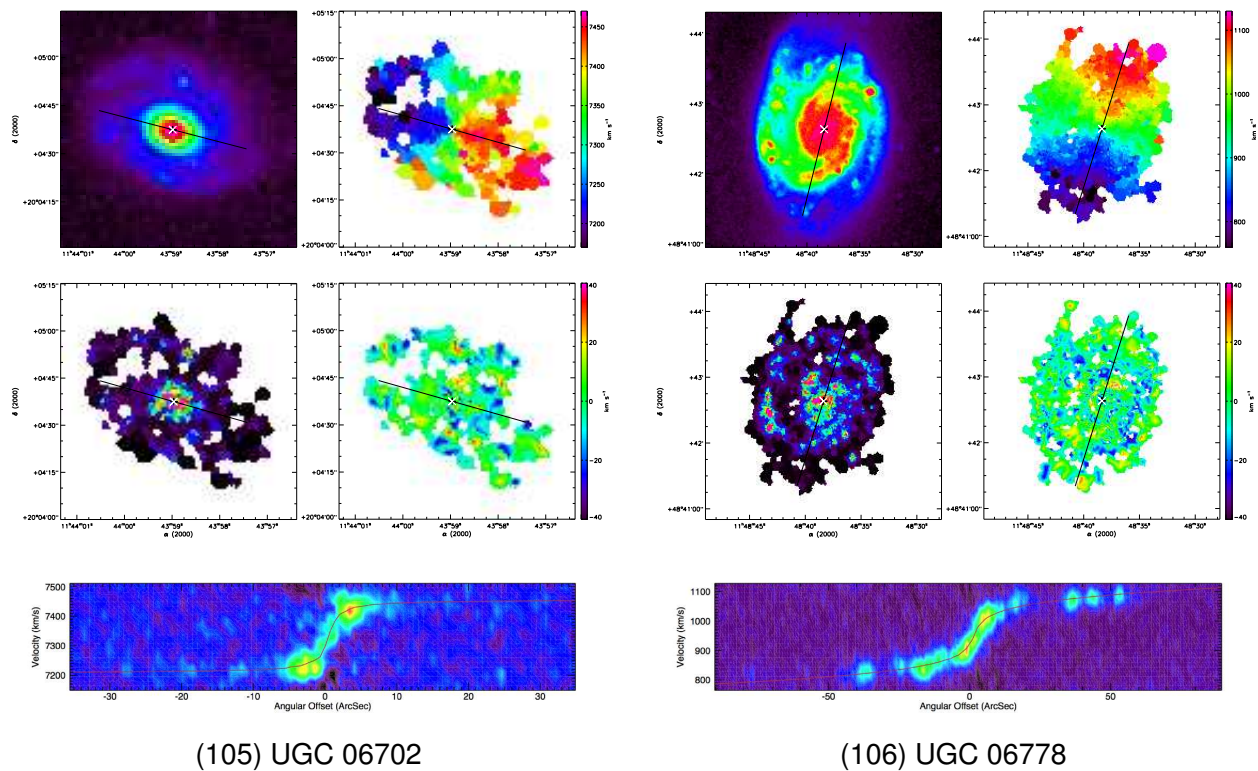
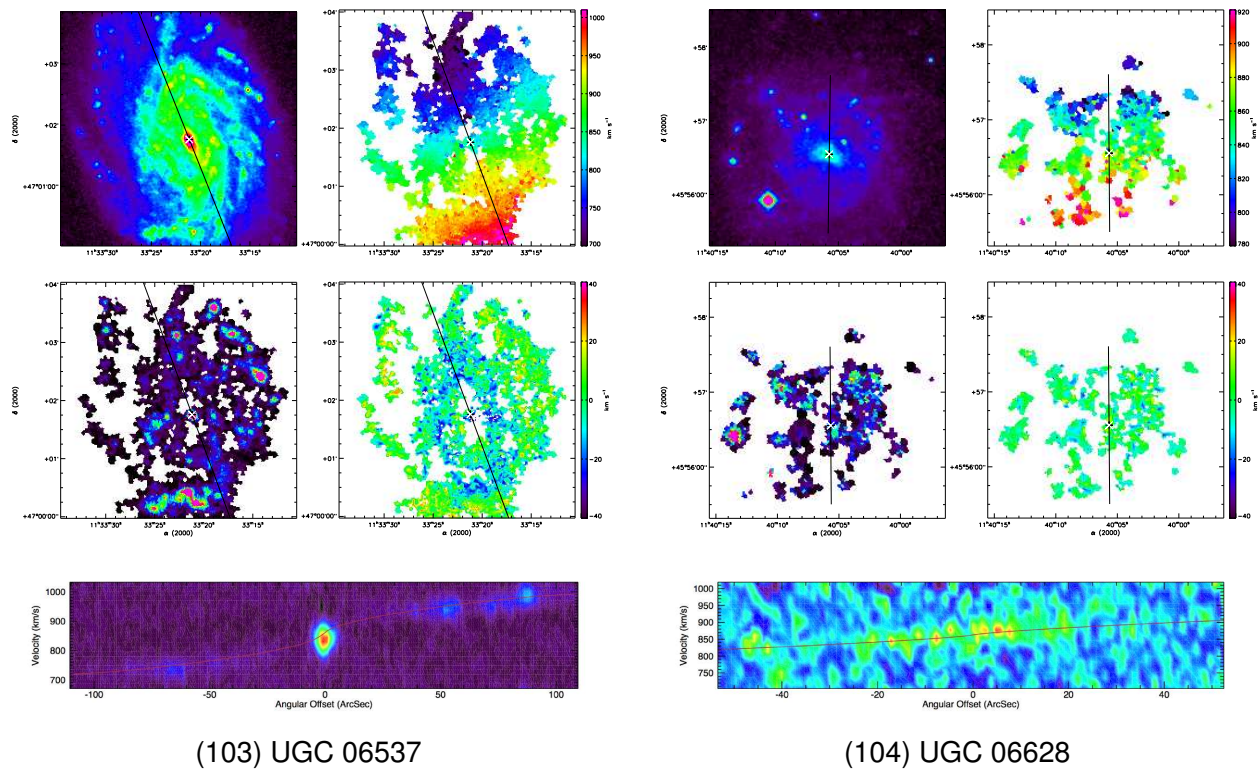
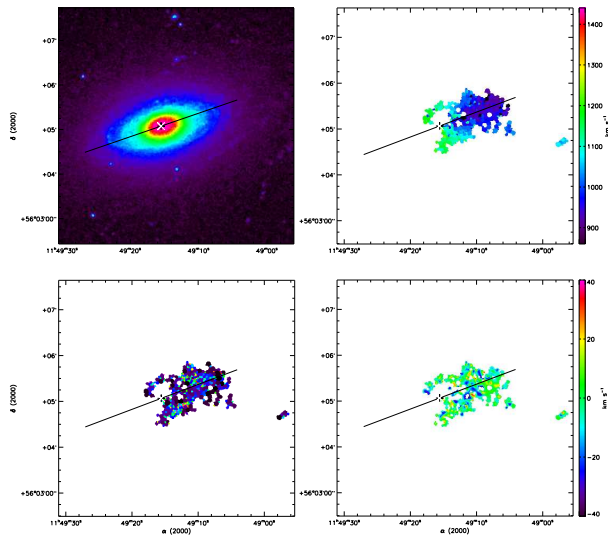
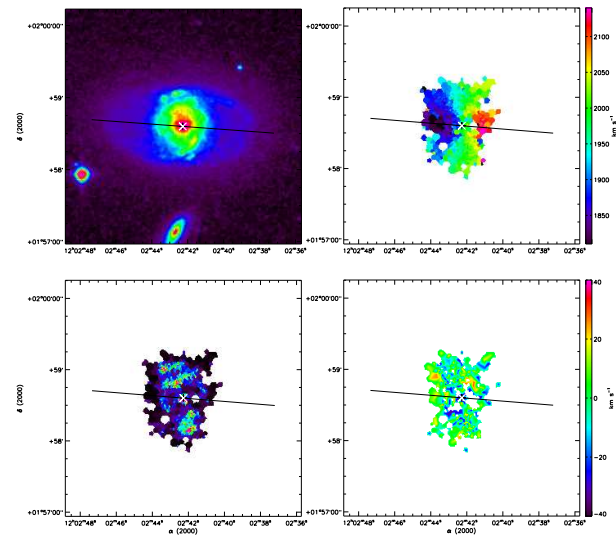


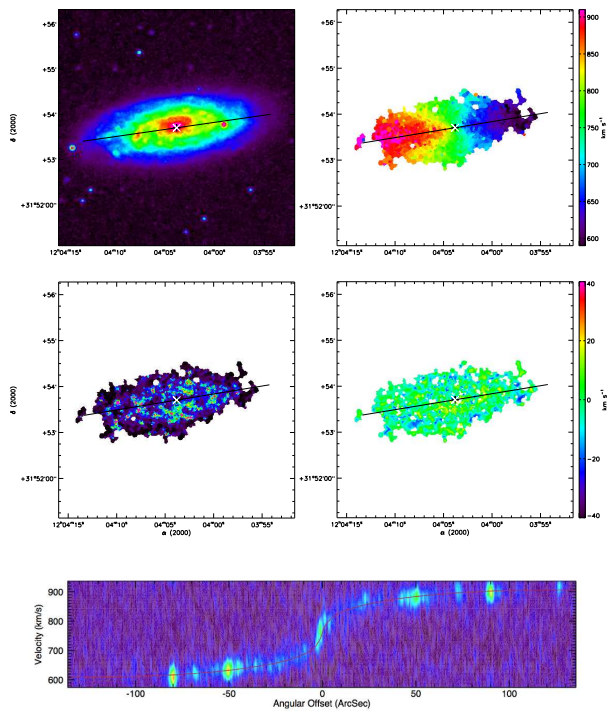
FIG. D.1 : suite



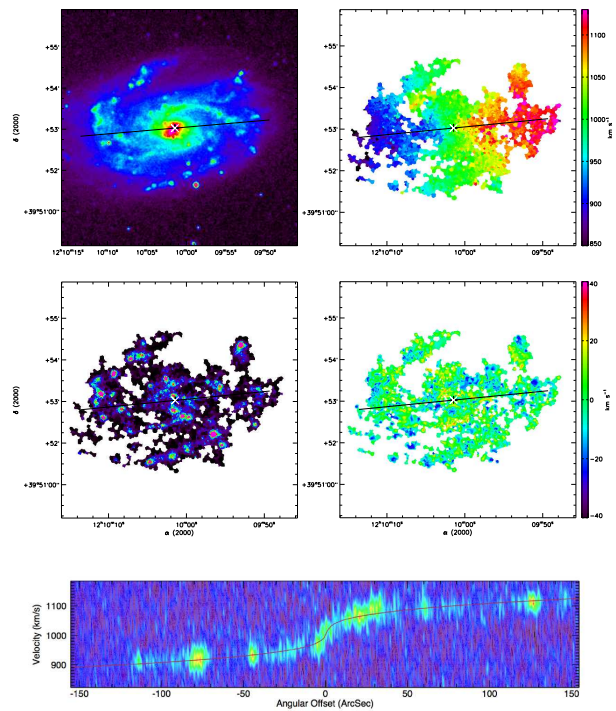
(107) UGC 06787



(108) UGC 07021

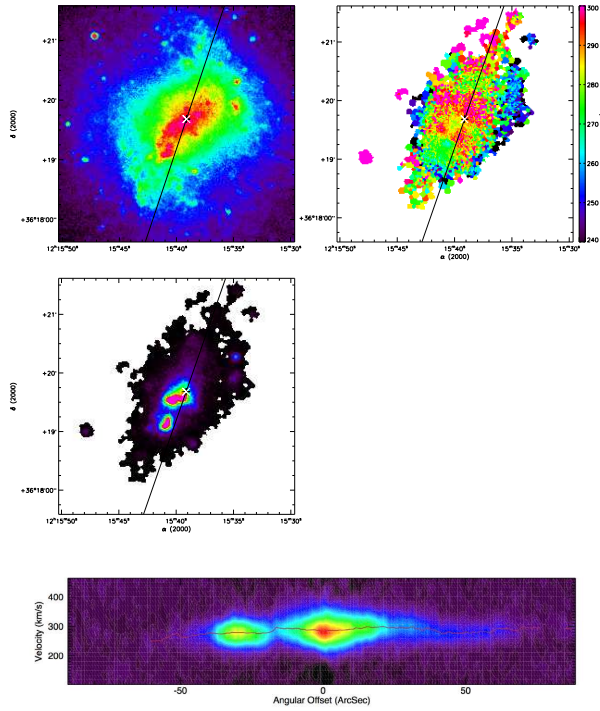


(109) UGC 07045

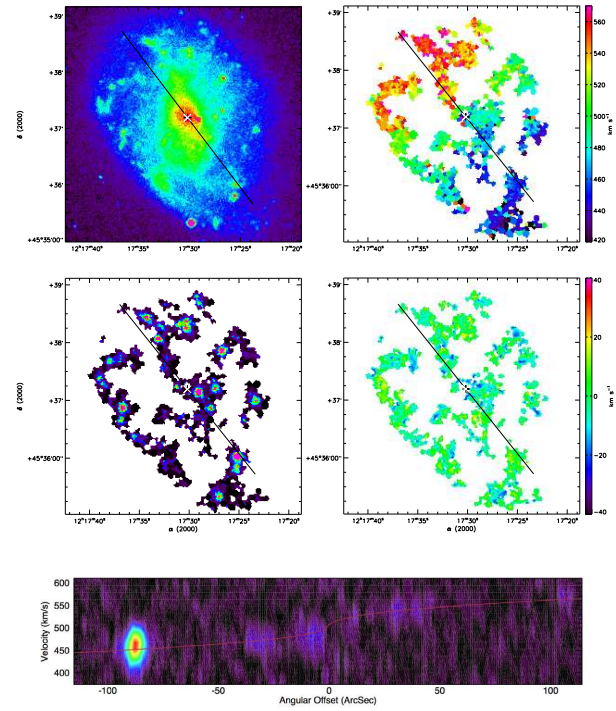


(110) UGC 07154

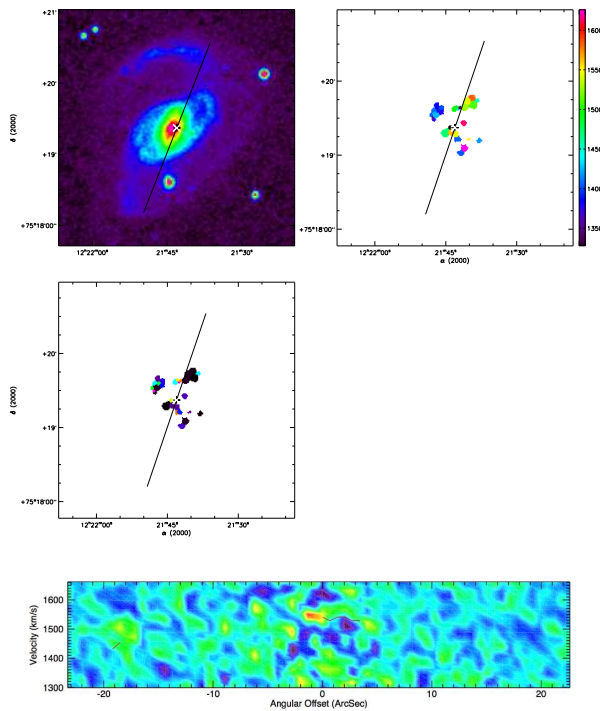
FIG. D.1 : suite



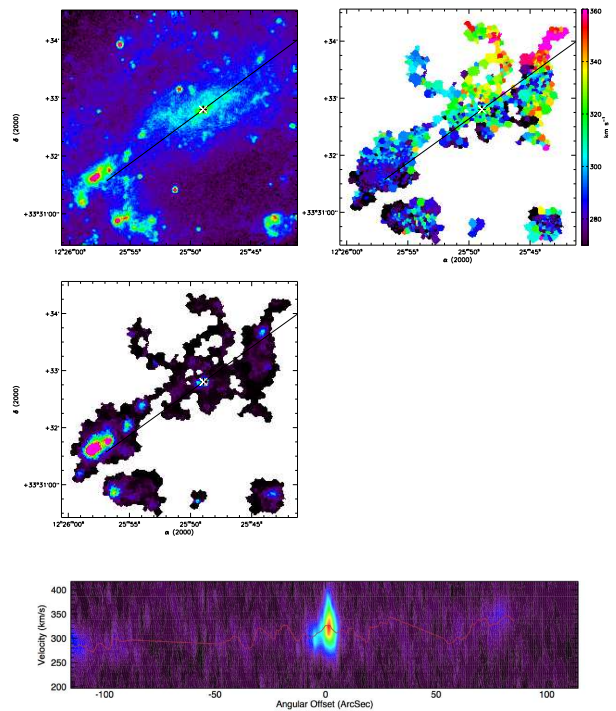
(111) UGC 07278



(112) UGC 07323

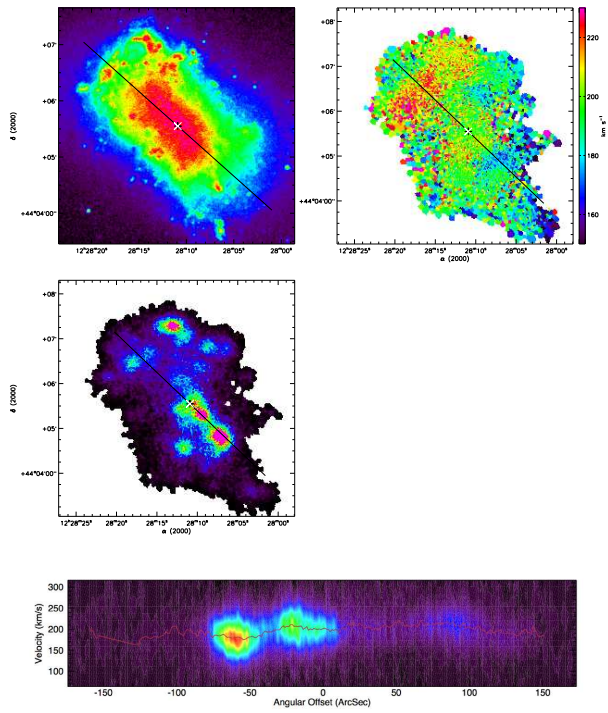


(113) UGC 07429

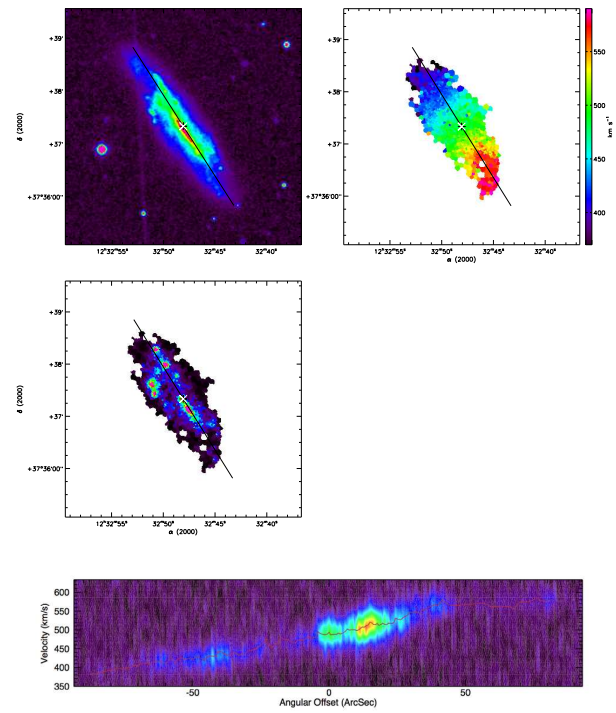


(114) UGC 07524

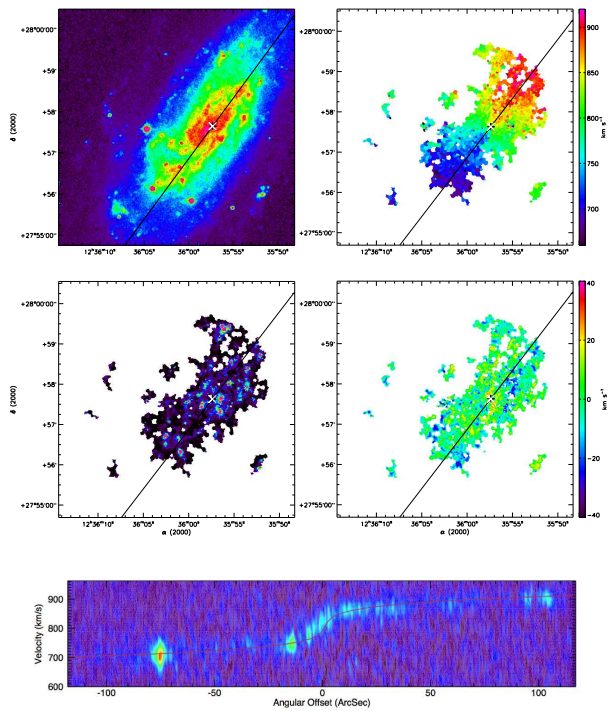
FIG. D.1 : suite



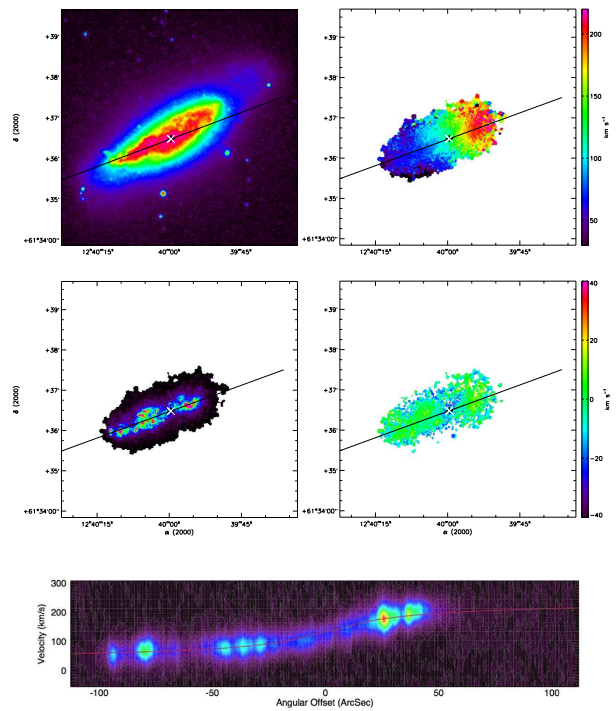
(115) UGC 07592



(116) UGC 07699

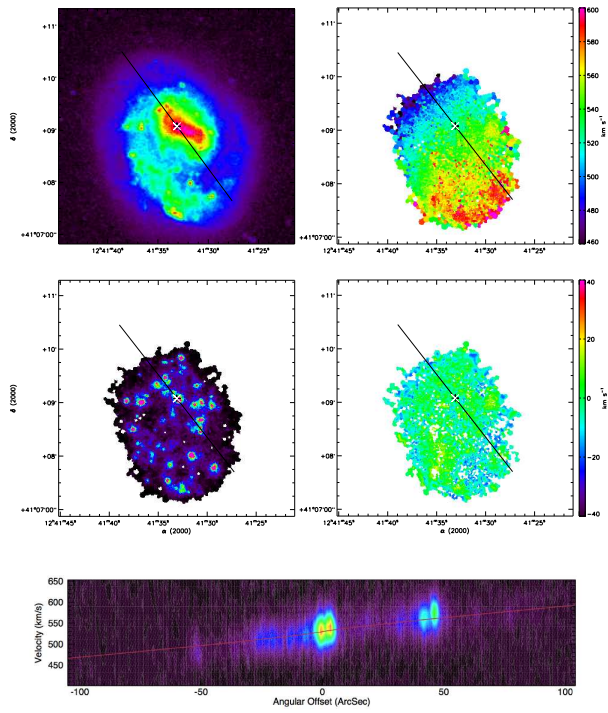


(117) UGC 07766

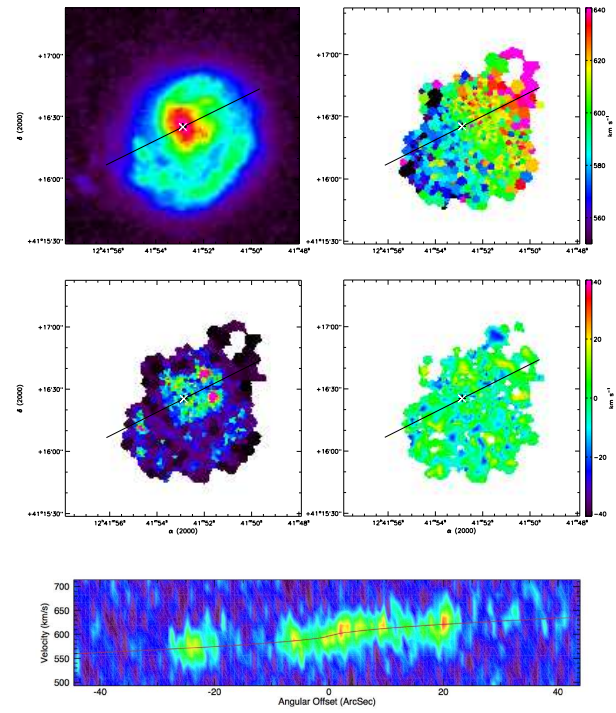


(118) UGC 07831

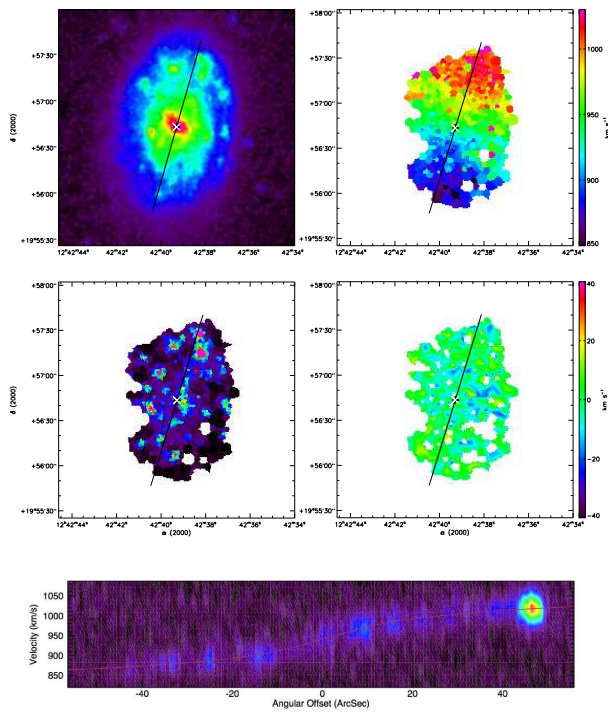
FIG. D.1 : suite



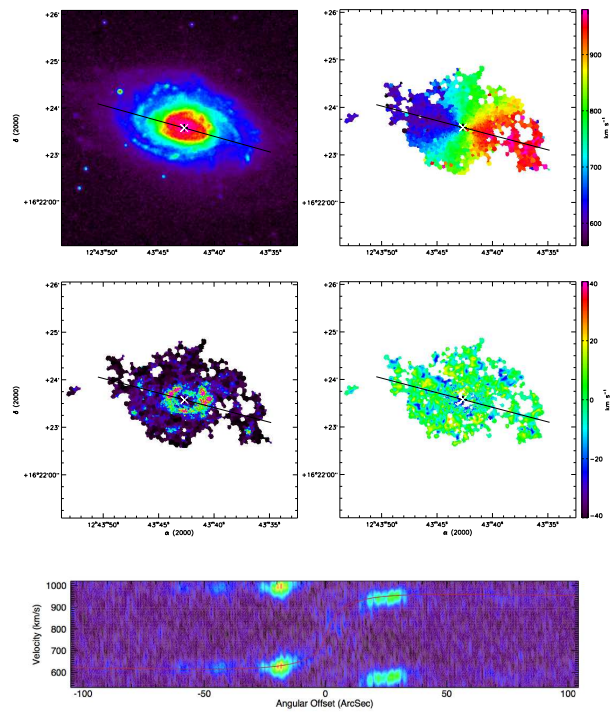
(119) UGC 07853



(120) UGC 07861

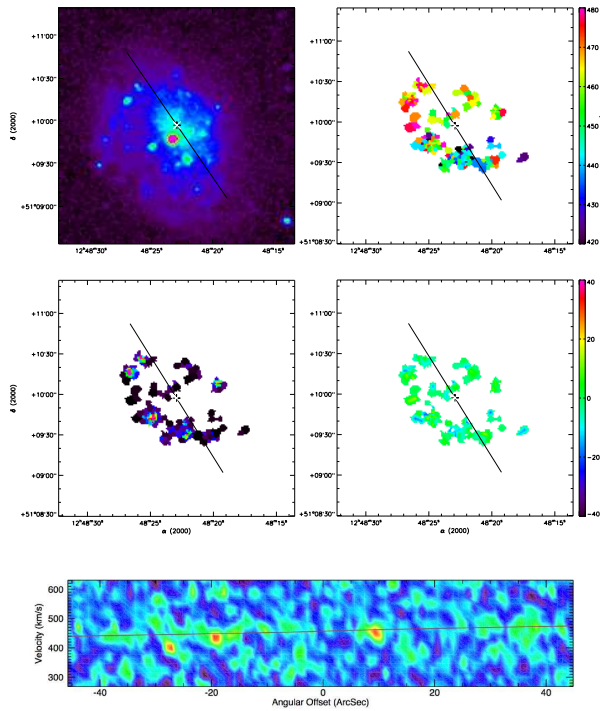


(121) UGC 07876

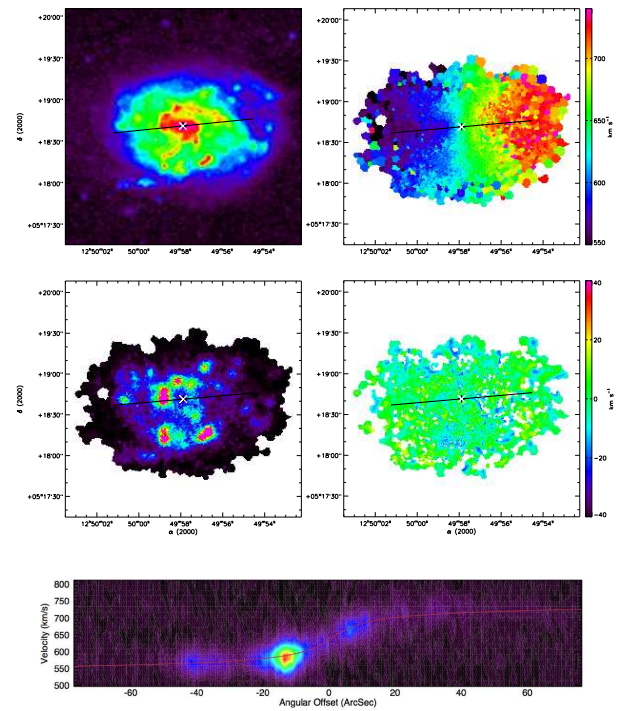


(122) UGC 07901

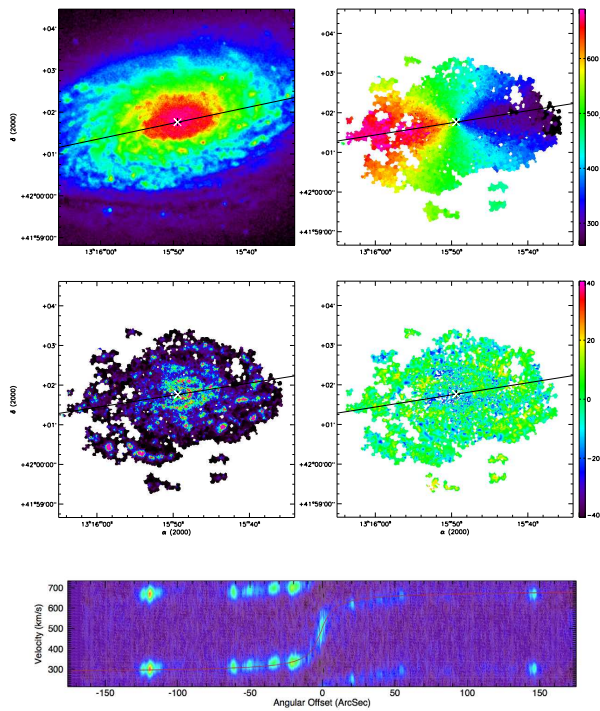
FIG. D.1 : suite



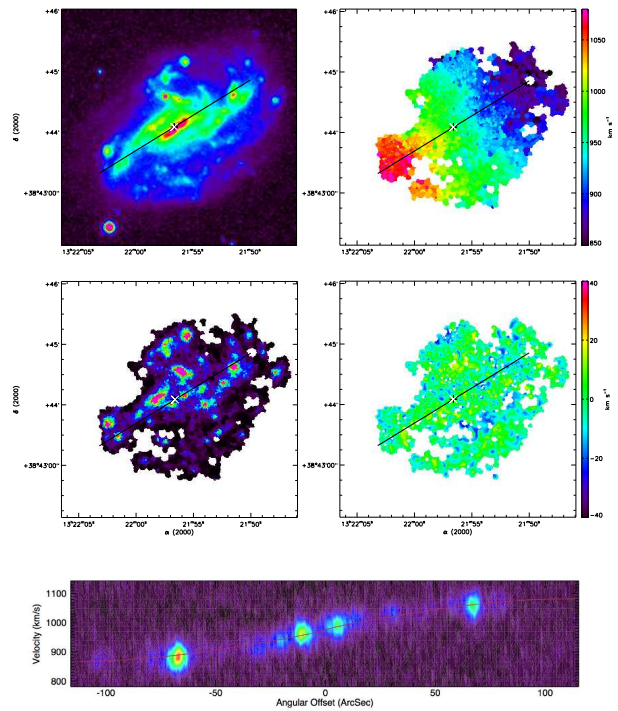
(123) UGC 07971



(124) UGC 07985

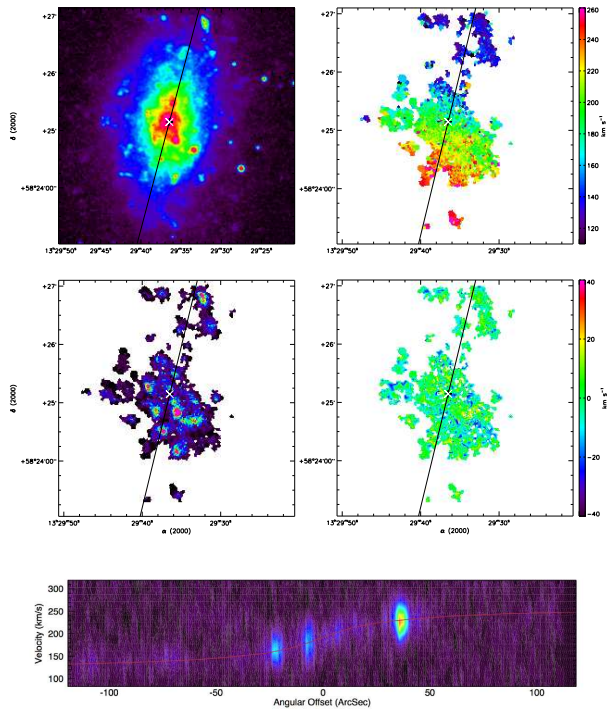


(125) UGC 08334

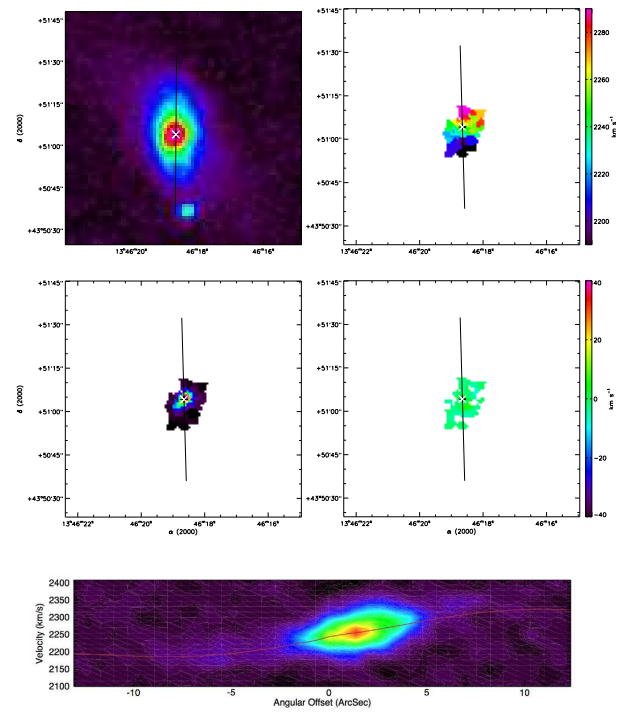


(126) UGC 08403

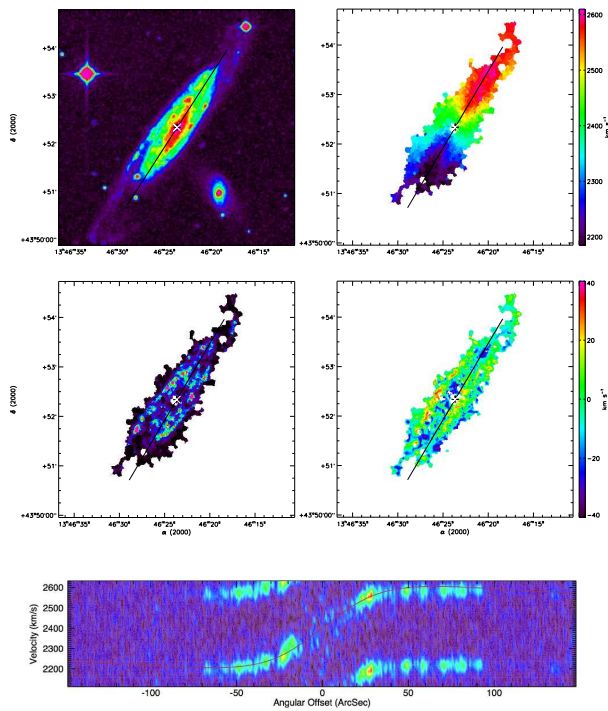
FIG. D.1 : suite



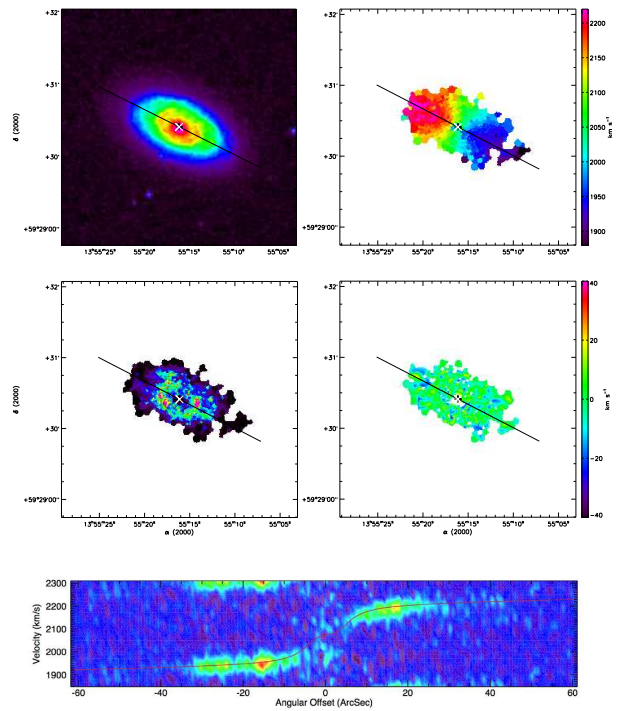
(127) UGC 08490



(128) NGC 5296

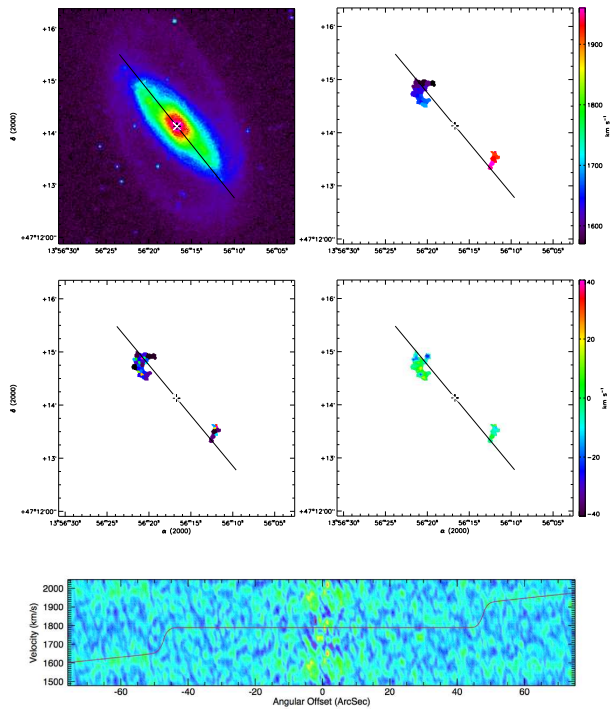


(129) UGC 08709

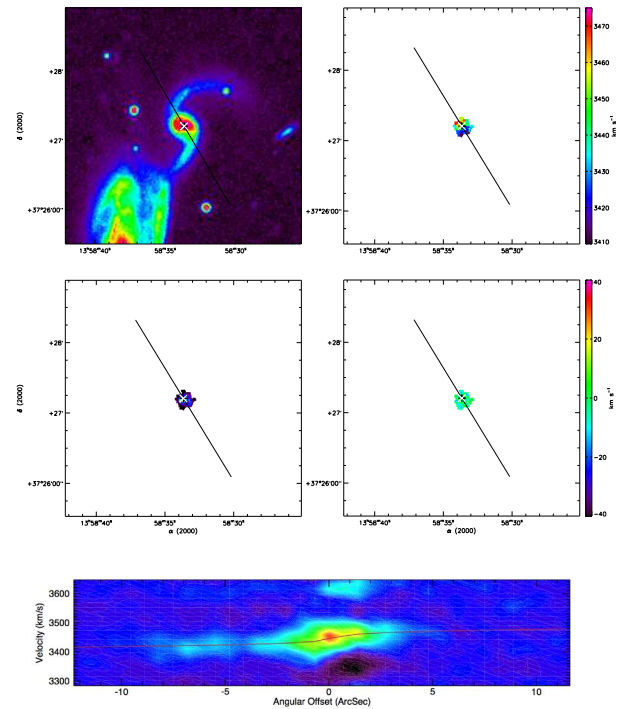


(130) UGC 08852

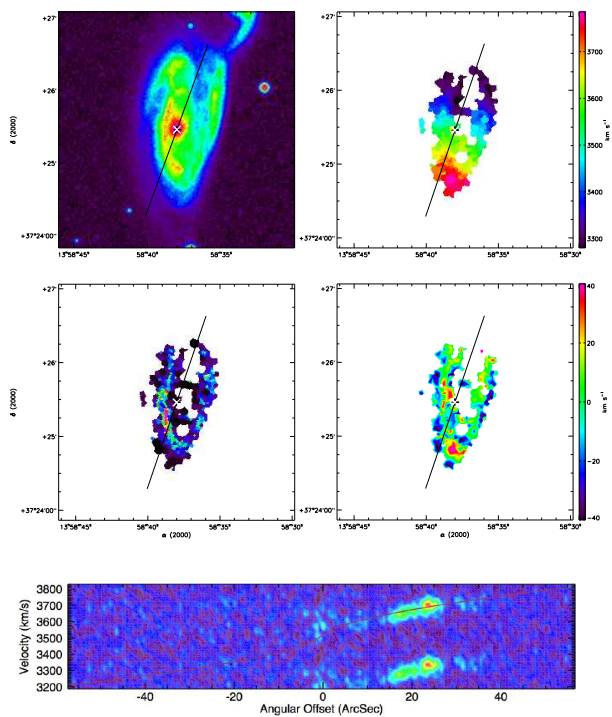
FIG. D.1 : suite



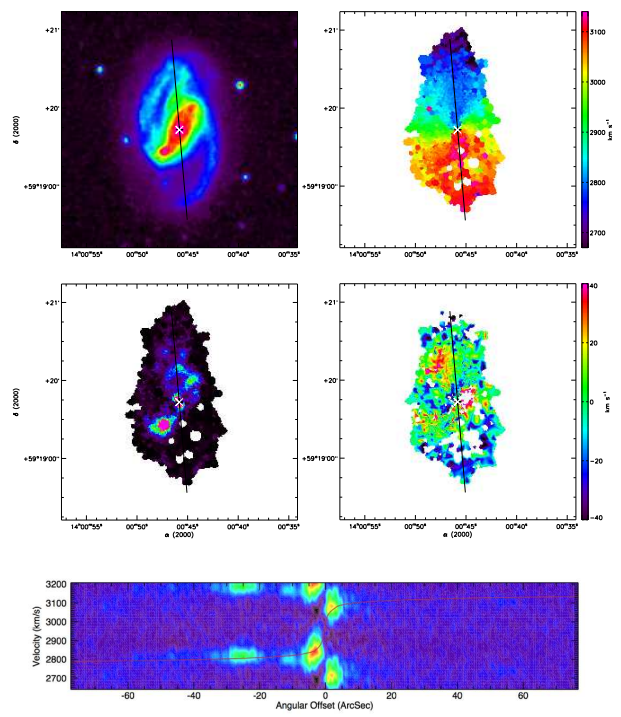
(131) UGC 08863



(132) UGC 08898

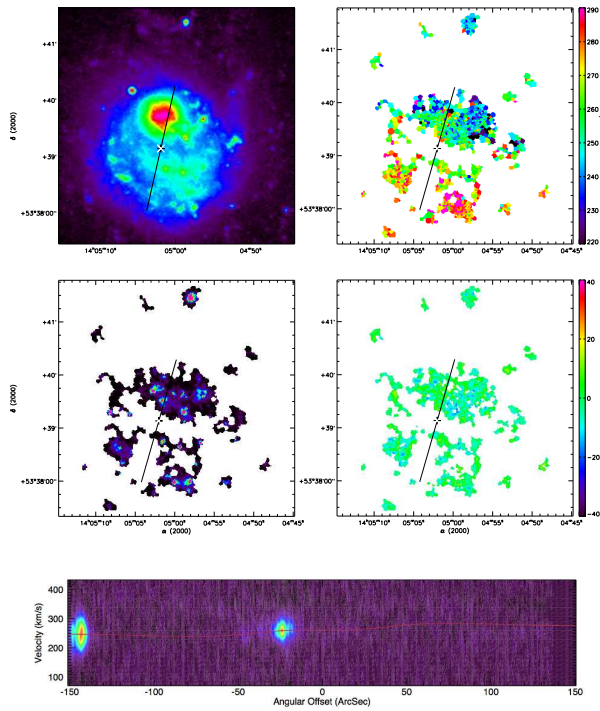


(133) UGC 08900

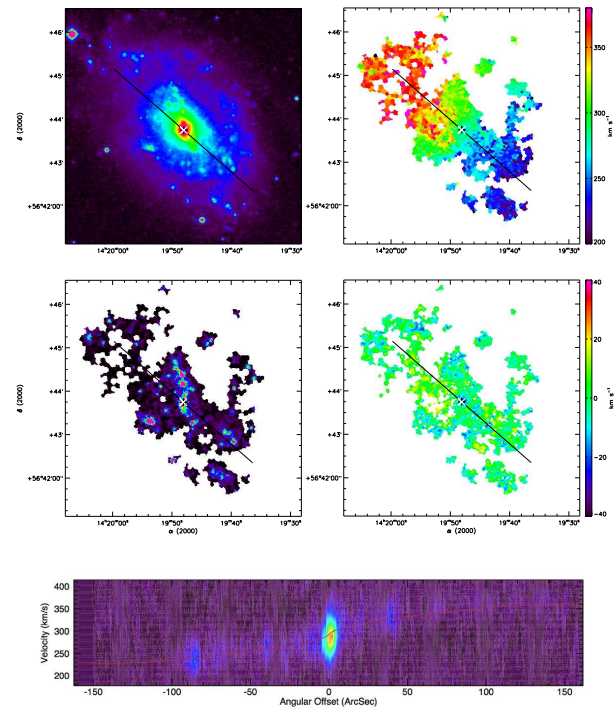


(134) UGC 08937

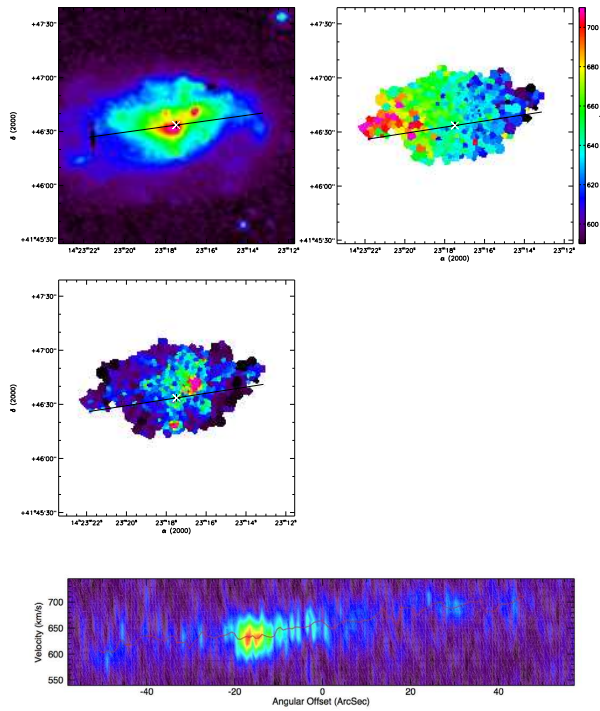
FIG. D.1 : suite



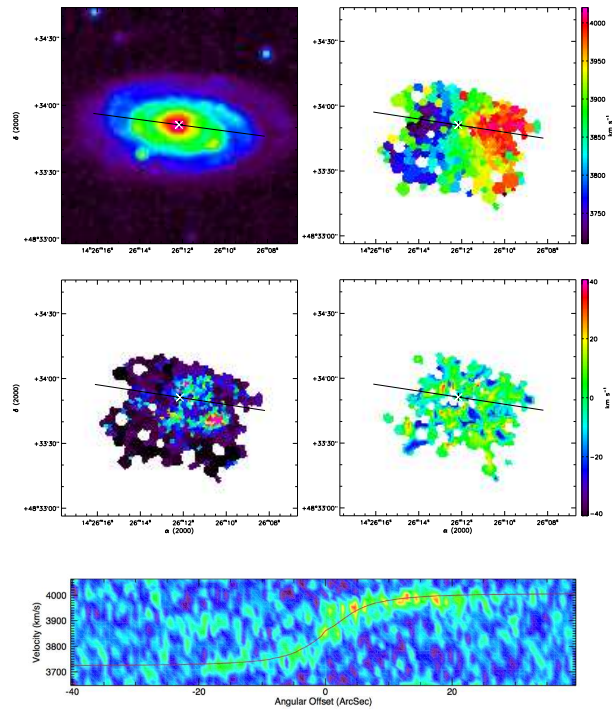
(135) UGC 09013



(136) UGC 09179

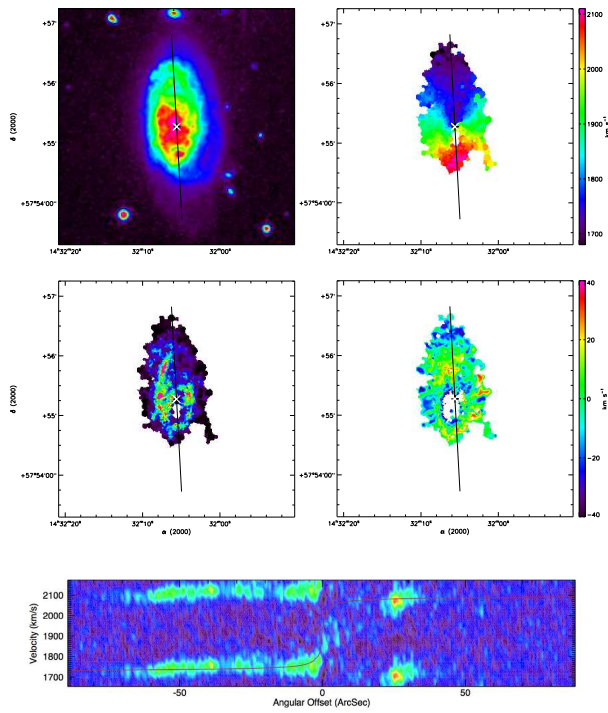


(137) UGC 09219

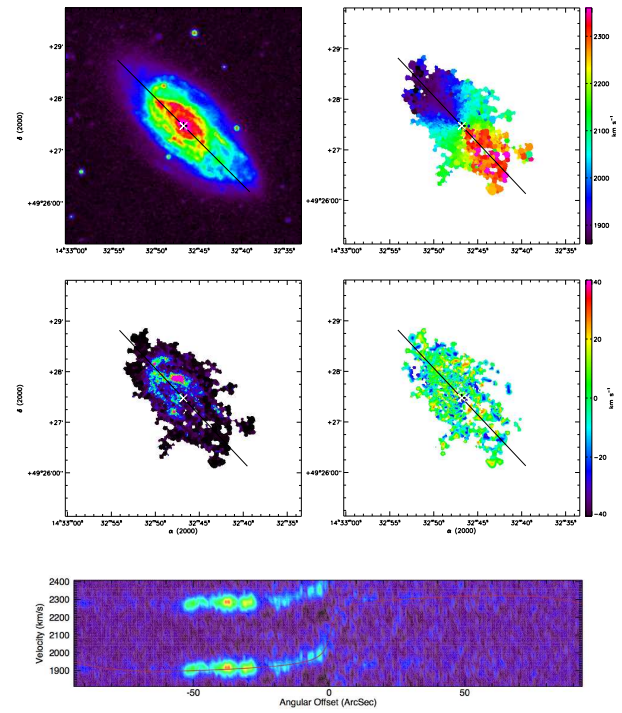


(138) UGC 09248

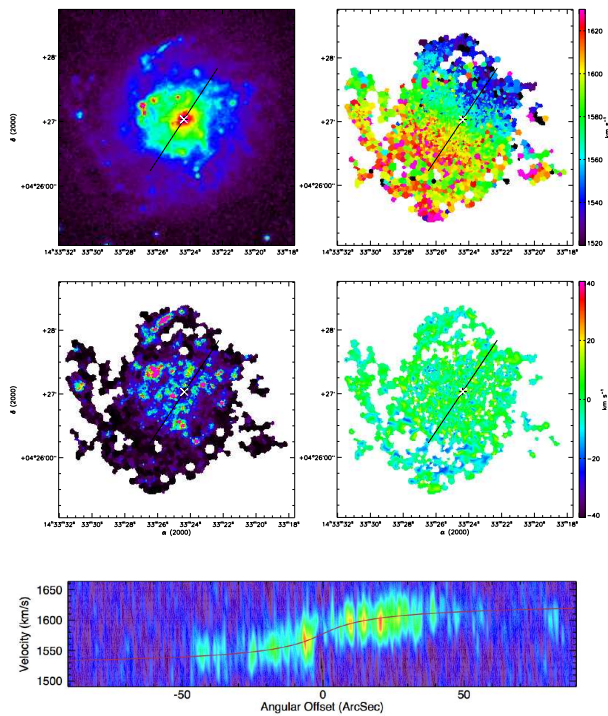
FIG. D.1 : suite



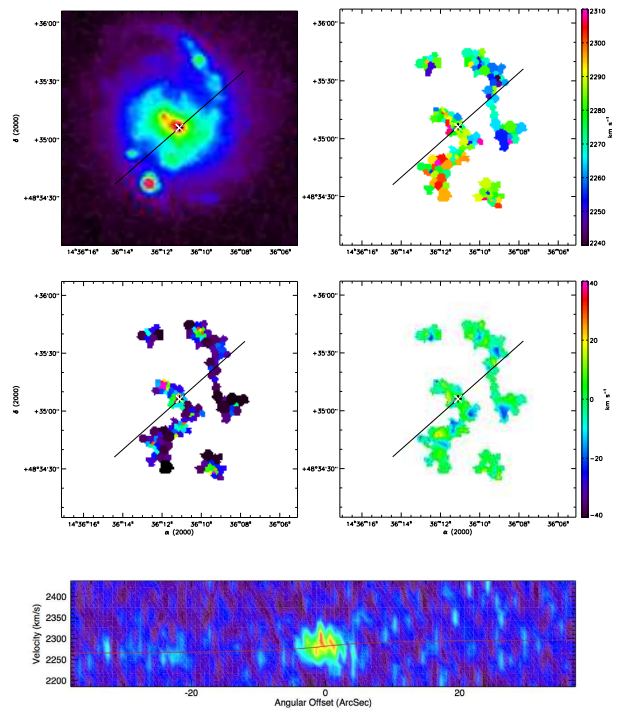
(139) UGC 09358



(140) UGC 09366

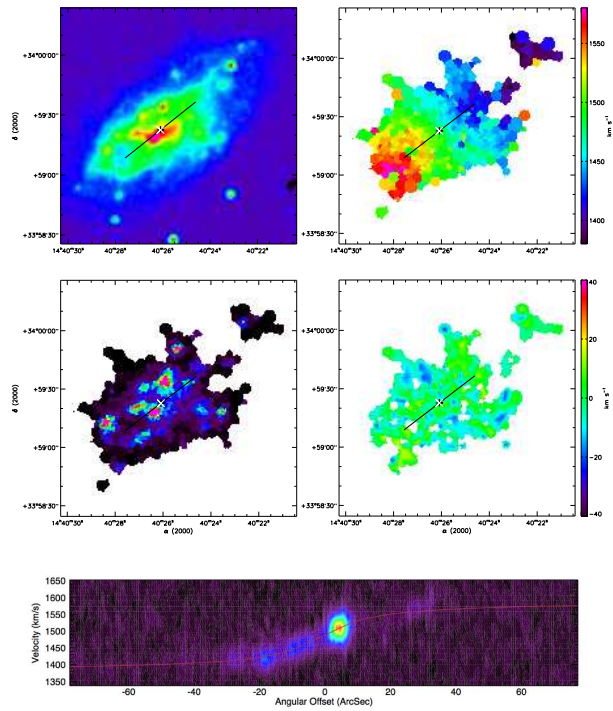


(141) UGC 09363

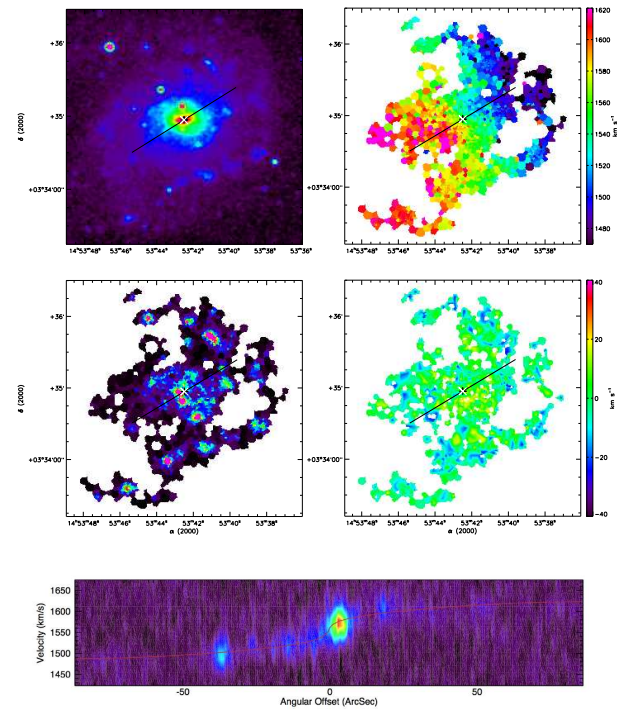


(142) UGC 09406

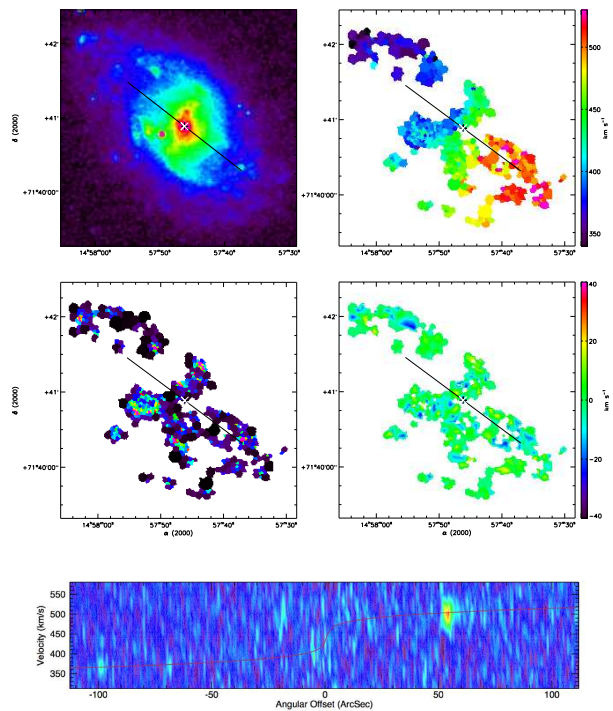
FIG. D.1 : suite



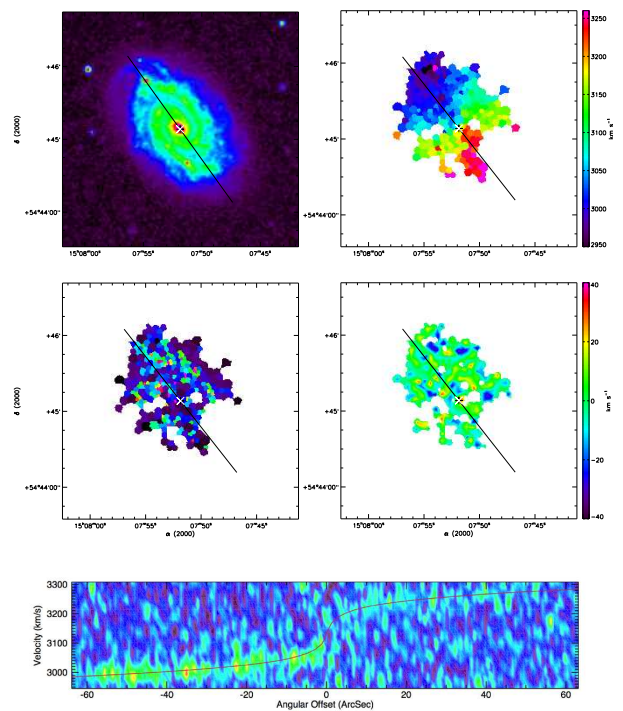
(143) UGC 09465



(144) UGC 09576 (XDSS en bande R)

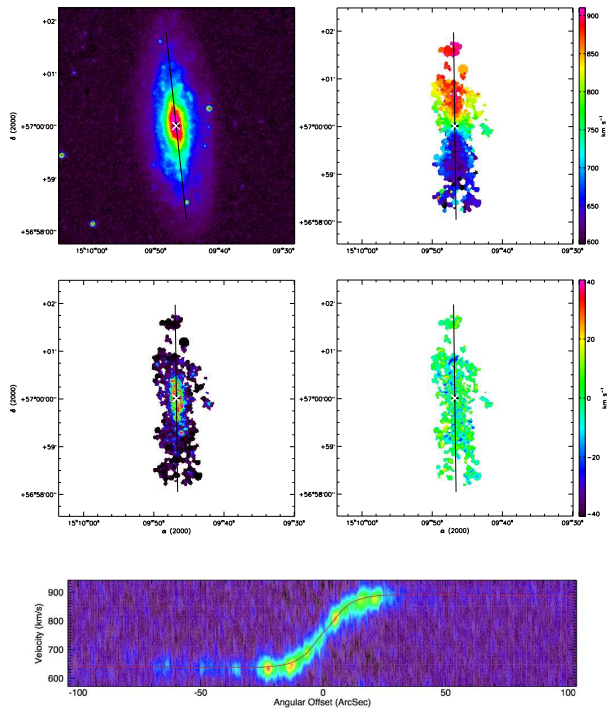


(145) UGC 09649

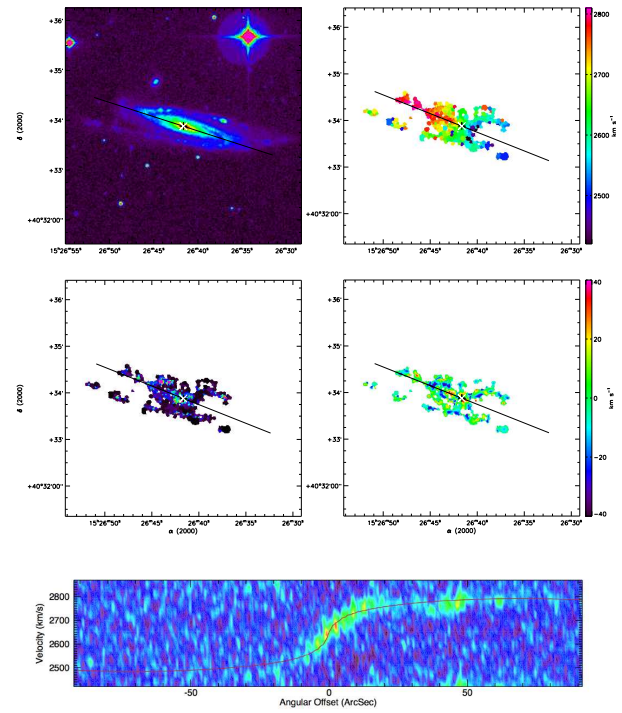


(146) UGC 09736

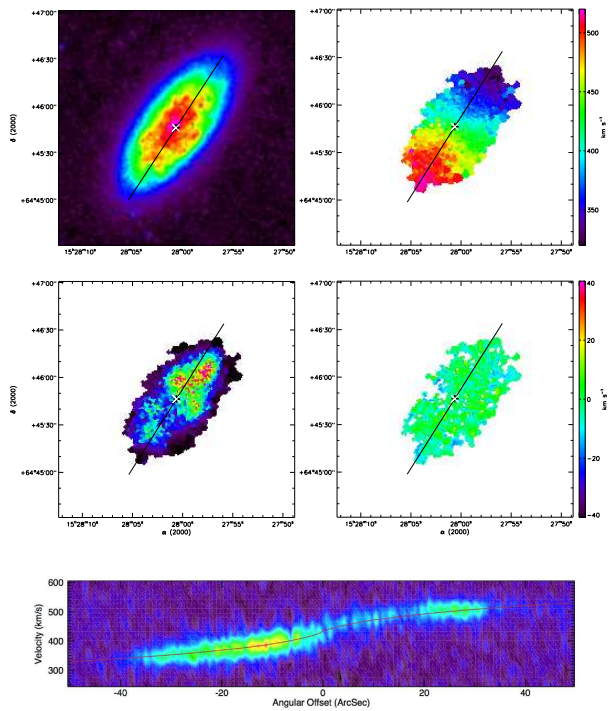
FIG. D.1 : suite



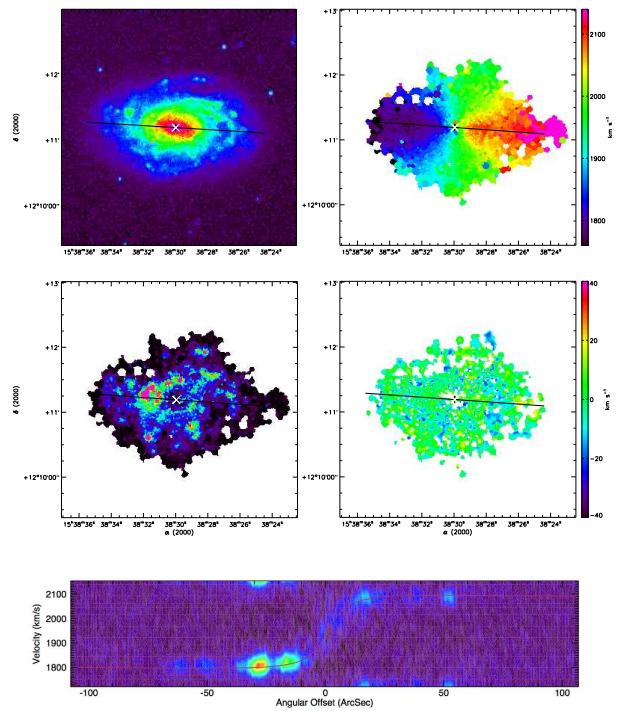
(147) UGC 09753



(148) UGC 09858

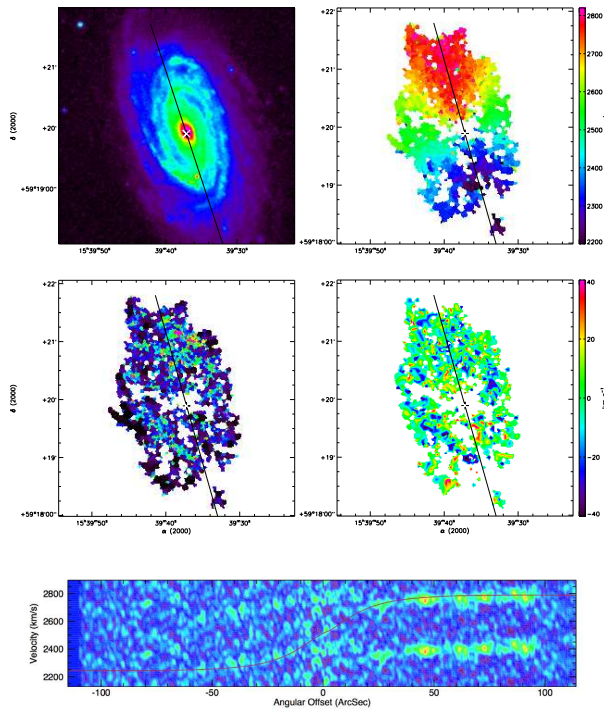


(149) UGC 09866

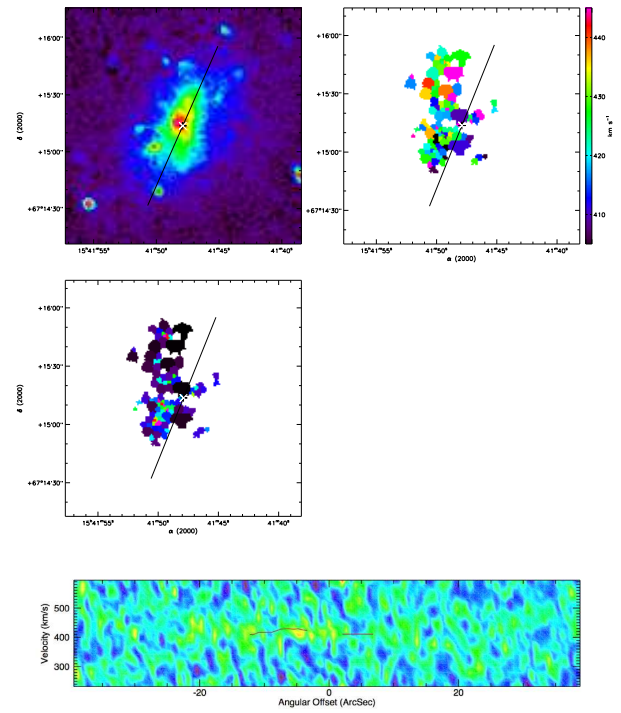


(150) UGC 09943

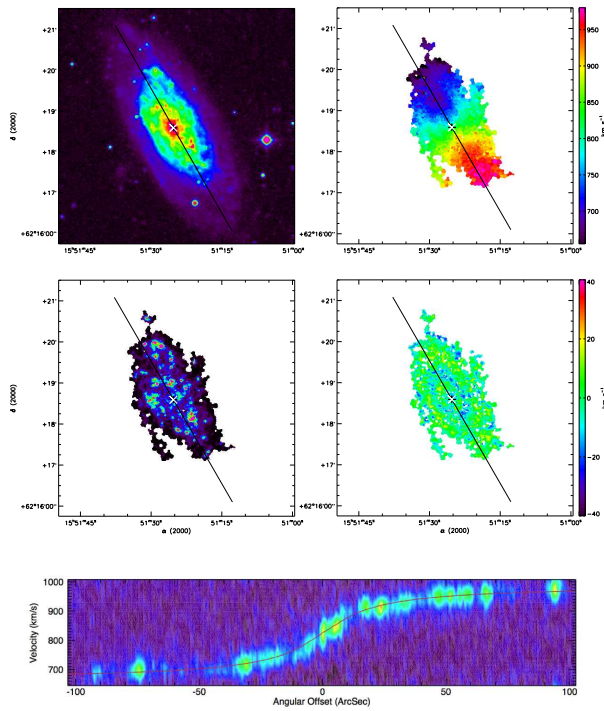
FIG. D.1 : suite



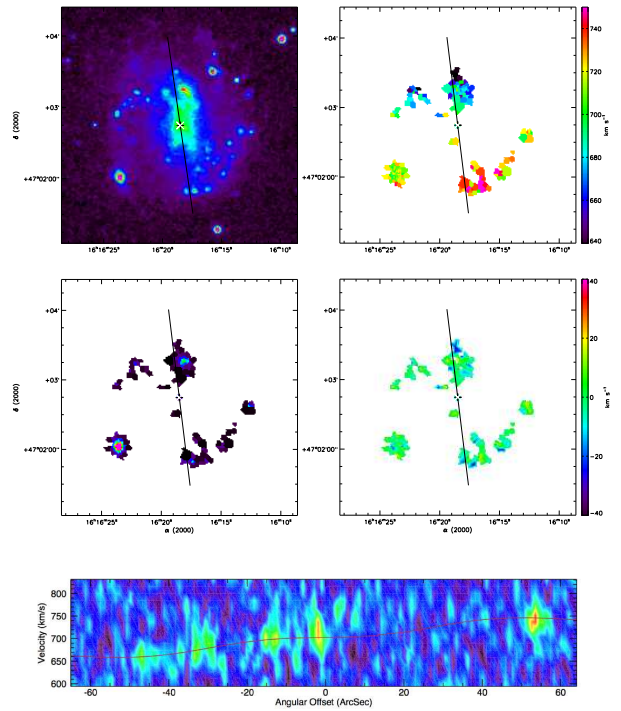
(151) UGC 09969



(152) UGC 09992

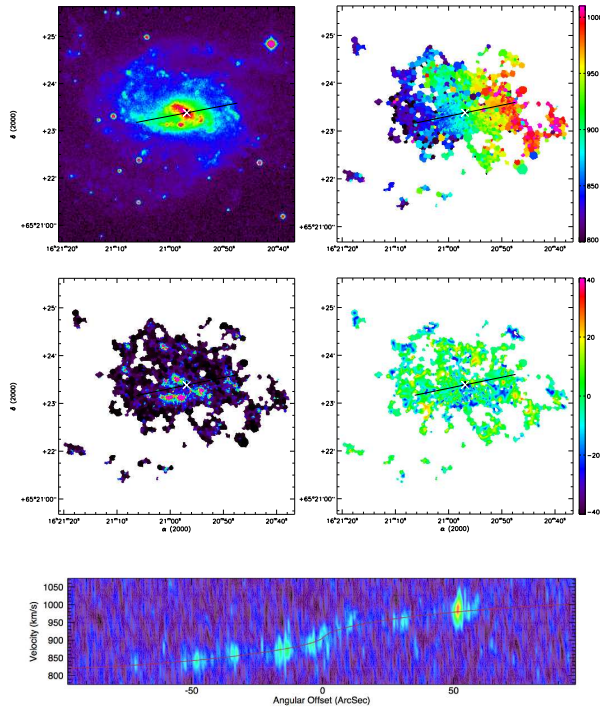


(153) UGC 10075

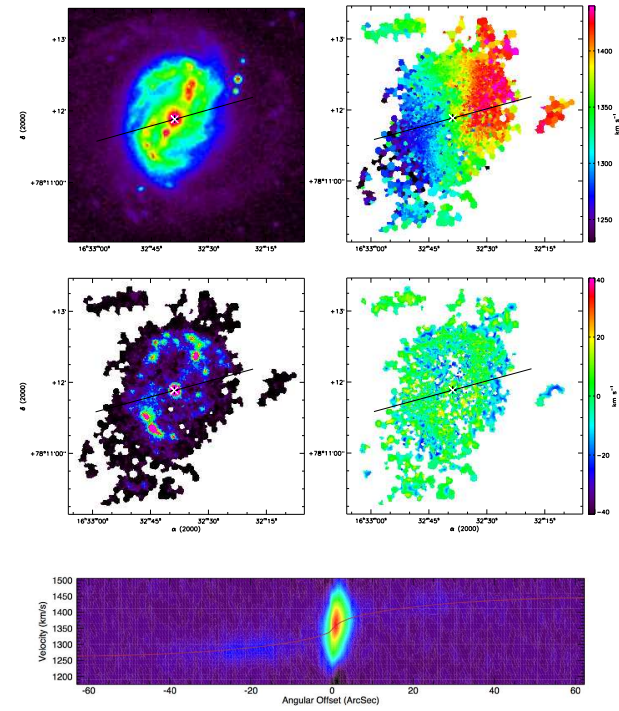


(154) UGC 10310

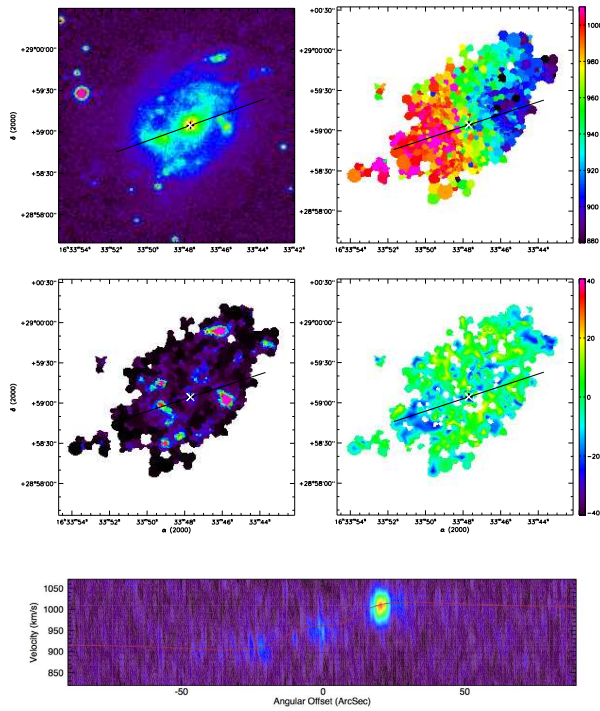
FIG. D.1 : suite



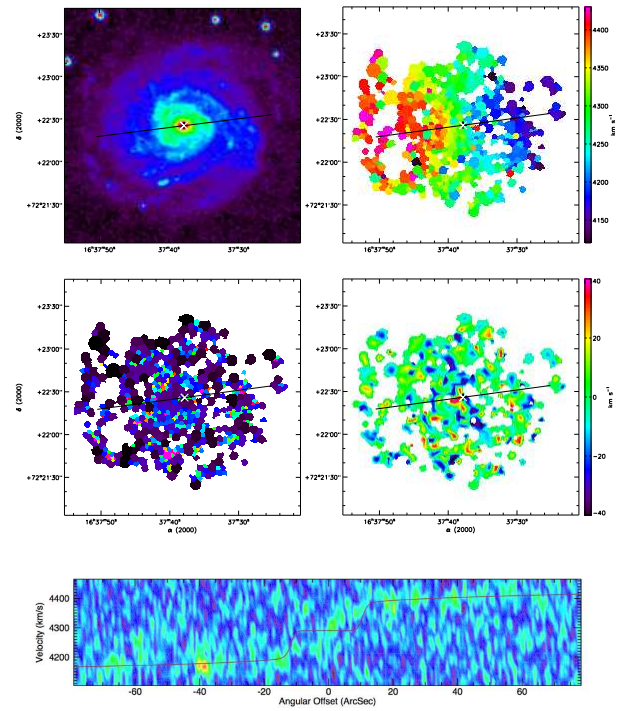
(155) UGC 10359



(156) UGC 10470

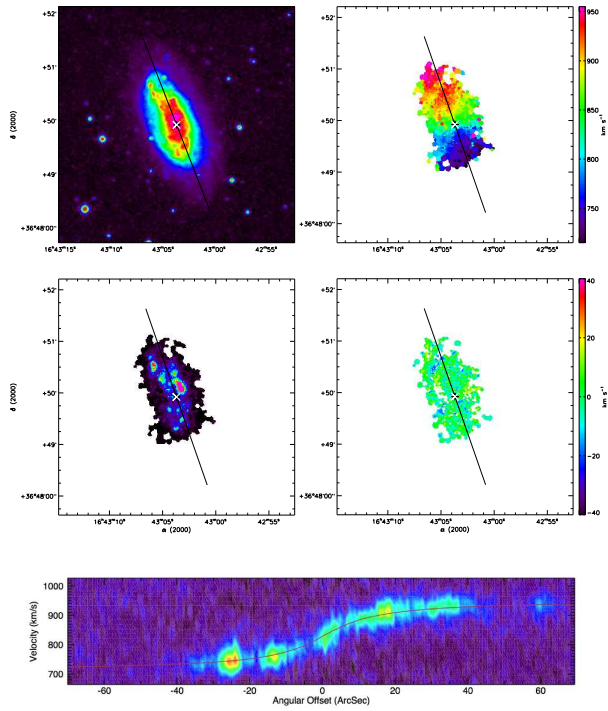


(157) UGC 10445

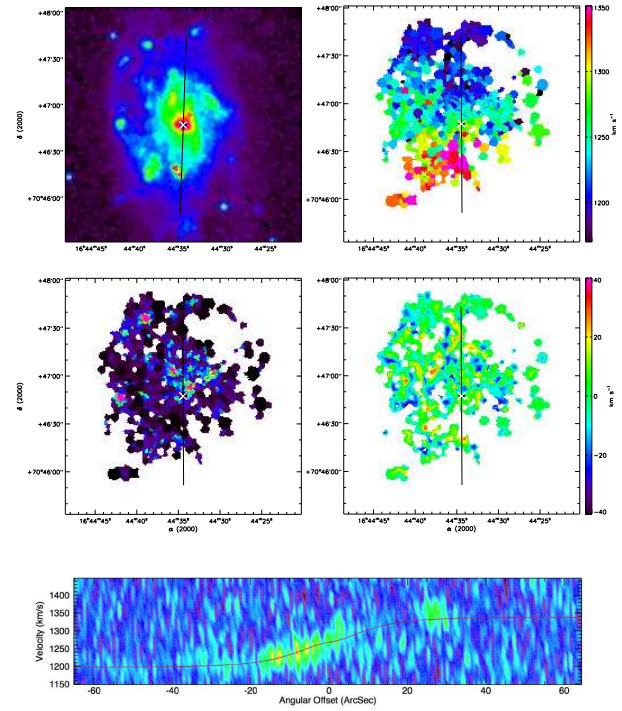


(158) UGC 10502

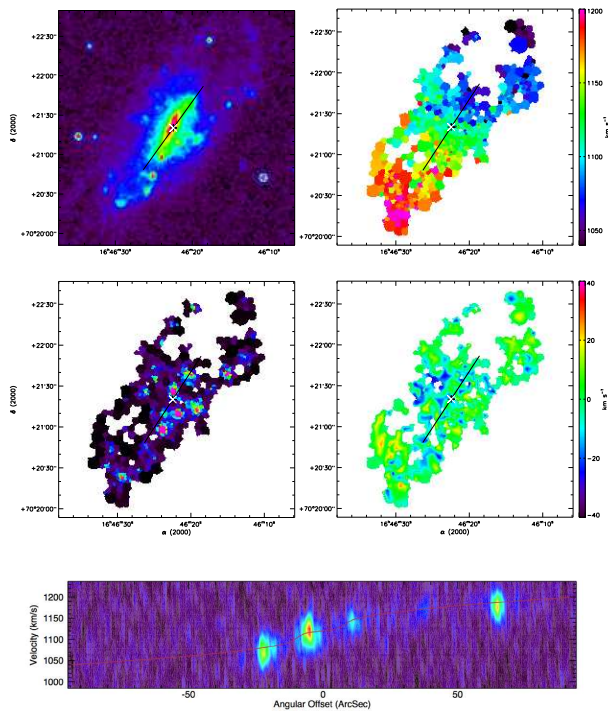
FIG. D.1 : suite



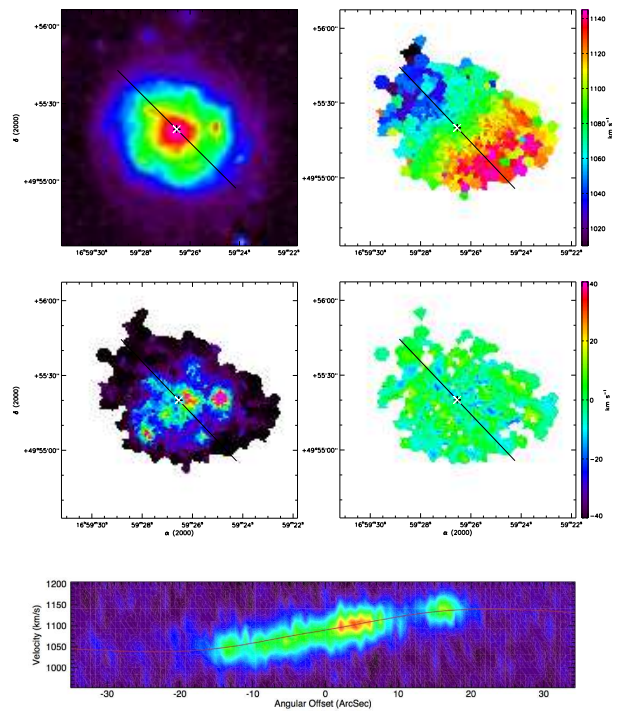
(159) UGC 10521



(160) UGC 10546

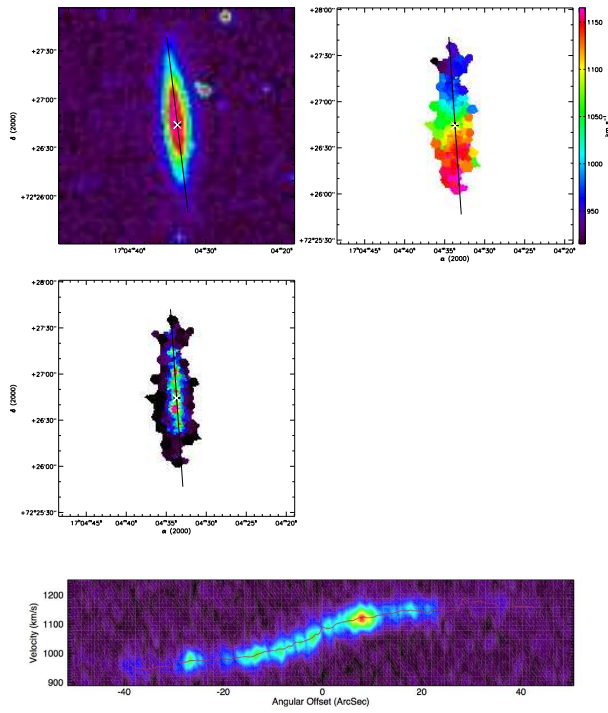


(161) UGC 10564

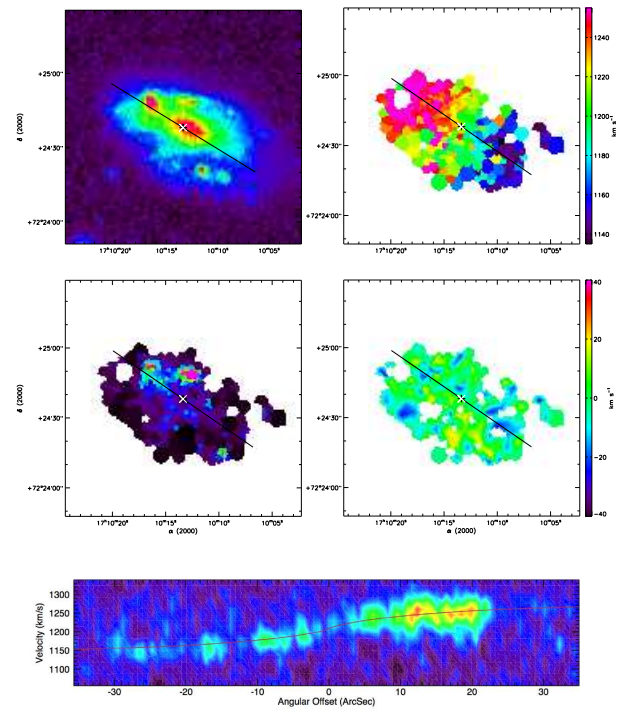


(162) UGC 10652

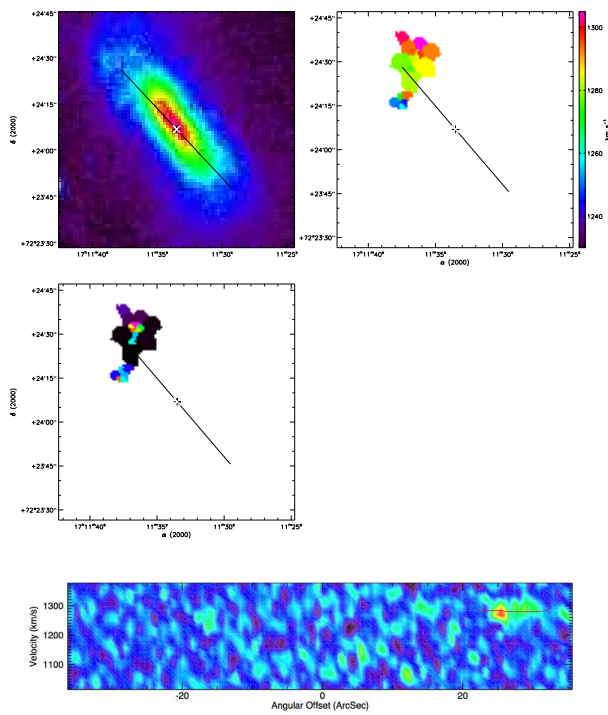
FIG. D.1 : suite



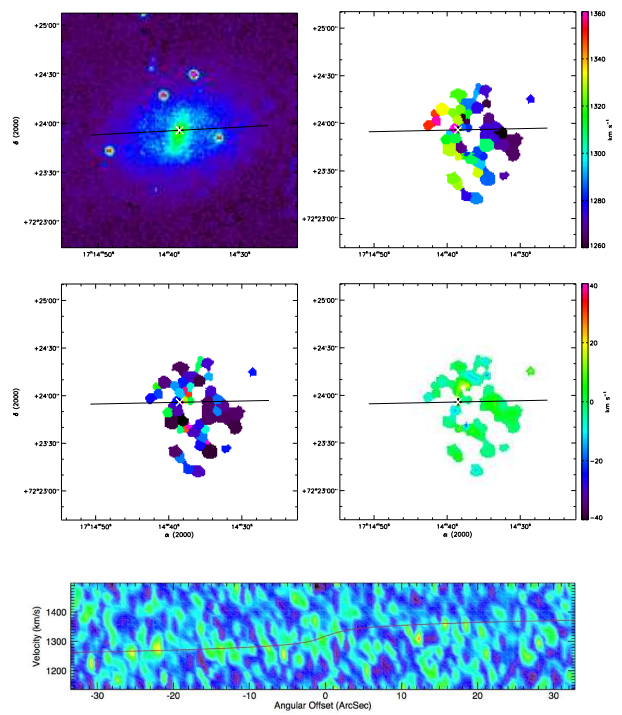
(163) UGC 10713 (XDSS en bande R)



(164) UGC 10757

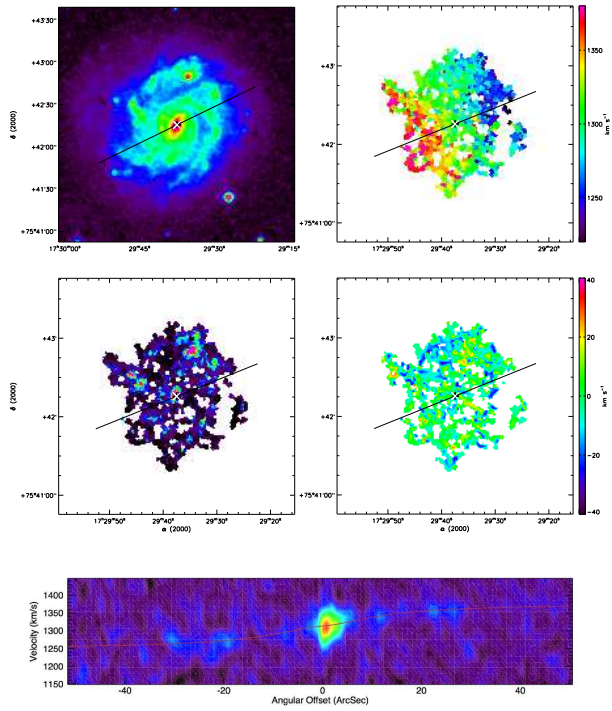


(165) UGC 10769

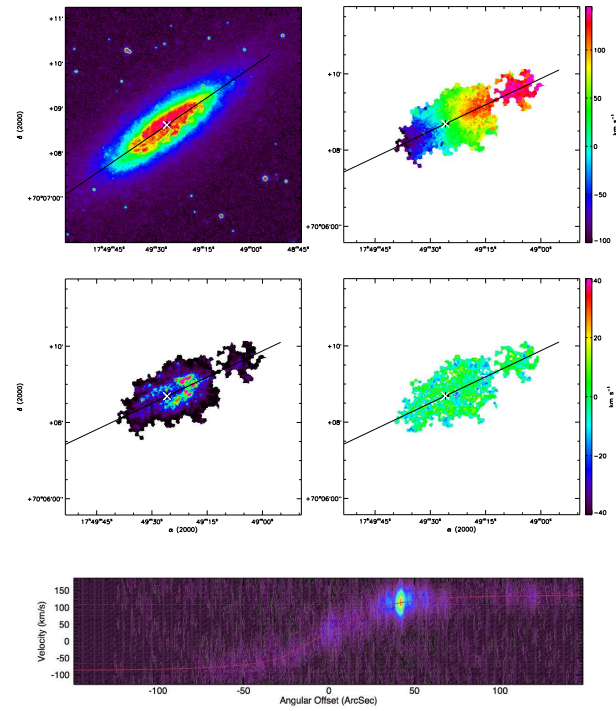


(166) UGC 10791

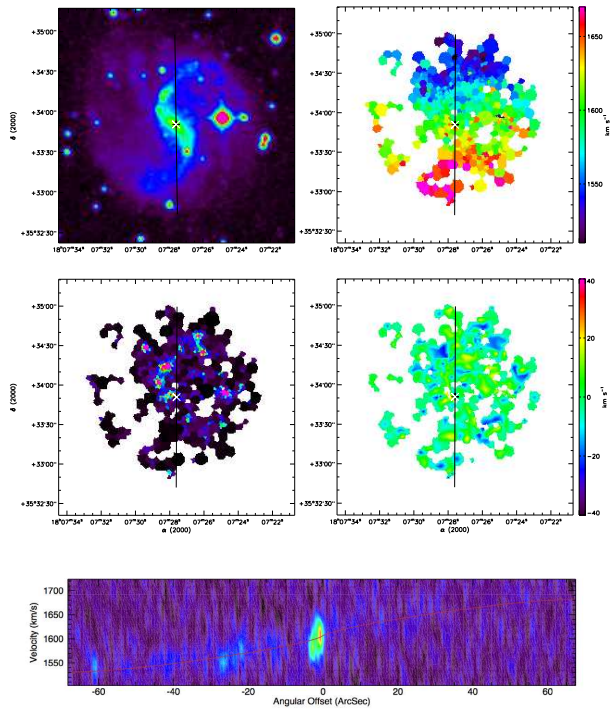
FIG. D.1 : suite



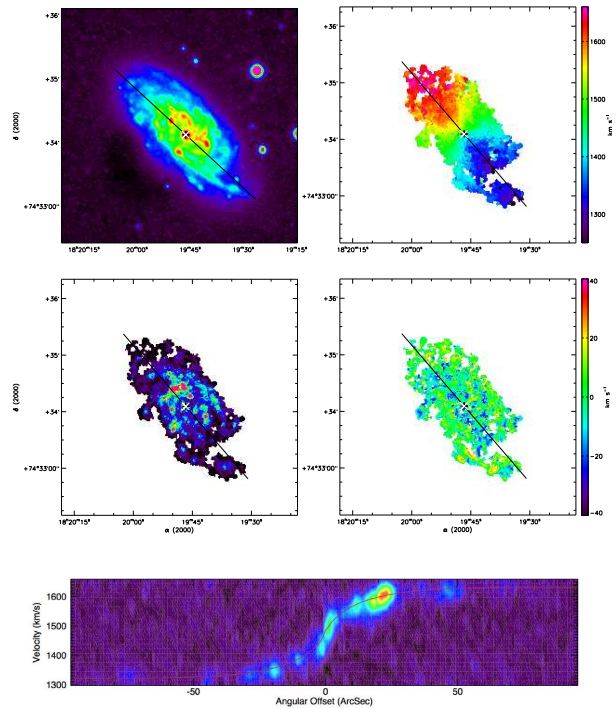
(167) UGC 10897



(168) UGC 11012

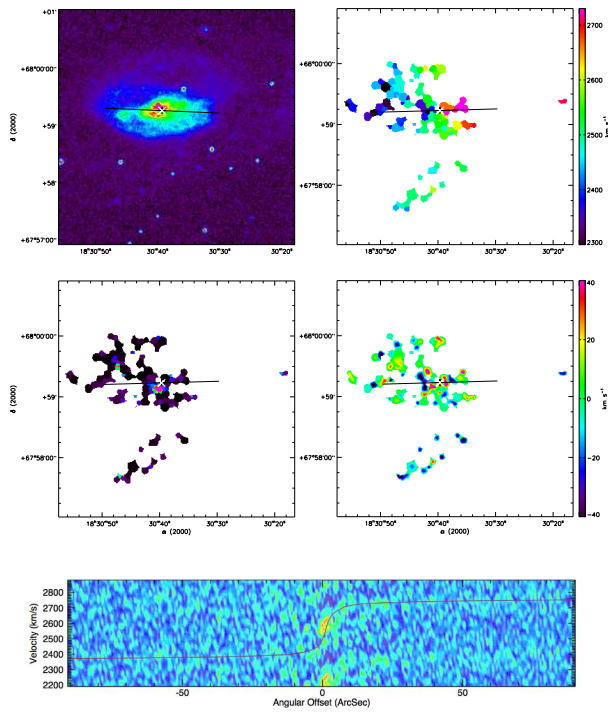


(169) UGC 11124

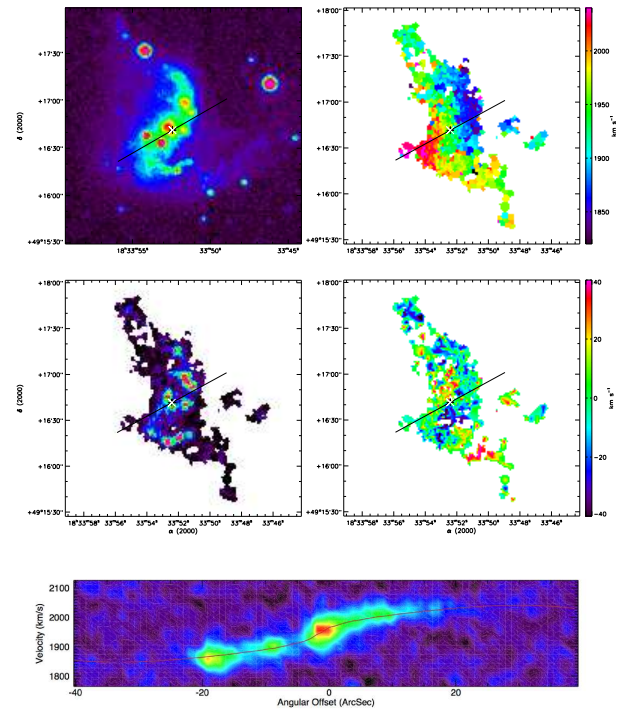


(170) UGC 11218

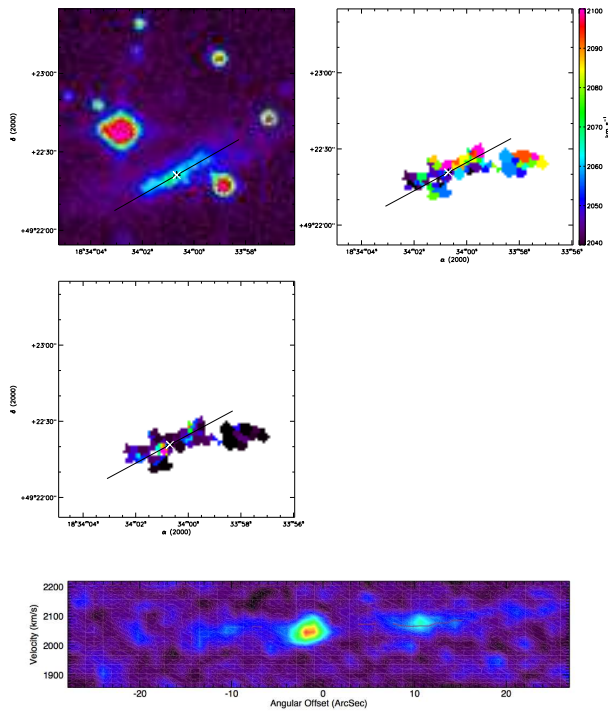
FIG. D.1 : suite



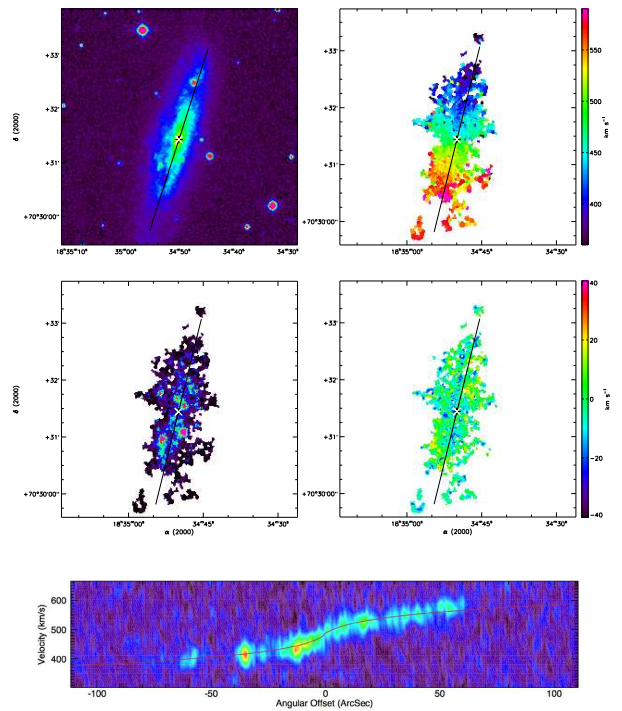
(171) UGC 11269



(172) UGC 11283

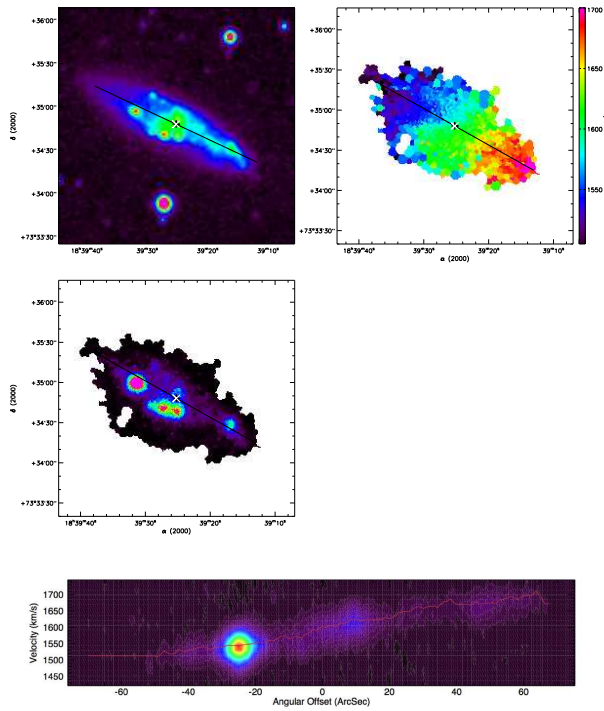


(173) UGC 11283C

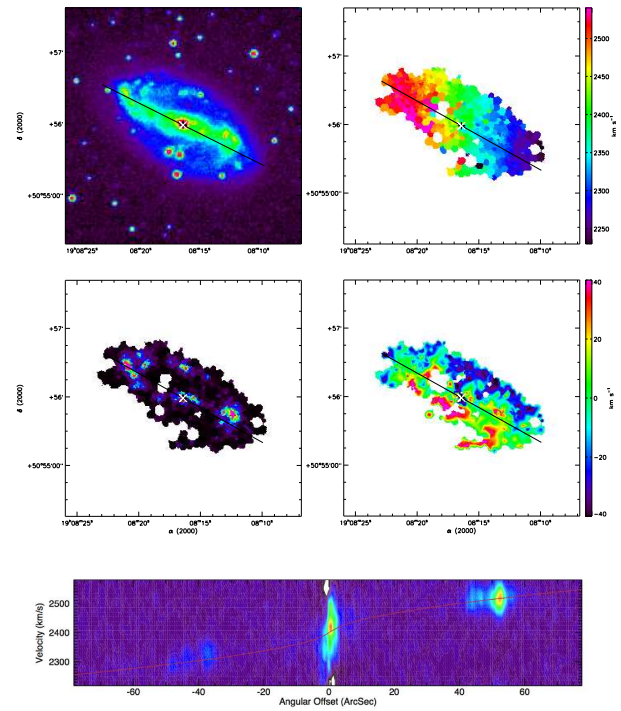


(174) UGC 11300

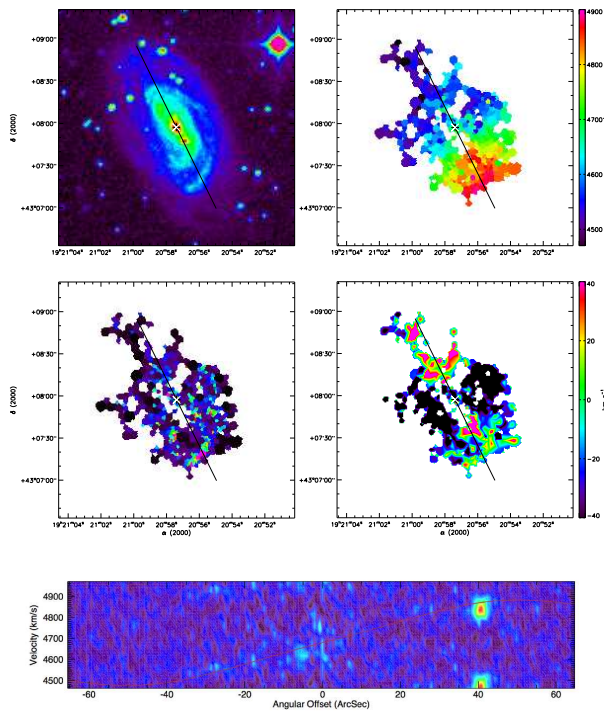
FIG. D.1 : suite



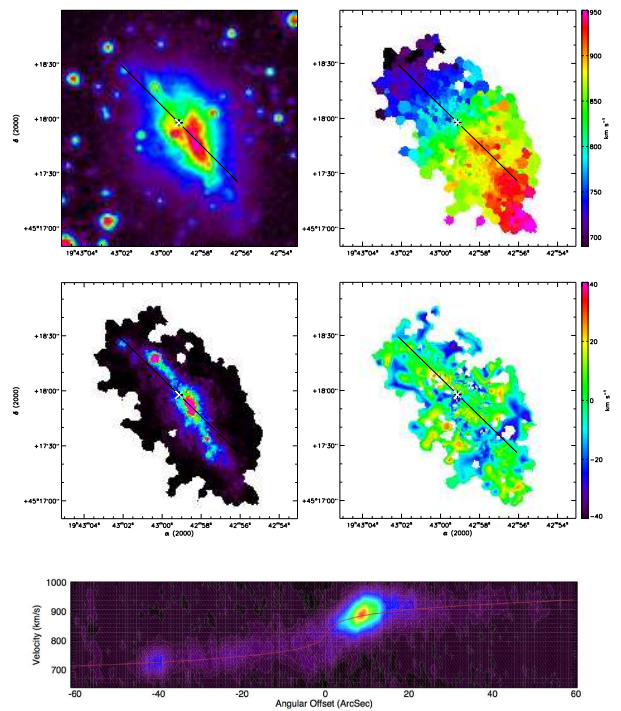
(175) UGC 11332



(176) UGC 11407

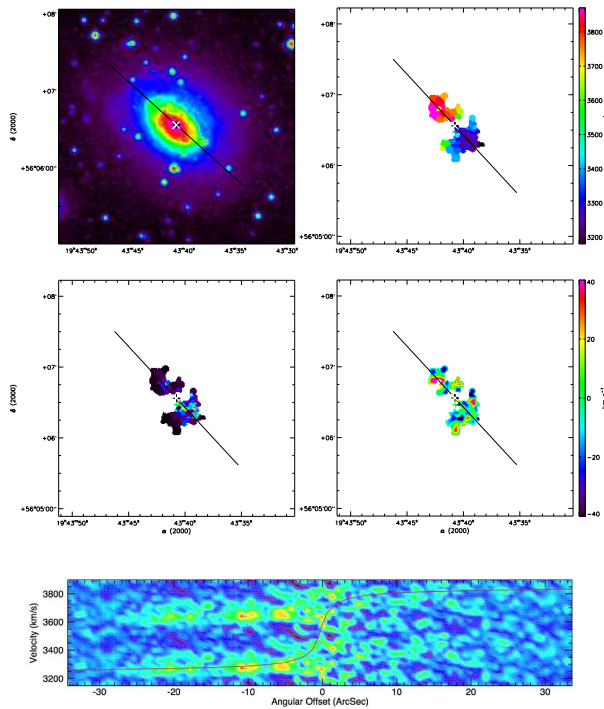


(177) UGC 11429

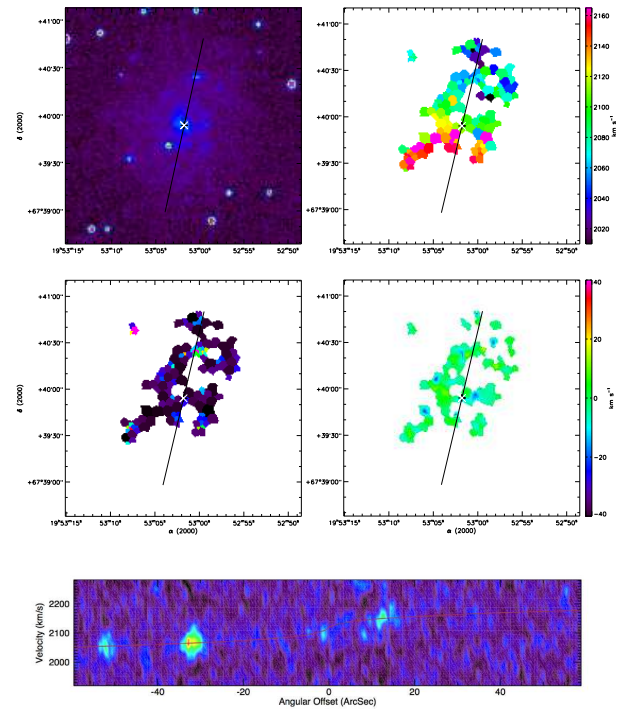


(178) UGC 11466

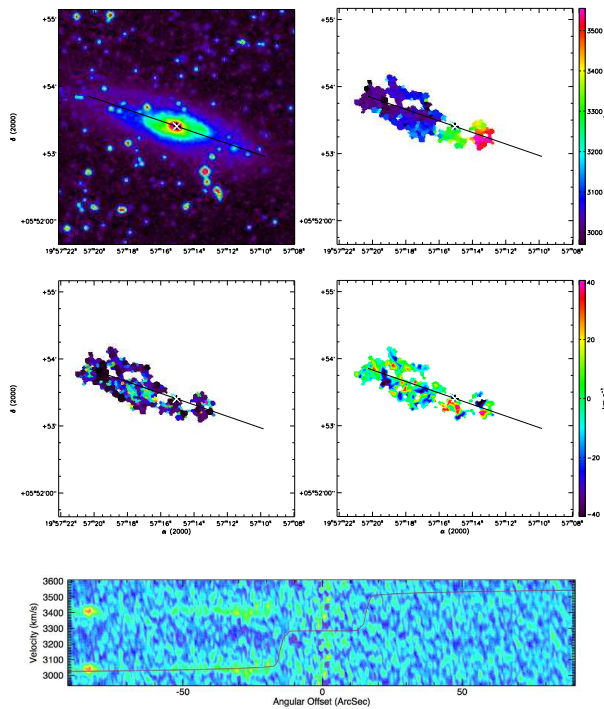
FIG. D.1 : suite



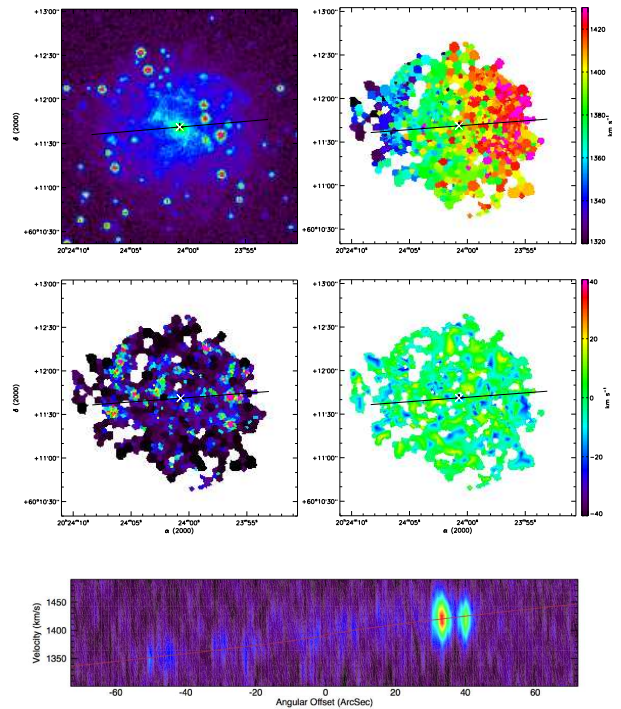
(179) UGC 11470



(180) UGC 11496

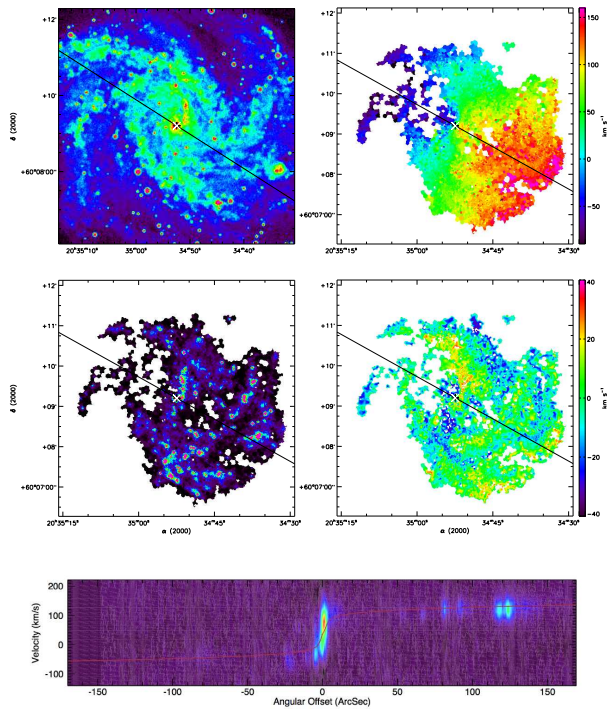


(181) UGC 11498 (XDSS en bande R)

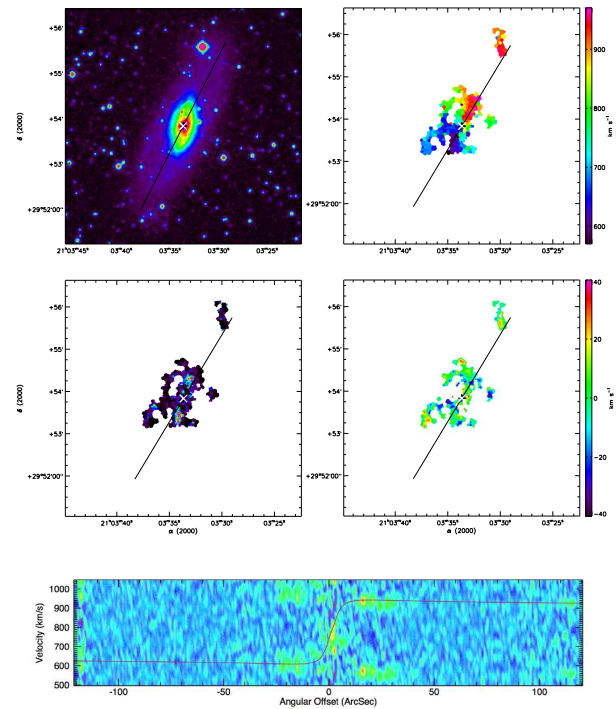


(182) UGC 11557

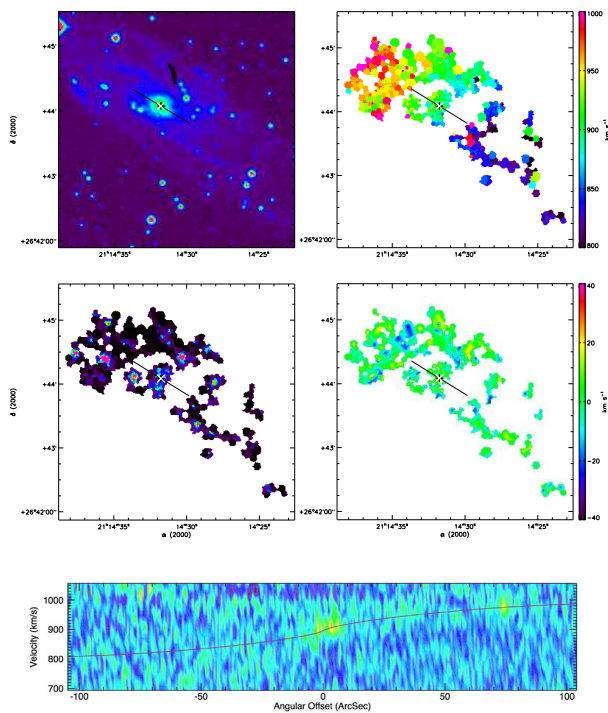
FIG. D.1 : suite



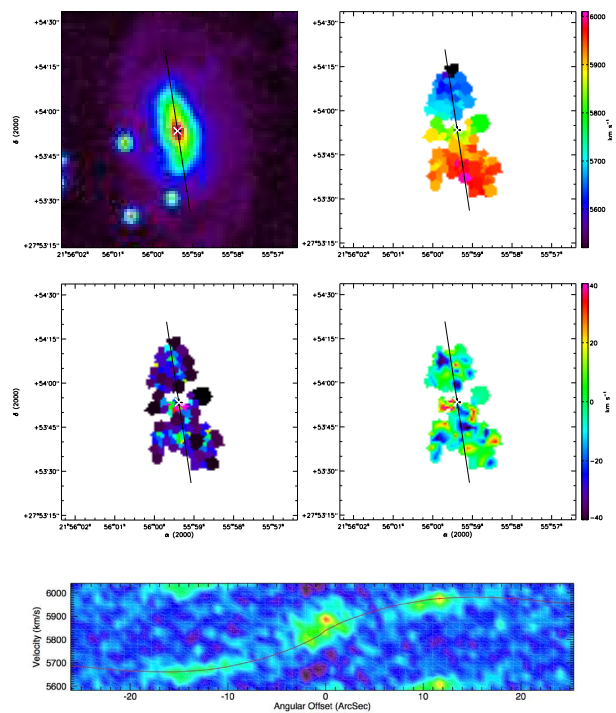
(183) UGC 11597



(184) UGC 11670

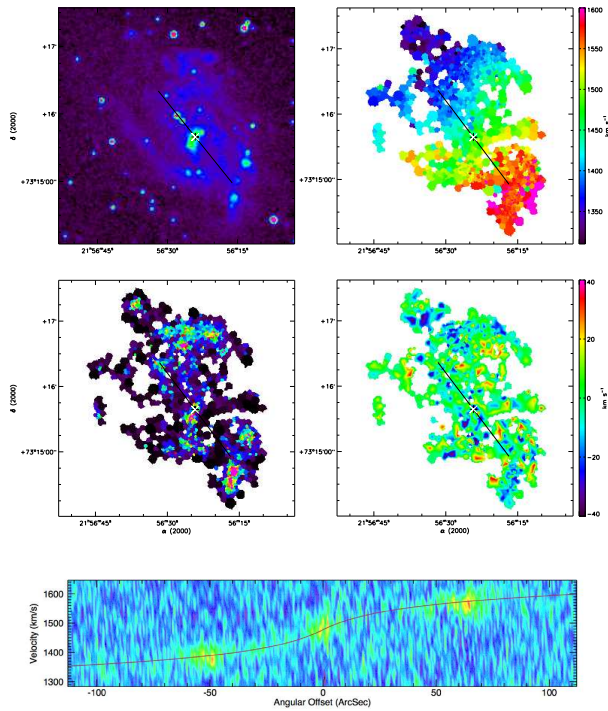


(185) UGC 11707

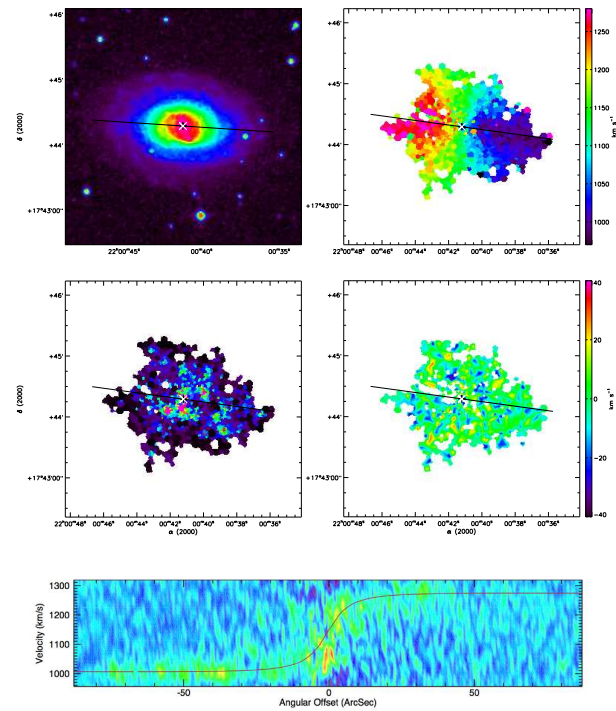


(186) UGC 11852

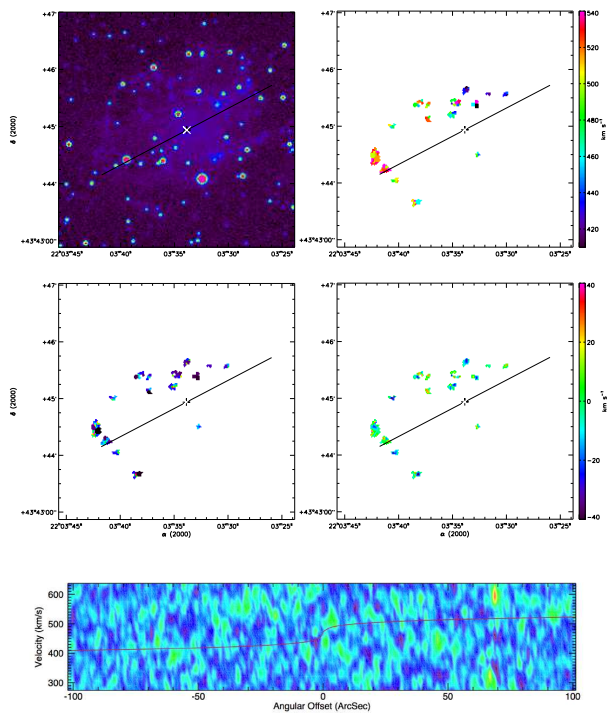
FIG. D.1 : suite



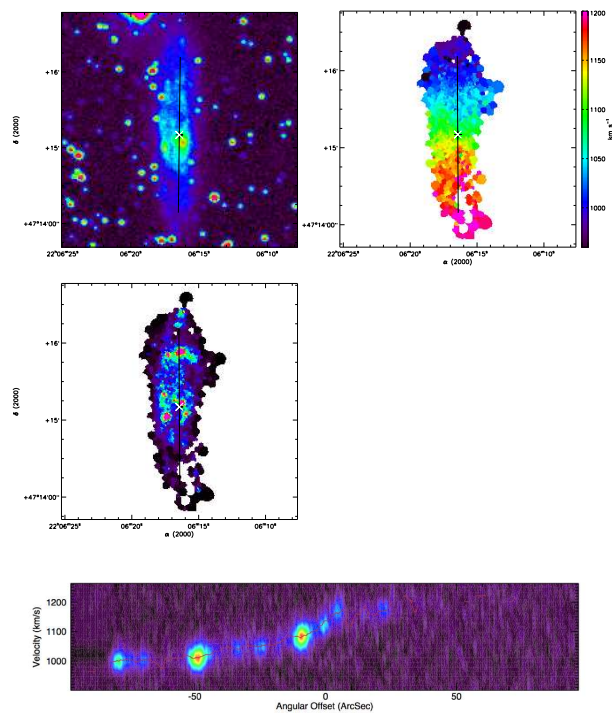
(187) UGC 11861



(188) UGC 11872

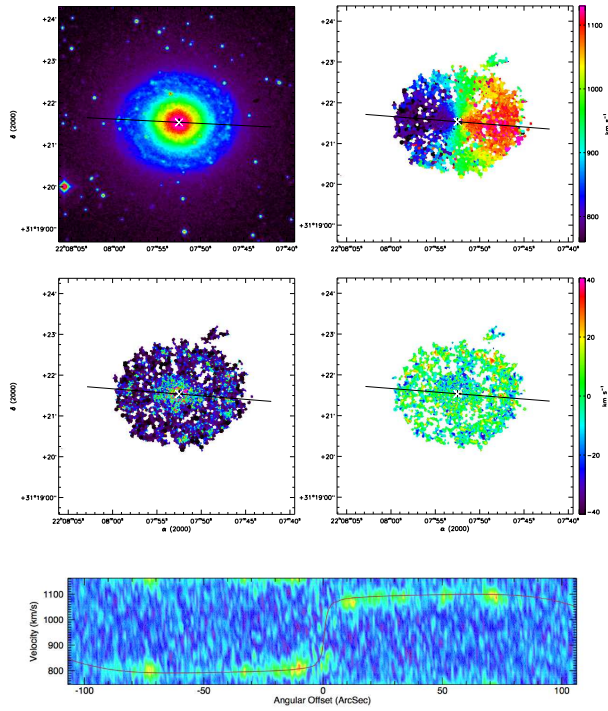


(189) UGC 11891

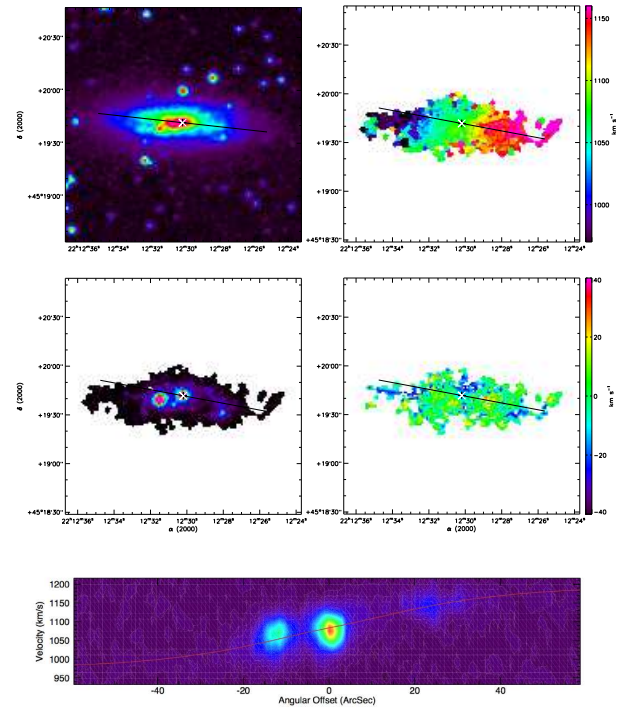


(190) UGC 11909

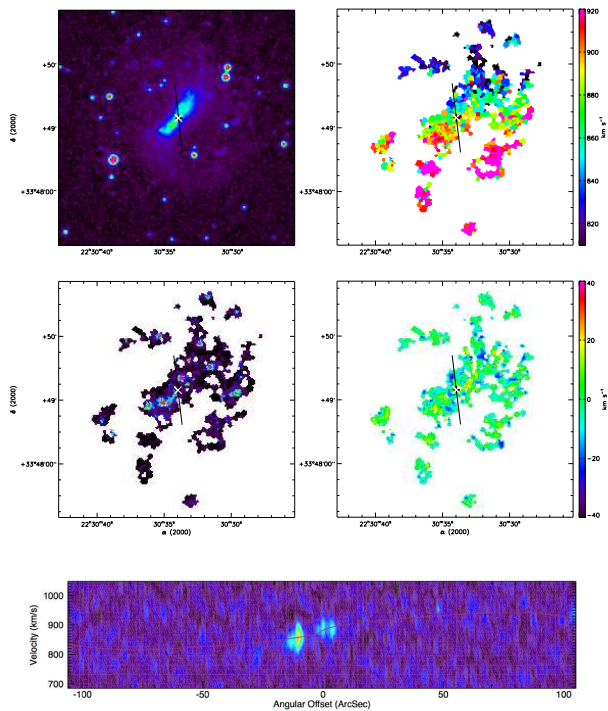
FIG. D.1 : suite



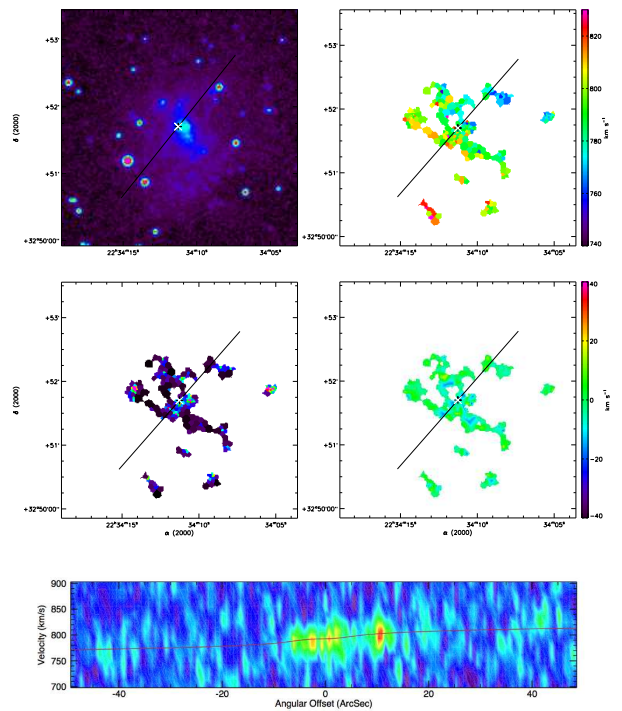
(191) UGC 11914



(192) UGC 11951

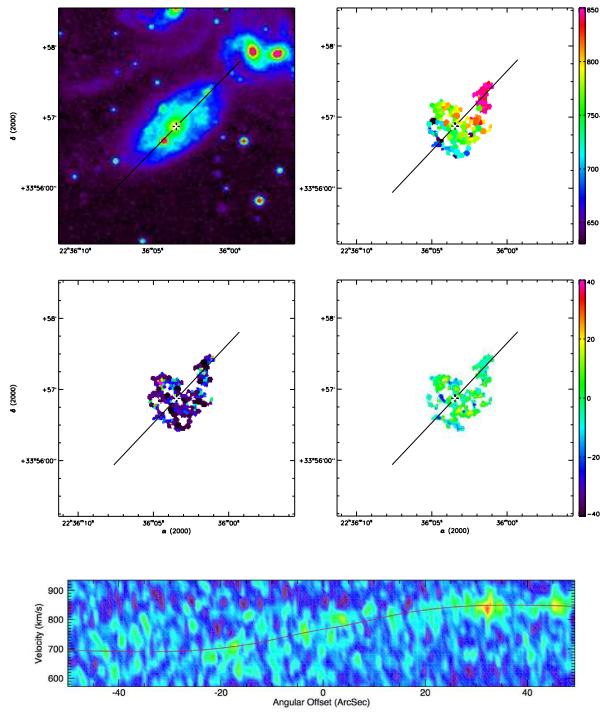


(193) UGC 12060

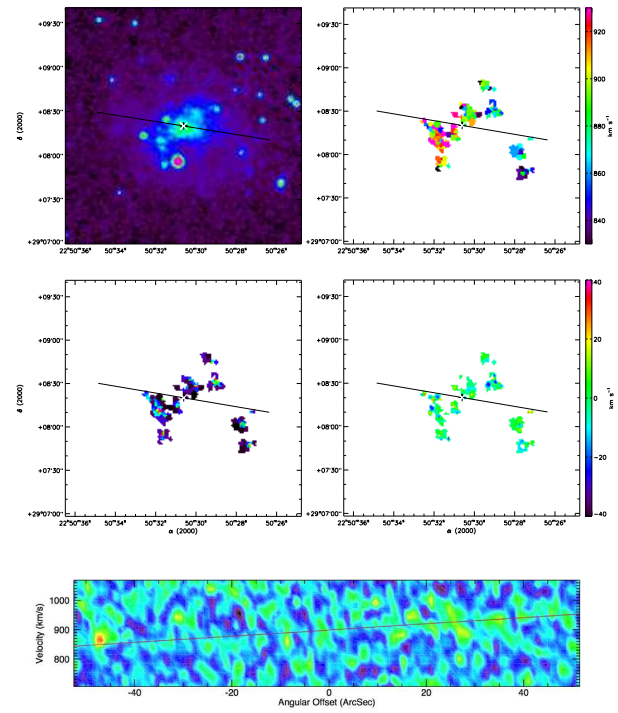


(194) UGC 12082

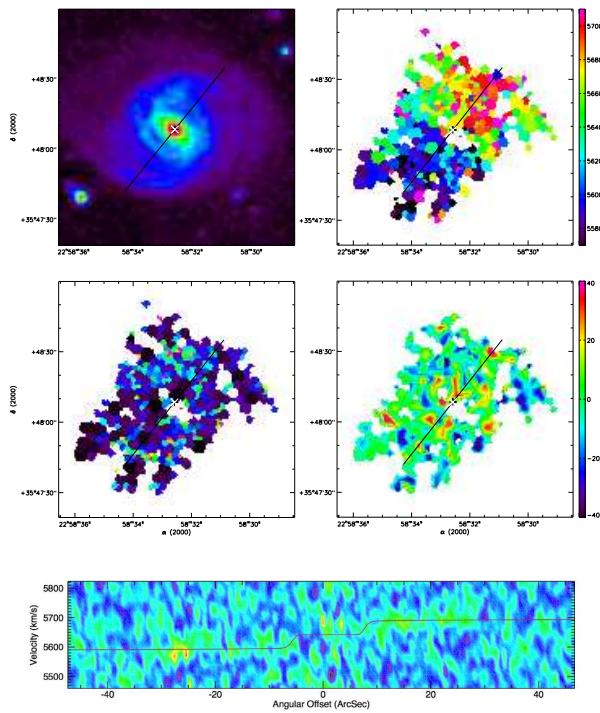
FIG. D.1 : suite



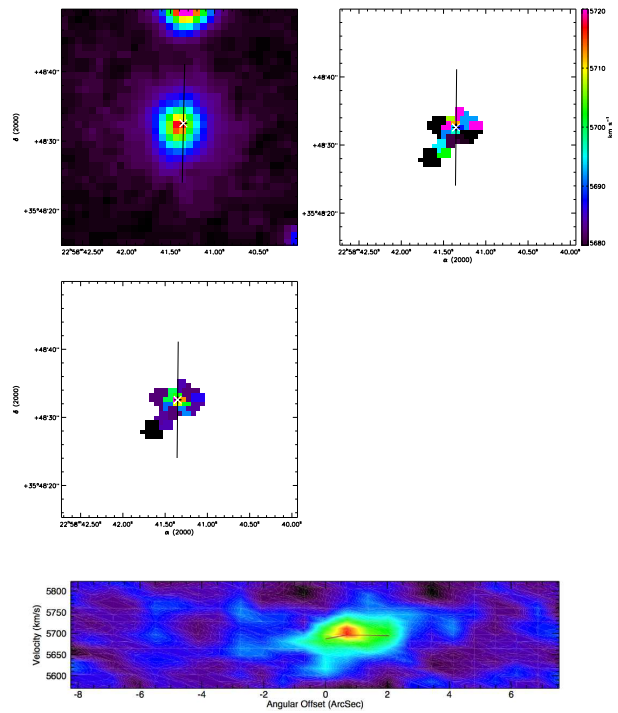
(195) UGC 12101



(196) UGC 12212

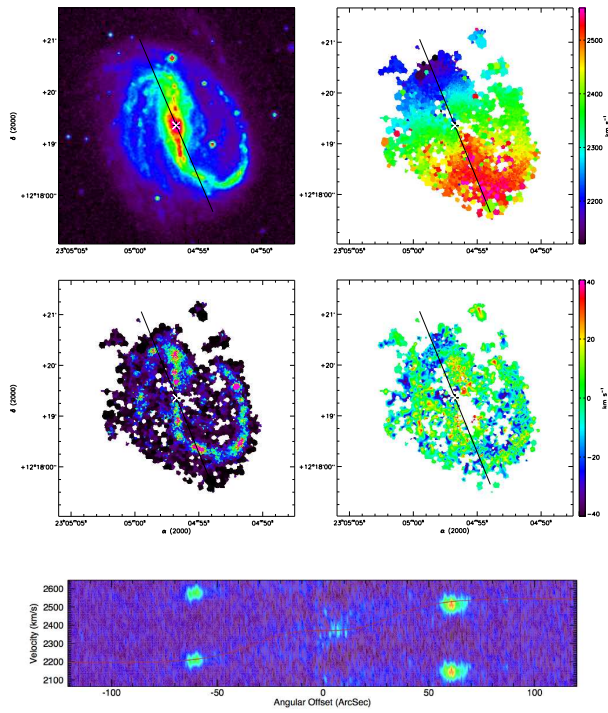


(197) UGC 12276

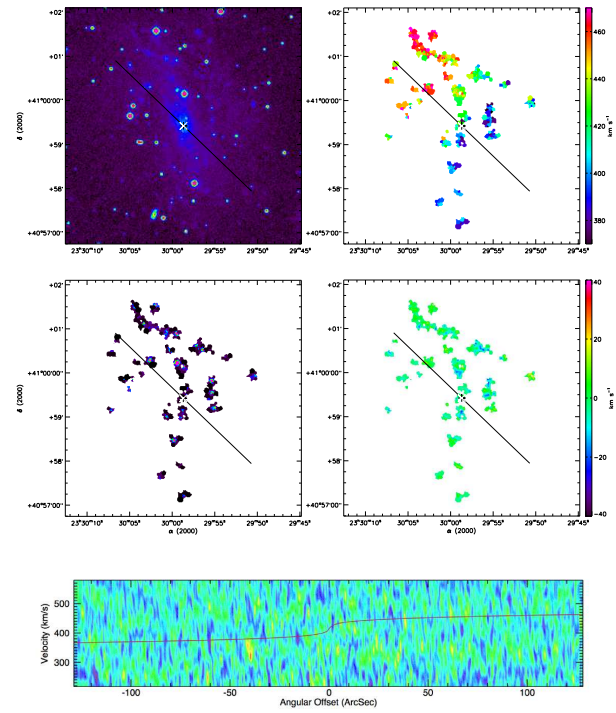


(198) UGC 12276C

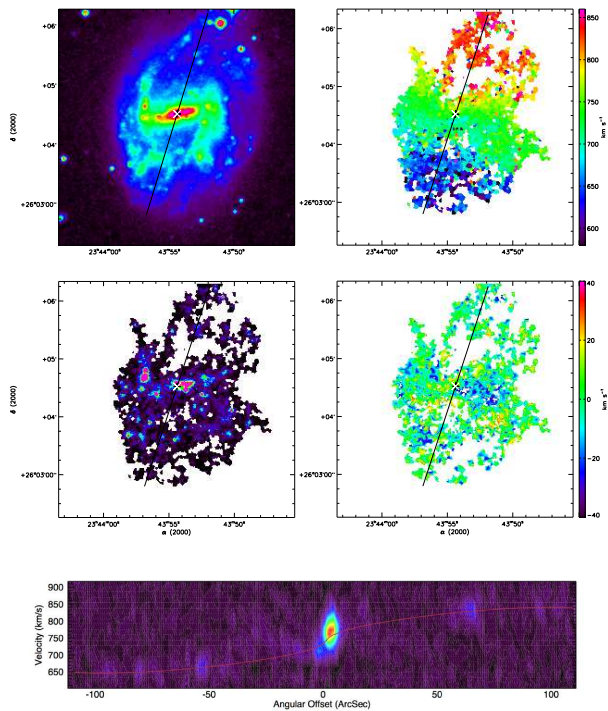
FIG. D.1 : suite



(199) UGC 12343



(200) UGC 12632



(201) UGC 12754

FIG. D.1 : suite

D.2 Courbes de rotation des galaxies GHASP

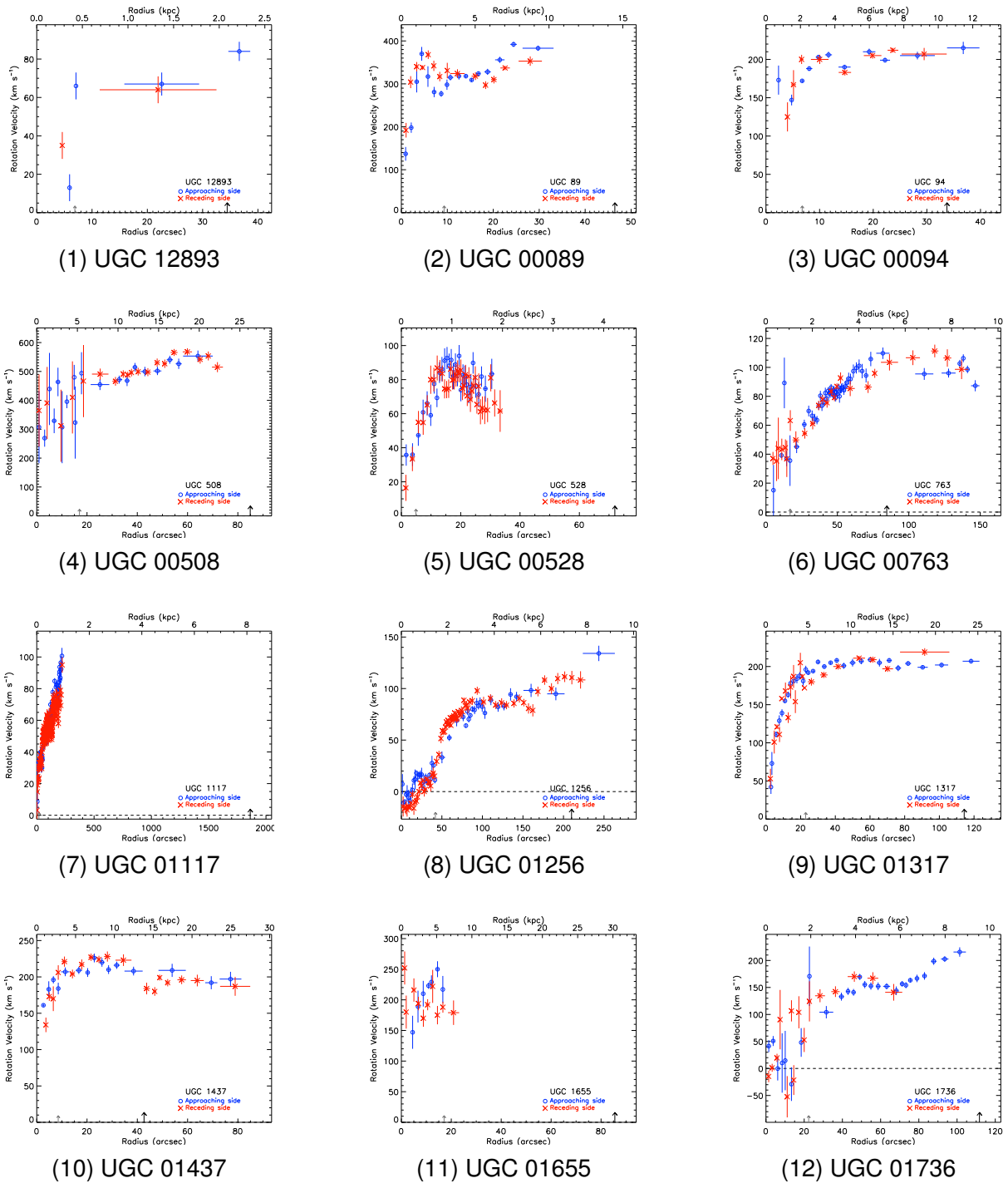
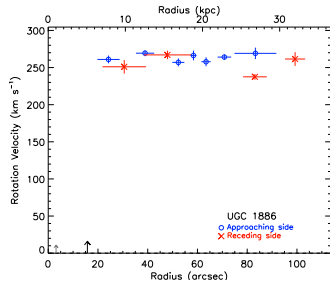
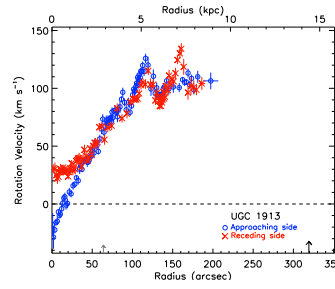


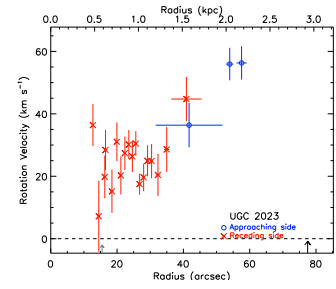
FIG. D.2: Courbes de rotation des galaxies GHASP. Les ronds bleus et les croix rouges identifient respectivement le côté qui s'approche et celui qui s'éloigne. La flèche noire indique le rayon optique ($D_{25}/2$, de Vaucouleurs et al., 1995), la flèche grise indique le rayon de transition.



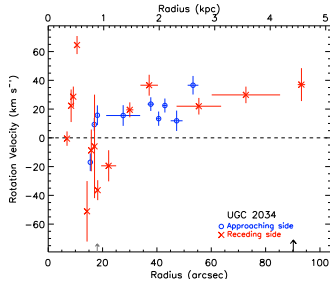
(13) UGC 01886



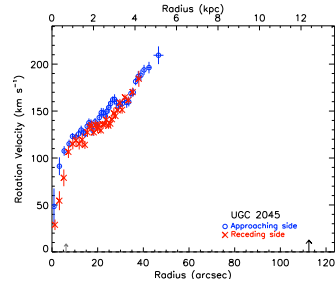
(14) UGC 01913



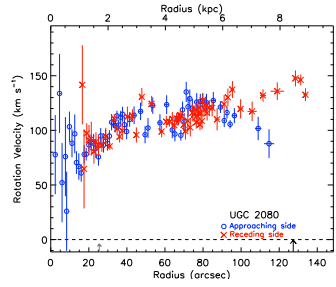
(15) UGC 02023



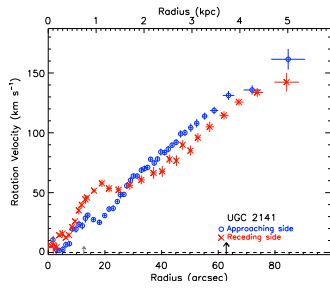
(16) UGC 02034



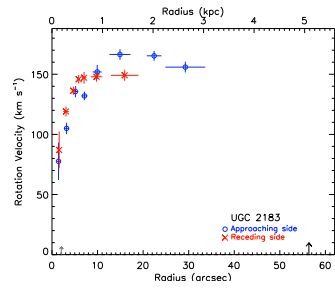
(17) UGC 02045



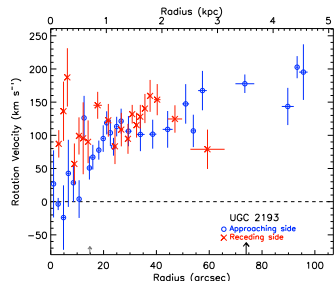
(18) UGC 02080



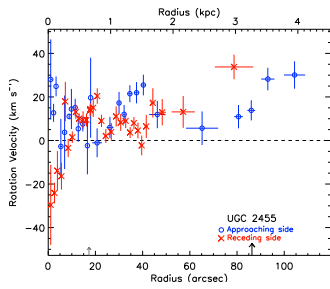
(19) UGC 02141



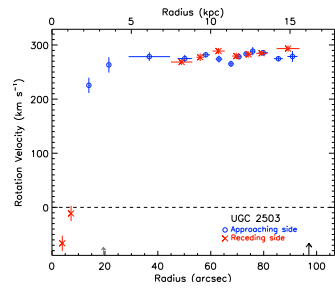
(20) UGC 02183



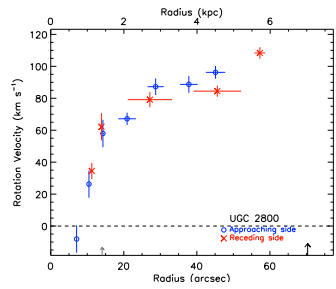
(21) UGC 02193



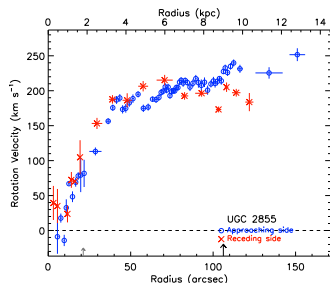
(22) UGC 02455



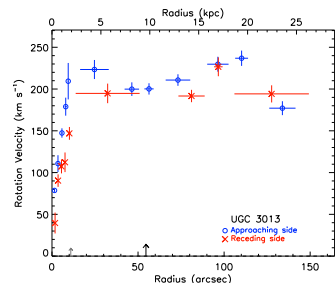
(23) UGC 02503



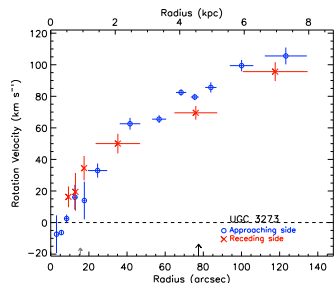
(24) UGC 02800



(25) UGC 02855

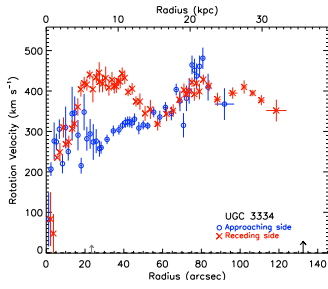


(26) UGC 03013

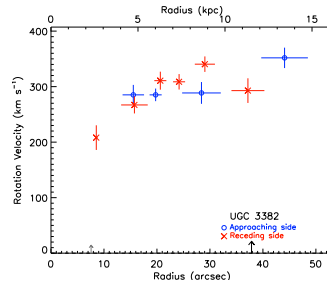


(27) UGC 03273

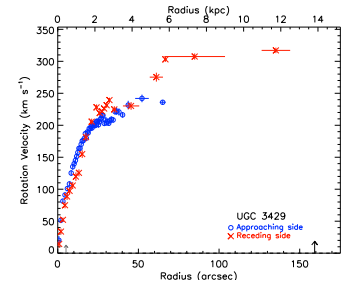
FIG. D.2 : suite



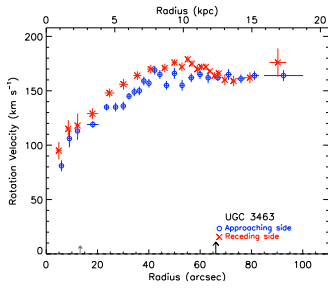
(28) UGC 03334



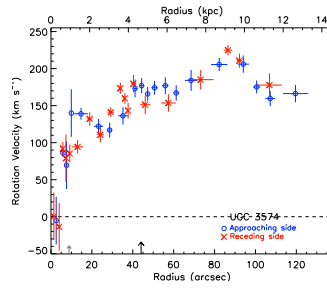
(29) UGC 03382



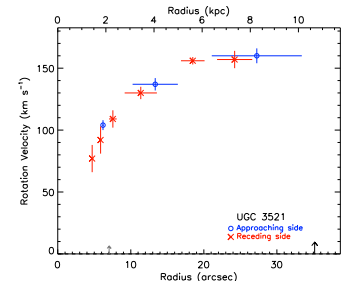
(30) UGC 03429



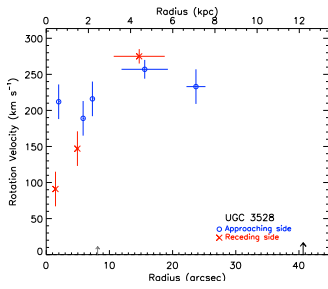
(31) UGC 03463



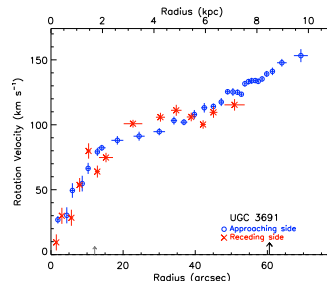
(32) UGC 03574



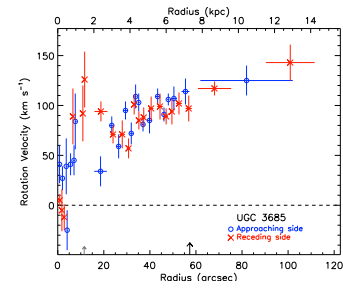
(33) UGC 03521



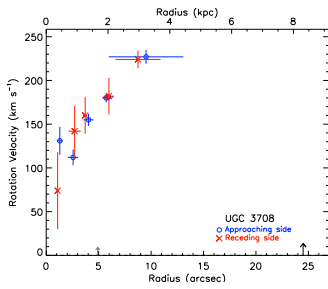
(34) UGC 03528



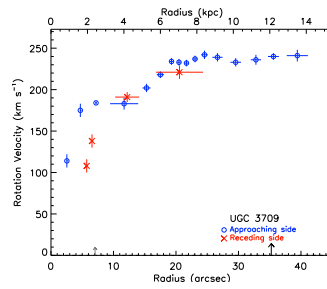
(35) UGC 03691



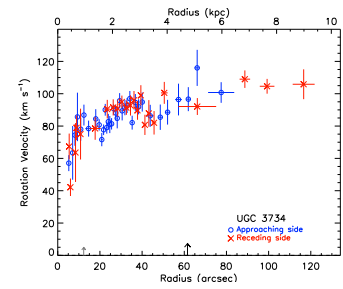
(36) UGC 03685



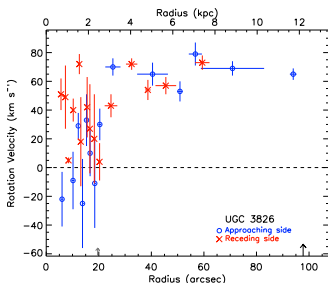
(37) UGC 03708



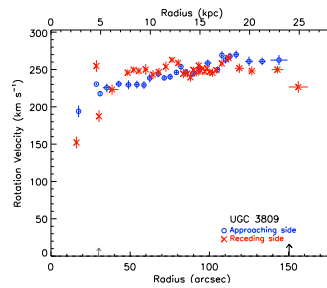
(38) UGC 03709



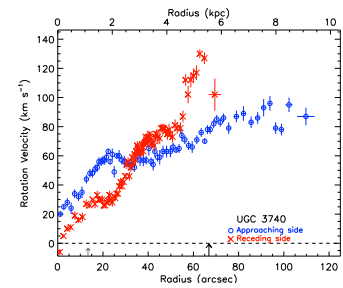
(39) UGC 03734



(40) UGC 03826

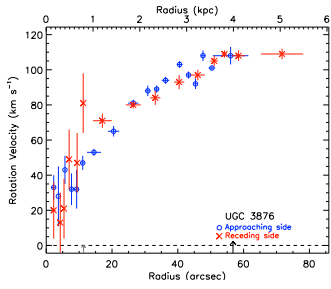


(41) UGC 03809

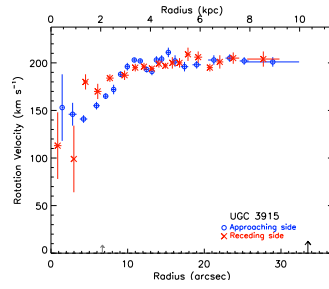


(42) UGC 03740

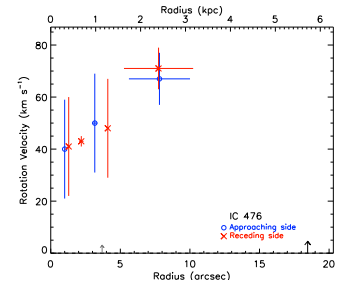
FIG. D.2 : suite



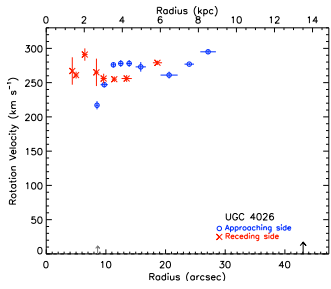
(43) UGC 03876



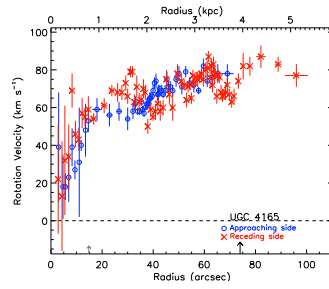
(44) UGC 03915



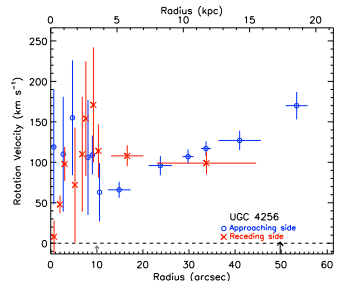
(45) IC 476



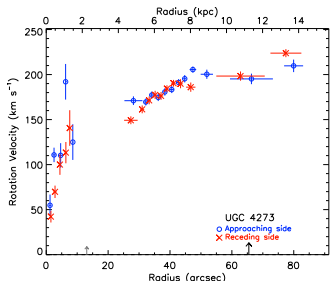
(46) UGC 04026



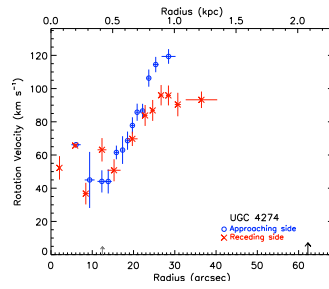
(47) UGC 04165



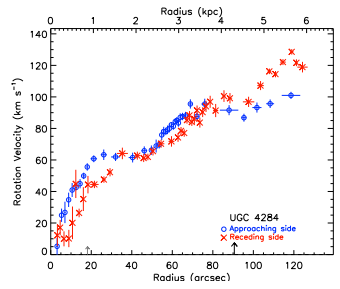
(48) UGC 04256



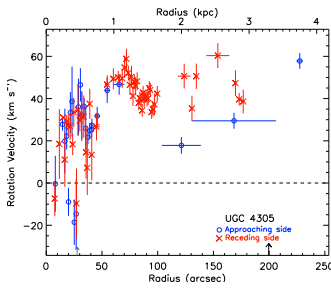
(49) UGC 04273



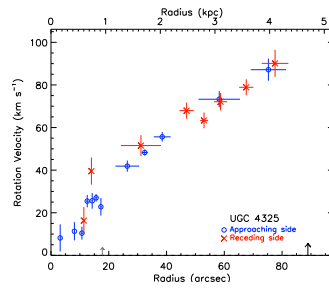
(50) UGC 04274



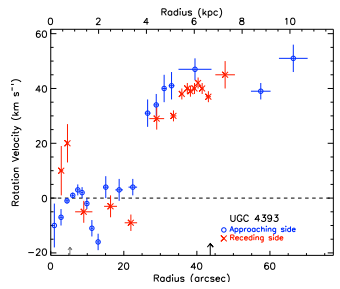
(51) UGC 04284



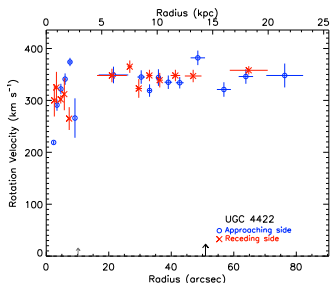
(52) UGC 04305



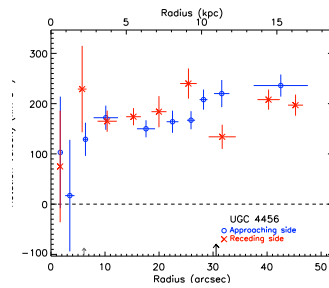
(53) UGC 04325



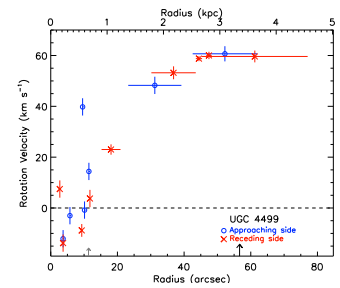
(54) UGC 04393



(55) UGC 04422

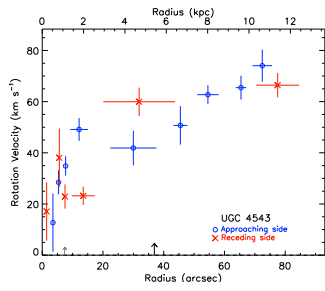


(56) UGC 04456

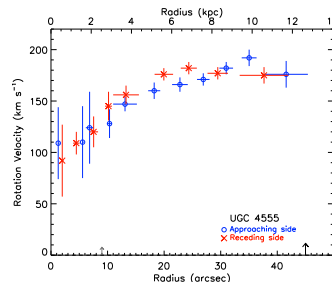


(57) UGC 04499

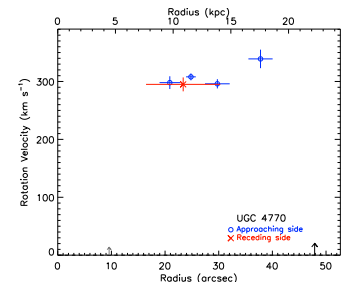
FIG. D.2 : suite



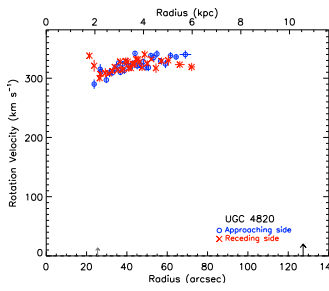
(58) UGC 04543



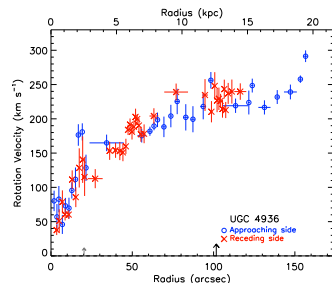
(59) UGC 04555



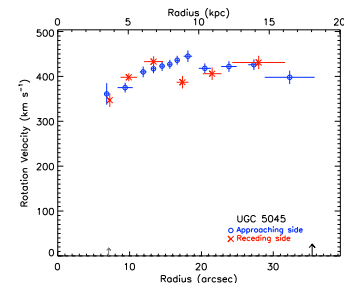
(60) UGC 04770



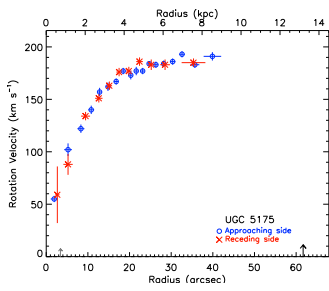
(61) UGC 04820



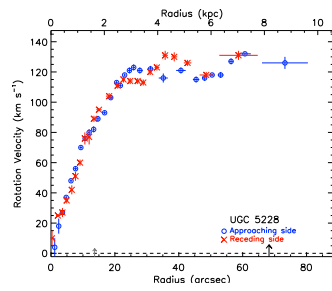
(62) UGC 04936



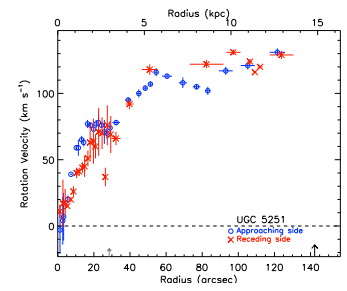
(63) UGC 05045



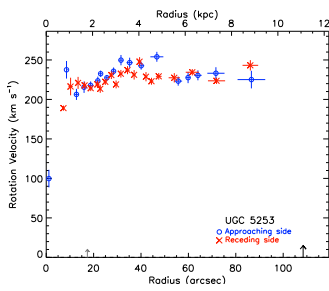
(64) UGC 05175



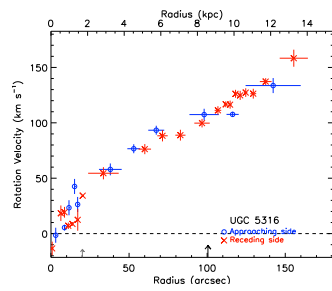
(65) UGC 05228



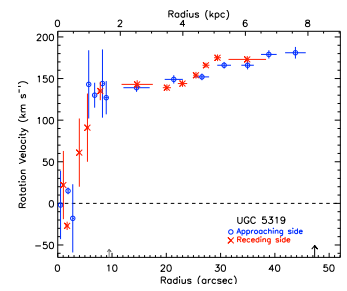
(66) UGC 05251



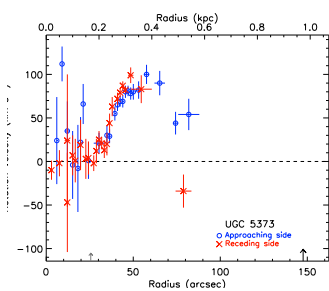
(67) UGC 05253



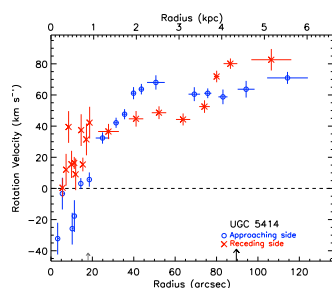
(68) UGC 05316



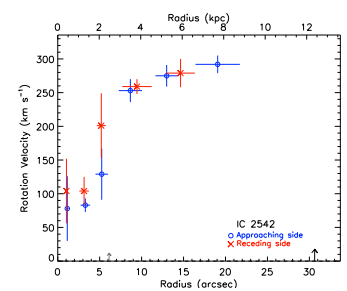
(69) UGC 05319



(70) UGC 05373

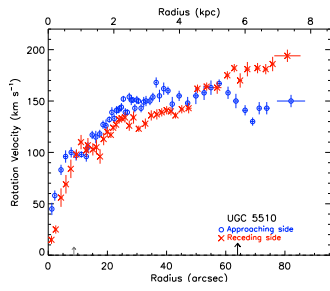


(71) UGC 05414

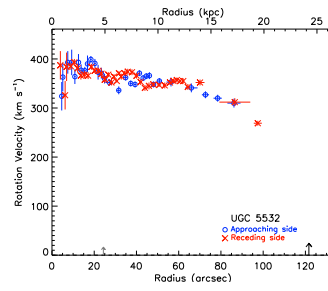


(72) IC 2542

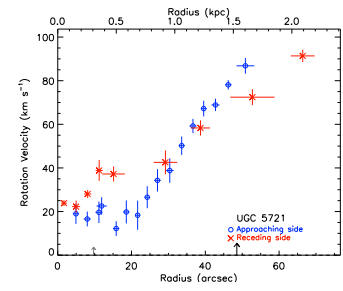
FIG. D.2 : suite



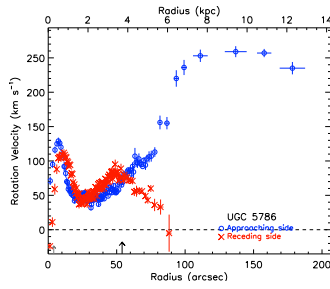
(73) UGC 05510



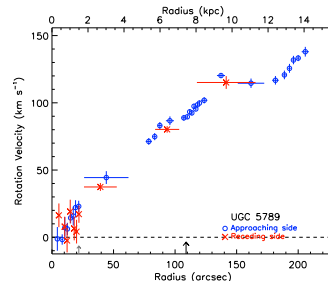
(74) UGC 05532



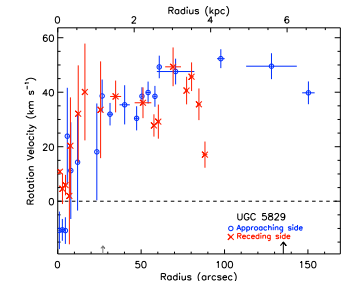
(75) UGC 05721



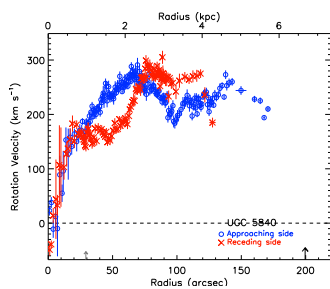
(76) UGC 05786



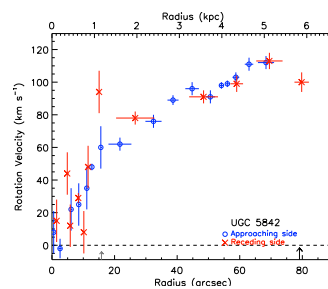
(77) UGC 05789



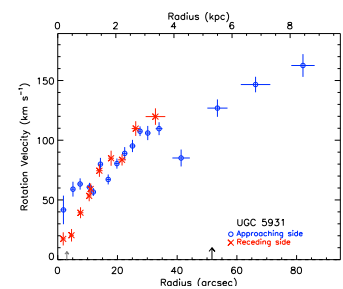
(78) UGC 05829



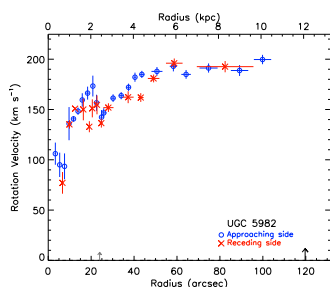
(79) UGC 05840



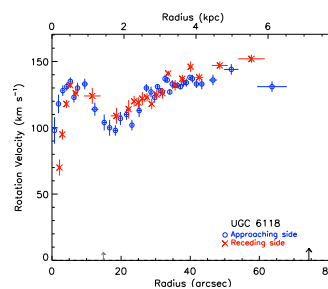
(80) UGC 05842



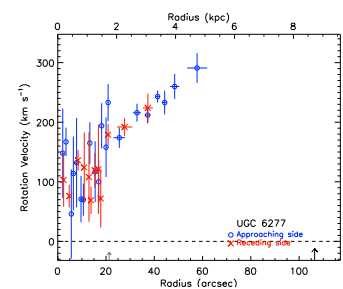
(81) UGC 05931



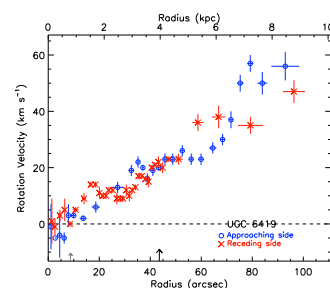
(82) UGC 05982



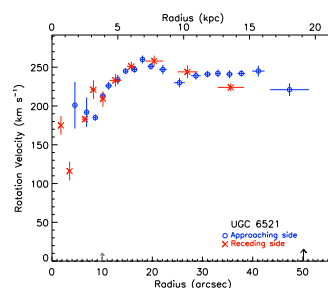
(83) UGC 06118



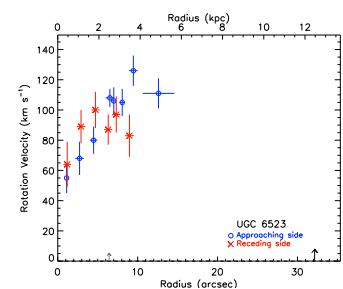
(84) UGC 06277



(85) UGC 06419

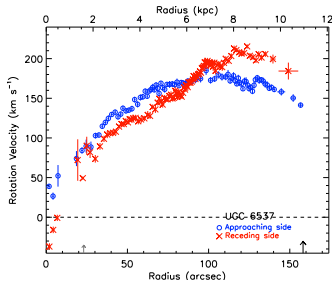


(86) UGC 06521

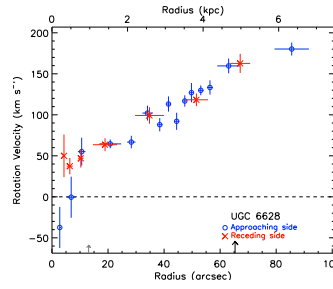


(87) UGC 06523

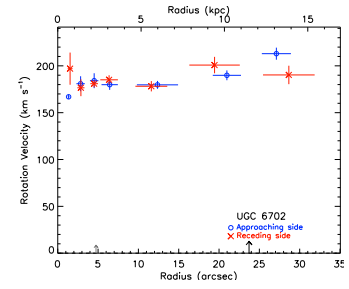
FIG. D.2 : suite



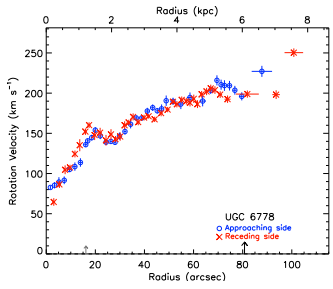
(88) UGC 06537



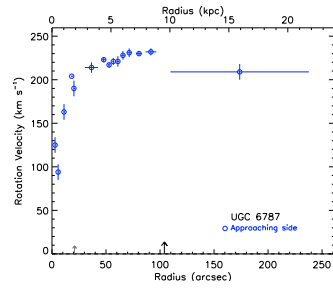
(89) UGC 06628



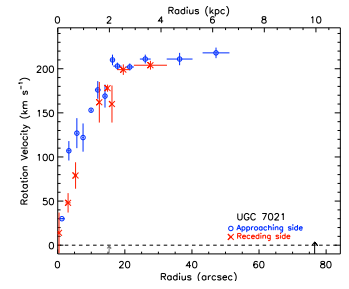
(90) UGC 06702



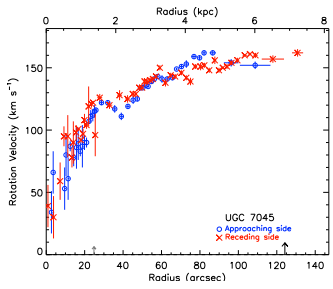
(91) UGC 06778



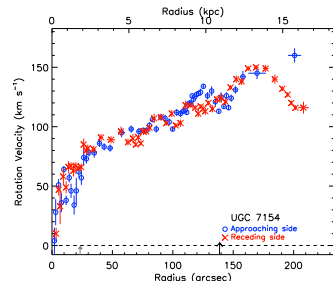
(92) UGC 06787



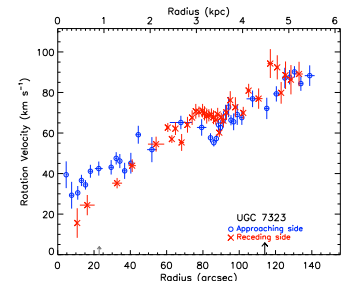
(93) UGC 07021



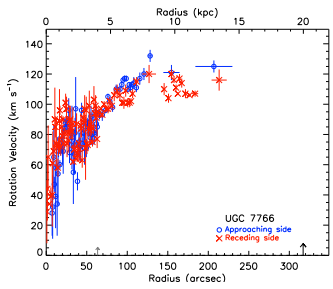
(94) UGC 07045



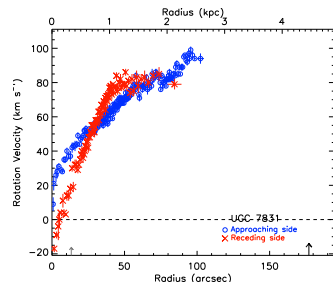
(95) UGC 07154



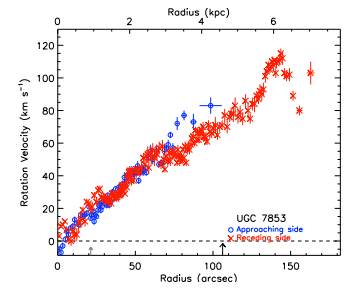
(96) UGC 07323



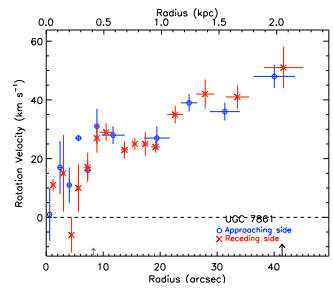
(97) UGC 07766



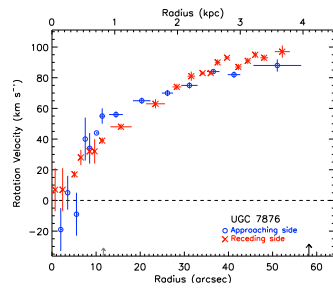
(98) UGC 07831



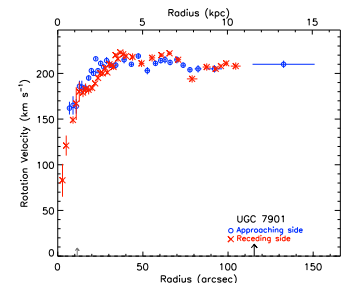
(99) UGC 07853



(100) UGC 07861

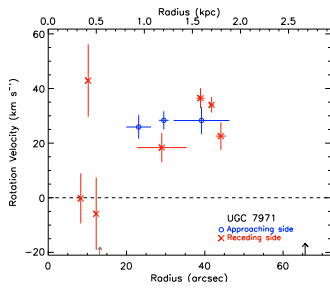


(101) UGC 07876

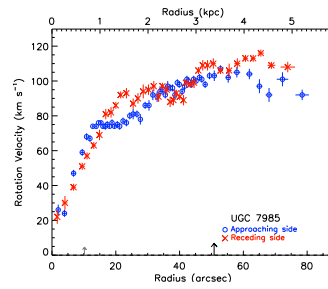


(102) UGC 07901

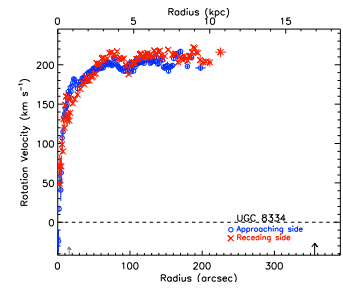
FIG. D.2 : suite



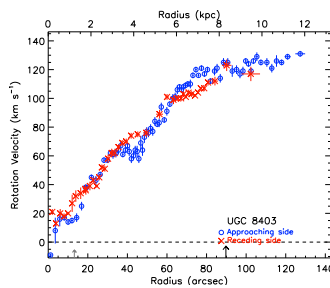
(103) UGC 07971



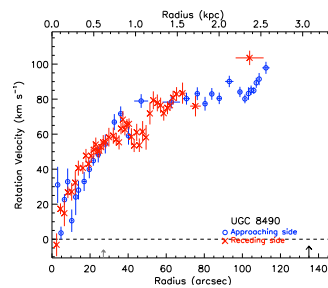
(104) UGC 07985



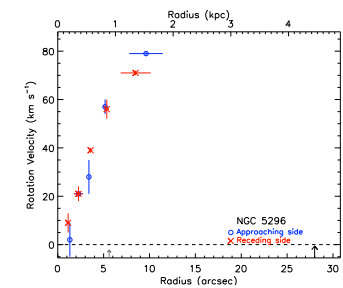
(105) UGC 8334



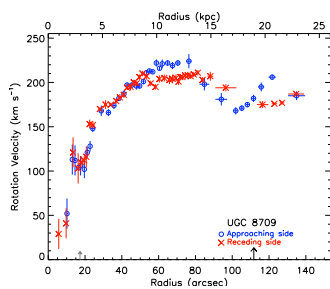
(106) UGC 8403



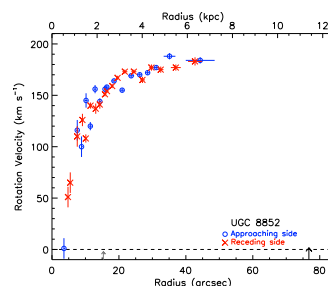
(107) UGC 8490



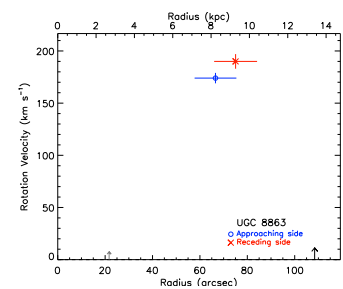
(108) NGC 5296



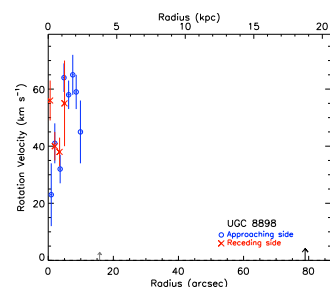
(109) UGC 8709



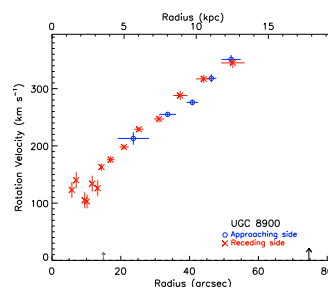
(110) UGC 8852



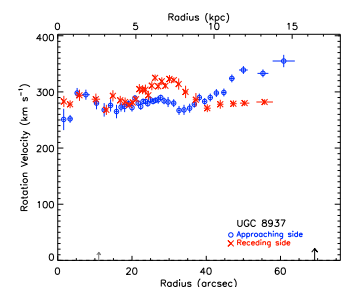
(111) UGC 8863



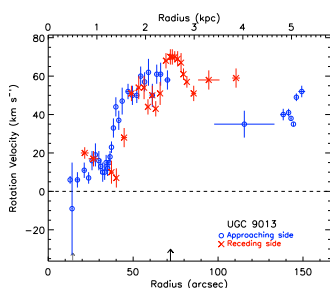
(112) UGC 8898



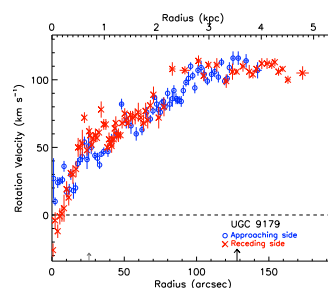
(113) UGC 8900



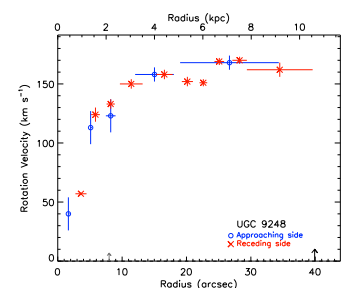
(114) UGC 8937



(115) UGC 9013

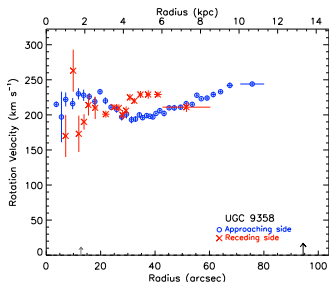


(116) UGC 9179

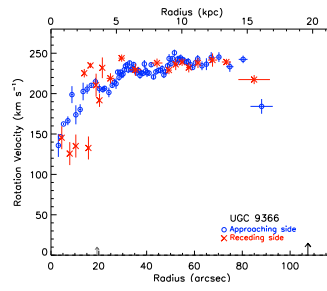


(117) UGC 9248

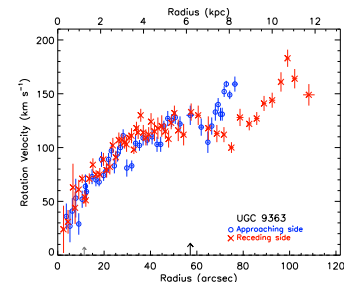
FIG. D.2 : suite



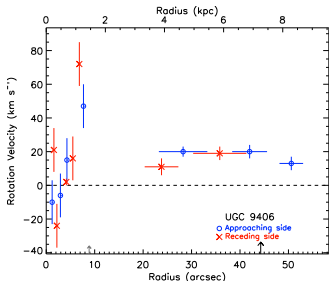
(118) UGC 09358



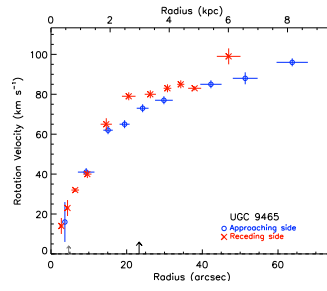
(119) UGC 09366



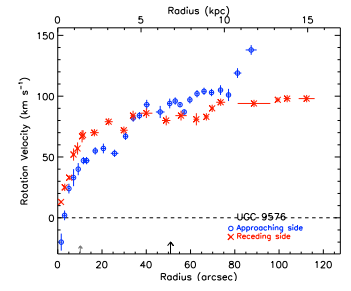
(120) UGC 09363



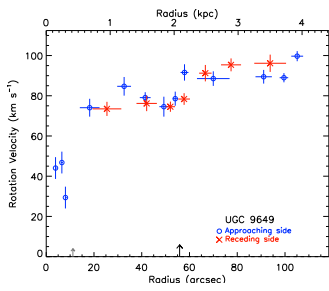
(121) UGC 09406



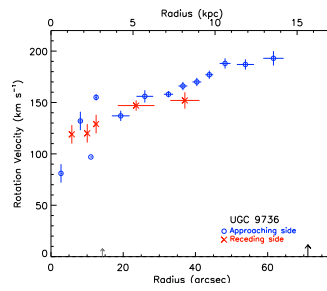
(122) UGC 09465



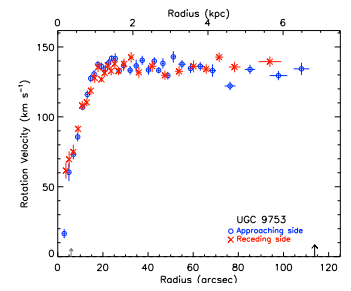
(123) UGC 09576



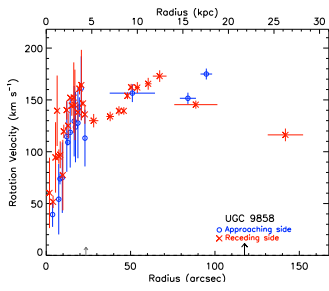
(124) UGC 09649



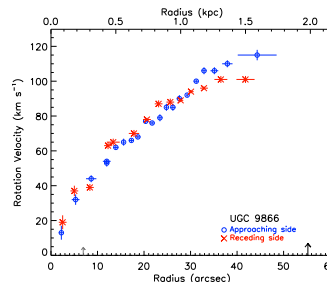
(125) UGC 09736



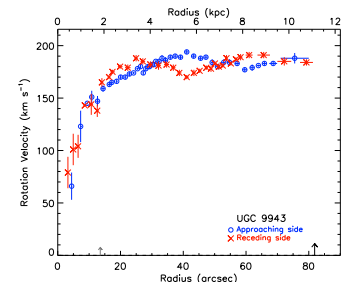
(126) UGC 09753



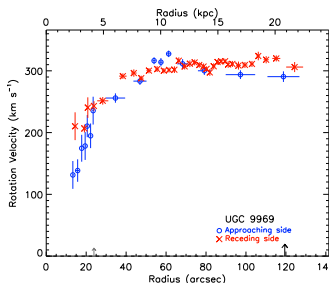
(127) UGC 09858



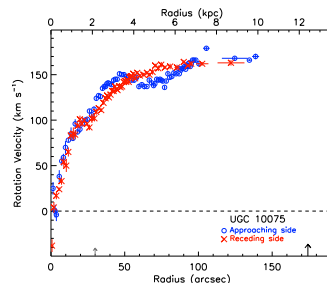
(128) UGC 09866



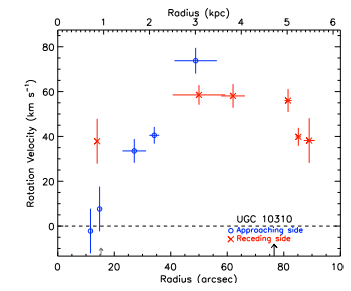
(129) UGC 09943



(130) UGC 9969

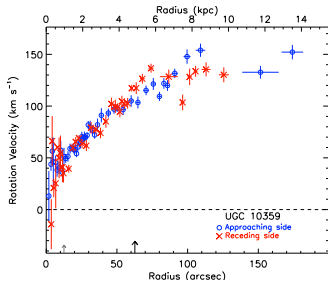


(131) UGC 10075

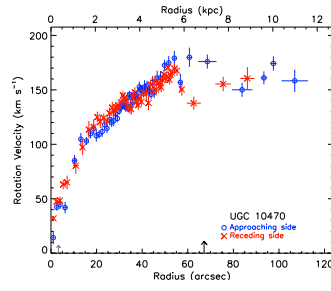


(132) UGC 10310

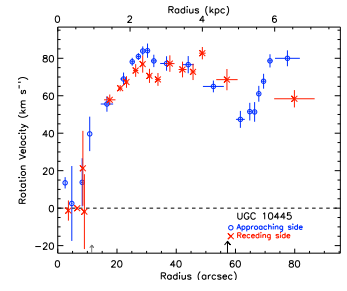
FIG. D.2 : suite



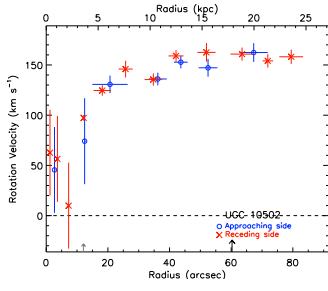
(133) UGC 10359



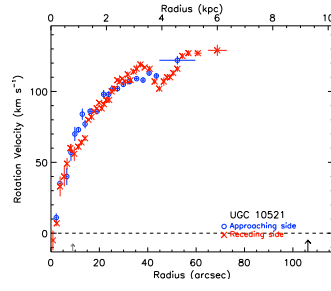
(134) UGC 10470



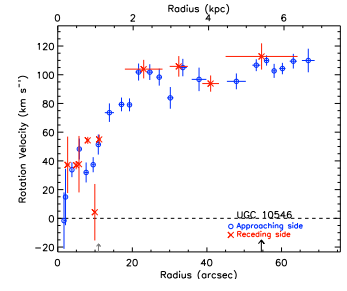
(135) UGC 10445



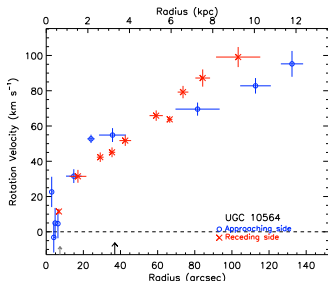
(136) UGC 10502



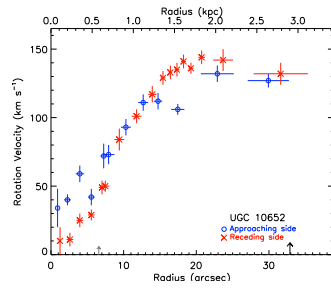
(137) UGC 10521



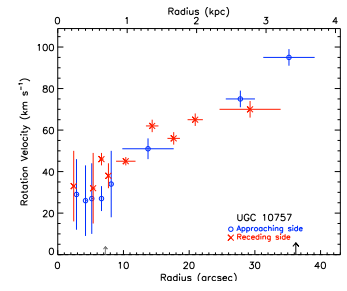
(138) UGC 10546



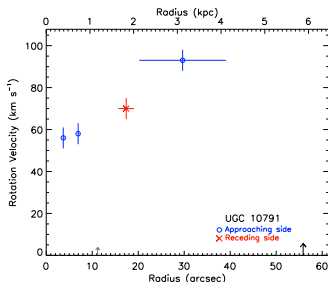
(139) UGC 10564



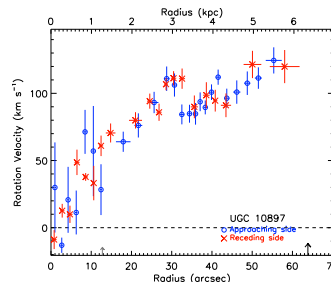
(140) UGC 10652



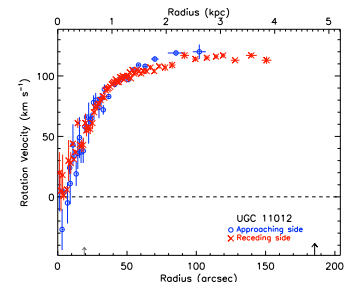
(141) UGC 10757



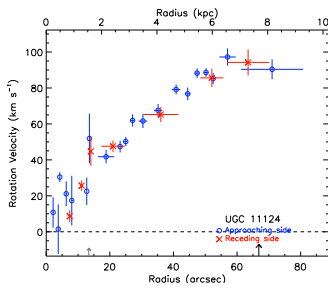
(142) UGC 10791



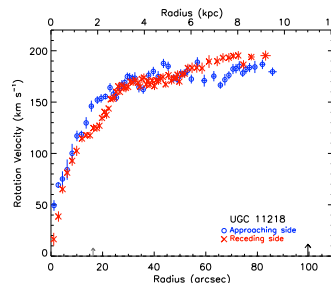
(143) UGC 10897



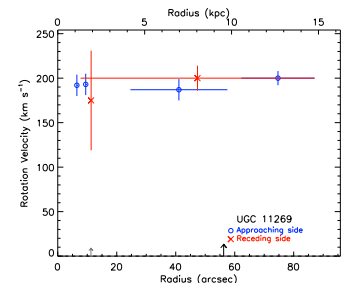
(144) UGC 11012



(145) UGC 11124

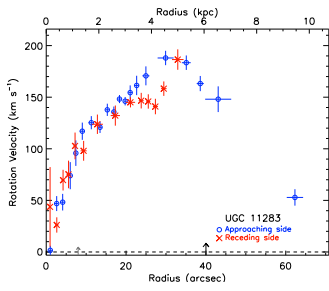


(146) UGC 11218

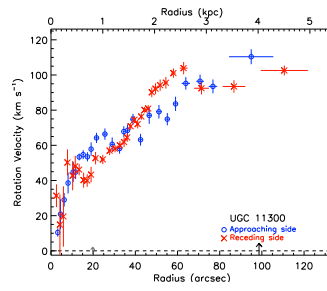


(147) UGC 11269

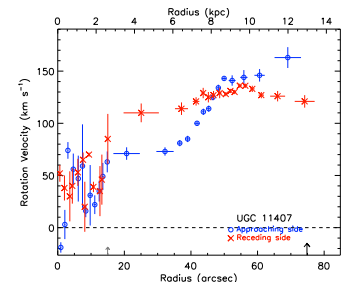
FIG. D.2 : suite



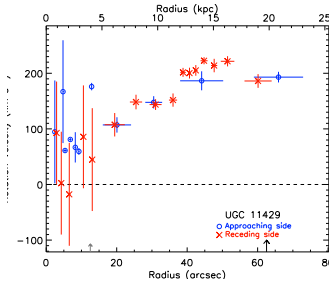
(148) UGC 11283



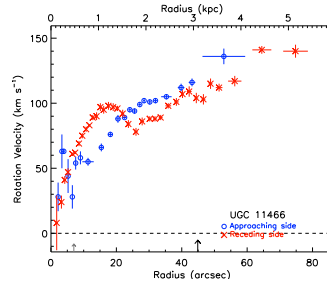
(149) UGC 11300



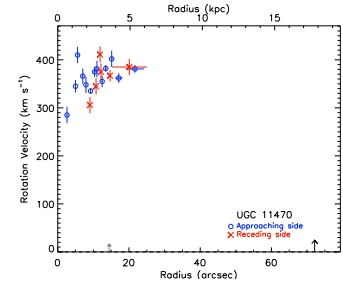
(150) UGC 11407



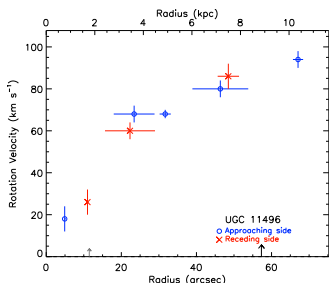
(151) UGC 11429



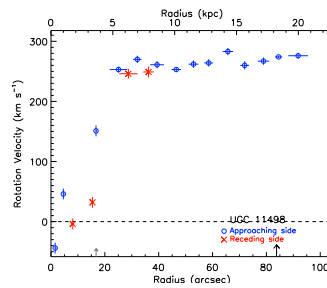
(152) UGC 11466



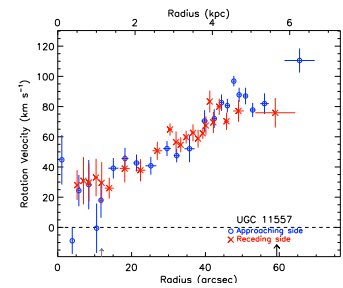
(153) UGC 11470



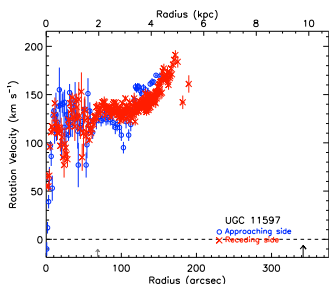
(154) UGC 11496



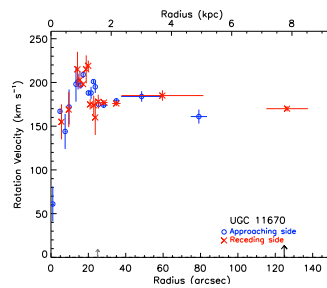
(155) UGC 11498



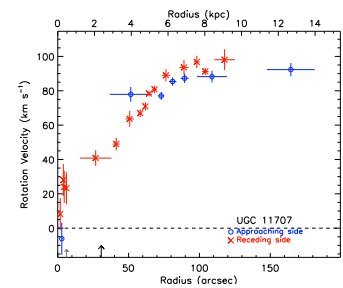
(156) UGC 11557



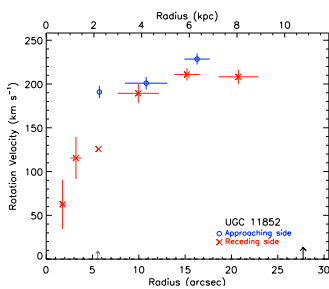
(157) UGC 11597



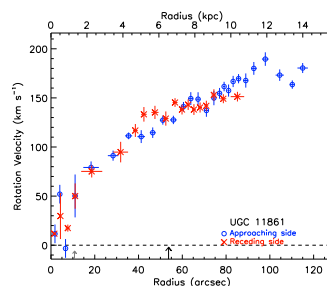
(158) UGC 11670



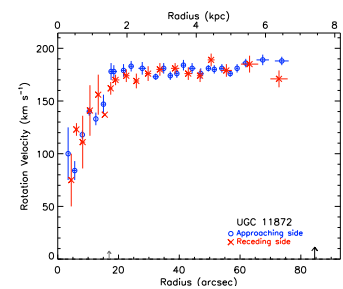
(159) UGC 11707



(160) UGC 11852

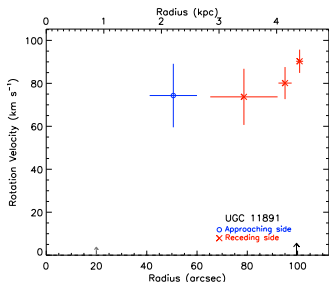


(161) UGC 11861

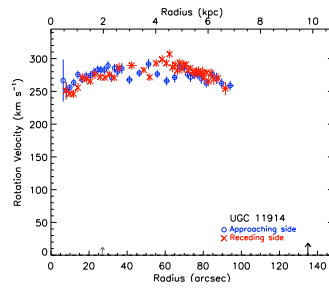


(162) UGC 11872

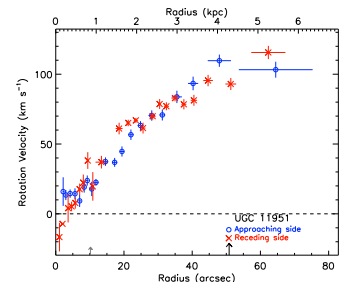
FIG. D.2 : suite



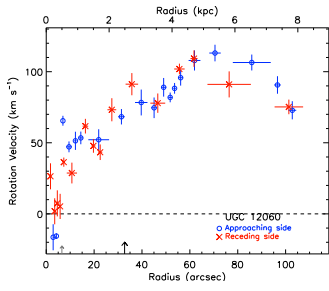
(163) UGC 11891



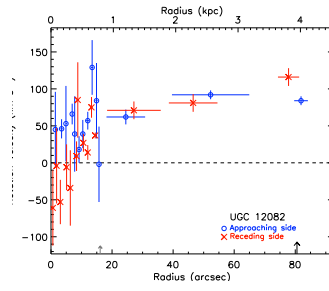
(164) UGC 11914



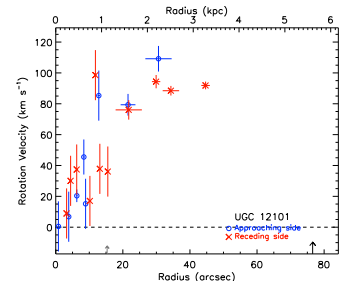
(165) UGC 11951



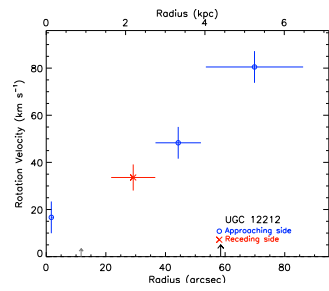
(166) UGC 12060



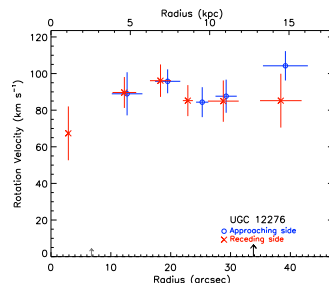
(167) UGC 12082



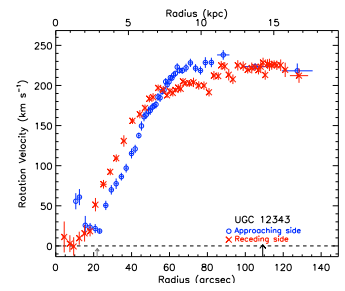
(168) UGC 12101



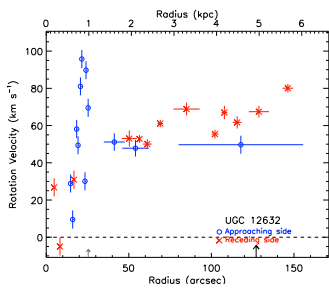
(169) UGC 12212



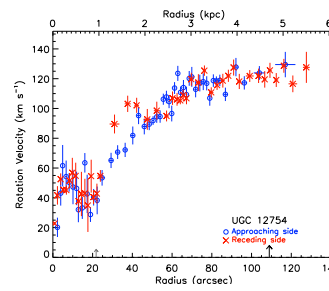
(170) UGC 12276



(171) UGC 12343



(172) UGC 12632



(173) UGC 12754

FIG. D.2 : suite

D.3 Cartes et profils de dispersion de vitesses des galaxies GHASP

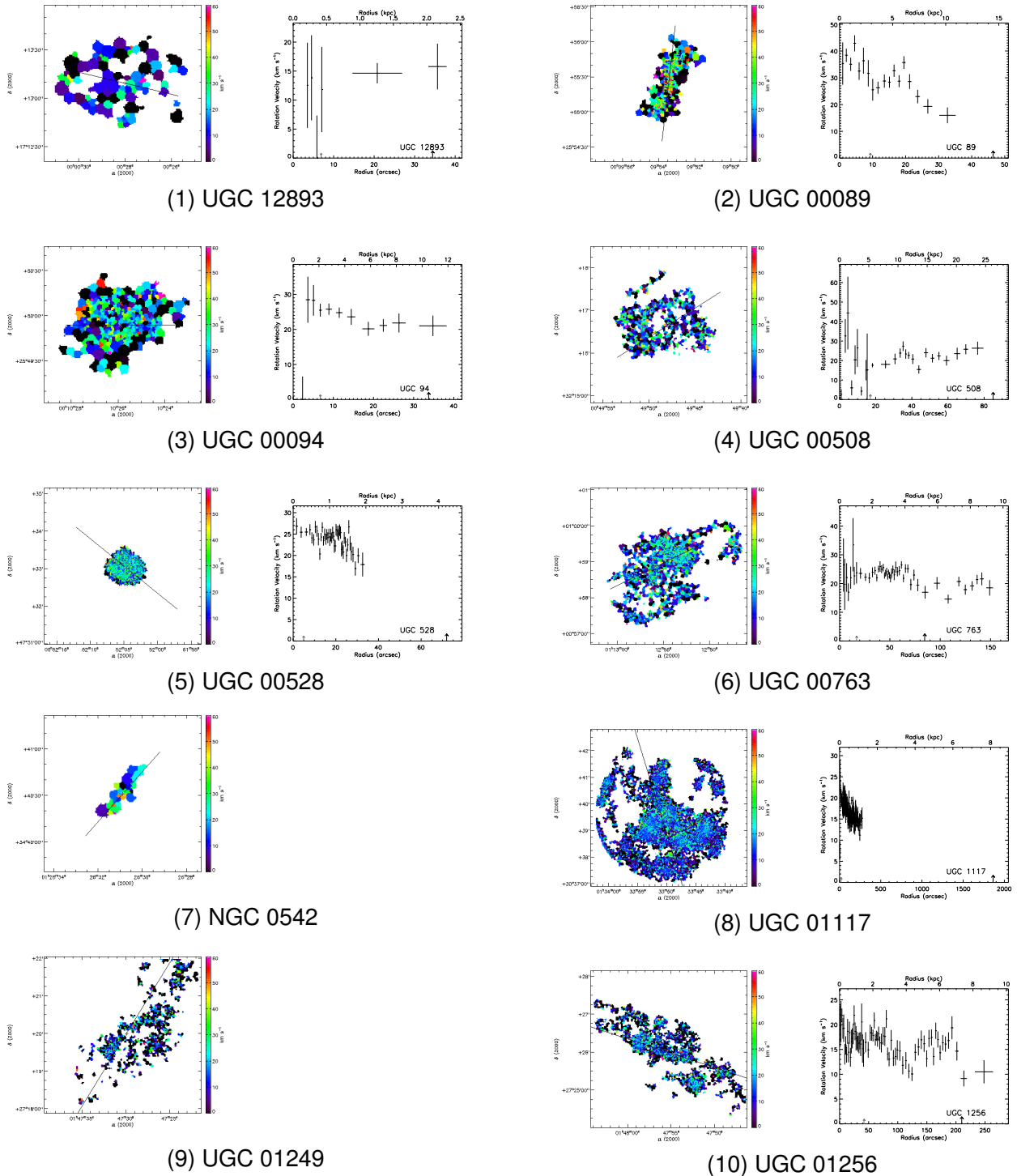
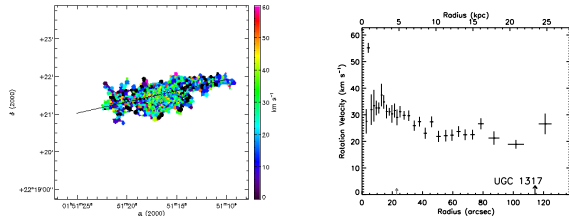
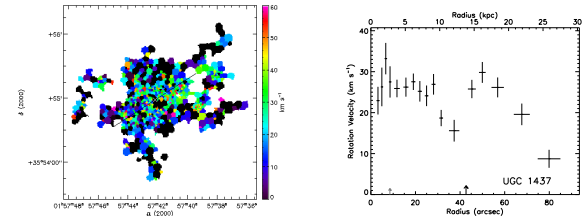


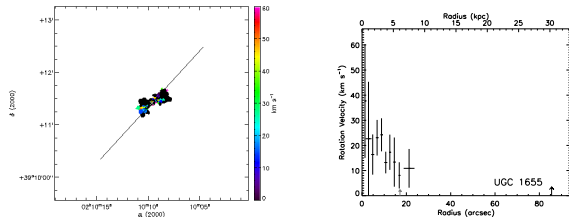
FIG. D.3: Dispersion de vitesses des galaxies GHASP. **À gauche** : Carte de dispersion de vitesses. La double croix blanche et noire représente le centre cinématique. La ligne noire représente le grand axe et s'arrête au rayon optique ($D_{25}/2$, de Vaucouleurs et al., 1995). **À droite** : Profil radial de dispersion de vitesses. La flèche noire indique le rayon optique, la flèche grise indique le rayon de transition.



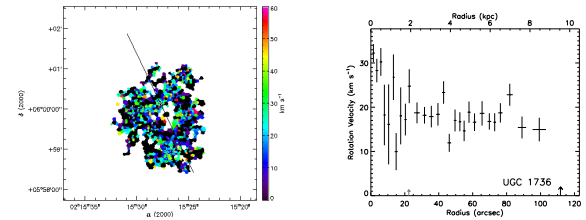
(11) UGC 01317



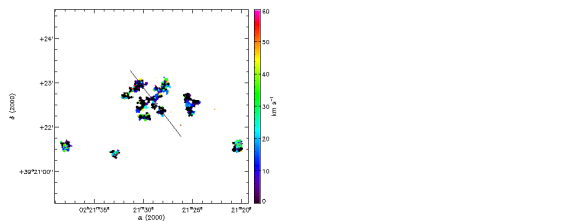
(12) UGC 01437



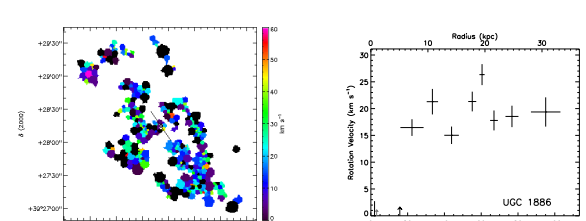
(13) UGC 01655



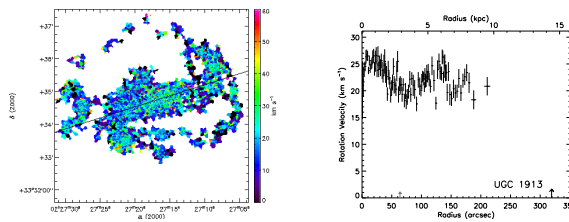
(14) UGC 01736



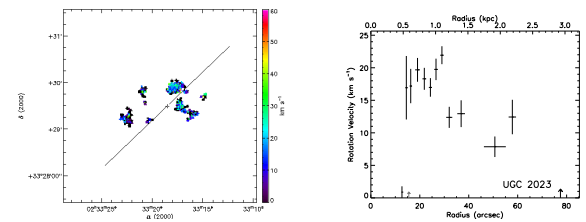
(15) UGC 01810



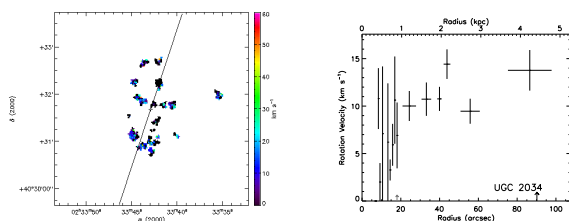
(16) UGC 01886



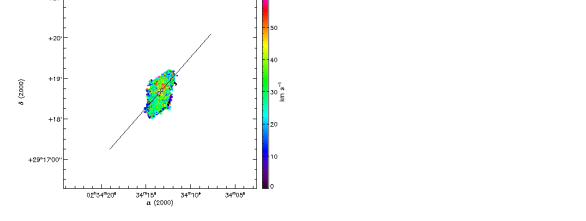
(17) UGC 01913



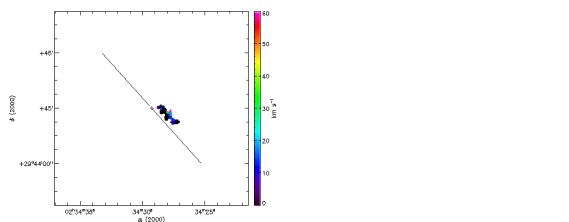
(18) UGC 02023



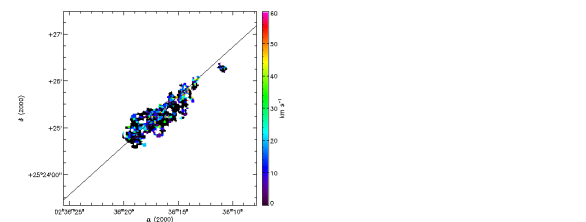
(19) UGC 02034



(20) UGC 02045

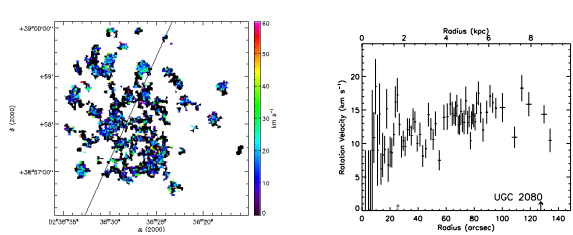


(21) UGC 02053

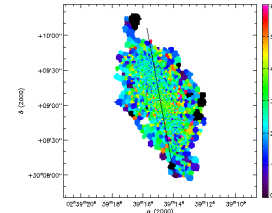


(22) UGC 02082

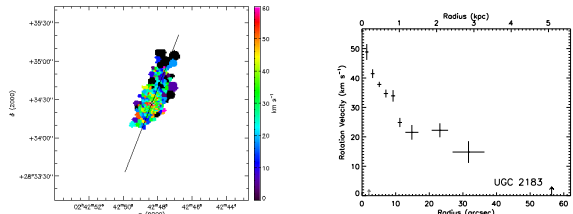
FIG. D.3 : suite



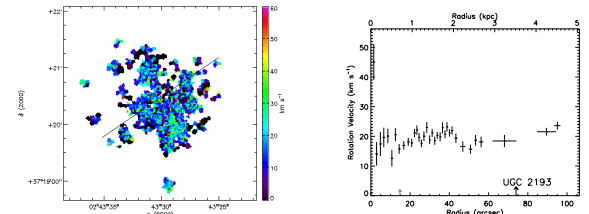
(23) UGC 02080



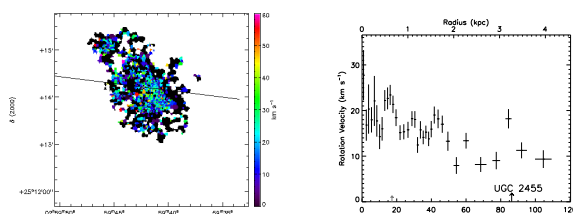
(24) UGC 02141



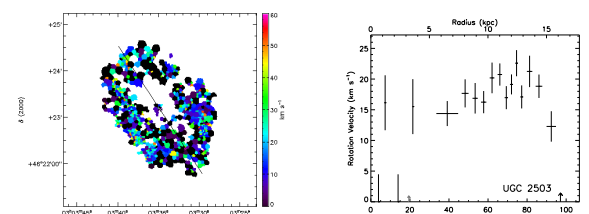
(25) UGC 02183



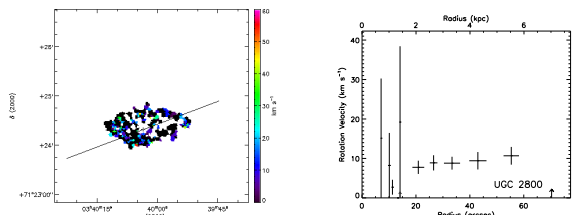
(26) UGC 02193



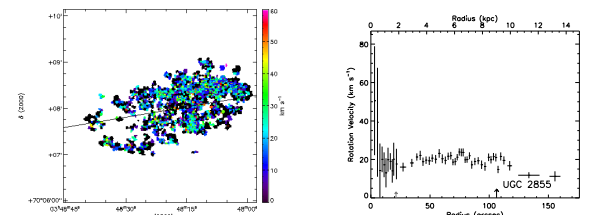
(27) UGC 02455



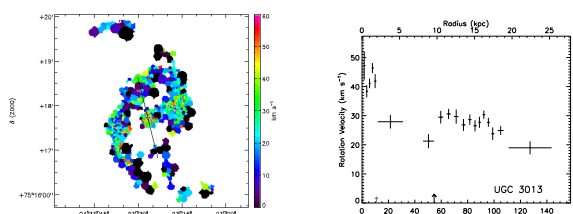
(28) UGC 02503



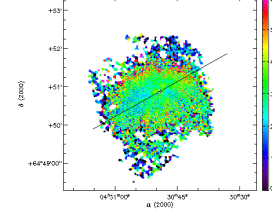
(29) UGC 02800



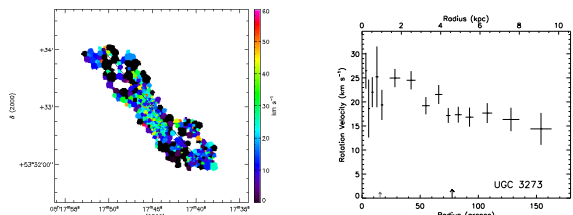
(30) UGC 02855



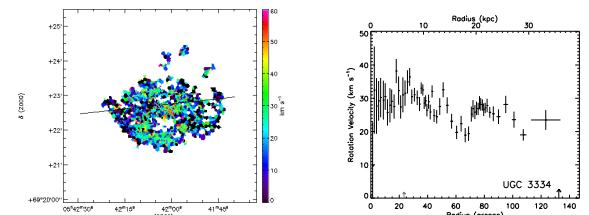
(31) UGC 03013



(32) UGC 03056

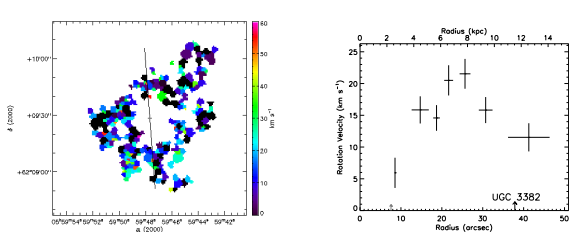


(33) UGC 03273

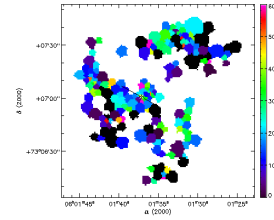


(34) UGC 03334

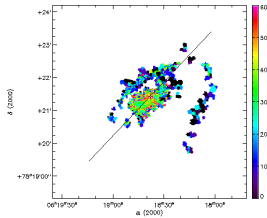
FIG. D.3 : suite



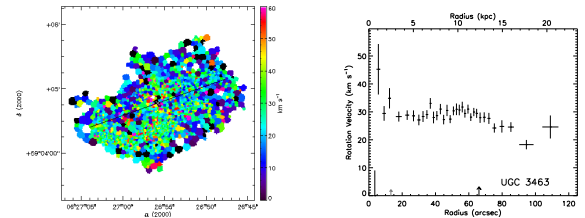
(35) UGC 03382



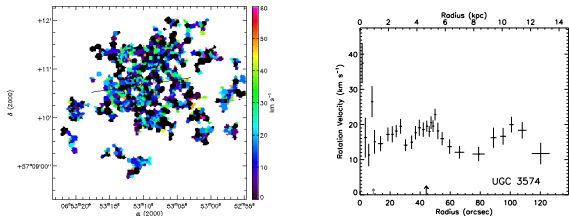
(36) UGC 03384



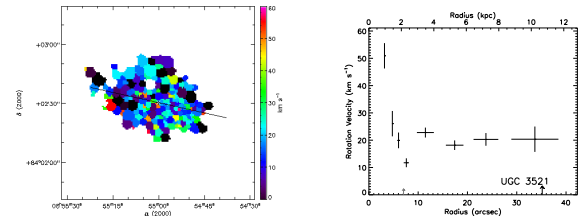
(37) UGC 03429



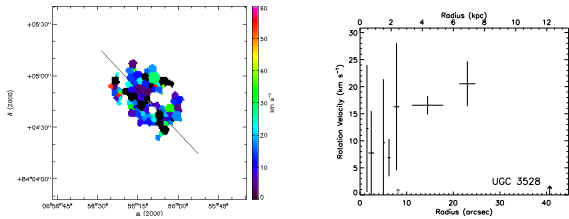
(38) UGC 03463



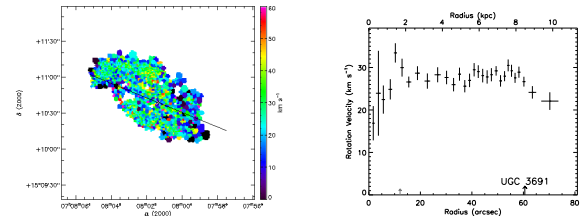
(39) UGC 03574



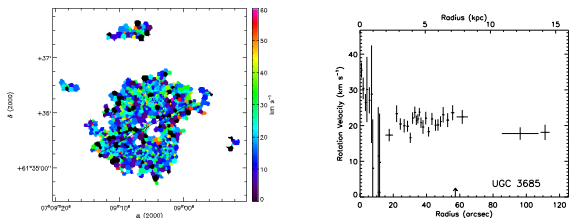
(40) UGC 03521



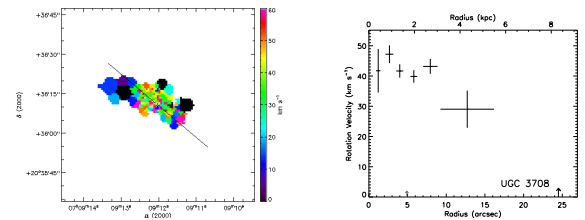
(41) UGC 03528



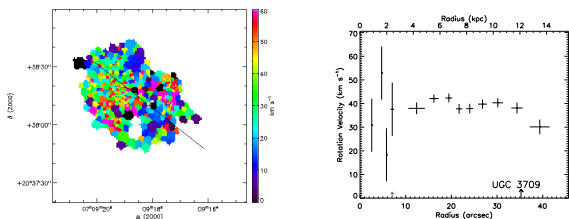
(42) UGC 03691



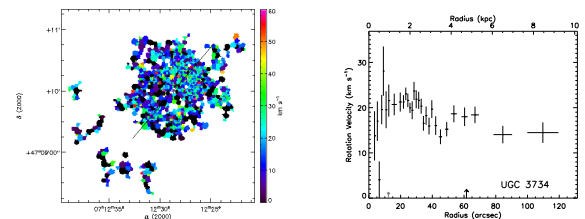
(43) UGC 03685



(44) UGC 03708

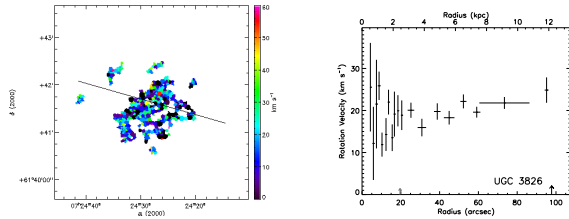


(45) UGC 03709

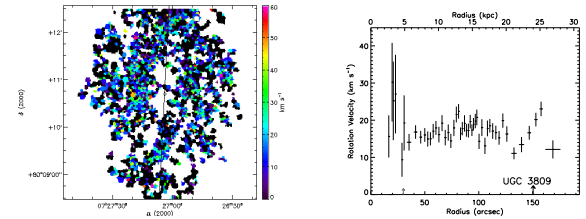


(46) UGC 03734

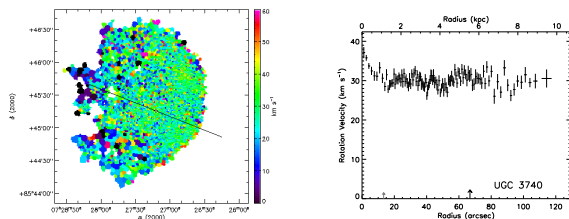
FIG. D.3 : suite



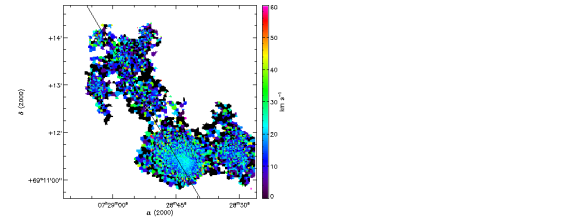
(47) UGC 03826



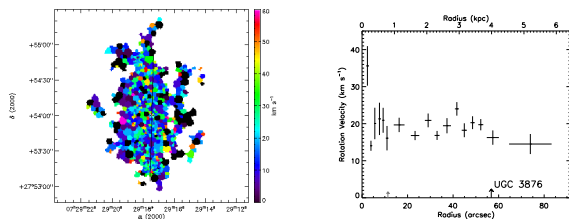
(48) UGC 03809



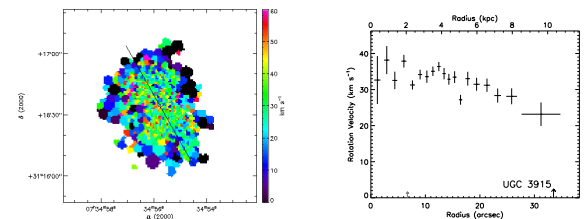
(49) UGC 03740



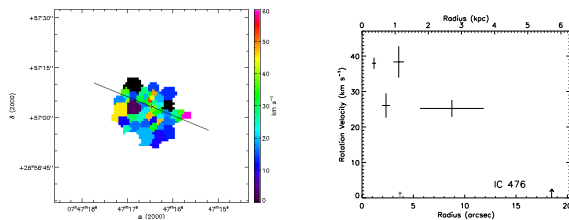
(50) UGC 03851



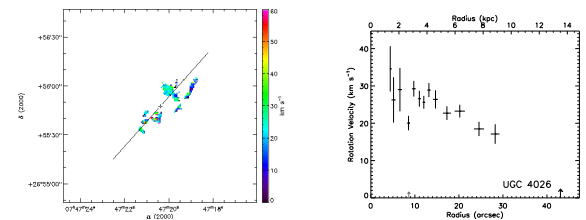
(51) UGC 03876



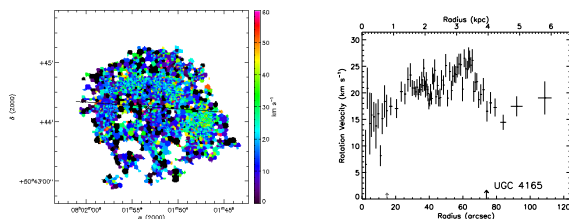
(52) UGC 03915



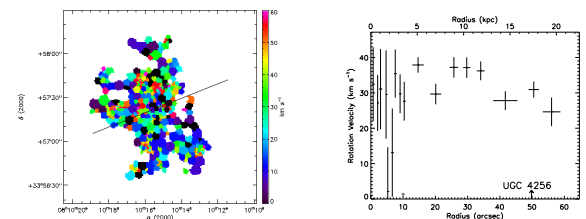
(53) IC 476



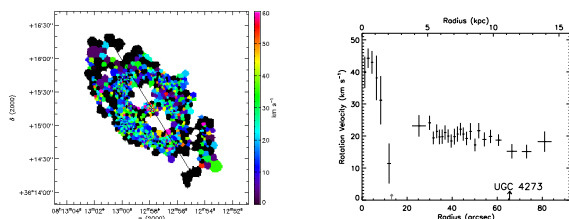
(54) UGC 04026



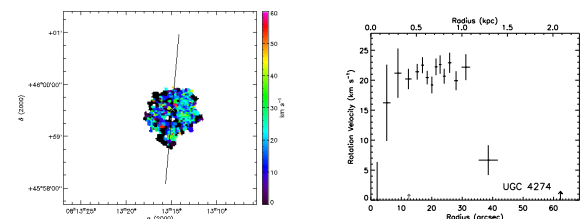
(55) UGC 04165



(56) UGC 04256

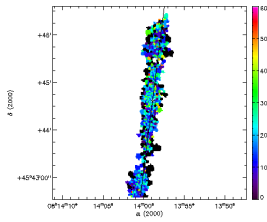


(57) UGC 04273

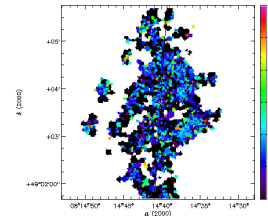


(58) UGC 04274

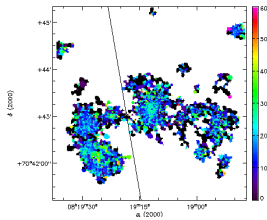
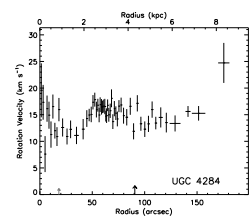
FIG. D.3 : suite



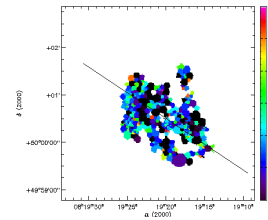
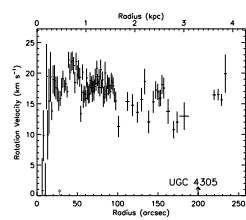
(59) UGC 04278



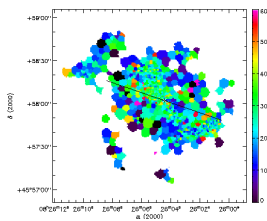
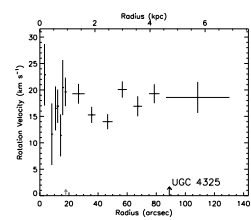
(60) UGC 04284



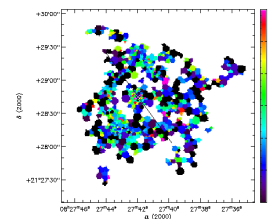
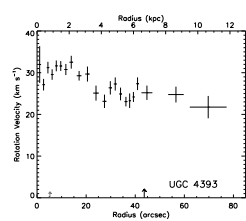
(61) UGC 04305



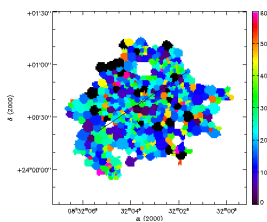
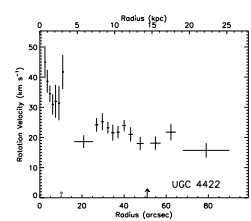
(62) UGC 04325



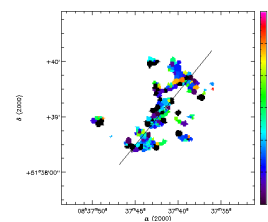
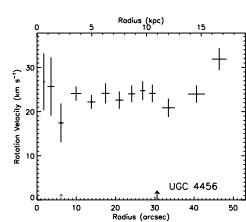
(63) UGC 04393



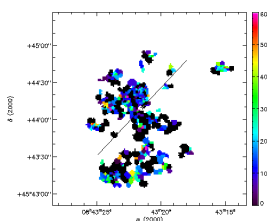
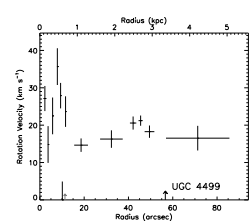
(64) UGC 04422



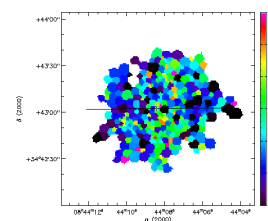
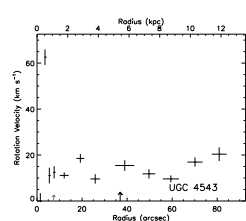
(65) UGC 04456



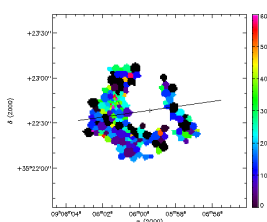
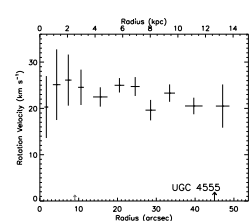
(66) UGC 04499



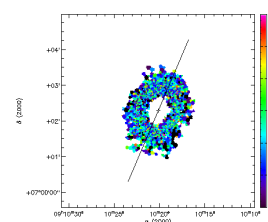
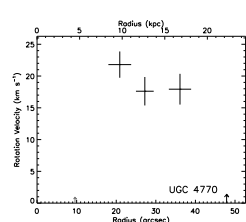
(67) UGC 04543



(68) UGC 04555



(69) UGC 04770



(70) UGC 04820

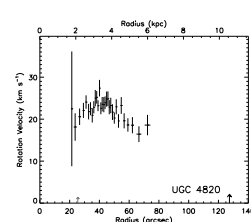
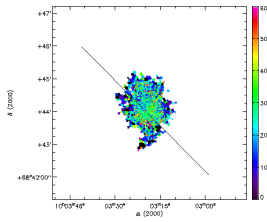
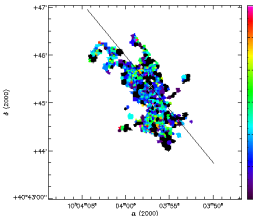


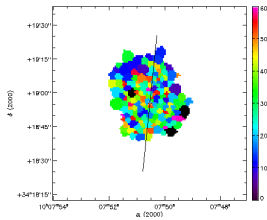
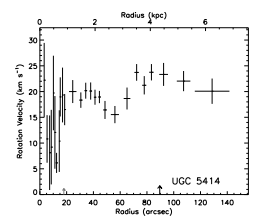
FIG. D.3 : suite



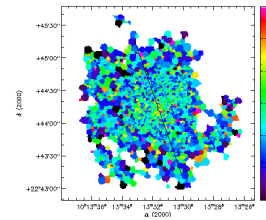
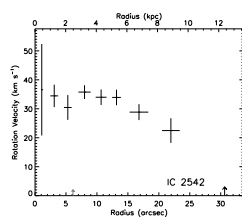
(83) UGC 05398



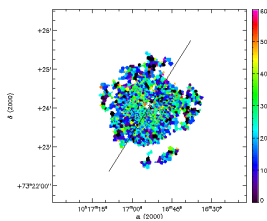
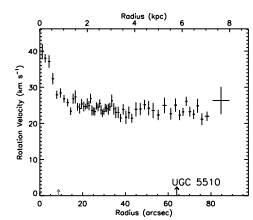
(84) UGC 05414



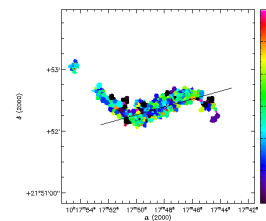
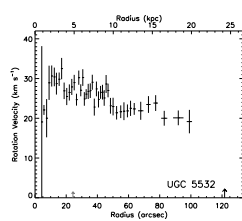
(85) IC 2542



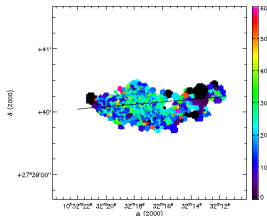
(86) UGC 05510



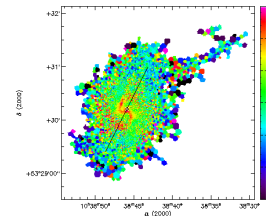
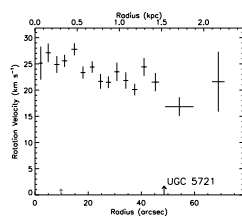
(87) UGC 05532



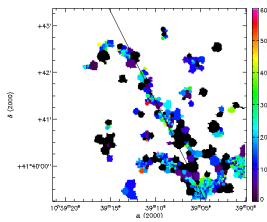
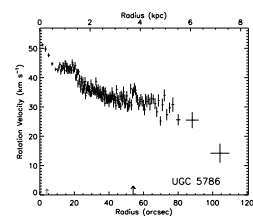
(88) UGC 05556



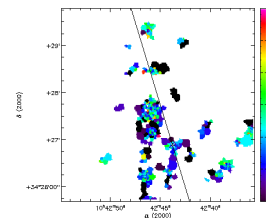
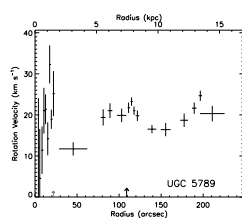
(89) UGC 05721



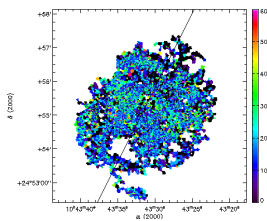
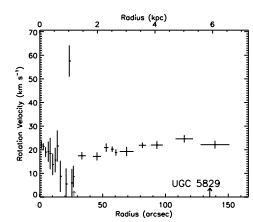
(90) UGC 05786



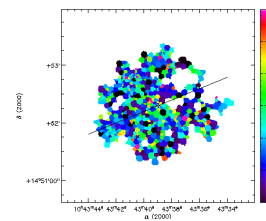
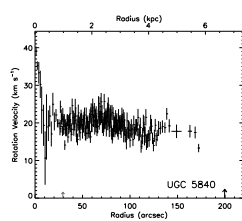
(91) UGC 05789



(92) UGC 05829



(93) UGC 05840



(94) UGC 05842

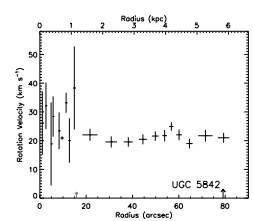


FIG. D.3 : suite

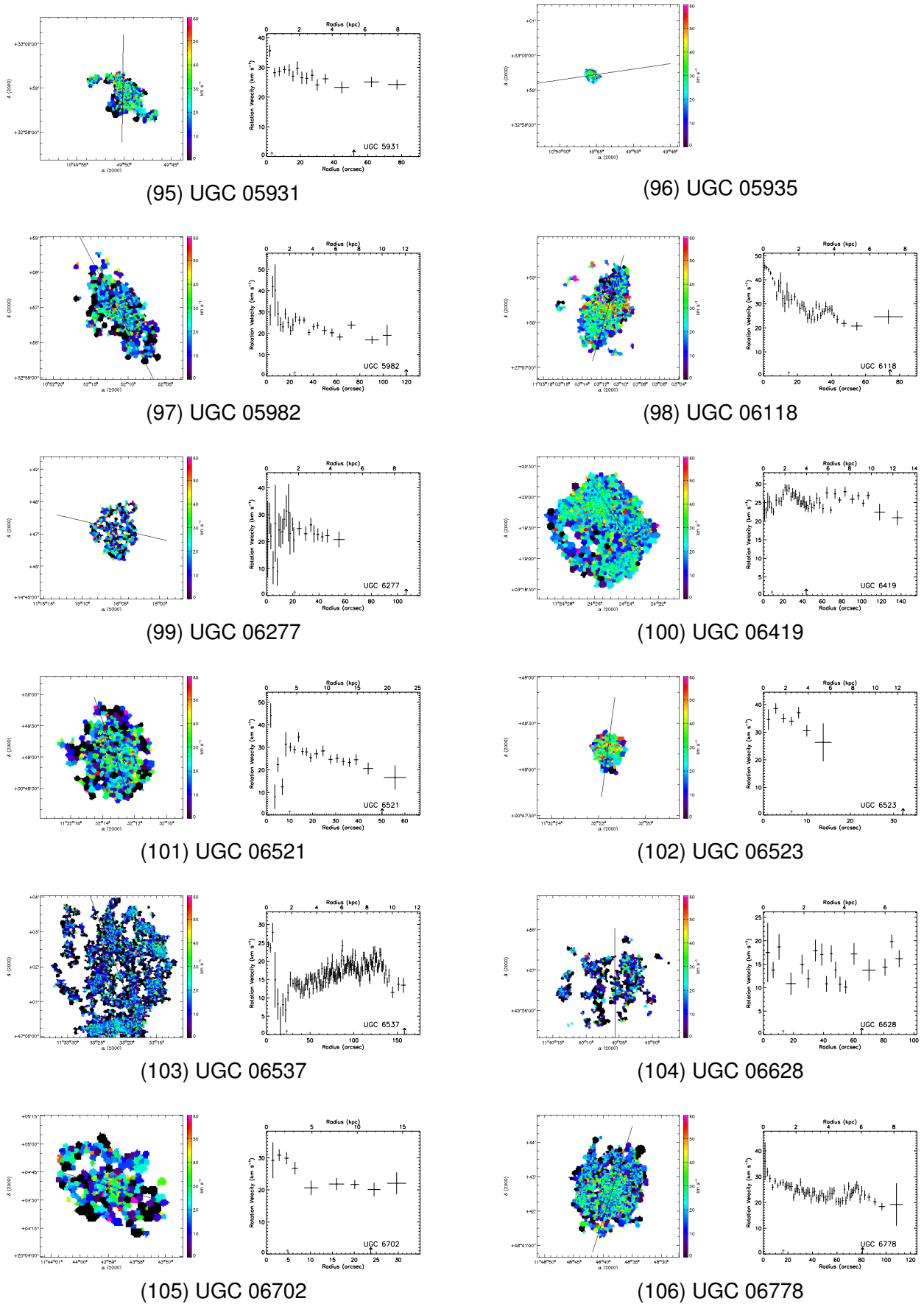
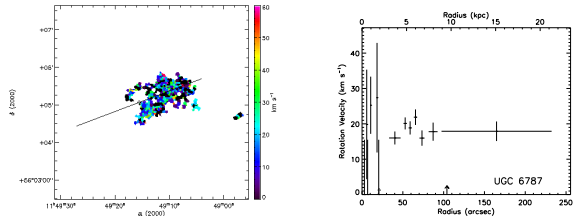
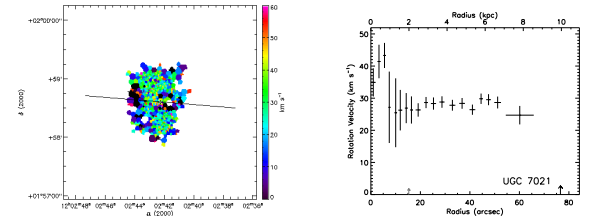


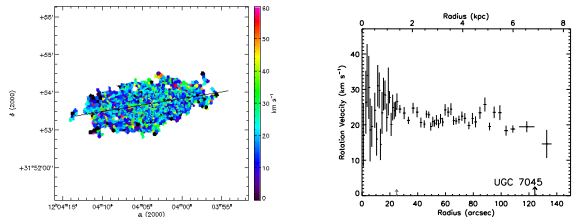
FIG. D.3 : suite



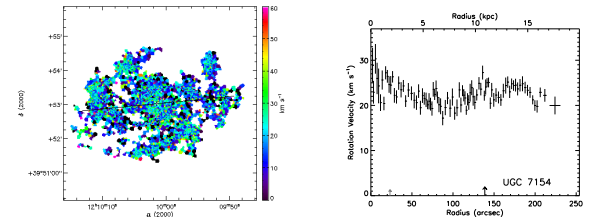
(107) UGC 06787



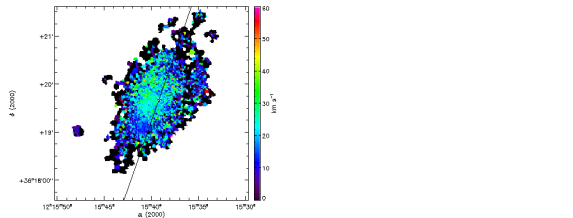
(108) UGC 07021



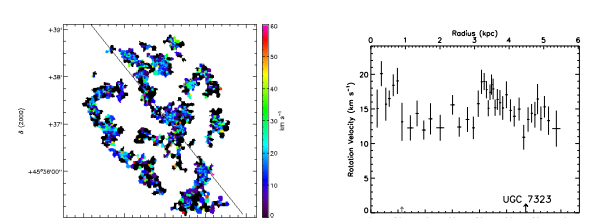
(109) UGC 07045



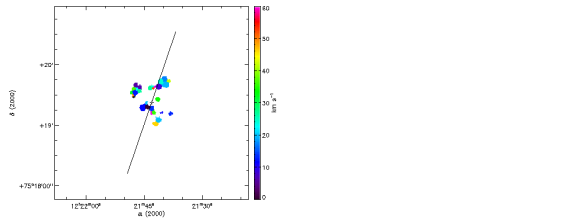
(110) UGC 07154



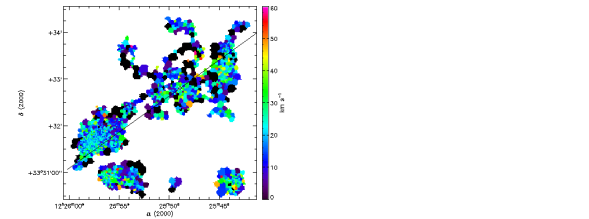
(111) UGC 07278



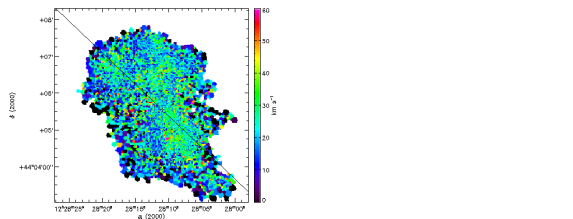
(112) UGC 07323



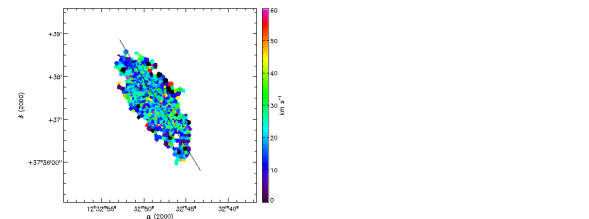
(113) UGC 07429



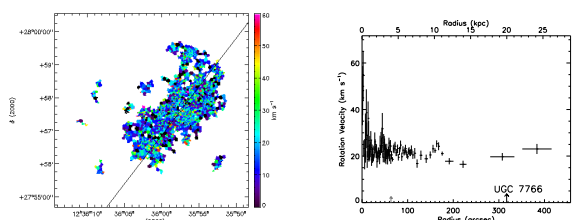
(114) UGC 07524



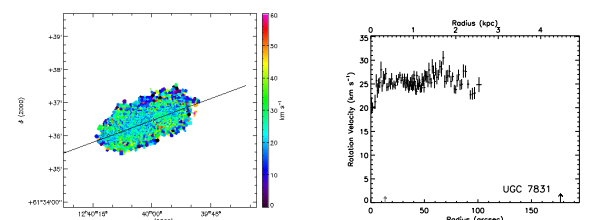
(115) UGC 07592



(116) UGC 07699

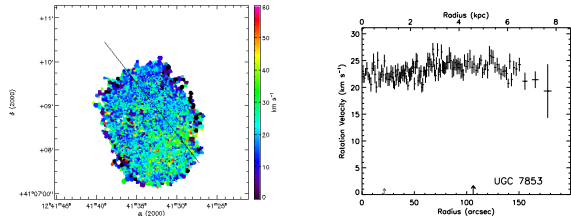


(117) UGC 07766

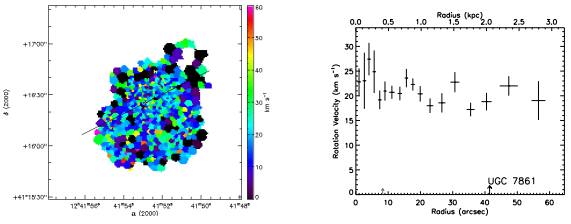


(118) UGC 07831

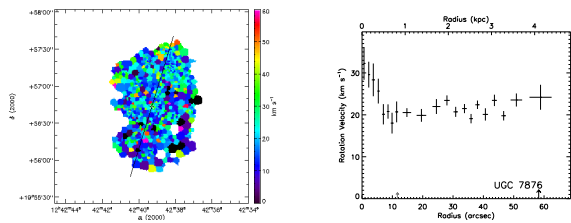
FIG. D.3 : suite



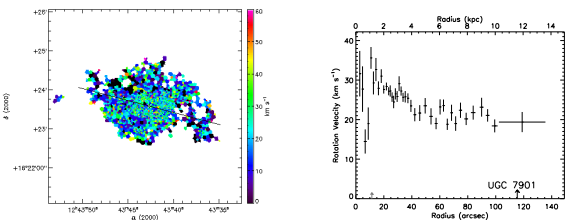
(119) UGC 07853



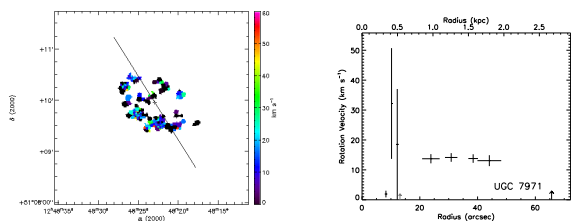
(120) UGC 07861



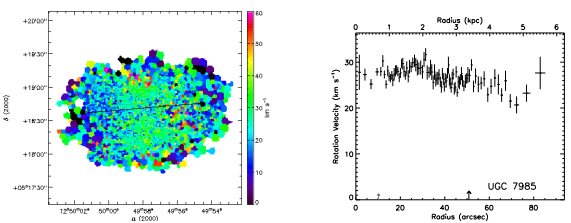
(121) UGC 07876



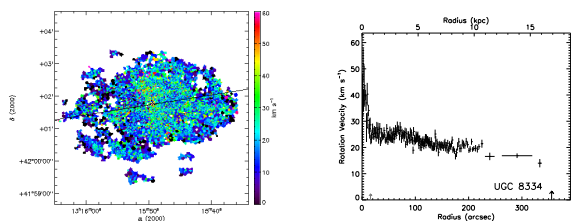
(122) UGC 07901



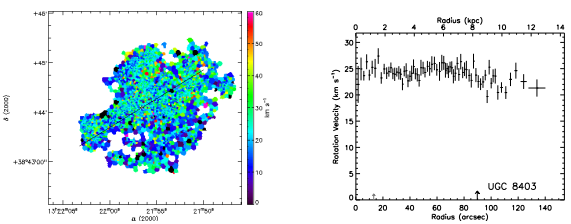
(123) UGC 07971



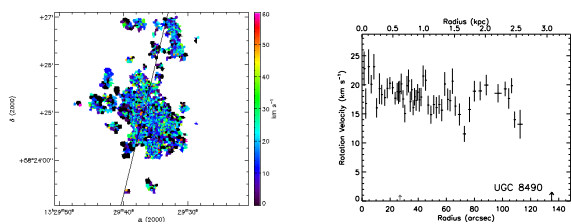
(124) UGC 07985



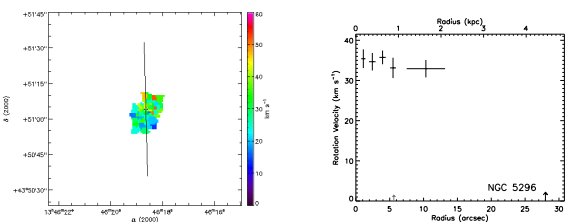
(125) UGC 08334



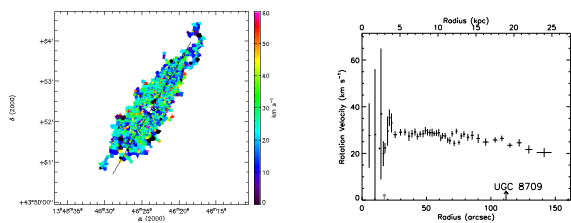
(126) UGC 08403



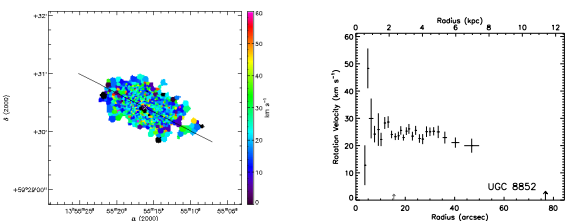
(127) UGC 08490



(128) NGC 5296

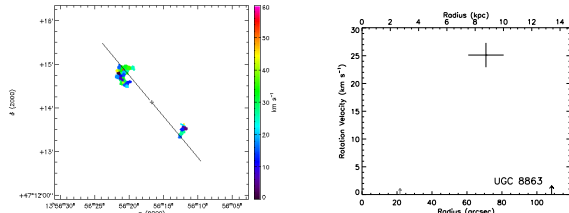


(129) UGC 08709

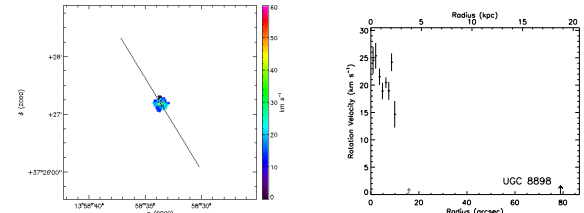


(130) UGC 08852

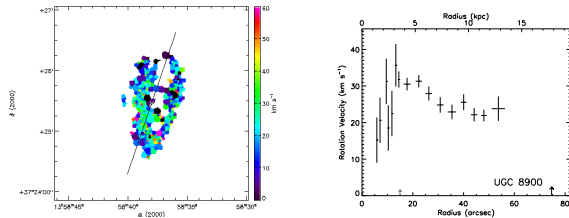
FIG. D.3 : suite



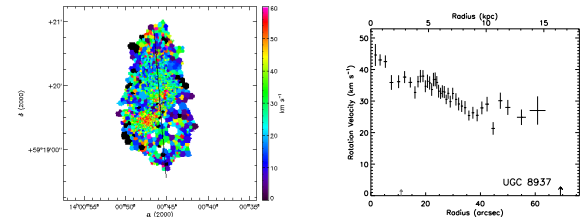
(131) UGC 08863



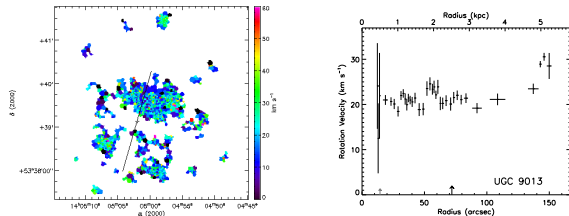
(132) UGC 08898



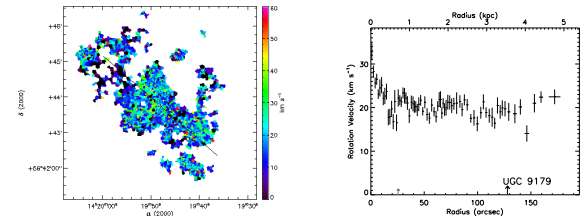
(133) UGC 08900



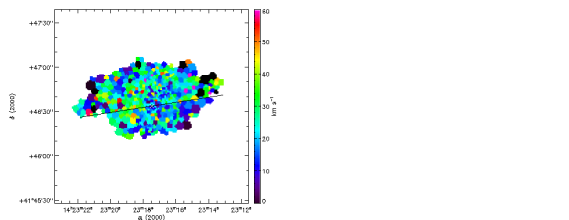
(134) UGC 08937



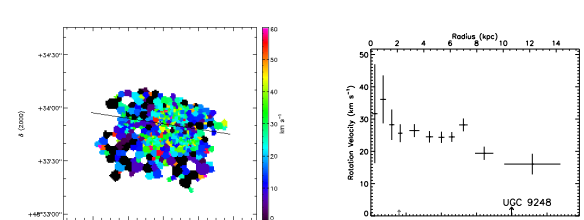
(135) UGC 09013



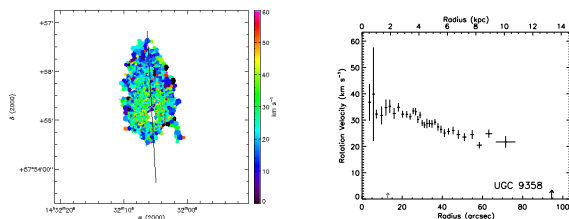
(136) UGC 09179



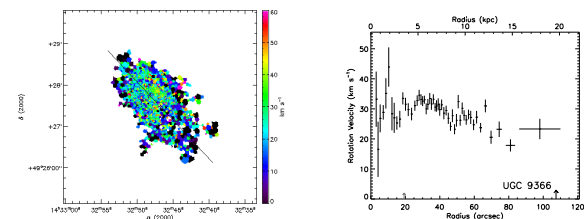
(137) UGC 09219



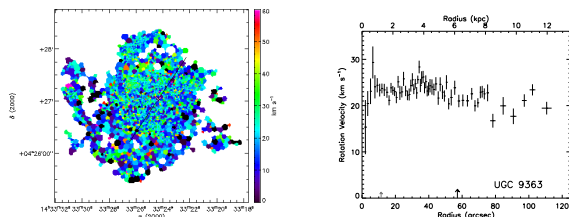
(138) UGC 09248



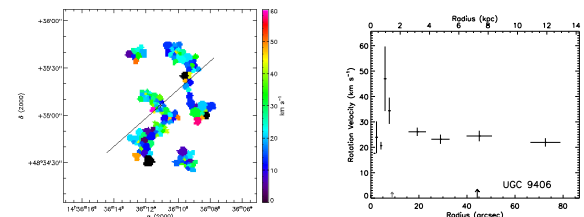
(139) UGC 09358



(140) UGC 09366

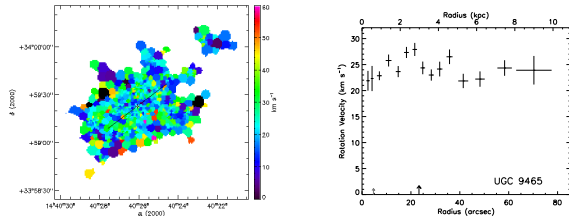


(141) UGC 09363

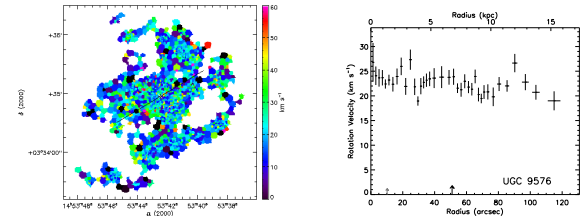


(142) UGC 09406

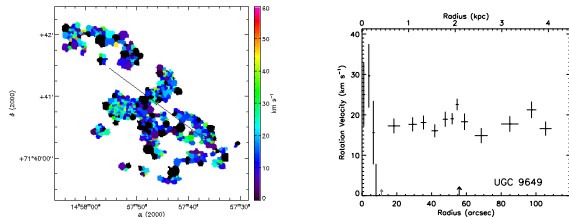
FIG. D.3 : suite



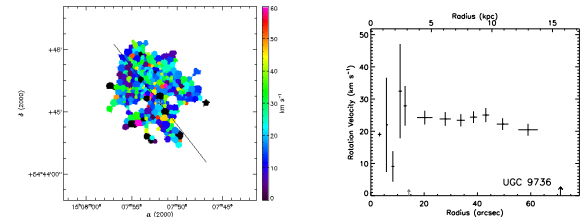
(143) UGC 09465



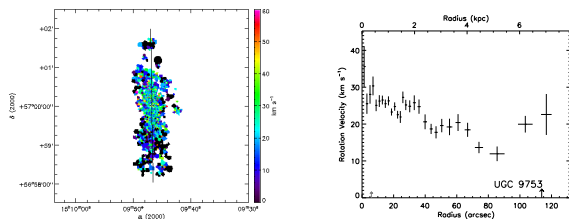
(144) UGC 09576



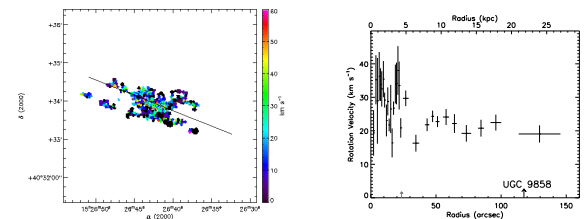
(145) UGC 09649



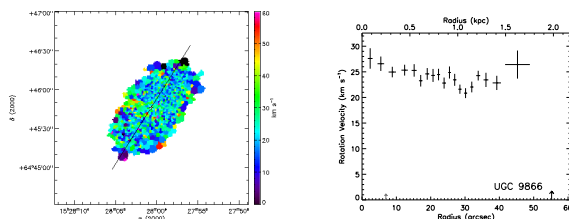
(146) UGC 09736



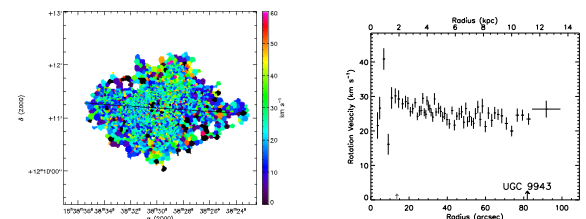
(147) UGC 09753



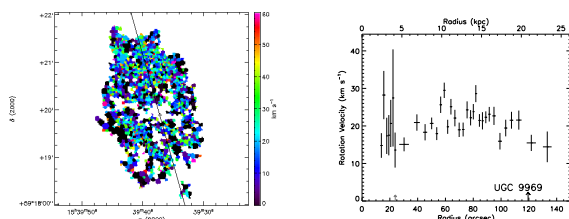
(148) UGC 09858



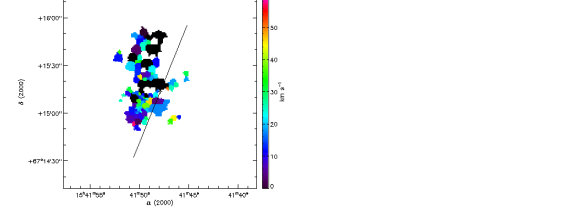
(149) UGC 09866



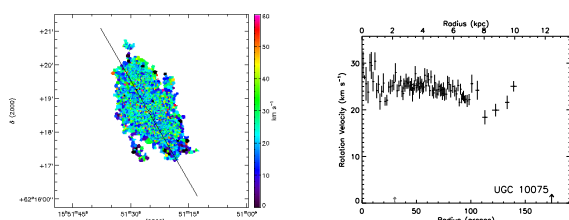
(150) UGC 09943



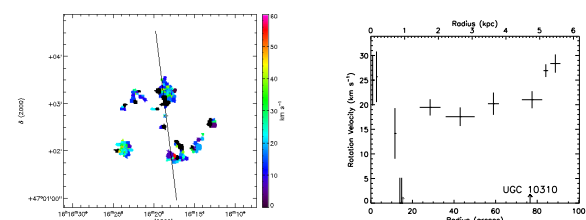
(151) UGC 09969



(152) UGC 09992

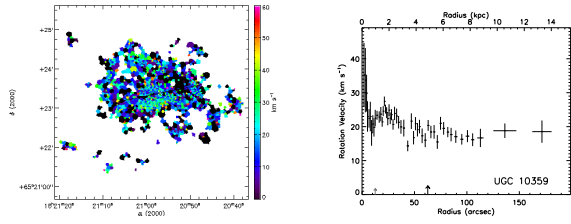


(153) UGC 10075

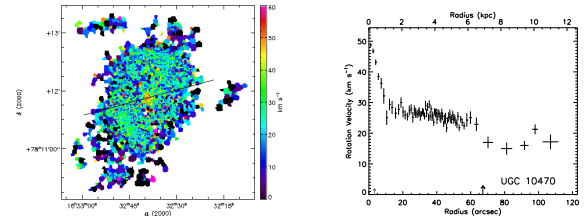


(154) UGC 10310

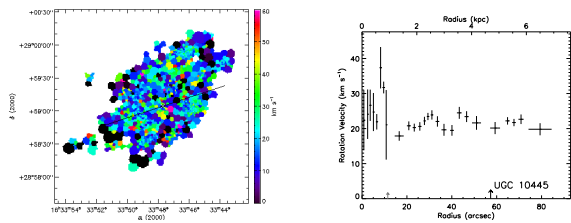
FIG. D.3 : suite



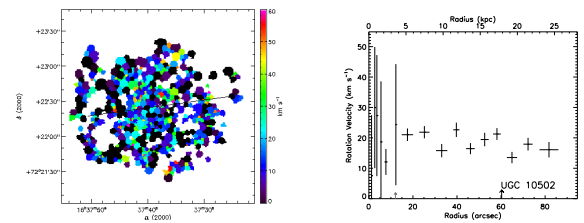
(155) UGC 10359



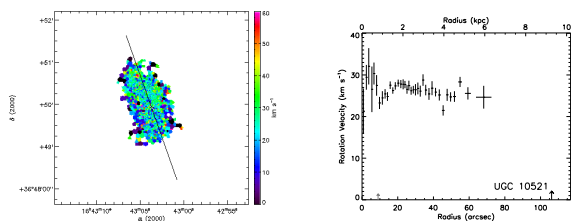
(156) UGC 10470



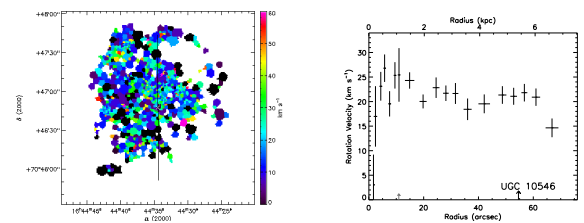
(157) UGC 10445



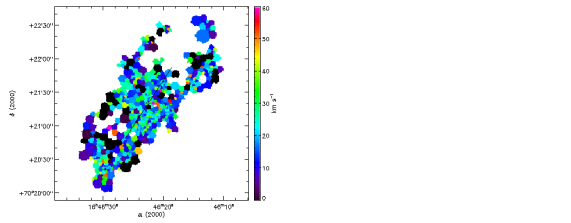
(158) UGC 10502



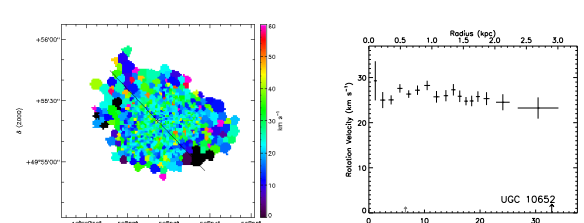
(159) UGC 10521



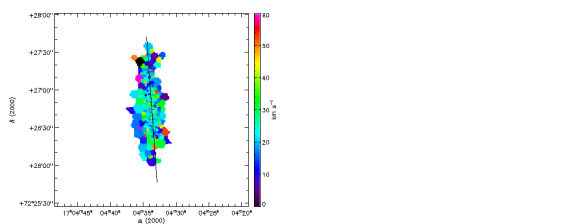
(160) UGC 10546



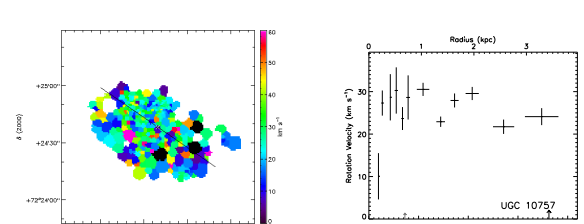
(161) UGC 10564



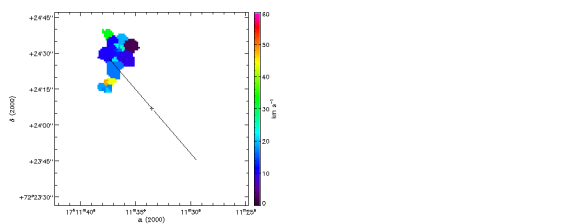
(162) UGC 10652



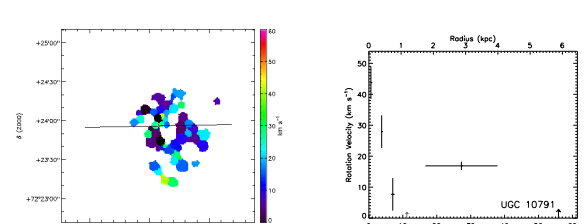
(163) UGC 10713



(164) UGC 10757

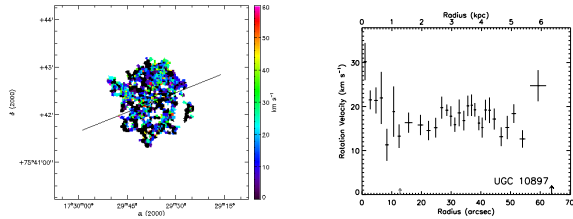


(165) UGC 10769

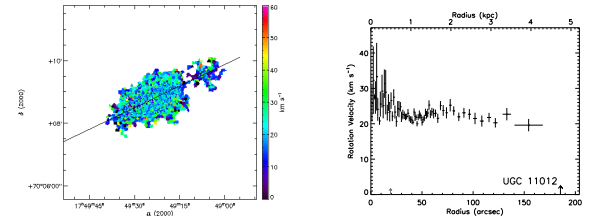


(166) UGC 10791

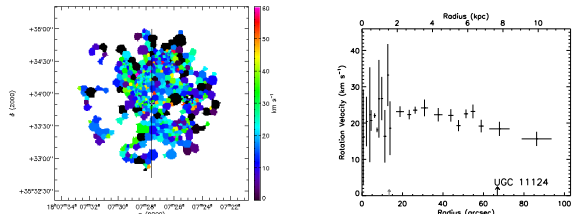
FIG. D.3 : suite



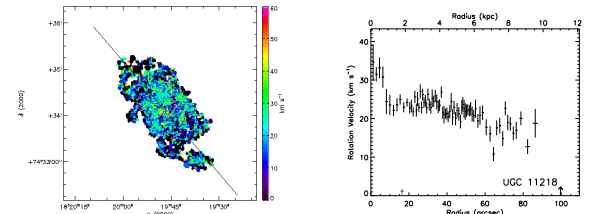
(167) UGC 10897



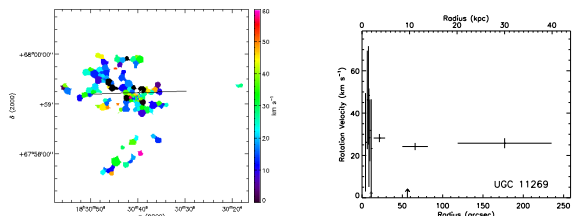
(168) UGC 11012



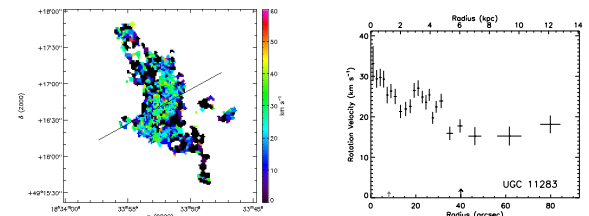
(169) UGC 11124



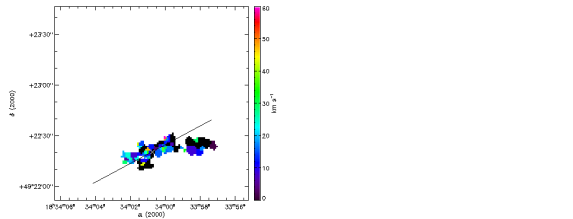
(170) UGC 11218



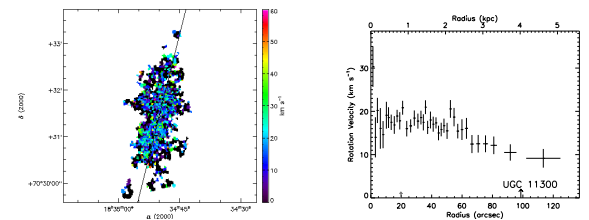
(171) UGC 11269



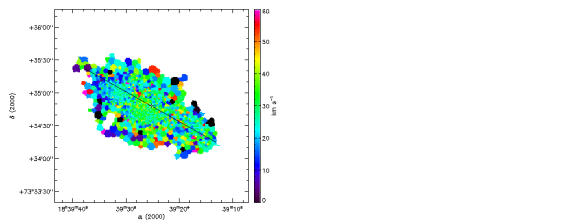
(172) UGC 11283



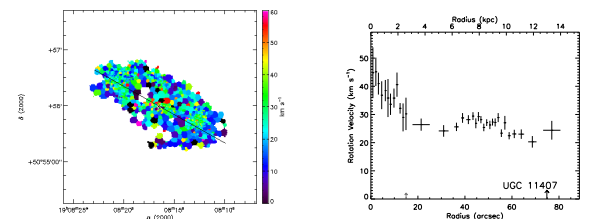
(173) UGC 11283C



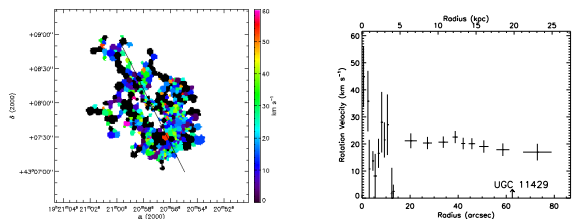
(174) UGC 11300



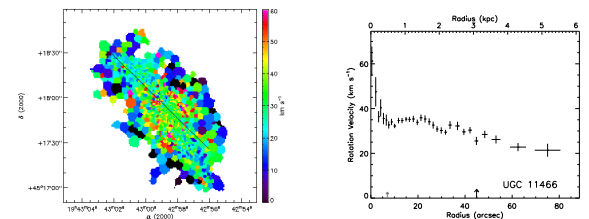
(175) UGC 11332



(176) UGC 11407

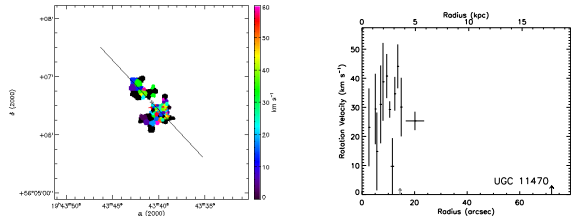


(177) UGC 11429

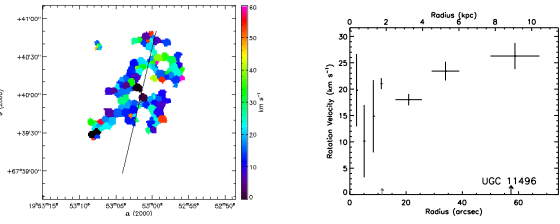


(178) UGC 11466

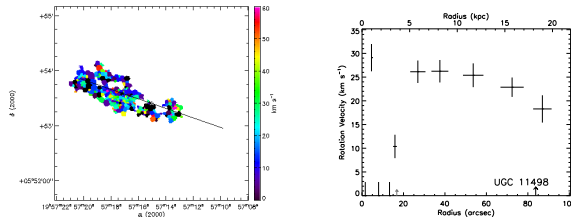
FIG. D.3 : suite



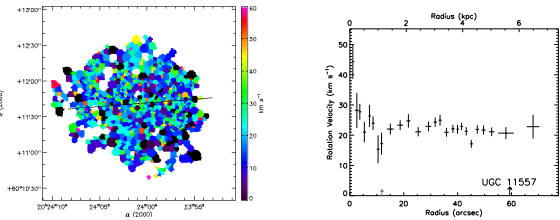
(179) UGC 11470



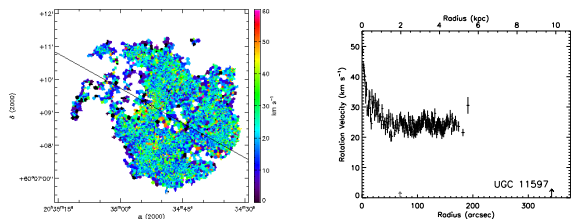
(180) UGC 11496



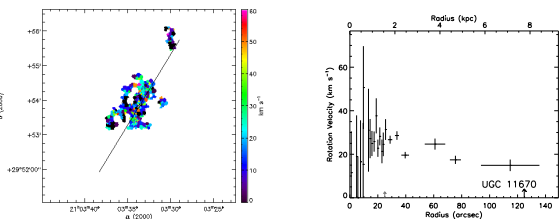
(181) UGC 11498



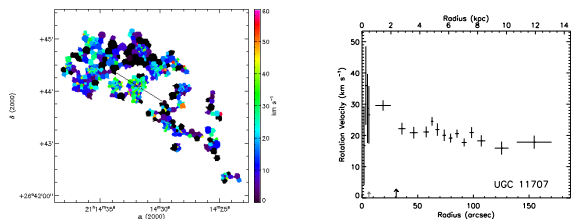
(182) UGC 11557



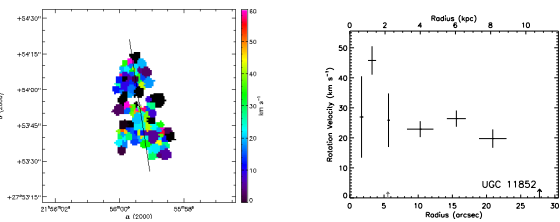
(183) UGC 11597



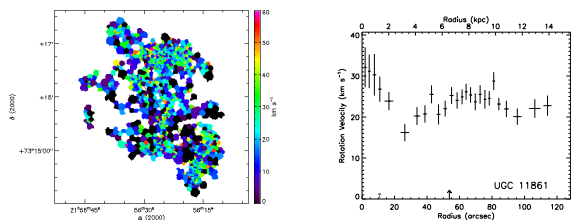
(184) UGC 11670



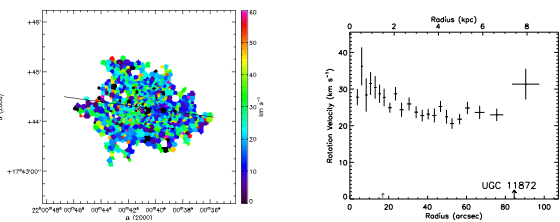
(185) UGC 11707



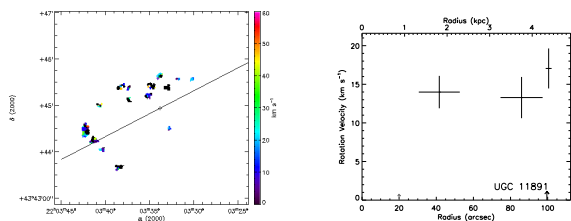
(186) UGC 11852



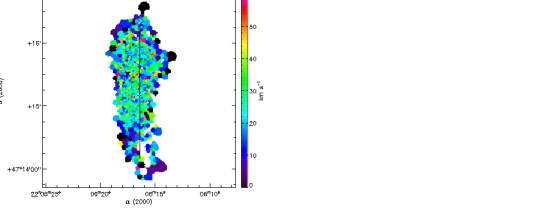
(187) UGC 11861



(188) UGC 11872



(189) UGC 11891



(190) UGC 11909

FIG. D.3 : suite

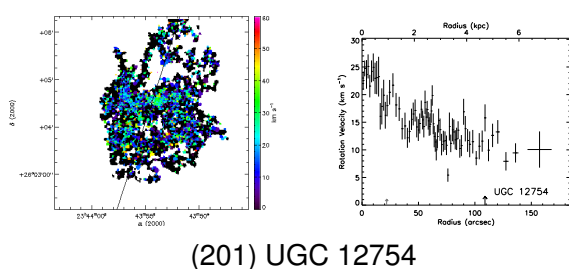
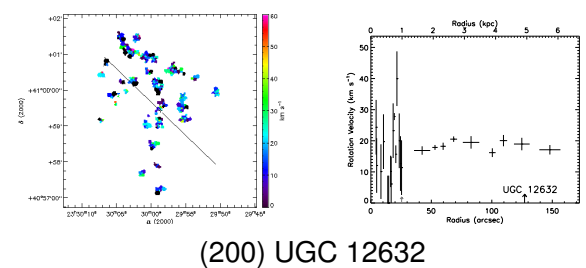
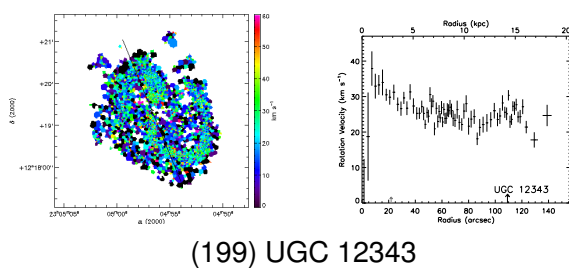
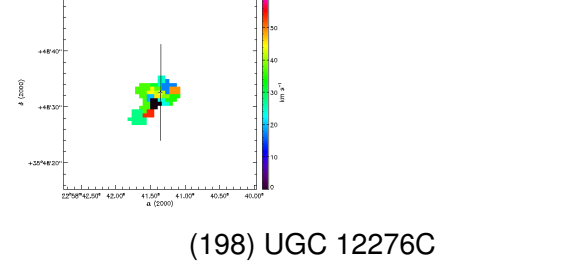
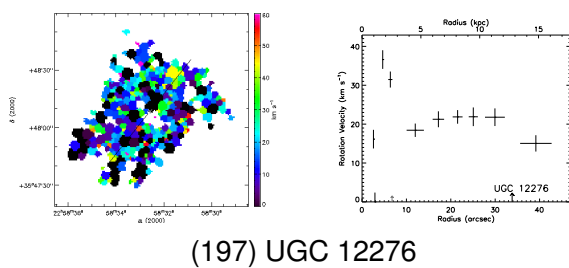
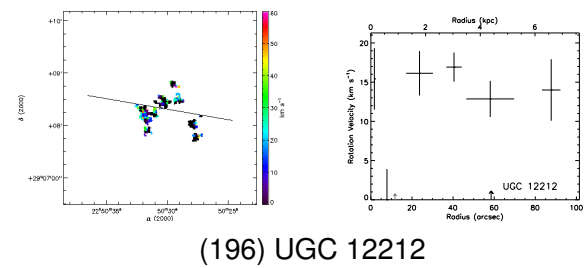
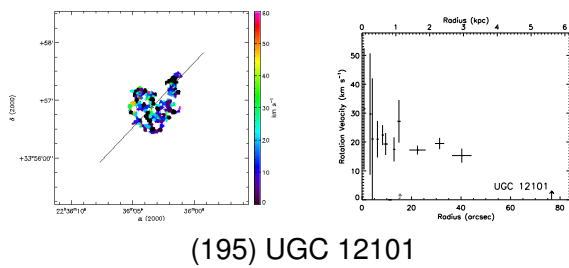
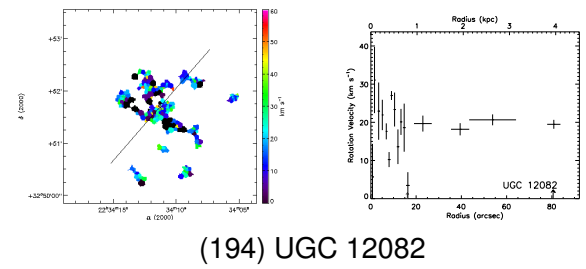
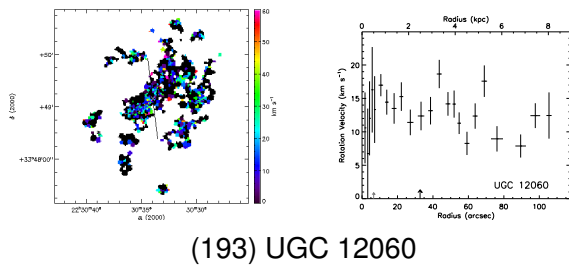
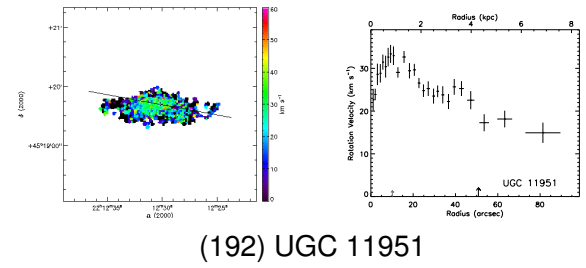
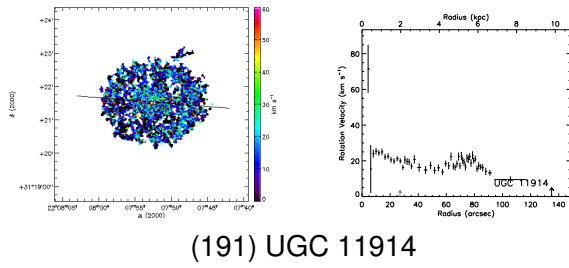


FIG. D.3 : suite

D.4 Base de données Fabry-Perot

J'ai participé à l'élaboration de la base de données Fabry-Perot, une collaboration entre le LAM, le GÉPI et le LAE de Montréal. Cette base de données est disponible à l'adresse <http://FabryPerot.oamp.fr/>. Elle est en cours de construction et sera compatible avec le projet VO. A terme, elle regroupera toutes les données Fabry-Perot obtenues par les instruments présentés dans le chapitre 1 de cette thèse. Elle mettra à disposition de la communauté scientifique les données réduites ainsi que les produits dérivés tels que les courbes de rotation, les diagrammes position-vitesse, les paramètres cinématiques déduits des analyses. Il sera également possible de récupérer les données brutes. Les différents logiciels de réduction des données seront également disponibles. Un outil de sélection de galaxies sur des critères de type morphologique, de magnitude, d'inclinaison, etc., est d'ores et déjà partiellement en place.

Dans un deuxième temps, des outils élaborés seront proposés aux utilisateurs de la base de données. En particulier, un outil de projection des données à un décalage spectral voulu, avec résolutions et échantillonnages spatiaux et spectraux définis par l'utilisateur sera mis en place afin de généraliser les études du type de celle exposée dans la partie 3.4.

Annexe E

Étude des modèles de masse (chapitre 2)

Résumé

E.1 Article VIII : GHASP : an Hα kinematic survey of spiral and irregular galaxies - V. Dark matter distribution in 36 nearby spiral galaxies	377
--	------------

Cette annexe présente un article contenant les premiers résultats concernant l'étude de la distribution de masse des halos de matière sombre à partir des courbes de rotation d'une partie de l'échantillon GHASP. Cette étude s'insère dans les objectifs scientifiques du projet GHASP et est introduite dans la partie 2.3. À terme, l'ensemble de l'échantillon GHASP sera utilisé.

E.1 Article VIII : GHASP : an H α kinematic survey of spiral and irregular galaxies - V. Dark matter distribution in 36 nearby spiral galaxies

L'étude de la distribution de masse à partir de galaxies de l'échantillon GHASP a donné lieu à une publication dans un journal à comité de lecture¹ (Spano et al., 2008). Cet article est présenté ici.

Les résultats d'une étude de la distribution de masse sur 36 galaxies spirales sont présentés. Ces galaxies ont été observées avec un interféromètre de Fabry-Perot dans le cadre du programme GHASP. L'obtention de champs de vitesses 2D de haute résolution en utilisant la raie H α a pour objectif majeur de définir de manière détaillée la partie interne croissante des courbes de rotation, ce qui devrait permettre de mieux contraindre les paramètres de la distribution de masse. Lorsque des données HI (de plus faible résolution spatiale) étaient disponibles dans la littérature, elles ont été combinées aux vitesses H α . En combinant données cinématiques et photométriques, des modèles de masse ont été déterminés à partir de ces courbes de rotation en utilisant deux modèles de halo de matière sombre : une sphère isotherme (ISO) et un profil de Navarro-Frenk-White (NFW). Les résultats obtenus pour les galaxies ayant déjà fait l'objet d'études similaires par d'autres auteurs tendent à être concordants. Nos résultats mettent en évidence l'existence d'une densité de cœur au centre des halos de matière sombre constante plutôt qu'un cœur piqué et ce, quel que soit le type de galaxie de Sab à Im. Cela généralise à tous les types morphologiques le résultat déjà obtenu par d'autres auteurs à

¹Monthly Notices of the Royal Astronomical Society

partir d'études de galaxies naines et de galaxies à faible brillance de surface, même s'il est encore nécessaire d'utiliser un échantillon plus important afin de conclure plus fermement. Quel que soit le modèle utilisé (ISO ou NFW), les halos de faible rayon de cœur possèdent de plus grandes densités centrales, une fois encore indépendamment du type morphologique. Nous confirmons différentes lois d'échelle des halos, comme les corrélations entre le rayon de cœur, la densité centrale des halos et la magnitude absolue des galaxies : les galaxies de faible luminosité ont un petit rayon de cœur et une grande densité centrale. Nous trouvons que le produit de la densité centrale et du rayon de cœur du halo est presque constant quel que soit le modèle et quelle que soit la magnitude absolue de la galaxie. Cela suggère que la densité de surface du halo est indépendante du type morphologique de la galaxie.

GHASP: an H α kinematic survey of spiral and irregular galaxies – V. Dark matter distribution in 36 nearby spiral galaxies

M. Spano,^{1*} M. Marcelin,¹ P. Amram,¹ C. Carignan,² B. Epinat¹ and O. Hernandez^{2*}†

¹Laboratoire d'Astrophysique de Marseille, OAMP, 2 Place Le Verrier, 13248 Marseille Cedex 04, France

²Laboratoire d'Astrophysique Expérimentale, Université de Montréal, CP 6218, Succ. Centre-ville, Montréal, QC, Canada H3C 3J7

Accepted 2007 October 3. Received 2007 September 26; in original form 2007 May 4

ABSTRACT

The results obtained from a study of the mass distribution of 36 spiral galaxies are presented. The galaxies were observed using Fabry–Perot interferometry as part of the GHASP survey. The main aim of obtaining high-resolution H α 2D velocity fields is to define more accurately the rising part of the rotation curves which should allow to better constrain the parameters of the mass distribution. The H α velocities were combined with low resolution H I data from the literature, when available. Combining the kinematical data with photometric data, mass models were derived from these rotation curves using two different functional forms for the halo: an isothermal sphere (ISO) and a Navarro–Frenk–White (NFW) profile. For the galaxies already modelled by other authors, the results tend to agree. Our results point at the existence of a constant density core in the centre of the dark matter haloes rather than a cuspy core, whatever the type of the galaxy from Sab to Im. This extends to all types the result already obtained by other authors studying dwarf and low surface brightness galaxies but would necessitate a larger sample of galaxies to conclude more strongly. Whatever model is used (ISO or NFW), small core radius haloes have higher central densities, again for all morphological types. We confirm different halo scaling laws, such as the correlations between the core radius and the central density of the halo with the absolute magnitude of a galaxy: low-luminosity galaxies have small core radius and high central density. We find that the product of the central density with the core radius of the dark matter halo is nearly constant, whatever the model and whatever the absolute magnitude of the galaxy. This suggests that the halo surface density is independent from the galaxy type.

Key words: galaxies: dwarf – galaxies: haloes – galaxies: irregular – galaxies: kinematics and dynamics – galaxies: spiral – dark matter.

1 INTRODUCTION

Rotation curves are a fundamental tool for studying the dynamics and mass distribution in galaxies. The distribution of the total mass can then be compared with the distribution of visible light, assuming a certain mass-to-light ratio (M/L). Observations have clearly established that dark matter (DM) is needed for explaining the rotation velocities observed in the outer parts of spirals. The DM is most often considered as being distributed in a spherical dark halo but its density profile, especially at small radii, is still a matter of debate (Blais-Ouellette, Amram & Carignan 2001; de Blok & Bosma 2002; Swaters et al. 2003; Navarro 2004; Graham et al. 2006; Kuzio de Naray et al. 2006; Hayashi, Navarro & Springel 2007).

However, mass models of spiral and dwarf galaxies have well-known degeneracies (Barnes, Sellwood & Kosowsky 2004) that prevent a unique mass decomposition, the most important being the unknown value of the stellar M/L (Dutton et al. 2005). Unfortunately, stellar population models (e.g. de Jong & Bell 2006) still cannot predict accurately the (M/L) values of the stellar discs based on their colours. The main problem comes from the fact that the normalization of this relation (colour versus M/L) depends critically on the shape of the stellar initial mass function at the low-mass end. It is well known that the faint stars contribute significantly to the mass but not to the luminosity and colour of the stellar discs. This means that it will prove difficult to tighten this relation and lessen the effect of the disc–halo degeneracy.

Cosmological numerical simulations favour cuspy dark haloes, although the value of the inner slope γ of the radial density profile, where $\rho \propto r^\gamma$ (see equation 6 of Section 4) depends on the authors, with $\gamma = -1.5$ for Moore et al. (1999) as well as Fukushige &

*E-mail: Maxime.Spano@obs.unige.ch

†Based on observations collected at the observatoire de Haute Provence.

Makino (2001) or -1.0 for Navarro, Frenk & White (1997) (hereafter NFW). Recent simulations (Graham et al. 2006) have extrapolated inner logarithmic profile slope ranging from -0.2 to -1.5 , with a typical value at 0.1 kpc around -0.7 .

Most observers conclude, however, that γ is closer to 0.0 than to -1.0 and that mass models give better results with an isothermal (or pseudo-isothermal) sphere halo rather than an NFW profile (e.g. Blais-Ouellette, Amram & Carignan 2001; de Blok & Bosma 2002; de Blok, Bosma & McGaugh 2003; Swaters et al. 2003; de Blok 2005; Kassin, de Jong & Pogge 2006a). Most of these observations are based on the rotation curves of dwarf and low surface brightness (LSB) galaxies (Kuzio de Naray et al. 2006). It is still unclear if this is true also for high surface brightness (HSB) systems and for all morphological types.

One problem in this cusp–core debate is that numerical simulations mainly predict the halo density profile shape at the time of formation while galaxies are observed after many Gyr of evolution. The problem is that internal dynamics and interaction between the dark halo and the luminous disc (e.g. adiabatic contraction: Dutton et al. 2005) and interaction with the environment (Maccio et al. 2007) may have altered the shape of the halo density profile.

Moreover, the shape of the gravitational potential in cold dark matter (CDM) haloes may explain the core-like halo density profiles seen in LSB systems. Hayashi et al. (2007) suggest that galactic discs may be forming in elliptical gravitational potential. This could result in significant non-circular motions in systems such as LSBs which would mimic constant density cores. Thus, taking into account the 3D shape of the dark mass distribution could reconcile the constant density cores observed in LSBs with the predicted cuspy mass profiles of CDM haloes.

Finally, it is unclear if CDM simulations, mainly obtained to compare with the large scale structure, have sufficient resolution to reliably probe the kpc scales necessary to compare with the observationally derived DM halo density profiles on the scale of a few halo core radii. As discussed by Navarro (2004), unfortunately rotation curves constraints are strongest where numerical simulations are the least reliable. In fact, rotation curves are usually compared with extrapolations of the simulation data that rely heavily on the applicability and accuracy of fitting formulae such as the NFW profile to regions that may be compromised by numerical artefact. This is especially true for LSB and dwarf galaxies (for instance Dutton et al. 2005).

Blais-Ouellette et al. (1999) and Barnes et al. (2004) have shown the necessity of optical integral field spectroscopy to accurately determine the rotation curves in the inner parts of spiral and dwarf galaxies, for which the H I data are affected by beam smearing (Swaters, Madore & Trewhella 2000; van den Bosch et al. 2000). While the use of two-dimensional data does not necessarily alter the halo parameters derived from optical long-slit data, it, however, decreases the uncertainties by roughly a factor of 2 (Kuzio de Naray et al. 2006). Blais-Ouellette et al. (2001) and Blais-Ouellette et al. (2004) also pointed out the great sensitivity of the mass distribution parameters to the inner rotation curve. The ideal rotation curve will therefore combine high-resolution optical data, for the inner part, with radio data, for the outer part extending well beyond the luminous disc.

2 THE SAMPLE

The sample of 36 galaxies studied in this paper is composed of nearby galaxies observed for the GHASP survey. These 36 galaxies are simply the GHASP galaxies already reduced (113 out of a total

of ~ 200 observed galaxies) for which there is photometry available in the literature and for which we could draw an acceptable rotation curve at H α wavelength. Half of them has been already published and another half has been reduced recently and only available on the GHASP website. For 19 of them, the velocity fields and rotation curves have been published in Garrido et al. (2002, 2003, 2004) and Garrido et al. (2005); 17 other galaxies (observed in 2004) have been reduced recently and the data will be published later (Epinat et al., in preparation). However, their monochromatic images, velocity fields and rotation curves are already available on the GHASP website: <http://www.oamp.fr/interferometrie/GHASP/ghasp.html>.

Eight other galaxies from the same observing run (2004) are also presented on the GHASP website but they are not analysed here, because no photometry is available (UGC 4770, 5319, 5373 and IC 2542) or because of problems with the rotation curve (UGC 4393, 6277, 8863 and 9358), as explained in the next paragraph.

The GHASP survey provides high-resolution velocity fields of nearby galaxies at the H α wavelength. For the analysis done in this paper, we selected the galaxies for which photometric data were available in the literature. We then excluded all the galaxies with strong differences between the red and the blue side of the rotation curve or displaying high velocity dispersions hence difficult to fit properly with mass models. These galaxies are: UGC 4278 (seen edge-on), UGC 4305 (strong velocity dispersion and counter rotation in the centre), UGC 4393 (anomalous rotation curve with counter rotation in the centre), UGC 5414 (strong dispersion and asymmetry of the velocities between receding and approaching sides), UGC 6277 (rotation curve abnormally flat in the central part), UGC 7971 (strong dispersion and asymmetry of the velocities between receding and approaching side), UGC 8863 (not enough H α emission to get a correct rotation curve) and UGC 9358 (very strong asymmetry: plateau immediately reached for the approaching side and solid body rotation for the receding side).

In Table 1, the morphological type is completed by an additional mention: LSB for low surface brightness galaxies and dS for dwarf spirals. We have adopted the same criterion as Pizzella et al. (2005), considering that LSB have a disc with a central face-on surface brightness $\mu_B \geq 22.6$ mag arcsec $^{-2}$. The criteria for dwarf spirals are those defined by Schombert et al. (1995). We thus find that nine galaxies of our sample are LSB and five are dwarf spirals, UGC 2034 and 5272 being both. All of them are late-type galaxies: two Scd, two Sdm, one Sm and four Im for the nine LSB galaxies, one Sd, one Sm and three Im for the five dS.

Since there are only nine LSB and five dS in our sample, it is not possible, however, to make any significant study for these classes. Our whole sample is in fact not big enough to reach strong conclusions and most results presented here are trends to be confirmed.

When H I data were available (which is the case for more than half of the selected sample) we derived a hybrid rotation curve, by combining our optical data with the H I data from the literature. Table 1 gives the origin of the H I data (when available) and of the photometry data used to derive our mass models. The morphological types are also given in that table, together with the main parameters adopted for the galaxies analysed in this paper (distance, radius at 25 B mag arcsec $^{-2}$, axial ratio and Galactic absorption).

The distances for each galaxy are also given together with the corresponding references in the literature. Some of these distances are based on local indicators such as the brightest supergiants, cepheids, red giant branch position or group membership but most of them are based on the Hubble law, assuming $H_0 = 75$ km s $^{-1}$ Mpc $^{-1}$ and taking into account the Virgo infall. When no precise value

Table 1. Data used for the analysis of our sample.

N° UGC (1)	N° NGC (2)	Type (3)	Distance Mpc (4)	M_B (5)	$D_{25/2}$ arcmin (6)	b/a (7)	i $^{\circ}$ (8)	$A_G(R)$ (9)	Σ_{HI} (10)	H I RC (11)	Photometry/band (12)	h kpc (13)	Rlast kpc (14)
2034		Im/LSB/dS	10.1 (Sw02)	-16.41	1.3	0.79	19	0.15	Sw02a	Sw99	Sw02b/R	1.26 \pm 0.02	5.9
2455	1156	IB(s)m	7.8 (Sw02)	-18.05	1.7	0.68	51	0.60	Sw02a	Sw99	Sw02b/R	0.87 \pm 0.07	4.5
2503	1169	SABb	34.4 (Koo06)	-21.82	2.1	0.74	53	0.58		vD94	vD94/R	5.14 \pm 0.01	38
3876		SA(s)d	14.5 (Jam04)	-17.65	1.1	0.58	59	0.12			Cou96/R	1.37 \pm 0.02	5.1
4256	2532	SAB(rs)c	71.7	-21.65	1.1	0.83	38	0.14			Dej94/R	5.15 \pm 0.01	18
4274	2537	SB(s)m	6.9 (Kar04)	-17.17	0.9	0.85	40	0.14	Sw02a	S02	Sw02b/R	0.68 \pm 0.17	4.0
4325	2552	SA(s)m	10.1 (Sw02)	-17.76	1.7	0.66	41	0.12	Sw02a	Sw99	Sw02b/R	1.73 \pm 0.01	7.1
4456		SA(rs)c	74.0	-20.93	0.9	0.89	27	0.10			OHP120/R	4.71 \pm 0.01	29
4499		SABdm	13.0	-17.36	1.3	0.74	50	0.09	Sw02a	Sw99	Sw02b/R	1.40 \pm 0.02	8.5
4555	2649	SAB(rs)bc	58.0	-20.91	0.8	0.95	35	0.09			OHP120/R	4.25 \pm 0.01	17
5175	2977	Sb	44.1	-20.62	0.9	0.44	62	0.08			OHP120/R	2.36 \pm 0.01	9.6
5272		Im/LSB/dS	7.1 (Kar04)	-15.27	1.0	0.38	59	0.06	Sw02a	Sw99	Sw02b/R	0.89 \pm 0.12	2.2
5279	3026	Im/LSB	21.2	-18.53	1.3	0.30	78	0.06			OHP120/R	2.44 \pm 0.01	8.8
5721	3274	SABd/dS	6.5 (Kar04)	-16.38	1.1	0.48	61	0.06	Sw02a	Sw99	Sw02b/R	0.43 \pm 0.22	7.1
5789	3319	SB(rs)cd/LSB	14.1 (Saha06)	-19.62	3.1	0.55	65	0.04	Mo98	Mo98	Kas06/R	6.19 \pm 0.01	24
5842	3346	SB(rs)cd	15.2 (Sha01)	-18.67	1.4	0.87	47	0.07			Dej94/R	1.75 \pm 0.02	5.8
6537	3726	SAB(r)c	14.3	-20.11	3.1	0.69	50	0.04	Ver01	Ver01	Kas06/R	3.07 \pm 0.01	26
6778	3893	SAB(rs)c	15.5 (Shap01)	-20.27	0.5	0.62	49	0.06	Ver01	Ver01	Kas06/R	2.06 \pm 0.04	17
7045	4062	SA(s)c	11.4 (Mou06)	-19.00	2.0	0.43	69	0.07	Bro94		Kas06/R	1.89 \pm 0.01	7.6
7323	4242	SAB(s)dm	8.1 (Sw02)	-18.24	2.5	0.76	50	0.03	Sw02a	Sw99	Sw02b/R	2.04 \pm 0.01	5.9
7524	4395	SAB(s)m/LSB	4.6 (Kar04)	-17.74	6.6	0.83	46	0.05	Sw02a	Sw99	Sw02b/R	3.00 \pm 0.01	10
7699		SBcd/LSB	9.3	-17.51	1.9	0.27	78	0.03	Bro94		Jan00/R	0.67 \pm 0.16	6.3
7876	4635	SAB(s)d	12.8	-17.68	1.0	0.70	44	0.07			Dej94/R	1.17 \pm 0.04	3.0
7901	4651	SA(rs)c	20.6 (Sha01)	-20.53	2.0	0.66	53	0.07	War88		Dej94/R	2.69 \pm 0.01	15
8490	5204	SA(s)m/dS	4.7 (Kar04)	-16.88	2.5	0.60	50	0.03	Sw02a	Sw99	Sw02b/R	0.67 \pm 0.07	10
9179	5585	SAB(s)d	5.7 (Kar04)	-17.73	2.9	0.65	54	0.04	Cot91	Cot91	Cot91/R	1.07 \pm 0.05	8.8
9219	5608	Im/dS	10.2 (Jam04)	-16.35	1.3	0.51	59	0.03			Jan00/R	0.69 \pm 0.23	3.7
9248	5622	Sb	54.9	-20.11	0.9	0.58	55	0.06			Cou96/R	2.79 \pm 0.01	11
9465	5727	SABdm/LSB	26.4 (Jam04)	-18.25	1.1	0.52	73	0.04			Her96/I	2.29 \pm 0.01	12
9866	5949	SA(r)bc	7.4 (Jam04)	-17.07	1.1	0.47	57	0.06			Cou96/R	0.54 \pm 0.27	1.6
10075	6015	SA(s)cd	14.7 (Jam04)	-19.78	2.7	0.40	65	0.03			Her96/I	2.49 \pm 0.01	12
10310		SB(s)m	12.7 (Jam04)	-17.00	1.4	0.79	34	0.03	Sw02a	Sw99	VZ00/B	1.50 \pm 0.03	7.4
11557		SAB(s)dm	19.7 (Jam04)	-19.12	1.1	0.80	30	0.63	Sw02a	Sw99	Sw02b/R	1.70 \pm 0.02	8.6
11707		SAdm/LSB	15.9 (Sw02)	-17.54	1.8	0.52	55	0.44	Sw02a	Sw99	Sw02b/R	3.04 \pm 0.01	15
11914	7217	SA(r)ab	15.0 (Koo06)	-20.35	1.9	0.83	28	0.24	VM95	VM95	VM95/R	1.76 \pm 0.20	9.1
12060		IBm/LSB	15.7 (Sw02)	-16.60	0.8	0.65	40	0.24	Sw02a	Sw99	Sw02b/R	1.58 \pm 0.01	12

Column (1): name of the galaxy in the UGC catalogue. Column (2): name in the NGC catalogue when available. Column (3): morphological type from the RC3 catalogue, completed by a mention LSB and dS as explained in Section 2 of the text. Column (4): distance and source. When no reference is given, the distance has been computed as explained in Section 2 of the text. *References:* Jam04 = James et al. (2004); Kar04 = Karachentsev et al. (2004); Koo06 = Koopmann, Haynes & Catinella (2006); Mou06 = Moustakas & Kennicutt (2006); Saha06 = Saha et al. (2006); Sha01 = Shapley, Fabbiano & Eskridge (2001); Sw02 = Swaters & Balcells (2002). Column (5): Absolute B magnitude computed from the corrected apparent B magnitude B_T from the RC3 using the distance of column 4. Column (6): radius at 25 B mag/arcsec² from the RC3. Column (7): axial ratio at 25 B mag/arcsec² from the RC3. Column (8): inclination adopted for deriving the rotation curve. Column (9): Galactic absorption in the R band, computed as explained in Section 2 of the text. Column (10): source of total H I distribution. *References.* Bro94 = Broeils & van Woerden (1994); Cot91 = Coté, Carignan & Sancisi (1991); Mo98 = Moore & Gottesman (1998); Sw02a = Swaters & Balcells (2002); Ver01 = Verheijen & Sancisi (2001); VM95 = Verdes-Montenegro, Bosma & Athanassoula (1995); War88 = Warmels (1988). Column (11): source of H I rotation curve. *References.* Cot91 = Coté et al. (1991); Mo98 = Moore & Gottesman (1998); S02 = Stil & Israel (2002); Sw99 = Swaters (1999); vD94 = van Driel & van Woerden (1994); Ver01 = Verheijen & Sancisi (2001). Column (12): source of photometry and corresponding band. *References.* Cot91 = Coté et al. (1991); Cou96 = Courteau (1996); Dej94 = de Jong & Vander Kruit (1994); Her96 = Héraudeau & Simien (1996); Jan00 = Jansen et al. (2000); Kas06 = Kassim et al. (2006b); OHP120 = Observed by Spano with 1.20-m OHP in 2006 March; Sw02b = Swaters et al. (2002); vD94 = van Driel & van Woerden (1994); VZ00 = van den Bosch et al. (2000). Column (13): disc scalelength, in kpc, derived from the photometric profile of column 12, with distance of column 4. Column (14): radius of the last point, in kpc, of the rotation curve.

of distance was found in the literature, we simply divided by $H_0 = 75 \text{ km s}^{-1} \text{ Mpc}^{-1}$, using the velocity correction for infall of the Local Group towards Virgo (vvir) given in the HyperLeda database.

The Galactic absorption in the R band has been determined from that in the B band given in the HyperLeda database, assuming $A(R)/A(B) = 0.62$ [from the values of $A(R)/A(V)$ and $A(B)/A(V)$ given in table 6 of Schlegel, Finkbeiner & Davis 1998, evaluated using the $R_V = 3.1$ extinction laws of Cardelli, Clayton & Mathis

1989 and O'Donnell 1994]. The value of $A(R)/A(B) = 0.62$ has been confirmed by Choloniewski & Valentijn (2003) using a new method for the determination of the extinction in our Galaxy, based on the observation of surface brightnesses of external galaxies in the B and R bands. Only four galaxies of our sample are affected by a relatively strong Galactic absorption in the R band [between 0.4 and 0.6 (see column 8 of Table1)] which should not affect our conclusions.

3 THE DATA SET

3.1 The hybrid rotation curve

The hybrid rotation curve was obtained with the following method.

In the central part of the galaxy, we preferred the $H\alpha$ curve because of its higher spatial resolution. The curve was extended in the outer parts with the $H\text{I}$ data when available.

The rotation curves given in Figs A1–A9, in the appendix, show the hybrid rotation curve used for the fit of the models, with full dots for the $H\alpha$ velocities and open circles for the $H\text{I}$ velocities. The $H\text{I}$ data in the inner parts are displayed as crosses, for comparison with our $H\alpha$ data, but they are not used when fitting the models.

The $H\alpha$ rotation curves of the GHASP survey are derived from the 2D velocity fields obtained from the scan of the $H\alpha$ line with a Fabry–Perot. Each velocity field is composed of a lot of individual radial velocity points (hereafter mentioned as velocity pixels) since a velocity is computed for each pixel as soon as the signal to noise ratio is sufficient. The error bars of our rotation curves were computed up to now, for every point of the curve, from the velocity dispersion found among the velocity pixels contributing to that very point. Each galaxy being considered as a rotating disc, the velocity pixels contributing to a given point of the rotation curve are found to be lying within an elliptical ring in the sky. However, we do not take into account the points too close from the minor axis (otherwise the dispersion increases rapidly because the non circular motions are then amplified when converting radial velocities into rotational velocities). Also, when computing the final rotation curve, both approaching and receding sides are averaged.

The velocity points of the rotation curve resulting from the average of a large number of velocity pixels are much more accurate and reliable than those obtained from a limited number of pixels. That is why we weight the original dispersion by the number of velocity pixels contributing to a given point of the rotation curve. To do that, we simply divide the original error bar by the square root of this number.

Whenever a rotation velocity point is computed from a too small number of velocity pixels we simply attribute to this point the average error bar found for the other points of the rotation curve.

The inclination adopted for deriving the rotation curves from the radial velocities (given in Table 1) are generally close from the values found in the literature and deduced from the photometric axial ratio (also given in Table 1). However, in some cases we found a significantly smaller dispersion of the rotation velocities when adopting a different inclination. Note also that the inclination has been changed for two GHASP galaxies previously published in Garrido et al. (2005): for UGC 11557 it is now 30° instead of 37° and for UGC 11914 it is now 28° instead of 35° . The highest rotation velocity dispersions are found for the smallest inclinations since the original radial velocities are then divided by the sine of the inclination, leading to large error bars on the rotation curves of almost face-on galaxies. This effect remains marginal for inclinations between 40° and 30° (five galaxies of our sample are concerned) but becomes noticeable for inclinations smaller than 30° because it more than doubles any velocity fluctuation. Only three galaxies of our sample have such small inclinations: UGC 11914 at 28° , UGC 4456 at 27° and, the closest to face-on, UGC 2034 at 19° . Note that it is one of the three irregular galaxies excluded from the fits in Figs 2–5 because of chaotic behaviour and large error bars of the rotation curve.

Most of the galaxies of our sample are rather nearby. However, 6 of them have distances larger than 30 Mpc. They are of Sb, Sbc

or Sc type and large enough on the sky so that there is no problem of sampling or spatial resolution for deriving their rotation curve. Indeed these six galaxies exhibit well-behaved rotation curves with rather small error bars.

We defined a ‘quality parameter’ for each rotation curve, going from 1 (for best quality curves) to 4 (for very low quality curves). This parameter was estimated from characteristics such as asymmetry, velocity dispersion, bar, etc. Surprisingly, no significant difference was found on our plots between low and high quality points (indeed the dispersion was about the same, whatever the quality parameter) and we finally decided not to use this parameter for the plots. Nevertheless, it is worth being mentioned that 12 galaxies of our sample have good-quality rotation curve (hereafter RC) (class 1): UGC 3876, 4499, 5175, 5721, 6778, 7323, 7524, 8490, 9866, 11557, 11707, 11914; 11 galaxies have acceptable-quality RC (class 2): UGC 4256, 4456, 4555, 5279, 7876, 9179, 9219, 9248, 9465, 10075, 12060; nine galaxies have low-quality RC (class 3): UGC 2034, 2455, 2503, 4325, 5272, 5842, 7045, 7901, 10310; four galaxies have very low quality RC (class 4): UGC 4274, 5789, 6537, 7699.

3.2 The luminosity profile

We used the photometric data in the R band from the literature in order to derive the distribution of stellar mass. Additionally, four galaxies were observed in 2006 March, with the 1.20-m telescope at OHP, in order to get their luminosity profile in the R band (see Table 1 for details). For UGC 9465 and UGC 10075, only the I band was available in the literature and we used the colour indices to derive the R band. For this purpose we used the effective colour indices $V - I$ and $I - R$ given by Prugniel & Héroudeau (1998) as a function of the morphological type of galaxies. Same thing for UGC 10310 for which only the B band was found in the literature, we derived the R band now using $B - V$ and $V - R$ from Prugniel & Héroudeau (1998). An exponential was then fitted to the outer parts of the photometric profile and subtracted in order to check for the presence of a central bulge. Whenever a bulge was seen on the residual luminosity profile we decomposed the profile into two components. However, some of these residuals were found to be a mere nucleus and not kept into account. Also, we assumed that galaxies later than Scd type had no bulge and discarded any central component for these galaxies. As a result, only four galaxies of our sample were decomposed into bulge and disc components (see Table 2). Best-fitting models for extracting the disc and bulge components were carried out by minimizing the χ^2 using the MINUIT package, with the SIMPLEX and MILGRAD routines from Fletcher (1970).

The bulge component has been extracted from the observed luminosity profile in the central part of the galaxy, after extrapolating the exponential profile of the underlying disc by an exponential law:

$$\mu_{\text{disc}}(r) = \mu_o + 1.0857 \left(\frac{r}{h} \right) \quad (1)$$

where μ_o is the central surface brightness of the disc and h the disc scalelength.

The remaining luminosity profile has been fitted by a de Vaucouleurs law:

$$\mu_{\text{bulge}}(r) = \mu_c + 8.3268 \left[\left(\frac{r}{r_c} \right)^{1/4} + \left(\frac{r}{r_t} \right)^4 \right], \quad (2)$$

where μ_c is the central surface brightness of the bulge and r_c the bulge scalefactor. r_t is the truncation radius (limit beyond which the bulge is no more detected, taken here as the radius where the luminosity of the bulge reaches the magnitude 30 arcsec²).

Table 2. Results of the best fits of rotation curves with ISO and NFW models of halo profiles

N°	N°	M/L	M/L	R_o	ρ_o	χ^2	M/L	M/L	R_o	ρ_o	χ^2	Best	Class
UGC	NGC	Disc	Bulge	kpc	$10^{-3} M_{\odot} \text{pc}^{-3}$		Disc	Bulge	kpc	$10^{-3} M_{\odot} \text{pc}^{-3}$		model	
(1)	(2)	(3)	(4)	(5)	(6)	(7)	NFW	NFW	NFW	NFW	(12)	(13)	(14)
2034		1.9		184	1	0.97	0.83		10	1	0.90	Both	4
2455	1156	0.10		30	5	1.24	0.10		5.8	1	2.33	ISO	3
2503	1169	6.8	1.5	188	1	1.27	6.0	0.73	57	1	1.91	Both	2
3876		7.9		100	23	0.60	0.19		33	5	0.47	Both	4
4256		0.27		3.4	49	0.60	0.10		6.8	19	0.74	Both	1
4274		0.42		1.0	253	2.34	0.43		2.3	60	1.73	NFW	0
4325	2552	2.6		1.9	121	2.50	9.00		2.7	1	2.90	Both	4
4456		1.0		15	1	1.54	0.20		14	2	1.48	Both	1
4499		1.7		2.2	43	0.90	0.15		4.3	19	0.76	Both	4
4555	2649	8.1		100	5	5.23	0.21		20	14	3.07	NFW	4
5175	2977	5.3		2.0	200	2.16	6.4		3.8	54	4.52	ISO	2
5272		2.6		25	14	1.10	0.21		25	1	1.44	Both	4
5279	3026	0.10		3.2	95	1.23	0.85		35	3	2.78	ISO	0
5721	3274	0.10		1.0	408	1.58	0.10		2.6	84	3.57	ISO	0
5789	3319	0.10		7.4	11	3.20	0.10		35	1	5.04	ISO	0
5842	3346	0.10		1.7	251	1.58	0.23		5.0	43	2.52	ISO	0
6537	3726	0.21		4.7	8.0	7.04	0.10		16	12	15.57	ISO	1
6778	3893	0.10	2.2	2.8	282	2.04	0.25	0.47	5.8	95	2.59	ISO	1
7045	4062	5.4		12	10	2.77	0.74		5.2	75	1.90	NFW	4
7323	4242	1.5		7.7	12	1.99	0.10		20	3	2.58	ISO	4
7524	4395	0.77		3.4	24	1.10	0.40		19	2	1.70	Both	1
7699		0.10		2.7	29	0.69	0.10		15	2	1.82	ISO	0
7876	4635	0.45		1.6	239	0.87	0.10		9.3	18	2.41	ISO	0
7901	4651	0.84	2.5	5.8	48	4.47	0.10	1.2	4.0	179	4.01	Both	1
8490	5204	1.1		1.9	95	0.62	0.16		4.5	26	2.09	ISO	1
9179	5585	0.31		2.8	69	3.41	0.10		16	5	9.51	ISO	1
9219	5608	0.10		1.8	40	2.88	0.10		5.0	6	6.86	ISO	0
9248	5622	4.1		1.7	75	5.13	4.9		1.0	10	5.18	Both	2
9465	5727	3.6		13	10	1.32	0.10		61	1	1.63	ISO	4
9866	5949	3.5		1.0	426	1.01	4.1		12	10	1.41	ISO	2
10075	6015	5.6		2.8	182	2.96	11		11	16	2.82	Both	1
10310		2.1		4.8	10	1.71	0.74		14	3	1.72	Both	4
11557		0.22		5.0	18	1.53	0.10		37	1	2.16	ISO	1
11707		0.10		2.4	84	2.59	0.25		6.1	19	3.81	ISO	0
11914	7217	4.2	6.2	13	63	2.12	2.7	5.9	16	32	2.78	Both	3
12060		0.76		4.6	26	2.74	0.10		14	5	3.15	Both	0

Column (1): name of the galaxy in the UGC catalogue. Column (2): name in the NGC catalogue when available. Column (3): M/L of the disc in the R band for the ISO model. Column (4): M/L of the bulge in the R band for the ISO model. Column (5): core radius of the DM halo for the ISO model. Column (6): central density of the DM halo for the ISO model. Column (7): χ^2 for the ISO model. Columns (8)–(12): same as columns (3)–(7) but now with the NFW profile for the DM halo model. Column (13): best model: ISO, NFW or Both. Column (14): classification of the RC according to the following code: 0 when halo is the main component whatever be the model, 1 when halo is the main component except in the very centre Column (and for ISO only), 2 when disc is the main component at all radii whatever be the model, 3 when disc Column (or disc + bulge) is dominating at the centre whatever be the model, and 4 when the main component is changing with the model Column (ISO or NFW).

This bulge profile was then subtracted from the total luminosity profile observed in order to get the true disc component alone. It is this last component that was used for the mass modelling and not the pure exponential component given above (which was merely an intermediate step to get the bulge profile as best as possible). Some discrepancies with other authors must be mentioned, however. For instance we found no bulge component for UGC 7045, whereas Baggett, Baggett & Anderson (1998) found one. Conversely, we found a bulge for UGC 7901 and 11914, while Kassin et al. (2006a) considered the bulge as negligible for both of them (which is especially surprising for UGC 11914 since it is an Sab galaxy).

3.3 The distribution of neutral gas

The distribution of neutral hydrogen (found in the literature) has been multiplied by 1.33 in order to take into account helium. The

thickness of the disc was calculated for each galaxy, depending on its type, with the formula given by Bottinelli et al. (1983).

Then, the halo contribution is deduced from the contribution of the different components to the final rotation curve we observe:

$$V_{\text{rot}}(r) = \left(V_{\text{gaz}}^2 + V_{\text{disc}}^2 + V_{\text{bulge}}^2 + V_{\text{halo}}^2 \right)^{0.5}. \quad (3)$$

For 14 galaxies of our sample, there is no H I distribution in the literature (see Table 1). However, since the influence of the neutral gas is most often negligible in the central part of the rotation curves of galaxies, it should not change our conclusions about the shape of the DM halo in the centre.

In order to check that, we have run our models for the six galaxies of our sample having a strong H I contribution and set the H I component at zero. The comparison of the results, with and without H I, shows that the change in both R_o and ρ_o ranges from 0 per cent

302 *M. Spano et al.*

to 33 per cent, with an average around 15 per cent. The change in χ^2 is slightly smaller, with an average around 10 per cent.

4 DENSITY PROFILES AND FITTING PROCEDURE

The method used in this paper to model the mass distribution is the same as described in Blais-Ouellette et al. (2001).

Since we have no a priori knowledge of the DM halo shape, we assumed the simplest shape of a spherical and symmetric distribution of matter (isothermal sphere, hereafter ISO):

$$\rho(r) = \frac{\rho_0}{[1 + (r/R_0)^2]^{3/2}}, \quad (4)$$

where R_0 is the core radius, and ρ_0 the central density of DM. This kind of profile is flat in the centre. However, N -body simulations, in the framework of the Λ CDM theory, favour cuspy halo profiles, peaked in the centre (NFW; Moore et al. 1999; Fukushige & Makino 2001).

For instance, the NFW profile is

$$\rho_{\text{NFW}}(r) = \frac{\rho_0}{(r/R_0)[1 + (r/R_0)]^2}, \quad (5)$$

where R_0 is the core radius and ρ_0 is the central density of DM. The density $\rho(r)$ is thus proportional to r^{-1} when r is small.

We used for our fits the density profiles defined by Zhao (1996):

$$\rho(r) = \frac{\rho_0}{[c + (r/R_0)^{-\gamma}] [1 + (r/R_0)^\alpha]^{(\beta+\gamma)/\alpha}}, \quad (6)$$

where ρ_0 is the central density and R_0 the core radius. The density profiles are then defined by the set of parameters (c, α, β, γ). Our fitting procedure was led with the two following sets: (0, 2, 3, 0) corresponding to the ISO (equation 4) with a constant central density and (0, 1, 3, -1) corresponding to the NFW profile (equation 5), with a peaked central density.

For each of the 36 galaxies studied here, we have applied the best-fitting model technique for these two profiles (ISO and NFW). It consists in minimizing the χ^2 in the three dimensions of the parameter space defined by $((M/L)_{\text{disc}}, \rho_0, R_0)$. Whenever a bulge component is taken into account, a fourth dimension is added with $(M/L)_{\text{bulge}}$.

Some constraints were added to these parameters in order to avoid non physical values. We thus limited M/L to a minimum value of 0.1 for both disc and bulge, R_0 to a minimum value of 1 kpc and ρ_0 to a minimum value of $10^{-3} M_\odot \text{pc}^{-3}$. These minima values were arbitrarily chosen (although suggested by the current values encountered for these parameters).

Table 2 summarizes the results of the best fits obtained with our mass models (for both NFW and ISO profiles of the DM halo) in terms of luminosity ratios of the visible components, central density and core radius of the DM halo together with the corresponding χ^2 .

For the calculation of our mass–luminosity ratios, we adopted 4.28 for the absolute magnitude of the sun in the R band (Allen Astrophysical Quantities, 4th edition, 2000).

Figs A1–A9, given in the appendix, show the plots of the best fits obtained using the two different density profiles for the DM halo (ISO and NFW) for the 36 rotation curves of our sample. The observed rotation curves are coded as explained in Section 3.1. The dotted blue (light) line is for the H I component. The dash–dotted blue line is for the disc component. The dash–dotted pink line is for the bulge component. The dashed green line is for the halo component. The continuous red line is for the total (quadratic sum of all components).

5 RESULTS OF THE FITS

5.1 Best-fitting model

For 10 galaxies, the halo is clearly the dominating component at all radii, whatever the model (NFW or ISO). They are UGC 4274, 5279, 5721, 5789, 5842, 7699, 7876, 9219, 11707 and 12060. All of them are late-type spirals (from Scd to Im).

For 10 galaxies, the halo is dominating except in the very centre (where the disc – or bulge – is the main component) and for ISO model only. They are UGC 4256, 4499, 6537, 6778, 7524, 7901, 8490, 9179, 10075 and 11557 (types ranging from Sc to Sm).

For four galaxies, the disc is dominating at all radii whatever the model. They are UGC 2503, 5175, 9248 and 9866. All of them being rather early type galaxies (Sb or Sbc).

For two galaxies, the disc (or disc + bulge) is dominating in the centre whatever the model. They are UGC 2455 and UGC 11914. The result is not so surprising for this last one (being of Sab type) and more surprising for UGC 2455 (of Im type) but it must be taken with care because both models (NFW and ISO) led to abnormally low (non physical) values of M/L for this galaxy (blocked at 0.1 adopted here as the lowest acceptable value).

For the 10 remaining galaxies, the main component changes with the model but the disc is almost always dominating with the ISO model, whereas the halo is dominating with the NFW model (the only exception being UGC 4325, for which the main component is the halo with the ISO model and the disc with the NFW model). These galaxies are mainly UGC 2034, 3876, 4555, and 7045, ranging from Sbc type to Im. Things are not so clear for UGC 4456, 5272, 7323, 9465 and 10310 (one Sc and four magellanic galaxies) because the disc is then overtaken by the halo in the outer parts with the ISO model.

Following the above discussion, we defined a classification code given in the last column of Table 2. To summarize, we find 10 galaxies in class 0, 10 in class 1, four in class 2, two in class 3 and 10 in class 4.

This quick review of the results of the best fits confirms the well-known fact that later-type galaxies are more DM-dominated.

Some galaxies of our sample have already been observed by other authors and their rotation curves have been analysed in terms of mass models.

Four galaxies have been already observed by de Blok & Bosma (2002) all of them being LSB-type galaxies: UGC 4325, 5272, 5721, 7524. They also observed UGC 10310 but could not derive mass models (except a minimum disc one) because they had no surface photometry. Our results are in good agreement for UGC 4325 and 5272, since they find good fits with their pseudo-isothermal model and bad ones with the NFW model. We also agree for UGC 7524, where they find that both models give acceptable fits. As for UGC 5721, we also find that the ISO provides a good fit but the fit we obtain with the NFW model is not satisfying (we find a χ^2 which is more than twice that obtained with the ISO), whereas they find it almost as good.

UGC 7323 (a dwarf galaxy of Sdm type) has been already observed by van den Bosch & Swaters (2001) who concluded that ‘no meaningful fit can be obtained for this galaxy’. Our fits do not look so bad, however, even with the NFW model for which we had to push down to the minimum acceptable value of M/L for the disc (0.1). Our best fit (smaller χ^2) was obtained with the ISO model, with a quite normal set of parameters.

Six dwarf or LSB galaxies have been already observed and analysed in terms of mass models by Swaters et al. (2003): UGC 4325,

4499, 5721, 8490, 11557 and 11707. They find better results for four of them (UGC 4325, 4499, 8490 and 11557) with a pseudo-isothermal model rather than with NFW (in agreement with our results except for UGC4499 that we discuss below) but they have a reverse for UGC 5721 (which is in contradiction with de Blok & Bosma 2002 and with our results) as well as for UGC 11707. About UGC 5721, we must confess that our ISO model gives a better solution to the price of minimal accepted values for both M/L (0.1) and R_0 (1 kpc) thus casting a doubt on the validity of the result hence to the comparison that can be done with the NFW model for this galaxy. As for UGC 11707, we have H α points on the rotation curve hovering significantly above the H I curve for radii going from 3 to 6 kpc (see Fig. A9), exactly where the pseudo-ISO model from Swaters et al. is too low to fit correctly the observed curve (see their fig. 3). The difference between our H α curves may be explained by the smaller value of inclination we adopted for that galaxy (55° instead of 68°) but also because with Fabry–Perot observations we take into account data from a large part of the disc instead of getting points only along a slit. We agree with Swaters et al. who find that NFW overpredicts the inner slope of the rotation curve for UGC 4325 (also in agreement with de Blok & Bosma 2002, fig. 8) and for UGC 8490 (as can be seen in their fig. 3) but not for UGC 4499 where the slope of our H α rotation curve can be fitted correctly with our models (even slightly better with the NFW model although it is not very significant). Indeed, the inner slope of their rotation curve is not much different from the slope of the H I curve (plotted as crosses on our Fig. A3) whereas our H α curve is clearly above. This discrepancy is maybe due to the fact that the authors use slit spectroscopy to get the H α rotation curve in the central part of the galaxy (we adopted here the same inclination of 50°), although they note that it generally provides a steeper slope than the H I curve, this last one being biased by beam smearing. As for the three other galaxies (UGC 5721, 11557 and 11707) we do find that NFW overpredicts the inner slope, more or less strongly but systematically.

Six galaxies of our sample have been studied by Kassín, de Jong & Weiner (2006b) (UGC 5789, 6537, 6778, 7045, 7901 and 11914, of respective types Scd, Sc, Sc, Sc, Sc and Sab) with another approach since they decompose the rotation curves found in the literature into baryonic and DM components (stellar mass profiles are created by applying colour– M/L relations to near-infrared and optical photometry). As a consequence, no straightforward comparison could be done with our results. However, it is interesting to note that Kassín et al. find that for two of them (UGC 5789 = NGC 3319 and UGC 7045 = NGC 4062) the baryons underpredict the rotation curve, although they conclude that the case is not so clear for NGC4062 when taking into account all the uncertainties. Indeed, for UGC 5789 our models (NFW and ISO) both point at an M/L of the disc at the minimum accepted value, 0.1, suggesting that it is dominated by the DM halo component. As for UGC 7045, the disc alone (with $M/L = 5.4$) is almost sufficient to explain the rotation curve with the ISO model (which is then very close to a maximum disc model) whereas it is the contrary with the NFW model where the halo alone can explain the rotation curve (M/L is then found to be close to 1 for the disc). For the four other galaxies (UGC 6537, 6778, 7901 and 11914), we find that the fits obtained with the ISO model are not far from the fits provided by a maximum disc, more especially for UGC 6537 and 11914 where the match is perfect (we applied maximum disc models to the 36 galaxies studied in this paper but the resulting graphs are not presented here). Our analysis of the rotation curves in terms of mass models for these six galaxies

is thus in good agreement with the conclusions reached by Kassín et al.

In summary, in the cases where some of our galaxies have already been modelled by other authors, the results tend to agree pretty well. In the few cases which differ, the reason for the discrepancy has most of the time been identified.

6 DISCUSSION

In order to allow a direct comparison, the χ^2 given in Table 2 have been computed using the same variation range for the parameters and the same step of calculus for both the ISO and the NFW mass models.

The comparison of the values of the χ^2 found for the best fits of both models clearly shows that the ISO profile for the DM halo gives better results than the NFW profile when fitting the observed rotation curves. In Fig. 1, we plotted the minimum value of the χ^2 found with the ISO model as a function of that obtained with the NFW model for each galaxy. These last χ^2 are systematically larger. The column ‘best model’ in Table 2 indicates which one, from ISO or NFW, gives the best results as can be judged from the fits displayed in Figs A1–A9, with the mention ‘Both’ when they give comparable results. It appears that there is a clear difference between ISO and NFW models as soon as there is a 20 per cent difference in the corresponding χ^2 . It also confirms what the χ^2 values suggest, namely that the ISO model provides better fits than the NFW in most of the cases.

Indeed, the NFW model, because of its steep rise in the centre, is often unable to fit correctly the observed rotation curve. Typical examples can be seen with UGC 5279, 5842, 7699, 7876, 9219, 9465 or 11557. For these galaxies (all of late type, ranging from Scd to Im) the central rising part of the rotation curves is completely missed by the NFW model, although the M/L of the disc is most often pushed to its lowest acceptable value of 0.1 (except for UGC 5279 and UGC 5842 where it is found to be respectively 0.56 and 0.16).

In particular, in the case where the χ^2 value is lower for the NFW model, the M/L value found is smaller than for the ISO model,

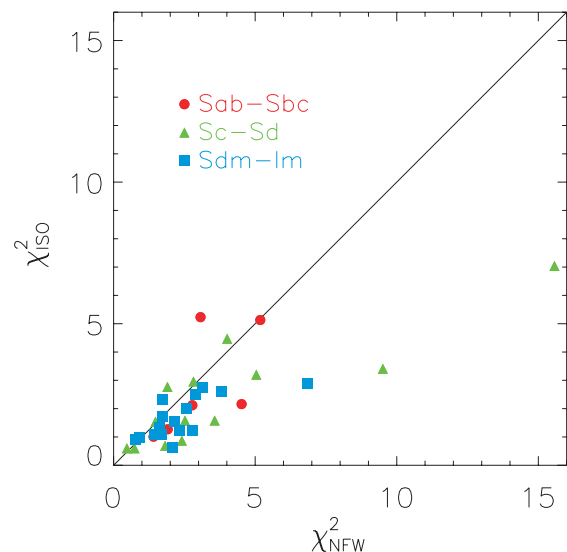


Figure 1. Minimum χ^2 obtained with an ISO profile versus an NFW profile. For Figs 1–5 we used three different symbols for the main classes of morphological types of spiral galaxies (early, late and Magellanic).

304 *M. Spano et al.*

leading to a poor match between the RC and the disc contribution in the central region of the galaxy. More generally, because of the small M/L found for the NFW models, this solution rarely allows the first 1–2 kpc of the RC to be fitted by the disc component contribution, even when the shape of the RC should make it possible. Indeed, the ISO model solutions, which are often close to maximum disc solutions, lead to better matches between the stellar mass and the total mass distributions in the inner region of the galaxies. This is a strong argument in favour of the ISO solutions.

The NFW profile cannot account for rotation curves with a linear rise in velocity with radius, as shown by Hayashi & Navarro (2006) in their fig. 1. The ISO model, on the contrary, provides good fits in the central part for such slowly rising rotation curves and, more generally, systematically better fits than the NFW model for most of the galaxies of our sample. The position of the points in Fig. 1 shows no special trend with morphological type. More generally, it can be seen that the NFW best fits tend to give systematically unphysical low values for the disc M/L (0.1). This is even a stronger argument than the smaller χ^2 to favour the ISO solutions. Also, whenever the χ^2 is smaller for the NFW model, it appears that the M/L is systematically smaller (or equal in one case) than with the ISO model, leading to abnormally low values of M/L.

Looking at Tables 1 and 2, one can see that nearly half (16/36) of the galaxies do not have H I velocities such that the RC is only defined in the inner parts. Since, as mentioned earlier, the kinematics in the inner parts can be affected by non-circular motions (such as the presence of bars), it is interesting to see if this alters significantly the results when trying to see which model (ISO or NFW) fits best the kinematics. In fact, for the whole sample (36) we get that 50 per cent are best represented by an ISO model, 8 per cent by an NFW model and 42 per cent are equally well represented by both models while for the subsample having only an optical RC for the inner parts, those numbers are 50, 12 and 38 per cent. Thus, the main conclusions hold even when only optical data are available for the inner parts.

In Fig. 2, we plotted the central density of the DM density profile versus the core radius of the dark halo for both models (top panel: ISO profile; bottom panel: NFW profile). The central density and the core radius of the halo are clearly correlated: the higher the central density, the smaller the core radius, whatever the model and independent of morphological type. This is in good agreement with the results found by other authors (Burket 1995; Kravtsov et al. 1998; Blais-Ouellette 2000) who claim that one free parameter is enough for describing the distribution of DM. More recently, Barnes et al. (2004) and Kormendy & Freeman (2004) also found the same type of correlation. However, the slope of our correlation is close to that found by Kormendy & Freeman, whereas the slope found by Barnes et al. is clearly steeper. Indeed, as detailed hereafter, we find a slope of -0.93 (for ISO fits) which is very close to that found by Kormendy & Freeman (-1.04 for ISO fits and -1.20 for pseudo-isothermal fits) while Barnes et al. find a steeper slope, around ~ -2 (estimated from their fig. 4) for pseudo-ISO fits.

All these values are in agreement when considering the accuracy for the slopes. The error bars on our data show that the permitted range for the slope deduced from our Fig. 2 (top panel) goes from 0.5 to 2.0. One can estimate this range from 1.5 to 2.5 for Barnes et al. and from 0.5 to 1.5 for Kormendy & Freeman.

When taking into account only the points for which the ISO model is clearly the best (see column 13 of Table 2) we also find a steeper slope (-1.38 instead of -0.93) intermediate between that found

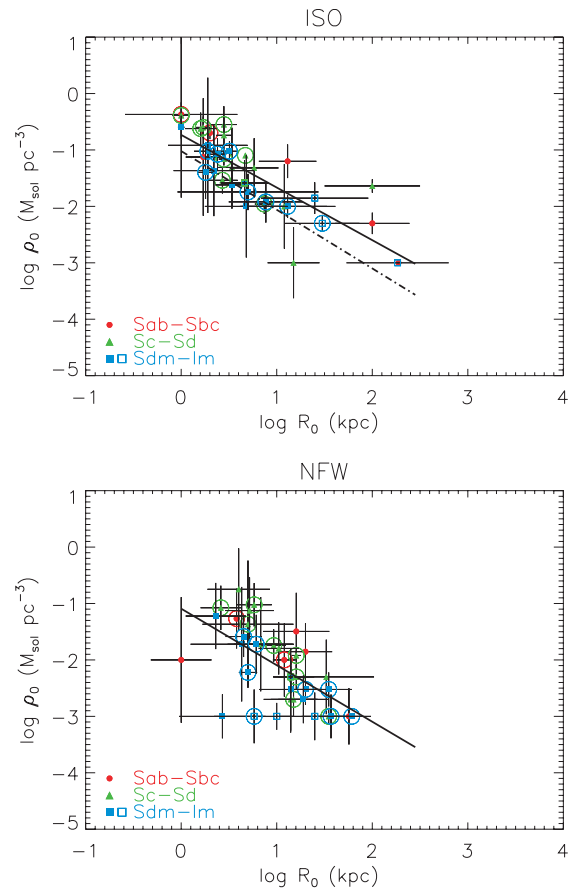


Figure 2. Top panel: Central density (log) of DM versus the core radius (log) of DM for the ISO profile (ISO). Bottom panel: Same for the NFW profile. The solid lines are least-squares fits to our data (excluding the three open squares discussed in Section 6). The dashed line (top panel) is the least-squares fit extracted from fig. 3 of Kormendy & Freeman (2004). The circles surround the points for which ISO is clearly the best model.

by Kormendy & Freeman and that found by Barnes et al. These points are surrounded by a circle in Figs 2–4. In Fig. 2 (bottom panel, NFW model), these points also lead to a steeper slope than the whole set (-1.48 instead of -1.00). In Fig. 4 too, they suggest a slightly steeper slope (albeit the least-squares fit remains very flat and almost horizontal) than the whole set. In Fig. 3, on the contrary, the points for which ISO is the best suggest a lower slope than the whole set for both graphs (top and bottom). For all these Figs 2–4, these points tend to have a smaller dispersion than the whole set.

Based on published mass models for 37 galaxies, from Sc to Im type, Kormendy & Freeman found the following least-squares fit for isothermal haloes:

$$\log \rho_0 = -1.04 \log R_0 - 1.02 \text{ (rms} = 0.17\text{dex)}.$$

Our data of Fig. 2 give the following least-squares fits excluding the three points plotted as the open squares corresponding to Im galaxies discussed below (Fig. 3):

$$\log \rho_0 = -0.93 \log R_0 - 0.74 \text{ (} R^2 = 0.61 \text{) for ISO,}$$

$$\log \rho_0 = -1.00 \log R_0 - 1.03 \text{ (} R^2 = 0.42 \text{) for NFW.}$$

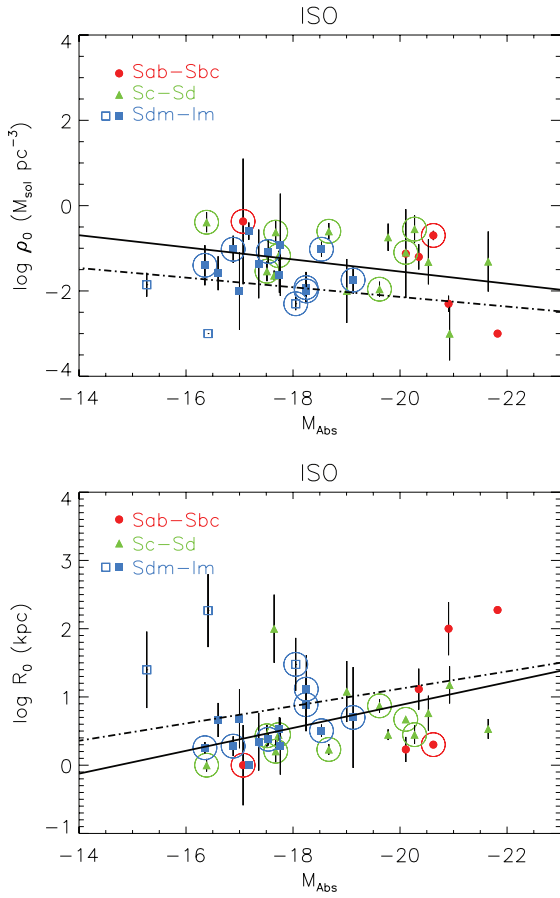


Figure 3. Top panel: central density (log) of dark halo versus absolute magnitude. Bottom panel: core radius (log) of dark halo versus absolute magnitude. Both are for the ISO models. The solid lines are least-squares fits for our data (excluding the three open squares discussed in Section 6). The dashed lines are the least-squares fits extracted from fig. 3 of Kormendy & Freeman (2004). The circles surround the points for which ISO is clearly the best model.

We conclude that, on average, $\log \rho_0 \sim -\log R_0 - 0.8$, which implies that the product $\rho_0 R_0$ is almost constant.

Fig. 3 shows the correlation of the central density (top panel) and of the core radius (bottom panel) as a function of absolute magnitude. From those two plots it is clear that faint galaxies (dwarfs) have higher central density and smaller core radius. In other words, dwarf galaxies have a more highly concentrated DM content than massive spirals. This result had already been seen quite convincingly in the study of the Sculptor group dwarfs by Coté, Carignan & Freeman (2000) in their figs 8 and 9 (see also the figs 2 and 3 of Kormendy & Freeman 2004).

For three out of the six Im galaxies of our sample (namely UGC2034, 2455 and 5272) the optical part of the rotation curve is very chaotic, with large error bars, and the resulting best-fitting models are not very reliable. The correlation is much clearer when these three galaxies are removed from the sample. Anyway we plotted them on the graphs as open squares but do not take them into account when fitting the data points. The same thing has been done for the two plots of Fig. 2, where one can see that the corresponding points have a normal behaviour in the top panel diagram (ISO model), whereas all of them appear in the lower part of the

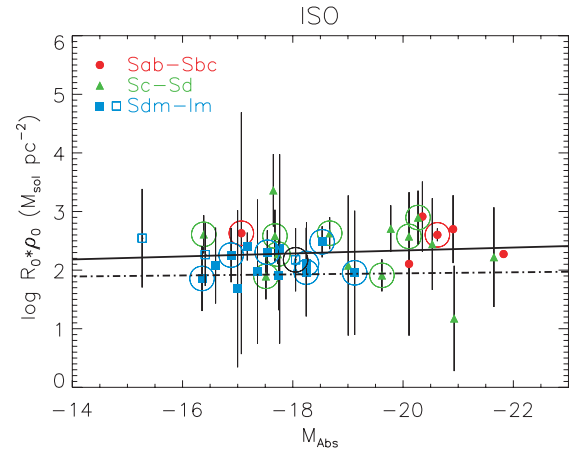


Figure 4. Central surface density (log) of DM (ISO model) as a function of absolute magnitude (given in Table 1, determined from $B_T(0)$ found in the RC3 and our adopted distance). The solid line is a least-squares fit for our data (excluding the three open squares discussed in Section 6). The dashed line is the least-squares fit extracted from fig. 5 of Kormendy & Freeman (2004). The circles surround the points for which ISO is clearly the best model.

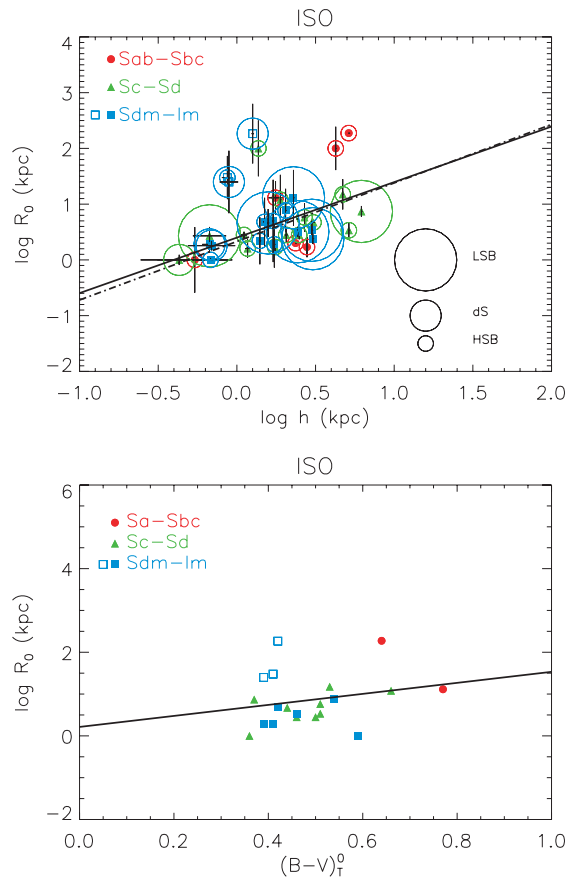


Figure 5. Core radius (log) of the DM halo (ISO models) as a function of optical disc scalelength (top panel) and $(B - V)_T$ colour (bottom panel). This last parameter, extracted from the RC3 catalog, could be found for 20 of our galaxies only. The solid lines are least-squares fits obtained with our data (excluding the three open squares discussed in Section 6). The dashed line on the top diagram is the least-squares fit from fig. 1 of Donato et al. (2004). On that diagram we have surrounded HSB, dS and LSB galaxies by circles of growing sizes.

306 *M. Spano et al.*

bottom panel diagram (NFW model) since they reach the minimum accepted value of ρ_0 .

Kormendy & Freeman found the following least-squares fit for isothermal haloes:

$$\log \rho_0 = 0.113M_B + 0.12 \quad (\text{rms} = 0.28 \text{ dex}),$$

$$\log R_0 = -0.127M_B - 1.42 \quad (\text{rms} = 0.16 \text{ dex}).$$

Our plots in Fig. 3 give the following least-squares fits (also for the isothermal models):

$$\log \rho_0 = 0.142M_B + 1.29 \quad (R^2 = 0.12),$$

$$\log R_0 = -0.167M_B - 2.47 \quad (R^2 = 0.23).$$

The agreement is fairly good, as can be seen in Fig. 3, and strengthens the validity of these scaling laws.

Salucci et al. (2007) also get such a relation between the central density and the core radius of the halo (see fig. 1 of their paper) although for a different fitting model.

The obvious next step is to look at the product of R_0 and ρ_0 as a function of absolute magnitude. This is done in Fig. 4. Our mass models, applied to galaxies ranging from Sab to Im, suggest a nearly constant halo surface density around $\sim 150 M_\odot \text{pc}^{-2}$, slightly higher than the value found by Kormendy & Freeman which is just below $\sim 100 M_\odot \text{pc}^{-2}$ (according to their fig. 5). Clearly, the halo surface density is nearly independent of galaxy luminosity. A small part of the offset (~ 0.06 for the log) observed in Fig. 4 between our least-squares fit and that of Kormendy & Freeman may be explained by the adopted value of $H_0 = 75 \text{ km s}^{-1} \text{ Mpc}^{-1}$, whereas they use $H_0 = 70 \text{ km s}^{-1} \text{ Mpc}^{-1}$, anyway the offset is smaller than the error bars.

Another interesting correlation is the one found by Donato, Gentile & Salucci (2004) between the core radius of the DM halo and the exponential disc scalelength h . They find (from a sample of 25 galaxies of different morphological types found in the literature) the following relation:

$$\log R_0 = (1.05 \pm 0.11) \log h + (0.33 \pm 0.04),$$

$$\text{corr} = 0.90 \text{rms} = 0.16 \text{ dex}.$$

Our data are in good agreement with that result since our plot of Fig. 5 (top panel) shows the following relation (least-squares fit excluding the three Im galaxies already mentioned above and plotted as open squares):

$$\log R_0 = 0.996 \log h + 0.40 \quad (R^2 = 0.28).$$

The different types (LSB, dS, HSB) of galaxies are distinguished in Fig. 5 (top panel) by circles of different sizes surrounding them. (NB: For those who are both LSB and dS, we preferred marking only the last classification.) Unfortunately, two out of the five dS of our sample are among the group of three galaxies already excluded from the fits in Figs 2–5 (where they are plotted as open squares). As a matter of fact, only three ‘bona fide’ dS remain. Luckily, all of them are on the lower left side of the diagram, as expected, but of course it is not very significant and prevents to draw any significant conclusion.

Finally, as seen in Coté et al. (2000), there is a trend in Fig. 5 (bottom panel) between the core radius and the $(B - V)$ colour. The different types of galaxies are not distinguished in that figure because there are too few points to conclude efficiently about the different subtypes. Furthermore, it is just a trend that is shown, needing to be confirmed with a larger sample.

7 SUMMARY AND CONCLUSION

Our study, based on 36 galaxies of different morphological types, confirms the result already claimed by other authors about the shape of the DM halo in the centre of spiral galaxies, namely that its density profile is probably closer to an ISO profile than to an NFW profile: DM haloes are rather flat than cuspy. Our mass models (ISO and NFW) are compared when fitting the rotation curve as a whole, however, a comparison of the χ^2 values limited to the central regions would be still clearer since the inner slope of the RC found with the NFW model is systematically steeper and above the data points, compared with the ISO model.

Thus far, most of the results found in the literature concerned dwarf or LSB galaxies. Nine galaxies of our sample are LSB (UGC 2304, 5272, 5279, 5789, 7524, 7699, 9465, 11707 and 12060, with types going from Scd to Im) and, for all of them, we systematically find better results with the ISO model (smaller χ^2) than with NFW, except UGC 2304 for which both are equivalent. Interestingly, our study suggests that this holds for most spirals since the 36 galaxies of this study have morphological types ranging from Sab to Im. For almost all of them, the best fit is obtained with the ISO model (the reverse is found only for four galaxies out of 36). Also, no significant difference can be seen when comparing the quality of the fits obtained with the NFW and the ISO model as a function of the morphological type.

However, a difference can be seen in the way the rotation curves are decomposed into several components, with the halo being the main component for late types and the disc (or disc + bulge) the main component for early types. This result, although needing to be confirmed with a larger sample, merely reflects the well-known fact that later-type galaxies are more DM-dominated.

Finally, we confirm different halo scaling laws seen previously by other authors such as Coté et al. (2000), Kormendy & Freeman (2004) and Barnes et al. (2004). Among those, it appears clearly that low-luminosity galaxies have small core radius and high central density, the product of the two parameters being nearly constant with absolute magnitude. This means that the galaxy halo surface density is independent of galaxy type or luminosity. Trends are also seen for the core radius as a function of luminosity and colour but should be confirmed with a larger sample.

ACKNOWLEDGMENTS

The authors wish to thank the anonymous referee who helped improve this paper. They thank the Groupement de Recherche Galaxies (now Programme National Galaxies) for its support for observing time and the Observatoire de Haute-Provence team for its technical assistance during the observations. They also thank O. Garrido, J. L. Gach, O. Boissin and P. Balard for their help during the observing runs and J. Boulesteix for constantly improving the ADHOCW software used for the data acquisition and reduction. The authors thank Chantal Balkowski, Laurent Chemin, Henri Plana and Olivier Daigle for fruitful discussions. This research has made use of the NASA/IPAC Extragalactic Database (NED) which is operated by the Jet Propulsion Laboratory, California Institute of Technology, under contract with the National Aeronautics and Space Administration. The authors have also made an extensive use of the LEDA database (<http://leda.univ-lyon1.fr>). CC and OH acknowledge support from the Natural Sciences and Engineering Research Council of Canada and le Fonds québécois de la recherche sur la nature et les technologies.

REFERENCES

- Allen C. W., 2000, in Cox A. N., ed., *Allen's Astrophysical Quantities*, 4th edn. Am. Inst. Phys., New York
- Baggett W. E., Baggett S. M., Anderson K. S. J., 1998, *AJ*, 116, 1626
- Barnes E. I., Sellwood J. A., Kosowsky A., 2004, *AJ*, 128, 2724
- Blais-Ouellette S., 2000, PhD thesis, Univ. Montréal
- Blais-Ouellette S., Carignan C., Amram P., Côté S., 1999, *AJ*, 118, 2123
- Blais-Ouellette S., Amram P., Carignan C., 2001, *AJ*, 121, 1952
- Blais-Ouellette S., Amram P., Carignan C., Swaters R., 2004, *A&A*, 420, 147
- Bottinelli L., Gouguenheim L., Paturel G., de Vaucouleurs G., 1983, *A&A*, 118, 4
- Broeils A. H., van Woerden H., 1994, *A&AS*, 107, 129B
- Burket A., 1995, *ApJ*, 447, L25
- Cardelli J. A., Clayton G. C., Mathis J. S., 1989, *ApJ*, 345, 245
- Choloniewski J., Valentijn E. A., 2003, *Acta Astron.*, 53, 249
- Côté S., Carignan C., Sancisi R., 1991, *AJ*, 102, 904
- Côté S., Carignan C., Freeman K. C., 2000, *AJ*, 120, 3027
- Courteau S., 1996, *ApJS*, 103, 363C
- de Blok W. J. G., 2005, *ApJ*, 634, 227
- de Blok W. J. G., Bosma A., 2002, *A&A*, 385, 816
- de Blok W. J. G., Bosma A., McGaugh S., 2003, *MNRAS*, 340, 657
- de Jong R. S., van der Kruit P. C., 1994, *A&AS*, 106, 451D
- de Jong R. S., Bell E., 2006, in de Jong R. S., ed., *Astrophys. Space Sci. Proc., Island Universes, Structure and Evolution of Disk Galaxies*. Springer, Dordrecht, p. 107
- Donato F., Gentile G., Salucci P., 2004, *MNRAS*, 353, L17
- Dutton A. A., Courteau S., de Jong R., Carignan C., 2005, *ApJ*, 619, 218
- Fletcher R., 1970, *Comp. J.*, 13, 317
- Fukushige T., Makino J., 2001, *ApJ*, 557, 533
- Garrido O., Marcelin M., Amram P., Boulesteix J., 2002, *A&A*, 387, 821
- Garrido O., Marcelin M., Amram P., Boissin O., 2003, *A&A*, 399, 51
- Garrido O., Marcelin M., Amram P., 2004, *MNRAS*, 349, 225
- Garrido O., Marcelin M., Amram P., Balkowski C., Gach J. L., Boulesteix J., 2005, *MNRAS*, 362, 127
- Graham A. W., Merritt D., Moore B., Diemand J., Terzic B., 2006, *AJ*, 132, 2701
- Hayashi E., Navarro J. F., 2006, *MNRAS*, 373, 1117
- Hayashi E., Navarro J. F., Springel V., 2007, *MNRAS*, 377, 50
- Héraudeau P., Simien F., 1996, *A&AS*, 118, 111
- James P. A. et al., 2004, *A&A*, 414, 23
- Jansen R. A., Franx M., Fabricant D., Caldwell N., 2000, *ApJS*, 126, 271J
- Karachentsev I. D., Karachentseva V. E., Huchtmeier W. K., Makarov D. I., 2004, *AJ*, 127, 2031
- Kassin S. A., de Jong R. S., Pogge R. W., 2006a, *ApJS*, 162, 80
- Kassin S. A., de Jong R. S., Weiner B. J., 2006b, *ApJ*, 643, 804
- Koopmann R. A., Haynes M. P., Catinella B., 2006, *AJ*, 131, 716
- Kormendy J., Freeman K. C., 2004, in Ryder S., Pisano D. J., Walker M., Freeman K. C., eds, *Proc. IAU Symp. 220, Dark Matter in Galaxies*. Astron. Soc. Pac., San Francisco, p. 377
- Kravtsov A., Klypin A., Bullock J., Primack J., 1998, *ApJ*, 502, 48
- Kuzio de Naray R., McGaugh S. S., de Blok W. J. G., Bosma A., 2006, *ApJS*, 165, 461
- Maccio A. V., Dutton A. A., van den Bosch F. C., Moore B., Potter D., Stadel J., 2007, *MNRAS*, 378, 55
- Moore B., Quinn T., Governato F., Stadel J., Lake G., 1999, *MNRAS*, 310, 1147
- Moore E., Gottesman S., 1998, *MNRAS*, 294, 353
- Moustakas J., Kennicutt R. C., 2006, *ApJS*, 164, 81
- Navarro J., 2004, in Ryder S., Pisano D. J., Walker M., Freeman K. C., eds, *Proc. IAU Symp. Dark Matter in Galaxies*. Astron. Soc. Pac., San Francisco, 220, p. 61
- Navarro J., Frenk C., White S., 1997, *ApJ*, 490, 493 (NFJ)
- O'Donnell J. E., 1994, *ApJ*, 422, 1580
- Pizzella A., Corsini E. M., Dalla Bonta E. D., Sarzi M., Cocconi L., Bertola F., 2005, *ApJ*, 631, 785
- Prugniel P., Héraudeau P., 1998, *A&AS*, 128, 299
- Saha A., Thim F., Tammann G. A., Reindl B., Sandage A., 2006, *ApJS*, 165, 108
- Salucci P., Lapi A., Tonini C., Gentile G., Yegorova I., Klein U., 2007, *MNRAS*, 378, 41
- Schlegel D. J., Finkbeiner D. P., Davis M., 1998, *ApJ*, 500, 525
- Schombert J. M., Pildis R. A., Eder J. A., Oemler A., 1995, *AJ*, 110, 2067
- Shapley A., Fabbiano G., Eskridge P. B., 2001, *ApJS*, 137, 139
- Stil J., Israel F., 2002, *A&A*, 392, 473
- Swaters R. A., 1999, PhD thesis, Rijksuniv. Groningen
- Swaters R. A., Balcells M., 2002, *A&A*, 390, 863
- Swaters R. A., Madore B. F., Trewhella M., 2000, *ApJ*, 531, L107
- Swaters R. A., van Albada T. S., van der Hulst J. M., Sancisi R., 2002, *A&A*, 390, 829
- Swaters R. A., Madore B. F., van den Bosch F. C., Balcells M., 2003, *ApJ*, 583, 732
- van den Bosch F. C., Robertson B. E., Dalcanton J. J., de Blok W. J. G., 2000, *AJ*, 119, 1579
- van den Bosch F. C., Swaters R. A., 2001, *MNRAS*, 325, 1017
- van Driel W., van Woerden H., 1994, *A&A*, 286, 395
- van Zee L., 2000, *AJ*, 119, 2757
- Verdes-Montenegro L., Bosma A., Athanassoula E., 1995, *A&A*, 300, 65
- Verheijen M., Sancisi R., 2001, *A&A*, 370, 765
- Warmels R. H., 1988, *A&AS*, 72, 427W
- Zhao H., 1996, *MNRAS*, 278, 488.

APPENDIX A

Best fitting models for the rotation curves (Figs A1–A14).

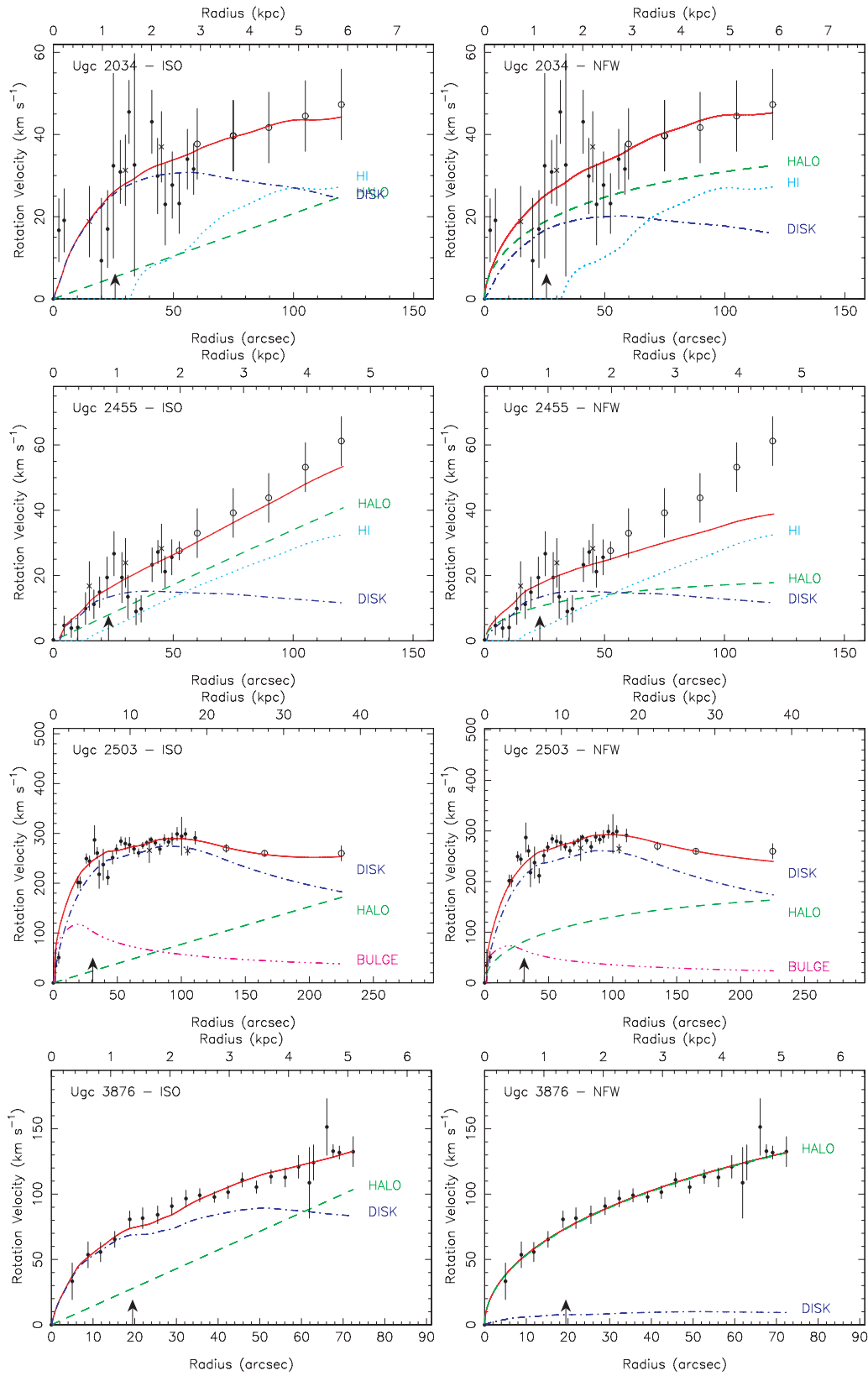
308 *M. Spano et al.*

Figure A1. Best-fitting model for the rotation curve of UGC 2034, UGC 2455, UGC 2503 and UGC 3876 with ISO profile (left) and NFW profile (right-hand panel). The dots are for optical velocities, the open circles for HI velocities and the crosses for HI in the central part, not taken into account. The arrow on the X-axis indicates the disc scalelength.

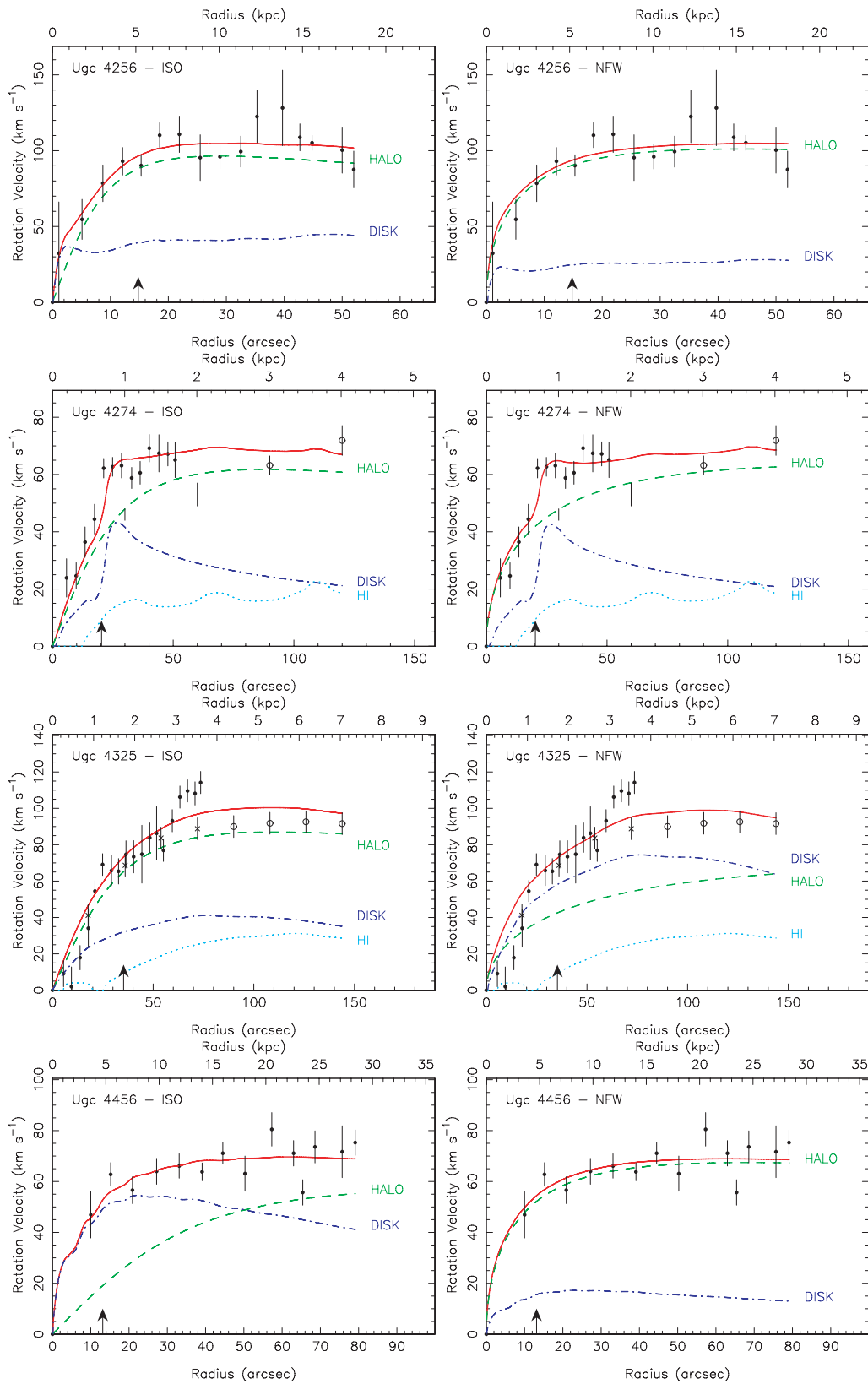


Figure A2. Best-fitting model for the rotation curve of UGC 4256, UGC 4274, UGC 4325 and UGC 4456 with ISO profile (left-hand panel) and NFW profile (right-hand panel). The dots are for optical velocities, open circles for H I velocities and crosses for H I in the central part, not taken into account. The arrow on the X-axis indicates the disc scalelength.

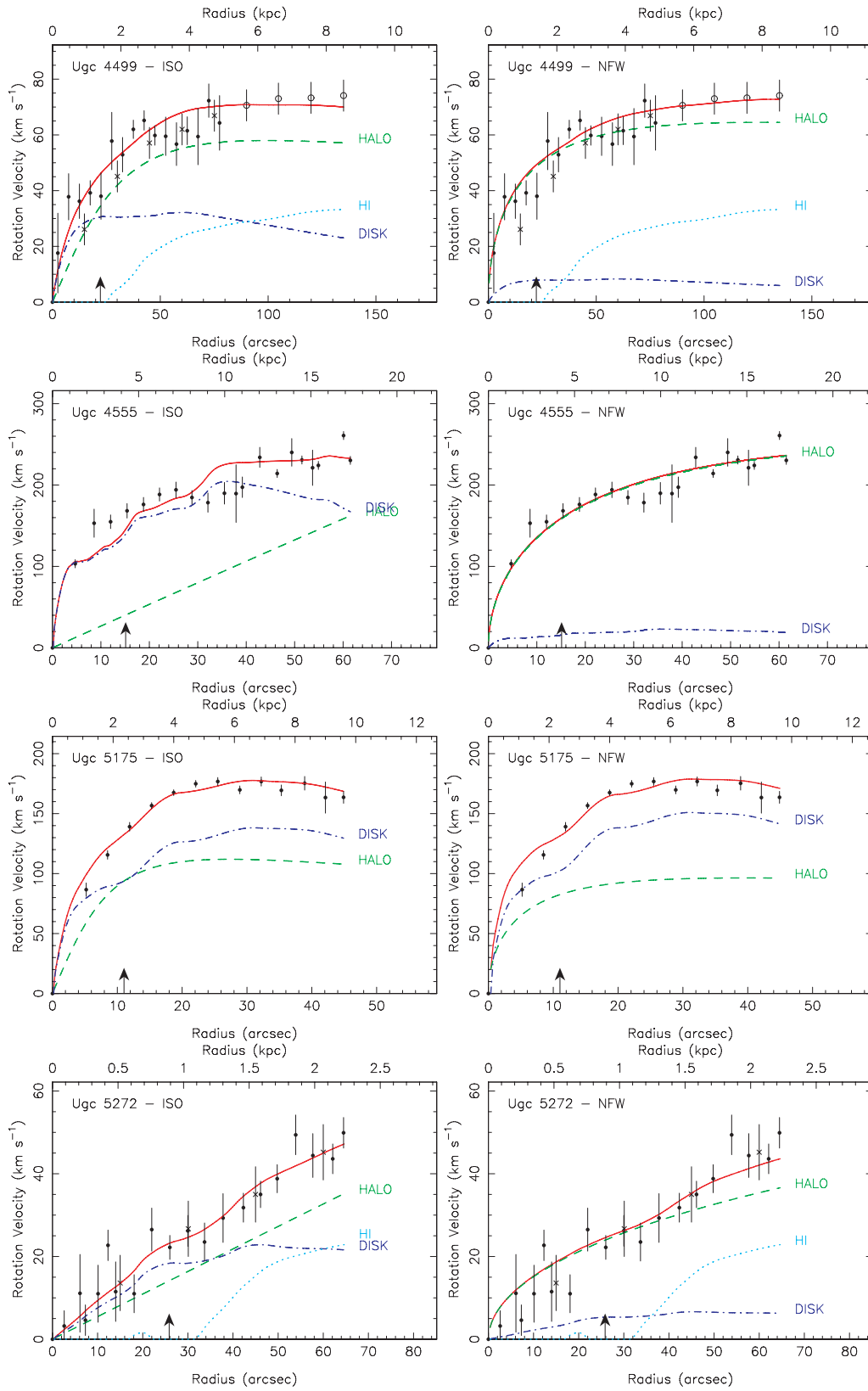
310 *M. Spano et al.*

Figure A3. Best-fitting model for the rotation curve of UGC 4499, UGC 4555, UGC 5175 and UGC 5272 with ISO profile (left-hand panel) and NFW profile (right-hand panel). The dots are for optical velocities, the open circles for H I velocities and the crosses for H I in the central part, not taken into account. The arrow on the X-axis indicates the disc scalelength.

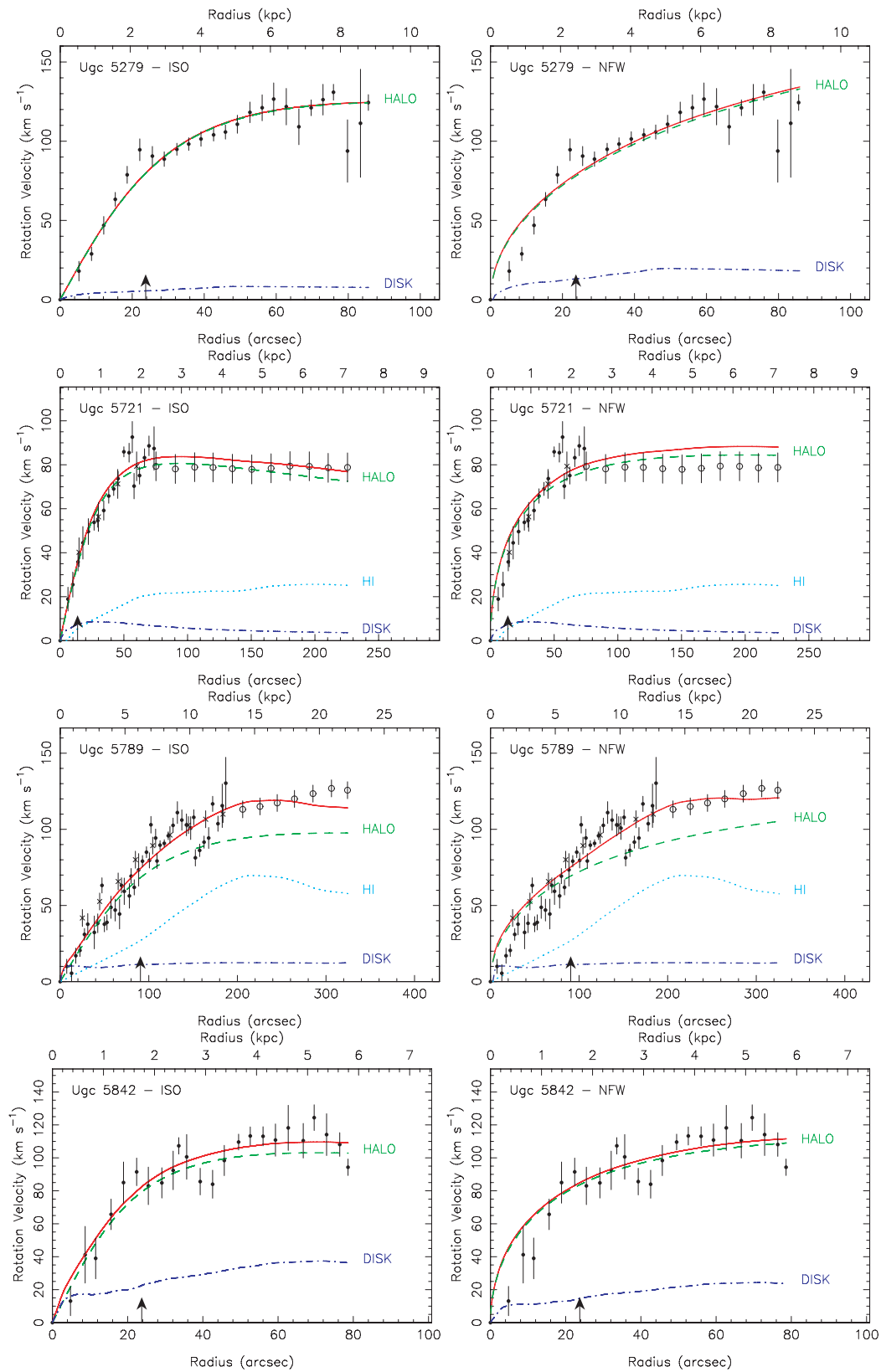


Figure A4. Best-fitting model for the rotation curve of UGC 5279, UGC 5721, UGC 5789 and UGC 5842 with ISO profile (left-hand panel) and NFW profile (right-hand panel). the dots are for optical velocities, open circles for H I velocities and crosses for H I in the central part, not taken into account. The arrow on the X-axis indicates the disc scalelength.

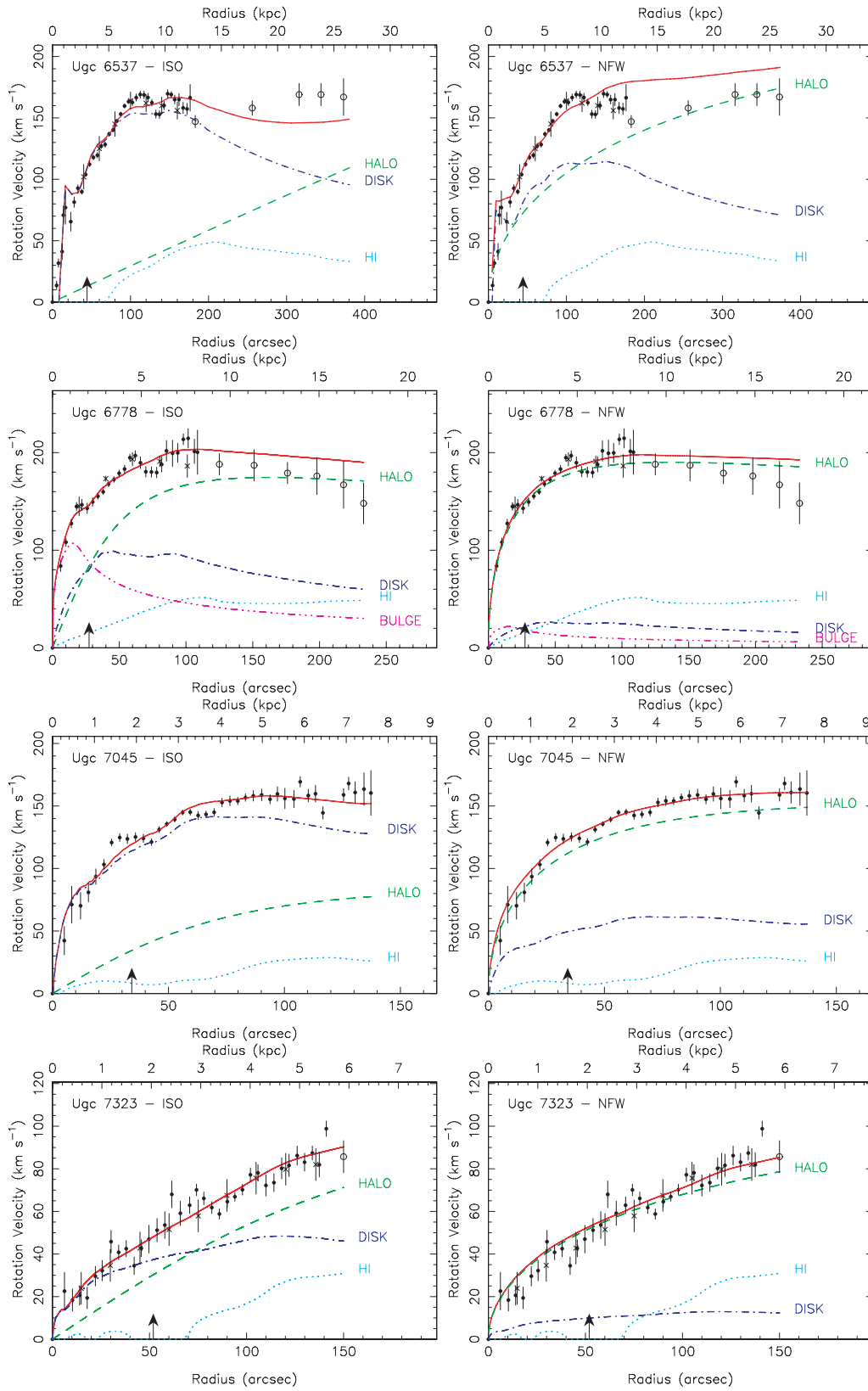
312 *M. Spano et al.*

Figure A5. Best-fitting model for the rotation curve of UGC 6537, UGC 6778, UGC 7045 and UGC 7323 with ISO profile (left-hand panel) and NFW profile (right-hand panel). The dots are for optical velocities, open circles for HI velocities and crosses for HI in the central part, not taken into account. The arrow on the X-axis indicates the disc scalelength.

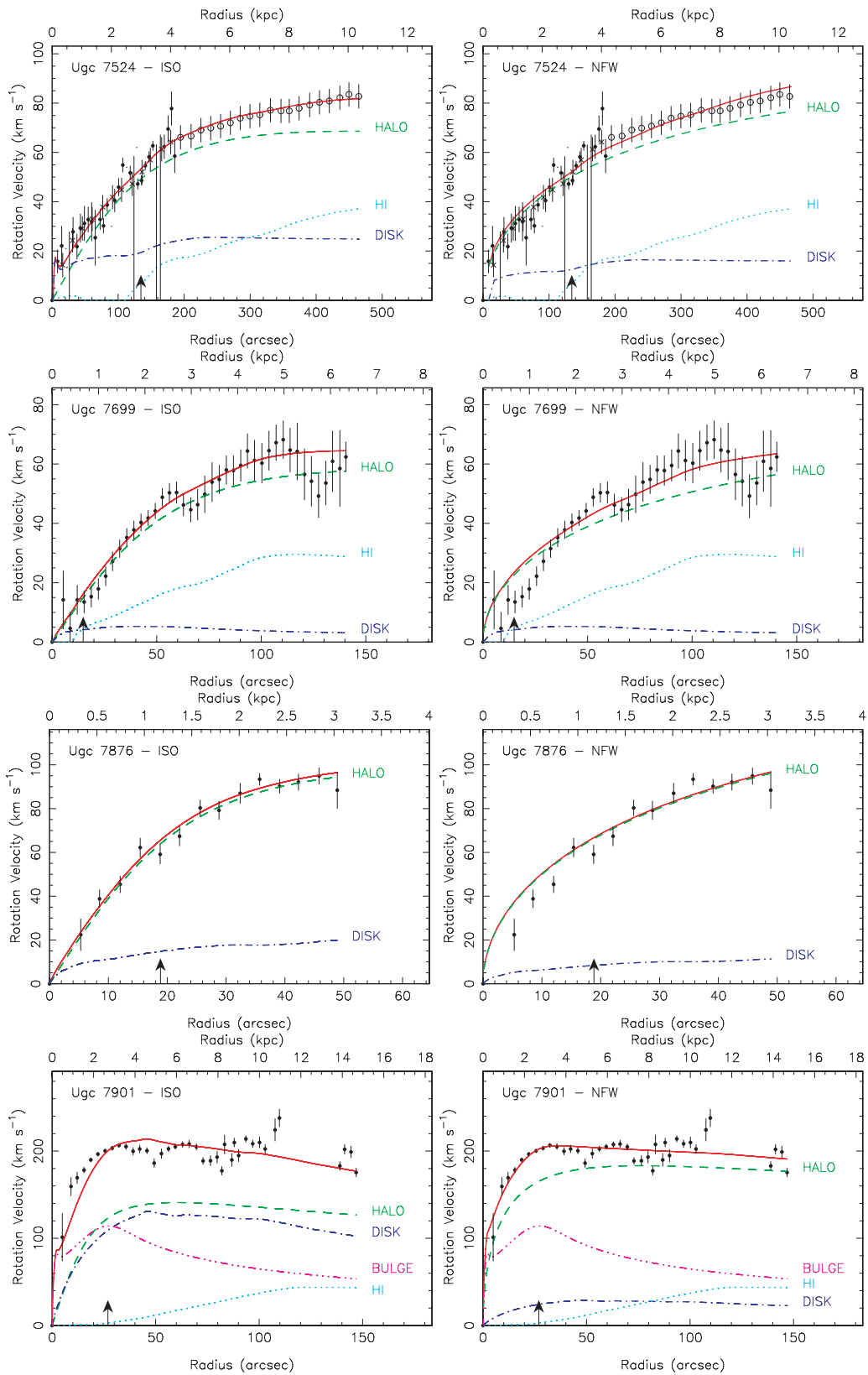


Figure A6. Best-fitting model for the rotation curve of UGC 7524, UGC 7699, UGC 7876 and UGC 7901 with ISO profile (left-hand panel) and NFW profile (right-hand panel). The dots are for optical velocities, open circles for H I velocities and crosses for H I in the central part, not taken into account. The arrow on the X-axis indicates the disc scalelength.

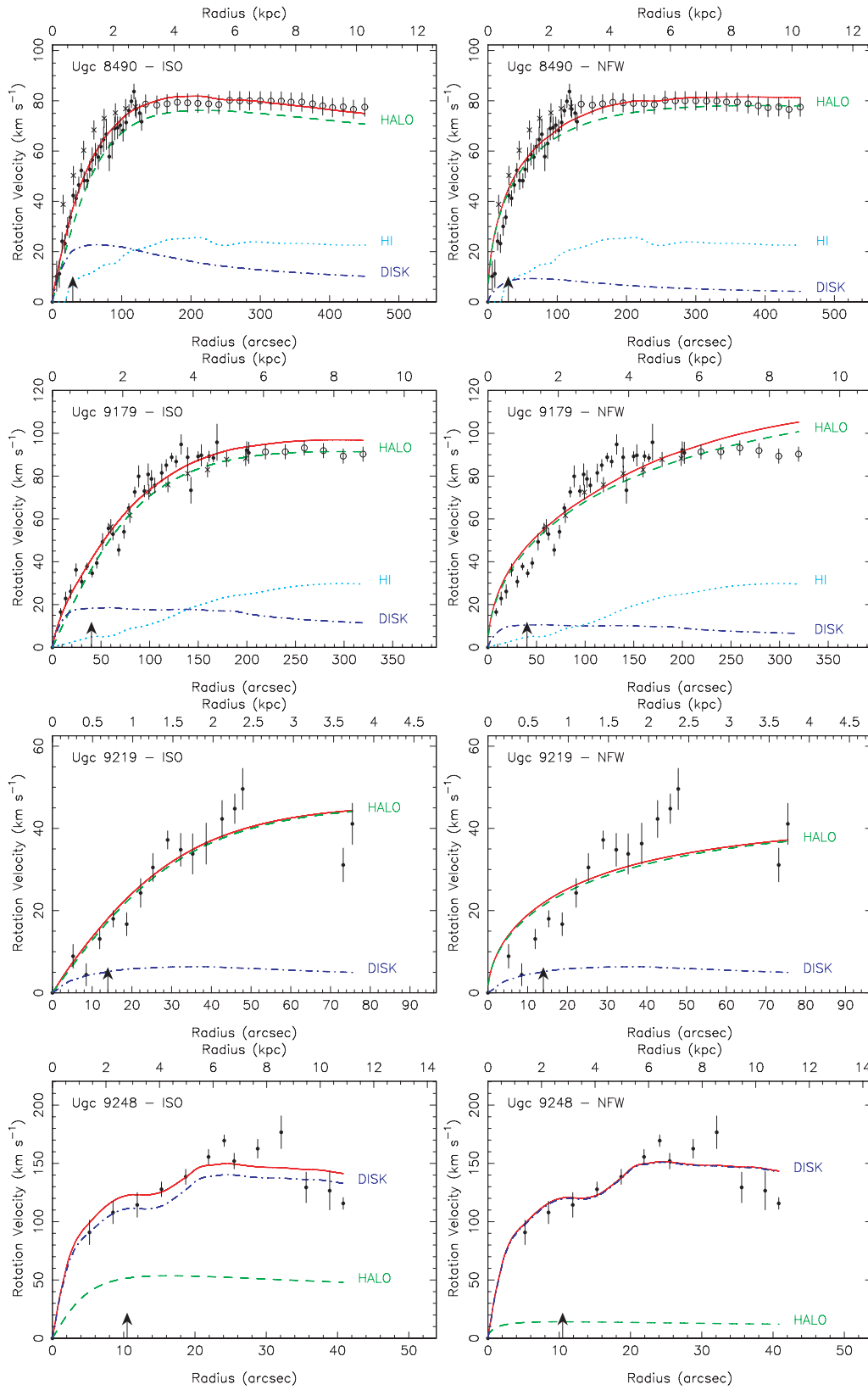
314 *M. Spano et al.*

Figure A7. Best-fitting model for the rotation curve of UGC 8490, UGC 9179, UGC 9219 and UGC 9248 with ISO profile (left-hand panel) and NFW profile (right-hand panel). The dots are for optical velocities, open circles for H I velocities and crosses for H I in the central part, not taken into account. The arrow on the X-axis indicates the disc scalelength.

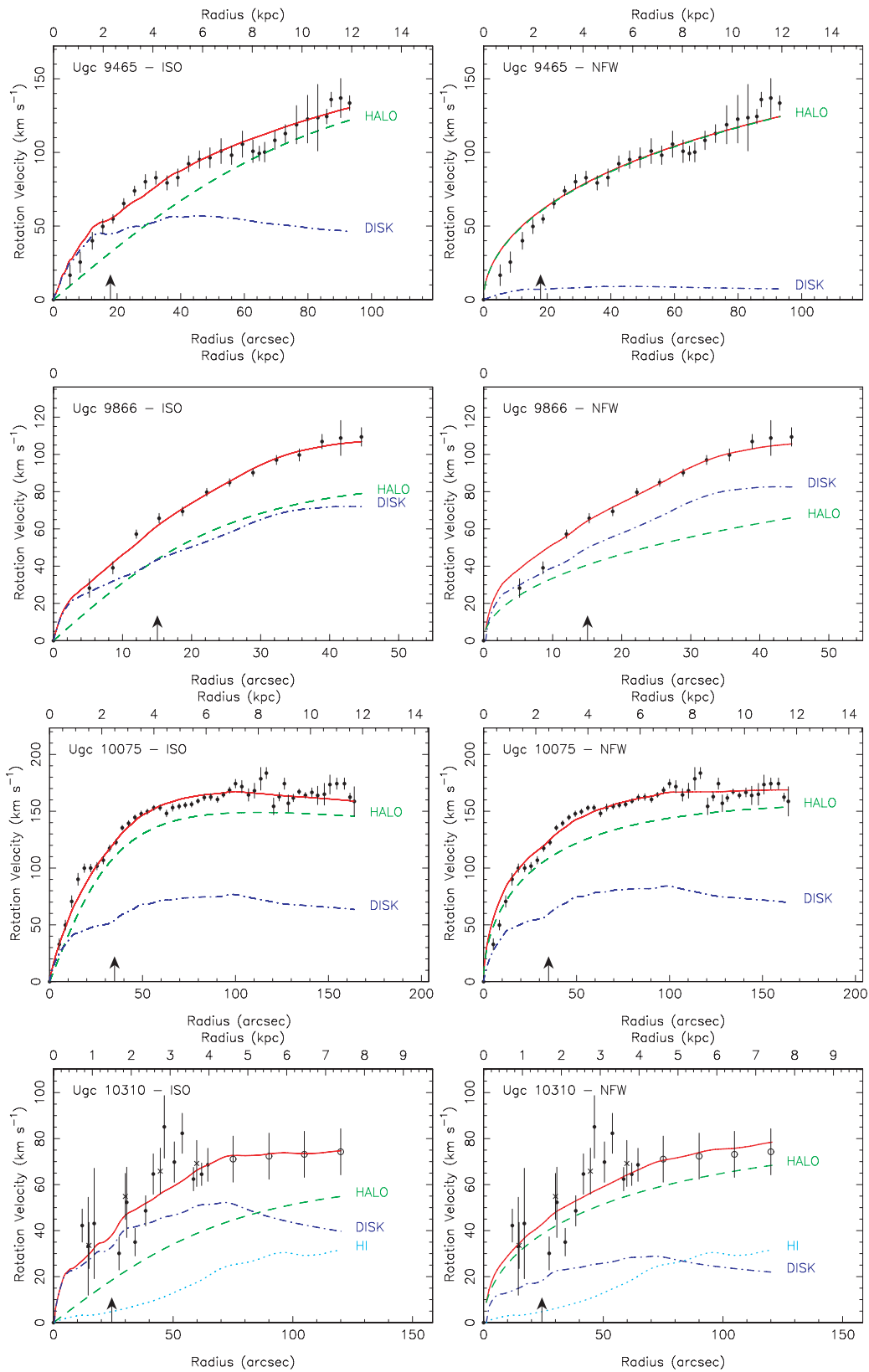


Figure A8. Best-fitting model for the rotation curve of UGC 9465, UGC 9866, UGC 10075 and UGC 10310 with ISO profile (left-hand panel) and NFW profile (right-hand panel). The dots are for optical velocities, open circles for H I velocities and crosses for H I in the central part, not taken into account. The arrow on the X-axis indicates the disc scalelength.

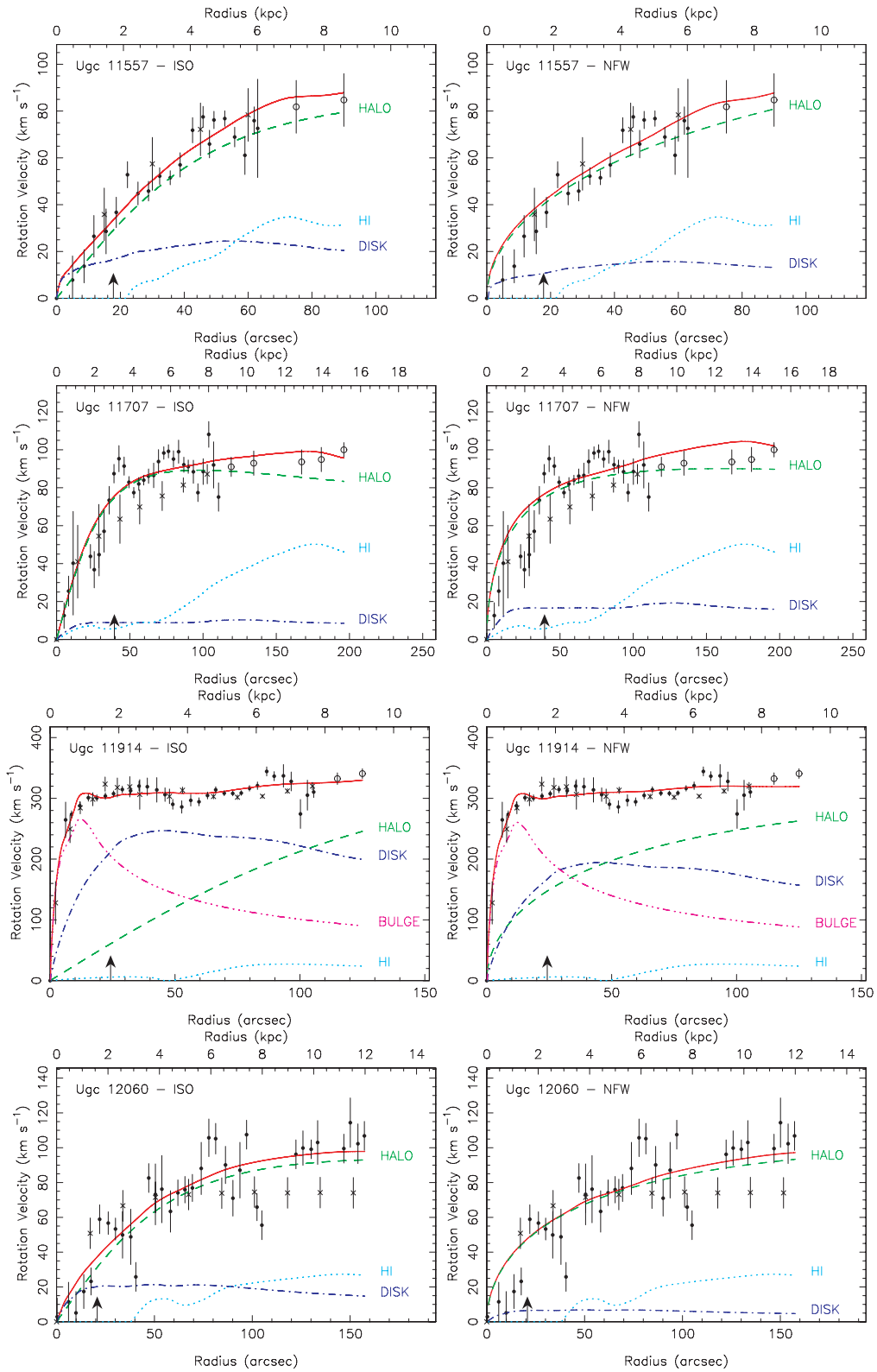


Figure A9. Best-fitting model for the rotation curve of UGC 11557, UGC 11707, UGC 11914 and UGC 12060 with ISO profile (left-hand panel) and NFW profile (right-hand panel). The dots are for optical velocities, open circles for H I velocities and crosses for H I in the central part, not taken into account. The arrow on the X-axis indicates the disc scalelength.

This paper has been typeset from a $\text{T}_{\text{E}}\text{X}/\text{L}_{\text{A}}\text{T}_{\text{E}}\text{X}$ file prepared by the author.

Annexe F

Étude de données à grand décalage spectral (chapitre 3)

Résumé

F.1 Article IX : IMAGES III. The evolution of the near-infrared Tully-Fisher relation over the last 6 Gyr	399
--	------------

Cette annexe contient un article sur des observations à grand décalage spectral auquel j'ai contribué. Cet article présente des résultats concernant la relation de Tully-Fisher obtenus à partir d'observations de galaxies dont le décalage spectral est voisin de 0.6 avec GIRAFFE. Quelques galaxies GHASP projetées de la manière décrite dans la partie 3.4 ont été utilisées afin de vérifier les biais de la méthode de mesure des vitesses de rotation.

F.1 Article IX : IMAGES III. The evolution of the near-infrared Tully-Fisher relation over the last 6 Gyr

Le programme IMAGES (PI : F. Hammer), est un échantillon possédant actuellement 68 galaxies observées à un décalage spectral $z \sim 0.6$ par FLAMES/GIRAFFE dans le visible dont l'objectif est d'étudier l'assemblage de masses des galaxies depuis $z = 1$. Une dizaine de galaxies de l'échantillon GHASP que j'ai projetées à un décalage spectral de 0.6 dans les conditions d'observations de l'échantillon IMAGES (un pixel de $0.52''$ pour un seeing de $0.8''$) ont été utilisées lors d'une étude sur l'évolution de la relation de Tully-Fisher à ce décalage spectral. Cette étude a été publiée dans un journal à comité de lecture¹ (Puech et al., 2008).

À partir d'un échantillon représentatif de 65 galaxies à raies d'émission ($W_0(OII) \geq 15 \text{ \AA}$) observées avec le spectrographe à multiples champs intégraux (multi-IFU) GIRAFFE sur le VLT, nous avons déterminé la relation de Tully-Fisher en bande K (TFR) à $z \sim 0.6$. Nous confirmons que la dispersion observée dans la TFR à $z \sim 0.6$ est due à des galaxies possédant une cinématique anormale, et nous trouvons une forte corrélation entre la complexité de la cinématique des galaxies et la dispersion dans la TFR à laquelle elles contribuent. En ne considérant que les disques en rotation relaxés, la dispersion ainsi que la pente de la TFR ne semblent pas évoluer avec le décalage spectral. Nous détectons

¹Astronomy & Astrophysics

cependant une évolution du point zéro de la TFR en bande K entre $z \sim 0.6$ et $z = 0$ qui impliquerait une augmentation de la luminosité des disques en rotation de 0.66 ± 0.14 mag entre $z \sim 0.6$ et $z = 0$. Les désaccords avec les résultats de Flores et al. (2006, A&A, 455, 107) sont attribués à la fois à l'amélioration de la TFR locale et aux mesures plus précises des vitesses de rotation de l'échantillon distant. Les incertitudes s'expliquent globalement par la relativement basse résolution spatiale des données cinématiques. Puisque la plupart des disques en rotation à $z \sim 0.6$ semblent ne pas être sujets à de futurs épisodes de fusions, leur vitesse de rotation, qui est utilisée comme un traceur de la masse totale des galaxies, ne devrait pas varier de manière significative. Si cette hypothèse est vérifiée, notre résultat implique que les disques en rotation observés à $z \sim 0.6$ convertissent rapidement leur gaz en étoiles, de manière à doubler leur masse stellaire et être ainsi observés sur la TFR à $z = 0$. Les disques en rotation observés sont en effet des galaxies à raies d'émission qui sont soit des pépinières d'étoiles (starbursts) soit des LIRGs, ce qui implique qu'elles ont un fort taux de formation d'étoiles. Pour une fraction significative des disques en rotation, la majeure partie des étoiles se forment en 6 à 8 milliards d'années, ce qui est en bon accord avec les précédentes études concernant l'évolution de la relation masse-métallicité.

IMAGES

III. The evolution of the near-infrared Tully-Fisher relation over the last 6 Gyr[★]

M. Puech^{1,2}, H. Flores², F. Hammer², Y. Yang², B. Neichel², M. Lehnert², L. Chemin², N. Nesvadba², B. Epinat⁵, P. Amram⁵, C. Balkowski², C. Cesarsky¹, H. Dannerbauer⁶, S. di Serego Alighieri⁷, I. Fuentes-Carrera², B. Guiderdoni⁸, A. Kembhavi³, Y. C. Liang⁹, G. Östlin¹⁰, L. Pozzetti⁴, C. D. Ravikumar¹¹, A. Rawat^{2,3}, D. Vergani¹², J. Vernet¹, and H. Wozniak⁸

¹ ESO, Karl-Schwarzschild-Strasse 2, 85748 Garching bei München, Germany
 e-mail: mpuech@eso.org

² GEPI, Observatoire de Paris, CNRS, University Paris Diderot, 5 Place Jules Janssen, 92190 Meudon, France

³ Inter-University Centre for Astronomy and Astrophysics, Post Bag 4, Ganeshkhind, Pune 411007, India

⁴ INAF – Osservatorio Astronomico di Bologna, via Ranzani 1, 40127 Bologna, Italy

⁵ Laboratoire d’Astrophysique de Marseille, Observatoire Astronomique de Marseille-Provence, 2 Place Le Verrier, 13248 Marseille, France

⁶ MPA, Königstuhl 17, 69117 Heidelberg, Germany

⁷ INAF – Osservatorio Astrofisico di Arcetri, Largo Enrico Fermi 5, 50125 Florence, Italy

⁸ Centre de Recherche Astronomique de Lyon, 9 Avenue Charles André, 69561 Saint-Genis-Laval Cedex, France

⁹ National Astronomical Observatories, Chinese Academy of Sciences, 20A Datun Road, Chaoyang District, Beijing 100012, PR China

¹⁰ Stockholm Observatory, AlbaNova University Center, Stockholms Center for Physics, Astronomy and Biotechnology, Roslagstullsbacken 21, 10691 Stockholm, Sweden

¹¹ Department of Physics, University of Calicut, Kerala 673635, India

¹² IASF – INAF, via Bassini 15, 20133 Milano, Italy

Received 21 December 2007 / Accepted 17 March 2008

ABSTRACT

Using the multi-integral field spectrograph GIRAFFE at VLT, we have derived the *K*-band Tully-Fisher relation (TFR) at $z \sim 0.6$ for a representative sample of 65 galaxies with emission lines ($W_0(\text{OII}) \geq 15 \text{ \AA}$). We confirm that the scatter in the $z \sim 0.6$ TFR is caused by galaxies with anomalous kinematics, and find a positive and strong correlation between the complexity of the kinematics and the scatter that they contribute to the TFR. Considering only relaxed-rotating disks, the scatter, and possibly also the slope, of the TFR, do not appear to evolve with redshift. We detect an evolution of the *K*-band TFR zero point between $z \sim 0.6$ and $z = 0$, which, if interpreted as an evolution of the *K*-band luminosity of rotating disks, would imply that a brightening of $0.66 \pm 0.14 \text{ mag}$ occurs between $z \sim 0.6$ and $z = 0$. Any disagreement with the results of Flores et al. (2006, A&A, 455, 107) are attributed to both an improvement of the local TFR and the more detailed accurate measurement of the rotation velocities in the distant sample. Most of the uncertainty can be explained by the relatively coarse spatial-resolution of the kinematical data. Because most rotating disks at $z \sim 0.6$ are unlikely to experience further merging events, one may assume that their rotational velocity, which is taken as a proxy of the total mass, does not evolve dramatically. If true, our result implies that rotating disks observed at $z \sim 0.6$ are rapidly transforming their gas into stars, to be able to double their stellar masses and be observed on the TFR at $z = 0$. The rotating disks observed are indeed emission-line galaxies that are either starbursts or LIRGs, which implies that they are forming stars at a high rate. Thus, a significant fraction of the rotating disks are forming the bulk of their stars within 6 to 8 Gyr, in good agreement with former studies of the evolution of the mass-metallicity relationship.

Key words. galaxies: evolution – galaxies: kinematics and dynamics – galaxies: high-redshift – galaxies: general – galaxies: interactions – galaxies: spiral

1. Introduction

Since the first rotation curves were measured at intermediate redshifts (Vogt et al. 1993), many studies have been devoted to the evolution of the Tully-Fisher Relation (TFR, Tully & Fisher 1977), given its prominent role in constraining galaxy-formation models (e.g., Dutton et al. 2007). Early work using *B*-band imaging found only modest luminosity evolution (Vogt et al. 1996, 1997), but subsequent studies using data of the same band have

suggested a more significant evolution (Simard & Pritchett 1998; Bamford et al. 2006; Weiner et al. 2006; Chiu et al. 2007). In almost all of these studies, the *B*-band TFR shows a large dispersion in comparison with the local relation, especially at the low-luminosity (or velocity) end (e.g., Böhm et al. 2004). Böhm & Ziegler (2007) showed that this effect could be attributed to an incompleteness in magnitude provided that the scatter decreased by a factor of at least three between $z \sim 0.5$ and $z = 0$, with no evolution of slope or zero point. Alternatively, they proposed a possible luminosity-dependent evolution, in which distant low-luminosity galaxies would have lower mass-to-light ratios [M/L]

[★] Intermediate MAss Galaxy Evolution Sequence, ESO programs 174.B-0328(A), 174.B-0328(E).

than their local counterparts, while higher-luminosity galaxies would not undergo strong M/L evolution. Therefore, the situation for B -band data remains unclear, particularly concerning the large scatter in measurements found at high redshift.

To minimize observational biases and enable easier comparisons with models, a progressive interest has been devoted to the K -band and stellar-mass TFRs (hereafter, smTFR). Long-slit spectroscopy of distant galaxies revealed an smTFR of significant scatter, with detectable evolution of neither zero point nor slope, up to $z \sim 1$ (Conselice et al. 2005). This much larger dispersion appears to be linked to “kinematically anomalous galaxies”, as inferred from local studies (Kannappan & Barton 2004), or, from a morphological point of view, with disturbed, compact, or merging galaxies (Kassin et al. 2007; Atkinson et al. 2007). Weiner et al. (2006) and Kassin et al. (2007) defined a new tracer of the galaxy dark-halo potential called S , which corrects the rotation velocity for disordered, non-circular motions. Once expressed using this new kinematical estimator, the distant smTFR shows significantly-reduced scatter, with no detectable evolution in either zero point or slope. This suggests an important role of non-ordered motions in increasing the scatter of the distant TFR.

In this respect, 3D spectroscopy provides a unique way to distinguish relaxed rotating disks from other kinematically-disturbed galaxies. Kinematically-selected relaxed (or pure) rotating disks at $z \sim 0.6$ present a TFR that appears to evolve neither in slope, zero point, nor *dispersion* (Flores et al. 2006): kinematically-anomalous galaxies, which range from perturbed rotators where a rotation can be detected to galaxies with complex kinematics but no noticeable rotation, appear to be responsible for the increased scatter of the distant TFR. Therefore, 3D spectroscopy allows us to establish a direct connection between non-ordered motions and kinematical and morphological anomalies. In this paper, we double the sample previously available (see Yang et al. 2007, hereafter Paper I) to test robustly the results obtained in Flores et al. (2006).

This paper is organized as follows: Sect. 2 introduces the data used in this study; Sect. 3 details the methodology used for the analysis; Sect. 4 presents the K -band TFR obtained from GIRAFFE data, and Sect. 5 draws the conclusions from this work. In the Appendix, we derive the stellar-mass TFR in the GIRAFFE sample. Throughout, we adopt $H_0 = 70 \text{ km s}^{-1} \text{ Mpc}^{-1}$, $\Omega_M = 0.3$, and $\Omega_\Lambda = 0.7$, and the AB magnitude system.

2. Data

2.1. Distant sample

2.1.1. Kinematics

We used the multi-object integral field spectrograph FLAMES-GIRAFFE at VLT, to obtain the [OII] spatially-resolved kinematics of a sample of 68 galaxies at $0.4 \leq z \leq 0.75$. The median redshift of the sample was $z_{\text{med}} \sim 0.61$, which corresponds to a look-back time ~ 5.8 Gyr, while the 25 and 75 percentiles of the redshift distribution are $z_{25} \sim 0.49$ and $z_{75} \sim 0.67$. This sample represents well the luminosity function of $z \sim 0.6$ galaxies with stellar masses $[M_{\text{stellar}}]$ in the $1.5\text{--}15 \times 10^{10} M_\odot$ range, and is unaffected by field-to-field variations within Poisson statistics, as targets were observed in four different fields (see Paper I).

Flores et al. (2006) and Paper I used GIRAFFE velocity fields [VF] and velocity dispersion maps [σ -maps], to define three kinematical classes, namely the *rotating disks* [RD], which correspond to relaxed rotators, the *perturbed rotators* [PR], corresponding to rotating disks showing some weak disturbances,

and *kinematically-complex* [CK] galaxies, corresponding to dynamically non-relaxed galaxies, probably associated with major mergers (see also Puech et al. 2006a, 2007a). This classification takes into account the residuals between the observed VF and σ -map and those predicted by a rotating-disk model (see Paper I), which mitigates the subjectivity of a fully visual classification.

2.1.2. Morphology

A detailed morphological analysis of a subsample of 52 galaxies, which had multi-band HST/ACS imaging data, was completed by Neichel et al. (2008, hereafter, Paper II). They found a good agreement between both kinematical and morphological classifications. Only 16% of galaxies in this subsample are both kinematically-classified as RDs and morphologically-classified as spirals. These “rotating spiral disks” were selected to have a redder bulge than the disk and to be therefore quite similar to local spirals, apart their much bluer integrated colors and [OII] equivalent widths (see Paper II, for a detailed discussion). Furthermore, they showed no special trend in size nor in Bulge-to-Total luminosity ratio $[B/T]$ compared to local galaxies, and we do not expect any bias in the distant TFR that could be due to morphological variation of the TFR along the Hubble Sequence (see, e.g., Russell 2004). In the following, we use the inclinations $[i]$ and half light radii $[R_{\text{half}}]$ derived in Paper II.

The comparison between kinematics and morphology revealed two special cases of RDs. First, J033230.78-275455.0 was detected in emission only on one half of the galaxy, which was caused by the superposition of a skyline on an [OII] emission line. This galaxy was classified as a RD, but the amplitude of its VF is affected by large uncertainty. Second, J033241.88-274853.9 was classified as a Tadpole galaxy in Paper II because of its highly-asymmetric shape. In the following (see Sect. 3.2), we assume that all RD flux distributions can be approximated by an exponential disk, which, obviously, does not apply to this galaxy. Therefore, in this paper, “RDs” refers to galaxies classified as rotating disks in Paper I *excluding* J033230.78-275455.0 and J033241.88-274853.9, while “RD+” refers to all RDs *including* J033230.78-275455.0 and J033241.88-274853.9.

2.1.3. Absolute K -band magnitudes

Absolute K -band magnitudes M_K were taken from Flores et al. (2006) and Ravikumar et al. (2007). They were derived using Bruzual & Charlot 2001 stellar-population models, assuming a CSP template with solar metallicity and an exponential star-formation history with $\tau = 0.5$ Gyr, which describes the properties of most galaxies between $z = 0.4$ and 1 (Hammer et al. 2001). For each galaxy, an optimal SED was found by matching the observed $J - K$ color. This method was preferred to complete SED fitting because 50% of the selected galaxies, from the CFRS and the HDFs, did not have similar multiwavelength photometric data to galaxies in the remaining 50%, which were selected from the CDFS; SED fitting would, therefore, not have been able to measure an M_K of similar quality for all galaxies studied. We compared, for galaxies from the CDFS, the impact of this simple “color-matching” method relatively to a full SED fitting (using optical photometry only): we found an excellent agreement between J -band absolute magnitudes with a $1\text{-}\sigma$ dispersion ~ 0.01 mag, and no systematic effect (Hammer & Pozzetti, private communication). We compared absolute J -band and not K -band magnitudes because whatever the method used,

these are not extrapolations. A potential drawback of the “color-matching” method is that M_K is extrapolated, since the reddest photometric point used is the observed K -band, which falls roughly in the middle of the rest-frame J and H band at $z \sim 0.6$. For galaxies in the CDFS, IRAC 3.6 μm fluxes were publicly available, which allowed us to compare the M_K obtained using this method with those obtained taking into account the IR 3.6 μm flux: we found a residual $1 - \sigma$ dispersion of 0.12 mag between both estimates, with no systematic effect. Using two independent photometric datasets for galaxies in the CDFS (i.e., EIS and ACS), we derived a random uncertainty of $\lesssim 0.2$ mag on M_K , with no noticeable systematic uncertainties. Therefore, we adopted a random uncertainty of 0.2 mag and neglected systematic uncertainties.

Absolute magnitudes were corrected for internal extinction, using the mass-dependent method of Tully et al. (1998). We applied an additional correction of 0.04 mag that accounted for extinction in face-on galaxies (Tully et al. 1998, 1985). We note that within the sample of 68 objects, three do not have NIR photometry (see Table 1).

2.1.4. Summary

For the distant sample, all measurements used are listed in Table 1. The columns of the table are as follows: (1) IAU ID, (2) Internal ID, (3) Redshift z , (4) Inclination i (in deg, ± 5 deg, see Sect. 2.1.2), (5) Dynamical Class D.C., (6) Projected radial velocity $\Delta V_{\text{obs}} \sin(i)$ (in km s^{-1} , see Sect. 3.1), (7) Rotation velocity corrected for inclination and spatial-resolution effects V_{flat} (in km s^{-1} , see Sect. 3.1), (8) Total uncertainty in V_{flat} (in km s^{-1} , see Sect. 3.4), (9) Absolute K -band magnitude M_K (uncorrected for extinction), (10) Absolute K -band magnitude M_K^c corrected for extinction (± 0.2 mag, see Sect. 2.1.3), and (11) Stellar mass in $\log(M_{\text{stellar}}/M_{\odot})$ (± 0.3 dex, see Appendix A).

2.2. Local sample

As a local reference, we adopt the K -band TFR derived by Hammer et al. (2007) for a complete subsample of the SDSS (Pizagno et al. 2007), which allows us to control systematic effects that can occur when comparing local and distant samples.

One important choice for studying the TFR is the kinematic estimator used for the rotation velocity V_{rot} . Studies of the local TFR have shown that using different estimators (e.g., the maximal rotation velocity V_{max} , the plateau rotation curve velocity V_{flat} , the velocity measured at the radius containing 80% of the light V_{80} , and the velocity $V_{2.2}$ measured at 2.2 disk scale length) can lead to different results (see, e.g., Verheijen 2001; Pizagno et al. 2007). V_{flat} has been shown to be correlated with V_{rot} , since it is less influenced by the bulge dynamics, which can produce a central “bump” with $V_{\text{max}} > V_{\text{flat}}$. This can then lead to a tighter TF relation (e.g., Verheijen 2001), and a significant improvement in the linearity of the K -band relation at the high-mass end (Noordermeer & Verheijen 2007). For the local sample, we adopted the V_{80} measurements of Pizagno et al. (2007) using arctan fits to the RCs. To limit uncertainties, we restricted the local sample to galaxies for which V_{80} is a good proxy for V_{flat} (i.e., Pizagno et al. 2007, flags 1 and 2), as shown by Hammer et al. (2007).

Rotation velocities were corrected for inclination using estimates derived from their morphological axis ratio. When well-resolved 2D kinematics is available, it is possible to derive the inclination directly from the fit of the VF. However, large

differences (up to ~ 10 deg) can be found between such kinematically-derived inclinations and the ones inferred from the morphological axis ratio (e.g., Chemin et al. 2006). Since we do not have 2D kinematics for galaxies in the local sample, we use morphologically-derived inclinations exclusively. This provides us with homogeneous estimates for the local and distant samples, since in the latter we also use such inclinations.

Hammer et al. (2007) combined the Pizagno et al. (2007) kinematic measurements with 2MASS K_s -photometry. We estimated absolute magnitudes in the local sample following a similar method to that used for the distant sample, including corrections for extinctions (see Sect. 2.1.3). The 2MASS K_s filter has the advantage of being close to the ISAAC K_s filter used in the distant sample. Both filters match well the K -band LCO filter designed to establish the faint IR standard-star system of Persson et al. (1998) (Mason et al. 2007; Carpenter 2001). We assumed that both filters are identical during the SED-fitting procedure, which did not introduce any systematic effect. We note that 2MASS K -band magnitudes were converted into AB magnitudes using $K_s(\text{AB}) = K_s(\text{Vega}) + 1.85$, following Blanton et al. (2005).

Since we are exploring the higher tail of the stellar-mass distribution and the TFR is highly sensitive to stellar mass (see, e.g., McGaugh 2005), we restrict the K -band TFR to $\log(V_{\text{flat}}) \geq 2.2$ and find from Hammer et al. (2007):

$$M_K(\text{AB}) = -6.54 \pm 1.33 - (6.88 \pm 0.57) \times \log(V_{\text{flat}}), \quad (1)$$

with a residual dispersion $\sigma_{\text{res}} = 0.38$ mag. Since we used uniform M_K error bars, we used direct fits to the TFR, i.e., with M_K as a V_{flat} -dependent variable (using the IDL MPFITFUN procedure of Markwardt, translated from the MINPACK-1 package¹).

3. Methodology

3.1. Derivation of the rotation velocity

For each galaxy, we estimated the deprojected VF half-amplitude using $\Delta V_{\text{obs}} = (V_{\text{max}}^{\text{IFU}} - V_{\text{min}}^{\text{IFU}})/(2 \sin(i))$, where $V_{\text{max}}^{\text{IFU}}$ and $V_{\text{min}}^{\text{IFU}}$ are respectively the maximal and minimal values of the VF sampled by the IFU (see Table 1).

Because of the influence of the relatively coarse spatial-resolution of the kinematic data, ΔV_{obs} underestimates the true rotation velocity V_{rot} (see Flores et al. 2006; Puech et al. 2006a). Rather than applying a mean correction factor to the entire sample as in Flores et al. (2006), we corrected each galaxy *individually* by modeling its data-cube. We used a method developed from that used by Flores et al. (2006) and in Paper I, to model the σ -map. Assuming that all galaxies are thin-rotating disks, we modeled their data-cube, from their observed VF and σ -map, in the following way.

First, for each galaxy, we constructed a grid of rotation curves (RC) with V_{rot} spaced at 10 km s^{-1} intervals, which roughly corresponded to the typical uncertainty in ΔV_{obs} (see Sect. 3.4). Because of a lack of spatial resolution, the precise shape of distant RCs remains largely unknown. Therefore, we chose a simple arctan defined as $V_0 \times (2/\pi) \times \arctan(r/r_t)$, which depends only on two parameters, i.e., the asymptotic velocity V_0 , and the “turnover” radius r_t (see, e.g., Courteau 1997). This RC shape was used in Paper I to model the VF of each distant galaxy. In the RD+ subsample, such models provided good matches to the observed VFs, which demonstrated that such a

¹ <http://cow.physics.wisc.edu/~craigm/idl/mpfittut.html>

Table 1. Principle properties of the sample of 68 galaxies used in this study, ordered by increasing RA (see text).

IAU ID	Internal ID	z	i	DC	$\Delta V_{\text{obs}} \sin(i)$	V_{flat}	ΔV_{flat}	M_K	M_K^c	$\log(M_{\text{stellar}}/M_{\odot})$
J030225.28+001325.1	CFRS030085	0.6100	71	RD	127	170	23	-20.83	-20.98	10.21
J030228.72+001333.9	CFRS030046	0.5120	66	RD	148	200	29	-21.68	-21.82	10.64
J030232.16+000639.1	CFRS039003	0.6189	29	RD	110	290	79	99.99	99.99	99.99
J030238.74+000611.5	CFRS031032	0.6180	37	PR	83	200	36	-22.64	-22.70	11.00
J030239.38+001327.1	CFRS030523	0.6508	41	CK	63	130	38	-21.55	-21.61	10.48
J030240.45+001359.4	CFRS030508	0.4642	38	CK	47	100	40	-20.34	-20.40	10.00
J030240.99+000655.4	CFRS031016	0.7054	67	CK	15	30	25	-21.24	-21.25	10.37
J030242.19+001324.3	CFRS030488	0.6069	41	CK	36	70	36	-20.84	-20.89	10.20
J030245.67+001027.9	CFRS030645	0.5275	45	CK	89	150	38	-21.34	-21.42	10.40
J030246.94+001032.6	CFRS030619	0.4854	27	RD	70	210	76	-21.93	-21.99	10.63
J030248.41+000916.5	CFRS031353	0.6340	57	RD	174	260	41	-22.42	-22.54	10.85
J030249.10+001002.1	CFRS031349	0.6155	48	PR	175	290	46	-22.92	-23.01	11.04
J030252.03+001033.4	CFRS031309	0.6170	71	CK	84	150	22	-22.91	-23.05	11.03
J033210.25-274819.5	CDFS4301297	0.6100	69	PR	110	150	26	-20.83	-20.96	10.29
J033210.76-274234.6	CDFS4402679	0.4180	26	CK	186	550	123	-23.62	-23.68	11.44
J033212.39-274353.6	CDFS3400803	0.4230	90	RD	105	180	22	-21.55	-21.85	10.61
J033213.06-274204.8	CDFS3500001	0.4220	79	CK	90	130	22	-20.56	-20.73	10.19
J033214.97-275005.5	CDFS3300063	0.6680	22	PR	62	190	90	-22.45	-22.50	10.92
J033217.62-274257.4	CDFS3401109	0.6470	46	CK	131	250	43	-21.15	-21.24	10.38
J033219.32-274514.0	CDFS3400329	0.7250	72	CK	116	270	29	-21.16	-21.36	10.39
J033219.61-274831.0	CDFS3300651	0.6710	49	PR	82	190	33	-20.90	-20.98	10.27
J033219.68-275023.6	CDFS3202670	0.5610	58	RD	161	230	33	-22.30	-21.42	10.88
J033220.48-275143.9	CDFS3202141	0.6790	63	CK	39	70	24	-20.63	-20.70	10.18
J033224.60-274428.1	CDFS3400618	0.5380	65	CK	63	90	27	-20.35	-20.44	10.08
J033225.26-274524.0	CDFS3400279	0.6660	60	CK	47	80	26	-21.54	-21.61	10.56
J033226.23-274222.8	CDFS3401338	0.6679	76	PR	150	200	24	-21.93	-22.13	10.72
J033227.07-274404.7	CDFS3400743	0.7390	84	CK	71	110	21	-20.95	-21.15	10.26
J033228.48-274826.6	CDFS3300684	0.6697	22	CK	23	130	66	-21.68	-21.73	10.63
J033230.43-275304.0	CDFS2200433	0.6460	70	CK	219	380	29	-21.68	-21.90	10.64
J033230.57-274518.2	CDFS2400243	0.6810	34	CK	41	80	46	-22.86	-22.91	11.08
J033230.78-275455.0	CDFS2102060	0.6870	66	RD+	90	200	43	-21.82	-21.96	10.66
J033231.58-274121.6	CDFS2500322	0.7047	42	RD	81	140	41	-20.51	-20.57	10.10
J033232.96-274106.8	CDFS2500425	0.4690	16	PR	31	210	117	-20.13	-20.17	10.01
J033233.90-274237.9	CDFS2401349	0.6190	17	PR	46	200	107	-21.82	-21.96	10.66
J033234.04-275009.7	CDFS2300055	0.7030	59	RD	104	160	29	-20.50	-20.60	10.09
J033234.12-273953.5	CDFS2500971	0.6280	32	CK	25	110	44	99.99	99.99	99.99
J033237.54-274838.9	CDFS2300477	0.6650	31	RD	106	230	71	-21.98	-22.03	10.70
J033238.60-274631.4	CDFS2301047	0.6220	60	RD	118	210	33	-21.45	-21.57	10.53
J033239.04-274132.4	CDFS2500233	0.7330	43	PR	58	130	39	-20.62	-20.68	10.14
J033239.72-275154.7	CDFS2200829	0.4160	35	CK	16	30	36	-20.94	-20.98	10.31
J033240.04-274418.6	CDFS2400536	0.5223	16	CK	108	470	214	-21.95	-22.00	10.77
J033241.88-274853.9	CDFS2300404	0.6680	67	RD+	80	120	27	-20.90	-21.01	10.27
J033243.62-275232.6	CDFS2200611	0.6800	71	PR	38	60	23	-19.94	-20.01	9.86
J033244.20-274733.5	CDFS2300750	0.7365	39	CK	46	170	40	-21.76	-21.83	10.62
J033245.11-274724.0	CDFS2300800	0.4360	43	RD	95	270	44	-22.03	-22.11	10.80
J033248.28-275028.9	CDFS1202537	0.4462	81	PR	76	110	22	-20.38	-20.54	10.09
J033249.53-274630.0	CDFS1302369	0.5230	46	PR	74	150	39	-21.00	-21.07	10.34
J033250.24-274538.9	CDFS1400714	0.7318	31	CK	82	240	67	-20.59	-20.65	10.12
J033250.53-274800.7	CDFS1301018	0.7370	62	PR	71	110	26	-20.34	-20.43	10.01
J221741.46+001854.8	CFRS221119	0.5138	41	RD	135	250	47	99.99	99.99	99.99
J221743.08+001508.3	CFRS221064	0.5383	48	PR	93	250	29	-21.64	-22.74	10.53
J221745.12+001447.4	CFRS220975	0.4211	50	CK	313	410	44	-22.53	-22.64	10.95
J221746.48+001653.5	CFRS220919	0.4738	60	CK	39	30	23	-19.53	-19.55	9.67
J221754.56+001900.3	CFRS220619	0.4676	68	PR	62	90	24	-19.33	-19.42	9.63
J221758.07+002137.5	CFRS220504	0.5379	42	RD	93	170	42	-21.36	-21.43	10.43
J221802.92+001428.0	CFRS220321	0.4230	42	PR	104	220	46	-20.79	-20.87	10.21
J221803.55+002131.9	CFRS220293	0.5420	45	CK	89	160	40	-20.89	-20.97	10.24

Table 1. continued.

IAU ID	Internal ID	z	i	DC	$\Delta V_{\text{obs}} \sin(i)$	V_{flat}	ΔV_{flat}	M_K	M_K^c	$\log(M_{\text{stellar}}/M_{\odot})$
J223241.45-603516.1	HDFS4130	0.4054	36	CK	90	220	53	-22.13	-22.20	10.76
J223245.56-603418.8	HDFS4170	0.4602	51	RD	134	230	37	-22.60	-22.70	10.96
J223252.74-603207.3	HDFS4040	0.4650	51	PR	75	120	32	-20.04	-20.11	9.88
J223254.05-603251.6	HDFS4090	0.5162	45	CK	14	20	30	-19.83	-19.85	9.80
J223256.07-603148.8	HDFS4020	0.5138	50	RD	88	140	36	-20.12	-20.20	9.96
J223256.08-603414.1	HDFS5140	0.5649	50	CK	171	220	42	-20.46	-20.56	10.04
J223257.52-603305.9	HDFS5030	0.5821	25	CK	31	130	69	-22.68	-22.73	10.94
J223258.01-603525.9	HDFS4180	0.4647	64	RD	104	140	26	-20.38	-20.49	10.04
J223258.23-603331.4	HDFS4070	0.4230	40	CK	36	70	43	-19.67	-19.72	9.75
J223300.09-603529.9	HDFS5190	0.6952	59	RD	144	230	23	-21.92	-22.04	10.64
J223302.45-603346.5	HDFS5150	0.6956	42	PR	51	120	39	-21.02	-21.09	10.27

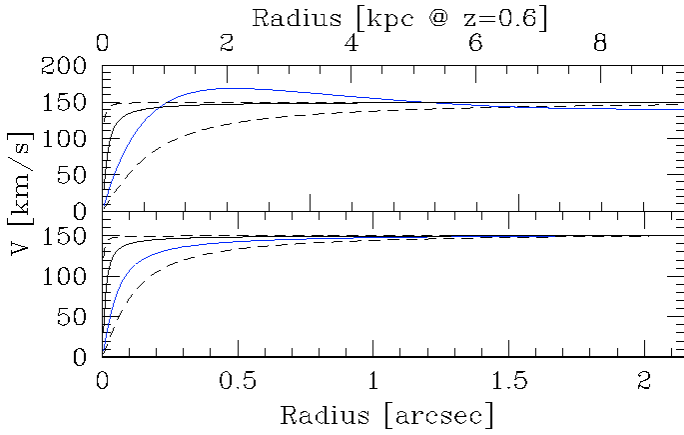


Fig. 1. Illustration of the ΔV_{obs} correction method, for an early-type RC (*upper panel*, note that $V_{\text{max}} > V_{\text{flat}}$) and a late-type RC (*bottom panel*). The blue thick curves represent the input RC of the test, the black curves the best models (see text), and the dash-lines the two alternative RCs with non-optimal r_t . We note that typical r_t values lead to velocity gradients on spatial scales that are much smaller than the typical seeing of ~ 0.8 arcsec.

RC shape is a reasonable choice. The same shape was adopted in the local sample (see Sect. 2.2), which provided us with homogeneous estimates of the rotation velocity in both the local and distant samples. We chose not to fit a wide range of values for r_t because a visual inspection of VFs revealed that for almost all RDs, the gradient of the RC fell inside a single GIRAFFE IFU pixel (Flores et al. 2006 and Paper I). We therefore explored only three fixed values for r_t (see Fig. 1), which allowed us to investigate more extreme cases where the RC is relatively steep or, in contrast, relatively flat.

The arctan RC model cannot reproduce the central “bump” observed in some early-type galaxies (see, e.g., Fig. 1). Given the coarse spatial resolution of the GIRAFFE IFU (0.52 arcsec/pix, i.e., ~ 3.5 kpc at $z = 0.6$) and the large size of the seeing disk compared to the typical scalelengths of distant galaxies, it might however be impossible to distinguish clearly between V_{max} or V_{flat} in distant galaxies. It might be expected that the asymptotic velocity V_0 , corresponding to an arctan RC, is probably, in this case, an average value between V_{max} and V_{flat} . Because we rely on V_{flat} as a kinematic measure of the rotation velocity in the local sample (see Sect. 2.2), we are naturally led to quantify all random and systematic uncertainties relative to V_{flat} . Finally, we note that even for late-type RCs, $V_0 \sim V_{\text{flat}}$

only if the RC has a well-defined plateau and if this plateau can be observed in terms of spatial coverage or SNR.

From each RC, a high-resolution data-cube was constructed, assuming a simple Gaussian shape for the emission line. For simplicity, we did not include noise in the simulations, assuming that the global uncertainty can be derived by estimating separately the influence of the noise and other effects (see Sect. 3.4). As a consequence, neglecting the doublet spectral nature of the [OII] emission line should not impact severally the results. The velocity width was assumed to be the minimal value observed in the σ -map, and the emission-line flux was taken from an exponential flux distribution, assuming $R_d \sim R_{\text{half}}/1.6$ (Persic & Salucci 1991) and limiting the spatial extent to a radius $2R_{\text{half}} \sim 3R_d \sim R_{\text{opt}}$, where R_d is the disk scale-length, and R_{opt} is the optical radius. We chose to use R_{half} rather than direct R_d measurements because more than 80% of galaxies in the sample were not classified as simple spirals but had more complex morphologies (see Paper II), which could lead to meaningless R_d values. In contrast, R_{half} provides us with a uniform and well-defined size-parameter, which can be safely converted into R_d for thin exponential disks: using the bulge/disk decomposition of the RD subsample done in Paper II, we compared R_d with $R_{\text{half}}/1.6$, and found a *maximal* difference of ~ 0.1 arcsec, which is much smaller than the typical seeing during the observations (see also Puech et al. 2007a). Thus, such an error in R_d has little influence on the model, and we chose not to explore this parameter.

Each high-resolution data-cube was convolved by a 0.8 arcsec seeing, which corresponded to the median condition of the observations, and then rebinned to the GIRAFFE sampling, i.e., 0.52 arcsec/pix. From these simulated GIRAFFE data-cubes, simulated VFs and simulated ΔV_{model} were derived as for real GIRAFFE data. We checked the influence of changing the seeing from 0.8 to 1.0 arcsec, on the ΔV_{model} : using Monte-Carlo simulations of 100 GIRAFFE data-cubes (see next section), we found a good linear correlation between the ΔV_{model} obtained for a 1 arcsec seeing and that obtained for a 0.8 arcsec seeing, all other properties being equal. This fit indicated that for a 1 arcsec seeing, ΔV_{model} was reduced by $\sim 0.05\%$ compared to that obtained for a 0.8 arcsec seeing (see Fig. 2). Therefore, the maximal uncertainty on ΔV_{model} due to seeing variations is $\sim 12 \text{ km s}^{-1}$, which corresponds roughly to the velocity spacing adopted for the searching grid used to correct ΔV_{obs} (see above), which implies that this velocity grid was well adapted for our purpose.

To find the best model, we finally looked for the (r_t, V_{flat}) pair minimizing the difference between ΔV_{model} and ΔV_{obs} . We checked that, in all simulations, such a criterion gives a unique

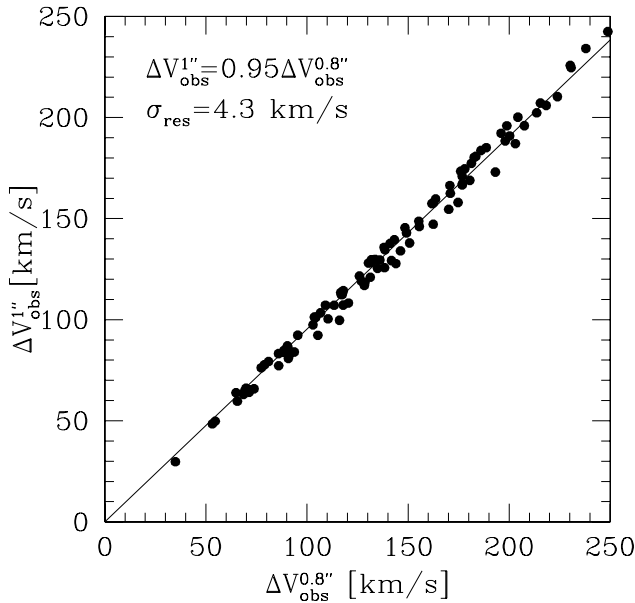


Fig. 2. Comparison between the ΔV_{model} values obtained in Monte-Carlo simulations of 100 GIRAFFE data-cubes using a 0.8 and 1 arcsec seeing (see text). The black line is a linear fit fixing the intercept to zero. The residual dispersion is $\sim 4.3 \text{ km s}^{-1}$.

solution. Results are listed in Table 1, and representative examples of this kinematical fitting for three RD galaxies are shown in Fig. 3.

3.2. Testing the method of correction

To test the correction method, we performed Monte-Carlo simulations of 100 GIRAFFE data-cubes. The parameter space investigated encompassed the inclination, half-light radius, PA, rotation velocity, and RC gradient, of values randomly chosen from the typical values observed for the GIRAFFE sample. Half of the Monte-Carlo simulations were generated using an arctan RC shape model, and the other half using an exponential term combined with a second-order polynomial term. This polynomial term allowed us to create a central velocity “bump” as observed in some early-type galaxies (see Fig. 1). We note, for late-type RCs, that the V_{flat} did not have to be located within the IFU, which allowed us to test how the correction procedure operated in this case. For early-type galaxies, V_{flat} should be located within the IFU, as V_{max} is generally located close to $2.2R_d \sim 1.375R_{\text{half}}$ (e.g., Courteau 1997), which almost always falls within the IFU (Flores et al. 2006). We note, however, that in some cases, because of the dynamical influence of the bulge, the RC of some early-type galaxies can show an extended velocity peak up to large distances (see, e.g., M31, Carignan et al. 2006). The limited spatial coverage of the GIRAFFE IFU would probably provide us with an overestimation of the rotation velocity. In the RD sample, all galaxies besides one have $B/T < 0.2$, which means that such an effect cannot affect significantly the RD sample.

These simulated RCs were used to simulate GIRAFFE observations following the method outlined in Sect. 3.2. These simulated data-cubes were in turn used as inputs to test the method of correction on ΔV_{obs} . In Fig. 4, we compare the input rotation velocity V_{flat} , with the asymptotic velocity V_0 of the best arctan model obtained using the method detailed above. We find a good linear correlation with $V_0 = [0.65 \pm 6.22] + [1.00 \pm 0.03]V_{\text{flat}}$,

consistent with $V_0 = V_{\text{flat}}$, and a residual dispersion $\sim 17 \text{ km s}^{-1}$. In this figure, we have distinguished between simulations where V_{flat} is sampled by the IFU (black circles) from those where this is not the case (black squares). If we compare the corrected velocity V_0 with the last point of the RC sampled by the IFU V_{end} , both sets of simulations fall on the same region. In such a plot (not shown here), we find a similar result, with $V_0 = [-1.23 \pm 4.47] + [1.03 \pm 0.02]V_{\text{end}}$, also consistent with $V_0 = V_{\text{end}}$.

We checked that r_t had little influence on the ΔV_{obs} correction by comparing the corrected rotation velocity, derived by allowing r_t to vary between the three values defined in Sect. 3.1, with that obtained by fixing r_t to the middle value of this grid, i.e. the one that makes most of the RC gradient fell inside one GIRAFFE pixel as observed in most cases. We found that both sets of values correlated well within $\sim 6 \text{ km s}^{-1}$ ($1 - \sigma$), i.e., as expected, r_t has a negligible impact on the derived correction. This is due mainly to the large seeing size (~ 0.8 arcsec) compared to velocity gradients associated with typical r_t values (see Fig. 1), which significantly dilutes the variations of the RC gradient, once projected onto the IFU.

It is important to check whether or not these simulations are representative of real galaxies. To do this, we selected a few galaxies from the GHASP survey (Amram et al. 2002), which provides us with high spatial-resolution data-cubes for a morphologically-complete sample of local galaxies using Fabry-Perot interferometry. The analysis of the GHASP sample is still underway (Epinat et al. 2008), and a full comparison between local 3D data and distant 3D GIRAFFE data will be addressed in a future work. Here, we check whether or not the simulations are representative of local galaxies, especially in the range of velocity and size spanned by distant RDs. We restrict our choice to galaxies for which an arctan shape provides a relatively good representation of the RC, because we probe the accuracy of the correction applied to ΔV_{obs} , and not to the measurement itself, which is an independent issue. Given the limited number of galaxies meeting these criteria, we chose to restrict our choice to 7 such galaxies with rotation velocities ranging from 190 to 220 km s^{-1} , where are typical measurements for most distant RDs (see next Sect. 4). This choice allows us to sample roughly the most relevant velocity range for distant RDs, rather than testing a few isolated points spread over the full velocity range of the distant sample. We simulated GIRAFFE observations by degrading the Fabry-Perot high-resolution data-cube to the resolution of GIRAFFE observation (0.8 arcsec seeing) and then to the GIRAFFE IFU spatial sampling. From these data-cubes, we extracted a VF and ΔV_{obs} as for real GIRAFFE data, and corrected them. These simulation results are shown as blue stars datapoints in Fig. 4, which agree with the Monte-Carlo simulations that fall in the same velocity range, reproducing the dispersion of the correlation. This confirms that we can confidently rely on the correction applied to ΔV_{obs} .

In Fig. 5, we plot all correction factors $\alpha = V_{\text{flat}}/\Delta V_{\text{obs}}$ obtained for the Monte-Carlo simulations. Both simulations of redshifted local galaxies and real GIRAFFE rotating disk galaxies fall in the same region of the plot, apart from three galaxies (J033212.39-274353.6, J033230.78-275455.0, J033245.11-274724.0), that show relatively large α . One is a compact galaxy (J033245.11-274724.0, see Paper II), while another one is seen almost edge-on (J033212.39-274353.6), which might explain the relatively high α . The last galaxy (J033230.78-275455.0) is a special case, because only half of the galaxy is detected in emission (this galaxy was shifted into the RD+ class in Sect. 2.1). We checked that the results presented in this paper are not

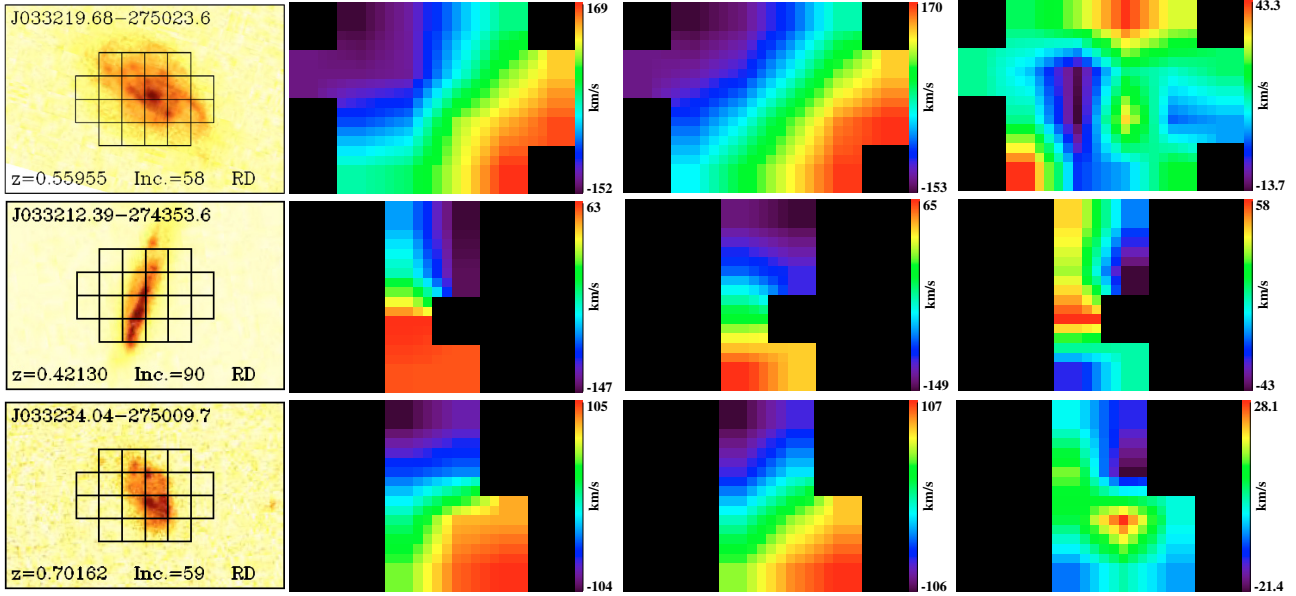


Fig. 3. Examples of kinematical fitting of three $z \sim 0.6$ RD galaxies. *From left to right:* HST/ACS F775W image with the GIRAFFE IFU superimposed (from Paper I), observed VF (shown with a 5×5 interpolation see Paper I), best modeled VF (shown with a 5×5 interpolation), residual map between the observed and modeled VFs. Relatively large differences are found only close to the minor axis, where departure from pure circular motion is artificially exaggerated by projection effects (see a discussion of this effect in, e.g., Chemin et al. 2006).

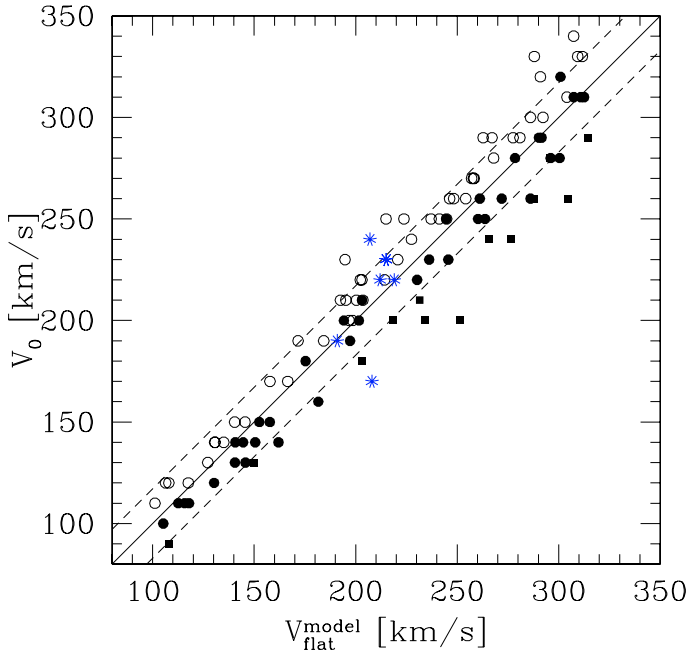


Fig. 4. Comparison between the V_{flat} used as inputs to the Monte-Carlo simulations of 100 GIRAFFE data-cubes, with the V_0 values obtained after using the method of correction described in Sect. 3.2. Black dots represent RCs generated using an arctan model (i.e., late-type like RCs), while open circles represent RCs typical of early-type galaxies. Black squares represent simulations where the rotation velocity is not sampled by the IFU (see text). The black line is a linear fit, and the dash lines represent the $1 - \sigma$ residual dispersion $\sim 17 \text{ km s}^{-1}$. Blue stars represent real observations of local galaxies artificially redshifted to $z \sim 0.6$ (see text).

significantly affected when these three special objects are removed from the sample. In the RD subsample, we found a median $\alpha \sim 1.26$, consistent with what is found in the Monte-Carlo simulations, with a mean $\alpha = 1.25 \pm 0.12$.

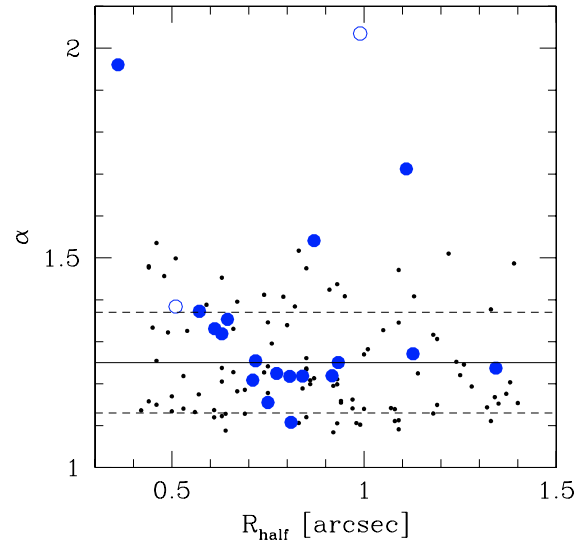


Fig. 5. Correction factors α used to correct ΔV_{obs} for RDs (blue dots; open blue dots represent the two RD+ galaxies). Small black dots correspond to Monte-Carlo simulations of 100 GIRAFFE data-cubes in the same range of half-light radius, PA, inclination, rotation velocity, and RC gradient (see text). The horizontal dash line represents to the mean correcting factor of 1.25 derived from Monte-Carlo simulations, while the $1 - \sigma$ dispersion around the mean is shown in dash lines.

3.3. Random uncertainty budget of the rotation velocity derivation

The uncertainty budget can be decomposed into uncertainties related to ΔV_{obs} , and those related to the correction applied to ΔV_{obs} to obtain V_{flat} .

The main source of uncertainty that can affect ΔV_{obs} is that associated with a finite spectroscopic SNR in the measurement of $V_{\text{max}}^{\text{IFU}}$ and $V_{\text{min}}^{\text{IFU}}$, which can be quantified using Monte-Carlo simulations (see Fig. 6). For each galaxy, we used the SNR maps derived in Paper I to estimate the mean SNR uncertainty on $V_{\text{max}}^{\text{IFU}}$

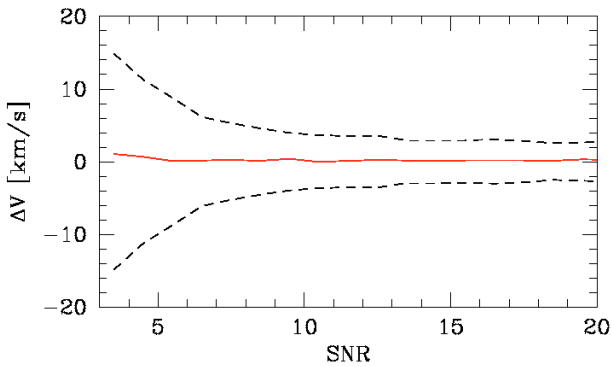


Fig. 6. Monte-Carlo simulations of the velocity measurement accuracy (see Paper I, for details). The red line shows the corresponding bias (almost zero), while the black dashed lines shows the $1 - \sigma$ error: $\sim 12 \text{ km s}^{-1}$ between $\text{SNR} = 3-5$, $\sim 5 \text{ km s}^{-1}$ between $\text{SNR} = 5-10$, and ≤ 2 for $\text{SNR} \geq 10$.

and $V_{\text{min}}^{\text{IFU}}$, i.e., on ΔV_{obs} . We found a median (mean) uncertainty due to a finite SNR of $\sim 9 \text{ km s}^{-1}$ (8 km s^{-1}).

We used Fig. 4 to quantify the uncertainty associated with the correction made to ΔV_{obs} . We found 17 km s^{-1} ($1 - \sigma$ residual dispersion), with no noticeable systematic uncertainties. We note that this uncertainty takes into account cases where the RC is not fully sampled by the IFU. As we have already pointed out, one galaxy in the sample deserves more consideration. Only part of the galaxy J033230.78-275455.0, which was classified as RD+ (see Sect. 2.1), was detected in emission (see Paper I). ΔV_{obs} does not encompass a symmetric range along the RC, which biases the rotation-velocity input of the model to a lower value. Considering a rough RC model, composed of a first, linear, rising part up to $R_{\text{max}} = 2.2R_{\text{D}}$ (Persic & Salucci 1991), and a second flat part, we estimate a $\sim 30 \text{ km s}^{-1}$ correction to “symmetrize” ΔV_{obs} . This correction is convolved directly by the other uncertainty factors on ΔV_{obs} . Following Sects. 3.1 and 3.2, we also took into account uncertainties due to seeing and r_t variations (~ 5 and 6 km s^{-1} , respectively), which produced a total uncertainty for the correction on ΔV_{obs} of $\sim 19 \text{ km s}^{-1}$.

The total uncertainty on $V_{\text{flat}} \times \sin(i)$ (i.e., the radial rotation velocity uncorrected for inclination) was derived by adding in quadrature all the previous terms. We finally propagate the uncertainty associated with the inclination, which is ± 5 degrees, according to Paper I. We finally found a median (mean) total uncertainty on V_{flat} of $\sim 37 \text{ km s}^{-1}$ (44 km s^{-1}). The $1 - \sigma$ dispersion of the total uncertainties around the mean is $\sim 30 \text{ km s}^{-1}$.

4. The K-band Tully-Fisher relation at $z \sim 0.6$

4.1. Results

We compare both the distant and local K-band TFR in Fig. 7. Holding the slope to the local value, σ_{res} increases from RDs (0.31 mag), to PRs (0.80 mag), and CKs (2.08 mag). Restricting the distant TFR to dynamically well-relaxed RDs, the local and distant relations have comparable σ_{res} : we therefore confirm quantitatively the previous findings of Flores et al. (2006) that all of the enlarged dispersion of the distant TFR comes from non-relaxed galaxies. If we allow the slope to vary during the fit, we find a residual dispersion of 0.31 mag. This indicates that assuming no evolution in slope appears to be a reasonable assumption.

The zero point of the TFR of distant RD galaxies is found to be -5.88 ± 0.09 ($1 - \sigma$ bootstrapped error, slope fixed), i.e., 0.66 mag fainter than the local zero point. Allowing the slope

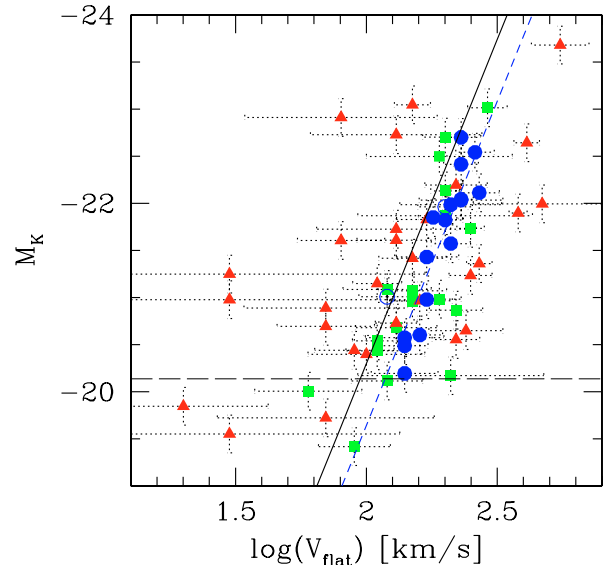


Fig. 7. Evolution of the K-band TFR (AB magnitudes). The completeness limit $M_K \sim -20.14$ (corresponding to $M_J = -20.3$, see Sect. 2) is indicated by an horizontal dash line. Blue dots represent RDs (the two RD+ galaxies are represented with open blue dots), green squares PRs, and red triangles CK galaxies. The black line is the local TFR, while the blue dash-line represent a linear fit to the $z \sim 0.6$ TFR (see text).

Table 2. Fits to the local and distant K-band TFRs, using $M_K(AB) = a + b \times \log(V_{\text{flat}})$.

K-band TFR	Slope a	Zero point b	Comments
Local relation	-6.88 ± 0.57	-6.54 ± 1.33	SDSS subsample
Distant RDs	-6.88	-5.88 ± 0.09	Using local slope
Distant RDs	-7.24 ± 1.04	-5.07 ± 2.37	Slope free
Distant RD/RD+	-6.88	-5.92 ± 0.10	Using local slope
Distant RD/RD+	-6.47 ± 1.30	-6.85 ± 2.98	Slope free

to vary during the fit, we find a zero point of -5.07 ± 2.37 and a slope of -7.24 ± 1.04 in agreement (within the corresponding uncertainties) with those derived by fixing the slope to the local value. This strongly suggests no evolution in slope of the K-band TFR. Given the limited number of RDs in the distant sample (16), we adopt the zero-point value derived by keeping the slope to the local value. We note that if we consider the RD+ class (18 galaxies, see Sect. 2), we find similar results (see Table 2).

We find in the distribution of M_K residuals, a skewness and a kurtosis of -0.22 and -0.99 , respectively for RDs: this is roughly consistent with the Gaussian residuals, within the $1 - \sigma$ expected thresholds². This indicates that residuals are not biased significantly on any side of the relation. A Welcher’s t-test then provides a probability $\ll 1\%$ that the local and distant relations have the same zero point. We note that during the fitting procedure, we weighted all the rotation velocities by their associated uncertainties. Therefore, the result of the Welcher’s t-test means that within random uncertainties, the zero-point difference of 0.66 mag between the distant and the local relations is statistically significant.

² For a distribution of n points, these thresholds are $\sqrt{6/n}$ and $\sqrt{21/n}$ respectively ($n = 16$ is the present case).

4.2. Systematic uncertainty budget

We investigate which systematic effects could bias the evolution of TFR zero point detected between $z \sim 0.6$ and $z = 0$.

4.2.1. Photometric systematic uncertainty

As stated in Sect. 2, we do not expect any noticeable systematic-effect on measurements due to photometric measurement or calibration. However, one possible exception is the extinction correction made on both local and distant galaxies. Even if we follow exactly the same procedure for the two samples, one might wonder whether or not the low surface-brightness outer-regions in distant galaxies could be far less well detected compared to local galaxies, which would create a bias in the derivation of their axis ratios and extinction corrections. However, we found in Paper II that the HST/ACS imaging used to derive the axis ratio in distant galaxies allows us to reach the optical radius ($\sim 3.2 \times R_d$), which limits such a bias. We note that extinction corrections are relatively small in the K -band: in the distant sample, we find a mean/median correction of 0.11 ± 0.05 mag ($1 - \sigma$ dispersion), while in the local sample, the mean (median) correction is found to be $0.15(0.14) \pm 0.05$, which are consistent within the respective uncertainties.

4.2.2. Effects related to the comparison to the local relation

One important aspect about the evolution of the TFR is to control systematic effects between the distant and local relations. These considerations have led us to adopt as a local reference the TFR derived by Hammer et al. (2007) for a complete subsample of the SDSS (Pizagno et al. 2007, see Sect. 2.2). However, there are several differences between the local and distant samples that could lead to possible biases when comparing the corresponding TFRs.

First, kinematical data are obtained using different techniques (3D spectroscopy vs. long-slit spectroscopy). We mitigated this effect by restricting the local sample to galaxies having a well-defined RC (see details in Hammer et al. 2007). This also mitigates the assumption that both local and distant galaxies have RC shapes than can be well described by an arctan (see Sects. 2.2 and 3.2). Second, a different emission line is used for deriving the rotation velocity ($[\text{OII}]$ and H_α). However, both emission lines are found to provide similar estimates of the rotation velocity (e.g., Saintonge 2007). Third, in the local sample, V_{80} (defined as the velocity at a radius that encompasses 80% of the light) is used as a proxy for V_{flat} , while we directly used the asymptotic V_0 from the arctan RC in the distant sample. V_{80} is a reliable proxy for V_{flat} , as shown in Hammer et al. (2007) (see also Pizagno et al. 2007). Finally, one possible caveat about the use of 2MASS K -band magnitudes was recently pointed out by Noordermeer & Verheijen (2007), i.e. that 2MASS underestimates the K -band luminosity in relatively low surface brightness galaxies. We note that this bias would go in the opposite trend compared to the evolution seen in the TFRs, i.e., to shift the local relations towards brighter magnitudes or larger stellar masses. However, we have also mitigated this effect by restricting the local relation to galaxies having $\text{Log}(V_{\text{flat}}) \geq 2.2$, i.e. to the most massive galaxies (see Sect. 2.2).

4.2.3. Kinematic systematic uncertainty

We restricted the analysis of the TFR evolution to well-relaxed RDs. In distant TFR studies, it is often assumed that the (gas)

rotation velocity can be simply derived as the half-amplitude of the VF divided by $\sin(i)$ (modulo spatial-resolution effects): an important assumption behind this simple prescription is that the azimuthal velocity component of the 3D velocity vector within the galaxy (i.e., the rotation) dominates its projection along the line-of-sight. This assumption should always be checked a posteriori, by showing that residuals between a rotating-disk model and the observed VF are small compared to the amplitude of rotation motions. In the case of GIRAFFE RDs, there are few doubts that this assumption is correct, because their modeled VFs match the observed ones (see Paper I).

Conversely, CK galaxies are clearly out of dynamical equilibrium (see Flores et al. 2006 and Paper I). As a consequence, one does no longer know which component of the 3D velocity vector dominates its projection along the line-of-sight. If these galaxies are associated with mergers, as we will discuss below, deriving the rotation velocity in this way is probably uncertain, if not meaningless. This is the reason why in this study, we restricted the analysis of the TFR to well-relaxed RDs.

In Sect. 3, we tested extensively the method of correction used to correct ΔV_{obs} for spatial-resolution effects. All galaxies were assumed to be RDs, regardless of their kinematical class (see Puech et al. 2006a, 2007a). However, this provides uniform α values that are independent of kinematical class: a misclassification of a galaxy has no impact on the way α is derived. This approach helps to compare with long-slit spectroscopy results, where all galaxies are implicitly assumed to be RDs (e.g., Conselice et al. 2005). As explained above, the fit to the TFR is restricted to RDs only, and therefore this cannot affect the evolution of the zero point of the TFR.

One might wonder whether or not the slight bias found in Fig. 4 between early- and late-type galaxies could influence significantly the results. Once translated into $\text{log}(V_{\text{flat}})$ (using Eq. (1)), the offset of the distant TFR is found to be -0.1 dex between $z \sim 0.6$ and $z = 0$, which is much larger than that found in Fig. 4 for early-type galaxies (~ 0.025 dex). Late-type galaxies have the opposite trend, which provides a -0.014 dex offset in Fig. 4. It is impossible to explain all of the shift in the distant TFR zero point in terms of such a morphological bias. Looking at the TFR residuals against B/T for RDs analyzed in Paper II, we find no special trend, which excludes the presence of a bias.

Another source of systematic uncertainty could be the limited spatial coverage of the GIRAFFE IFU. Figure 4 (see the black squares) shows that when the plateau of the RC is not sampled by the IFU, the recovered rotation velocity is underestimated on average by ~ 0.03 dex. We note that this effect generally leads to the underestimation of V_{flat} , which would increase the shift of the zero point between the local and the distant TFRs. However, most of the RDs are well spatially covered by the IFU (see Flores et al. 2006 and Paper I), and this could affect a few galaxies in our sample. It is thus unlikely that such an effect could affect significantly the results in a systematic way.

Finally, the most important possible systematic uncertainty likely comes from our limited knowledge of the seeing during observations. Individual variations from galaxy to galaxy leads to relatively small random uncertainties (see Sect. 3.2). However, we assumed a uniform value of 0.8 arcsec during the rotation-velocity correction process. According to Fig. 2, changing the seeing in the simulations from 0.8 to 1.0 arcsec implies a systematic effect of -0.02 dex on the rotation velocity correction.

4.2.4. Total systematic uncertainty

The only possible systematic effect we can identify so far is that associated with the kinematics, due to the correction for the rotation velocity. Using Eq. (1), this translates into a possible systematic uncertainty of ± 0.14 mag in the 0.66 mag evolution of the K -band TFR zero point between $z \sim 0.6$ and $z = 0$, which represents 20% of the shift.

5. Discussion

5.1. Comparison with Flores et al. (2006)

In Flores et al. (2006; see also Puech et al. 2007a), we used hydro-dynamical simulations of an Sbc galaxy to infer a mean correction factor $\alpha = 1.2 \pm 0.05$ on V_{\max} for galaxies of typical diameters between 2 and 3 arcsec: this value is less than that found here using Monte-Carlo simulations. At first sight, it is surprising to find a larger mean α for V_{flat} than for V_{\max} (since $V_{\text{flat}} \leq V_{\max}$). The explanation is likely linked to the fact that in Flores et al. (2006), we did not consider all possible ranges of size, PA, inclination, rotation velocity and RC gradient to derive this mean correction, because we were limited by the hydro-dynamical models of spiral galaxies available to us at that time. Another difference is the exponential dependence of α with galaxy size found in Flores et al. (2006), which is not reproduced here. The reason for this is that in Flores et al. (2006), we used the same simulation of an Sbc galaxy to simulate distant galaxies of different sizes, which induced an intrinsic correlation between the RC gradient and the galaxy size. Our tests show that if we introduce this correlation in the Monte-Carlo simulations, we then recover the exponential variation of α with R_{half} .

The brightening found in the K -band TFR was not initially detected by Flores et al. (2006). In Fig. 8, we show the K -band TFR obtained following the Flores et al. (2006) method to correct ΔV_{obs} , i.e., applying a constant correction factor of 1.2. The black line shows the Verheijen (2001) K -band local TFR using V_{flat} as a kinematical tracer for the rotation velocity, i.e., the relation used as a local reference by Flores et al. (2006). Both the local and distant relation are then in good agreement: if we fix the slope of the distant relation to the local one, we find a shift ~ 0.1 mag between the zero point of the distant and the local relations. Therefore, we retrieve the Flores et al. (2006) results that no significant evolution in zero point can be detected. The reason for such a difference is twofold.

First, as detailed in Hammer et al. (2007), we found a discrepancy between the K -band TFR derived in the Verheijen (2001) sample, compared to those derived in two other local samples (Courteau 1997; Pizagno et al. 2007). We show in Hammer et al. (2007) that this discrepancy is due to the larger fraction of faint and slow rotating galaxies in the Verheijen (2001) sample compared to the two other ones. Such galaxies have a larger gas fraction, which results in a different slope at the low-mass end of the TFR (McGaugh 2005). Noordermeer & Verheijen (2007) derived a new K -band local TFR: they found a slope similar to the one inferred by Hammer et al. (2007) after restricting the Verheijen (2001) TFR to the high-mass end. In Flores et al. (2006), the relation used as a local reference was however the Verheijen (2001) relation. If we refit the distant RD subsample using the rotation velocities derived following Flores et al. (2006), but using the slope of the SDSS local relation (i.e., the one used in Fig. 7, see the blue lines in Fig. 8), we find a shift ~ 0.4 mag between the distant and the local zero points. Compared to Flores et al. (2006), we use a different local sample, which provides a better control of systematic effects

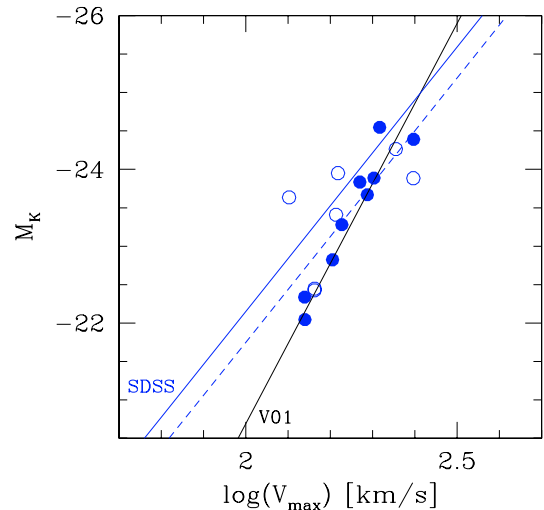


Fig. 8. K -band TFR derived following the Flores et al. (2006) methodology, for the RD subsample. The black line is the local relation of Verheijen (2001), i.e., the one used as a reference by Flores et al. (2006). Note that K -band magnitudes in the distant sample have been converted into the Vega system using $M_K(\text{Vega}) = M_K(\text{AB}) - 1.85$. For simplicity, we assume that the K' magnitudes of Verheijen (2001) are roughly equivalent to those derived in the distant sample using the ISAAC K s filter. The blue line is the SDSS local TFR used as a reference in this study (converted into the Vega system). The blue dash line is a linear fit to the distant RDs, which has a zero point 0.4 mag lower than the local one, fixing the slope to the local value. Open symbols represent galaxies from the new CDFS sample, while full symbols represent galaxies used in Flores et al. (2006).

that can occur in the comparison with the distant sample (see Sect. 4.2.2): this rigorous approach allows us to explain $\sim 60\%$ of the TFR zero-point shift, previously hidden by spurious effects.

Second, we have significantly improved the method for correcting the rotation velocity since the preliminary work of Flores et al. (2006). This is illustrated in Fig. 9, where we compare the rotation velocities derived following Flores et al. (2006) and those derived in this study: this figure reveals that Flores et al. (2006) underestimated the rotation velocity in RDs by 11% on average, which corresponds to a ~ 0.05 dex shift in $\log(V_{\text{flat}})$, or ~ 0.3 mag once converted into a M_K shift using Eq. (1). Therefore, we attribute the remaining $\sim 40\%$ of shift in the TFR zero point, previously undetected, to the improvement in the rotation-velocity derivation.

Finally, Fig. 8 provides us with a useful cross-check of the new method used in this study to correct the rotation velocity. In Fig. 8, one RD galaxy (J033212.39-274353.6) appears to be shifted to lower velocities compared to other distant rotating disks. This galaxy was identified as having a particularly high α value in Sect. 3.3, while its data are well described by the TFR in Fig. 7. This suggests that the new method of correction appears to be better suited for deriving rotation velocities: comparing Fig. 8 with 7, we note that the dispersion of the RD subsample is significantly reduced using the new method of correction.

5.2. Origin of the scatter in the distant relation

Using the spatially-resolved kinematics provided by 3D spectroscopy, we confirm earlier results that the dispersion of the distant relations can be explained by the presence of dynamically non-relaxed galaxies (Flores et al. 2006). These galaxies are found to be out of dynamical equilibrium, with random

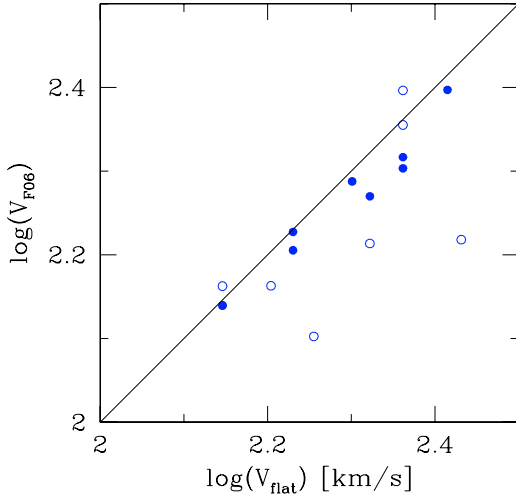


Fig. 9. Comparison between the rotation velocities V_{F06} obtained using the method of Flores et al. (2006) (i.e., a constant correction factor of 1.2) vs. rotation velocities V_{flat} derived using the new method used in this paper, for the subsample of RDs. V_{F06} underestimates V_{flat} by $\sim 11\%$ on average. Open symbols represent galaxies from the new CDFS sample, while full symbols represent galaxies used in Flores et al. (2006).

motions instead of ordered motions, especially for the most compact galaxies (Puech et al. 2006a; Weiner et al. 2006). Ongoing comparisons between hydrodynamical simulations of galaxy mergers with GIRAFFE data reveal that they could be associated with major mergers (Puech et al. 2007a; Puech et al., in prep.). Such events provide a natural link between CK galaxies and morphologically-peculiar galaxies (see Paper II), which causes an increase in the dispersion of the TFR at high redshift (Kassin et al. 2007; Atkinson et al. 2007).

On the other hand, it is still unclear whether or not more quiescent processes, such as secular gas accretion through internal processes (bars), or cold-gas flows (Dekel & Birnboim 2006; Keres et al. 2005), could explain such anomalous kinematics on a relatively large spatial scales, especially for CK galaxies (see Paper I). More work is required to compare dynamical predictions of such events with observations.

5.3. Comparison with the evolution of the K-band luminosity density

Finding a 0.66 mag *brightening* of the K-band TFR between $z \sim 0.6$ and $z = 0$ appears to be quite surprising, given the opposite trend seen in the evolution of the K-band luminosity density in “blue” galaxies over the same redshift range. One may reasonably assume that “blue” star-forming galaxies and emission-line galaxies belong to the same population (Hammer et al. 1997): Arnouts et al. (2007) find that the K-band luminosity density of blue star-forming galaxies *fades* by 0.5–0.6 mag from $z \sim 0.6$ to $z = 0$, which is exactly the opposite trend. What appears to be a clear contradiction simply reflects two different methodologies.

As we have detailed above, the TFR allows us to compare two physically-connected populations of galaxies, i.e., the local spirals and the distant rotating disks: the evolution of this relation directly reflects the evolution of the K-band luminosity in *rotating disks of similar total mass* between $z \sim 0.6$ and $z = 0$, assuming that the rotation velocity can be used as a proxy for the total mass (Hammer et al. 2007). On the other hand, the color selection used to select “blue” galaxies at $z = 0$ and at $z \sim 0.6$ can produce heterogeneous galaxy populations, as

noticeable when comparing their luminosity densities. Optical colors are well known to be seriously affected by instantaneous star formation and extinction. The evolution of the K-band luminosity density in “blue” galaxies reflects the number evolution of “blue” galaxies, which are much more numerous at high redshift (e.g., Ellis 1997).

To check that there is no contradiction between the evolution of the TFR zero point and the evolution of the K-band luminosity density, we derived the K-band luminosity density in the complete GIRAFFE sample, i.e., including all dynamical classes. As stated in Sect. 2.1, the GIRAFFE sample is representative of $z \sim 0.6$ emission-line galaxies with $M_J(\text{AB}) \leq -20.3$ (i.e., with $M_{\text{stellar}} \geq 1.5 \times 10^{10} M_{\odot}$, see Paper I). We therefore expect a K-band luminosity density in this sample that represents the luminosity density of “blue” galaxies at these redshifts. We estimated the K-band luminosity in the GIRAFFE sample to be $\log(\rho_K) = 8.74 L_{\odot} \text{Mpc}^{-3}$, which agree well with the K-band luminosity density of “blue” star-forming galaxies found by Arnouts et al. (2007). This comparison confirms that the GIRAFFE sample is representative of $z \sim 0.6$ emission-line galaxies: the K-band luminosity density in the GIRAFFE sample is consistent with the results inferred from studies using far larger samples.

5.4. Did distant rotating disks double their stellar-mass over the last 6 Gyr?

Once restricted to well-relaxed RDs, we find, between $z \sim 0.6$ and $z = 0$, a shift in the TFR zero point of 0.66 ± 0.14 mag in M_K , or -0.1 ± 0.02 dex in $\log(V_{\text{flat}})$. We consider the interpretation of this shift in terms of galaxy evolution.

Could there be any so-called “progenitor bias” between distant RDs and local relaxed spirals, which could imply that the latter would not be the descendants of the former? Local RDs are found to be twice as numerous as distant ones (see Paper II), which implies that some were not in a relaxed dynamical state at $z \sim 0.6$ (being then PR or CK). However, local intermediate-mass spirals have only a low probability to have undergone a major merger since $z \sim 0.6$ (15–30%, as discussed in Puech et al. 2007a): this means that most distant RDs must dynamically evolve smoothly towards local relaxed spirals, which implies that distant RDs are the progenitors of a majority of local spirals. Therefore, it makes sense to interpret the evolution of the RD-restricted TFR as an evolution in luminosity, rotation velocity, or a combination of the two. We reiterate that we assume no evolution in slope (see Sect. 4.1): a larger sample would be required to tackle directly the possible evolution in slope of the TFR and determine the details of the evolutionary path between distant and local RDs.

We discuss the possibility that this shift could correspond to a pure luminosity brightening of 0.66 ± 0.14 mag in RDs over the past 6 Gyr. Such a luminosity-brightening in RDs would correspond to a growth in stellar-mass, which can be estimated in the following way. Between $z \sim 0.6$ and $z = 0$, the evolution in $\log(M_{\text{stellar}}/L_K)$ is found to range between 0.13 and 0.16 dex (Drory et al. 2004; Arnouts et al. 2007), depending on the selection criteria. Using $\log(M_{\text{stellar}}) = \log(M_{\text{stellar}}/L_K) + \log(L_K)$, one finally finds a stellar-mass evolution of 0.39–0.42 dex. A more exhaustive derivation, using the stellar-mass TFR, leads to a similar conclusion, with an evolution in zero point of $0.36_{-0.06}^{0.21}$ dex between $z \sim 0.6$ and $z = 0$ (see Appendix A). On the other hand, the evolution of the cosmic stellar-mass density over the same redshift range is found to be ~ 0.1 – 0.16 dex (Dickinson et al. 2003; Drory et al. 2004; Arnouts et al. 2007).

Hammer et al. (2005) found that most of the present-day stellar-mass formed since $z = 1$ occur in intermediate-mass galaxies (see also Bell et al. 2005), which include 60% of emission-line galaxies at $z \sim 0.6$ (Hammer et al. 1997). Hence, if we assume that, on average, quiescent galaxies do not evolve in stellar-mass, one can estimate the growth in stellar-mass between $z \sim 0.6$ and $z = 0$ in intermediate-mass, emission-line galaxies to be ~ 0.32 – 0.38 dex. Therefore, this interpretation of the TFR zero-point shift as a pure luminosity evolution is roughly in agreement with the evolution of the cosmic stellar-mass density over the same redshift range. This interpretation is supported by the fact that distant RDs are found to be LIRGs or at least star-bursting, i.e., they are actively forming stars at very high rates (see Paper II).

Interpreted in this way, the evolution of the zero point of the K -band TFR reflects the growth in stellar-mass of the most active population over the past 6 Gyr, i.e. star-forming intermediate-mass galaxies, by a factor ~ 2.5 – 2.6 . This compares well with the gaseous O/H phase abundance of $z \sim 0.6$ emission-line galaxies, which is, on average, half that of present-day spirals for a similar range of stellar mass (Liang et al. 2006). Such an evolution in stellar mass would imply that RDs converted an important amount of gas into stars over the past 6 Gyr. In other words, the main evolutionary path for RDs during the past 6 Gyr would be conversion of gas into star through gas supply, which is further supported by their relatively low gas-disk V/σ values (Puech et al. 2007a) and the inside-out build-up of their stellar disks (see a detailed discussion in Paper II).

The opposite interpretation is that the shift in the zero point of the K -band TFR corresponds to a pure rotation-velocity evolution of -0.1 ± 0.02 dex between $z \sim 0.6$ and $z = 0$. Even in this case, the observed evolution in M_{stellar}/L_K over this redshift range still implies, on average, a substantial growth in stellar mass of 0.13 – 0.16 dex in intermediate-mass galaxies (see above). As a consequence, the stellar mass growth in quiescent intermediate-mass galaxies should be approximately similar because the stellar mass growth in the entire population (i.e., quiescent or not) is observed to be similar in this redshift range. This is clearly not what is observed, because $\sim 80\%$ of the stellar mass formed since $z = 1$ occurred in star-forming galaxies (LIRGs, see Hammer et al. 2005). We can therefore rule out a pure evolution along the velocity axis.

The last possibility is a combined evolution along both axes, i.e. a simultaneous brightening in luminosity with a decrease in rotation velocity V_{rot} . According to the Virial theorem, V_{rot}^2 scales as the ratio of the total mass enclosed within the optical radius R_{opt} , over R_{opt} ($\sim 3.2R_d$ in both distant and local galaxies, see Paper II). A decrease in V_{rot} between $z \sim 0.6$ and $z = 0$ would then imply a decrease in this ratio, which in turn would imply that R_{opt} (or R_d) increases faster than the total mass over the same redshift range. Between $z \sim 0.6$ and $z = 0$, R_d does not seem to evolve strongly, at least in the RD subsample (see Paper II; see also Puech et al. 2007a). Therefore, only a moderate increase in the total mass enclosed within R_{opt} could occur over this redshift range. Such a scenario would agree with observations: as stated above, local intermediate-mass spirals have a low probability to have undergone a major merger since $z \sim 0.6$ (15–30%, see Puech et al. 2007a, and references therein). Therefore, most distant RDs should be already mostly assembled at $z \sim 0.6$, and should not undergo strong evolution in terms of total-mass from $z \sim 0.6$ to $z = 0$.

To explore the real evolution along both axes, we compare our results with the model of spherical gas accretion of Birnboim et al. (2007). Birnboim et al. (2007) present a model of accretion

for a star-bursting galaxy at $z \sim 0.7$ and describe its subsequent evolution in terms of mass, down to $z = 0$. Although it is not clear whether or not such a model could be representative of all properties of distant RDs, we assume that it can be used to constrain the average mass evolution in a typical RD halo. In that case, the results of Birnboim et al. (2007) would suggest that the baryonic mass in the disk remains constant between $z \sim 0.6$ and $z = 0$, while the *Virial* baryonic mass roughly doubles (see their Fig. 2). On the other hand, Conroy et al. (2007) found that the *Virial*-to-stellar mass ratio in intermediate-mass galaxies is roughly constant between $z = 1$ and $z = 0$. Assuming that the subsample of RDs follows the same trend, one can combine the Conroy et al. (2007) observational results with the model of Birnboim et al. (2007), and find that RDs would roughly double their stellar-mass between $z \sim 0.6$ and $z = 0$. Accounting for the evolution in mass-to-light ratio over this redshift range, this would translate into an evolution of 0.35 – 0.43 mag in luminosity, to be compared with the 0.66 mag found in the evolution of the TFR zero point. Once translated into $\log(V_{\text{flat}})$, this would allow a -0.04 dex evolution along the velocity axis, between $z \sim 0.6$ and $z = 0$.

In conclusion, we find that the most likely interpretation of the evolution of the TFR zero point is the one in which this shift reflects mostly a luminosity evolution of RDs. We estimated an upper limit to the contribution of an evolution along the velocity axis to be at most one half of the total shift of zero point. Such a brightening of distant RDs over the past 6 Gyr would indicate a doubling of their stellar-mass, which is independently supported by their other dynamical and morphological properties.

Finally, this could suggest that the *baryonic* (stars plus gas) TFR would not evolve with redshift: if one accounts for the (average) two times larger gas fraction of $z \sim 0.6$ galaxies compared to $z = 0$ (Liang et al. 2006), one finds that distant galaxies roughly fall back onto the local smTFR (see Appendix A). Studies of the local baryonic TFR have shown that galaxies having $V_{\text{flat}} \leq 100 \text{ km s}^{-1}$ systematically fall below the TFR defined by more massive galaxies (e.g., McGaugh 2005). However, once the gas fraction is accounted for, all galaxies follow the same *baryonic* TFR. Interpreted that way, our results suggest an evolution of this threshold toward higher masses (velocities) at higher redshifts, of at least $V_{\text{flat}} \sim 300 \text{ km s}^{-1}$ at $z \sim 0.6$. This supports the idea that the baryonic TFR would be much more “fundamental” than the stellar-mass TFR (McGaugh 2005).

6. Conclusion

We have studied the evolution of the K -band TFR, using a representative sample of 65 emission line, intermediate-mass galaxies at $z \sim 0.6$, unaffected by field-to-field variations within Poisson statistics, and observed using 3D spectroscopy. We have presented and tested a new method allowing us to safely recover V_{flat} of distant galaxies. We have also investigated possible sources of systematic effects, which can be particularly important when studying the evolution of the TFR. We have paid particular attention to the analysis of both the local and distant samples in as similar as possible ways. We draw the following conclusions:

1. The larger dispersion of the distant TFR is caused by galaxies with anomalous kinematics, ranging from perturbed rotators to very dynamically-disturbed galaxies. We find a positive and strong correlation between the complexity of the kinematics and the scatter contributed to the TF. Once restricted to relaxed rotating disks, the scatter of the TFR

appears to not have evolved, which might suggest no evolution in slope.

2. We detect for the first time a significant evolution of the K -band TFR zero point, which we attribute to an average brightening of $z \sim 0.6$ galaxies by 0.66 ± 0.14 mag. We attribute this evolution to the fact that selected distant galaxies are either starbursts or LIRGs. The distant emission-line rotating disks represent roughly one fourth to one fifth of present-day spiral progenitors, and one half of the whole population of $z \sim 0.6$ intermediate-mass rotating disks (see Paper II). Therefore, a significant part of spiral progenitors are doubling their stellar masses during the last ~ 6 Gyr, in good agreement with former studies on the evolution of the mass-metallicity relation (Liang et al. 2006), which would suggest no evolution of the baryonic TFR with redshift.
3. Current studies of the evolution of the TFR, even using spatially-resolved kinematics, are limited by important systematic uncertainties, which can be attributed to the limited spatial resolution of the kinematics, and to the derivation of the stellar-mass. These systematic uncertainties represent 20% of the evolution in zero point of the K -band TFR.

Further progress in the study of the evolution of the TFR will benefit from a forthcoming larger sample of RDs. This will allow us to reduce the random uncertainties, allow the slope to vary during the fit, and start studying TF residuals. Although we have limited the local sample to galaxies having a well-defined rotation curve, a decisive answer about the evolution of the TFR will require both local and distant representative samples processed in the same way, from the observational strategy (3D spectroscopy) to the data analysis itself, as we have done in this paper. A similar analysis of a representative local sample observed using 3D spectroscopy is required to confirm the above results. This point will be addressed in a future study, using the local kinematic GHASP survey, whose analysis is currently ongoing (Epinat et al. 2008). Finally, an important limitation remains linked to systematic uncertainties, which are mostly due to a lack of spatial resolution. The only way to overcome this limitation will be to develop a new generation of optical integral-field spectrographs with higher spatial-resolution, i.e., assisted by adaptive optics. In this respect, the future extremely large telescopes will allow us to make a decisive leap forward in our understanding of the TFR (Puech et al. 2008).

Acknowledgements. We thank all the GIRAFFE team at the Observatories of Paris and Geneva, and ESO for this unique instrument.

Appendix A: The evolution of the stellar-mass TFR

A.1. The local stellar-mass TFR

Stellar masses M_{stellar} were estimated from M_{stellar}/L_K ratios using the method of Bell et al. (2003). We used a solar luminosity in the K_s -band of 3.28 (Vega) and assumed a “diet” Salpeter IMF (Bell et al. 2003). This method takes advantage of the tight correlation found between rest-frame optical colors and M_{stellar}/L_K ratios, assuming a universal IMF. These correlations are found to be relatively insensitive to the details of galaxy SFH, dust content, and metallicity (Bell & de Jong 2001; Bell et al. 2003), which implies that they are invaluable for deriving stellar mass without being too sensitive to the details of the stellar population synthesis models. We note that following this method, M_{stellar}/L_K ratios are corrected for the amount of light due to red-giant stars using $g-r$ colors.

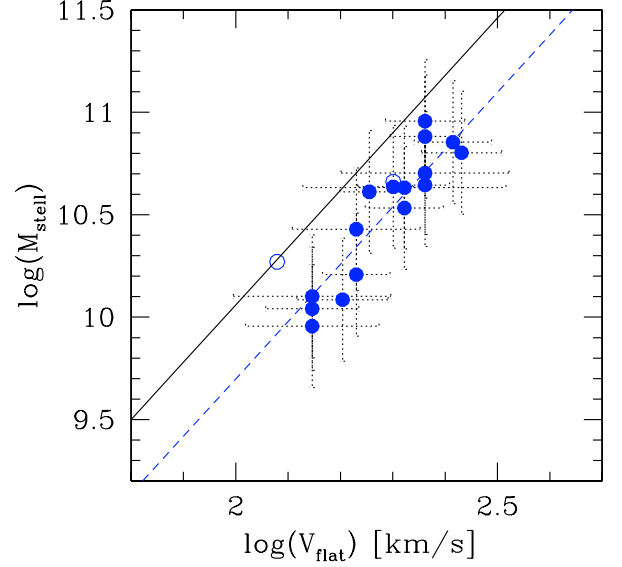


Fig. A.1. Evolution of the stellar-mass TFR in the RD subsample (the two RD+ galaxies are represented with open blue dots). The black line is the local smTFR, while the blue dash-line represents a linear fit to the $z \sim 0.6$ smTFR.

Table A.1. Fits to the local and distant smTFRs, using $\log(M_{\text{stellar}}/M_{\odot}) = a + b \times \log(V_{\text{flat}})$.

K -band TFR	Slope a	Zero point b	Comments
Local relation	2.8 ± 0.23	4.46 ± 0.53	SDSS subsample
Distant RDs	2.8	4.10 ± 0.16	Using local slope
Distant RDs	3.28 ± 1.10	3.01 ± 2.47	Slope free
Distant RD/RD+	2.8	4.13 ± 0.15	Using local slope
Distant RD/RD+	2.61 ± 1.33	4.56 ± 3.03	Slope free

According to Bell et al. (2003), using this method, the total random uncertainty on $\log(M_{\text{stellar}}/M_{\odot})$ at $z \sim 0$ should be lower than 0.1 dex, and the systematic uncertainties due to galaxy ages, dust, or bursts of star-formation can reach 0.1 dex. Finally, the influence of TP-AGB stars in the derivation of stellar masses could result in an overestimation of the stellar mass by ~ 0.14 dex (Maraston et al. 2006; Pozzetti et al. 2007) in a systematic way.

Using this method, we converted the local K -band TFR in the subsample of the SDSS (see Sect. 2.2) into stellar masses and found:

$$\log(M_{\text{stellar}}/M_{\odot}) = 4.46 \pm 0.53 + (2.8 \pm 0.23) \times \log(V_{\text{flat}}), \quad (\text{A.1})$$

with $\sigma_{\text{res}} = 0.15$ dex.

A.2. The distant stellar-mass TFR

To estimate stellar masses in the distant sample (see Table 1), we used the same method as in the local sample, i.e., the K -band luminosity and $B-V$ rest-frame colors. One important issue is whether or not the same correlations between color and M_{stellar}/L_K ratios found at $z = 0$ by Bell et al. (2003) can be directly applied at higher redshift. Borch et al. (2006) showed that this appears possible at least up to $z \sim 0.6$ (see their Fig. 4), with an associated random uncertainty of ~ 0.3 dex, and an average systematic uncertainty of up to -0.2 dex (i.e., towards an overestimation of the stellar-mass at high z).

We show the derived distant smTFR in Fig. A.1. The smTFR shows the same trend with the kinematic classification as the K -band TFR. Restricting ourselves to RDs, and holding the

Table A.2. Identified systematic uncertainties that could impact the shift of zero point between the local and the distant smTFRs. Systematic uncertainties on V_{flat} have been converted into M_{stellar} using Eq. (A.1). Negative values tend to reduce the shift of zero point, while positive values have the opposite trend.

Description	Bias on M_{stellar} (dex)	Comments
Photometry	~ 0	Comparison EIS vs. ACS in the CDFS
M/L_K Evolution with z	+0.1	Following Sect. A.3
IMF Evolution with z	+0.05	Following van Dokkum (2007)
Velocity correction	± 0.06	See Sect. 4.2.3
Total	-0.06/+0.21	

slope constant, the distant and local relations have similar dispersions ($\sigma_{\text{res}} = 0.12$ dex). If we allow the slope to vary during the fit, we find a residual dispersion of 0.12 dex, suggesting again that assuming no evolution in slope is acceptable. Maintaining the slope at its local value, the distant smTFR zero point is found to be 4.10 ± 0.16 (random) $_{-0.2}^{+0}$ (systematic, see above), i.e., 0.36 dex smaller than the local zero point (see Table A.1). A Welcher's t-test gives a probability $\ll 1\%$ that the two relations have the same zero point.

A.3. Stellar-mass systematic uncertainties

The most important systematic uncertainty is that associated with the mass-to-light ratios $[M/L]$ predicted by stellar population synthesis [SPS] models. Absolute values of M/L depend mostly on the SPS model and IMF used, and more particularly on the prescriptions for the TP-AGB stellar-evolution phase (Maraston 2005; Maraston et al. 2006). Pozzetti et al. (2007) compared M/L predictions between Bruzual & Charlot (2003) and Maraston (2005) SPS models and found a systematic difference of -0.14 dex due to different prescriptions for TP-AGB stars. However, they found that this systematic is constant with redshift, at least up to $z \sim 1.2$. In other words, at a given IMF, relative predictions between two different redshifts of SPS models are much more robust in terms of M/L predictions.

We therefore focus in Fig. A.2 on the evolution of $\log(M_{\text{stellar}}/L_K)$ between $z \sim 0.6$ and $z = 0$: we show the histograms of $\log(M_{\text{stellar}}/L_K)$ derived using the Bell et al. (2003) method, both in the distant and local samples. Both histograms were centered using the median $\log(M_{\text{stellar}}/L_K)$ of the local sample: we find that $\log(M_{\text{stellar}}/L_K)$ evolves from $z \sim 0.6$ to $z = 0$ by ~ 0.06 dex. In this figure, we show other determinations of the evolution of $\log(M_{\text{stellar}}/L_K)$ from the literature. Drory et al. (2004), using Maraston (1998) SPS models, found an evolution of 0.13 dex in galaxies with stellar masses between $4 \times 10^{10} M_{\odot}$ and $10^{11} M_{\odot}$, i.e., in a range of stellar-mass similar to GIRAFFE galaxies. This is similar to the 0.15 dex evolution found by Arnouts et al. (2007) in a flux-limited sample over the same redshift range, using Bruzual & Charlot (2003) SPS models. Furthermore, Arnouts et al. (2007) find an evolution of 0.16 dex once restricted to a sample of blue star-forming galaxies. Because such blue galaxies and emission-line galaxies probably belong to the same populations (Hammer et al. 1997), we conclude that we might be underestimating the evolution of $\log(M_{\text{stellar}}/L_K)$ by up to $\sim 0.16 - 0.06 = 0.1$ dex in a systematic way.

What is the origin of this systematic effect? As $\log(M_{\text{stellar}}/L_K)$ depends mostly on color and not on mass, Bell et al. (2003) used SPS models to predict their ‘‘average’’ correlations given a reasonable range of SPS parameters (e.g., metallicity, star formation histories). However, Bell et al. (2003) did not explicitly fit the age but assumed instead a reference age

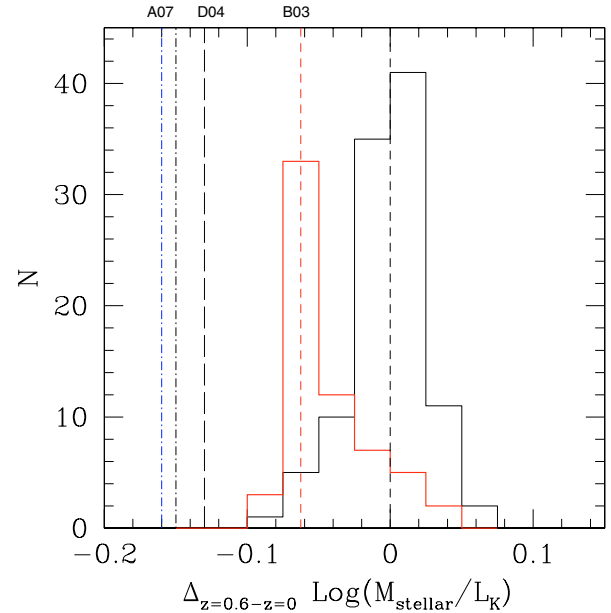


Fig. A.2. Histograms of $\log(M_{\text{stellar}}/L_K)$ found in the local and distant samples of galaxies using the method of Bell et al. (2003). Both histograms have been re-centered using the median found in the local samples, which allows us to directly infer the evolution of $\log(M_{\text{stellar}}/L_K)$ between $z \sim 0.6$ and $z = 0$, i.e., ~ 0.625 dex. Also shown, the evolution of $\log(M_{\text{stellar}}/L_K)$ found by Drory et al. (2004) in a sample of intermediate-mass galaxies (black long-dashed line), and Arnouts et al. (2007) in blue star-forming galaxies (blue mixed-line) or independently of the color (black mixed-line).

of 12 Gyr at $z = 0$. This introduces a systematic difference with other results where age is fitted explicitly. For instance, Drory et al. (2004) find an average age of 8.1 Gyr at $z = 0$. If one compares the median $\log(M_{\text{stellar}}/L_K)$ found in the local SDSS sample used in this study, with the average value found by Drory et al. (2004) in a similar mass range, one finds a difference of -0.08 dex (which accounts for the different IMF used). Similarly, we find a difference of -0.16 dex between the median $\log(M_{\text{stellar}}/L_K)$ found in the GIRAFFE sample, and the average value found by Drory et al. (2004) at $z = 0.6$. These values are consistent with the systematic error bars quoted above. They suggest that we underestimate the evolution of $\log(M_{\text{stellar}}/L_K)$ between $z = 0$ and $z \sim 0.6$ by -0.08 dex, which is consistent with Fig. A.2.

In summary, these comparisons show that we are probably underestimating the evolution of $\log(M_{\text{stellar}}/L_K)$ between $z = 0$ and $z \sim 0.6$ by -0.08 dex, and maybe up to -0.1 dex due to the use of the simplified prescriptions for M/L of Bell et al. (2003). This directly translates into a systematic effect of the evolution of smTFR zero point by up to $+0.1$ dex.

A.4. Total systematic uncertainty

We summarize all possible sources of systematic uncertainty identified so far in Table A.2. We expressed all in terms of their influence on the shift in the zero point between the distant and the local smTFRs. Taking into account all these uncertainties, we find a shift in the smTFR zero point of $0.36_{-0.06}^{+0.21}$ dex between $z \sim 0.6$ and $z = 0$. Systematic uncertainties represent up to $\sim 60\%$ (in dex) of the evolution detected in zero point, i.e., much larger than systematic uncertainties affecting the evolution of the K -band TFR zero point. The derivation of stellar mass is highly model-dependent, which implies a large additional uncertainty. However, we note that these effects tend to overestimate the stellar mass at high redshift, i.e., to minimize the evolution of the smTFR. Using $\log(M_{\text{stellar}}/L_K) = \log(M_{\text{stellar}}) - \log(L_K)$, one finds that $\log(M_{\text{stellar}}/L_K)$ evolves by ~ 0.1 dex ($=0.36-0.66/2.5$) between $z \sim 0.6$ and $z = 0$ in the subsample of RDs. Therefore, the evolution in the zero point of the smTFR is quite robust, in the sense that we might have minimized the evolution of M_{stellar}/L_K through the choice of method used to derive the stellar mass (see Sect. A.3).

References

- Amram, P., Adami, C., Balkowski, C., et al. 2002, *Ap&SS*, 281, 393
 Arnouts, S., Vandame, B., Benoist, C., et al. 2001, *A&A*, 379, 740
 Arnouts, S., Walcher, C. J., Le Fèvre, O., et al. 2007, *A&A*, submitted [arXiv:astro-ph/0705.2438]
 Atkinson, N., Conselice, C. J., & Fox, N. 2007, *MNRAS*, submitted [arXiv:astro-ph/0712.1316]
 Bamford, S. P., Aragon-Salamanca, A., & Milvang-Jensen, B. 2006, *MNRAS*, 366, 308
 Bell, E. F., & de Jong, R. S. 2001, *ApJ*, 550, 212
 Barnes, J. E. 2002, *MNRAS*, 333, 481
 Bell, E. F., McIntosh, D. H., Katz, N., & Weinberg, M. D. 2003, *ApJS*, 149, 289
 Bell, E. F., Papovich, C., Wolf, C., et al. 2005, *ApJ*, 625, 23
 Bell, E. F., Zheng, X. Z., Papovich, C., et al. 2007, *ApJ*, 663, 834
 Birnboim, Y., Dekel, A., & Neisten, E. 2007, *MNRAS*, submitted [arXiv:astro-ph/0703435]
 Blanton, M. R., Schlegel, D. J., Strauss, M. A., et al. 2005, *AJ*, 129, 2562
 Böhm, A., & Ziegler, B. L. 2007, *ApJ*, 668, 846
 Böhm, A., Ziegler, B. L., Saglia, R. P., et al. 2004, *A&A*, 420, 97
 Borch, A., Meisenheimer, K., Bell, E. F., et al. 2006, *A&A*, 453, 869
 Bruzual, G., & Charlot, S. 2003, *MNRAS*, 244, 1000
 Carignan, C., Chemin, L., Huchtmeier, W. K., & Lockman, F. J. 2006, *ApJ*, 641, 109
 Carpenter, J. M. 2001, *AJ*, 121, 2851
 Chemin, L., Balkowski, C., Cayatte, V., et al. 2006, *MNRAS*, 366, 812
 Chiu, K., Bamford, S. P., & Bunker, A. 2007, *MNRAS*, 377, 806
 Conselice, C. J., Bundy, K., Ellis, R. S., et al. 2005, *ApJ*, 628, 160
 Conroy, C., Prada, F., Newman, J. A., et al. 2007, *ApJ*, 654, 153
 Courteau, S. 1997, *AJ*, 114, 2402
 Davé, R. 2007, *MNRAS*, submitted [arXiv:astro-ph/0710.0381]
 De Rijcke, S., Zeilinger, W. W., Hau, G. K. T., et al. 2007, *ApJ*, 659, 1172
 Dekel, A., & Birnboim, Y. 2006, *MNRAS*, 368, 2
 Dickinson, M., Papovich, C., Ferguson, H. C., et al. 2003, *ApJ*, 587, 25
 Drory, N., Bender, R., Feulner, G., et al. 2003, *ApJ*, 595, 698
 Drory, N., Bender, R., Feulner, G., et al. 2004, *ApJ*, 608, 742
 Dutton, A. A., van den Bosch, F. C., Dekel, A., et al. 2007, *ApJ*, 654, 27
 Ellis, R. 1997, *ARA&A*, 25, 389
 Epinat, B., Amram, P., Marcelin, M., et al. 2008, *MNRAS*, submitted
 Flores, H., Hammer, F., Puech, M., Amram, P., & Balkowski, C. 2006, *A&A*, 455, 107
 Franceschini, A., Rodighiero, G., Cassata, P., et al. 2006, *A&A*, 453, 397
 Governato, F., Willman, B., Mayer, L., et al. 2007, *MNRAS*, 374, 1479
 Hammer, F., Flores, H., Lilly, S. J., et al. 1997, *ApJ*, 481, 49
 Hammer, F., Gruel, N., Thuan, T. X., et al. 2001, *ApJ*, 550, 570
 Hammer, F., Flores, H., Elbaz, D., et al. 2005, *A&A*, 430, 115
 Hammer, F., Puech, M., Chemin, L., Flores, H., & Lehnert, M. 2007, *ApJ*, 662, 322
 Hogg, D. W. 1999 [arXiv:astro-ph/9905116]
 Kannappan, S. J., & Barton, E. J. 2004, *AJ*, 127, 2694
 Kassin, S. A., Weiner, B. J., Faber, S. M., et al. 2007, *ApJ*, 660, 35
 Keres, D., Katz, N., Weinberg, D. H., & Davé, R. 2005, *MNRAS*, 363, 2
 Kroupa, P. 2001, *MNRAS*, 322, 231
 Liang, Y. C., Hammer, F., & Flores, H. 2006, *A&A*, 447, 113
 Maraston, C. 1998, *MNRAS*, 300, 872
 Maraston, C. 2005, *MNRAS*, 362, 799
 Maraston, C., Daddi, E., Renzini, A., et al. 2006, *ApJ*, 652, 85
 Mason, E., Kaufer, A., & Hainaut, O. 2007, *ISAAC Instrument data reduction cookbook*
 McLaugh, S. S. 2005, *ApJ*, 632, 859
 Mo, H. J., Mao, S., & White, D. M. 1998, *MNRAS*, 295, 319
 Neichel, B., et al. 2008, *A&A*, submitted
 Noordermeer, E., & Verheijen, M. A. W. 2007, *MNRAS*, accepted [arXiv:0708.2822]
 Okamoto, T., Eke, V. R., Frenk, C. S., & Jenkins, A. 2005, *MNRAS*, 363, 1299
 Persic, M., & Salucci, P. 1991, *ApJ*, 368, 60
 Persson, S. E., Murphy, D. C., Krzemiński, W., et al. 1998, *AJ*, 116, 2475
 Pizagno, J., Prada, F., Weinberg, D. H., et al. 2007, *AJ*, 134, 945
 Portinari, L., & Sommer-Larsen, J. 2007, *MNRAS*, 375, 913
 Press, W. H. 2002, *Numerical recipes in C++: the art of scientific computing* (Cambridge University Press)
 Puech, M., Flores, H., Hammer, F., & Lehnert, M. D. 2006a, *A&A*, 455, 131
 Puech, M., Hammer, F., Flores, H., Östlin, G., & Marquart, T. 2006b, *A&A*, 455, 119
 Puech, M., Hammer, F., Lehnert, M. D., & Flores, H. 2007a, *A&A*, 466, 83
 Puech, M., Hammer, F., Flores, H., et al. 2007b, *A&A*, accepted [arXiv:0711.0611]
 Puech, M., Flores, H., Lehnert, M. D., et al. 2008, *MNRAS*, submitted
 Pozzetti, L., Bolzonella, M., Lamareille, F., et al. 2007, *A&A*, 474, 443
 Ravikumar, C. D., Puech, M., Flores, H., et al. 2007, *A&A*, 465, 1099
 Robertson, B., Bullock, J. S., Cox, T. J., et al. 2006, *ApJ*, 645, 986
 Russell, D. G. 2004, *ApJ*, 607, 241
 Saintonge, A., Masters, K. L., Marinoni, C., et al. 2007, *A&A*, submitted [arXiv:0710.0760]
 Salpeter, E. E. 1955, *ApJ*, 121, 161
 Simard, L., & Pritchet, C. J. 1998, *ApJ*, 505, 96
 Tully, R., & Fisher, J. 1977, *A&A*, 54, 661
 Tully, R., & Fouqué, P. 1985, *ApJS*, 58, 67
 Tully, R., Pierce, M. J., Huang, J., et al. 1998, *AJ*, 115, 2264
 van der Wel, A., Holden, B. P., Franx, M., et al. 2007, submitted [arXiv:0707.2787]
 van Dokkum, P. G. 2007, *ApJ*, submitted [arXiv:astro-ph/0710.0875]
 Verheijen, M. A. W. 2001, *ApJ*, 563, 694
 Vogt, N., Herter, T., Haynes, M. P., et al. 1993, *ApJ*, 415, 95
 Vogt, N., Forbes, D. A., Philips, A. C., et al. 1996, *ApJ*, 465, 15
 Vogt, N., Philips, A. C., Faber, S. M., et al. 1997, *ApJ*, 479, 121
 Weiner, B. J., Willmer, C. N. A., Faber, S. M., et al. 2006, *ApJ*, 653, 1027
 Yang, Y., Flores, H., Hammer, F., et al. 2007, *A&A*, accepted [arXiv:0711.2305]

Résumé

L'étude cinématique des galaxies locales et lointaines permet de contraindre les scénarios de formation et d'évolution des galaxies. Pour cela, la spectroscopie à champ intégral permet une étude détaillée de la cinématique des galaxies proches et fournit depuis peu des indices sur la cinématique des galaxies lointaines. Cette thèse s'appuie principalement sur l'utilisation de l'échantillon cinématique de galaxies locales GHASP. Cet échantillon de référence composé de 203 galaxies spirales et irrégulières de l'Univers local dans des environnements peu denses observées par interférométrie de Fabry-Perot autour de la raie H α (6563 Å) est le plus grand échantillon de données Fabry-Perot à ce jour. Après un passage en revue des principes de l'interférométrie Fabry-Perot et des nouveautés apportées à la réduction des données Fabry-Perot, mon implication dans le développement du 3D-NTT, nouvel instrument utilisant deux Fabry-Perot est exposée de même que ma participation au projet de spectrographe à grand champ pour les ELT, WFSpec, dont l'objectif est l'étude de l'évolution des galaxies. Je présente dans une deuxième partie les données GHASP. Cet échantillon a été entièrement réduit et analysé à l'aide de nouvelles méthodes. L'analyse cinématique de l'échantillon à partir des cartes cinématiques 2D a été initiée en particulier avec l'étude de la distribution des halos de matière sombre, de la forme des courbes de rotation, de l'influence des potentiels barrés et de la dispersion de vitesses du gaz ionisé. Dans une troisième partie, cet échantillon local sert de point de référence pour l'étude de la cinématique des galaxies lointaines. L'échantillon GHASP est projeté à grand décalage spectral ($z = 1.7$) afin de déterminer les biais observationnels liés au manque de résolution spatiale des données cinématiques de galaxies lointaines obtenues par SINFONI, OSIRIS et GIRAFFE. L'analyse cinématique de nouvelles observations SINFONI y est également présentée, et l'ensemble des données cinématiques 2D de la littérature est mis en regard avec les résultats obtenus sur l'échantillon GHASP, mettant en évidence une évolution du support dynamique des galaxies avec le temps.

Mots-clés : Astronomie – Astrophysique – Galaxies – Spirales et Irrégulières – Spectroscopie – Fabry-Perot – Cinématique – Dynamique – Univers Local – Grand Décalage Spectral

Abstract

Kinematical studies of low and high redshift galaxies enables to probe galaxy formation and evolution scenarios. Integral field spectroscopy is a powerful tool to study with accuracy nearby galaxies kinematics. Recent observations also gives a new 2D vision of high redshift galaxies kinematics. This work mostly relies on the kinematical sample of galaxies GHASP. This control sample, composed of 203 local spiral and irregular galaxies in low density environments observed with Fabry-Perot techniques in the H α line (6563 Å), is by now the largest sample of Fabry-Perot data. After a revue on Fabry-Perot interferometry and a presentation of new data reduction procedures, my implications on both 3D-NTT Fabry-Perot instrument and the wide field spectrograph project (WFSpec) for galaxy evolution study with the european ELT are developed. The second section is dedicated to GHASP data. This sample have been fully reduced and analysed using new methods. The kinematical analysis of 2D kinematical maps has been undertaken with the study of the dark matter distribution, the rotation curves shape, bar signatures and the ionized gas velocity dispersion. In a third section, this local reference sample is used as a zero point for high redshift galaxies kinematical studies. The GHASP sample is projected at high redshift ($z = 1.7$) in order to disentangle evolution effects from distance biases in high redshift galaxies kinematical data observed with SINFONI, OSIRIS and GIRAFFE. The kinematical analysis of new SINFONI high redshift observations is also presented and high redshift data found in the literature are compared with GHASP projected sample, suggesting some evolution of the galaxy dynamical support within the ages.

Keywords : Astronomy – Astrophysics – Galaxies – Spiral and Irregular – Spectroscopy – Fabry-Perot – Kinematics – Dynamics – Local Universe – High Redshift
